Surface Current Measurements in The Juan de Fuca Strait Using the SeaSonde HF Radar

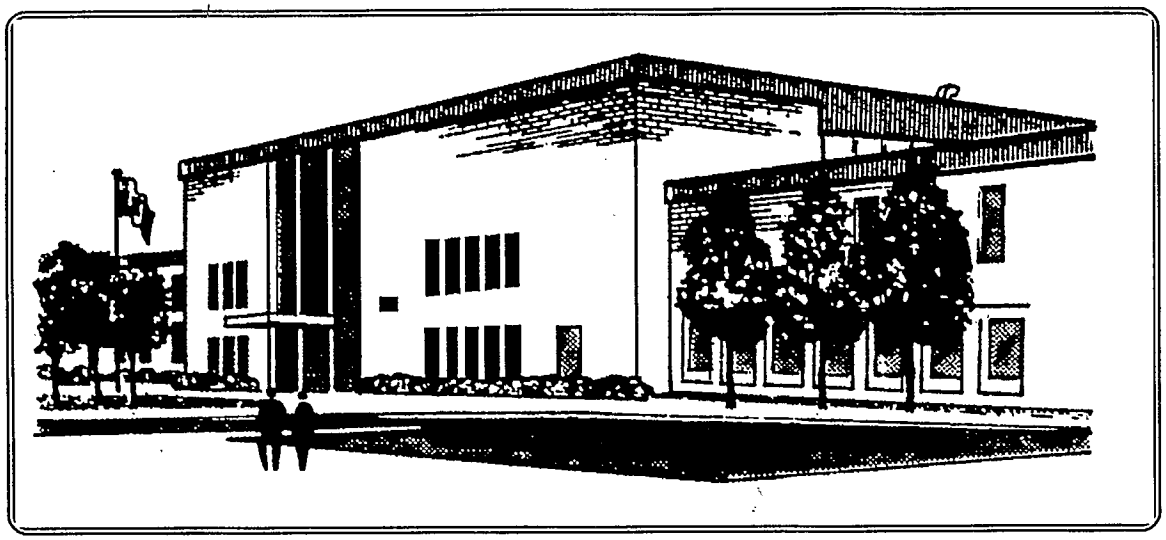

REPORT SERIES NO. **EE-149**

ENVIRONMENTAL TECHNOLOGY CENTRE
EMERGENCIES SCIENCE DIVISION

Environment Canada | Environnement Canada

Canada

Surface Current Measurements in Juan de Fuca Strait Using the SeaSonde HF Radar

by

Donald O. Hodgins
Seaconsult Marine Research Ltd.
8805 Osler Street
Vancouver, B.C.
V6P 4G1

Funding for this study was provided by the Canadian Coast Guard, Imperial Oil Resources Limited, NOAA/HAZMAT and the Emergencies Science Division of Environment Canada.

EE-149 **September, 1994**

EXECUTIVE SUMMARY

The SeaSonde 12.5 MHz HF radar system was deployed to measure surface currents in Juan de Fuca Strait for the month of July 1992. Two radars were installed, one located at the Race Rocks lightstation and one at the Ediz Hook U.S. Coast Guard base. In this configuration the radar baseline spanned the strait, providing coverage both to the east and west of the baseline. During the first few days of the month various tests were conducted on the radars, aimed at improving the siting for better antenna performance and remedying power interruptions at Race Rocks, as well as testing various data communication links. From July 8th to July 31st reliable data were obtained. Neither station had telephone line access, which precluded using direct modem transfer of data in real-time. Successful trials were conducted with the Infosat satellite link with a direct hook-up between the radar site Macintosh computer at Race Rocks and the central site PC computer in Vancouver, and this technology appears promising for remote operations. Cellular data transmission was attempted without success from Ediz Hook; however, opportunities to work on this data link were limited. Better communications software and some customization for the cellular network will overcome the difficulties encountered during these trials.

Data recovery from the SeaSonde was generally good, with maximum ranges varying from 15 km to over 30 km, at which point the radars became land-limited for this geographical area. Sea echo return strength at both radars was correlated with wind, consistent with lower Bragg scattering at lower wind speeds. Reduced Bragg scattering during flat calm conditions was the main reason for occasional reductions in range. A higher transmit frequency (20 to 30 MHz) is expected to give more consistent performance without a critical sacrifice in total range for protected waters such as Juan de Fuca Strait and the Strait of Georgia.

A simple surface current forecasting algorithm, based on decomposing the signal into tidal and residual bands, was examined. It was found that tides account for the greatest portion of the currents in this area, and could be forecasted out to 48 h with 1 to 2 days of input data. ARMA models of various orders were applied to the residual current band; however, the autocorrelation of residual currents was found to be weak in these data, and ARMA methods did not contribute substantially to the forecasted current. The non-predictable, fluctuating part of the current signal was isolated and its statistics were calculated. The algorithm tests showed that the SeaSonde data can be used to measure and predict the slowly-varying tidal and mean flow velocities, as well as the random part of the signal, both of which are important in oil spill modelling.

Surface flow patterns and time-series data from the SeaSonde measurements, and from a three-dimensional hydrodynamic model GF8 (Stronach, 1991) were compared from an oil spill modelling perspective. In general, the surface flow patterns from the model were smoother than observed; measured patterns contained considerable meandering structure, eddies and fronts, which were not reproduced by the model at fine scales. The differences were most noticeable in the cross-channel direction. The correlation of currents aligned with the EW orientation of the strait was good. The smoothness of modelled flows was attributed mainly to use of a uniform, constant horizontal eddy viscosity of 200 m^2/s. The radar data indicate that a flow-dependent eddy viscosity formulation, with coefficients calibrated to reproduce the features observed with the radar, would improve agreement and yield a good model for data assimilation. Combining modelling with radar data assimilation is expected to give better predictive capability than data alone, and affords the means to extend measured field spatially.

RÉSUMÉ

Le système radar HF SeaSonde de 12,5 MHz a été déployé pour mesurer les courants de surface dans le détroit Juan de Fuca au cours du mois de juillet 1992. Deux radars ont été installés, l'un au phare de Race Rocks et l'autre à la base Ediz Hook de la Garde côtière des États-Unis. Cette configuration faisait en sorte que la ligne de base du radar traverse le détroit et assurait une couverture vers l'est aussi bien que vers l'ouest de cette ligne. Durant les quelques premiers jours du mois, les radars ont été soumis à divers essais destinés à améliorer le positionnement pour une performance accrue de l'antenne, à remédier aux pannes de courant à Race Rocks et à vérifier diverses liaisons de transmission de données. Des données fiables ont été recueillies du 8 au 31 juillet. Ni l'une ni l'autre de ces stations n'était accessible par ligne téléphonique, ce qui empêchait le transfert direct par modem de données en temps réel. La liaison par satellite Infosat a été soumise à des essais par connexion directe entre l'ordinateur Macintosh du site radar de Race Rocks et l'ordinateur PC du site central à Vancouver; les résultats positifs de ces essais montrent que cette technologie semble prometteuse pour ce qui est de l'exploitation à distance. On a tenté, sans succès, la transmission cellulaire de données à partir d'Ediz Hook; toutefois les occasions de travailler à cette liaison de données ont été limitées. Un meilleur logiciel de communications et une certaine adaptation au réseau cellulaire permettront de surmonter les difficultés qui se sont présentées durant ces essais.

La récupération des données du SeaSonde s'est généralement révélée bonne, les distances maximales variant de 15 km à plus de 30 km, les radars devenant à ce point limités en terrain pour cette région géographique. On a établi la corrélation de l'intensité des échos de mer aux deux radars avec le vent, compte tenu de la diffusion de Bragg inférieure aux basses vitesses du vent. La diffusion de Bragg réduite par temps uniformément calme constituait la principale raison des réductions occasionnelles de distance. Une fréquence d'émission supérieure (20 à 30 MHz) devrait donner des performances plus uniformes, sans réduction importante de la distance totale dans les eaux protégées, comme celles du détroit Juan de Fuca et du détroit de Géorgie.

On a examiné un algorithme simple de prévision des courants de surface, fondé sur la décomposition du signal en bandes de marée et en bandes résiduelles. Il s'est avéré que les marées constituent la plus grande partie des courants dans cette région et qu'ils pourraient être prévus jusqu'à 48 heures à l'avance, avec des données d'entrée correspondant à 1 ou 2 jours. Des modèles ARMA de différents ordres ont été appliqués à la bande des courants résiduels, mais l'autocorrélation des courants résiduels s'est révélée faible pour ces données et les méthodes ARMA n'ont pas contribué substantiellement au courant prévu. La partie fluctuante non prévisible du signal de courant a été isolée, et ses statistiques ont été calculées. Les essais d'algorithme ont démontré que les données du SeaSonde peuvent servir à mesurer et à prévoir la vitesse des marées à variations lentes et leur écoulement moyen, ainsi que la partie aléatoire du signal, qui jouent toutes deux un rôle important dans la modélisation des déversements de pétrole.

Les structures de l'écoulement de surface et les données de série temporelle tirées des mesures du SeaSonde ainsi que d'un modèle hydrodynamique tridimensionnel GF8 (Stronach, 1991) ont été comparées dans la perspective de la modélisation des déversements de pétrole. En général, les structures de l'écoulement de surface tirées du modèle étaient plus uniformes que celles observées; les structures mesurées contenaient de nombreux méandres, remous et fronts que ne reproduisait pas le modèle aux échelles de grande précision. Les différences étaient particulièrement remarquables dans le sens transversal au cours d'eau. La corrélation des courants alignés par rapport à l'orientation est-ouest du détroit était bonne. La régularité des écoulements modélisés était attribuée principalement à l'utilisation d'une viscosité de remous horizontale uniforme et constante de 200 m^2/s. Les données radar indiquent qu'une formulation de viscosité des remous dépendant de l'écoulement, avec des coefficients réglés pour reproduire les caractéristiques observées par radar, améliorerait la correspondance et donnerait un bon modèle pour l'assimilation des données. La combinaison de la modélisation et de l'assimilation des données radar devrait procurer une capacité de prévision meilleure que celle des données seules et fournir les moyens d'étendre spatialement le champ mesuré.

TABLE OF CONTENTS

TABLE OF CONTENTS

LIST OF TABLES

LIST OF FIGURES

LIST OF FIGURES

LIST OF FIGURES

ACKNOWLEDGEMENTS

The surface current measurement program in Juan de Fuca Strait was jointly sponsored by Imperial Oil Resources Limited; Environment Canada, Emergency Sciences Division; the Canadian Coast Guard, Environmental Response Operations; and the United States National Oceanic and Atmospheric Administration, Hazardous Materials Response and Assessment Division. In addition, the Canadian Coast Guard, Pacific Region, provided generous logistics support with vessels and access to the lightstation at Race Rocks, and we extend our thanks to Colin Hendry and Capt. Cliff Crow for their cooperation. Similarly, we acknowledge the excellent support provided by the United States Coast Guard through access to facilities at the USCG Air Station in Port Angeles and thank Commander Larry Hall for his assistance. We also acknowledge the cooperation and support from the lightstation keepers at Race Rocks who kept an eye on the equipment and generally contributed to the success of the program. Infosat, from Vancouver, who supplied the satellite communications support, and Western Data Systems, Inc. in conjunction with ASA Consulting, Inc., who supplied and operated the RSI drifters, all contributed to the success of the experiment, and their support is gratefully acknowledged.

1.0 INTRODUCTION

SeaSonde is an integrated data acquisition and processing system for remotely mapping ocean surface currents, based on CODAR (Coastal Ocean Dynamics Applications Radar) principles. The system is comprised of two or more high-frequency (HF) radar units mounted on the shoreline separated by distances of 30 to 40 km. Each radar measures the radial component of surface current field, and the radial speeds from each site are combined to produce a map of the total surface current field.

HF radar principles for measuring surface currents are summarized in Hodgins (1991), Hardy et al. (1989), Leise (1984), and are described in detail for SeaSonde in Lipa and Barrick (1983). In the new instruments an FMCW (frequency-modulated continuous wave) signal format is used, centered at a frequency of 12.5 MHz. The radar design provides a theoretical range of just over 79 km resolved in 31 range cells. The sea echo spectra are averaged over one hour to provide stable estimates, and as a result the radars give a 1-h time average of the actual flow field. These parameters are fixed by the radar design and cannot be changed in the field.

The new SeaSonde HF radar system was first deployed in August of 1991 at the southern end of the Queen Charlotte Islands. Twenty-one days of hourly surface current maps were obtained over the open ocean. Although the radar was still under development at that time, the experiment was successful, and the remotely sensed currents were validated with both drifter and current meter data (Hodgins and Hardy, 1992; Hodgins, 1992). During that experiment all raw sea echo cross-spectra were logged for post-processing, and on-site data processing was confined to checking for correct radar operation.

By the spring of 1992, development work on the prototype SeaSonde was completed and the present demonstration project was launched in late June to collect surface current information in the more sheltered, but tidally-active waters of the Straits of Juan de Fuca and Georgia. Two radar units (Fig. 1.1) spanning the strait between Victoria and Port Angeles were deployed, and a series of tests with real-time data transmission to Seaconsult's office in Vancouver were carried out. The data collected over approximately a one-month period (July 1992) are presented and discussed in this report. In addition to the radar data collection program, four days of Orion buoy drifts were carried out, as well as deployment of a wood-chip slick to simulate oil-on-water motion during one of the drifter experiments. These drifts were targeted for the coverage area of the radars.

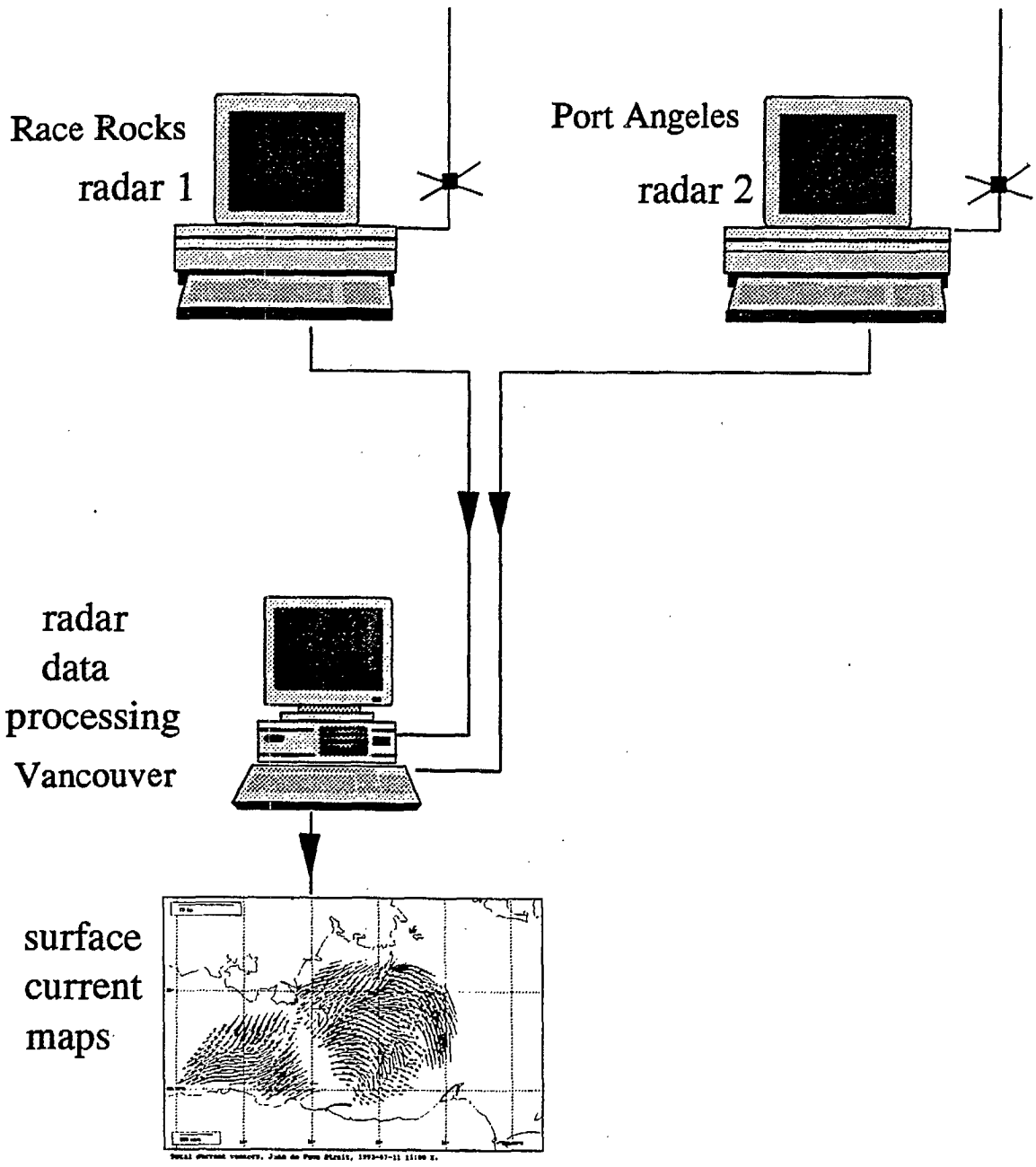

Figure 1.1 Schematic diagram of the SeaSonde experiment for Juan de Fuca Strait.

2.0 RADAR DEPLOYMENT

2.1 Siting and Operations

One remote site radar was deployed at the Race Rocks lightstation with a second radar unit situated on Ediz Spit, in Port Angeles, giving the combined coverage area illustrated in Fig. 2.1. Bathymetry contours are also plotted to show the bottom relief in this area. The dominant features in the coverage area are: (i) the ridge extending from Victoria, across the main axis of Juan de Fuca Strait to a point mid-way between Ediz Hook and Dungeness Spit, and (ii) the constriction in channel width at Race Rocks, essentially along the radar baseline. The photographs in Fig. 2.2 to 2.5 illustrate the instrumentation and installation. The radar sites were operational from June 29th until August 3rd.

The radar at Race Rocks was powered from the 110 V diesel generator that services the light and keeper's quarters. Between June 29th and July 8th data recovery at Race Rocks was intermittent, characterized by crashes of the data acquisition program which terminated all functions. During this early period, the radar was connected to a good-quality, un-interruptable power supply (UPS) designed to bridge power gaps while the diesel generators were serviced, and to smooth out power fluctuations. It was discovered that the UPS was too sensitive to voltage fluctuations in the 110 V supply, and was constantly drawing on its batteries to bridge apparent gaps. As a result the batteries were drawn down until they triggered a charge cycle; when this occurred the power was shut off to the radar eliminating all operation. This behaviour had not been encountered before although the same UPS units were used on previous deployments. Because a technician was required to re-start the program, data gaps arose between site visits.

After July 8th, the UPS was removed and most problems disappeared. We also gained the support of the lightkeeper, who checked on the Macintosh computer and eventually learned to re-start the program.

The availability of 110 V line supply at Port Angeles avoided all power problems, and the system operated without interruption except for a few instances when the mass storage devices were filled up and the system shut down awaiting re-initialization. However, examination of radial current plots in the first few days of deployment revealed an unexplained lack of coverage west of the baseline. Accordingly, on July 9th the receive and transmit antennas were re-positioned to give better direct coupling to the ocean, and to remove the receive antenna as far as possible from any pattern distortion caused by some large electrical wire reels stored near the site. The new antenna placement improved data recovery west of the baseline.

Key radar characteristics are summarized in Table 2.1.

2.2 Communications

At the inception of this experiment, the SeaSondes were configured for land-line communications using conventional modems between the remote site Macintosh computers and the central site Compaq computer. However, neither of the sites finally chosen had telephone access. Two different solutions for real-time data communications were attempted. Infosat, a Vancouver manufacturer of satellite voice/data communications equipment, agreed to participate in the demonstration, providing hardware at Race Rocks and communications

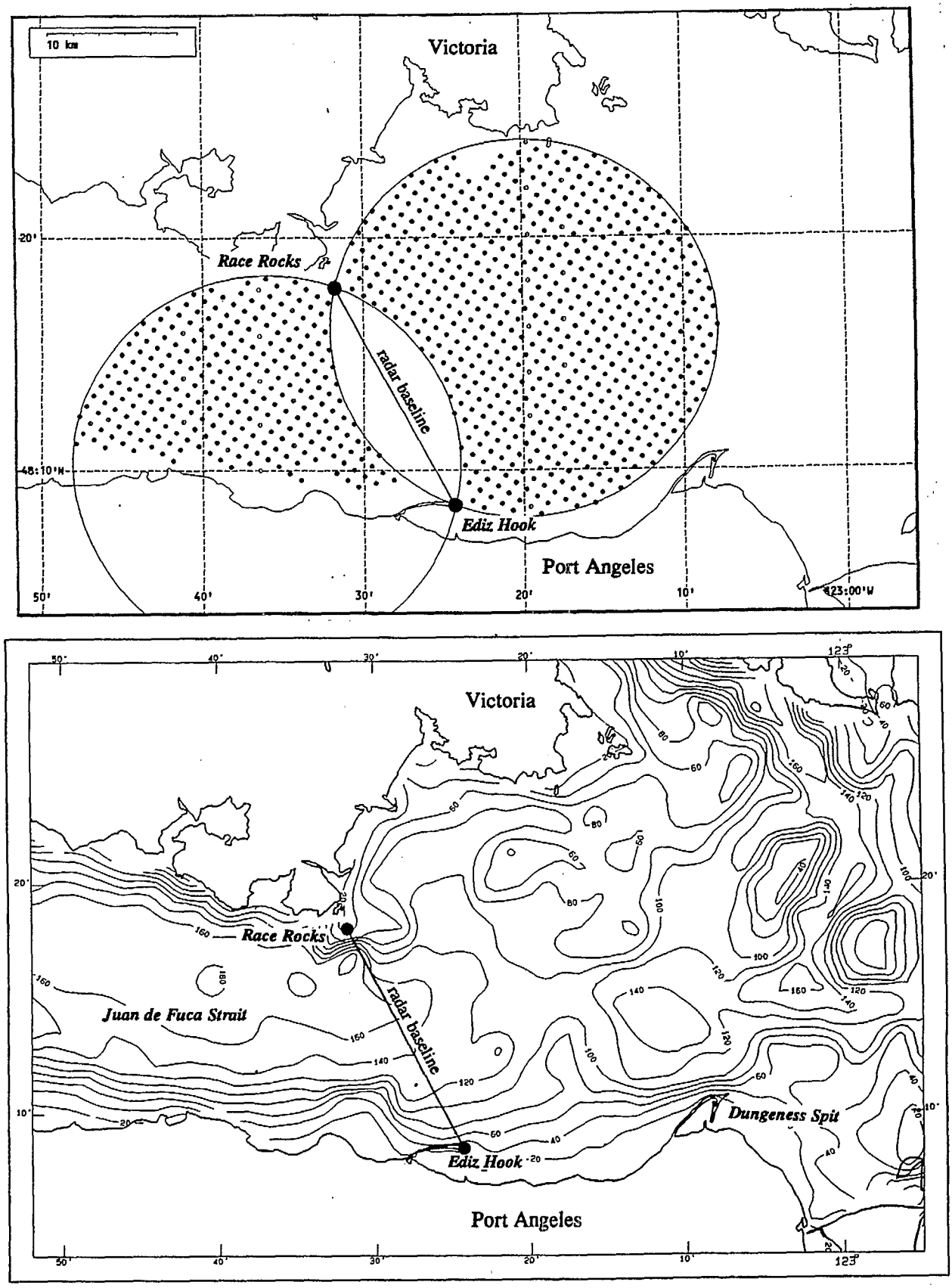

Figure 2.1 Site map of Juan de Fuca Strait showing the radar locations (●) and coverage area (upper panel). Bathymetry contour values in metres (lower panel).

Figure 2.2 View of Race Rocks (upper photograph) from the north. The SeaSonde hardware was installed in the light tower. The transmit and receive (lower photograph) antennas were deployed on the south side of the island.

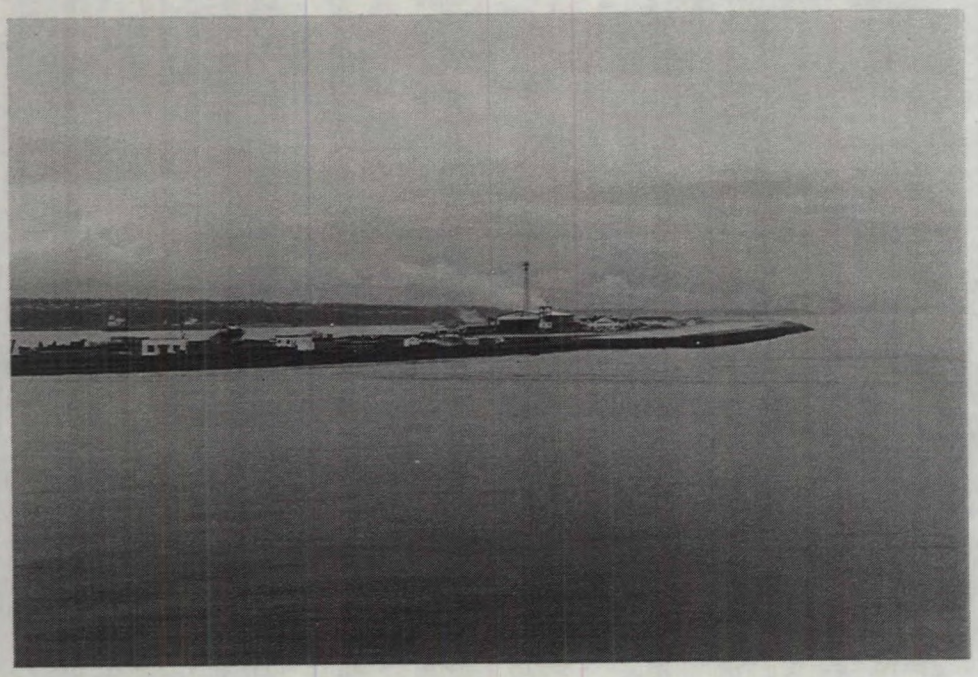

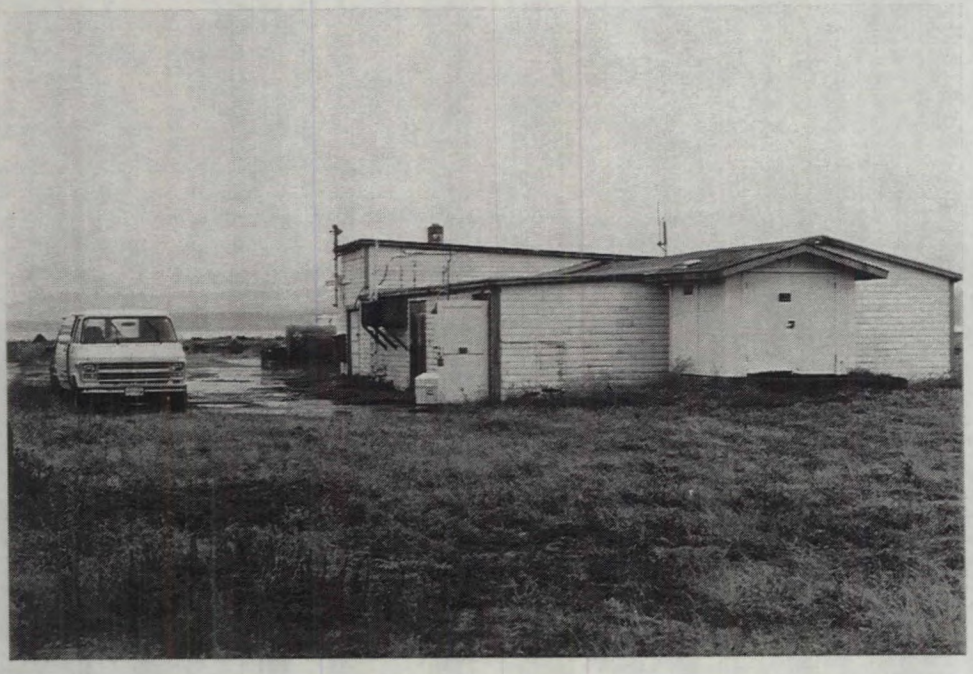

Figure 2.3 View of Port Angeles USCG airbase (upper photograph). The radar was installed at the end of the runway. The computer and RF equipment was located in the hut (lower photograph).

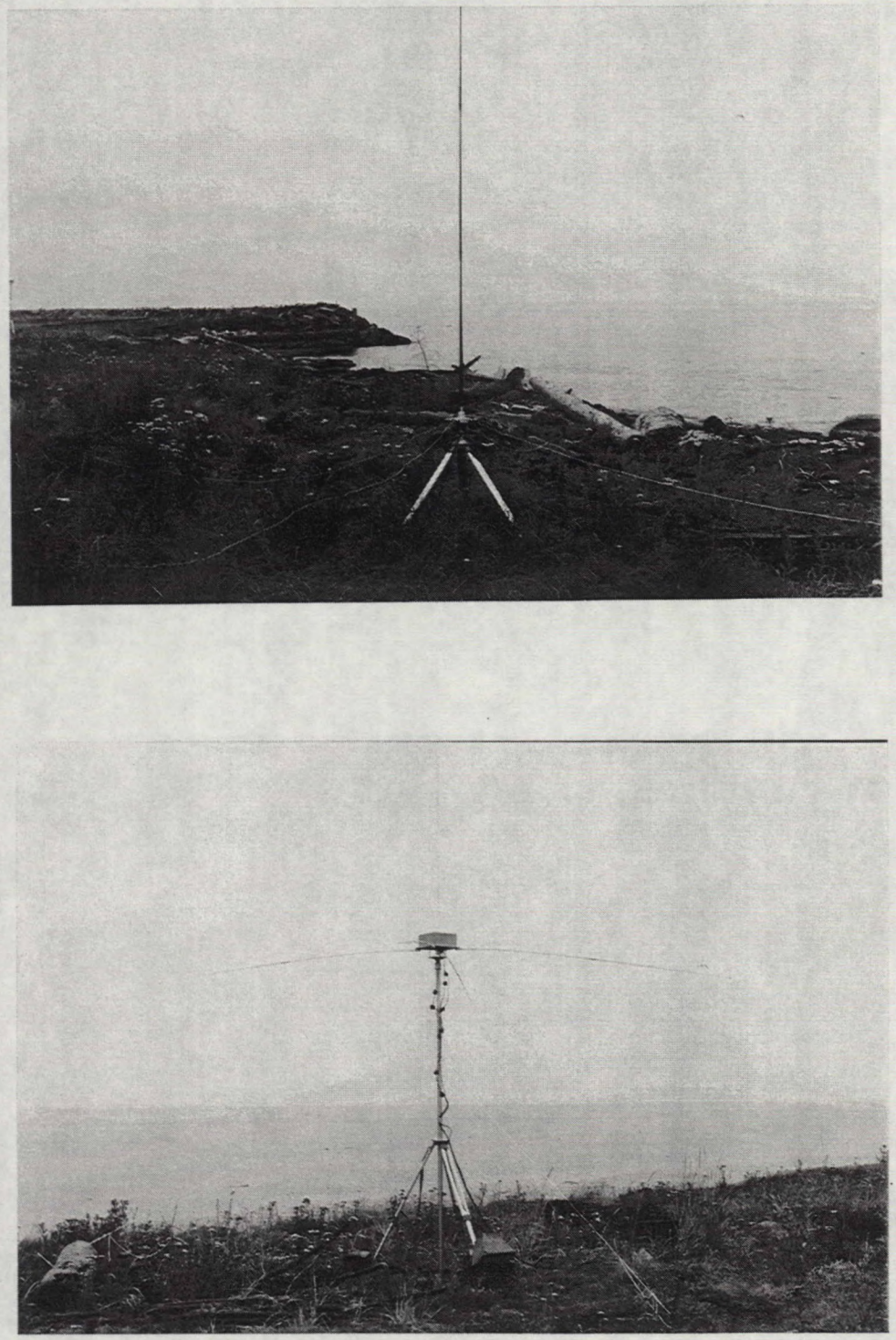

Figure 2.4 Transmit (upper panel) and receive (lower panel) antennas at Port Angeles in their first locations. The receive antenna was moved on July 9th to the end of the stone breakwater protecting the runway (see Fig. 2.3).

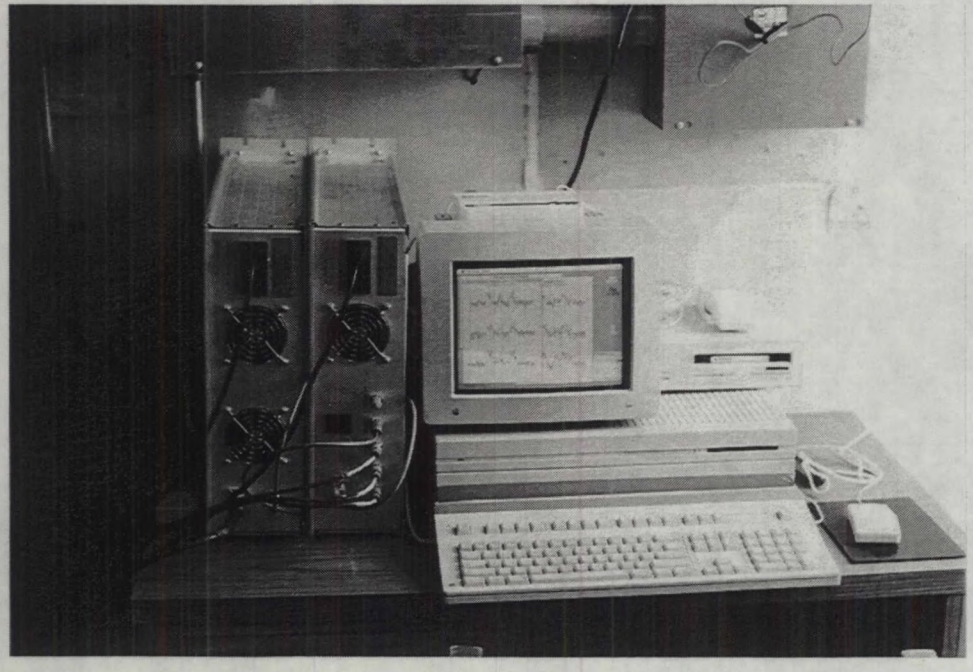

Figure 2.5 Examples of the equipment and screen displays at Port Angeles inside the hut.

Table 2.1

Characteristics of the SeaSonde Radars Deployed in Juan de Fuca Strait

Race Rocks Site 1	
Latitude	48° 17.89' N
Longitude	123° 31.77' W
Sampling interval	1 h
Transmit frequency	12.421875 MHz
Transmit power	< 100 W
Theoretical range	79.24 km
Range resolution	2.556 km
Radial velocity azimuth resolution	5°

Port Angeles Site 2	
Latitude	48° 08.50' N
Longitude	123° 24.28' W
Sampling interval	1 h
Transmit frequency	12.656250 MHz
Transmit power	< 100 W
Theoretical range	79.24 km
Range resolution	2.556 km
Radial velocity azimuth resolution	5°

support in Vancouver to which we connected the central site computer through a land-line modem. This system provided a direct satellite link between Race Rocks and Seaconsult's Vancouver office.

Different problems were encountered, but it appears that the modems, in conjunction with SeaSonde's Macintosh communications program, led to spurious characters that both rendered file transfer unreliable, and occasionally crashed the data acquisition program running on the Macintosh computer. On July 13th, the central site computer was connected directly to the satellite link at Infosat's Vancouver office, bypassing modems and telephone lines. Twenty-two files were successfully downloaded without difficulty. Consequently, our conclusion is that improved software to deal with extraneous characters introduced by the modems is required.

The second solution was to install a Motorola cellular data transceiver at Port Angeles supported by the USWEST Cellular network. USWEST has a repeater in Port Angeles providing excellent line-of-sight coverage to the radar site. Data were transferred over the cellular-land line link using standard data modems.

All tests conducted with the cellular transceiver were unsuccessful, but the number of tests was limited by the time and difficulty involved in travelling to Port Angeles to tend the remote site computer. Discussions with the cellular transceiver supplier suggest that this device will work with some re-programming and further tests are warranted.

The outcome of these tests indicates that data transfer over standard telephone land-lines using conventional modems, or a direct satellite link using equipment supplied by manufacturers such as Infosat, that bypasses any telephone-modem stage, will operate successfully. However, it appears that software to handle Macintosh-to-PC communications is not yet robust and can result in crashes of the radar during data acquisition. According to Motorola, the cellular data transceiver should work, but the difficulties encountered in this experiment are unresolved at present.

2.3 Data Recovery

The SeaSonde radar units produce two file types during regular operation: files of radial current vectors ranging in size from 10 to 16 Kbytes, and files containing the three Doppler cross-spectra that are 670 Kbytes each. The cross-spectral files are not normally saved; however, in this experiment these files were logged to provide the opportunity to post-process the data. This large quantity of data required servicing of the radar sites every 2 to 2.5 days using 44 MByte external cartridge drives for file storage. In mid-July, 240 MByte external hard disks were substituted to improve reliability, and to increase the servicing cycle to 6 to 8 days.

The data recovered are summarized in Fig. 2.6. As noted previously, the recovery was intermittent during early July as various operational problems were solved. On July 9th, the antennas at Port Angeles were re-positioned to the end of the breakwater, improving reception and data quality.

A gross measure of data recovery is given by the number of radial currents measured with each radar. In principle, given equally good siting and total aperture, both radar units should

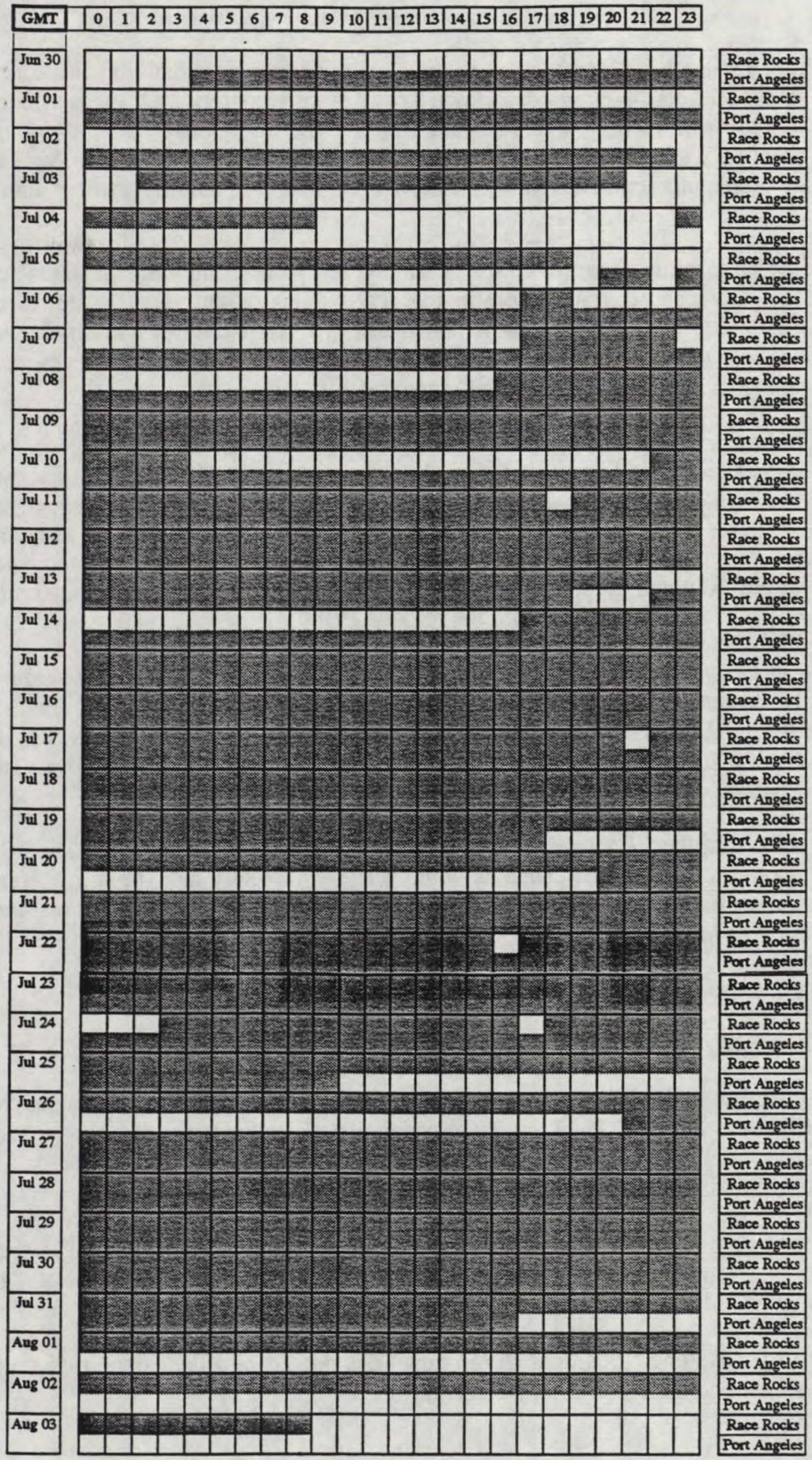

Figure 2.6 Summary of SeaSonde data recovery (shaded).

measure about equivalently in terms of range and density of derived radial current information. In this deployment the total view width at Race Rocks (approximately 270°) was wider than at Port Angeles (180°); however, antenna sheltering by the lighthouse and other structures reduced the effective width at Race Rocks to an average value closer to that at Port Angeles. As a result, the total radial current return at Race Rocks was only slightly greater than at Port Angeles.

This measure of data return is summarized in time-series format showing the radial count at each site versus wind speed at Race Rocks in Fig. 2.7. Radial count versus water level (tide) is plotted in Fig. 2.8. These figures show that the return was variable, and similar between sites. The latter observation indicates that factors external to the radars account for the variations, rather than a characteristic of one radar site.

The count data are correlated with the wind speed, which is logical, and reflects increased sea echo strength as resonant wind waves build with stronger winds. The variability shown here for Juan de Fuca Strait is slightly larger than has been experienced over the open ocean with other HF radars. This observation may be explained by the lower prevalence of resonant 12 m long waves in the strait compared with the open ocean. A higher operating frequency may decrease the variability noted here in radial returns by providing more constant range under all wind conditions.

As shown in Fig. 2.8, there is no apparent correlation of the radial returns with tidal phase. Although tidal currents are strong and highly modulated in this region, this result is also logical unless the tidal currents were modifying the wave field and thereby affecting the sea echo return. Such a modification is not expected; rather, the wave field will result from the local wind and will be closely coupled with the wind speed variations.

These results show that the 12.5 MHz radar is effective with moderate winds of 5 to 10 knots, but will suffer some loss in performance as winds abate completely and the sea becomes flat calm. Under calm conditions the range is decreased, as is the dual-radar coverage area over which total currents can be derived.

2.4 Surface Currents

2.4.1 Radial Velocity Extraction

Radial velocities were extracted from the sea echo spectra using the least-squares method described by Lipa and Barrick (1983). This procedure statistically tested the single and dual-angle models for radial currents and selected the one having the best fit to the data. The resulting hourly radial velocity fields consisted of a variable number of range cells, each separated by 2.557 km. Within each range cell, the data records were comprised of the speed, v, and corresponding direction indicated by the sign of the speed, a parameter, δv, expressing the uncertainty associated with the speed (see Lipa and Barrick, 1983), and an angular position, given at 5° intervals.

In principle, all over-water 5°-positions in the range cell should be filled if the radial speed is non-zero, but in practice there are always some gaps.

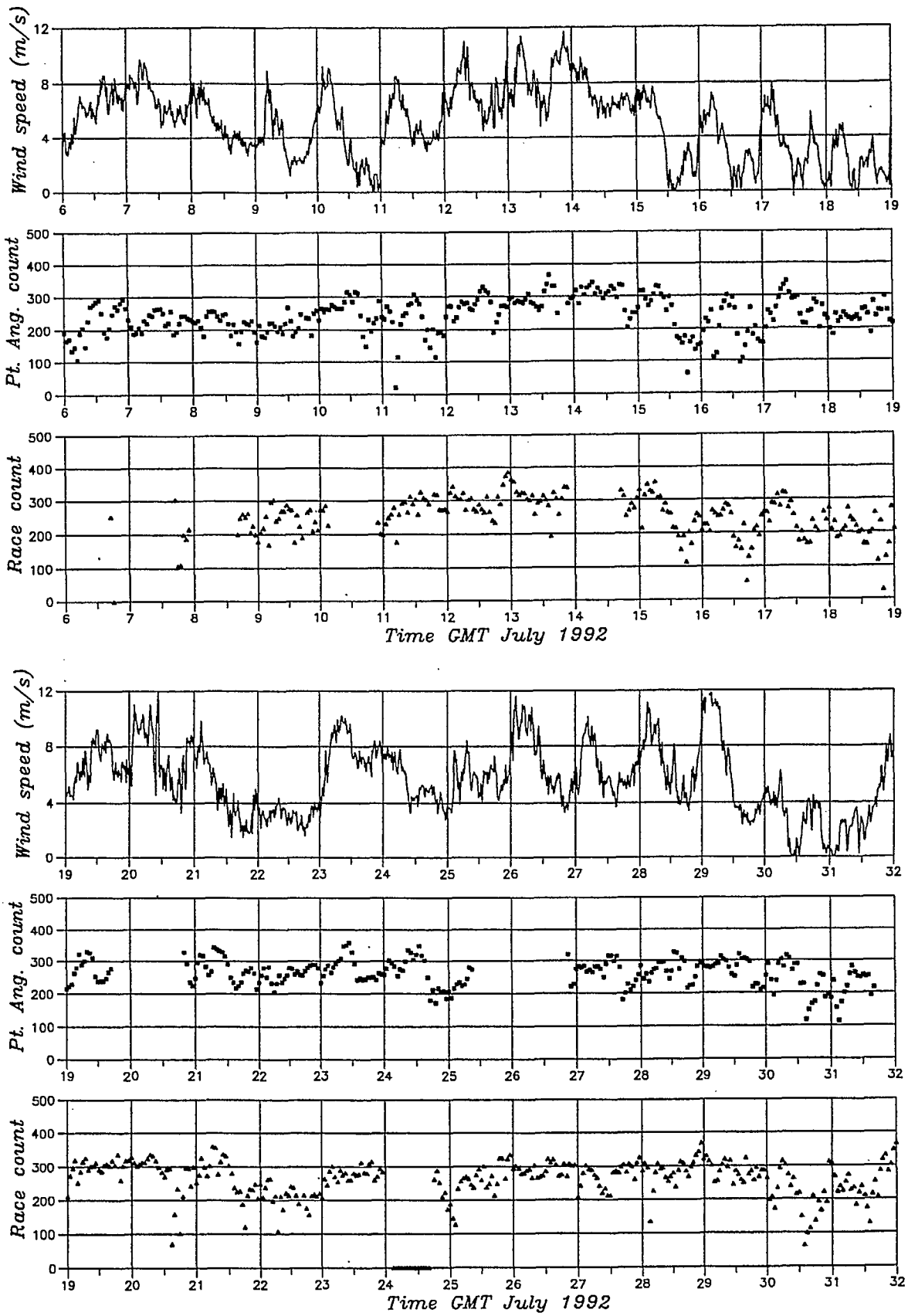

Figure 2.7 Time-series of wind speed measured at Race Rocks versus radial current count from each radar site.

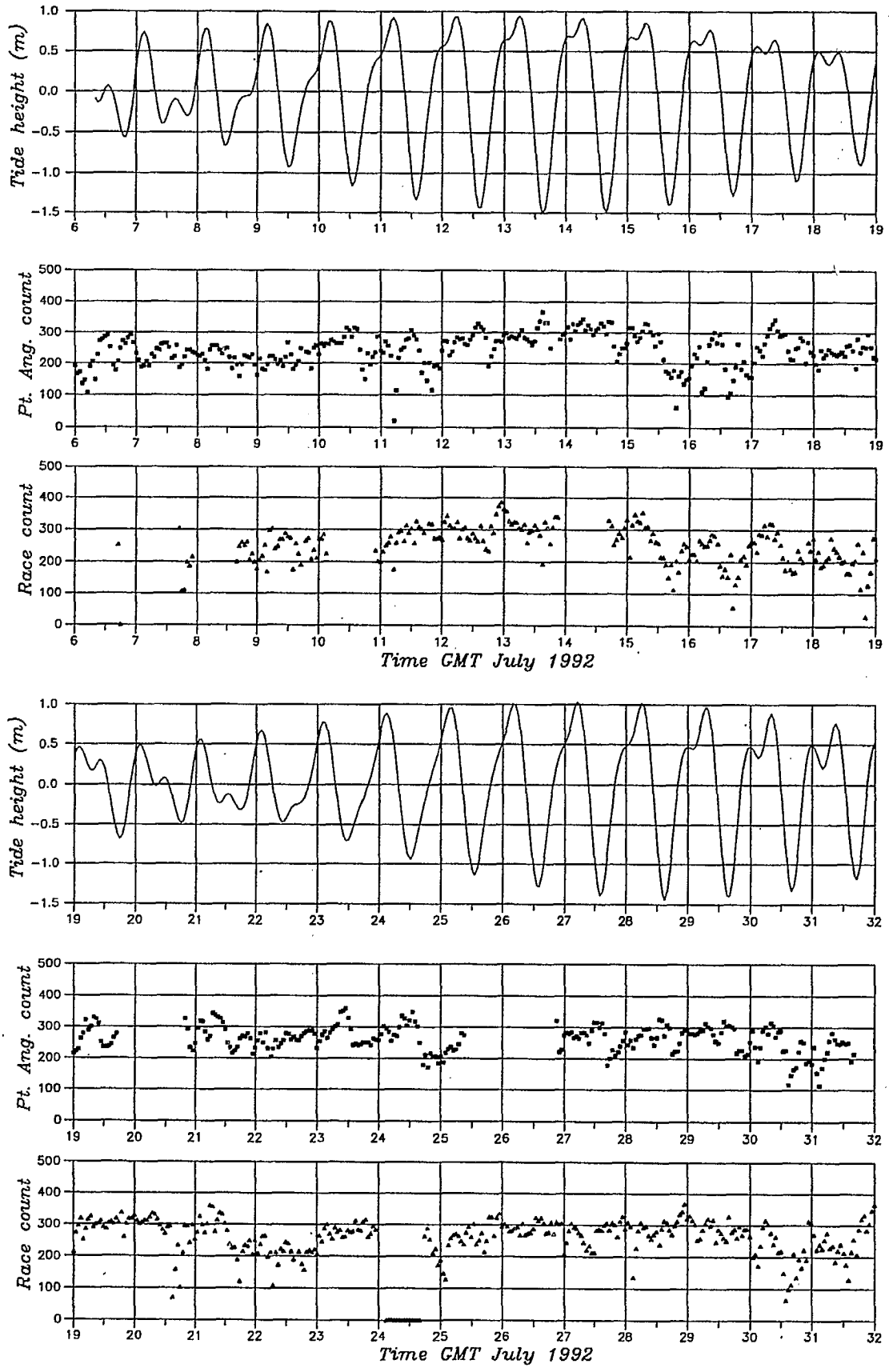

Figure 2.8 Time-series of tide height at Race Rocks versus radial current count from each radar site.

Inspection of the radial fields indicated a small percentage of questionable data, and some occasional, definite outliers. These fields also showed a tendency for systematic, small gaps along an axis bisecting the directions of the two cross-loop stick elements in the receive antenna. It was not clear whether such gaps arose because of the response characteristics of the antenna or because the radial current component was small in that part of the field. This characteristic was most noticeable at Port Angeles, for which the shore-normal flow in the gap area is small naturally.

In order to minimize gap occurrence, eliminate spurious data and give optimum coverage, all raw radar cross-spectral files were reprocessed following the field program. First, antenna phase information, used in calculation of radial currents, was estimated from the sea echo data (Lipa and Barrick, 1983) for each range ring, and compared over many hourly datasets to determine the optimum values for each receive antenna. At Port Angeles, the antenna phases were found to be stable in all cases and the standard processing software, which calculates the phase angles from the sea echo for each set of cross-spectra, was used without change to calculate the radial fields.

At Race Rocks, estimation of antenna phase was more complicated because one cross-stick element of the antenna was oriented such that it received sea echo return on both ends simultaneously. Although this condition violates an assumption in the phase extraction algorithm, experimentation with the cross-spectra showed that stable phases could be obtained from the software most of the time, and all Race Rocks spectra were reprocessed using constant phase angles, obtained from an average of many hourly measurements after discarding obvious outliers, to yield the final radial dataset.

Second, two thresholds were applied to remove questionable and bad data points. In order to set a limiting value for the uncertainty δv, bivariate distributions of the radial speed v versus δv were tabulated for the period July 11 to July 23, 1992. These distributions were heavily skewed toward smaller values of both v and δv, falling off to few occurrences of large δv. The frequency distributions of δv at the two radar sites are shown in Fig. 2.9, where the error bars correspond to $\pm$ one standard deviation of δv for all observations in the first 15 range rings. There are obvious outliers for which $\delta v > 100$ cm/s at each site, and a small percentage of values greater than 40 cm/s. Inspection of plotted radial maps did not revealed a systematic variation between δv and the consistency and magnitude of v in relation to neighbouring values. Consequently, no fixed threshold on δv, with which to filter out spurious values, could be identified, other than a relatively large value, greater than about 80 to 100 cm/s. In this study, $\delta v > 80$ cm/s has been used as the primary threshold to reject spurious radial estimates. This value represents less than 4% of the radial dataset.

A second threshold, using radial speed, was imposed for rejecting spurious data; i.e. $v \geq 250$ cm/s. This value exceeds the 1-hour averaged maximum current velocity that was expected anywhere within the coverage area of each radar. Using this threshold, only 0.12% of all data from both sites were eliminated.

Finally, gaps in the radial fields were filled by interpolation, using neighbouring points within the range ring. There is a trade-off in processing radial data to give combined total currents between interpolation at the level of radial currents versus averaging during the combining process. Inspection of both radial and total current fields in Juan de Fuca Strait showed high

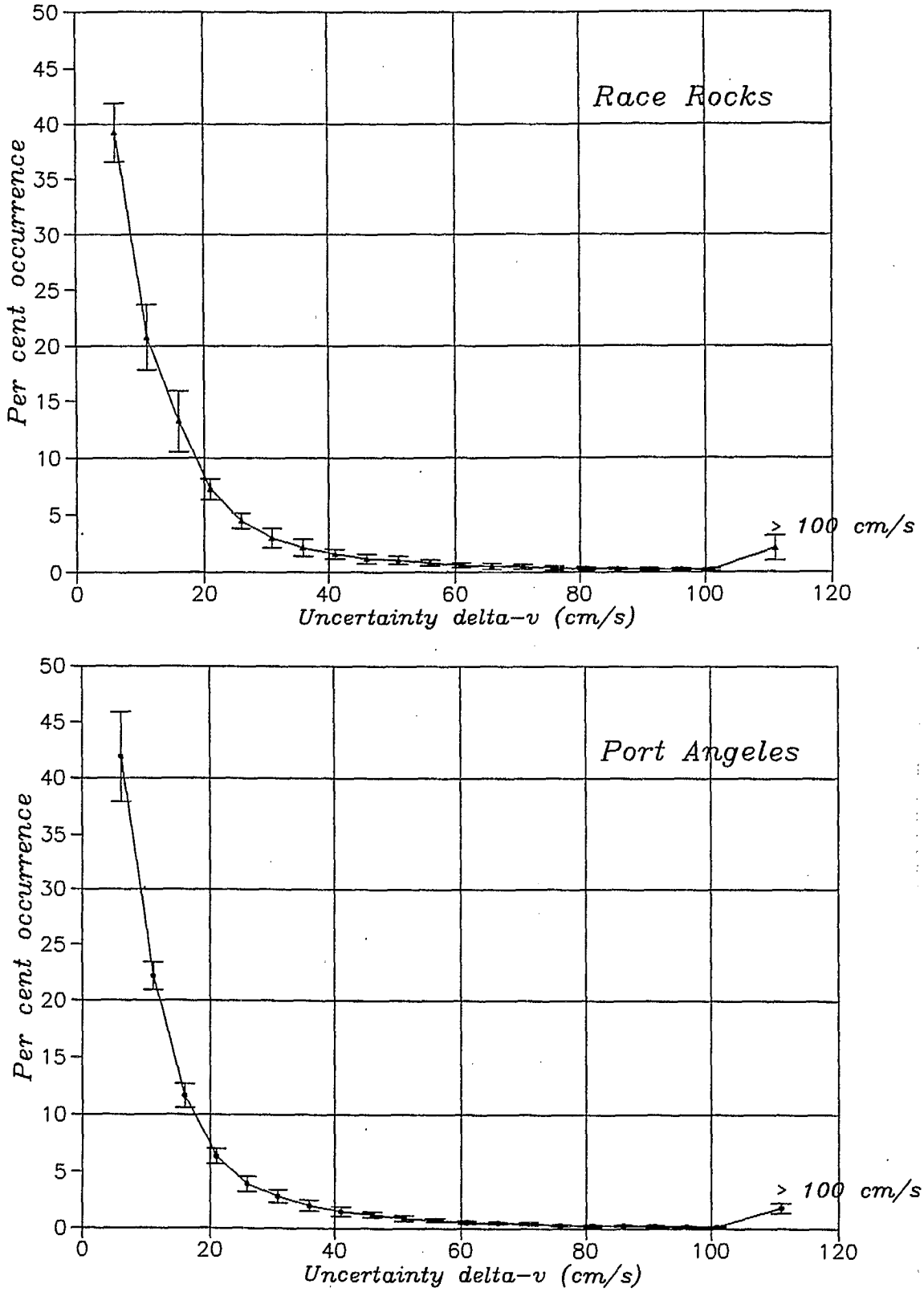

Figure 2.9 Per cent frequency of radial speed uncertainty δv for both radars. The error bars denote the variation with range ring for the first 15 ranges.

spatial variability, consistent with strongly sheared flows over irregular bathymetry and around shoreline features. In consequence, gross averaging of radials together, such as has been used in previous HF radar studies (Hodgins and Hardy, 1991; Leise, 1984) becomes increasingly inaccurate as the size of the averaging circle is increased. Given the scales of motion in Juan de Fuca Strait, more weight has been given in the present study to interpolating the radial currents to fill gaps than to averaging during the combining process. The interpolating function used was a one-dimensional spline under tension, with a tension factor of 10 (Anon., 1979), fitted to data within each view sector of the range ring. A view sector is an unbroken stretch of water within a single range cell, separated by land from other view sectors in the same range cell. The limiting gap width for interpolation was 10 km. No extrapolation beyond the range of data points was attempted.

The interpolated radial velocities were assigned an uncertainty equal to the average δv for the data used to calculate the interpolating spline function. Radial fields before and after thresholding and gap filling are shown in Fig. 2.10 for Race Rocks, and for Port Angeles in Fig. 2.11. These are examples of fairly gappy fields, slightly below average quality, and illustrate the strong speed variations that were found close to the radar units.

2.4.2 Calculation of Total Current Vectors

Synchronous radial data files were combined to yield total surface current on a Cartesian grid with a resolution of 1 km applied to the study area. The two-site coverage area was constrained by placing an upper bound on the triangulation angle between vectors from the two radar sites. This bound was defined by an error factor of $\epsilon=2$ (Leise, 1984) and corresponds to angles less than 138.6° between radials or greater than 41.4° between radials.

The radial information from each radar map required to form the total current at each grid point was found by linear interpolation using the four nearest neighbours. This procedure gives better accuracy for the total current near the radar units, and becomes nearly equivalent to the blending radius method (Hodgins and Hardy, 1992) when the Cartesian grid points are further away from both radar sites. The uncertainty of the final current vector was calculated by propagation of error from the speed and δv values of the radial data that enter the interpolation procedure.

An example of a combined current field is shown in Fig. 2.12. The complete set of current maps is contained in Appendix 1.

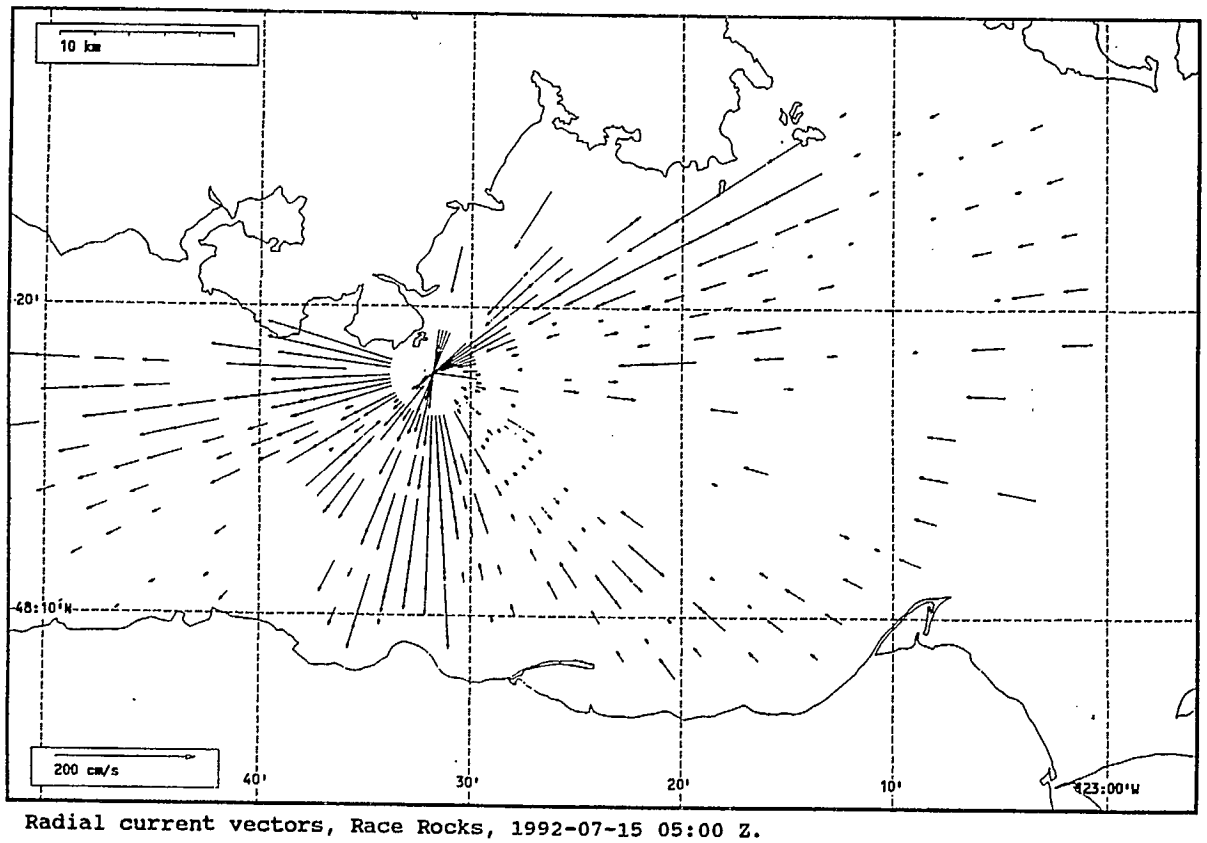

Radial current vectors, Race Rocks, 1992-07-15 05:00 Z.

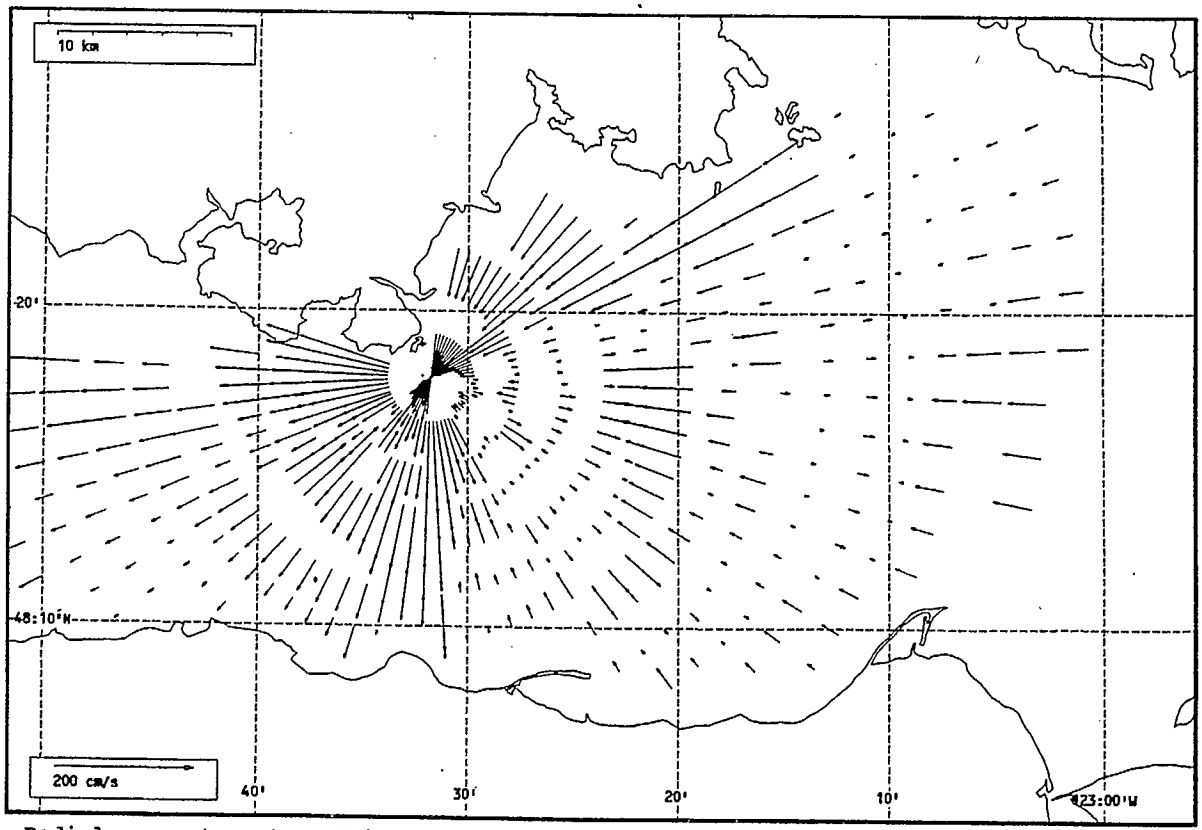

Radial current vectors (filled), Race Rocks, 1992-07-15 05:00 Z.

Figure 2.10 Example of radial current fields at Race Rocks before (upper panel) and after (lower panel) gap filling.

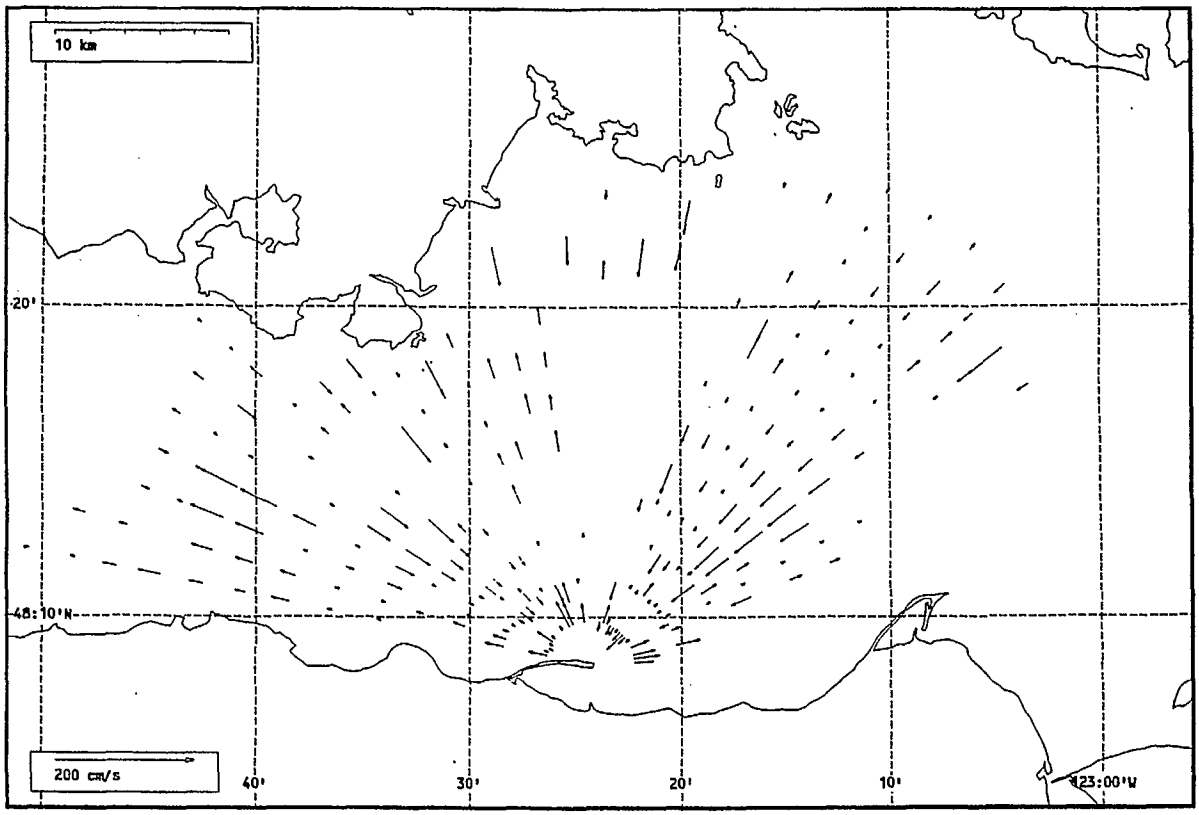

Radial current vectors, Port Angeles, 1992-07-11 04:00 Z.

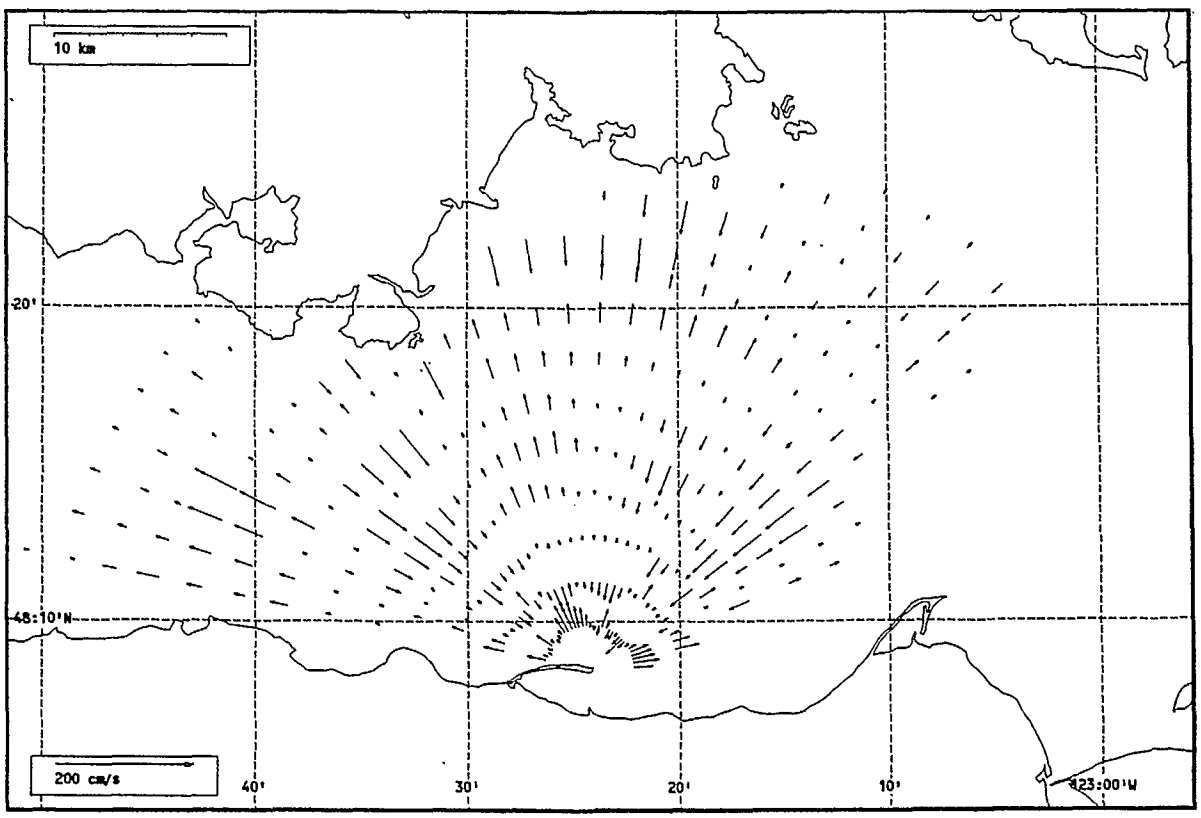

Radial current vectors (filled), Port Angeles, 1992-07-11 04:00 Z.

Figure 2.11 Example of radial current fields at Port Angeles before (upper panel) and after (lower panel) gap filling.

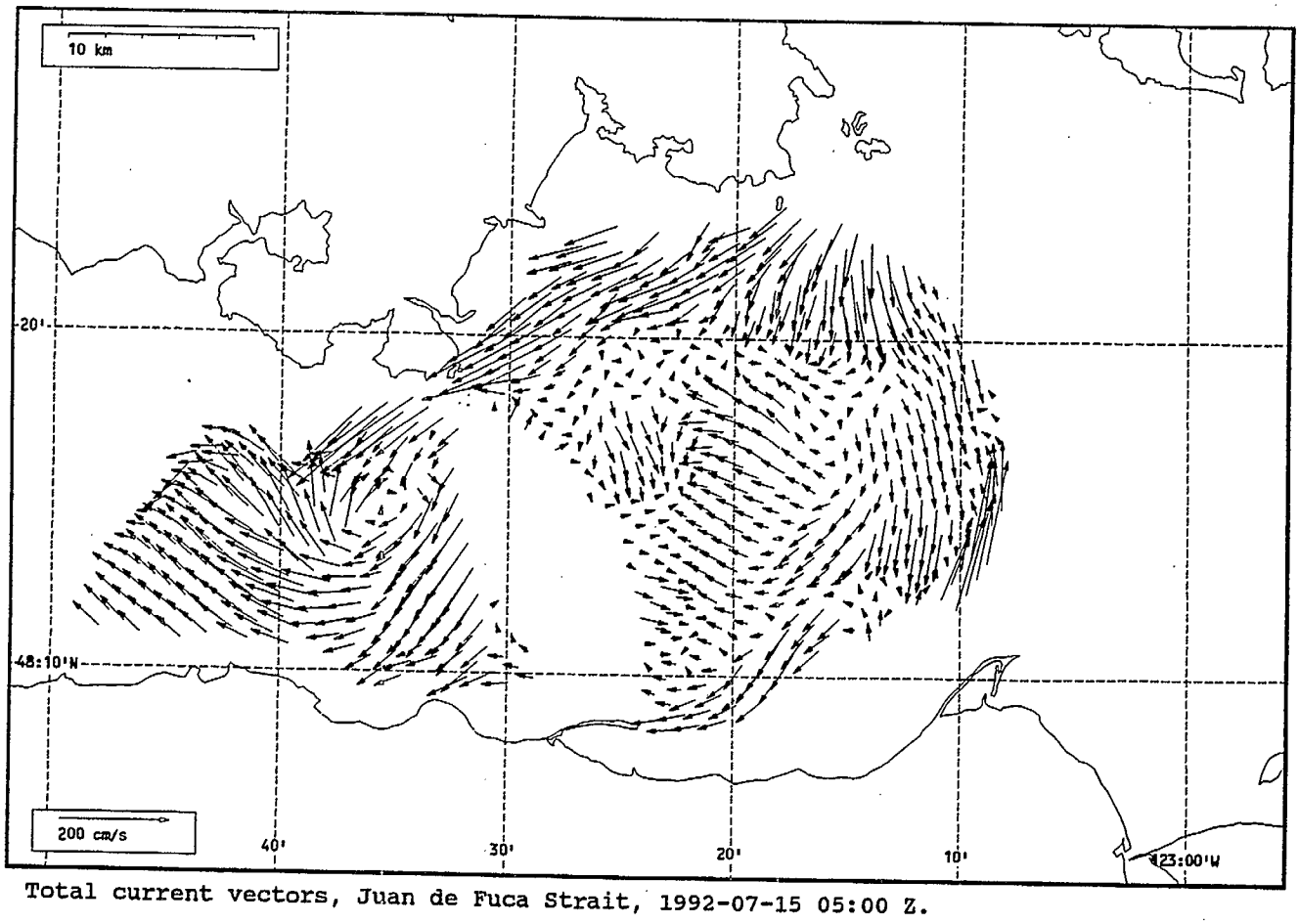

Total current vectors, Juan de Fuca Strait, 1992-07-15 05:00 Z.

Figure 2.12 Example of a surface current field calculated by combining radial current fields using a 4-point interpolation scheme.

3.0 CHIP-SLICK AND DRIFTER EXPERIMENT

3.1 Comparison of Slick and Drifters

On July 8, 1992 cedar chips were released in conjunction with four Orion buoys and one Oil Tracker GPS-positioned buoy, and a combined tracking experiment was carried out. The chips were deployed astern of the tracking vessel in 23 minutes, over an EW course. Green chips were laid first, to mark the initial position of the slick, and brown chips were used last to mark the tail of the slick. All positioning was done with non-differential GPS using the ship's system. Both chip and Orion positions were logged by hand and later entered into computer files. The Oil Tracker positions were logged directly to computer and made available by ASA Consulting Inc. The photographs in Fig. 3.1 illustrate the chip slick, and the two types of buoys. Winds at the time of the experiment were about 4 m/s from approximately 240° relative to true north, and held constant during the drift.

The experiment lasted roughly 3¼ hours, and positions were fixed approximately 30 to 40 minutes apart depending upon buoy separation. Chip and Orion buoy positions (as synchronous as possible) are plotted in the left-hand panel of Fig. 3.2, along with the green and brown chip locations. The Oil Tracker positions are plotted separately in the right-hand panel of Fig. 3.2. The motion of green chips (leading edge) is indicated by the solid line, while the motion of the brown chips is roughly illustrated by the dashed line. Observations from the boat revealed that the chip slick maintained a linear shape, which stretched during transport on the currents. Occasionally it was difficult to identify the brown chips uniquely with the tail of the slick, and these positions are less certain than the green chips which did delineate the leading edge well. Toward the end of tracking the slick had become quite diffuse, from both chip spreading and sinking, which reduced the density of chips at the surface.

The overall motion followed an elliptical path, spanning about 5,000 m NS and 3,000 m EW. The Orion buoys provided a close match with the chip motion throughout the experiment, and it is concluded that these buoys do follow the motion of material suspended in the upper few centimeters of the water column. The Orion buoys were largely unaffected by light winds in terms of differential movement with respect to the floating slick.

The Oil Tracker buoy followed the slick motion closely for the first 2 hours of drift, after which time positioning difficulties were encountered from a problem in the buoy electronics. Its position in Fig. 3.2, after 2 hours, lies outside the downwind edge of the slick. It appears that this buoy design was susceptible to greater wind-induced drift than the chips. It was recovered after 5 hours downwind of the chip position.

Figure 3.3 shows the displacement of the buoys from their original deployment positions, and that of the green chips for reference, as a function of elapsed time. These results also show how the Orion buoys conform to the chip motion, and indicate the trend to an increasing relative displacement of the Oil Tracker buoy.

3.2 Comparison of Drifter and SeaSonde Surface Currents

Orion buoy drifts were measured over four successive days, from July 6 to 9. The SeaSonde measurements on July 6 and 7 were intermittent as a result of shake-down problems at Race

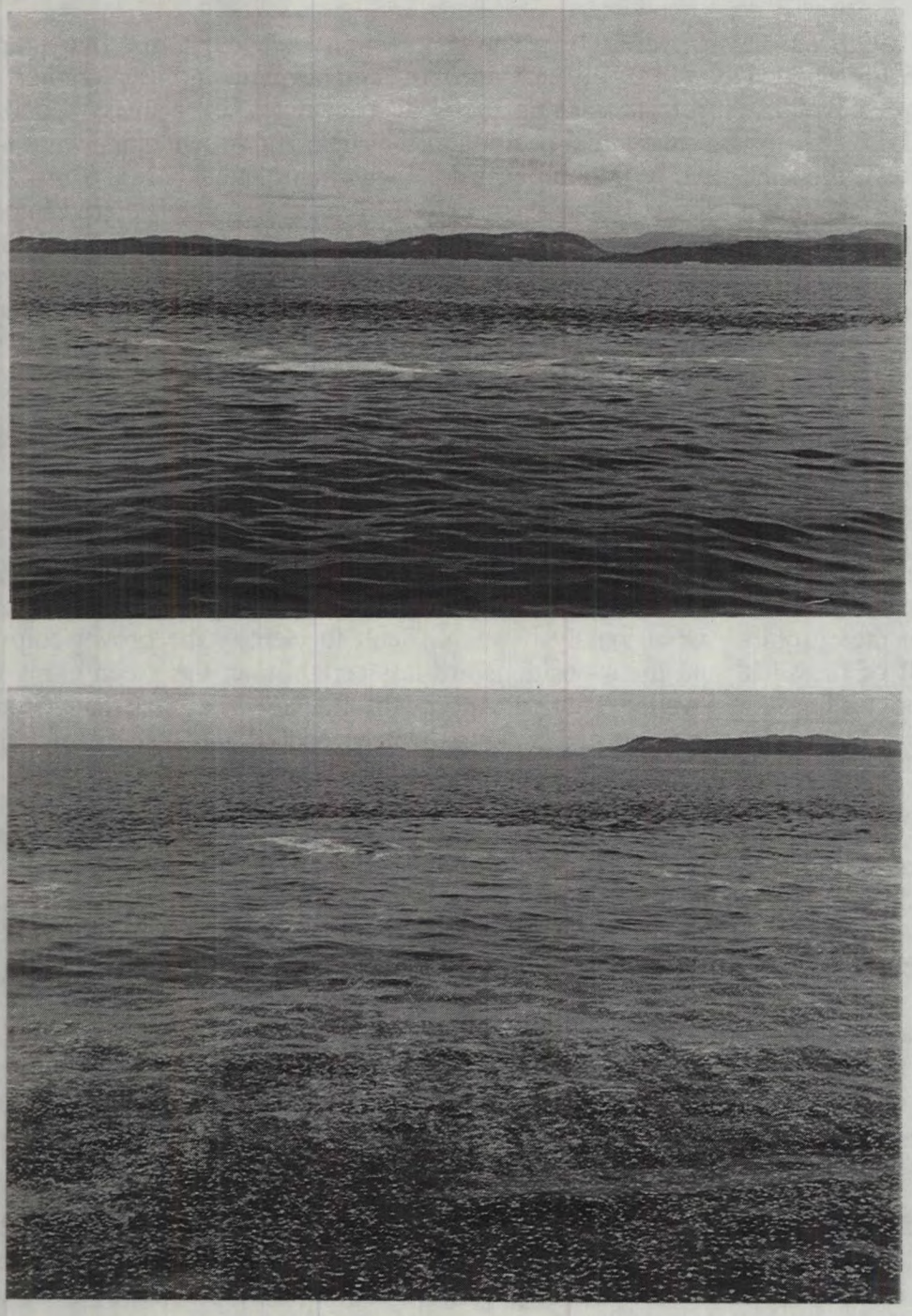

Figure 3.1 Chip slick near time of deployment, showing Orion buoys (upper panel), and later in a more wind-blown condition (lower panel) with the RSI buoy visible.

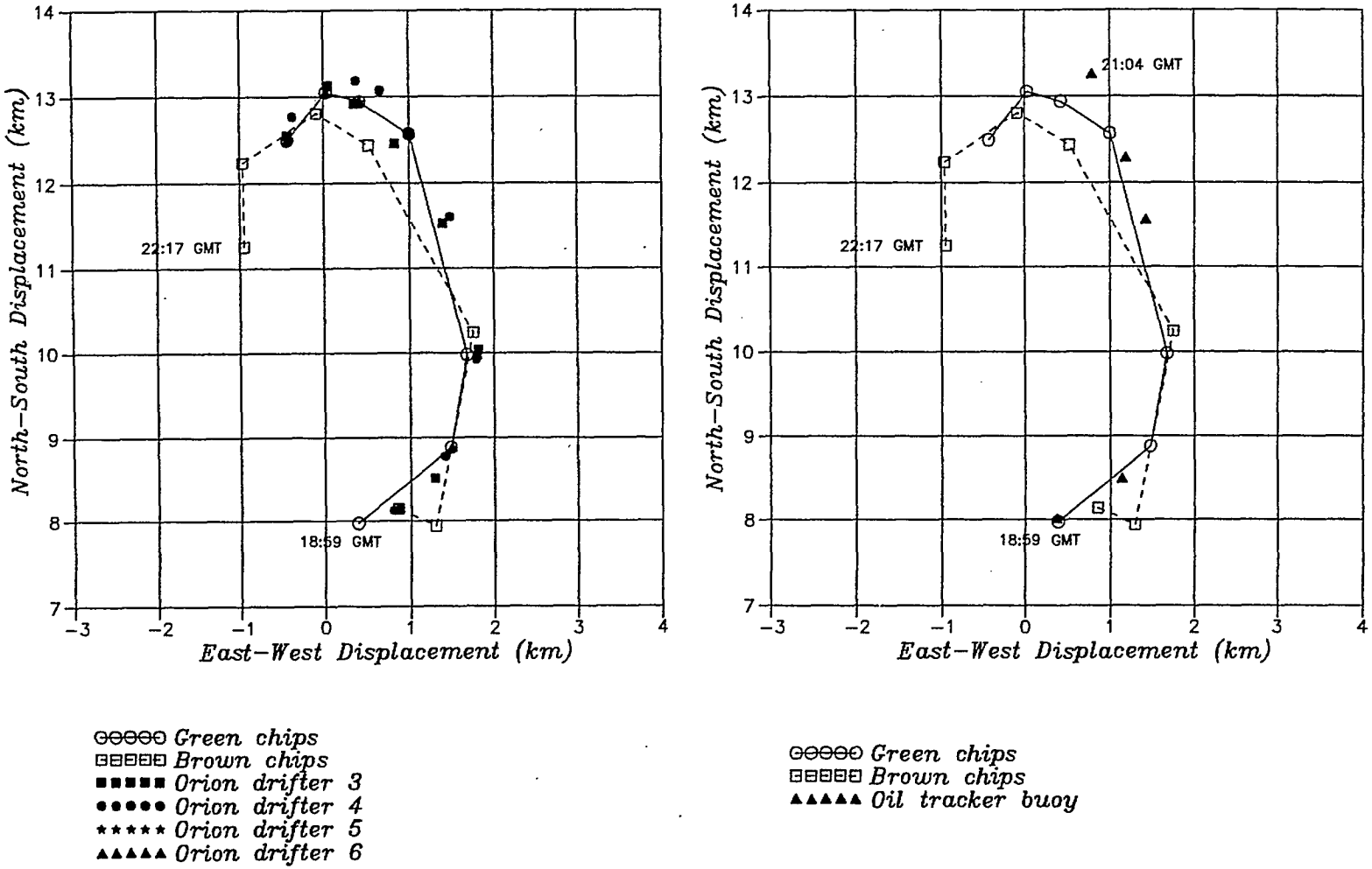

Figure 3.2 Graph showing the drift track of the chip slick and the Orion buoys (left-hand panel), and the chip slick and Oil Tracker buoy (right-hand panel), on July 8, 1992.

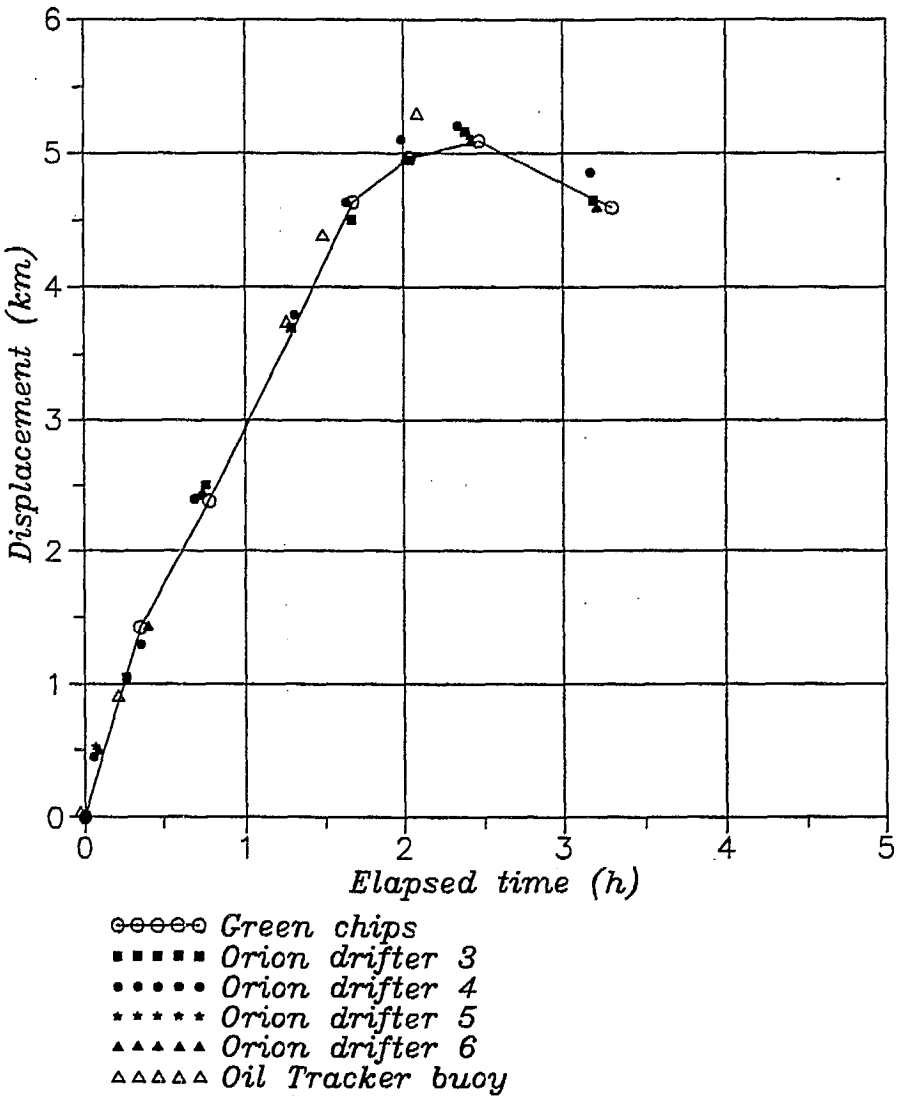

Figure 3.3 Total displacement of the chip slick and drifting buoys from their deployment positions versus elapsed time.

Rocks, and did not yield sufficient data for comparison with the Orion drifters. The situation improved on July 8 and 9, enabling limited comparison between the two datasets.

Given the short duration of each drift (2 to 3 hours), only point-estimates of the surface current were obtained by differencing the drifter positions and dividing by the elapsed time between fixes. The elapsed times typically ranged from 15 to 30 minutes. The positioning error has not been estimated, but with non-differential GPS and hand-logging to the nearest 1/100th of a degree, both the position and the speed errors are likely to be appreciable. Evidence of large error was found, for example, in the July 9th data for buoy 6 where consecutive speed values varied in the sequence 109, 396, 51, 306 cm/s while at the same time neighbouring buoys drifted steadily at about 100 cm/s.

For each point-estimate from the drifter, a radar-derived current for the mid-point location and same time has been calculated using bilinear interpolation of the Cartesian gridded currents. The total vector speeds are compared in Fig. 3.4. This graph shows that most drifter speeds exceeded the radar measurements, although occasionally the agreement was good. Examination of the components indicated that the difference was largely in the radar-measured NS component, which was consistently lower than the drifter data. The tendency for the drifter speeds to exceed those from the radar is consistent with anticipated higher speeds in the uppermost few centimetres of the water column under the light winds prevailing during these experiments, and the 1-hour averaging time of the radar.

The higher drifter speeds, and the more northeasterly set to the drift, may also reflect the influence of small scale surface flow features (eddies or meanders) that were poorly resolved by the radar during those two days. The interpolation scheme applied to the radial maps would have the tendency to smooth small-scale features, and yield lower flow speeds than obtained from the drifters.

It is not possible to resolve the differences and isolate the reasons with available data. However, the comparisons suggest that there are differences between the surface flow and the current field measured with the radar that would affect oil slick motion. Improvements in temporal and spatial resolution in the radar data will decrease these differences, and give a more accurate flow field. The influence of small-scale flow features is discussed further in later chapters.

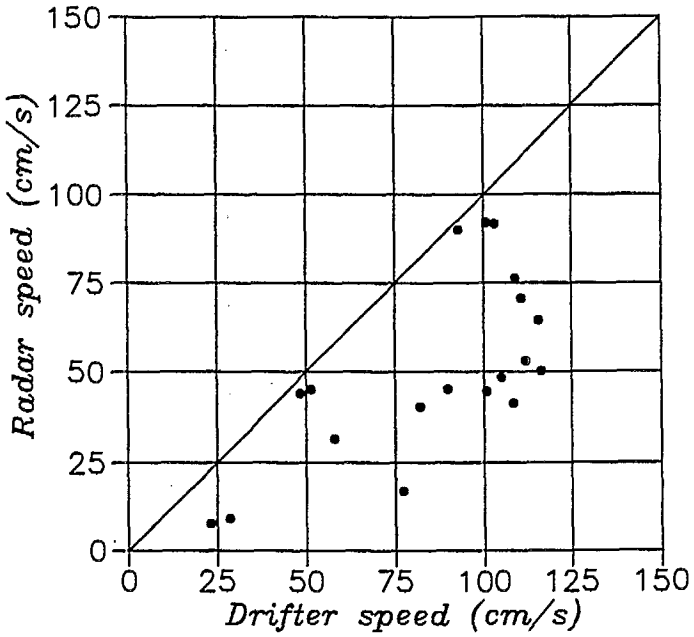

Figure 3.4 Comparison of total drifter current speed versus the radar-measured speed for drifts on July 8 and 9, 1992.

4.0 CURRENT PREDICTION FOR OIL SPILL MODELLING

4.1 A Simple Model

In order to utilize the radar data for real-time spill prediction, algorithms are required to forecast surface flows for lead times out to about 48 hours. Such algorithms could be based on measurements alone, on assimilation of observations into numerical hydrodynamic models, or a combination of these two approaches. In this section, a purely measurement-based algorithm is discussed. This approach is about the simplest that one could take to obtain an estimate of future flow conditions, incorporating the most recent history.

In most coastal areas surface currents result from a combination of tidal, buoyancy and wind-induced forces that occur over a range of frequencies from a few cycles per hour, to less than one cycle every few weeks. The tidal current component is deterministic and can be isolated in the total signal by harmonic analysis. The other components are less amenable to analysis and prediction.

The simple model examined here is based upon harmonic decomposition of the measured signal into its tidal and residual components, modelling each band separately to forecast 48 hours into the future, and recombining the components to give the total current. The residual component has not been further broken down into a low-frequency portion and a wind-driven current, although this is possible in practice if the wind data are available in both measured and forecast periods. Winds in Juan de Fuca Strait during the experiment showed a roughly diurnal cycle consistent with summer katabatic forcing, which is assumed to be modelled adequately in the treatment of the residual.

4.1.1 Analysis of the Tidal Current

The algorithm was applied with SeaSonde data in time-series of u(t) and v(t) at each grid point, in which data gaps were zero-filled. The tidal analysis method is described in Godin (1972) and Foreman (1978), and provided an estimate of the tidal signal $u_{tid}(t)$ and $v_{tid}(t)$ in terms of harmonics of tidal forces.

The accuracy of harmonically detiding the signal depends mainly upon the record length, which governs the number of constituents that can be resolved. The list in Table 4.1 shows the recovery of the major constituents as a function of the input record length in hours and days. The most important constituents are the semidiurnal M_2 and diurnal K_1 factors, which account for most of the tidal variance and which can be estimated with one day of data. Separation of the O_1 and K_1 diurnal components, and the S_2 and M_2 semi-diurnal constituents, is achieved with 15 days of input data.

Separation of the constituents becomes important for forecasts longer than 2 to 3 days since, after this time span, the fortnightly modulation will begin to noticeably affect the predictions. For short forecasts, based on input record lengths of 2 to 10 days, most of the semidiurnal and diurnal energy will be contained in the two extracted constituents, and the predicted tidal currents will agree well with the actual tidal flow.

Time-series of surface current have been extracted from the SeaSonde data set at point 1 in the centre of the coverage area, as shown in Fig. 4.1, and harmonically analyzed to give the tidal

Table 4.1

Extraction of Tidal Constituents for Various Record Lengths

Record Length (hours)	Record Length (days)	Period (hours)	Constituent	Magnitude (per cent M_2)
13	0.54	12.42	M_2	100
24	1.00	23.93	K_1	58.4
328	13.66	25.82	O_1	41.5
355	14.79	12.00	S_2	46.6
355	14.79	7.99	SK_3	< 10
662	27.58	22.31	OO_1	1.8
662	27.58	26.87	Q_1	8.0
662	27.58	24.83	NO_1	3.3
662	27.58	23.09	J_1	3.3
662	27.58	12.66	N_2	19.2

Source : LeBlond and Mysak, 1978. In practice, only those constituents of relative strength greater than 10 are of importance.

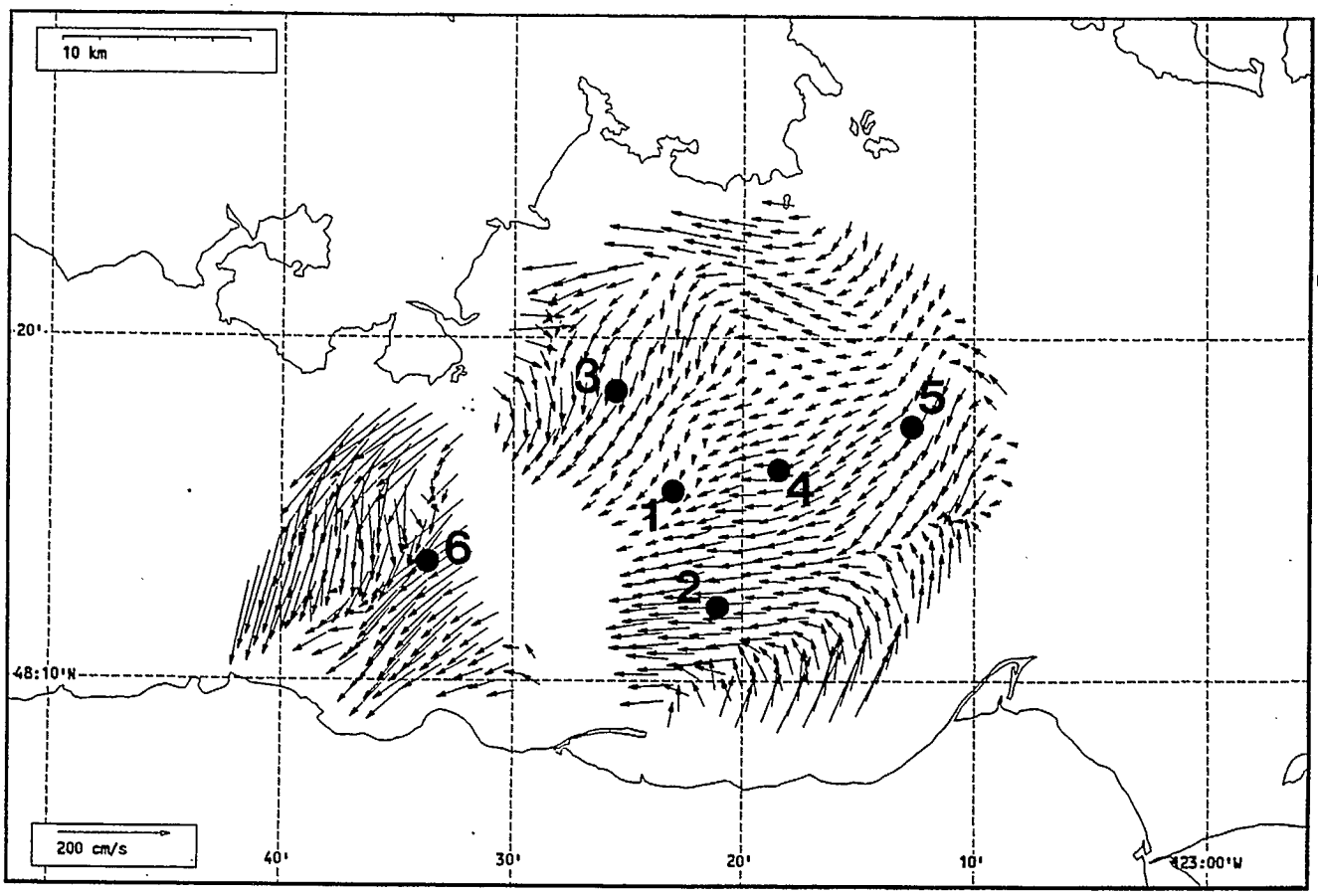

Total current vectors, Juan de Fuca Strait, 1992-07-18 09:00 Z.

Figure 4.1 Locations for time-series extraction.

portion of the signal. The tidal analysis was done for two input record lengths of 5 days and 21 days in order to examine the influence of discriminating the main diurnal and semidiurnal constitutents. The results for the 5-day analysis are shown in Fig. 4.2; it is clear that in this area, the tide accounts for the great majority of the signal, and that it is strongest in the east-west direction.

Figure 4.3 shows the measured signal versus the tidal components analyzed from the 21-day record (July 11-31). There is a closer correspondence between the tidal signal and the observed total current than obtained from the 5-day analysis, particularly during the last 18 hours of the prediction interval. The root-mean squared differences for the time-series in Fig. 4.2 and 4.3 are:

Tidal analysis	RMS-difference (cm/s)
5-day input series	u: 36.63 v: 18.55
21-day input series	u: 34.80 v: 16.36

These RMS differences express the amount by which the tidal signal deviates from the total measured current, and the longer input record for tidal analysis shows that the tide accounts for slightly more (6%) of the energy than is obtained from the shorter record. Although there is a small gain in overall accuracy from the longer time-series input, even a short record, giving the two main constituents, is able to model most of the observed variation in the currents.

4.1.2 Extrapolation of the Residual Current

The residual current is defined as:

$$u_{res} = u - u_{tid} \tag{4.1}$$

$$v_{res} = v - v_{tid} \tag{4.2}$$

dropping the time notation for clarity, and follows directly from the tidal analysis.

(a) The ARMA Model and an Example for an AR(2) Model

The time-series u_{res} and v_{res} were modelled as an autoregressive process of order m, denoted AR(m). This stochastic process is a special case of the class of models known as ARMA (autoregressive moving average). In the AR(m) model, z_t, the deviation from the mean at time t, is treated as being regressed on the m previous deviations z_t, z_{t-1}, z_{t-2}, z_{t-3}, ... z_{t-m} as follows:

$$z_t = \alpha_1 z_{t-1} + \alpha_2 z_{t-2} + \ldots + \alpha_m z_{t-m} + \epsilon_t \tag{4.3}$$

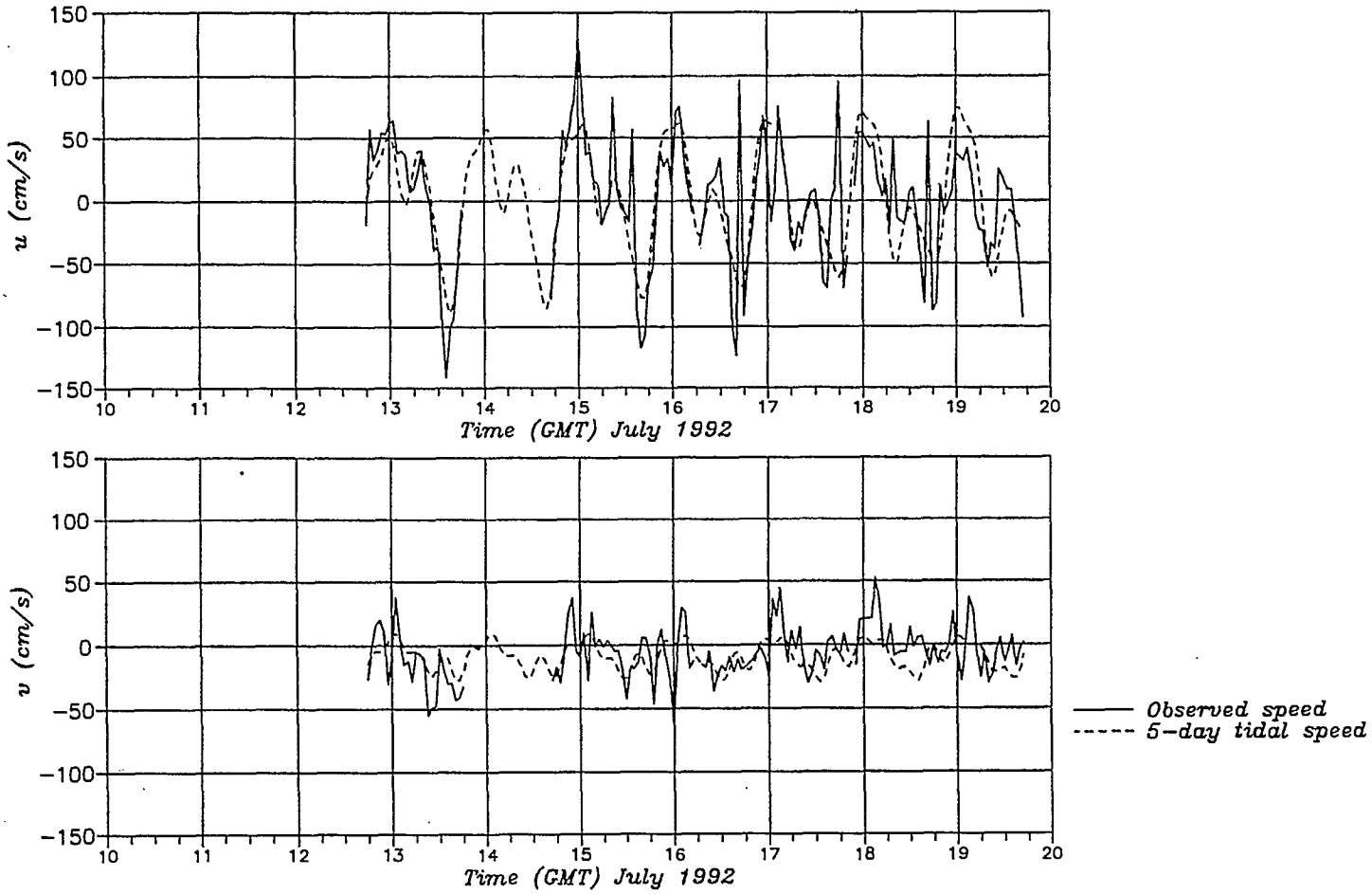

Figure 4.2 Comparison of the total current signal and the tidal signal based on a 5-day analysis for point 1.

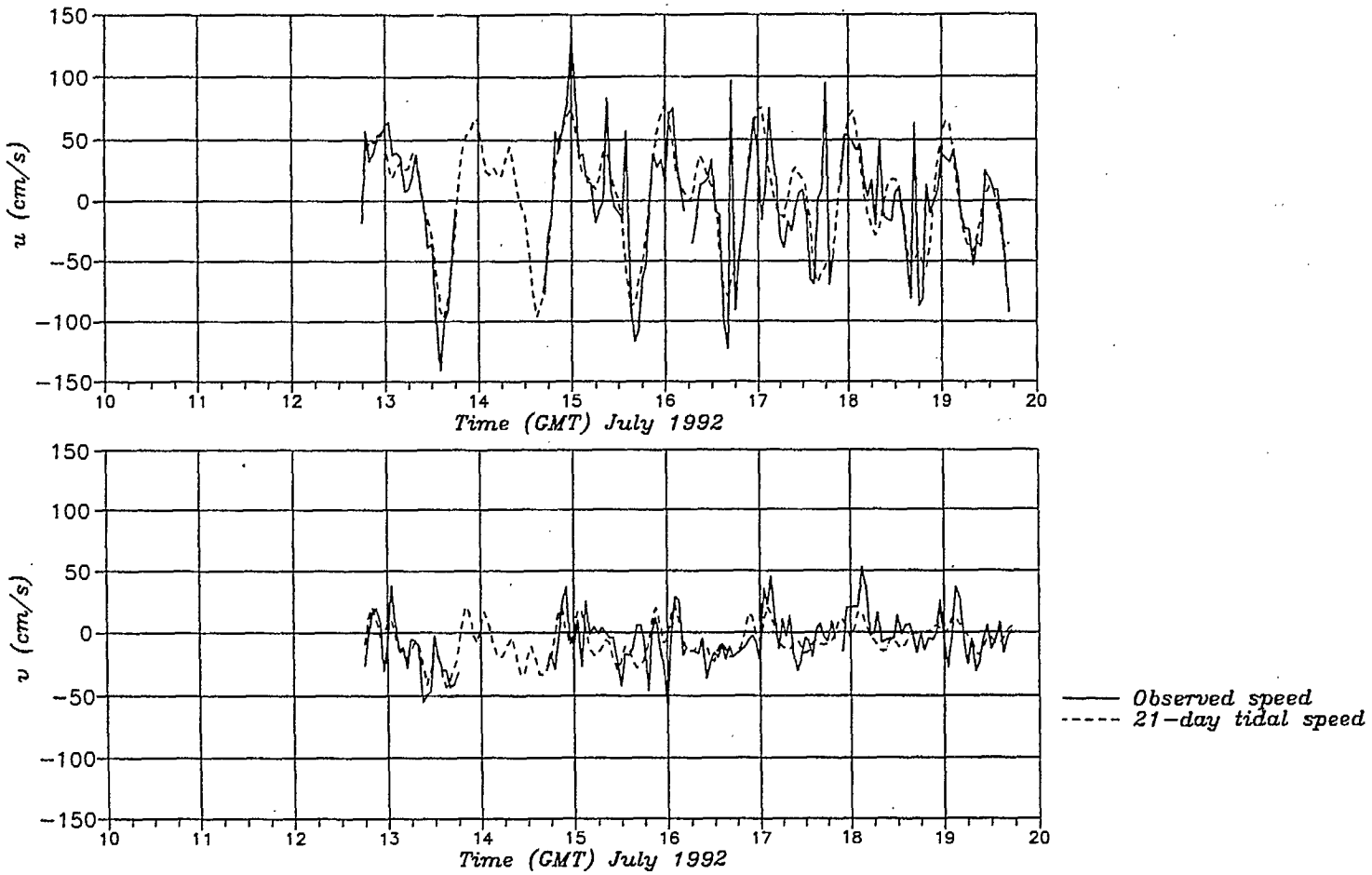

Figure 4.3 Comparison of the total current signal and the tidal signal based on a 21-day analysis for point 1.

where

$\alpha_1, \alpha_2, \alpha_3 \ldots \alpha_m$ are constant weights, and

ϵ_t is a time-series of uncorrelated random components with zero mean (white noise).

Such a model is capable of generating realistic environmental time-series. For example, even a second order model AR(2), which uses only the previous two values of the time-series to generate the next value, is capable of generating periodicity. This feature is illustrated in Fig. 4.4 and 4.5. In both cases, the white noise ϵ_t was generated from a rectangular probability distribution of half-width 0.5 and a mean of zero, and the initial values of the time-series were zero; i.e. $z_0 = z_1 = 0$. For Fig. 4.4, the values of α_1 and α_2 were 1.890 and -0.900, while in Fig. 4.5, the values of α_1 and α_2 were 1.985 and -0.992. These numbers were chosen so that the period of the oscillation was the same (75 time units) in both cases. [For AR(2), the frequency of the oscillation is given by the value of the expression $\sqrt{(-\alpha_1^2-4\alpha_2)}$; see Abraham and Ledolter (1983).] Various realizations of the process can be created by generating new sets of random variables ϵ_t. In Fig. 4.4 and 4.5, only one realization is shown for $t \leq 600$. In the upper panel of each figure, six realizations are shown for $t > 600$.

For the parameter values used for Fig. 4.4, it can be seen that the phase and amplitude of the projected oscillation beyond $t = 600$ rapidly lose any relationship to the previous series. It appears that it would be difficult to predict the future evolution of the time-series beyond $t = 625$ on the basis of its history up to $t = 600$. However, for the parameter values used for Fig. 4.5, the phase and amplitude of the projected oscillation beyond $t = 600$ retain their coherence for a longer period of time. In this case, it appears that it would be possible to predict the future evolution of the time-series with some confidence up to around $t = 800$. The difference in the predictability of the two time-series is associated with the fact that the autocorrelation function for the time-series shown in Fig. 4.5 is significantly non-zero for large time lags, while the autocorrelation function for the time-series shown in Fig. 4.4 is significantly non-zero only for small time lags, due to the random nature of the phase and amplitude of the oscillation.

In the lower panel of each figure, the time-series were projected beyond $t = 600$ using $\epsilon_t = 0$. This value is the best estimate for these random variables, since it is the mean of their probability distribution. The resulting time-series extension is deterministic, in that no random numbers are required for its generation. The difference in the predictability of the two time-series is evident in the more sustained oscillation shown for the evolution of the time-series in Fig. 4.5, compared with that in Fig. 4.4 which decays rapidly.

In the limiting case of white noise, with $z_t = \epsilon_t$, and $\alpha_1 = \alpha_2 = \alpha_3 = \ldots = \alpha_m = 0$, the best estimate for future values of the time-series is zero, since that is the mean of their probability distribution. There would be no advantage to generating a time-series of white noise as a prediction, since that time-series would, in fact, give a higher sum-of-squares error.

(b) A Predictive Model

The modelling objective is to determine the order m of the model, and to calculate the constant weights $\alpha_1, \alpha_2, \alpha_3 \ldots \alpha_m$, given the observed time-series. Equation (4.3) can then be used to

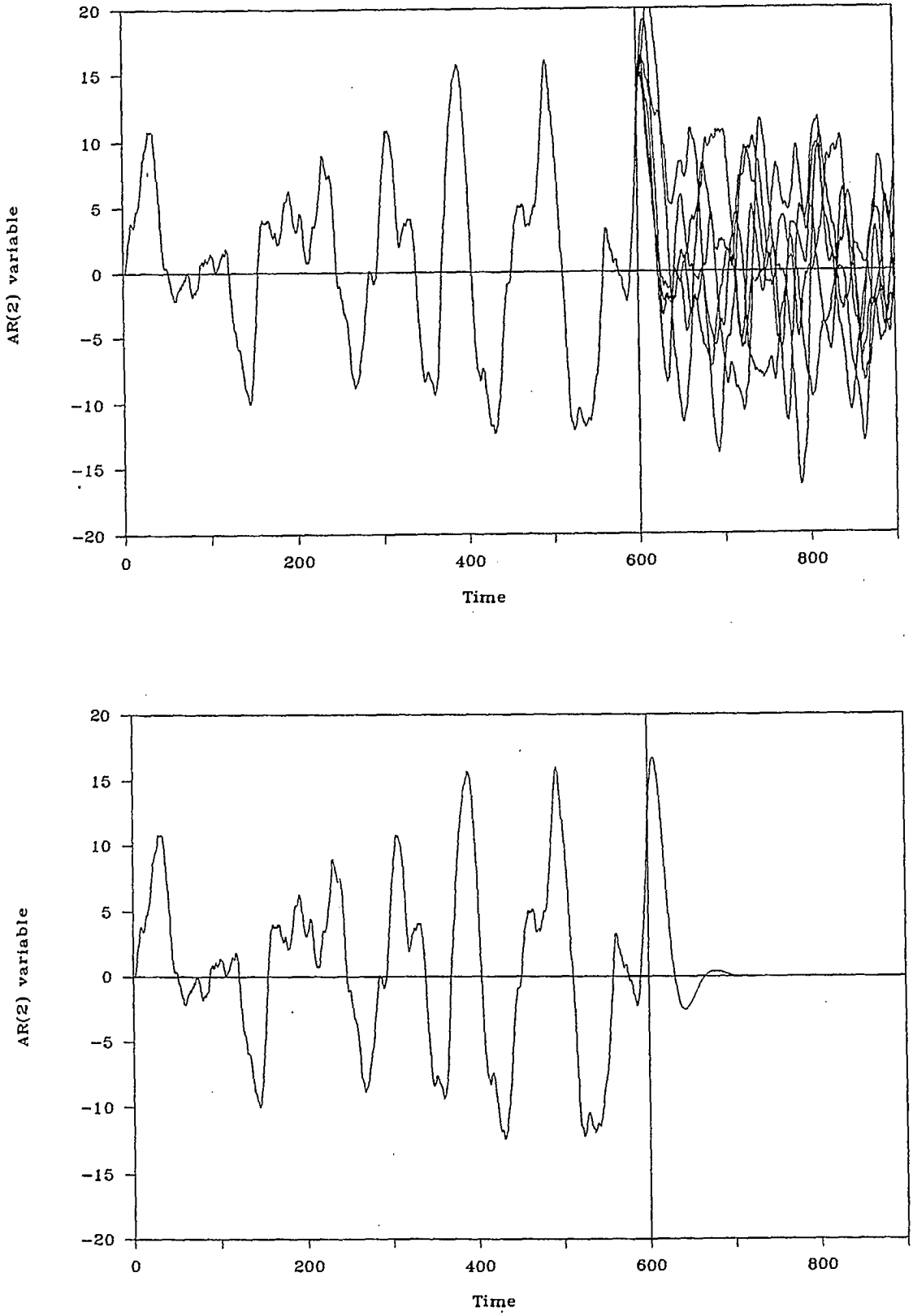

Figure 4.4 Example of a time-series generated by the AR(2) model with $\alpha_1 = 1.890$ and $\alpha_2 = -0.900$. Six examples of the possible evolution of the time-series beyond $t = 600$ are shown (upper panel), and best estimate of the evolution of the same time-series with $\epsilon_t = 0$ (lower panel).

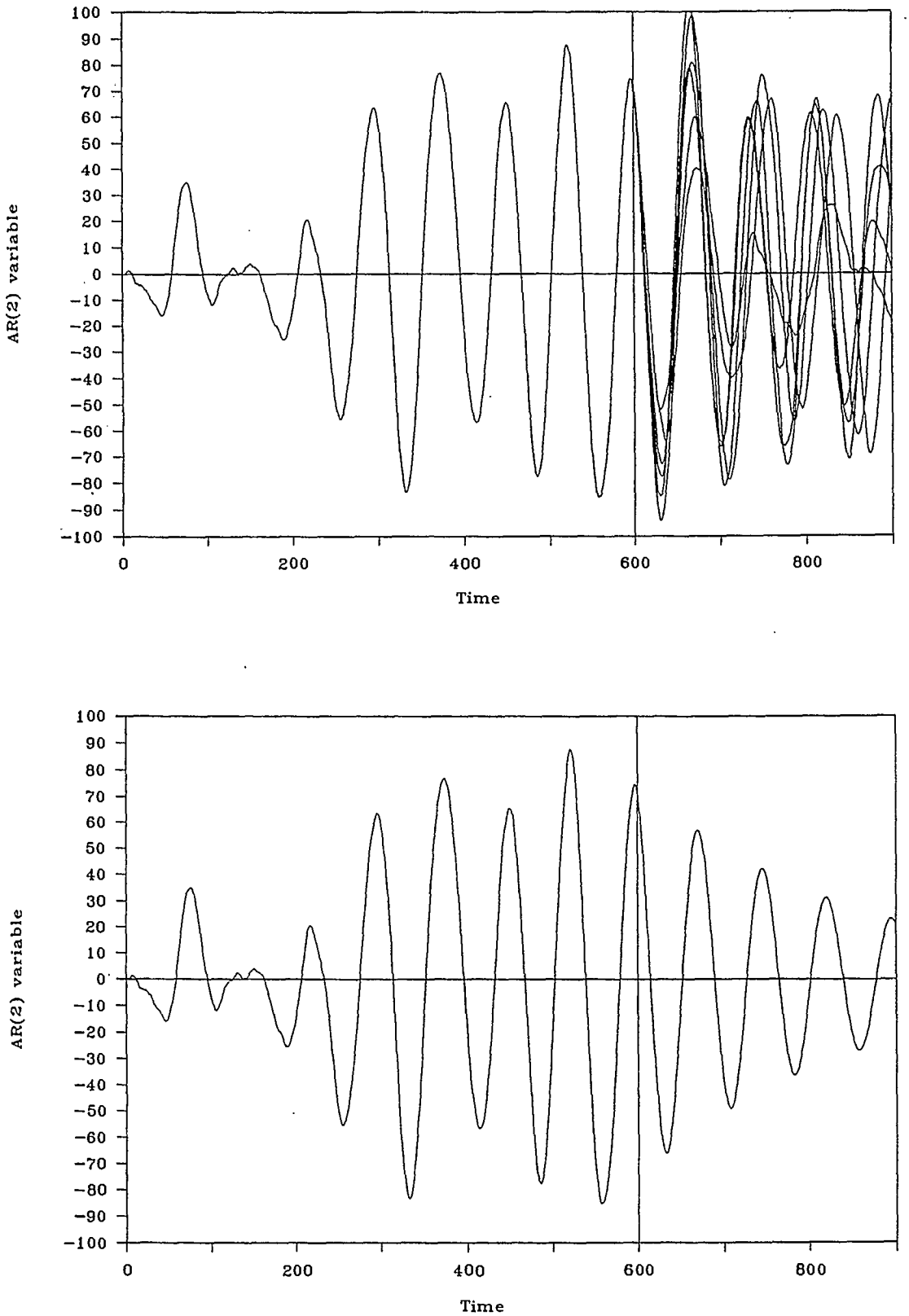

Figure 4.5 Example of a time-series generated by the AR(2) model with $\alpha_1 = 1.985$ and $\alpha_2 = -0.992$. Six examples of the possible evolution of the time-series beyond $t = 600$ are shown (upper panel) and best estimate of the evolution of the same time-series beyond $t = 600$ with $\epsilon_t = 0$ (lower panel).

generate a forecast for the future values of the time-series, using $\epsilon_t = 0$ as the best estimate of the future random component.

Each cartesian component of the residual velocity was processed and forecast independently. Gaps in the observed time-series were first filled by linear interpolation between the two bracketing values, to produce complete time-series with a 1-hour time interval. The mean μ of the time-series was calculated and subtracted, to yield the time-series $z_1, z_2, z_3, \ldots z_n$ with mean zero and length n hours.

The choice of the order m of the model was influenced by the following considerations. Models of high order are capable of detecting and parameterizing many superimposed oscillations at different frequencies, just as a linear differential equation of high order has solutions made up of a superposition of many damped harmonics. However, a limit to the ability to resolve these frequencies is imposed by the length of the observed time-series, analogous to the Nyquist criterion in Fourier analysis. Jenkins and Watts (1968) suggest that the order m be determined by fitting processes of different orders, and examining the residual variance for a number of test time-series.

The coefficients $\alpha_1, \alpha_2, \alpha_3 \ldots \alpha_m$ are calculated as solutions of the following m simultaneous linear equations:

$$\begin{aligned}
&\alpha_1\gamma_0 + \alpha_2\gamma_1 + \alpha_3\gamma_2 + \ldots + \alpha_m\gamma_{m-1} = \gamma_1 \\
&\alpha_1\gamma_1 + \alpha_2\gamma_0 + \alpha_3\gamma_1 + \ldots + \alpha_m\gamma_{m-2} = \gamma_2 \\
&\alpha_1\gamma_2 + \alpha_2\gamma_1 + \alpha_3\gamma_0 + \ldots + \alpha_m\gamma_{m-3} = \gamma_3 \\
&\cdot \quad \cdot \quad \cdot \quad \cdot \quad \cdot \\
&\cdot \quad \cdot \quad \cdot \quad \cdot \quad \cdot \\
&\alpha_1\gamma_{m-1} + \alpha_2\gamma_{m-2} + \alpha_3\gamma_{m-3} + \ldots + \alpha_m\gamma_0 = \gamma_m,
\end{aligned}$$

where

$$\gamma_k = \frac{1}{n}\sum_{i=k+1}^{n} z_i . z_{i-k} \qquad (4.4)$$

is the autocovariance at lag k.

Tests were carried out on n hours of residual current data from SeaSonde to investigate the effect of increasing the order of the model on the residual variance. In general, the residual variance decreased rapidly as the order was increased from zero to one, and continued to decrease slowly as the order was increased to around n/10. The residual variance then remained relatively constant, and started to rise as the order increased beyond n/3. There is a fundamental restriction that the order m cannot exceed the record length n. As a result of these tests, it was determined that a model of order m = n/4 would be used. In addition, a ceiling of 72 was placed on m, in order to avoid inverting an excessively large matrix for long time-series. Thus, values from no more than the previous 3 days are used in (4.3) to generate future values. However, all previous data are used in the calculation of the coefficients α_1, $\alpha_2, \alpha_3 \ldots \alpha_m$.

Equation (4.3) was then used to generate a 48-hour forecast for the future values of the time-series, with $\epsilon_t = 0$. Finally, the absolute residual current for each direction was calculated by adding the previously-subtracted mean μ to the forecast time-series u_{res}, v_{res}.

(c) Tests and Results

Five experiments using this algorithm were carried out on time-series data from point 1 (Fig. 4.1) to test the prediction method, and to examine the nature of the currents in Juan de Fuca Strait. A 9-day period, from 17:00 GMT on July 10, to 17:00 GMT on July 19, 1992, was selected for these tests. This period provided the longest input time-series of large tides followed by two days of good data against which to compare the forecast values. The last 48 hours were reserved as the prediction interval, and the analysis was carried out for:

Experiment	Input data record length (analysis period - days)	n (hours)
1	1	24
2	2	48
3	3	64
4	5	116
5	7	164

With these input data record lengths the same tidal constituents are estimated in each experiment, although with different amplitudes and phases, and the tests simulate conditions within the first few days of radar deployment during an incident response.

The ability of the ARMA model for predicting the residual current is governed to a large extent by the autocovariance properties of the signal. Estimated autocorrelation functions (acf) for n= 64 and n=164, for both u and v, are shown in Fig. 4.6. Since the ARMA order m = n/4, the number of lags analyzed is greater for experiment 5. Both functions have the same general shape, characterized by a rapid decrease in correlation at lag one, and an oscillatory behaviour about zero out to lag 40. The values of the acf for $k>1$ are low, less than 0.25, implying poor correlation between successive values, and low predictive skill.

The residual signals, and the predicted 48-h responses using the ARMA model, are shown in Fig. 4.7 to 4.9 for experiments 3, 4 and 5. The lower-order ARMA process for 3 days of input data, with these acf characteristics, yields a predicted signal that damps quickly over the first 48 hours. The higher-order ARMA processes associated with the 5- and 7-day input series yield greater variation in the predicted signal; however, the fit to the observed data is not better in any deterministic sense.

Given the nature of the observed residual flows in Juan de Fuca Strait, there is no benefit to a high-order ARMA process, and a second- or third-order process would be as justifiable as one with n/4 for an arbitrary-length input data record. These conclusions have been reached by examining the time-series at one location, and are limited by this small sample. Further analysis, using more of the dataset is recommended to characterize the acf and to quantify the variance of the signal that is not modelled by an ARMA process.

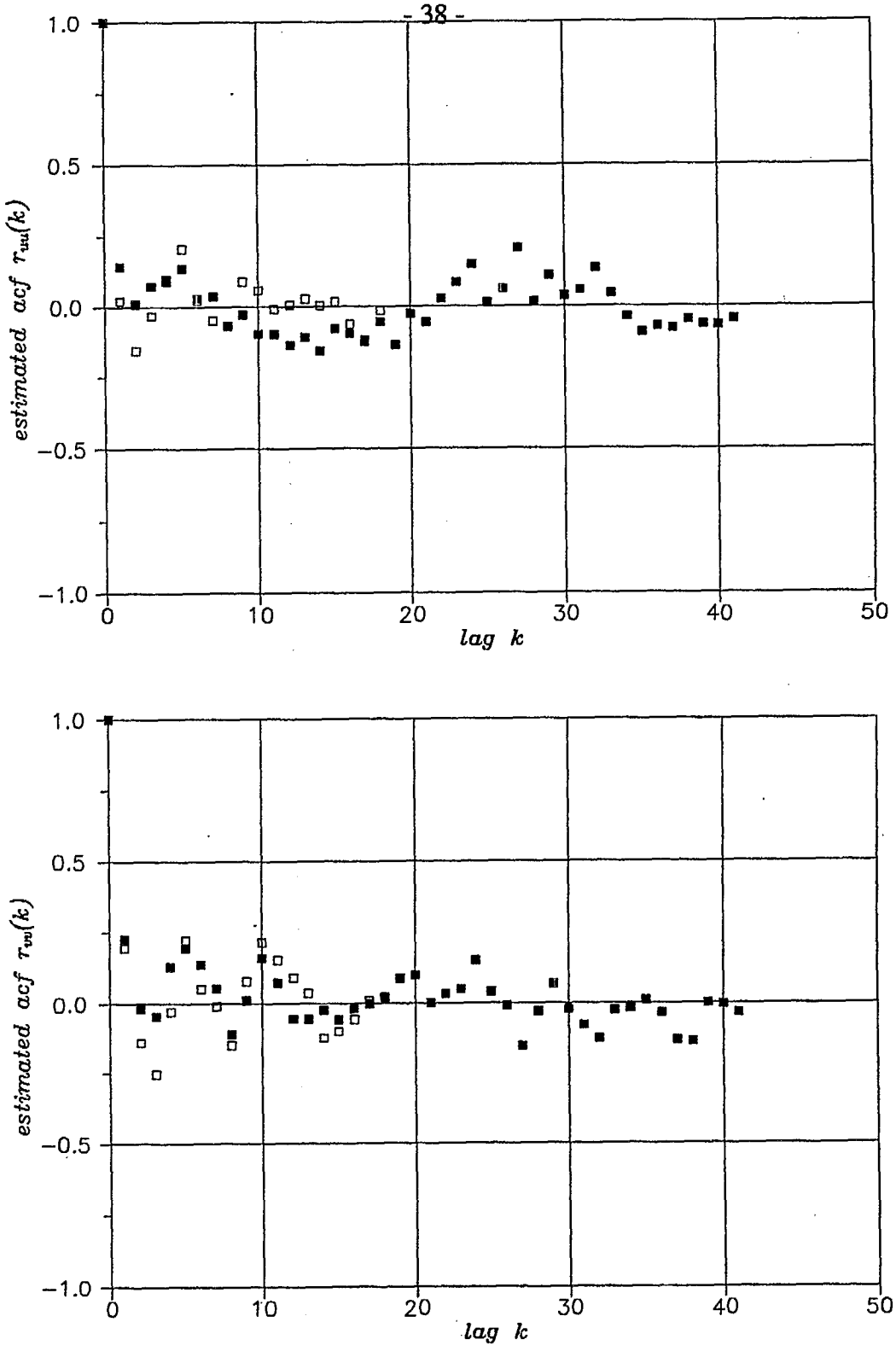

Figure 4.6 Estimated acfs for 3-day and 5-day input time-series at point 1.

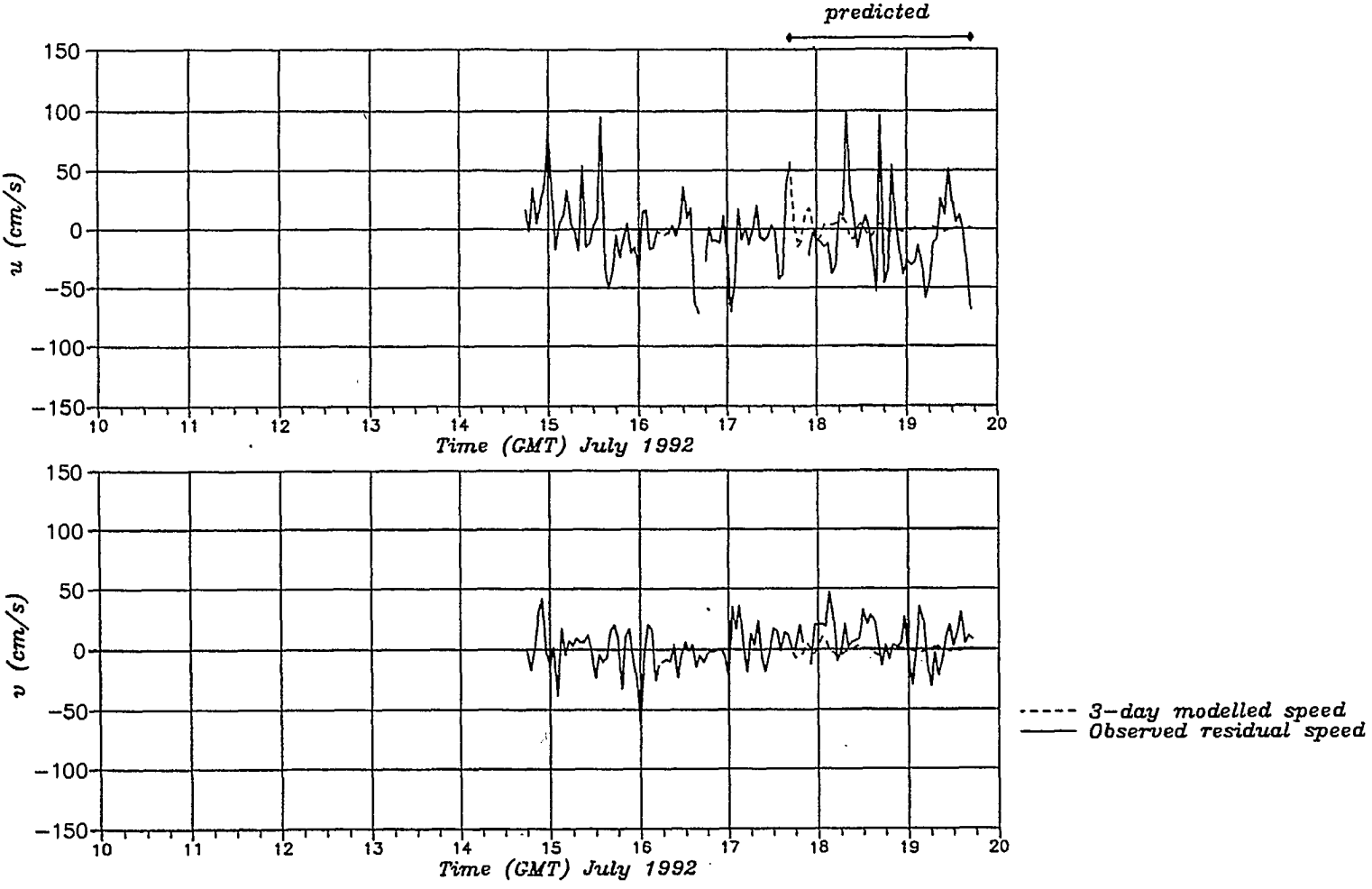

Figure 4.7 Comparison of the predicted and observed residual current signals for a 3-day analysis period.

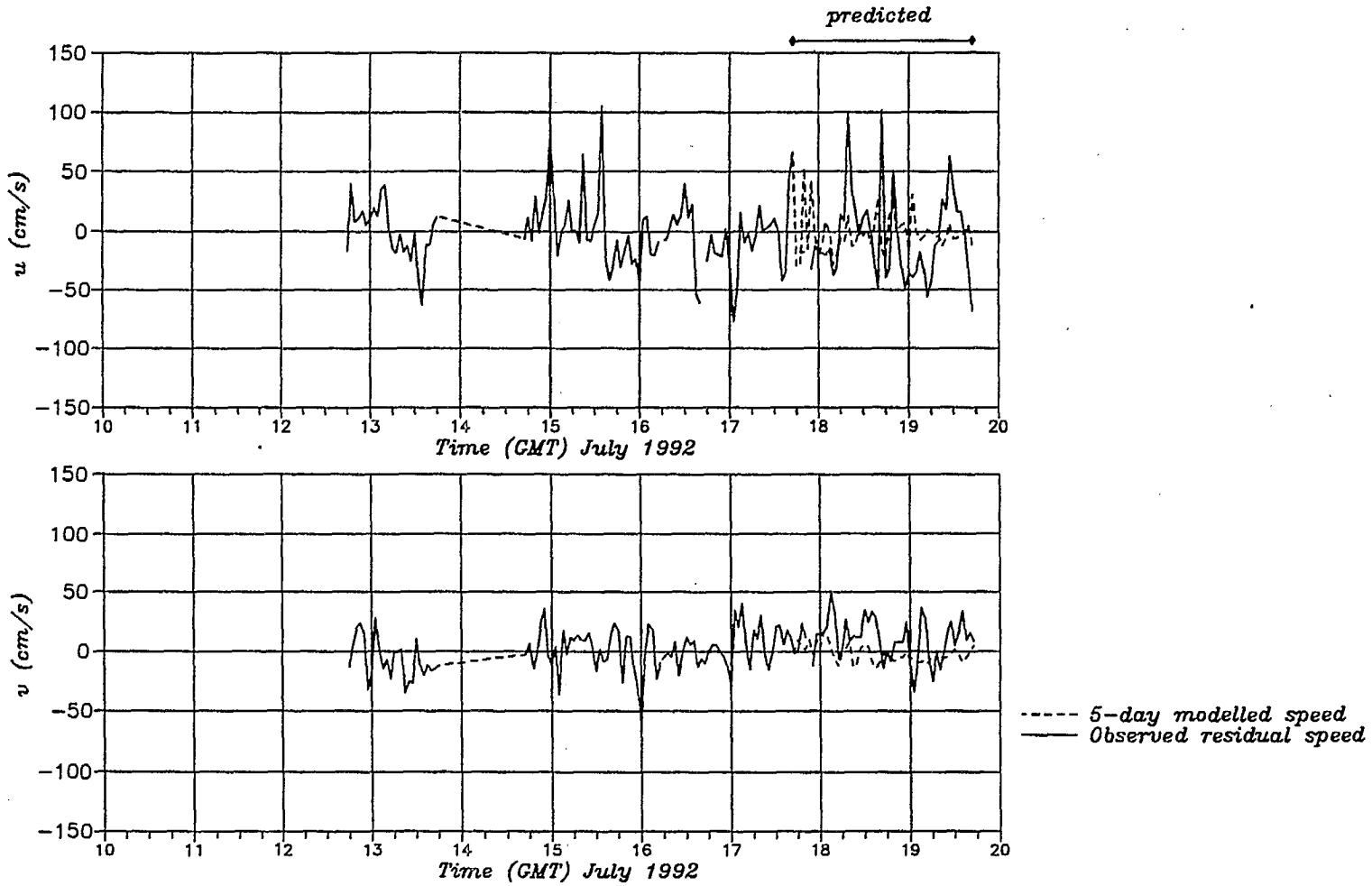

Figure 4.8 Comparison of the predicted and observed residual current signals for a 5-day analysis period at point 1.

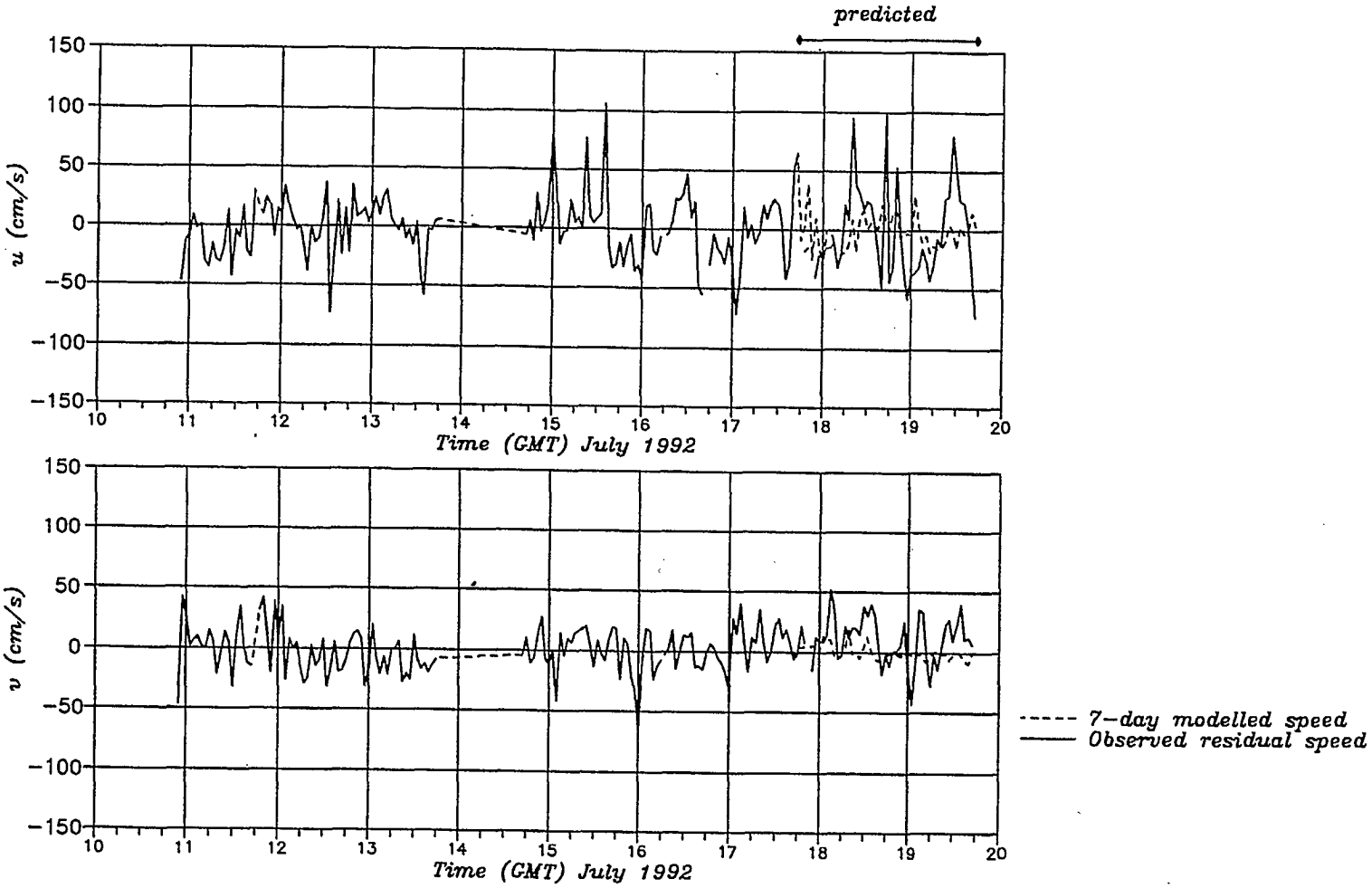

Figure 4.9 Comparison of the predicted and observed residual current signals for a 7-day analysis period at point 1.

4.1.3 Total Current

The total current prediction is given by:

$$u_{pred} = u_{tid} + u_{ARMA(m)} + \mu_u$$
$$v_{pred} = v_{tid} + v_{ARMA(m)} + \mu_v \qquad (4.7)$$

where $u,v_{ARMA(m)}$ are the m-th order ARMA model values, and $\mu_{u,v}$ is the mean of the residual current signal.

The five experiments discussed previously with the ARMA model were repeated, applying equation (4.7) for each different analysis period. The predicted u and v time-series for these experiments are shown in Fig. 4.10 to 4.14. Comparison of these forecasts with the tidal signals in Fig. 4.2 shows that most of the current is explained by the tide. The ARMA values make only a small additional contribution, and the predictive skill is largely determined by how well the tide is resolved.

The shortest analysis periods of 1 and 2 days provide the best prediction in terms of how well both u and v agree with the measured current based on visual inspection of the plotted time-series. The explanation lies with the large magnitude of the tidal band, and the resolution of the tidal constituents from records of less than 14 days. For input records 1 to 2 days long, the estimate of the amplitude of the diurnal and semidiurnal constituents is determined by the 2 to 4 waves contained in the input series. Since there is little fortnightly modulation over such a short period, these amplitudes are close to those of the tides occurring over the succeeding 48 hours. As a longer input record is used (but still less than 14 days) the diurnal and semidiurnal amplitudes found in the least-square harmonic analysis are modified from those of the short record by the fortnightly modulation of the input tidal waves. As a result of this amplitude modification, the predicted tide is slightly less accurate than that from the short record.

Since the residual component has a small influence, the short-term predictor is better than the 5- to 7-day predictor. As shown in Fig. 4.3, once the tidal analysis exceeds 14 days, then the fortnightly modulation becomes resolved and the accuracy improves. This improvement is evident by visually comparing the time-series plots in Fig. 4.3, 4.10 and 4.14.

The difference time-series for u and v velocity components (u,v_{obs}-u,v_{pred}) for the five experiments are plotted in Fig. 4.15, and illustrate that experiments 4 and 5 produce the largest differences, compared with the short-term predictors. Because of the tidal dominance and small residual contribution, the overall shape of each time-series is similar. The RMS differences between the five predictors and the measured total currents are listed in Table 4.2. Statistically, the 3-day input appears best, although in terms of a deterministic fit to some of the larger variations in current, which would dominate drift, it can be argued that the 1-day input predictor is preferable. However, there is little to choose between the 1-, 2- and 3-day input series.

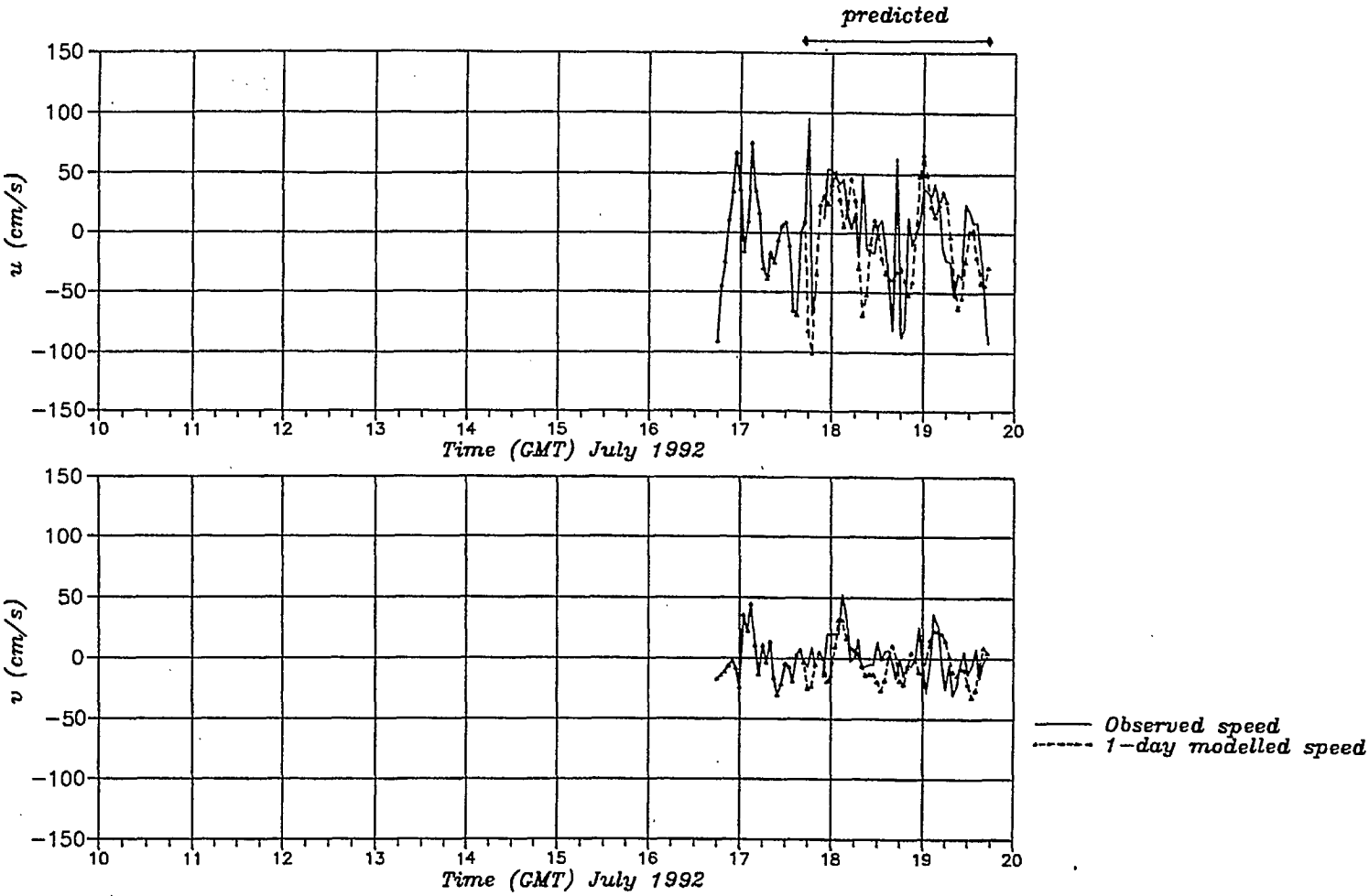

Figure 4.10 Comparison of predicted and observed total current for a 1-day analysis period at point 1.

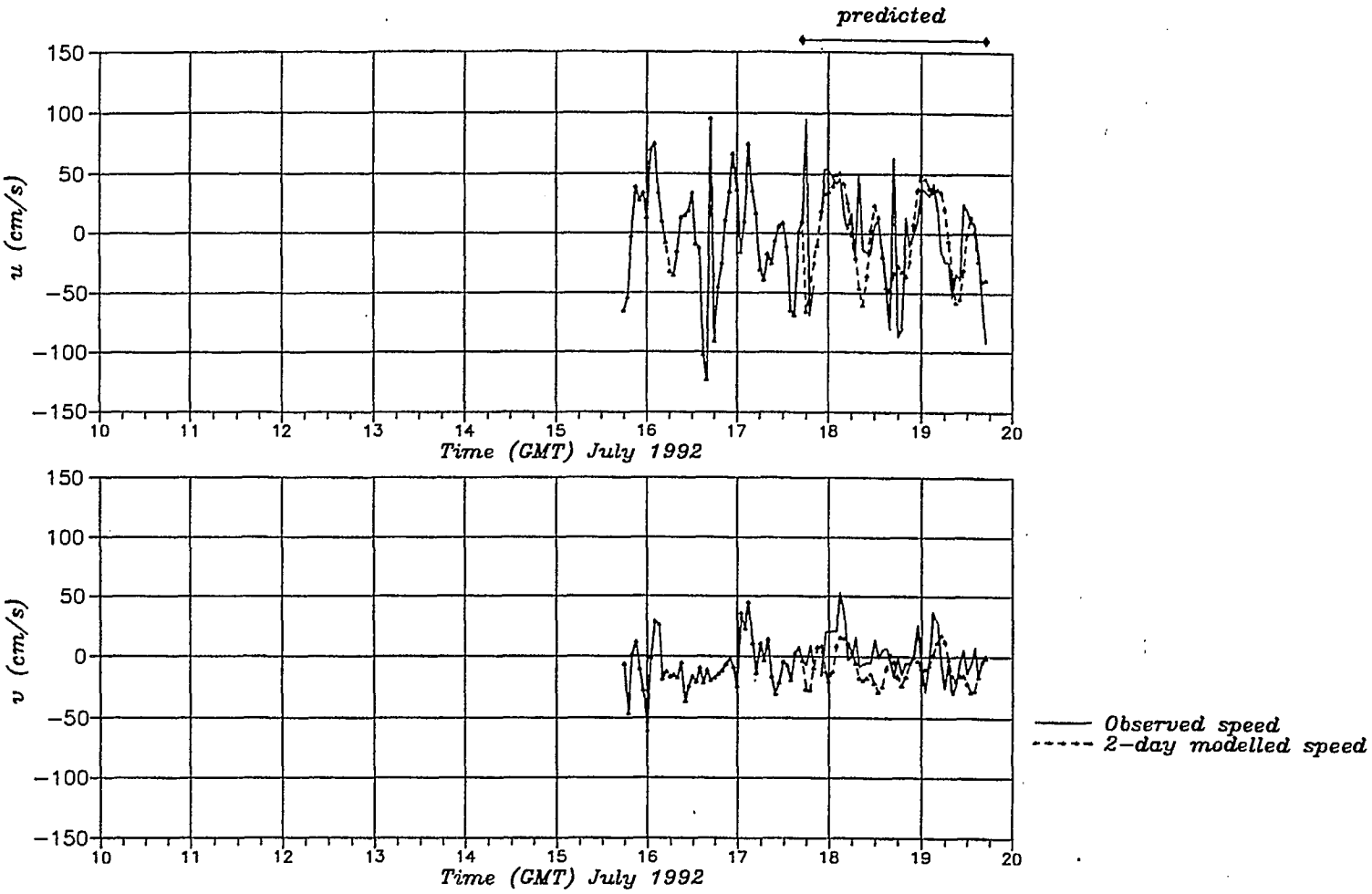

Figure 4.11 Comparison of predicted and observed total current for a 2-day analysis period at point 1.

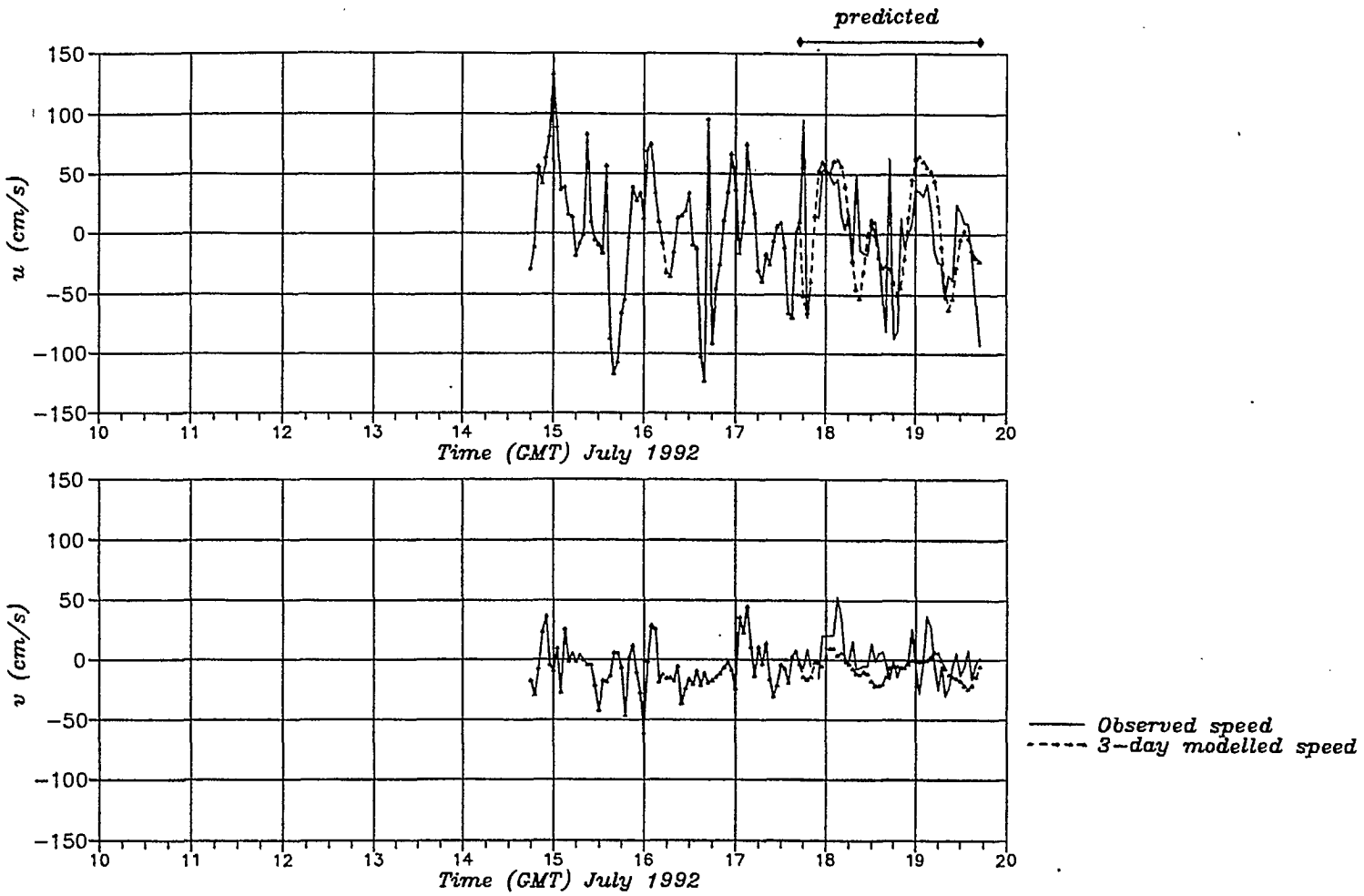

Figure 4.12 Comparison of predicted and observed total current for a 3-day analysis period at point 1.

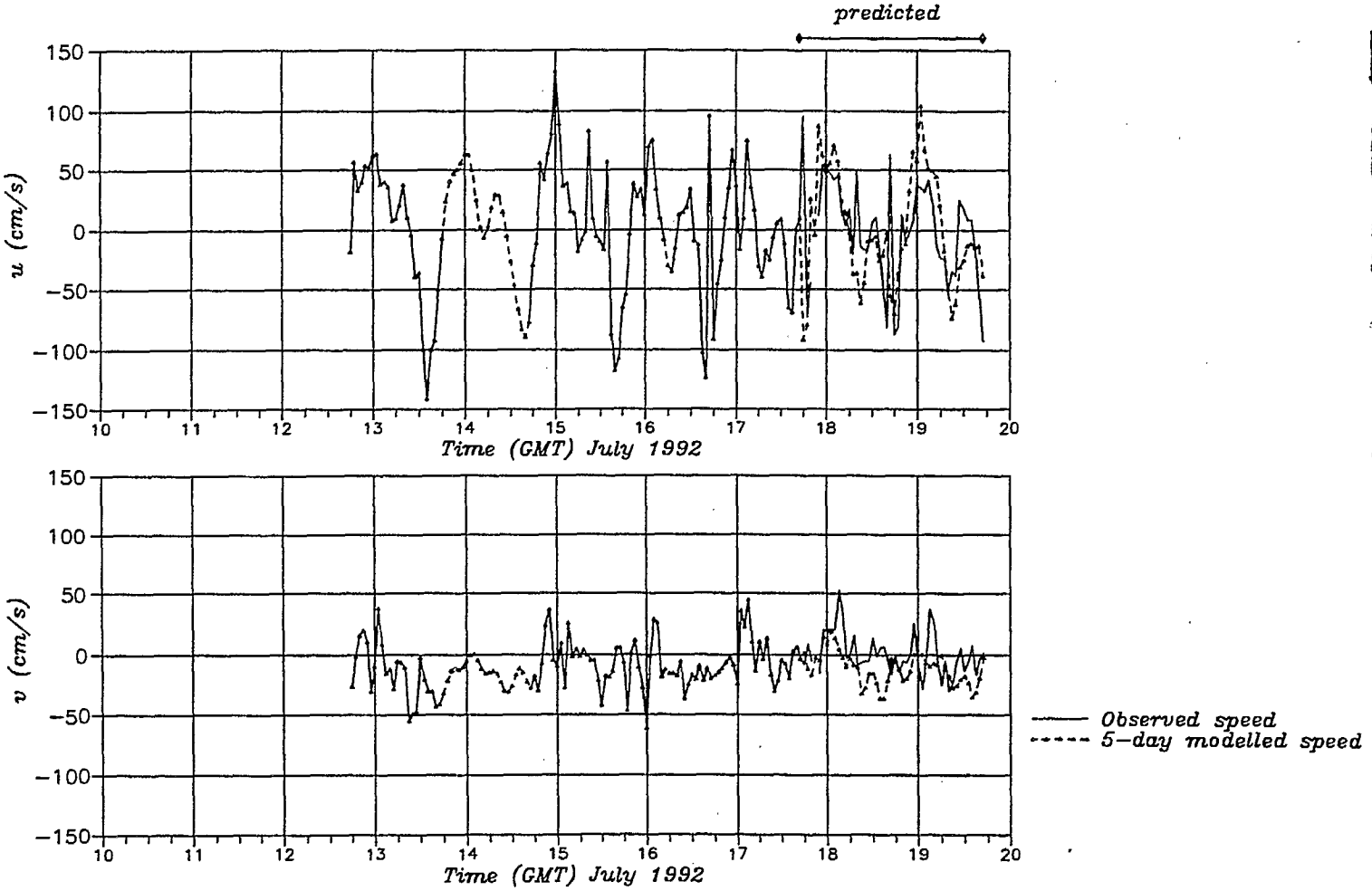

Figure 4.13 Comparison of predicted and observed total current for a 5-day analysis period at point 1.

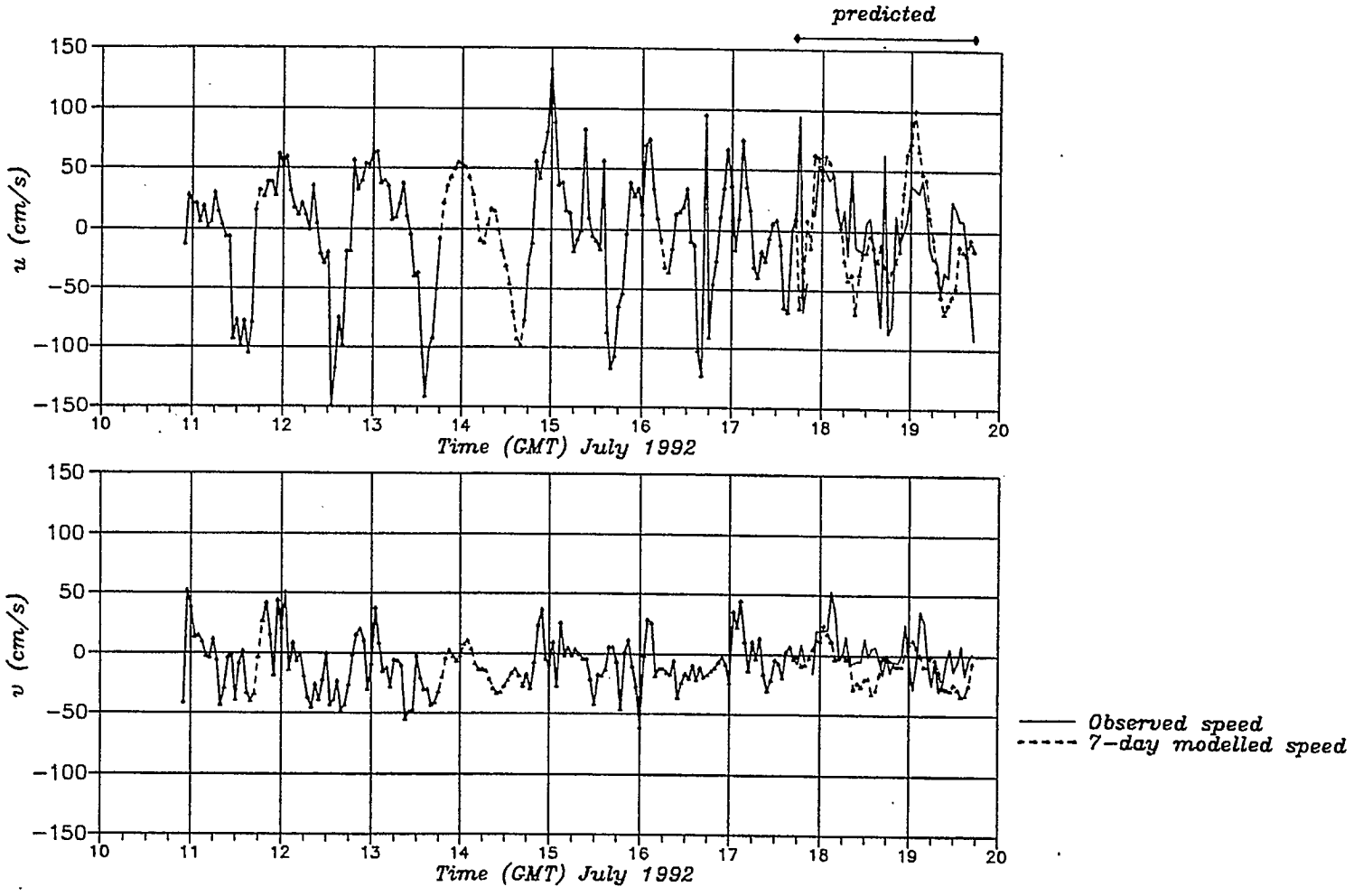

Figure 4.14 Comparison of predicted and observed total current for a 7-day analysis period at point 1.

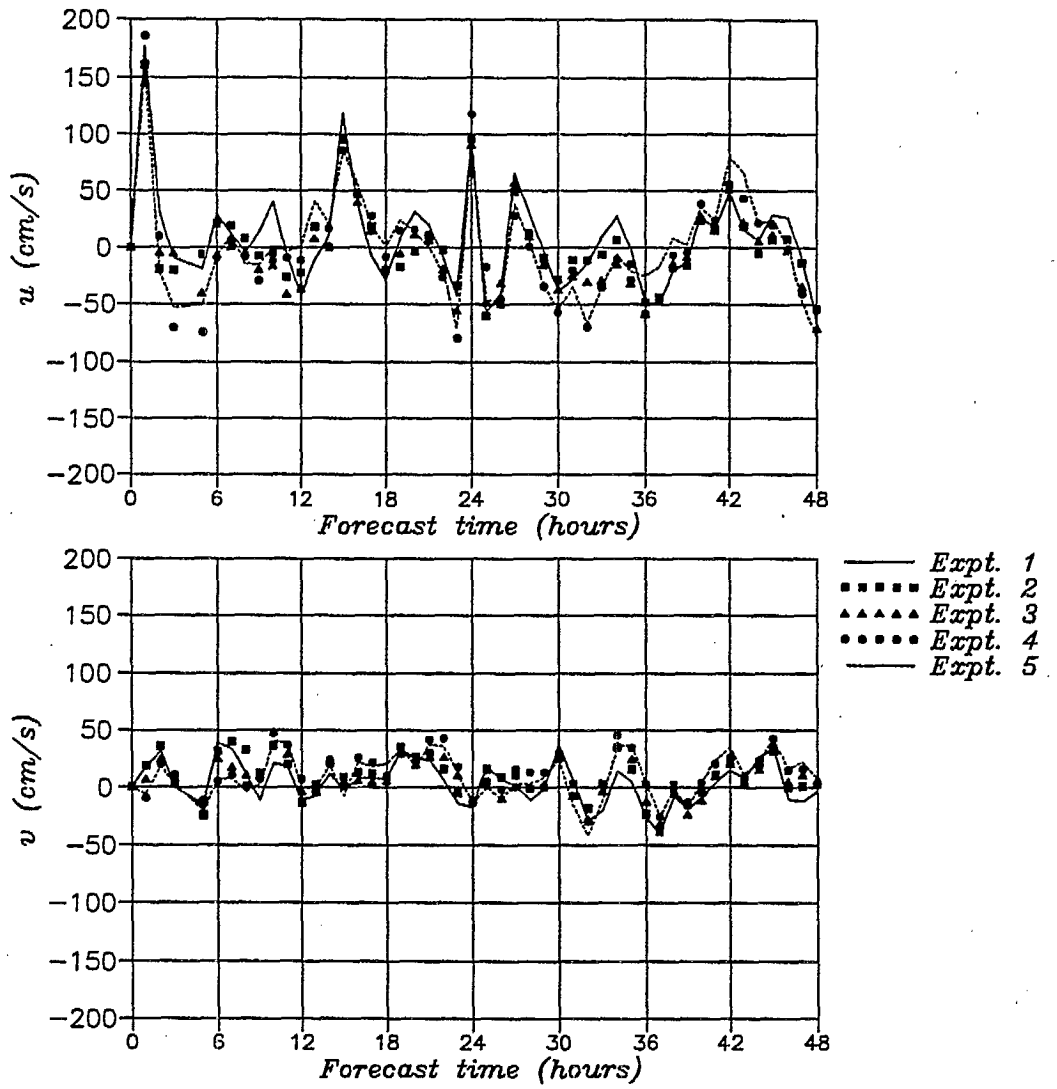

Figure 4.15 Difference between predicted and observed total current time-series as a function of forecast time for experiments 1 to 5 at point 1.

Table 4.2

RMS Difference In Current Components

$(u_{tot}-u_{pred})$ and $(v_{tot}-v_{pred})$

Experiment	u-component (cm/s)	v-component (cm/s)
1	44.97	19.10
2	39.72	20.62
3	40.67	18.70
4	48.77	21.65
5	46.18	21.59

4.1.4 Discussion of Results

It is apparent from the harmonic time-series analysis, and the nature of the acf of the residual currents, that there is a part of the observed flow that is unpredictable by tide and the autocorrelation structure of the non-tidal portion. Inspection of the current maps shows that much of the rapid variability in the residual time-series results from eddies that develop in the flow field at small scales, from fronts and convergences, and from meanders. These small scale features arise through non-linear interactions in the flow, and although they draw energy from the tidal currents, they are not predictable by harmonic analysis.

This type of current behaviour is observed in all coastal and oceanic time-series, and leads to treating the flow in terms of a deterministic part, and a random, turbulent part characterized by such statistical parameters as the RMS velocity. The SeaSonde data, and the simple model described here, provide the basis for forecasting the deterministic part, and for calculating the RMS velocity fluctuations, throughout the domain of an oil spill model. Further analysis of the SeaSonde data to refine the statistics of the non-predictable part of the flow is warranted. These analyses would include correlation with wind and possible isolation of a wind-induced component in the residual, tests with longer time-series over more of the coverage area to relate spatial variations with flow patterns, and examination of the influence of observation errors on the RMS velocities with a view to reducing the variance to match eddy scales in the flow field.

4.2 Oil Spill Model Formulation

Eddy fluctuations in the flow fields are responsible for horizontal turbulent mixing, and produce spreading of an oil slick that is usually much more rapid than gravity spreading after a few hours. Since the eddy fluctuating currents are unpredictable, except in a statistical sense, the consequence for oil spill modelling is that the forcing current must be parameterized into a slowly-varying deterministic part $\mathbf{U}_c$ (tide, buoyancy, wind forces) and a turbulent part $\mathbf{U}'$ (eddies, meanders, frontal affects at unresolved scales).

Oil spill models typically partition the total volume released into a number of parcels (Hodgins et al., 1991) or spillets. In order to model the diffusion of each parcel accurately, the effects of the fluctuating part of the current must be taken into account. If a parcel is represented by M particles, then the position vector $\mathbf{R}(t)$ of each particle at time t after release is written:

$$\mathbf{R}(t) = \int_0^t (\mathbf{U}_c + \mathbf{U}')\, dt \qquad (4.8)$$

where $\mathbf{U}_c$ denotes the smoothly-varying current derived from the radar data, including the residual prediction, and $\mathbf{U}'$ is modelled as a diffusive process with an RMS fluctuation also derived from the radar measurements (difference between the total signal and the predictable part).

The RMS fluctuations of $\mathbf{U}'$ depend upon location and the nature of the currents, and upon the resolution of the measurement of the total current field. By definition, current fluctuations that are not resolved appear in the random component, and in a poorly designed instrument, may

incorporate part of the deterministic signal. In that case, predictive modelling will be poor and may result in over-estimates of the spreading and lateral slick diffusion.

Hodgins et al. (1991) and Tayfun and Wang (1973), for example, model diffusion as a random walk process. The integral in (4.8) is solved in a sequence of N discrete time steps with increment Δt, for all M particles. The result is M position vectors:

$$\mathbf{R}_i(N\Delta t) = \sum_{n=1}^{N} (\mathbf{U}_c(n\Delta t)\cdot\Delta t + \mathbf{x}_n\cdot r_n); \quad i=1,2,\ldots,M \tag{4.9}$$

which is a form of the Lagrangian displacement integral, where r_n is a random number in the range (-1,1). The central problem for correctly modelling the turbulent diffusive process is to determine the length scale **x**.

This length scale is related to the Lagrangian velocity fluctuations and the integration time step. The radar data provide an estimate of the Eulerian velocity fluctuations at each grid point in the coverage area. It remains to derive an algorithm relating the statistics of the Eulerian measurements to the Lagrangian velocity, and hence determine **x**.

The principal advantage of the HF radar is that, for the first time, one can obtain estimates of the slowly varying flow over a wide coverage area, as well as estimates of the statistics of **U'** and their spatial variation. This latter feature eliminates much of the uncertainty associated with an important part of the spill modelling process.

5.0 COMPARISON OF RADAR MEASUREMENTS AND MODELLED CURRENTS

As shown by the present experiment, sea echo return to the radars is variable for several reasons, leading to temporal data gaps; the coverage area is limited by geometry and number of units deployed; and there is a baseline zone that requires filling. Even with improvements to radar range and coverage by moving to a higher transmit frequency, assimilation of data into a model is likely to provide the best means of filling gaps and the baseline zone, for extending the coverage area spatially, and for predicting currents two to three days ahead.

Numerical hydrodynamic models provide the correct dynamical basis for assimilating the radar data and extending its coverage. In this section we examine the behaviour of one such model, the three-dimensional primitive equation model named GF8 (Stronach, 1991), using the new SeaSonde dataset. This model has been developed and verified for the Juan de Fuca-Strait of Georgia-Puget Sound waterway.

5.1 Numerical Hydrodynamic Model

5.1.1 Form of Governing Equations

The model is formulated in terms of the conservation of horizontal momentum, conservation of mass, and conservation of density. The dependent variables in the hydrodynamic model consist of layer-averaged velocity components u,v; the vertical velocity between layers w; the free-surface elevation ζ; and the water density σ. The independent variables are distance in x, y and z, and time t. The treatment of the vertical dimension is in terms of a number of fixed layers of arbitrary thickness, bounded above by a free surface. The differential equations (Stronach, 1991) have the general form:

$$(uh)_x + (vh)_y = -(w_{upper} - w_{lower}) \tag{5.1}$$

$$u_t + [(uuh)_x + (uvh)_y - (wu)_{lower} + (wu)_{upper}]/h - fv = -g\zeta_x - (P_{baroclinic})_x + (A_H(u)_{xx} + A_H(u)_{yy}) + (\tau_{upper} - \tau_{lower})/h \tag{5.2}$$

$$v_t + [(uvh)_x + (vvh)_y - (wv)_{lower} + (wv)_{upper}]/h + fu = -g\zeta_y - (P_{baroclinic})_y + (A_H(v)_{xx} + A_H(v)_{yy}) + (\tau_{upper} - \tau_{lower})/h \tag{5.3}$$

$$\sigma_t + (u\sigma)_x + (v\sigma)_y = -[(w\sigma)_{upper} - (w\sigma)_{lower}]/h \tag{5.4}$$

In these equations f is the Coriolis parameter; g is gravitational acceleration; P is the pressure arising from density variations; A_H is the horizontal eddy diffusivity coefficient; τ is the horizontal stress component at the upper and lower boundaries of the layer; the subscripts "upper" and "lower" refer to the upper and lower bounding surfaces of the layer; and h is the layer thickness. In equation (5.4) σ denotes the sea water density, and in all four equations the

subscripts x,y,t denote partial differentiation with respect to distance in the coordinate x and y directions, and time.

The baroclinic pressure P is defined by the variations in σ and hence is known, as are the parameters f and g. The internal stresses τ are parameterized in terms of the flow variables u and v, and contain two coefficients that must be calibrated to reproduce observed vertical variations in the currents. At the free surface and sea bed these coefficients specify the magnitude of the wind stress and bottom friction stress. The coefficients linking the wind speed to the surface stress, and the current speed in the bottom layer to the sea bed stress, are reasonably well known from scientific research and previous modelling applications. However, the vertical eddy viscosity coefficient appearing in the internal stress terms varies as a function of the density gradient between layers, and the vertical velocity shear. These variations are not well understood and there is considerably more uncertainty in the vertical eddy viscosity term than in the wind and bed stress terms.

The horizontal eddy viscosity coefficient A_H must also be adjusted to calibrate the results to match observations. Thus there are five dependent variables, and five free calibration parameters.

Boundary conditions consist of the variation in tidal water level $\zeta(t)$ and the fluxes of σ and momentum at the mouth of Juan de Fuca Strait, the northern passes to the Strait of Georgia, and for σ at the mouths of local rivers, and the open sea boundaries. Initial conditions are specified for the dependent variables u,v,w, ζ and σ.

5.1.2 Solution Method and Model Validation

Equations (5.1) to (5.4) are solved using finite differences on a regular Cartesian grid with a uniform 1,950-m grid (Fig. 5.1). The independent variables are distributed on the grid in the Arakawa-C space-staggered scheme; thus, in the application to Juan de Fuca Strait, the separation between velocity points, and between elevation points, was 1,950 m. The model, consisting of 10 layers in the vertical, with a 5-m surface layer thickness, was applied during the period of SeaSonde measurements. Initial data for σ were extracted from historical surveys (Crean and Ages, 1972) since no suitable data were collected during the summer of 1992. Input wind data from coastal anemometers and lightstations were obtained from government agencies.

The horizontal eddy viscosity coefficient A_H was given a value of 200 m^2/s, applied uniformly over the grid based on the water level response at long-term gauging stations, and to achieve a reduction in the horizontal current variability that appeared reasonable in the absence of any suitable calibration data. The degree of flow smoothing achieved through the horizontal turbulent mixing terms is a critical aspect of flow modelling for transport and diffusion of contaminants and spills, and further comments on the parameterization of A_H will be presented at the end of this chapter.

The hydrodynamic model has been extensively calibrated and verified in the Strait of Georgia and Juan de Fuca by Stronach (1991) using tidal constants and water level measurements. Subsequently mid-channel current meter data were obtained in Admiralty Passage, close to the radar coverage area (Fig. 5.1). A time-series comparison of model versus observed currents

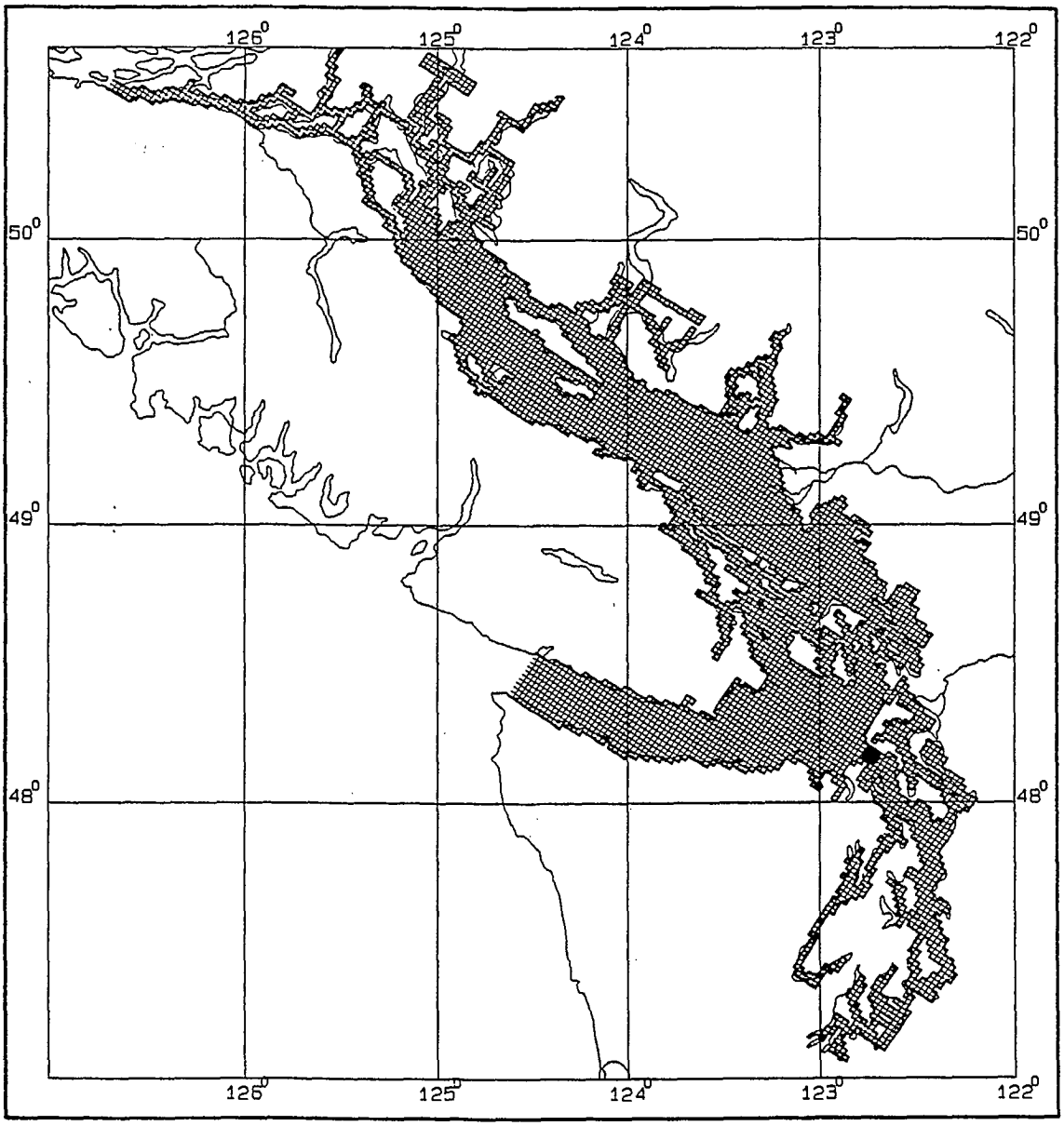

Figure 5.1 Map of Juan de Fuca Strait and the Strait of Georgia-Puget Sound waterway showing the 1,950-m GF8 model grid. The current meter comparison point is indicated by the (●).

at a depth of 39 m (Fig. 5.2) demonstrates the excellent correlation obtained over several tidal cycles. Both the phase of the strong tidal oscillations, and the magnitude of the peak flows agree well with most of the observations, and provide confidence that the model has the overall tidal flow largely correct.

5.2 Current Comparisons

Time-series data have been extracted from the SeaSonde current maps at locations marked 1, 2, 3, and 6 shown in Fig. 4.1. Upper layer currents were extracted from the numerical model predictions at the same four locations, and the u and v components are compared in Fig. 5.3 to 5.6.

Examination of the two mid-channel points west of the submarine ridge (points 1 and 6) shows the dominance of the EW currents and their tidal modulations. Agreement for phase and amplitude is excellent at point 6, and there is obviously a strong similarity at point 1. At the latter location, however, the radar measurements show that the flood flows are capped off, and the peak speeds are generally higher in the model. There is also a feature apparent in the radar data not found in the model; that is, the occurrence of a strong flow reversal associated with the ebbs on July 16, 17 and 18. It recurs every tide in the radar data over these three days, and corresponds with the formation of a short-lived (2 hours) front slightly east of this location. Such features are not evident in the smoother fields generated by the model.

In general, the v-component in both measurements and model is more variable than the u-component, and peak speeds are approximately one-half of the EW flows. The rapid variability in these data reduce the correlation between the two signals, particularly at point 6. In addition, over the last three days plotted here, there are strong southward pulses with sustained speeds exceeding 75 cm/s during morning hours. Current maps illustrating observed and modelled flows are shown in Fig. 5.7. The modelled flows are smoother, and more co-linear with the channel configuration, thus failing to reproduce the strong cross-channel flow south of Race Rocks.

At point 2 the phase and ebb amplitude of the EW signal shows excellent agreement; however, the flood peak currents are over-predicted by the model. The observed current maps show that towards the end of the large flood phase, a complex flow pattern develops, sweeping northward around Race Rocks and then bending southeastward to form a convergent front along a line northeast of Ediz Hook (Fig. 5.8, upper panel). To the west of the front, around point 2, flows are governed by the meander in the flooding current and the frontal features, leading to lower EW speeds than predicted by the modelled fields (Fig. 5.8, lower panel). The modelled flow patterns do not capture the meandering nature of the observed flows past Race Rocks; rather, they form more of a mid-channel jet, drawing water south past Race Rocks, and giving the strongest currents near point 1. The front is evident in the modelled field, but displaced further east than observed, bringing point 2 into the zone of strong flow. The north-south components show similar features to those from point 1, although at generally lower speeds.

By way of contrast, the NS component speeds at point 3 equals or exceeds those in the EW direction, and here both signals exhibit strong tidal fluctuations that are clearly well correlated with the modelled time-series. The main difference is evident in the EW component during

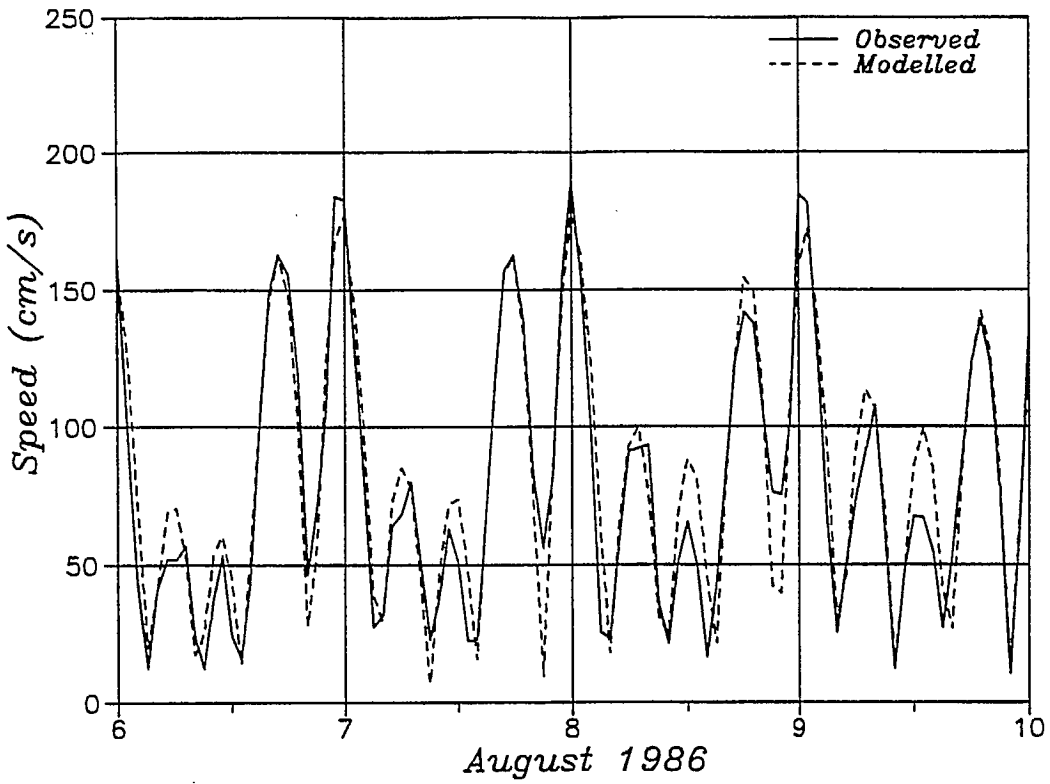

Figure 5.2 Comparison of modelled and observed flow speed in Admiralty Passage.

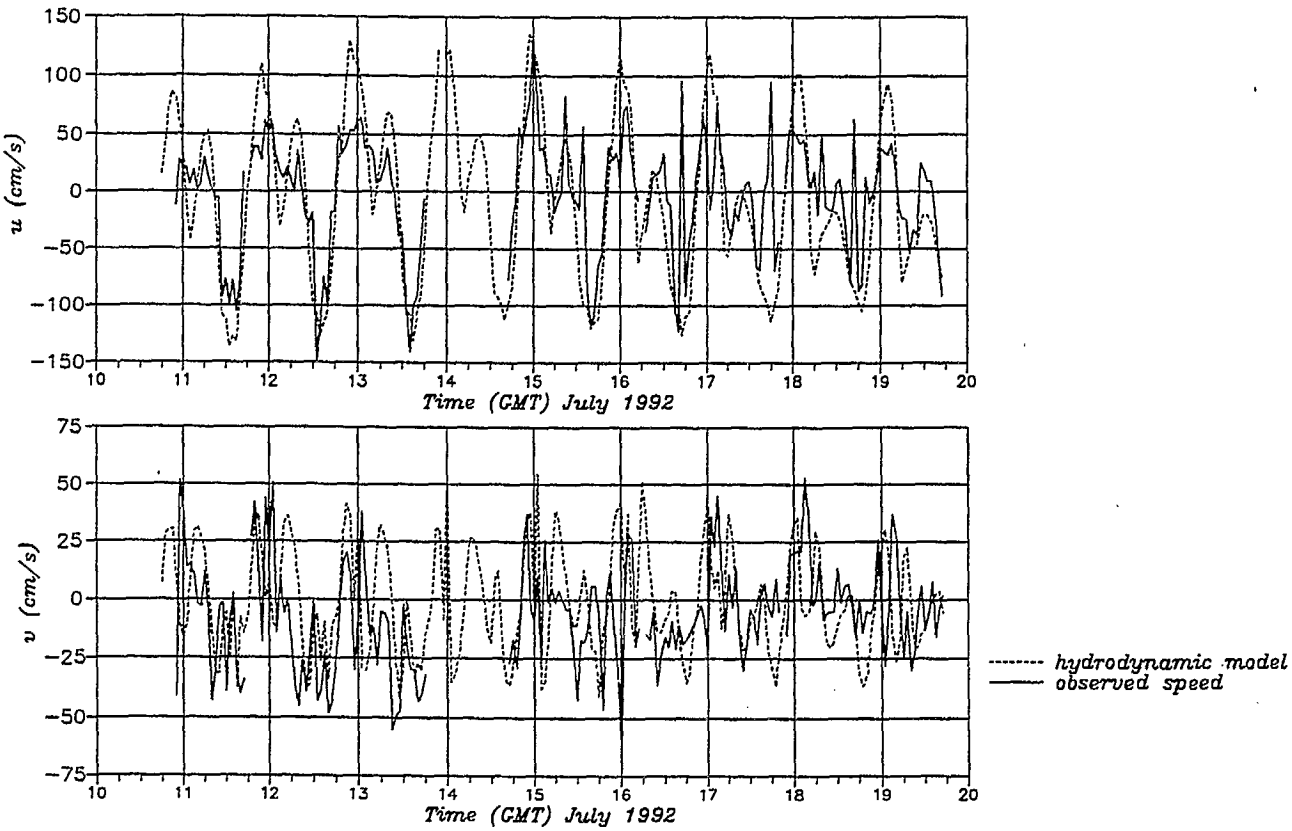

Figure 5.3 Comparison of modelled and observed surface currents at point 1 (see Fig. 4.1).

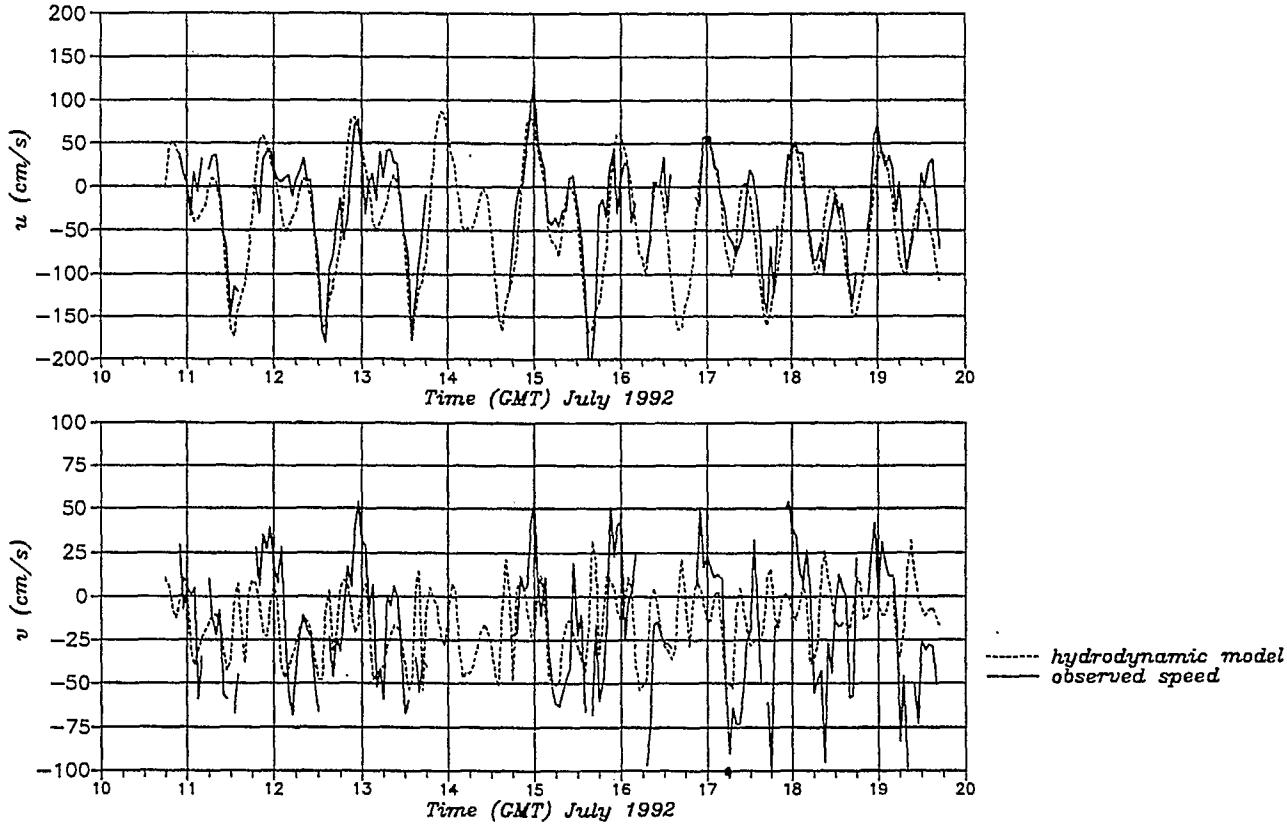

Figure 5.4 Comparison of modelled and observed surface currents at point 6 (see Fig. 4.1).

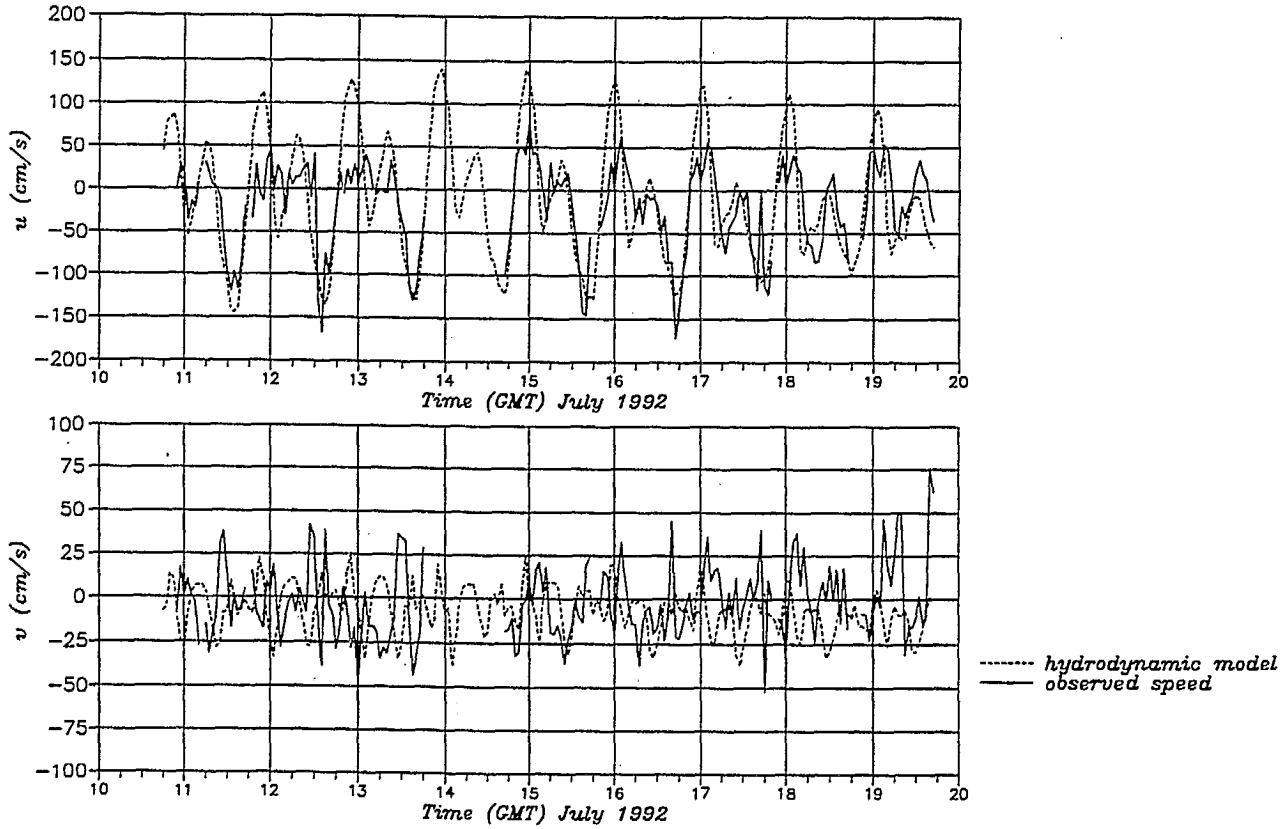

Figure 5.5 Comparison of modelled and observed surface currents at point 2 (see Fig. 4.1).

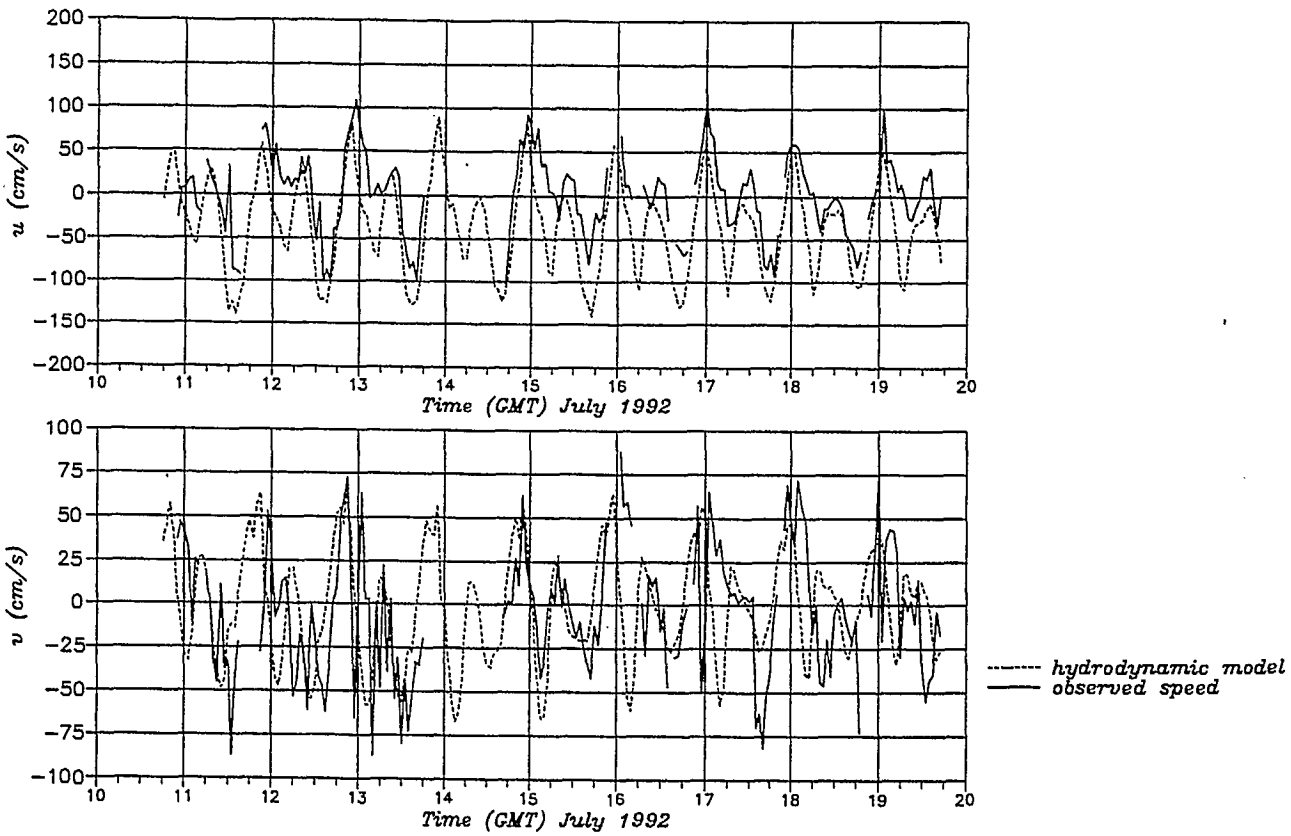

Figure 5.6 Comparison of modelled and observed surface currents at point 3 (see Fig. 4.1).

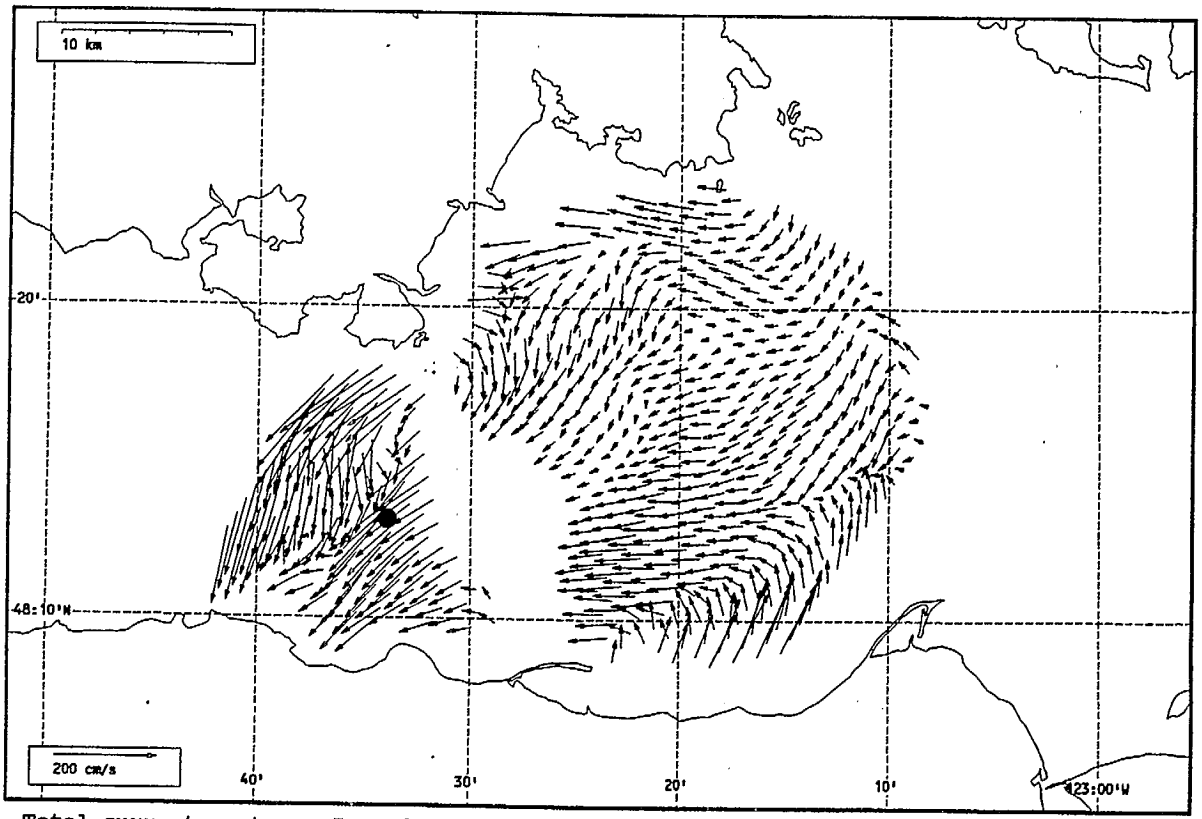

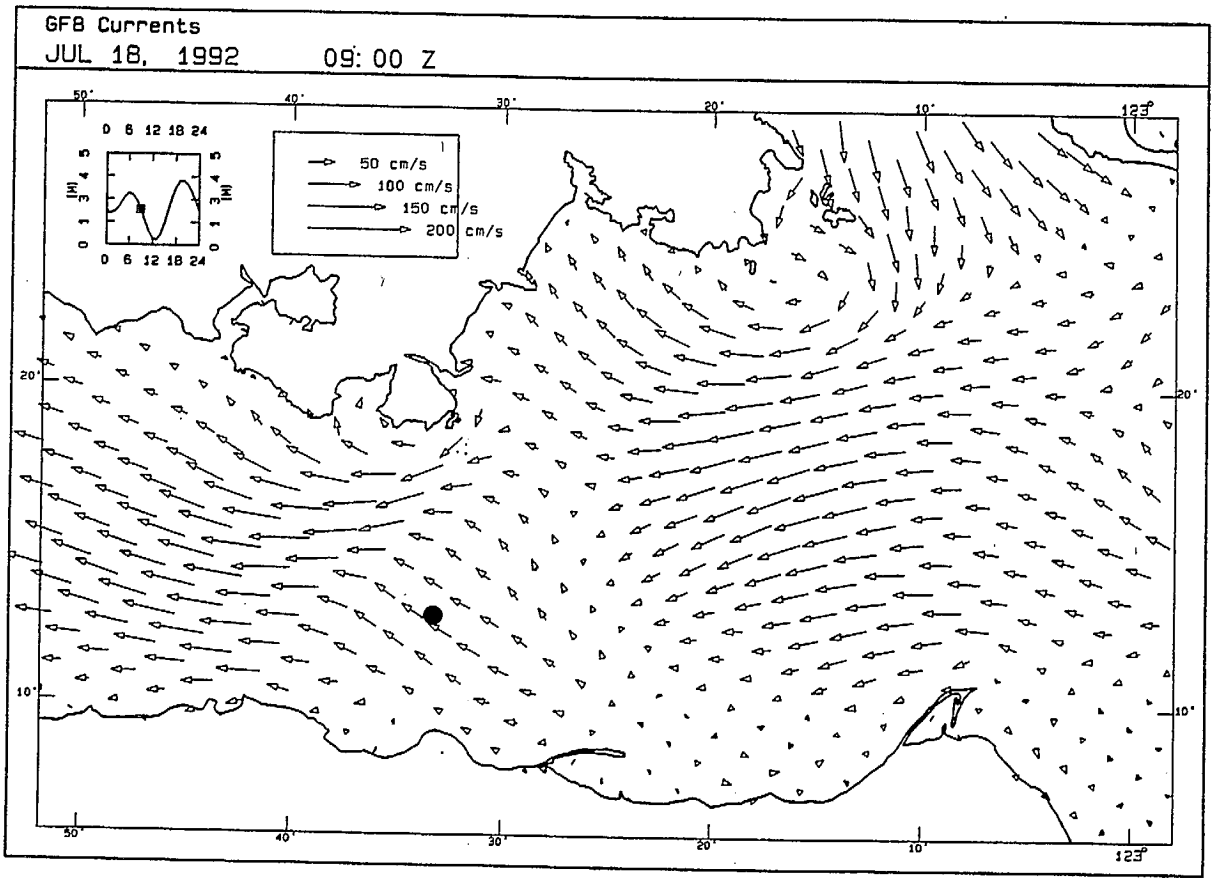

Figure 5.7 Ebb flows observed with the HF radar (upper panel) and modelled (lower panel). (●) time-series comparison point from Fig. 5.4.

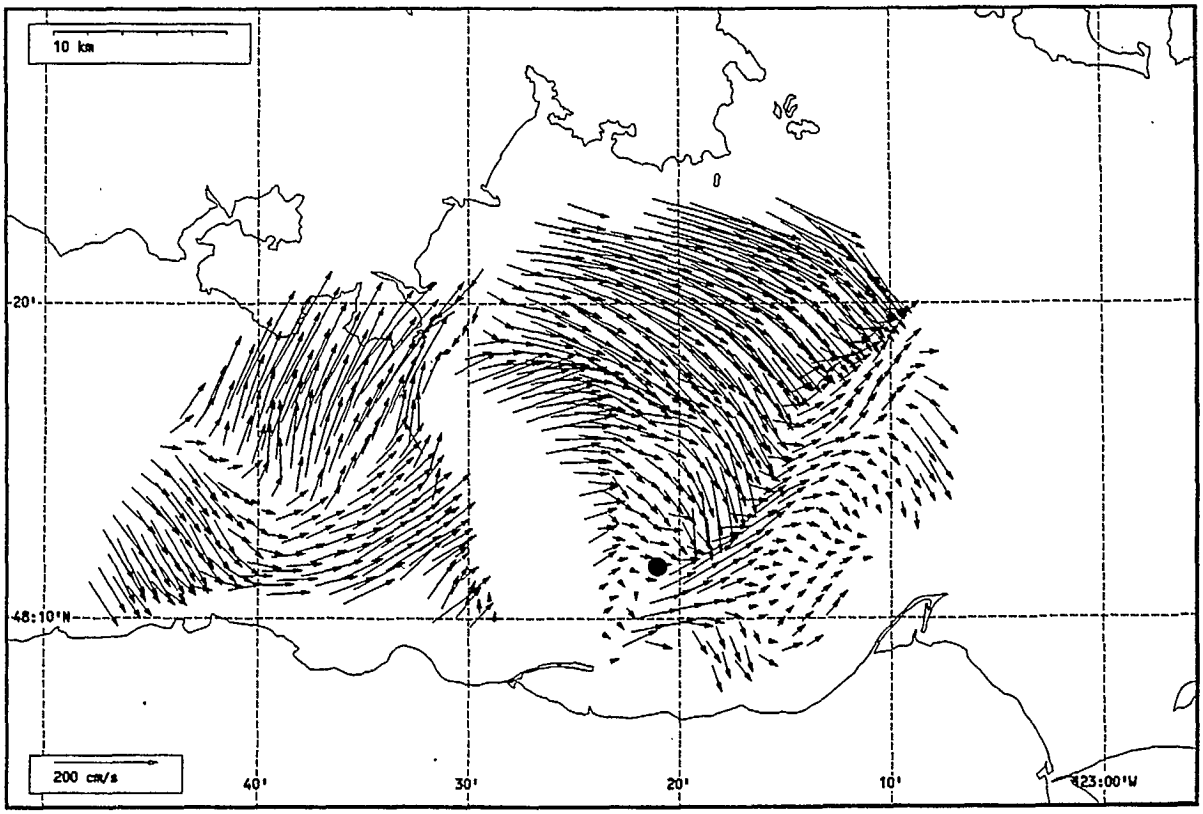

Total current vectors, Juan de Fuca Strait, 1992-07-12 23:00 Z.

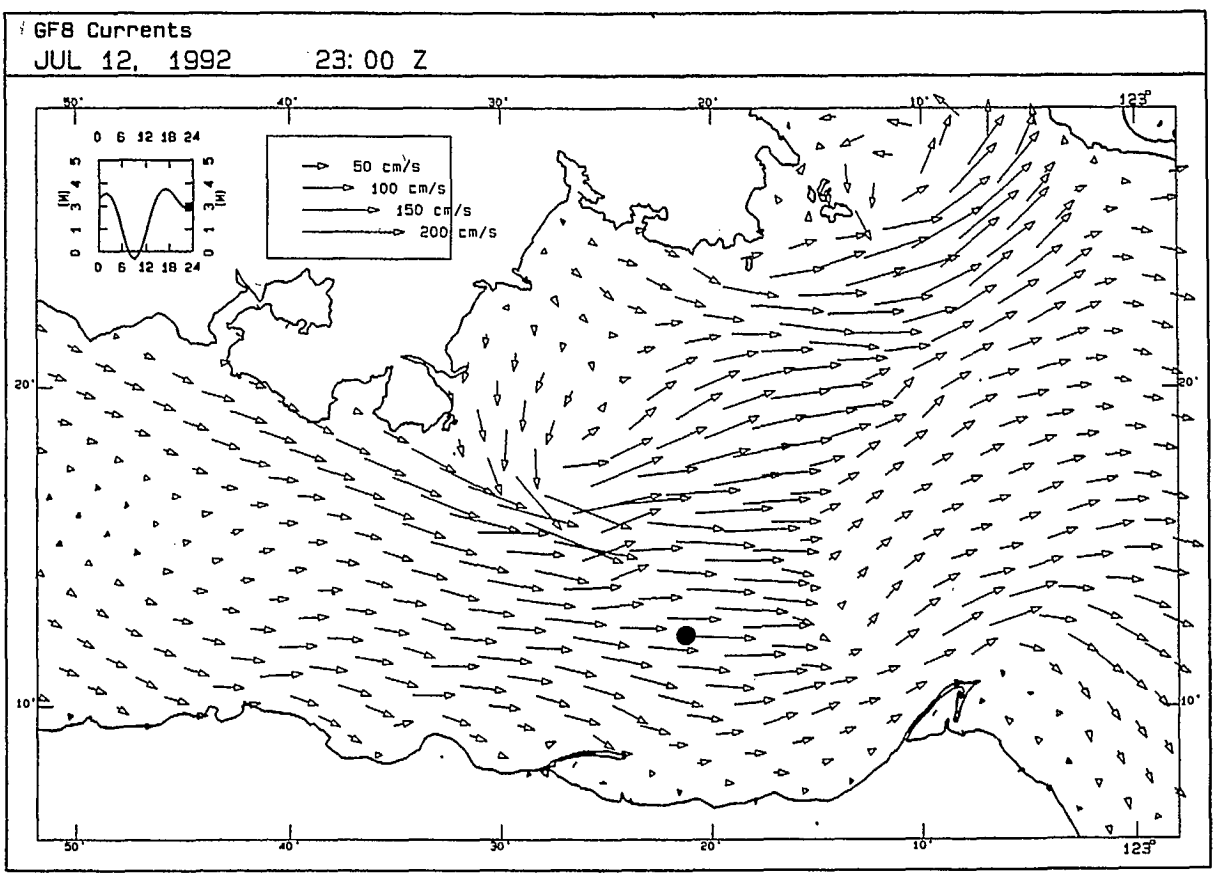

Figure 5.8 Flood flows observed with the HF radar (upper panel) and modelled (lower panel). (●) time-series comparison point from Fig. 5.5.

ebb flow, particularly on the weaker of the two ebbs each day. The model predicts two strong ebbs daily, compared with a much weaker observed flow following higher high water. The reason for this lies in the strongly sheared observed flow patterns, indicating a region of divergence near point 3 for this phase of the tide (Fig. 5.9, upper panel), compared with the smoother, more uniform fields produced by the model (Fig. 5.9, lower panel).

5.3 Discussion of Results

5.3.1 Model Calibration

The smoothness of modelled current fields depends on three factors: (i) horizontal resolution of the coastline and bathymetry; (ii) horizontal eddy viscosity through the value given to A_H; and (iii) vertical eddy viscosity through the value and parameterization of the coefficient A_V. The first two are likely the more important. In GF8 for the present application, A_H was treated as a universal constant and was not a property of the flow; the vertical eddy viscosity did have a bulk Richardson number dependence and, in this way, was a property of the flow, providing a realistic treatment of the process.

Assuming adequate horizontal resolution, the radar data provide an opportunity, for the first time, to examine formulations that make A_H a flow property (linked to the horizontal rate of strain) and to calibrate empirical coefficient in the formulation. Tests against the radar data would then show if such formulations modify the dynamics so as to give closer correspondence in the patterns of surface flow.

This aspect of model improvement is sufficiently important that it should be done before attempting radar data assimilation experiments. Otherwise the model errors would be large, and the perturbation provided from the radar data would be correspondingly large and is likely to slow down convergence of the model to true conditions. Such improvements are also warranted, of course, where models are to be used without radar data input.

5.3.2 Data Assimilation

It is clear that the radar observed currents contain greater small-scale but coherent horizontal structure, in the form of meanders, eddies, and fronts than the current fields from the model. This structure is not at the grid scale of model (2 km) or that of the radar, but has characteristic length scales of a few kilometres. These pattern differences are large enough that numerical experiments comparing slick motion computed with each source of input data would show large differences that increase with time. This type of calculation has been done before (Hodgins et al., 1992) and will not be repeated here.

The modelled currents have been shown to account for much of the observed variance in the flows, and to reproduce the large scale tidal response of the waterway and the distribution of the density fields over seasonal time-scales. Thus, the three-dimensional dynamical model provides a good basis for assimilating radar data in order to improve current predictions.

There are two general approaches to data assimilation: (i) variational/adjoint methods (see e.g. Courtier and Talagrand, 1990; Long and Thacker, 1989a,b), and (ii) sequential methods wherein model solutions are sequentially updated at every time step so as to provide convergence with observations (see e.g. Ghil and Malanotte-Rizzoli, 1991). Sequential

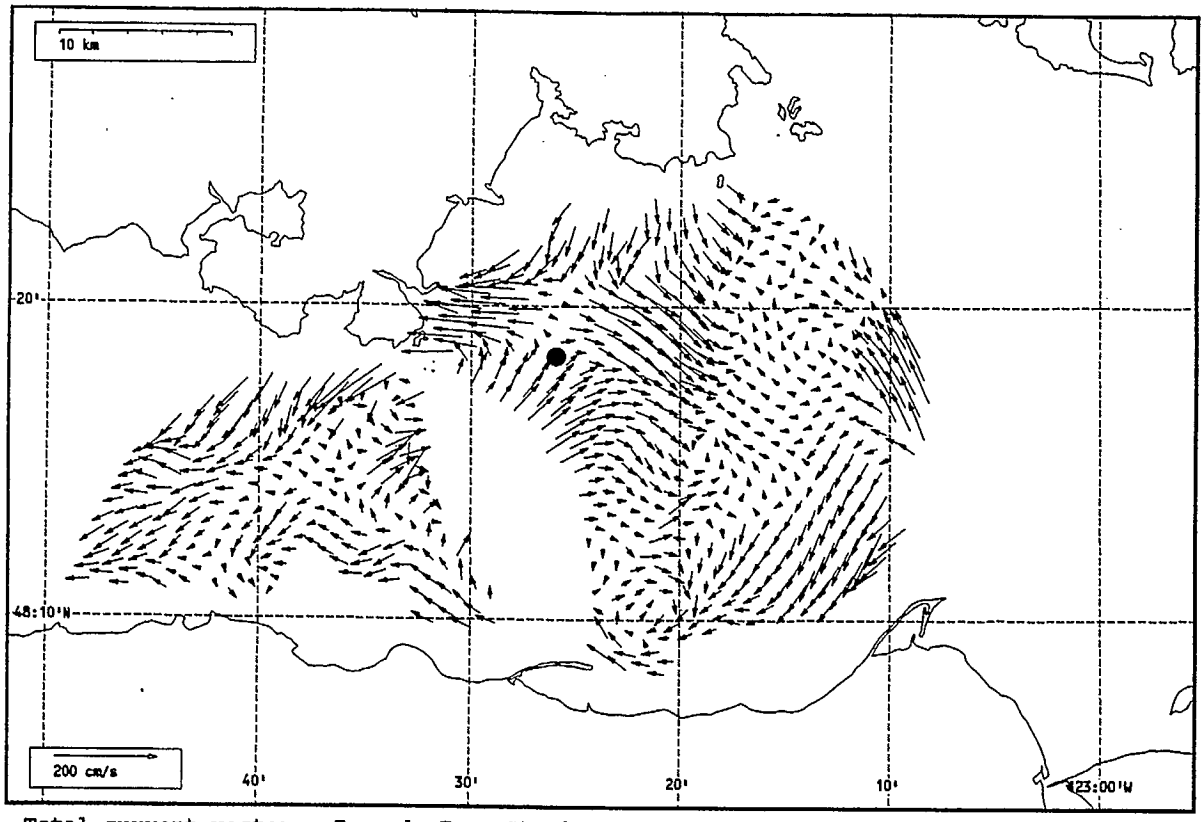

Total current vectors, Juan de Fuca Strait, 1992-07-12 02:00 Z.

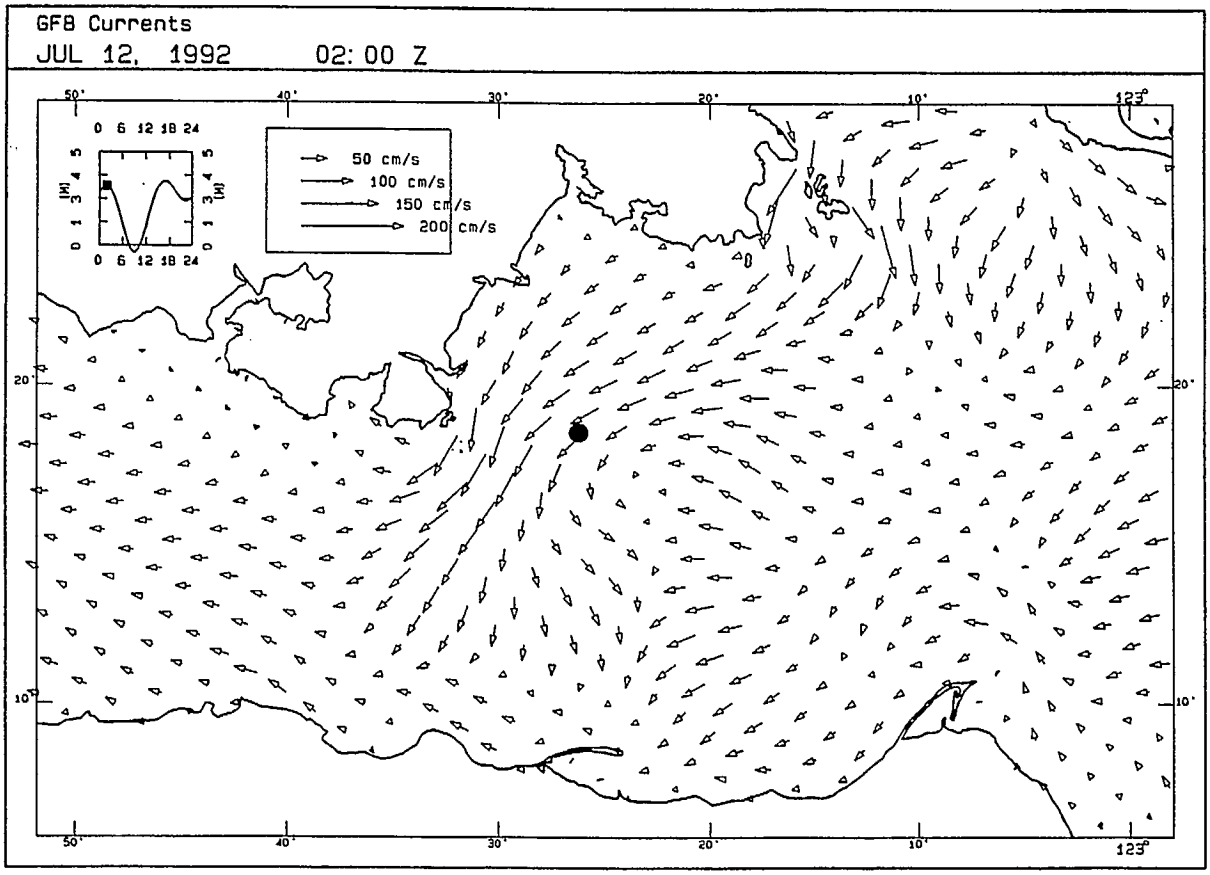

Figure 5.9 High water flow patterns observed with the HF radar (upper panel) and modelled (lower panel). (●) time-series comparison point from Fig. 5.6.

methods range from direct data insertion techniques, which are comparatively crude and may lead to discontinuities, to Kalman filtering methods, which provide optimal linear updates in a least squares sense but which are time-consuming to compute. There are a number of methods that fall in between, such as optimal interpolation (e.g. Rienecker and Miller, 1991) that are simpler to compute and which may be more appropriate to the problem at hand.

To date, methods to assimilate such spatially dense data as are obtained from radar observations into three-dimensional baroclinic ocean models are poorly understood and developed. A review of the latest methods and approaches being taken in this field is recommended, with the objective of identifying a starting algorithm for testing with the HF radar data and the GF8 model. The resulting system would be applicable initially to the Juan de Fuca-Georgia-Puget Sound waterway, but could be formulated generally enough to be widely applied once the benefits are demonstrated.

6.0 CONCLUSIONS

6.1 SeaSonde Performance

The SeaSonde HF radar system successfully collected surface current data in Juan de Fuca Strait over a 21-day period once some of the early problems with power supply and antenna siting were solved. Despite heavy ship and boat traffic through the centre of the coverage area, including the regular ferry run from Port Angeles to Victoria, the ship removal algorithm worked well and there was no detectable data loss to ship spike interference. Similarly, little or no RF interference was noticed.

Communications between the radar sites and the Vancouver central site computer were not effective and precluded true real-time operation. The successful test at Race Rocks with the Infosat satellite link indicates that the technology is available and will function well for remote sites without telephone service. To date the multi-site polling capability of the Infosat product has not been evaluated with SeaSonde. Cellular telephone technology was also tested at Port Angeles, without success; however, the number of opportunities to work on this data link were limited. It appears that better communications software, and some customization for the cellular network, will solve the problems encountered and more effort in this direction is warranted.

At 12.5 MHz maximum ranges varying from about 15 km to over 30 km. The sea echo returns at both radars were correlated with wind speed, which is consistent with better Bragg scattering wave heights at higher wind speeds. A higher transmit frequency, in the range of 20 to 30 MHz, is expected to achieve more consistent performance without a critical sacrifice in total range for the Straits of Juan de Fuca and Georgia. The higher frequency produces Bragg resonance from shorter waves that are likely to be more prevalent at lower winds in the inner waterway. The 12 to 13 MHz frequency range is expected to function well over more open-ocean conditions.

Analysis of the measured currents revealed a great deal of small-scale structure to the flows in this area, characterized by large shear in the current speeds. The SeaSonde parameters are not ideal for these conditions, and although hard to demonstrate, it is suspected that some features were under-resolved in more distant range rings. An increase in HF radar resolution is thus warranted for this area, in terms of both range ring spacing and azimuth angle spacing.

A change in transmission frequency and range ring spacing can be accommodated with minor impact to the SeaSonde hardware design, and an improved method for radial current extraction at smaller angle increments can be made in software.

6.2 Current Prediction

Currents in the coverage area are dominated by the tide. The tidal component can be successfully predicted using harmonic analysis. However, the residual current, including here the wind-driven part, was found to be poorly autocorrelated at lags of an hour and more. Consequently, the residual is essentially unpredictable using autoregressive models, and is random for all practical purposes. Since this random component is associated with the eddy-meander features of the flow fields it is largely responsible for horizontal turbulent mixing of a floating slick.

The SeaSonde data can be used to isolate this residual, and hence to provide a quantitative estimate of the RMS turbulent velocities that can be used to scale calculations of horizontal slick diffusion in spill models. The magnitude of the random component can be expected to vary spatially; thus, the radar data provide a unique means of mapping and predicting not only the tidal part, which accounts for most of the flow, but also for characterizing the horizontal spreading.

The conclusions reached here are based on one time-series from the centre of the coverage area. The analysis of the present data set should be extended to: (i) include all points with good data; (ii) examine the wind-residual correlation to see if more of the variance can be accounted for by the wind; (iii) calculate the Eulerian RMS velocity fluctuations; (iv) relate the Eulerian turbulent statistics to Lagrangian statistics; and (v) develop and test dispersion models using the whole dataset. The last step would involve numerical diffusion calculations scaled by the Lagrangian statistics and an assessment of whether the results are reasonable. The chip slick behaviour can be used as a guide in this assessment.

The outcome is expected to be a workable algorithm for predicting Lagrangian motion from analysis of HF remotely-sensed currents, both the slowly-varying and fluctuating parts, in a way that directly inputs to oil spill models.

6.3 SeaSonde-GF8 Model Current Comparisons

Comparison of time-series and current maps revealed that the GF8 numerical hydrodynamic model was well correlated with observations in terms of the tidal phase and amplitude, particularly in the EW direction, aligned with the channel. The agreement was poorer in the cross-channel NS direction, where both model and observations tend to be noisier.

In general, the model solutions are smoother than observed, and lack some of the smaller scale meanders and eddies found in the radar data. Fronts do form in the modelled fields, and coincide approximately in time and location with some observed features. However, the dissimilarity of the horizontal flow patterns at finer scales accounts, in large measure, for the differences in time-series examined at various locations, and would produce substantial differences in dispersion patterns for slicks.

The smoothness of the modelled fields results, in part, from the parameterization of horizontal eddy viscosity A_H and the relatively large, spatially uniform value given to it (200 m^2/s). In order to improve understanding of modelling flow dynamics, the radar dataset should be used to test better formulations for the horizontal eddy viscosity and the empirical coefficient. The testing could be carried out with the GF8 model, since there are no limiting restrictions in its formulation and the physics contained in the governing equations. The information gained would apply to all similarly formulated models, and would not be restricted to GF8. The following steps are recommended:

(a) Nest a 1-km grid subregion into the larger model grid to cover the area of interest around Victoria-Port Angeles. This finer grid would relieve concerns about bathymetric resolution.

(b) Formulate the lateral stress terms $((A_H\ u,v)_x)_x$ and $((A_H\ u,v)_y)_y$ in terms of local flow variables (strain rate).

(c) Run a series of numerical experiments adjusting A_H to give solutions matching the radar data to minimize differences. Some thought must be given to the function to be minimized since we are seeking a correspondence in the two-dimensional flow patterns.

Assuming the model converges to the measured fields in some systematic sense, then the model provides a basis for surface current data assimilation. These tests on the best formulation for horizontal dissipation are important since the expected improvement in model accuracy will greatly facilitate whatever assimilation scheme is adopted.

Combining modelling with radar data assimilation is expected to give better predictive capability than data alone (as examined in this study), and the means to extend the measured fields spatially, and to finer scales. Data assimilation schemes for the spatially dense data obtained from HF radars and baroclinic hydrodynamic models are poorly understood and will require further research to arrive at a scheme that is both computationally fast enough and convergent to the correct result. A review and assessment of potential schemes is recommended.

7.0 REFERENCES

Abraham, B. and J. Ledolter, 1983. *Statistical Methods for Forecasting*. John Wiley & Sons, New York.

Anon., 1979. Curve and Surface Fitting Using Splines Under Tension. University of British Columbia Computing Centre.

Courtier, P. and O. Talagrand, 1990. Variational Assimilation of Meteorological Observations with the Direct and Adjoint Shallow-water Equations. *Tellus*, **42A**(5), 531-549.

Crean, P.B. and A. Ages, 1971. Oceanographic Records from Twelve Cruises in the Strait of Georgia and Juan de Fuca Strait, 1968, Vol. 1-5. Unpublished Manuscript, Department of Energy, Mines and Resources, Canada.

Foreman, M.G.G., 1978.Manual for Tidal Currents Analysis and Prediction. Pacific Marine Sciences Report 78-6, Unpublished Manuscript, Institute of Ocean Sciences, Patricia Bay, Canada.

Ghil, M. and P. Malanotte-Rizzoli, 1991. Data Assimilation in Meteorology and Oceanography. *Adv. Geophys.*, 33, 141-266.

Godin, G., 1972. *The Analysis of Tides*. University of Toronto, Toronto.

Hardy, J.S., D.S. Dunbar and D.O. Hodgins, 1989. An Evaluation of Methods for Extracting Surface Currents from CODAR Data. Proc. IGARRS '89, 12th Canadian Symposium on Remote Sensing, Vancouver, Canada.

Hodgins, D.O., 1991. New Capabilities in Real-time Oil Spill and Fate Prediction Using HF Radar Remote Sensing. Proc. 14th AMOP Technical Seminar, June 12-14, 1991, Vancouver, Canada.

Hodgins, D.O., J-H. Huang, D.S. Dunbar and S.L.M. Hodgins, 1991. A High-resolution Coupled Hydrodynamic and Oil Spill Modelling System Applied to the Port of Vancouver. Proc. Arctic and Marine Oilspill Program (AMOP) Technical Seminar, June 1991, Vancouver.

Hodgins, D.O. and J.S. Hardy, 1992. Surface Current Data from Queen Charlotte Sound, B.C., Intercomparison of SeaSonde and Drifter Current Observations. Prepared for Fisheries & Oceans, Canada, Canadian Coast Guard, and Environment Canada by Seaconsult Marine Research Ltd.

Hodgins, D.O. J.H. Huang and M.F. Fingas, 1992. Oil Spill Modelling Using remote Sensed Surface Currents. Proc. Arctic and Marine Oilspill Program (AMOP) Technical Seminar, June 1992, Edmonton, 381-405.

Hodgins, D.O., 1992. The SeaSonde High-frequency Radar System for Surface Current Measurements. Proc. Third ASEAN Science and Technology Week, Singapore, Sept. 20-22, 1992.

Jenkins, G. M. and D. G. Watts, 1968. *Spectral Analysis and its Applications*. Holden-Day, San Fransisco.

Leise, J.A., 1984. The Analysis and Digital Signal Processing of NOAA's Surface Current Mapping System, *IEEE J. Ocean. Eng.*, **OE-9**(2), 106-113.

Lipa, B.J. and D.E. Barrick, 1983. Least-Squares Methods for the Extraction of Surface Currents From CODAR Crossed-Loop Data: Application at ARSLOE. IEEE *J. Oceanic Eng.*, **OE-8**(4), 226-253.

Long, R.B. and W.C. Thacker, 1989a. Data Assimilation into a Numerical Equatorial Ocean Model, I, The Model and the Assimilation Algorithm. *Dyn. Atmos. Oceans*, **13**(3-4), 379-412.

Long, R.B. and W.C. Thacker, 1989a. Data Assimilation into a Numerical Equatorial Ocean Model, II, Assimilation Experiments. *Dyn. Atmos. Oceans*, **13**(3-4), 413-439.

Rienecker, M.M. and R.N. Miller, 1991. Ocean Data Assimilation Using Optimal Interpolation with a Quasi-geostrophic Model. *J. Geophys. Res.*, **96**(C8), 15,093-15,103.

Stronach, J.A., 1991. The Development of GF8: A Three-dimensional Numerical Model of the Straits of Georgia and Juan de Fuca. Unpublished report prepared for Fisheries & Oceans Canada by Seaconsult Marine Research Ltd., Vancouver.

Tayfun, M.A. and H. Wang, 1973. Monte Carlo simulation of oil slick movements. *J. Waterways, Harbors and Coastal Engineering Div.*, ASCE, **WW3**, 309-324.

APPENDIX 1: SURFACE CURRENT MAPS

The following hourly surface current maps were measured using the SeaSonde HF radar between July 6, 1992 and July 31, 1992. The maps are presented chronologically, and each map is identified by data and time (GMT).

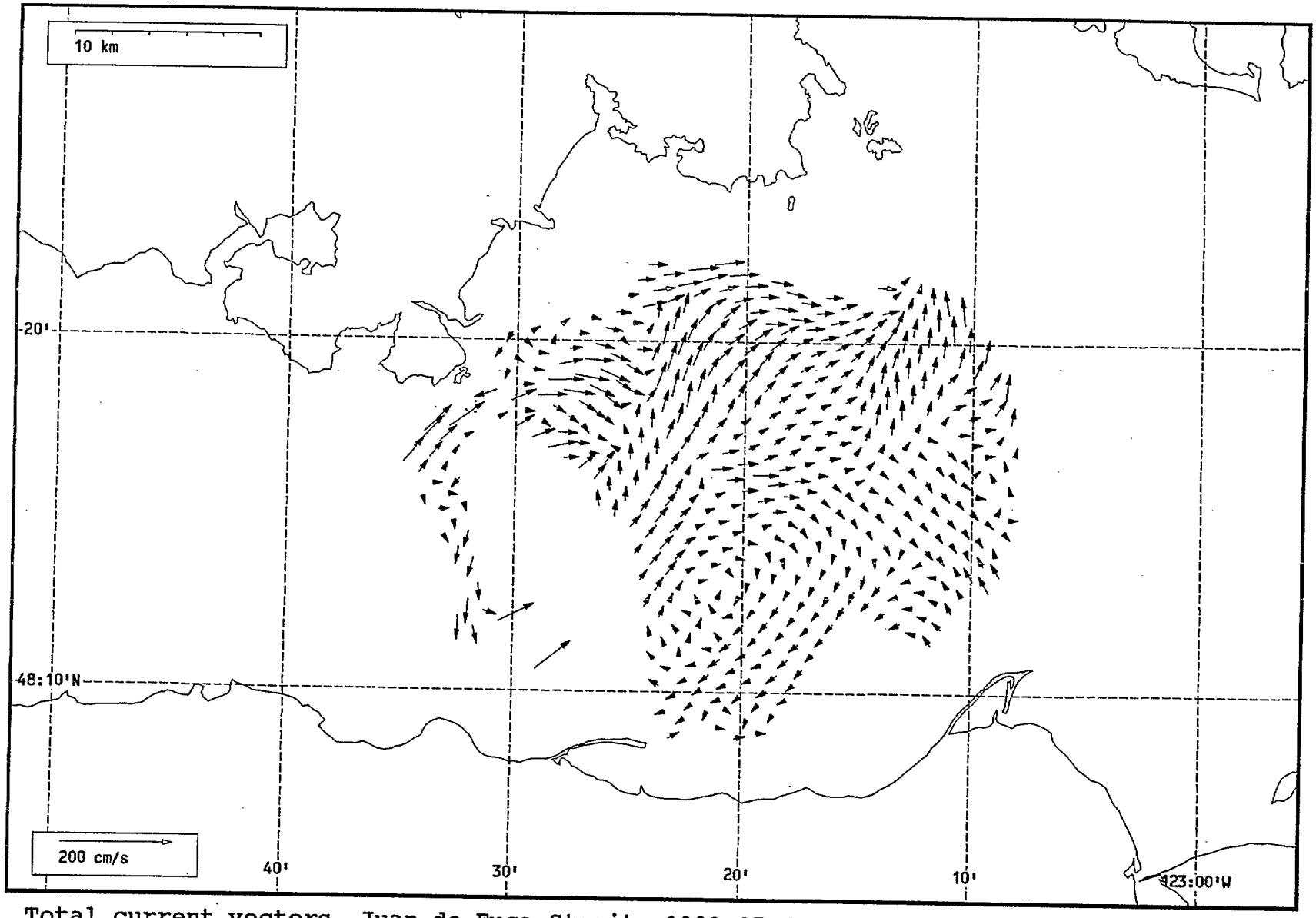

Total current vectors, Juan de Fuca Strait, 1992-07-6 17:00 Z.

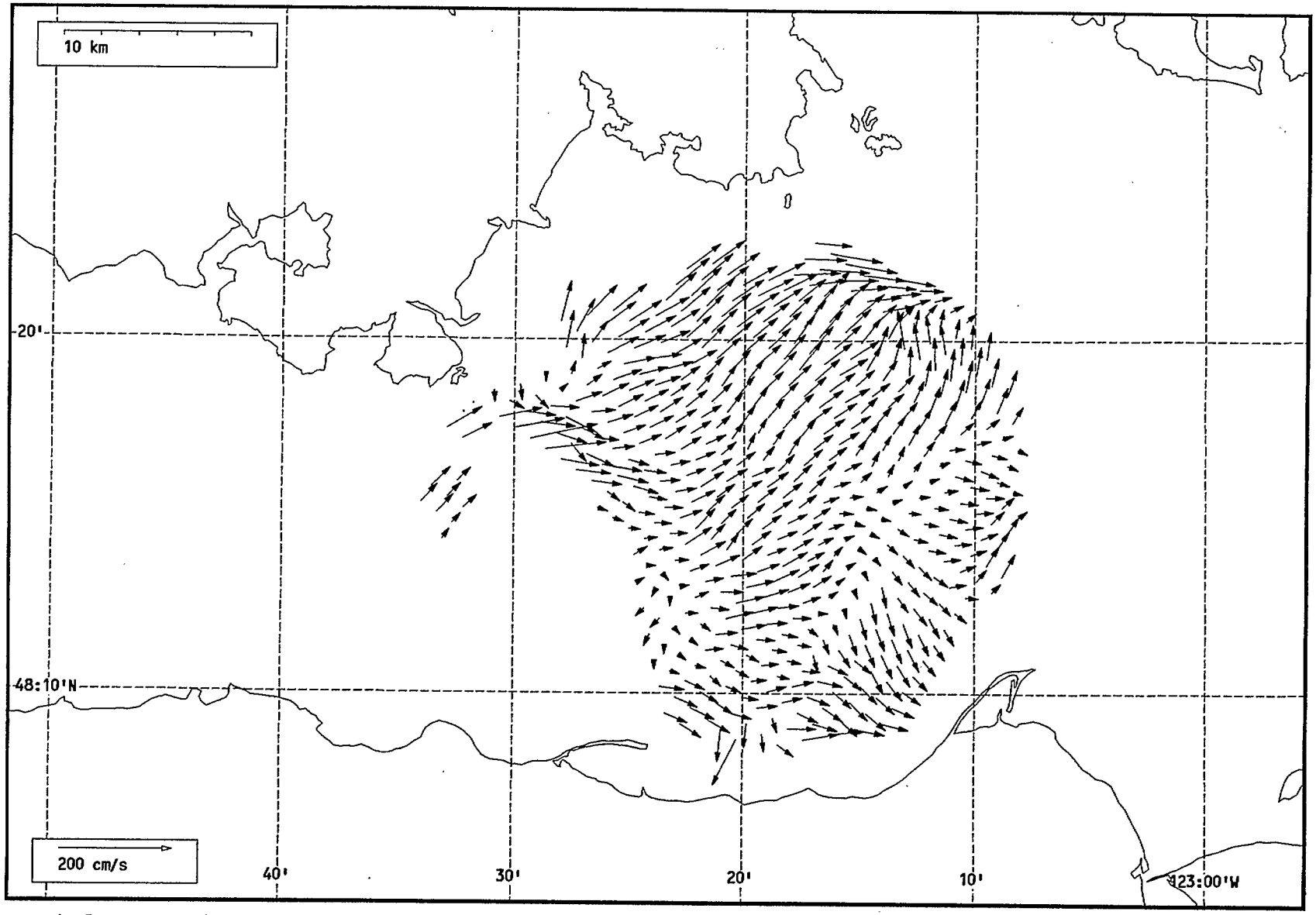

Total current vectors, Juan de Fuca Strait, 1992-07-7 17:00 Z.

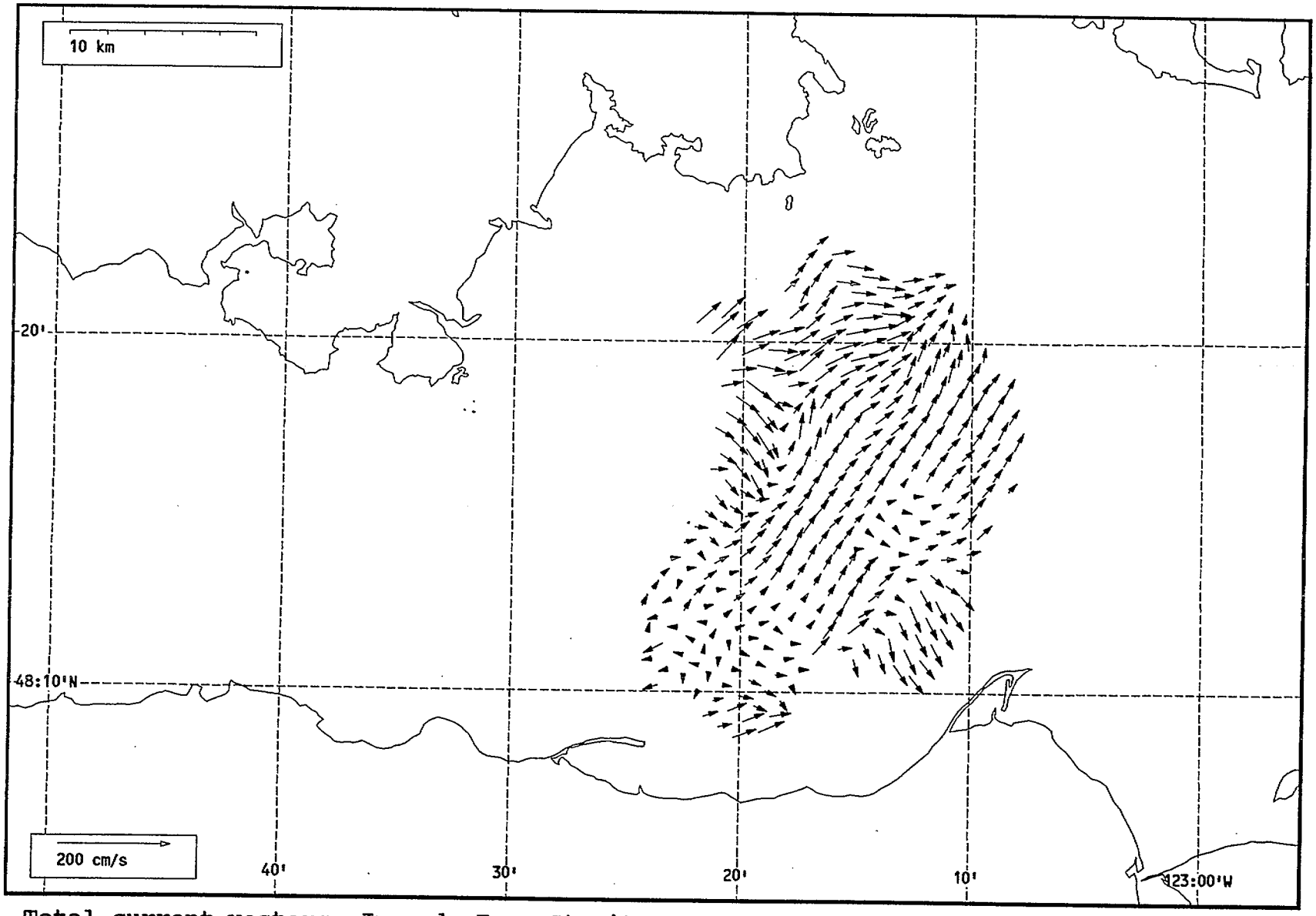

Total current vectors, Juan de Fuca Strait, 1992-07-7 18:00 Z.

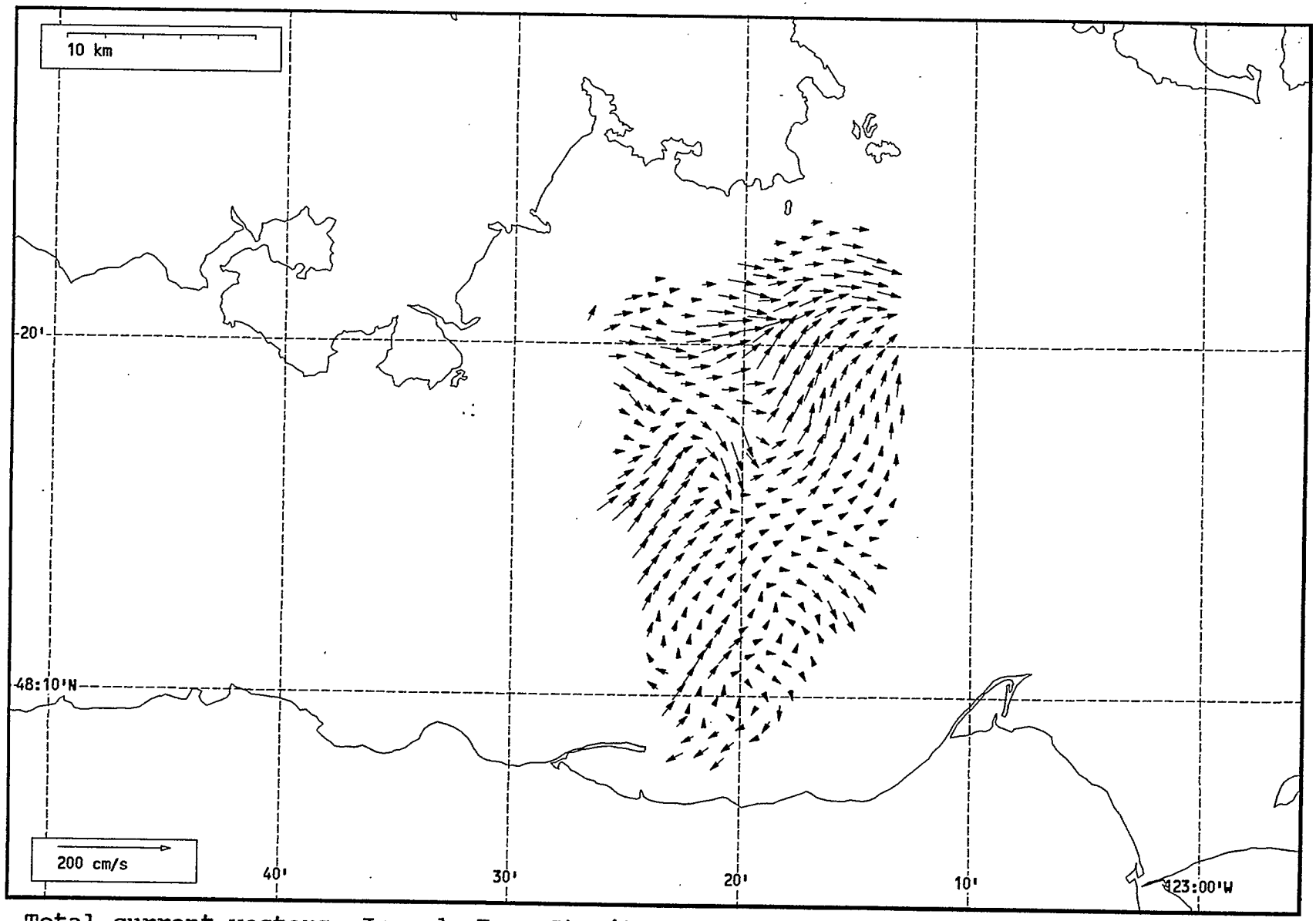

Total current vectors, Juan de Fuca Strait, 1992-07-7 19:00 Z.

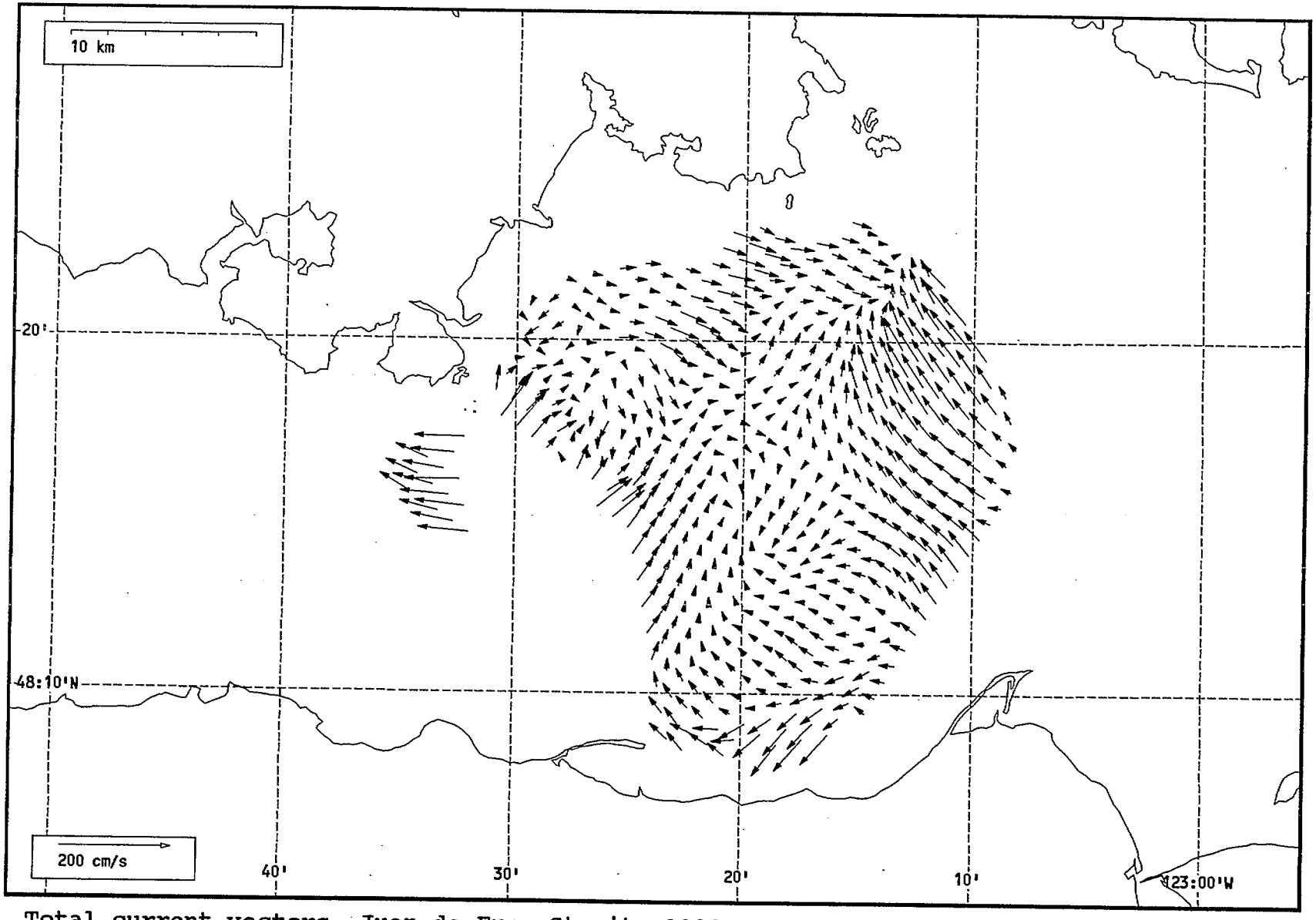

Total current vectors, Juan de Fuca Strait, 1992-07-7 20:00 Z.

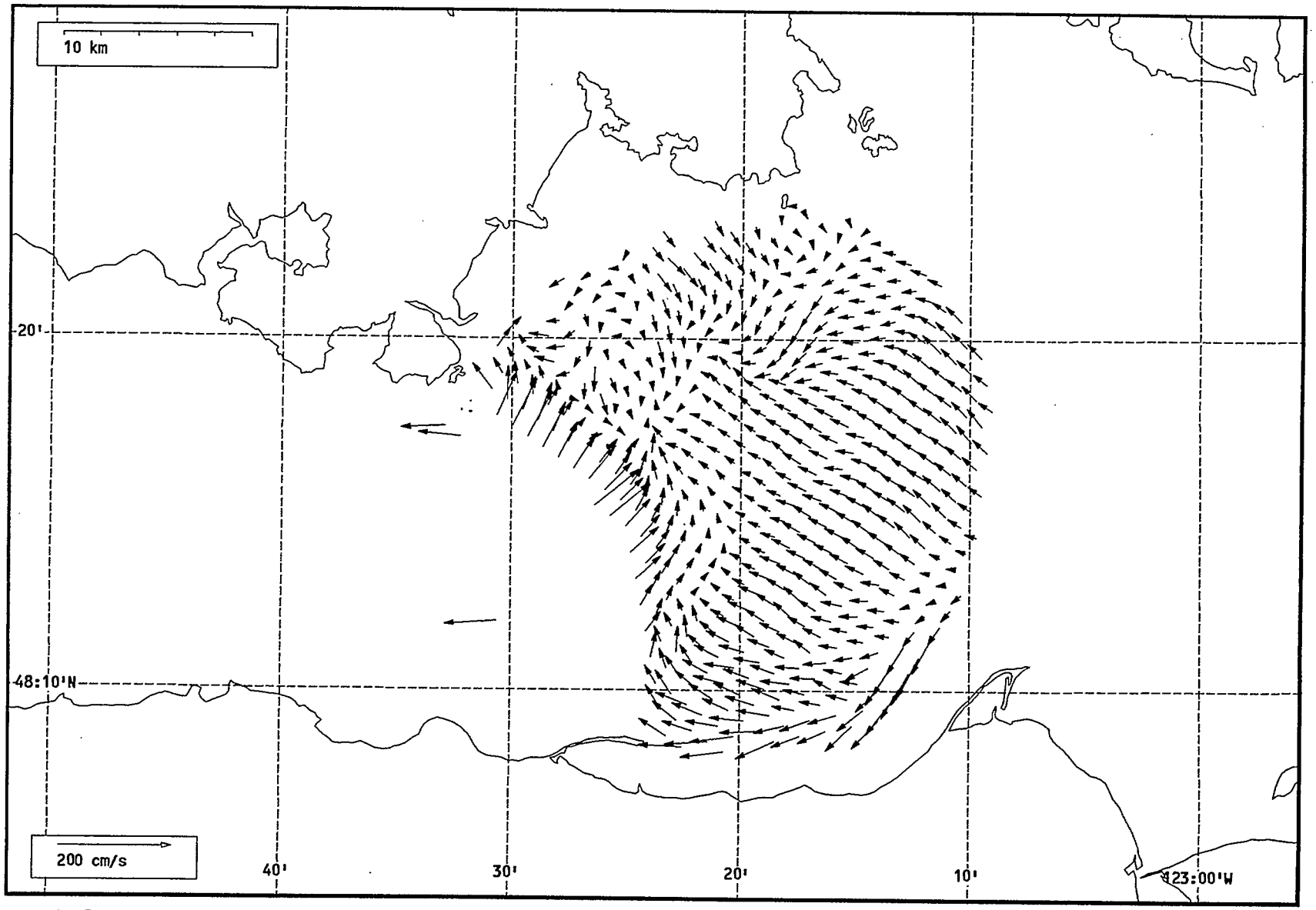

Total current vectors, Juan de Fuca Strait, 1992-07-7 21:00 Z.

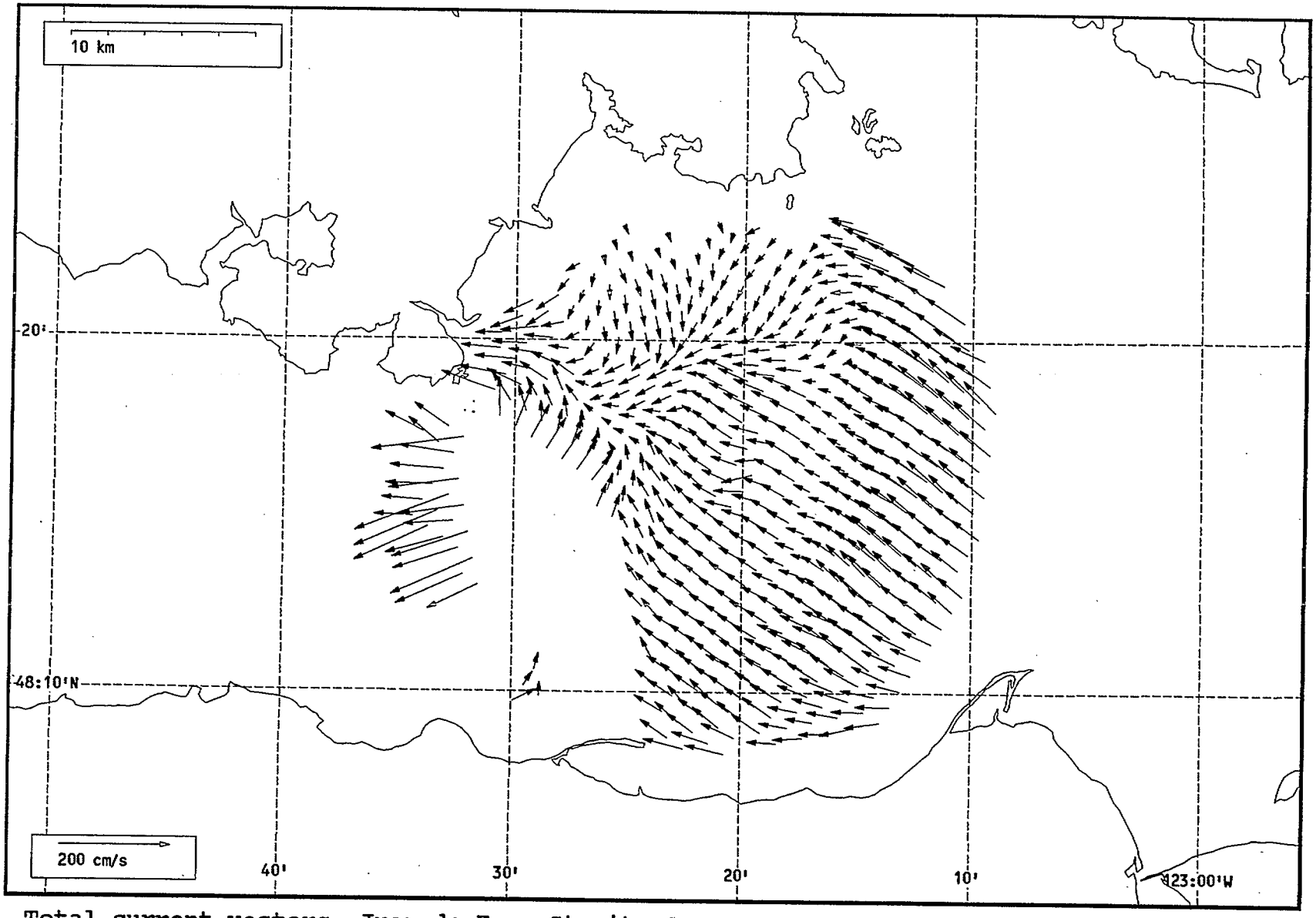

Total current vectors, Juan de Fuca Strait, 1992-07-7 22:00 Z.

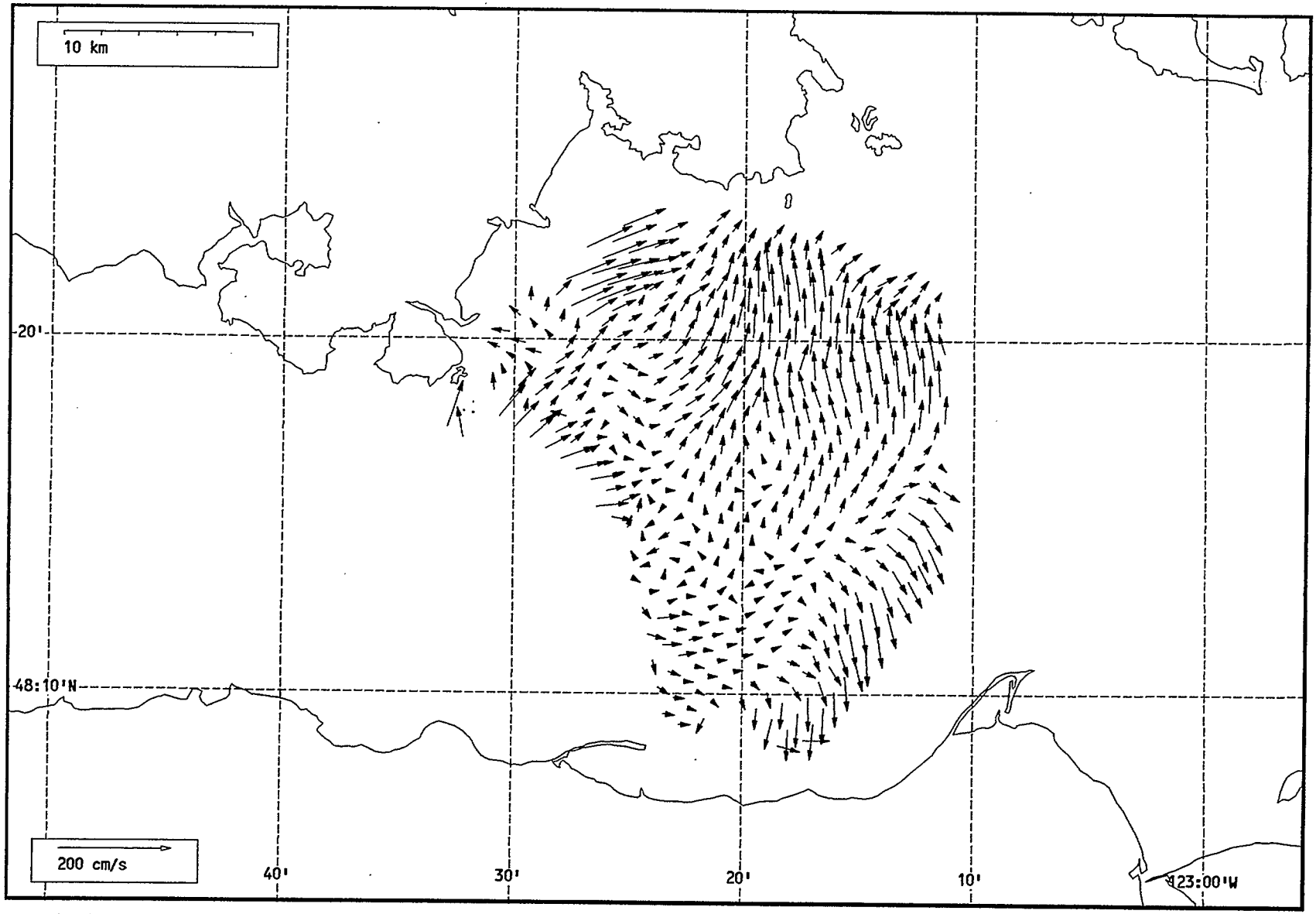

Total current vectors, Juan de Fuca Strait, 1992-07-8 16:00 Z.

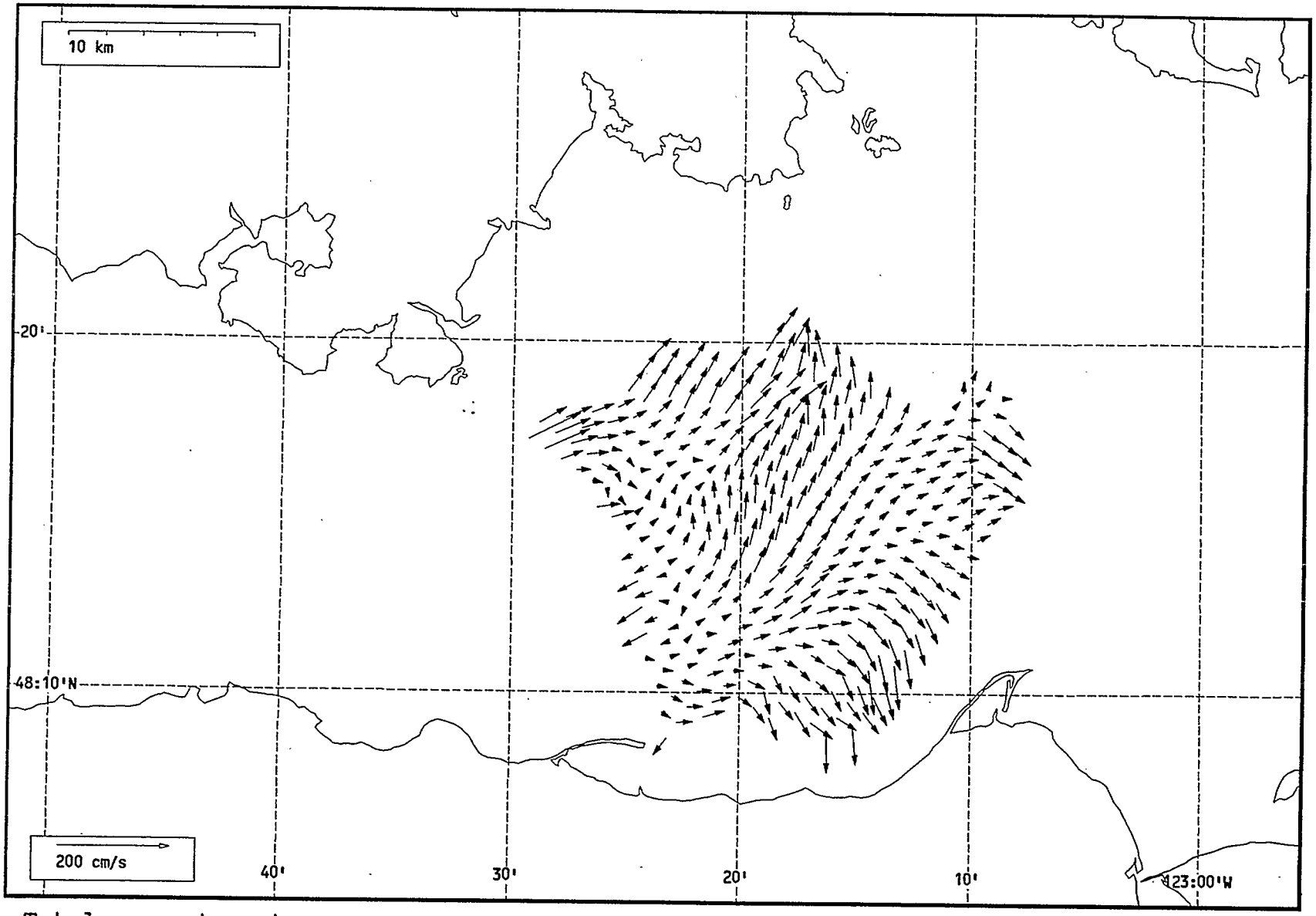

Total current vectors, Juan de Fuca Strait, 1992-07-8 17:00 Z.

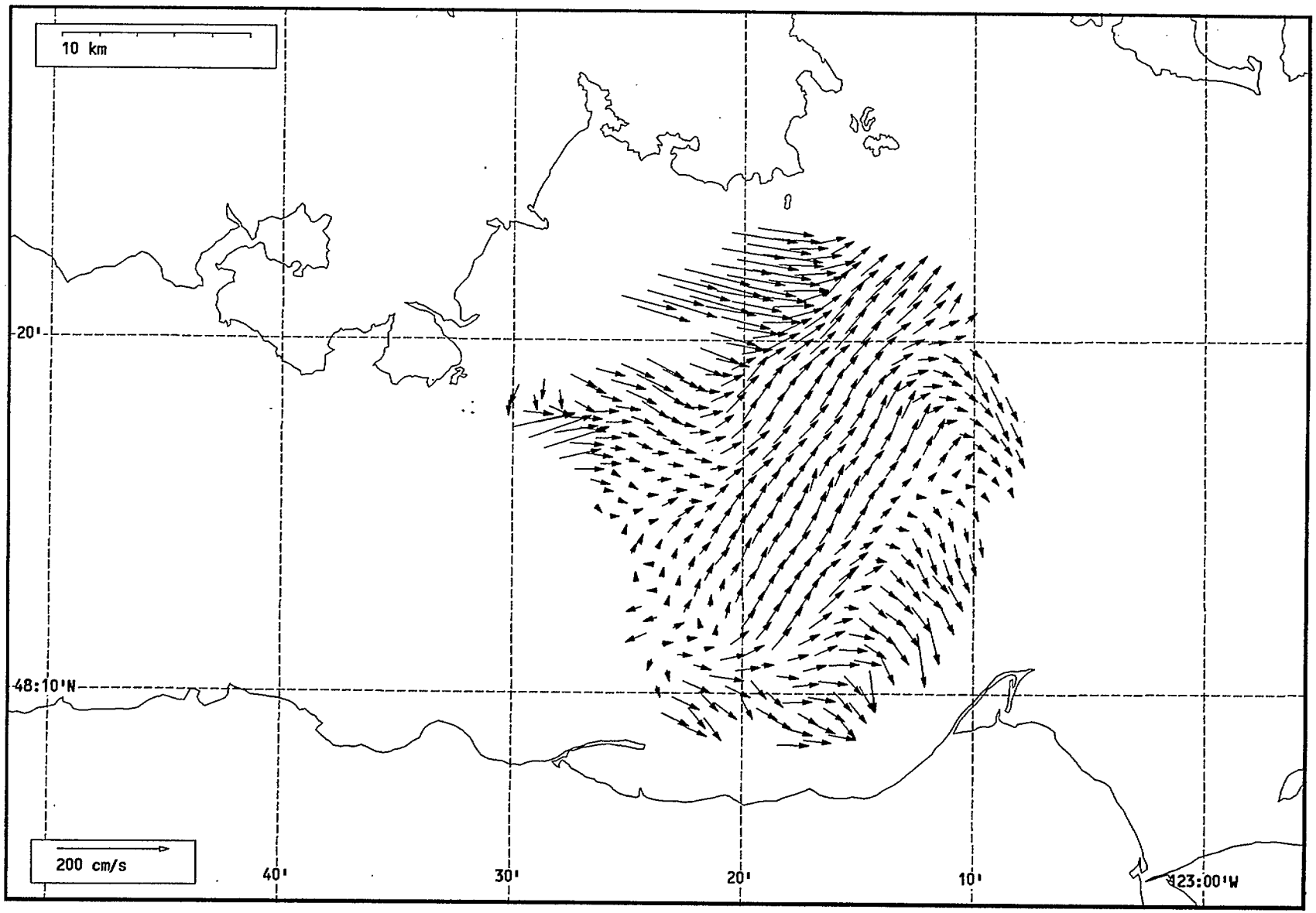

Total current vectors, Juan de Fuca Strait, 1992-07-8 18:00 Z.

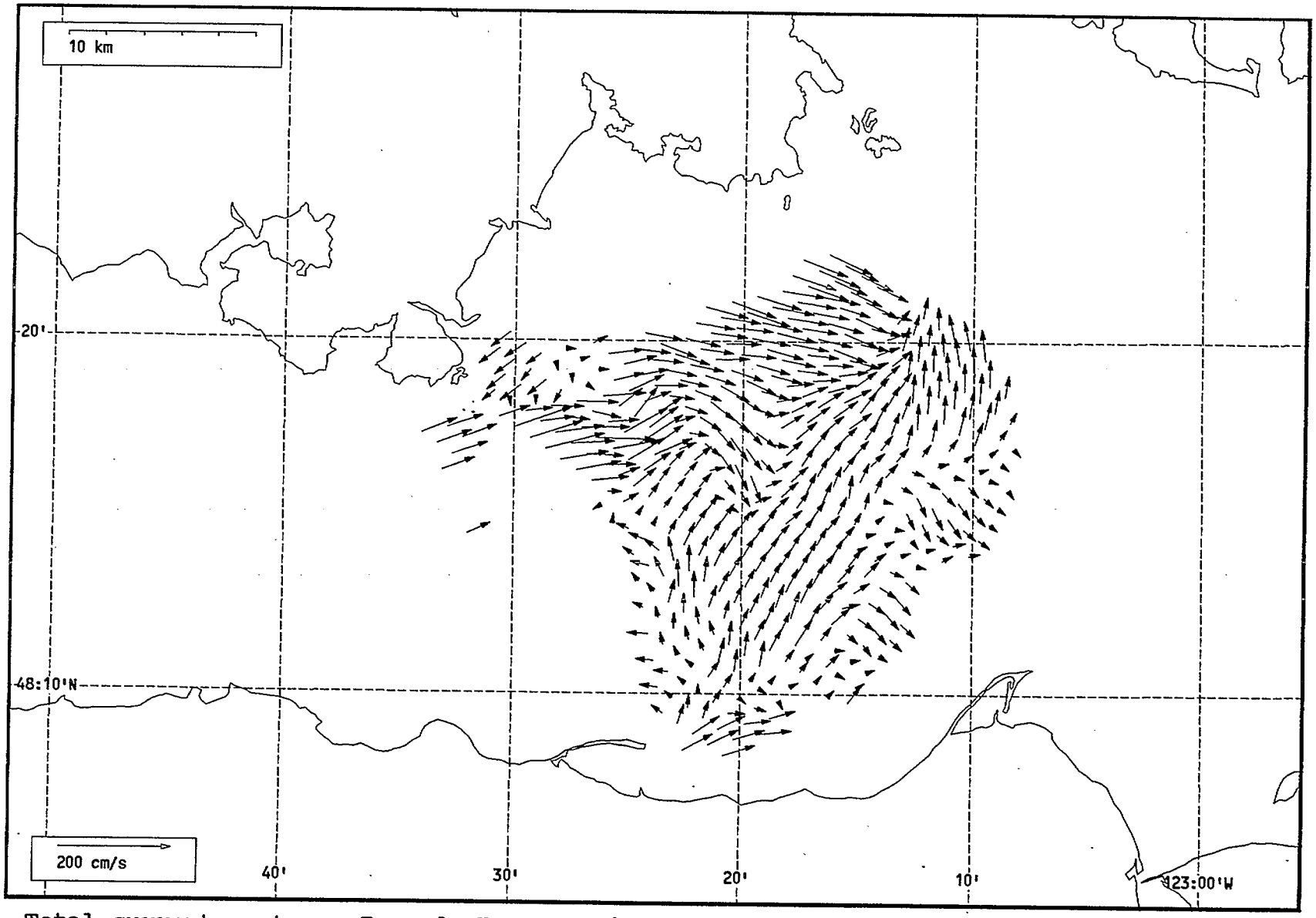

Total current vectors, Juan de Fuca Strait, 1992-07-8 19:00 Z.

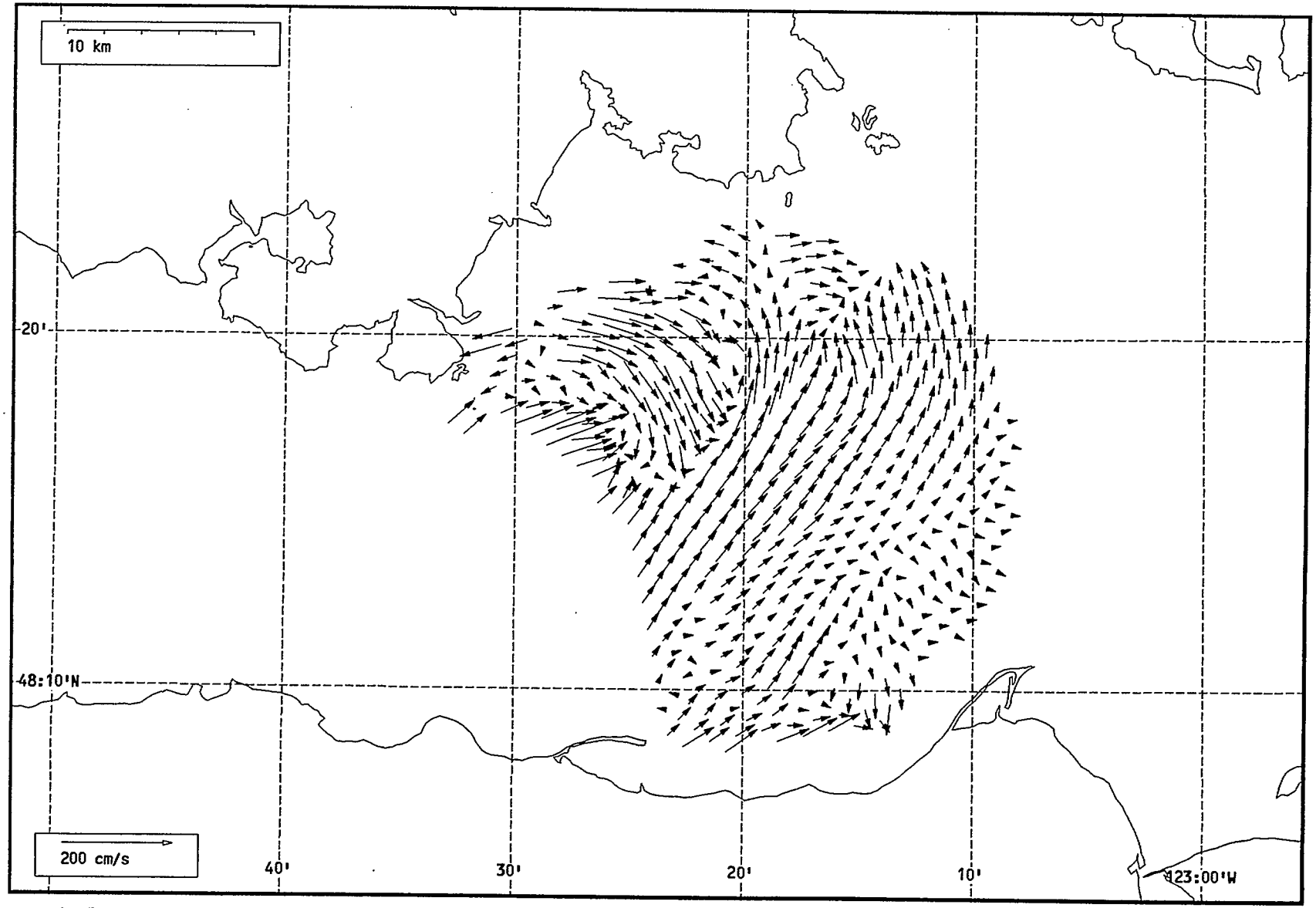

Total current vectors, Juan de Fuca Strait, 1992-07-8 20:00 Z.

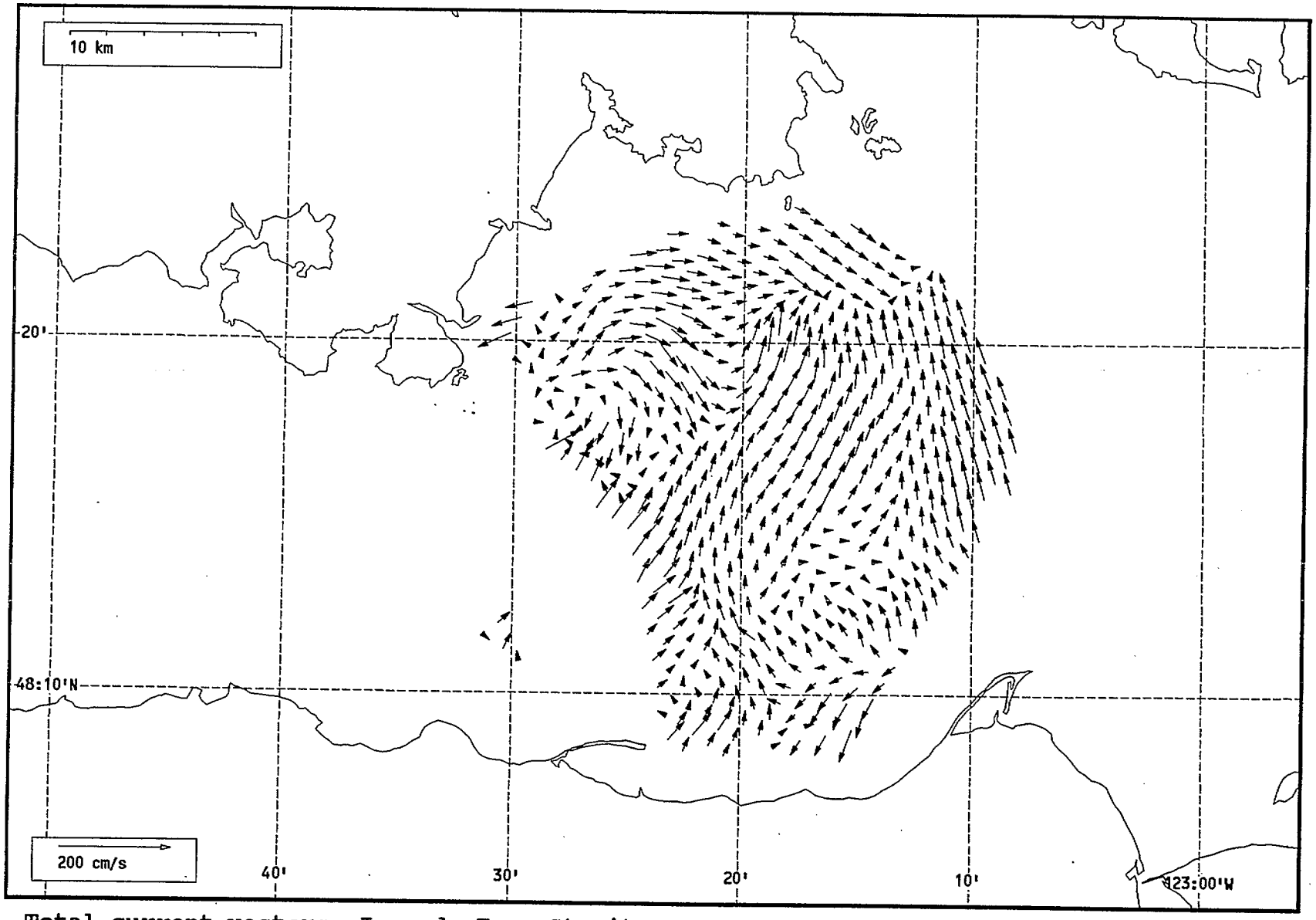

Total current vectors, Juan de Fuca Strait, 1992-07-8 21:00 Z.

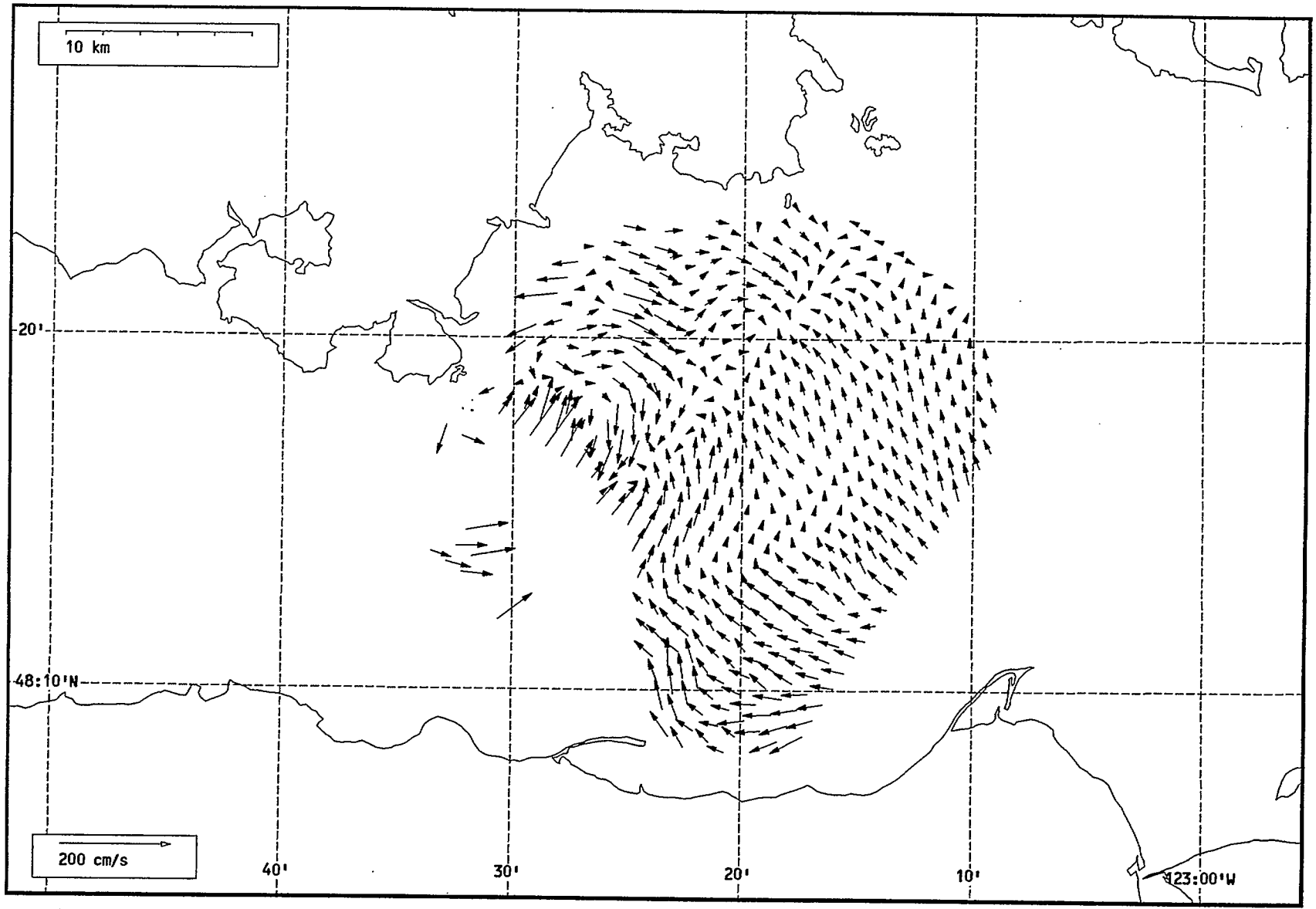

Total current vectors, Juan de Fuca Strait, 1992-07-8 22:00 Z.

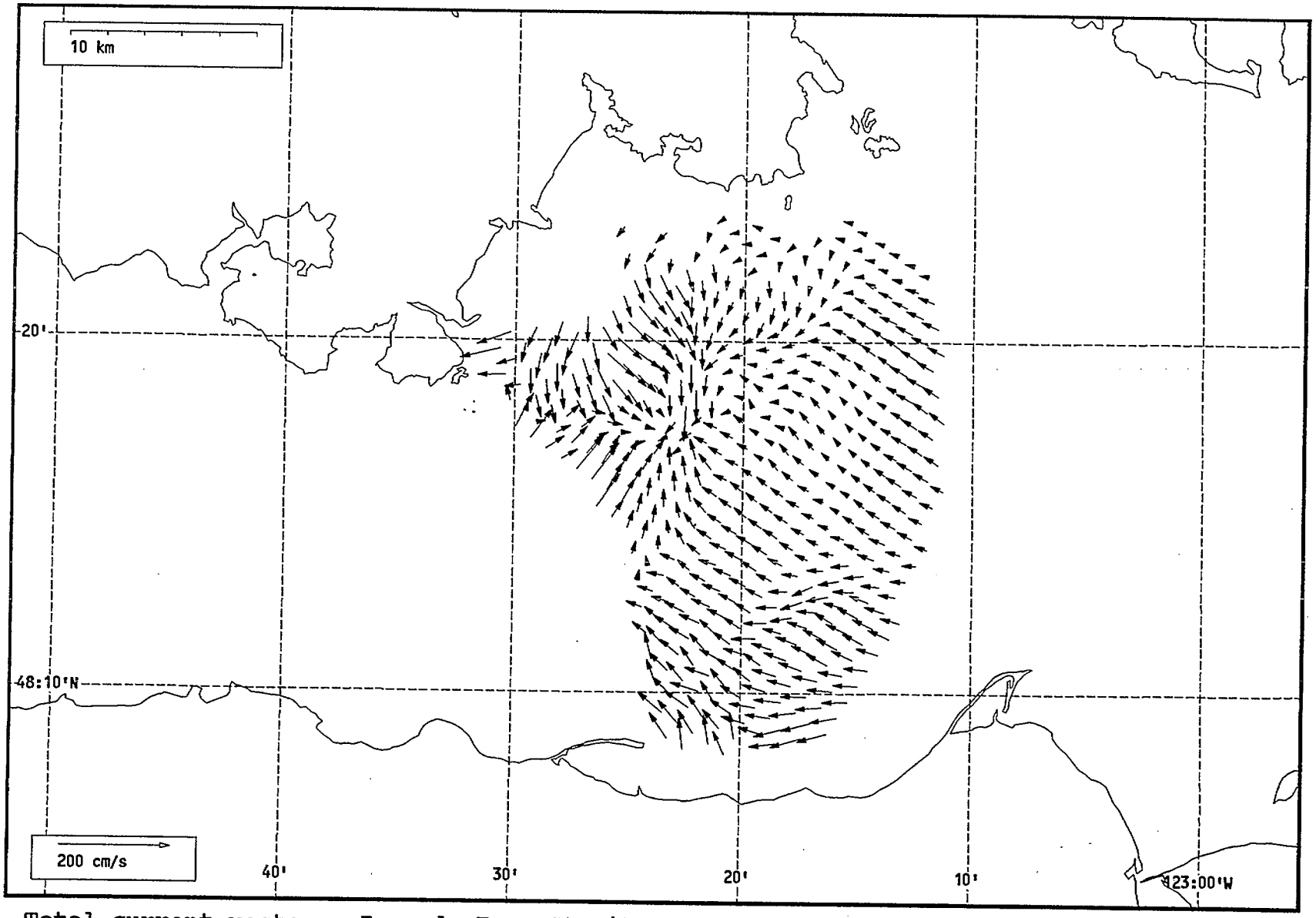

Total current vectors, Juan de Fuca Strait, 1992-07-8 23:00 Z.

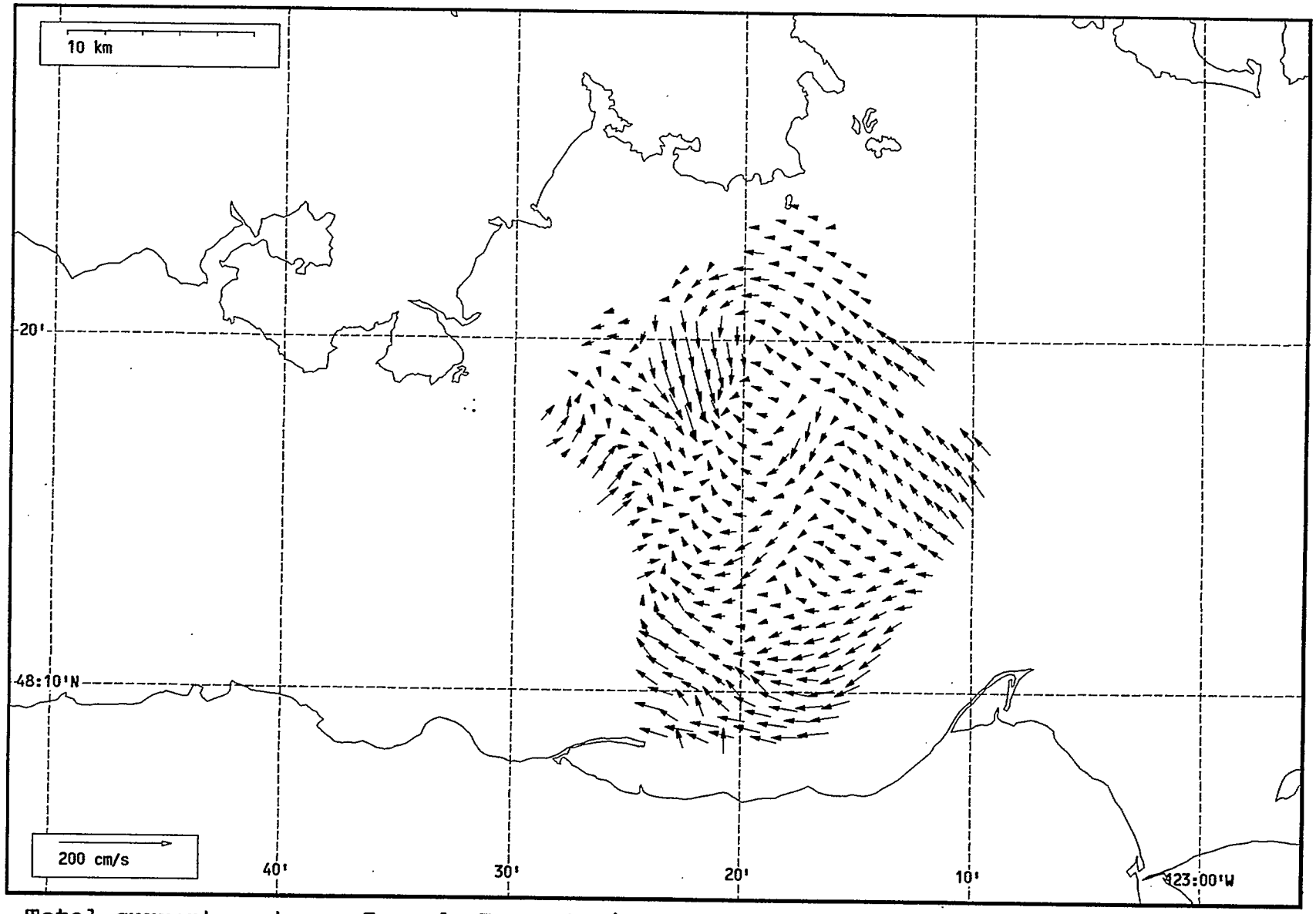

Total current vectors, Juan de Fuca Strait, 1992-07-9 00:00 Z.

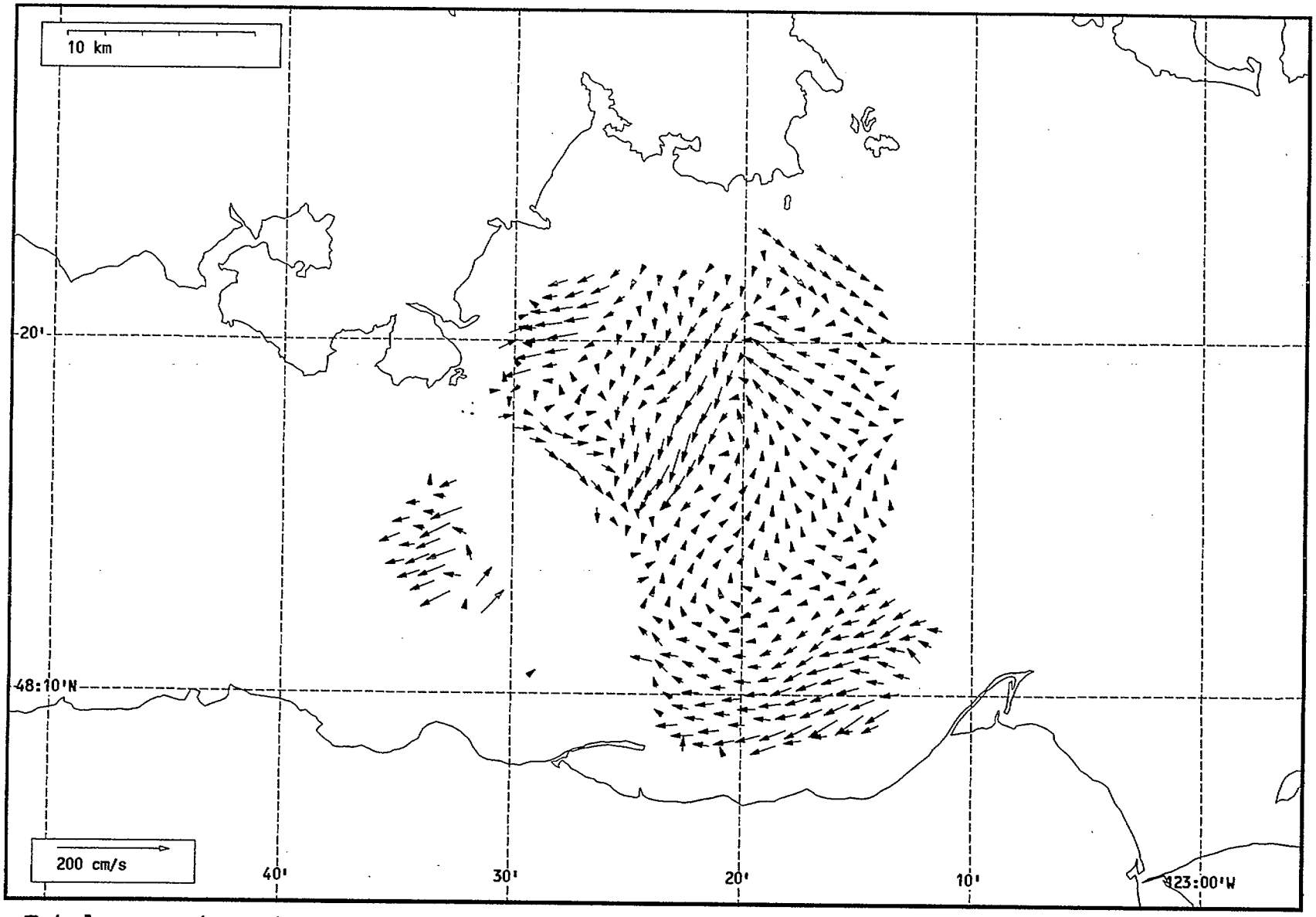

Total current vectors, Juan de Fuca Strait, 1992-07-9 01:00 Z.

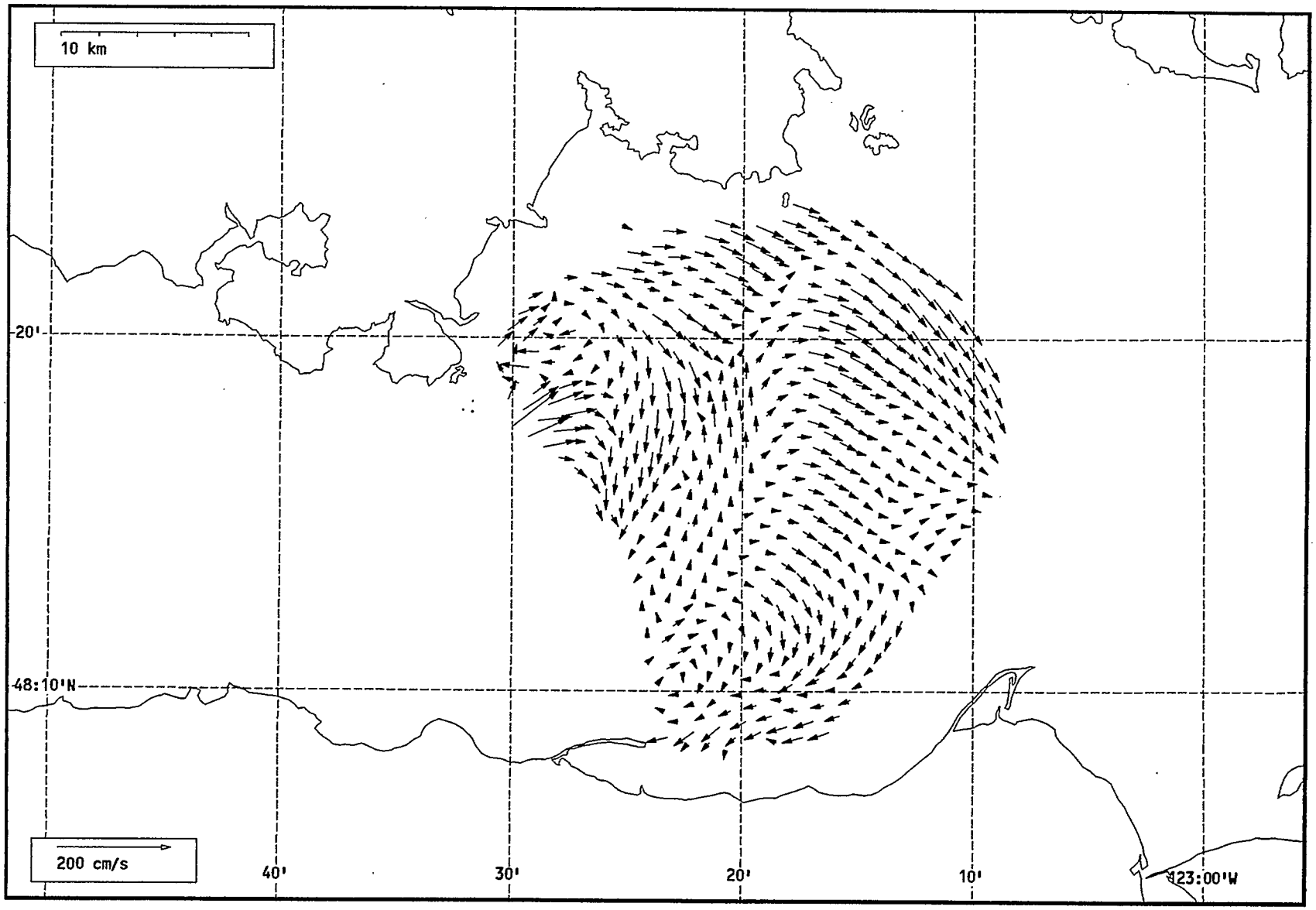

Total current vectors, Juan de Fuca Strait, 1992-07-9 02:00 Z.

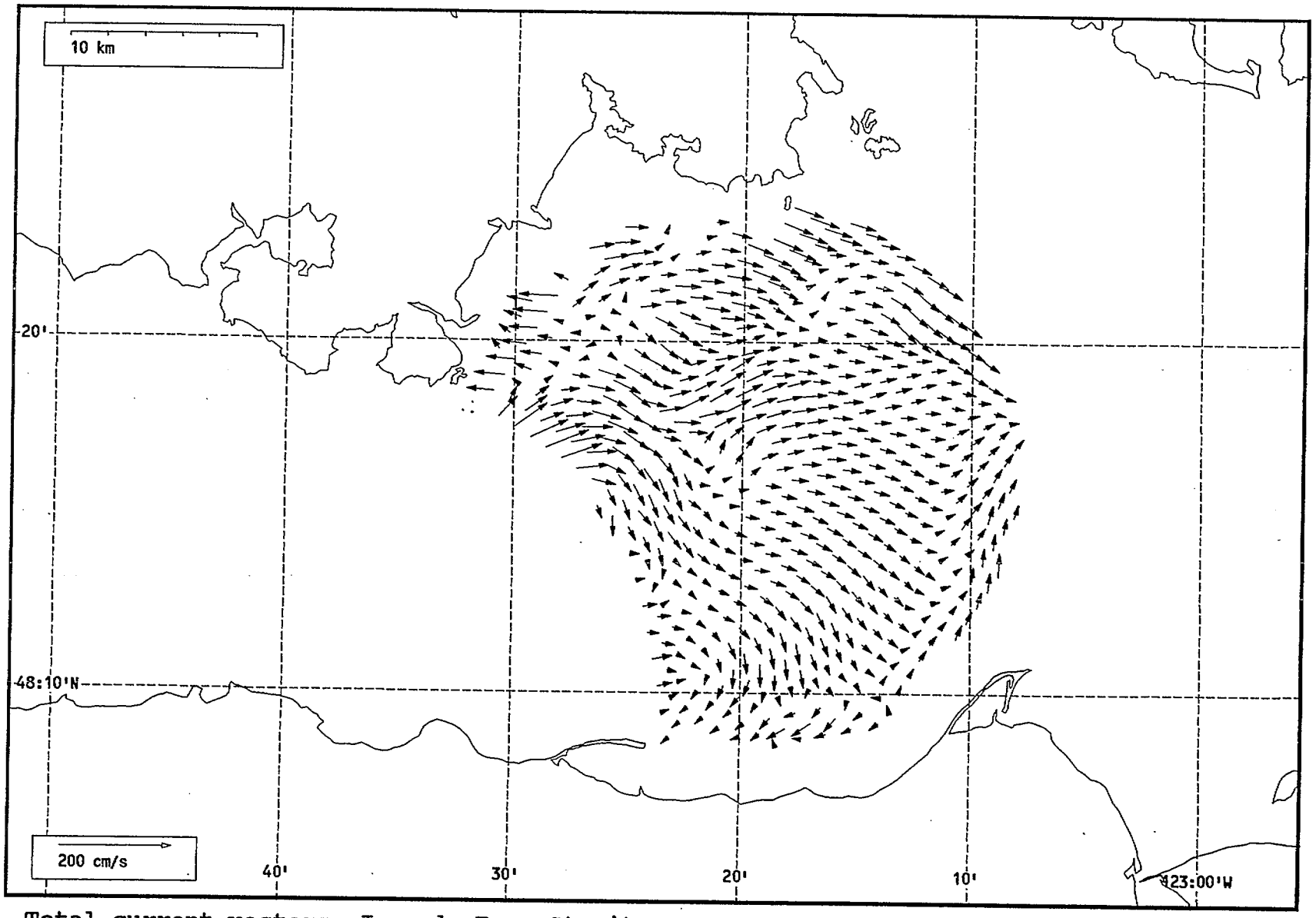

Total current vectors, Juan de Fuca Strait, 1992-07-9 03:00 Z.

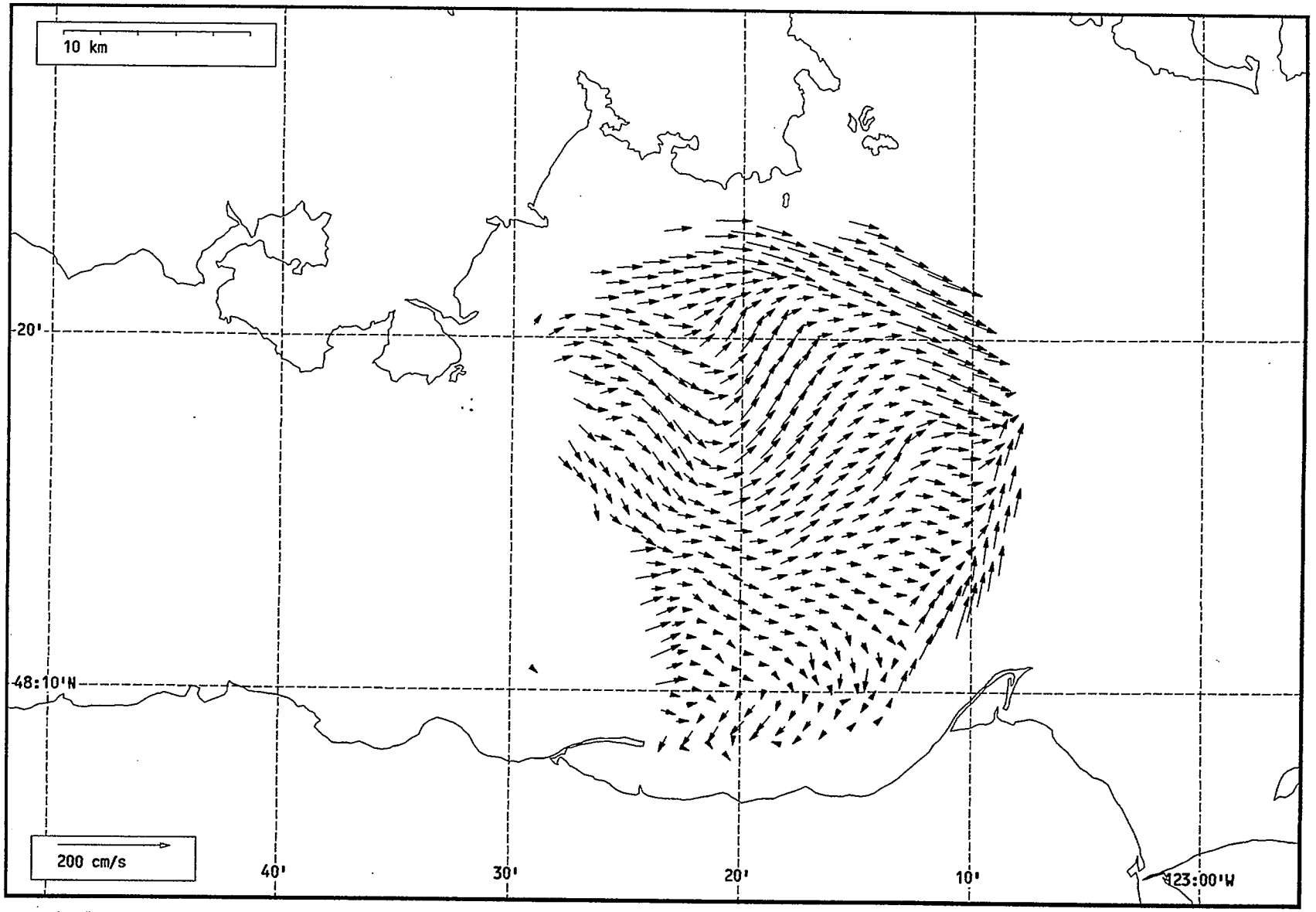

Total current vectors, Juan de Fuca Strait, 1992-07-9 04:00 Z.

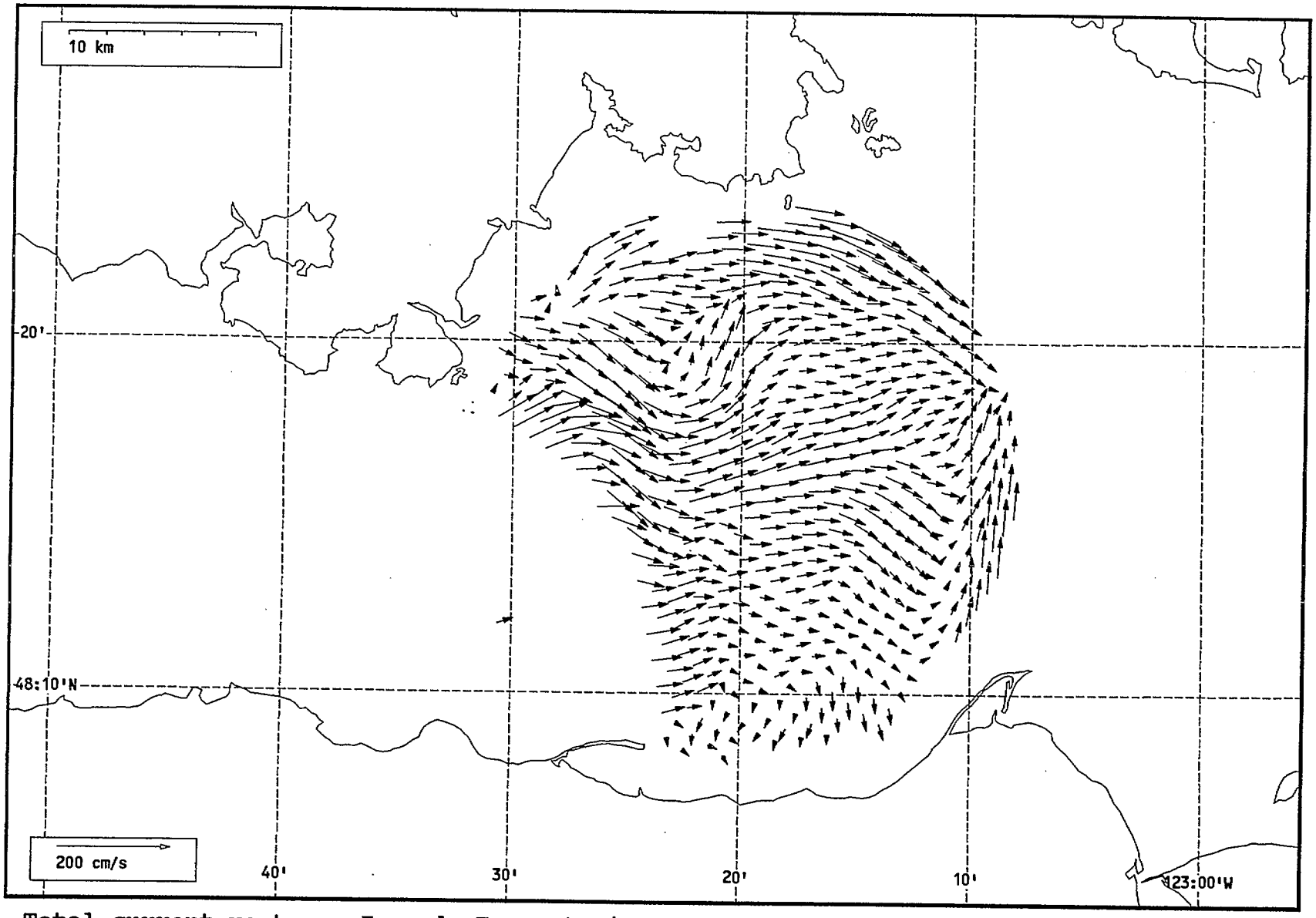

Total current vectors, Juan de Fuca Strait, 1992-07-9 05:00 Z.

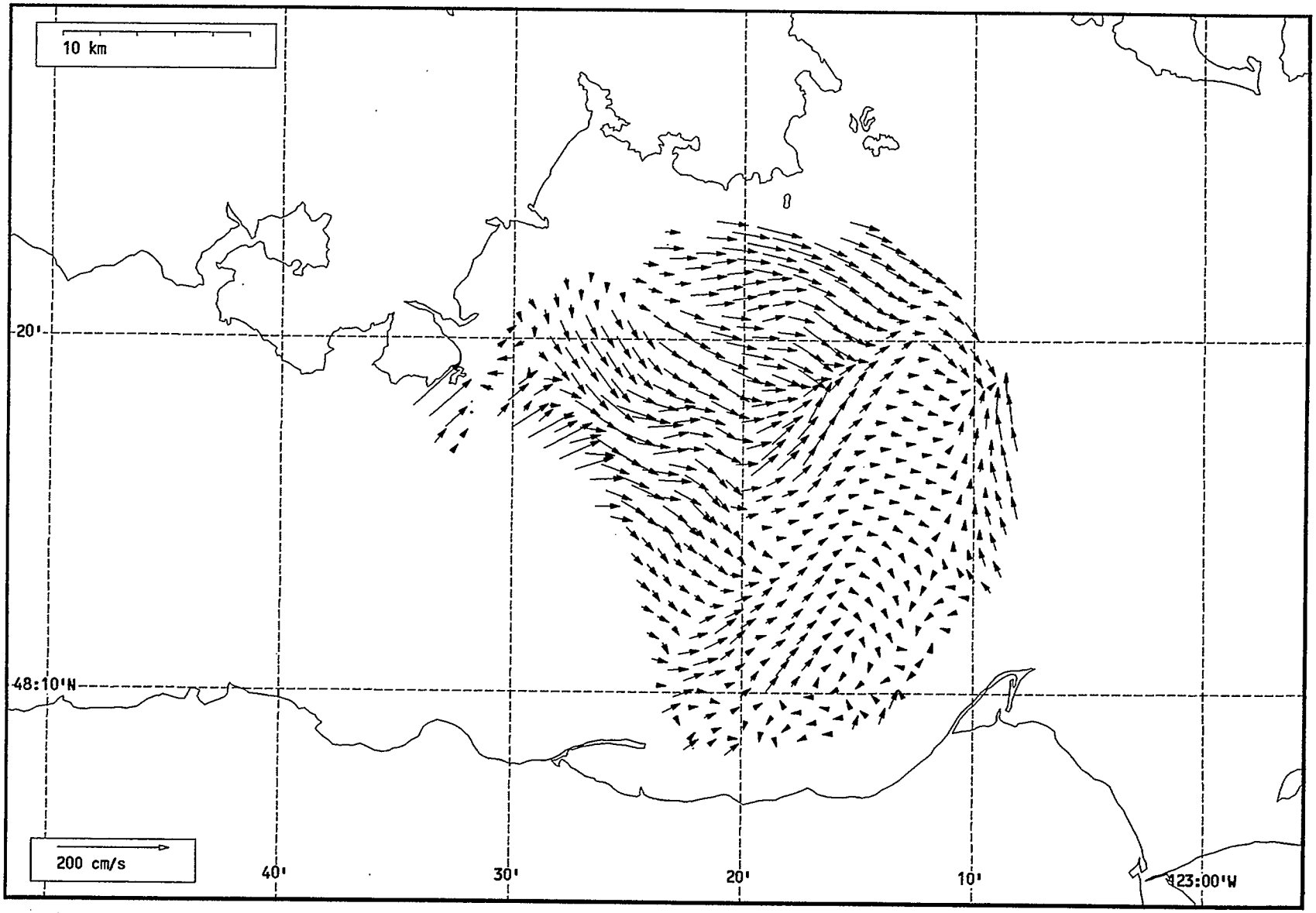

Total current vectors, Juan de Fuca Strait, 1992-07-9 06:00 Z.

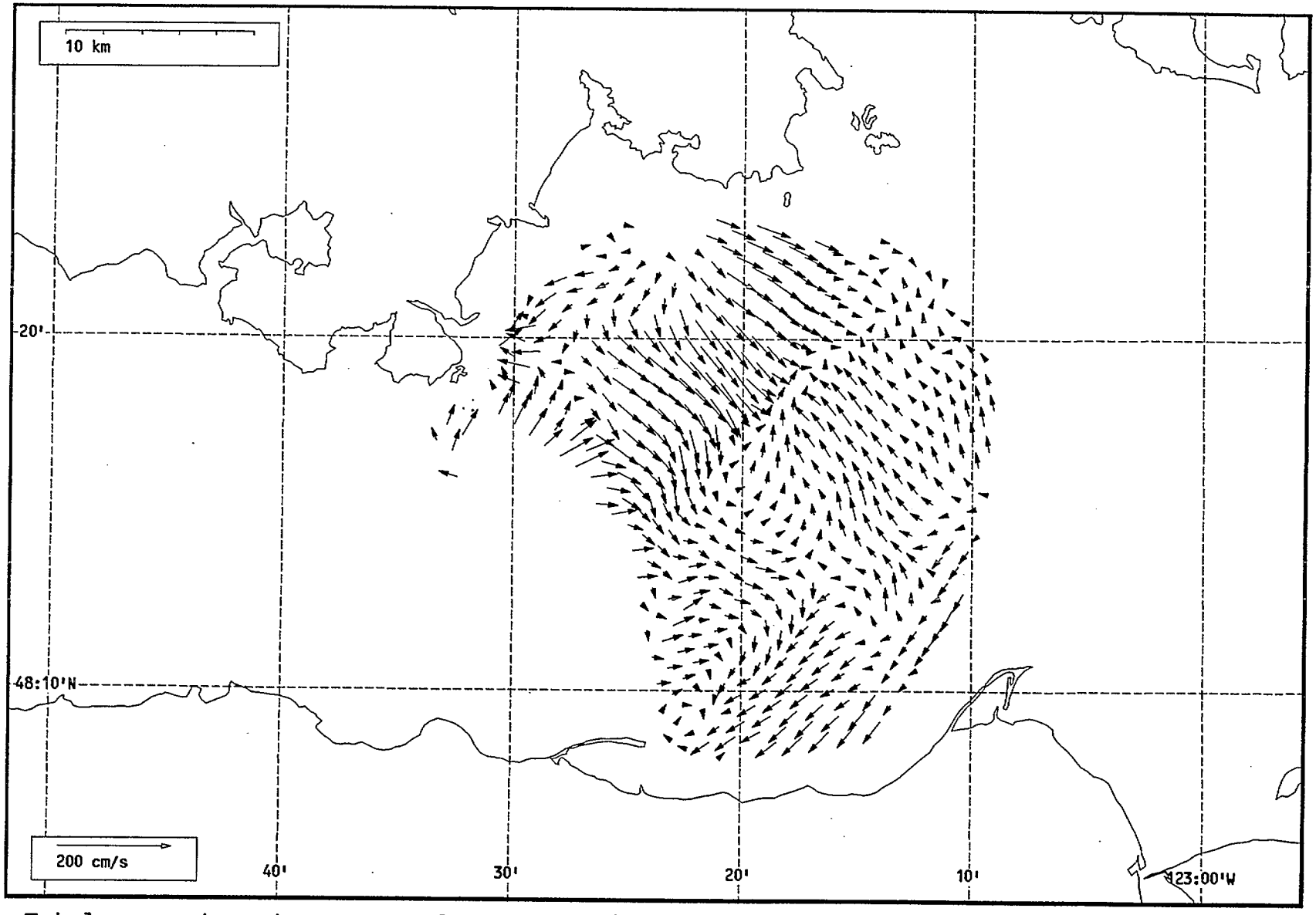

Total current vectors, Juan de Fuca Strait, 1992-07-9 07:00 Z.

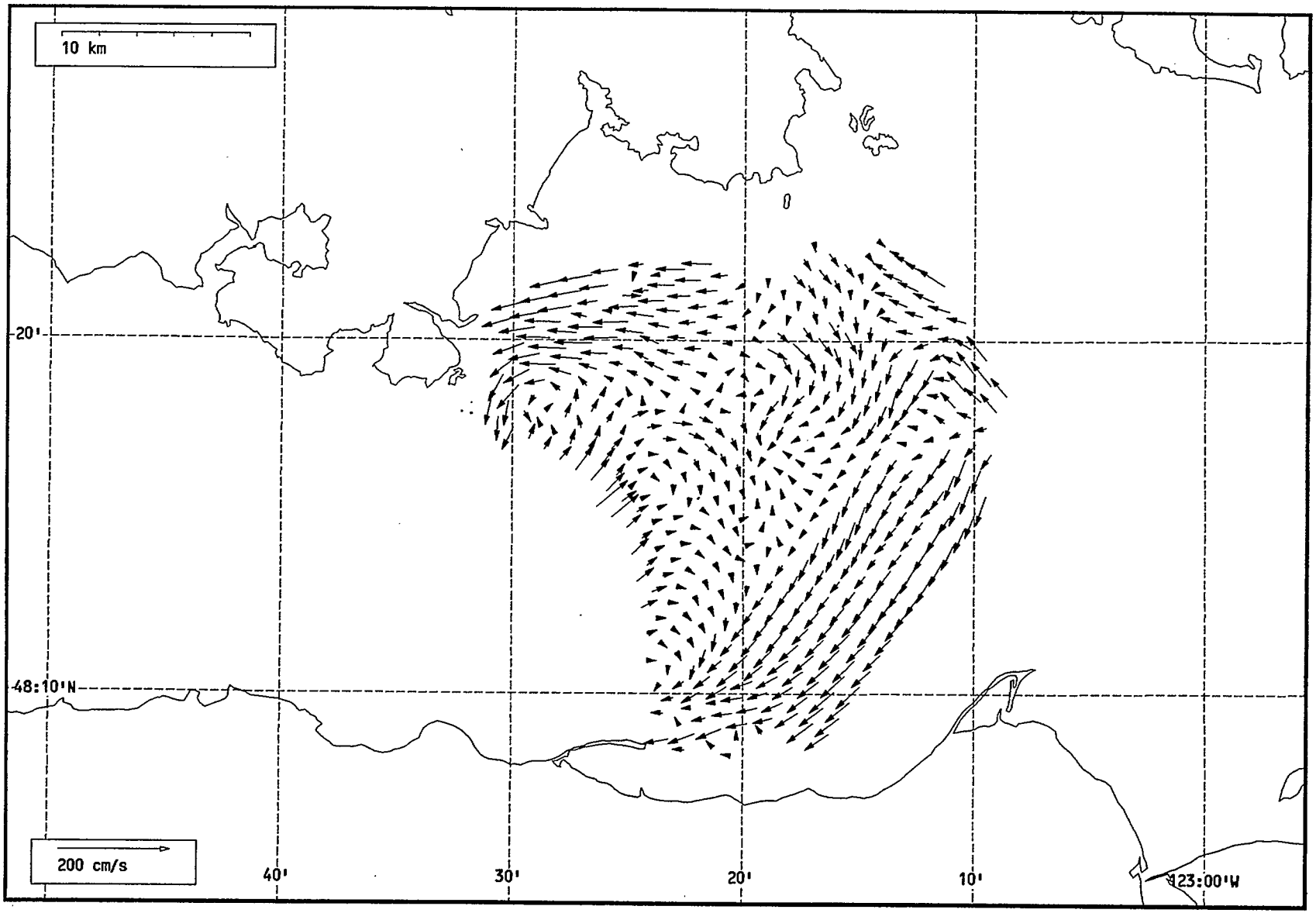

Total current vectors, Juan de Fuca Strait, 1992-07-9 08:00 Z.

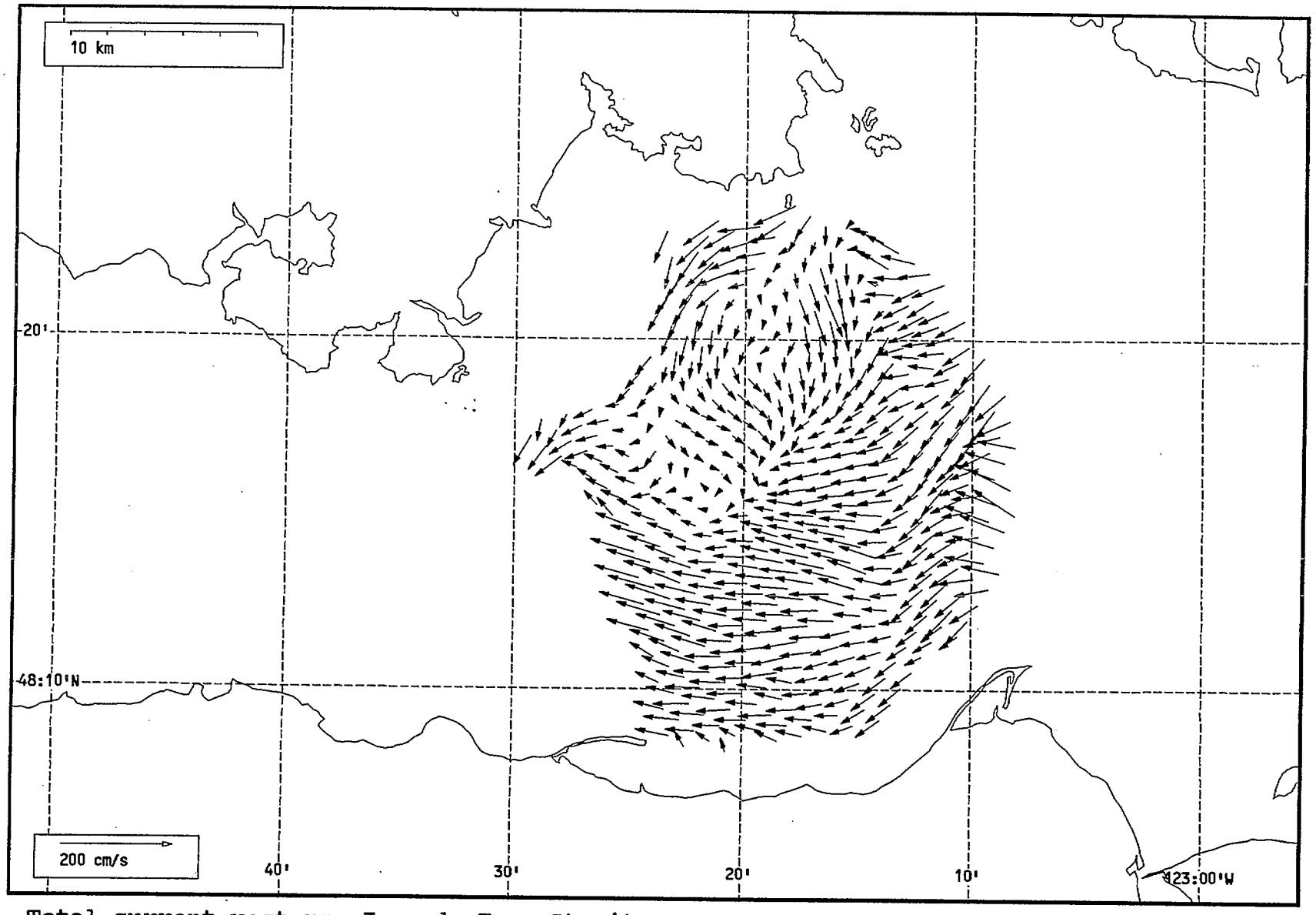

Total current vectors, Juan de Fuca Strait, 1992-07-9 09:00 Z.

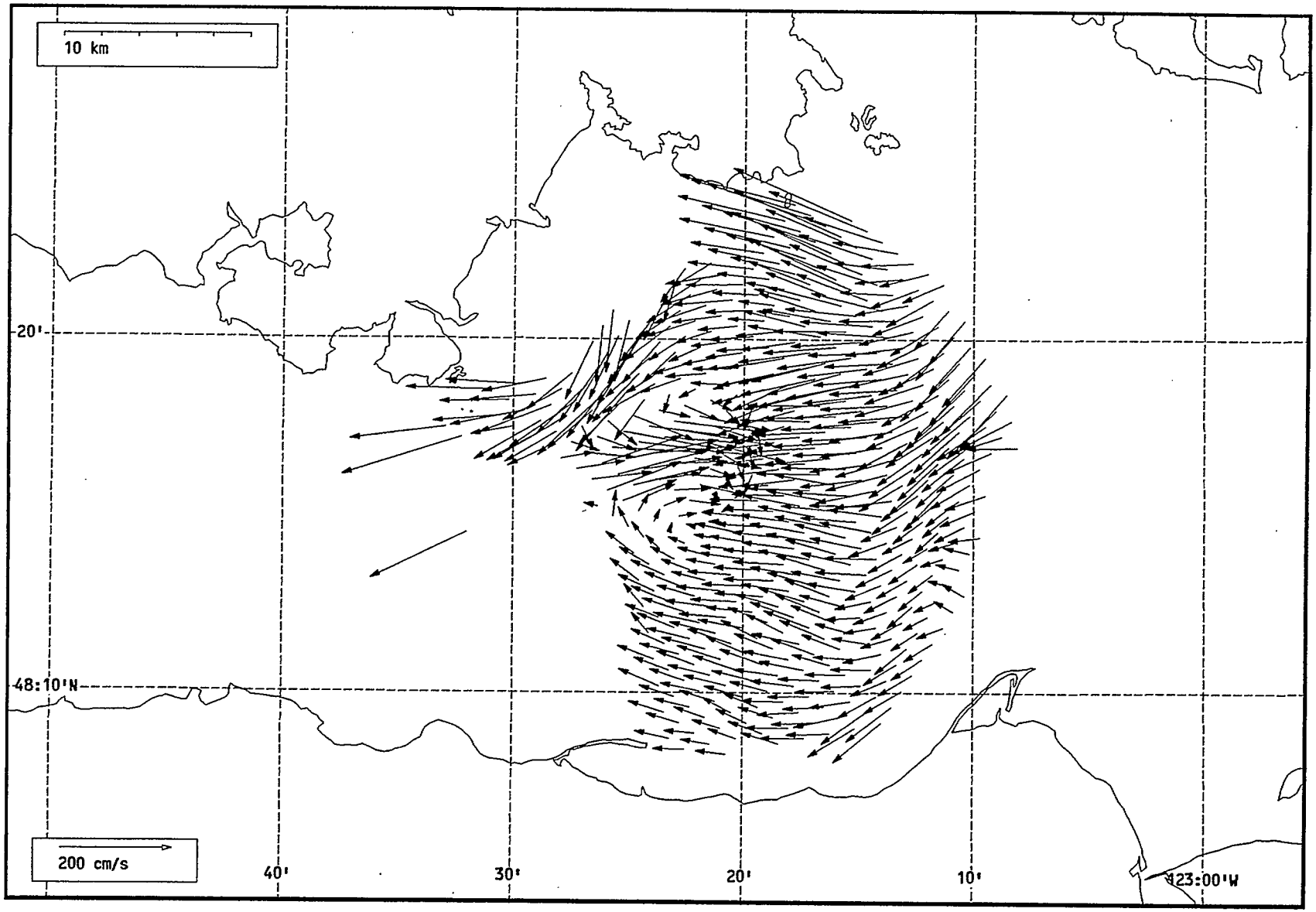

Total current vectors, Juan de Fuca Strait, 1992-07-9 10:00 Z.

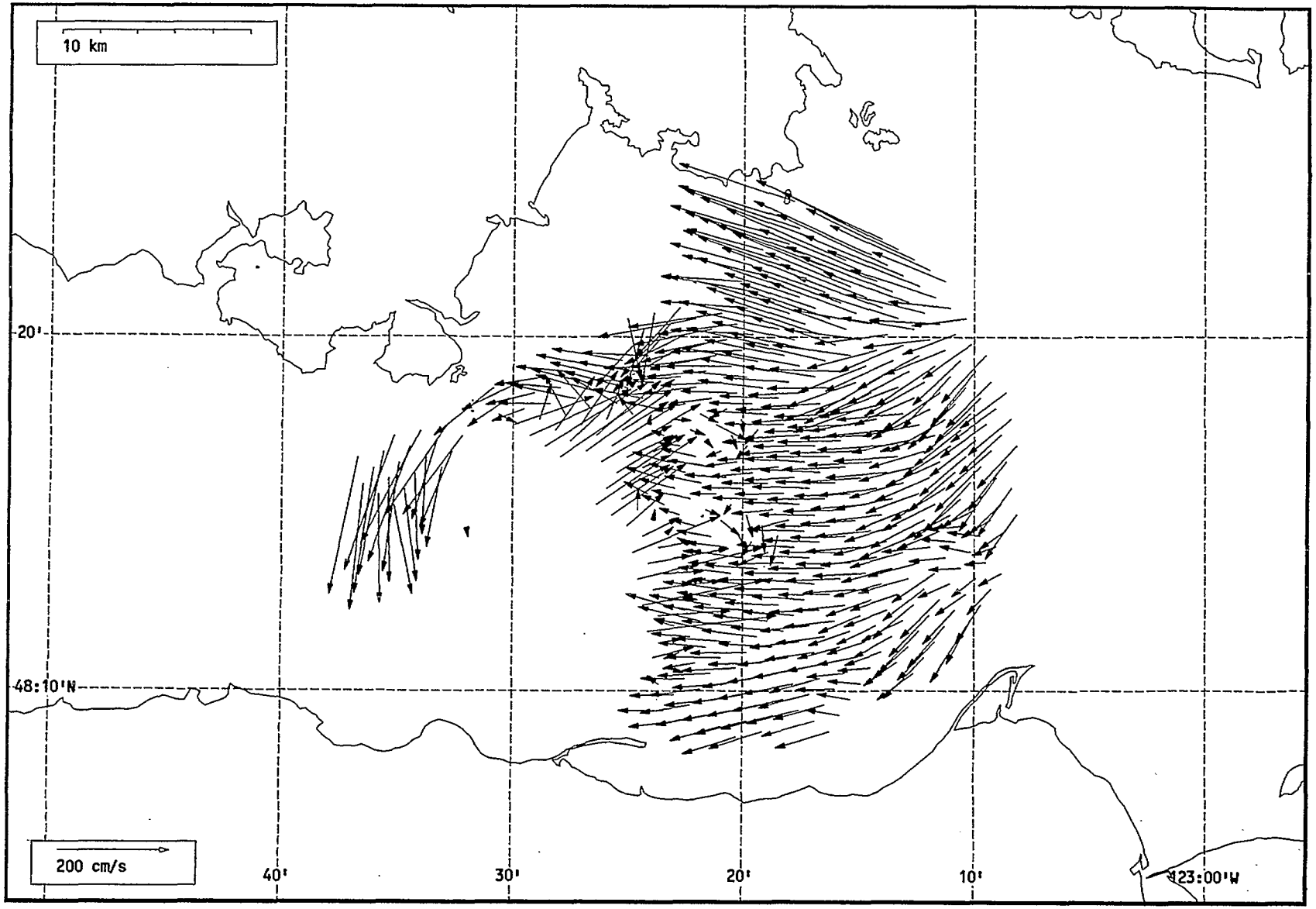

Total current vectors, Juan de Fuca Strait, 1992-07-9 11:00 Z.

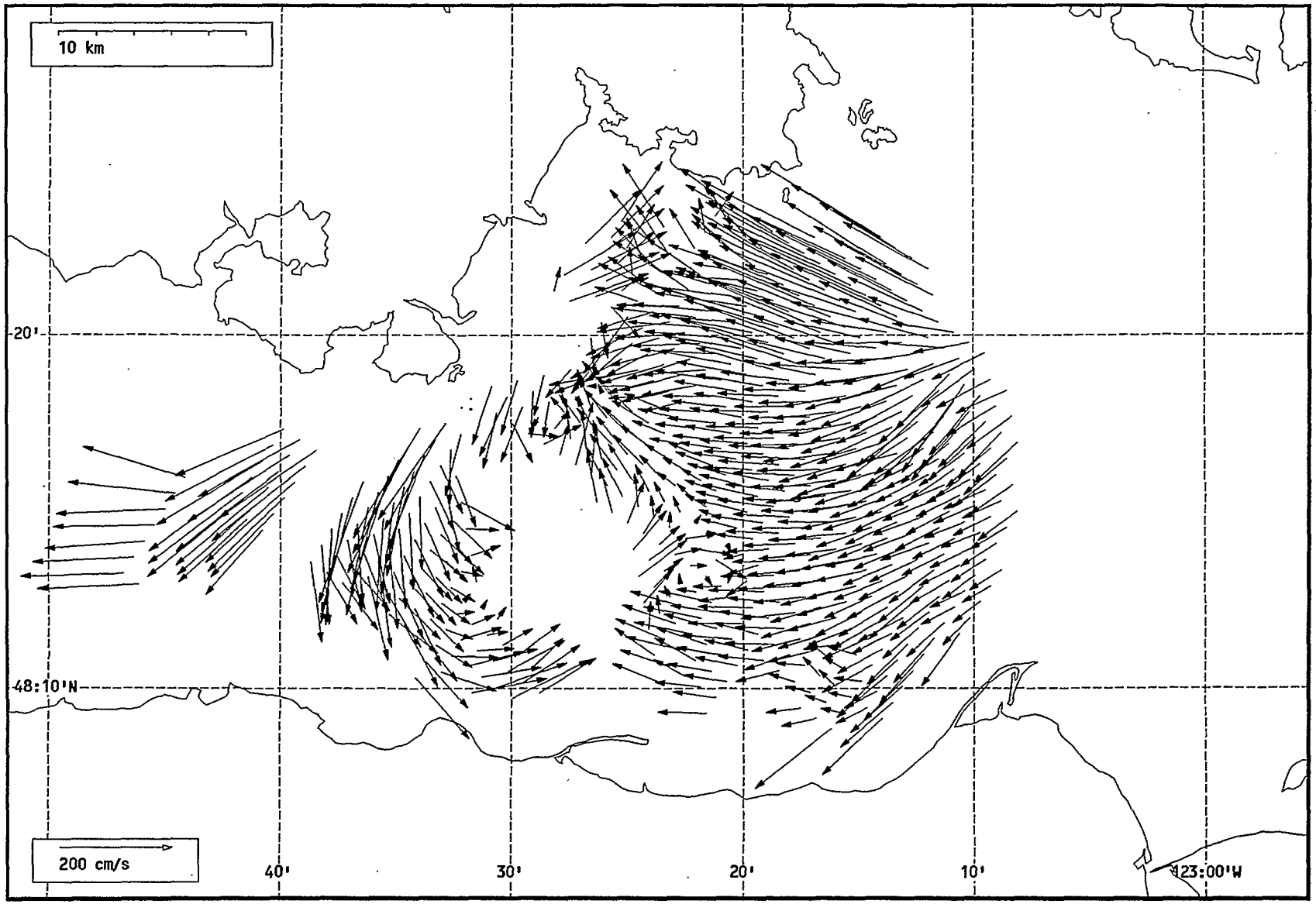

Total current vectors, Juan de Fuca Strait, 1992-07-9 12:00 Z.

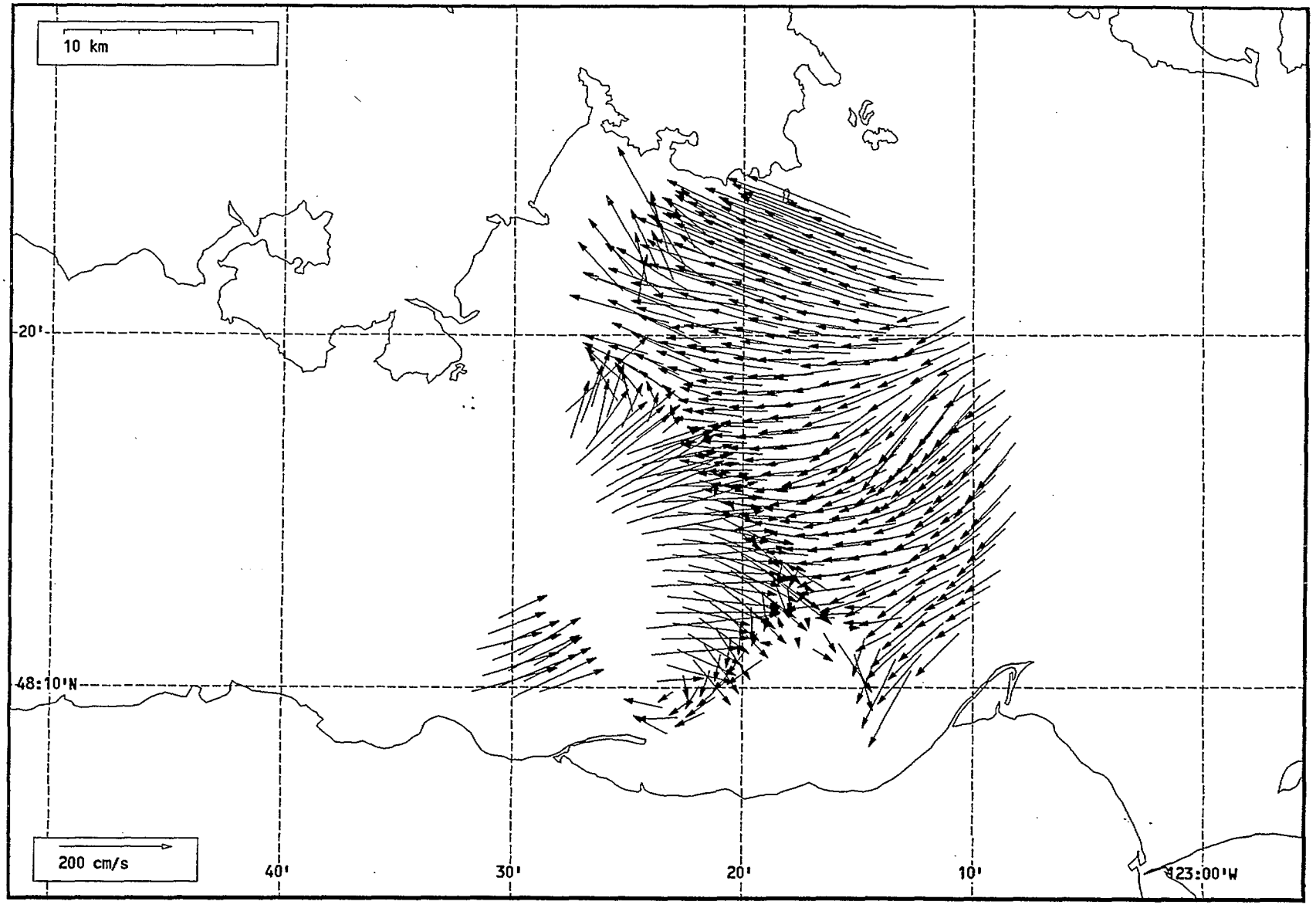

Total current vectors, Juan de Fuca Strait, 1992-07-9 13:00 Z.

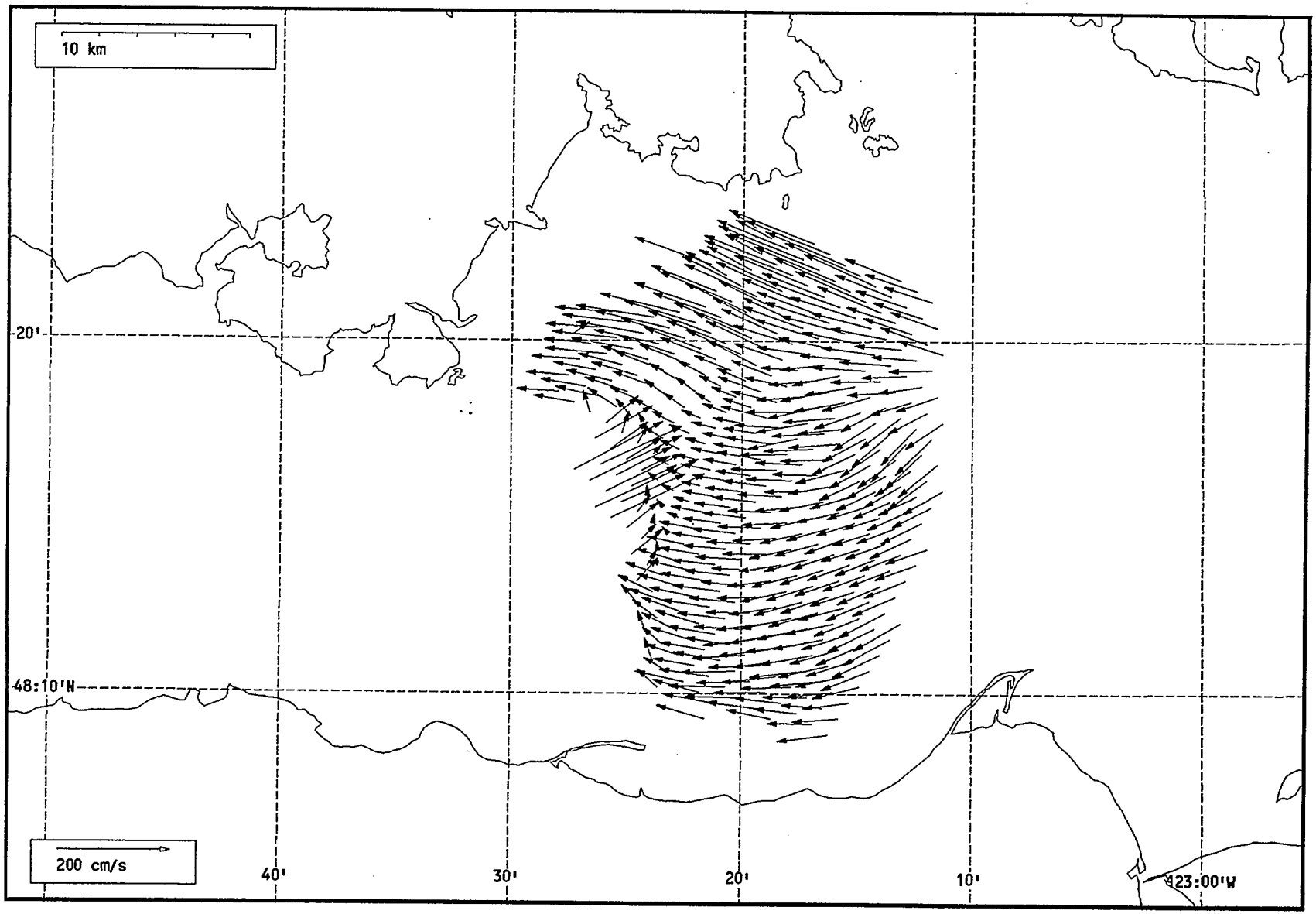

Total current vectors, Juan de Fuca Strait, 1992-07-9 14:00 Z.

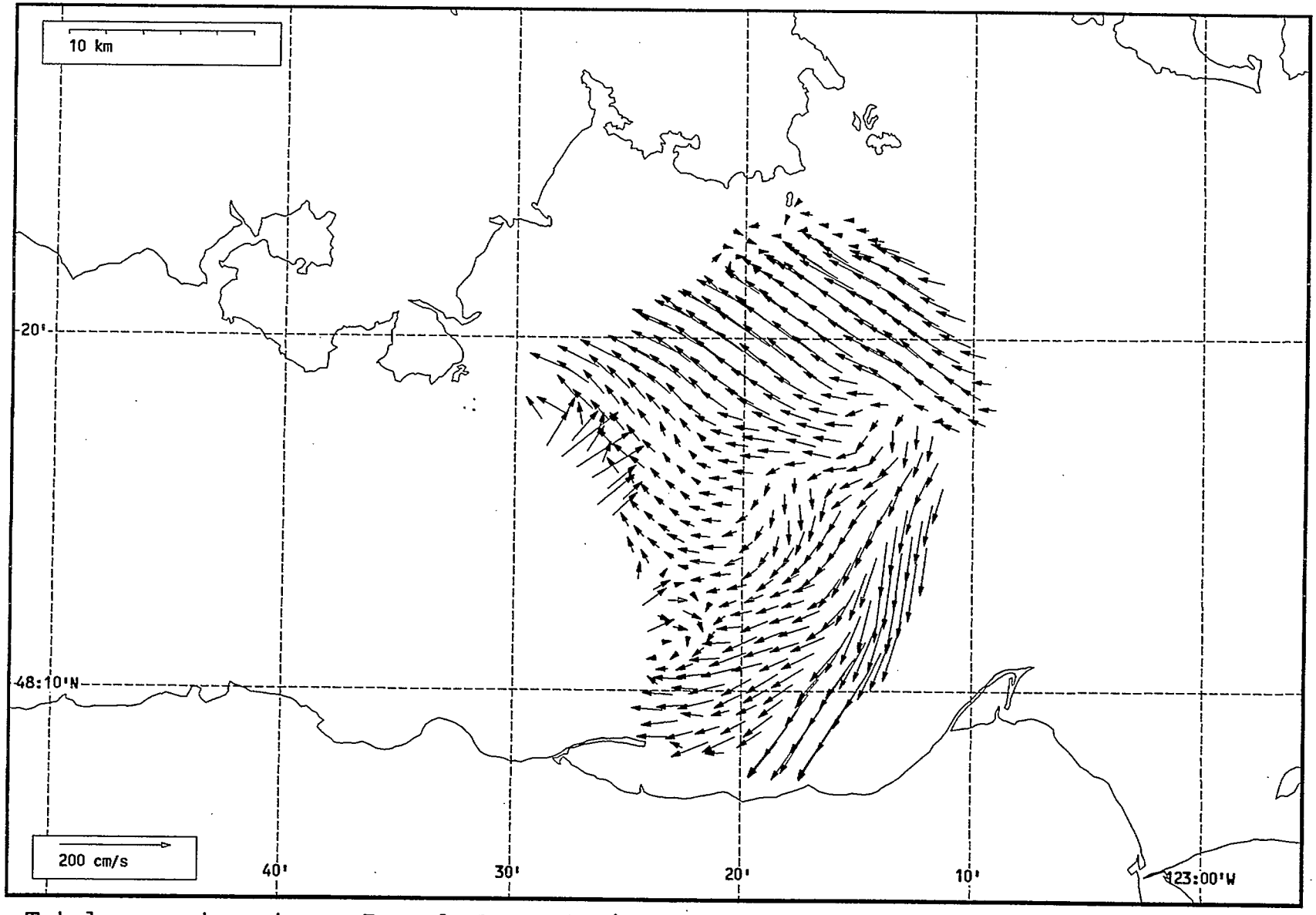

Total current vectors, Juan de Fuca Strait, 1992-07-9 15:00 Z.

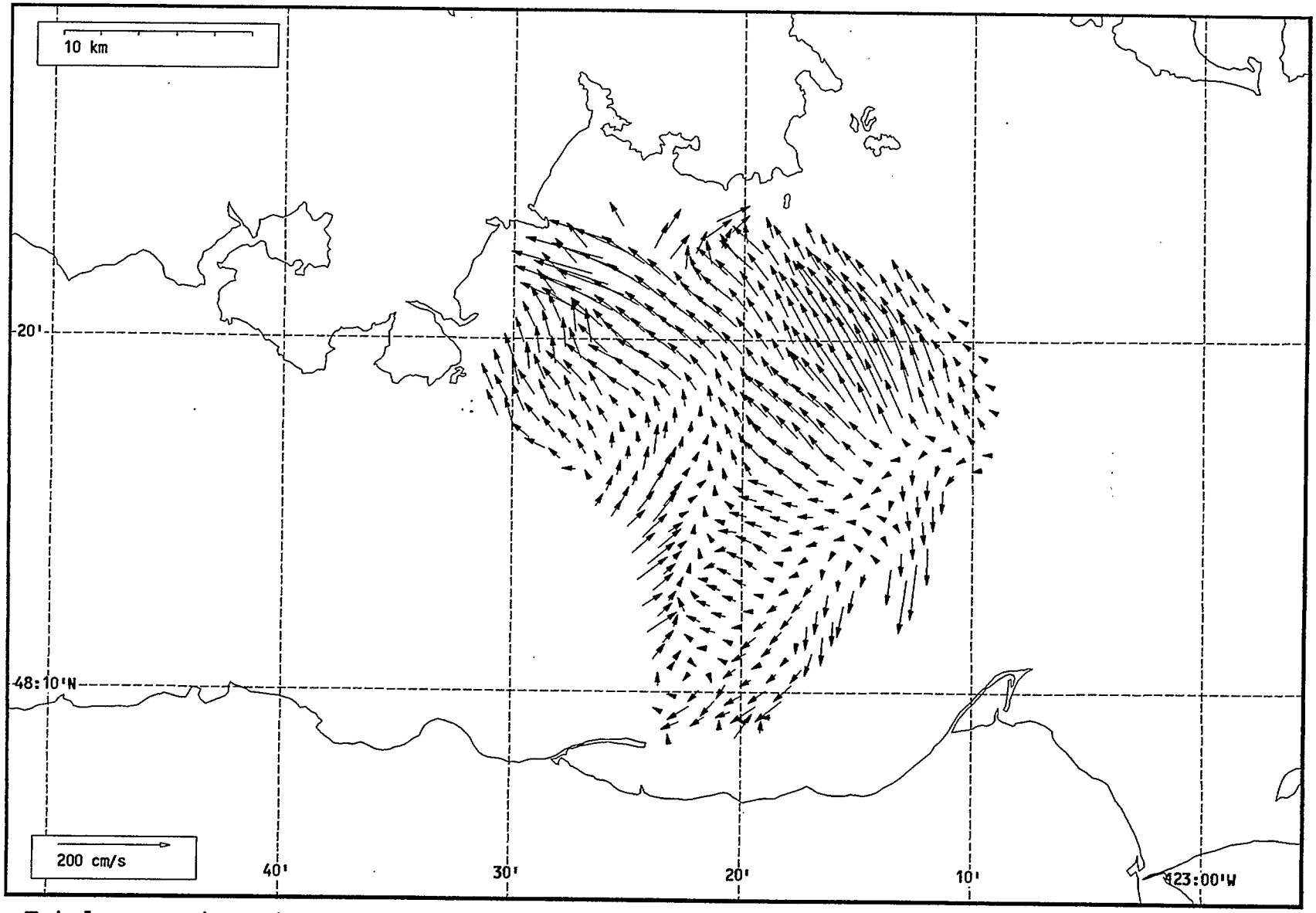

Total current vectors, Juan de Fuca Strait, 1992-07-9 16:00 Z.

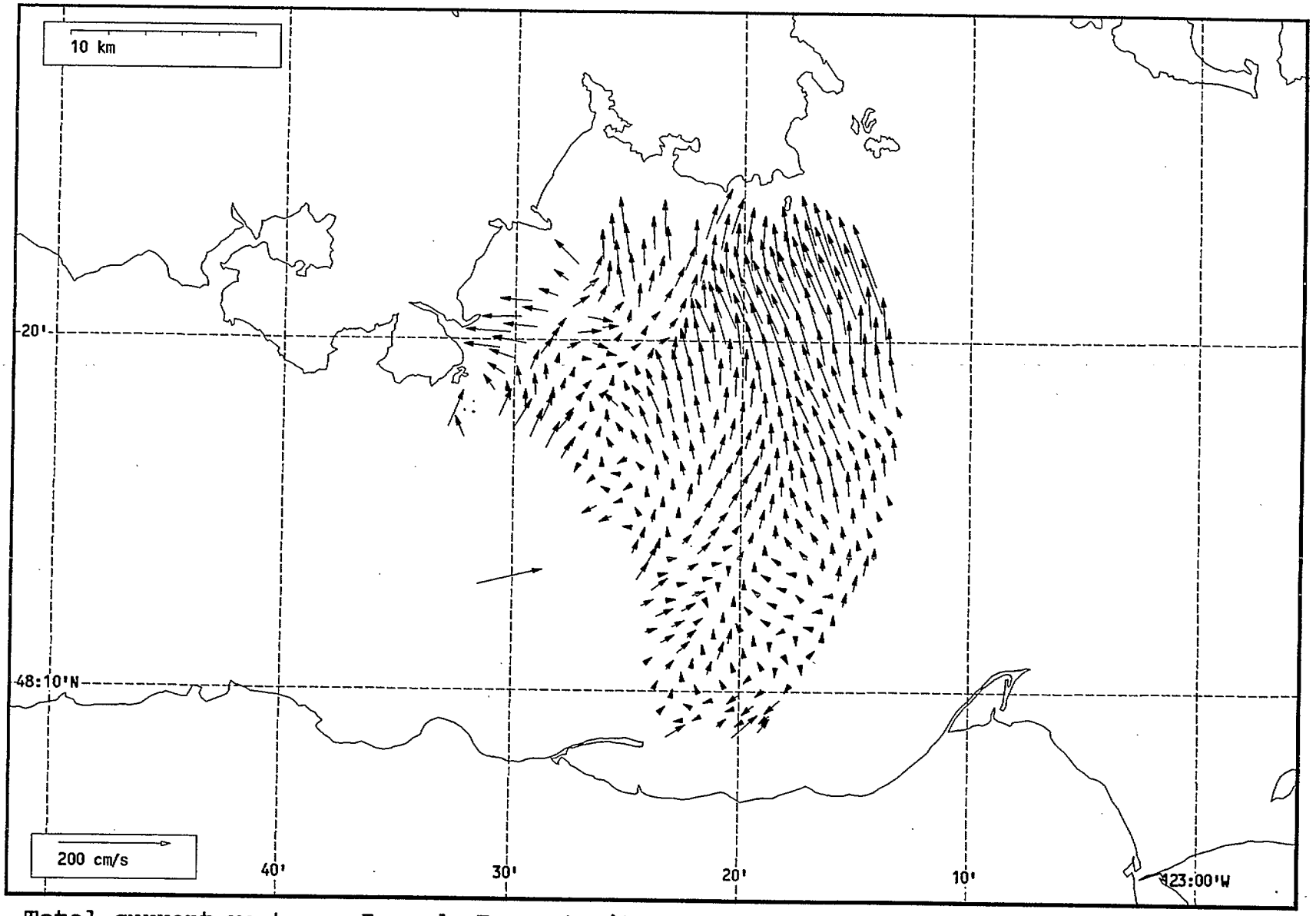

Total current vectors, Juan de Fuca Strait, 1992-07-9 17:00 Z.

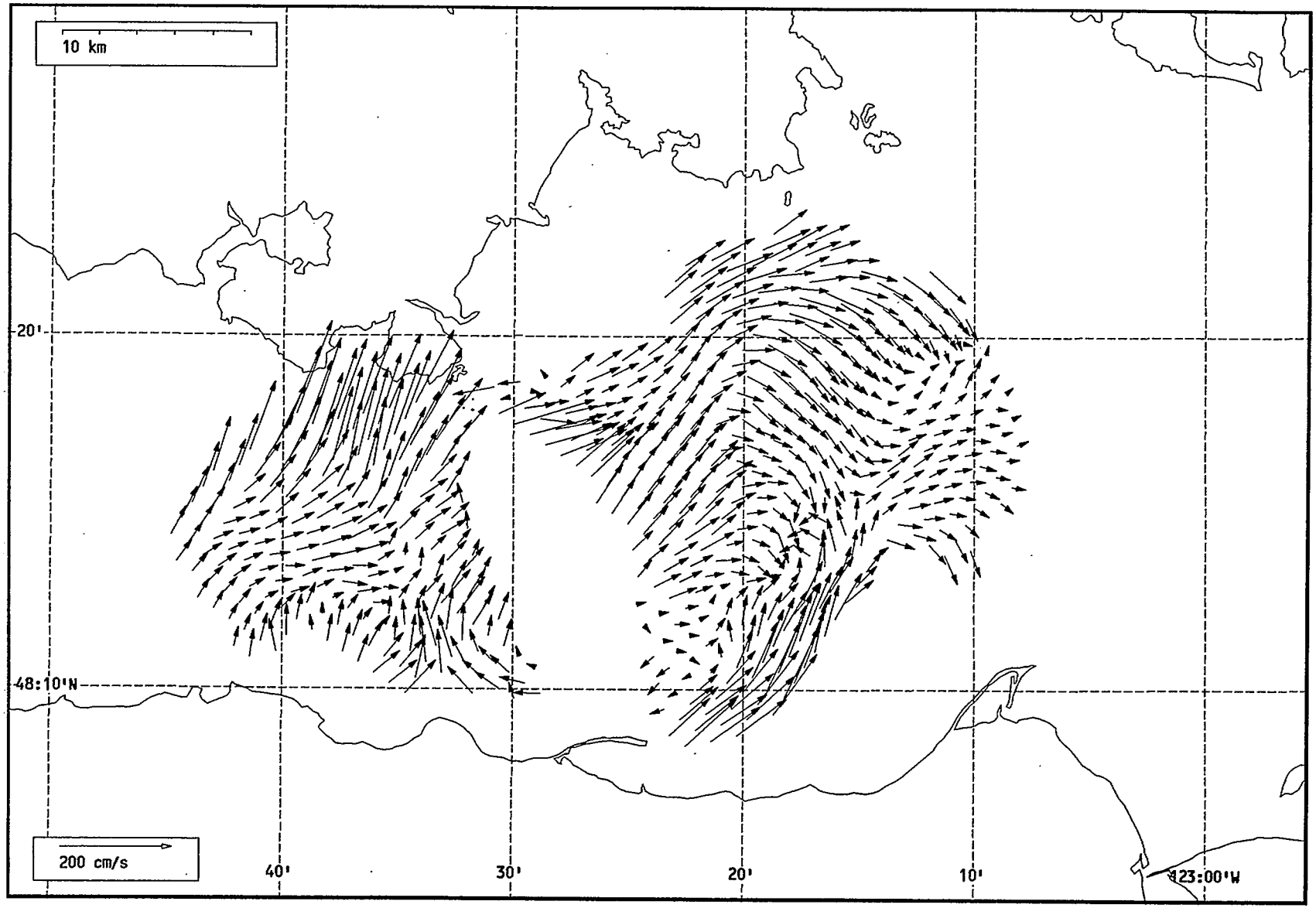

Total current vectors, Juan de Fuca Strait, 1992-07-9 19:00 Z.

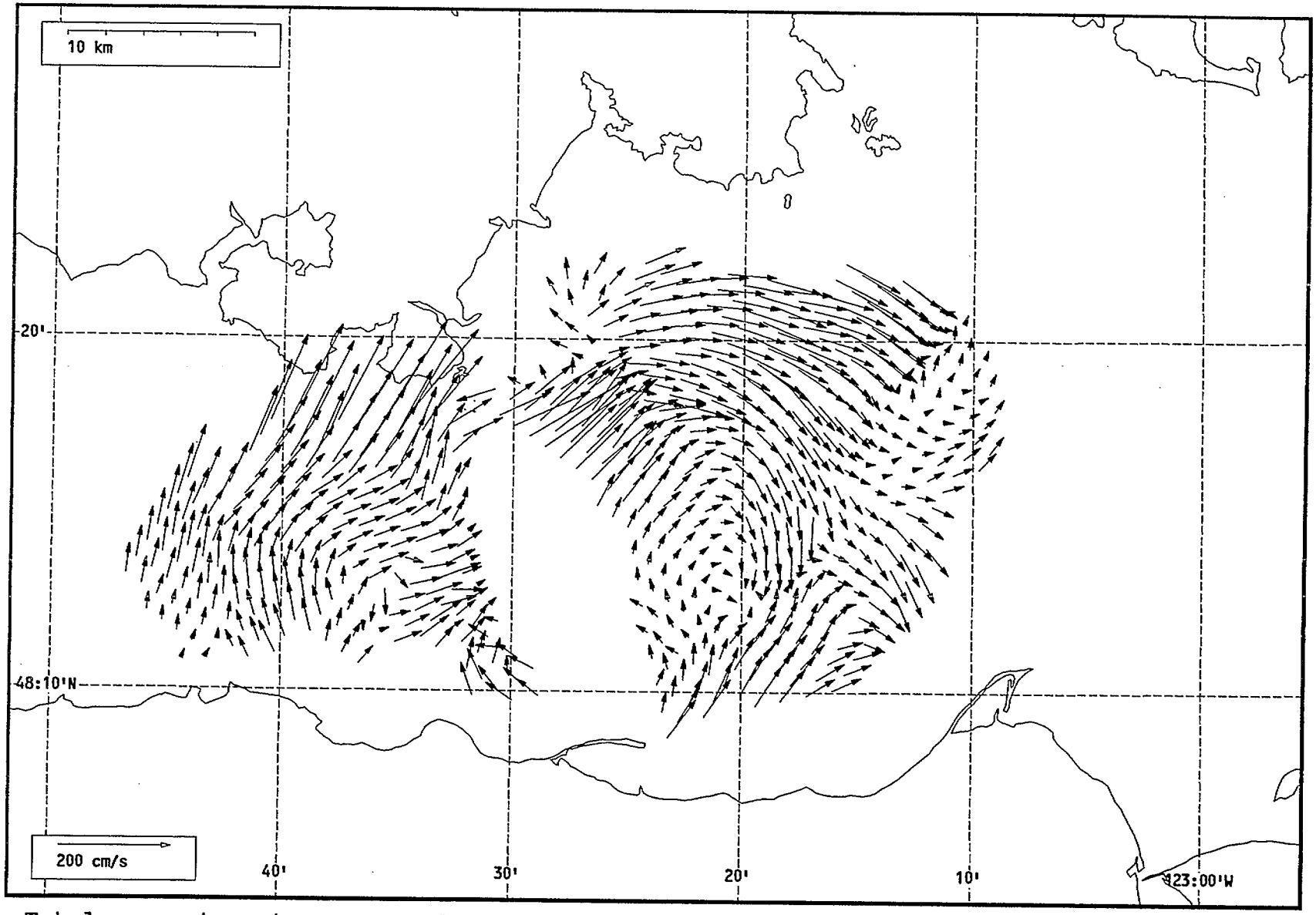

Total current vectors, Juan de Fuca Strait, 1992-07-9 20:00 Z.

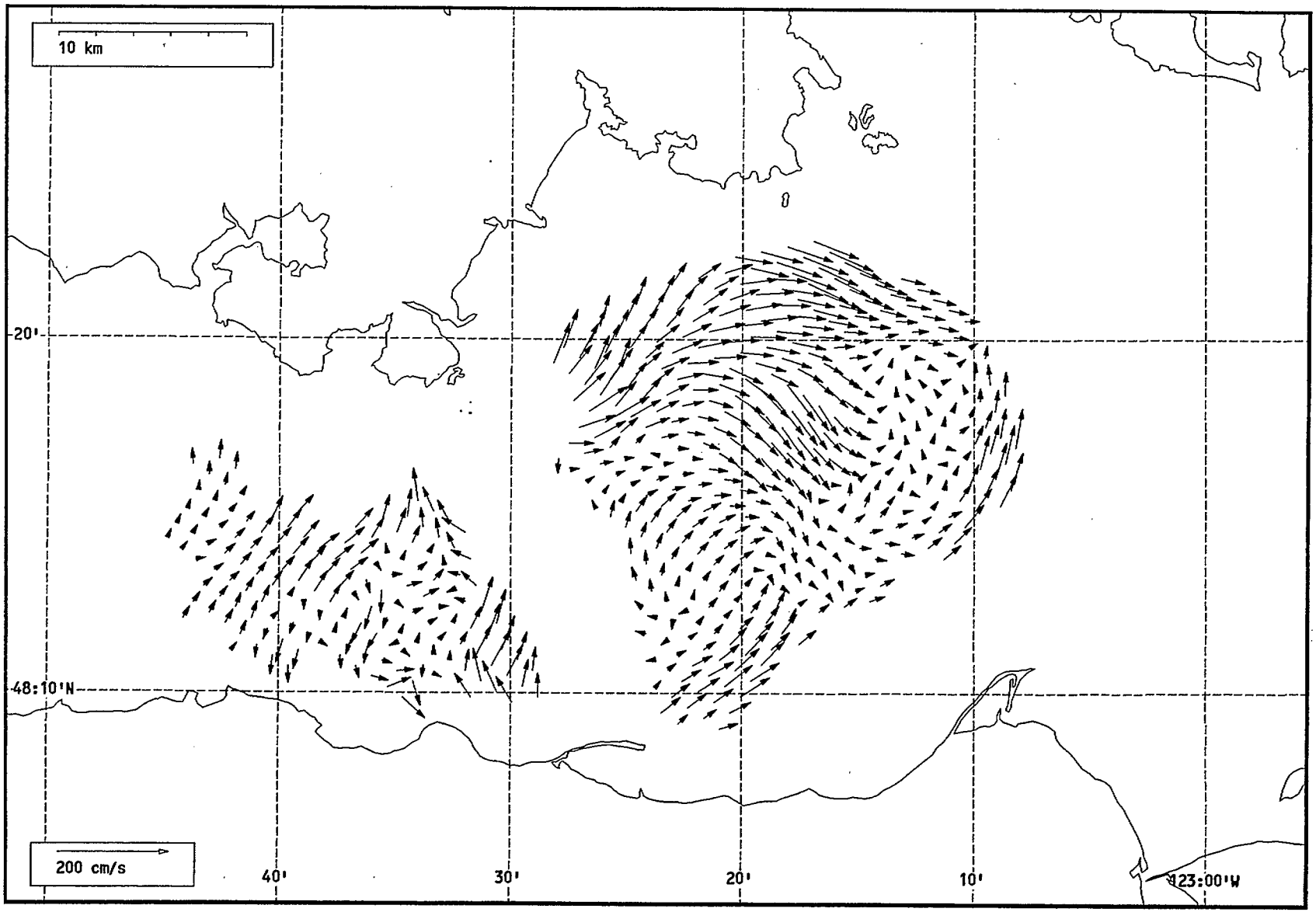

Total current vectors, Juan de Fuca Strait, 1992-07-9 21:00 Z.

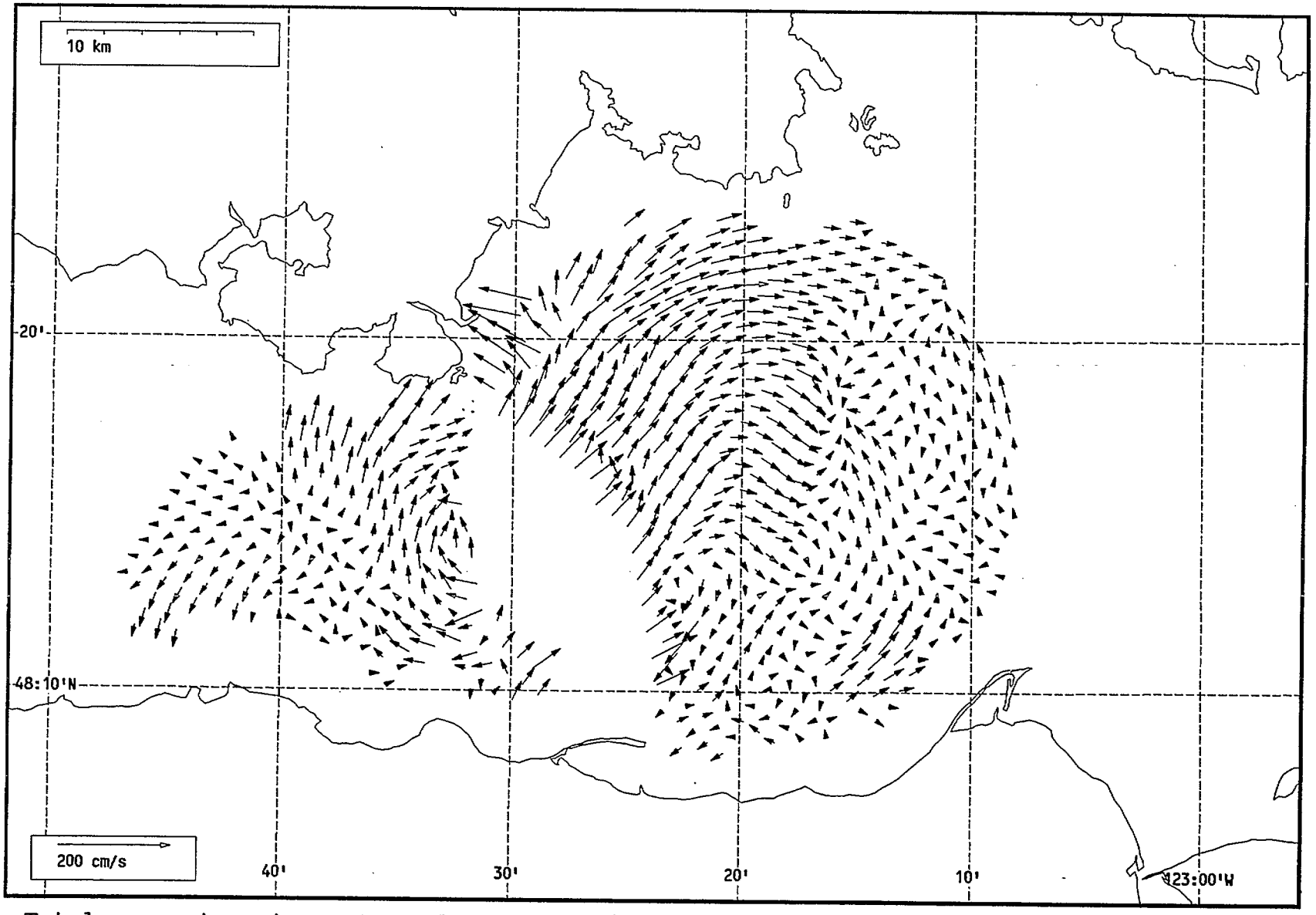

Total current vectors, Juan de Fuca Strait, 1992-07-9 22:00 Z.

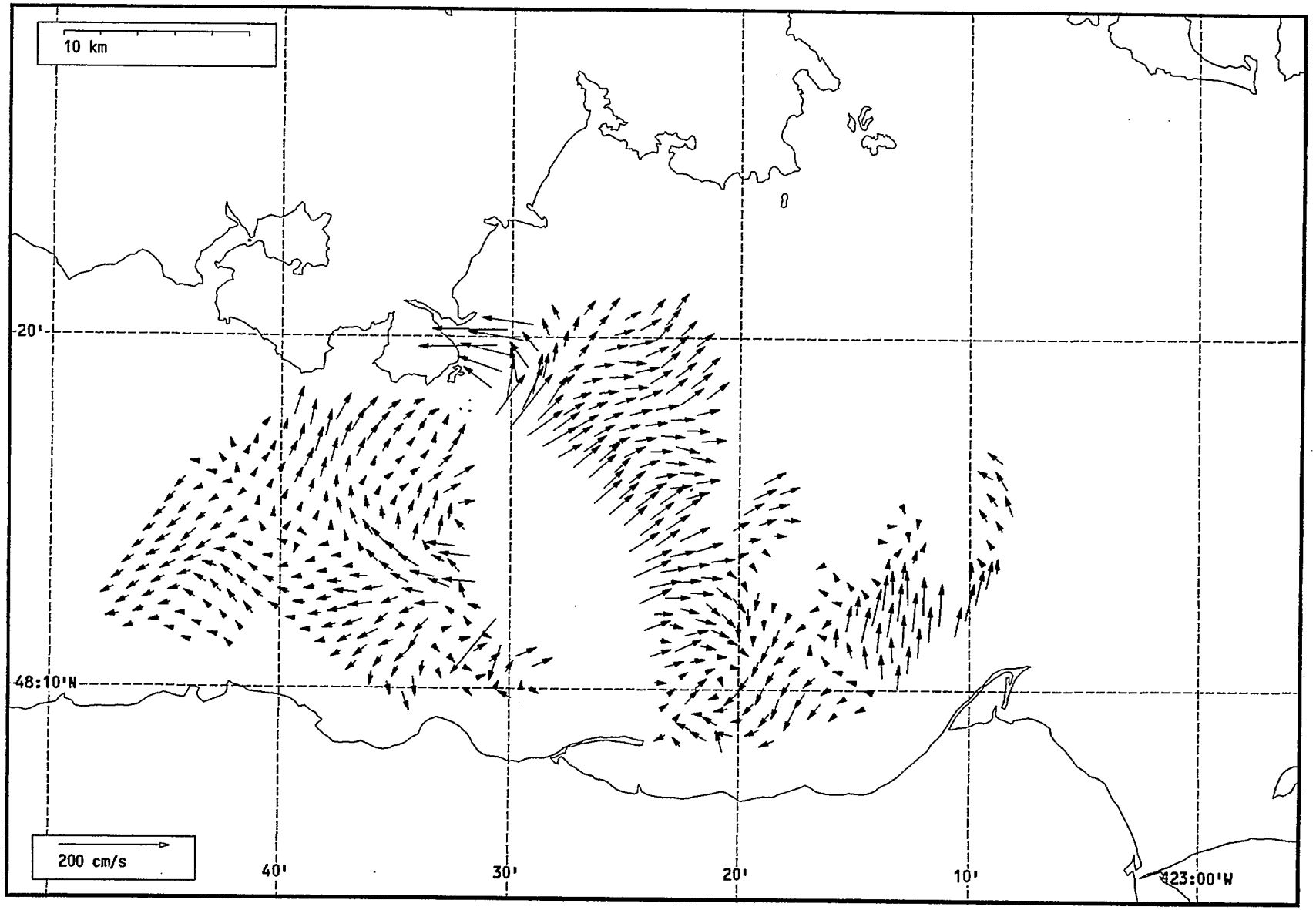

Total current vectors, Juan de Fuca Strait, 1992-07-9 23:00 Z.

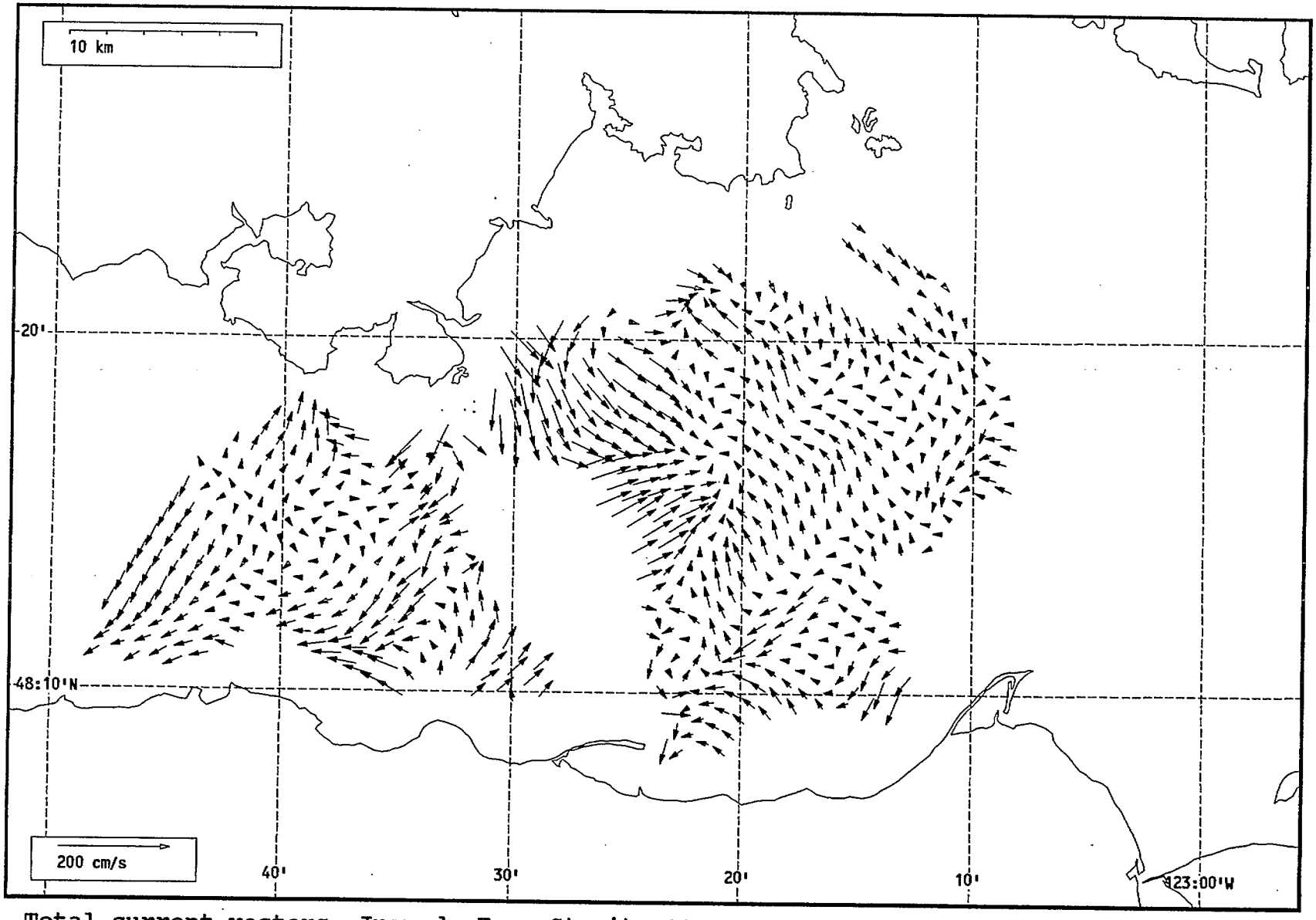

Total current vectors, Juan de Fuca Strait, 1992-07-10 00:00 Z.

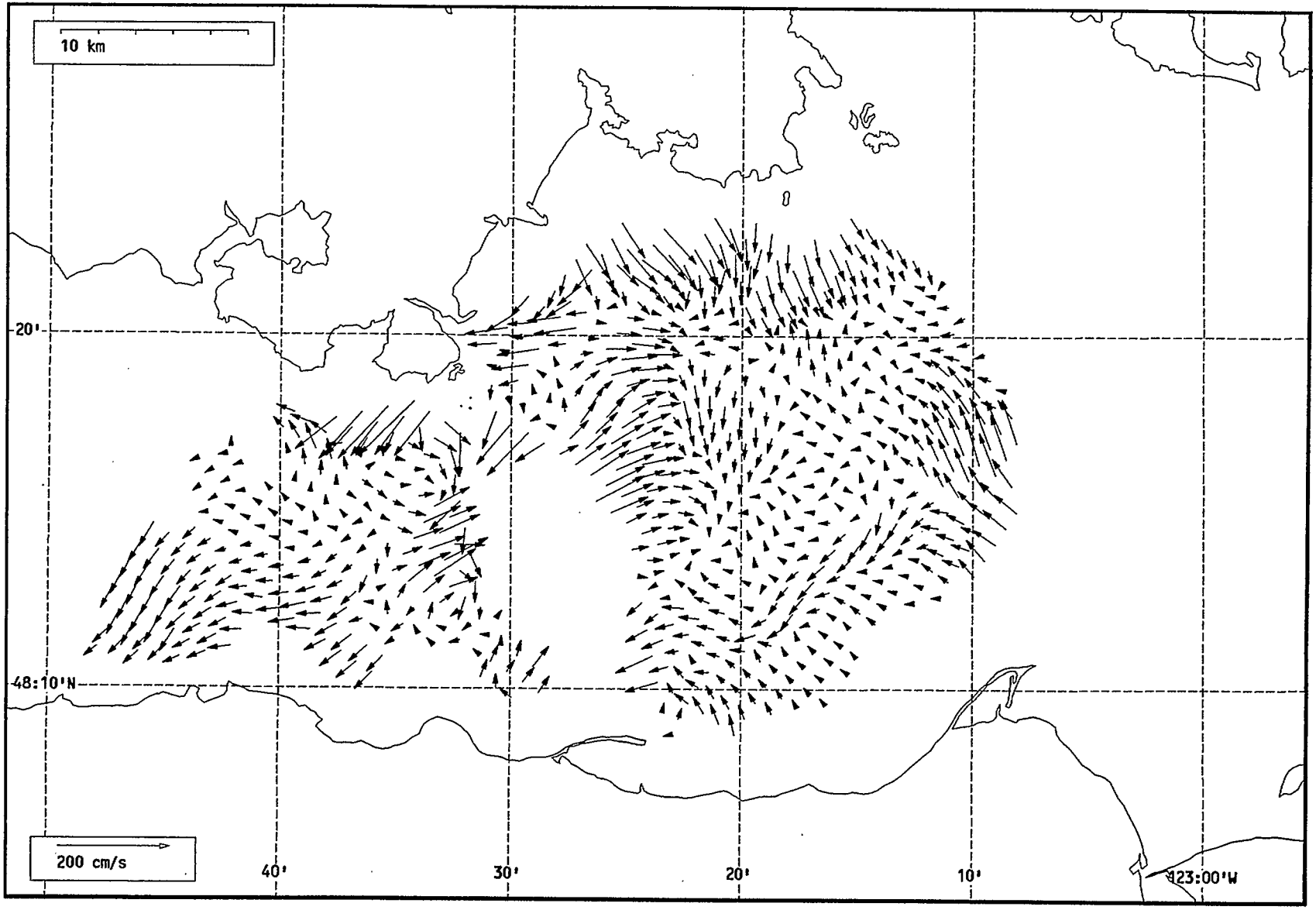

Total current vectors, Juan de Fuca Strait, 1992-07-10 01:00 Z.

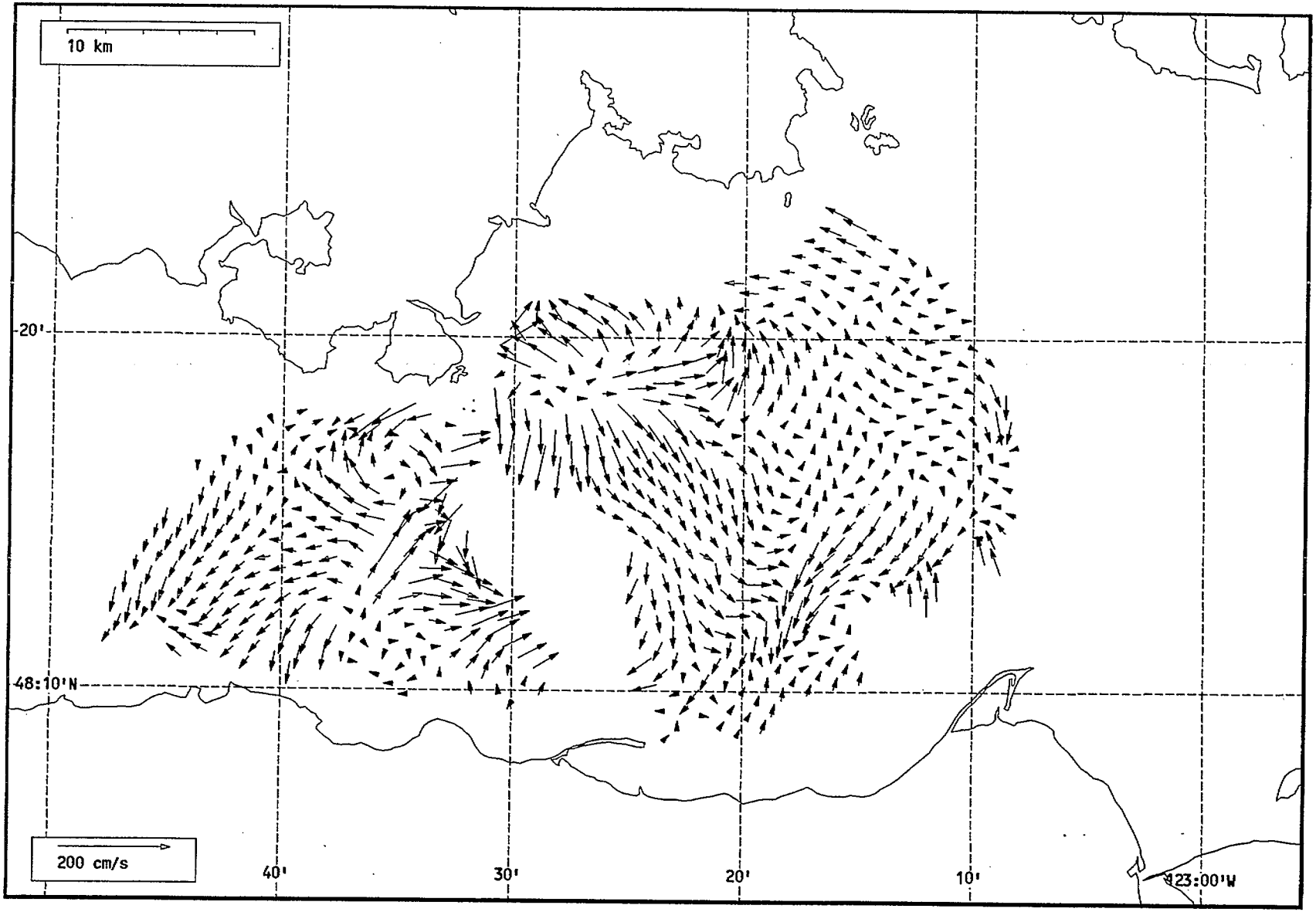

Total current vectors, Juan de Fuca Strait, 1992-07-10 02:00 Z.

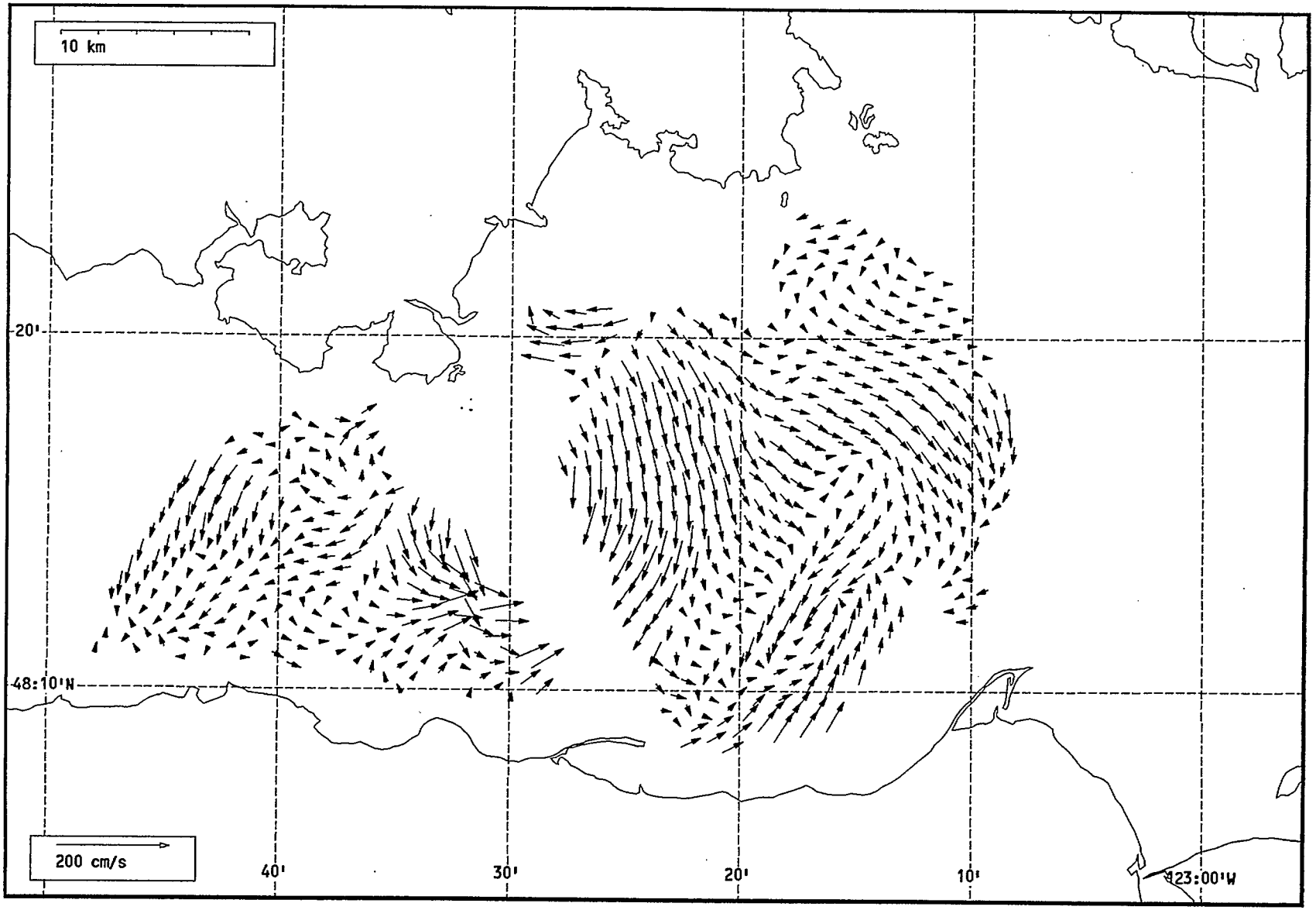

Total current vectors, Juan de Fuca Strait, 1992-07-10 03:00 Z.

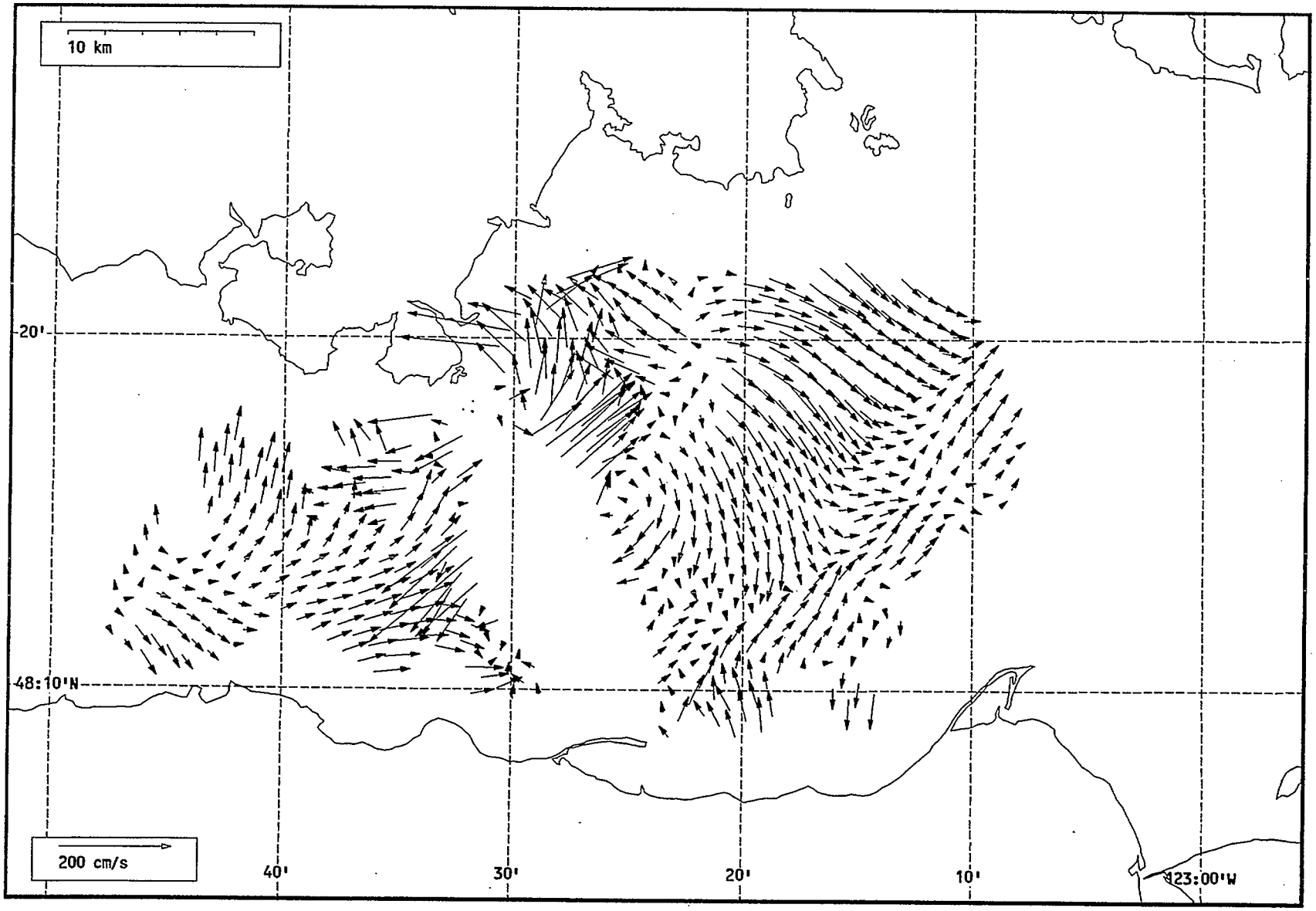

Total current vectors, Juan de Fuca Strait, 1992-07-10 22:00 Z.

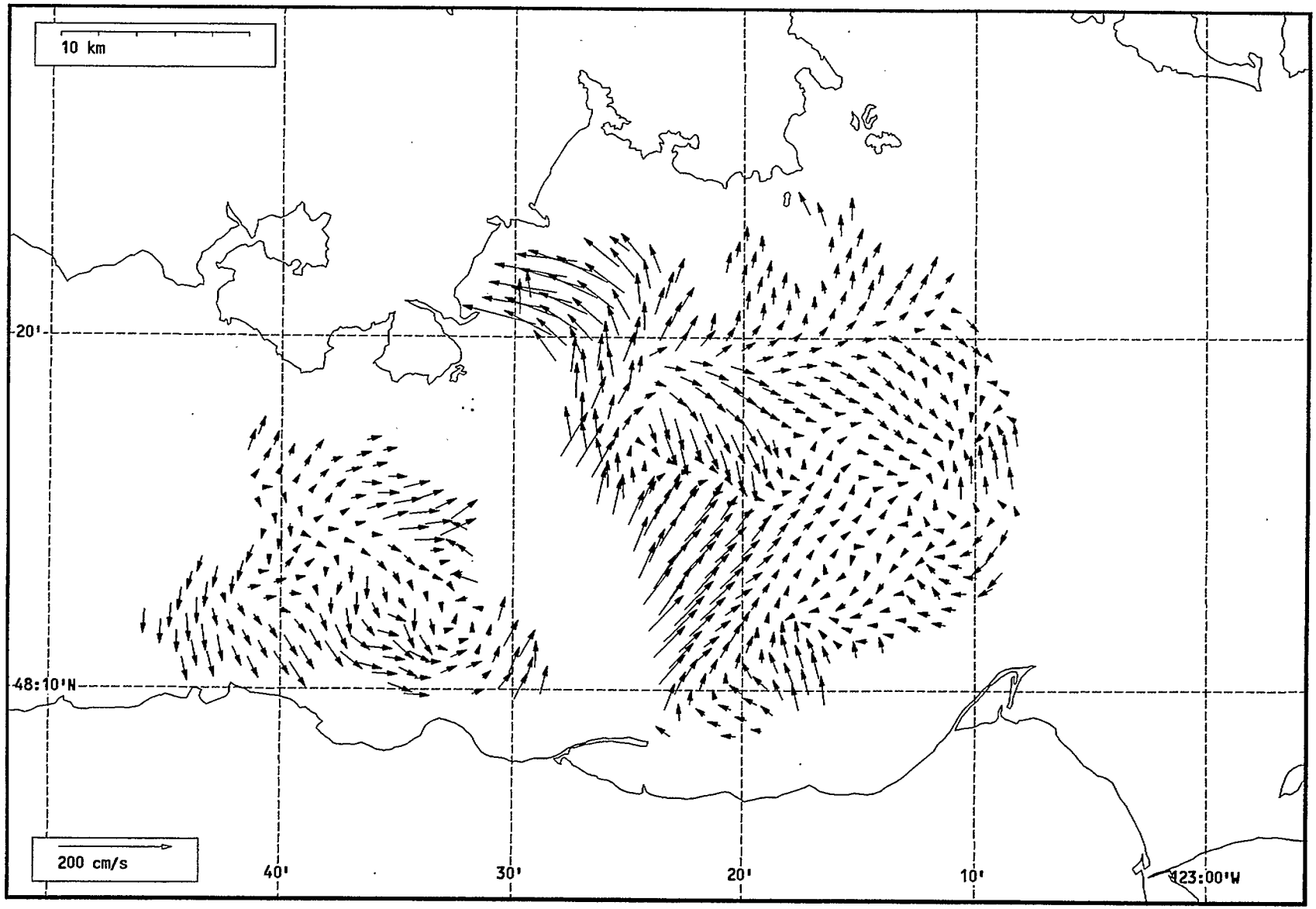

Total current vectors, Juan de Fuca Strait, 1992-07-10 23:00 Z.

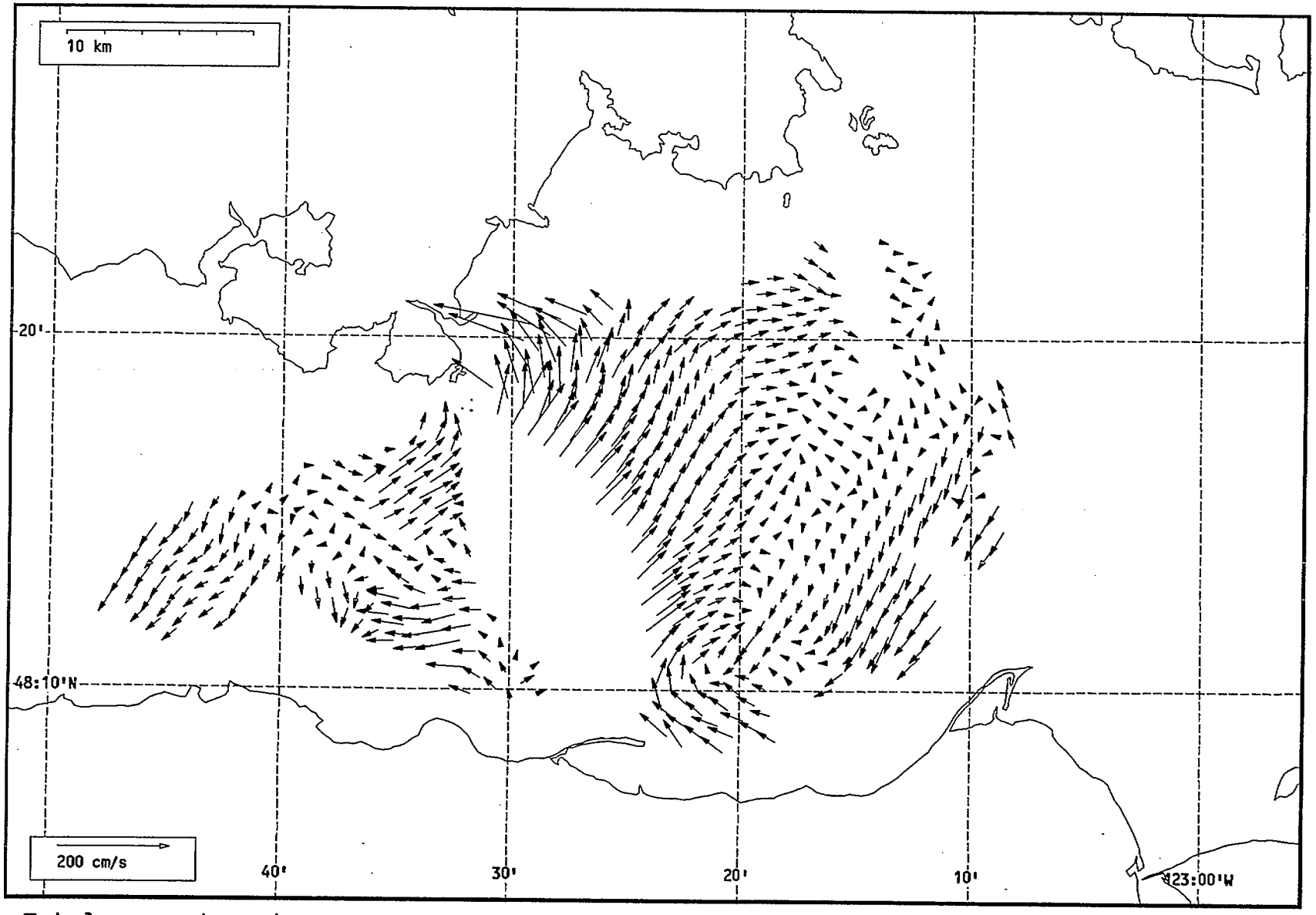

Total current vectors, Juan de Fuca Strait, 1992-07-11 00:00 Z.

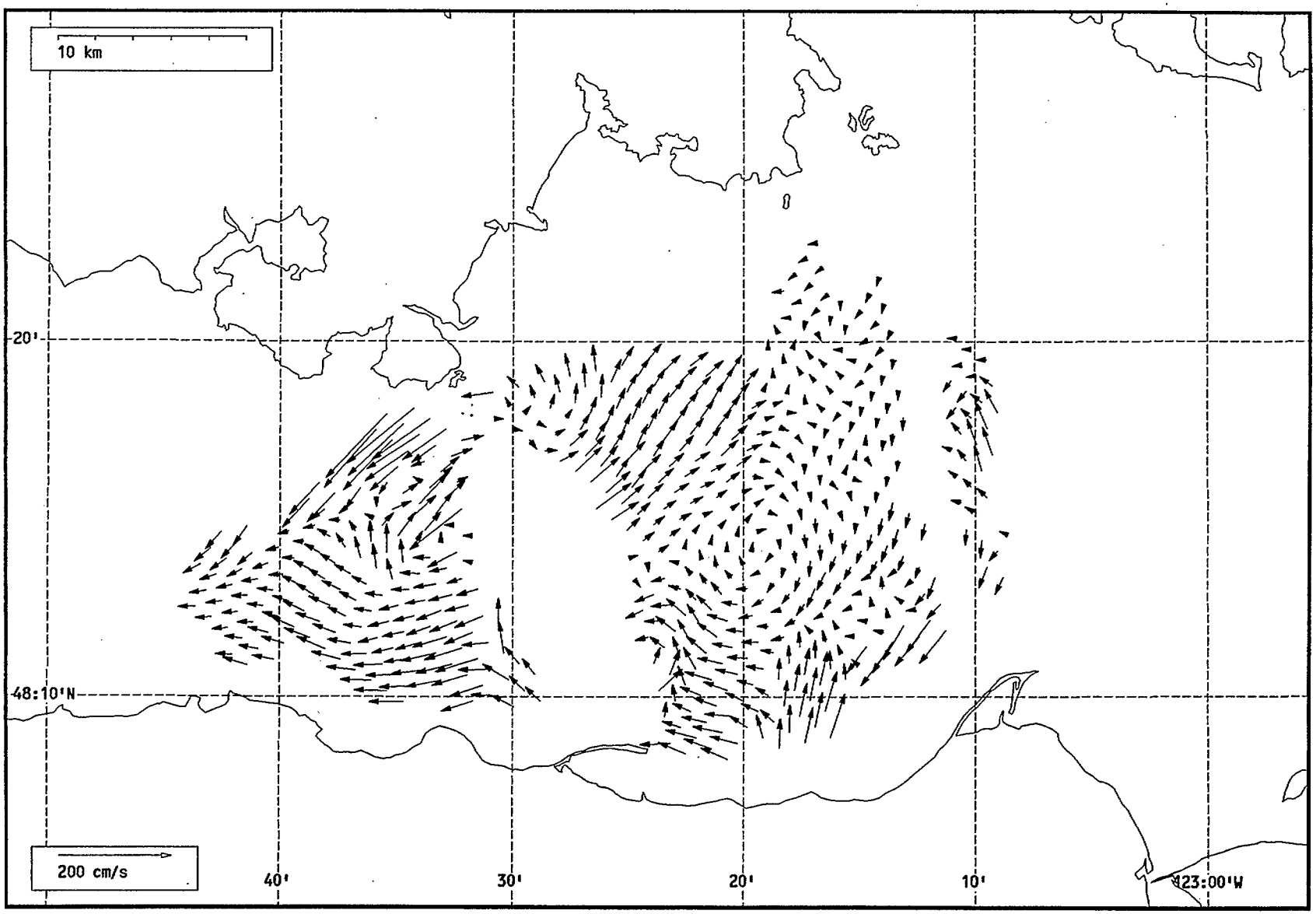

Total current vectors, Juan de Fuca Strait, 1992-07-11 01:00 Z.

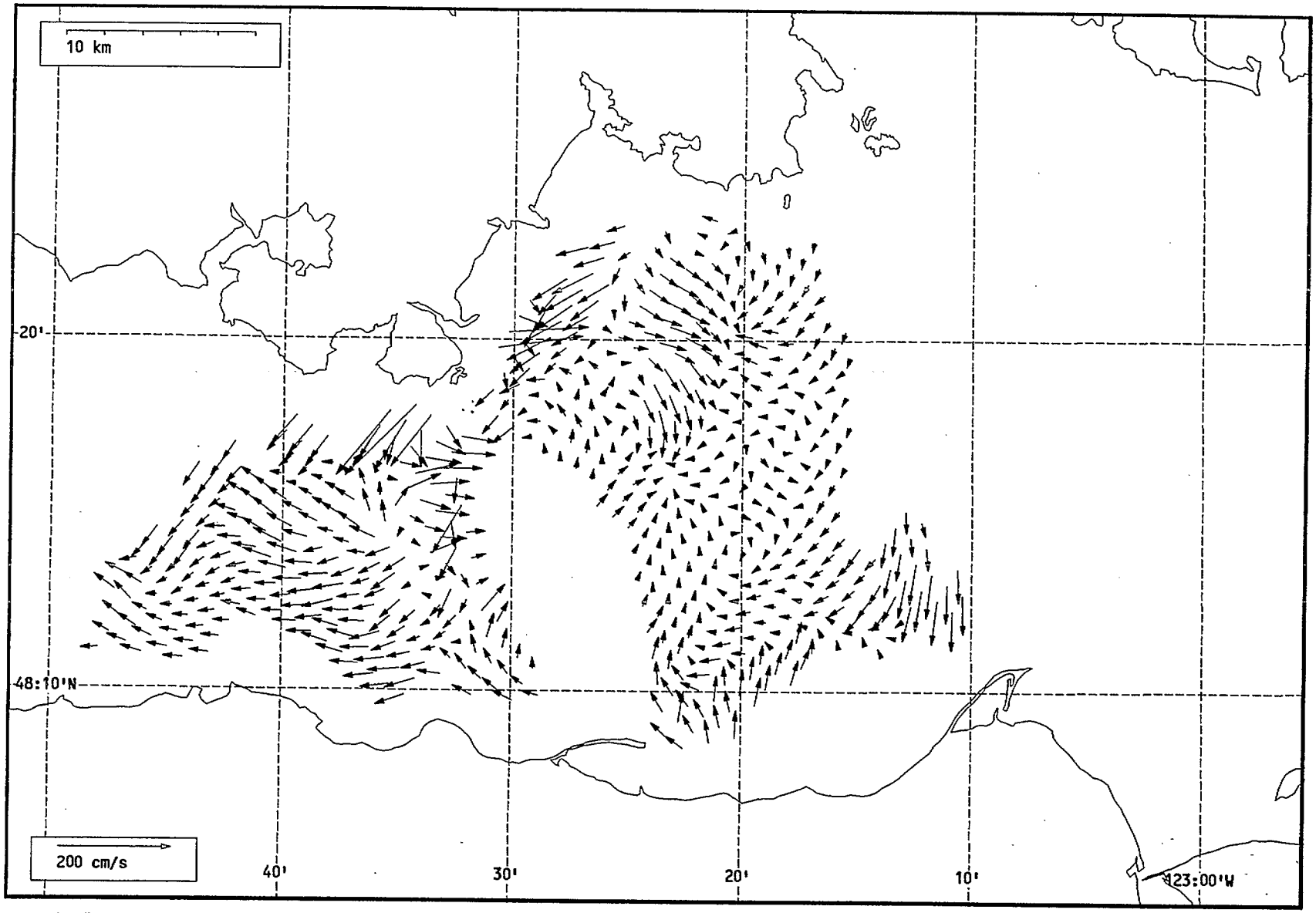

Total current vectors, Juan de Fuca Strait, 1992-07-11 02:00 Z.

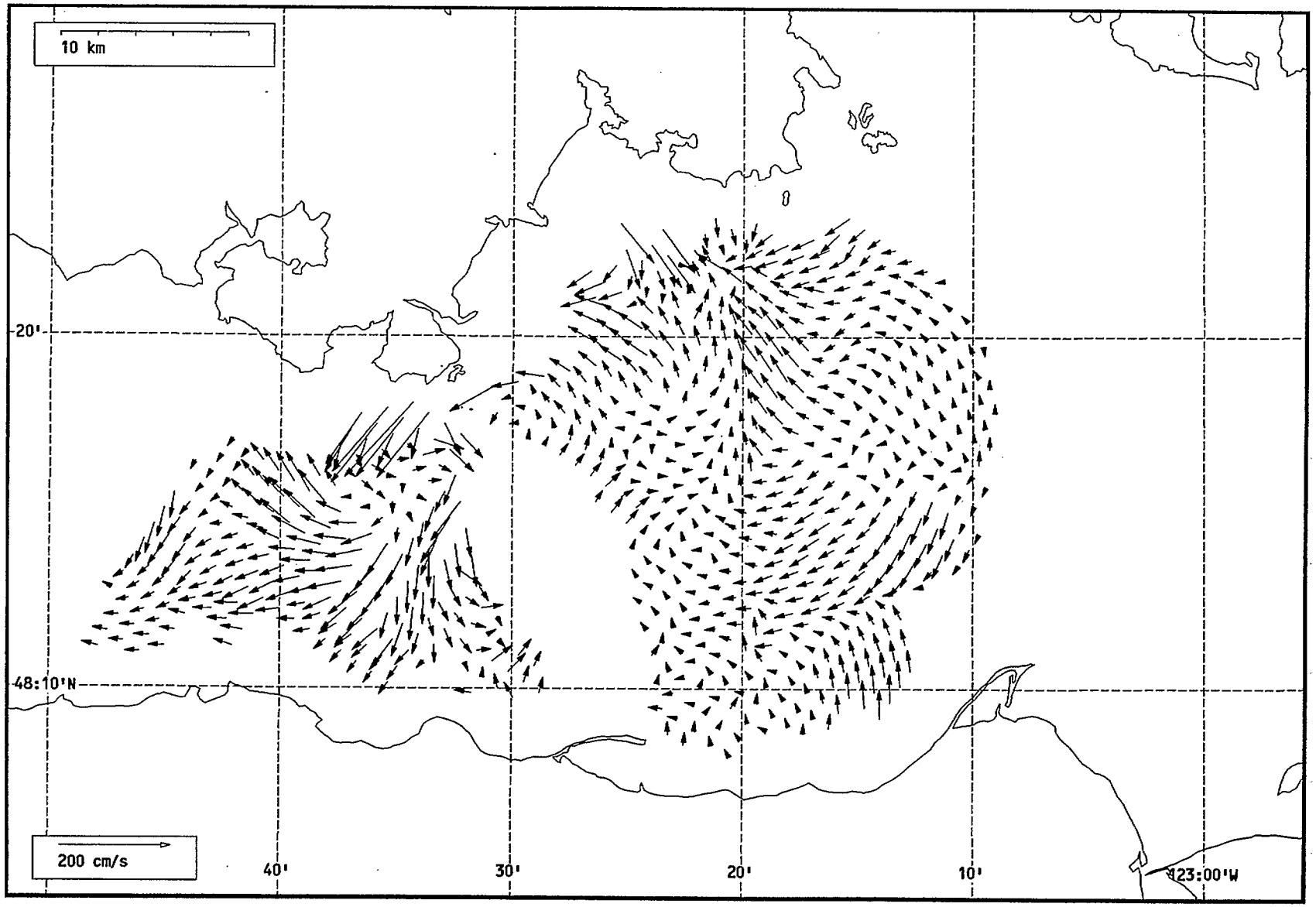

Total current vectors, Juan de Fuca Strait, 1992-07-11 03:00 Z.

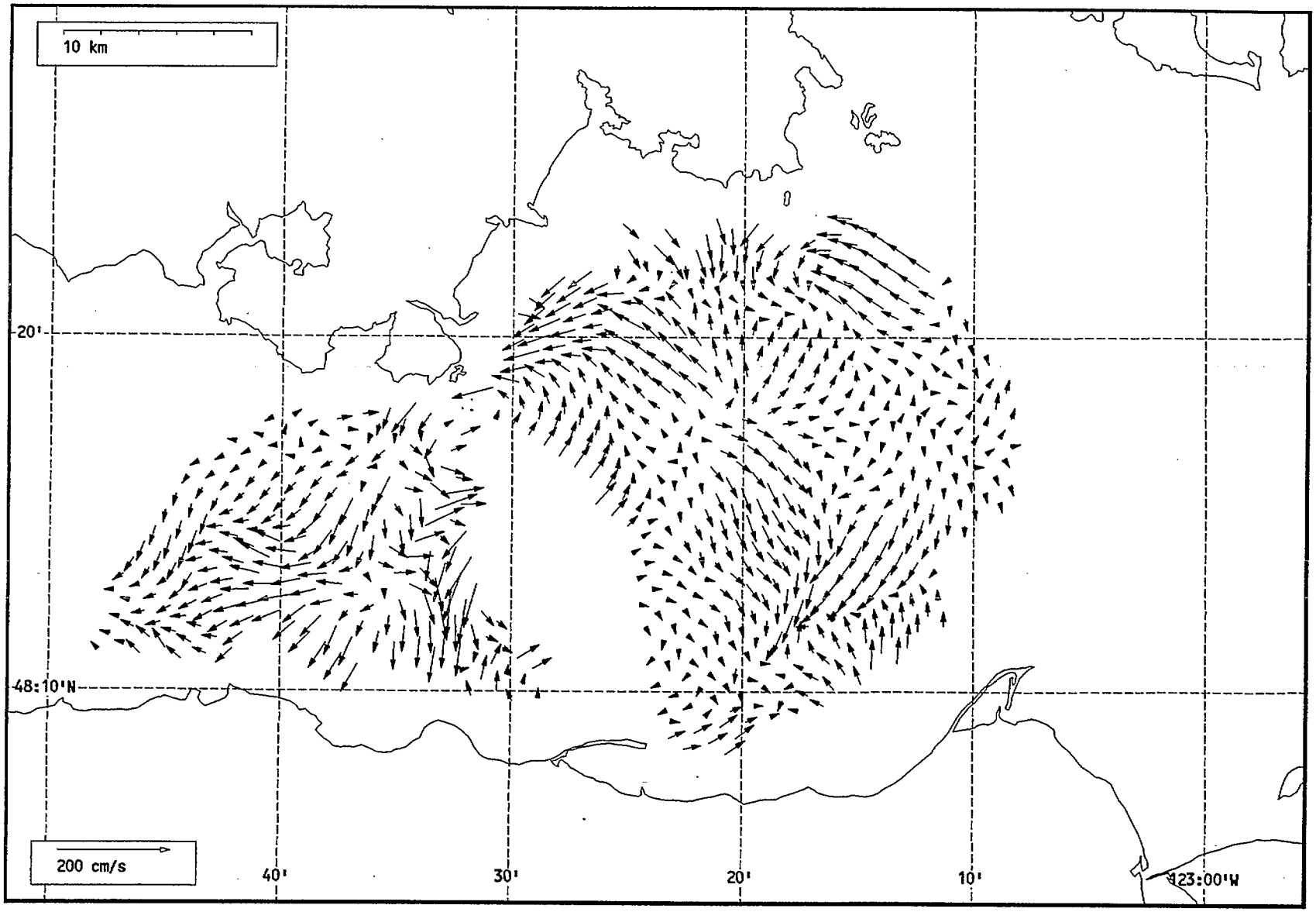

Total current vectors, Juan de Fuca Strait, 1992-07-11 04:00 Z.

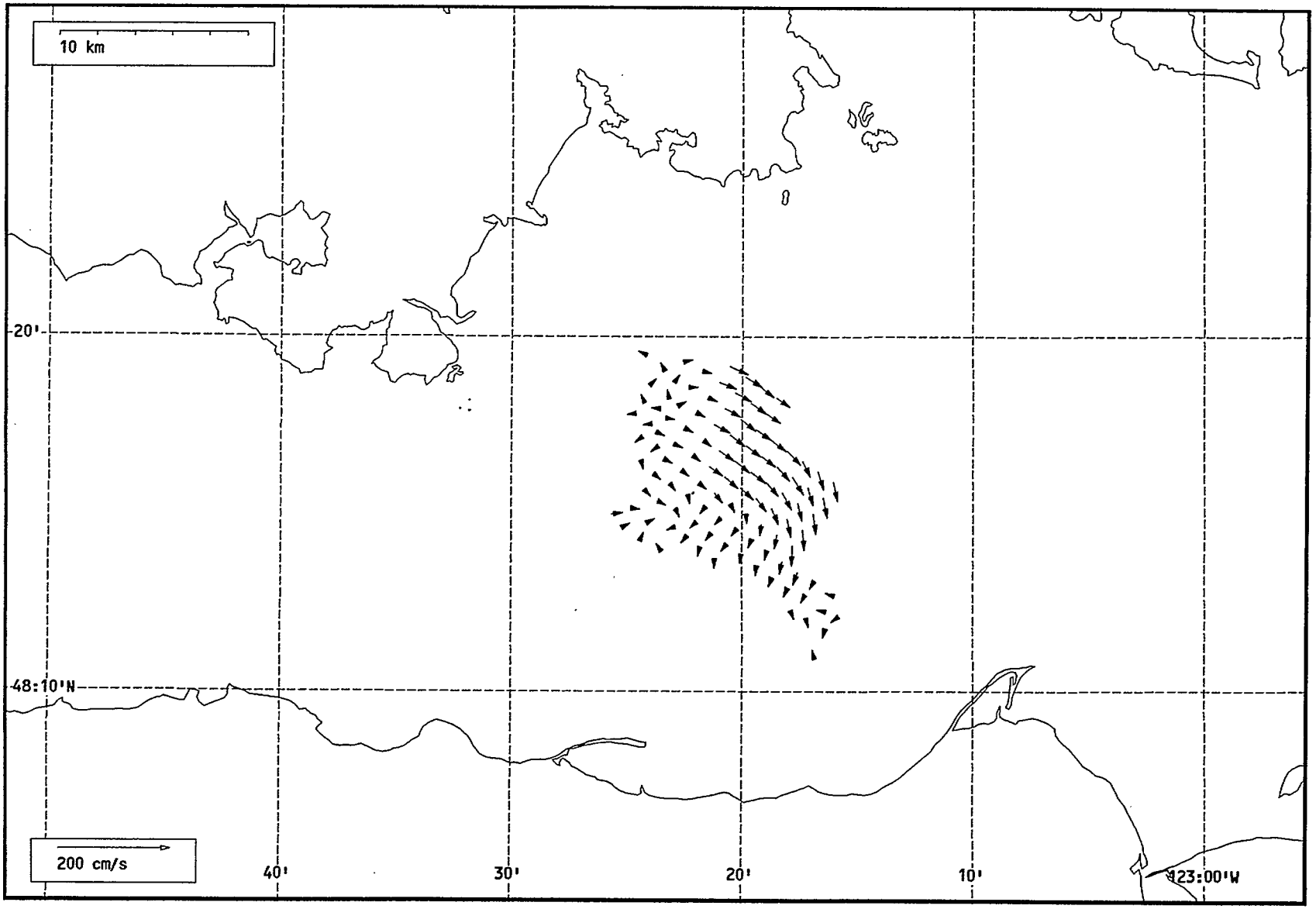

Total current vectors, Juan de Fuca Strait, 1992-07-11 05:00 Z.

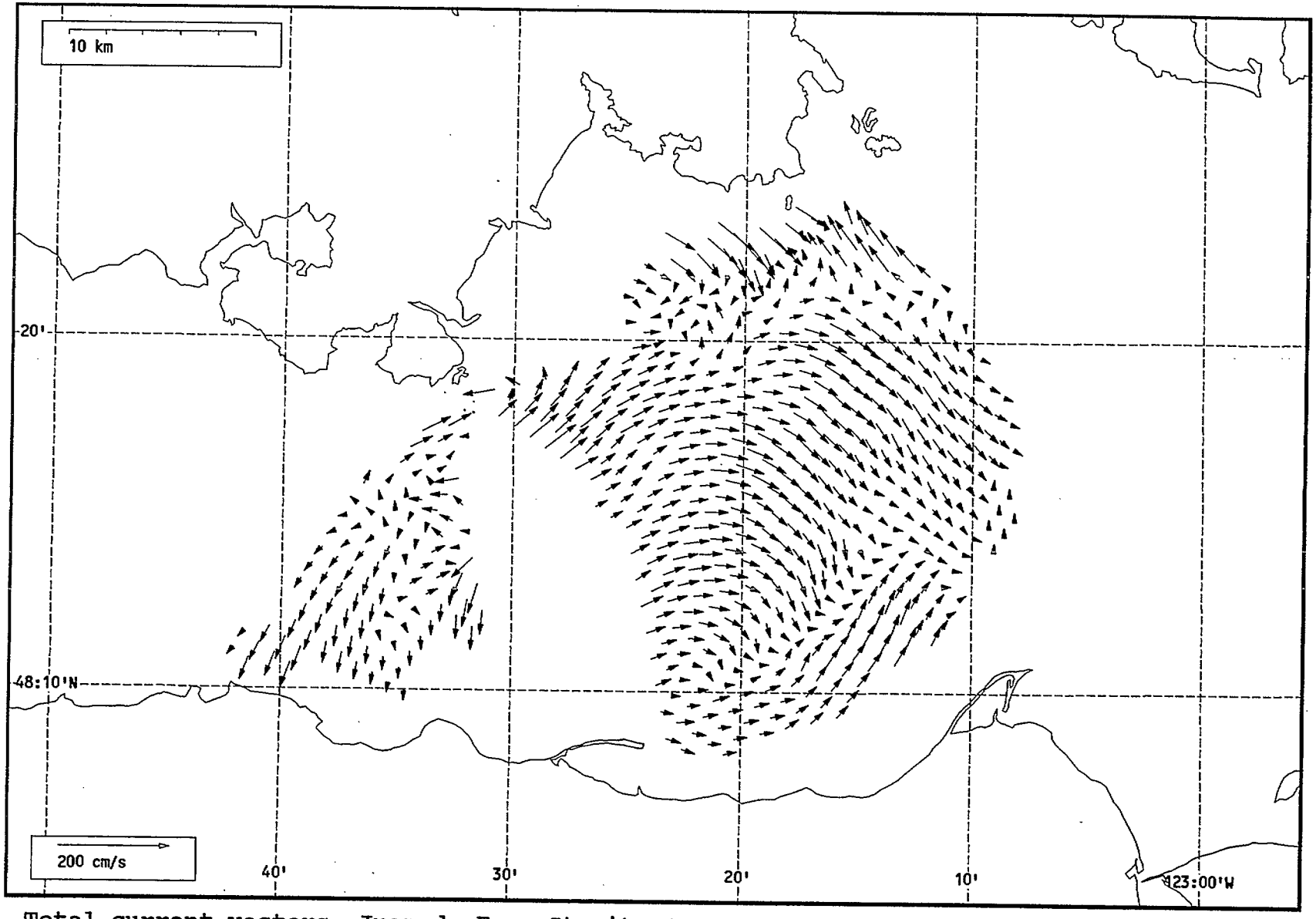

Total current vectors, Juan de Fuca Strait, 1992-07-11 06:00 Z.

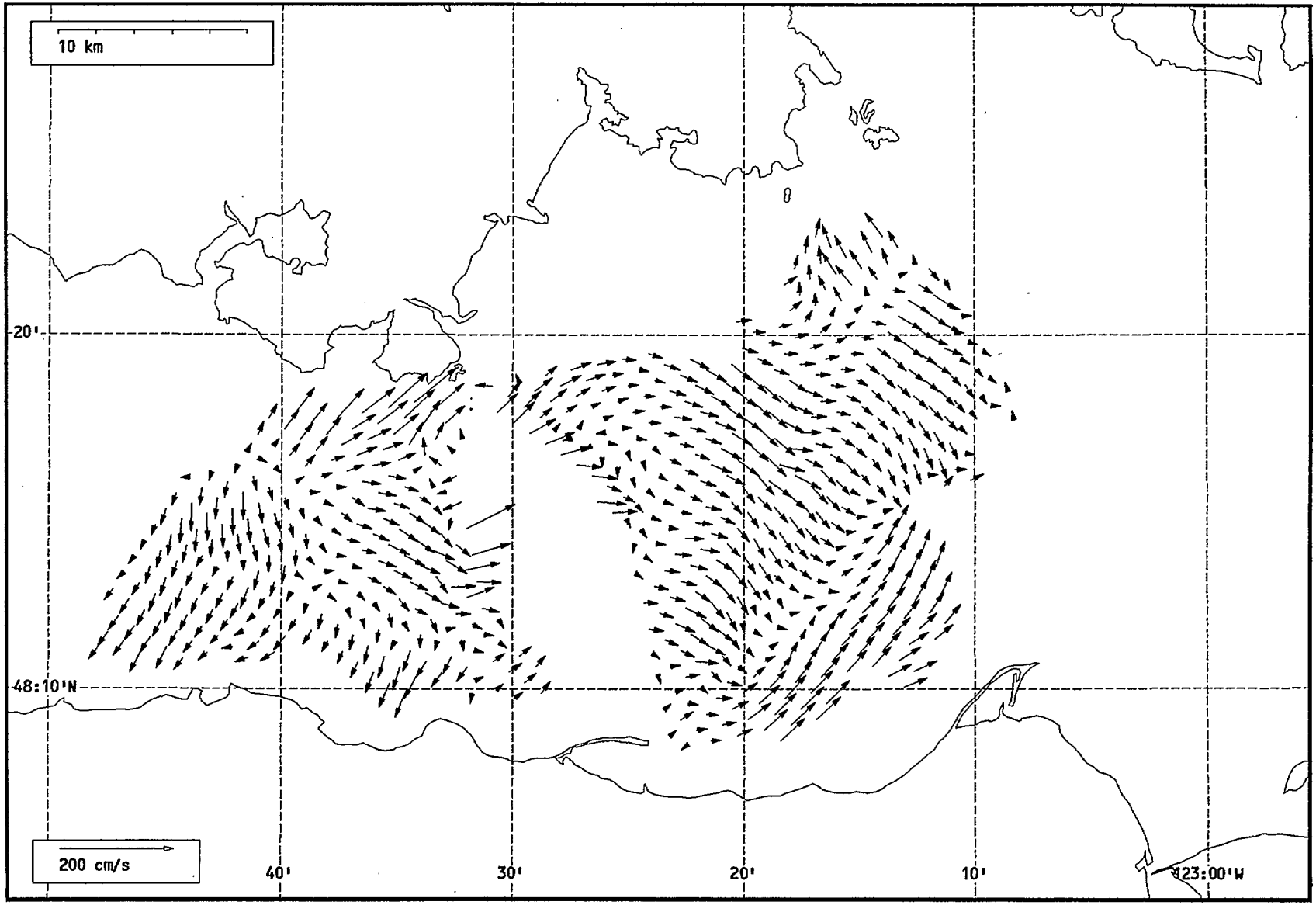

Total current vectors, Juan de Fuca Strait, 1992-07-11 07:00 Z.

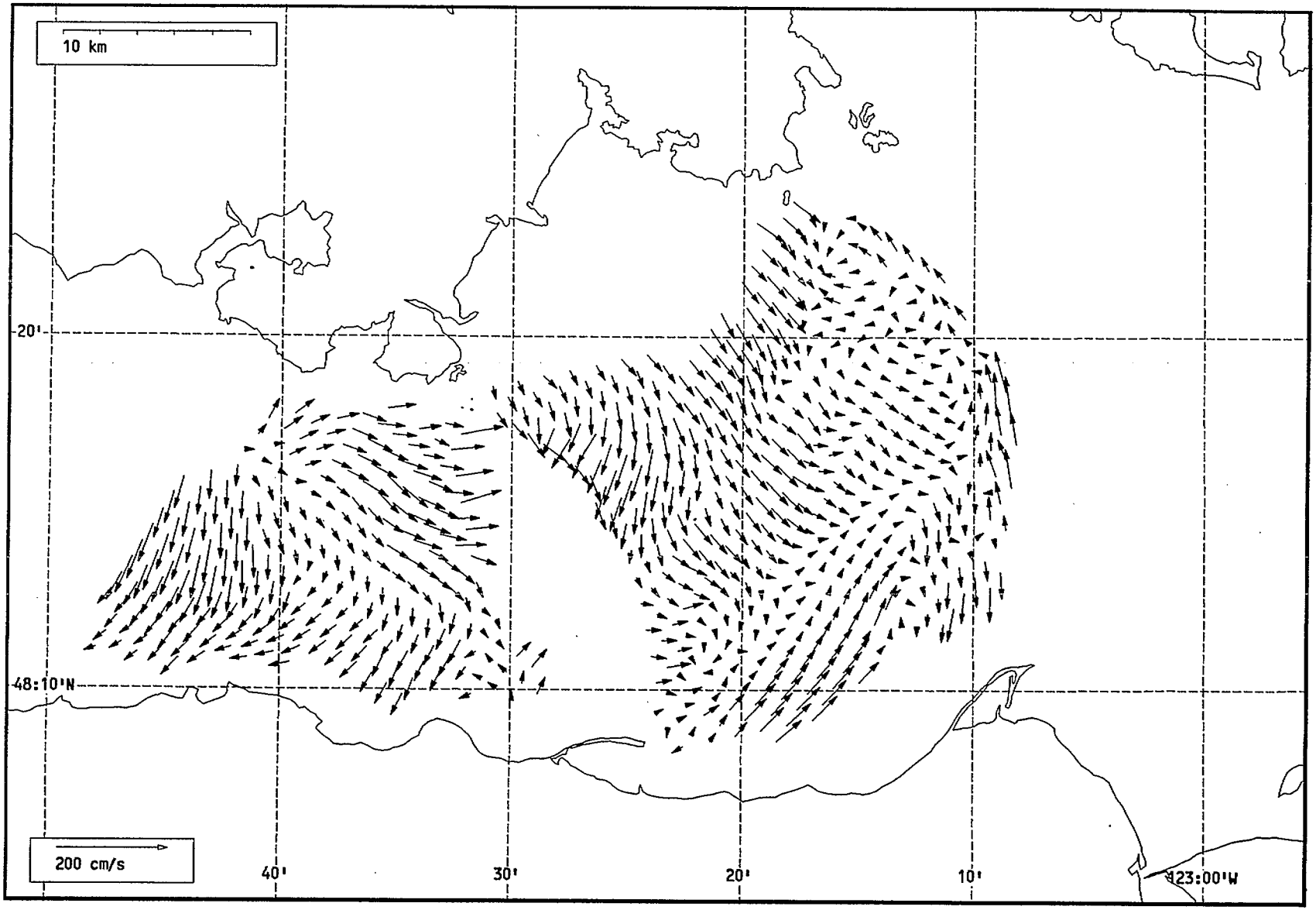

Total current vectors, Juan de Fuca Strait, 1992-07-11 08:00 Z.

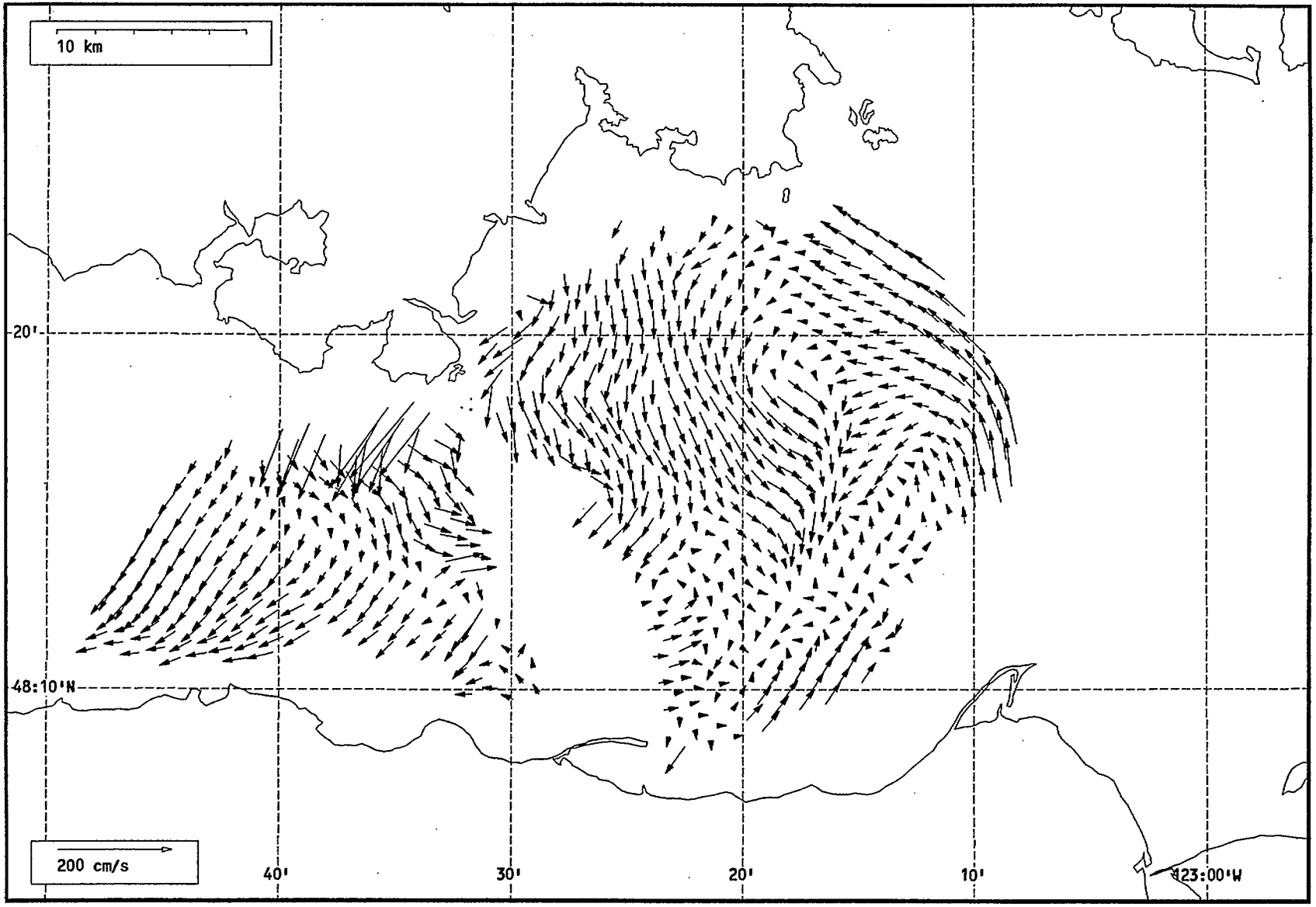

Total current vectors, Juan de Fuca Strait, 1992-07-11 09:00 Z.

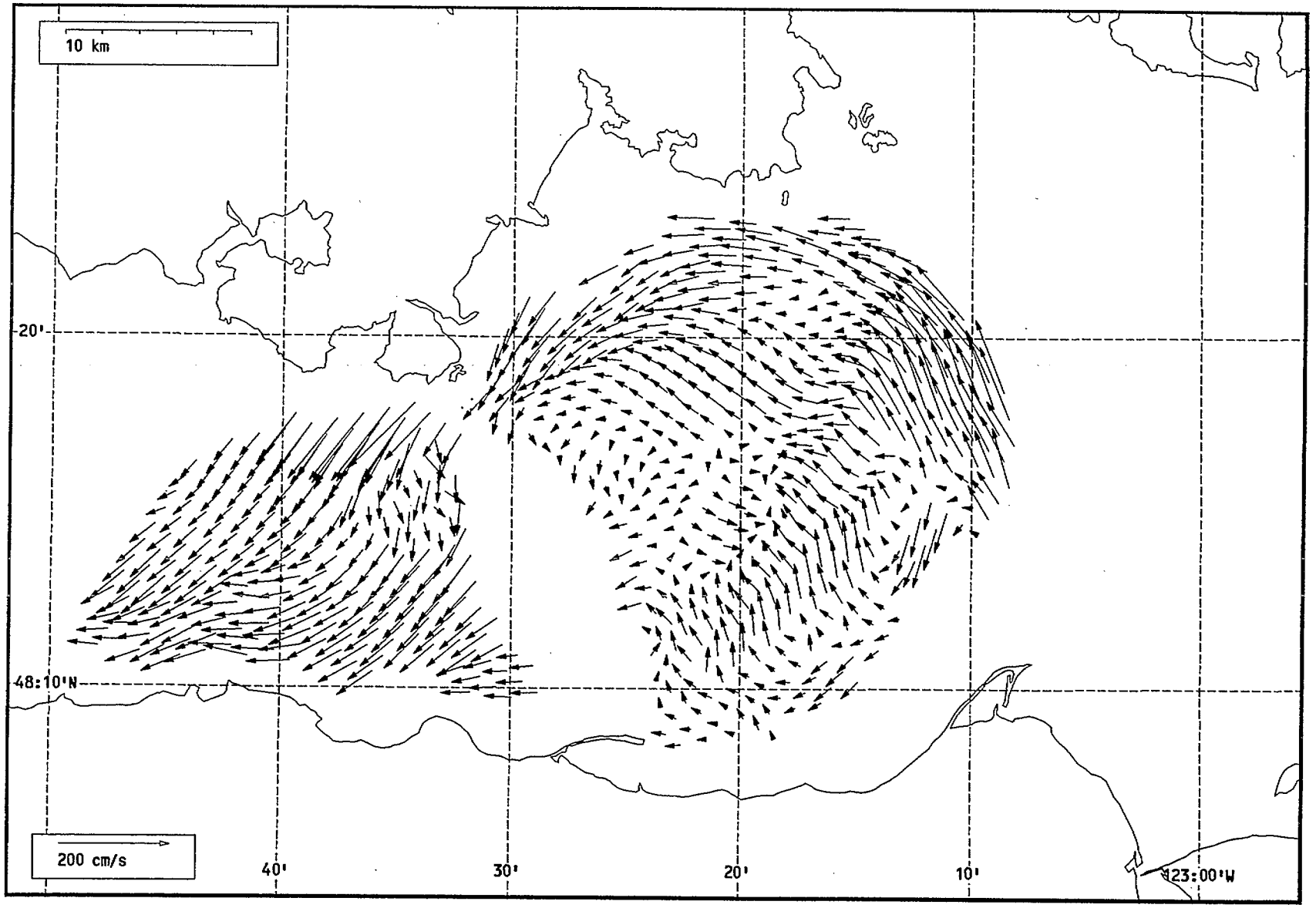

Total current vectors, Juan de Fuca Strait, 1992-07-11 10:00 Z.

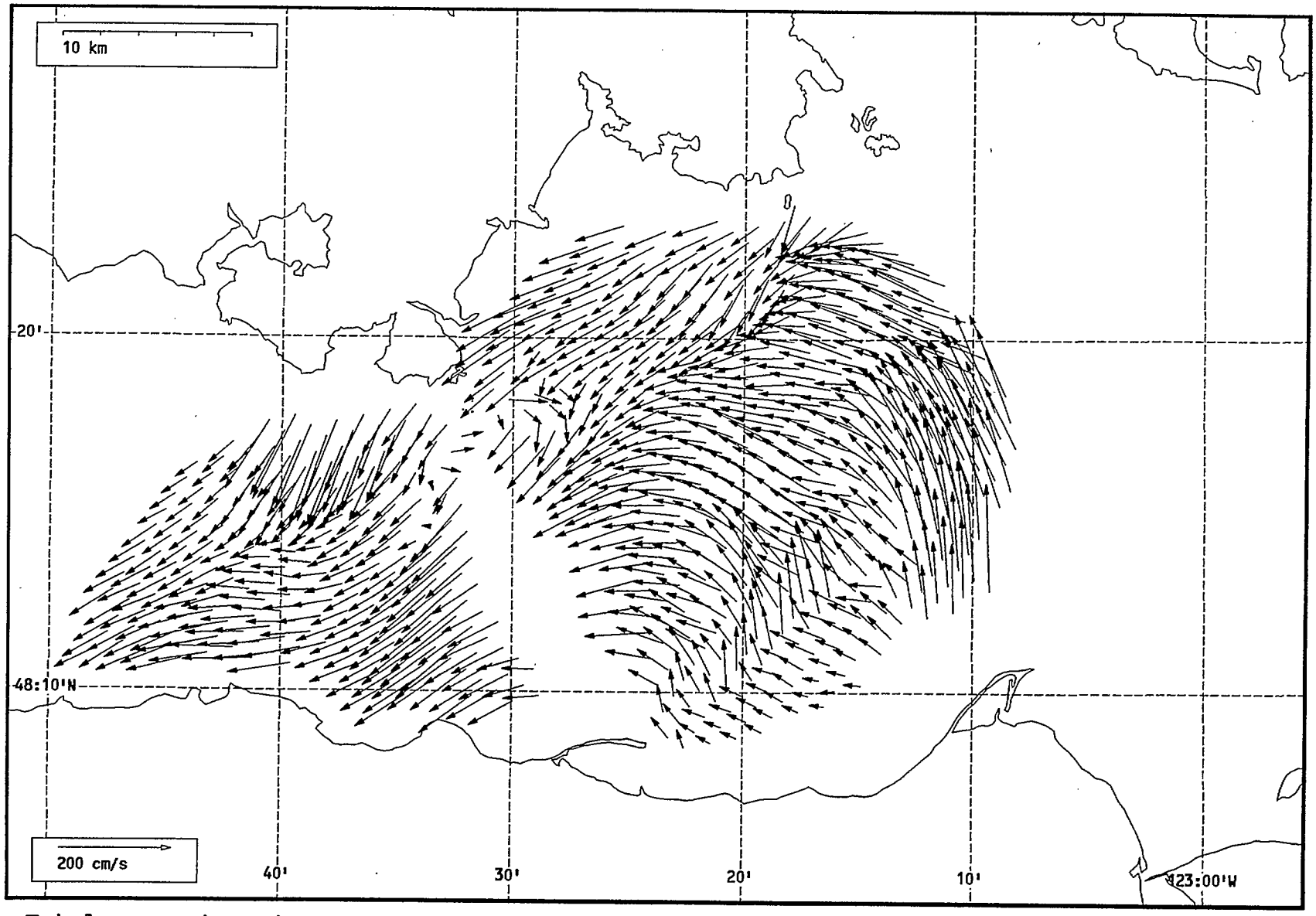

Total current vectors, Juan de Fuca Strait, 1992-07-11 11:00 Z.

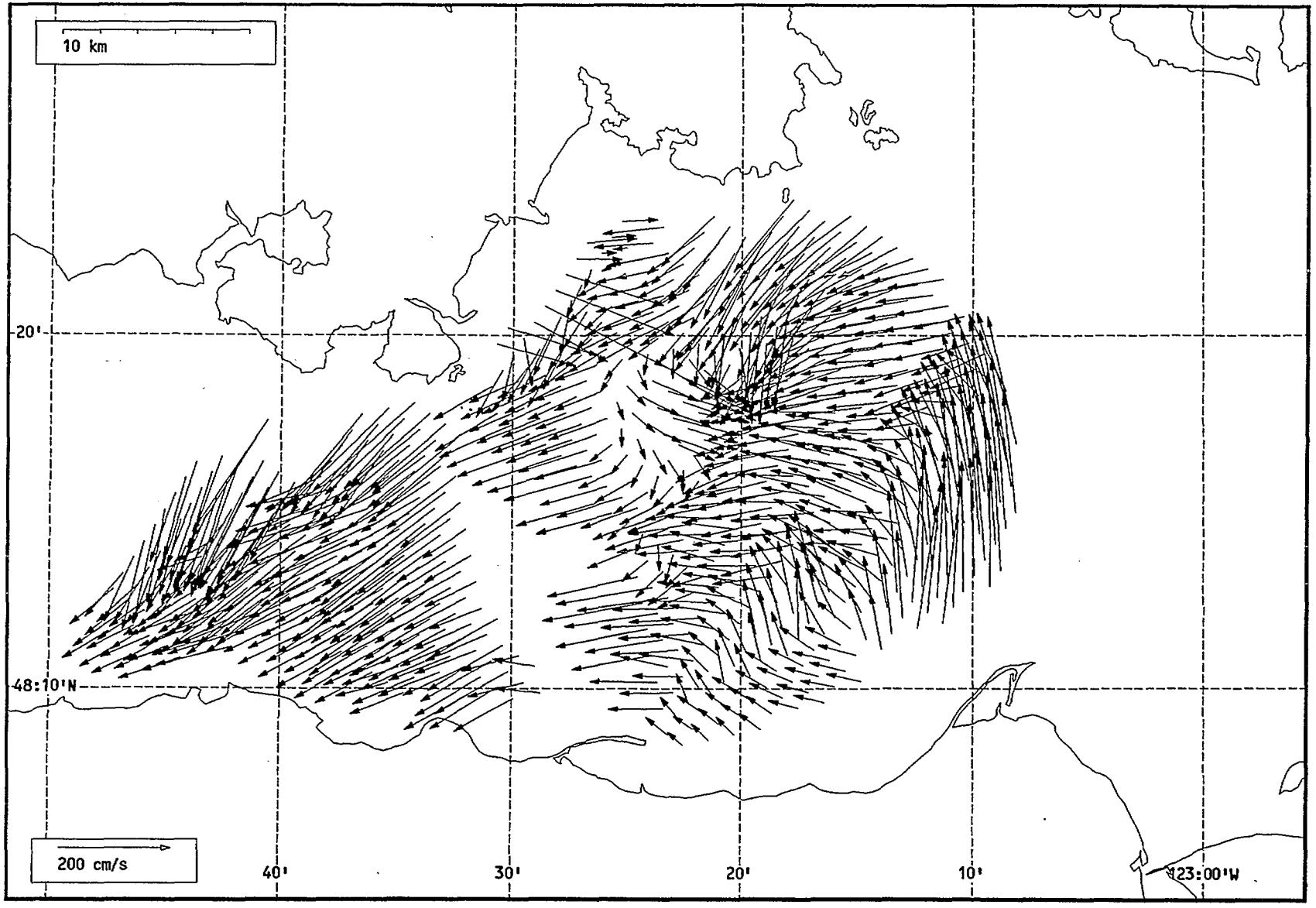

Total current vectors, Juan de Fuca Strait, 1992-07-11 12:00 Z.

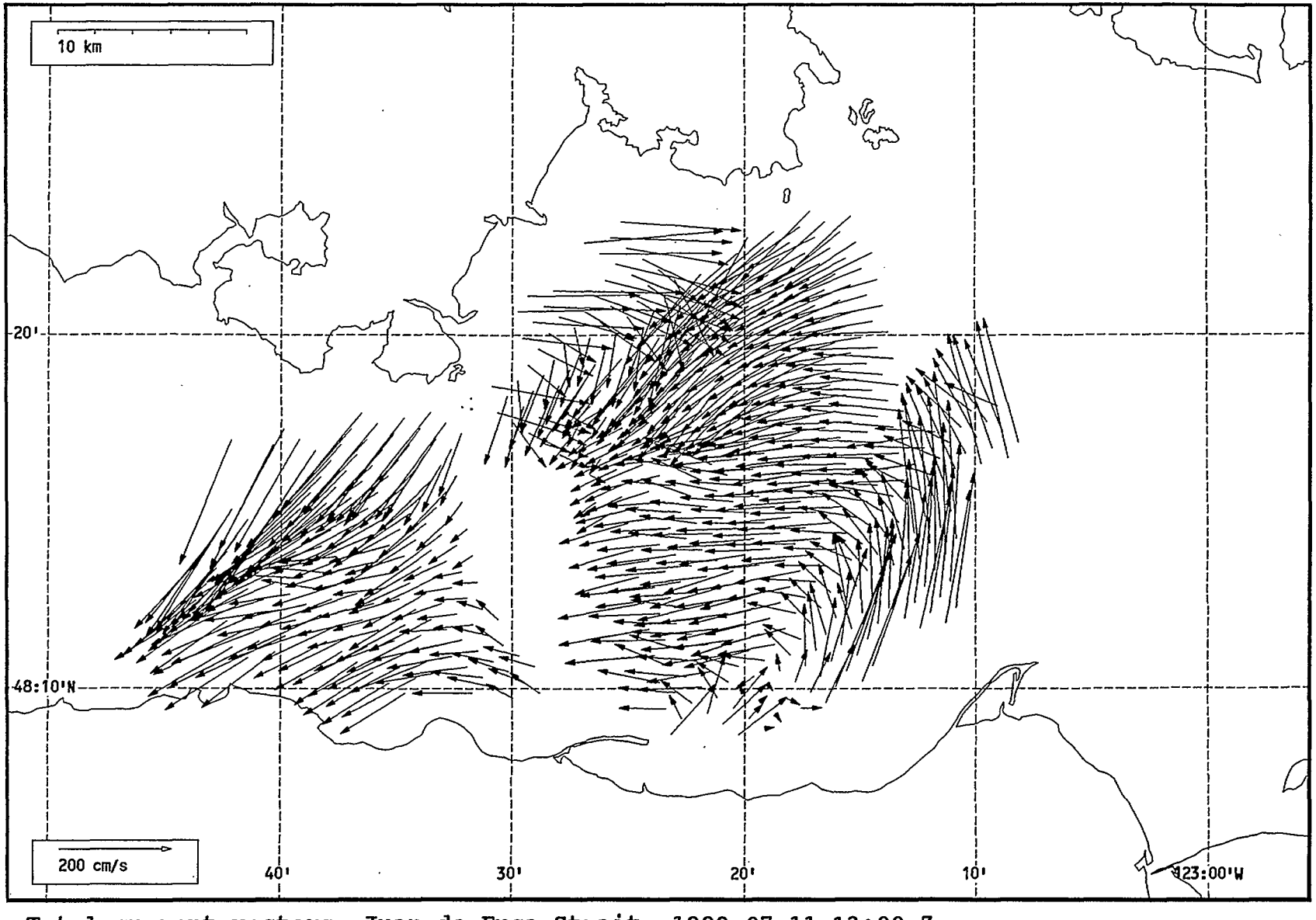

Total current vectors, Juan de Fuca Strait, 1992-07-11 13:00 Z.

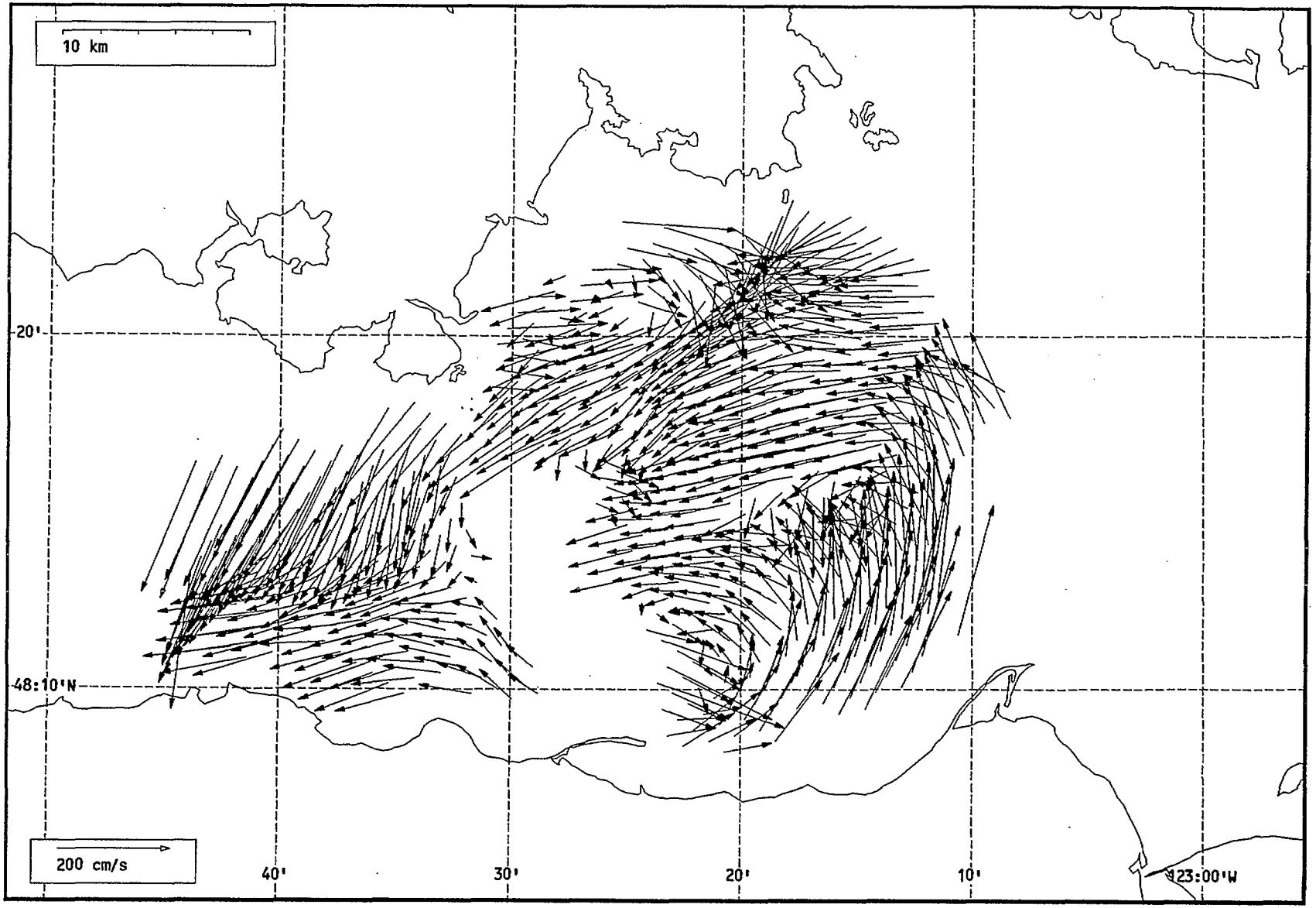

Total current vectors, Juan de Fuca Strait, 1992-07-11 14:00 Z.

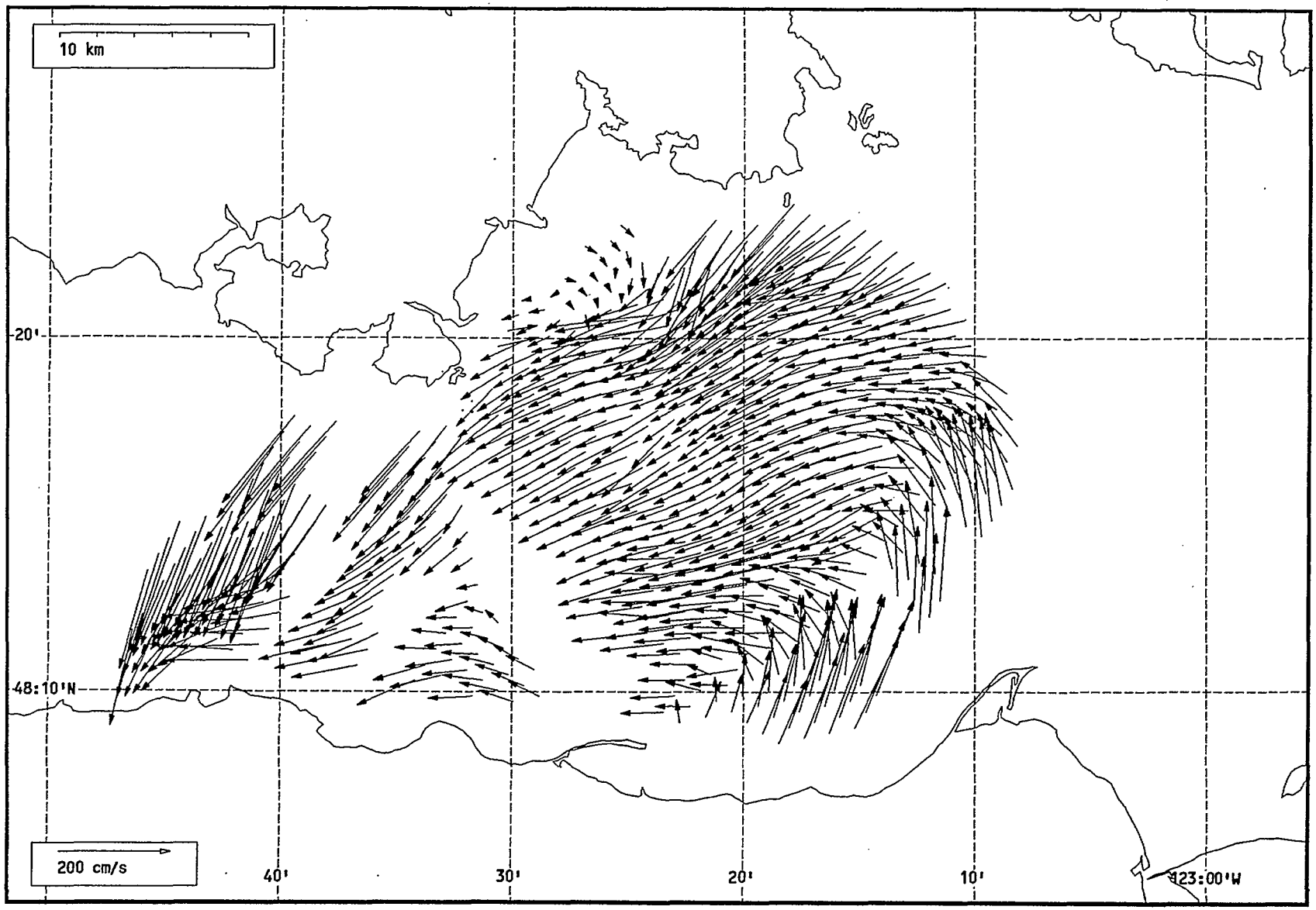

Total current vectors, Juan de Fuca Strait, 1992-07-11 15:00 Z.

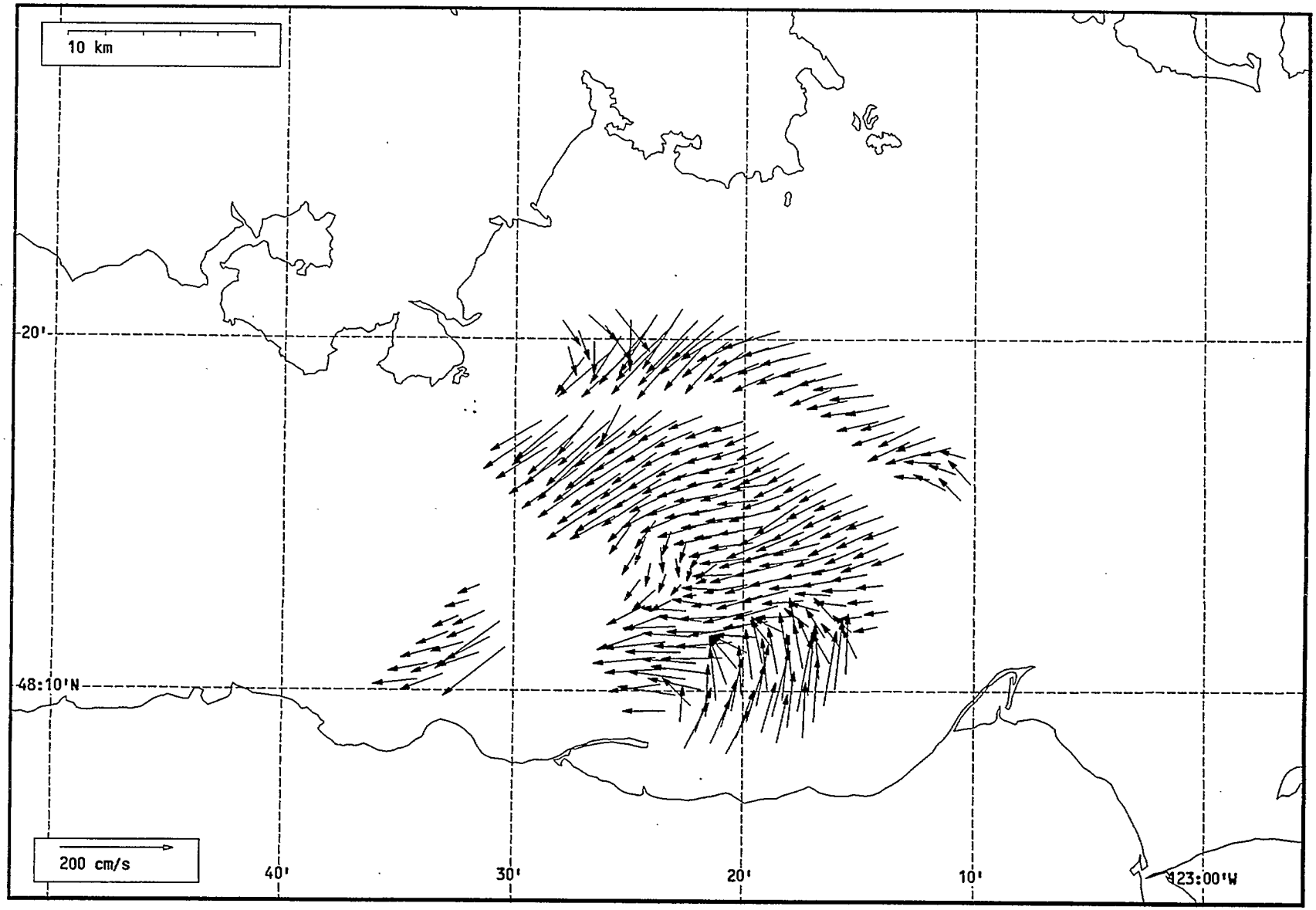

Total current vectors, Juan de Fuca Strait, 1992-07-11 16:00 Z.

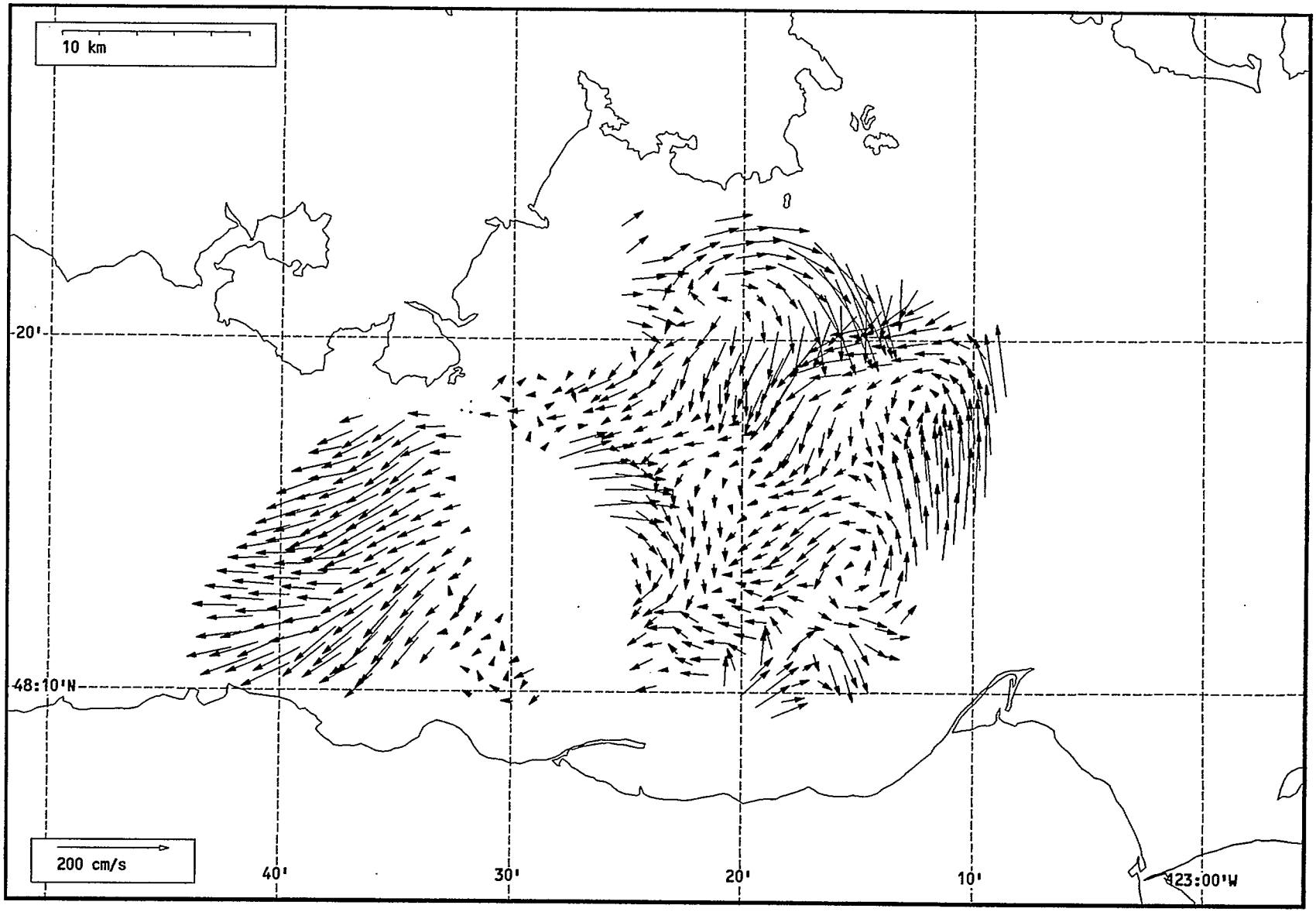

Total current vectors, Juan de Fuca Strait, 1992-07-11 17:00 Z.

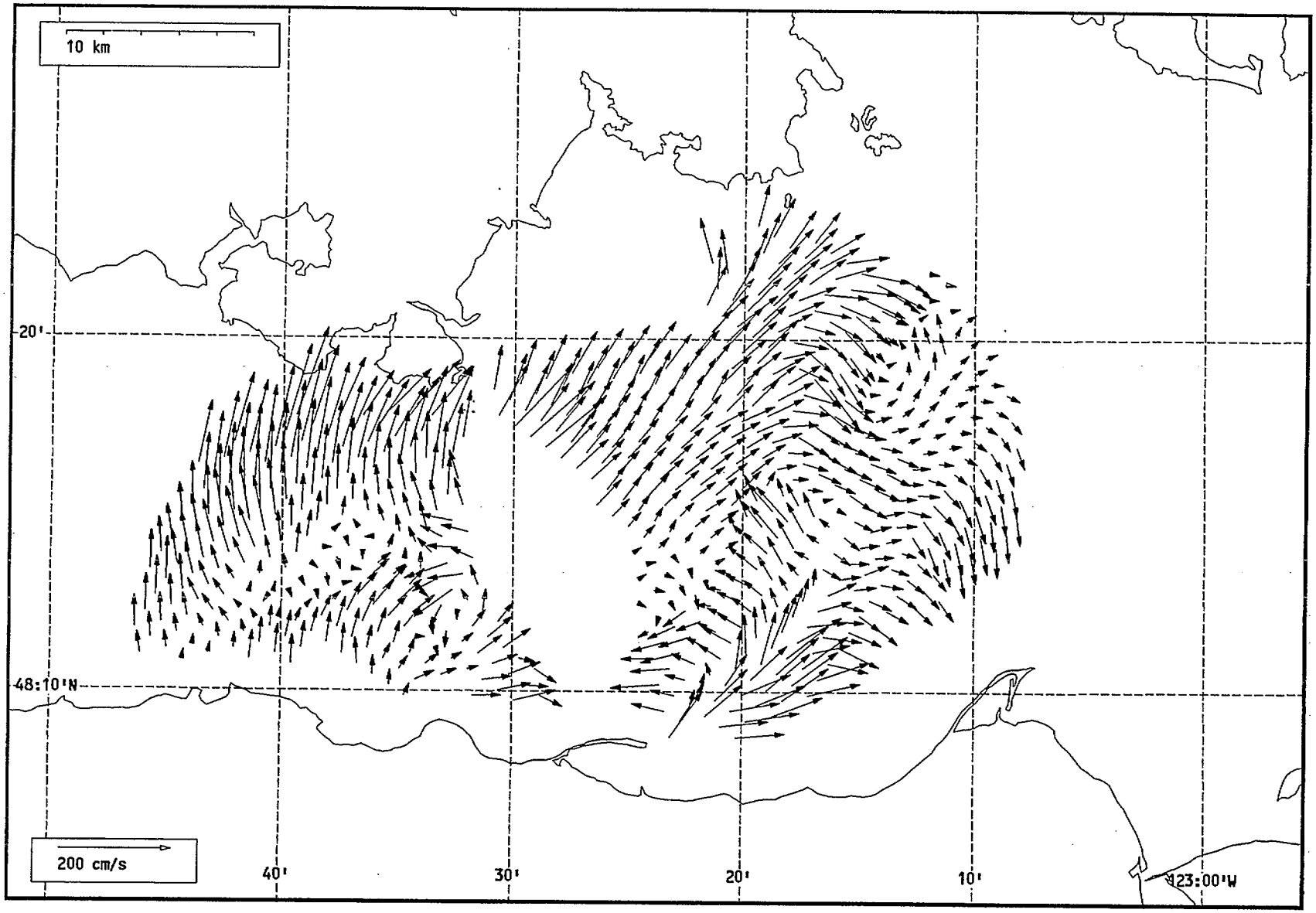

Total current vectors, Juan de Fuca Strait, 1992-07-11 19:00 Z.

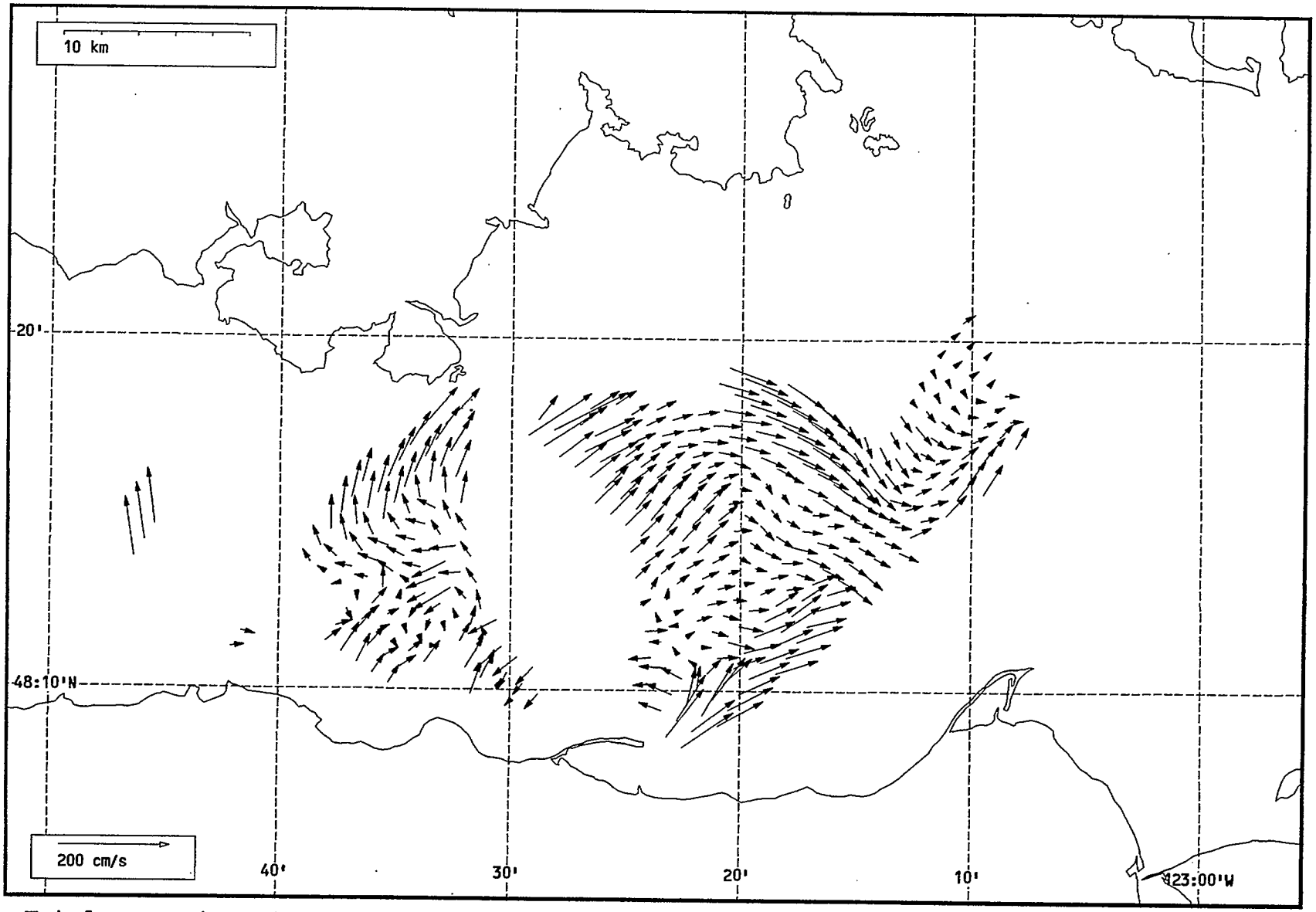

Total current vectors, Juan de Fuca Strait, 1992-07-11 20:00 Z.

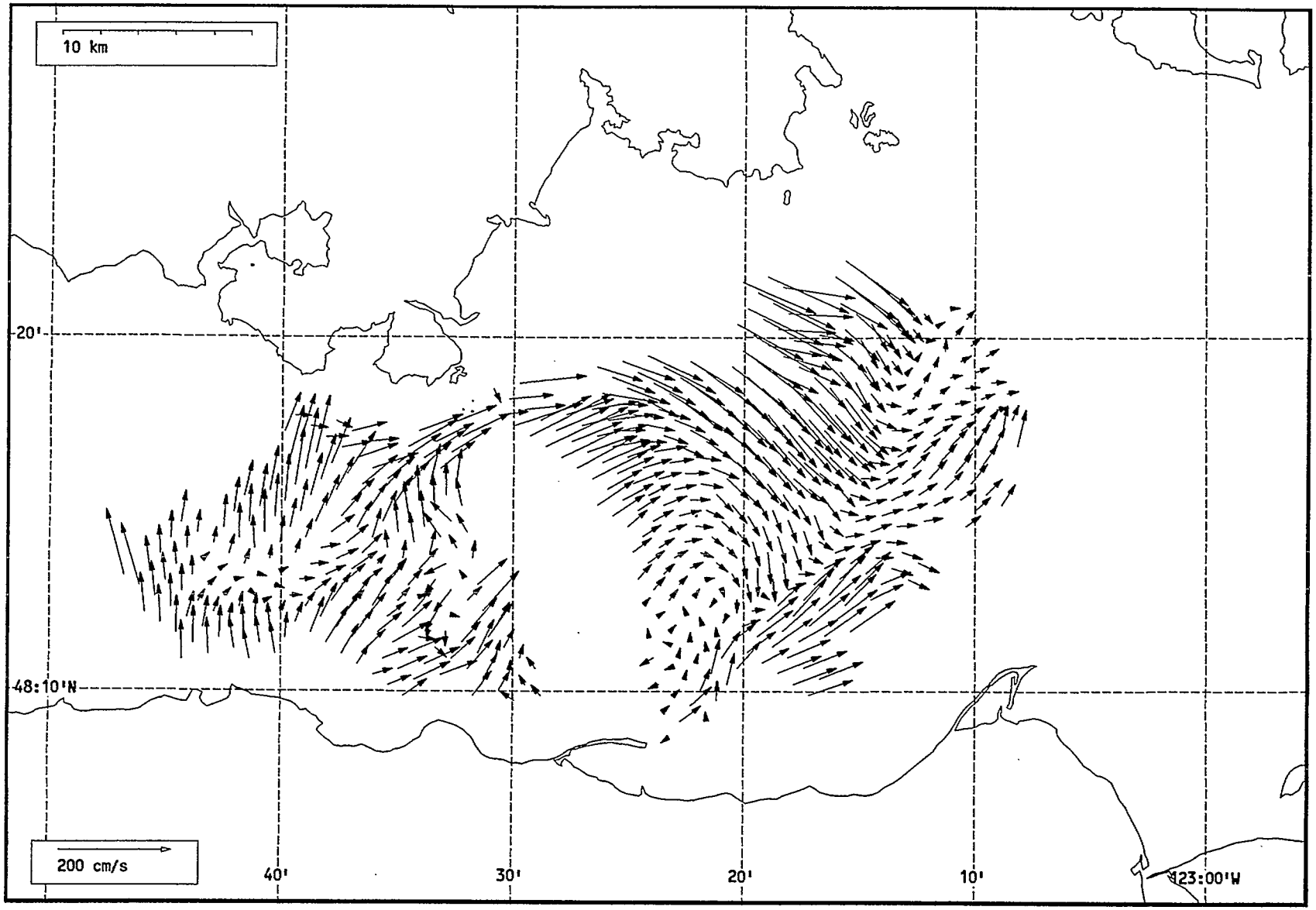

Total current vectors, Juan de Fuca Strait, 1992-07-11 21:00 Z.

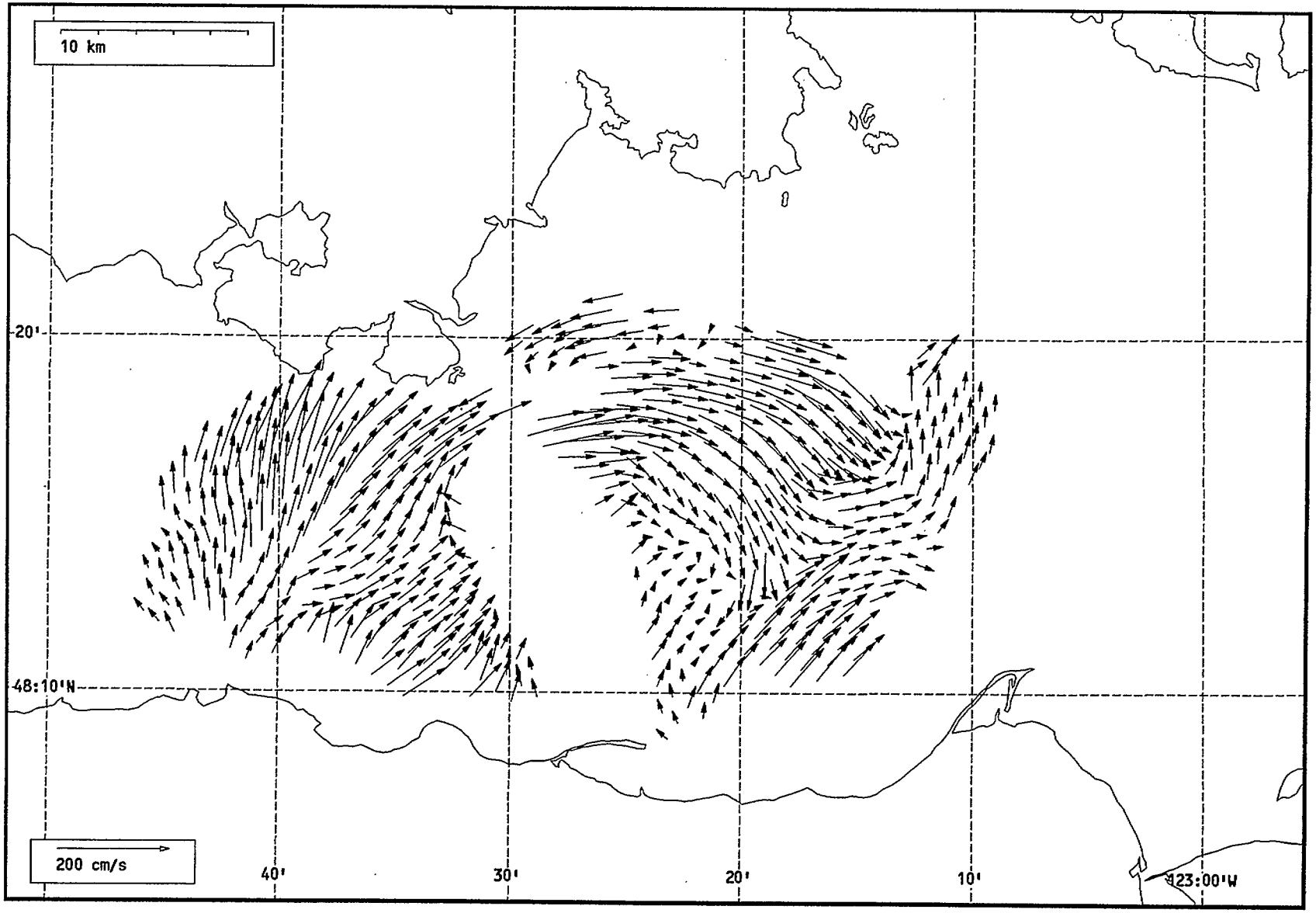

Total current vectors, Juan de Fuca Strait, 1992-07-11 22:00 Z.

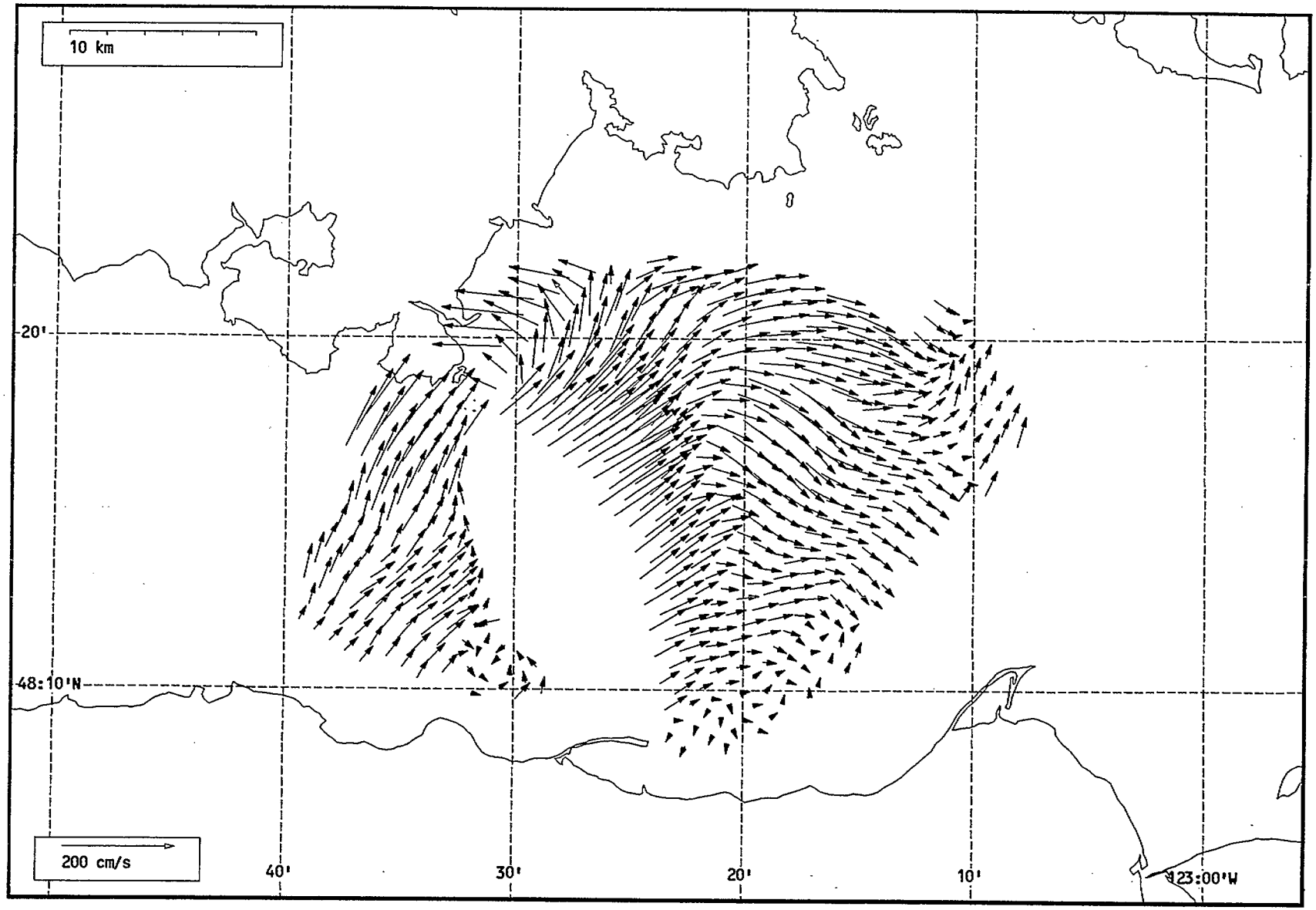

Total current vectors, Juan de Fuca Strait, 1992-07-11 23:00 Z.

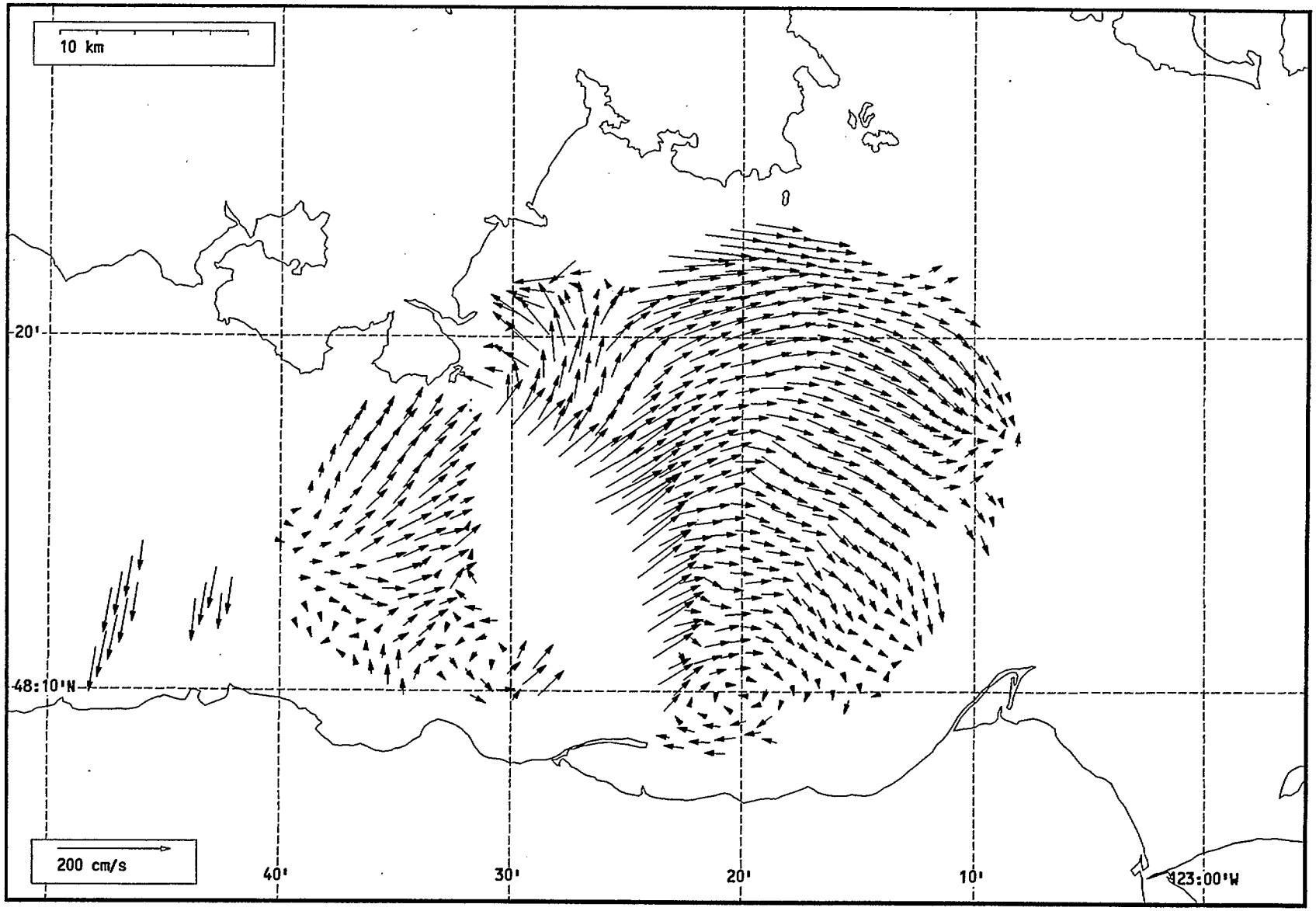

Total current vectors, Juan de Fuca Strait, 1992-07-12 00:00 Z.

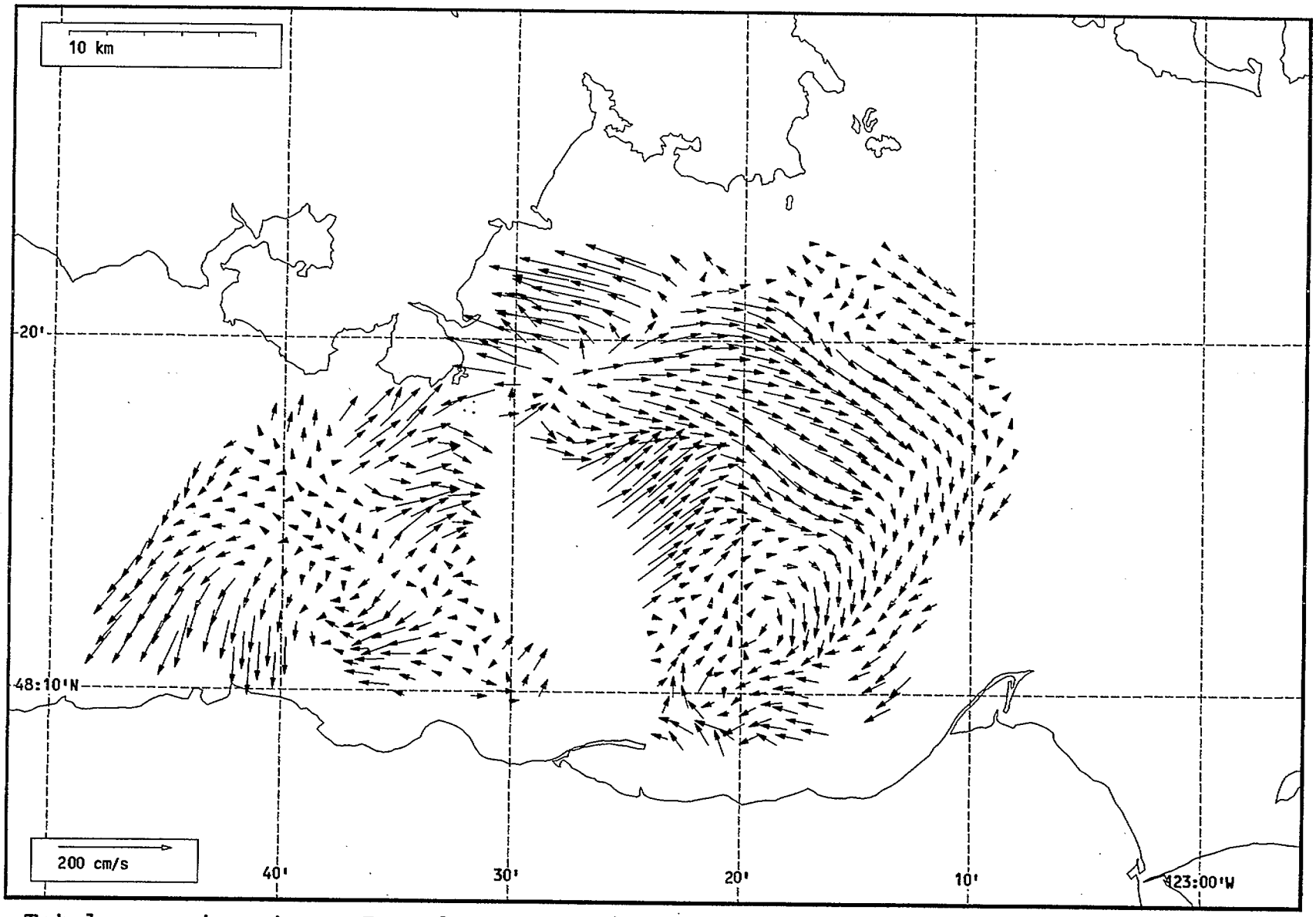

Total current vectors, Juan de Fuca Strait, 1992-07-12 01:00 Z.

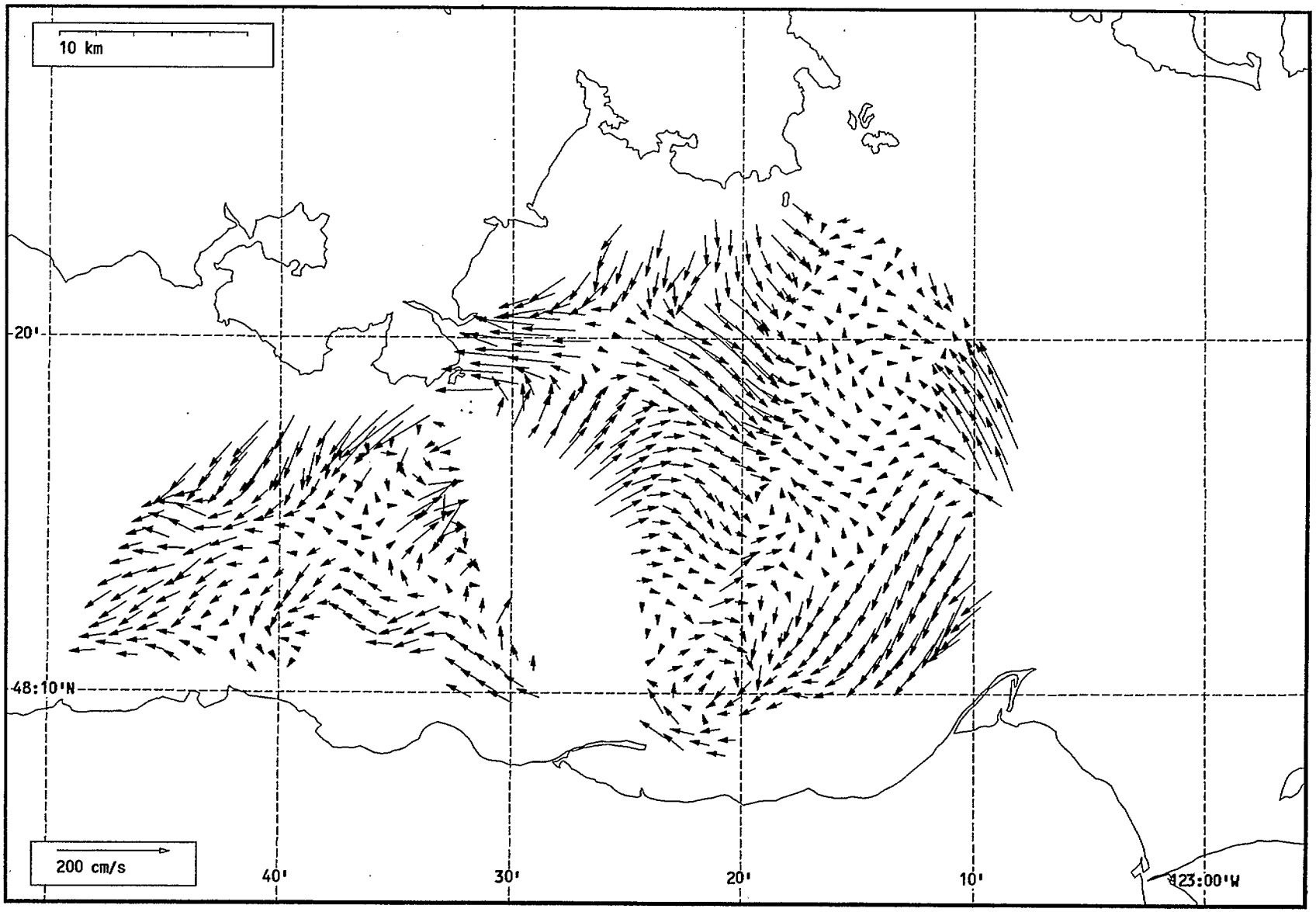

Total current vectors, Juan de Fuca Strait, 1992-07-12 02:00 Z.

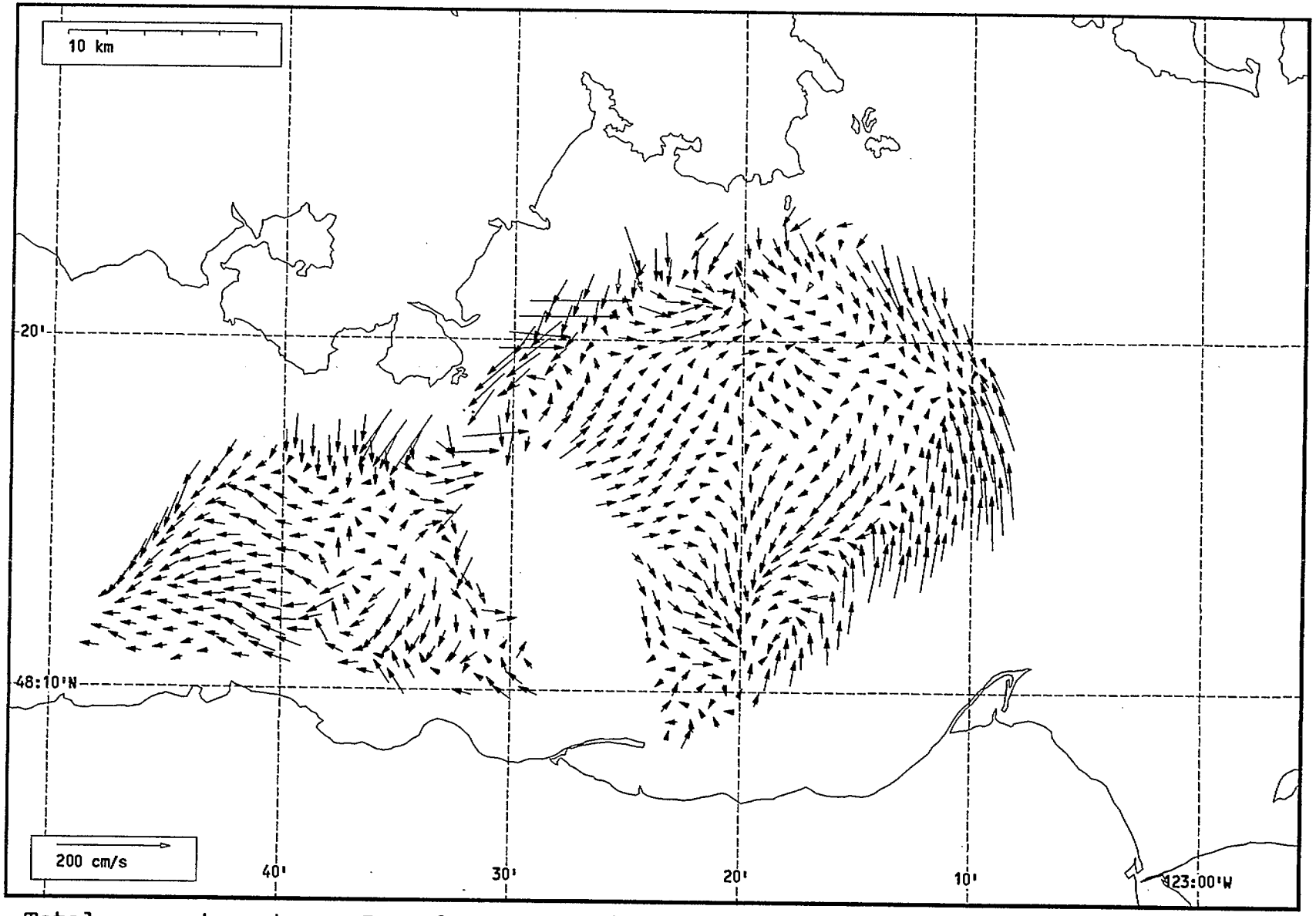

Total current vectors, Juan de Fuca Strait, 1992-07-12 03:00 Z.

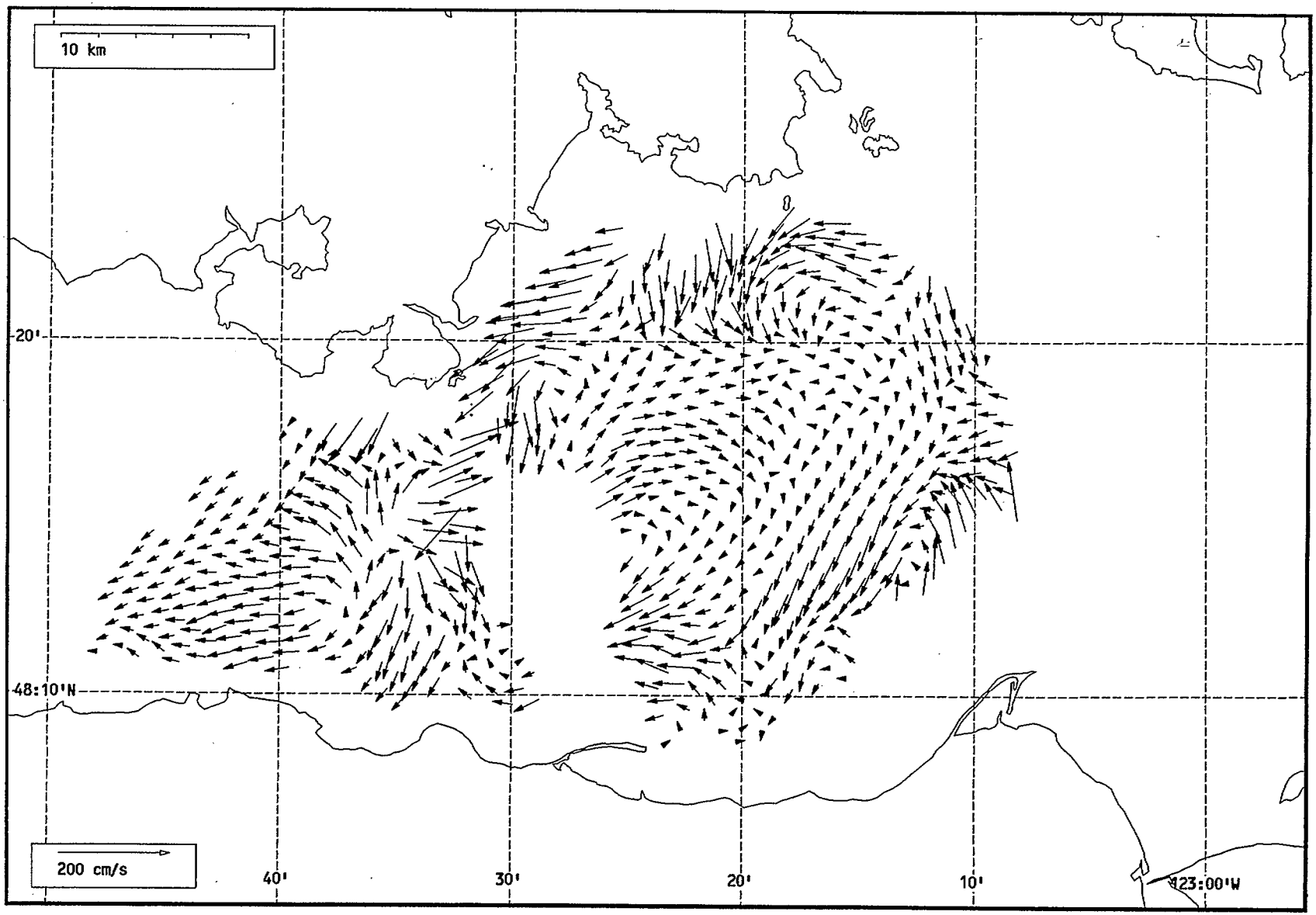

Total current vectors, Juan de Fuca Strait, 1992-07-12 04:00 Z.

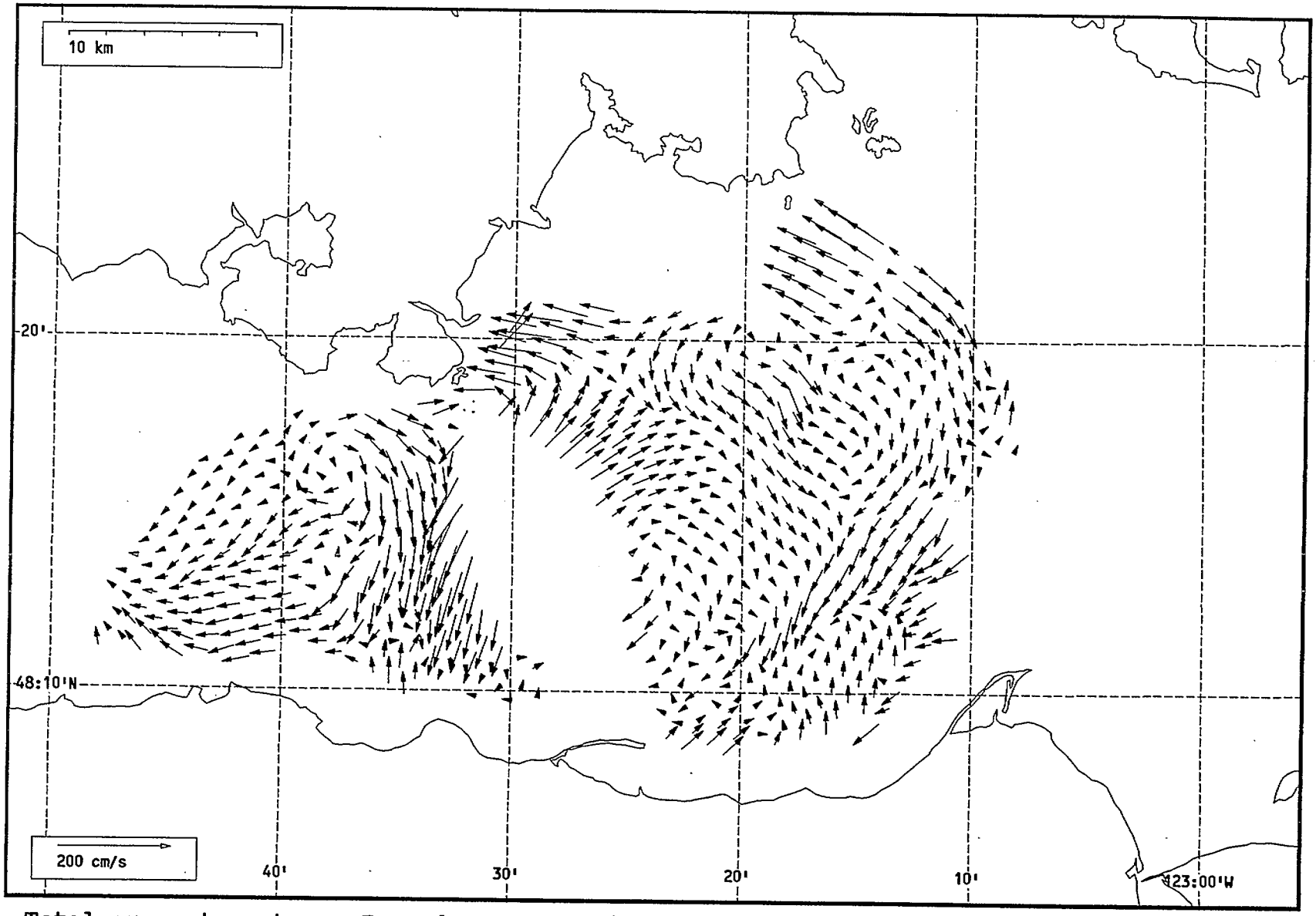

Total current vectors, Juan de Fuca Strait, 1992-07-12 05:00 Z.

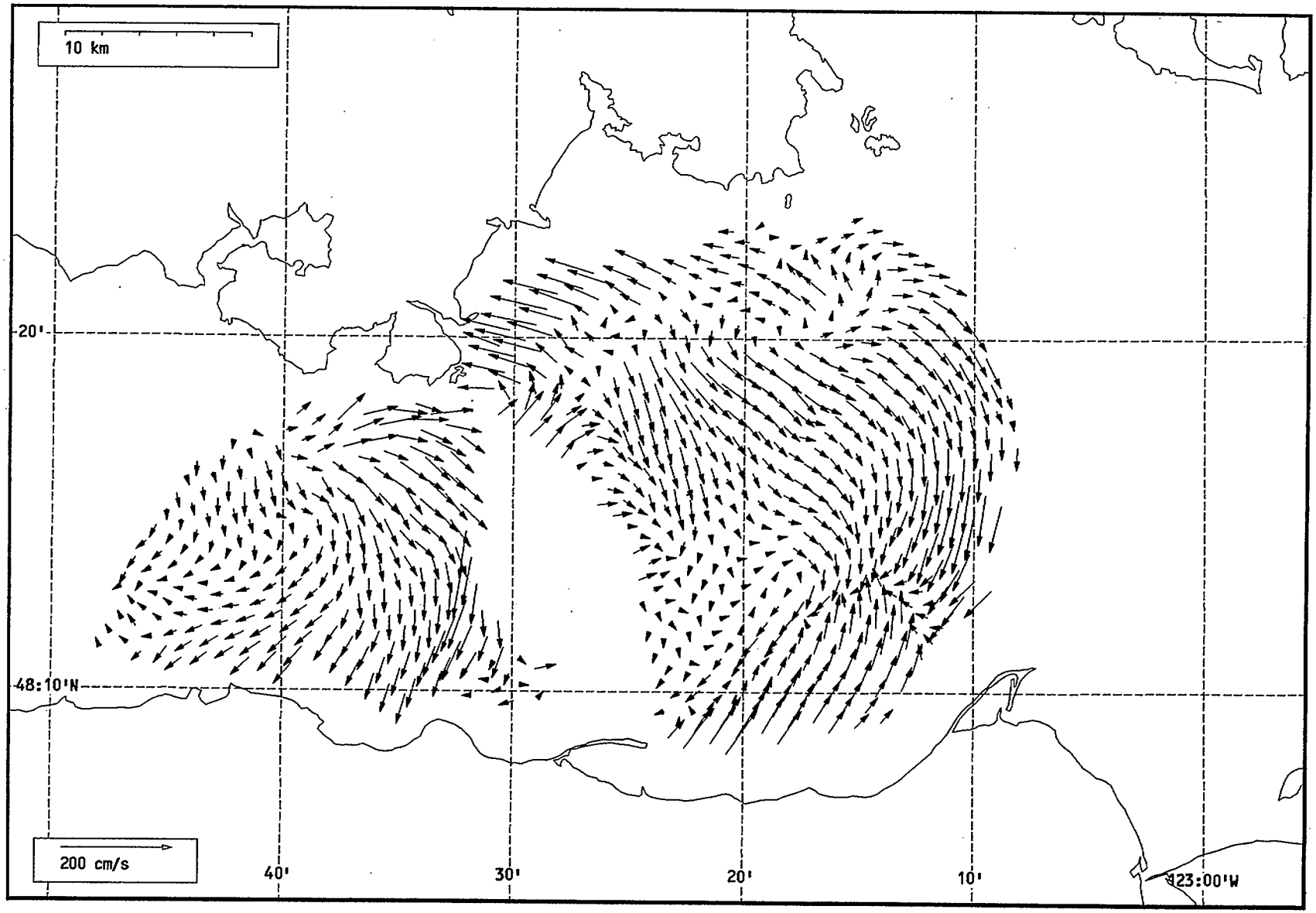

Total current vectors, Juan de Fuca Strait, 1992-07-12 06:00 Z.

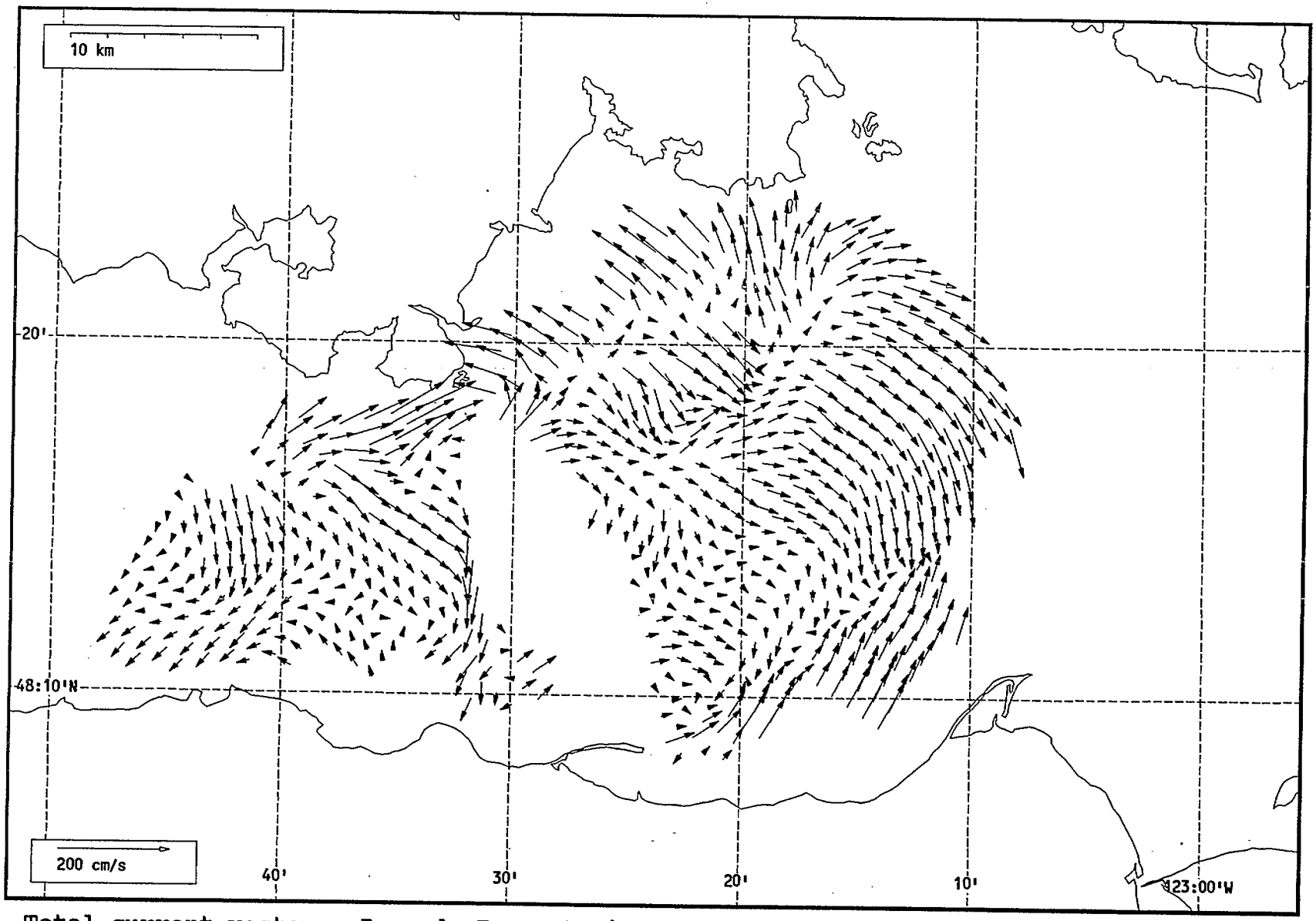

Total current vectors, Juan de Fuca Strait, 1992-07-12 07:00 Z.

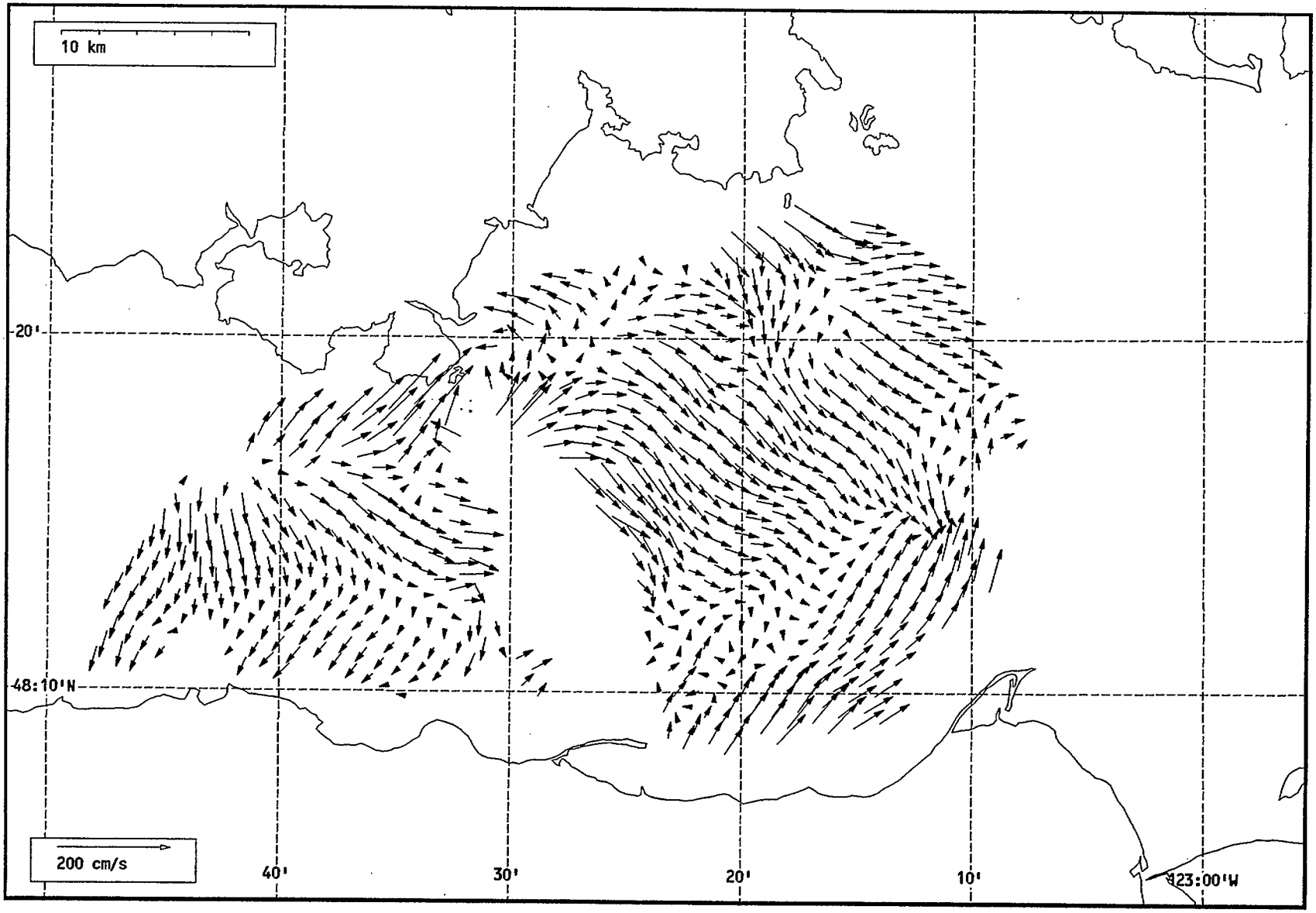

Total current vectors, Juan de Fuca Strait, 1992-07-12 08:00 Z.

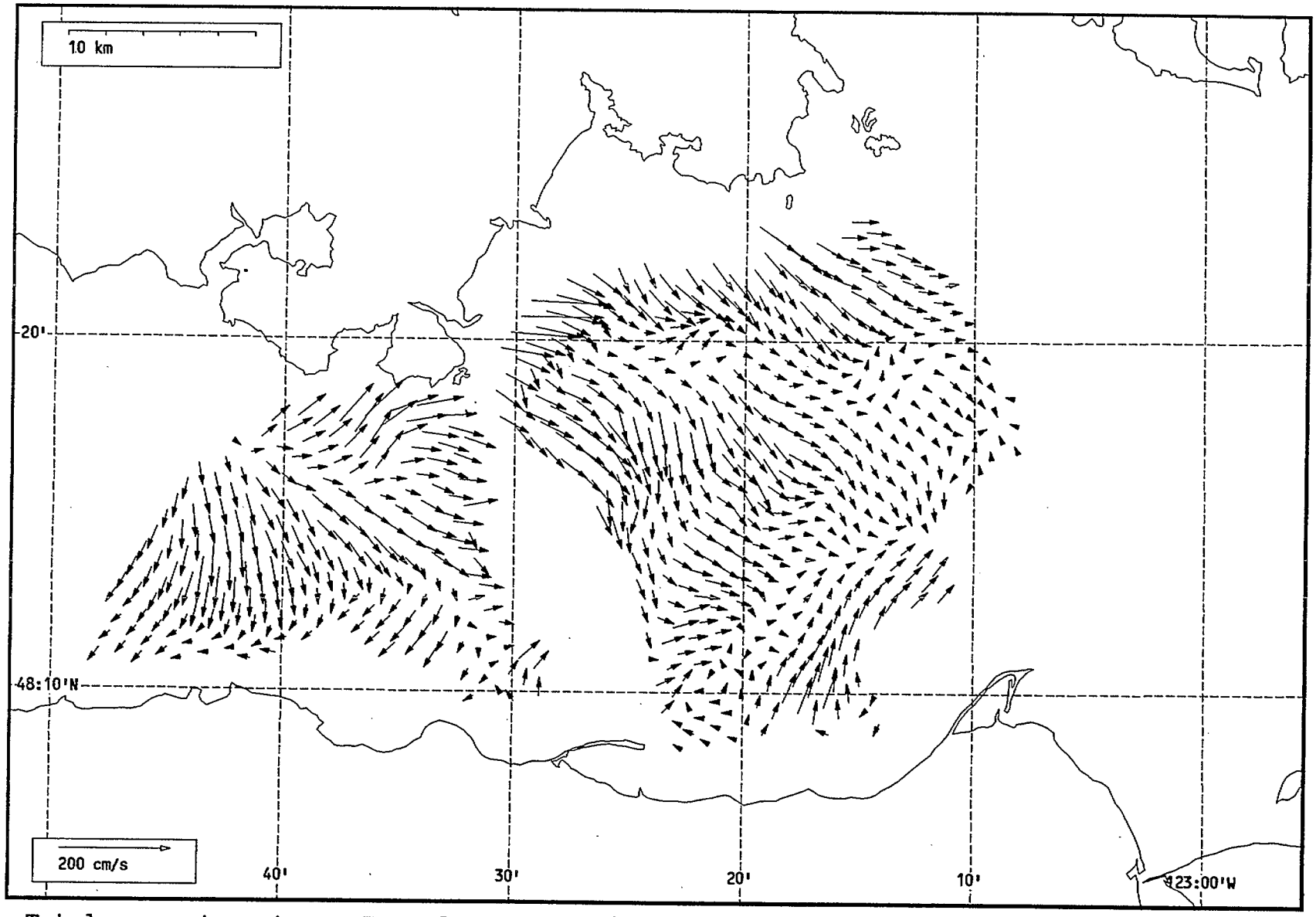

Total current vectors, Juan de Fuca Strait, 1992-07-12 09:00 Z.

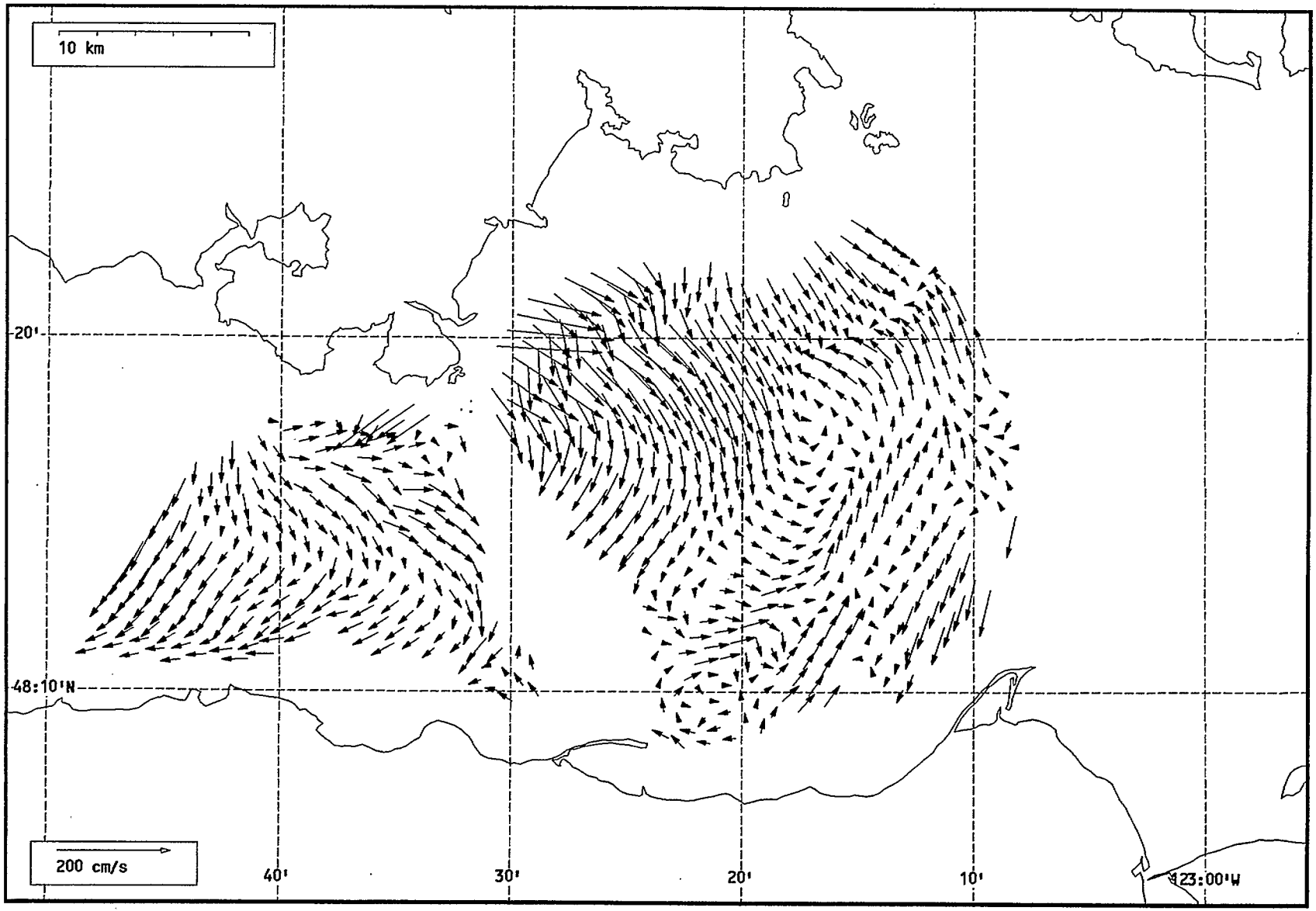

Total current vectors, Juan de Fuca Strait, 1992-07-12 10:00 Z.

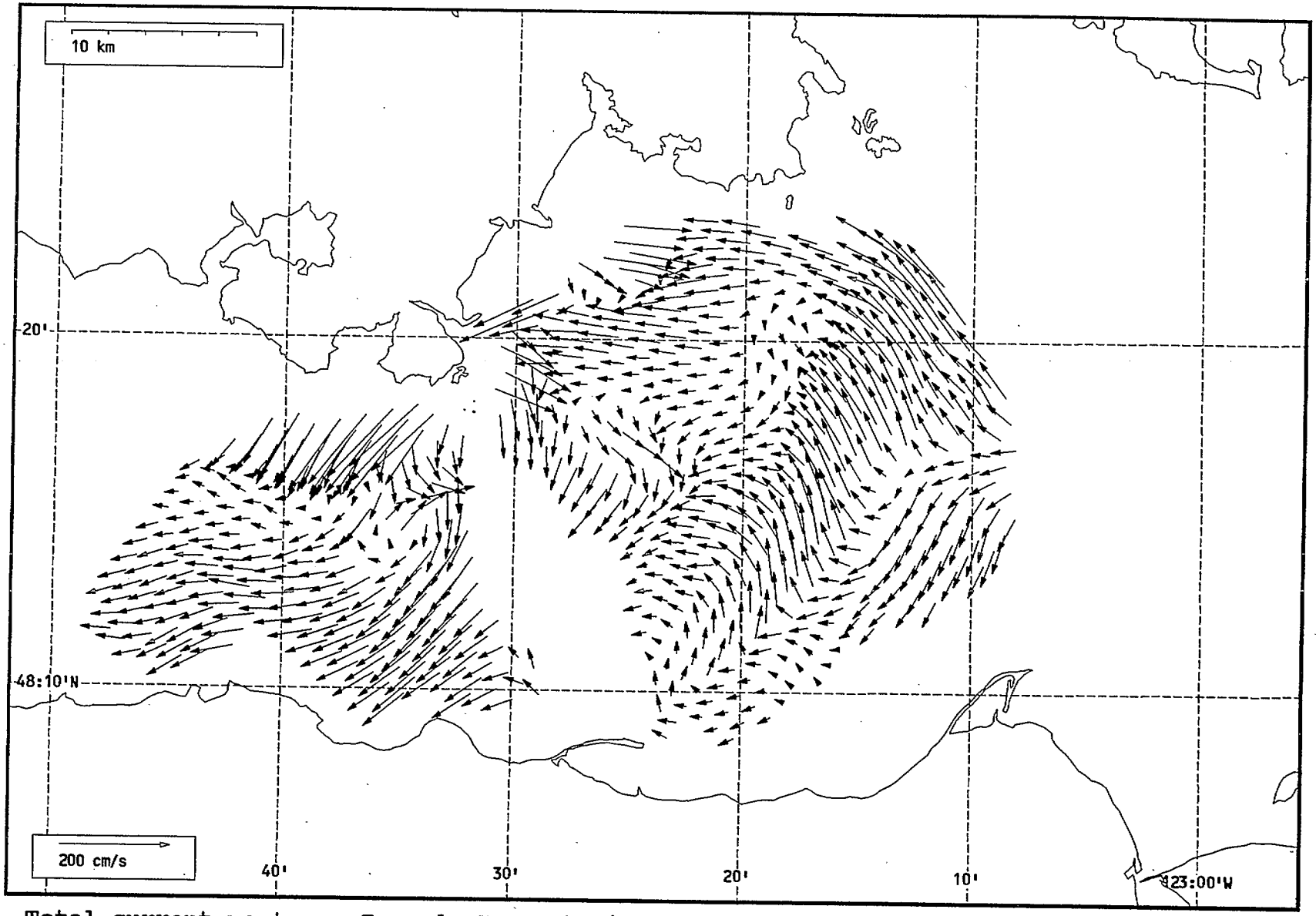

Total current vectors, Juan de Fuca Strait, 1992-07-12 11:00 Z.

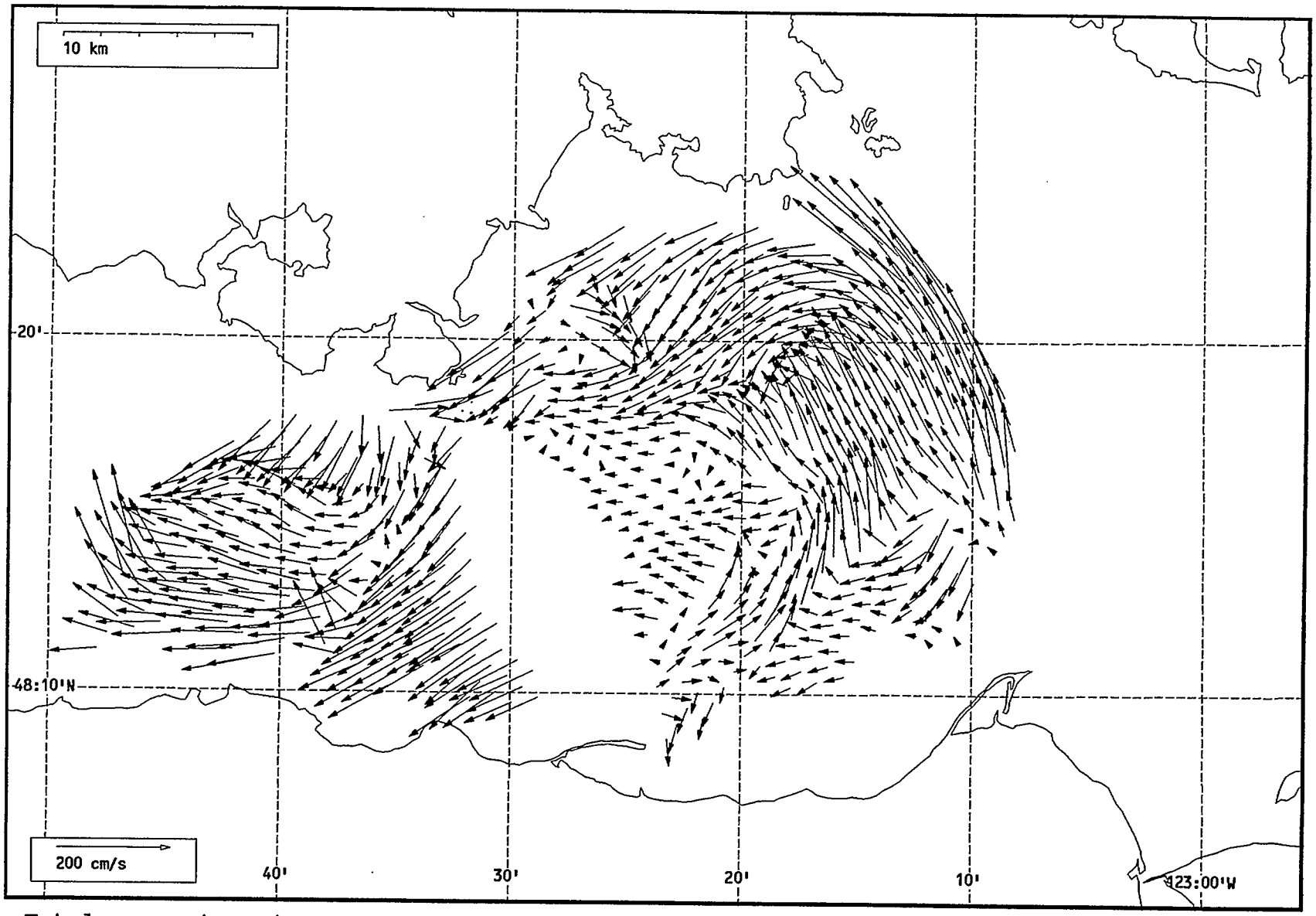

Total current vectors, Juan de Fuca Strait, 1992-07-12 12:00 Z.

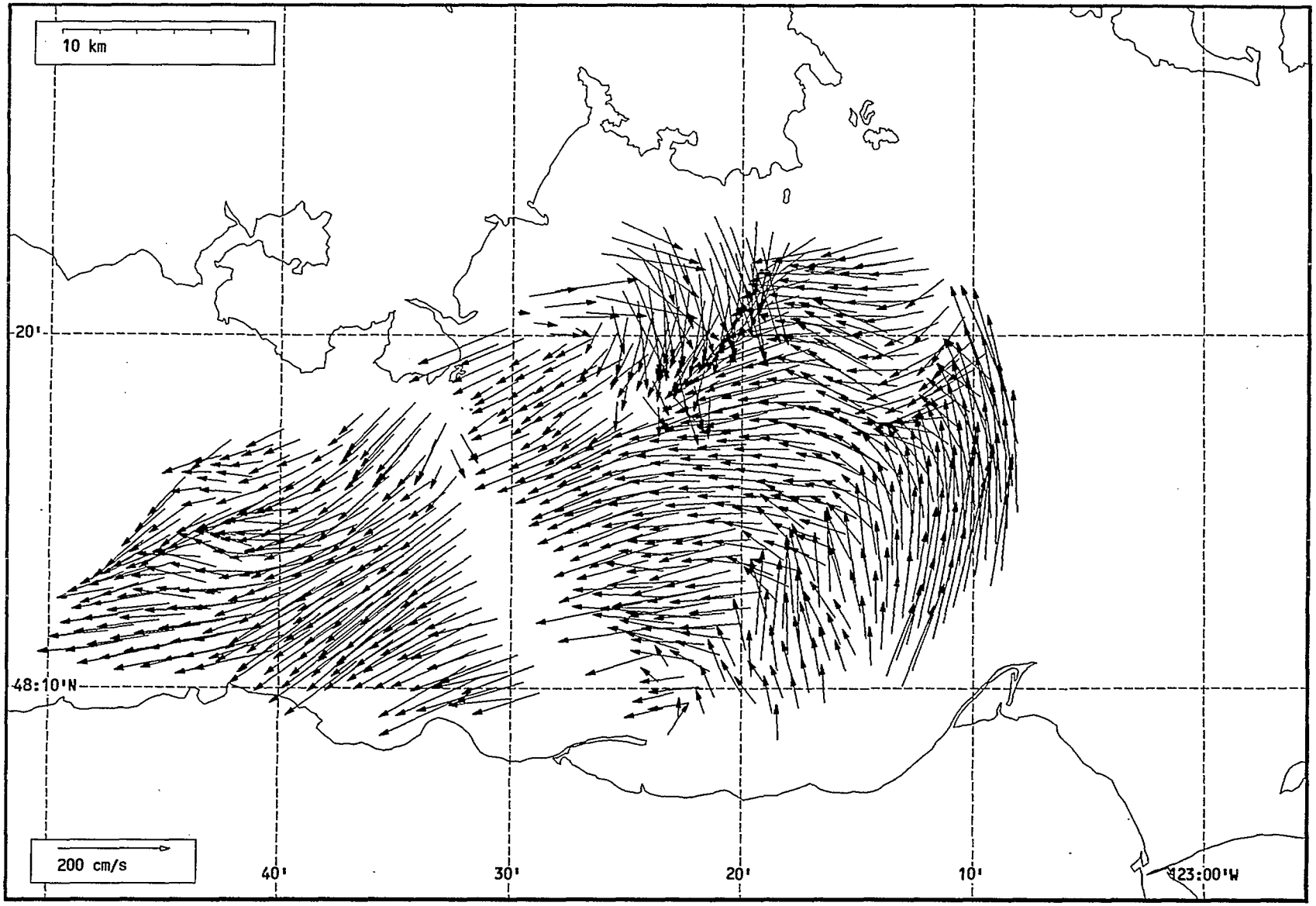

Total current vectors, Juan de Fuca Strait, 1992-07-12 13:00 Z.

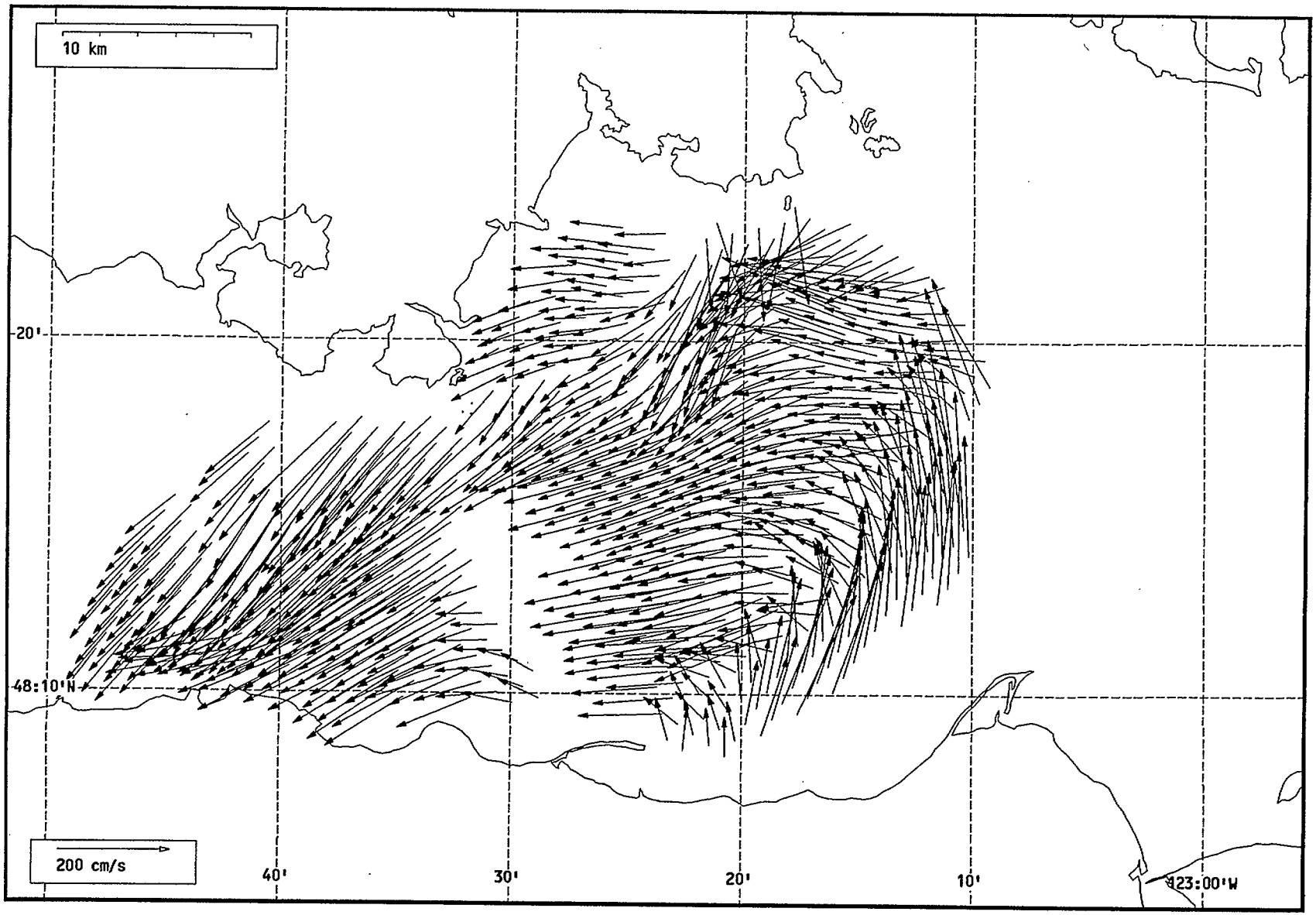

Total current vectors, Juan de Fuca Strait, 1992-07-12 14:00 Z.

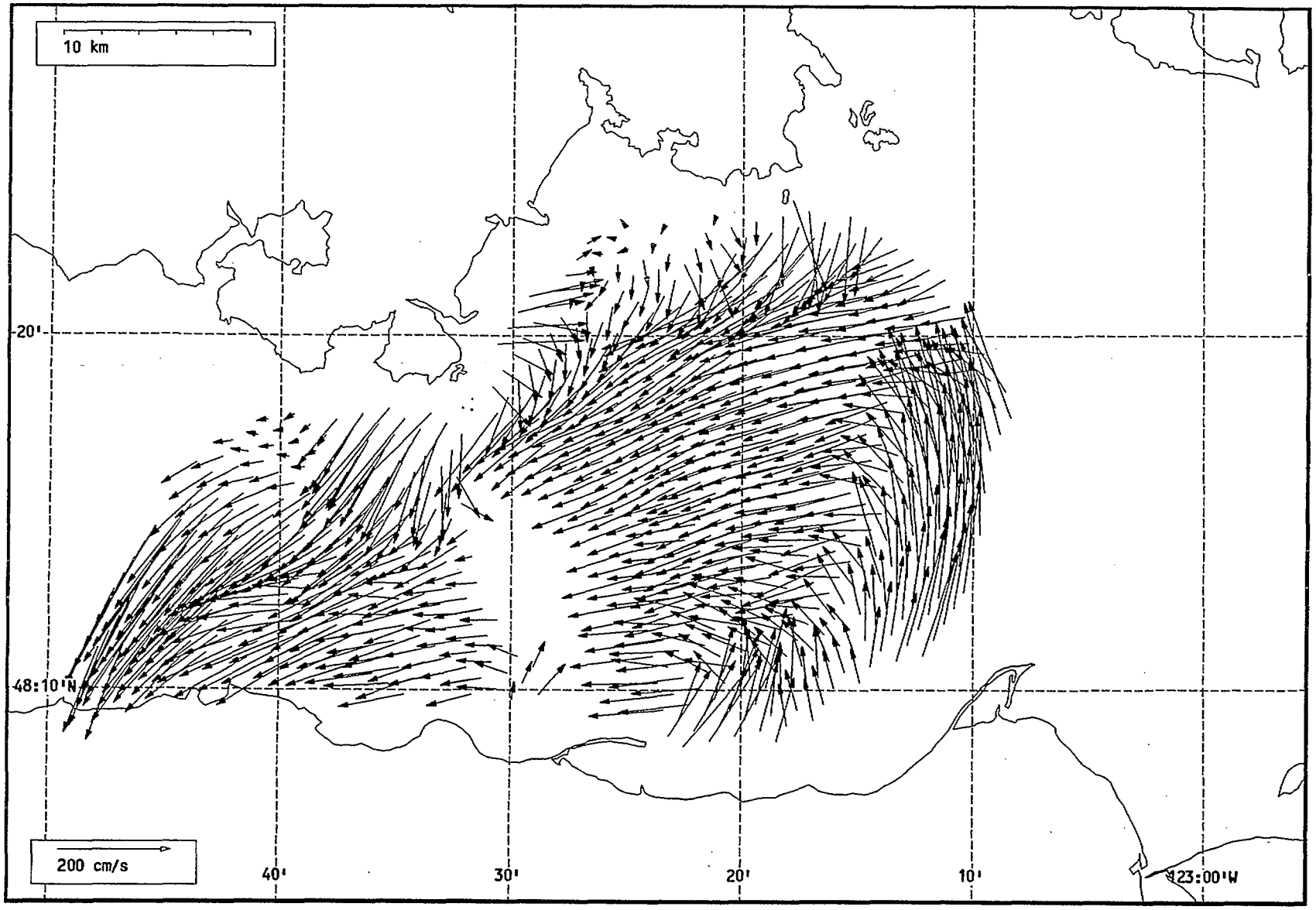

Total current vectors, Juan de Fuca Strait, 1992-07-12 15:00 Z.

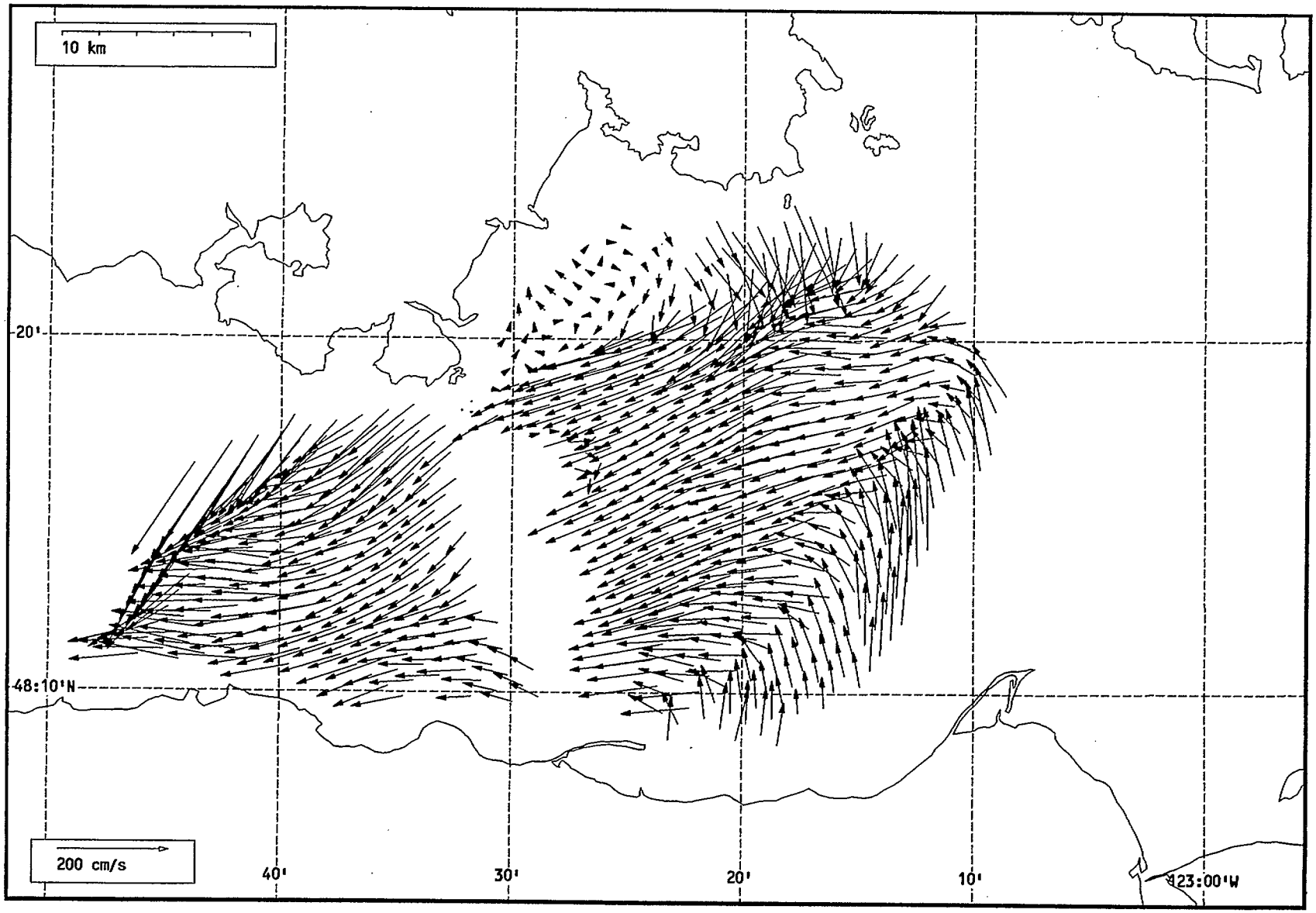

Total current vectors, Juan de Fuca Strait, 1992-07-12 16:00 Z.

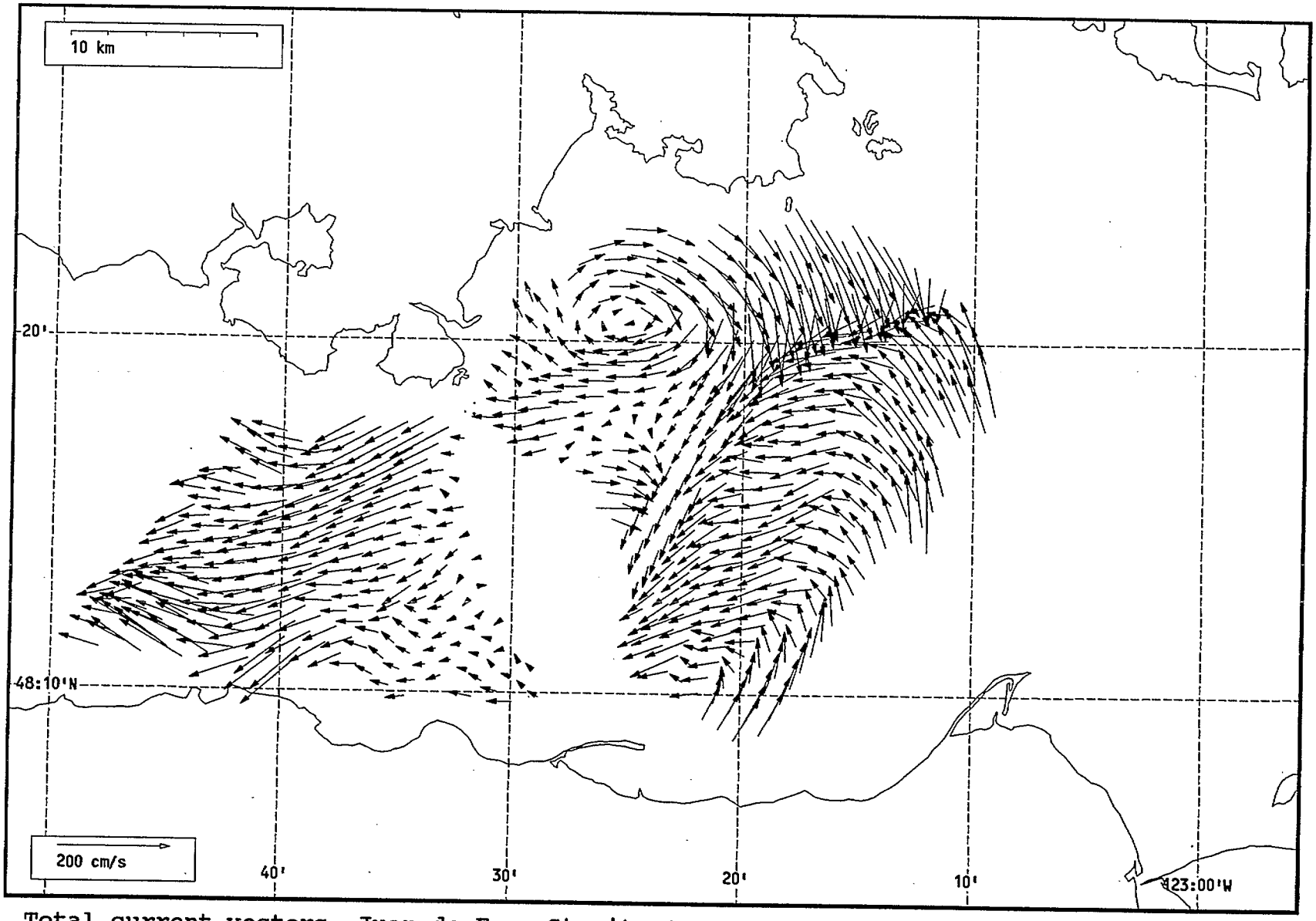

Total current vectors, Juan de Fuca Strait, 1992-07-12 17:00 Z.

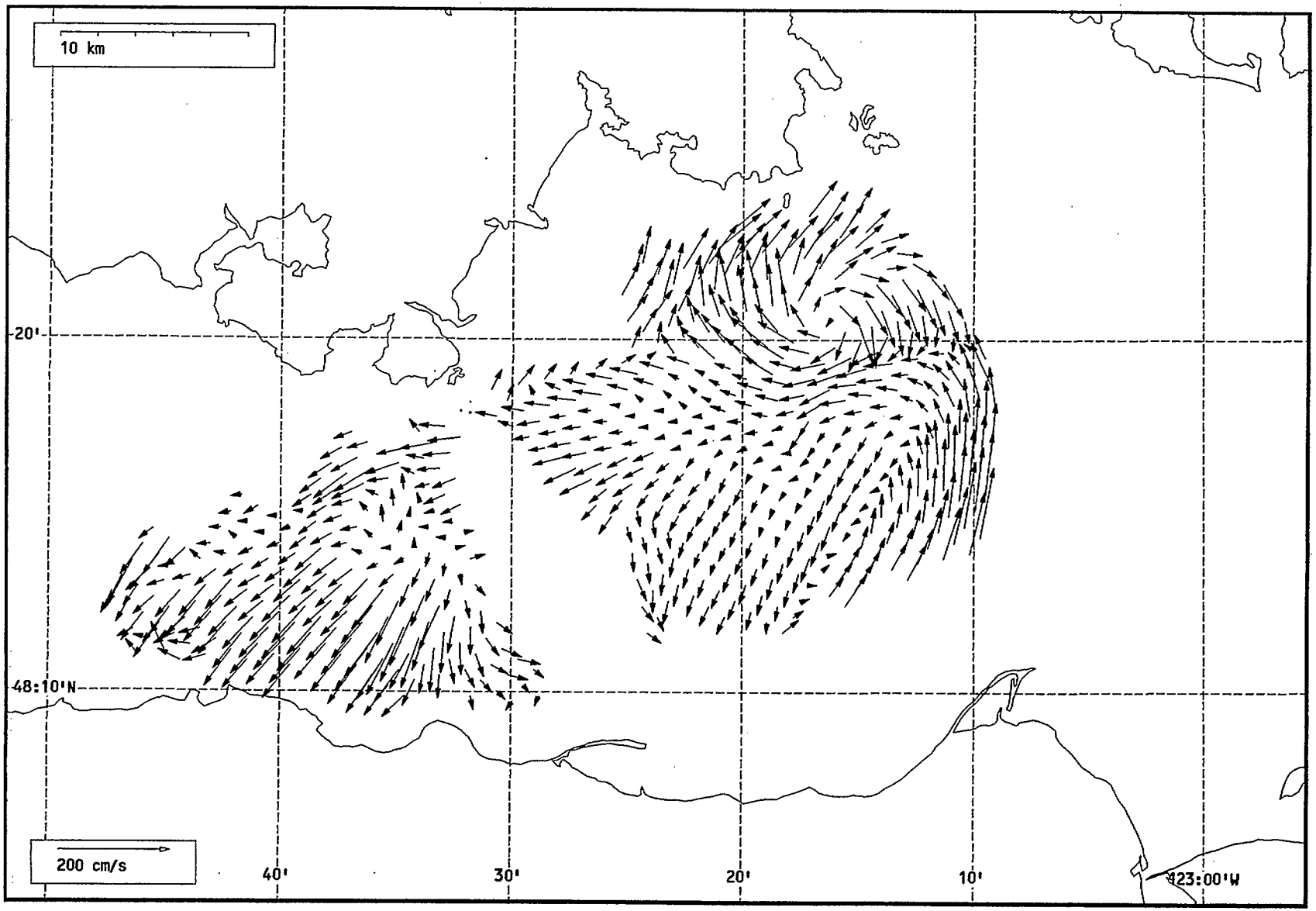

Total current vectors, Juan de Fuca Strait, 1992-07-12 18:00 Z.

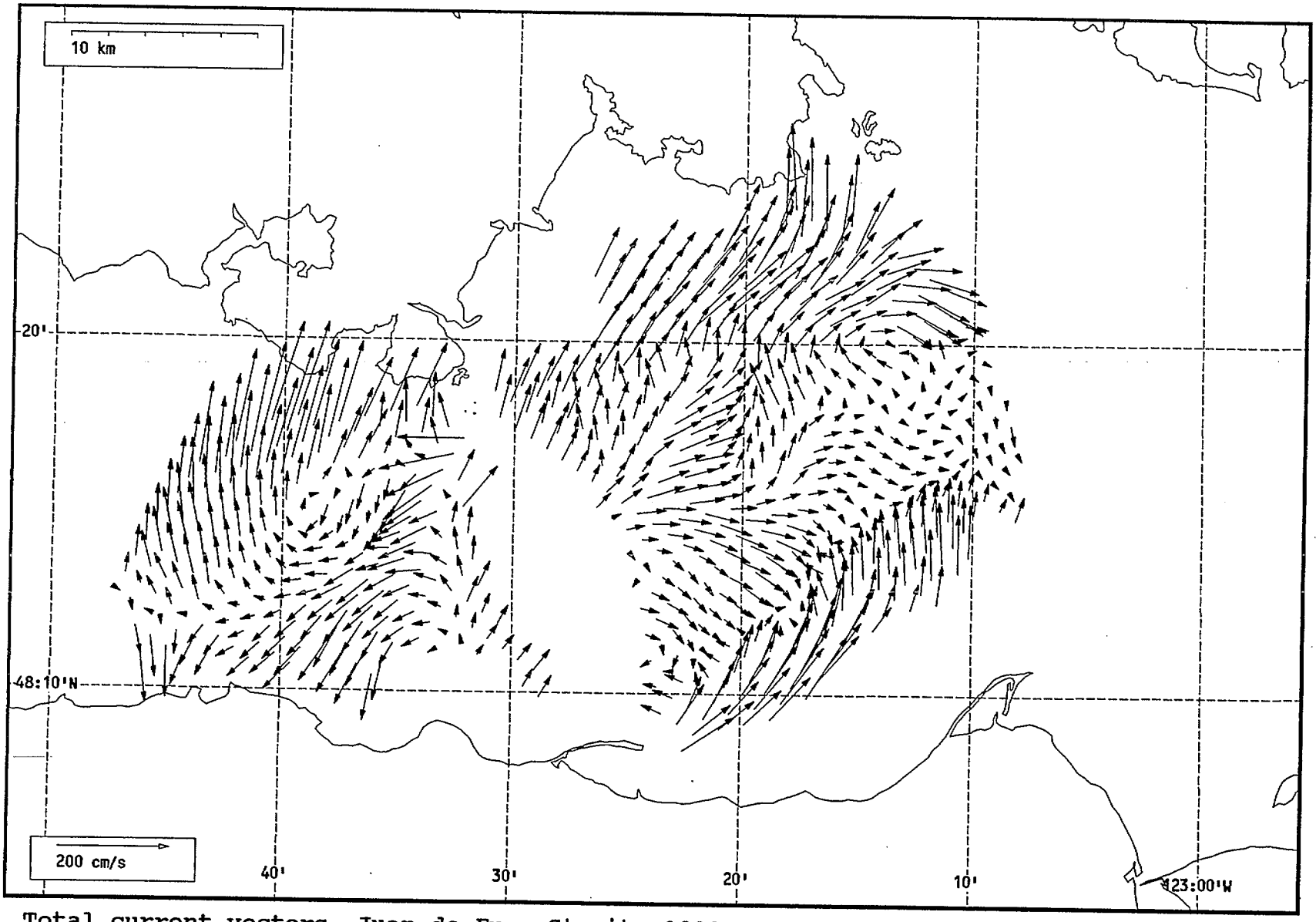

Total current vectors, Juan de Fuca Strait, 1992-07-12 19:00 Z.

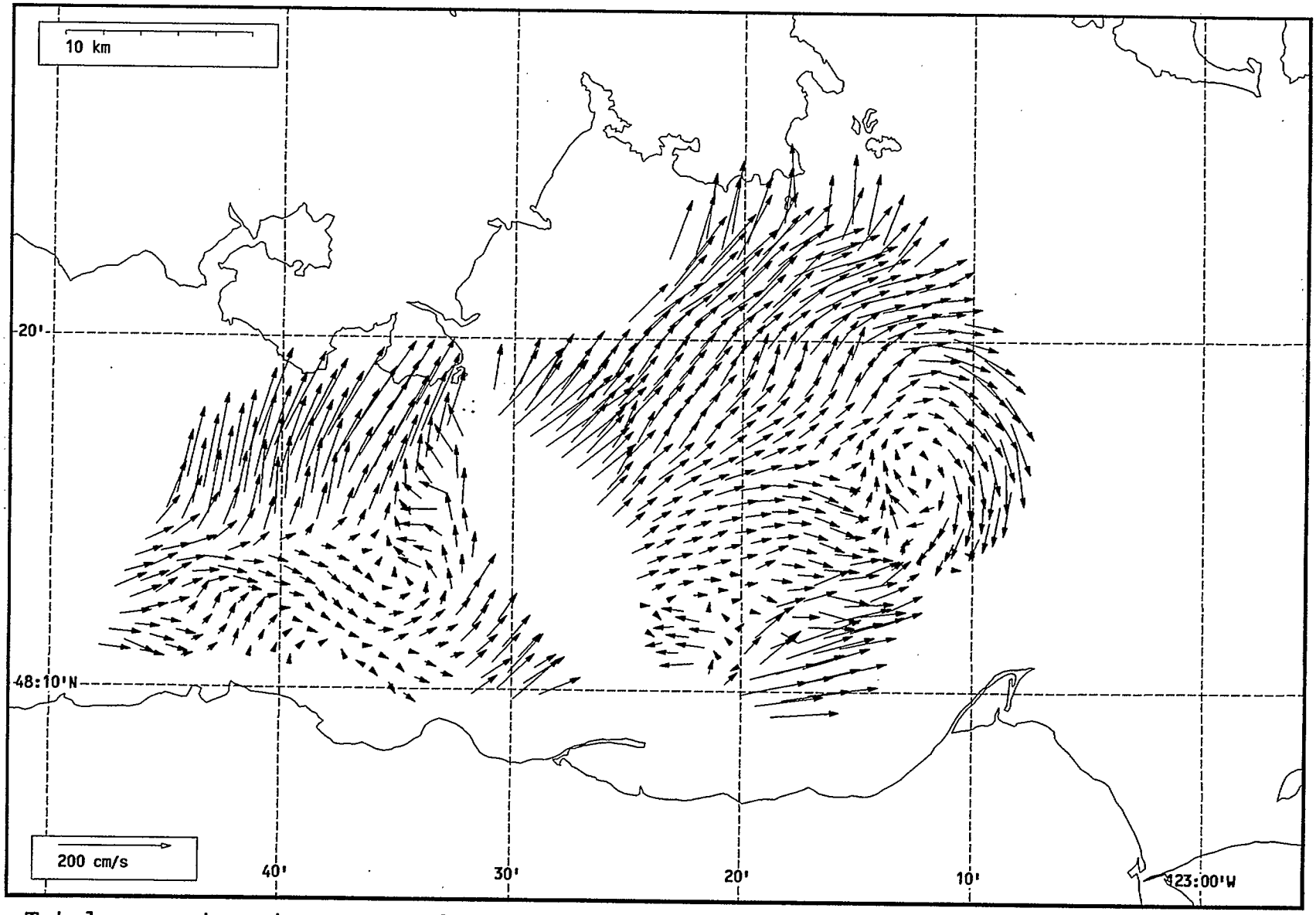

Total current vectors, Juan de Fuca Strait, 1992-07-12 20:00 Z.

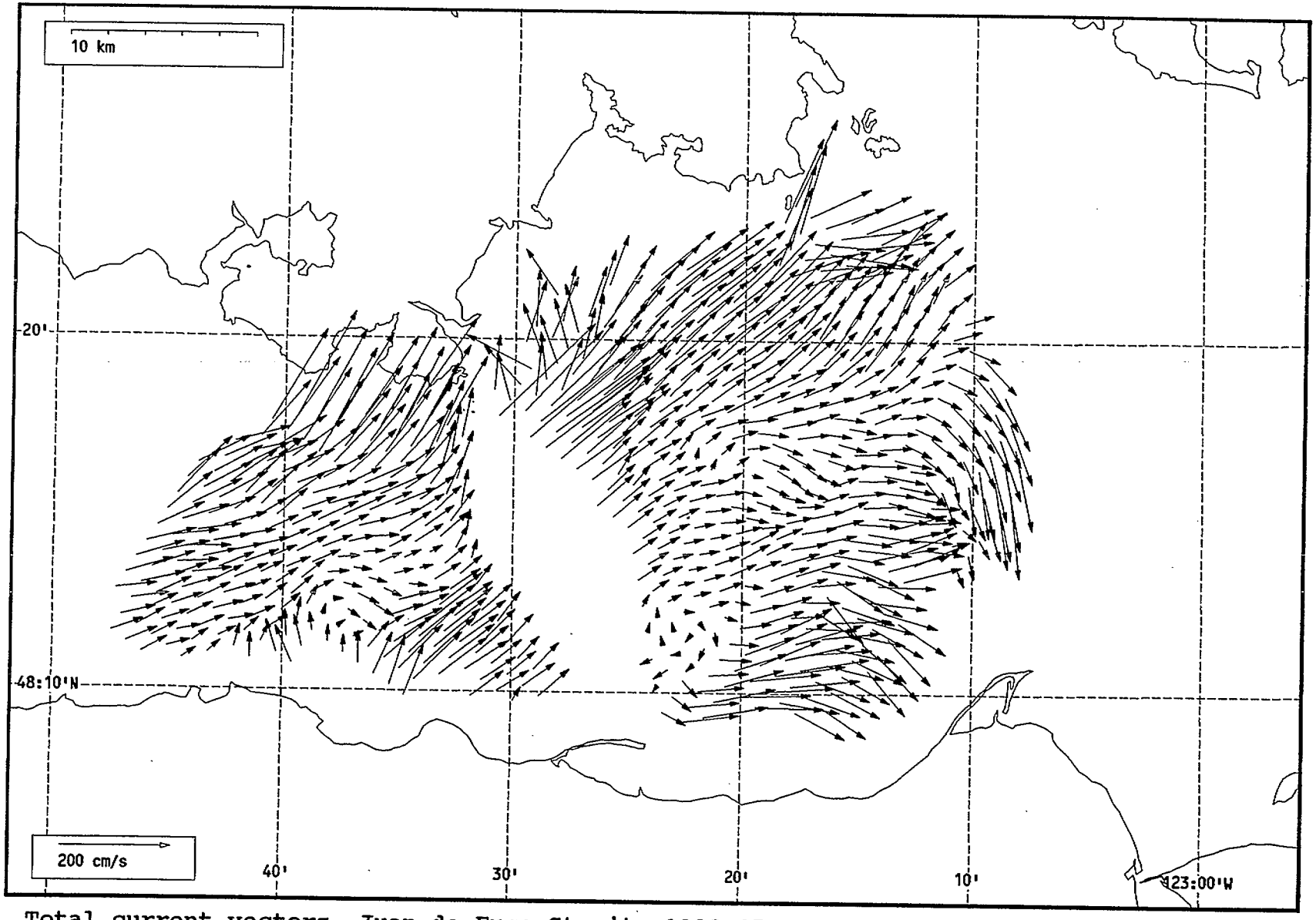

Total current vectors, Juan de Fuca Strait, 1992-07-12 21:00 Z.

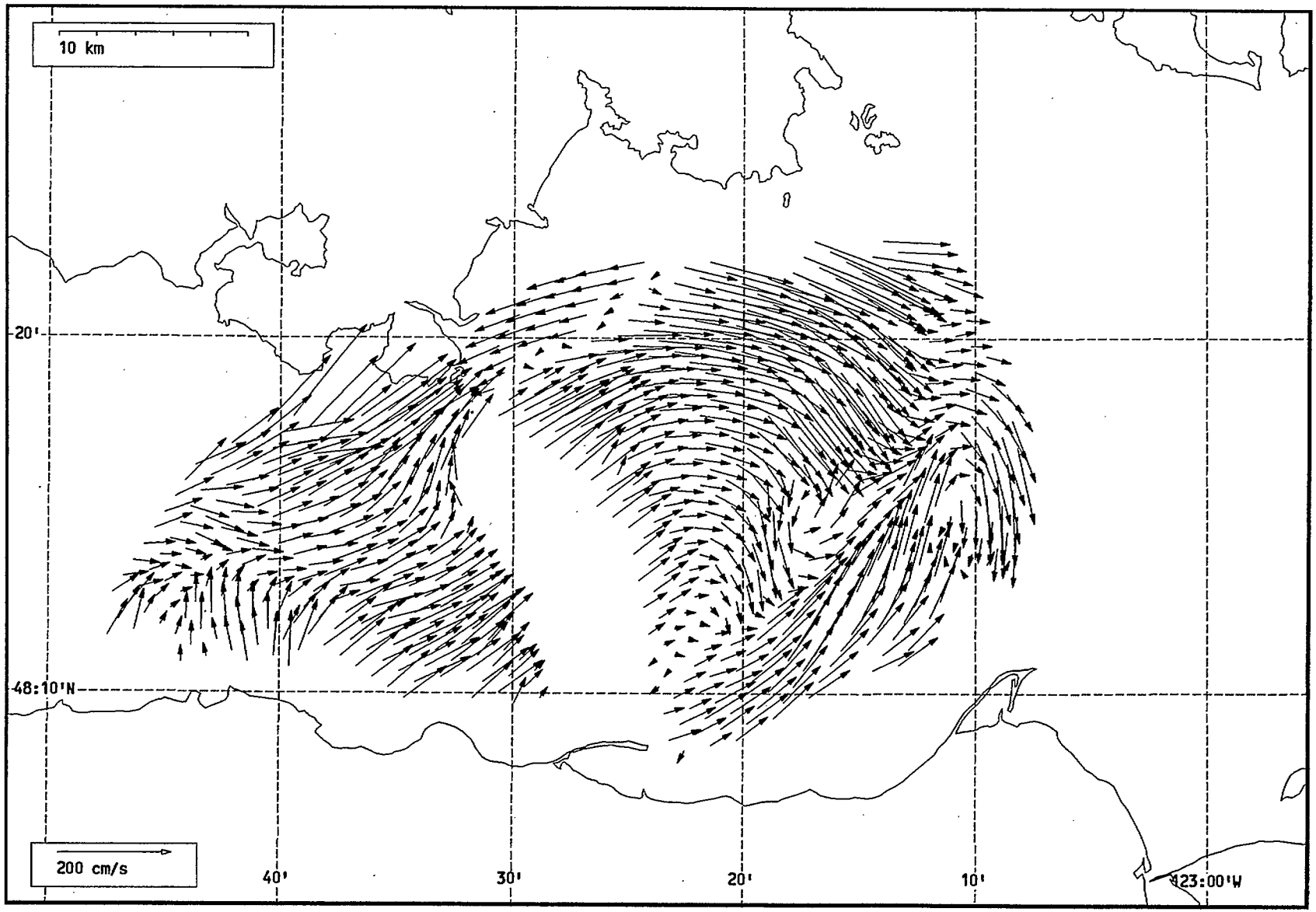

Total current vectors, Juan de Fuca Strait, 1992-07-12 22:00 Z.

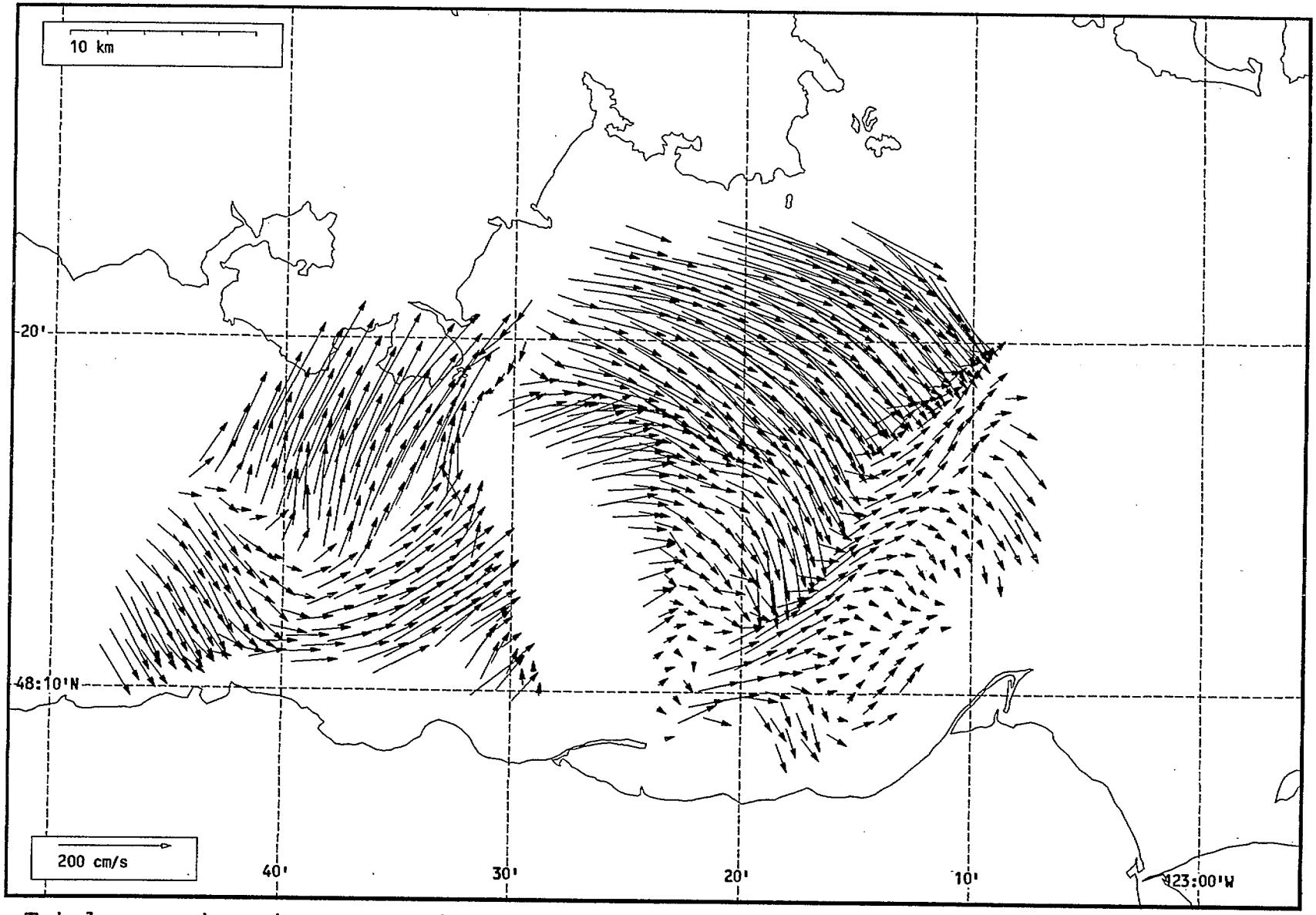

Total current vectors, Juan de Fuca Strait, 1992-07-12 23:00 Z.

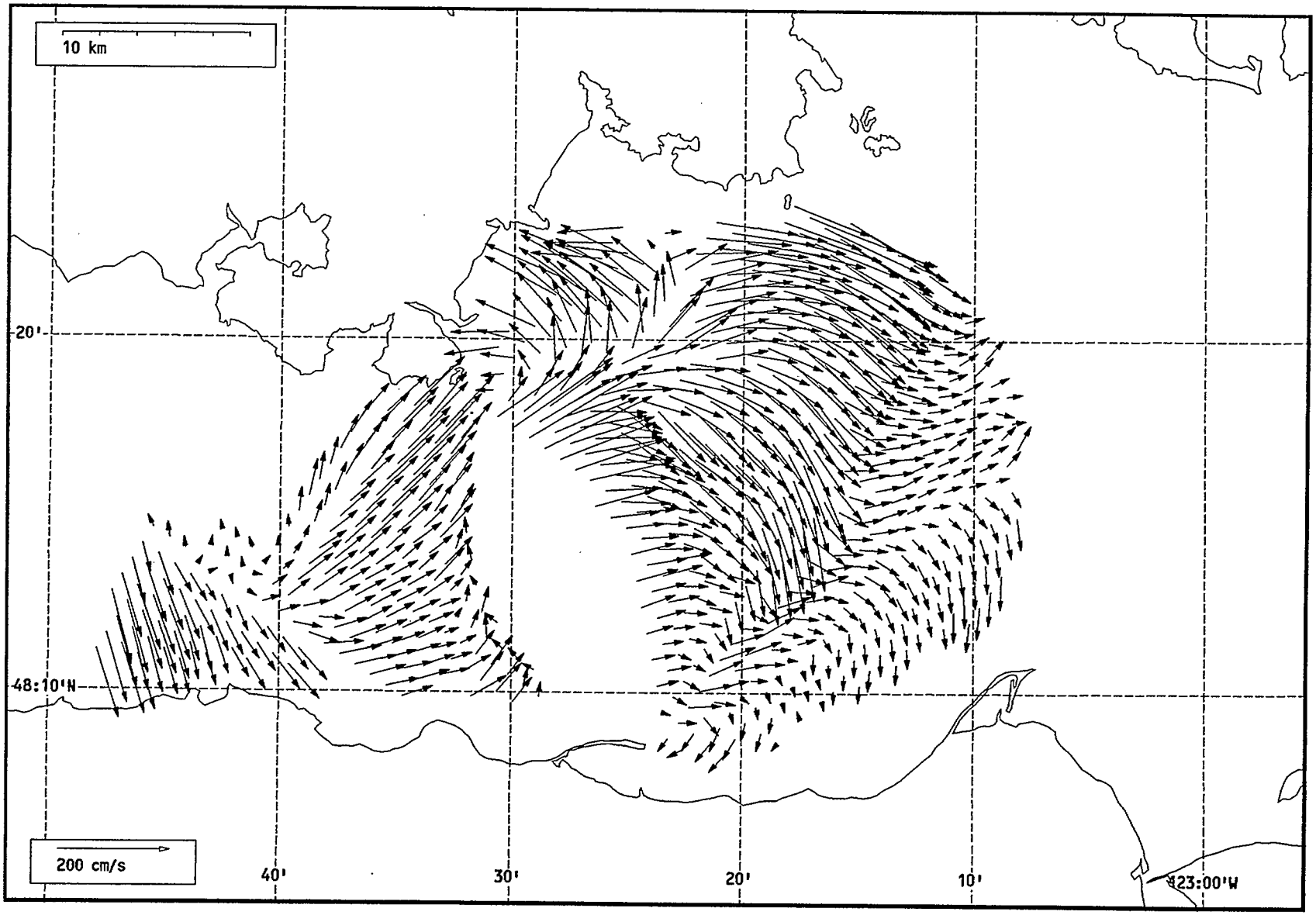

Total current vectors, Juan de Fuca Strait, 1992-07-13 00:00 Z.

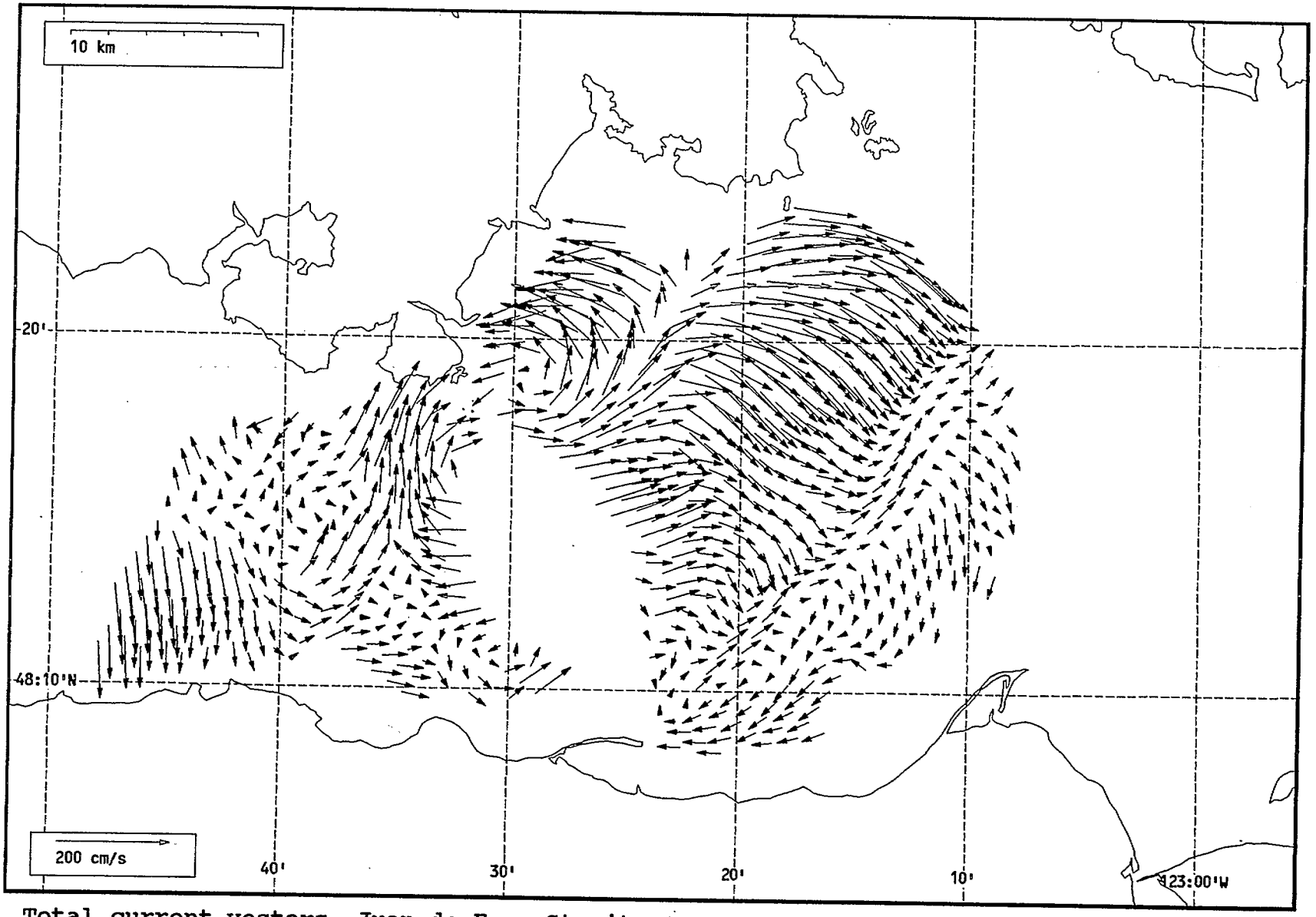

Total current vectors, Juan de Fuca Strait, 1992-07-13 01:00 Z.

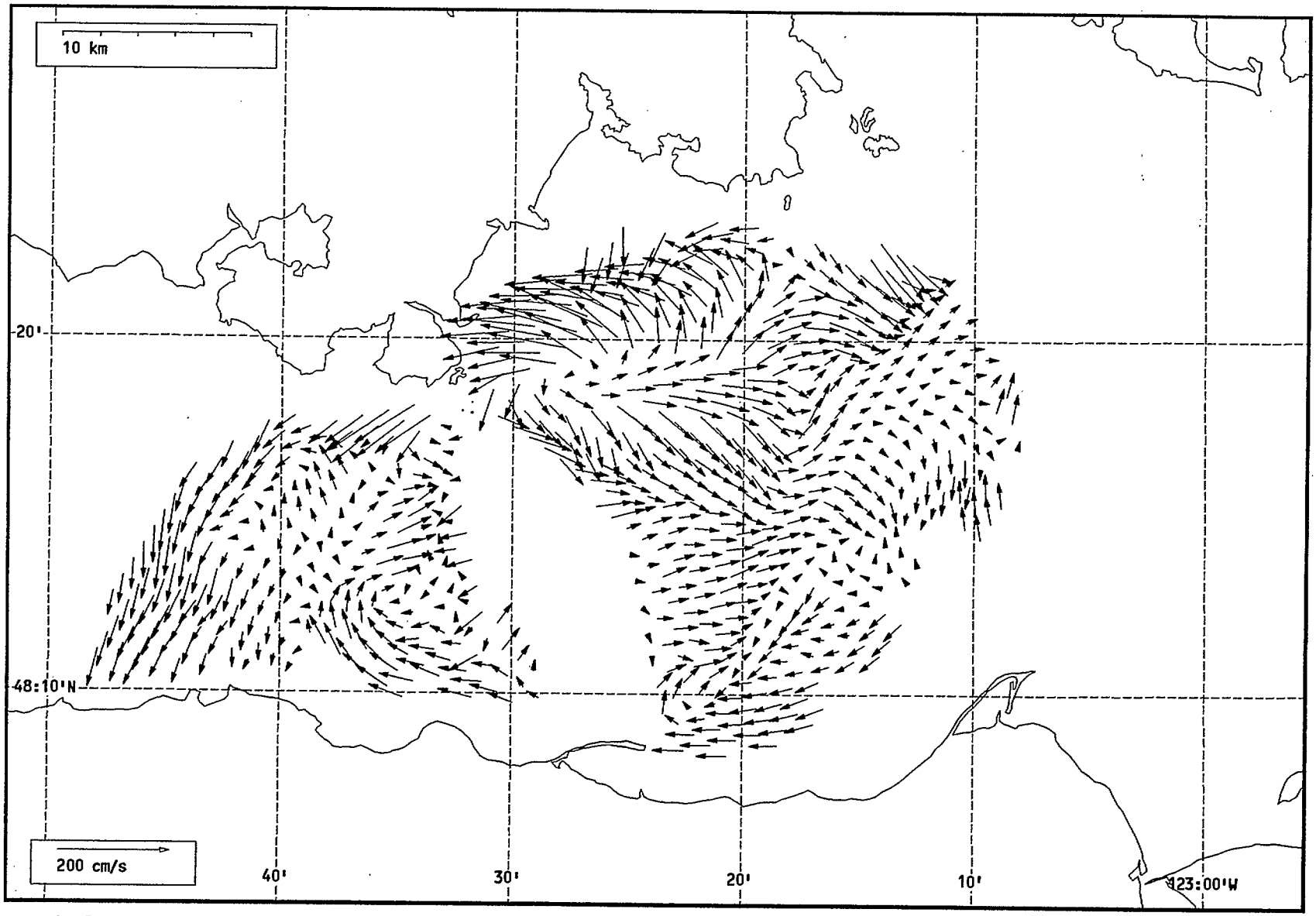

Total current vectors, Juan de Fuca Strait, 1992-07-13 02:00 Z.

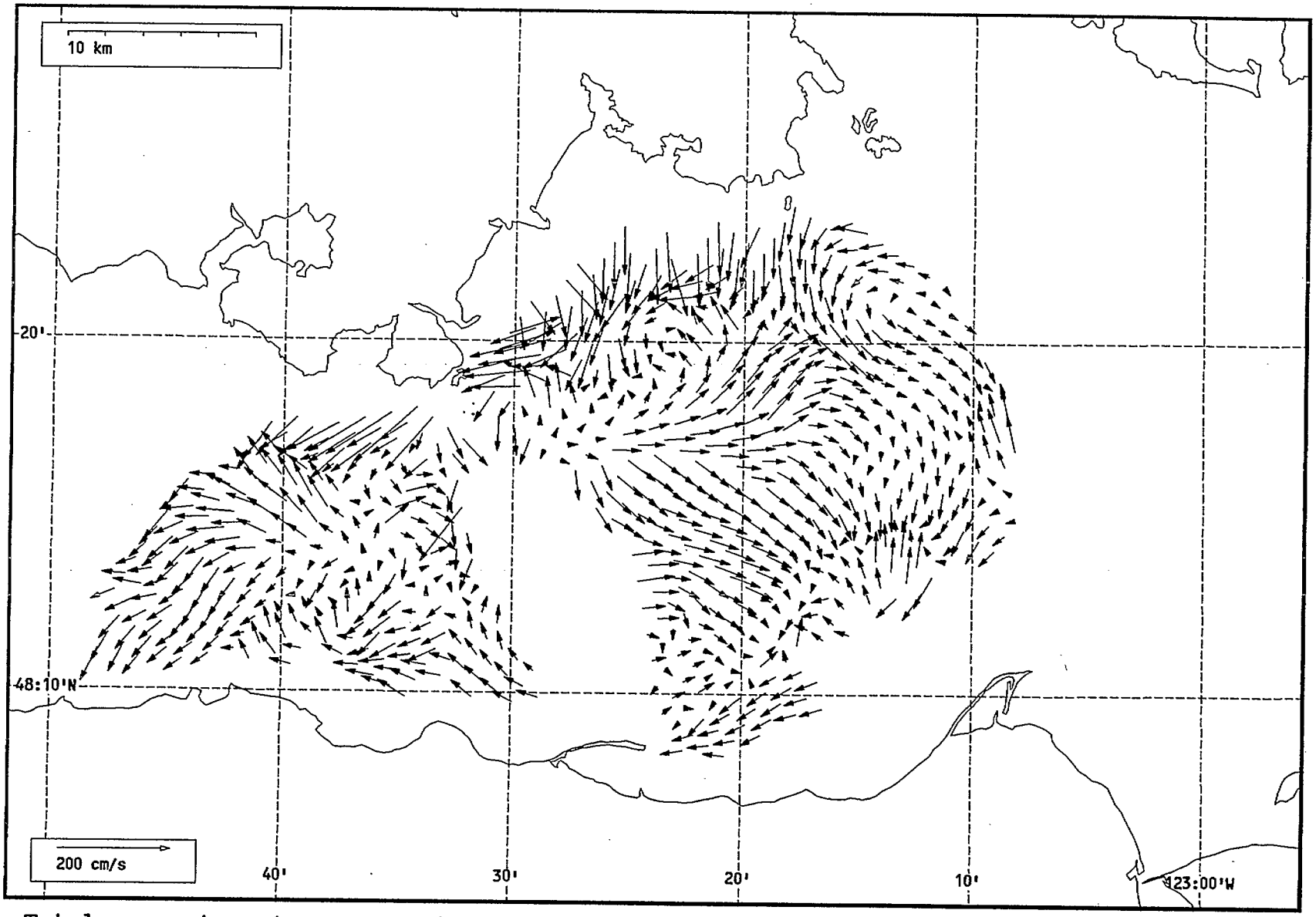

Total current vectors, Juan de Fuca Strait, 1992-07-13 03:00 Z.

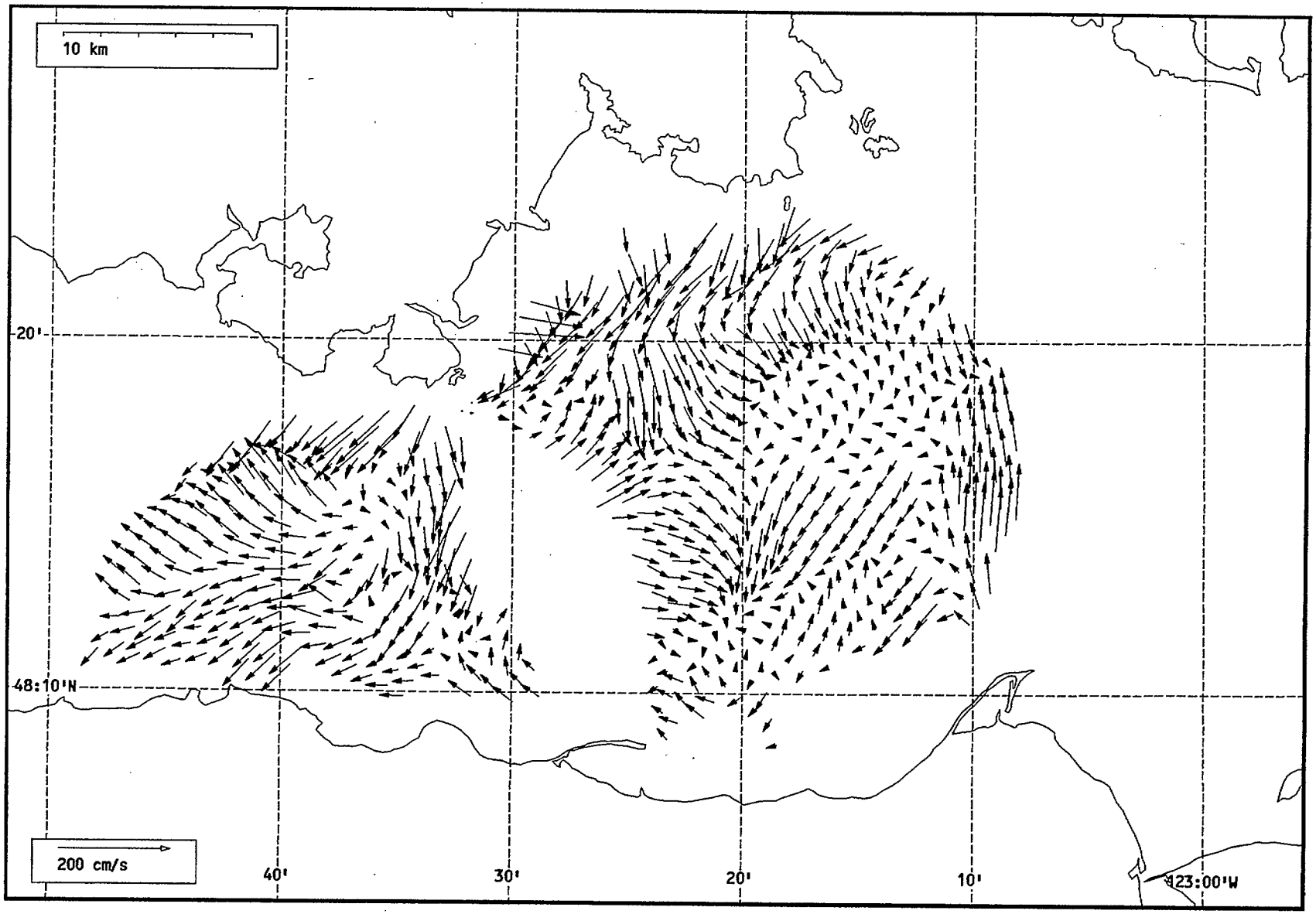

Total current vectors, Juan de Fuca Strait, 1992-07-13 04:00 Z.

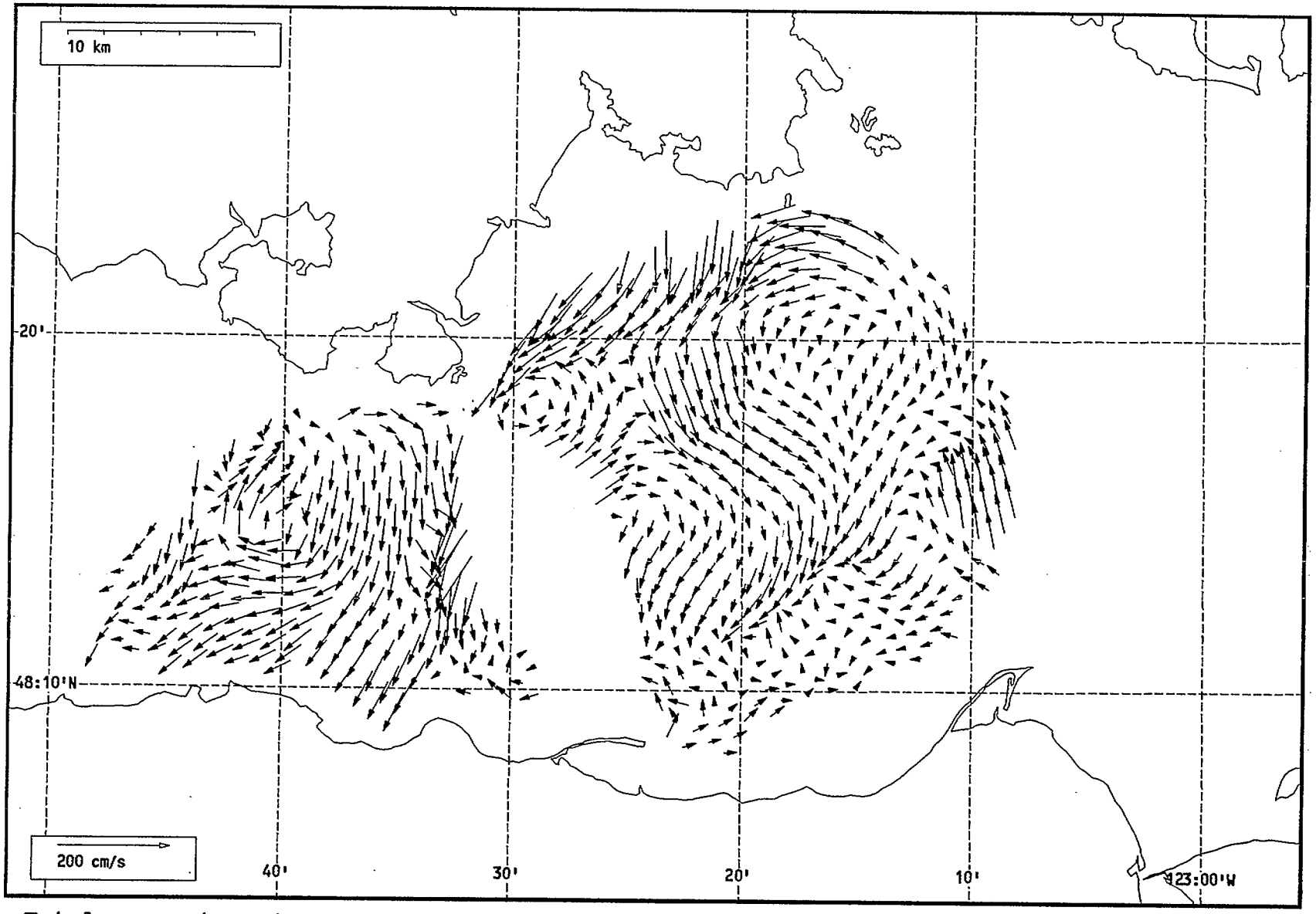

Total current vectors, Juan de Fuca Strait, 1992-07-13 05:00 Z.

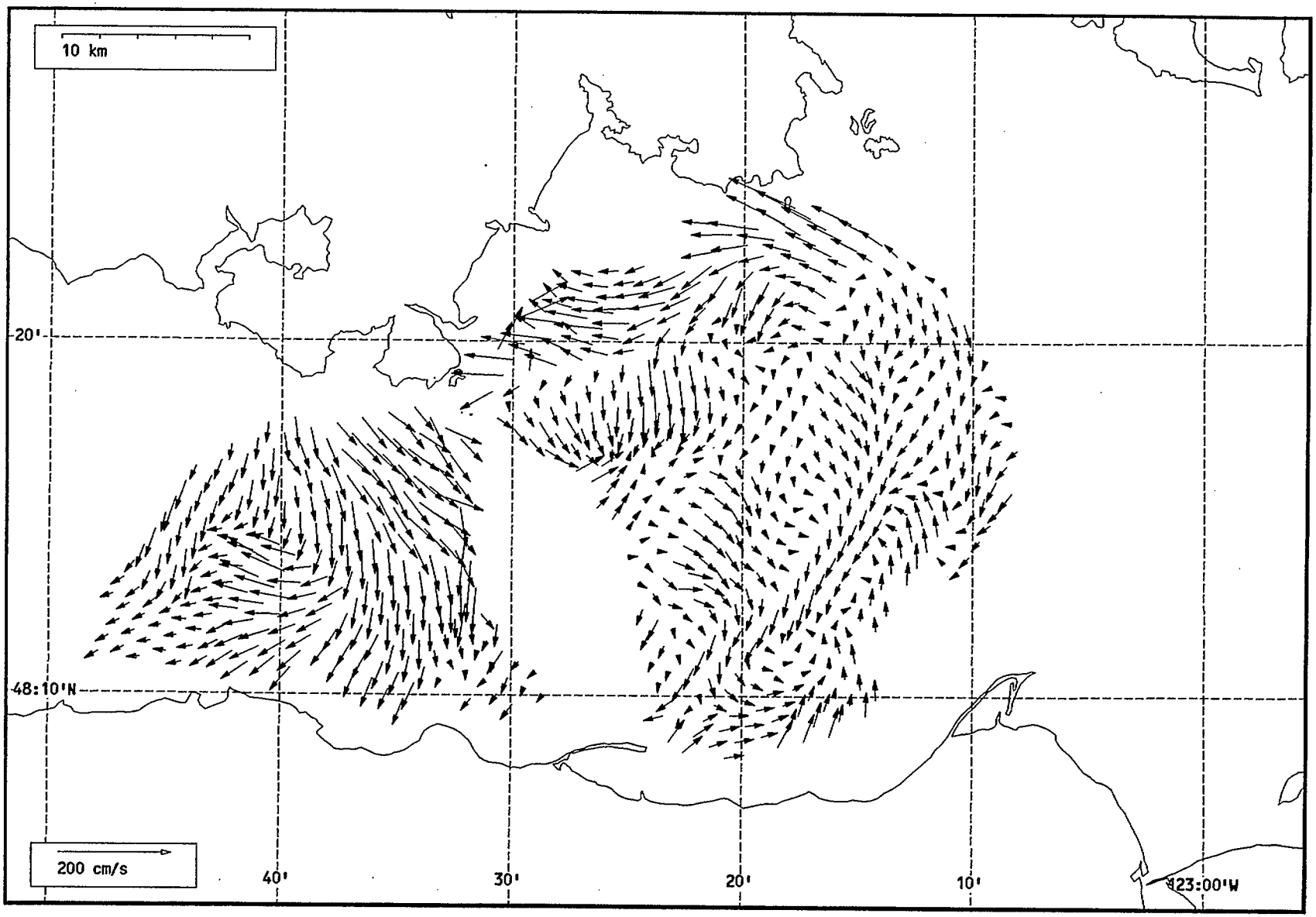

Total current vectors, Juan de Fuca Strait, 1992-07-13 06:00 Z.

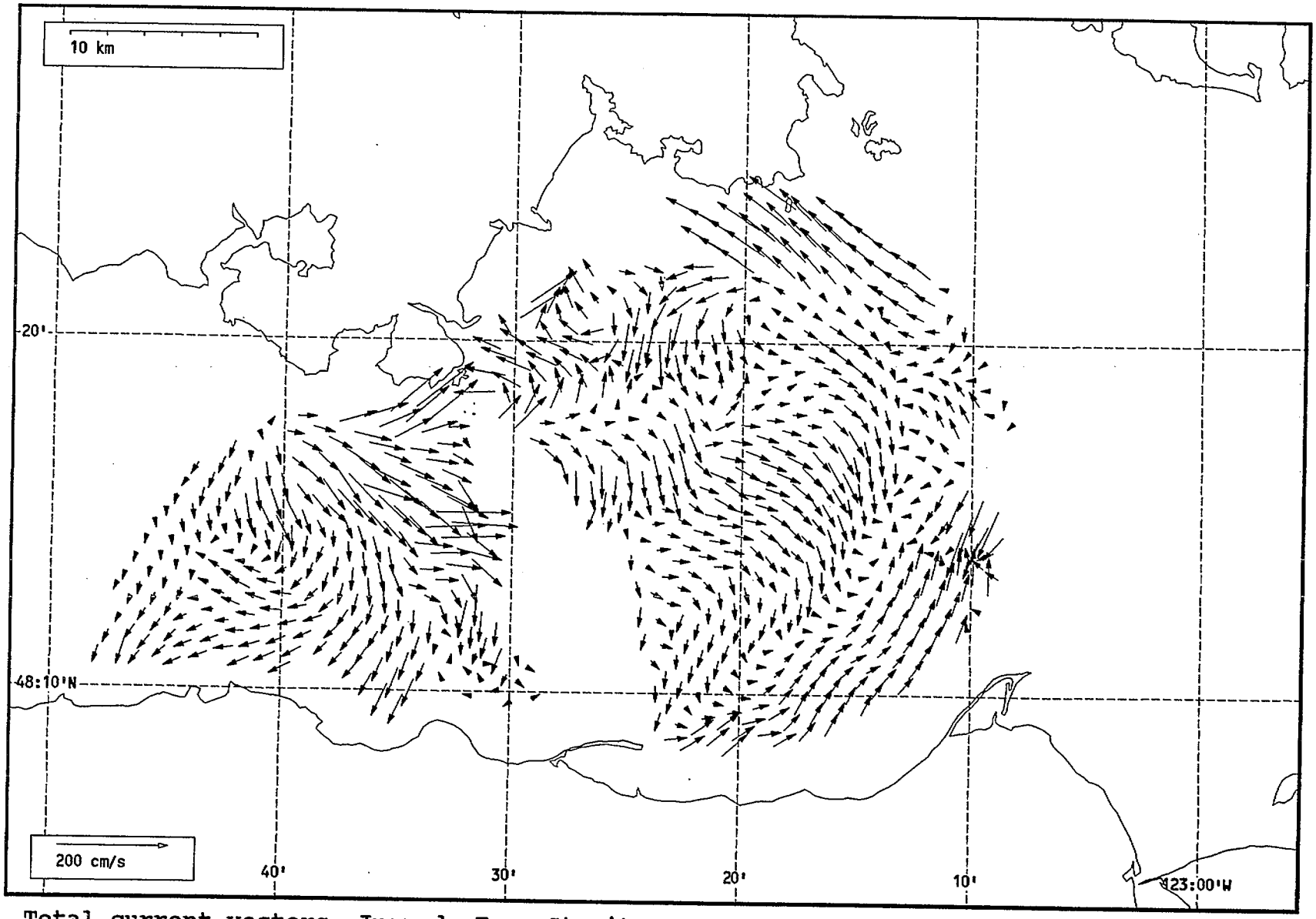

Total current vectors, Juan de Fuca Strait, 1992-07-13 07:00 Z.

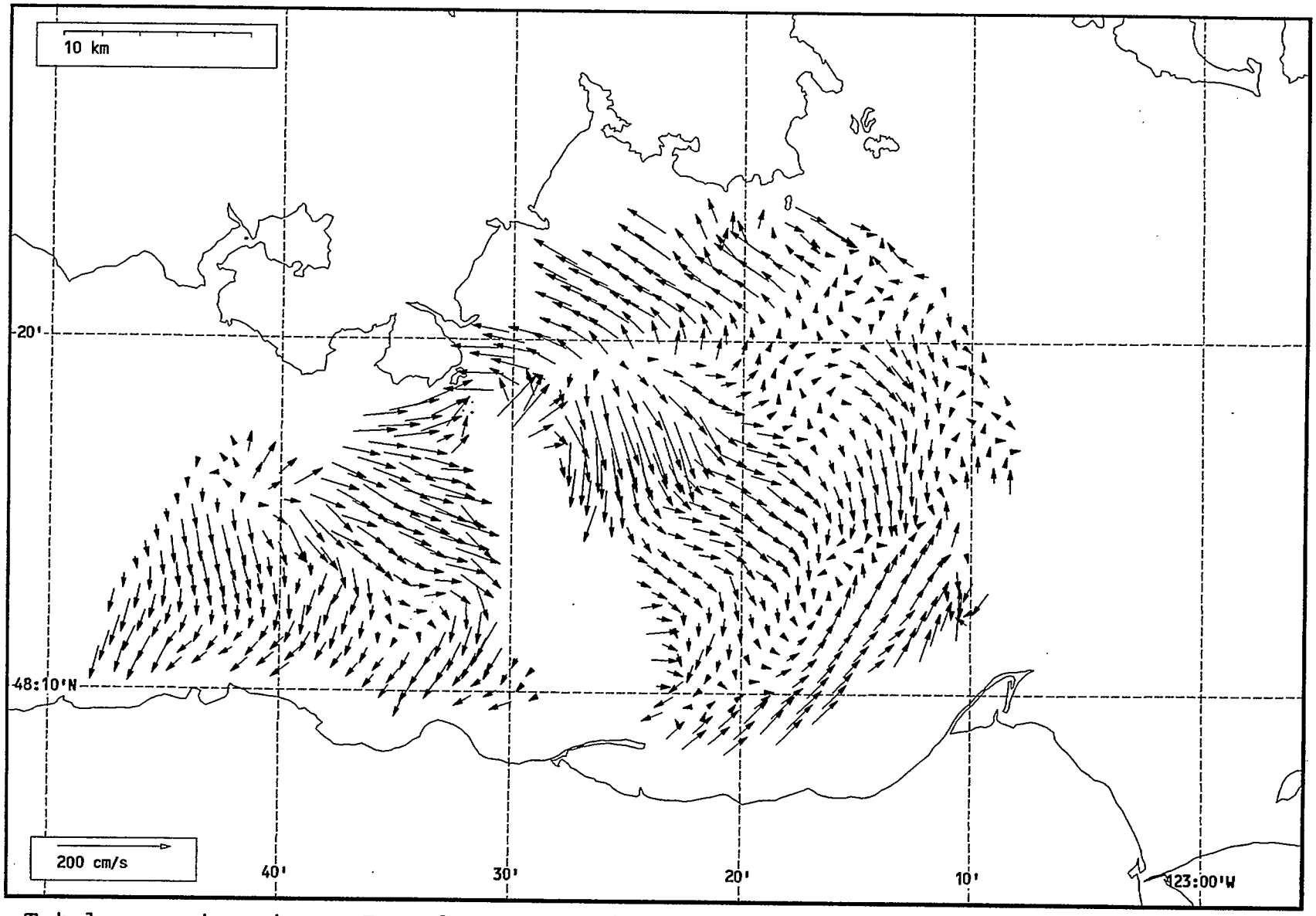

Total current vectors, Juan de Fuca Strait, 1992-07-13 08:00 Z.

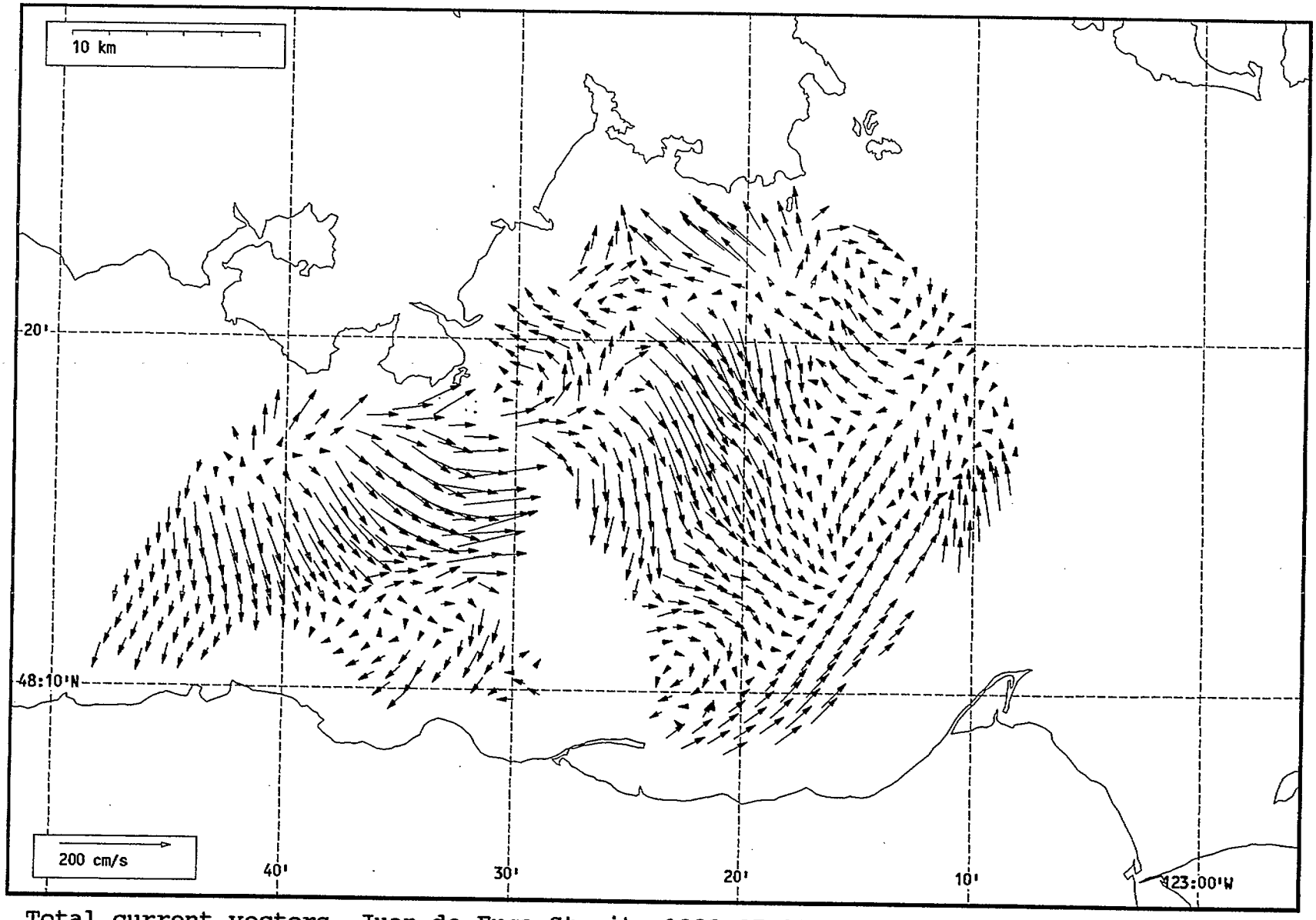

Total current vectors, Juan de Fuca Strait, 1992-07-13 09:00 Z.

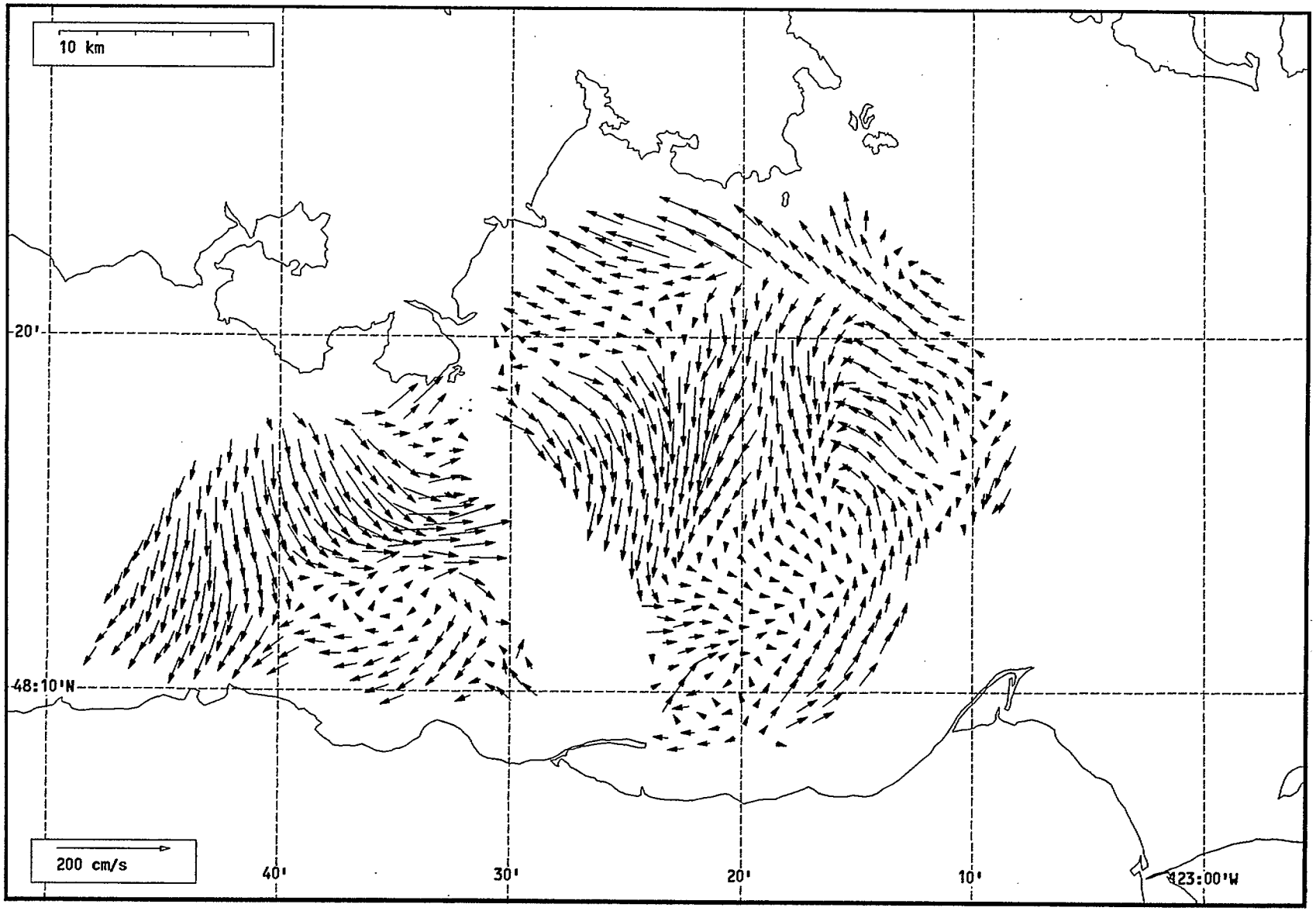

Total current vectors, Juan de Fuca Strait, 1992-07-13 10:00 Z.

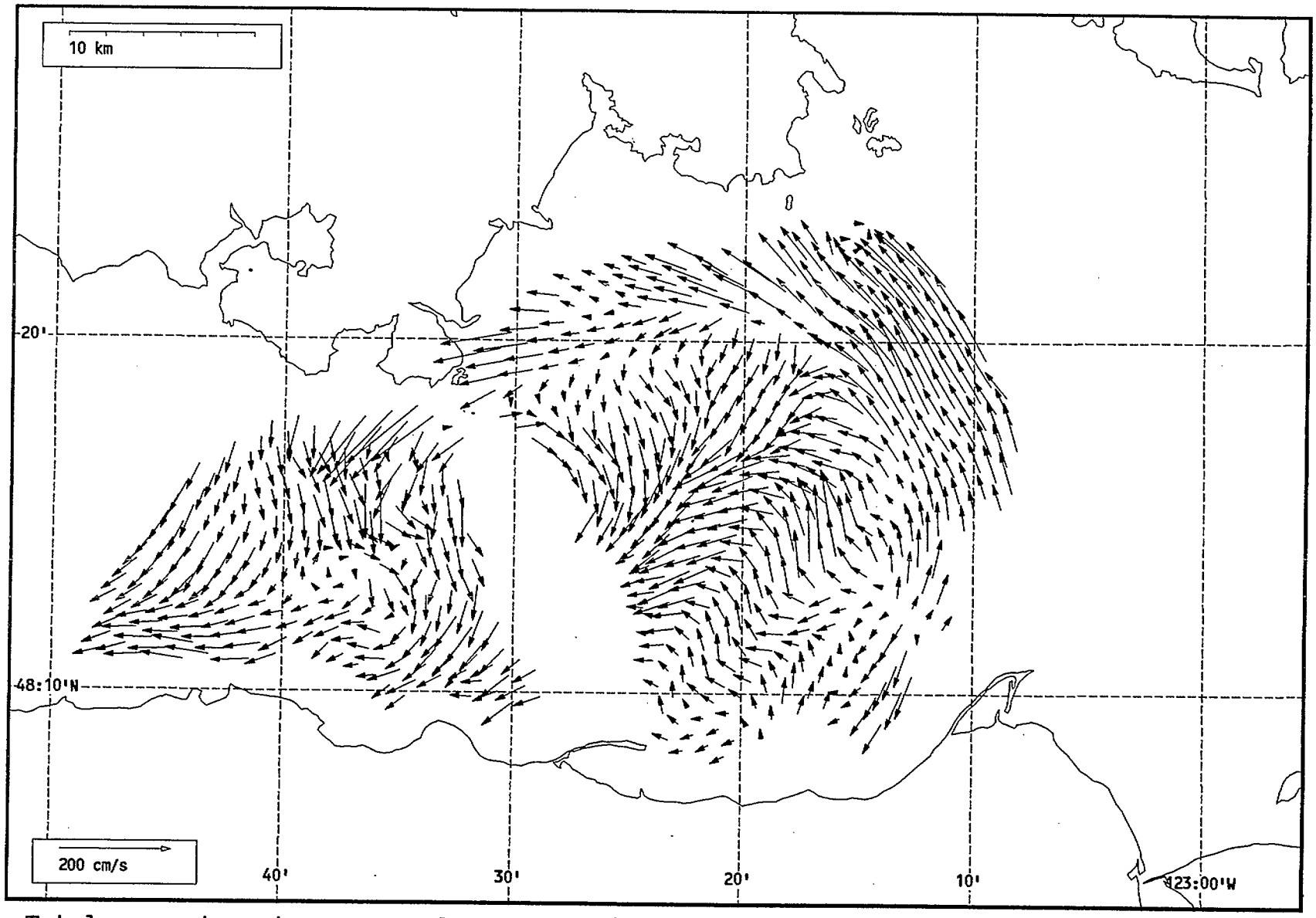

Total current vectors, Juan de Fuca Strait, 1992-07-13 11:00 Z.

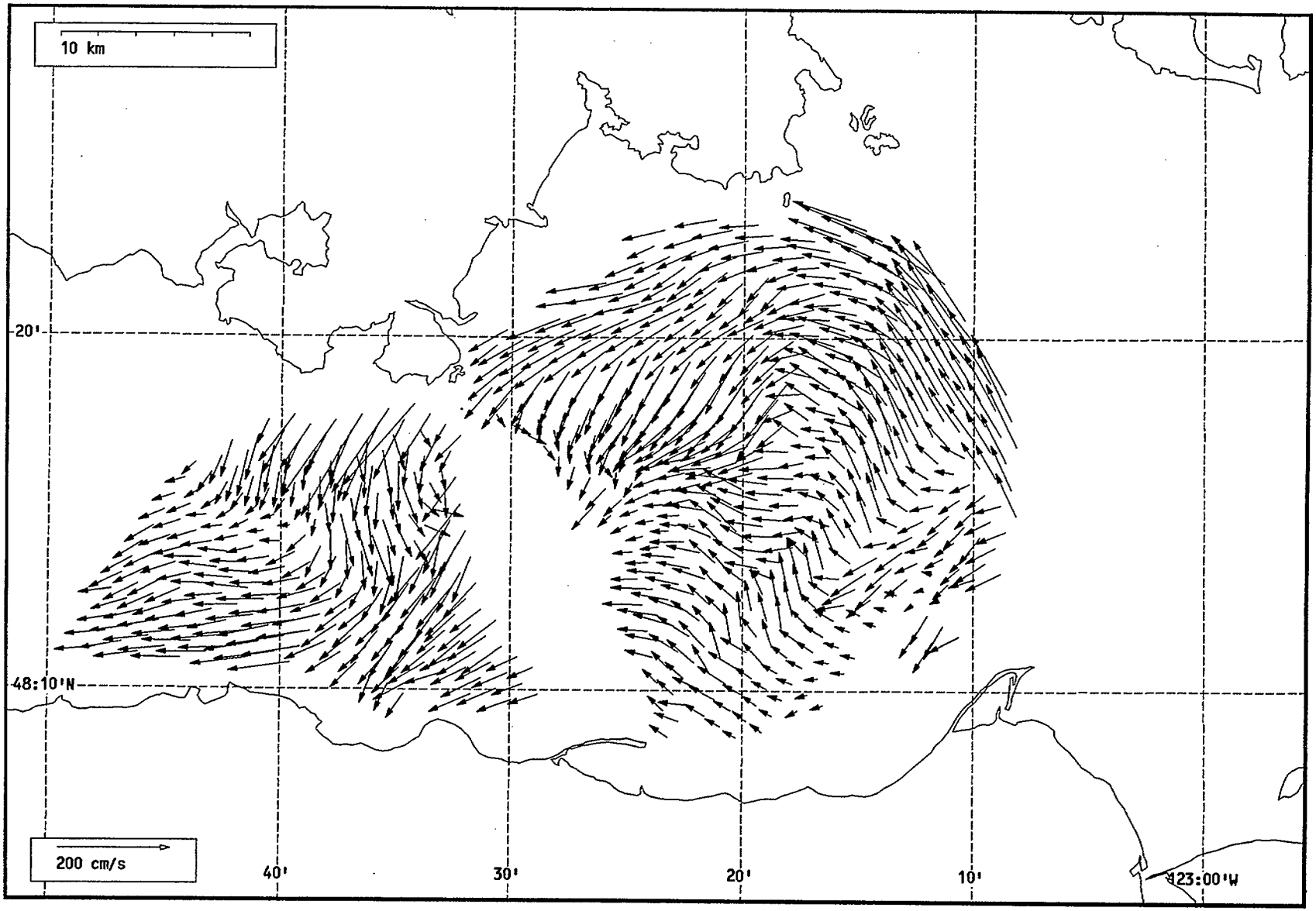

Total current vectors, Juan de Fuca Strait, 1992-07-13 12:00 Z.

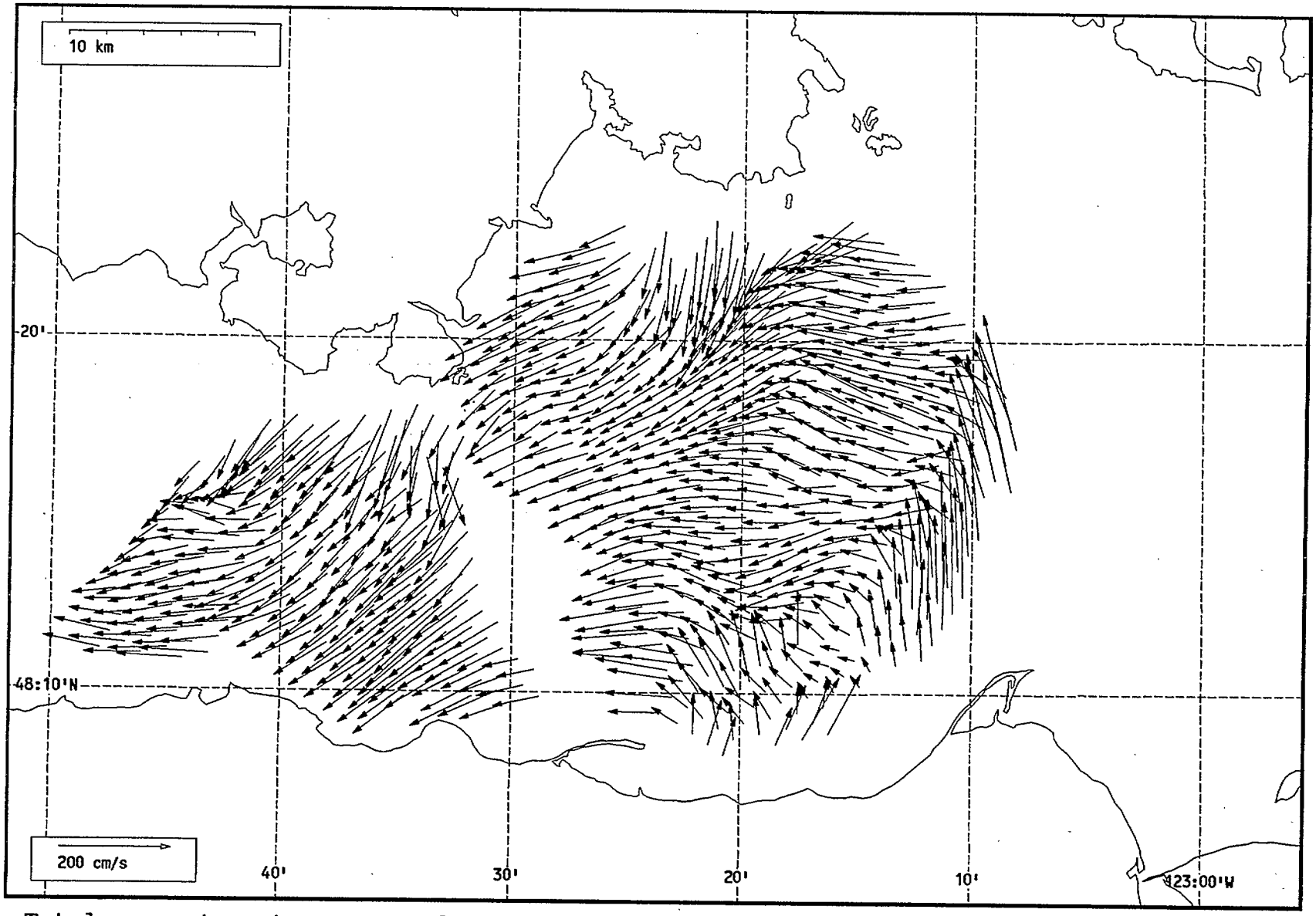

Total current vectors, Juan de Fuca Strait, 1992-07-13 13:00 Z.

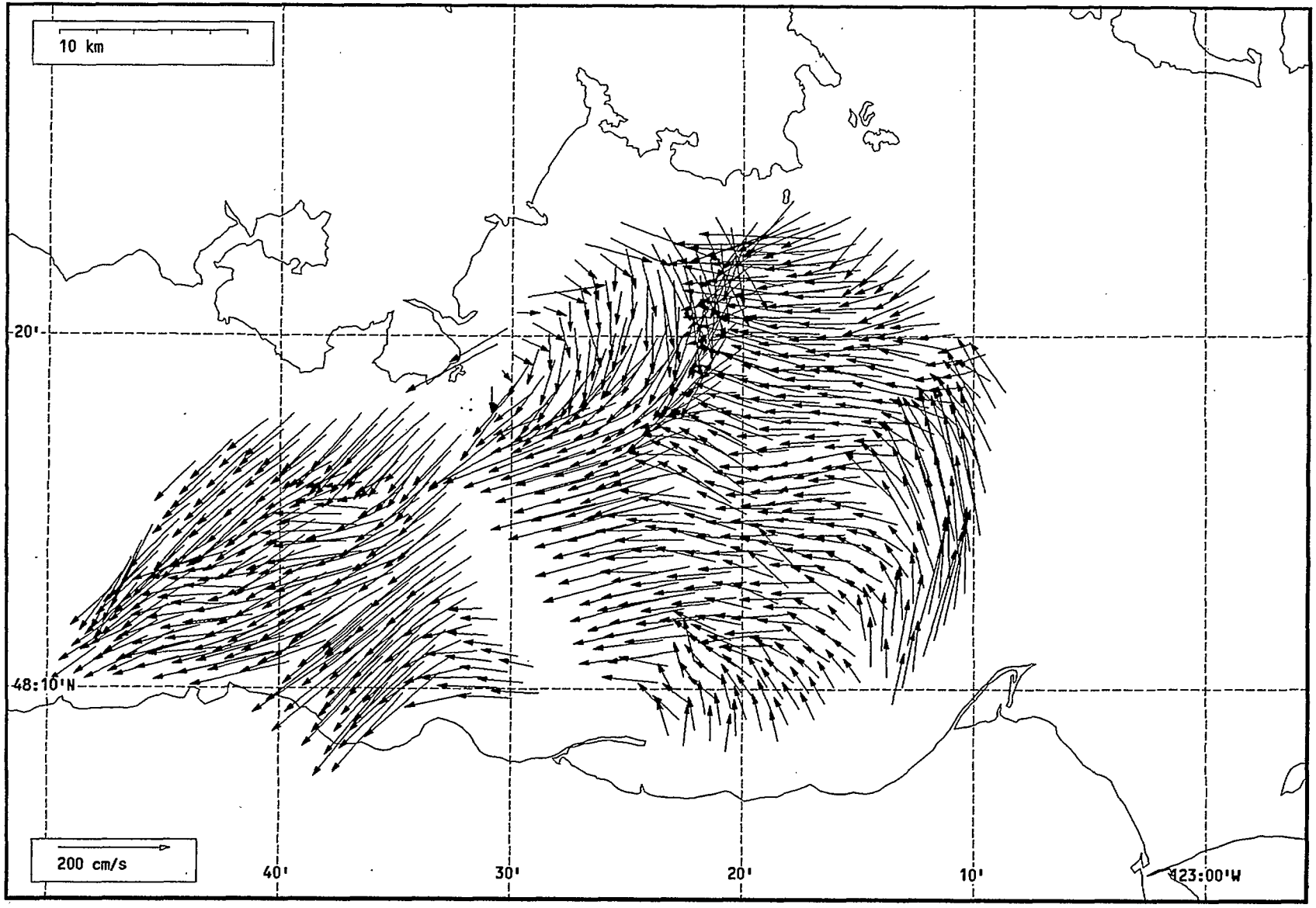

Total current vectors, Juan de Fuca Strait, 1992-07-13 14:00 Z.

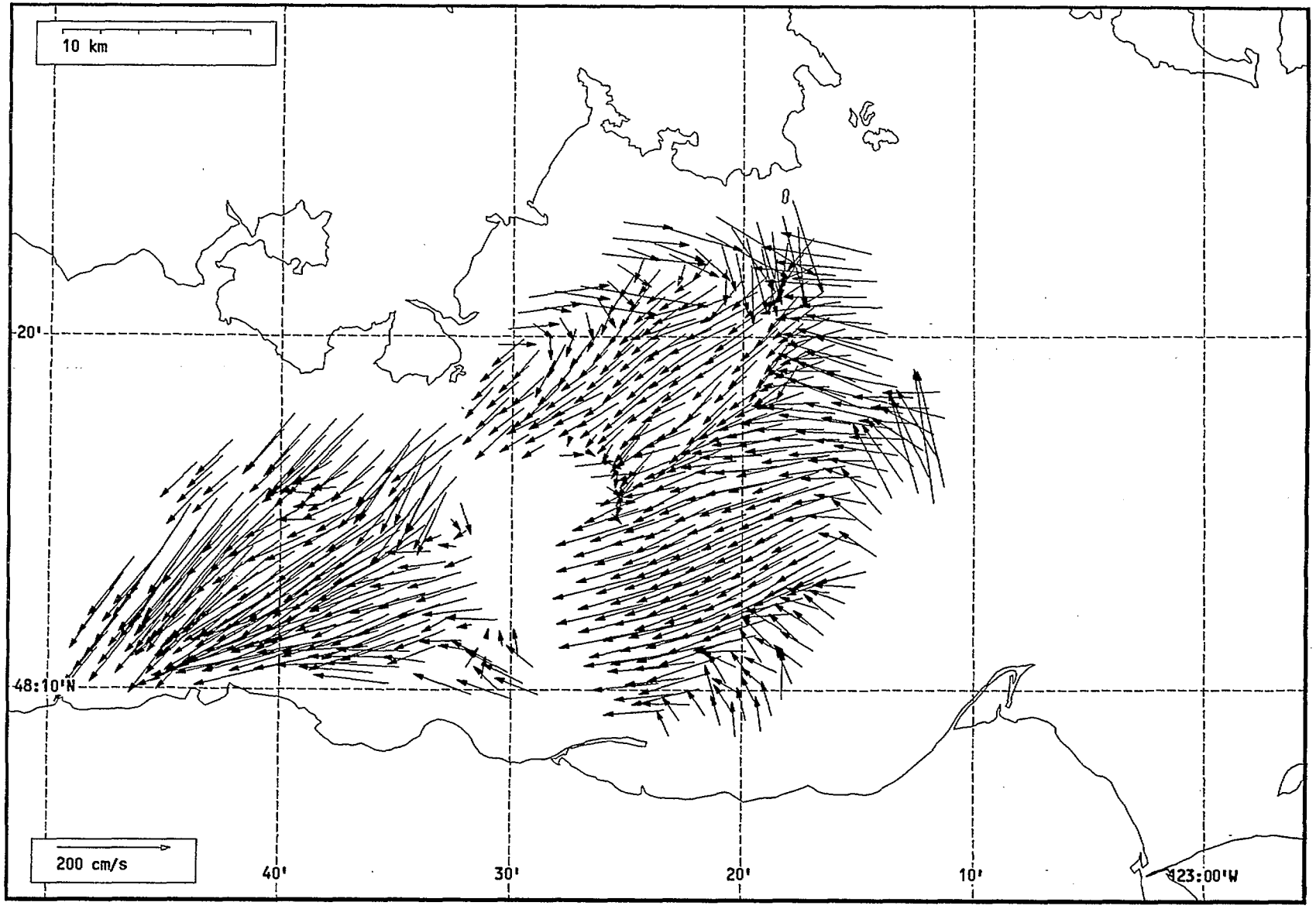

Total current vectors, Juan de Fuca Strait, 1992-07-13 15:00 Z.

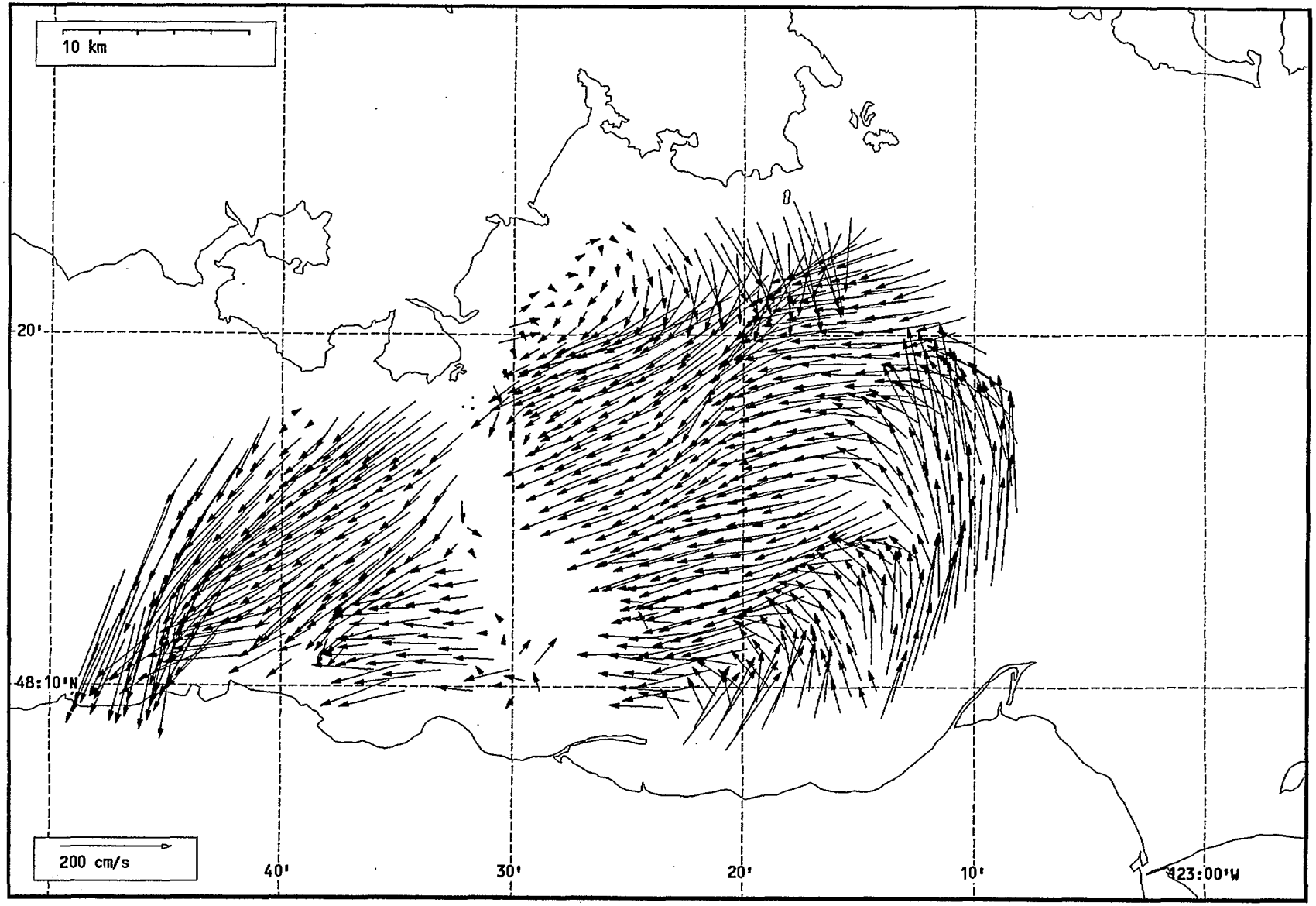

Total current vectors, Juan de Fuca Strait, 1992-07-13 16:00 Z.

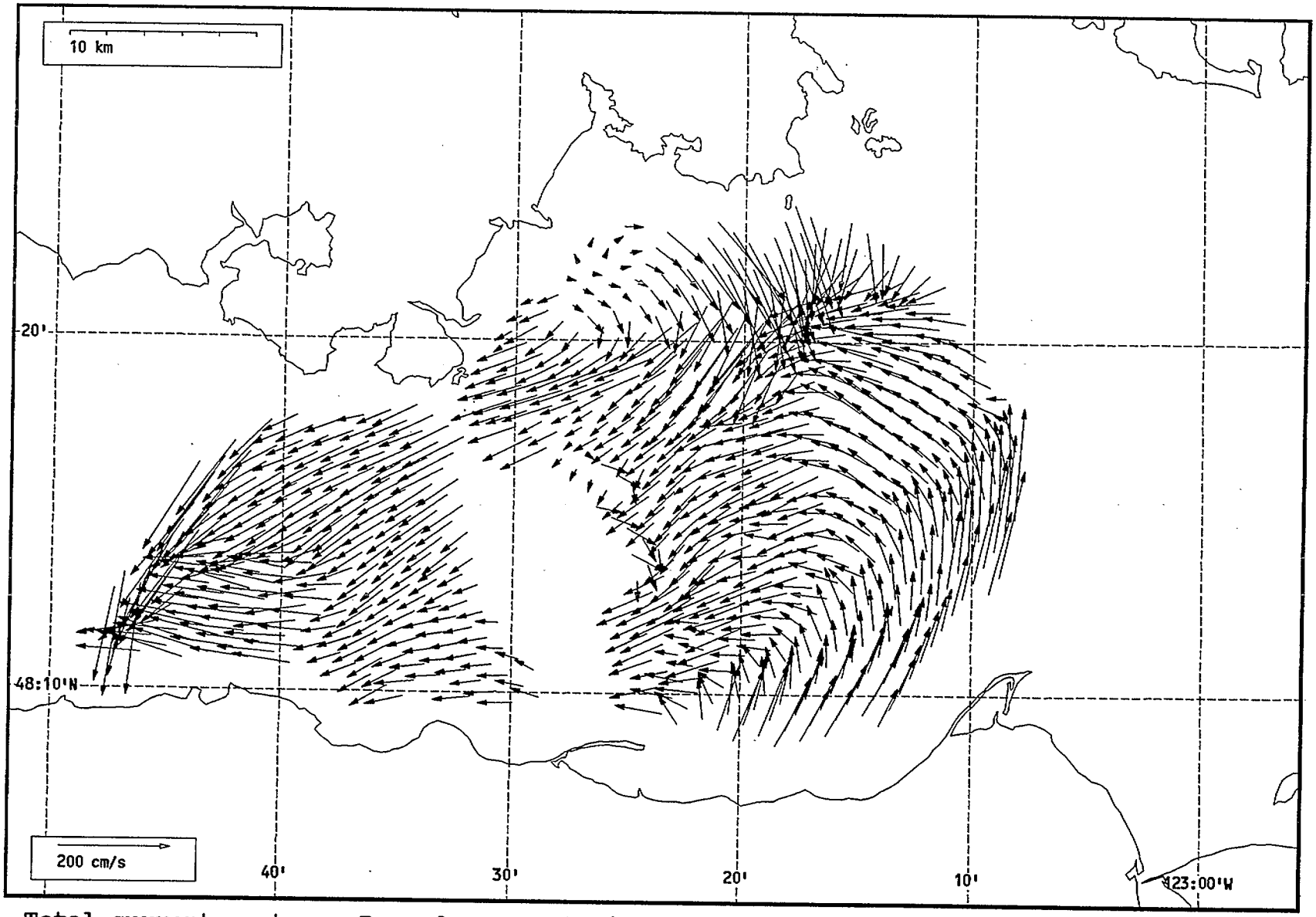

Total current vectors, Juan de Fuca Strait, 1992-07-13 17:00 Z.

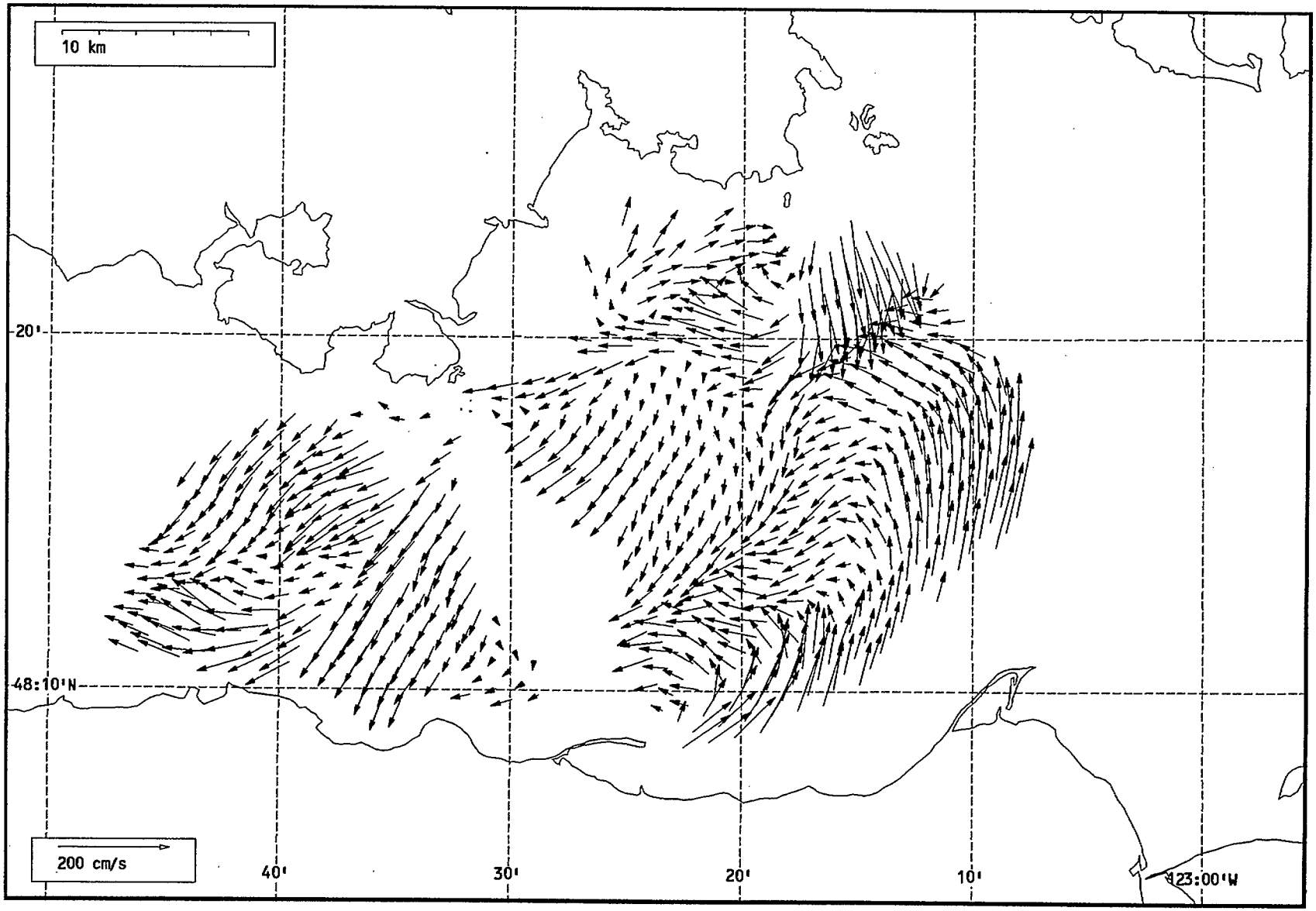

Total current vectors, Juan de Fuca Strait, 1992-07-13 18:00 Z.

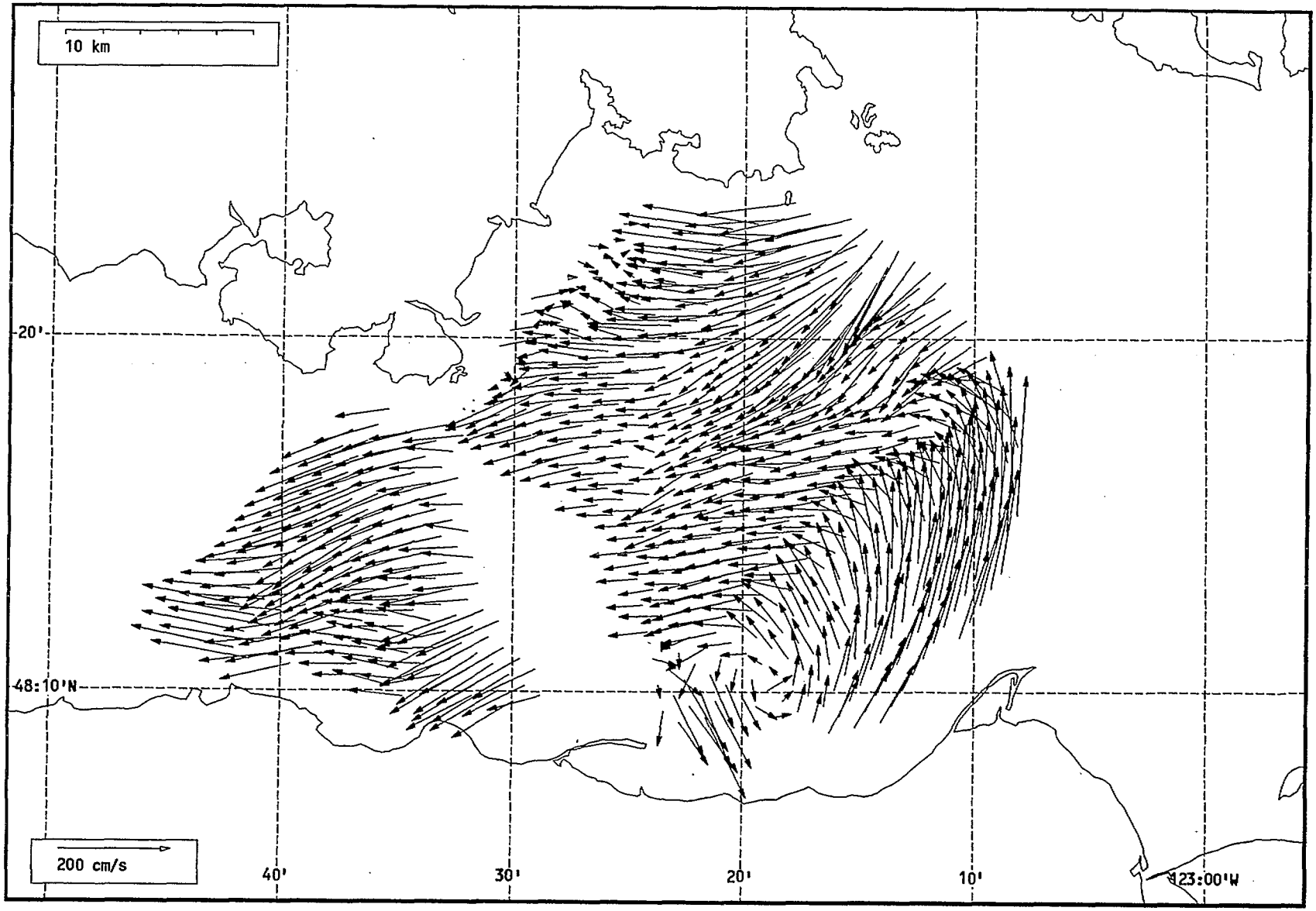

Total current vectors, Juan de Fuca Strait, 1992-07-14 17:00 Z.

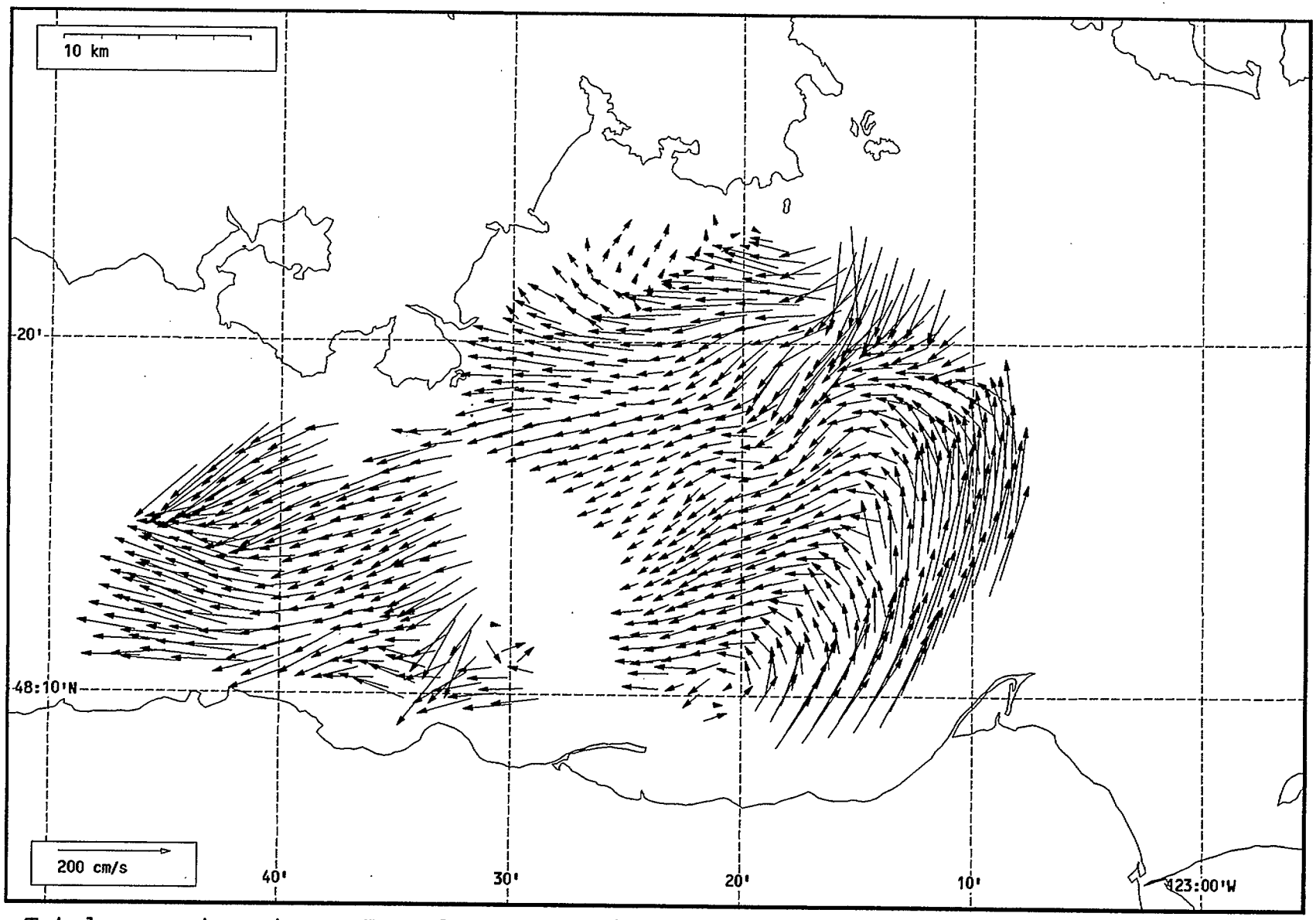

Total current vectors, Juan de Fuca Strait, 1992-07-14 18:00 Z.

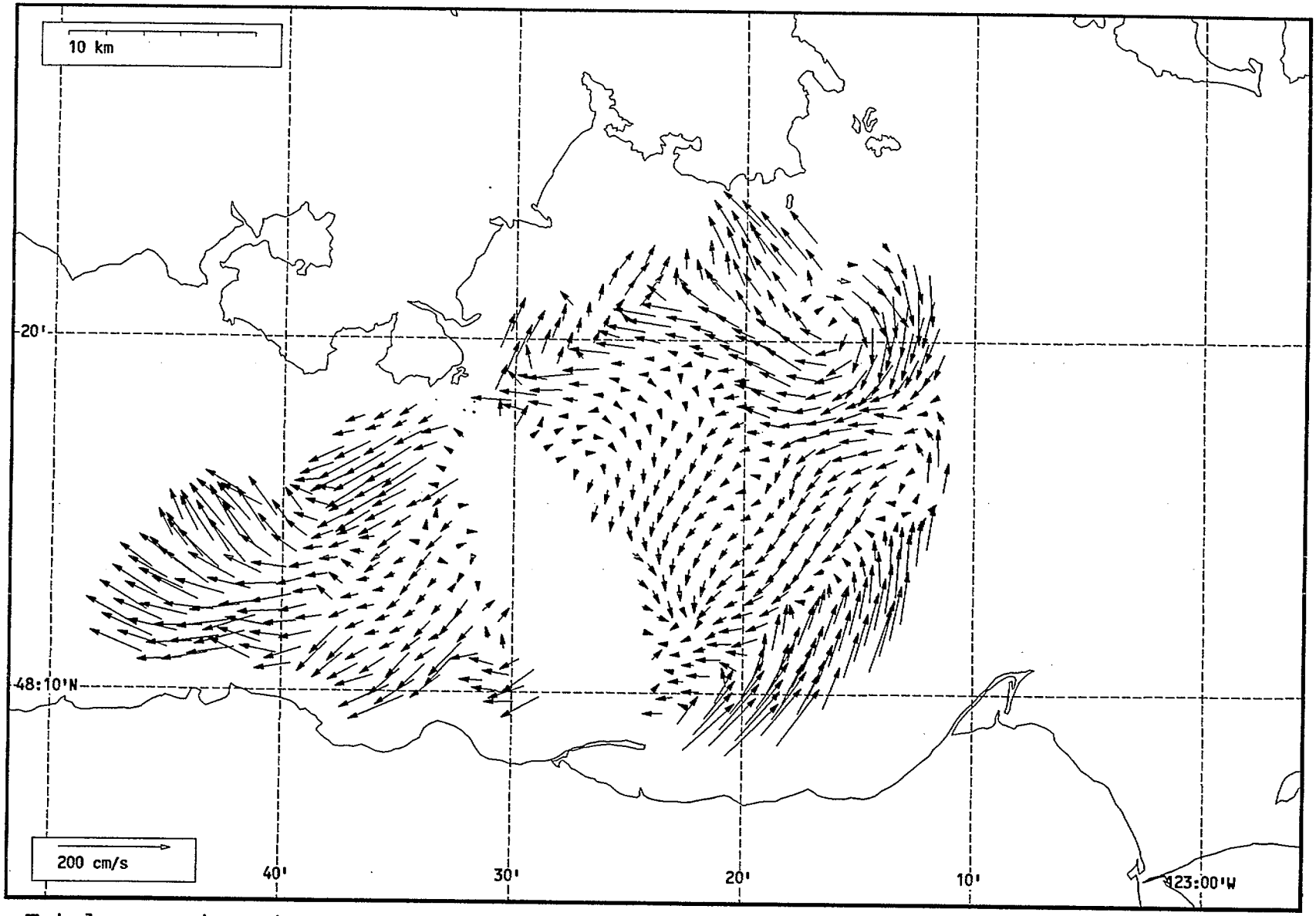

Total current vectors, Juan de Fuca Strait, 1992-07-14 19:00 Z.

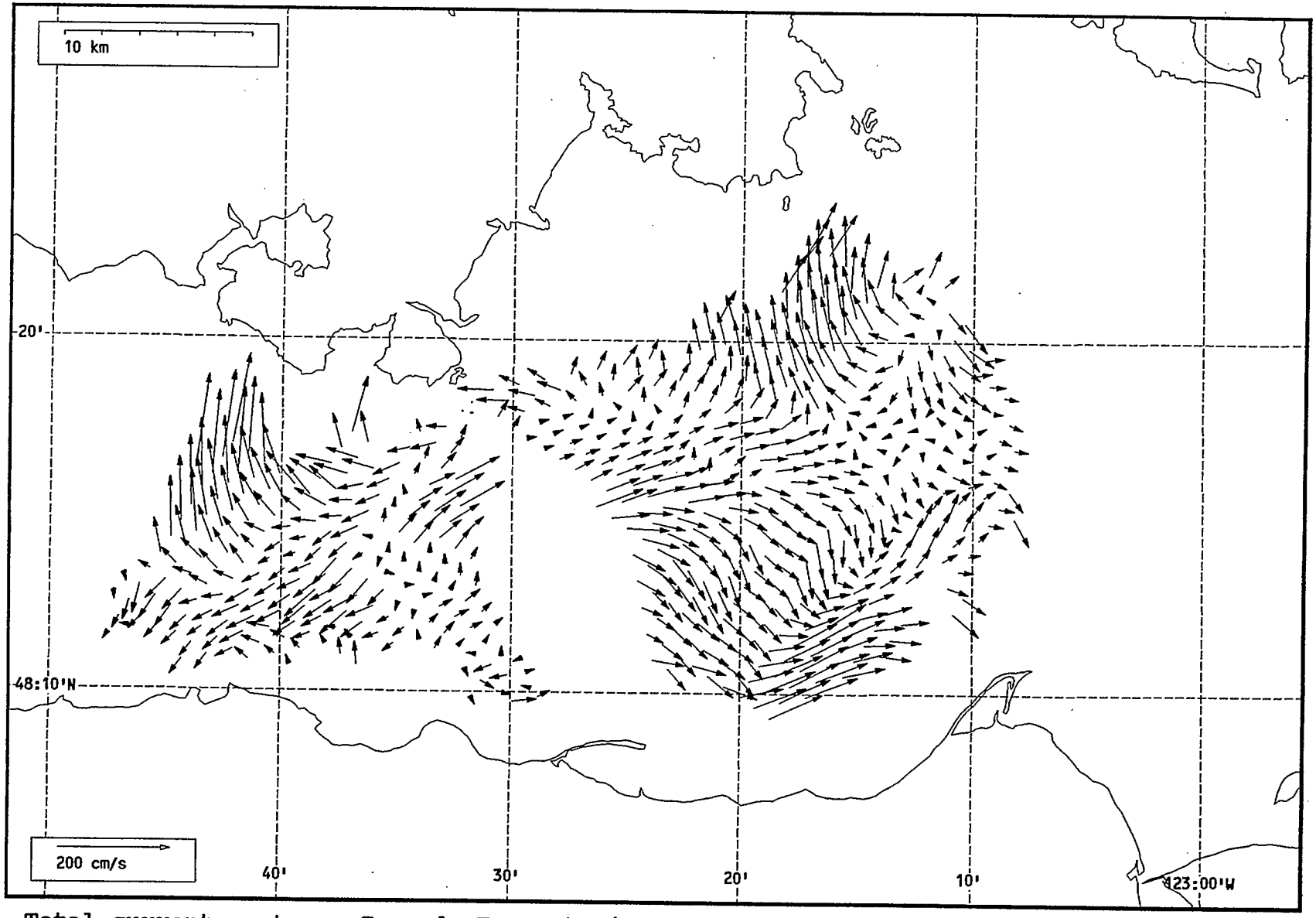

Total current vectors, Juan de Fuca Strait, 1992-07-14 20:00 Z.

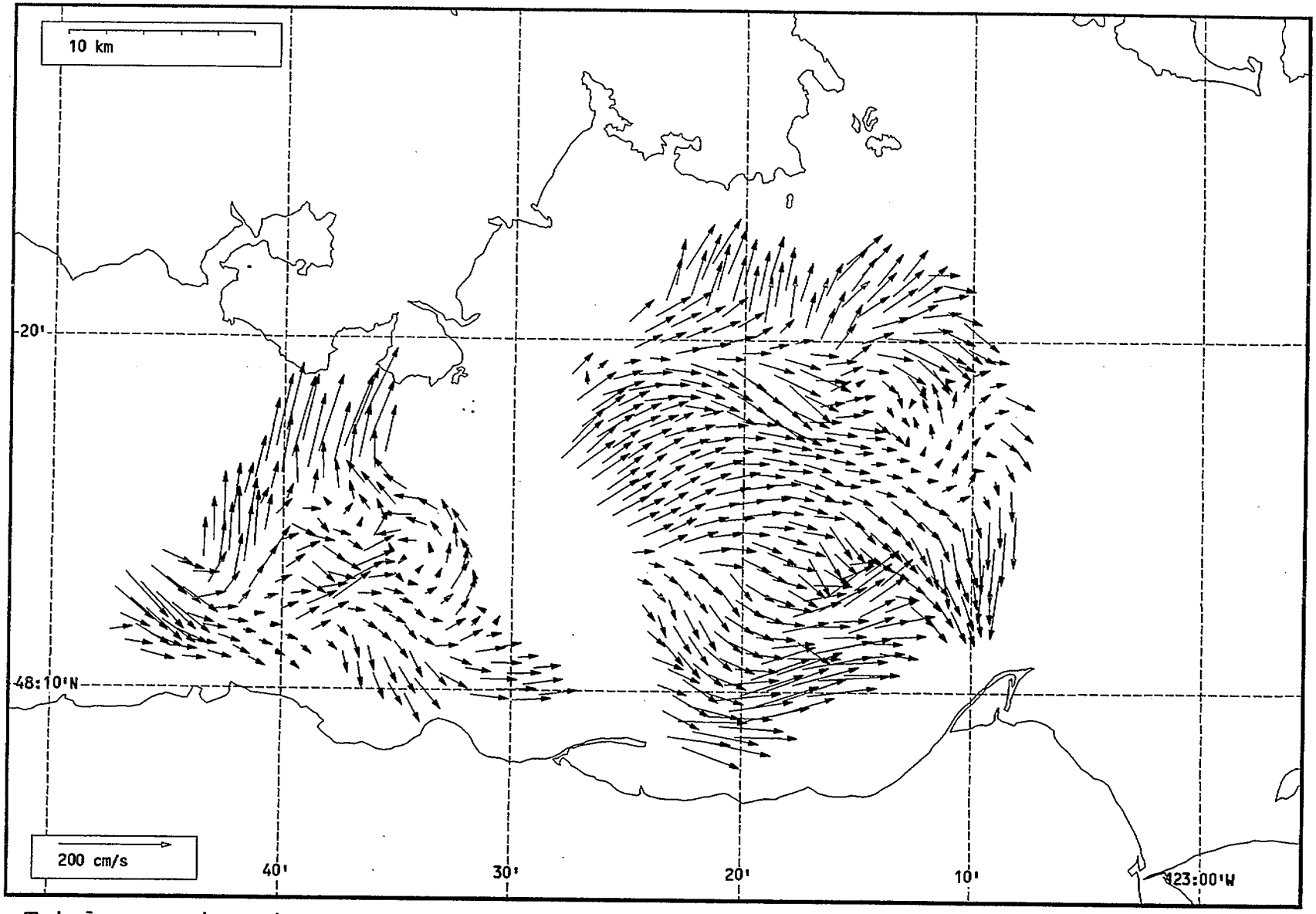

Total current vectors, Juan de Fuca Strait, 1992-07-14 21:00 Z.

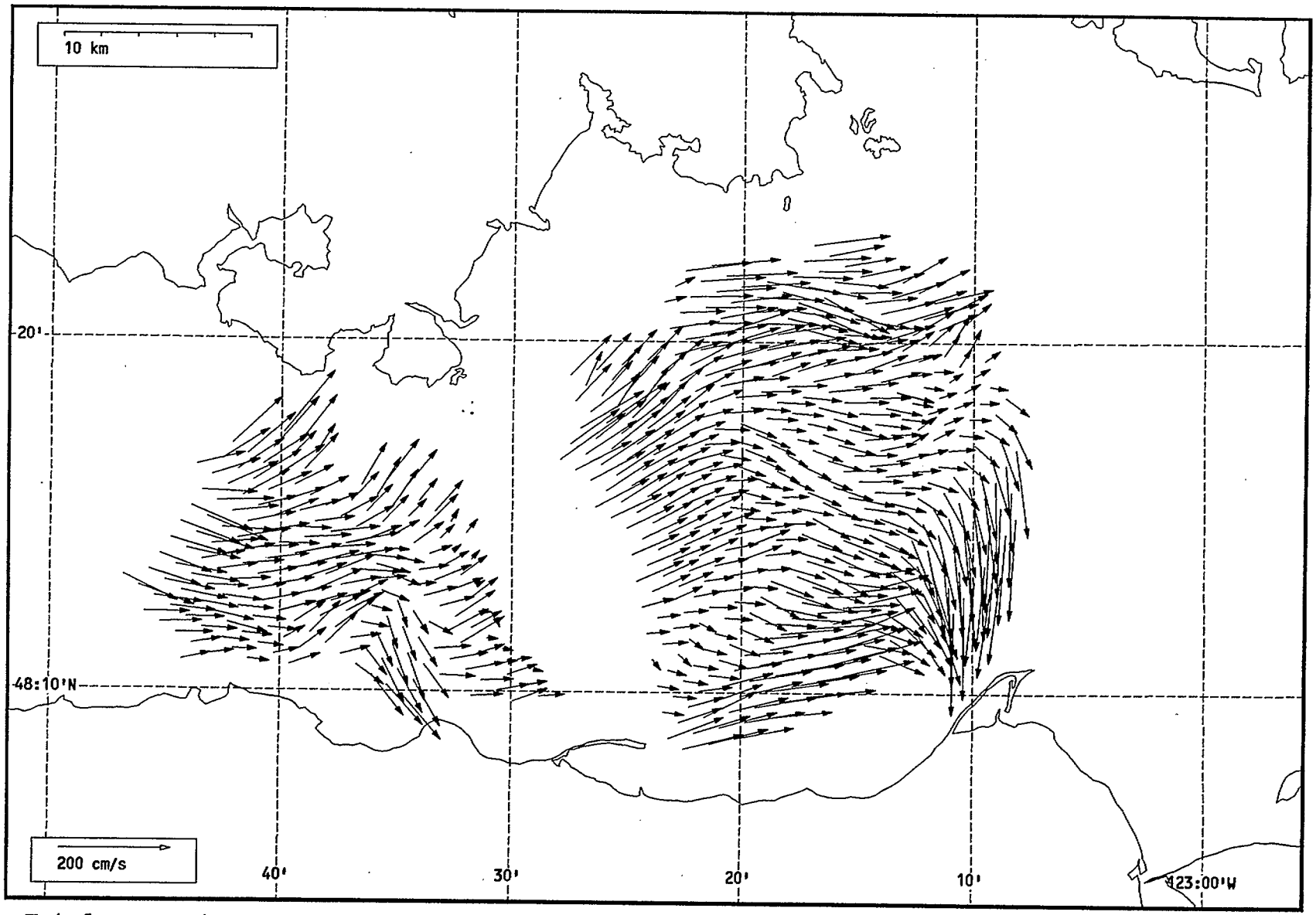

Total current vectors, Juan de Fuca Strait, 1992-07-14 22:00 Z.

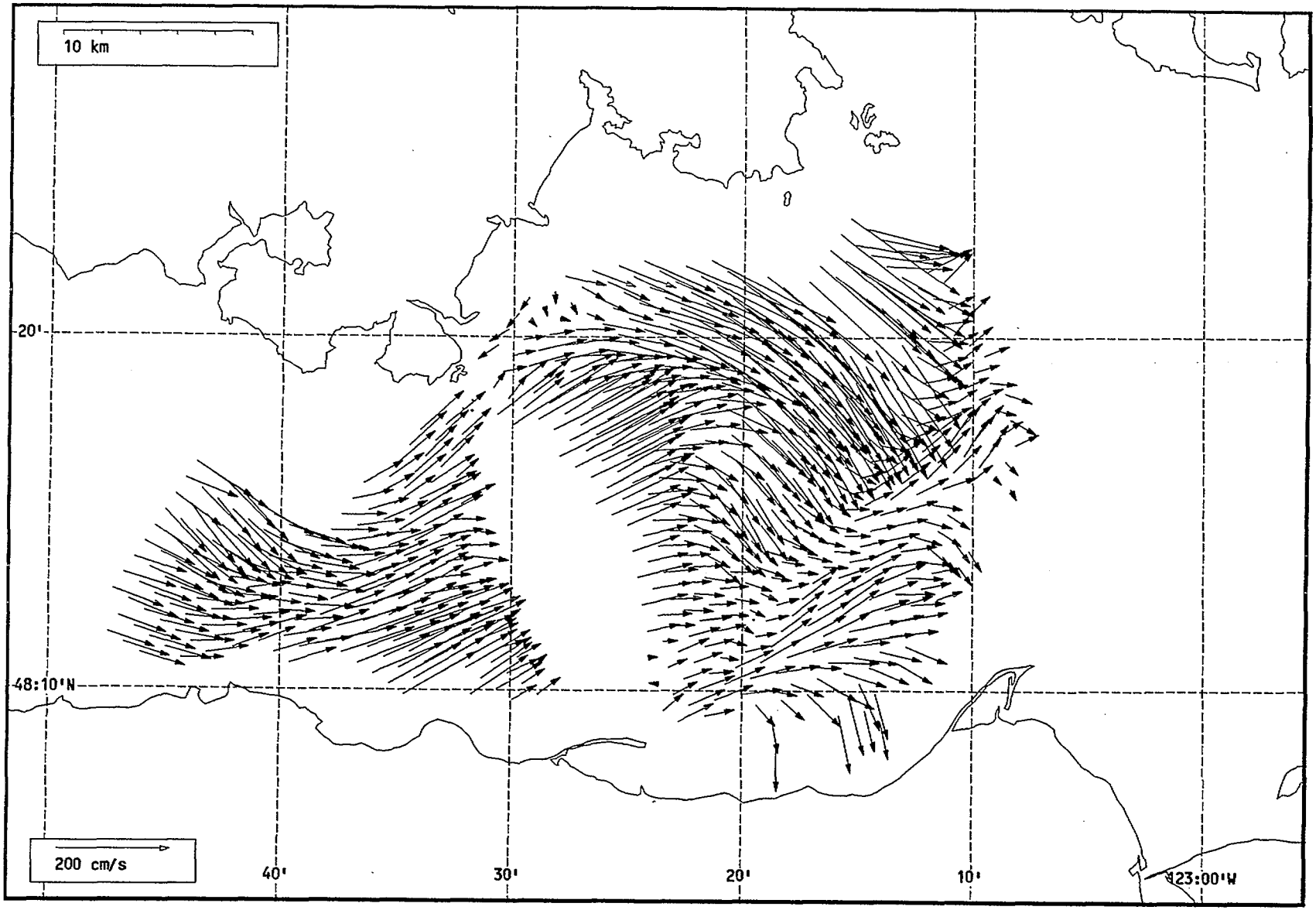

Total current vectors, Juan de Fuca Strait, 1992-07-14 23:00 Z.

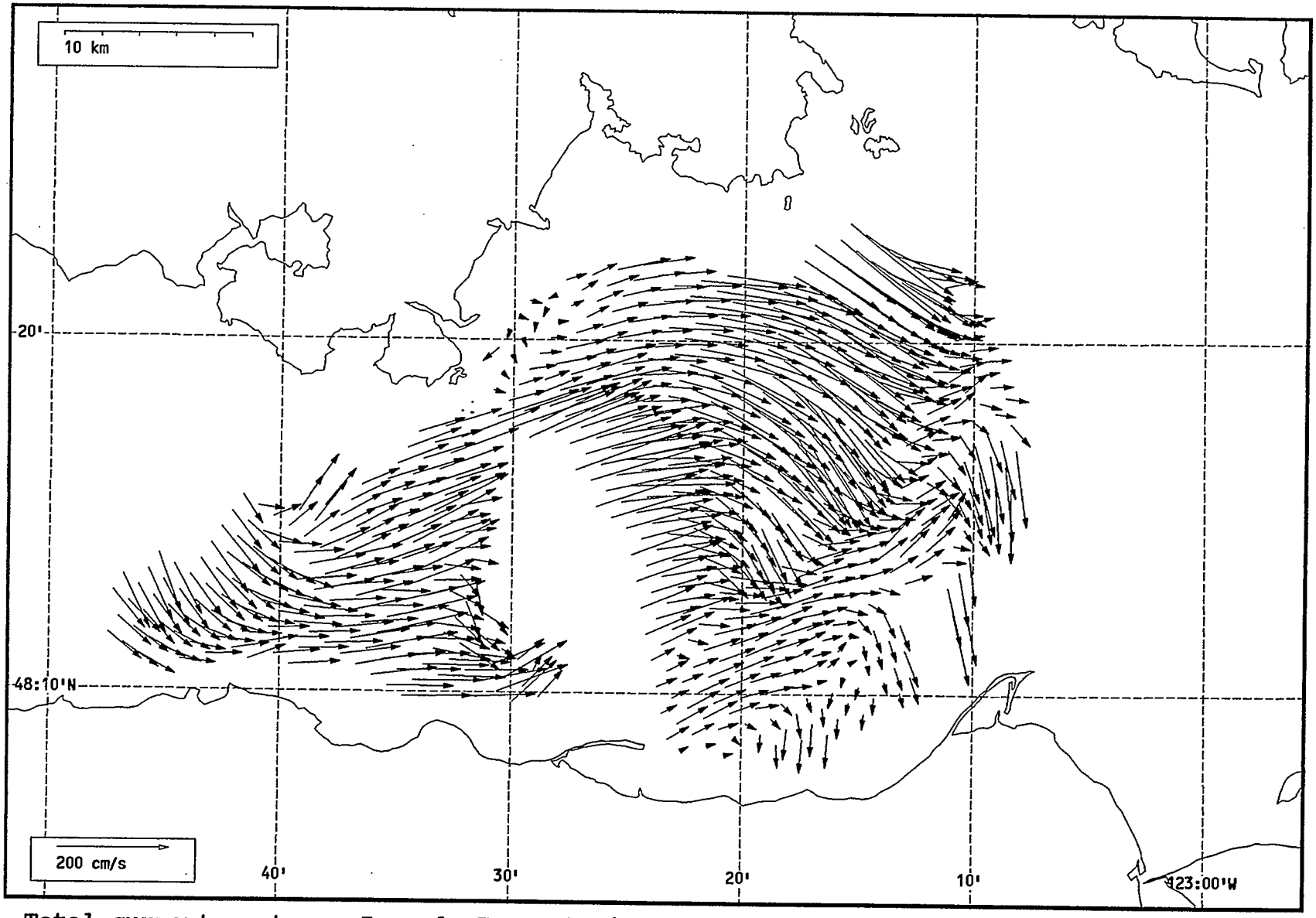

Total current vectors, Juan de Fuca Strait, 1992-07-15 00:00 Z.

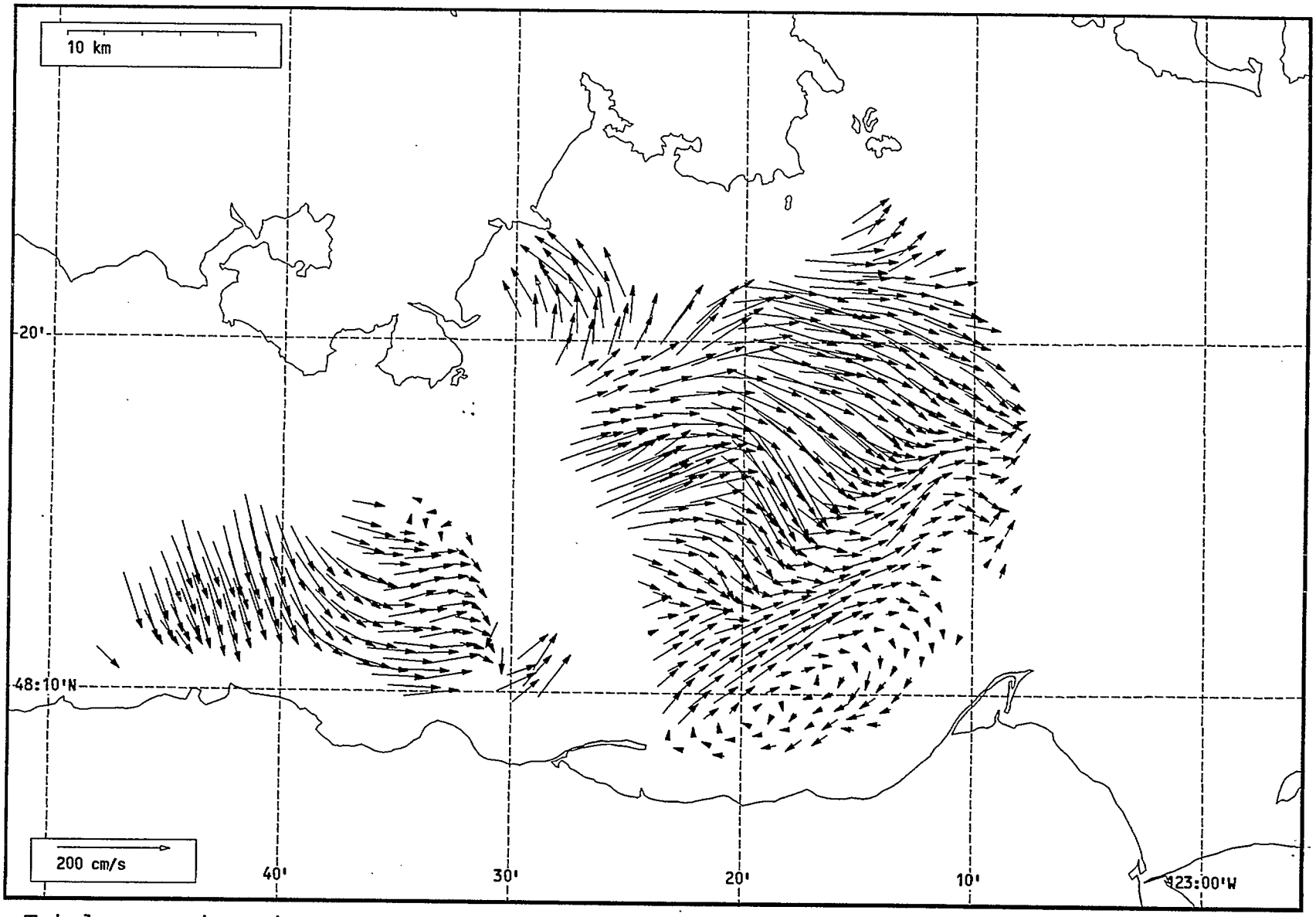

Total current vectors, Juan de Fuca Strait, 1992-07-15 01:00 Z.

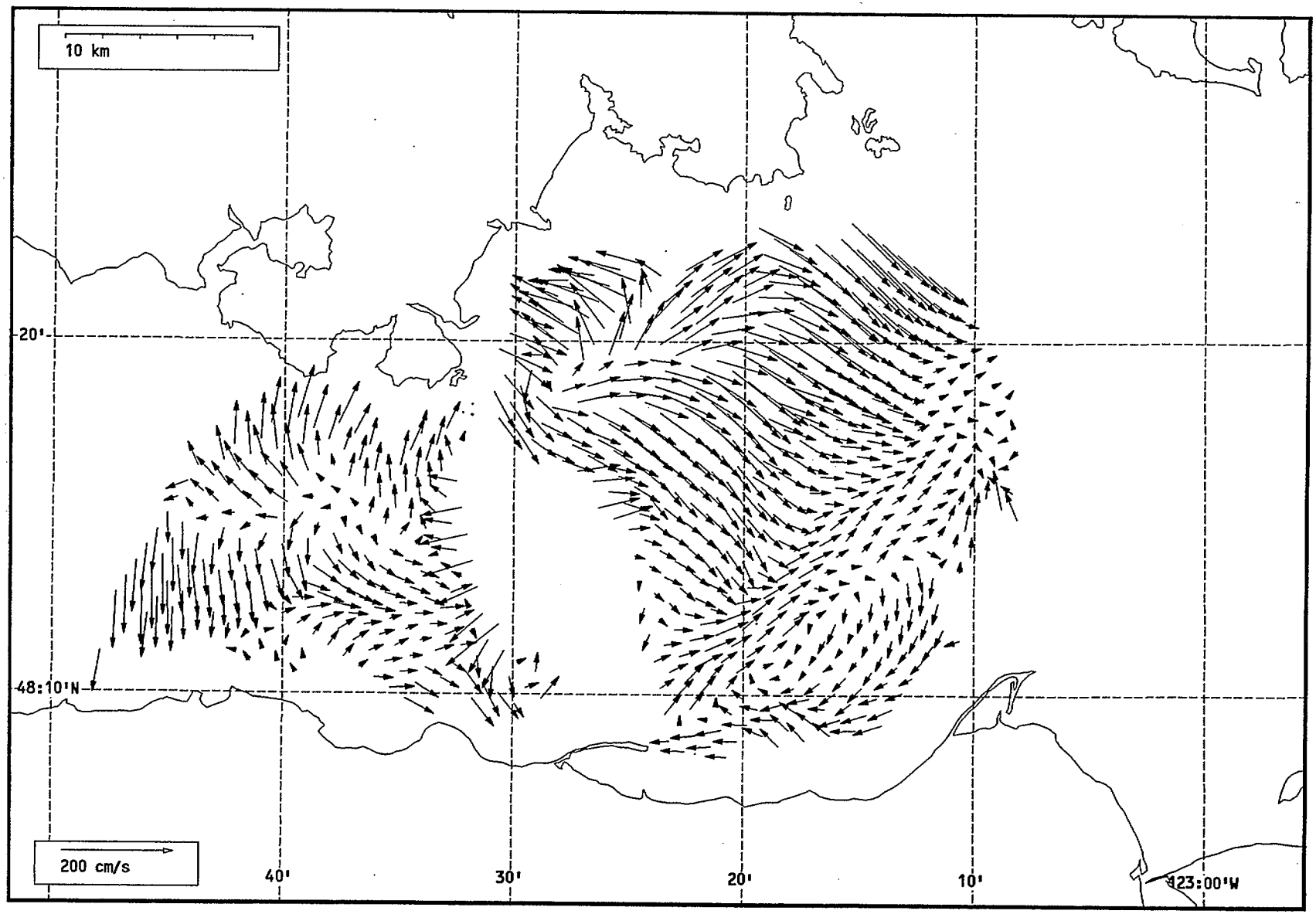

Total current vectors, Juan de Fuca Strait, 1992-07-15 02:00 Z.

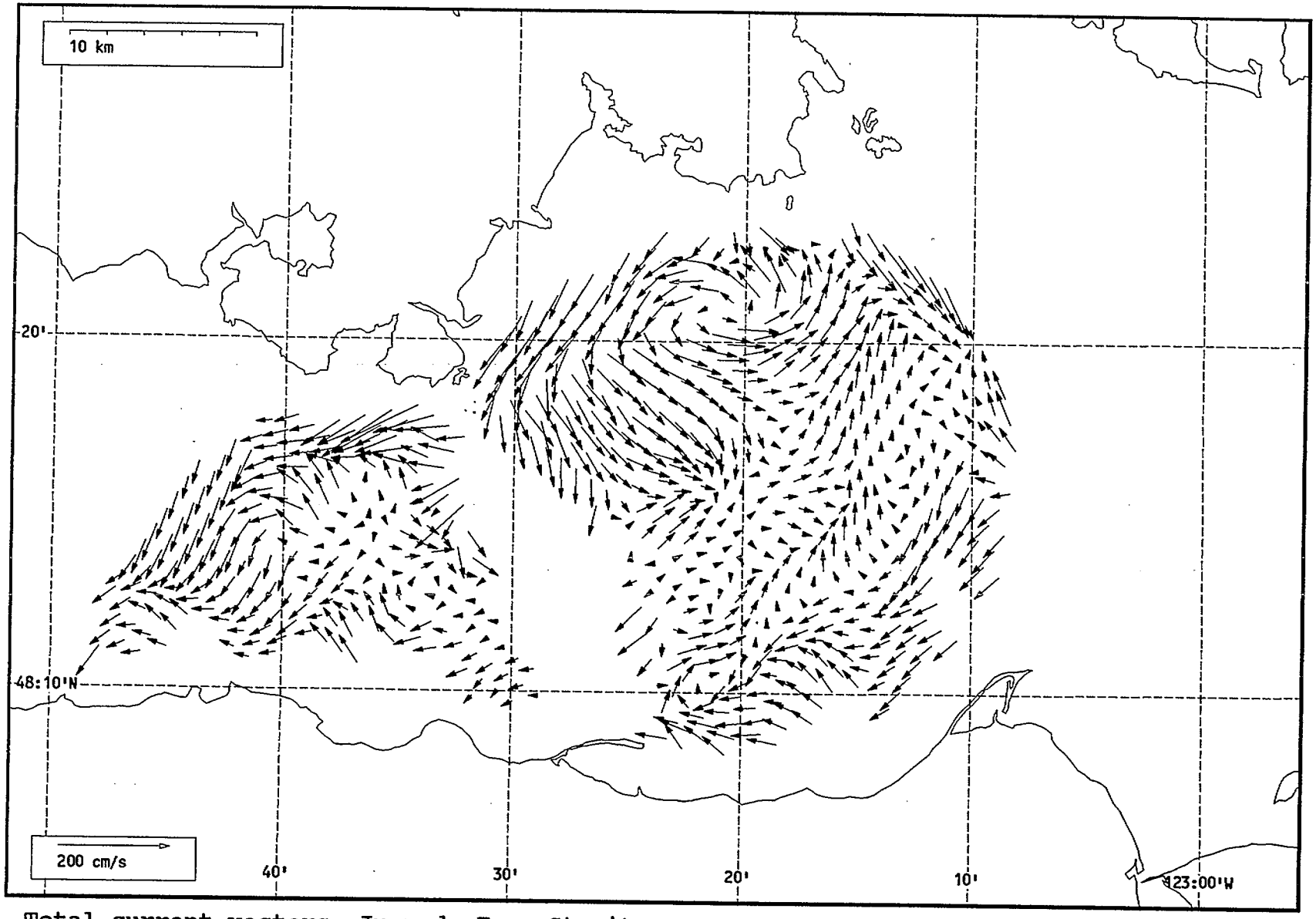

Total current vectors, Juan de Fuca Strait, 1992-07-15 03:00 Z.

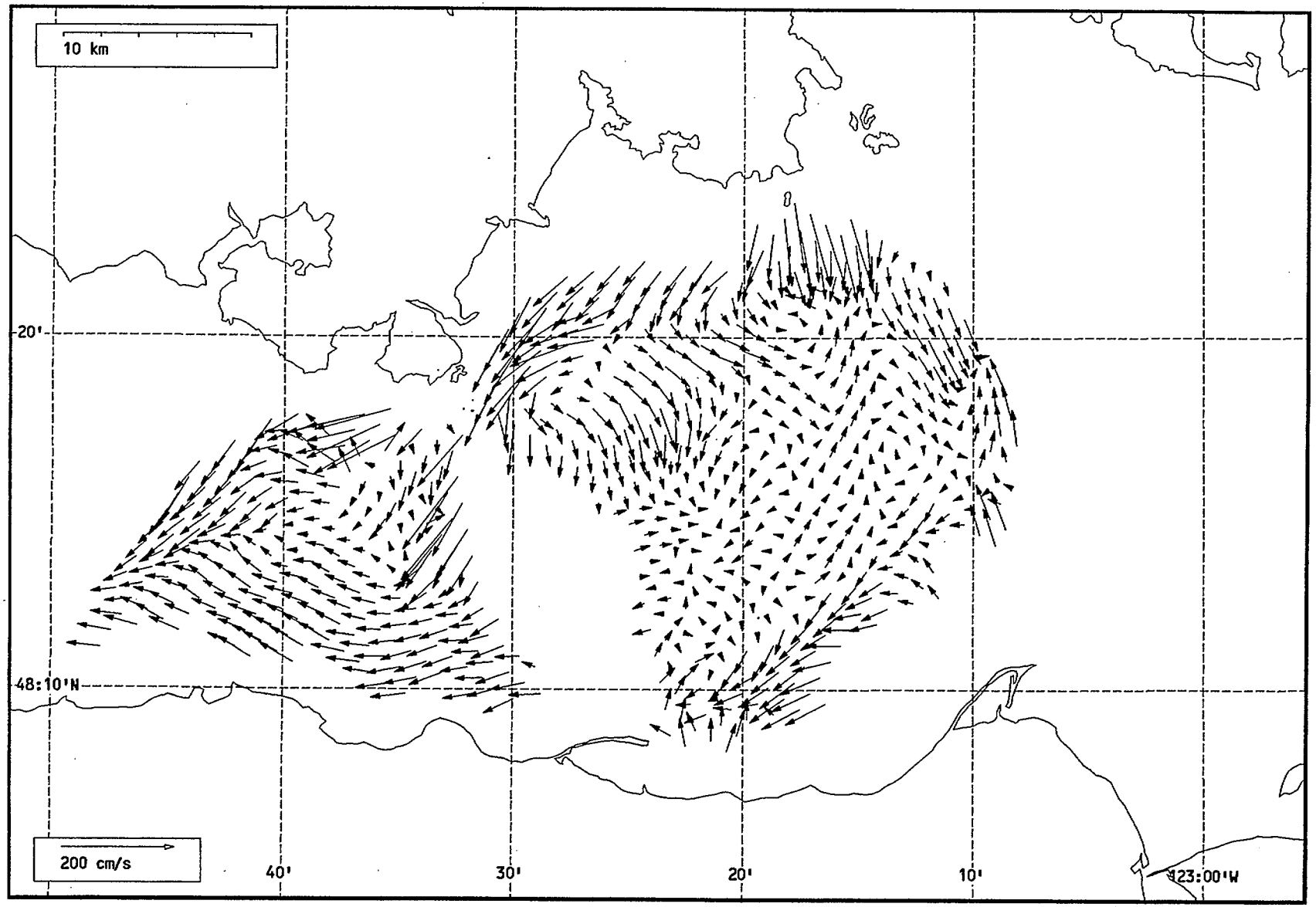

Total current vectors, Juan de Fuca Strait, 1992-07-15 04:00 Z.

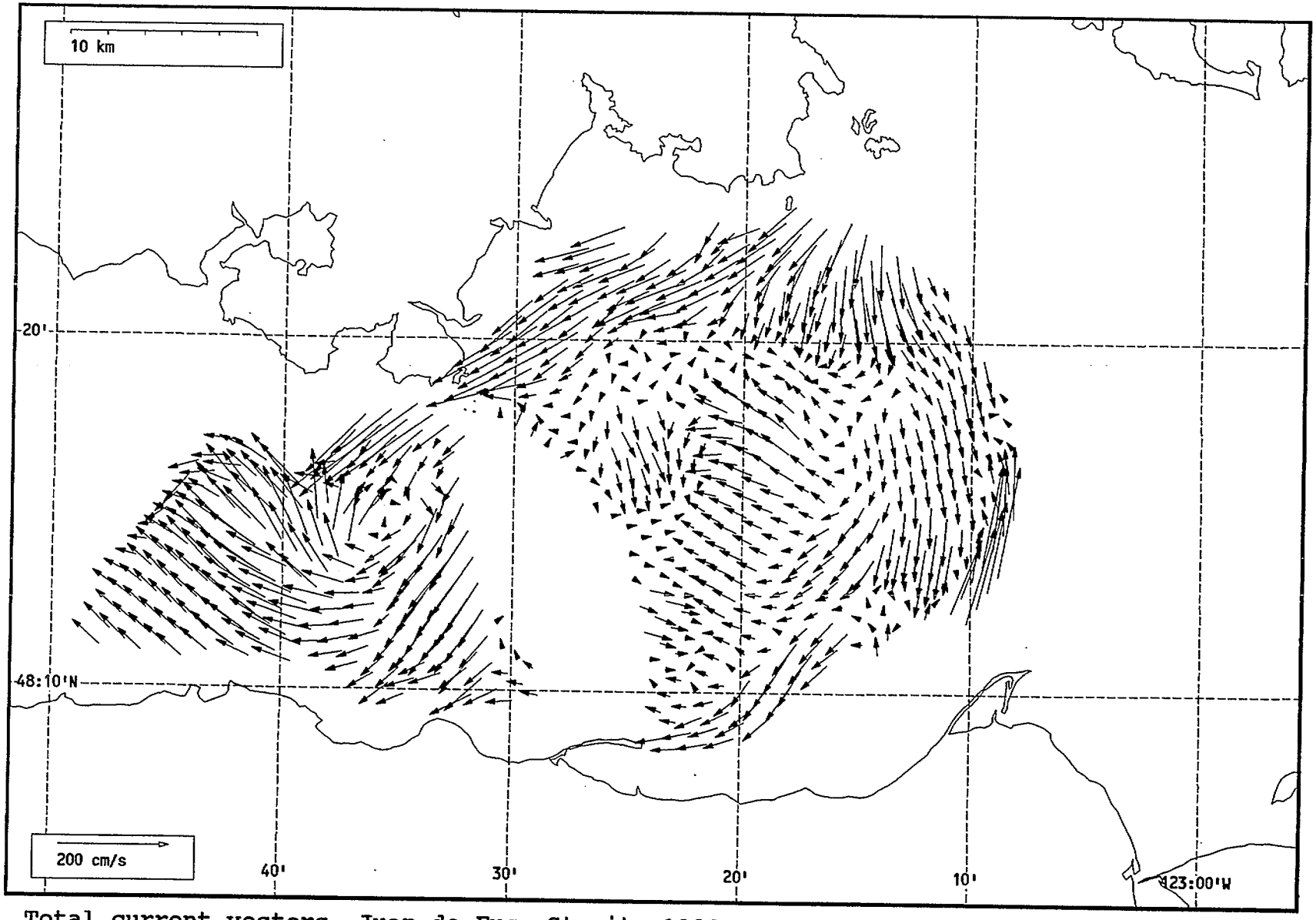

Total current vectors, Juan de Fuca Strait, 1992-07-15 05:00 Z.

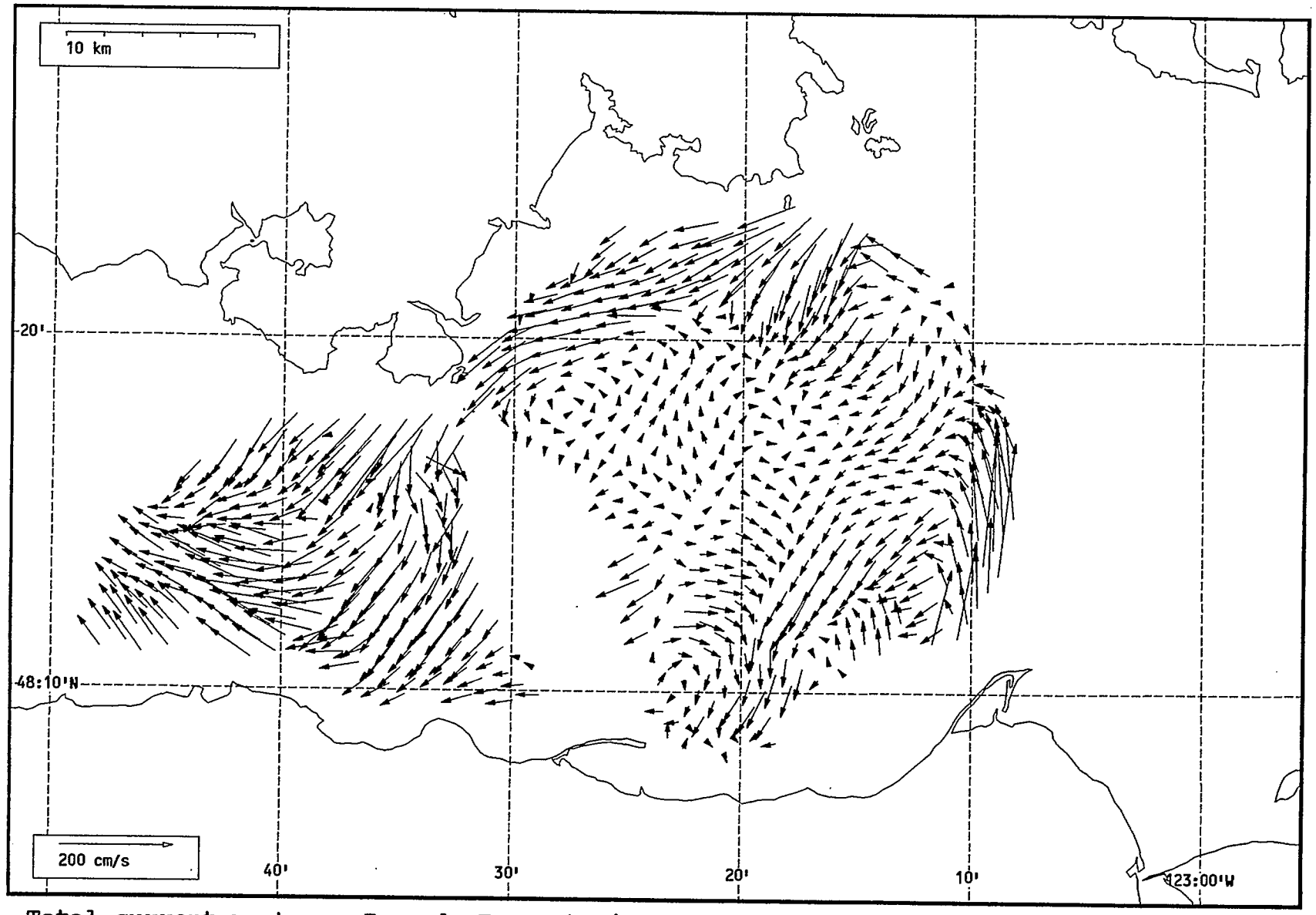

Total current vectors, Juan de Fuca Strait, 1992-07-15 06:00 Z.

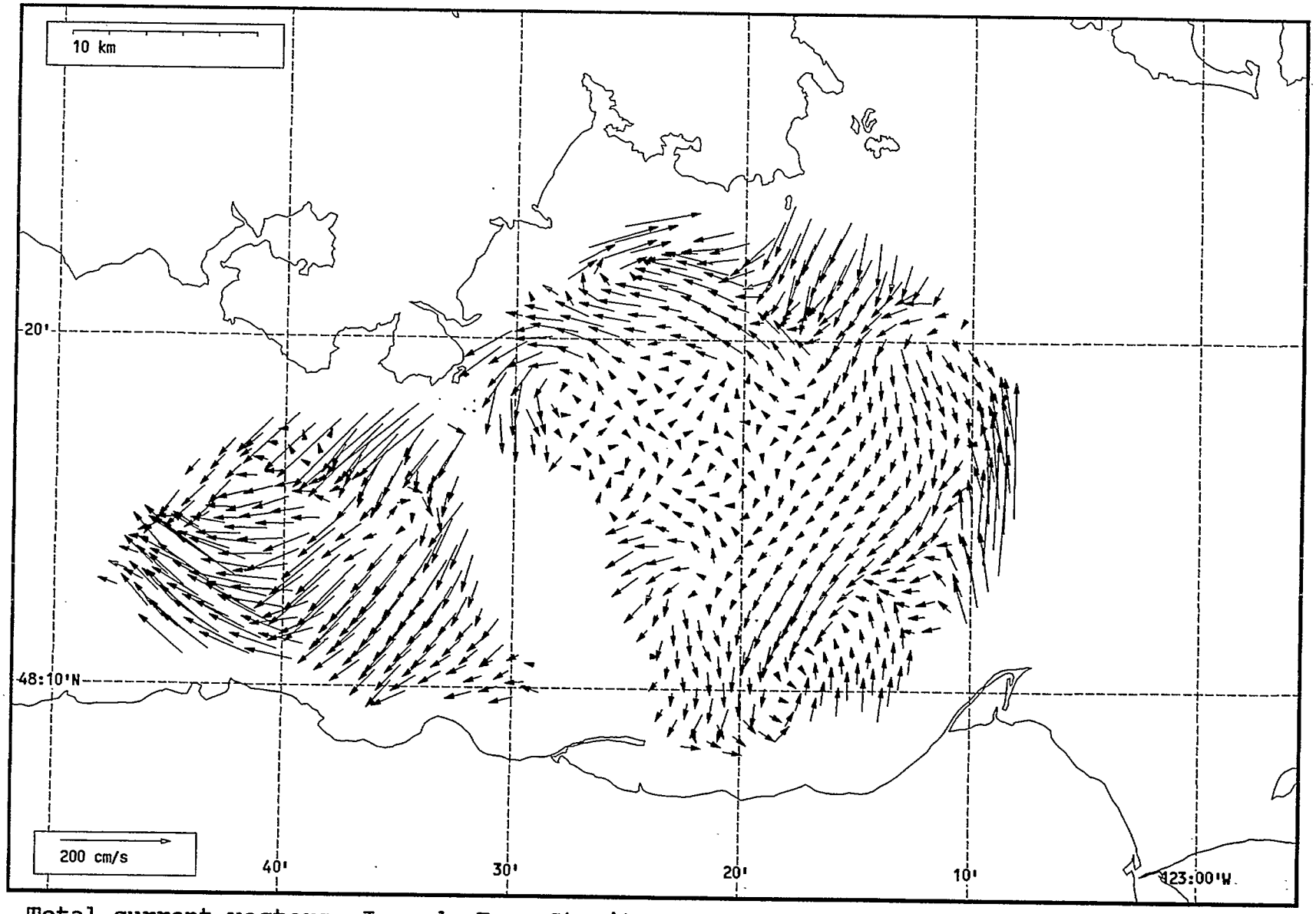

Total current vectors, Juan de Fuca Strait, 1992-07-15 07:00 Z.

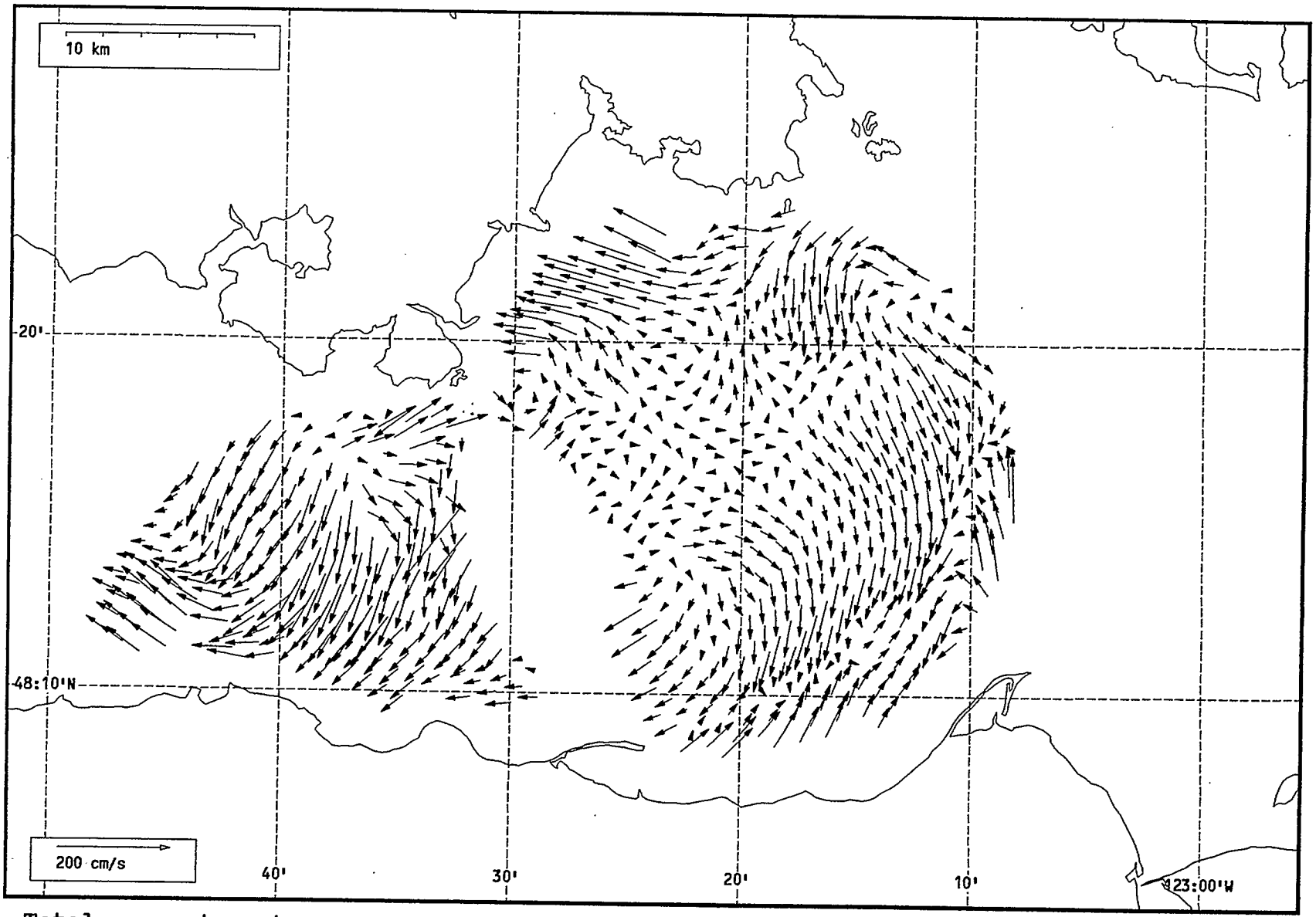

Total current vectors, Juan de Fuca Strait, 1992-07-15 08:00 Z.

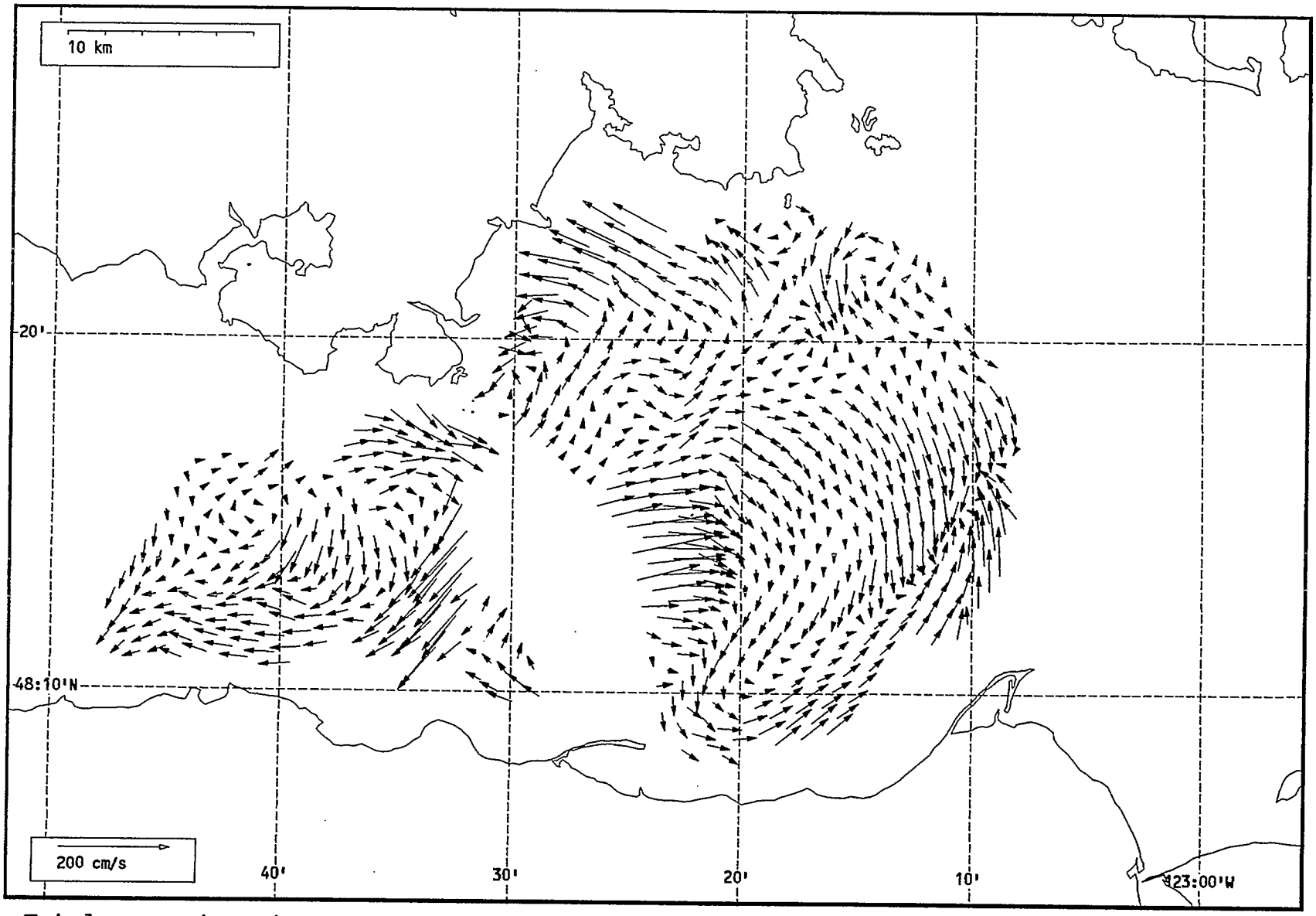

Total current vectors, Juan de Fuca Strait, 1992-07-15 09:00 Z.

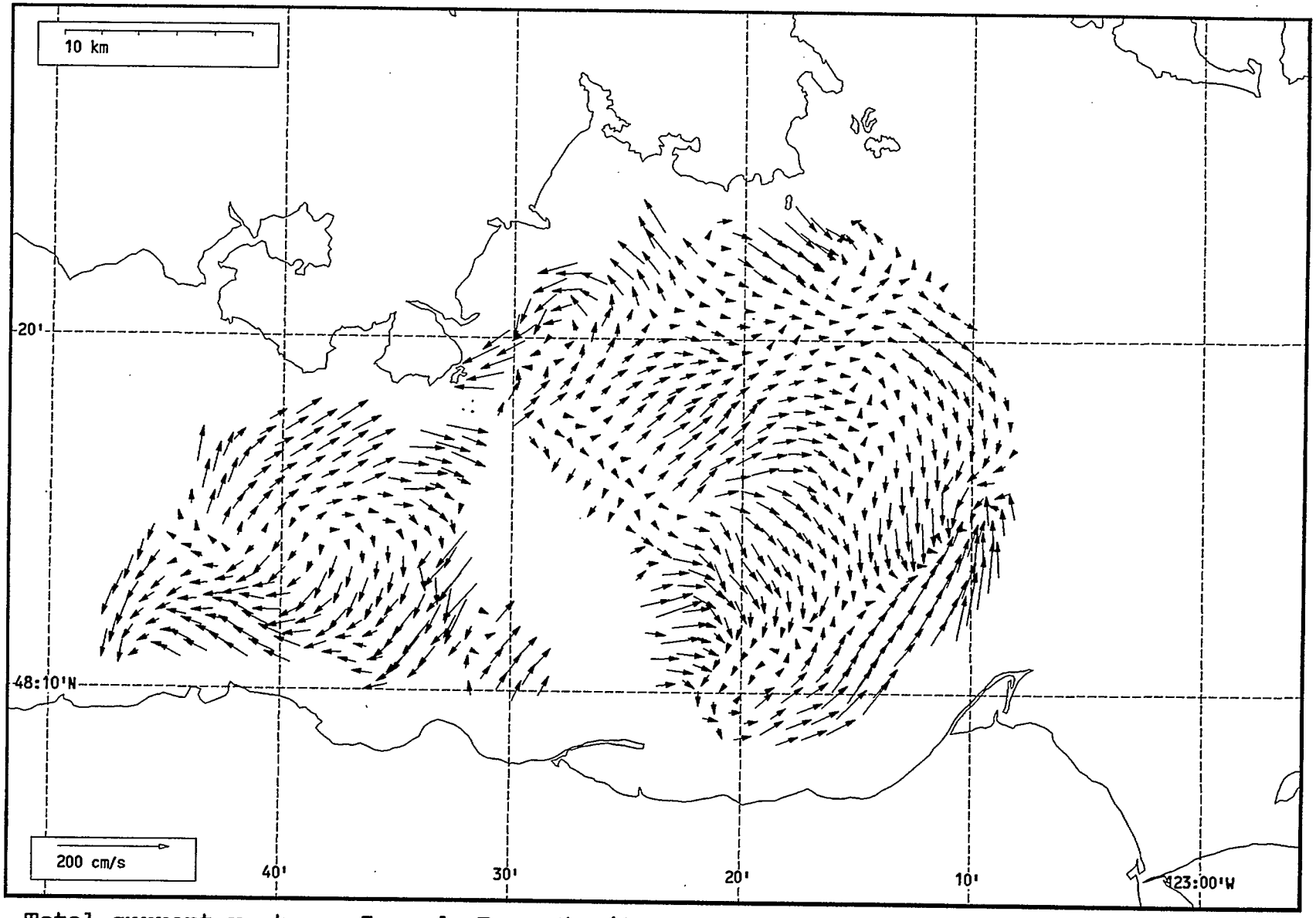

Total current vectors, Juan de Fuca Strait, 1992-07-15 10:00 Z.

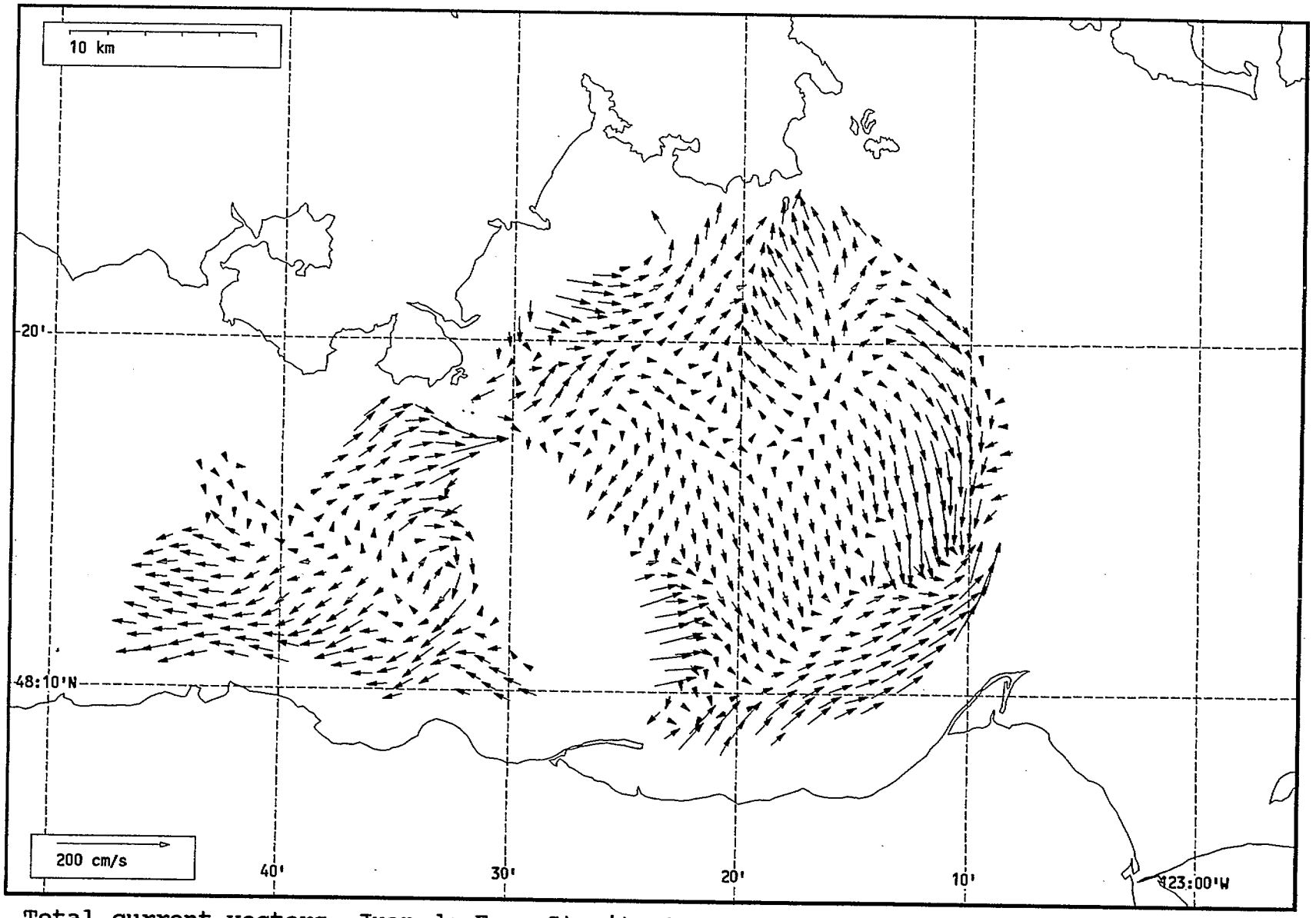

Total current vectors, Juan de Fuca Strait, 1992-07-15 11:00 Z.

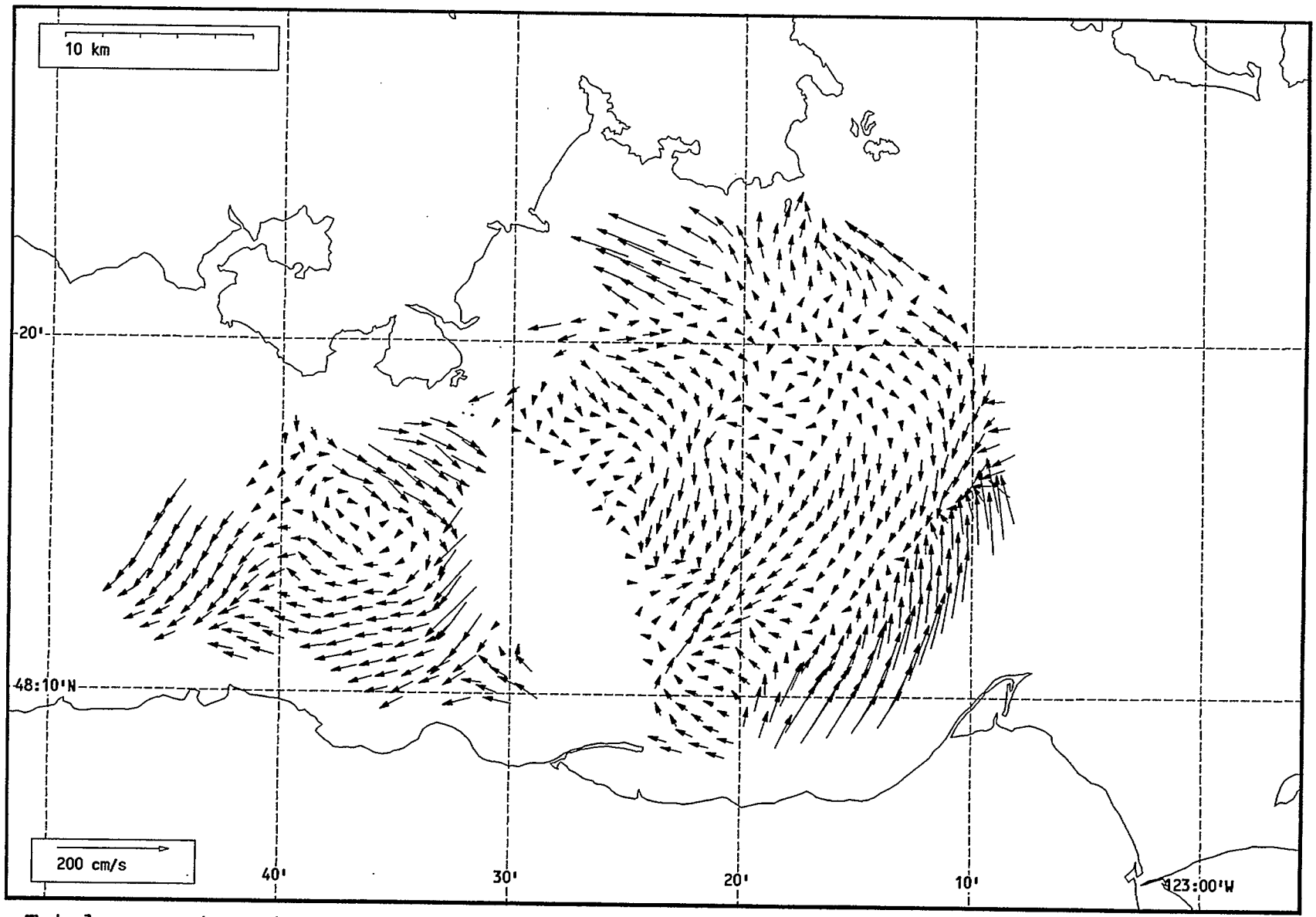

Total current vectors, Juan de Fuca Strait, 1992-07-15 12:00 Z.

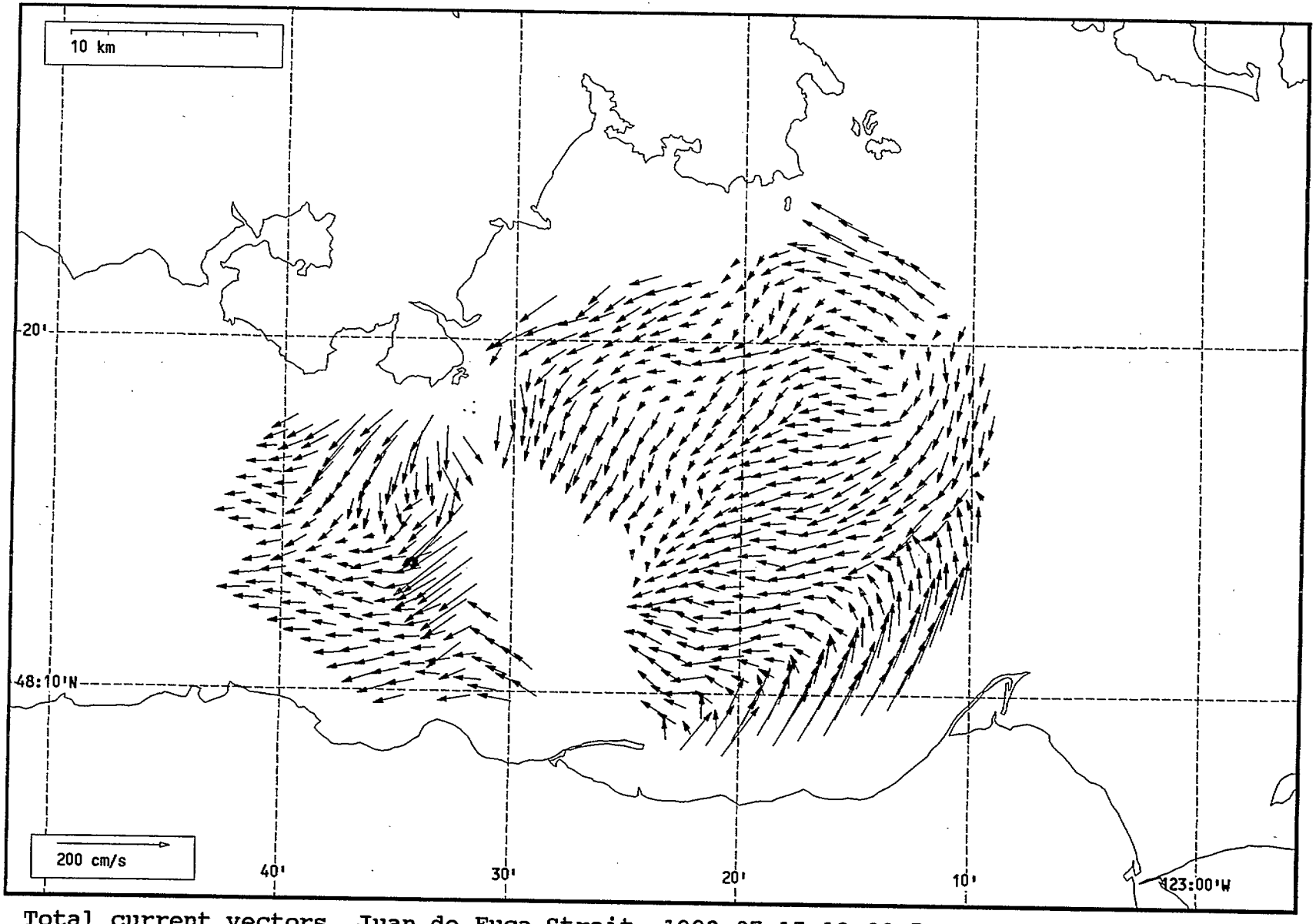

Total current vectors, Juan de Fuca Strait, 1992-07-15 13:00 Z.

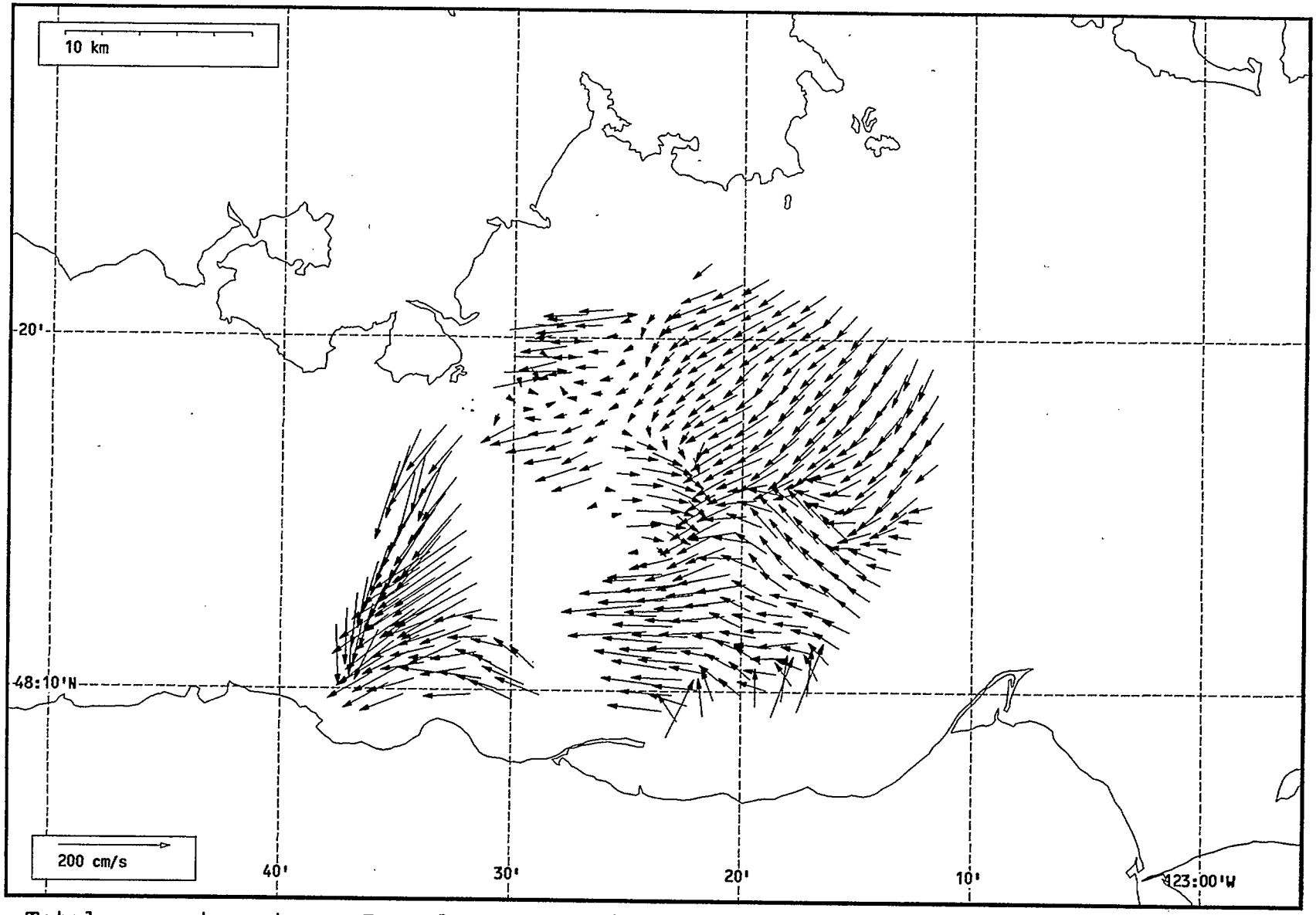

Total current vectors, Juan de Fuca Strait, 1992-07-15 14:00 Z.

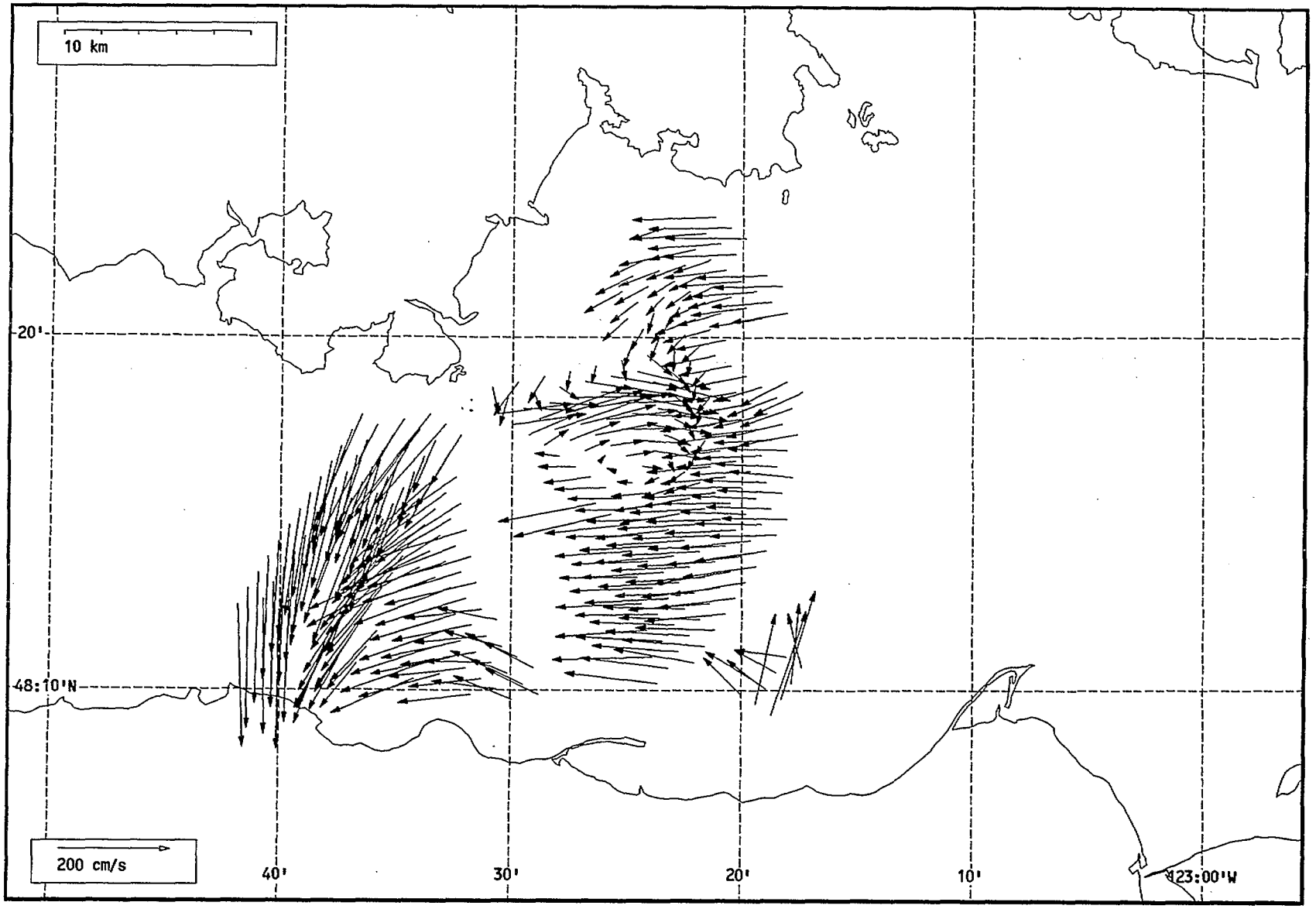

Total current vectors, Juan de Fuca Strait, 1992-07-15 15:00 Z.

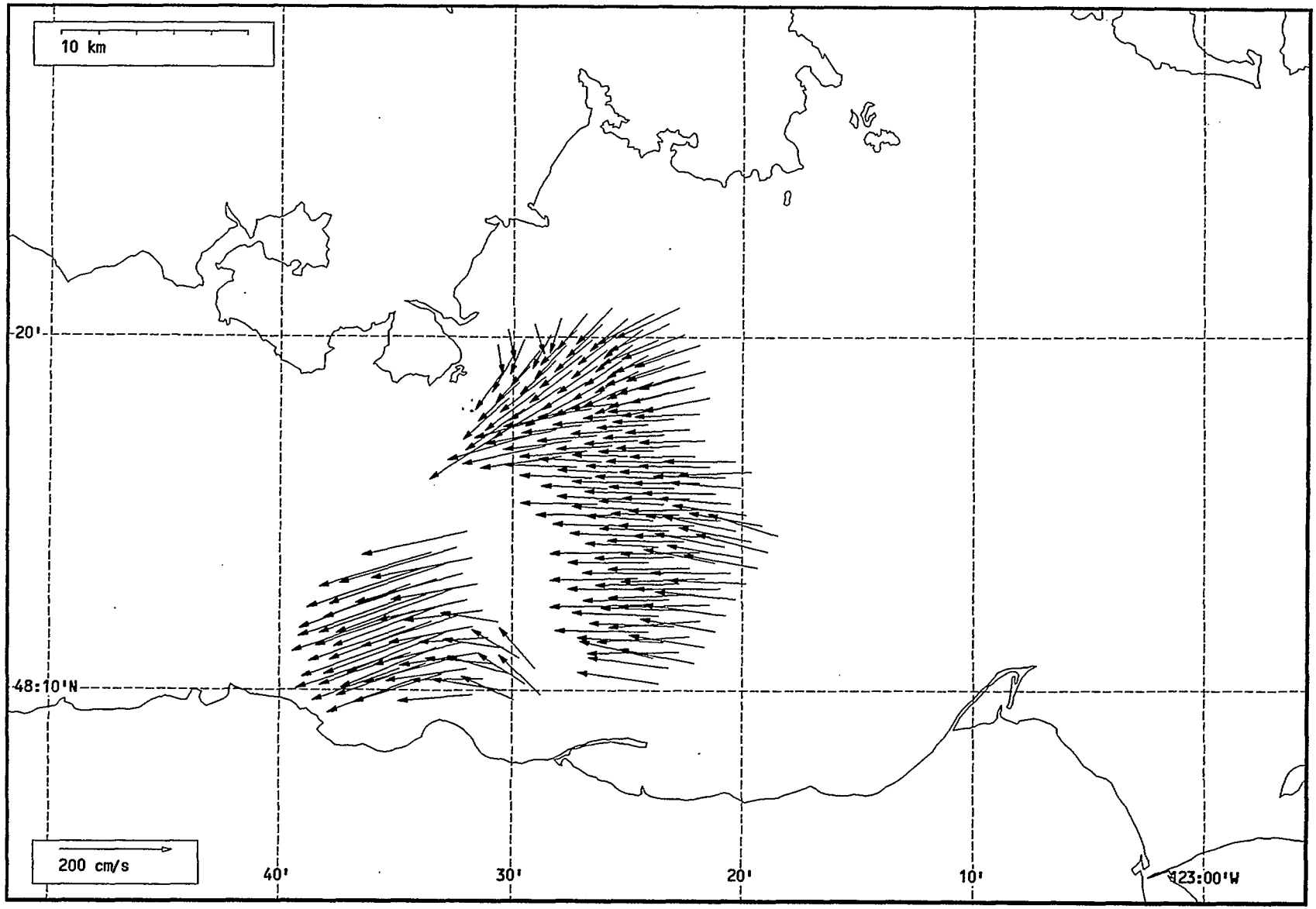

Total current vectors, Juan de Fuca Strait, 1992-07-15 16:00 Z.

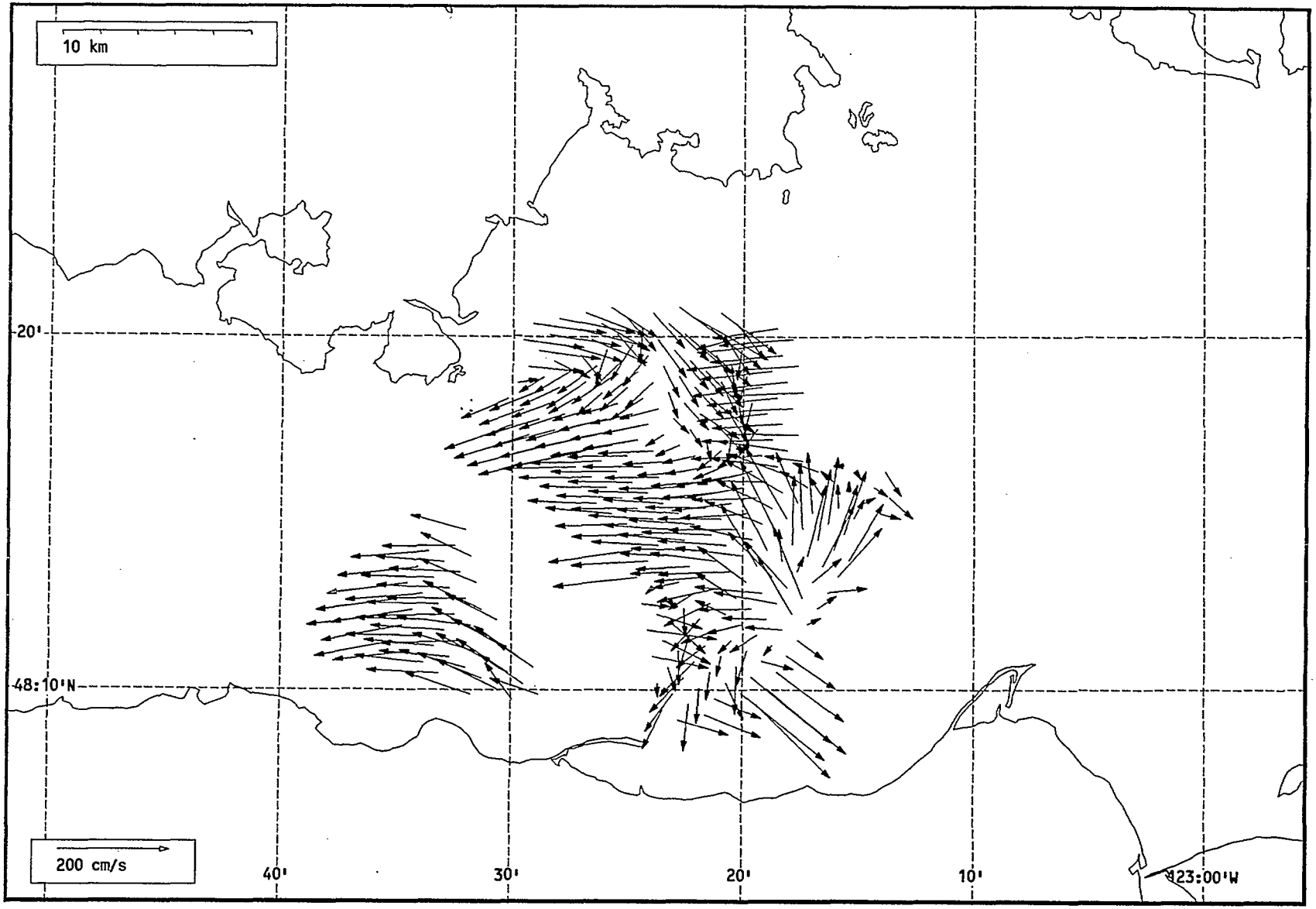

Total current vectors, Juan de Fuca Strait, 1992-07-15 17:00 Z.

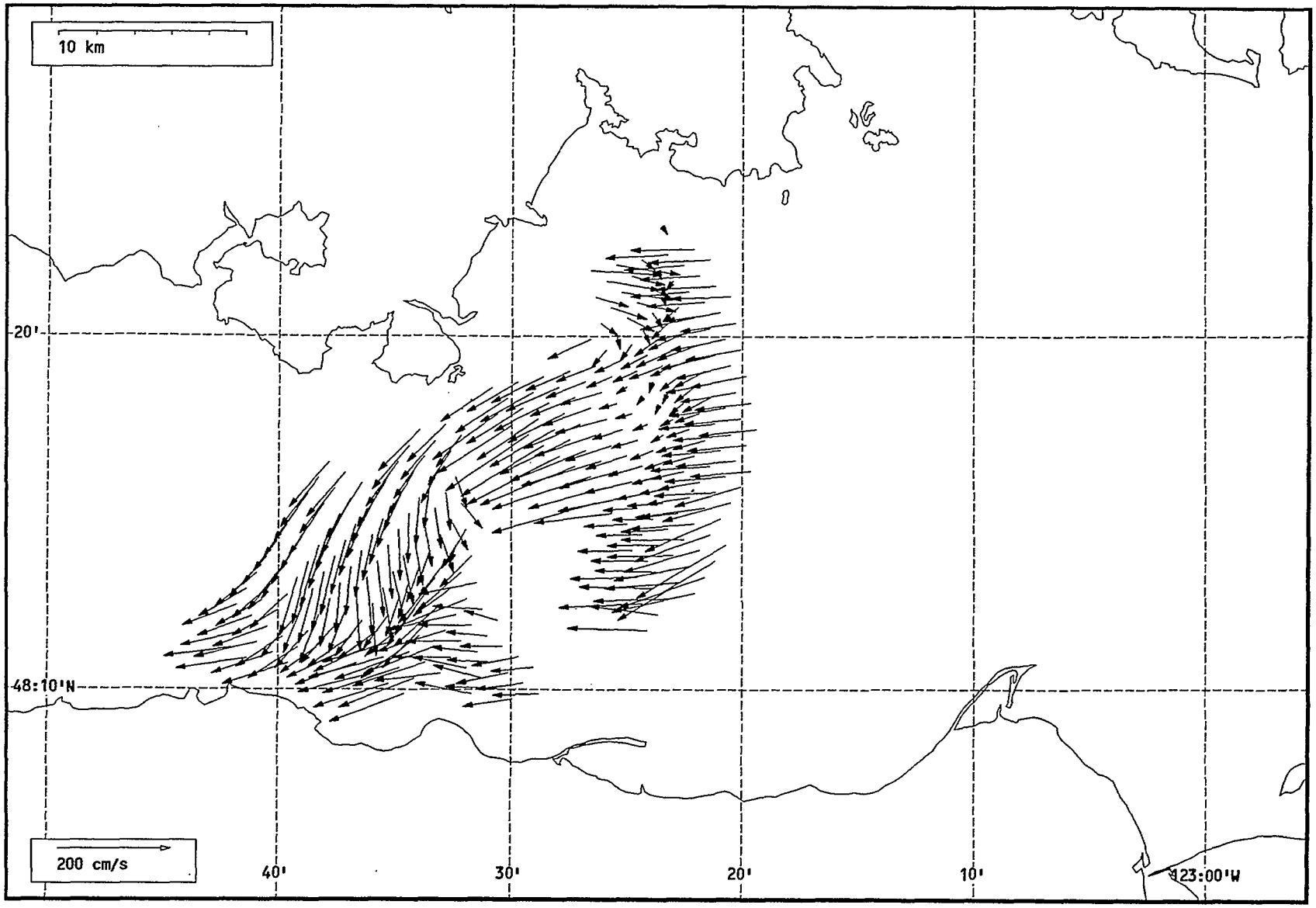

Total current vectors, Juan de Fuca Strait, 1992-07-15 18:00 Z.

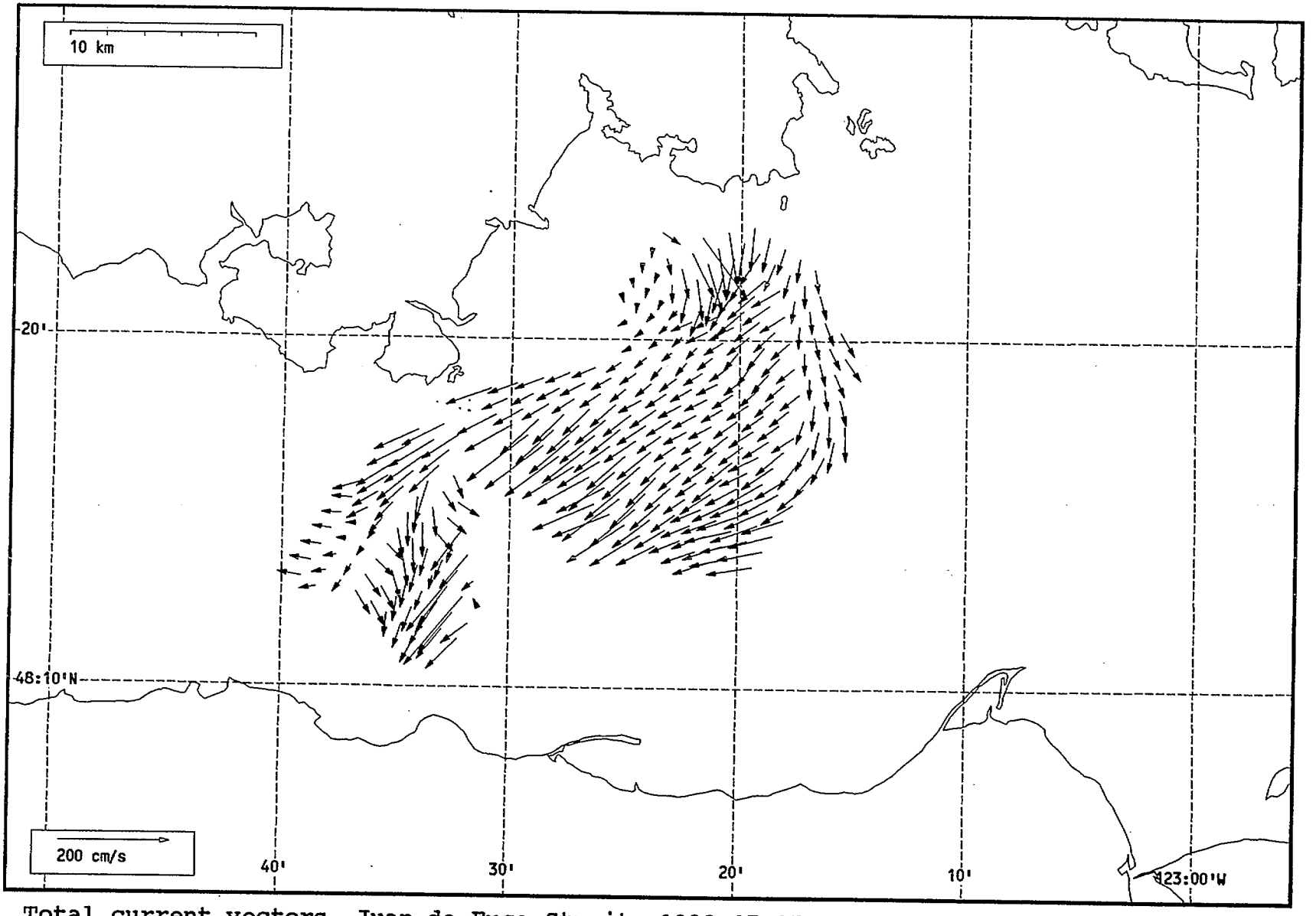

Total current vectors, Juan de Fuca Strait, 1992-07-15 19:00 Z.

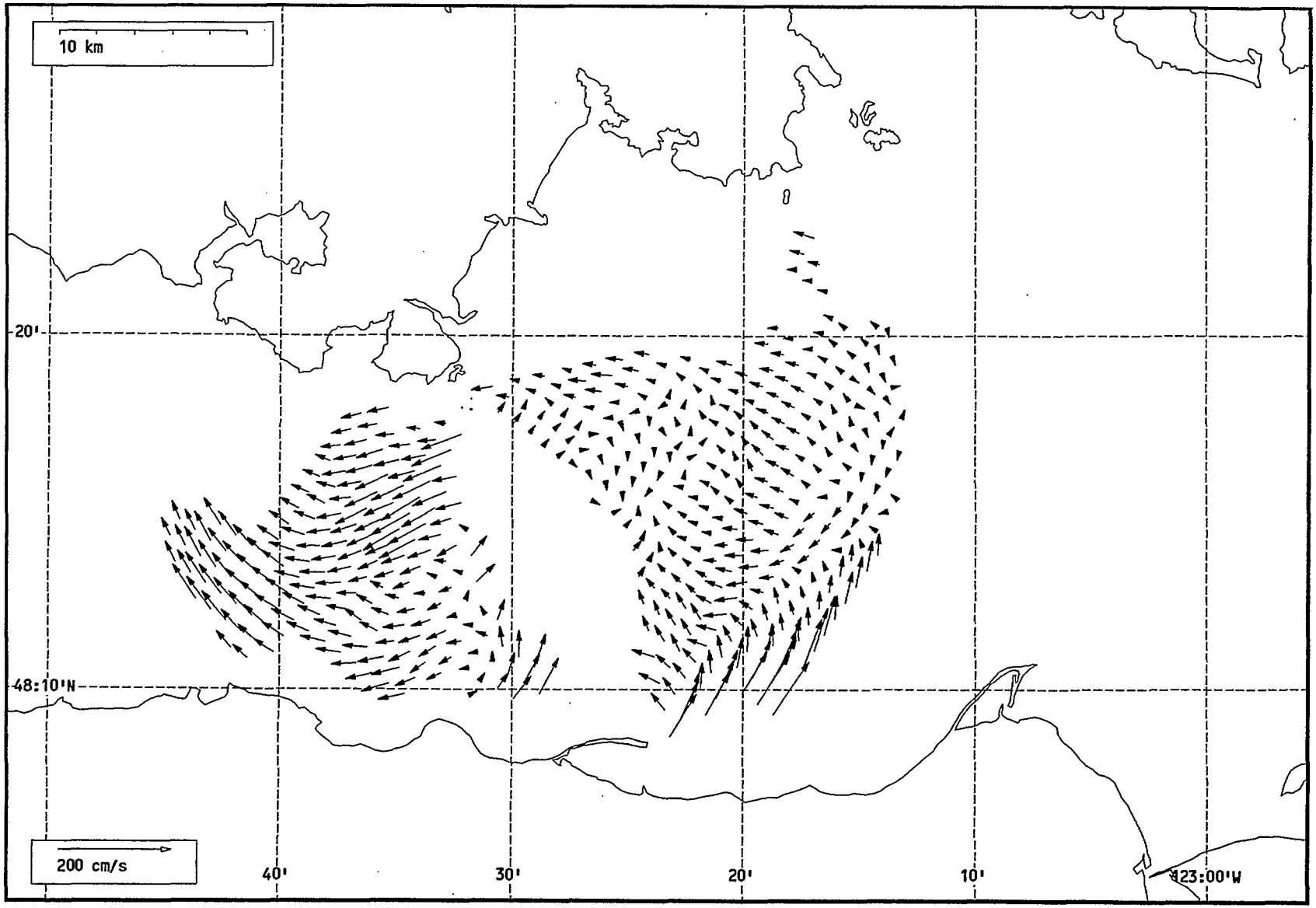

Total current vectors, Juan de Fuca Strait, 1992-07-15 20:00 Z.

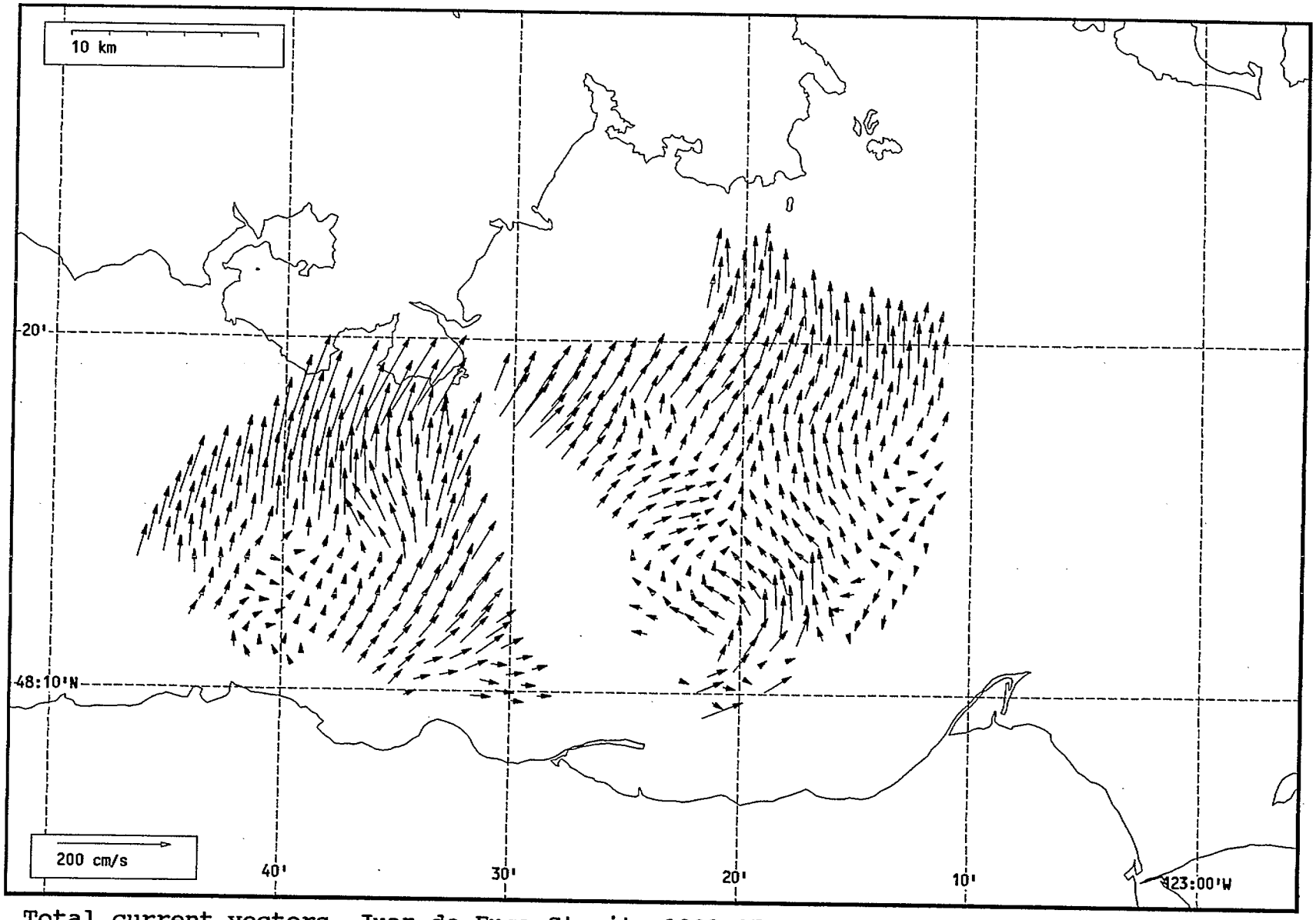

Total current vectors, Juan de Fuca Strait, 1992-07-15 21:00 Z.

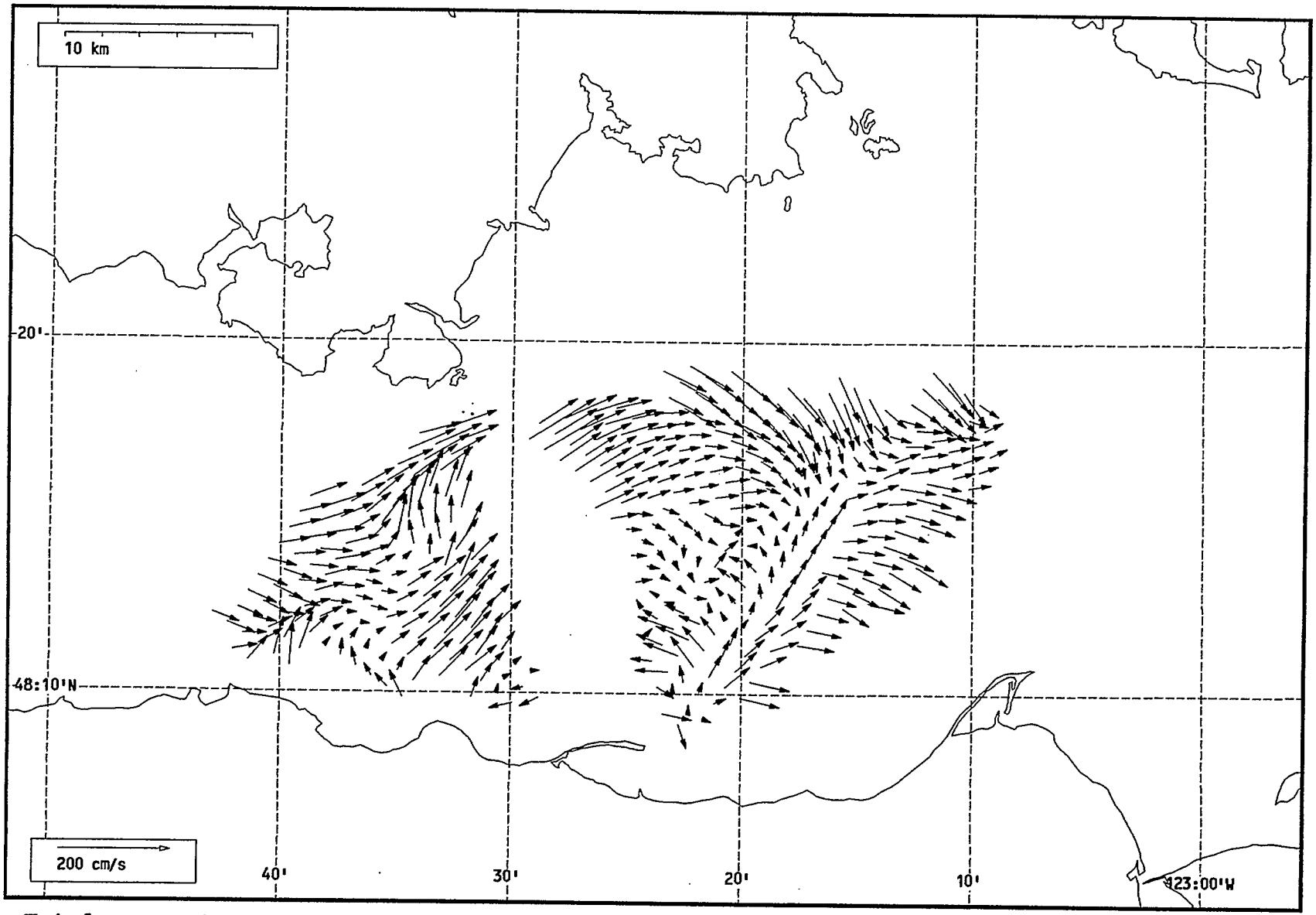

Total current vectors, Juan de Fuca Strait, 1992-07-15 22:00 Z.

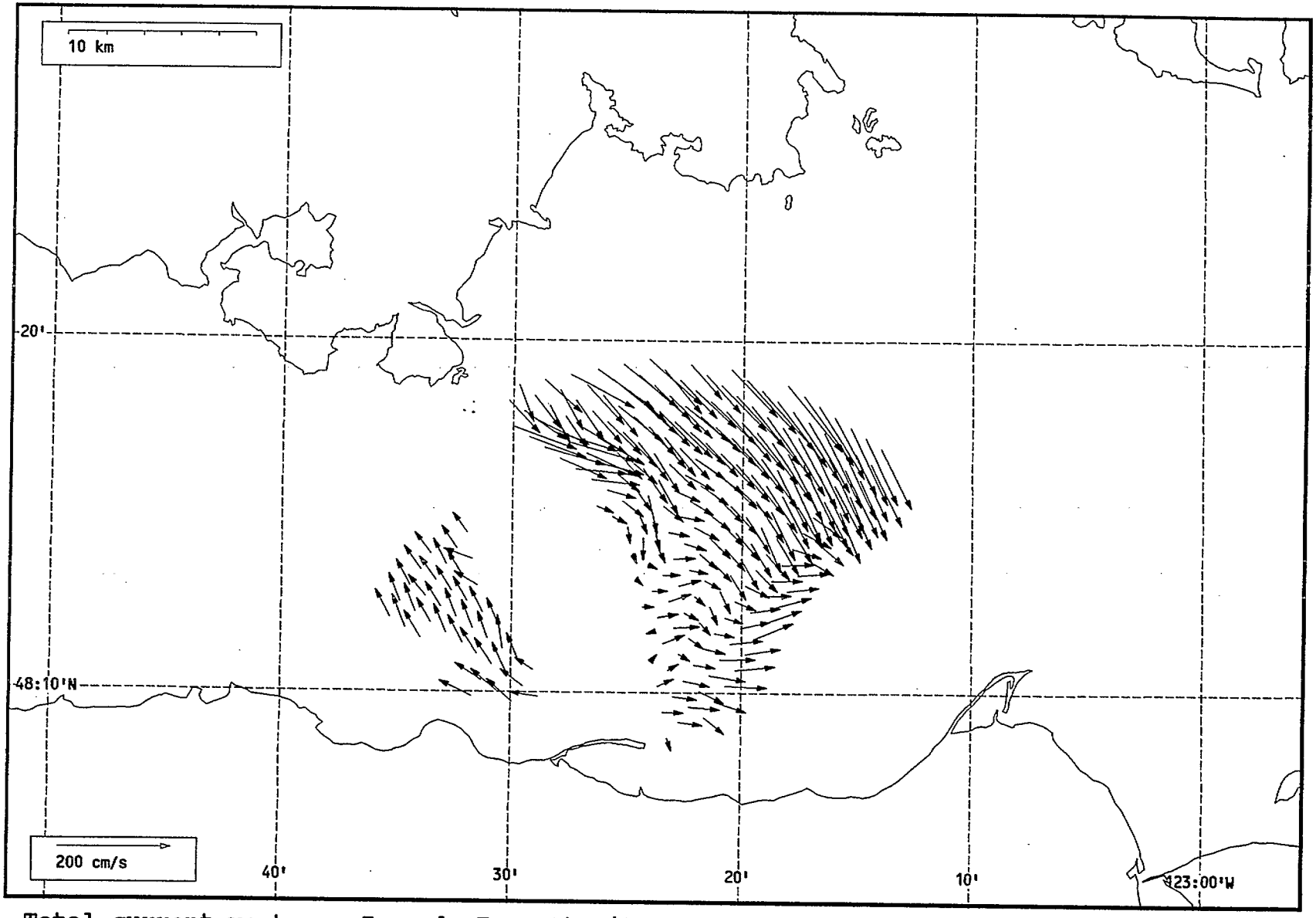

Total current vectors, Juan de Fuca Strait, 1992-07-15 23:00 Z.

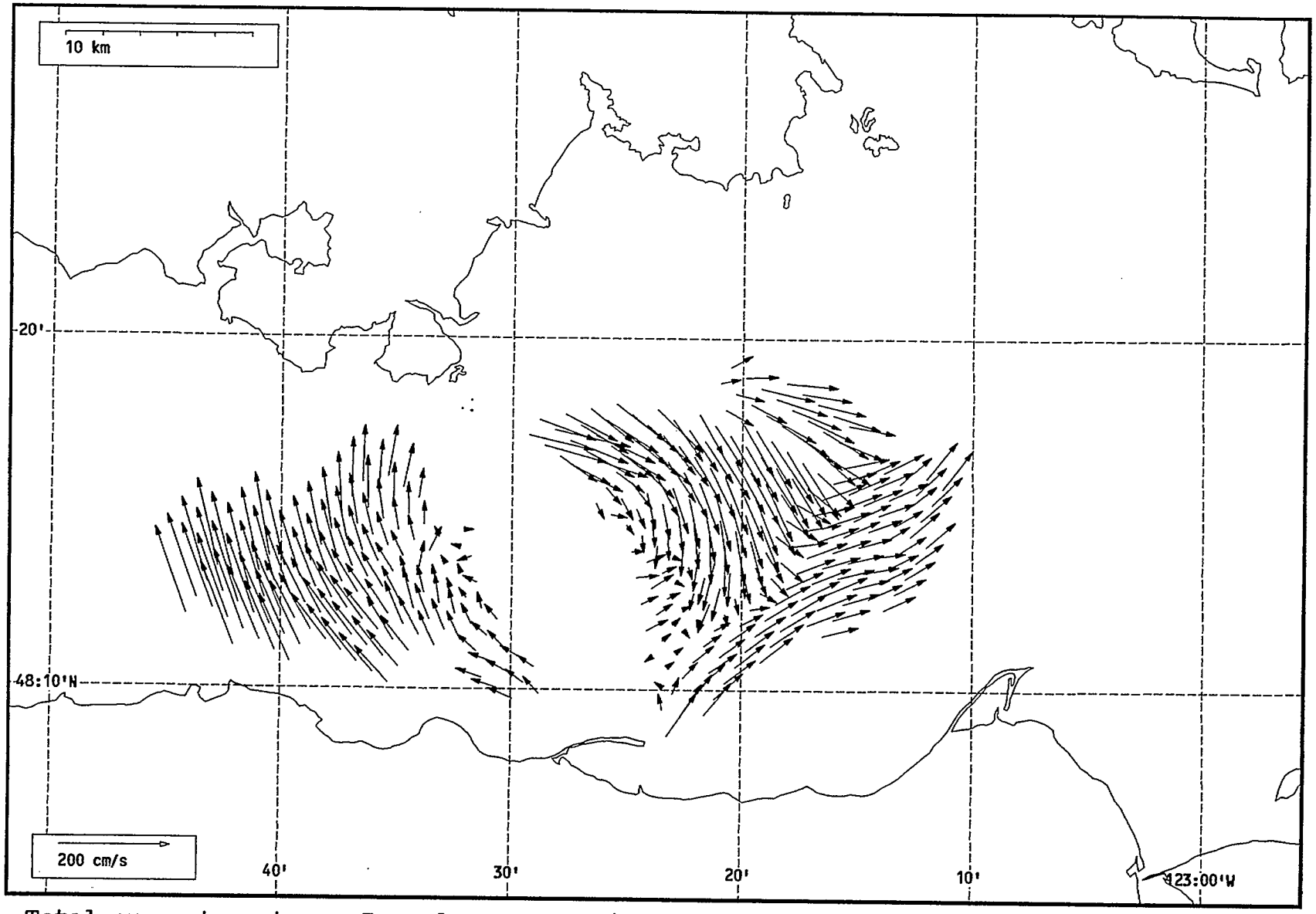

Total current vectors, Juan de Fuca Strait, 1992-07-16 00:00 Z.

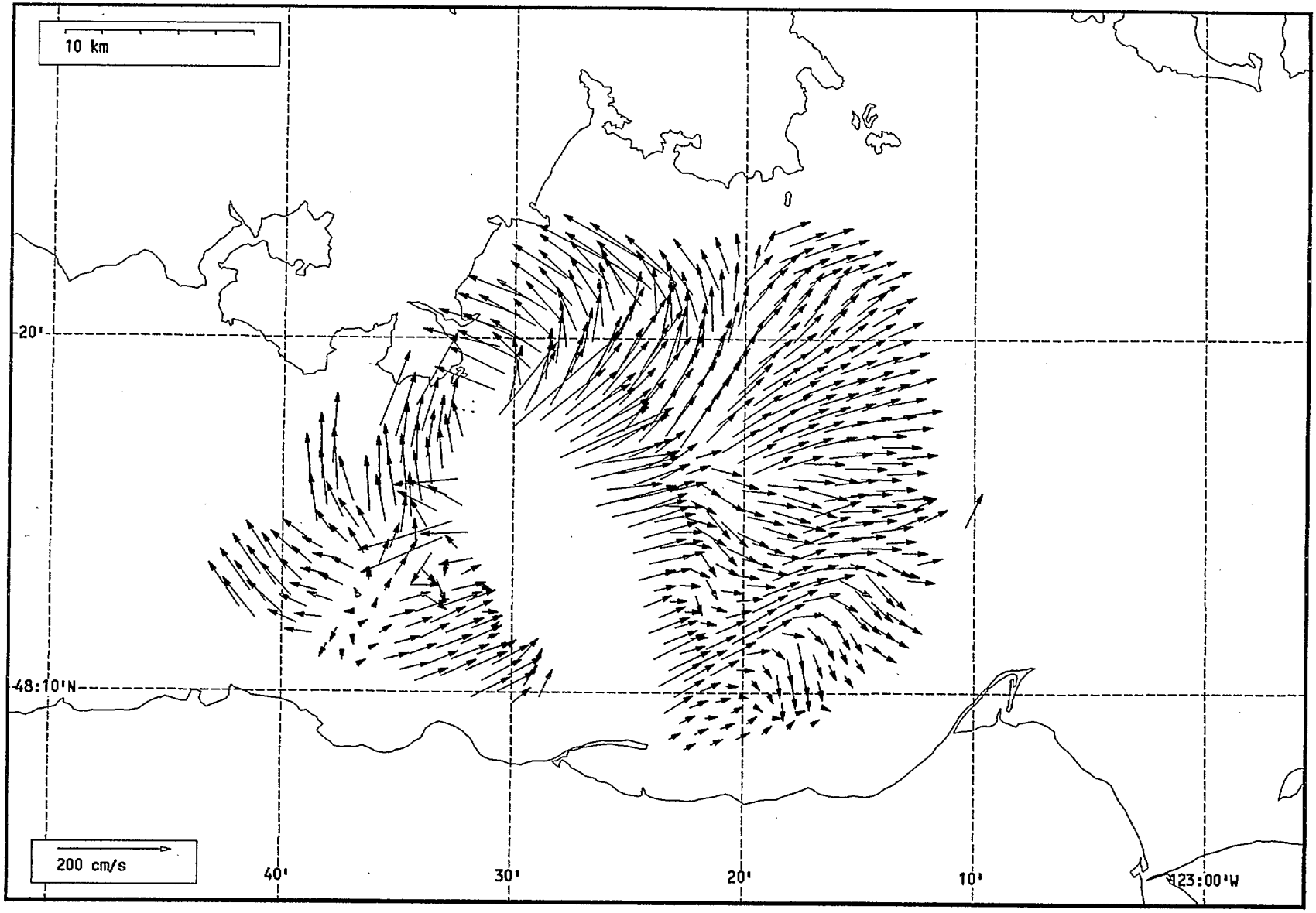

Total current vectors, Juan de Fuca Strait, 1992-07-16 01:00 Z.

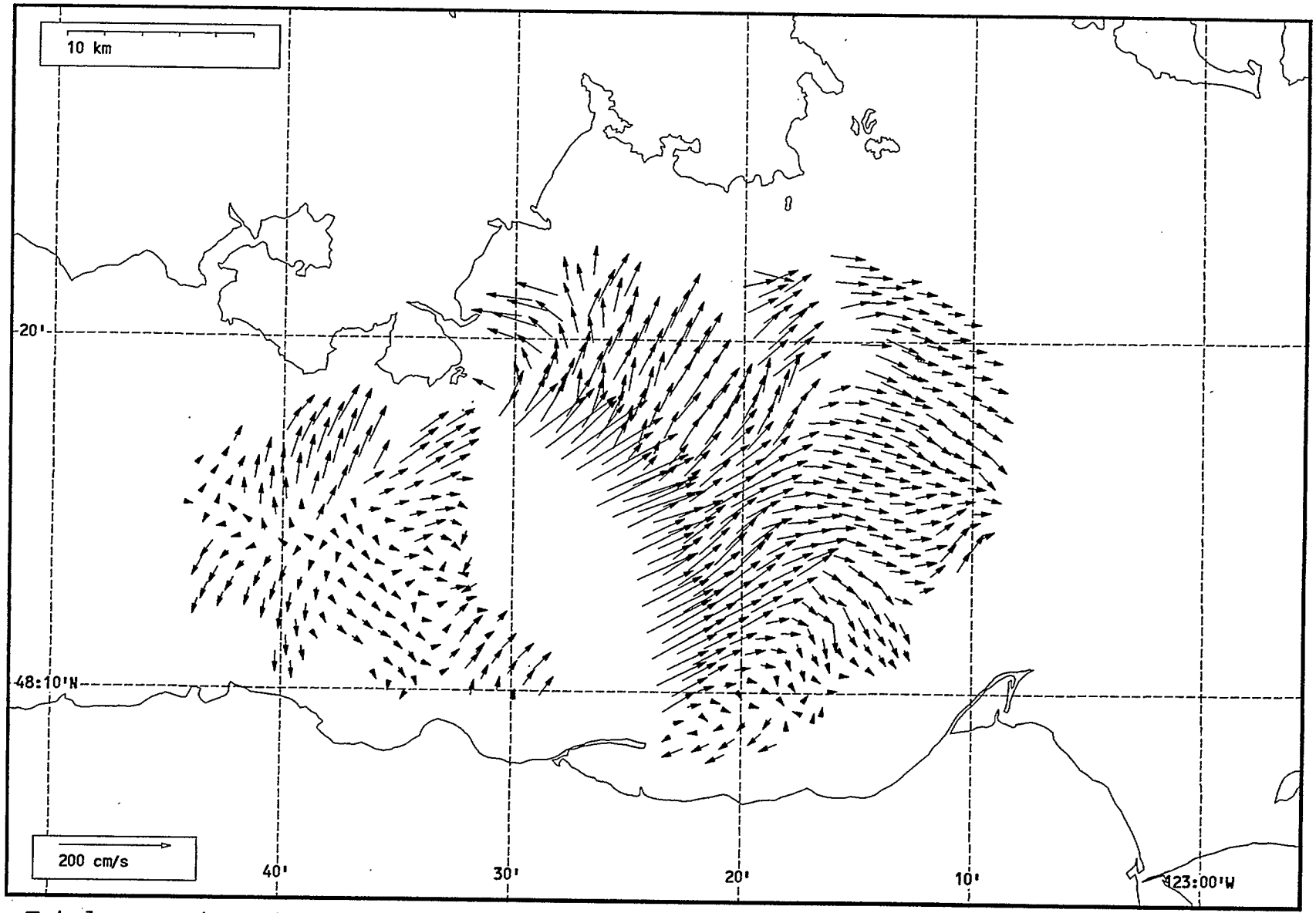

Total current vectors, Juan de Fuca Strait, 1992-07-16 02:00 Z.

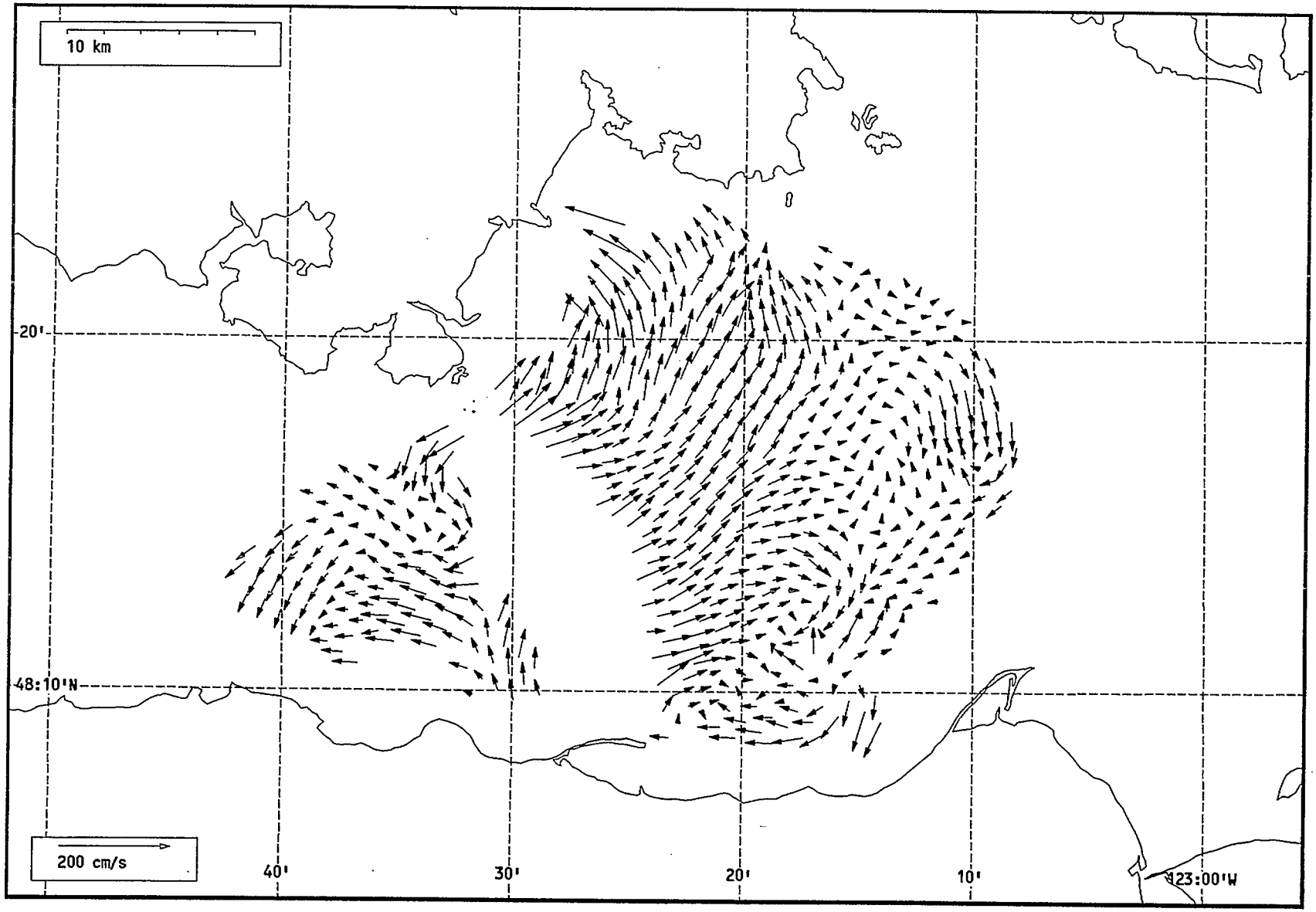

Total current vectors, Juan de Fuca Strait, 1992-07-16 03:00 Z.

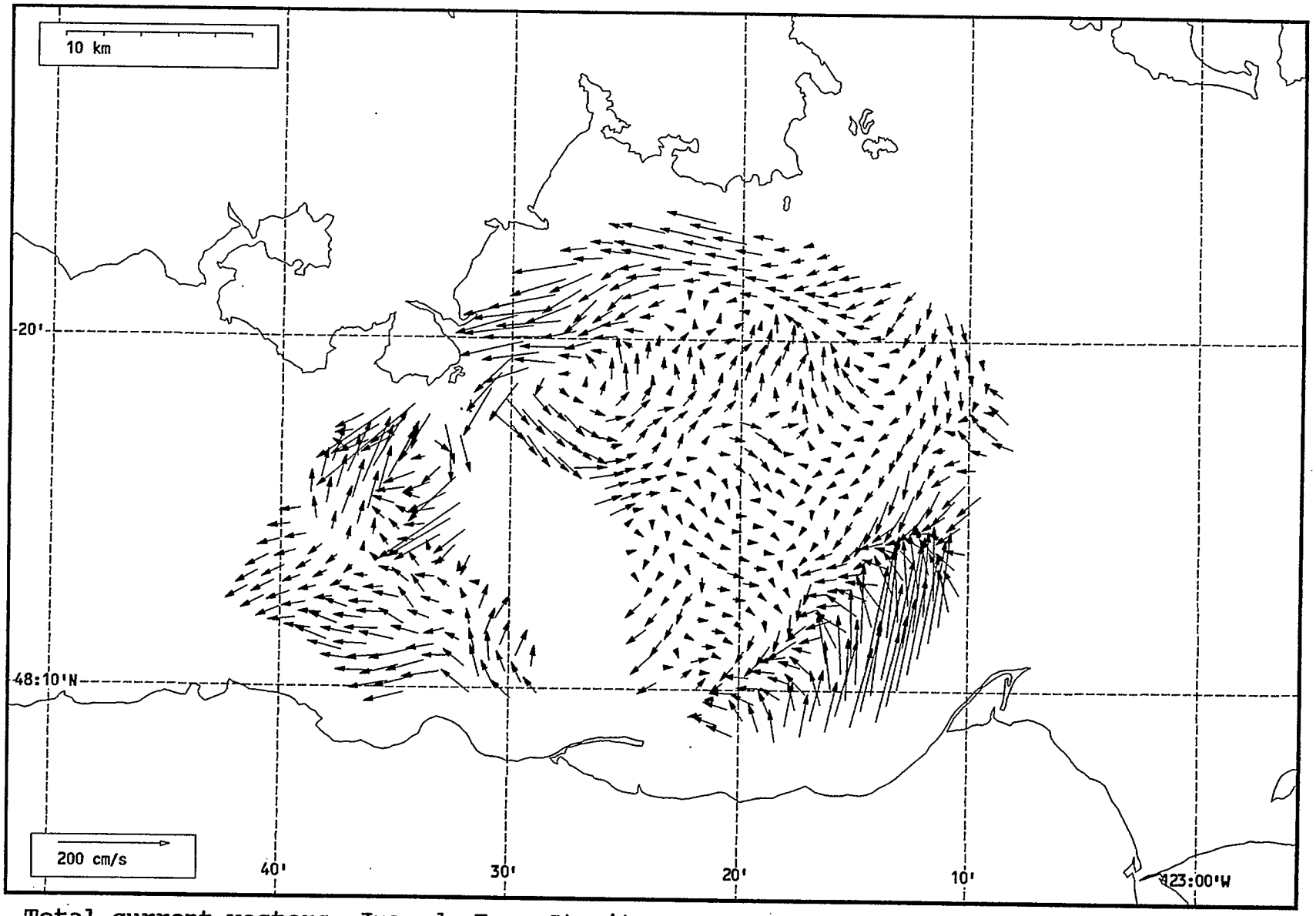

Total current vectors, Juan de Fuca Strait, 1992-07-16 04:00 Z.

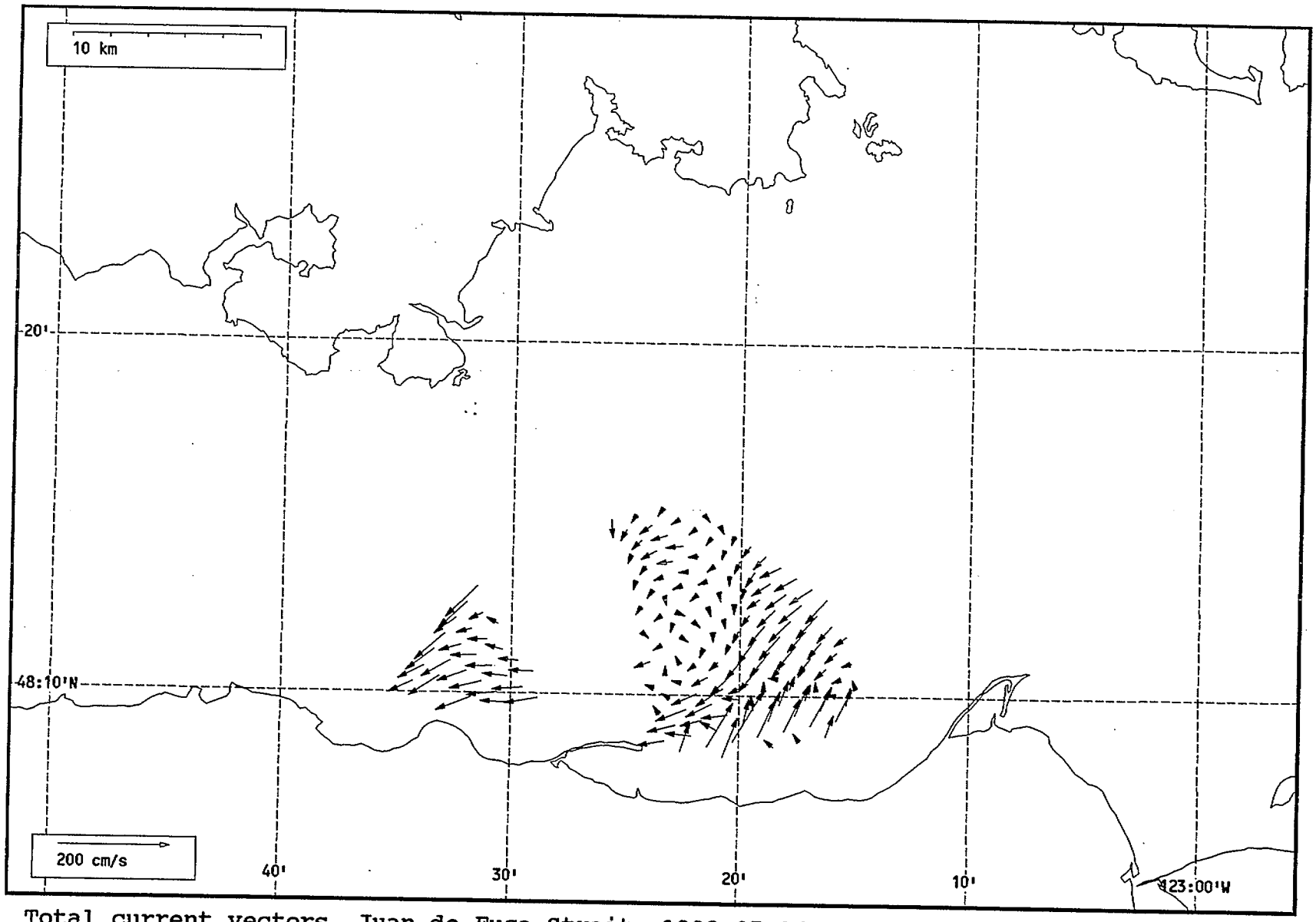

Total current vectors, Juan de Fuca Strait, 1992-07-16 05:00 Z.

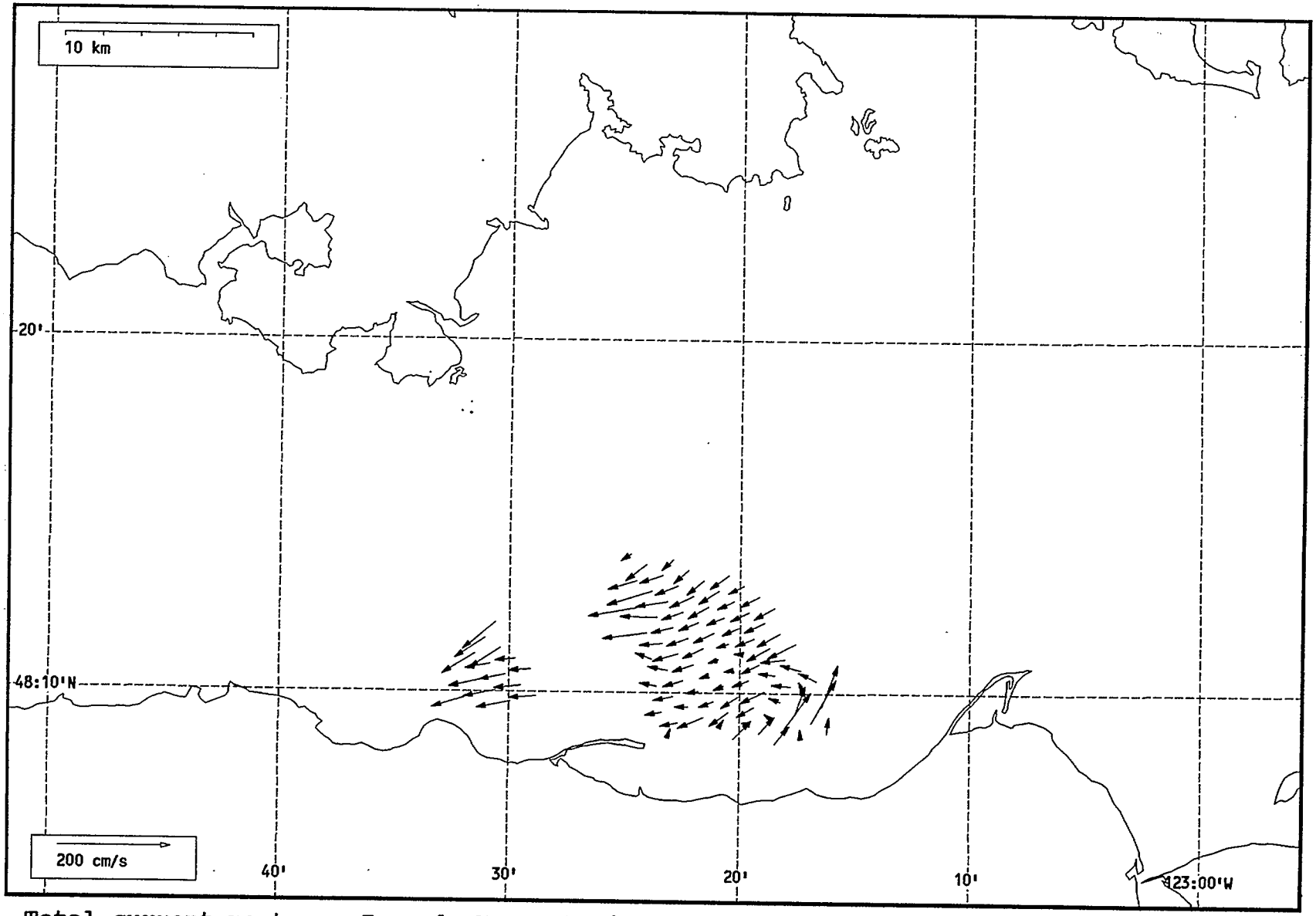

Total current vectors, Juan de Fuca Strait, 1992-07-16 06:00 Z.

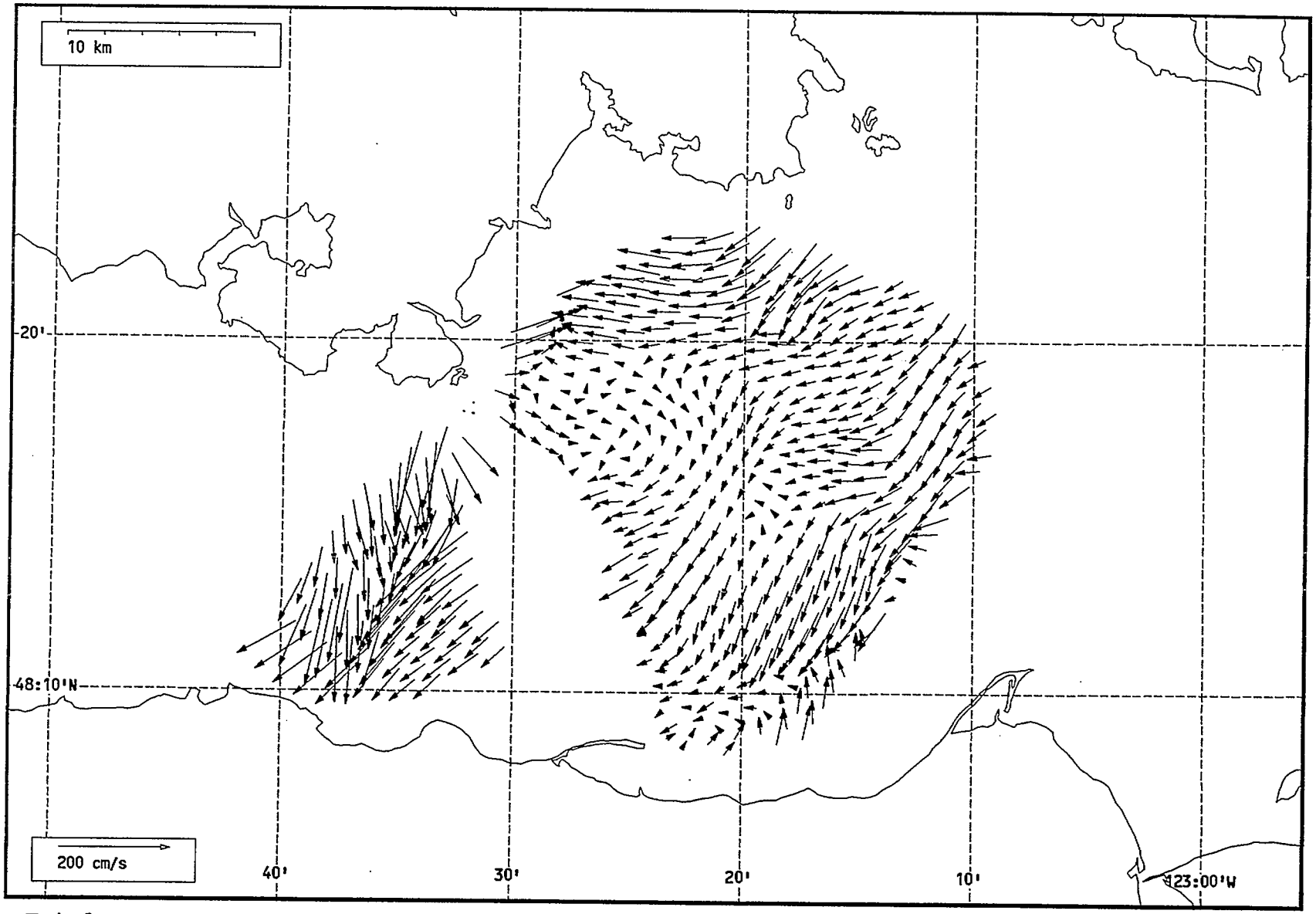

Total current vectors, Juan de Fuca Strait, 1992-07-16 07:00 Z.

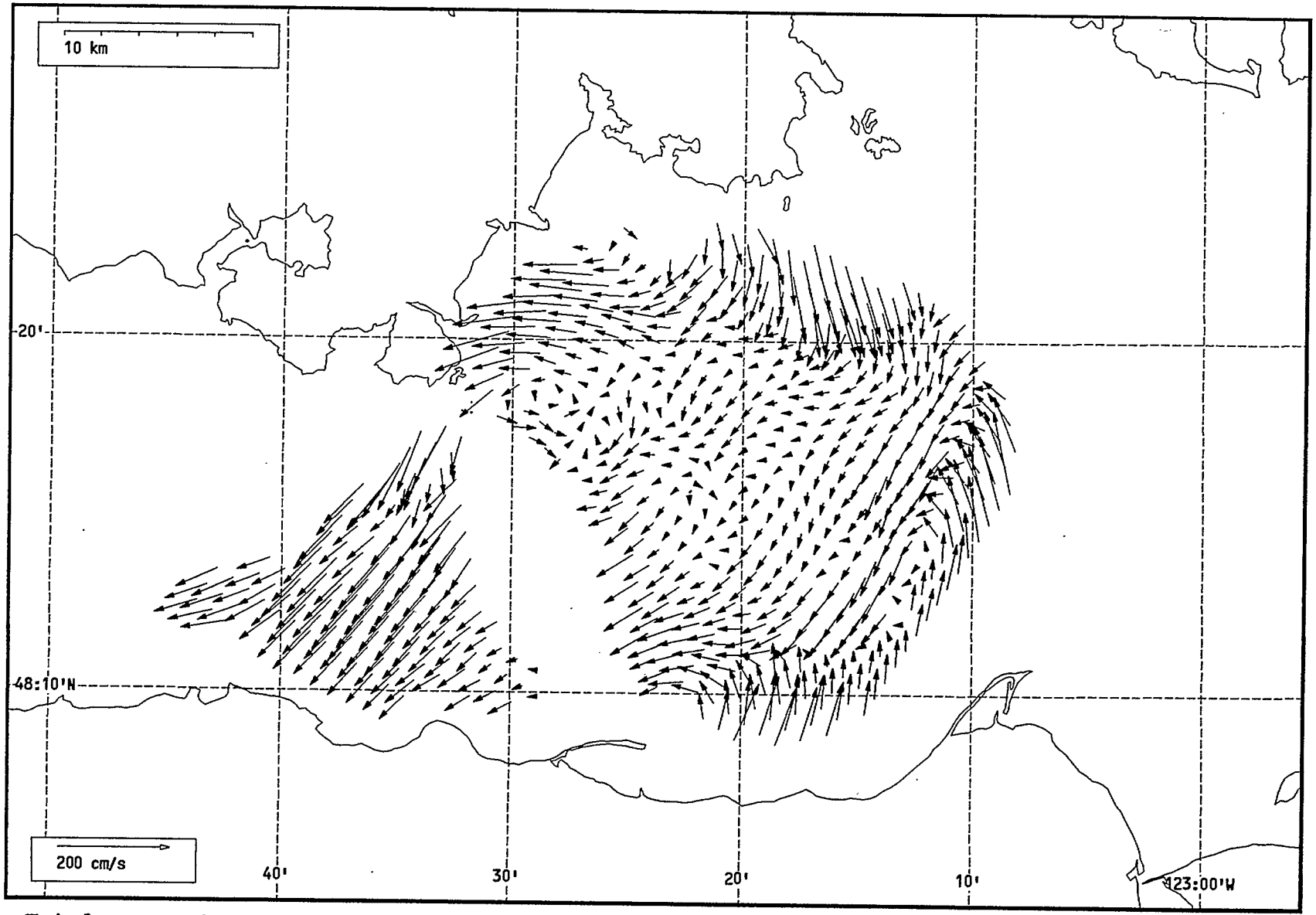

Total current vectors, Juan de Fuca Strait, 1992-07-16 08:00 Z.

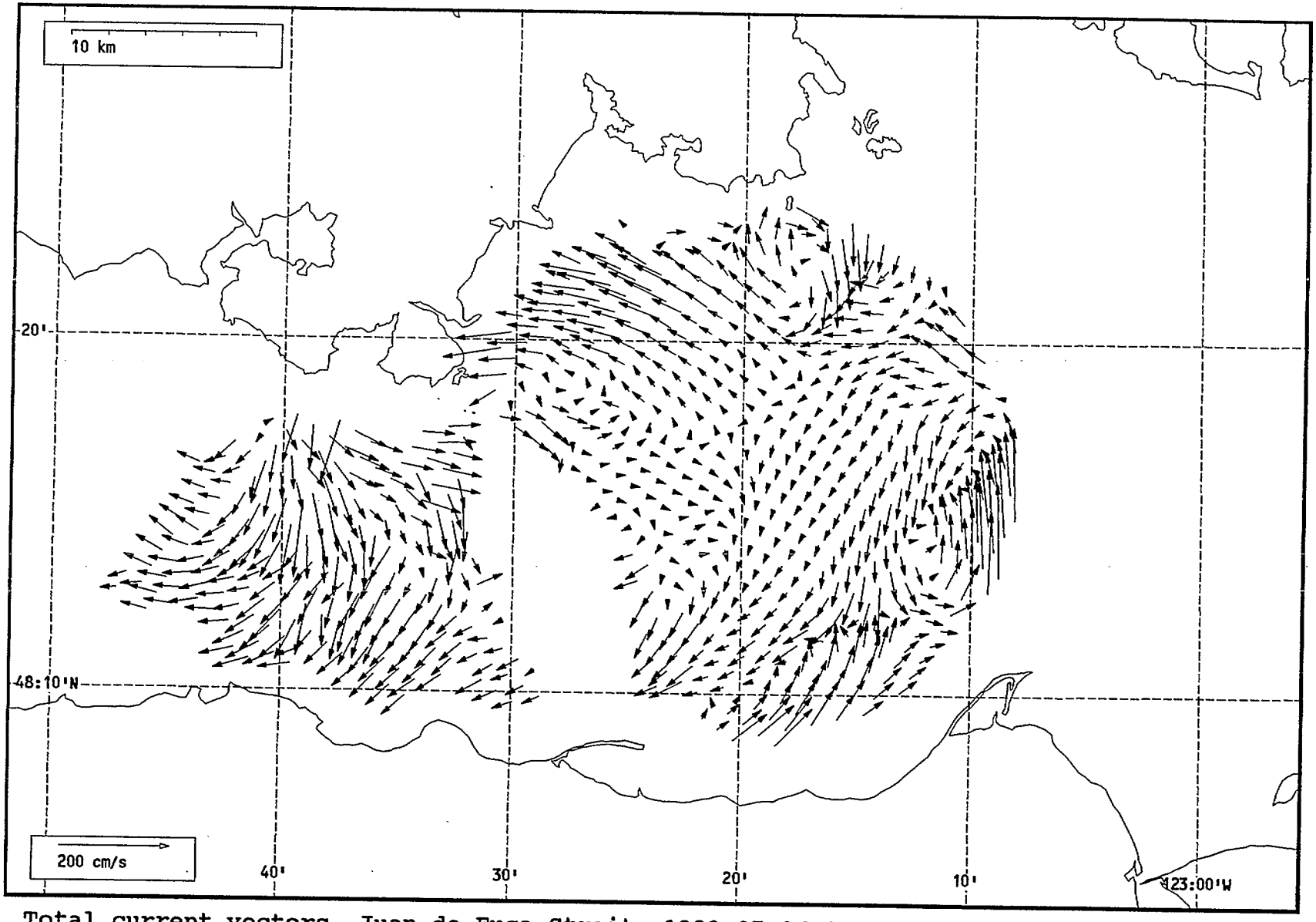

Total current vectors, Juan de Fuca Strait, 1992-07-16 09:00 Z.

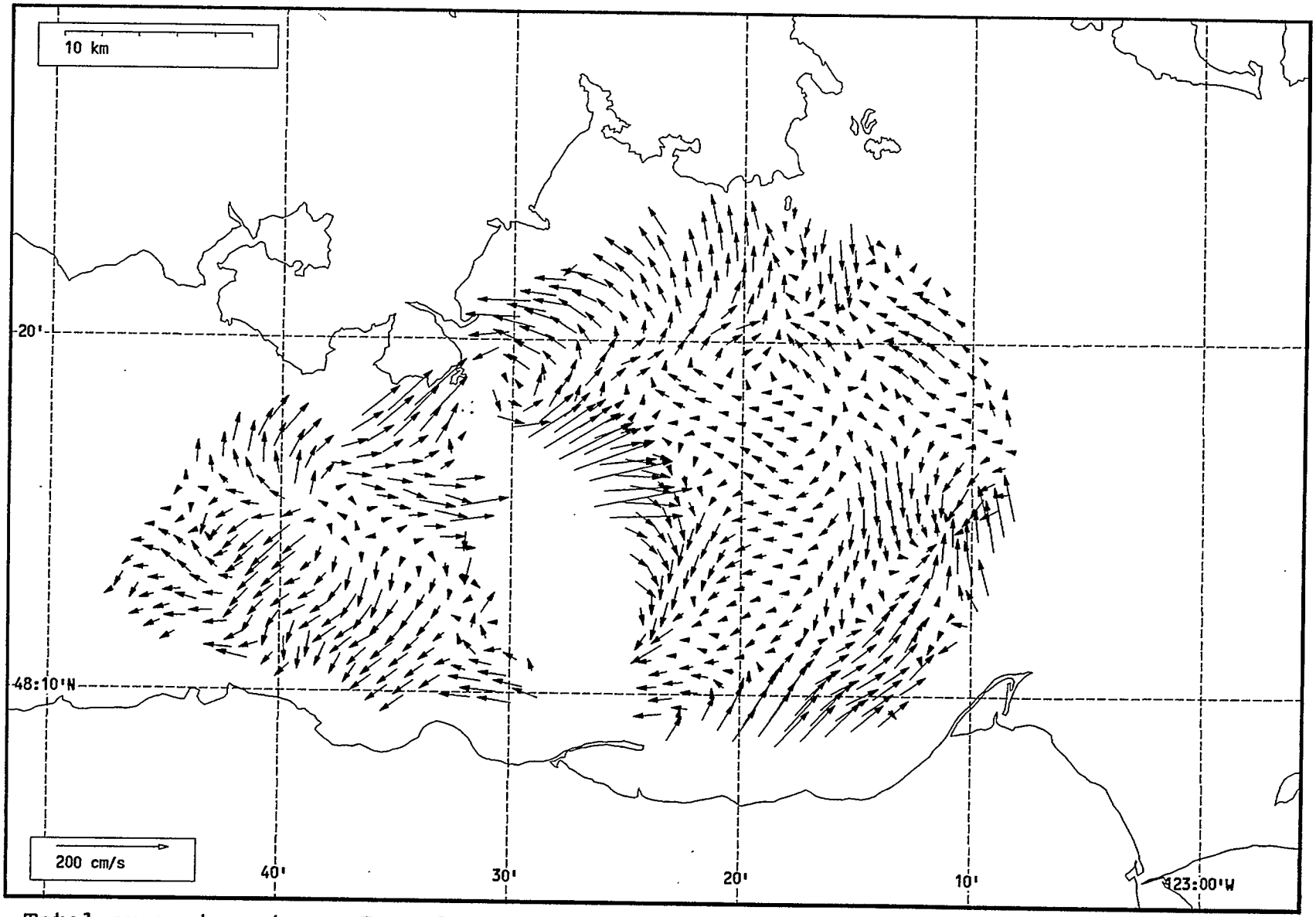

Total current vectors, Juan de Fuca Strait, 1992-07-16 10:00 Z.

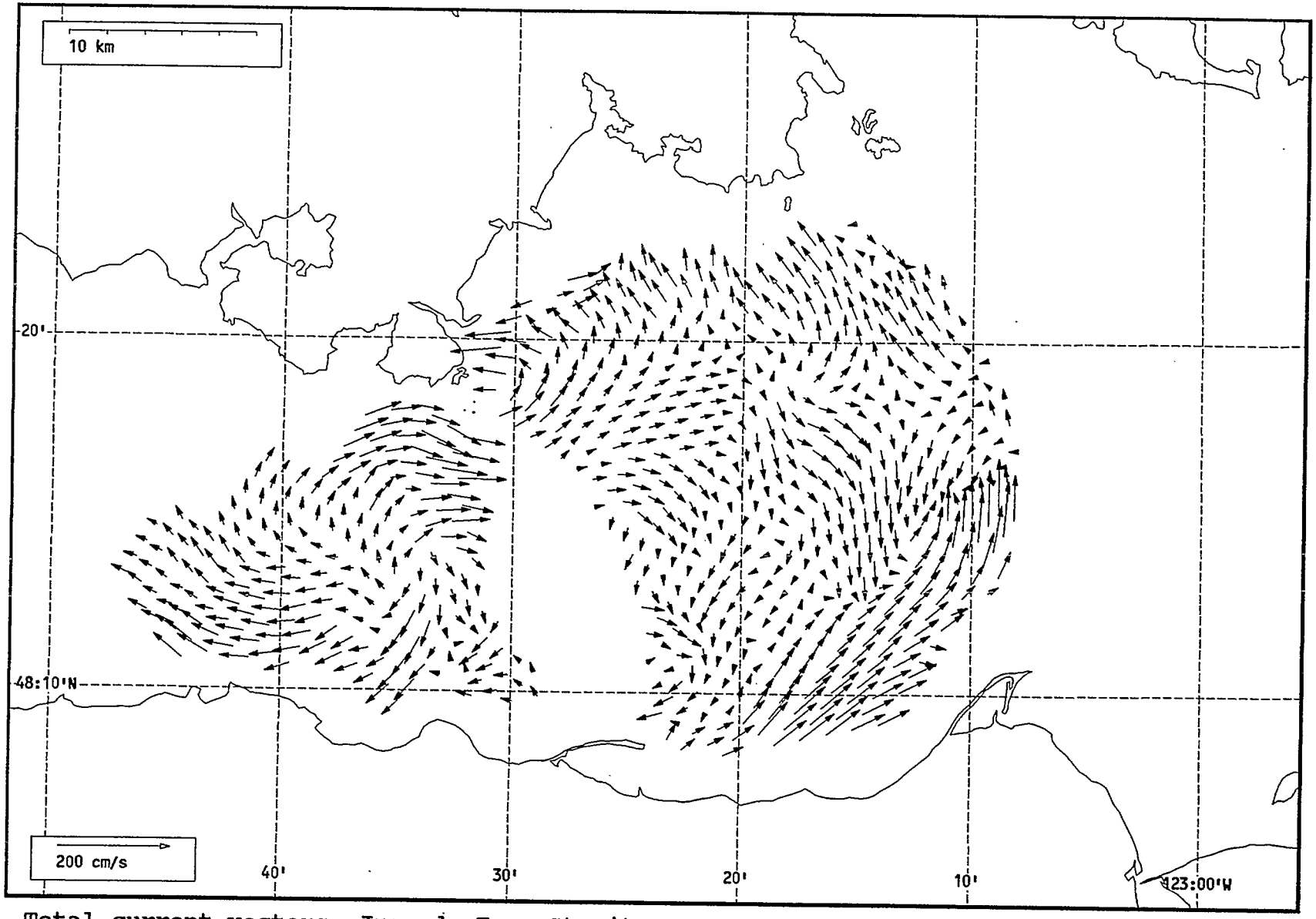

Total current vectors, Juan de Fuca Strait, 1992-07-16 11:00 Z.

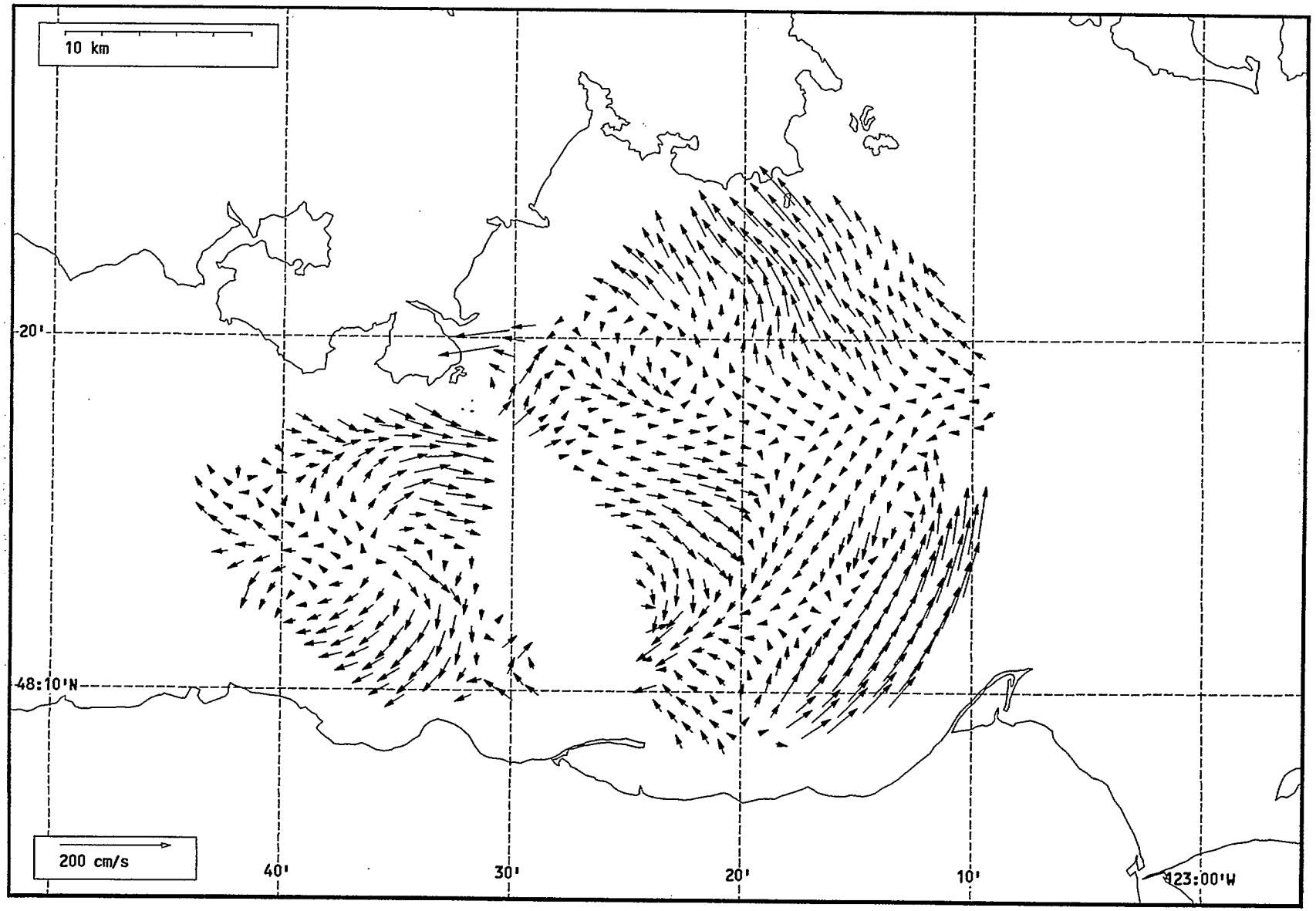

Total current vectors, Juan de Fuca Strait, 1992-07-16 12:00 Z.

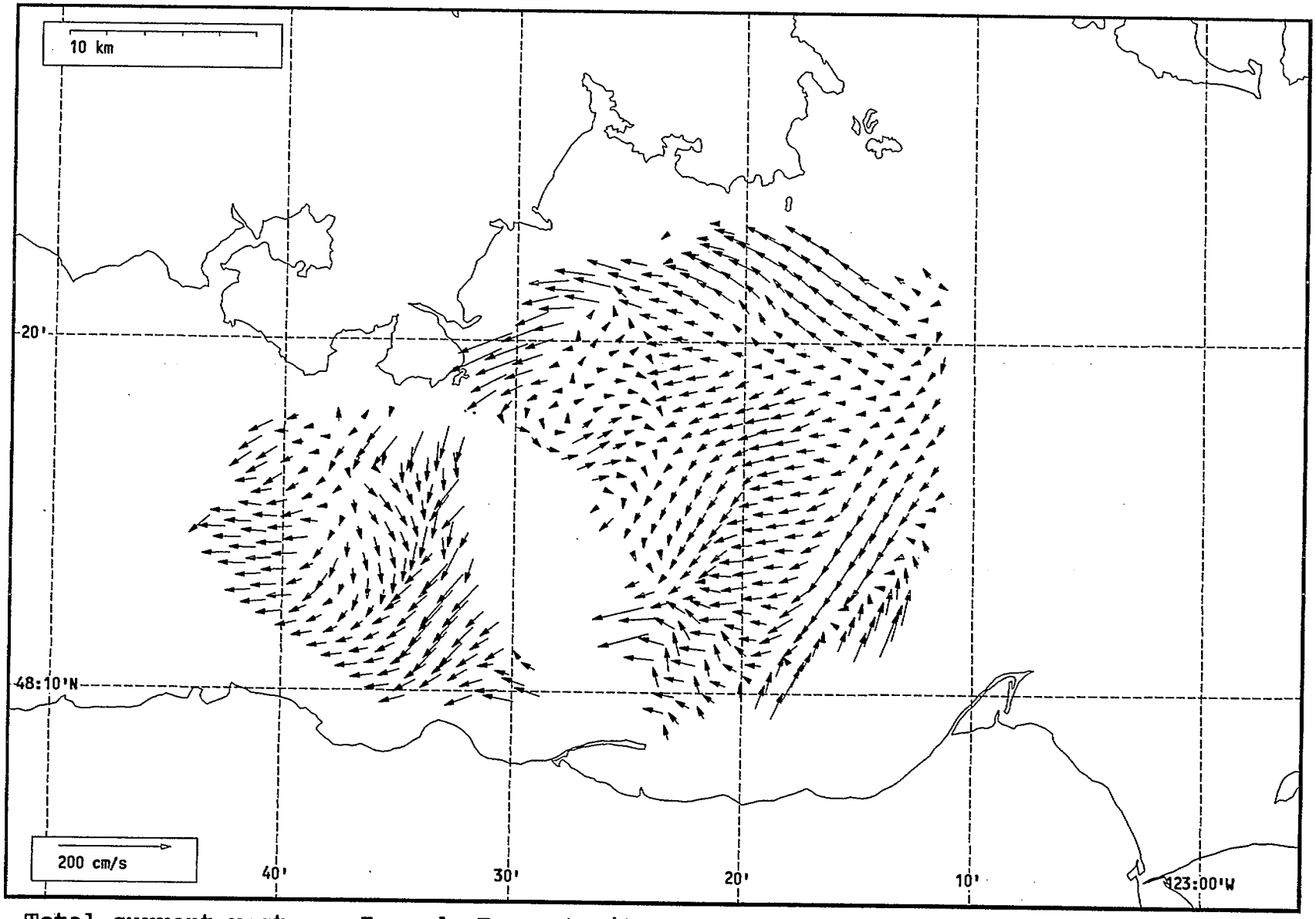

Total current vectors, Juan de Fuca Strait, 1992-07-16 13:00 Z.

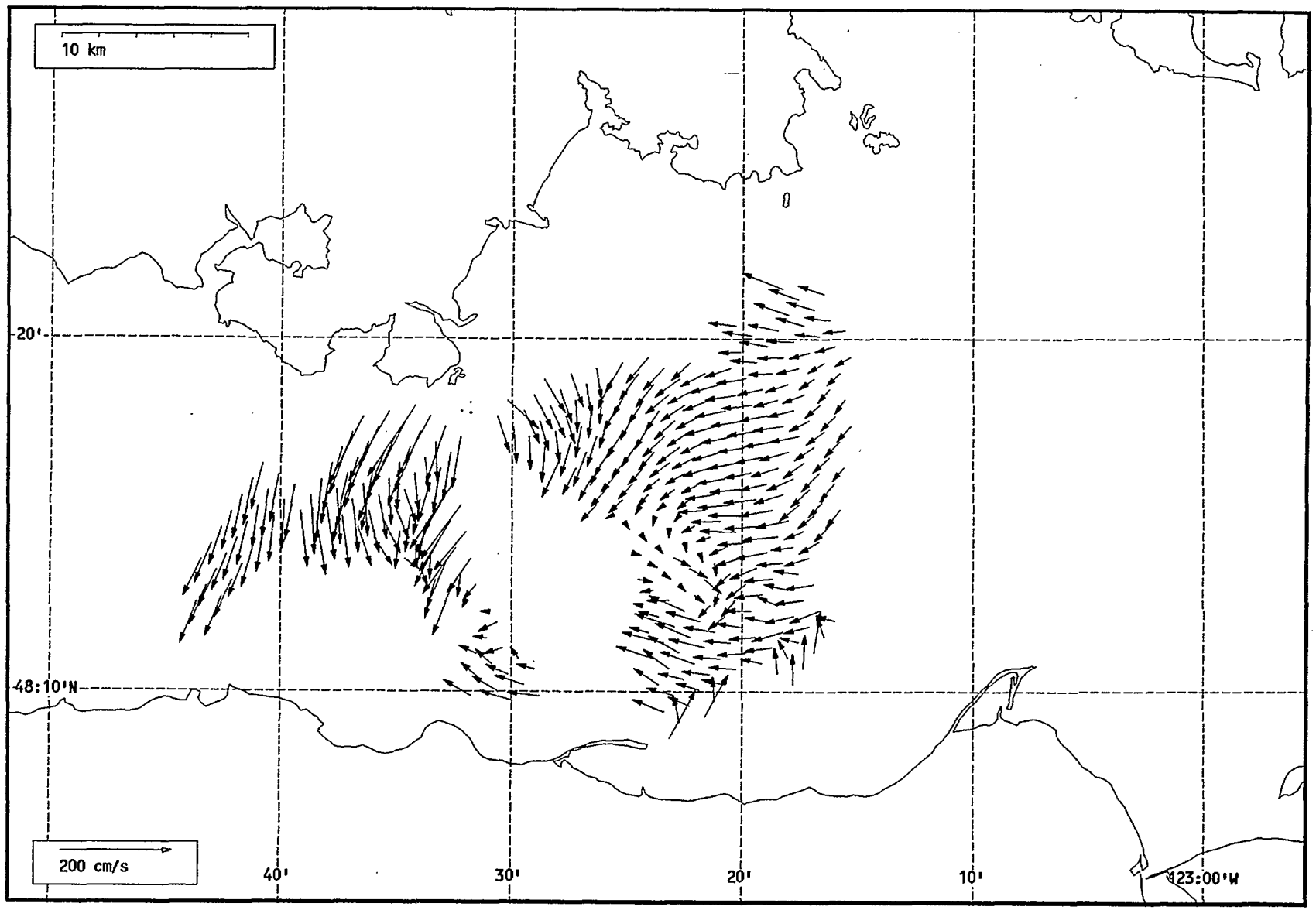

Total current vectors, Juan de Fuca Strait, 1992-07-16 14:00 Z.

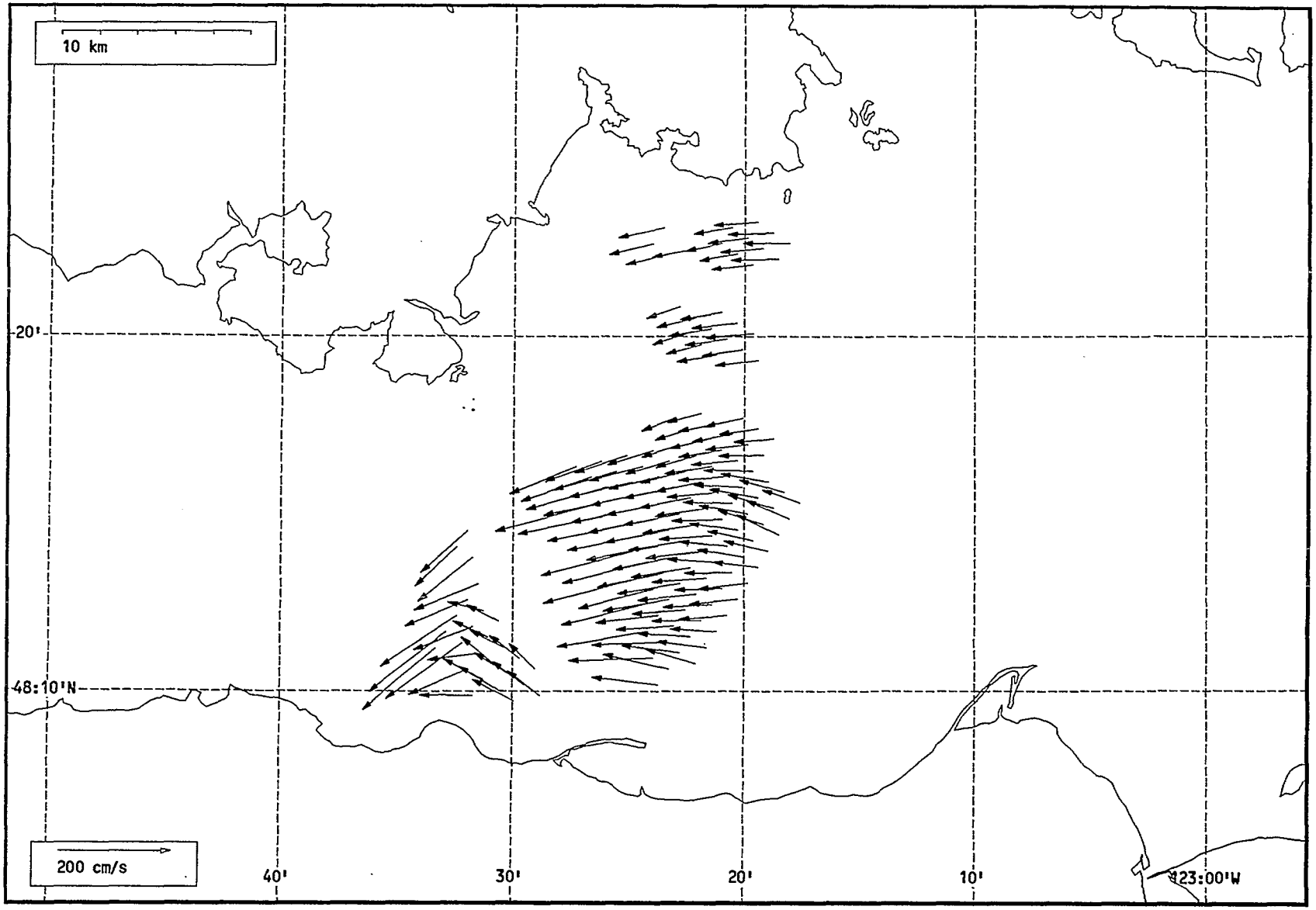

Total current vectors, Juan de Fuca Strait, 1992-07-16 15:00 Z.

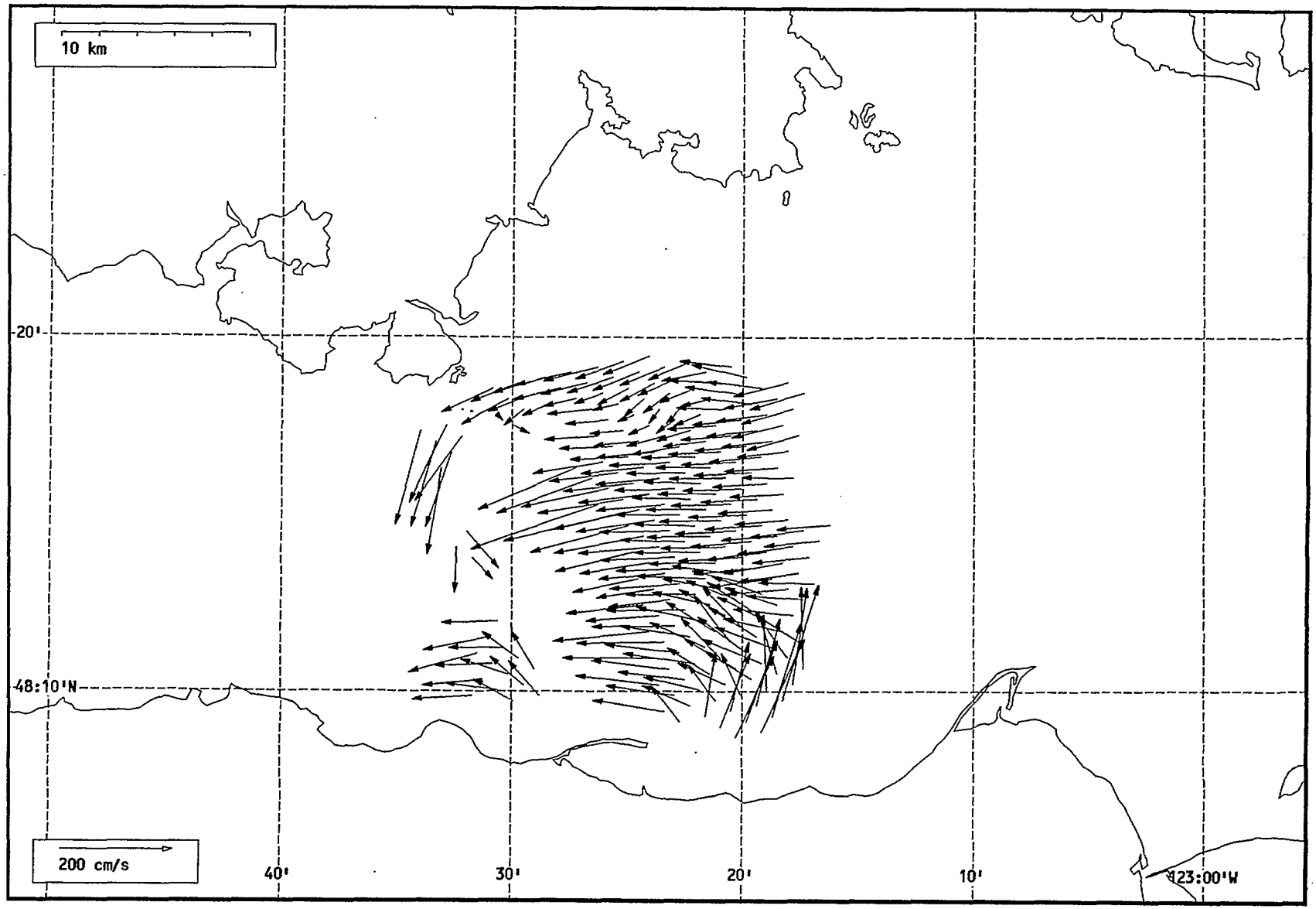

Total current vectors, Juan de Fuca Strait, 1992-07-16 16:00 Z.

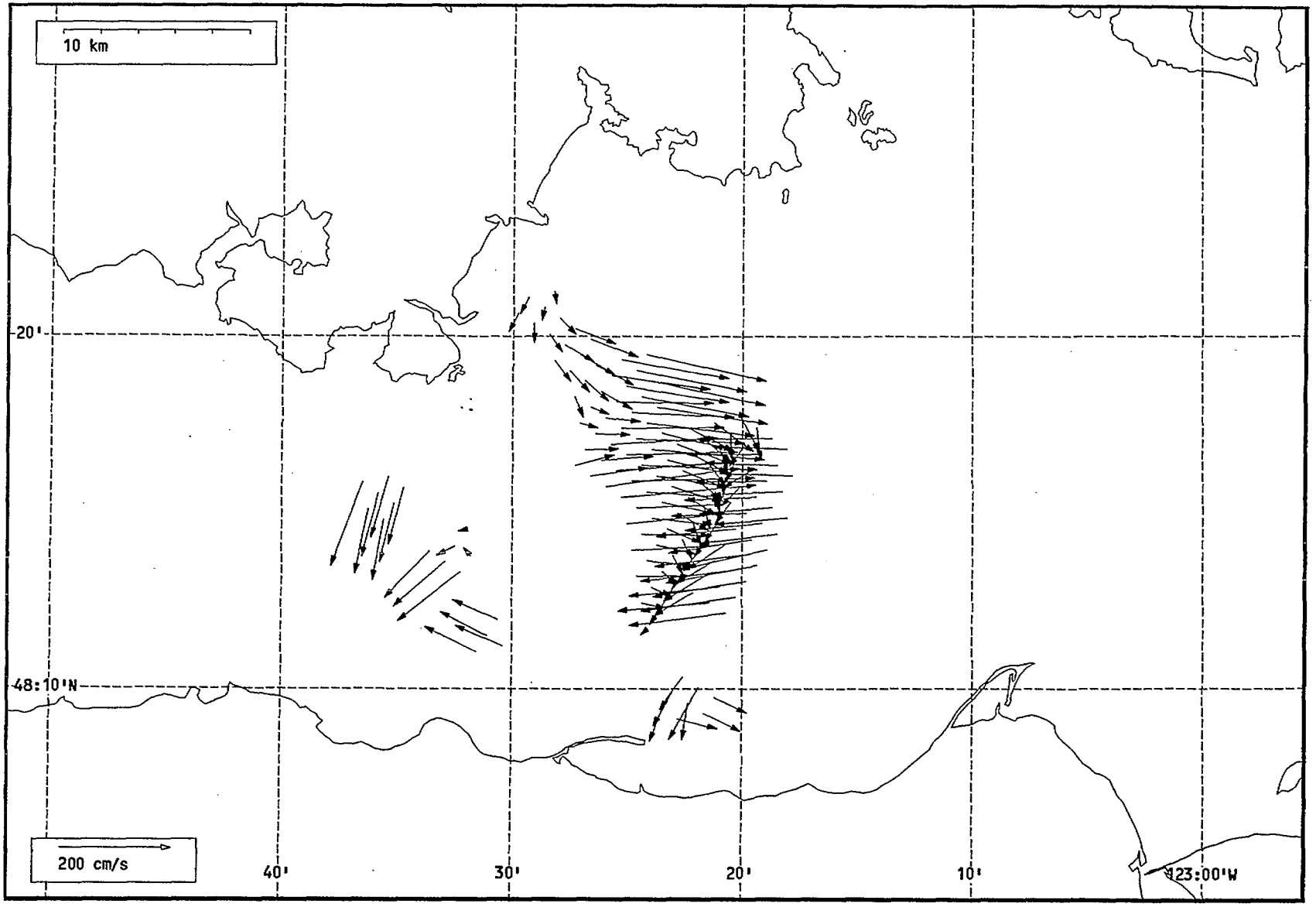

Total current vectors, Juan de Fuca Strait, 1992-07-16 17:00 Z.

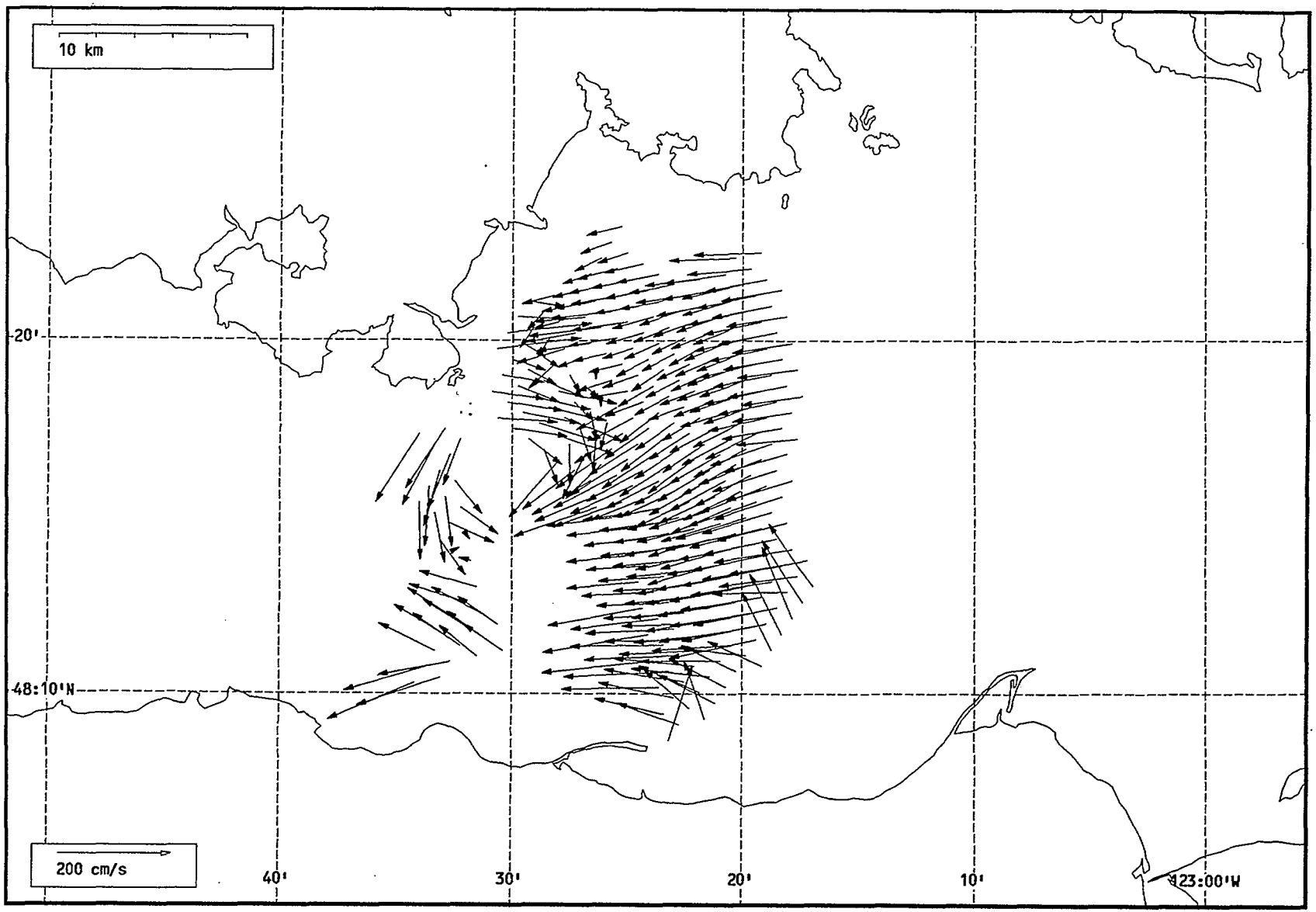

Total current vectors, Juan de Fuca Strait, 1992-07-16 18:00 Z.

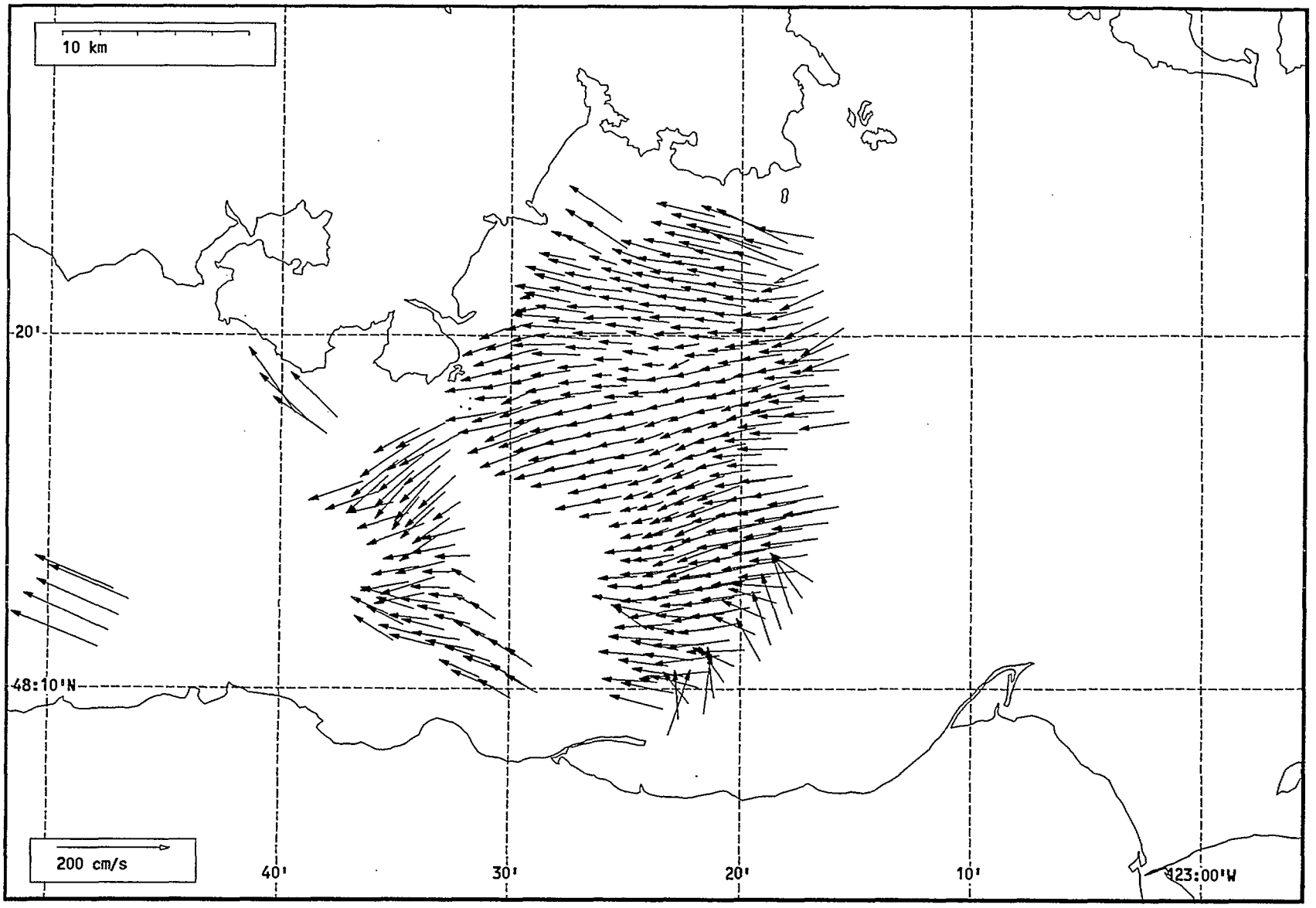

Total current vectors, Juan de Fuca Strait, 1992-07-16 19:00 Z.

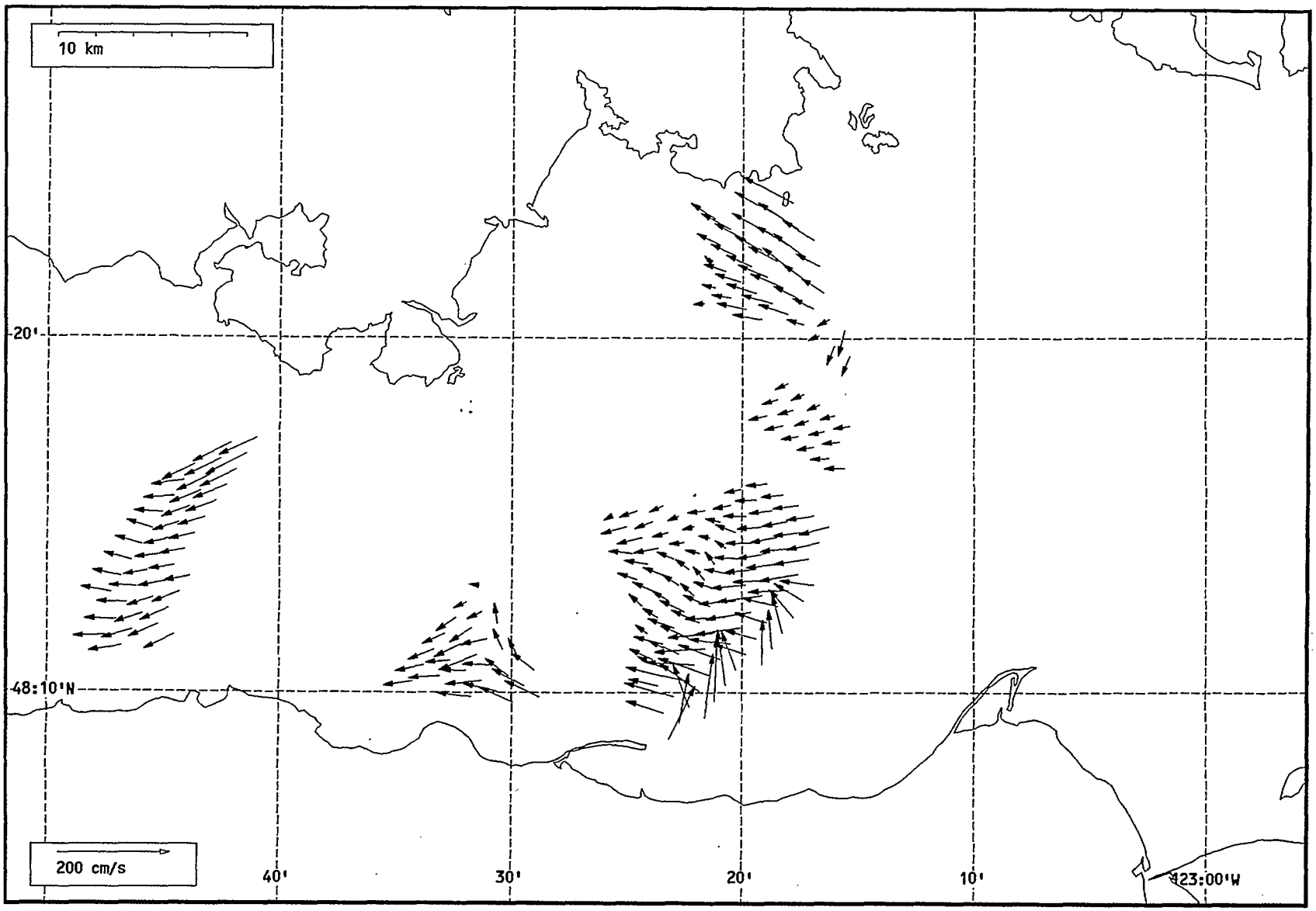

Total current vectors, Juan de Fuca Strait, 1992-07-16 20:00 Z.

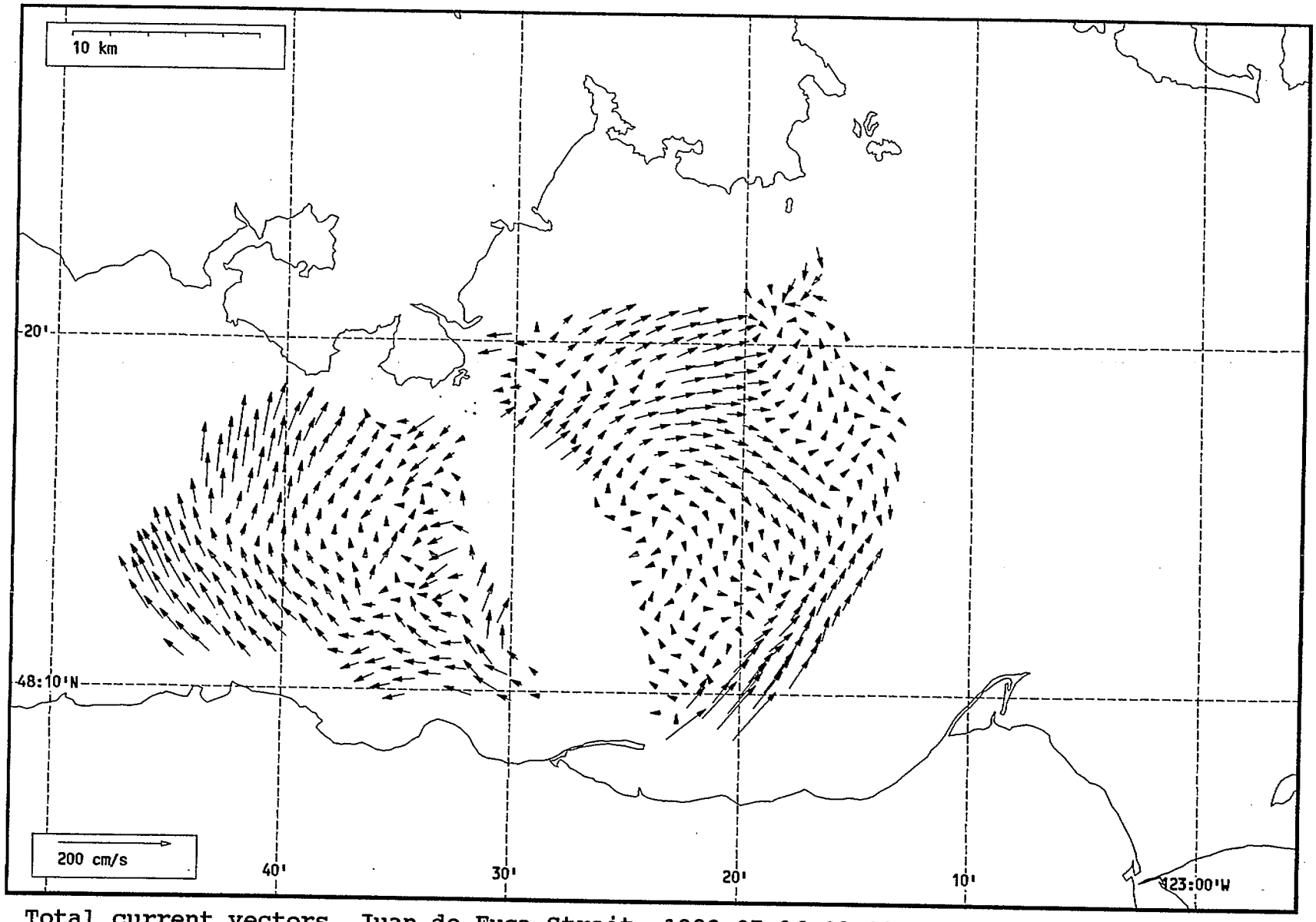

Total current vectors, Juan de Fuca Strait, 1992-07-16 21:00 Z.

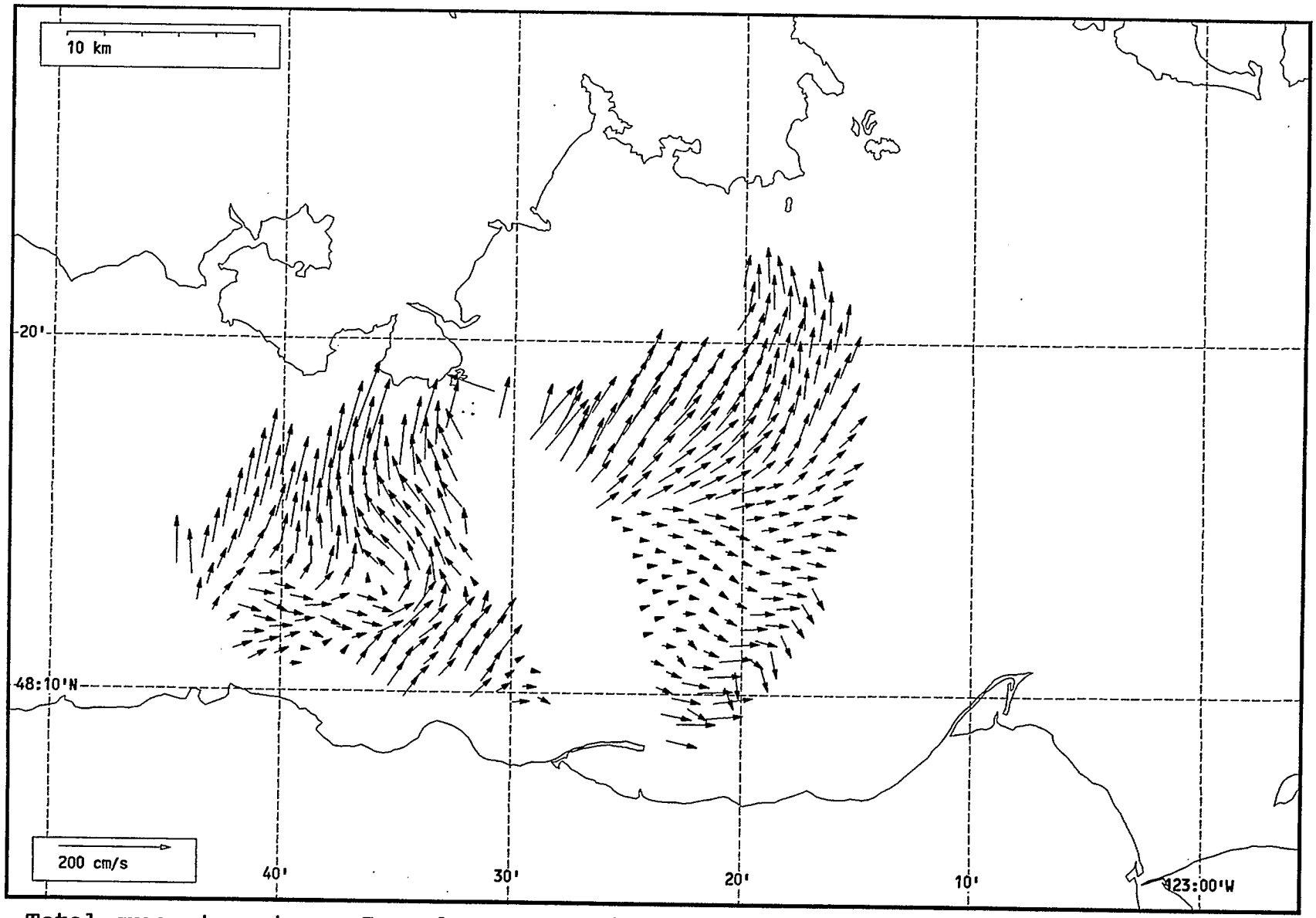

Total current vectors, Juan de Fuca Strait, 1992-07-16 22:00 Z.

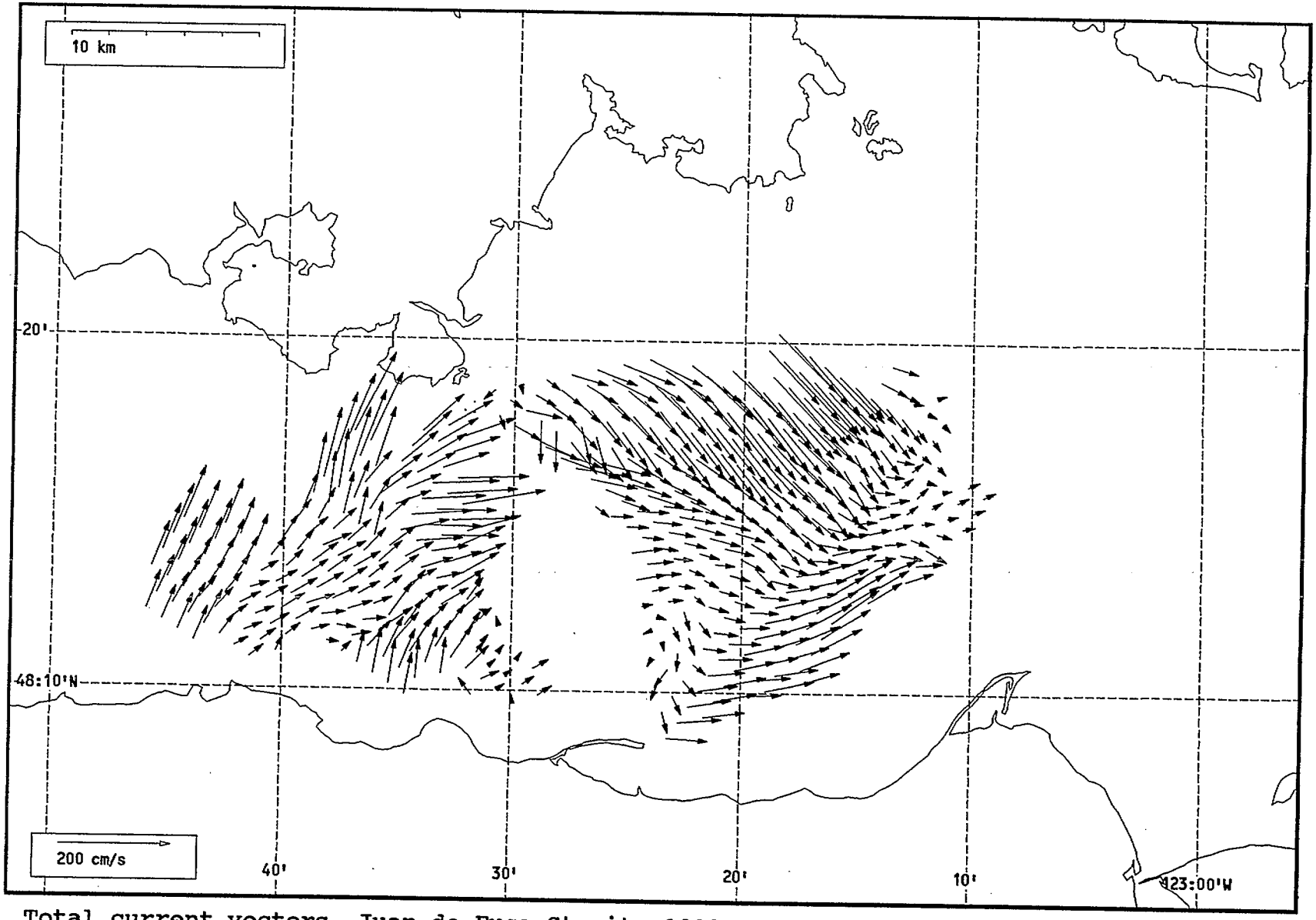

Total current vectors, Juan de Fuca Strait, 1992-07-16 23:00 Z.

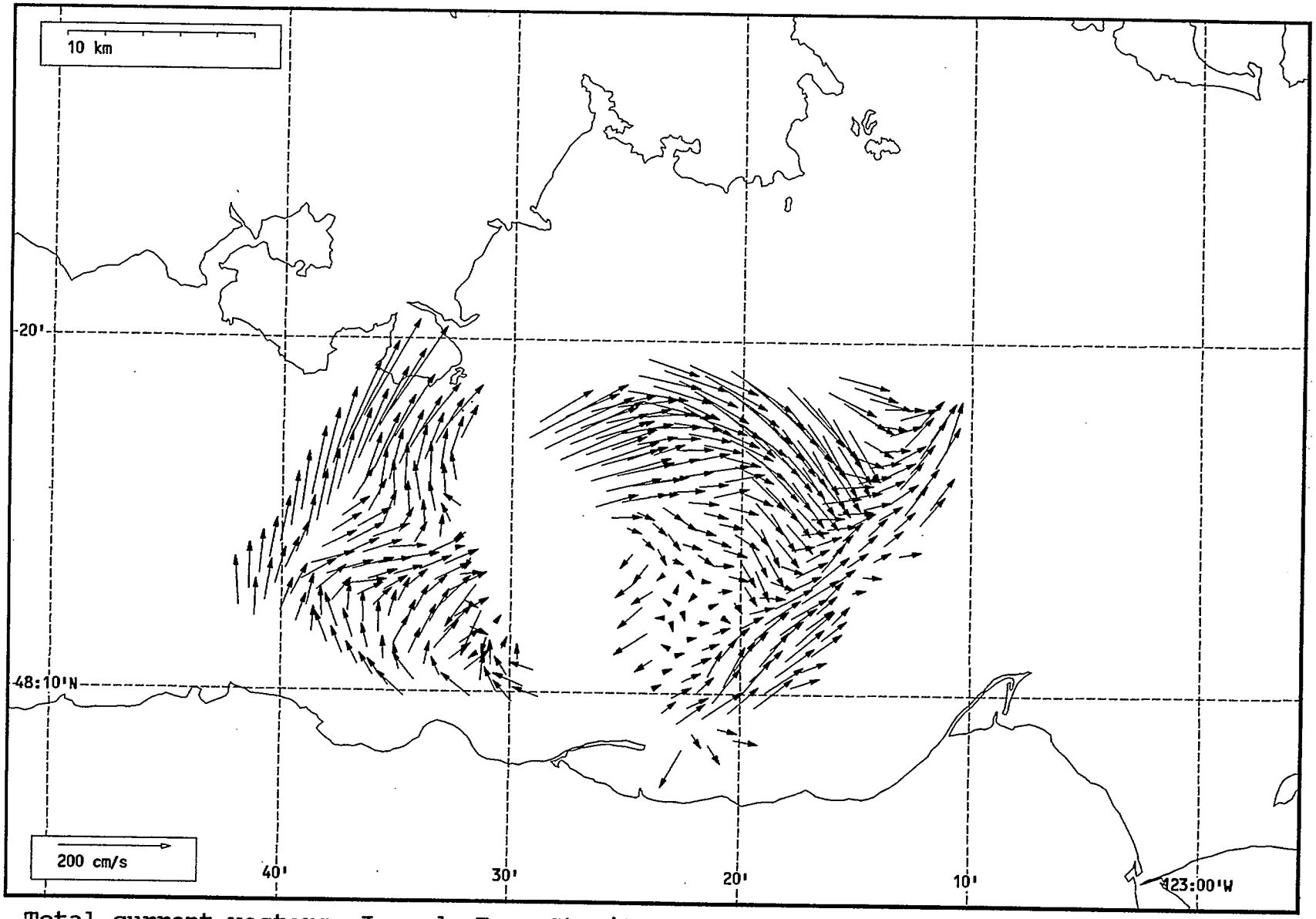

Total current vectors, Juan de Fuca Strait, 1992-07-17 00:00 Z.

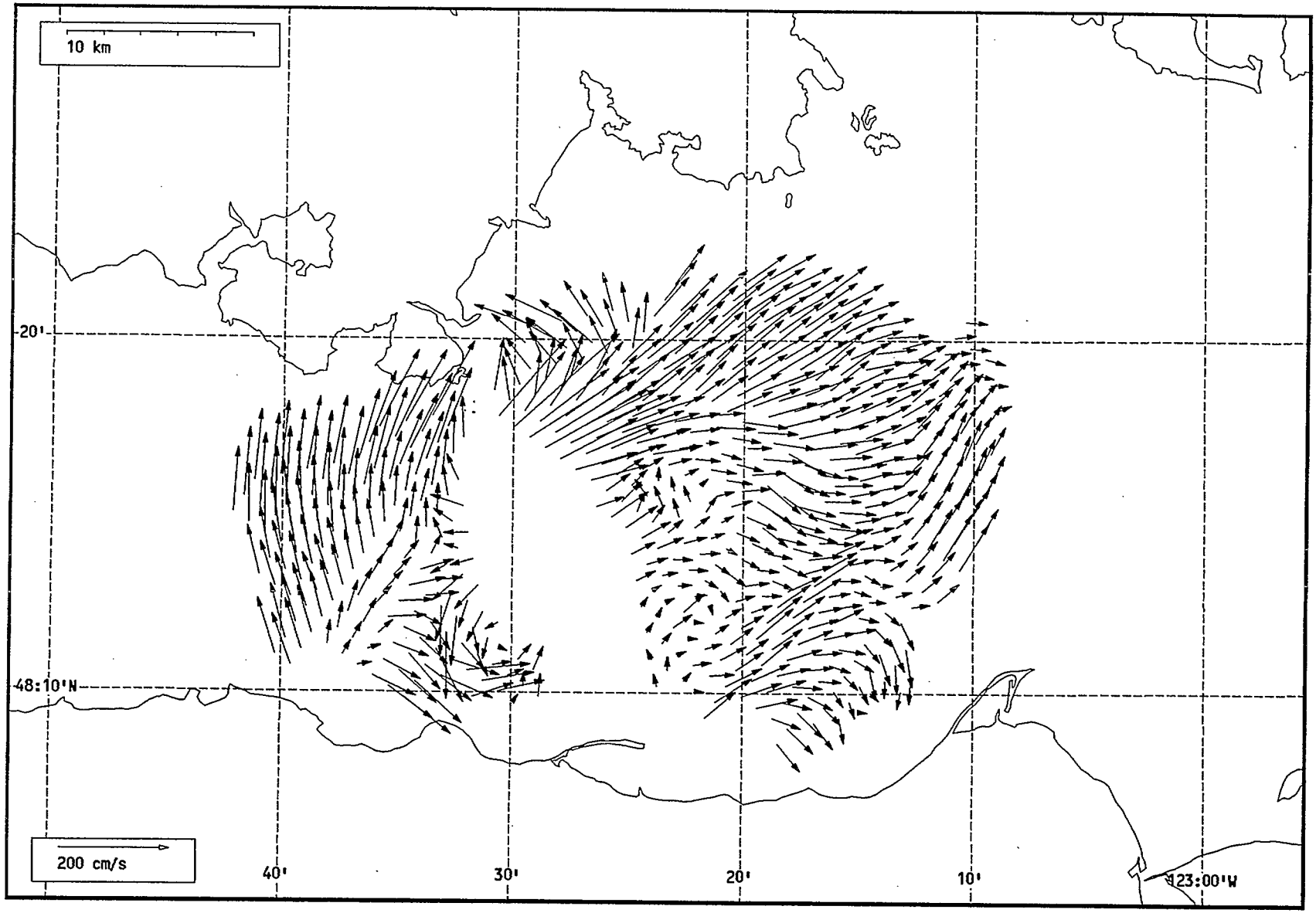

Total current vectors, Juan de Fuca Strait, 1992-07-17 01:00 Z.

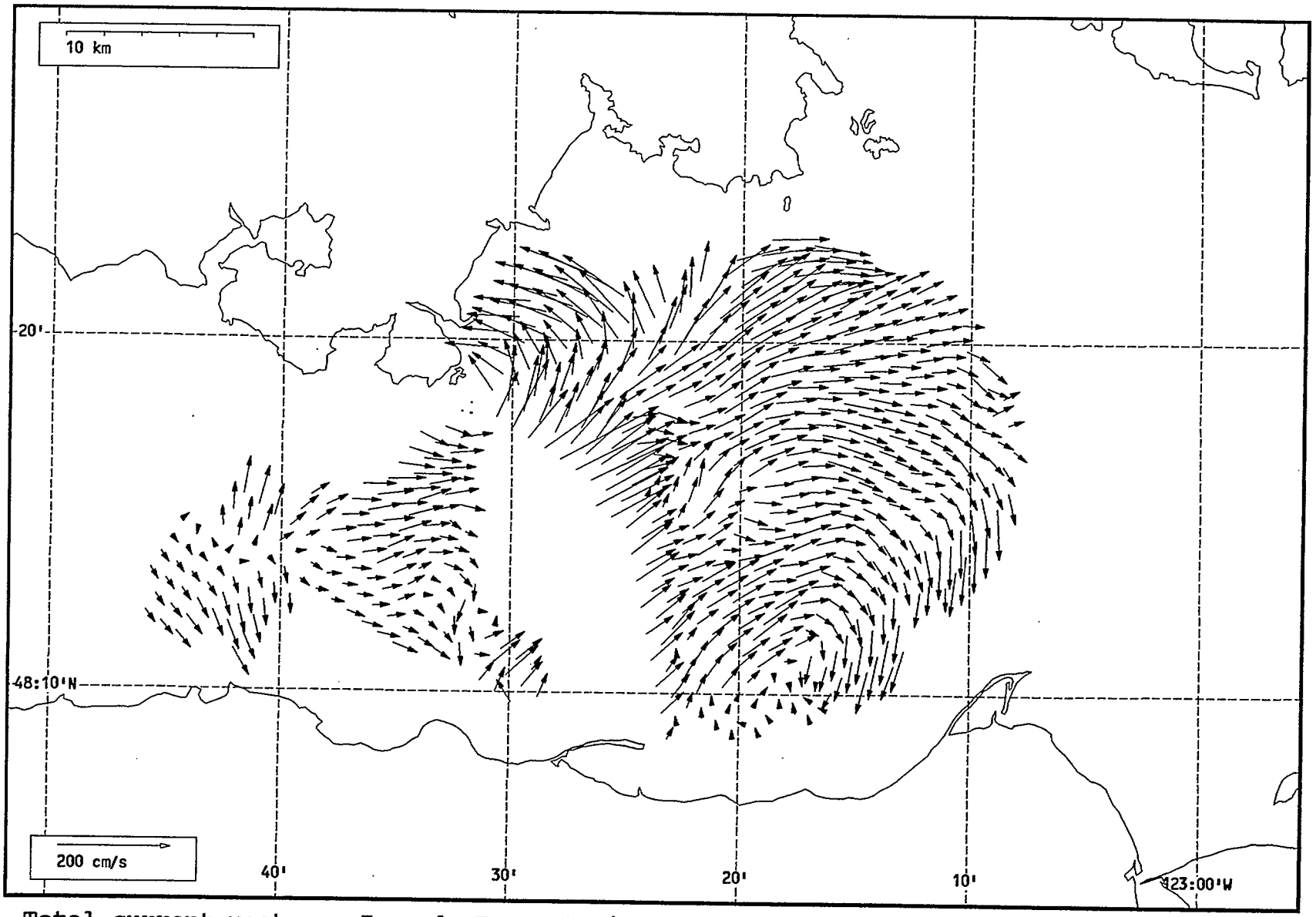

Total current vectors, Juan de Fuca Strait, 1992-07-17 02:00 Z.

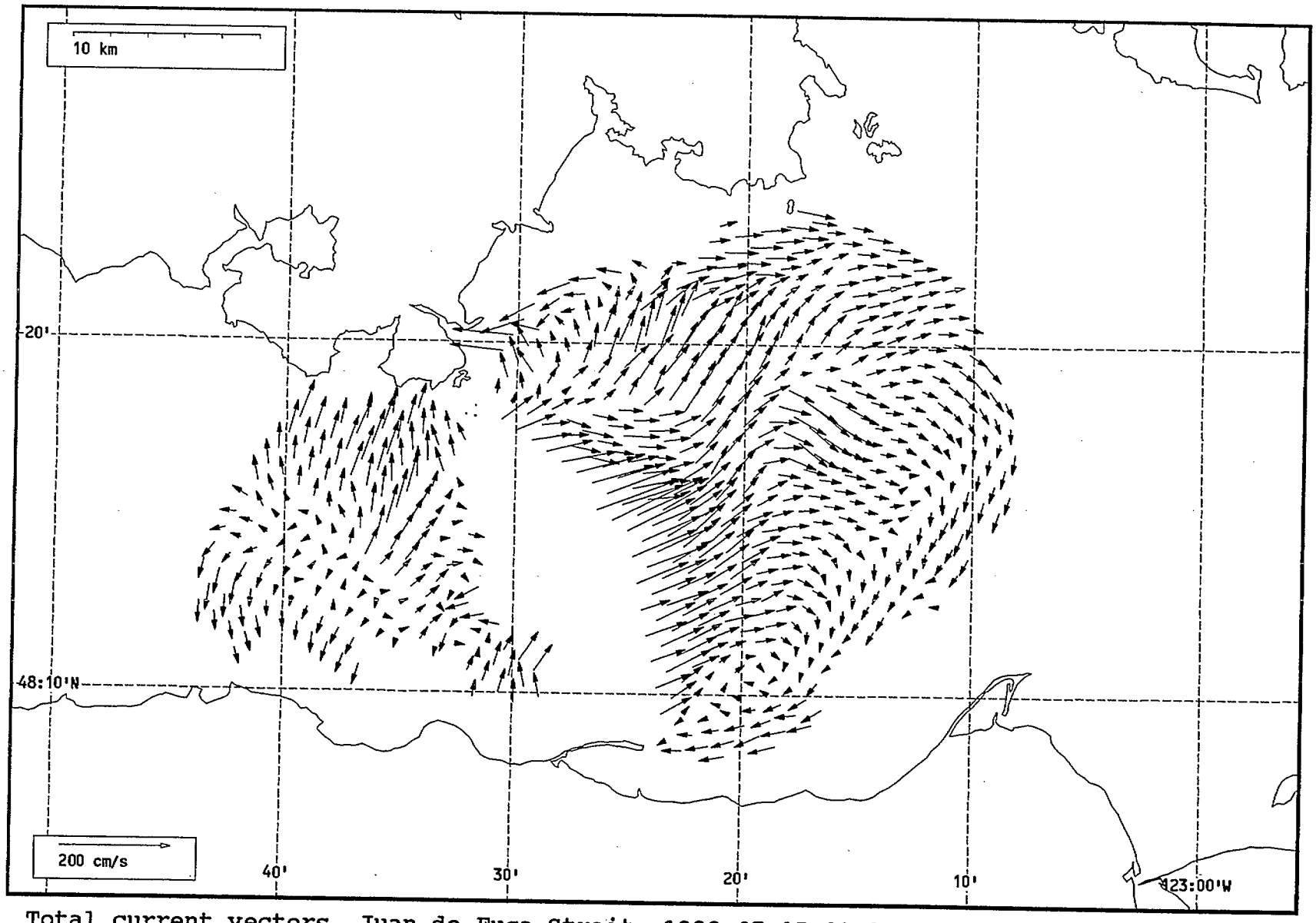

Total current vectors, Juan de Fuca Strait, 1992-07-17 03:00 Z.

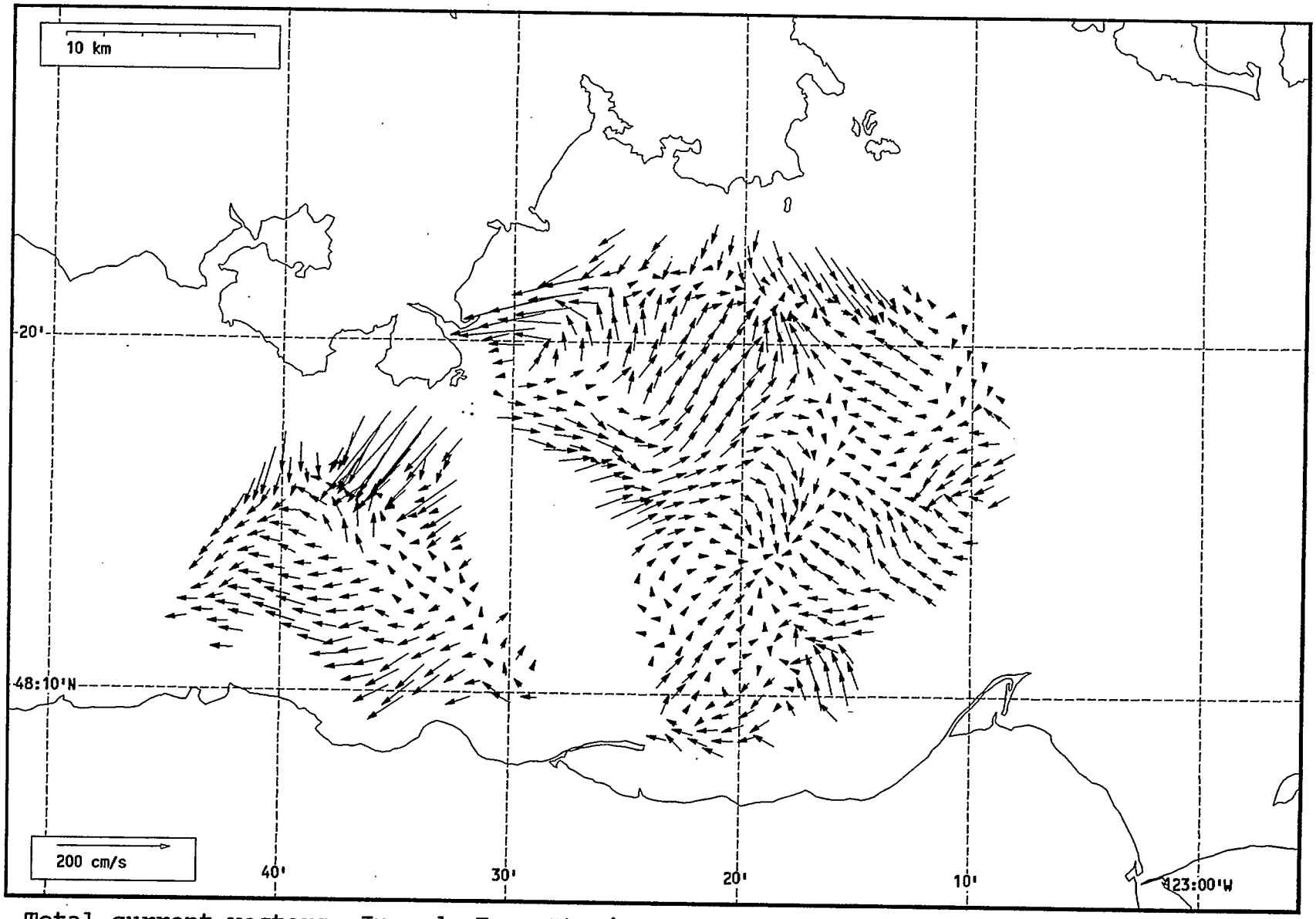

Total current vectors, Juan de Fuca Strait, 1992-07-17 04:00 Z.

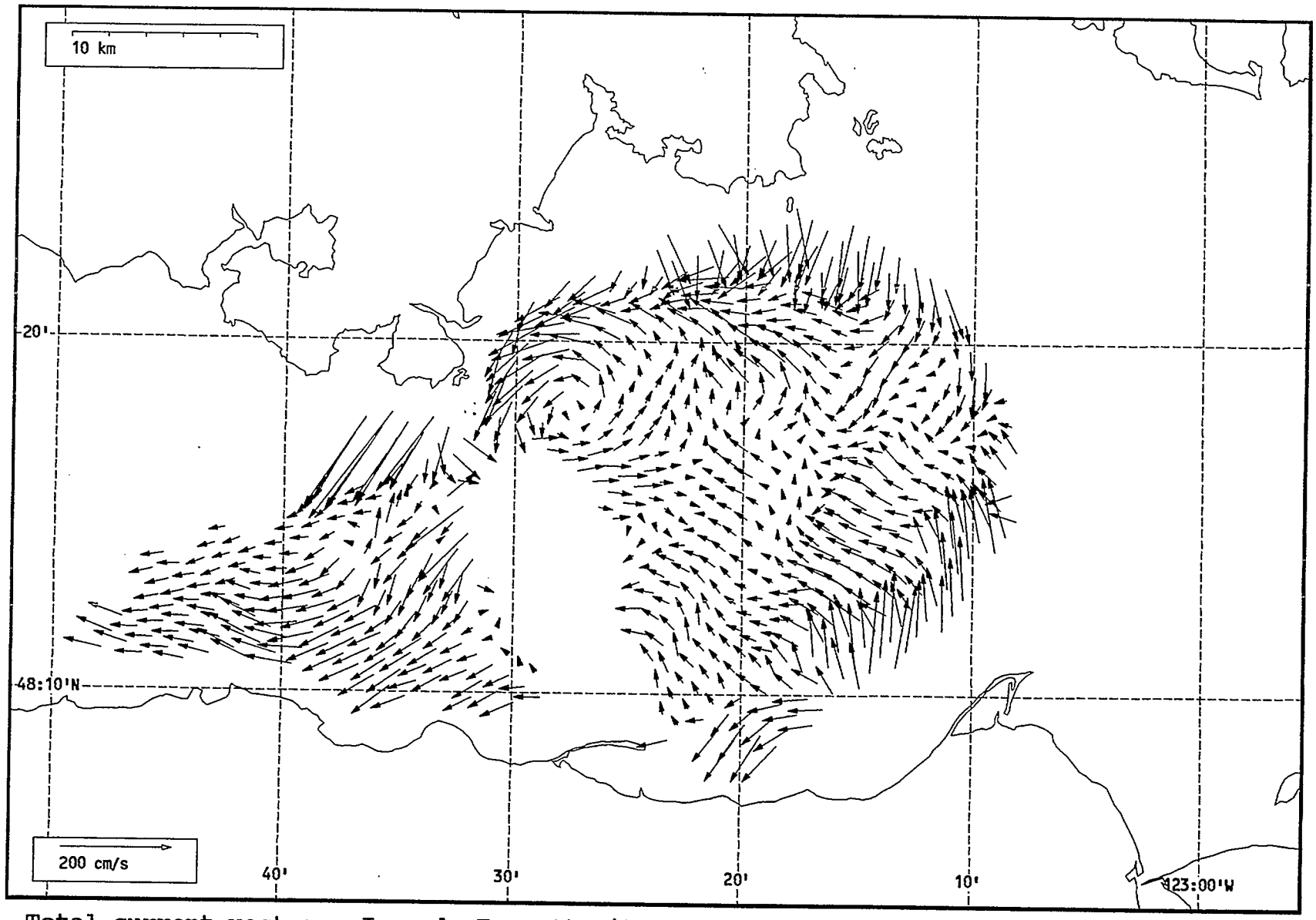

Total current vectors, Juan de Fuca Strait, 1992-07-17 05:00 Z.

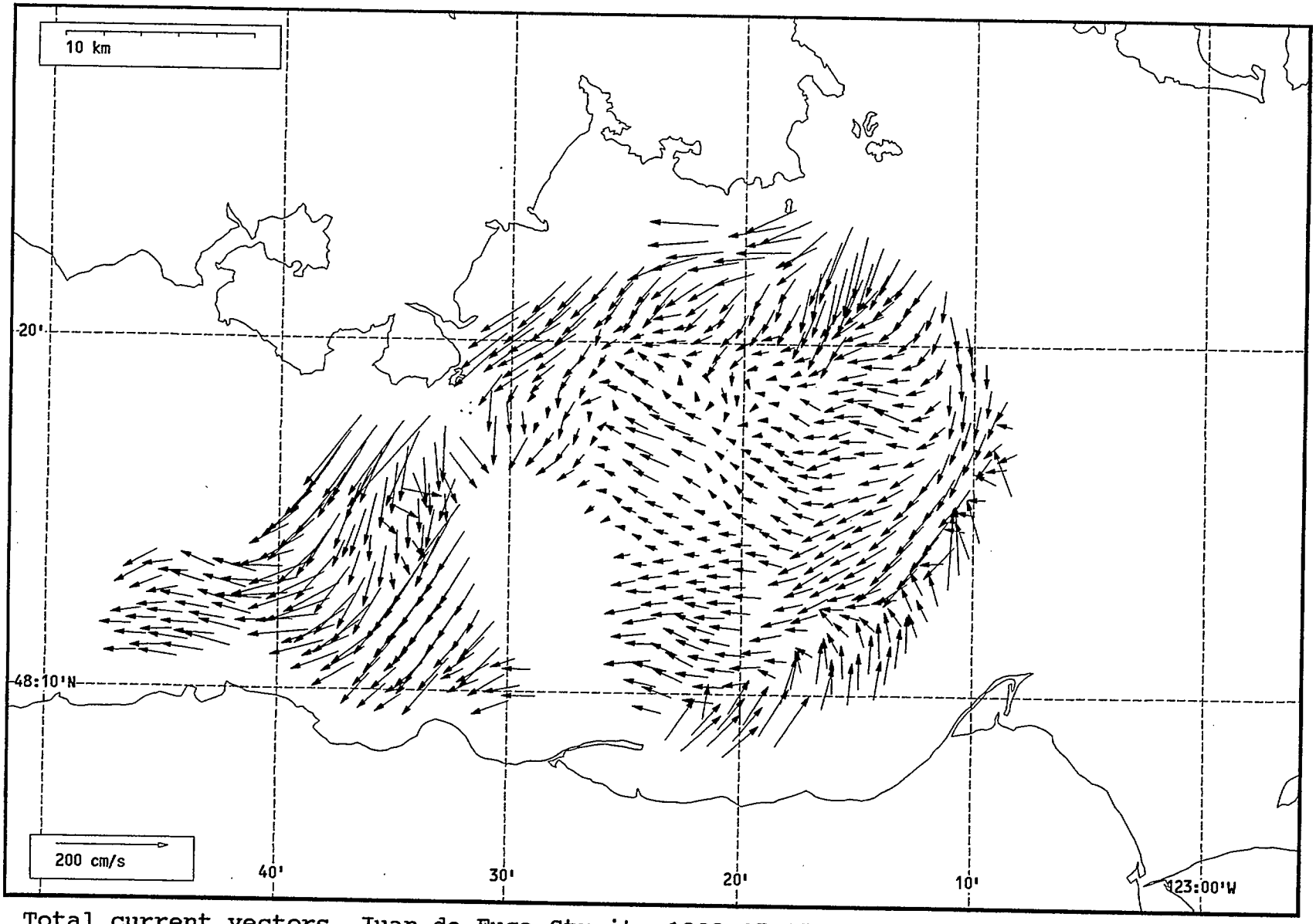

Total current vectors, Juan de Fuca Strait, 1992-07-17 06:00 Z.

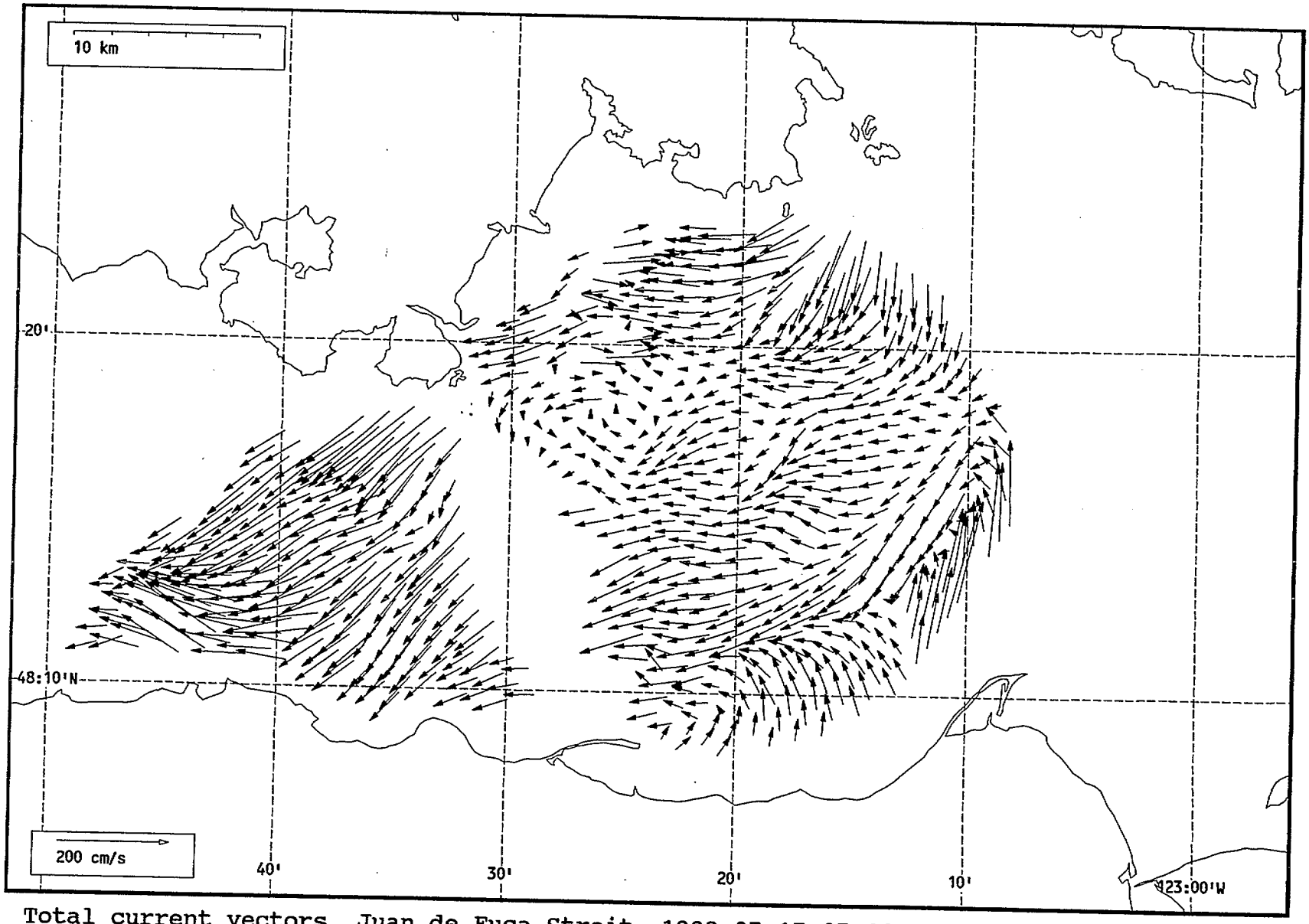

Total current vectors, Juan de Fuca Strait, 1992-07-17 07:00 Z.

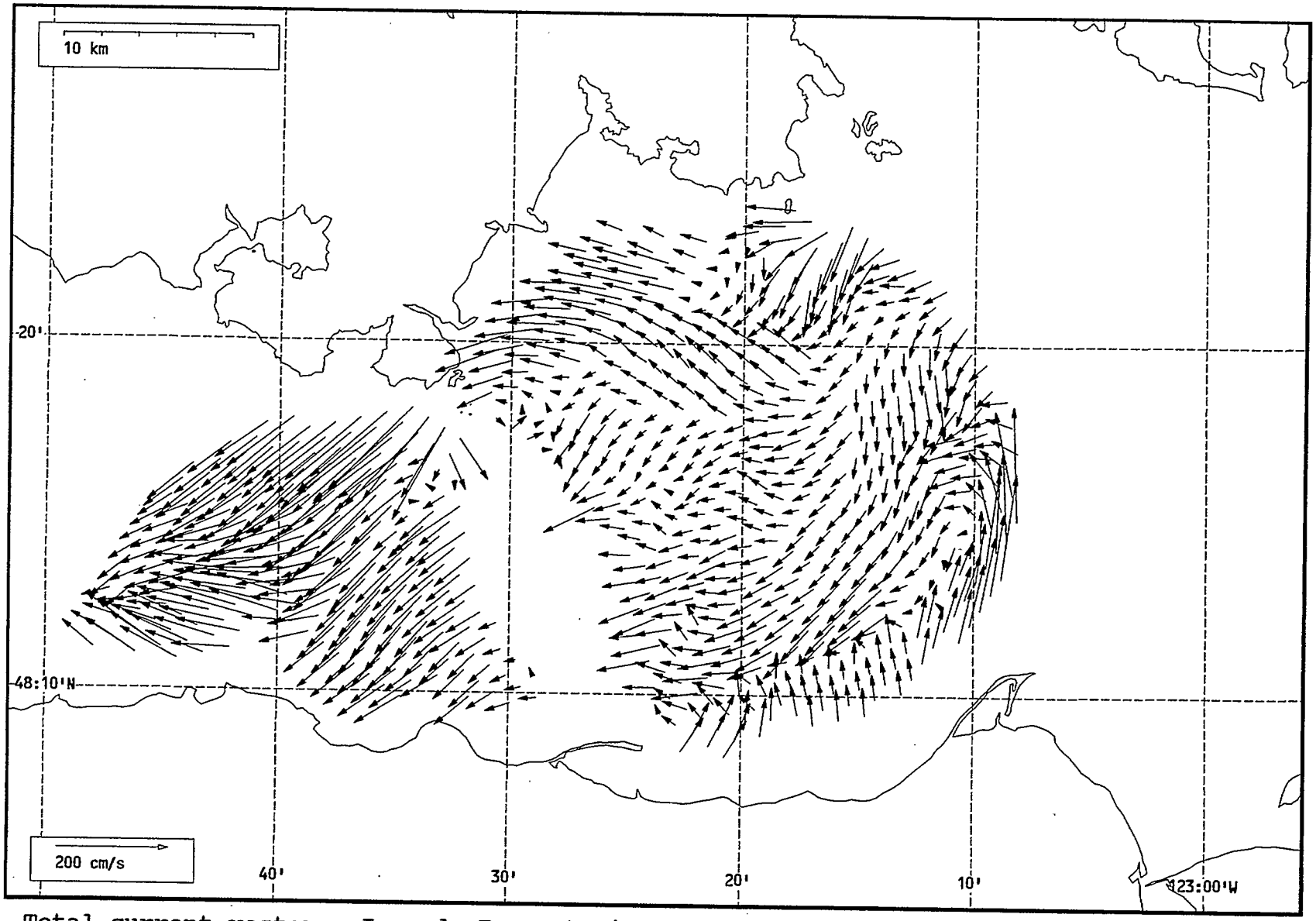

Total current vectors, Juan de Fuca Strait, 1992-07-17 08:00 Z.

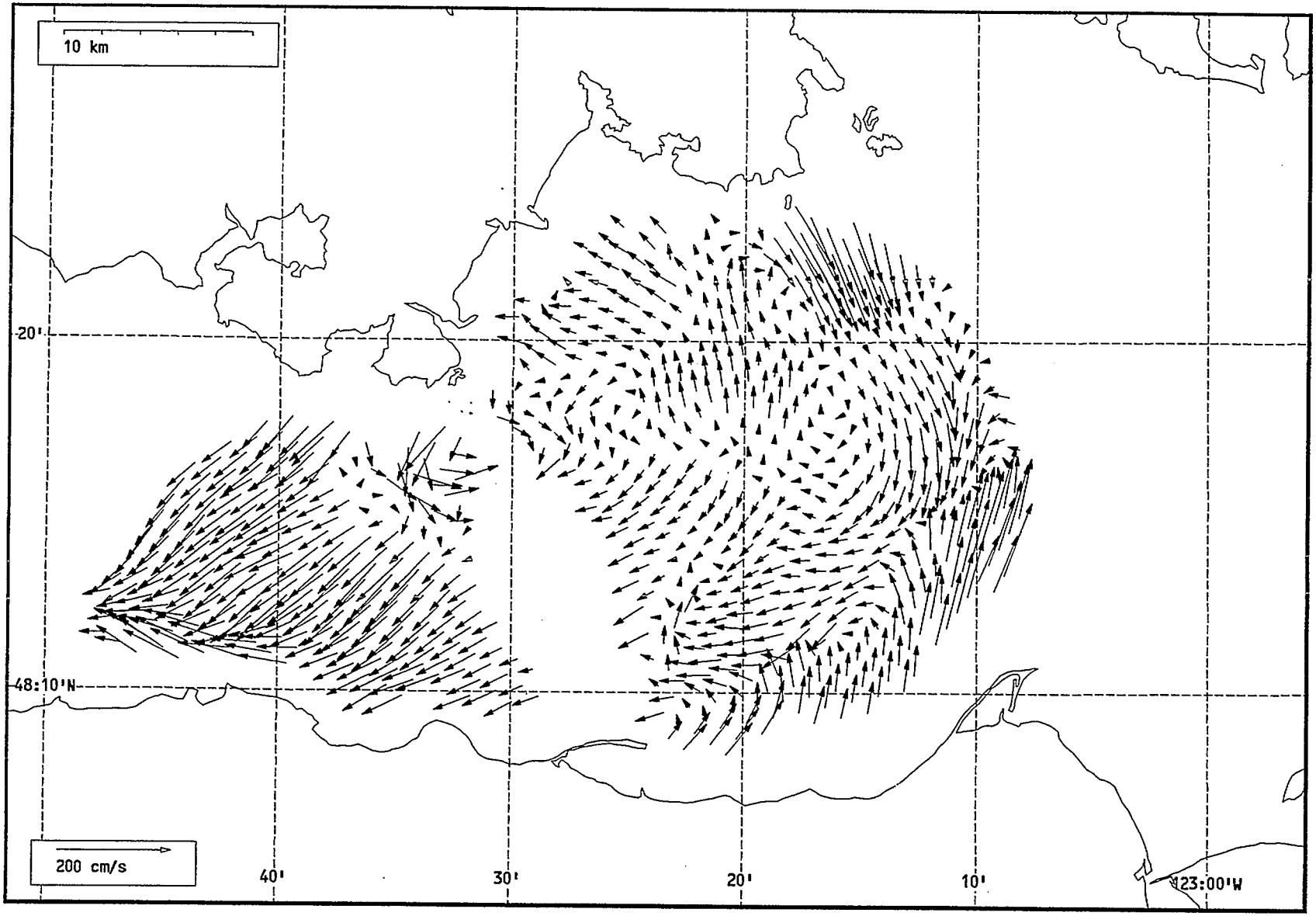

Total current vectors, Juan de Fuca Strait, 1992-07-17 09:00 Z.

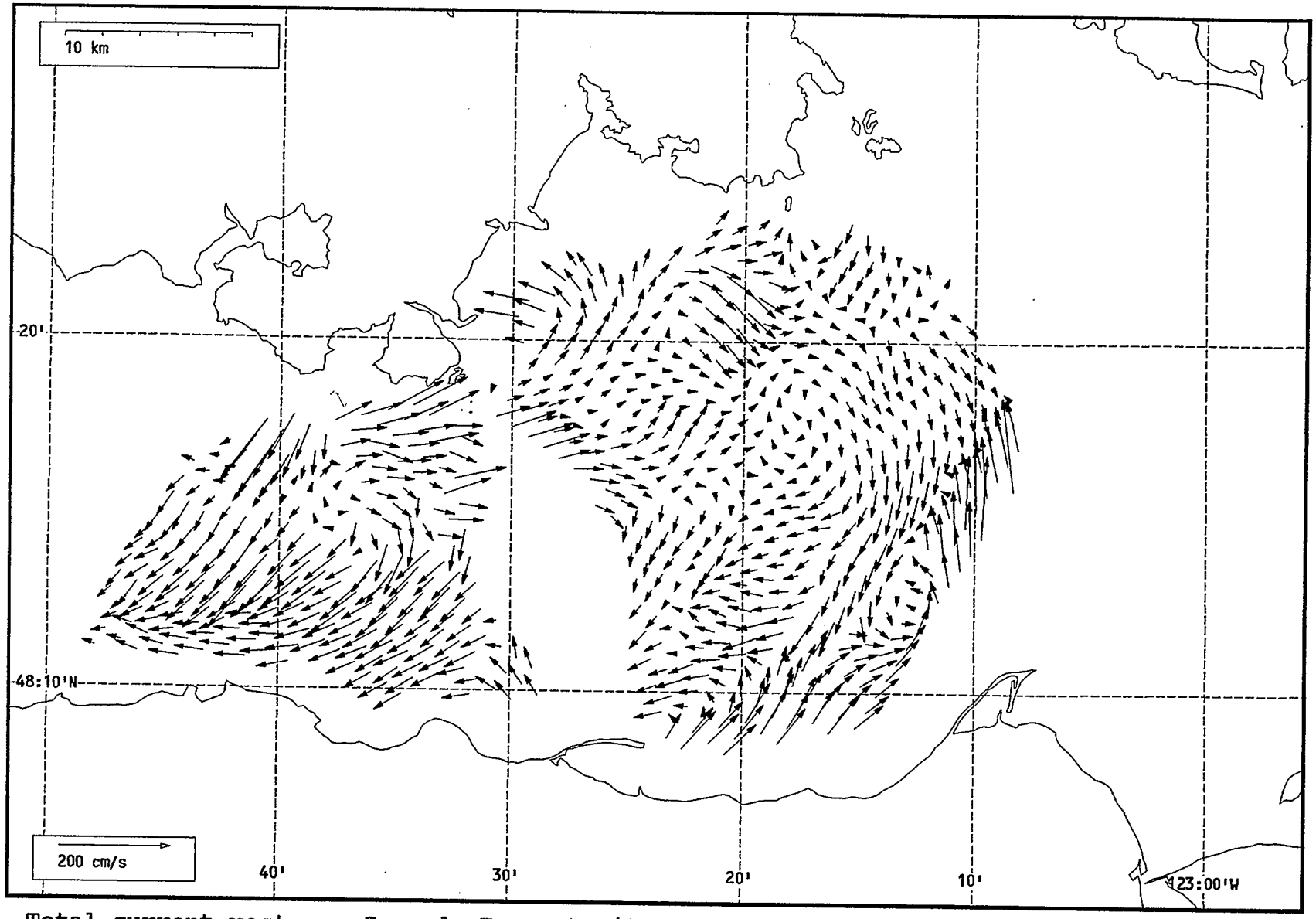

Total current vectors, Juan de Fuca Strait, 1992-07-17 10:00 Z.

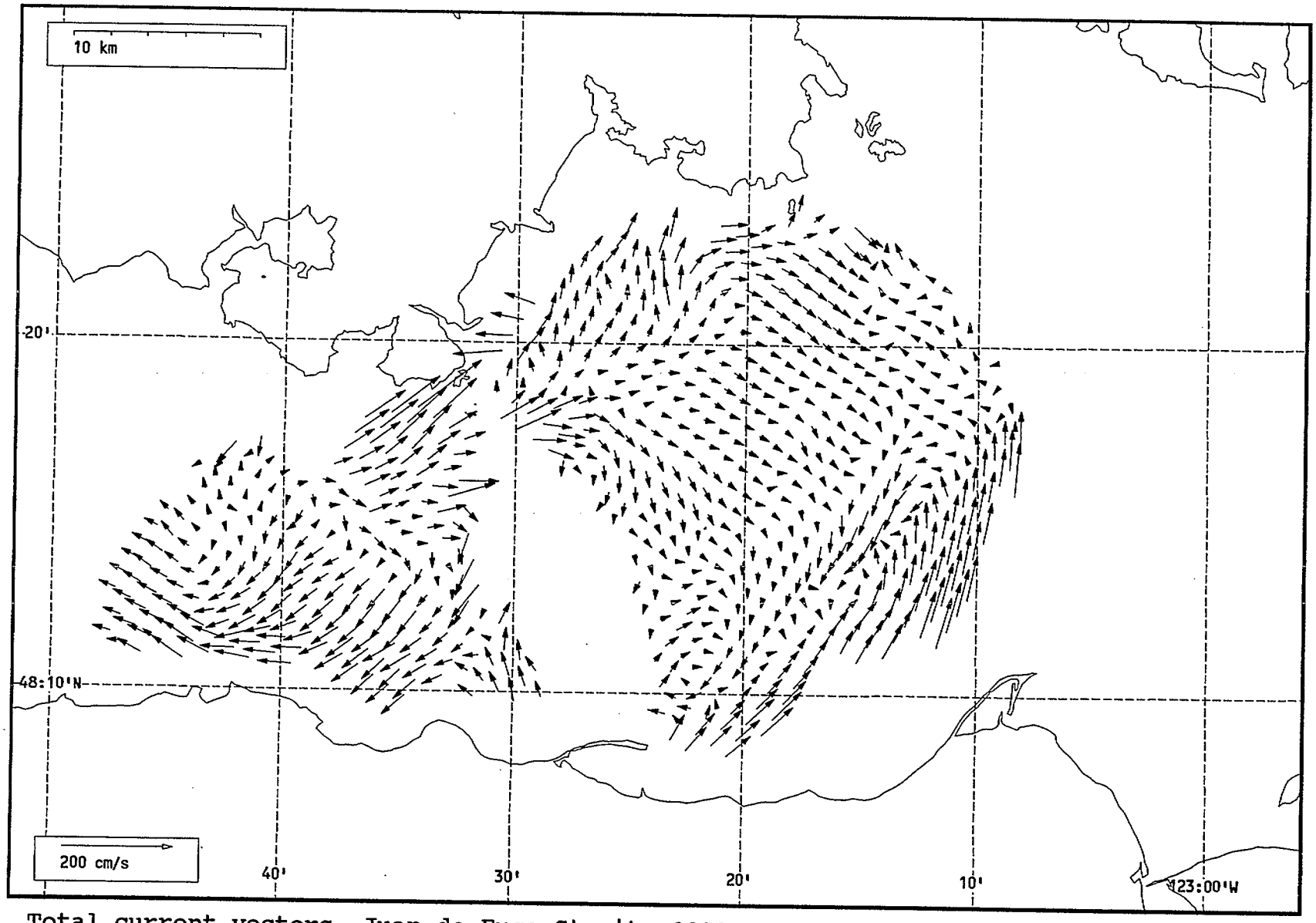

Total current vectors, Juan de Fuca Strait, 1992-07-17 11:00 Z.

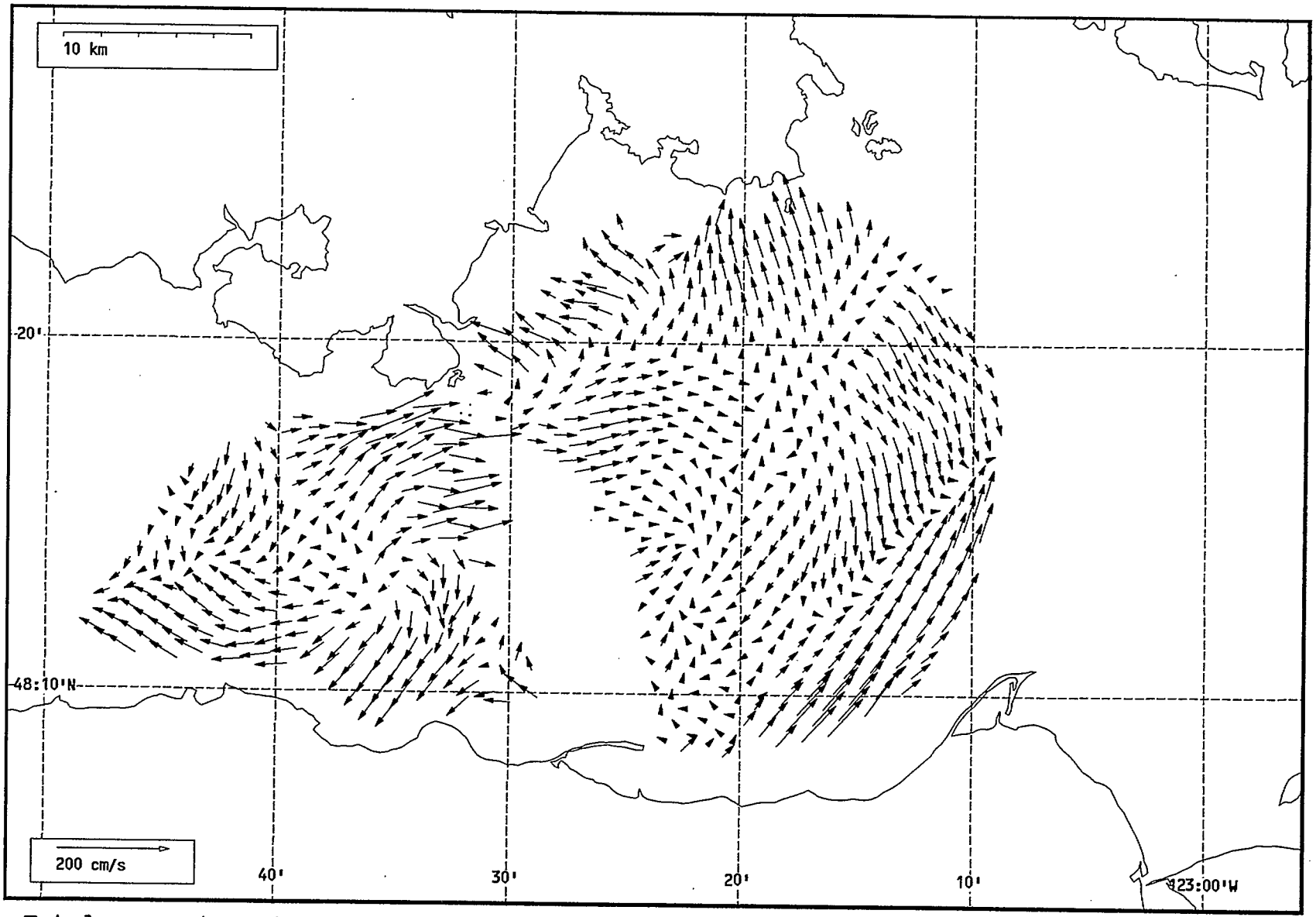

Total current vectors, Juan de Fuca Strait, 1992-07-17 12:00 Z.

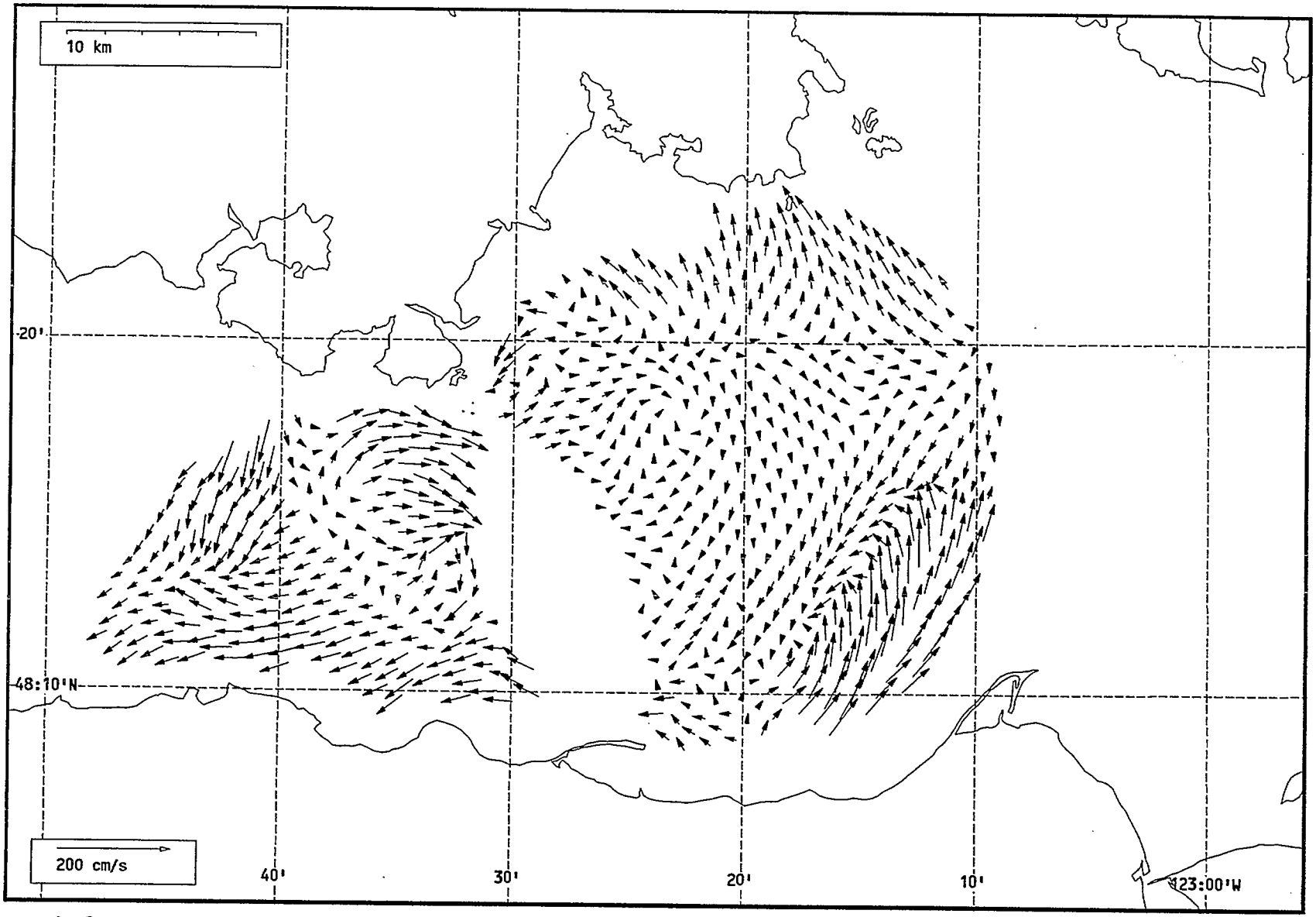

Total current vectors, Juan de Fuca Strait, 1992-07-17 13:00 Z.

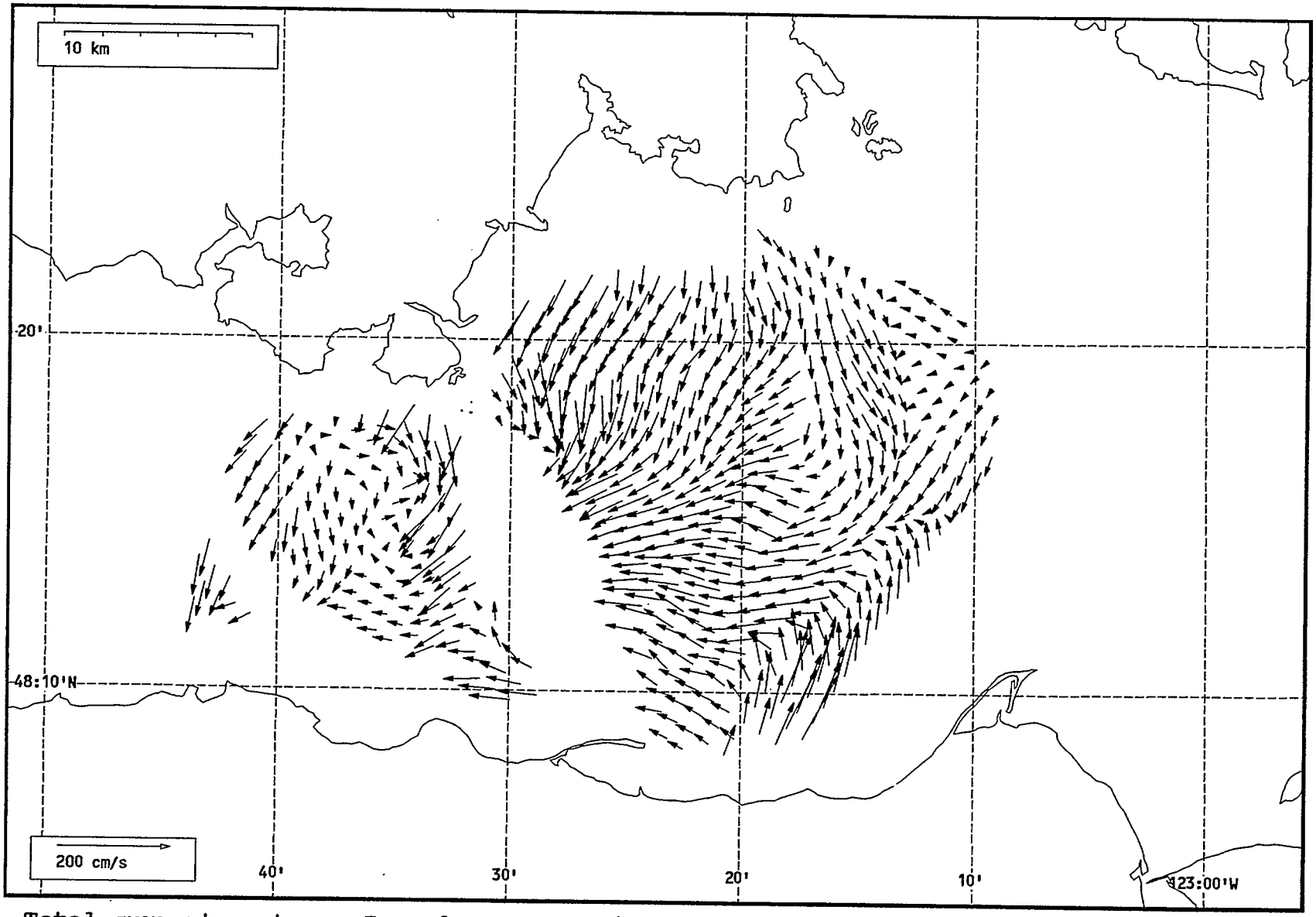

Total current vectors, Juan de Fuca Strait, 1992-07-17 14:00 Z.

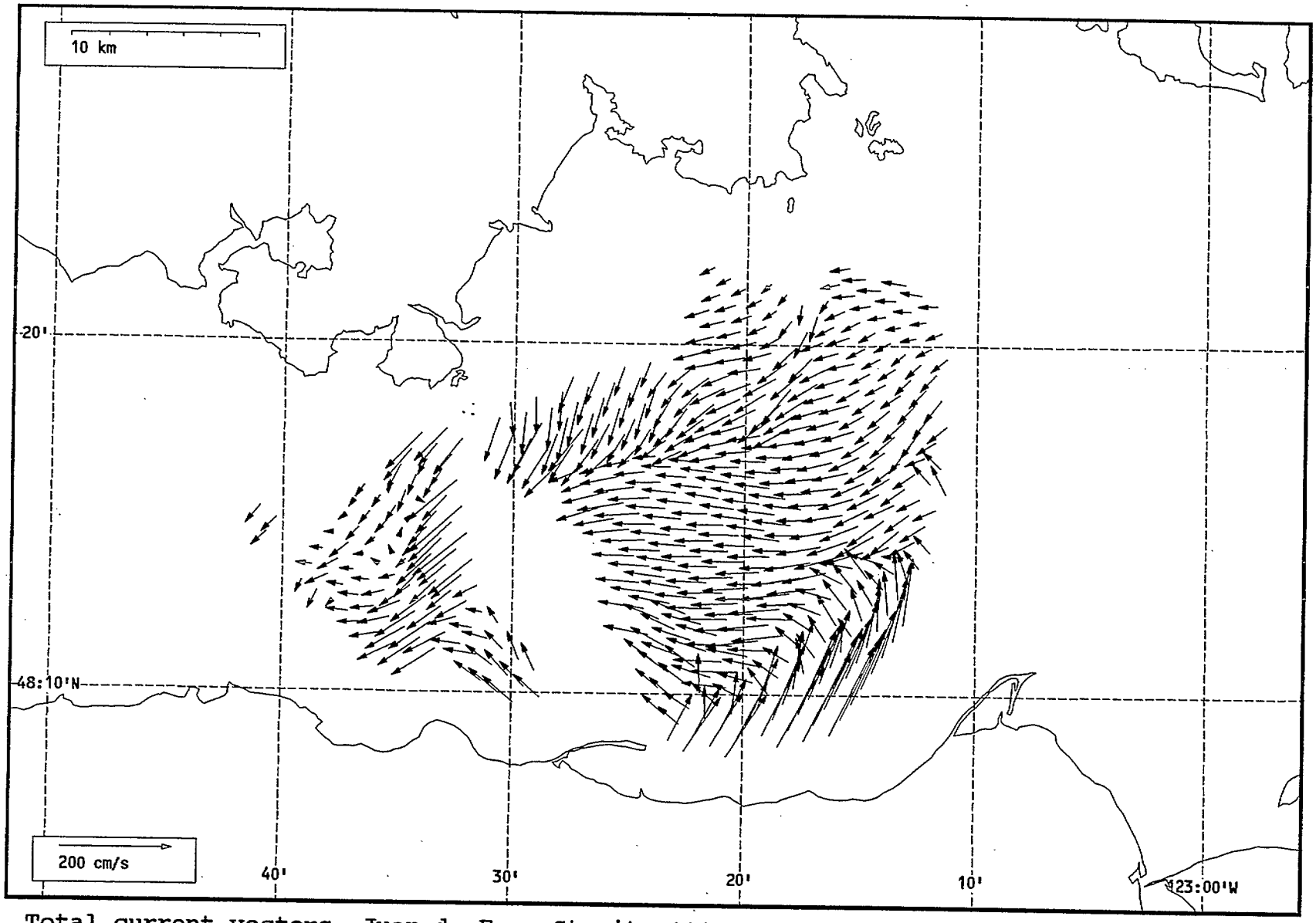

Total current vectors, Juan de Fuca Strait, 1992-07-17 15:00 Z.

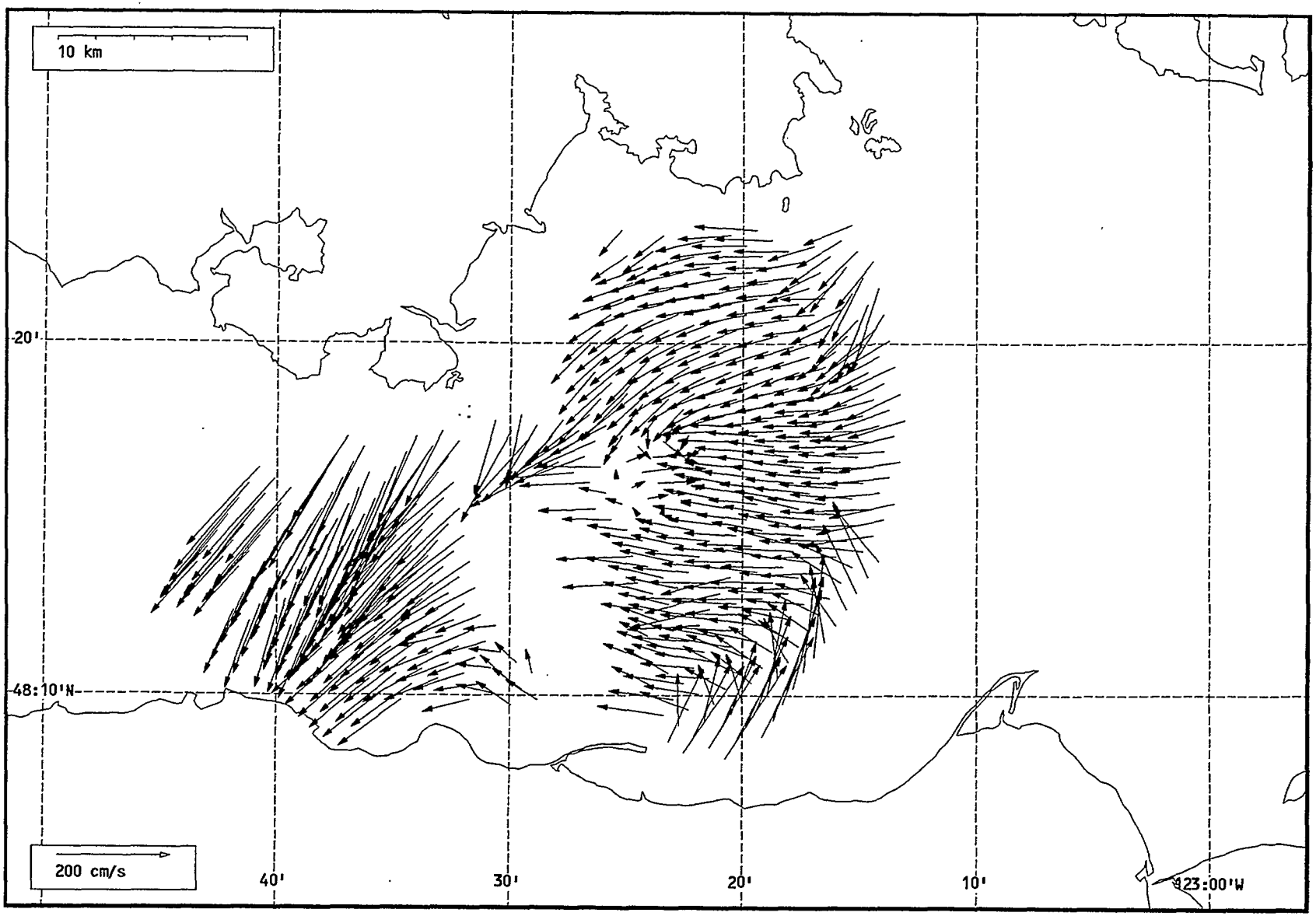

Total current vectors, Juan de Fuca Strait, 1992-07-17 16:00 Z.

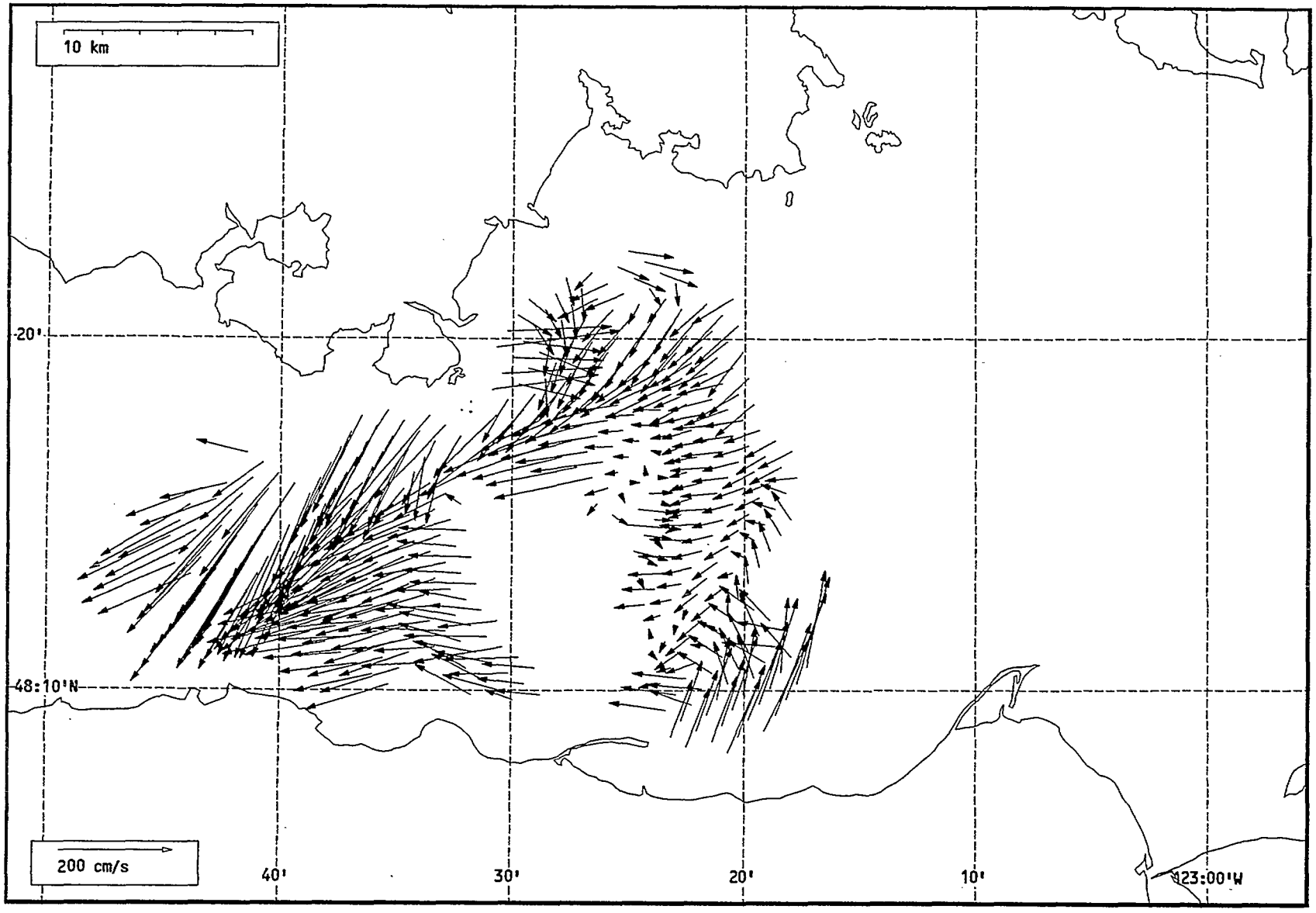

Total current vectors, Juan de Fuca Strait, 1992-07-17 17:00 Z.

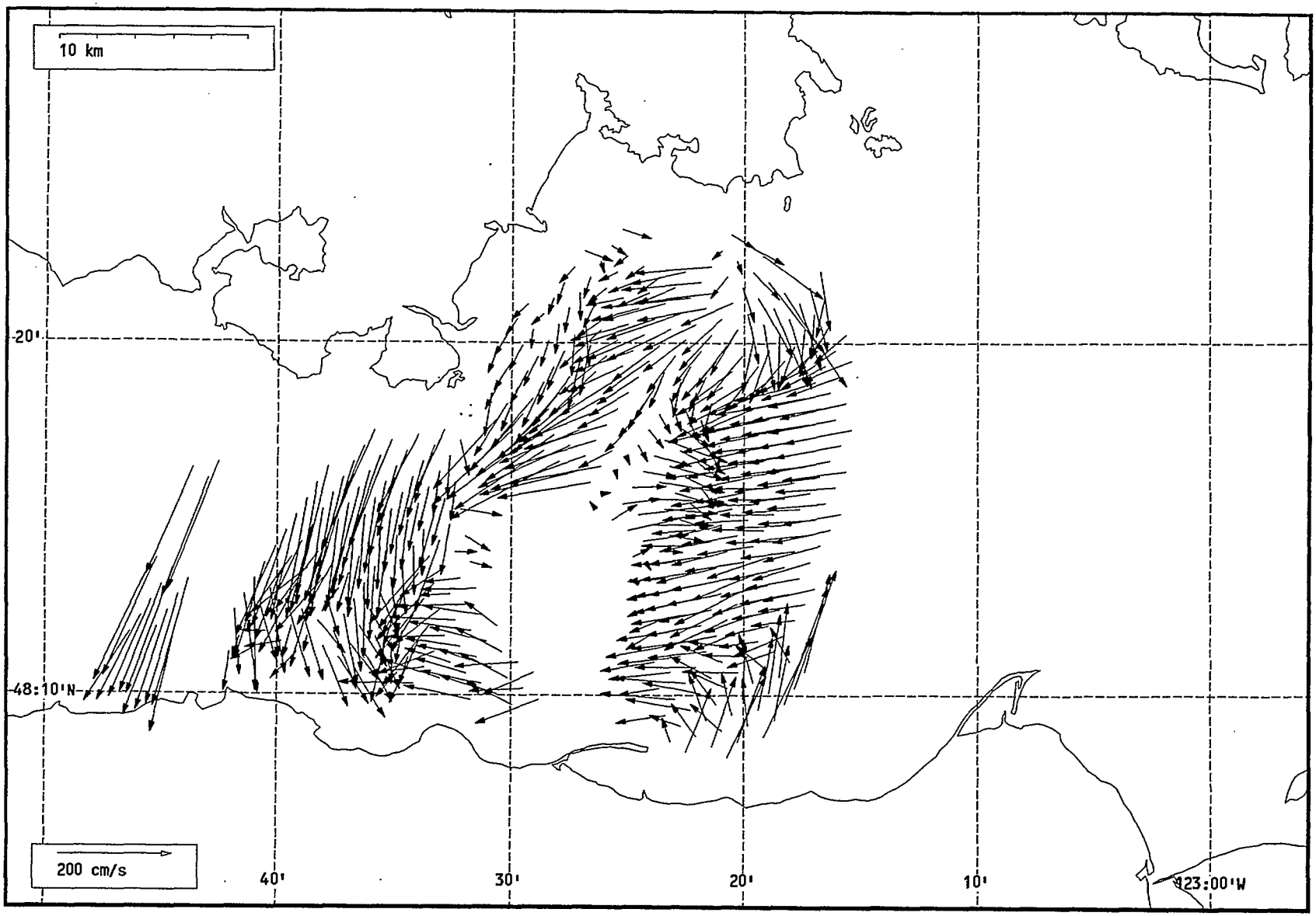

Total current vectors, Juan de Fuca Strait, 1992-07-17 18:00 Z.

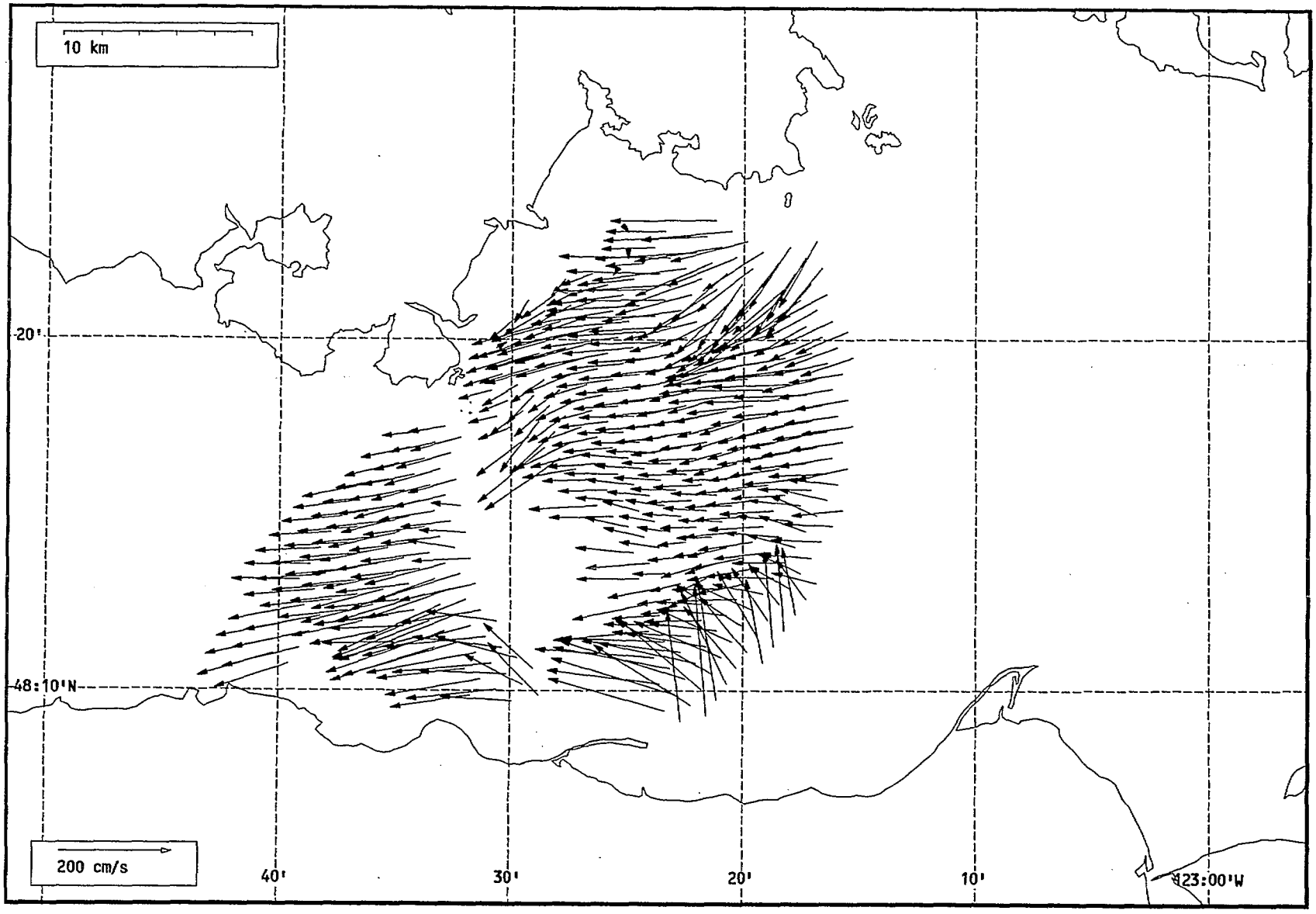

Total current vectors, Juan de Fuca Strait, 1992-07-17 19:00 Z.

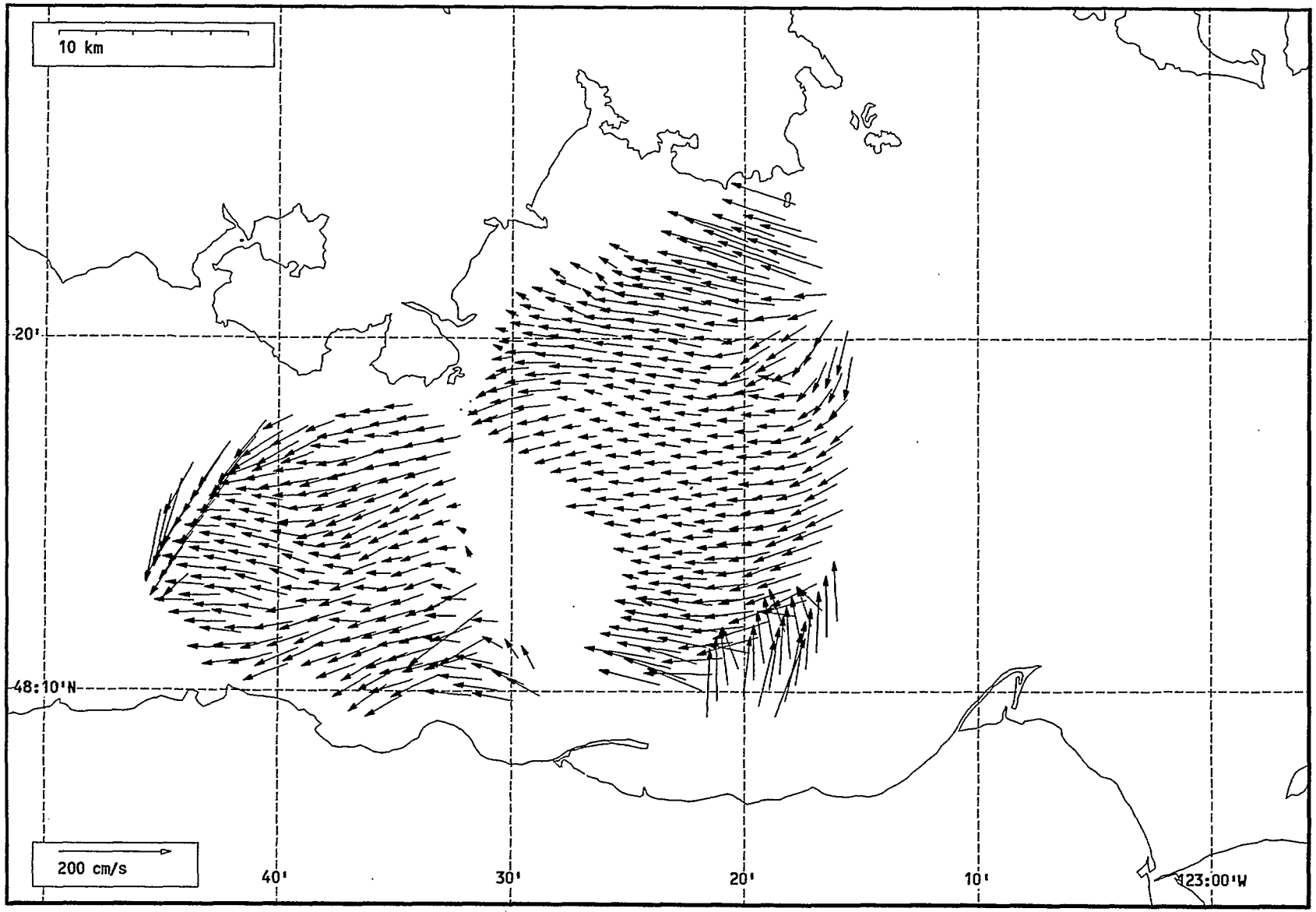

Total current vectors, Juan de Fuca Strait, 1992-07-17 20:00 Z.

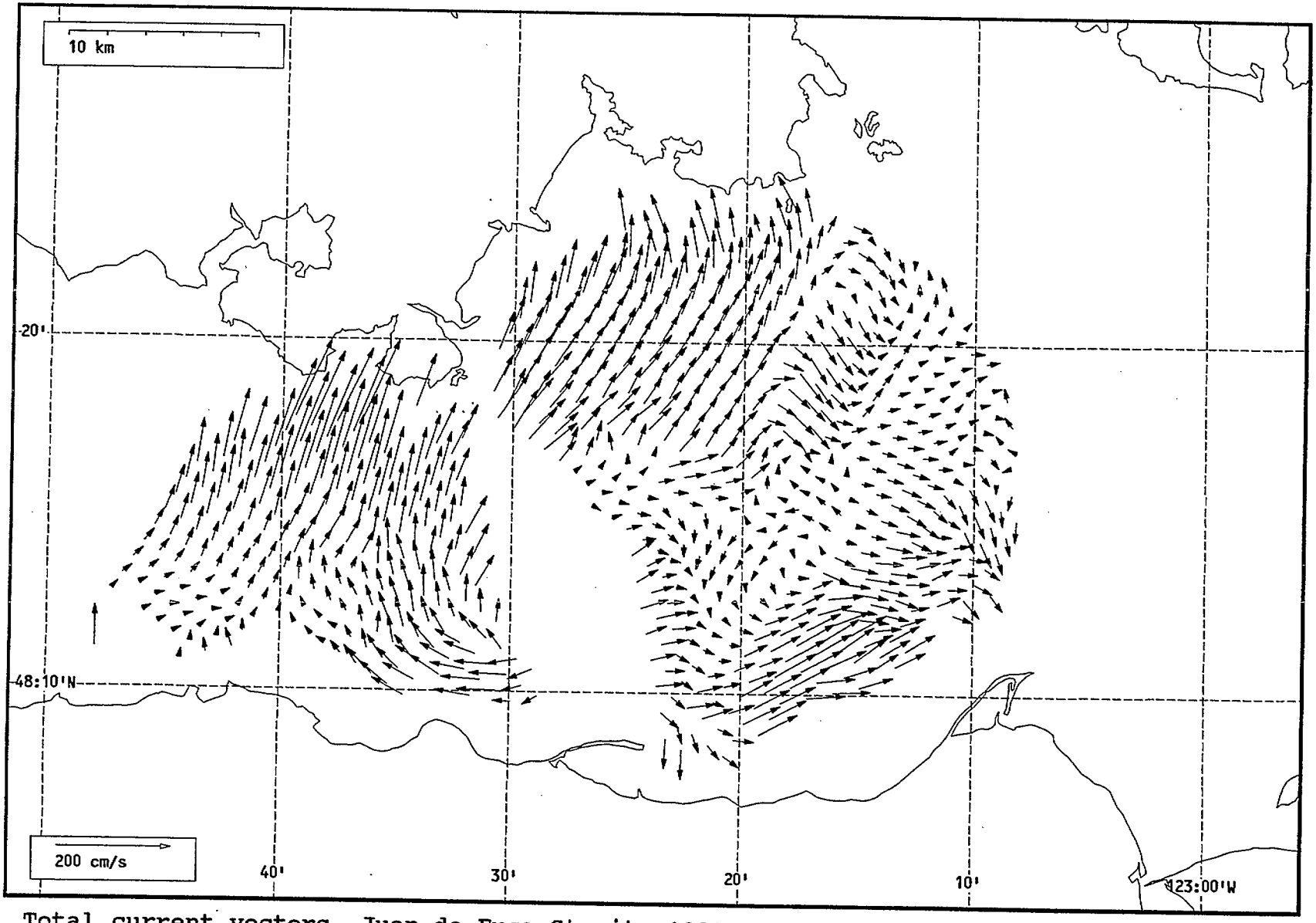

Total current vectors, Juan de Fuca Strait, 1992-07-17 22:00 Z.

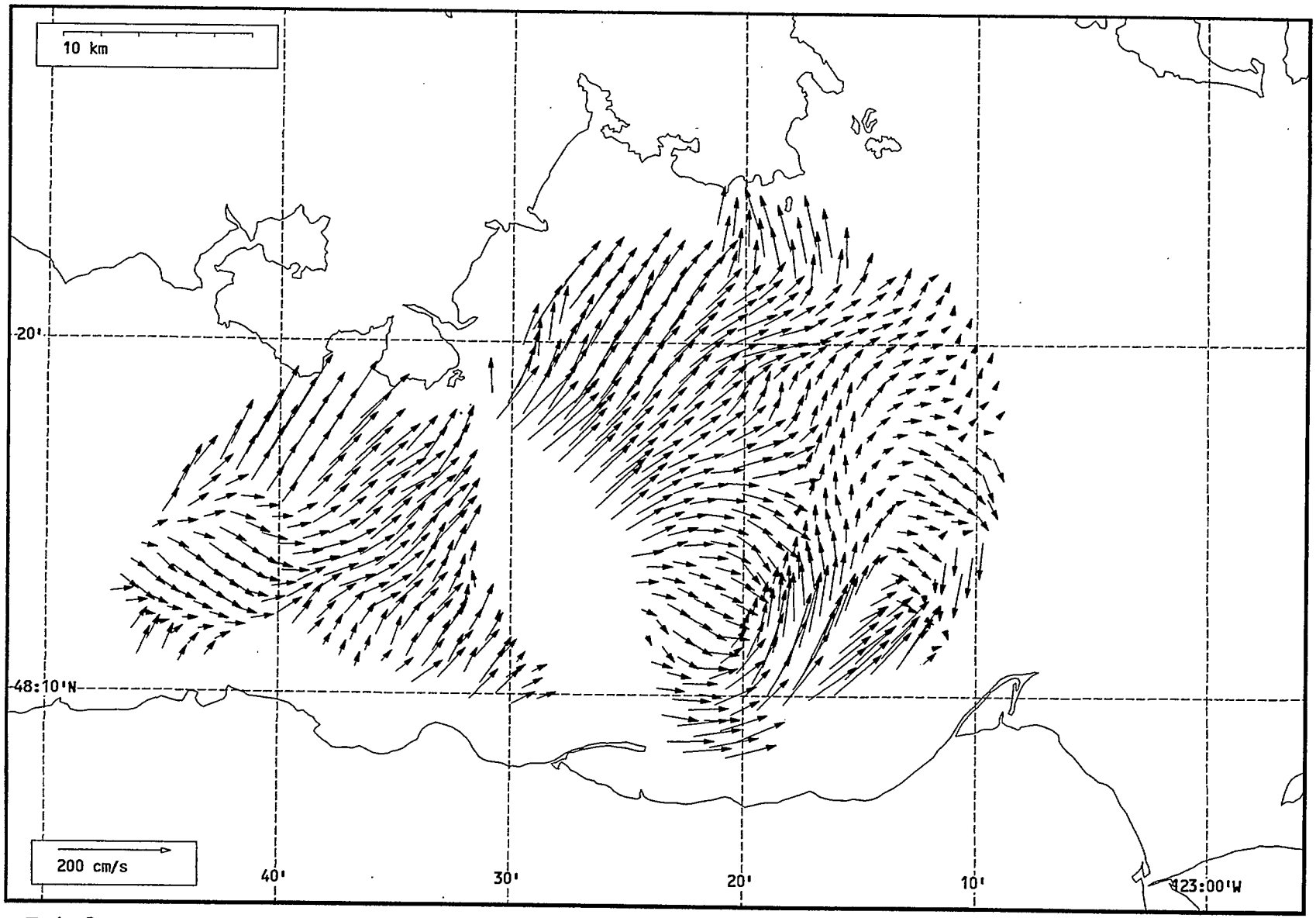

Total current vectors, Juan de Fuca Strait, 1992-07-17 23:00 Z.

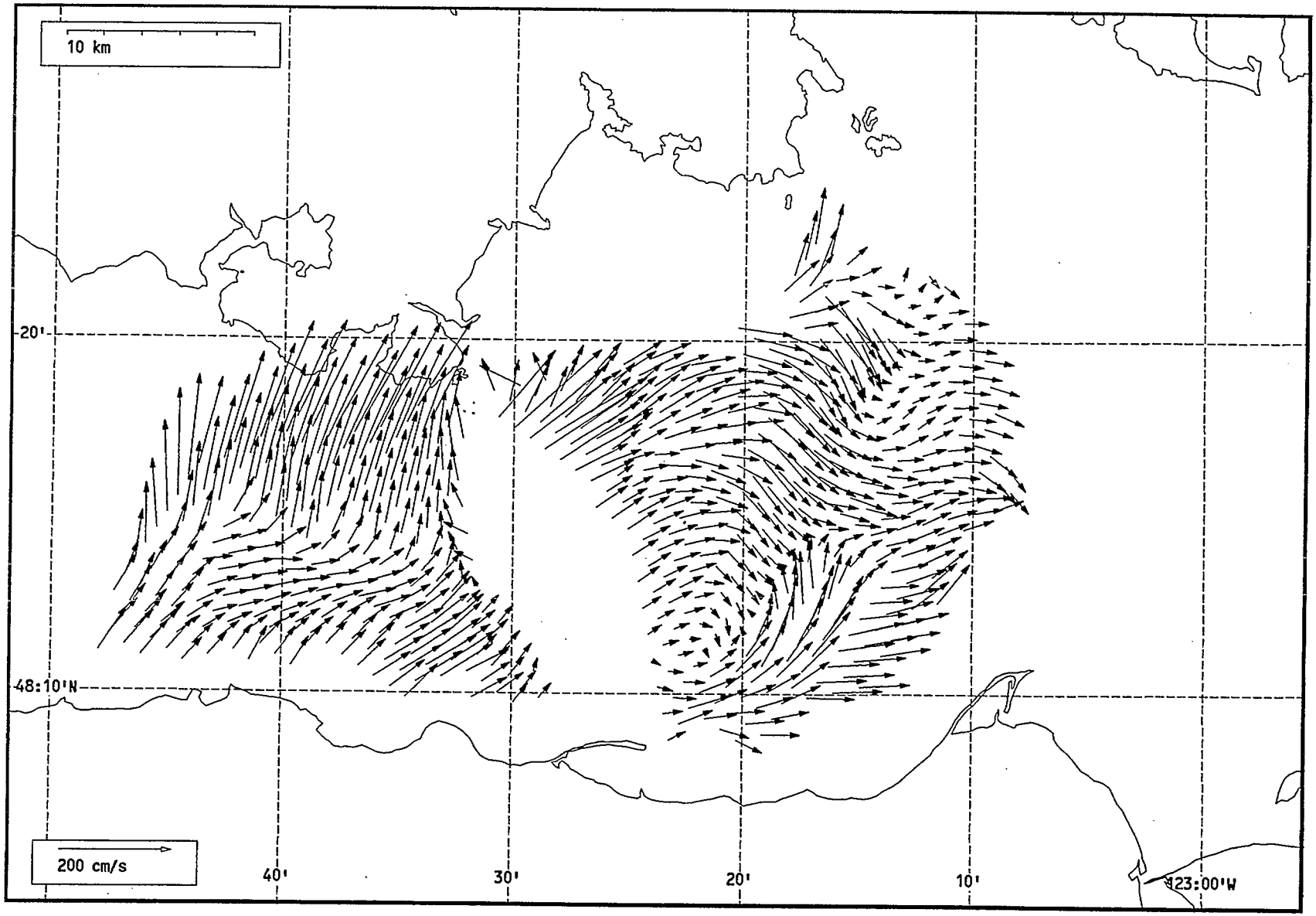

Total current vectors, Juan de Fuca Strait, 1992-07-18 00:00 Z.

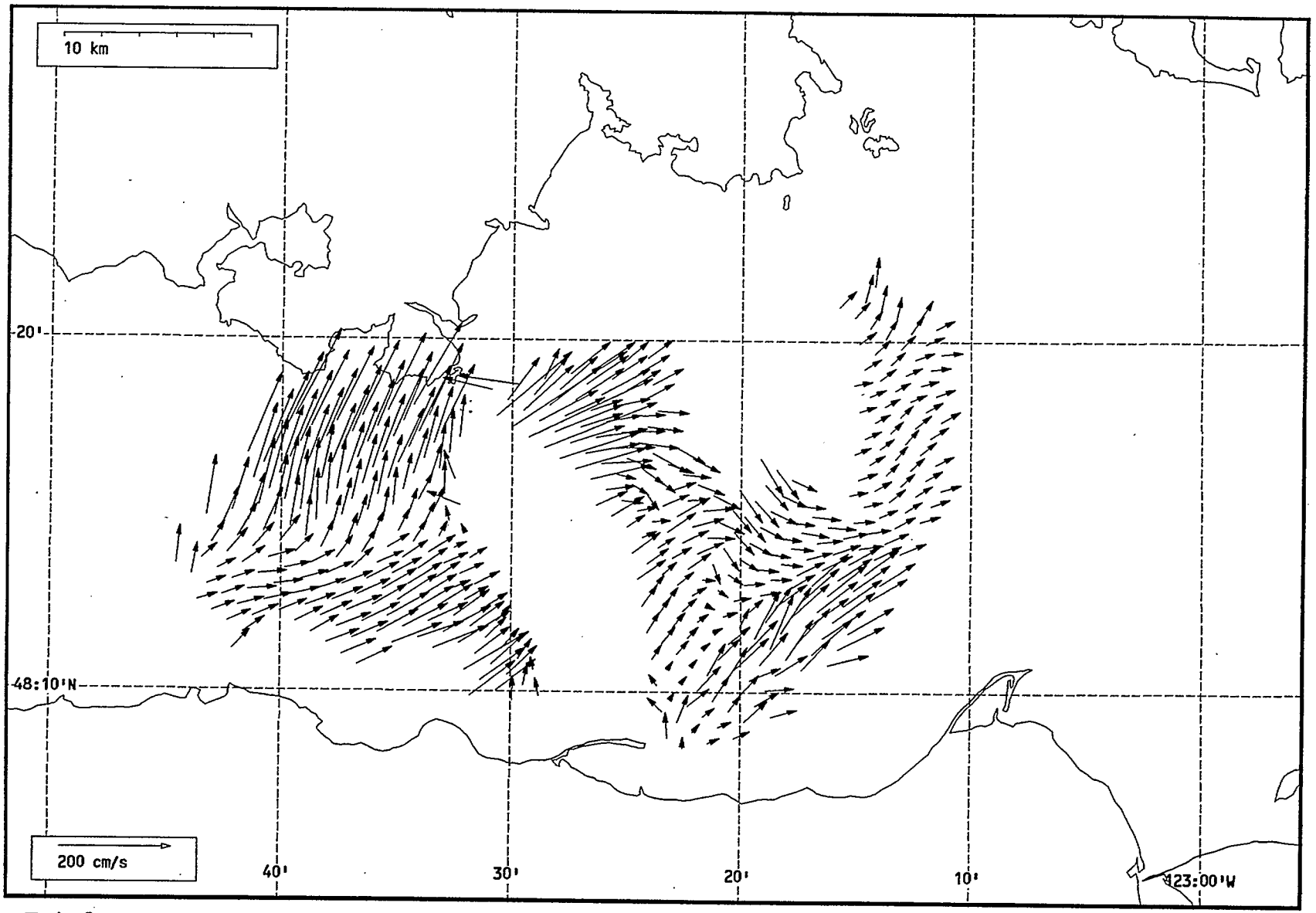

Total current vectors, Juan de Fuca Strait, 1992-07-18 01:00 Z.

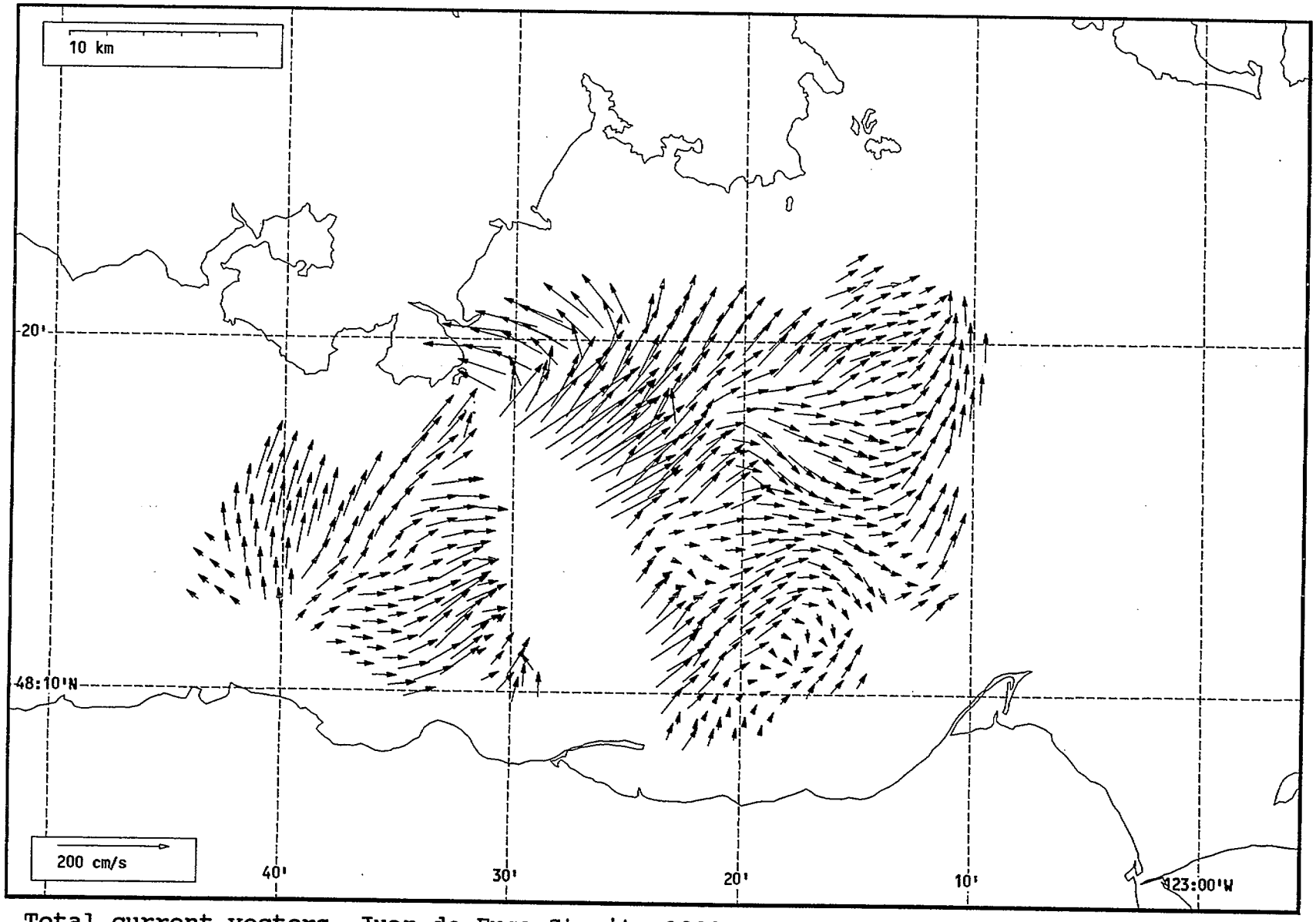

Total current vectors, Juan de Fuca Strait, 1992-07-18 02:00 Z.

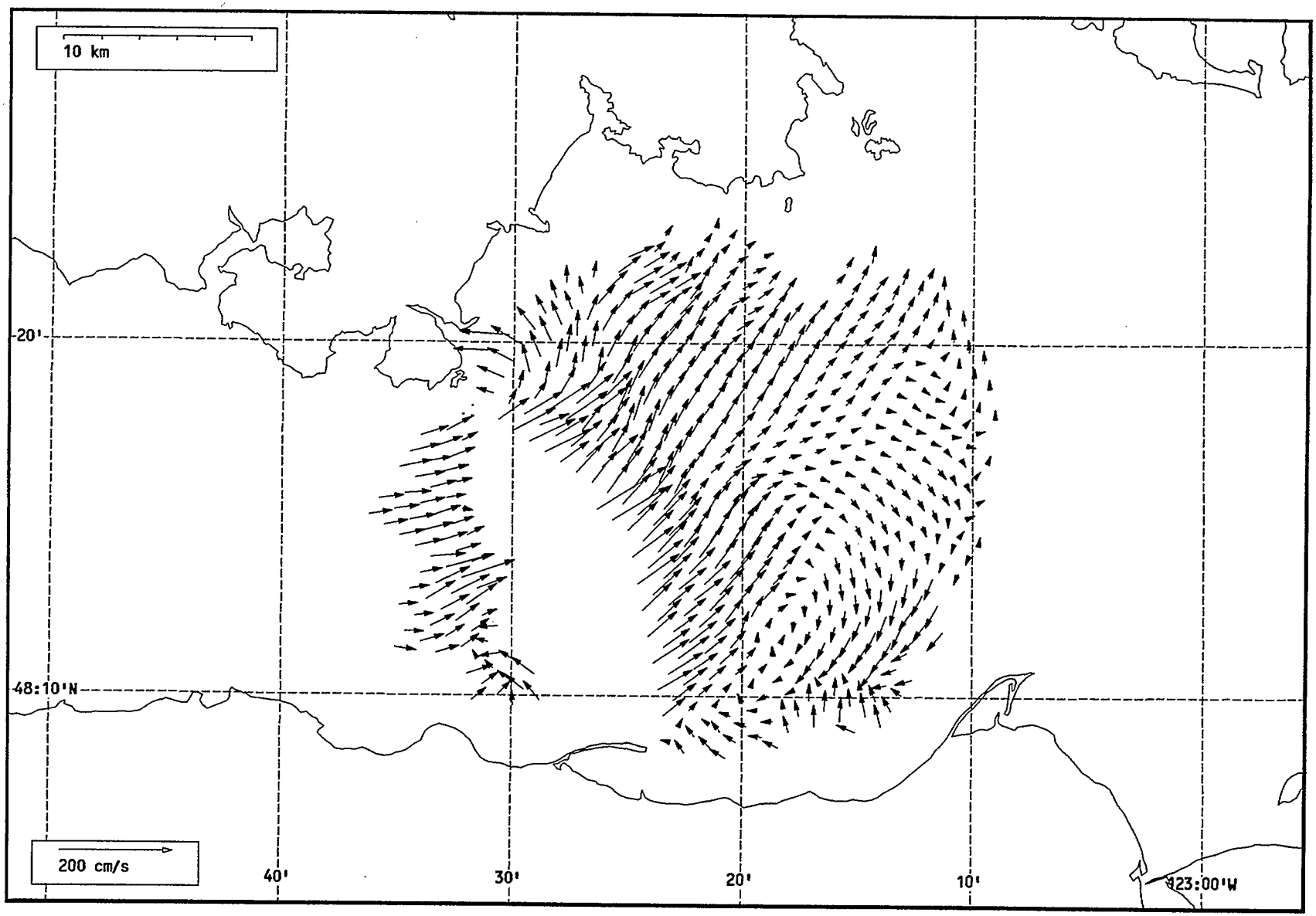

Total current vectors, Juan de Fuca Strait, 1992-07-18 03:00 Z.

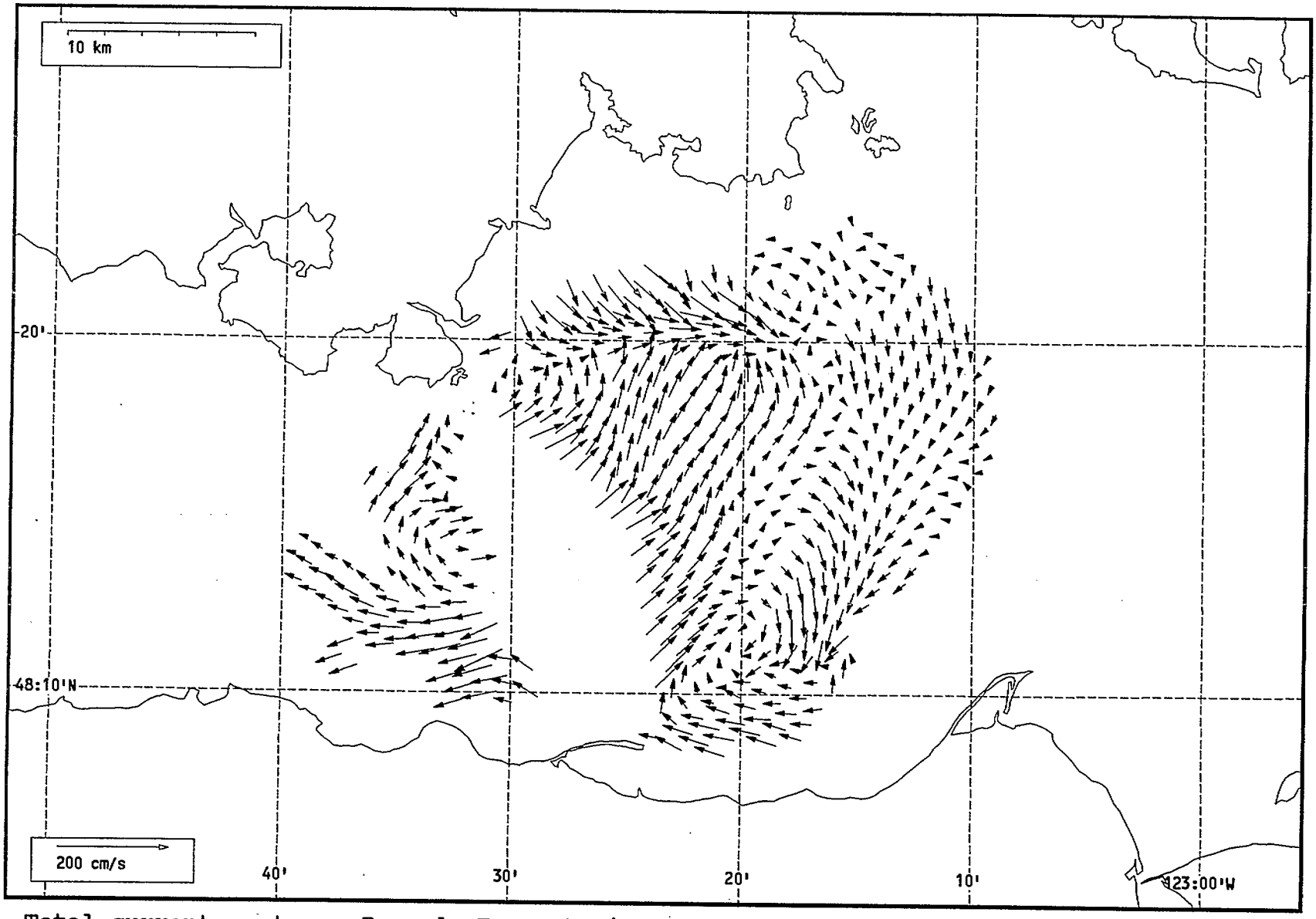

Total current vectors, Juan de Fuca Strait, 1992-07-18 04:00 Z.

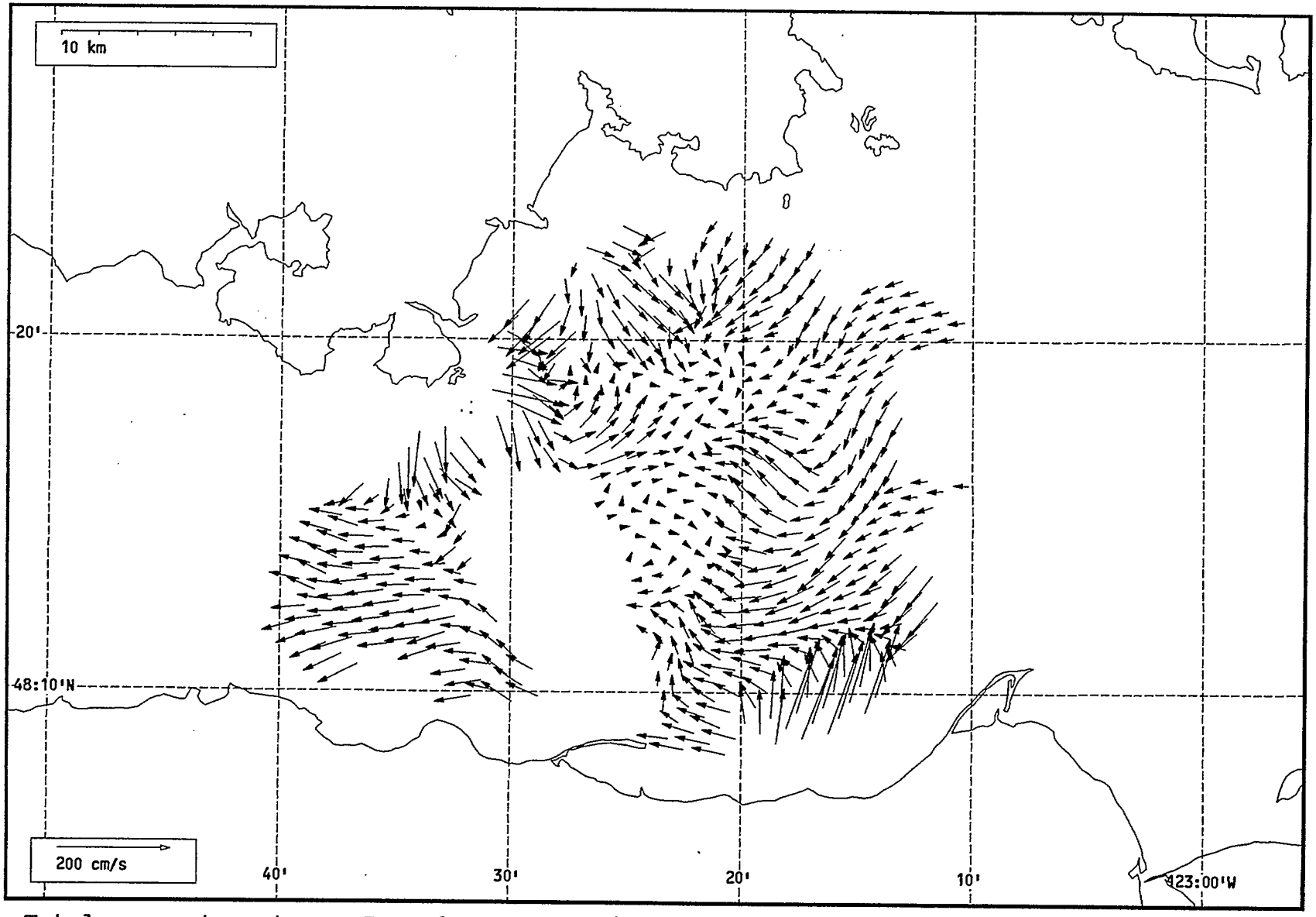

Total current vectors, Juan de Fuca Strait, 1992-07-18 05:00 Z.

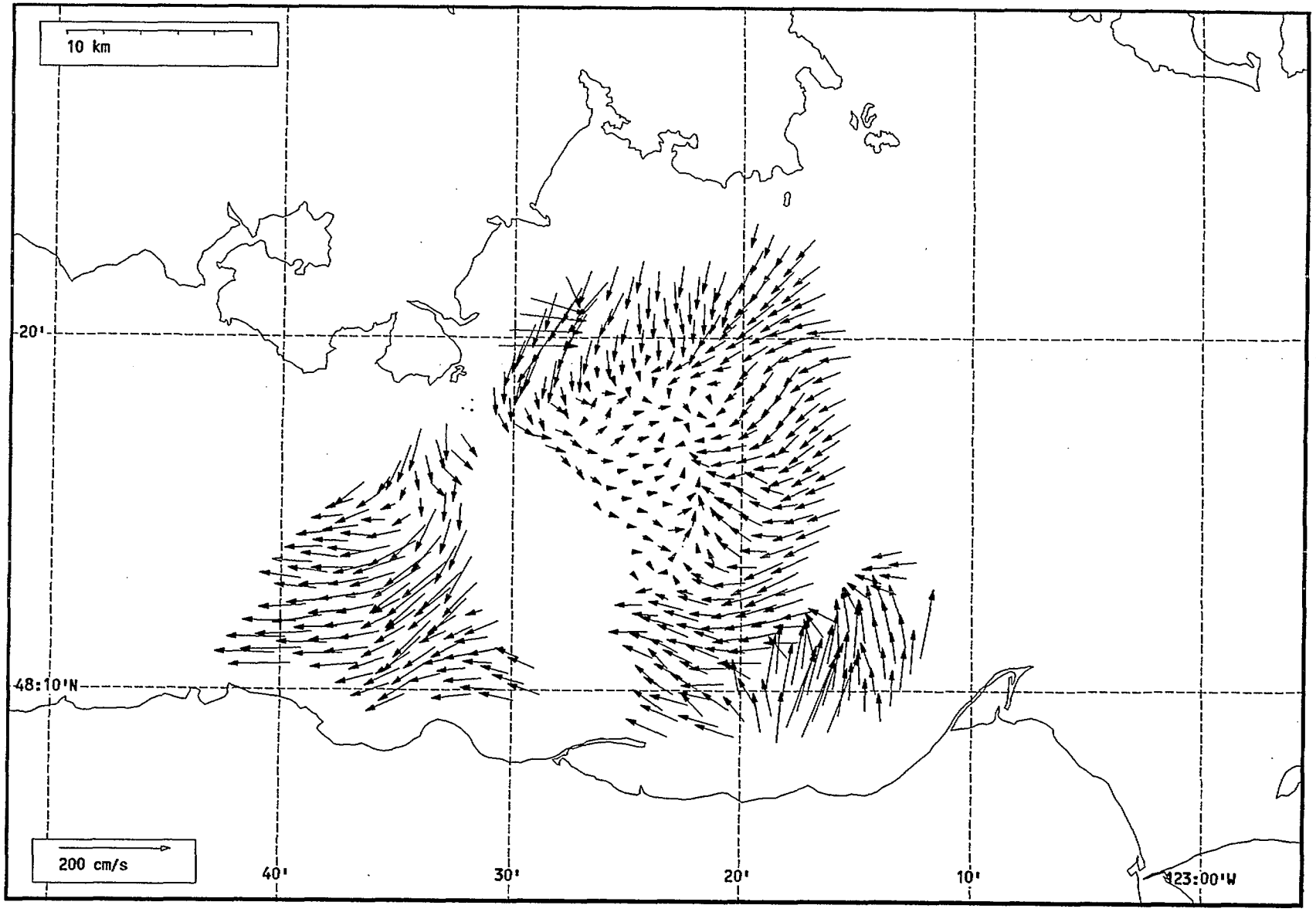

Total current vectors, Juan de Fuca Strait, 1992-07-18 06:00 Z.

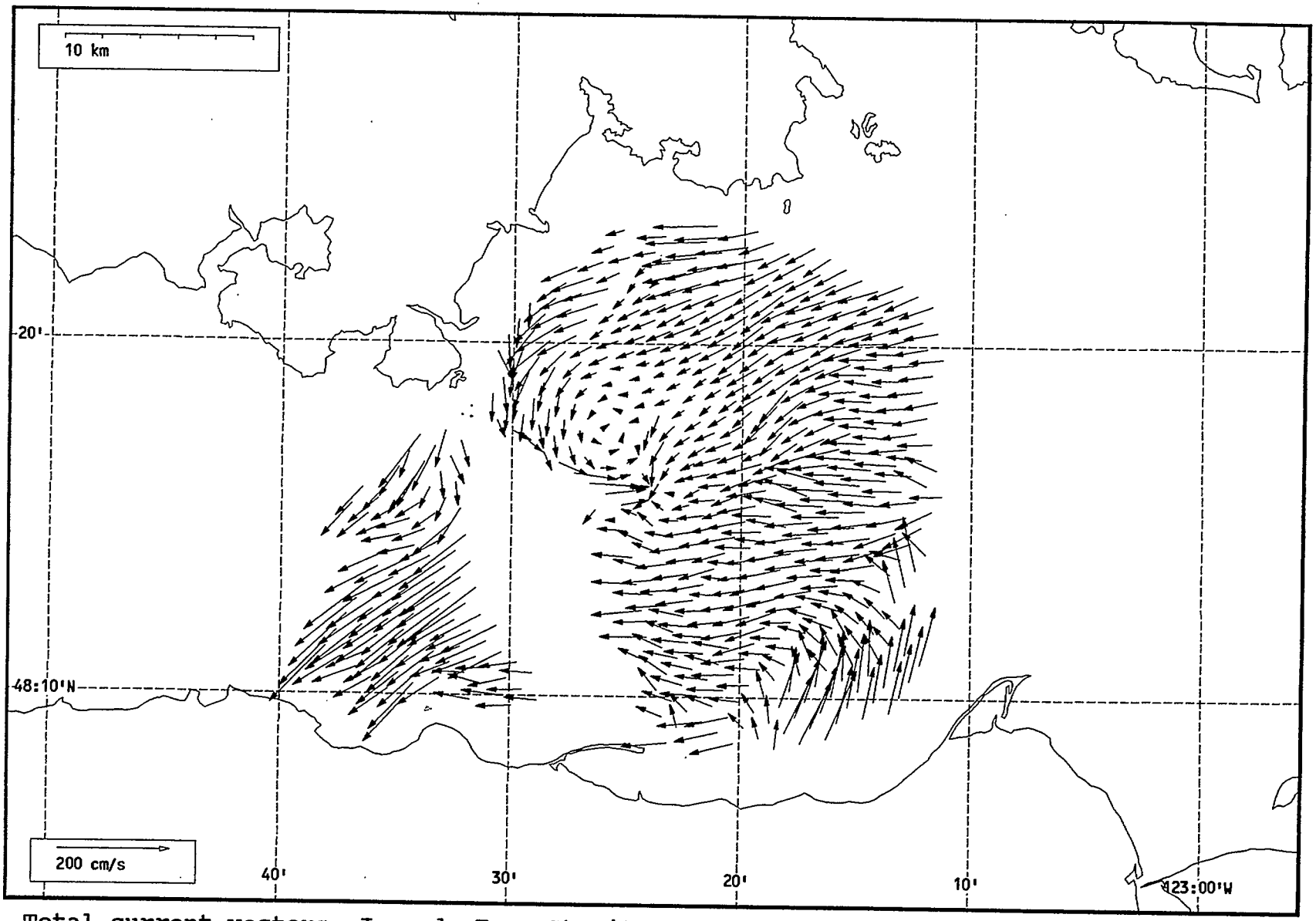

Total current vectors, Juan de Fuca Strait, 1992-07-18 07:00 Z.

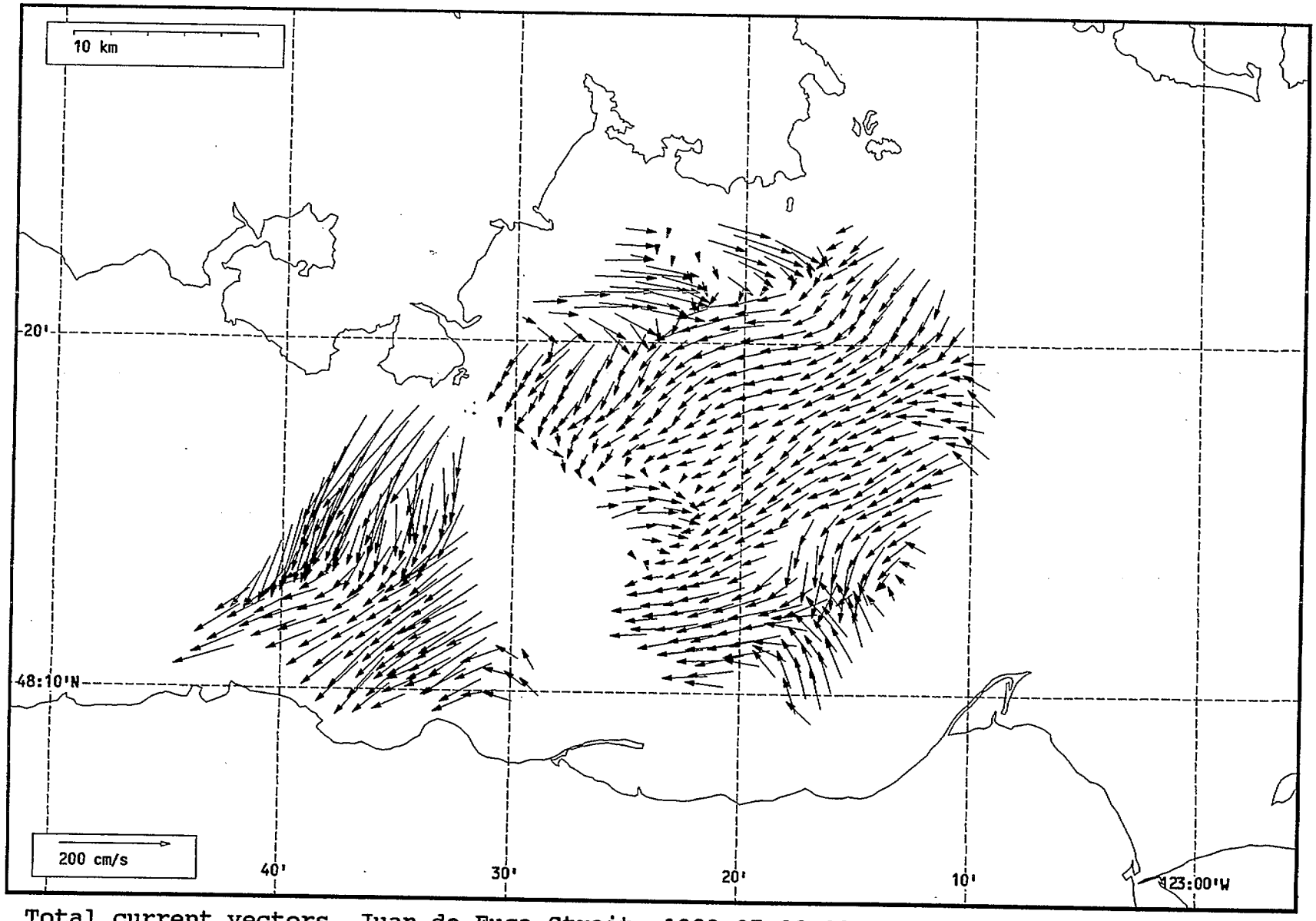

Total current vectors, Juan de Fuca Strait, 1992-07-18 08:00 Z.

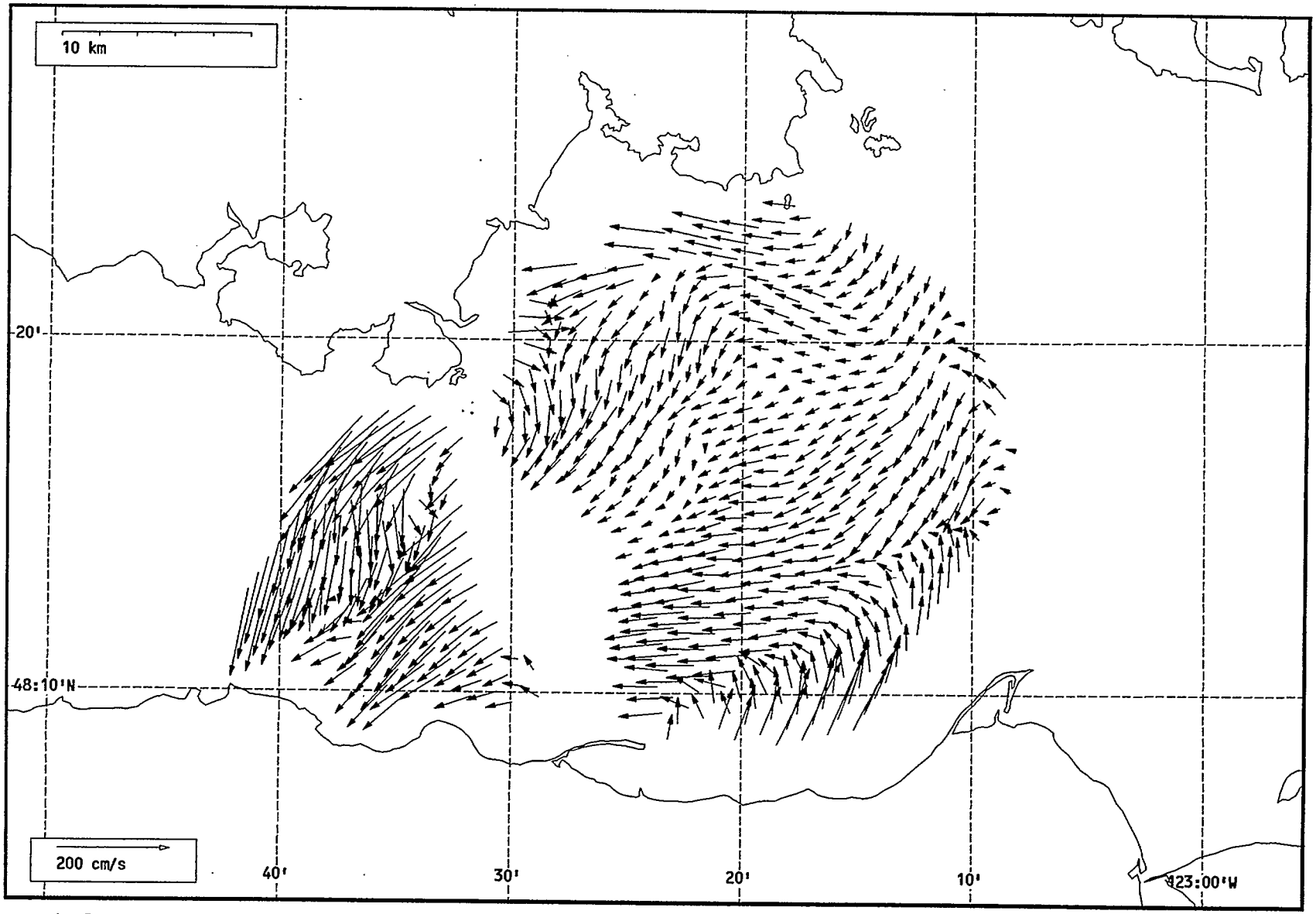

Total current vectors, Juan de Fuca Strait, 1992-07-18 09:00 Z.

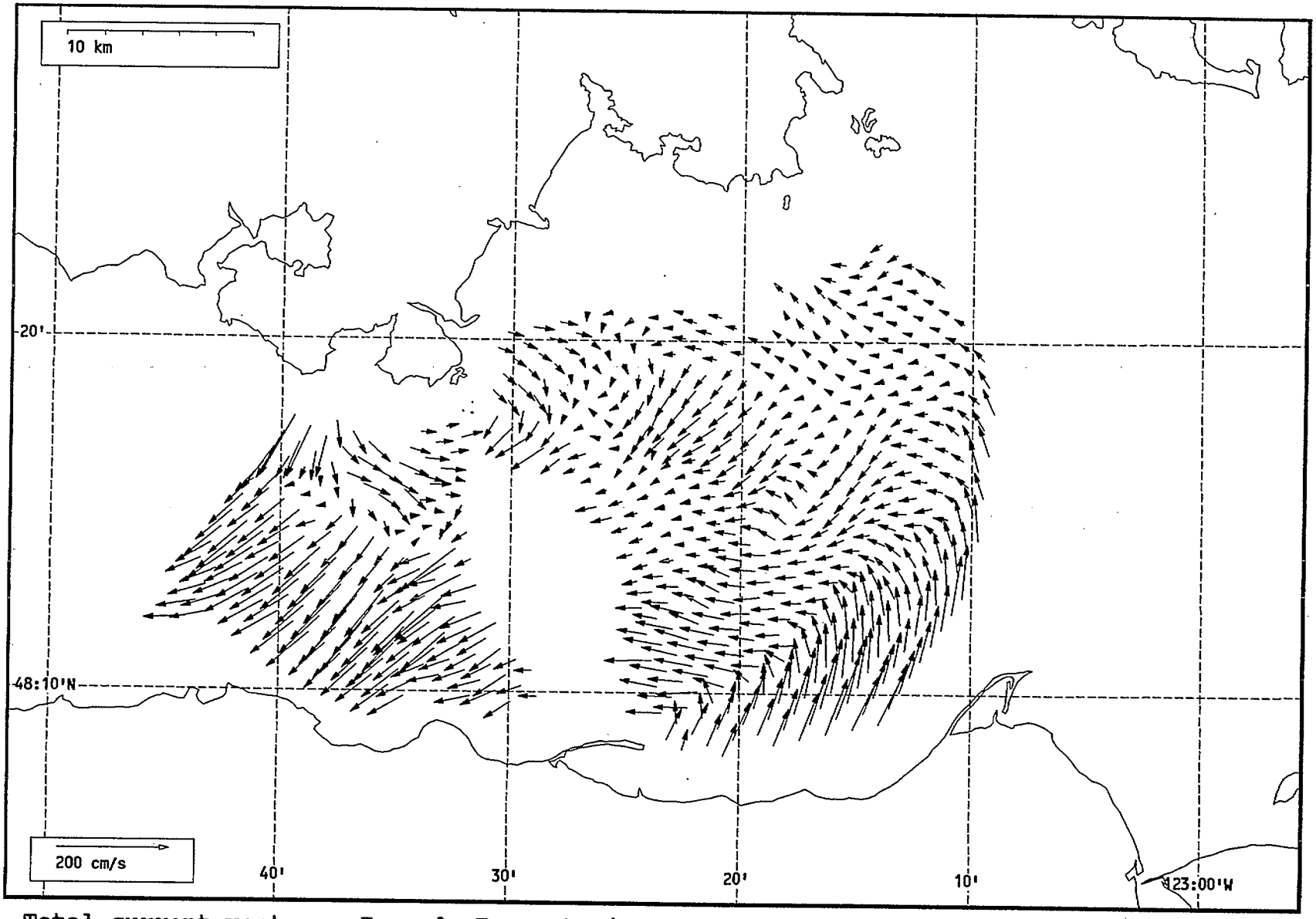

Total current vectors, Juan de Fuca Strait, 1992-07-18 10:00 Z.

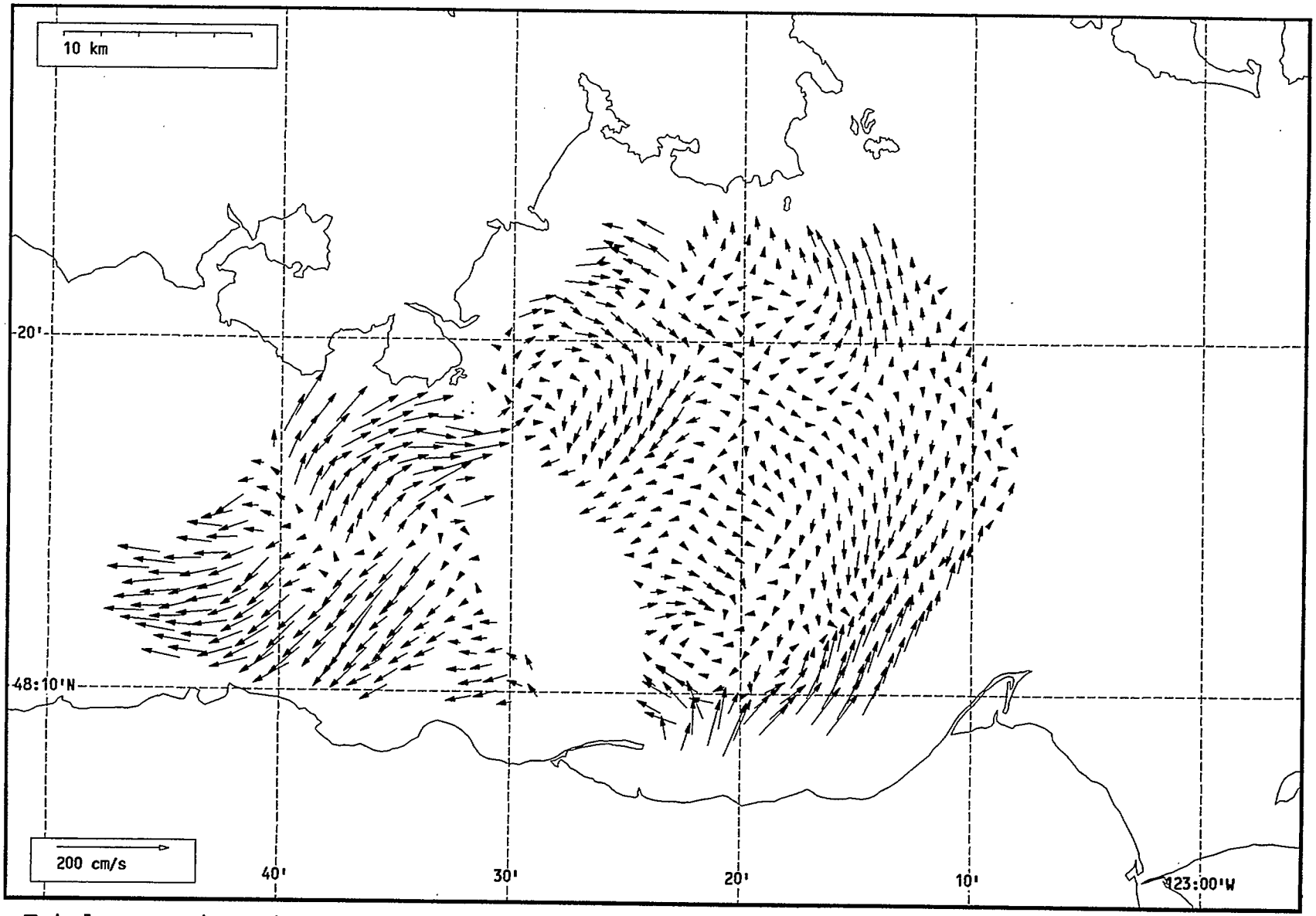

Total current vectors, Juan de Fuca Strait, 1992-07-18 11:00 Z.

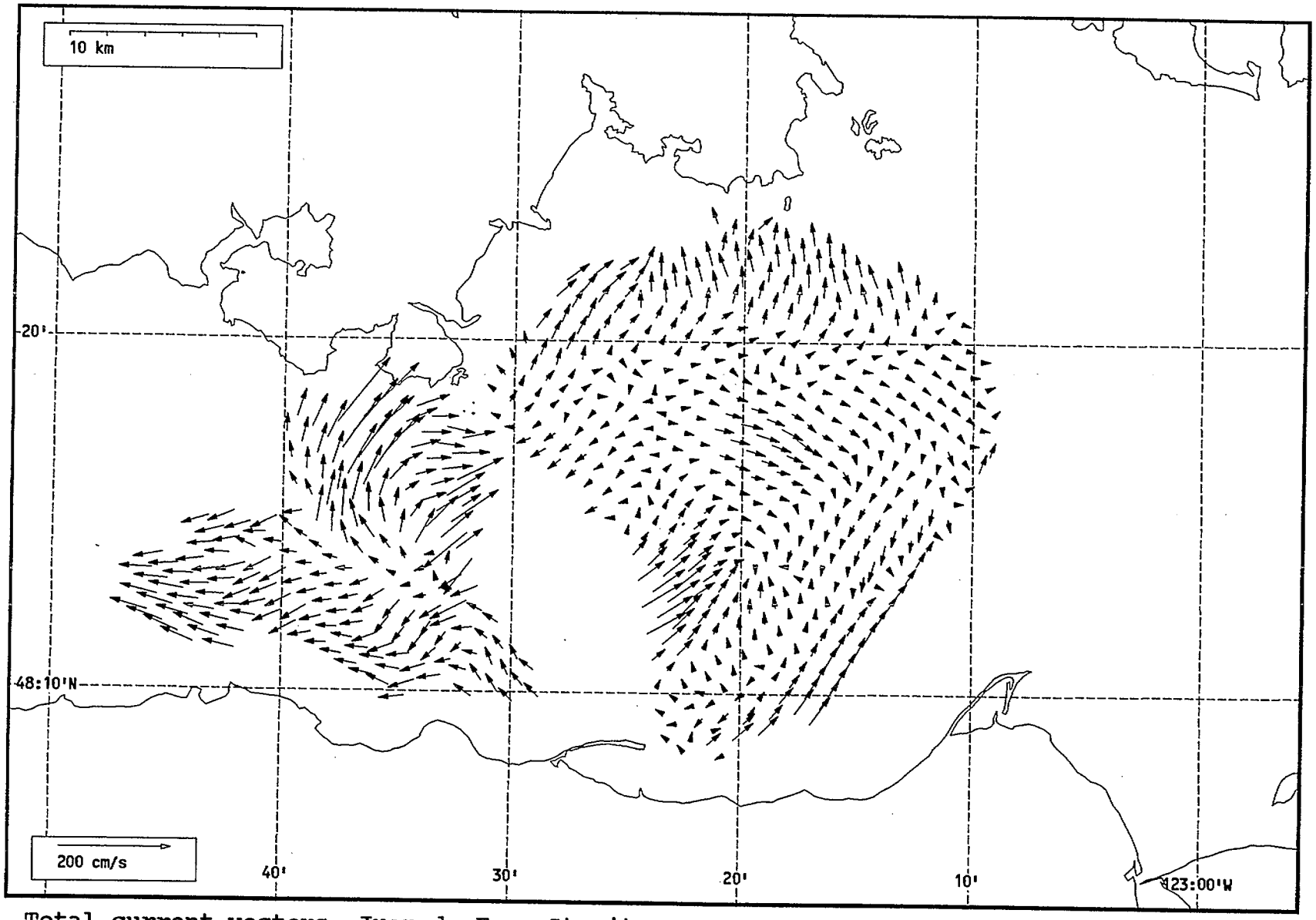

Total current vectors, Juan de Fuca Strait, 1992-07-18 12:00 Z.

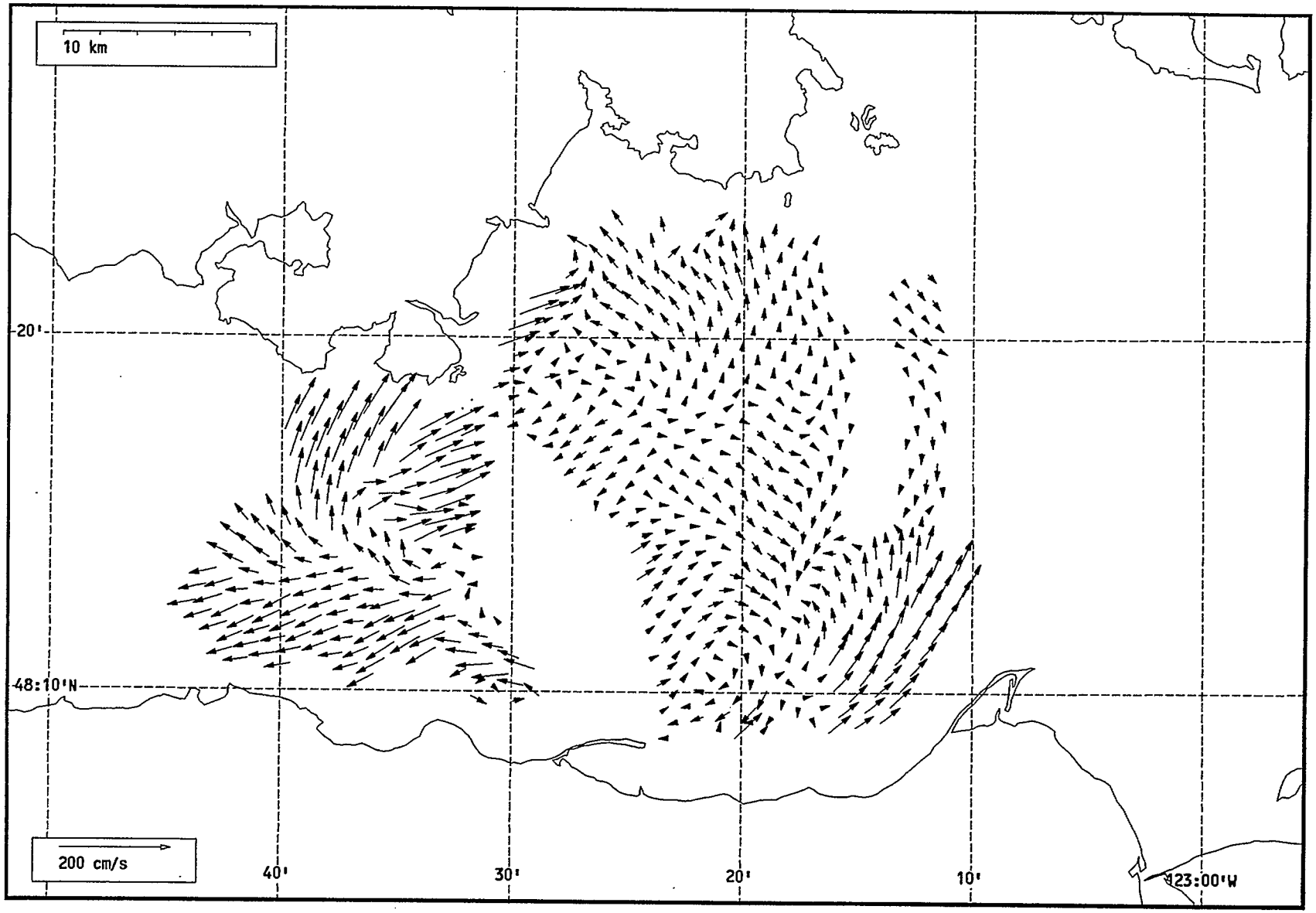

Total current vectors, Juan de Fuca Strait, 1992-07-18 13:00 Z.

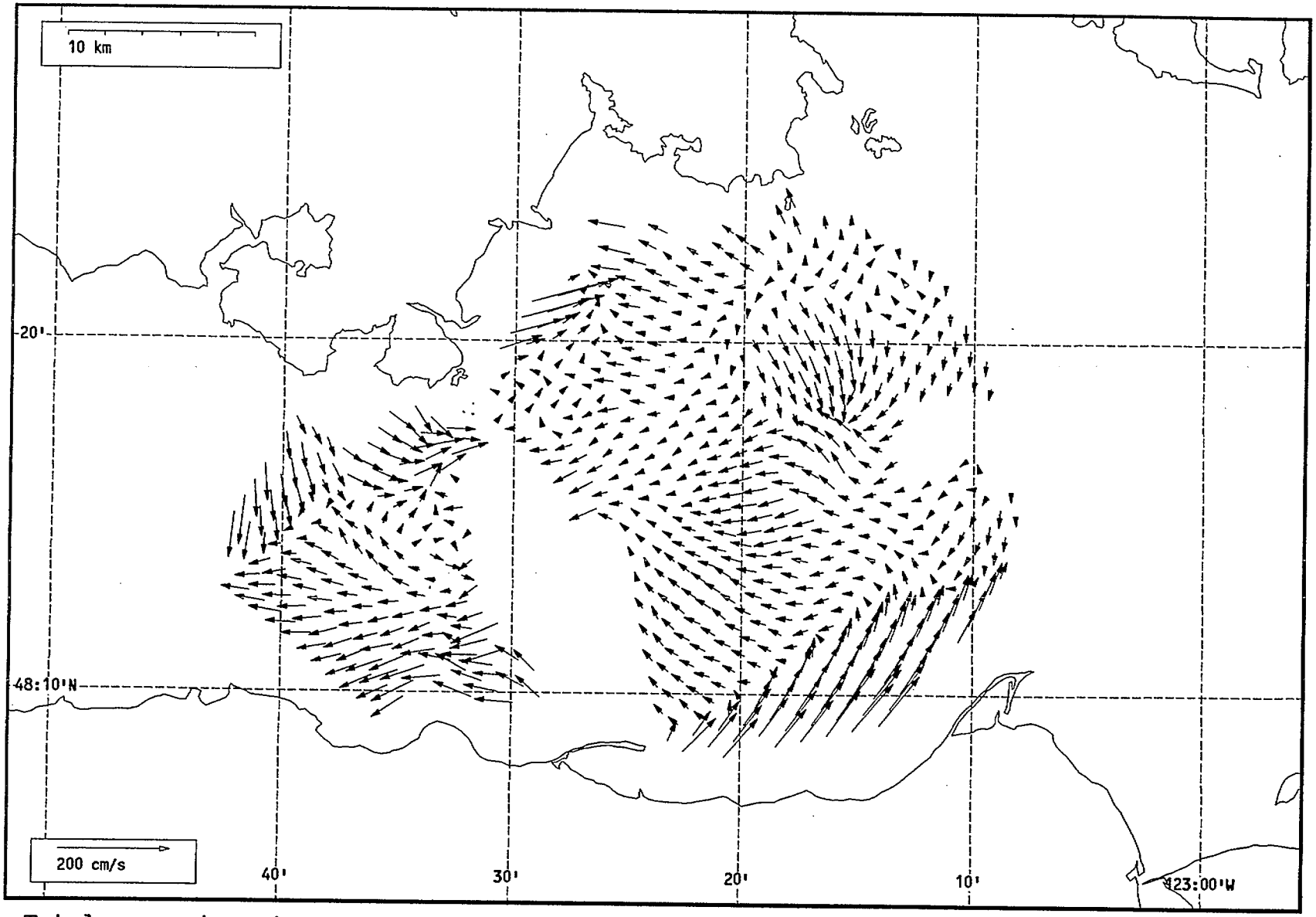

Total current vectors, Juan de Fuca Strait, 1992-07-18 14:00 Z.

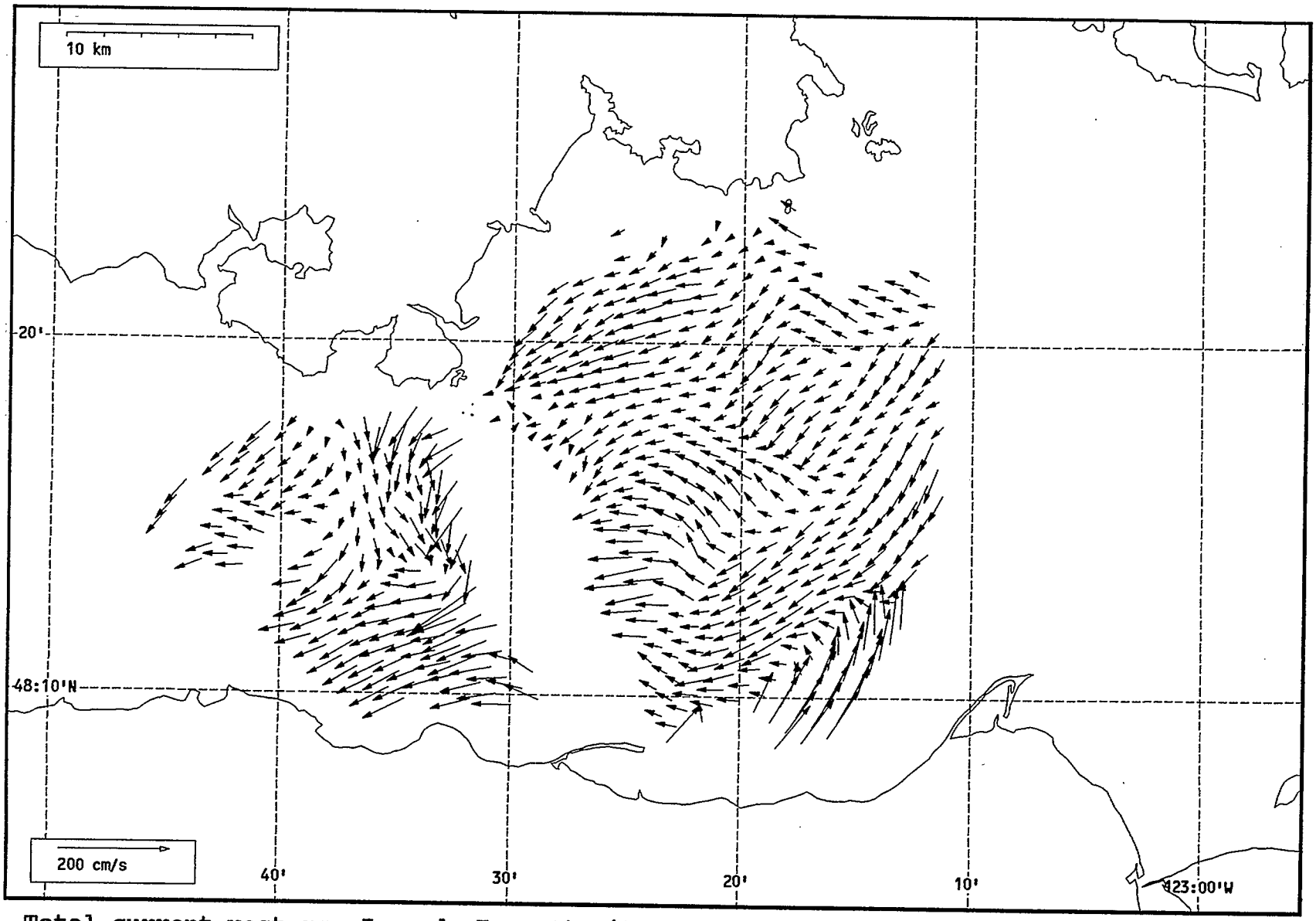

Total current vectors, Juan de Fuca Strait, 1992-07-18 15:00 Z.

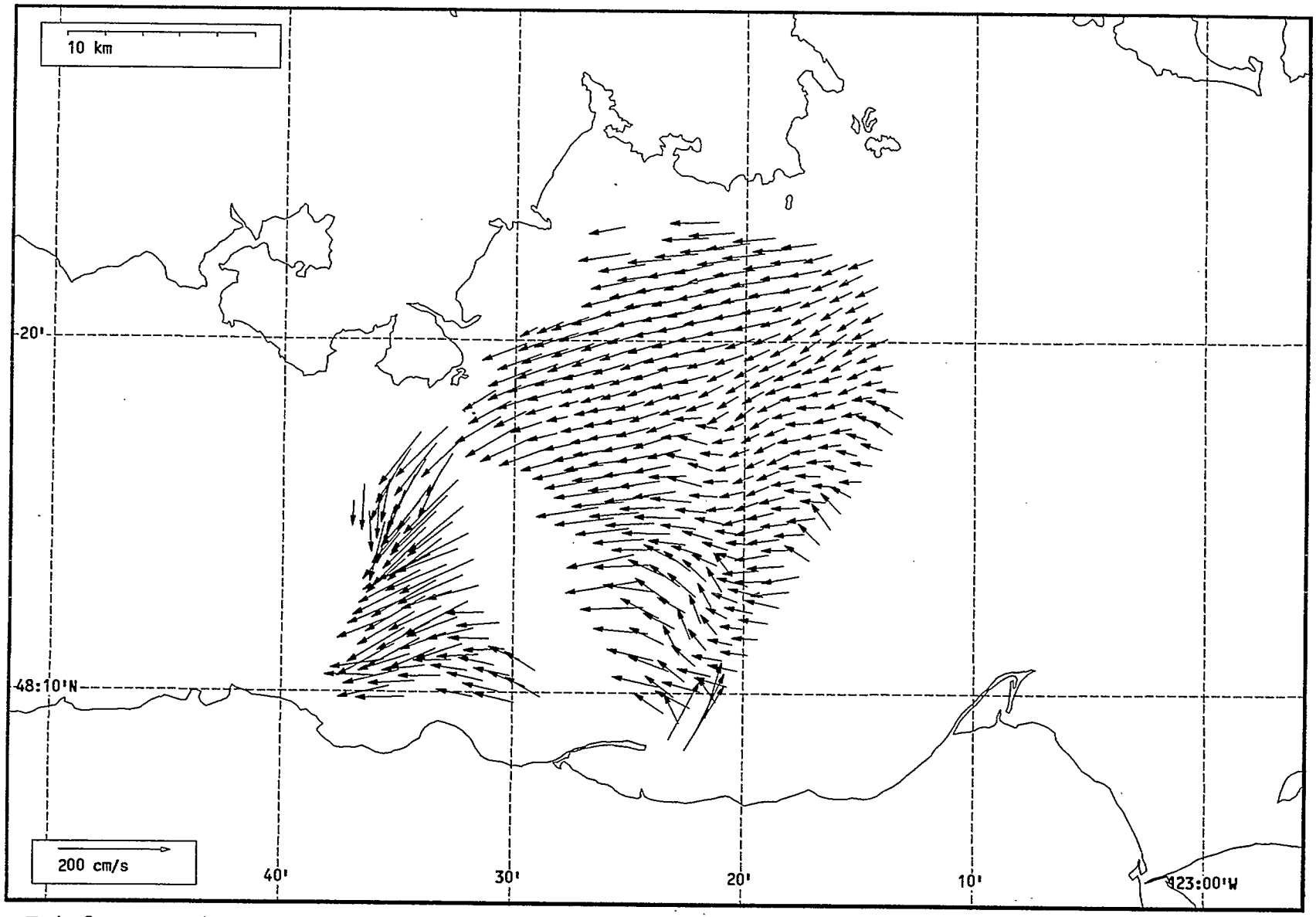

Total current vectors, Juan de Fuca Strait, 1992-07-18 16:00 Z.

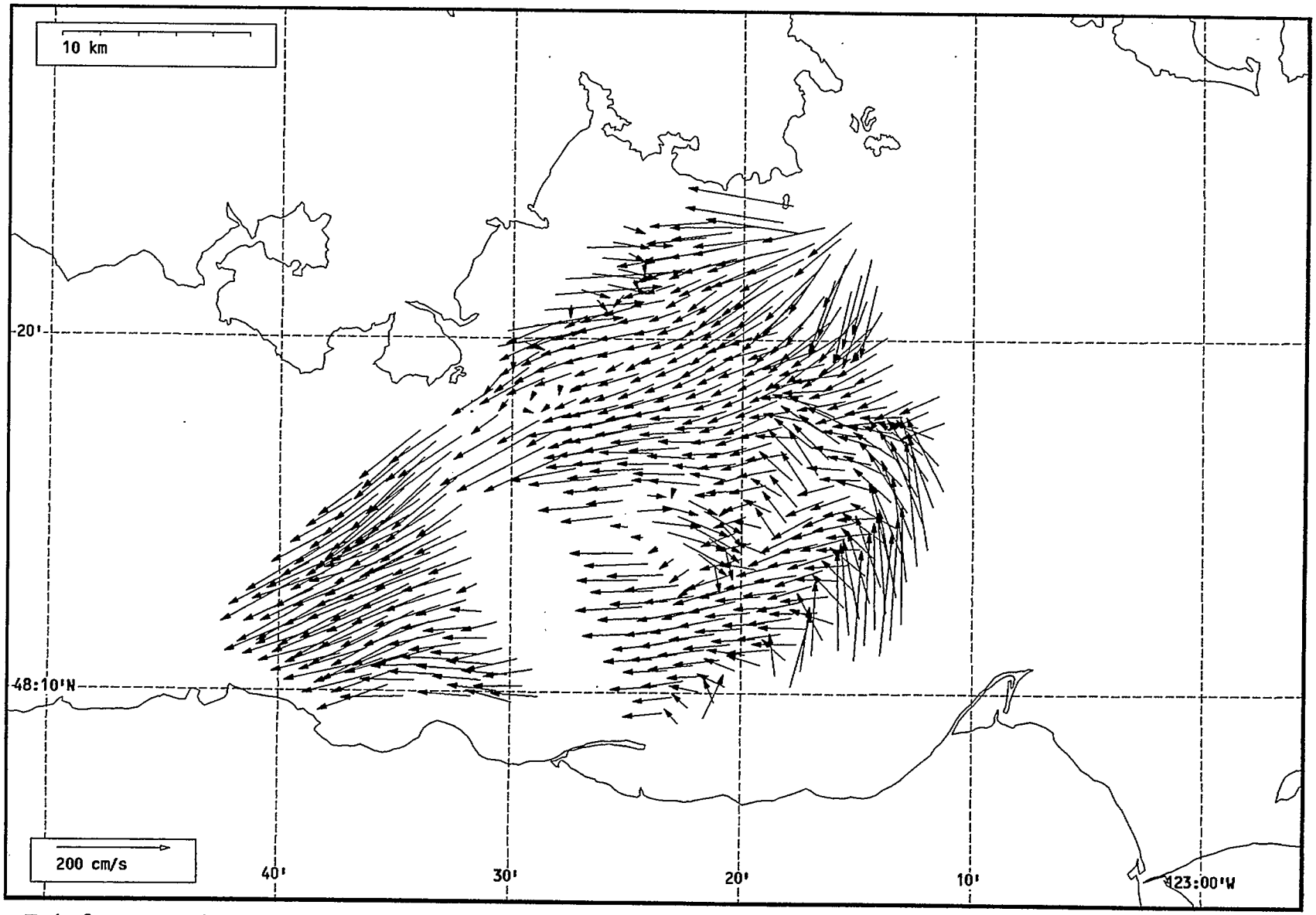

Total current vectors, Juan de Fuca Strait, 1992-07-18 17:00 Z.

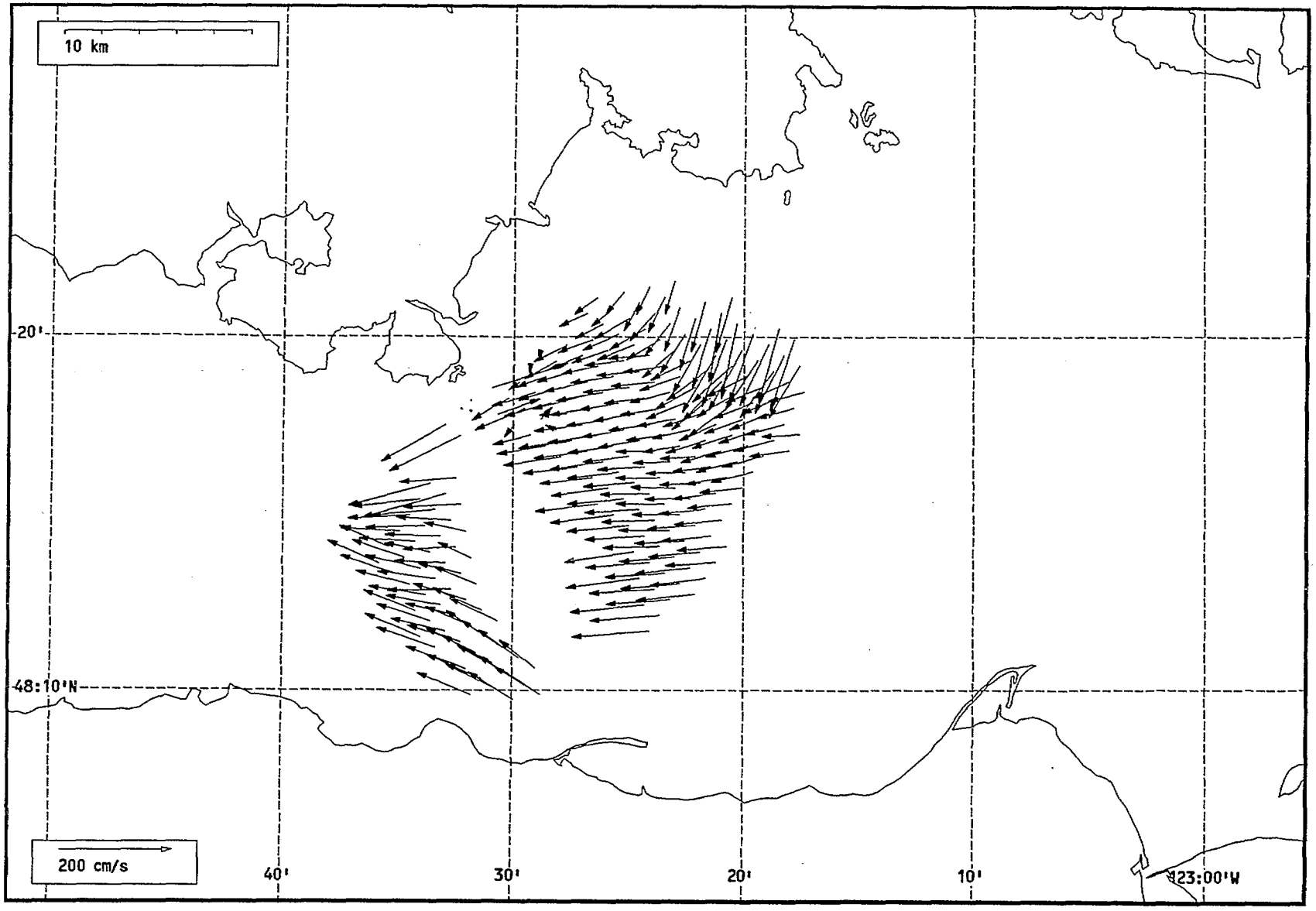

Total current vectors, Juan de Fuca Strait, 1992-07-18 18:00 Z.

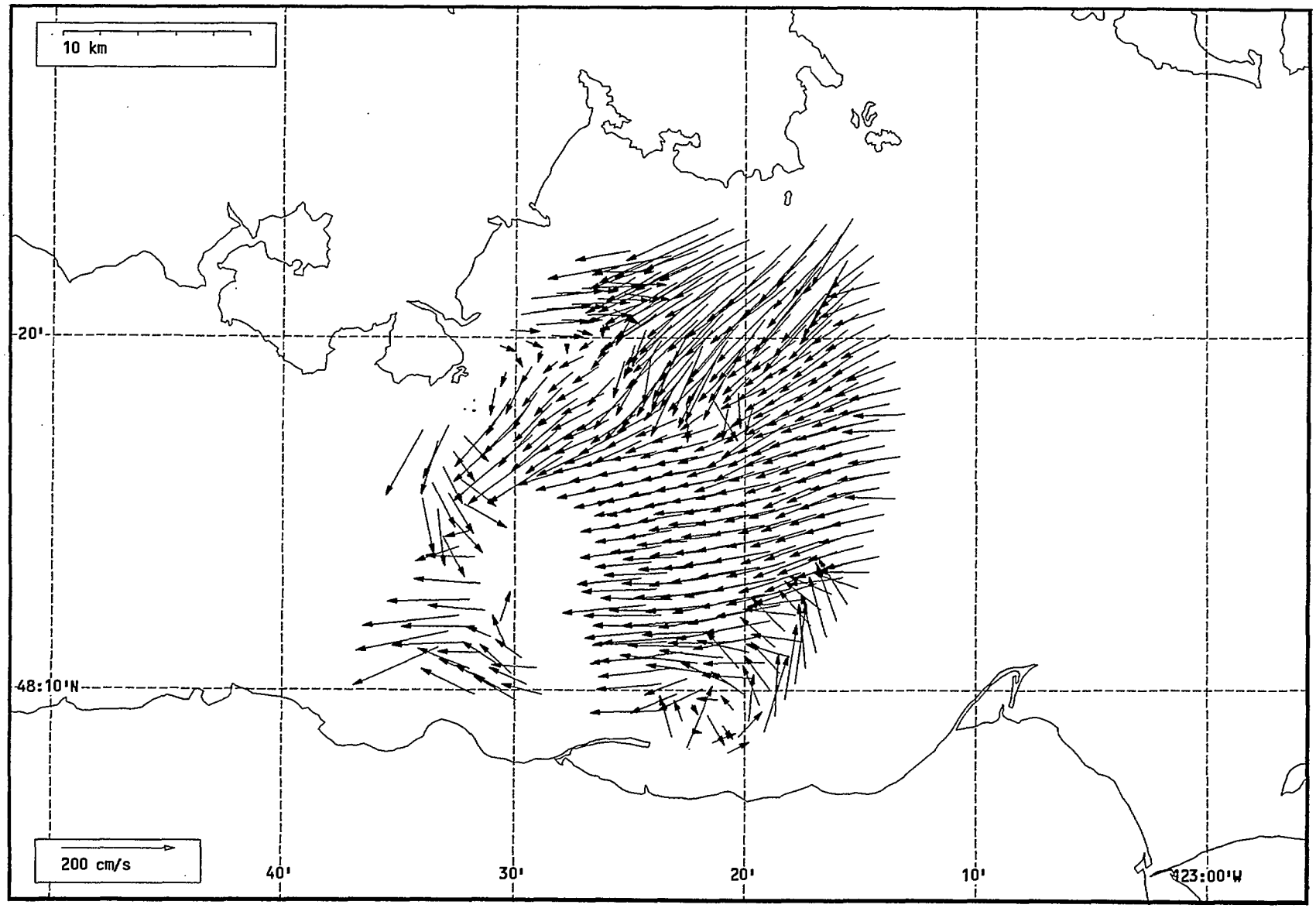

Total current vectors, Juan de Fuca Strait, 1992-07-18 19:00 Z.

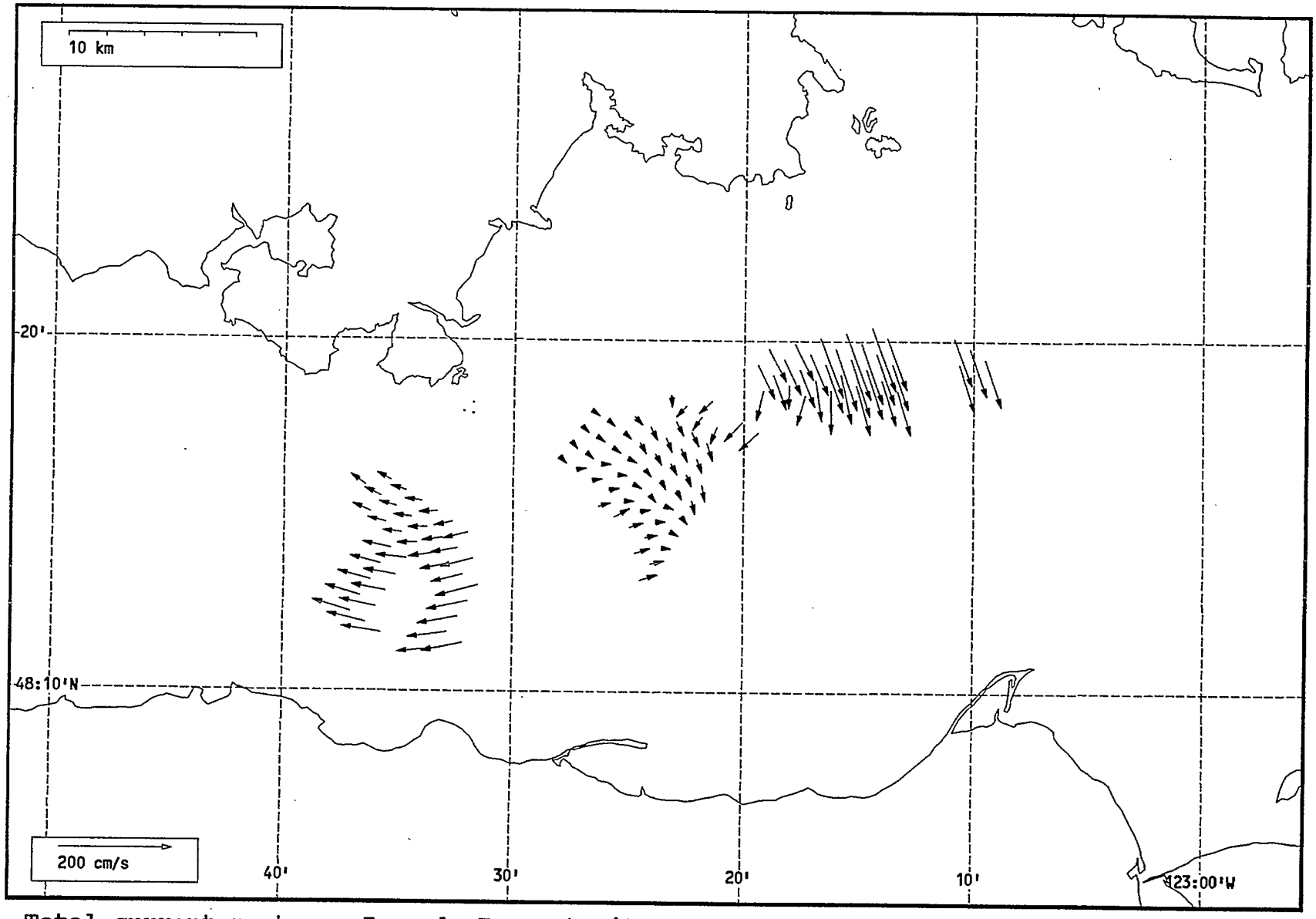

Total current vectors, Juan de Fuca Strait, 1992-07-18 20:00 Z.

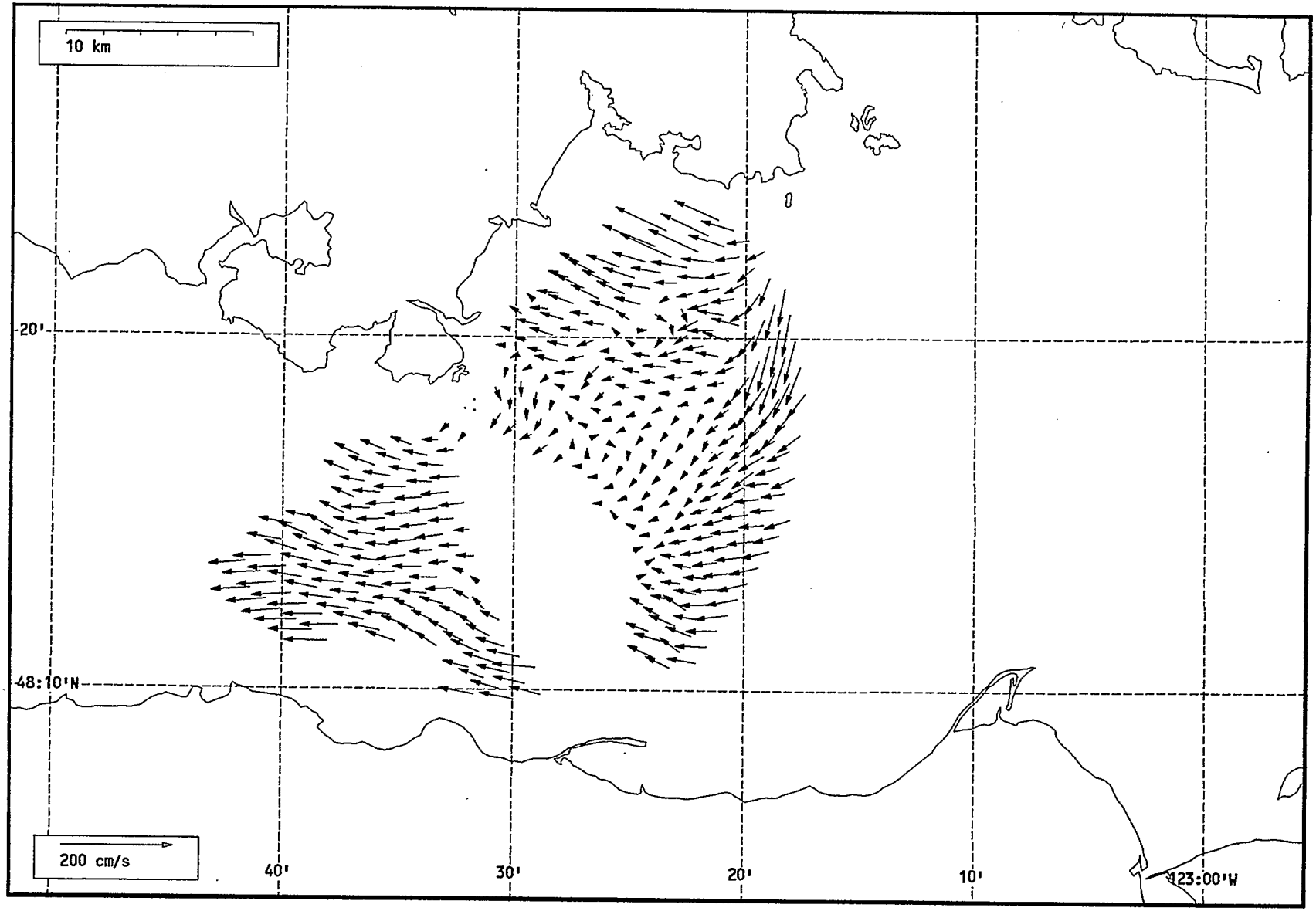

Total current vectors, Juan de Fuca Strait, 1992-07-18 21:00 Z.

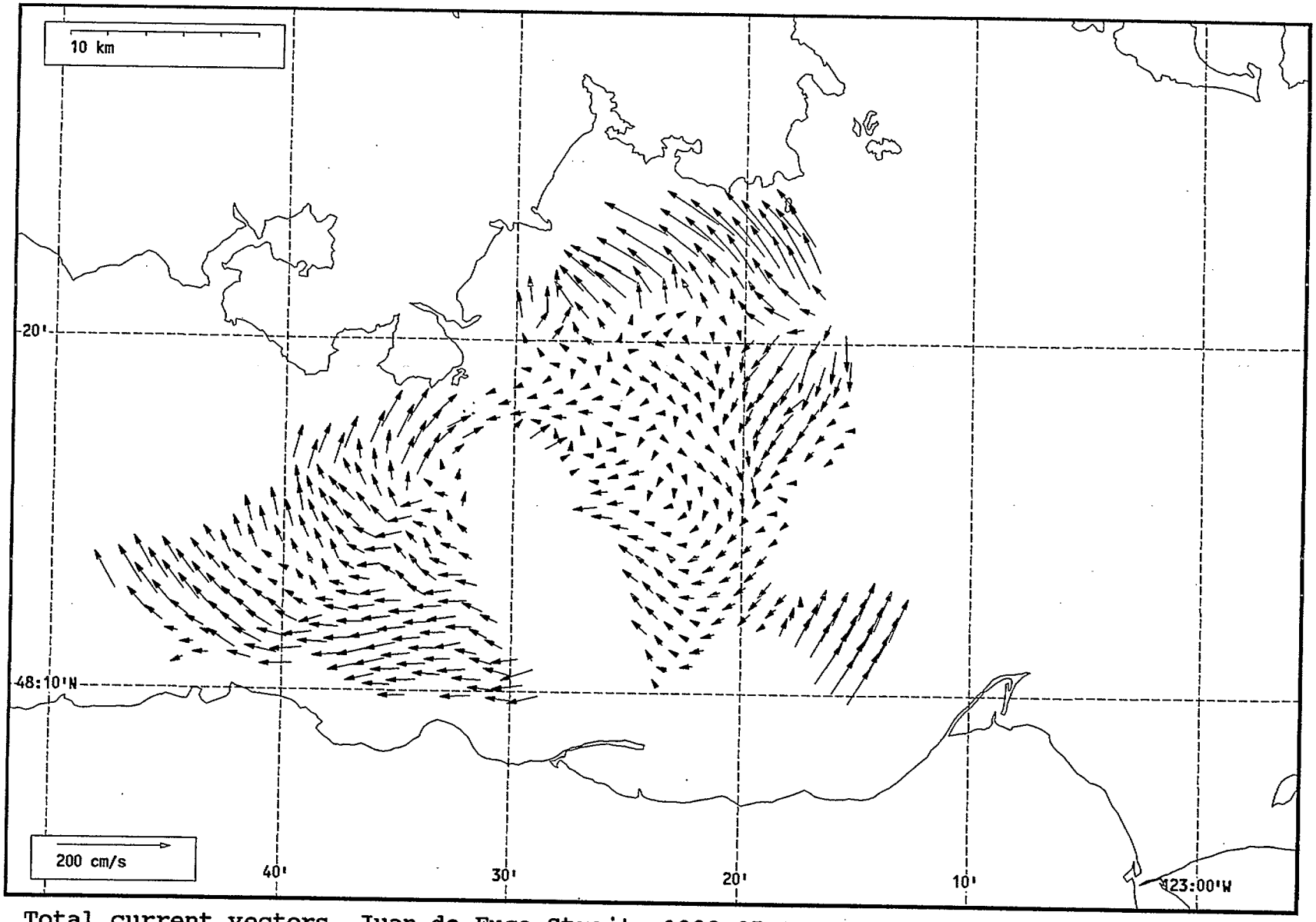

Total current vectors, Juan de Fuca Strait, 1992-07-18 22:00 Z.

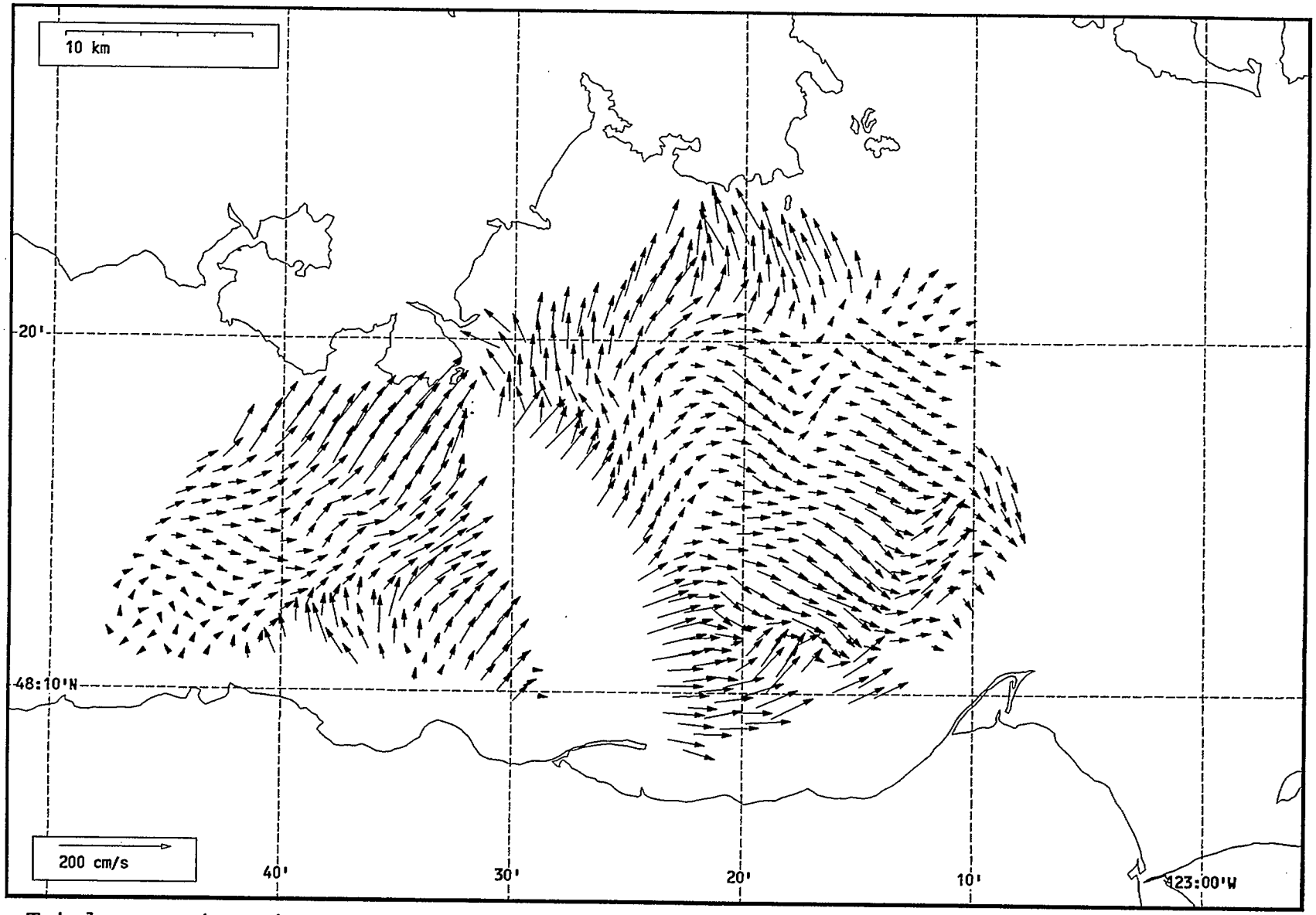

Total current vectors, Juan de Fuca Strait, 1992-07-18 23:00 Z.

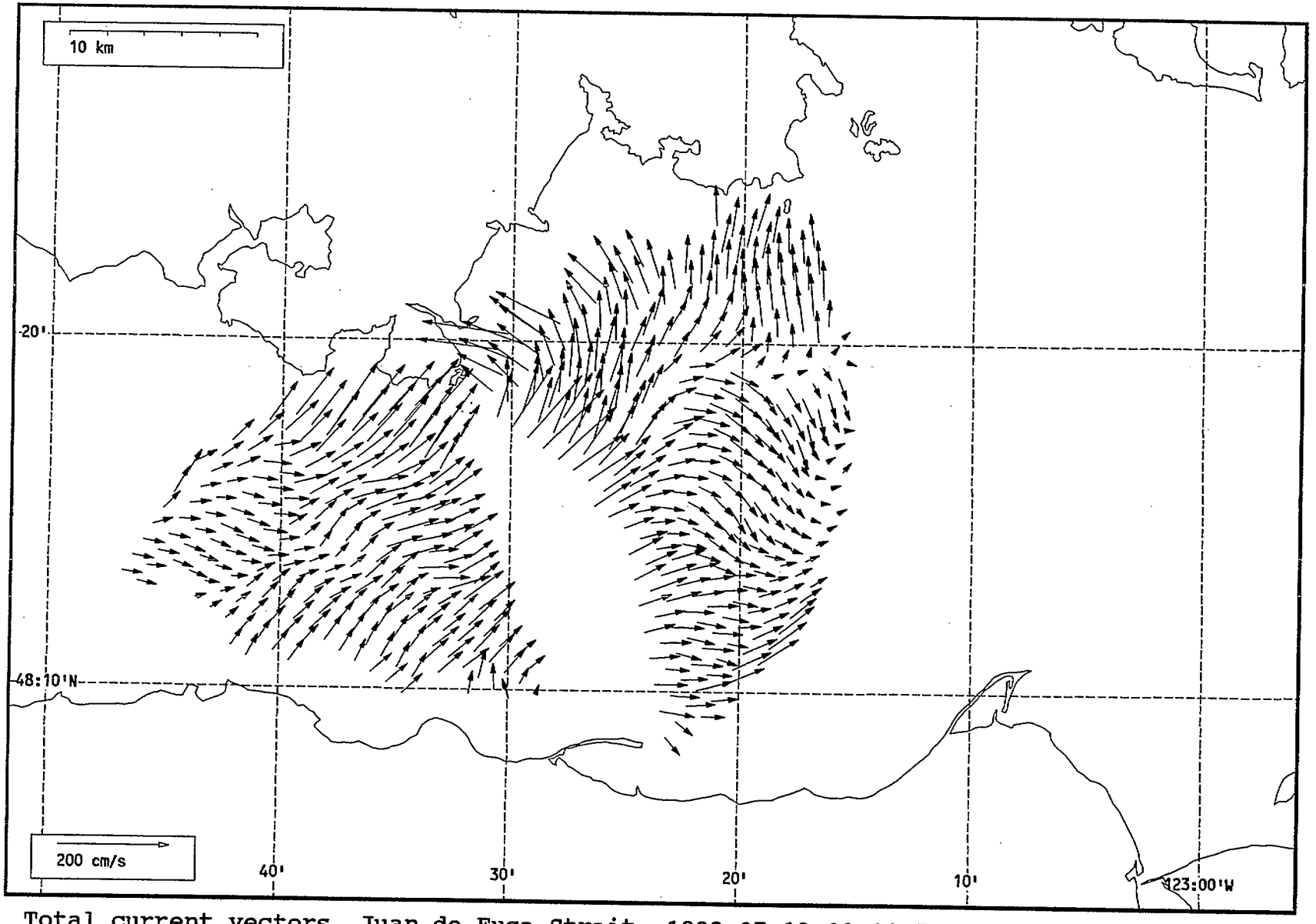

Total current vectors, Juan de Fuca Strait, 1992-07-19 00:00 Z.

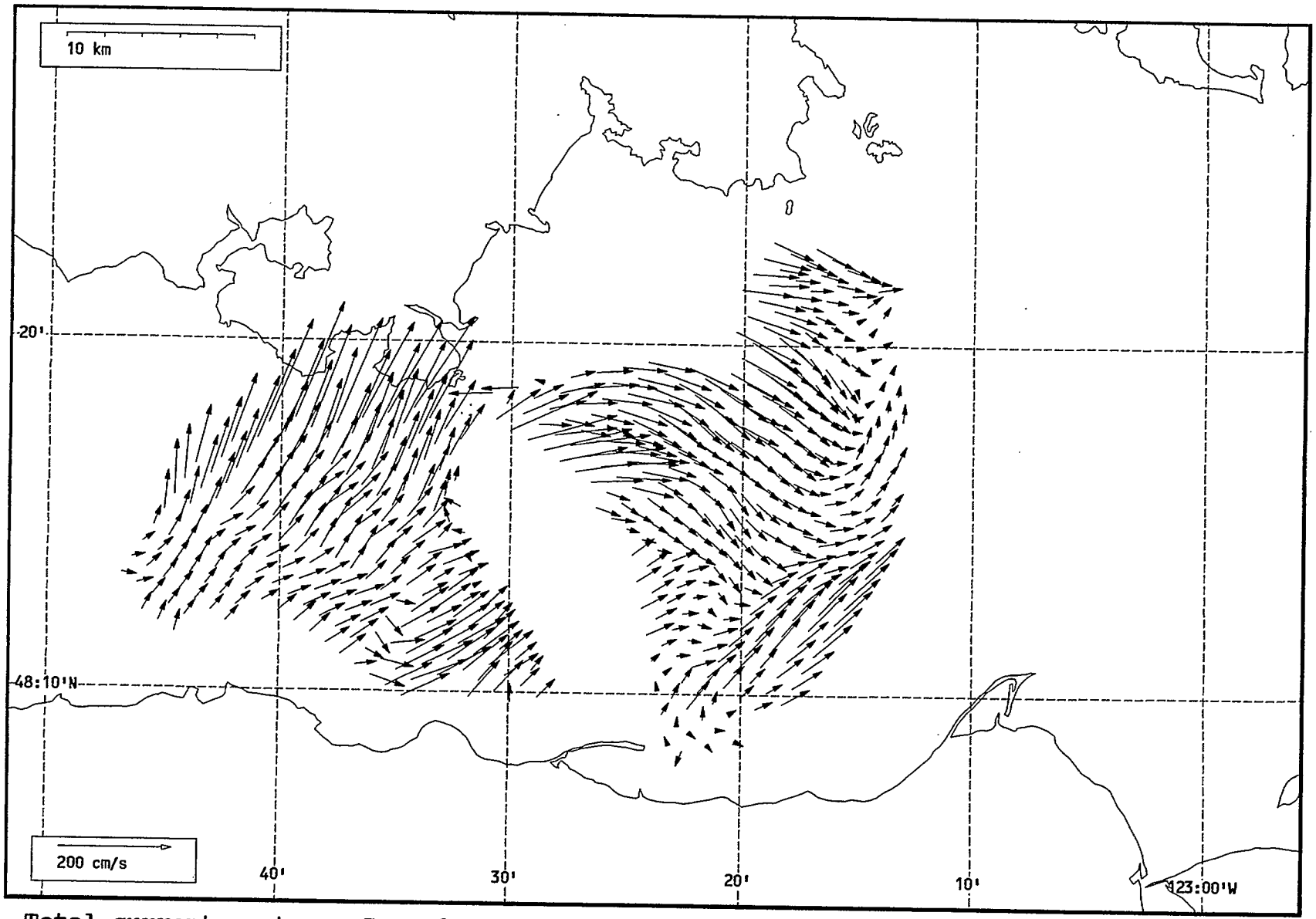

Total current vectors, Juan de Fuca Strait, 1992-07-19 01:00 Z.

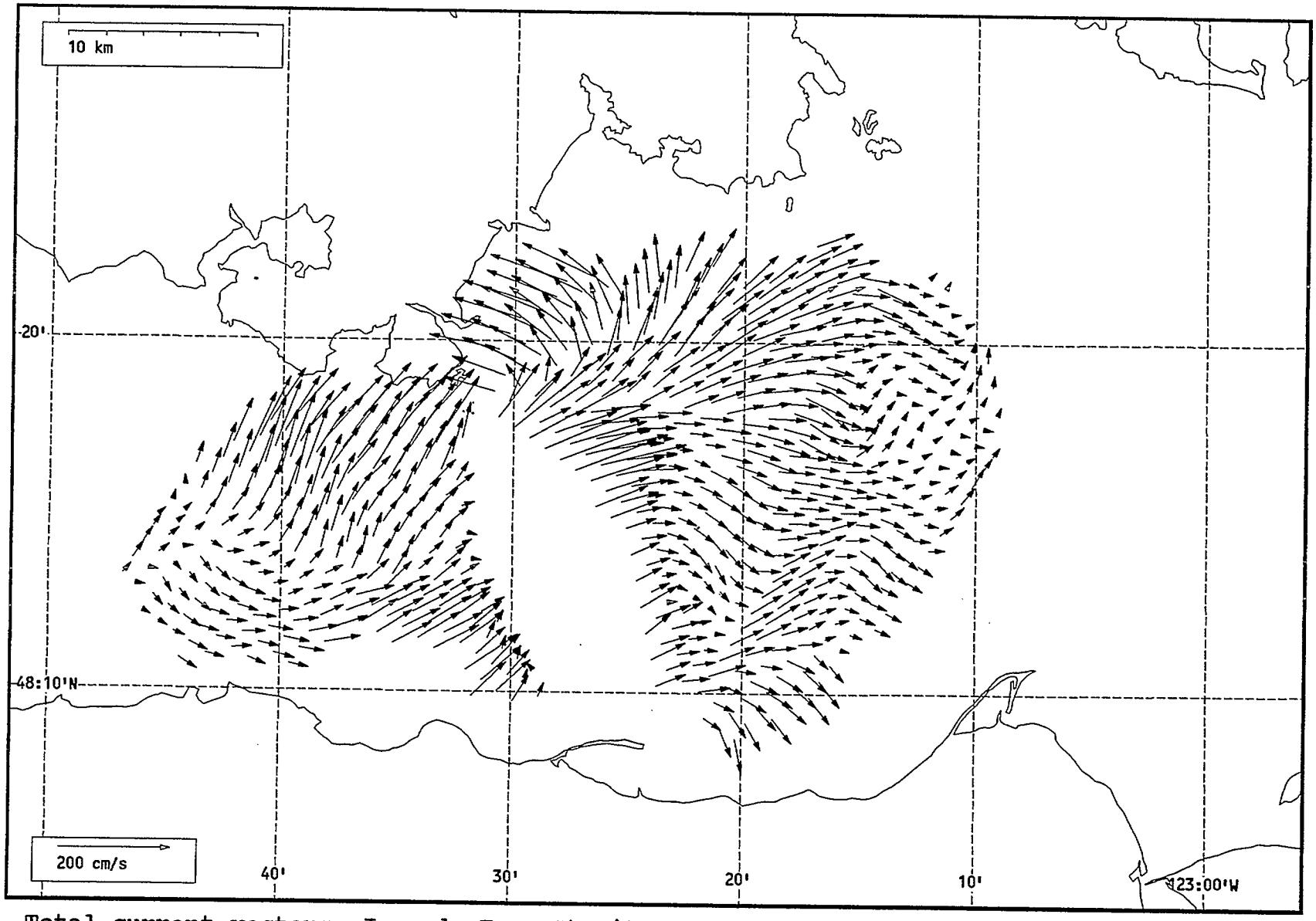

Total current vectors, Juan de Fuca Strait, 1992-07-19 02:00 Z.

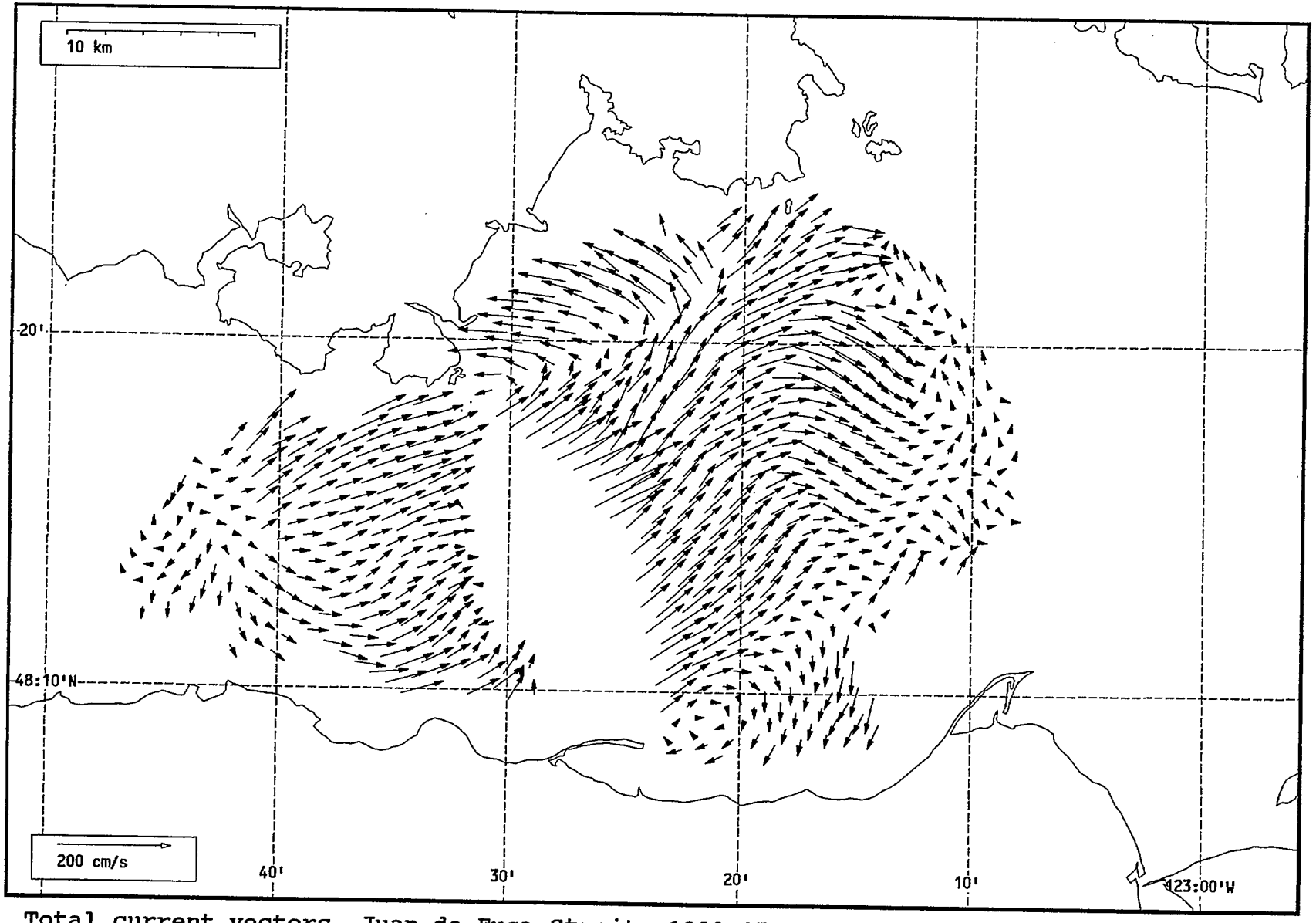

Total current vectors, Juan de Fuca Strait, 1992-07-19 03:00 Z.

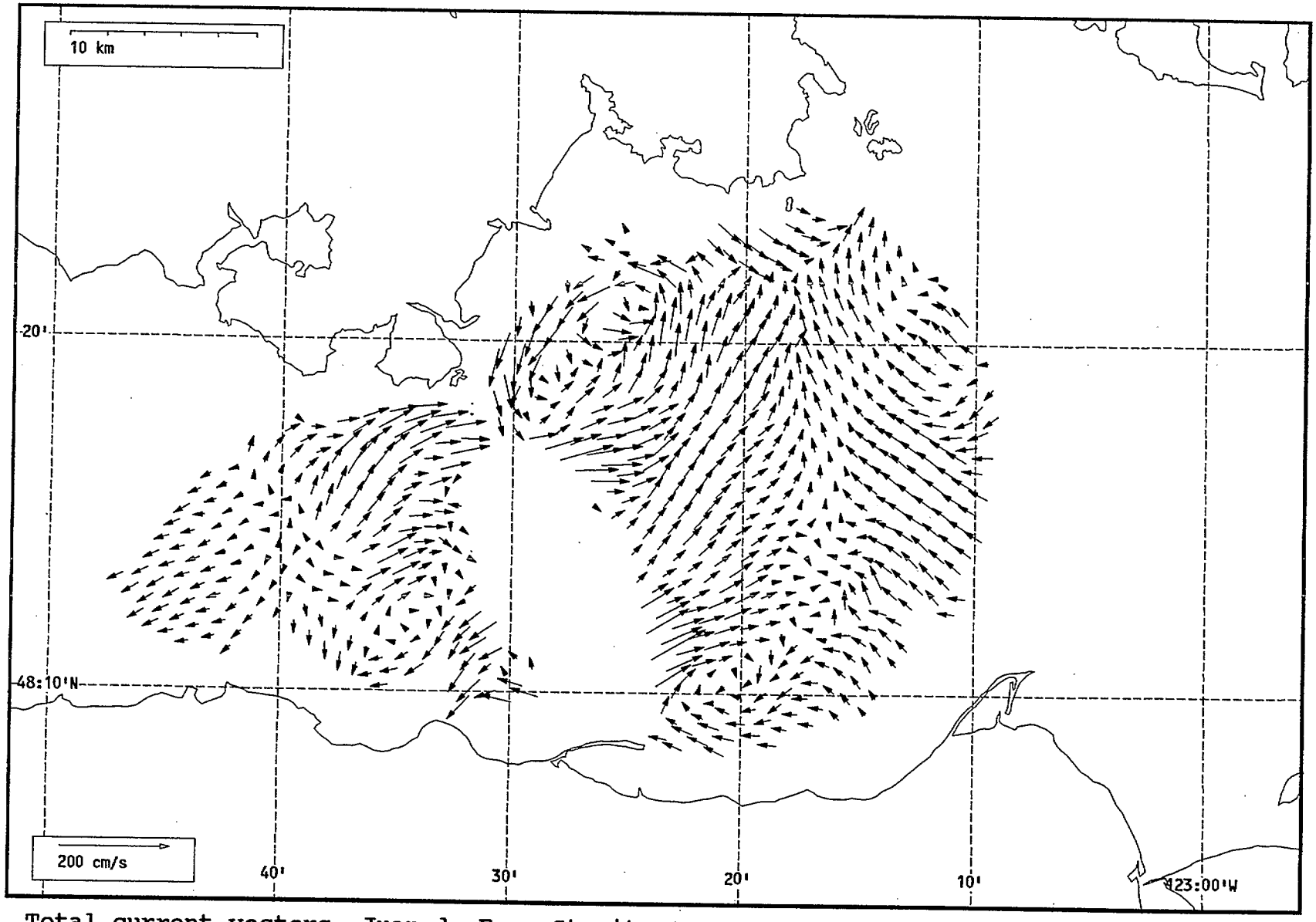

Total current vectors, Juan de Fuca Strait, 1992-07-19 04:00 Z.

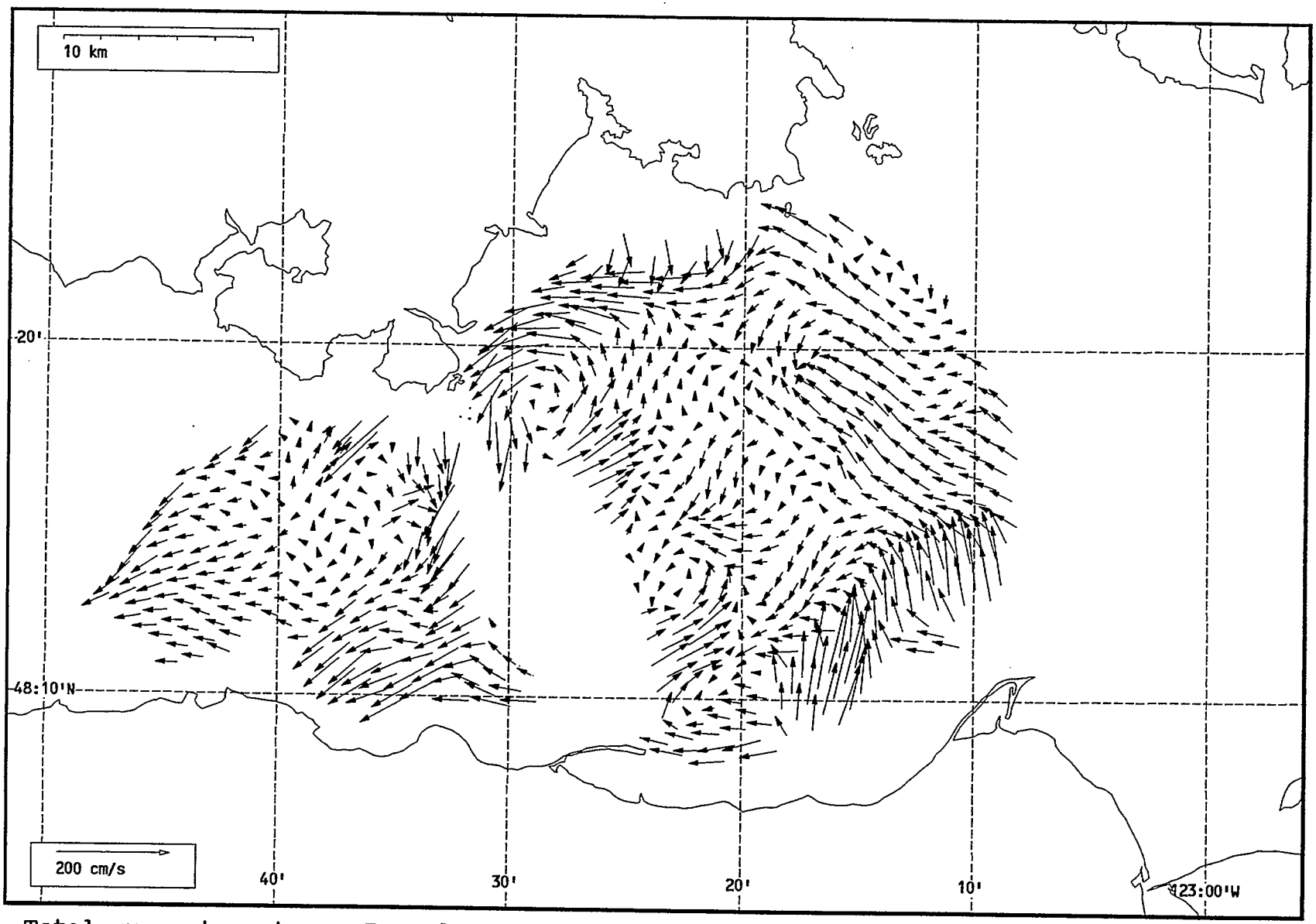

Total current vectors, Juan de Fuca Strait, 1992-07-19 05:00 Z.

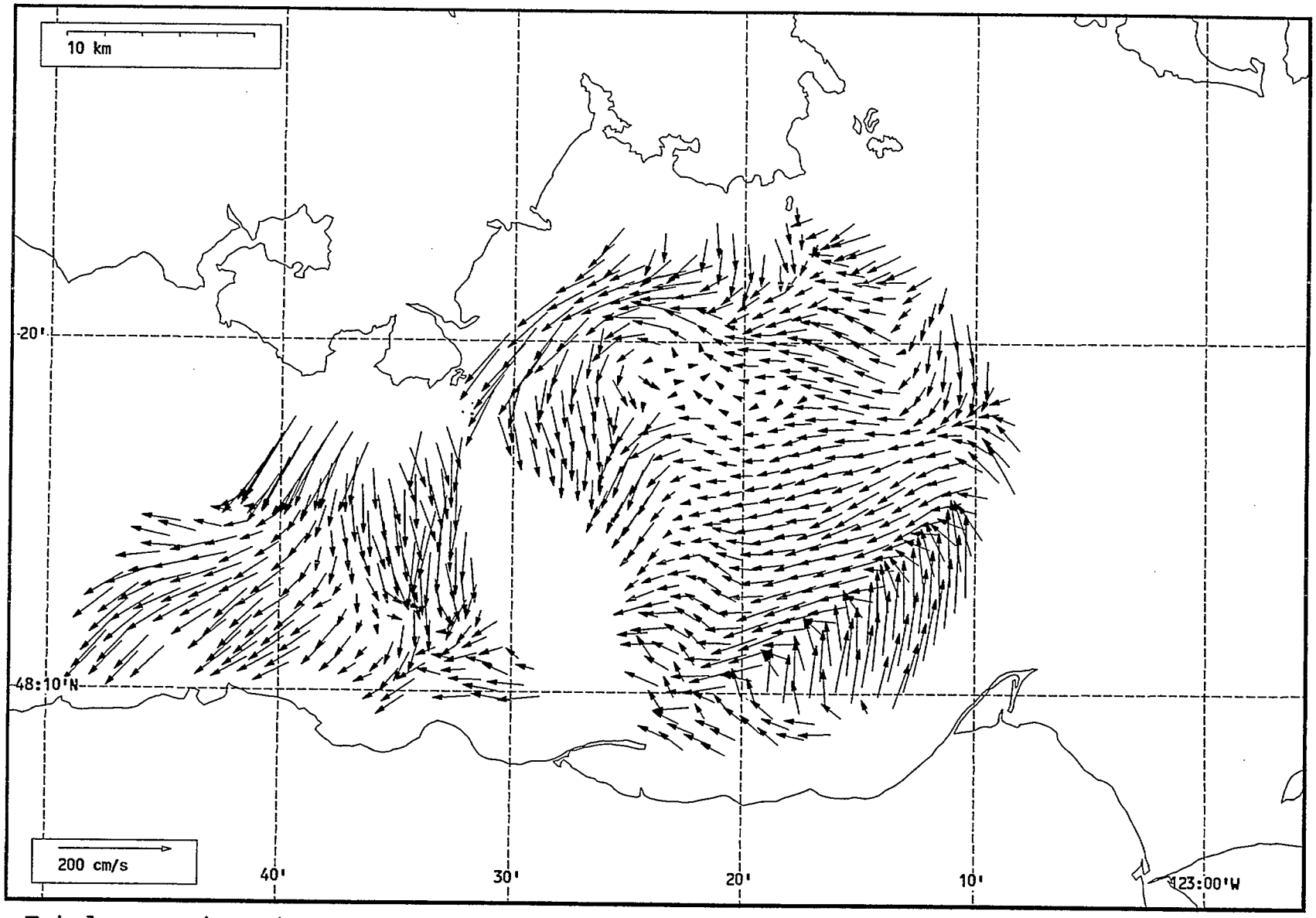

Total current vectors, Juan de Fuca Strait, 1992-07-19 06:00 Z.

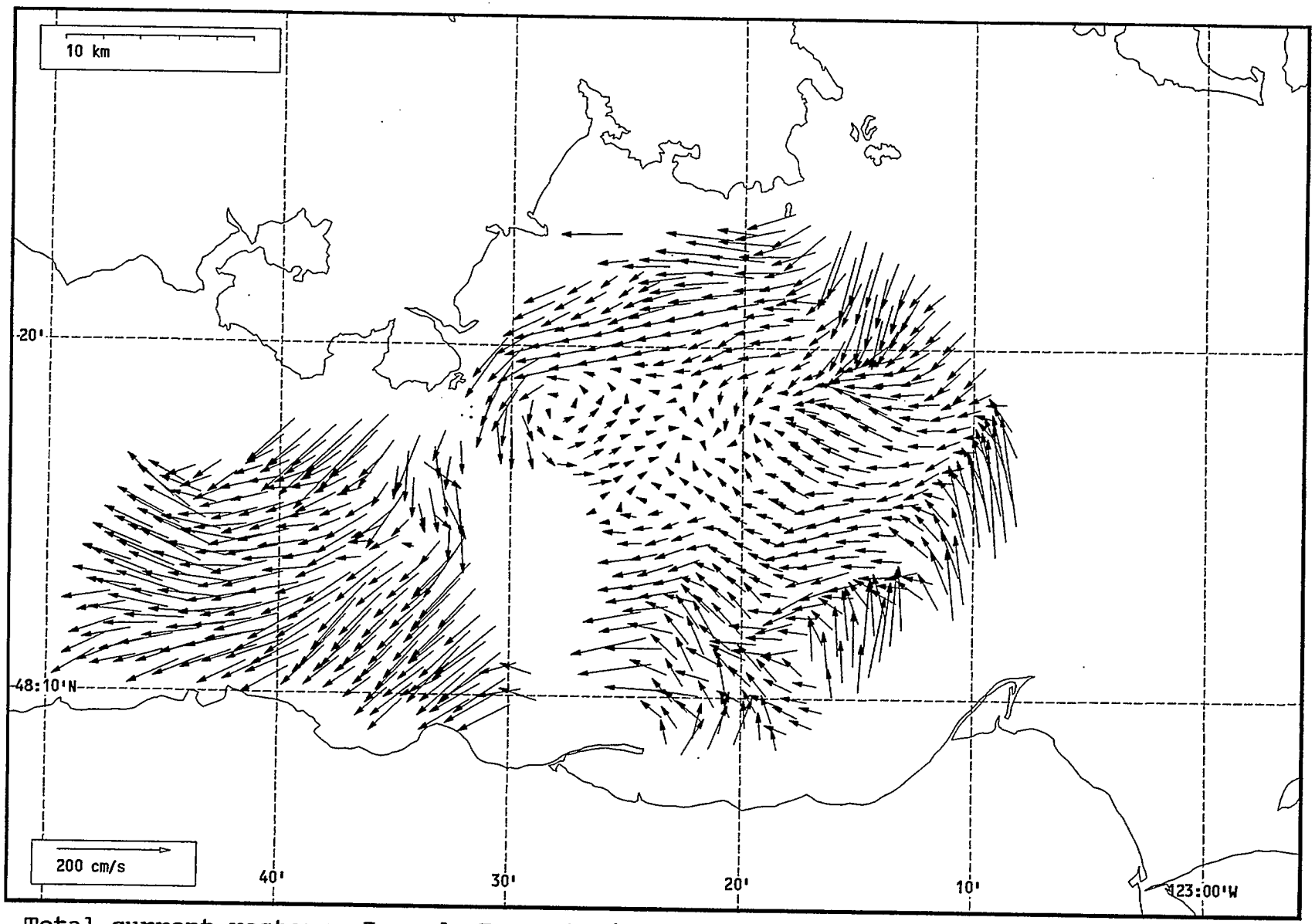

Total current vectors, Juan de Fuca Strait, 1992-07-19 07:00 Z.

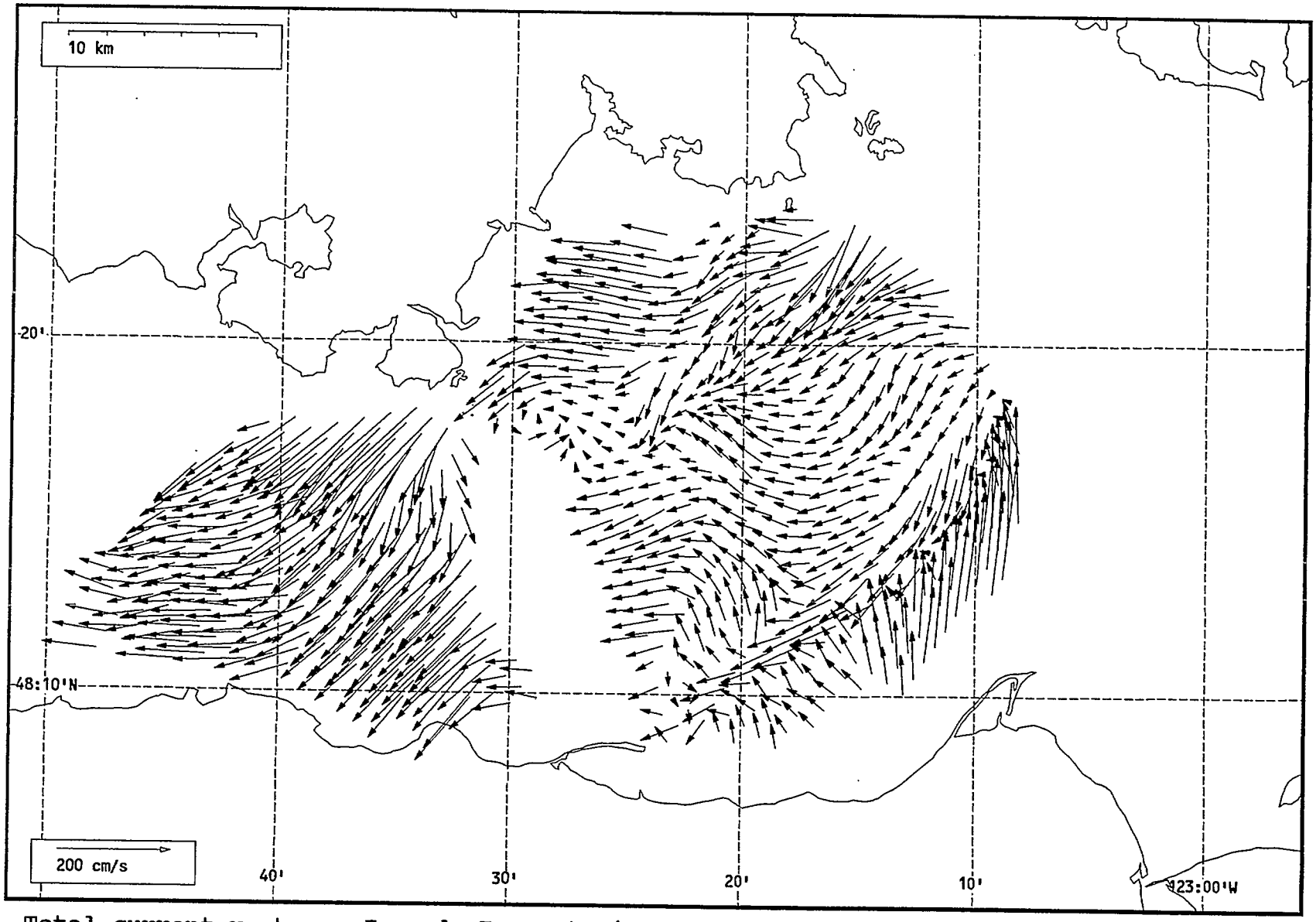

Total current vectors, Juan de Fuca Strait, 1992-07-19 08:00 Z.

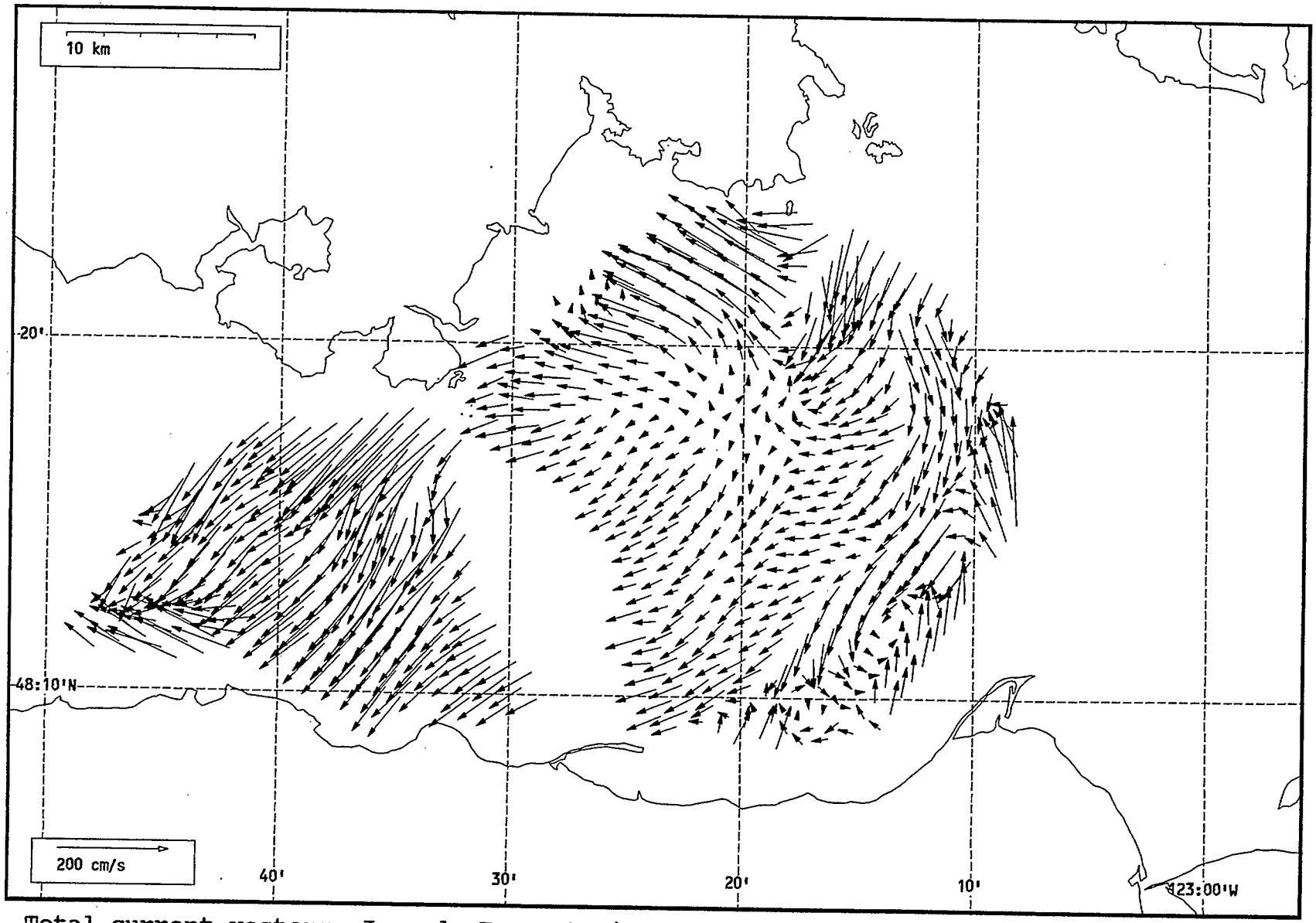

Total current vectors, Juan de Fuca Strait, 1992-07-19 09:00 Z.

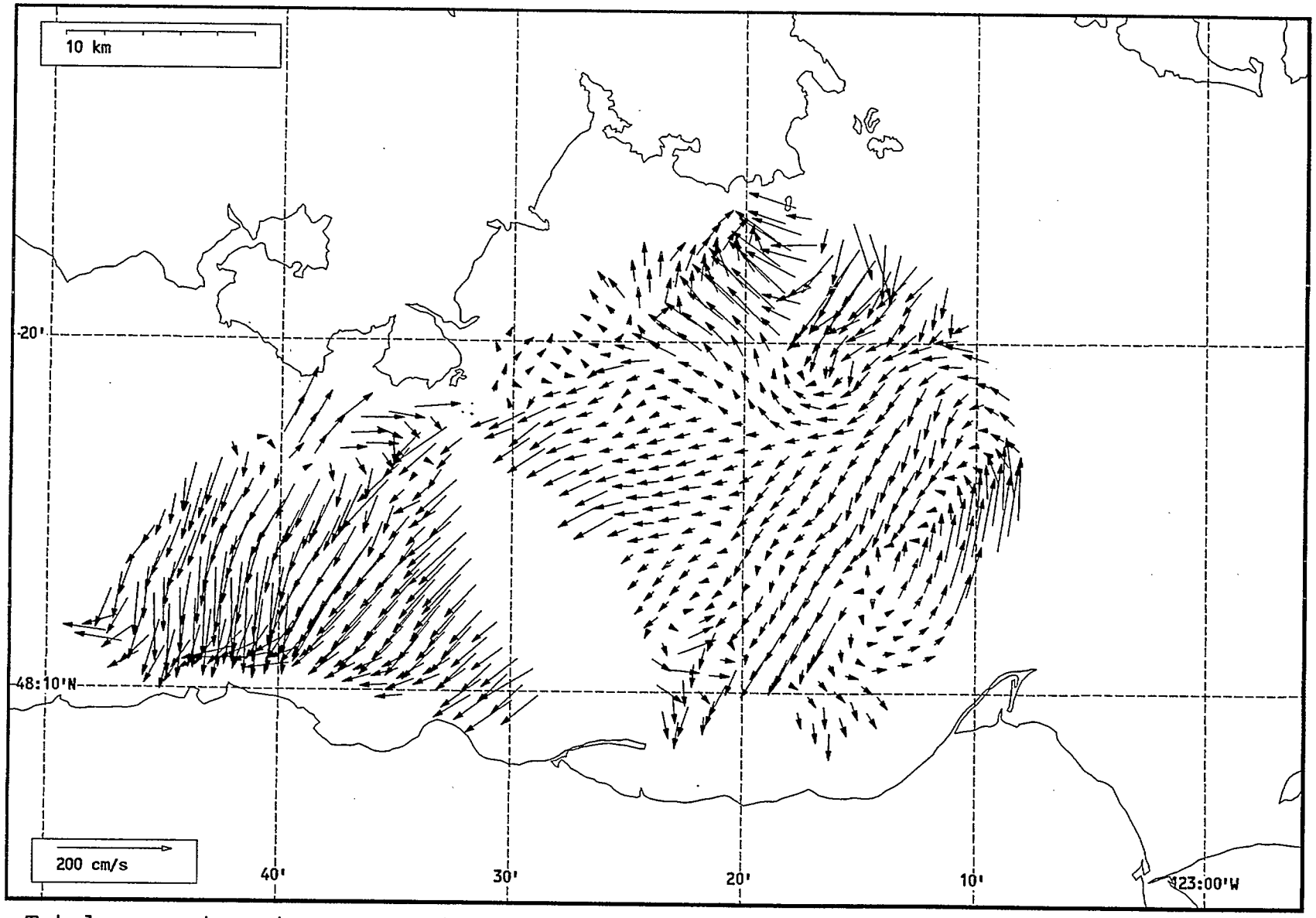

Total current vectors, Juan de Fuca Strait, 1992-07-19 10:00 Z.

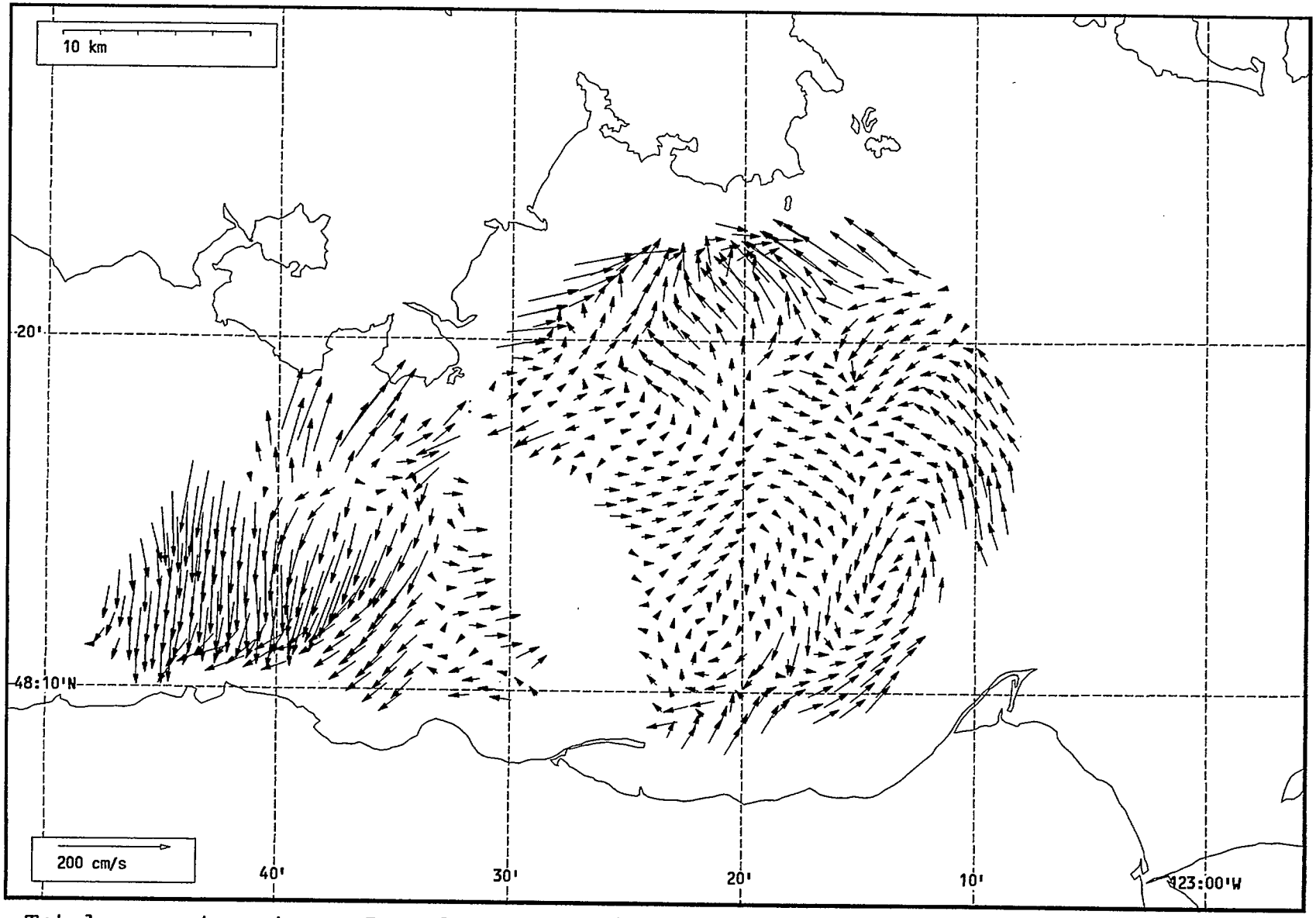

Total current vectors, Juan de Fuca Strait, 1992-07-19 11:00 Z.

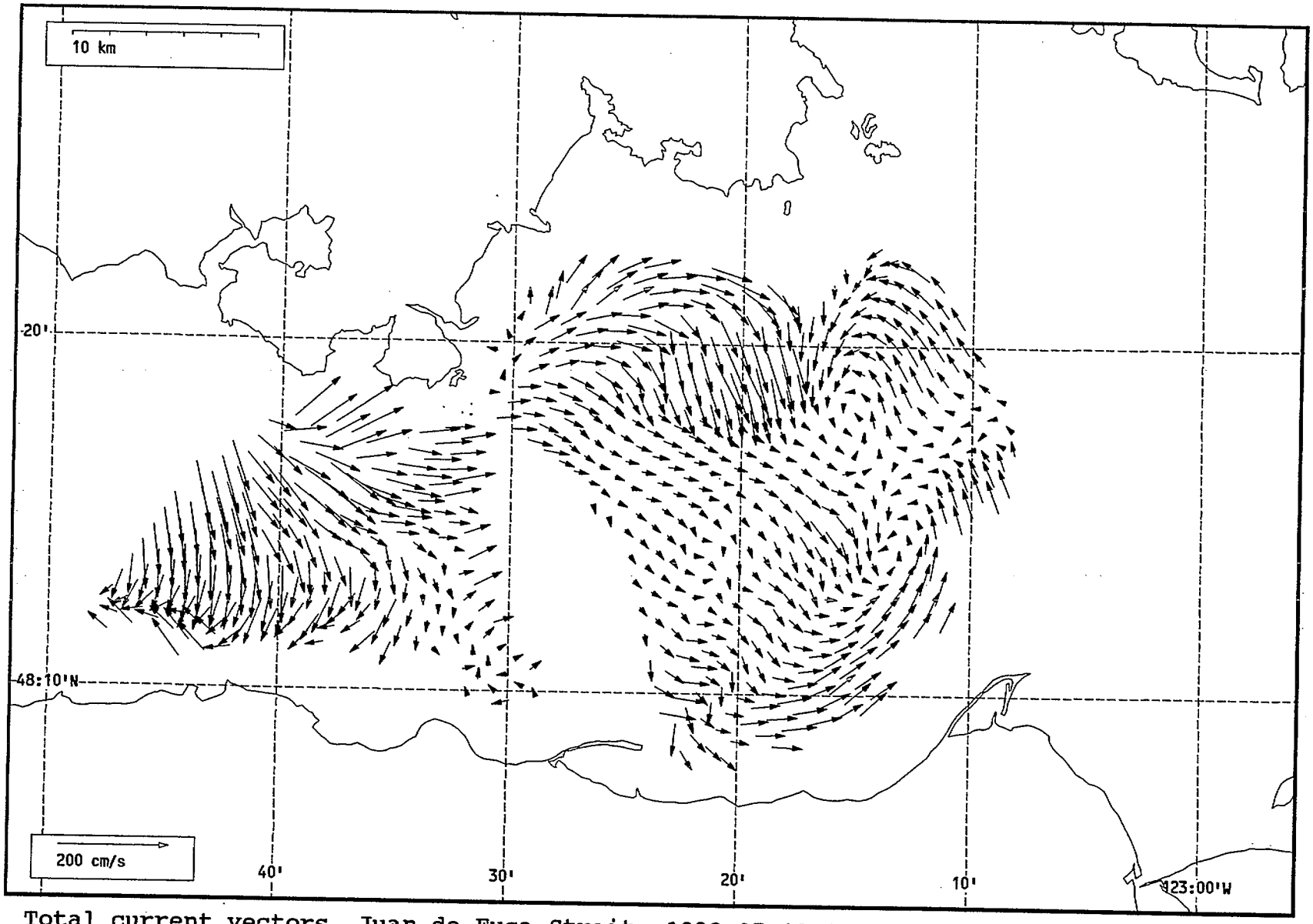

Total current vectors, Juan de Fuca Strait, 1992-07-19 12:00 Z.

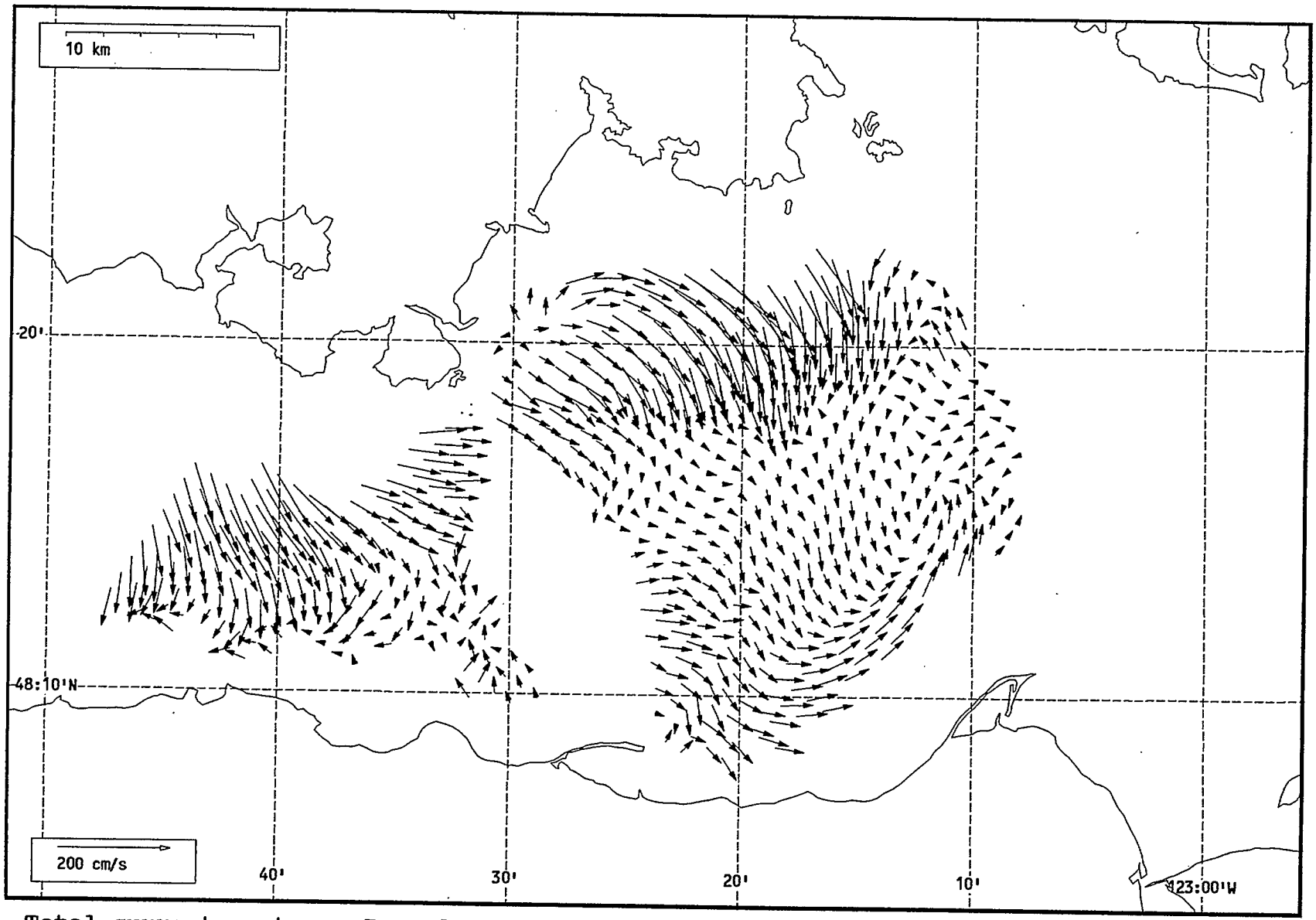

Total current vectors, Juan de Fuca Strait, 1992-07-19 13:00 Z.

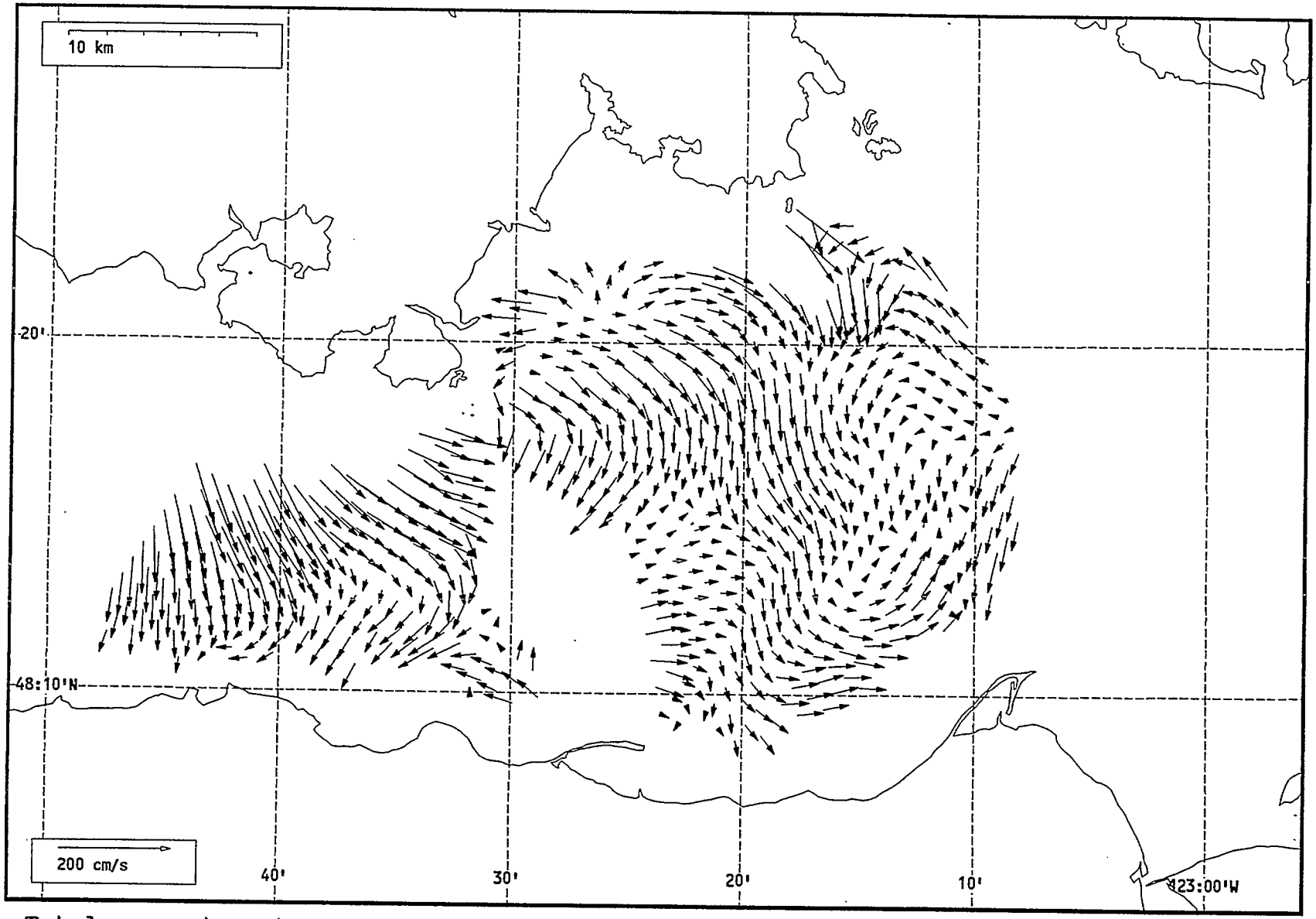

Total current vectors, Juan de Fuca Strait, 1992-07-19 14:00 Z.

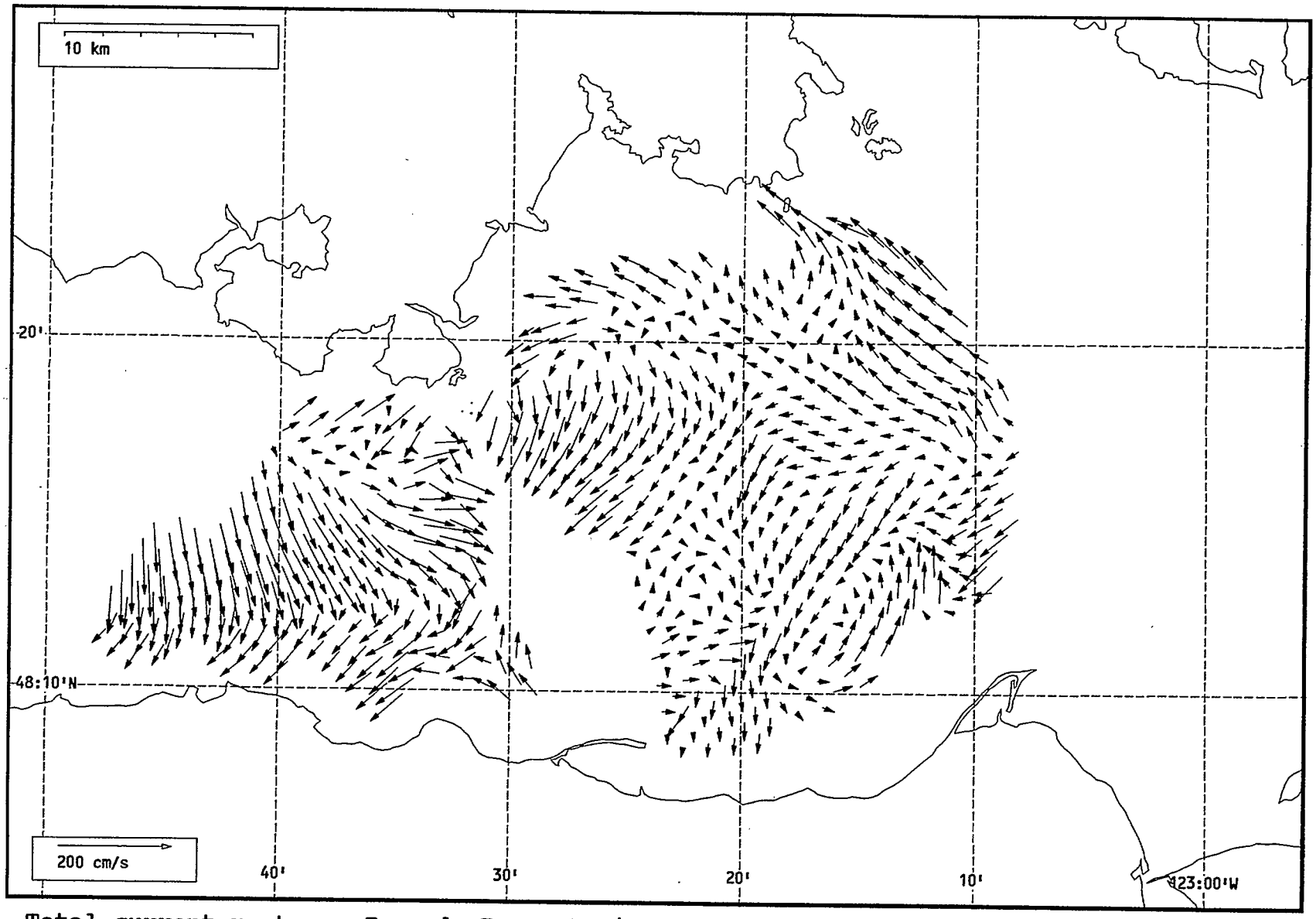

Total current vectors, Juan de Fuca Strait, 1992-07-19 15:00 Z.

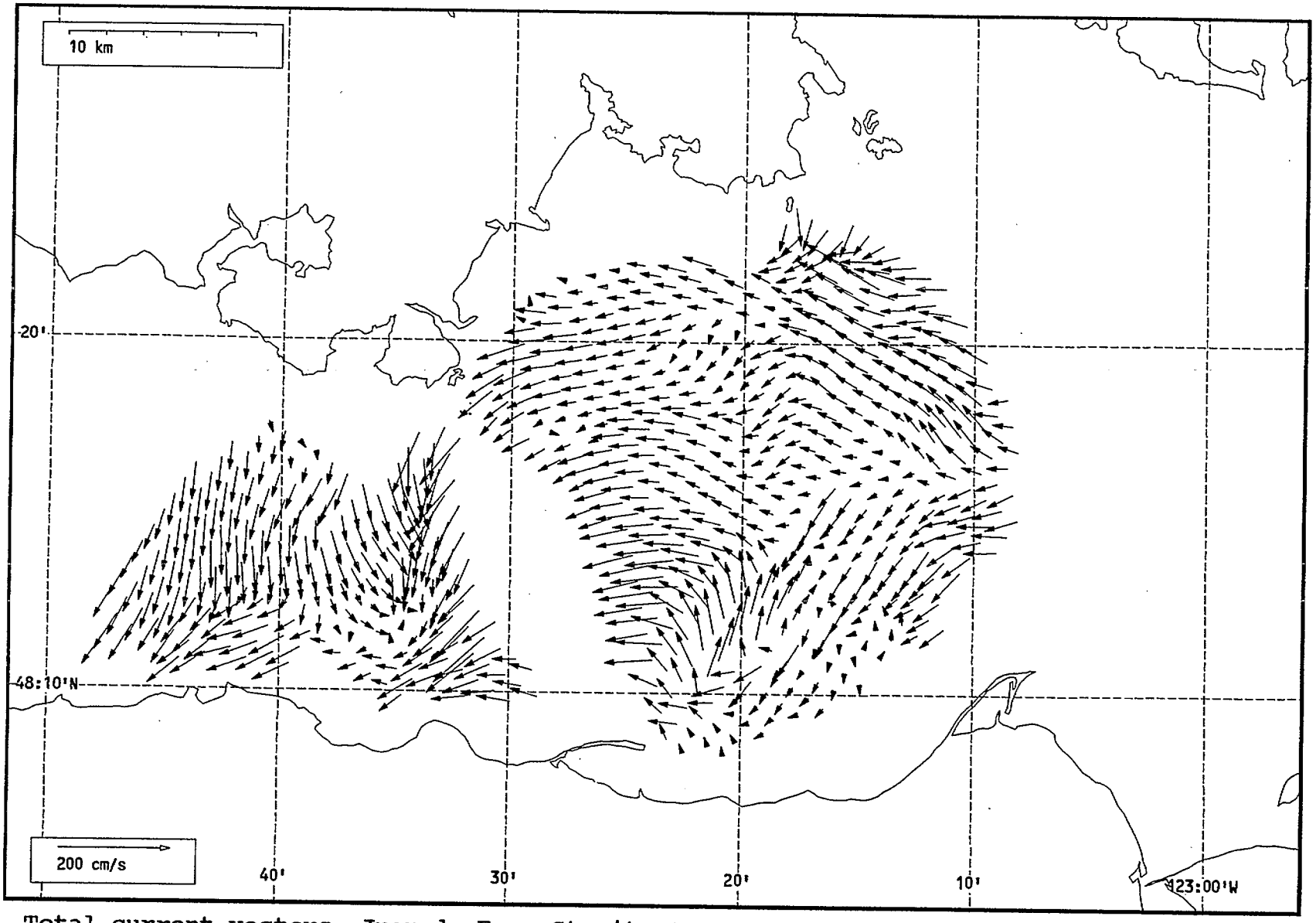

Total current vectors, Juan de Fuca Strait, 1992-07-19 16:00 Z.

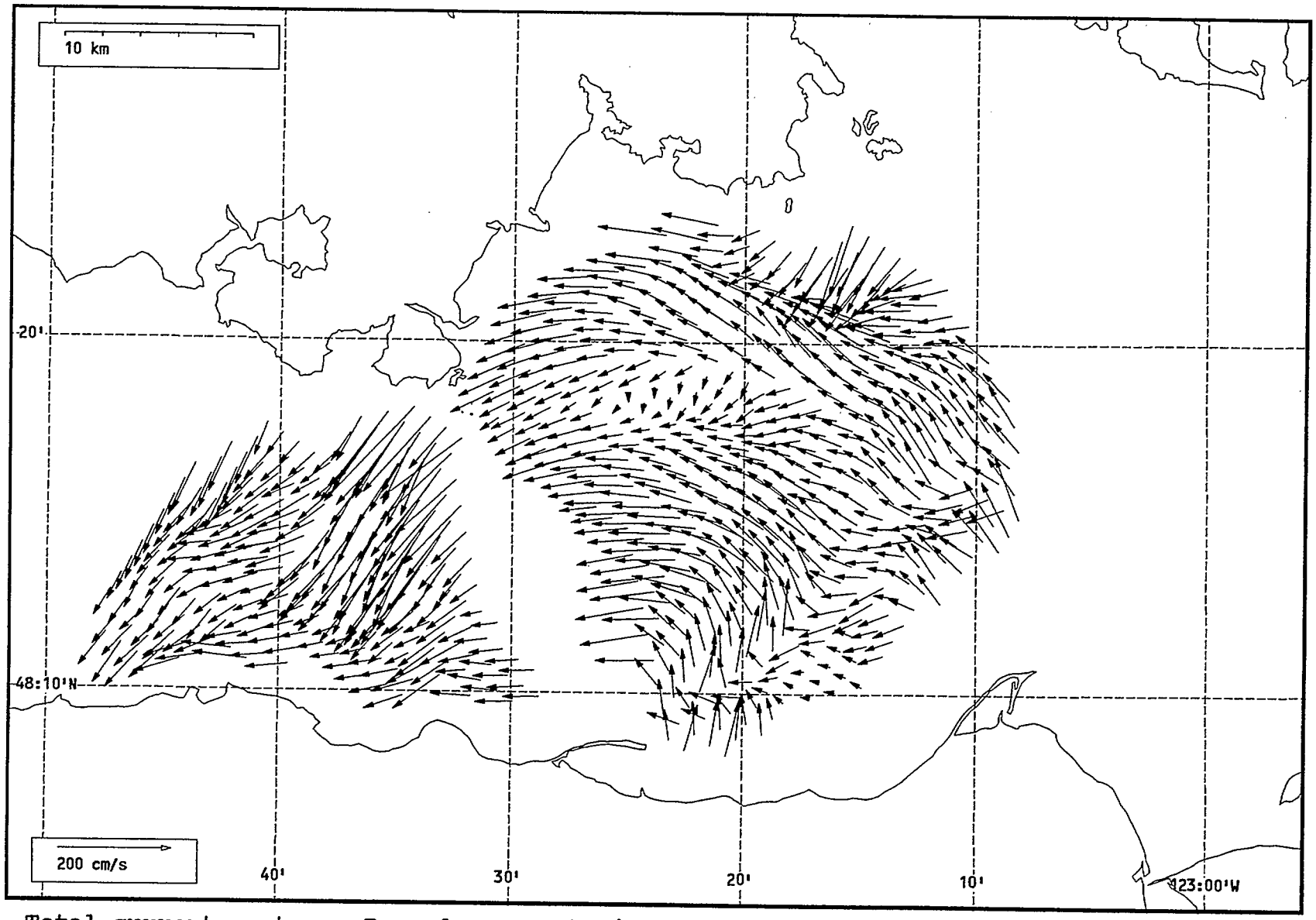

Total current vectors, Juan de Fuca Strait, 1992-07-19 17:00 Z.

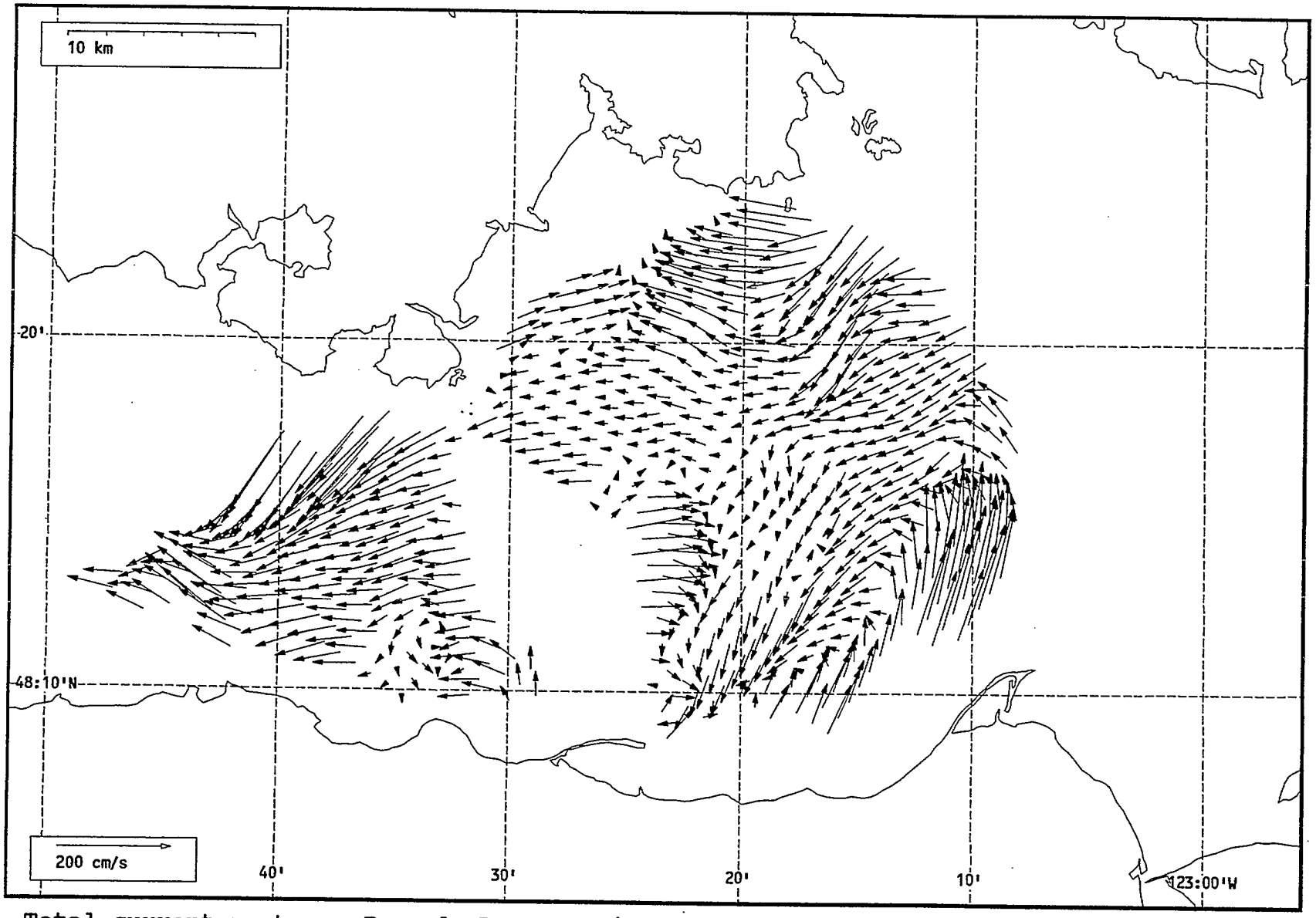

Total current vectors, Juan de Fuca Strait, 1992-07-20 20:00 Z.

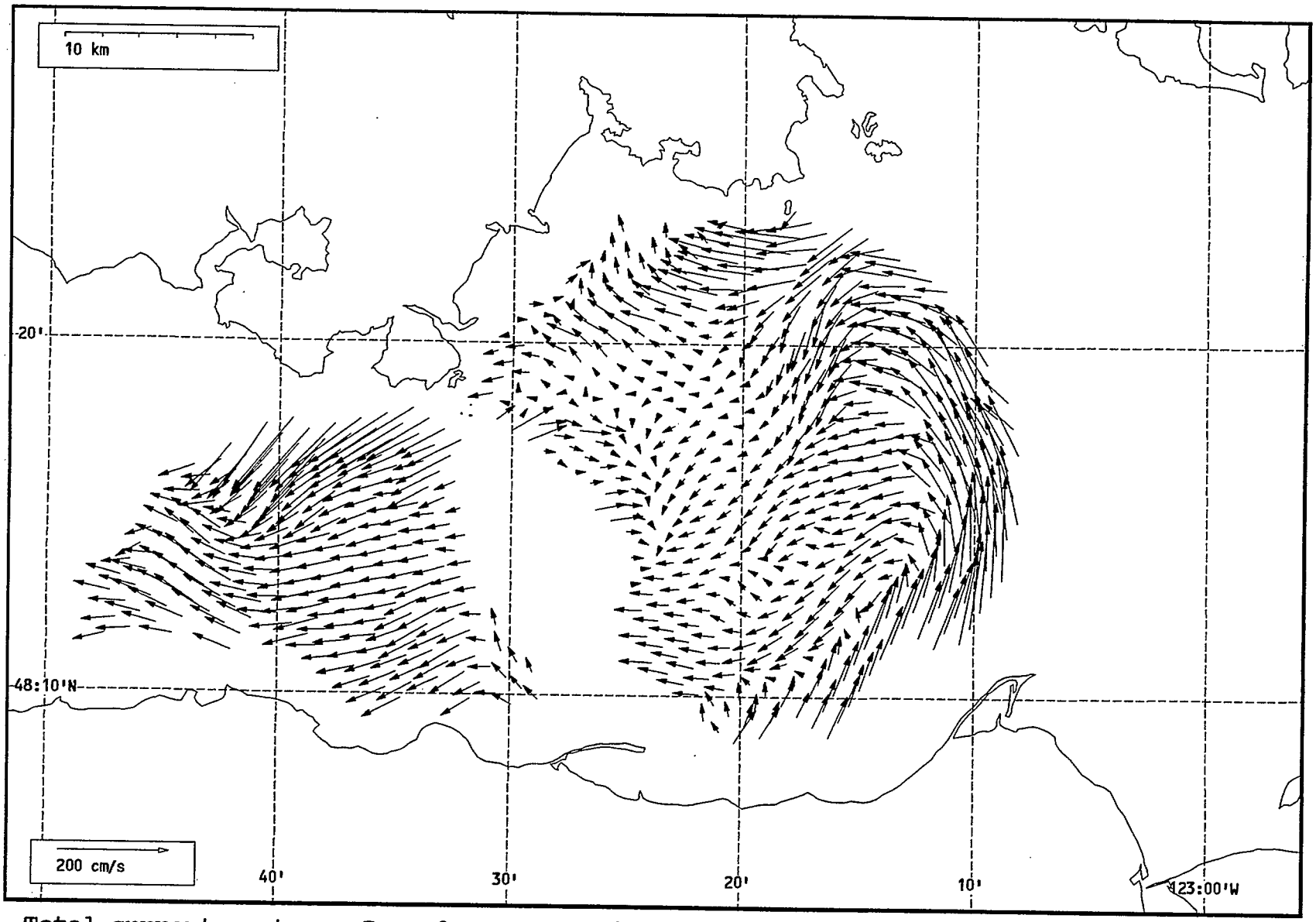

Total current vectors, Juan de Fuca Strait, 1992-07-20 21:00 Z.

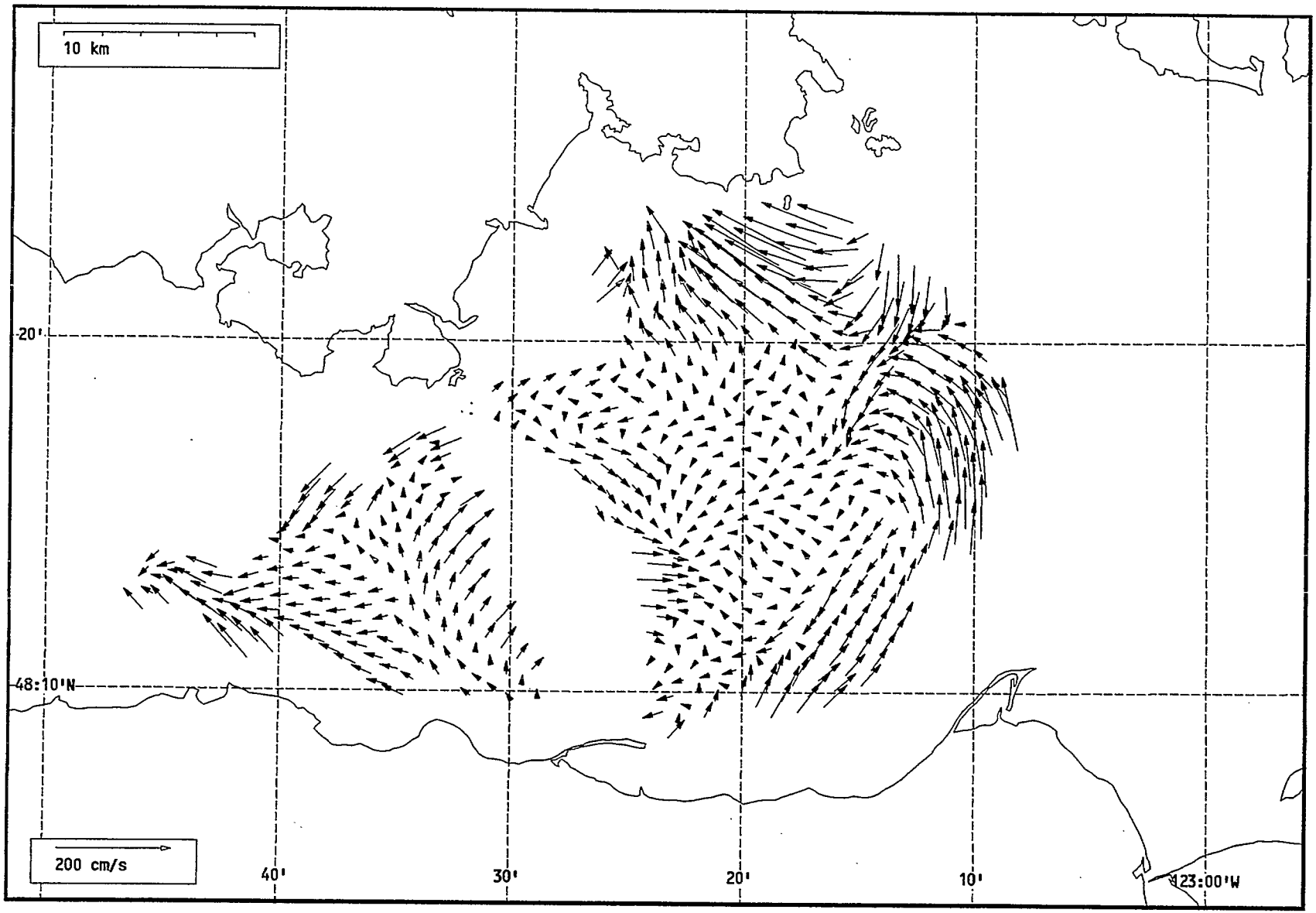

Total current vectors, Juan de Fuca Strait, 1992-07-20 22:00 Z.

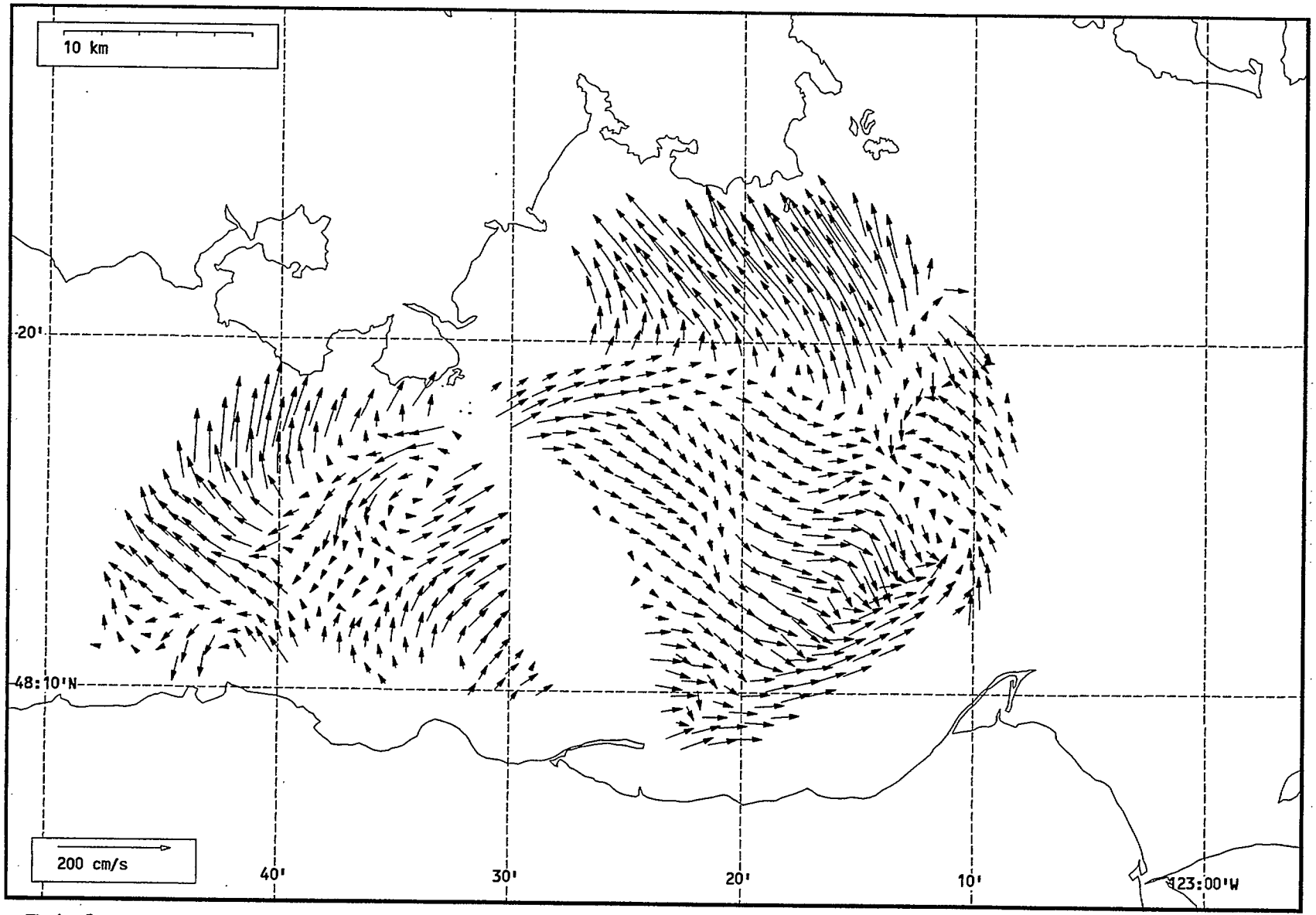

Total current vectors, Juan de Fuca Strait, 1992-07-20 23:00 Z..

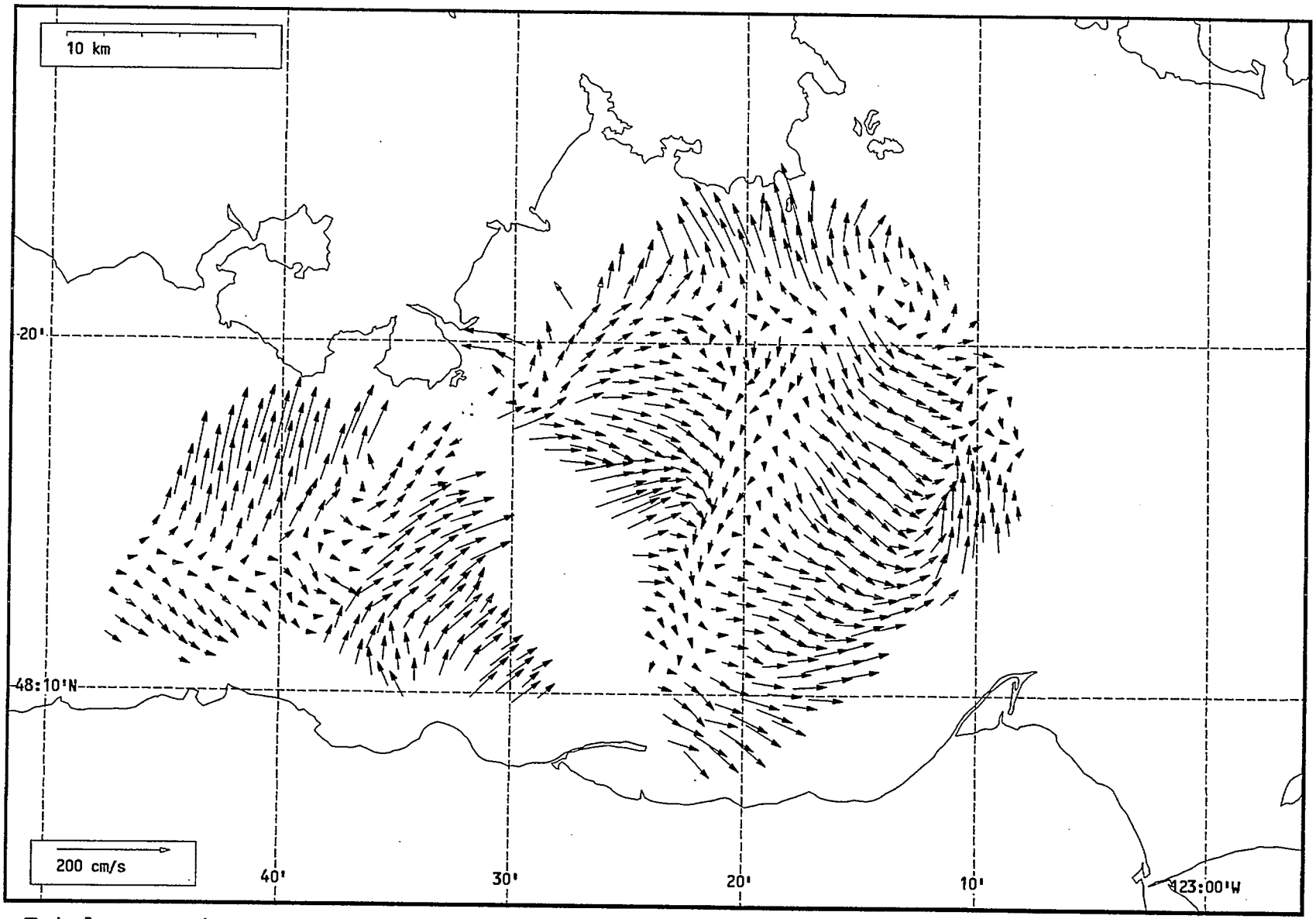

Total current vectors, Juan de Fuca Strait, 1992-07-21 00:00 Z.

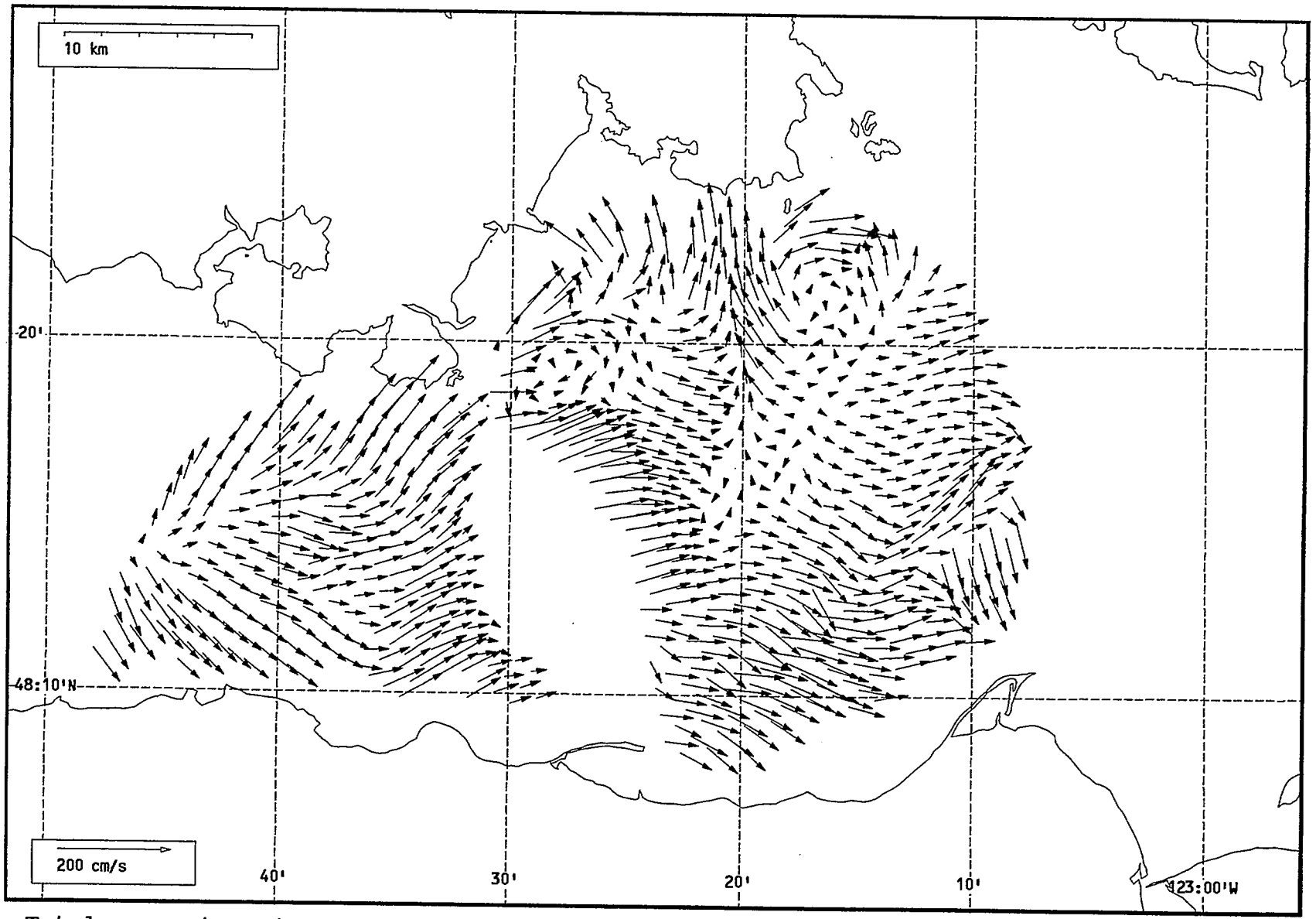

Total current vectors, Juan de Fuca Strait, 1992-07-21 01:00 Z.

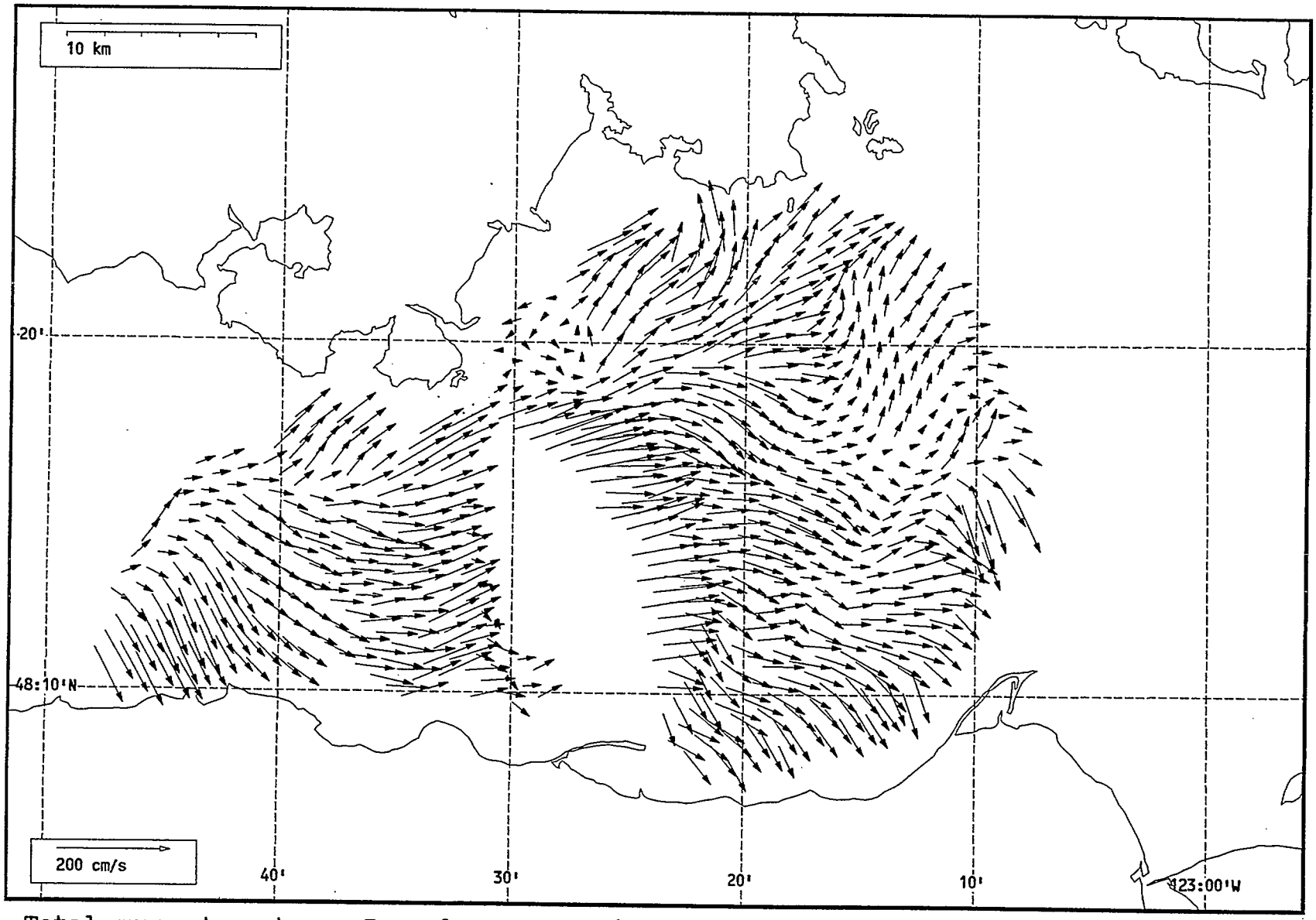

Total current vectors, Juan de Fuca Strait, 1992-07-21 02:00 Z.

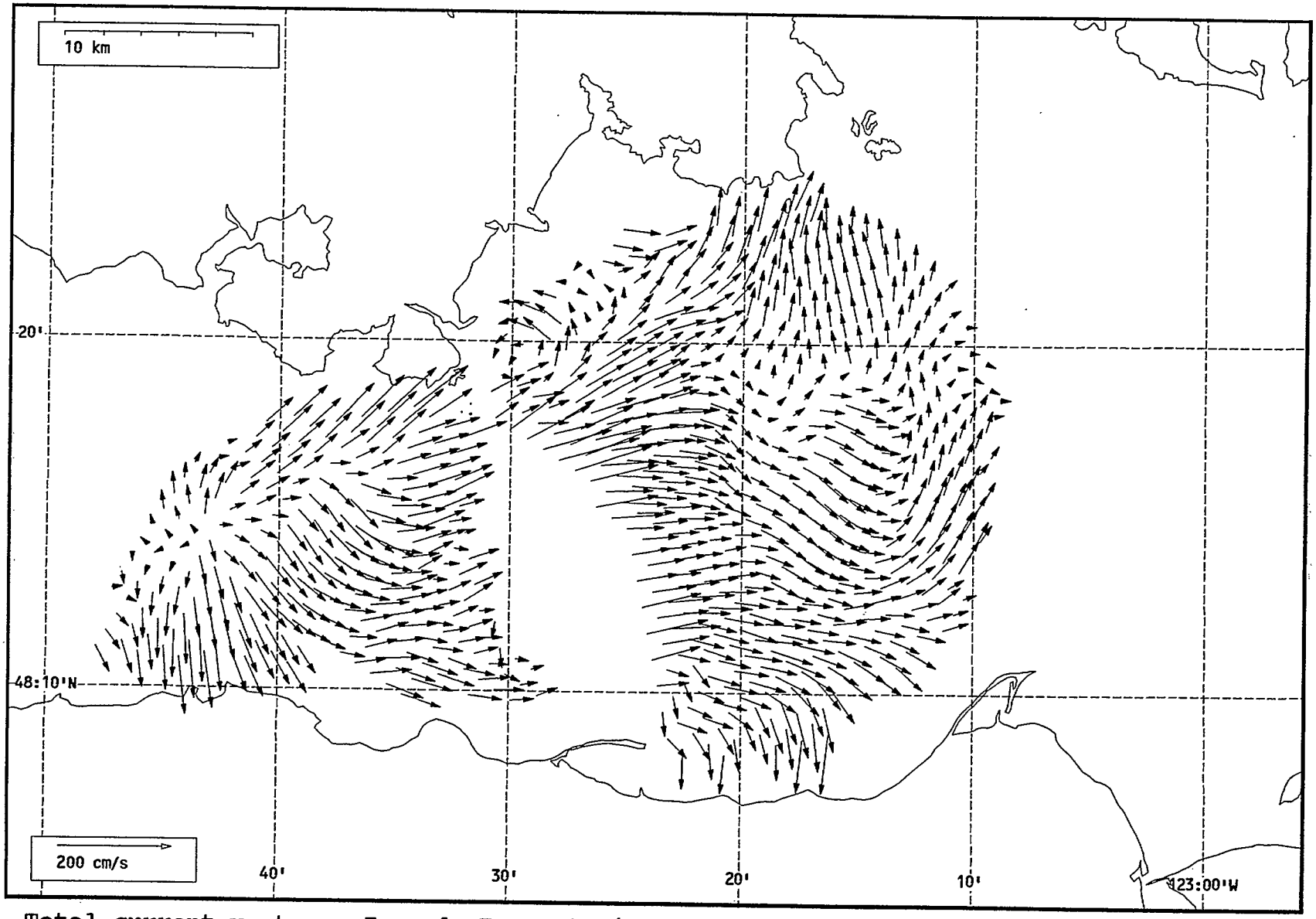

Total current vectors, Juan de Fuca Strait, 1992-07-21 03:00 Z.

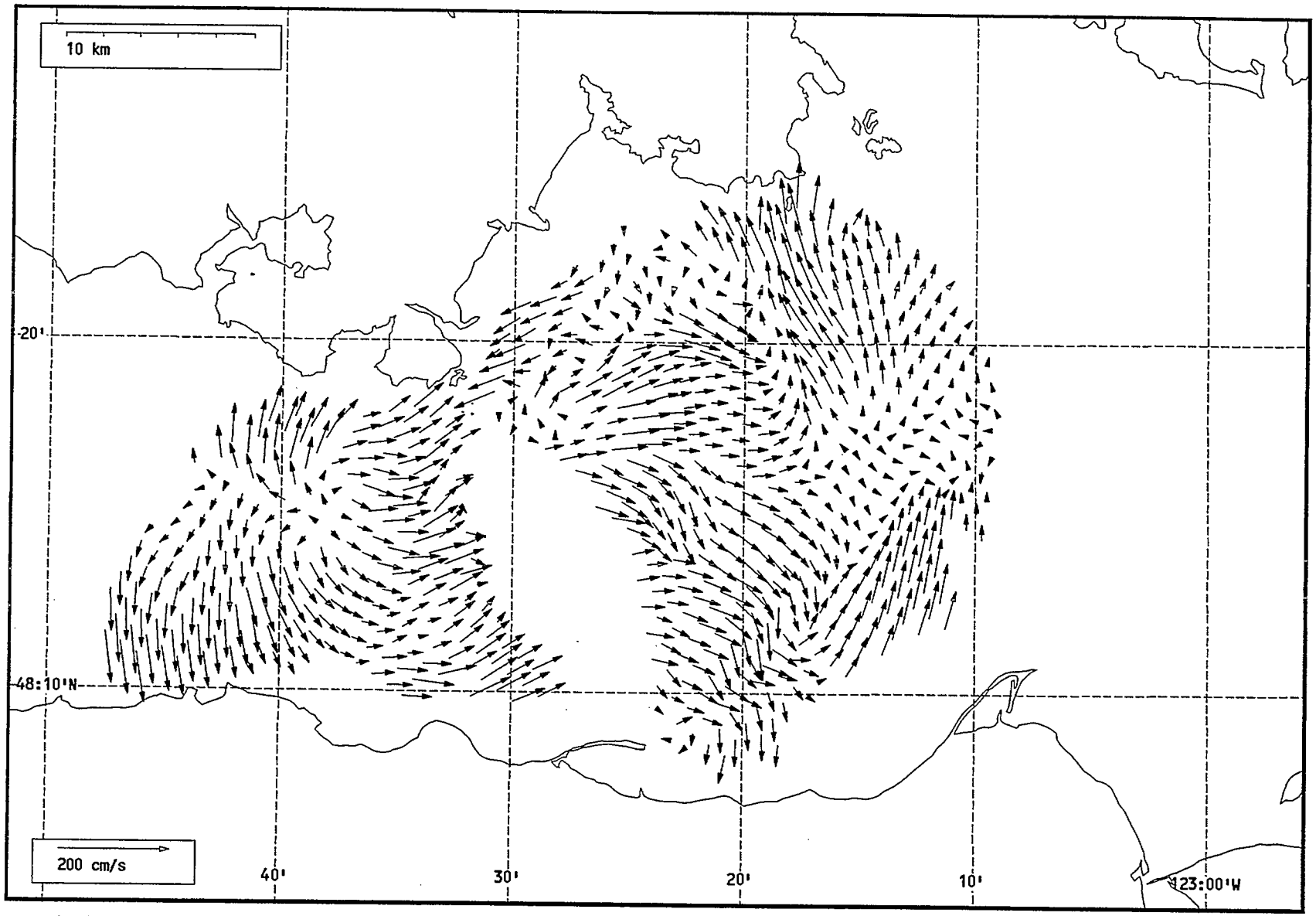

Total current vectors, Juan de Fuca Strait, 1992-07-21 04:00 Z.

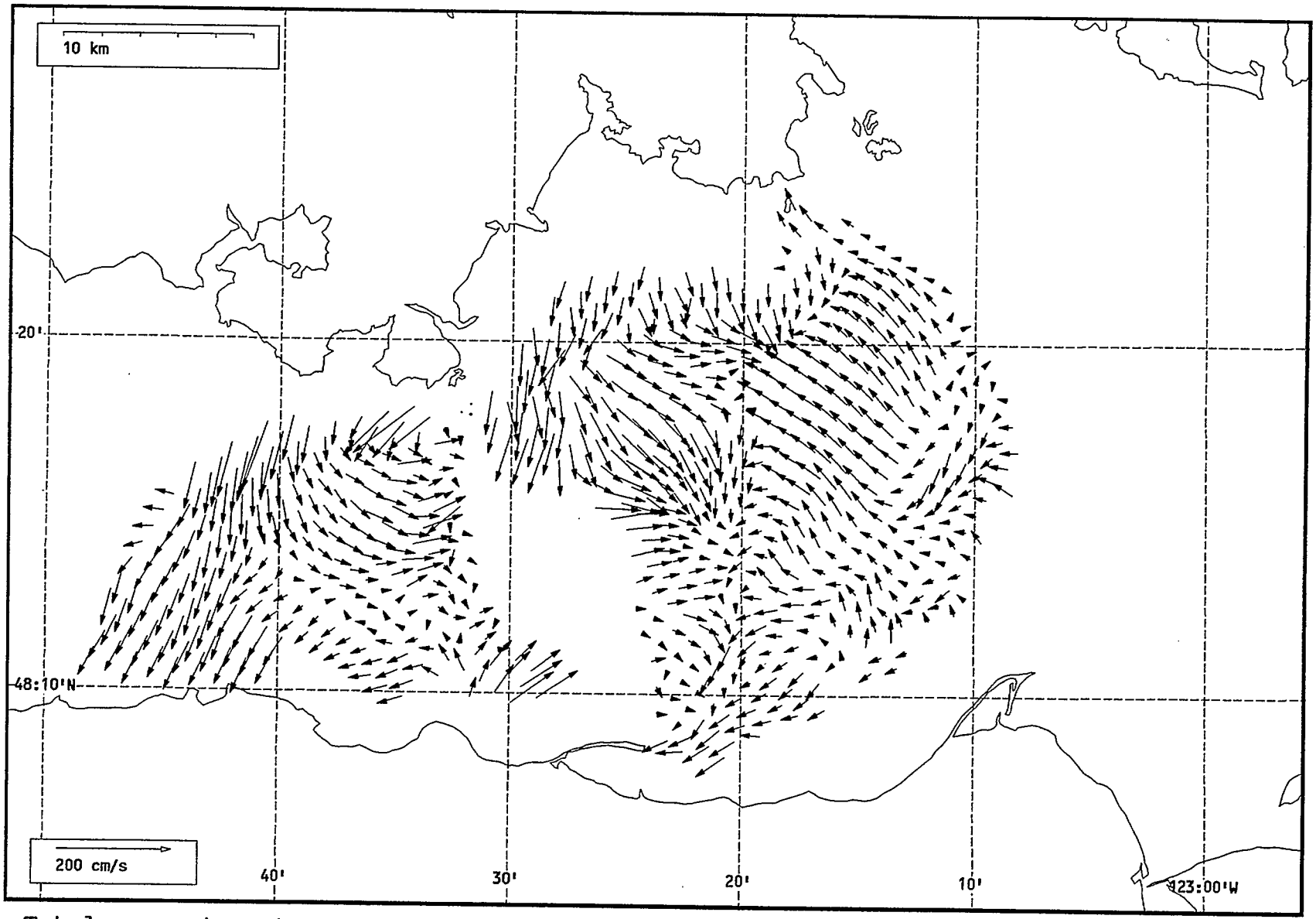

Total current vectors, Juan de Fuca Strait, 1992-07-21 05:00 Z.

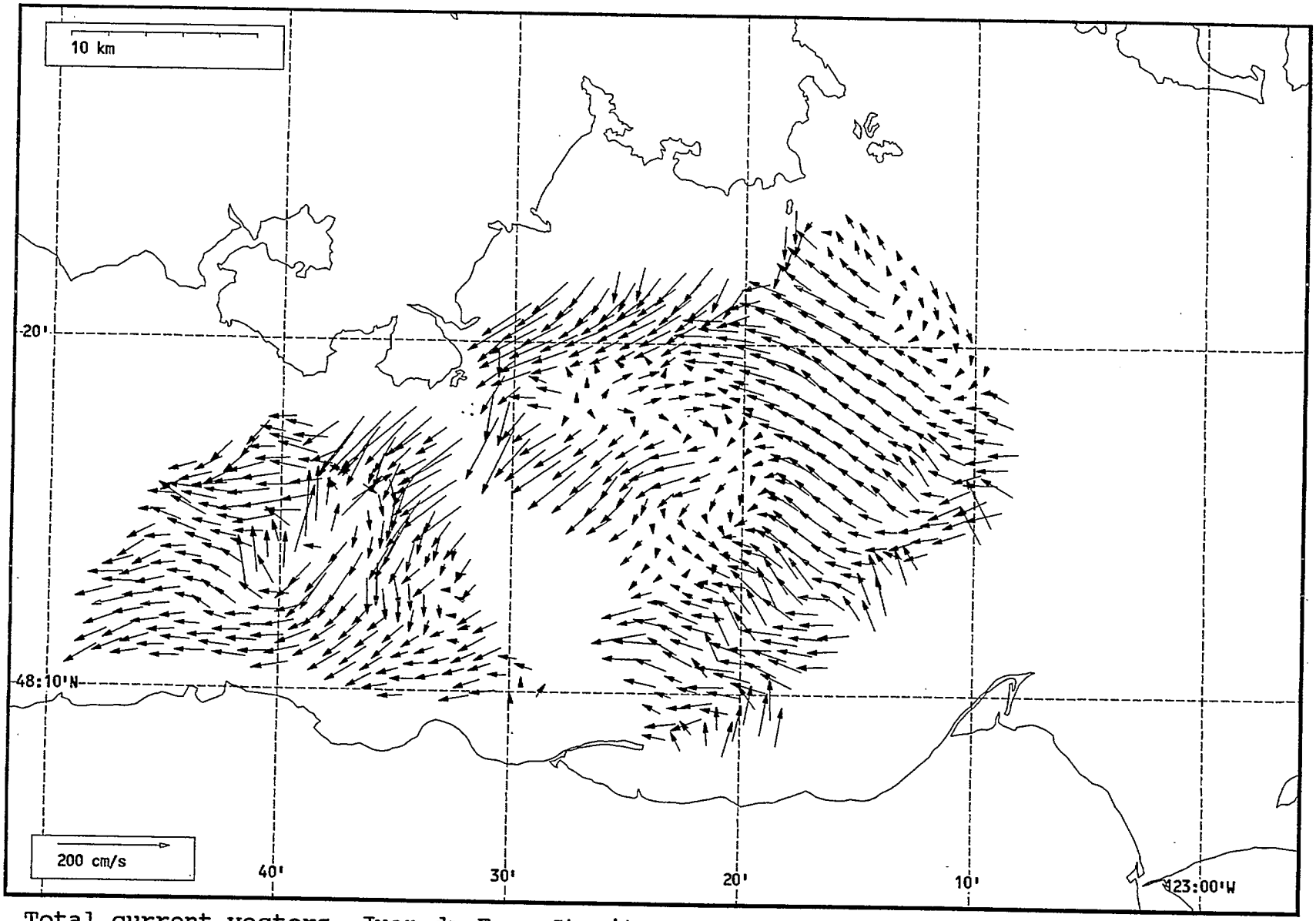

Total current vectors, Juan de Fuca Strait, 1992-07-21 06:00 Z.

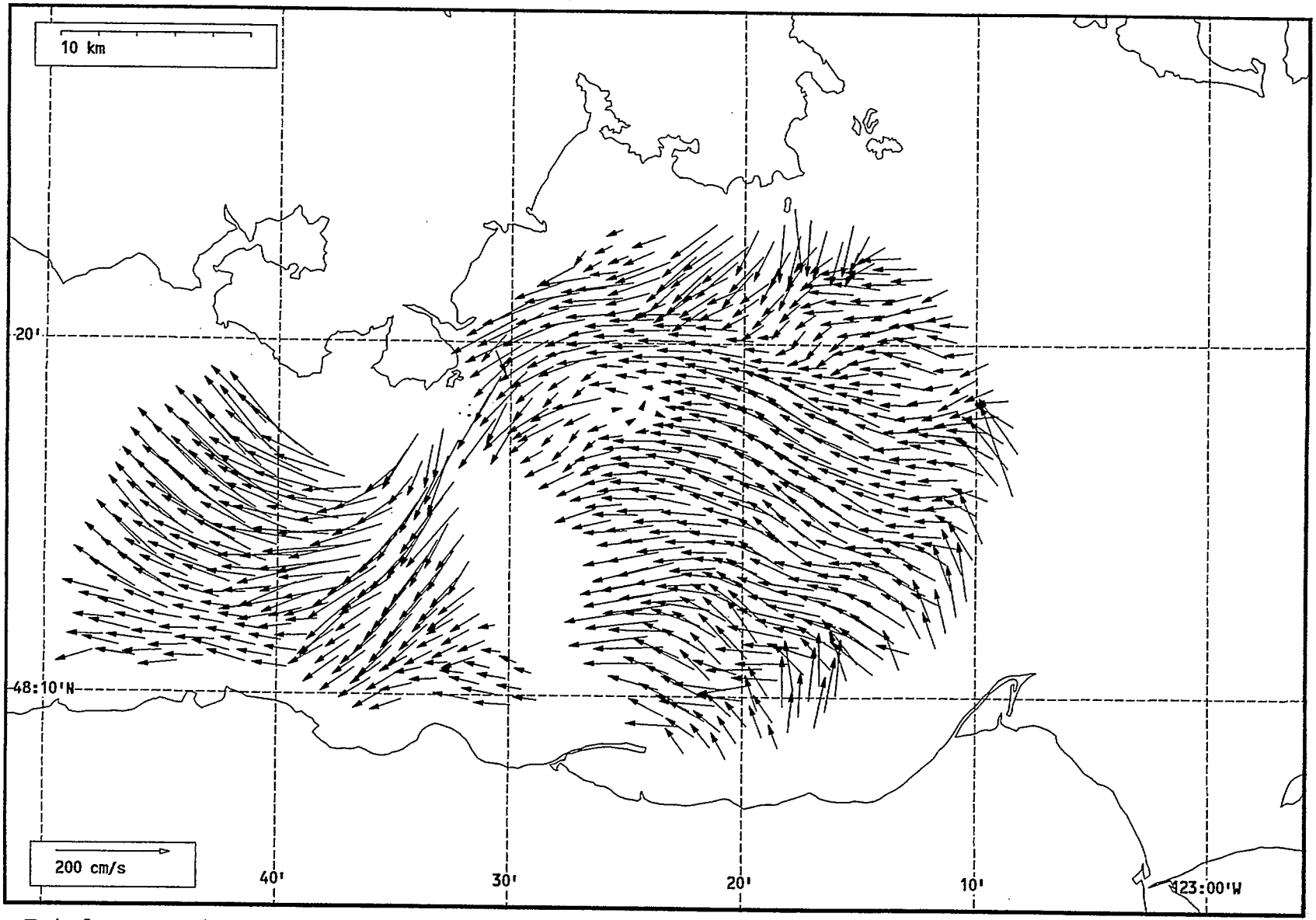

Total current vectors, Juan de Fuca Strait, 1992-07-21 07:00 Z.

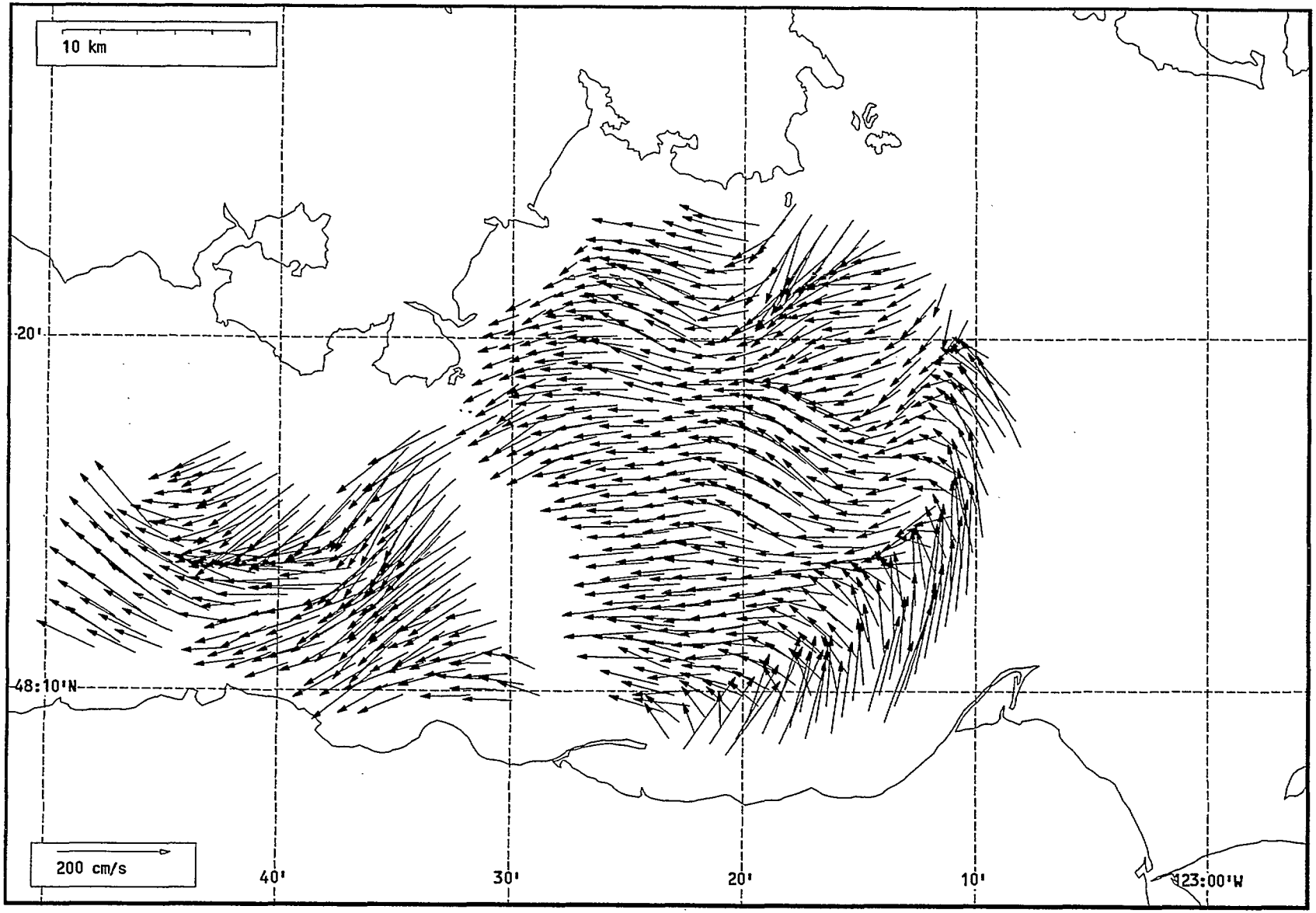

Total current vectors, Juan de Fuca Strait, 1992-07-21 08:00 Z.

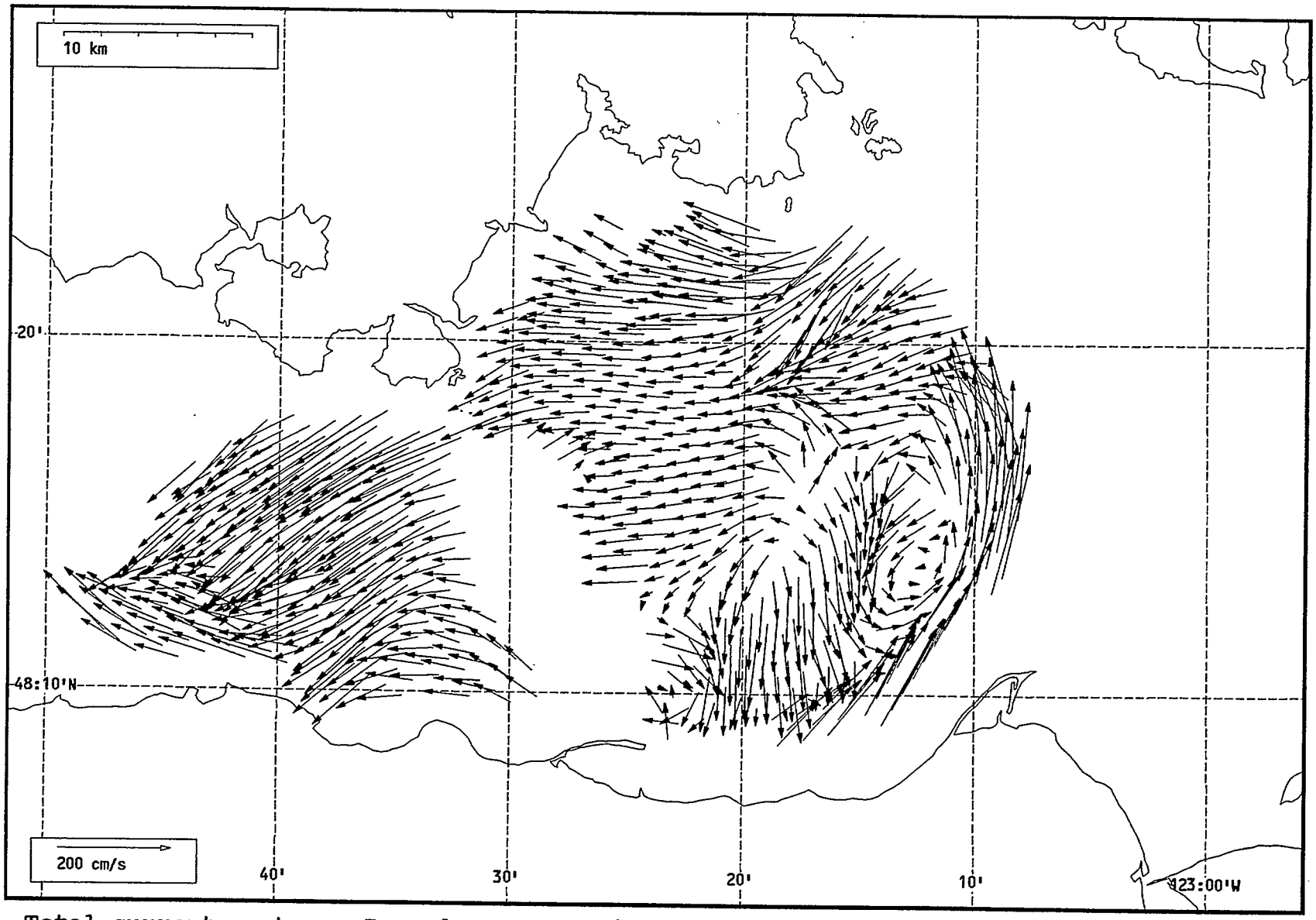

Total current vectors, Juan de Fuca Strait, 1992-07-21 09:00 Z.

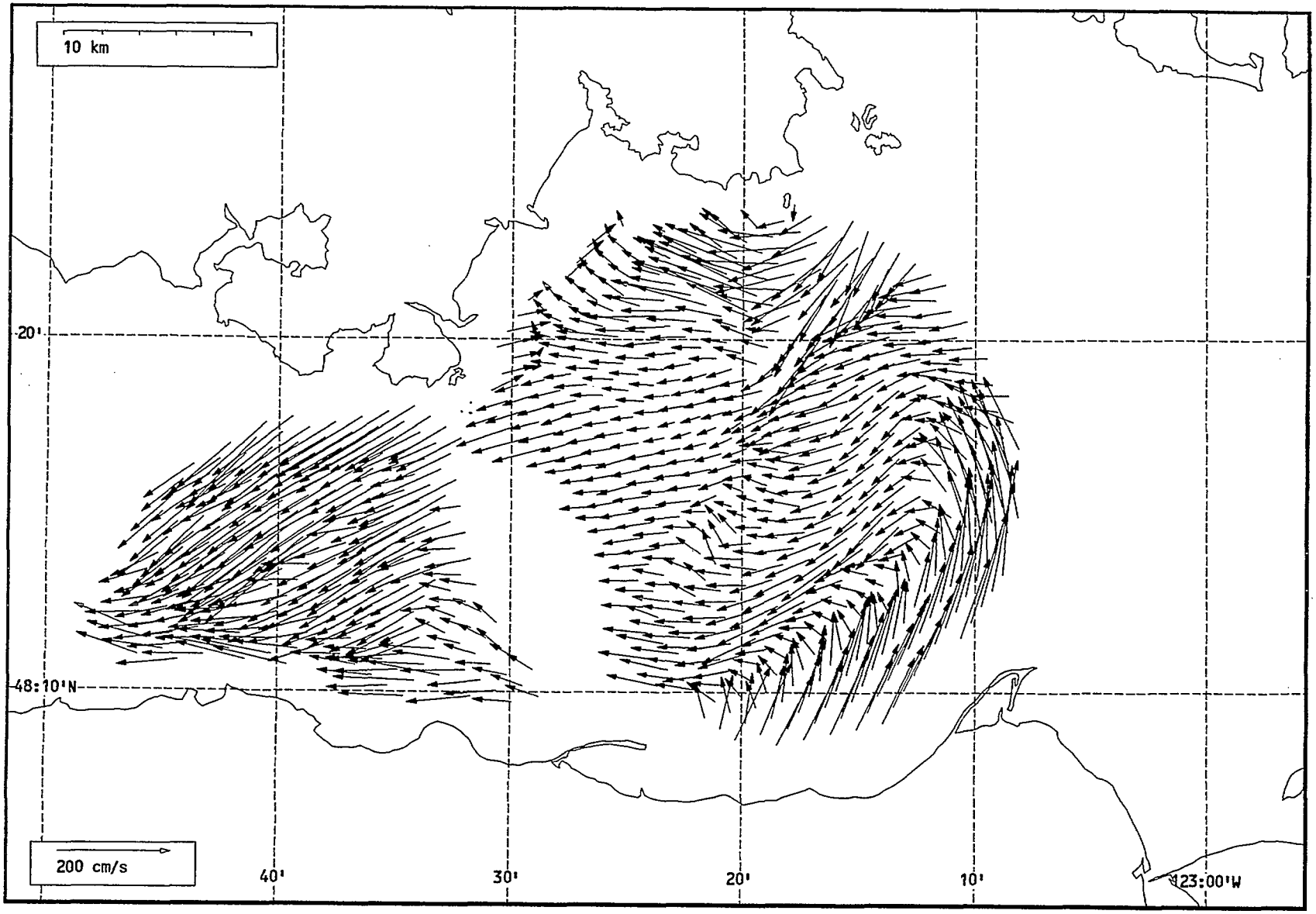

Total current vectors, Juan de Fuca Strait, 1992-07-21 10:00 Z.

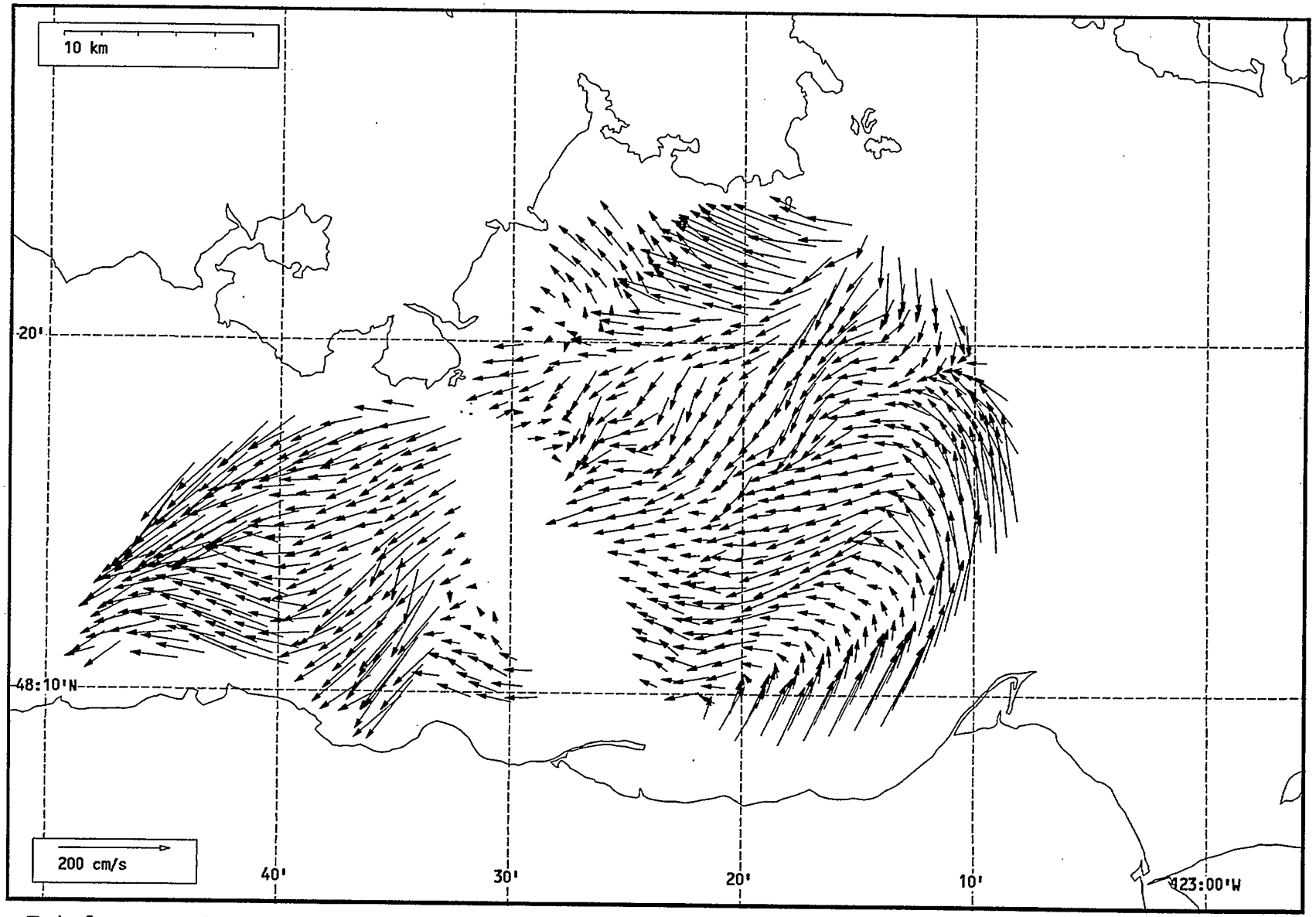

Total current vectors, Juan de Fuca Strait, 1992-07-21 11:00 Z.

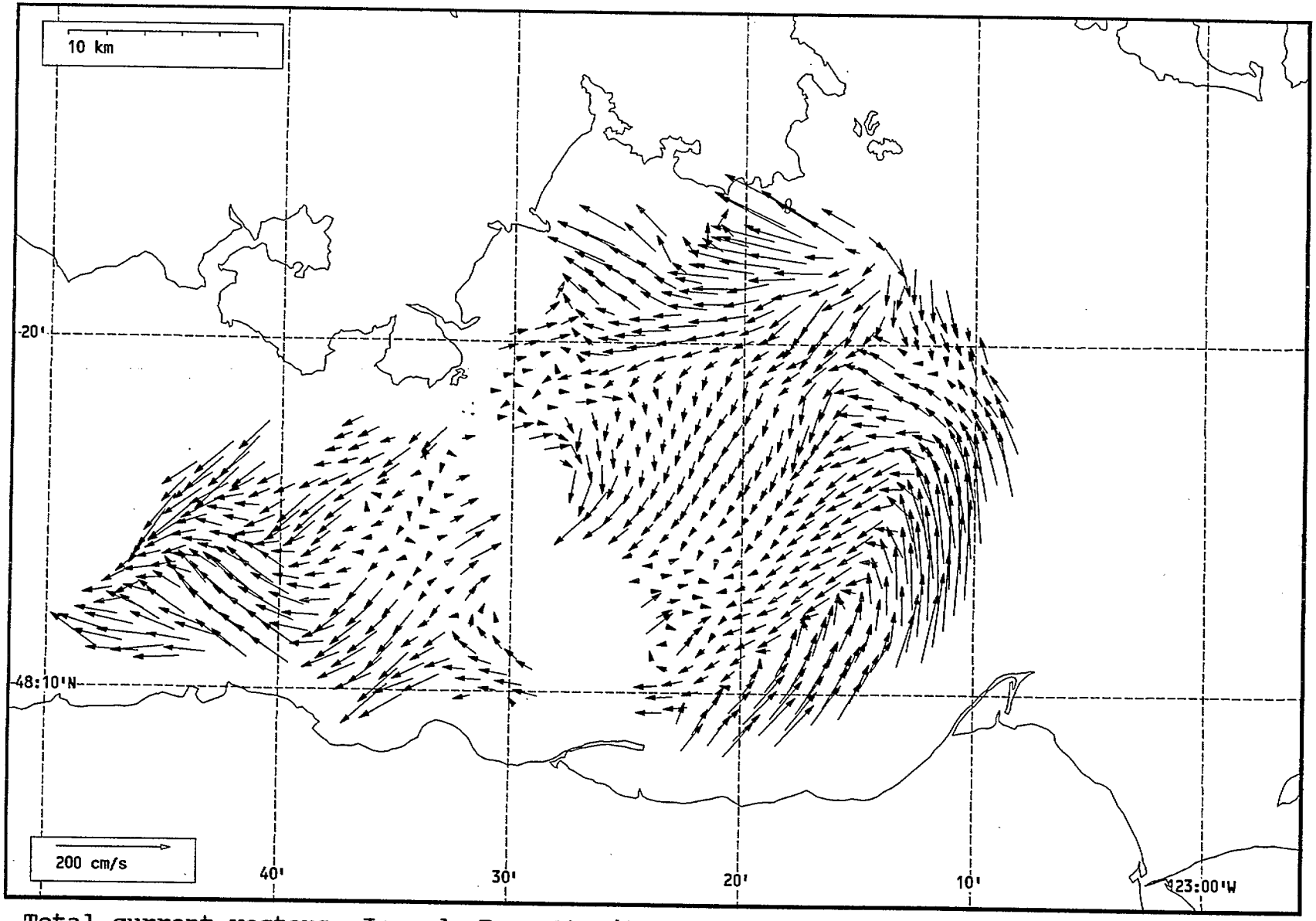

Total current vectors, Juan de Fuca Strait, 1992-07-21 12:00 Z.

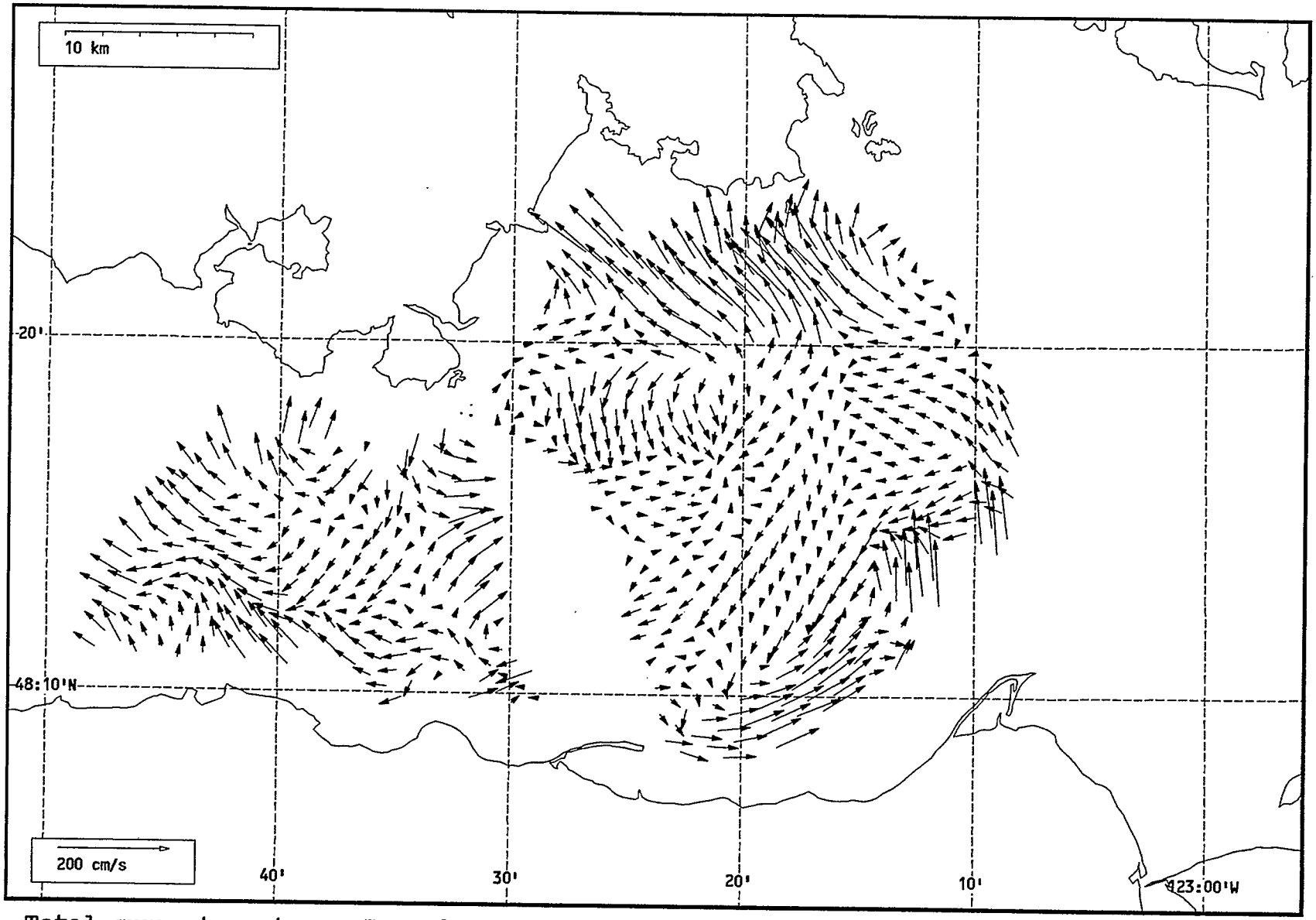

Total current vectors, Juan de Fuca Strait, 1992-07-21 13:00 Z.

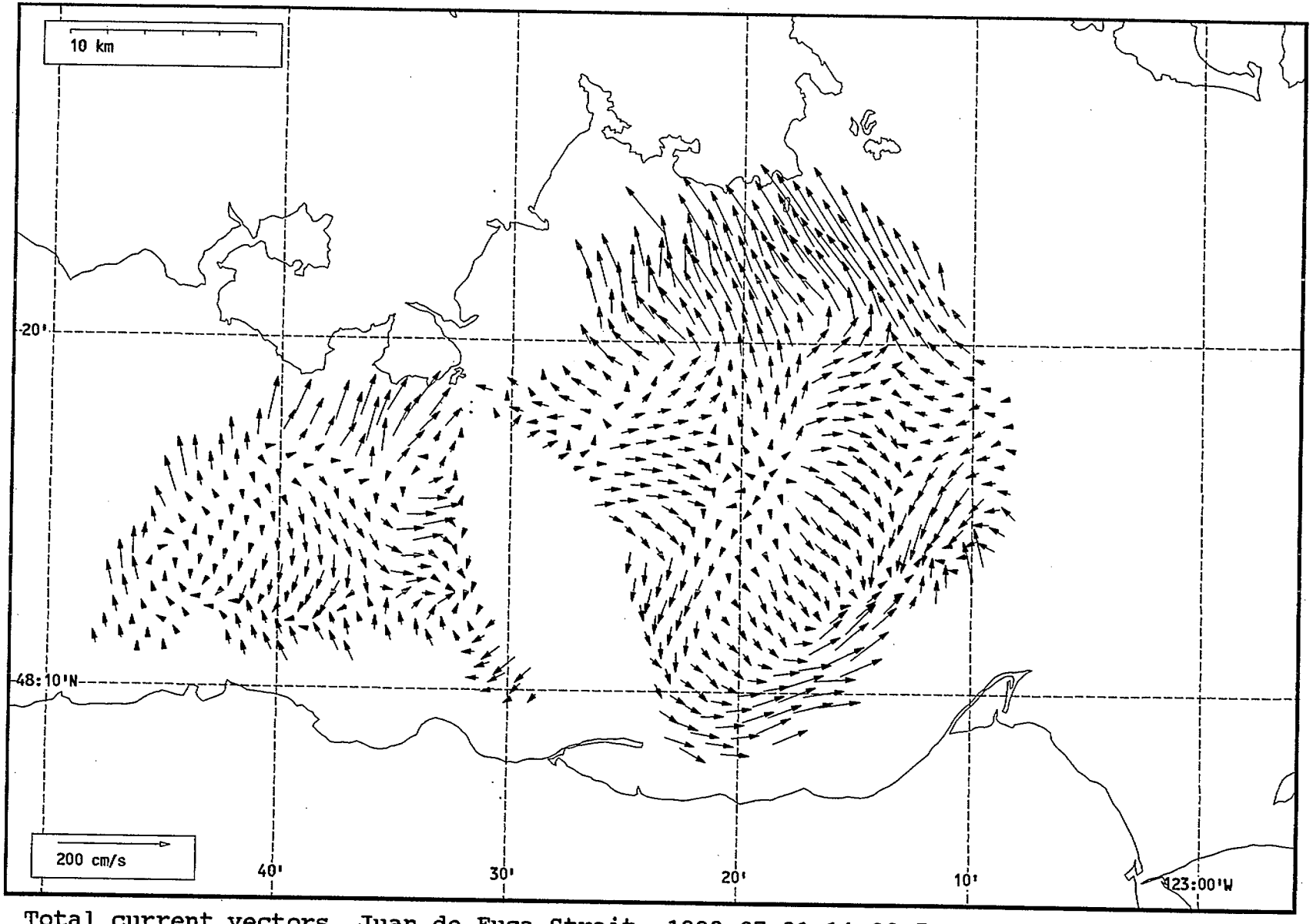

Total current vectors, Juan de Fuca Strait, 1992-07-21 14:00 Z.

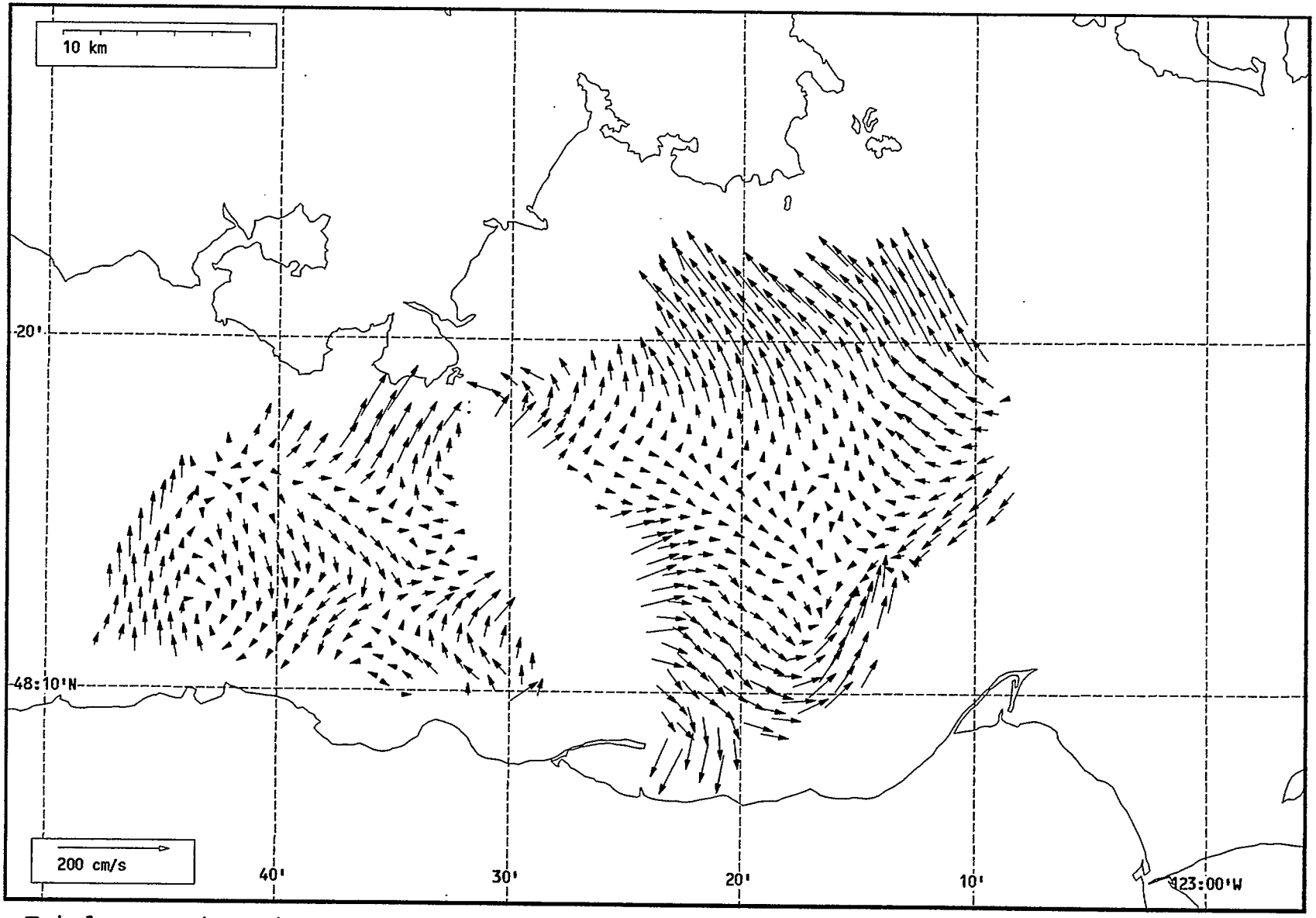

Total current vectors, Juan de Fuca Strait, 1992-07-21 15:00 Z.

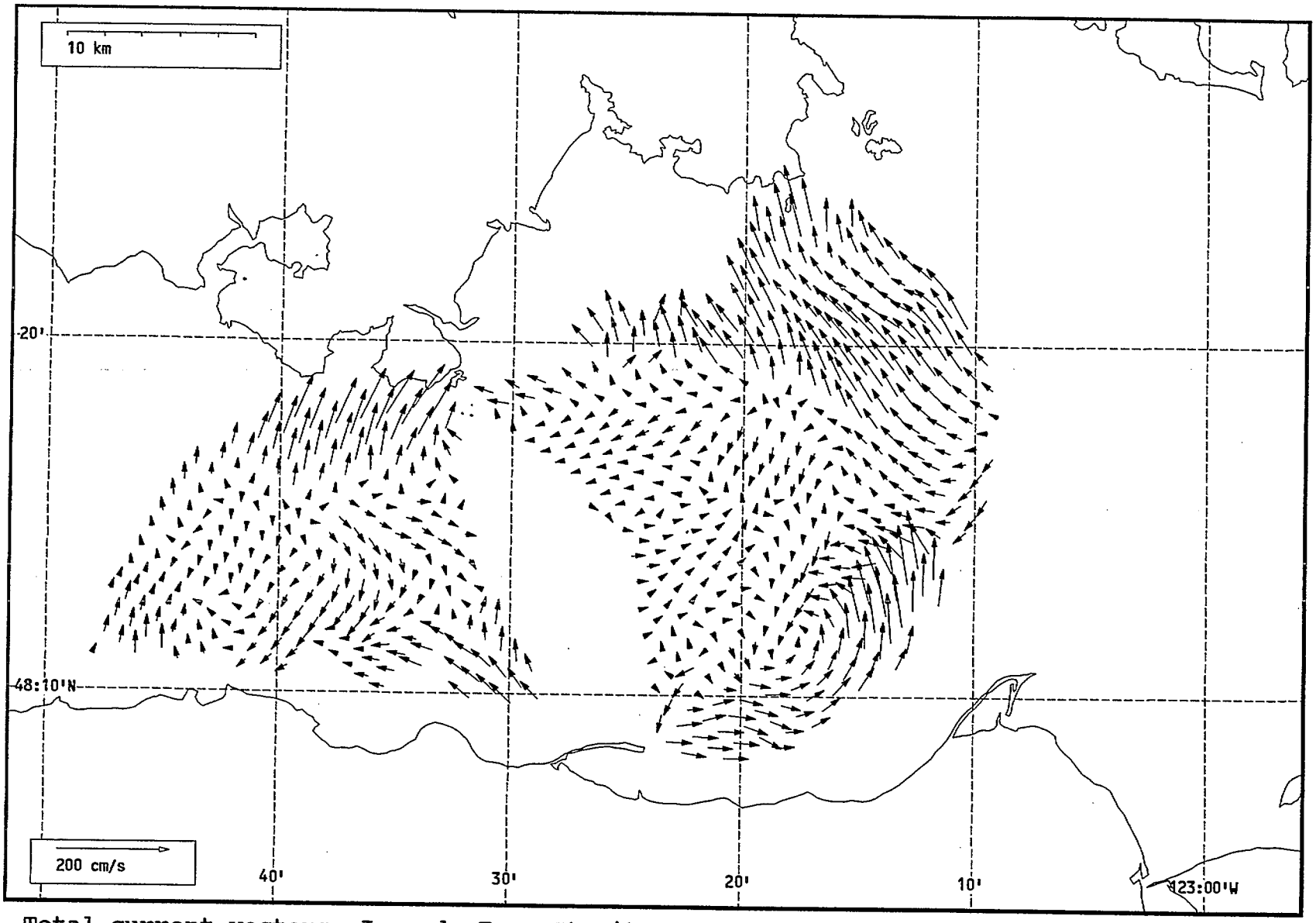

Total current vectors, Juan de Fuca Strait, 1992-07-21 16:00 Z.

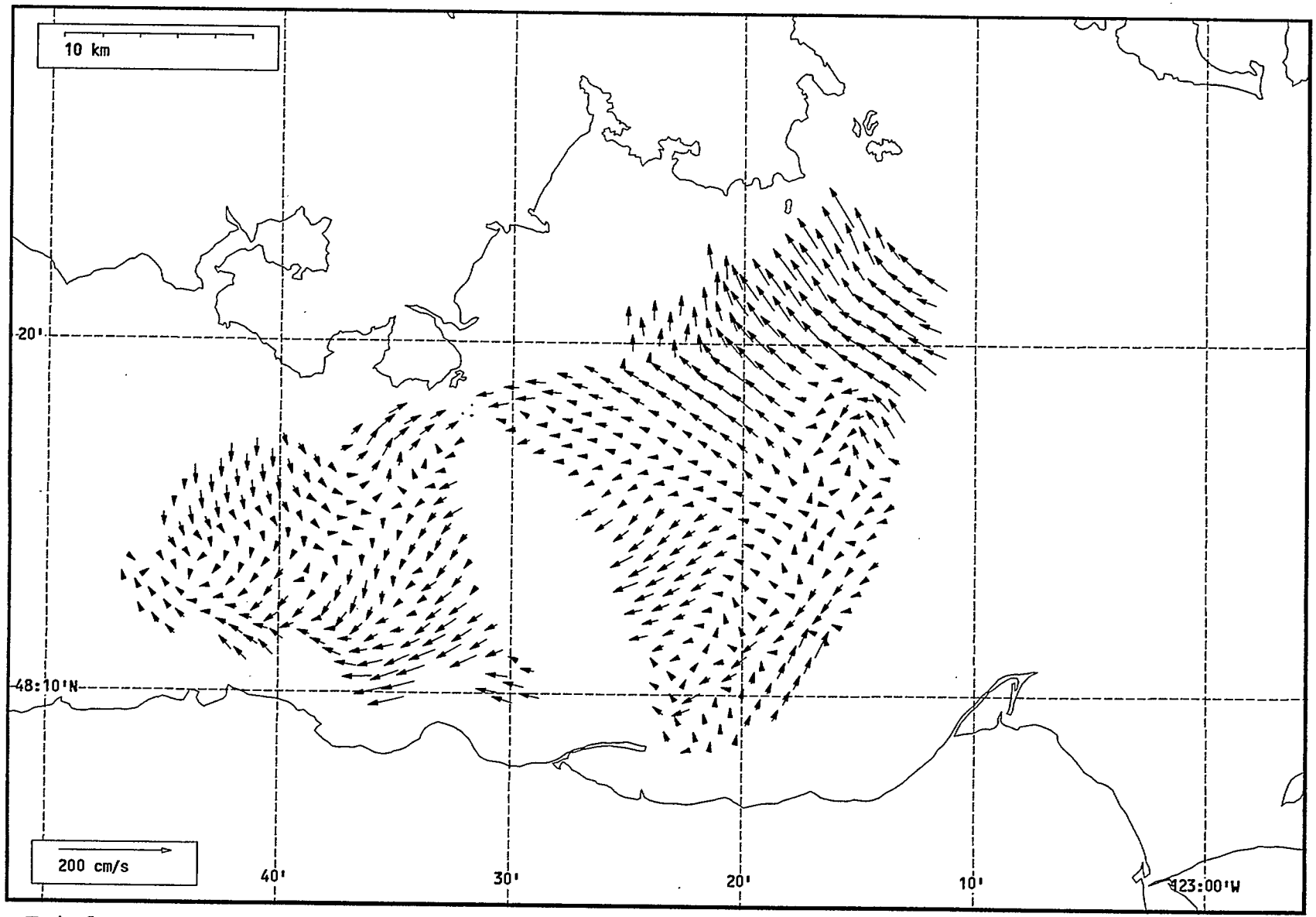

Total current vectors, Juan de Fuca Strait, 1992-07-21 17:00 Z.

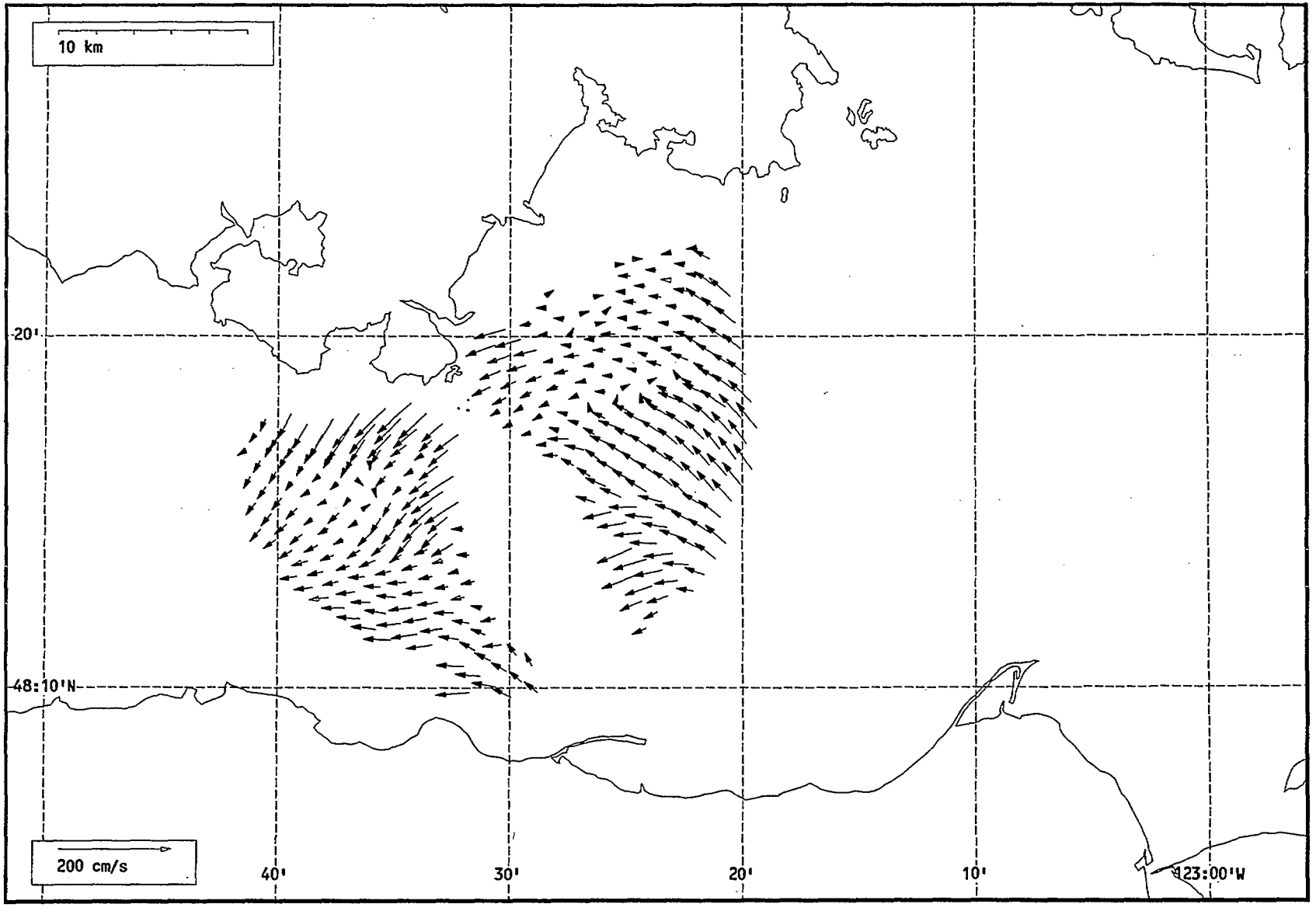

Total current vectors, Juan de Fuca Strait, 1992-07-21 18:00 Z.

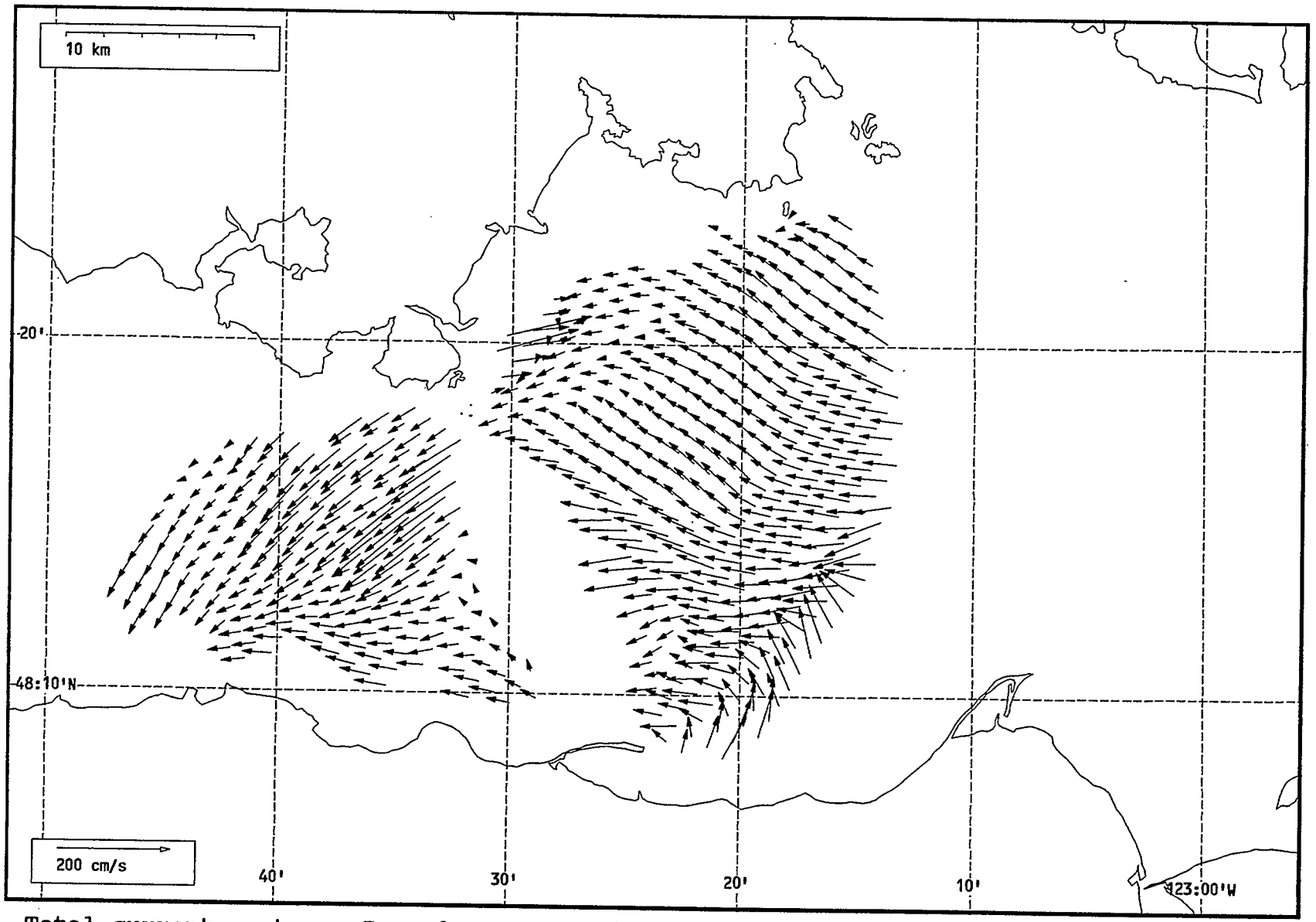

Total current vectors, Juan de Fuca Strait, 1992-07-21 19:00 Z.

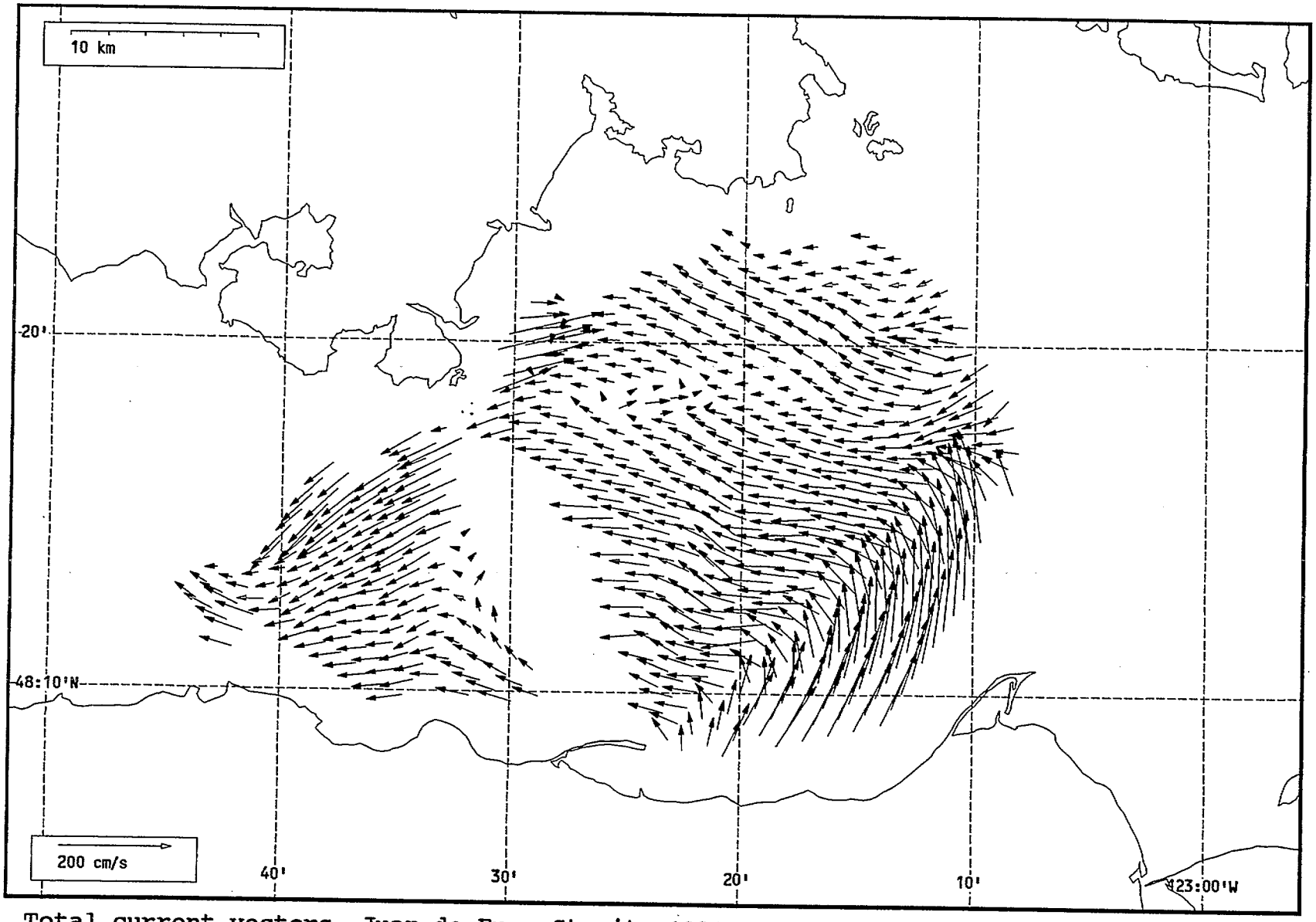

Total current vectors, Juan de Fuca Strait, 1992-07-21 20:00 Z.

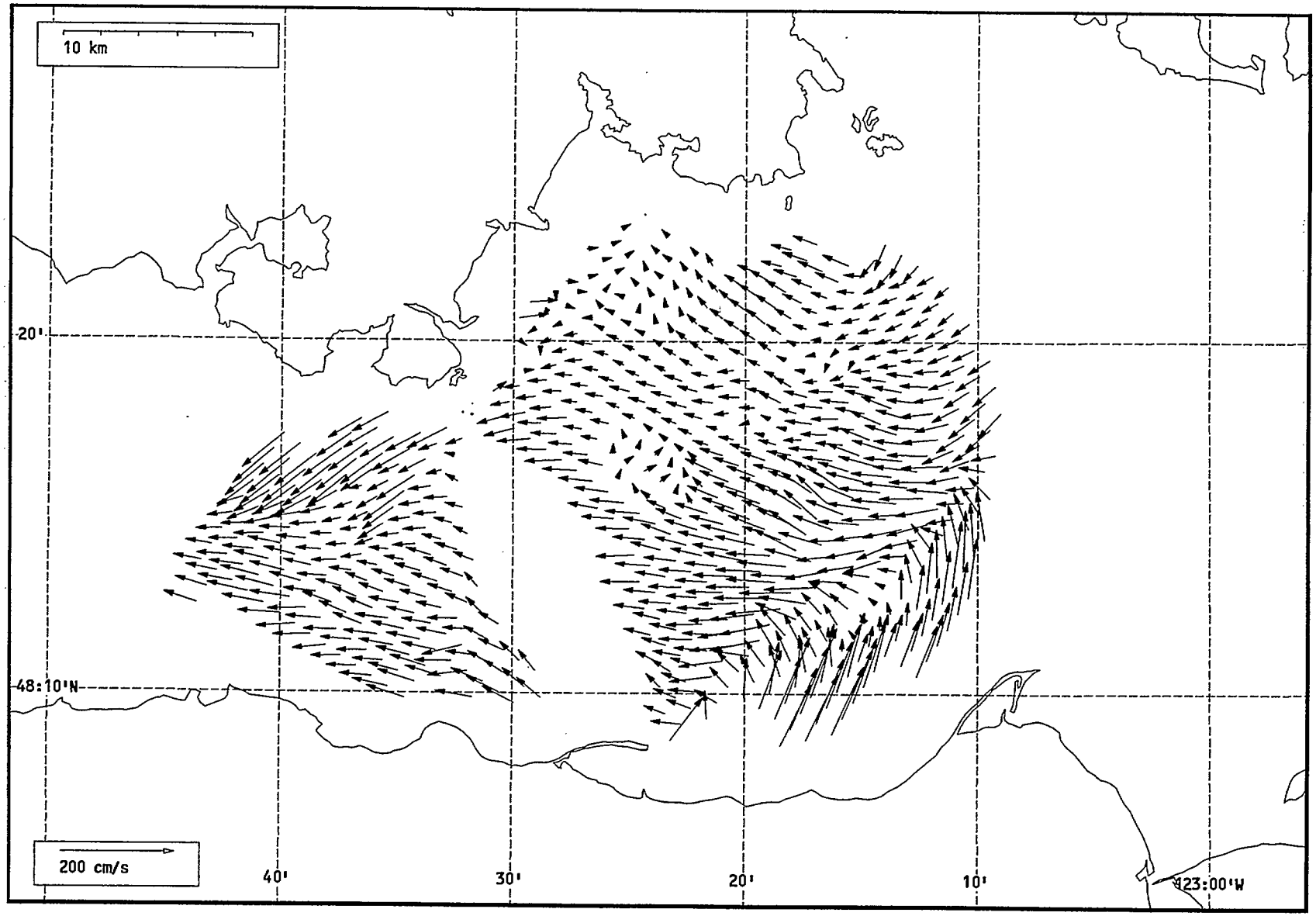

Total current vectors, Juan de Fuca Strait, 1992-07-21 21:00 Z.

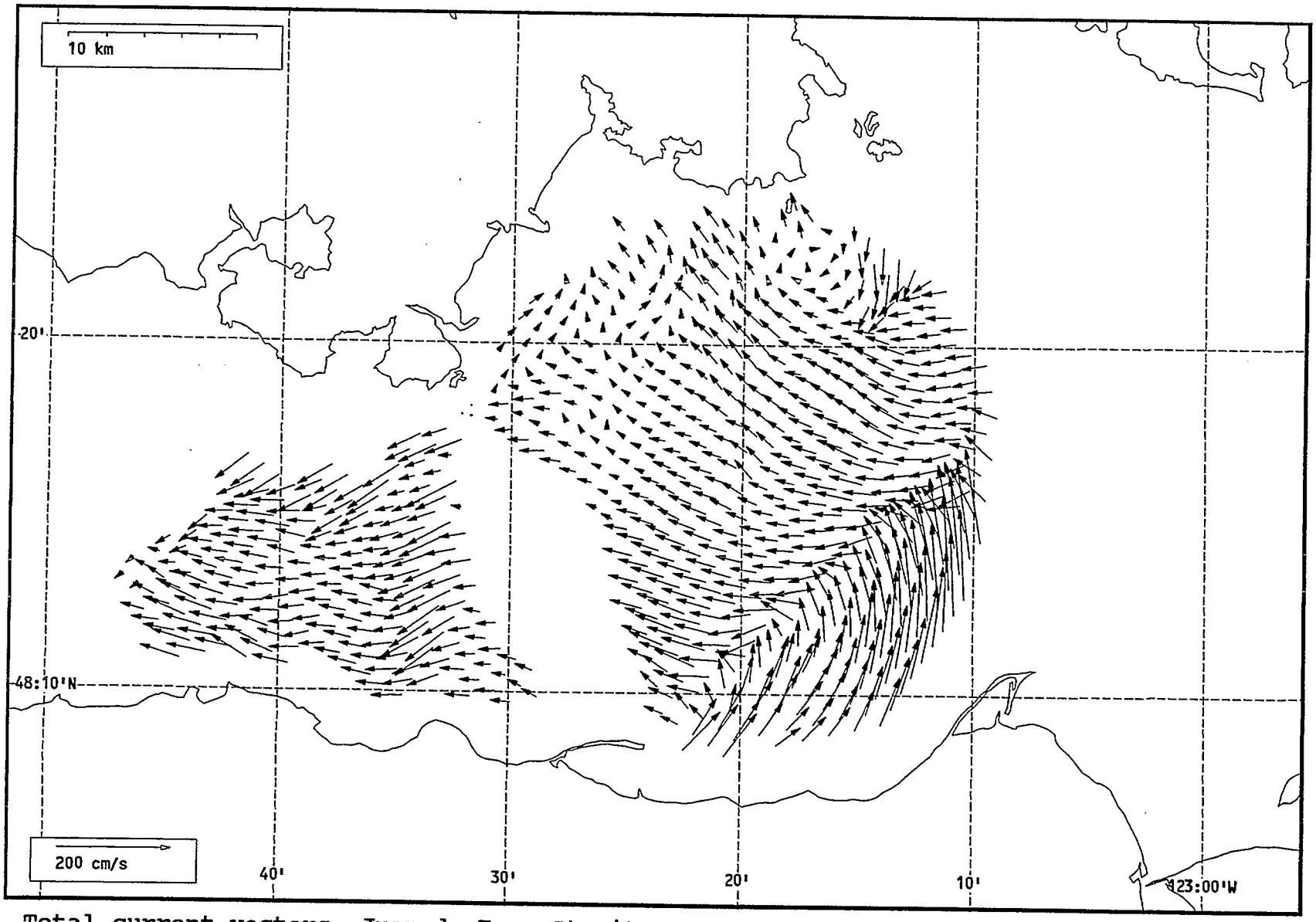

Total current vectors, Juan de Fuca Strait, 1992-07-21 22:00 Z.

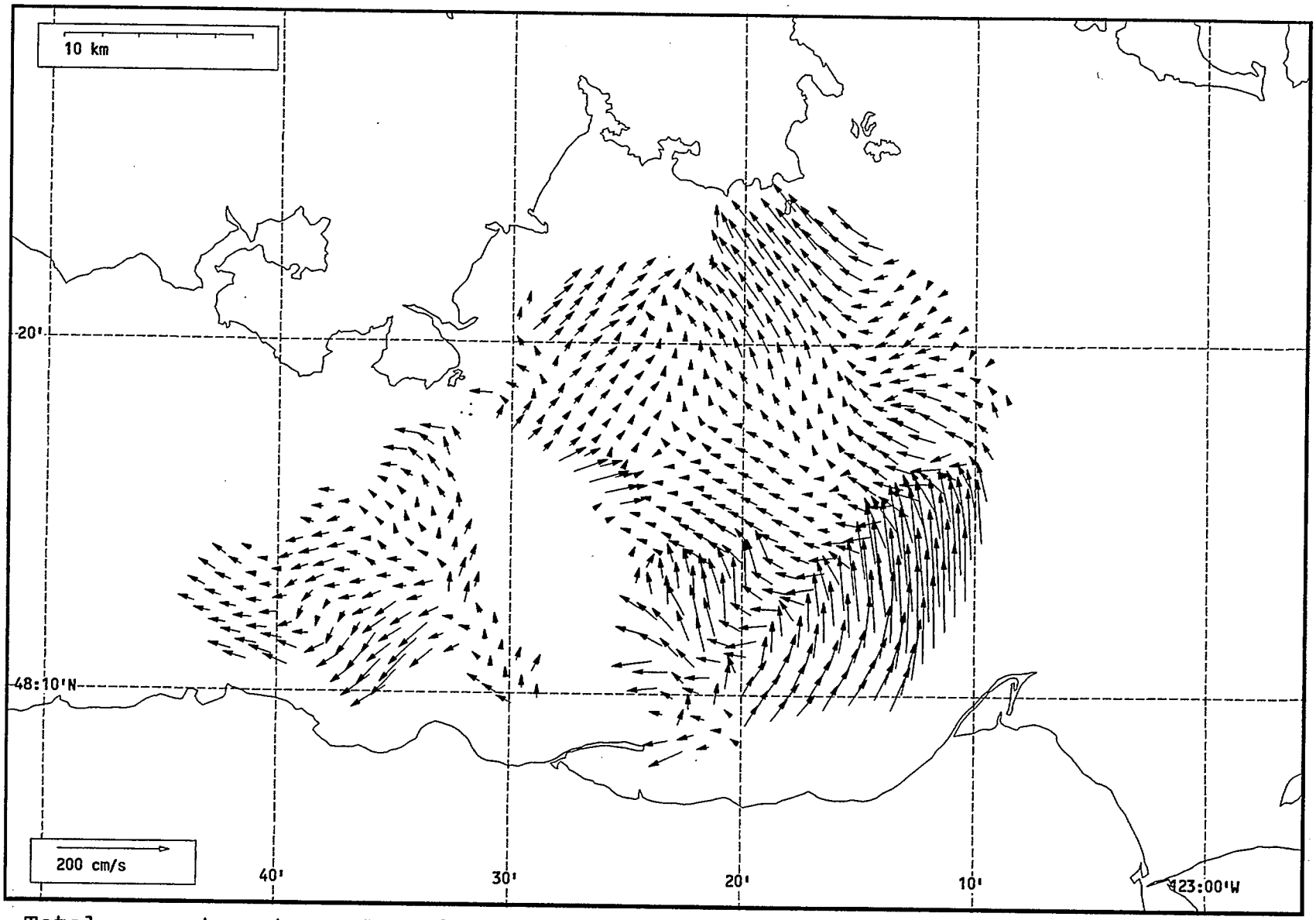

Total current vectors, Juan de Fuca Strait, 1992-07-21 23:00 Z.

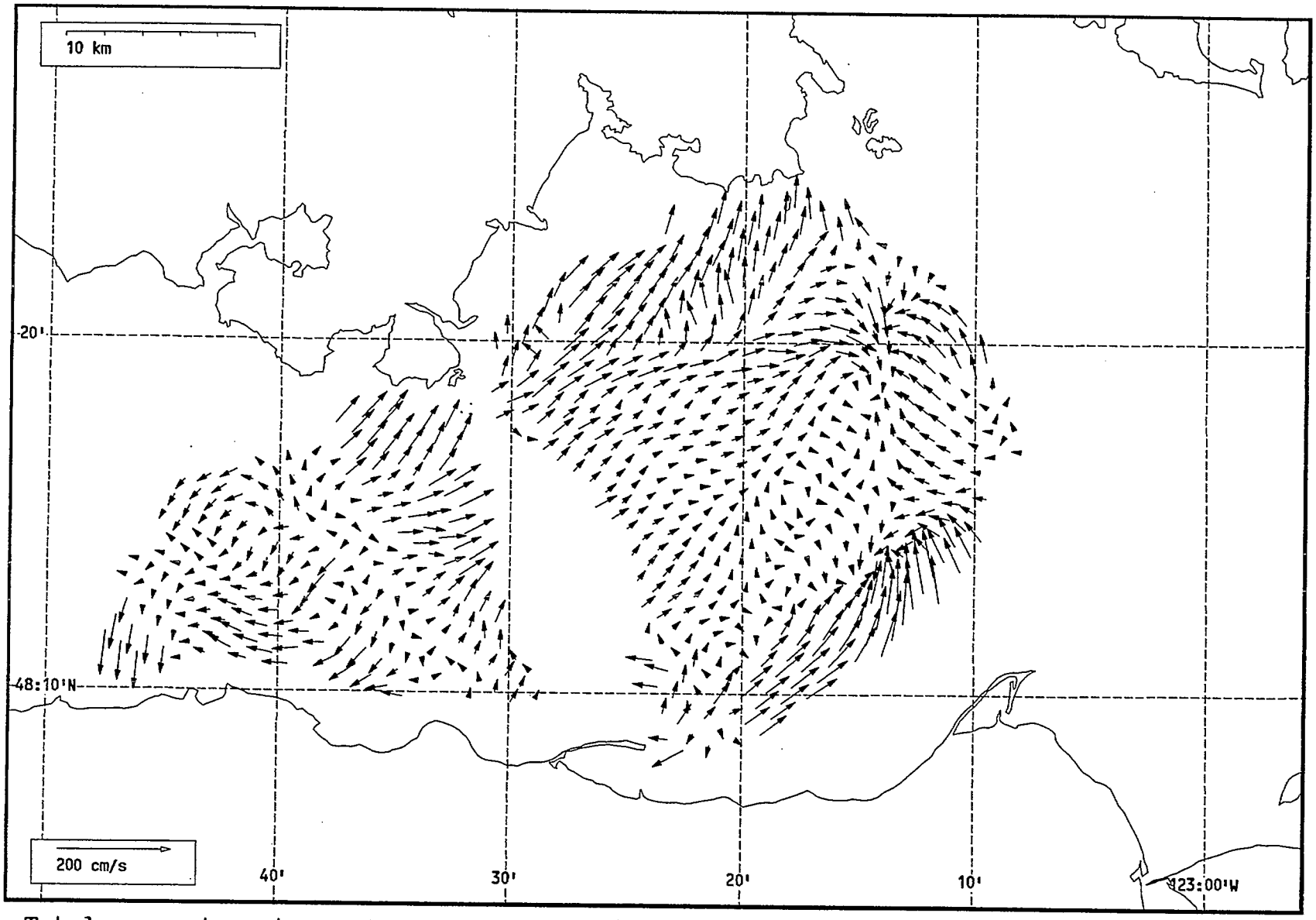

Total current vectors, Juan de Fuca Strait, 1992-07-22 00:00 Z.

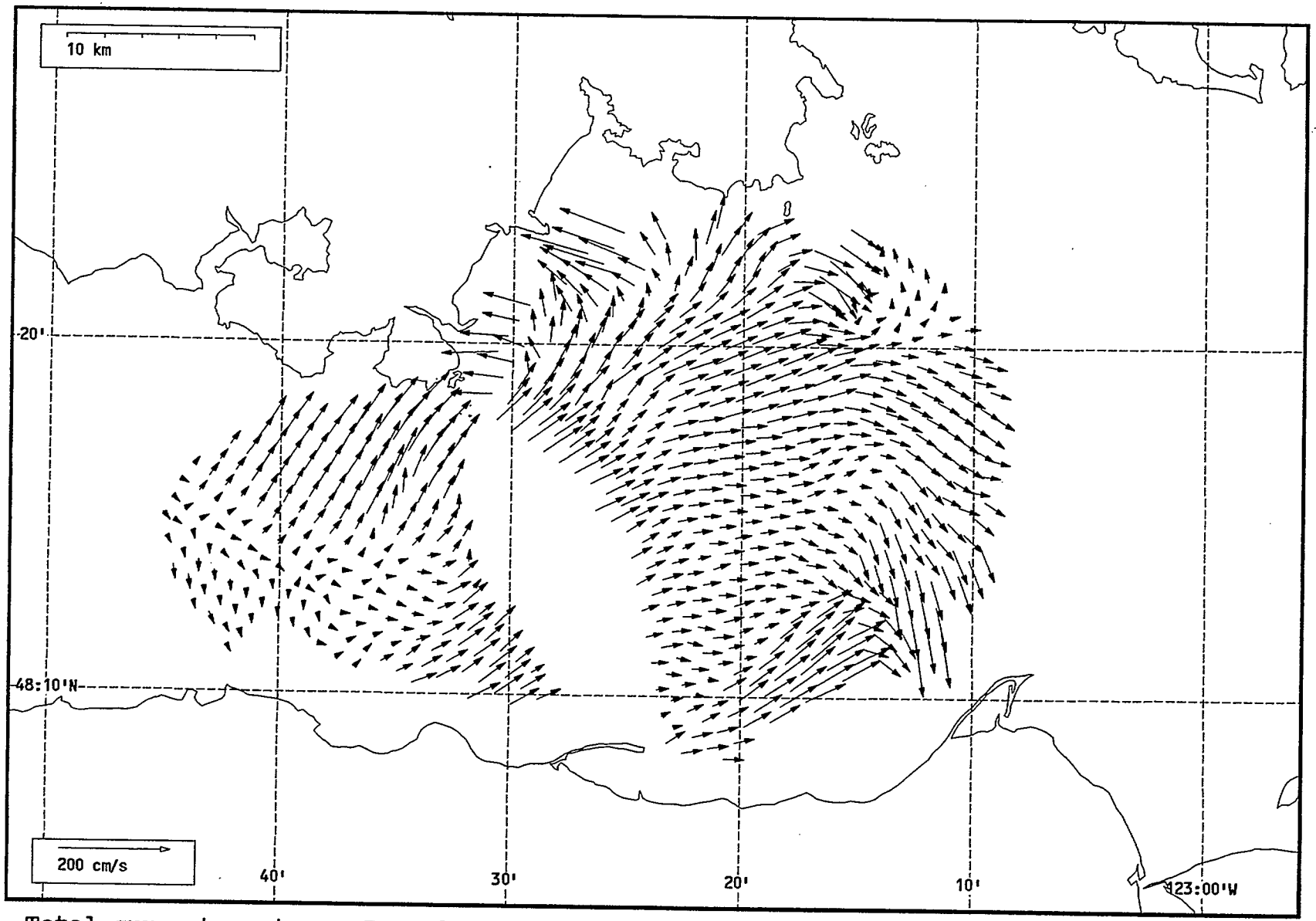

Total current vectors, Juan de Fuca Strait, 1992-07-22 01:00 Z.

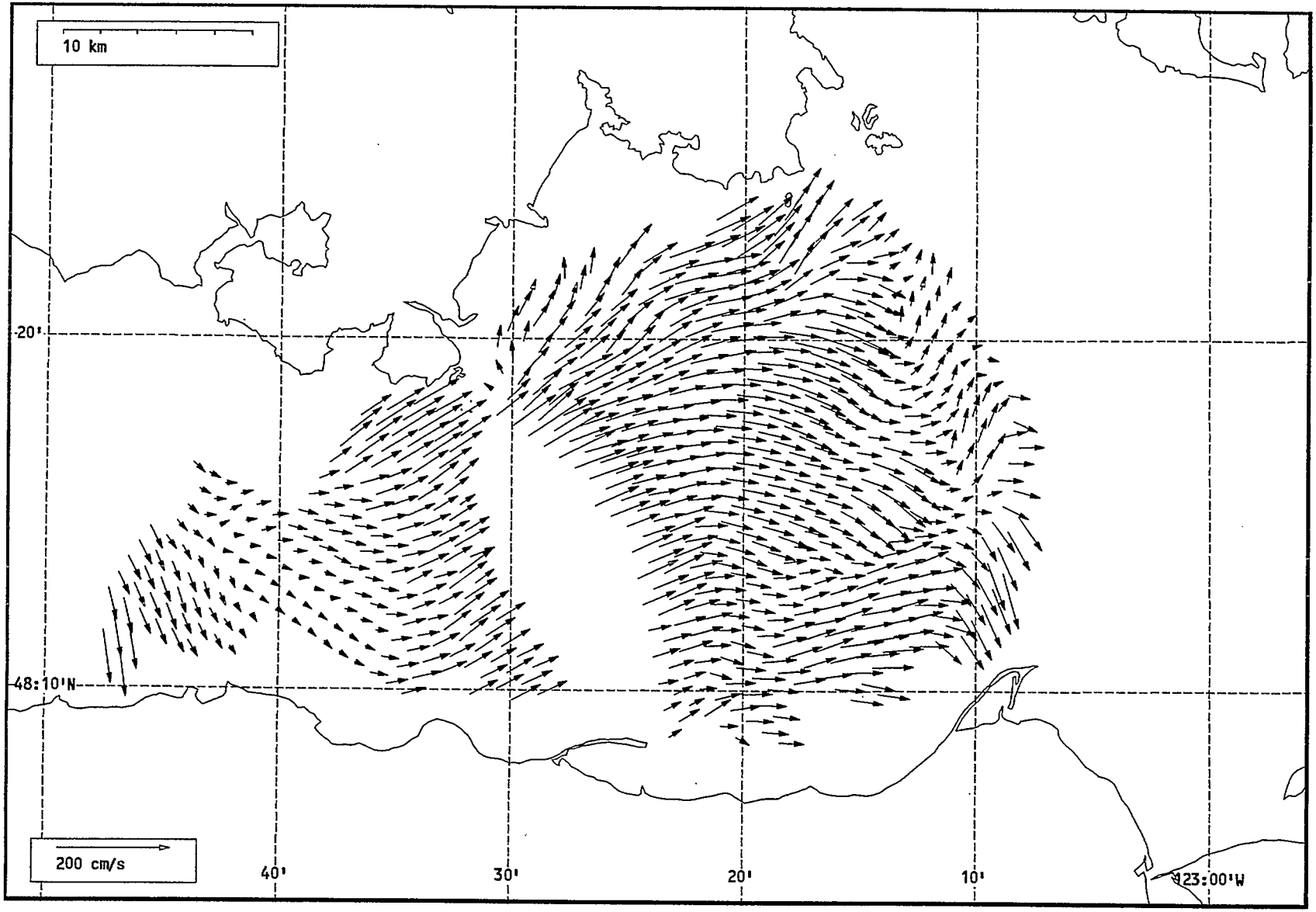

Total current vectors, Juan de Fuca Strait, 1992-07-22 02:00 Z.

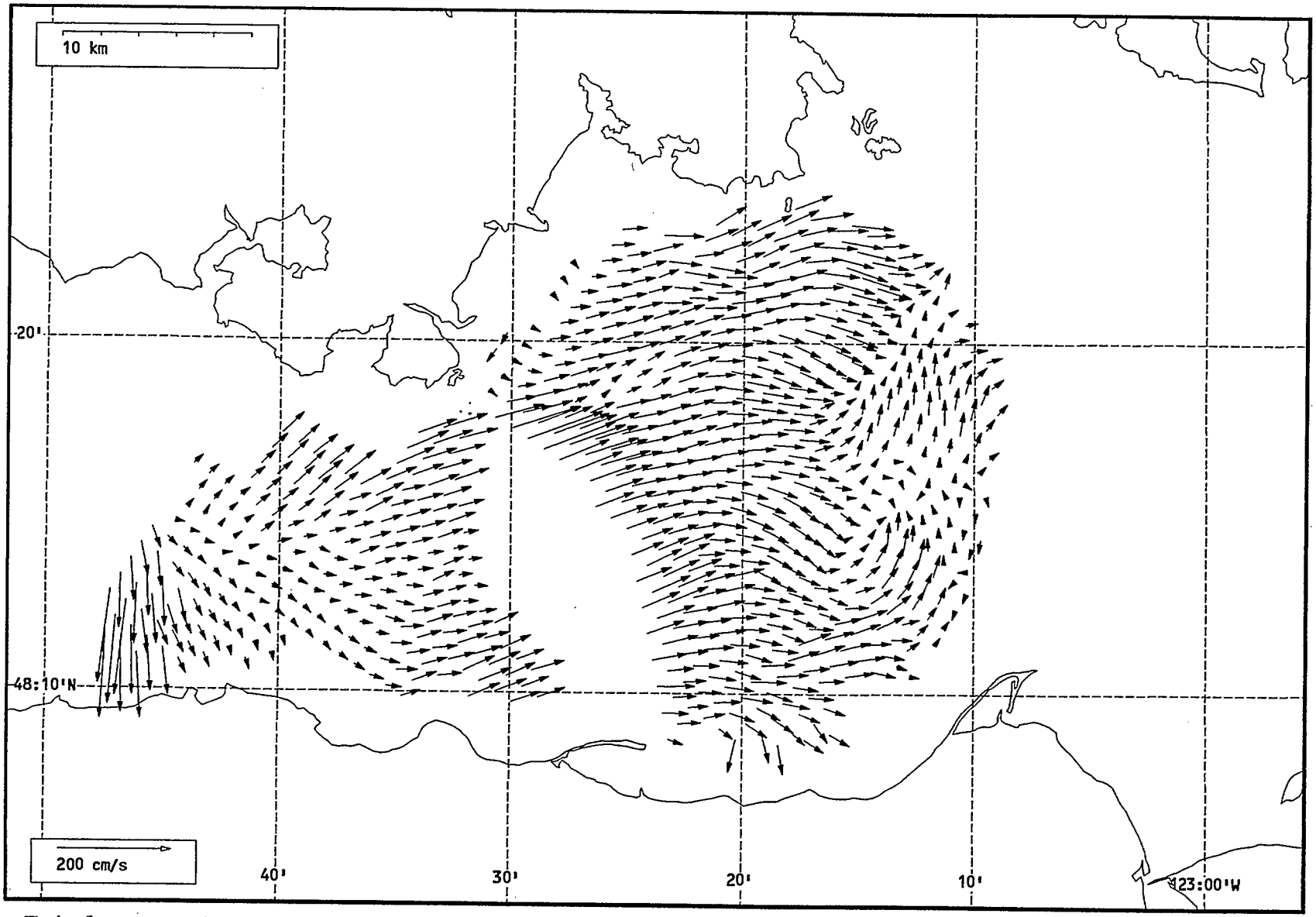

Total current vectors, Juan de Fuca Strait, 1992-07-22 03:00 Z.

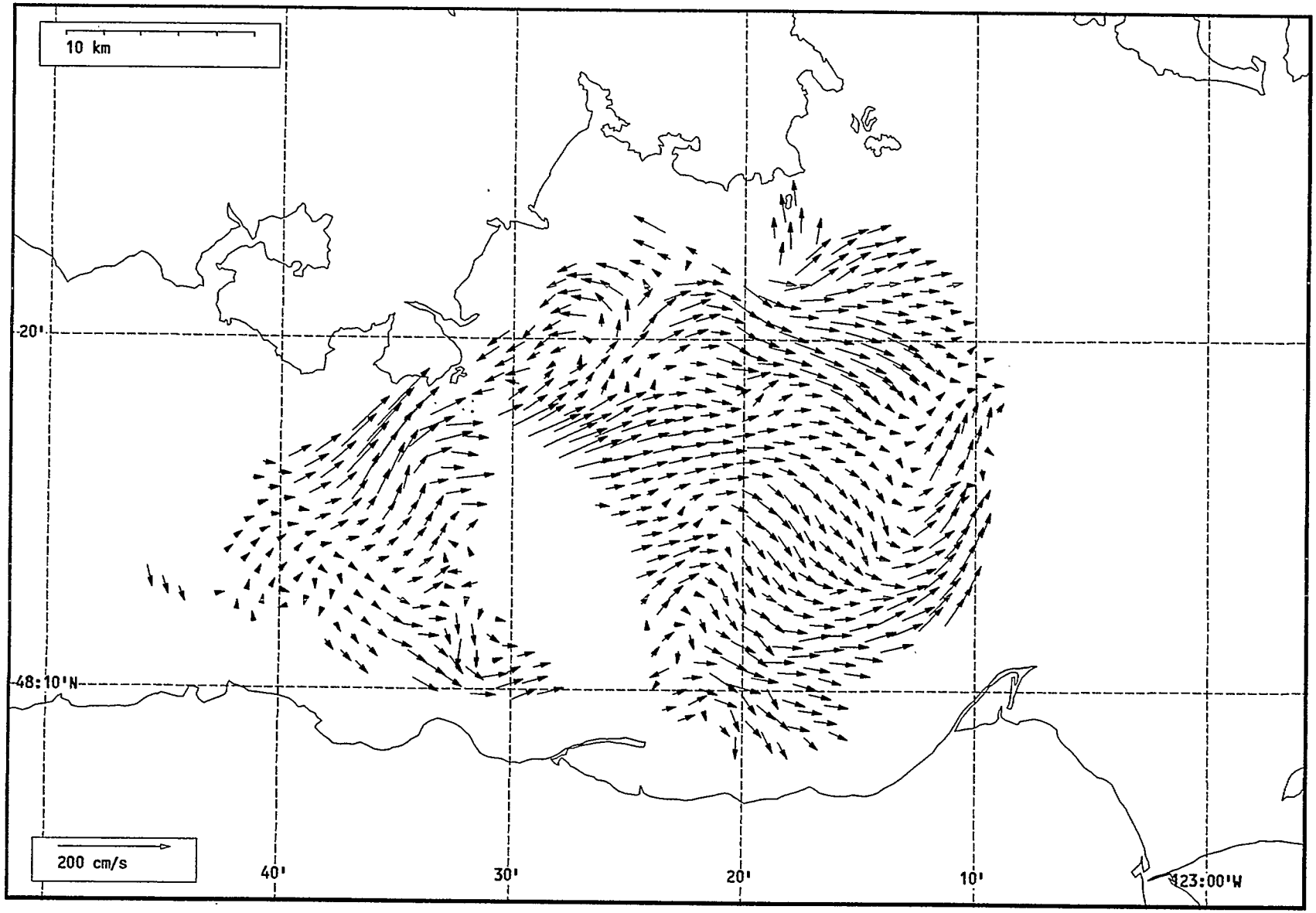

Total current vectors, Juan de Fuca Strait, 1992-07-22 04:00 Z.

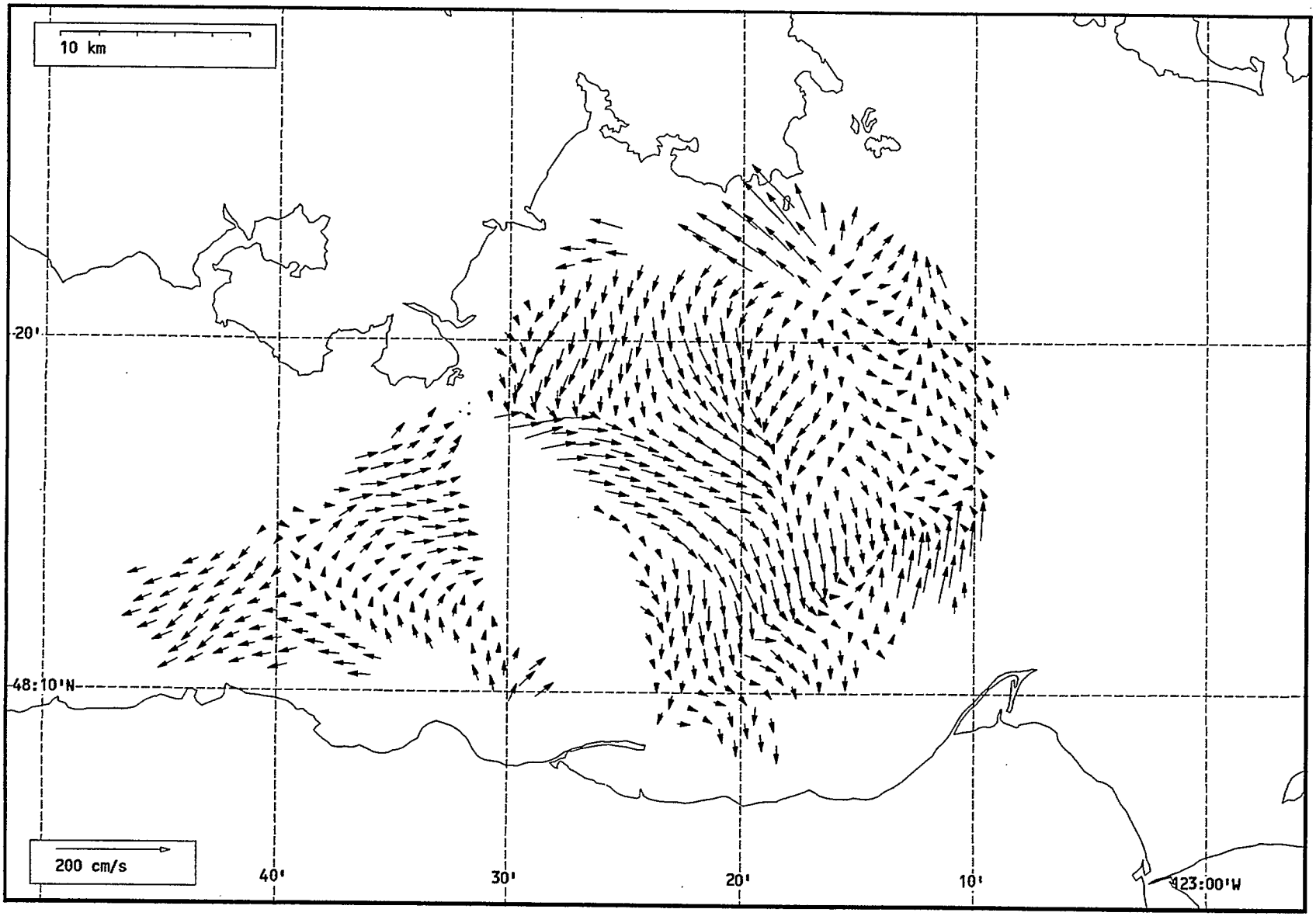

Total current vectors, Juan de Fuca Strait, 1992-07-22 05:00 Z.

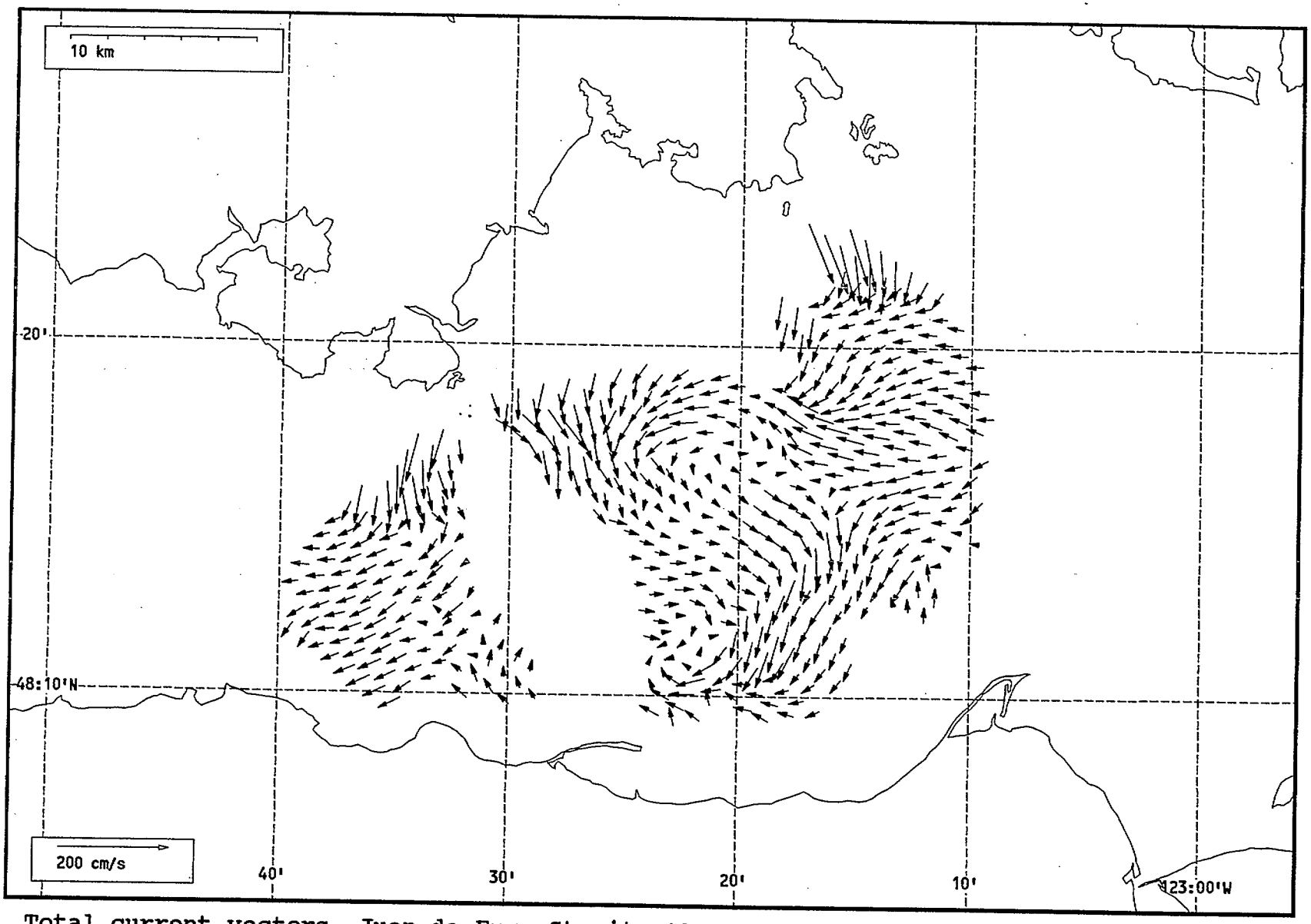

Total current vectors, Juan de Fuca Strait, 1992-07-22 06:00 Z.

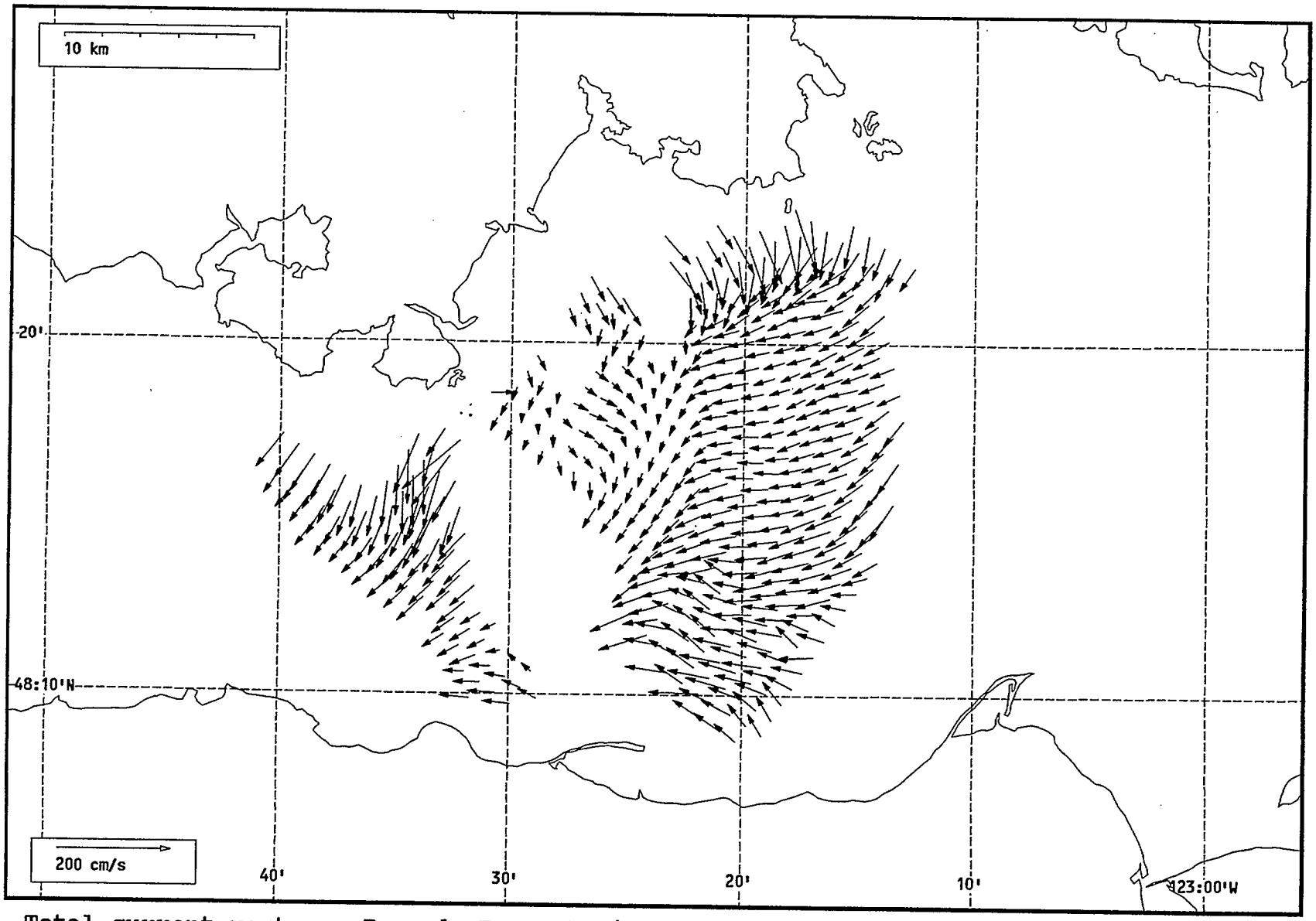

Total current vectors, Juan de Fuca Strait, 1992-07-22 07:00 Z.

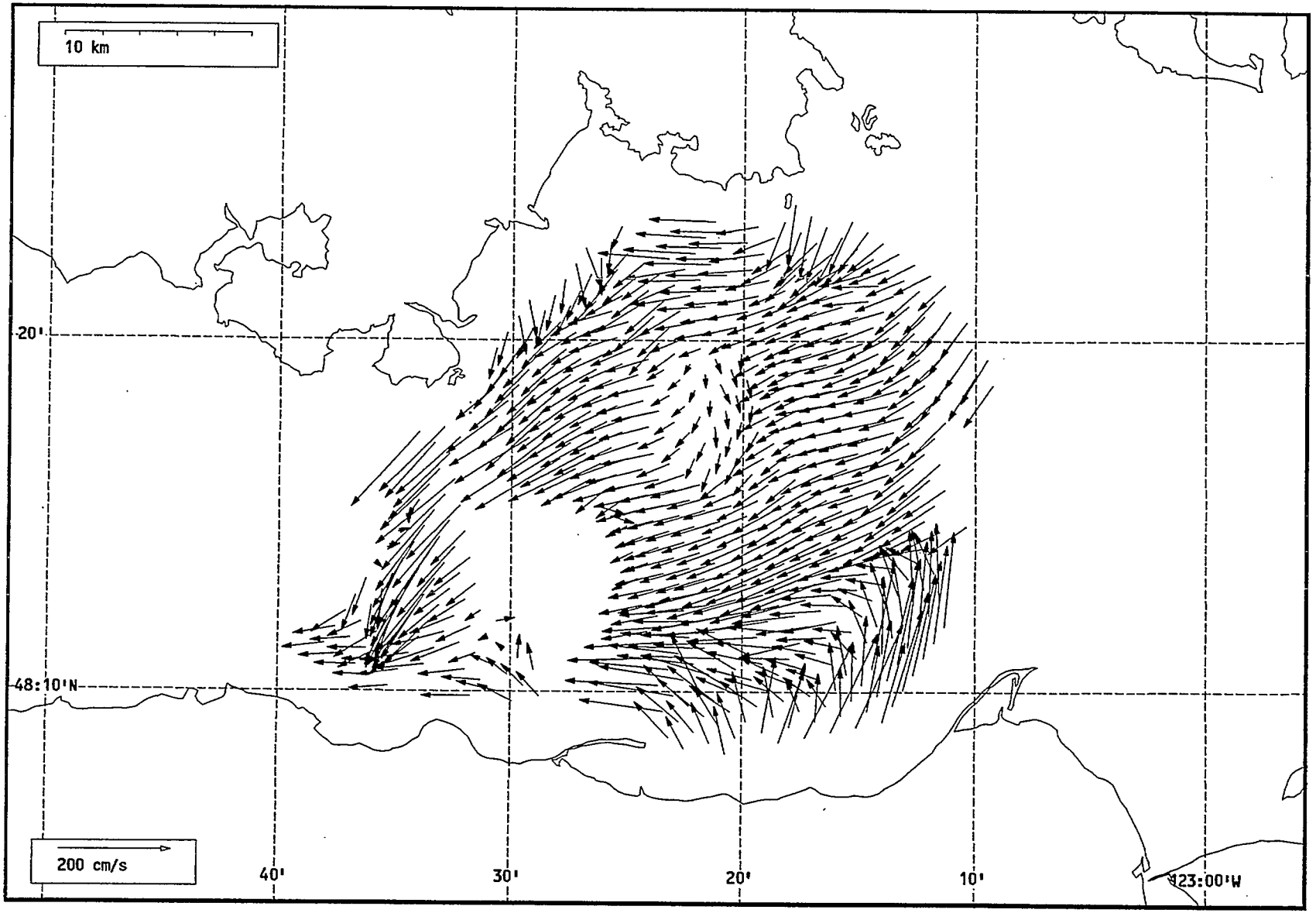

Total current vectors, Juan de Fuca Strait, 1992-07-22 08:00 Z.

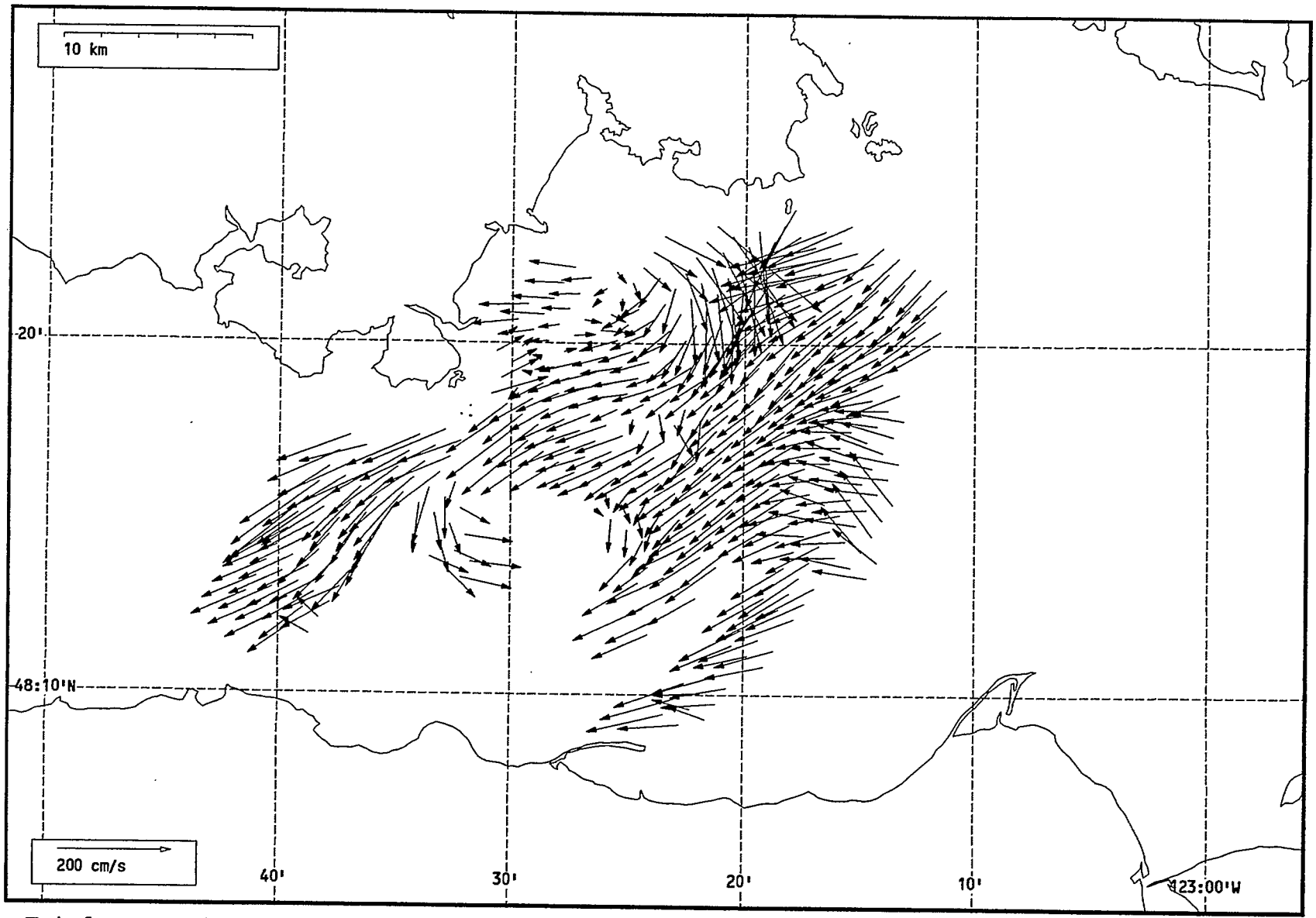

Total current vectors, Juan de Fuca Strait, 1992-07-22 09:00 Z.

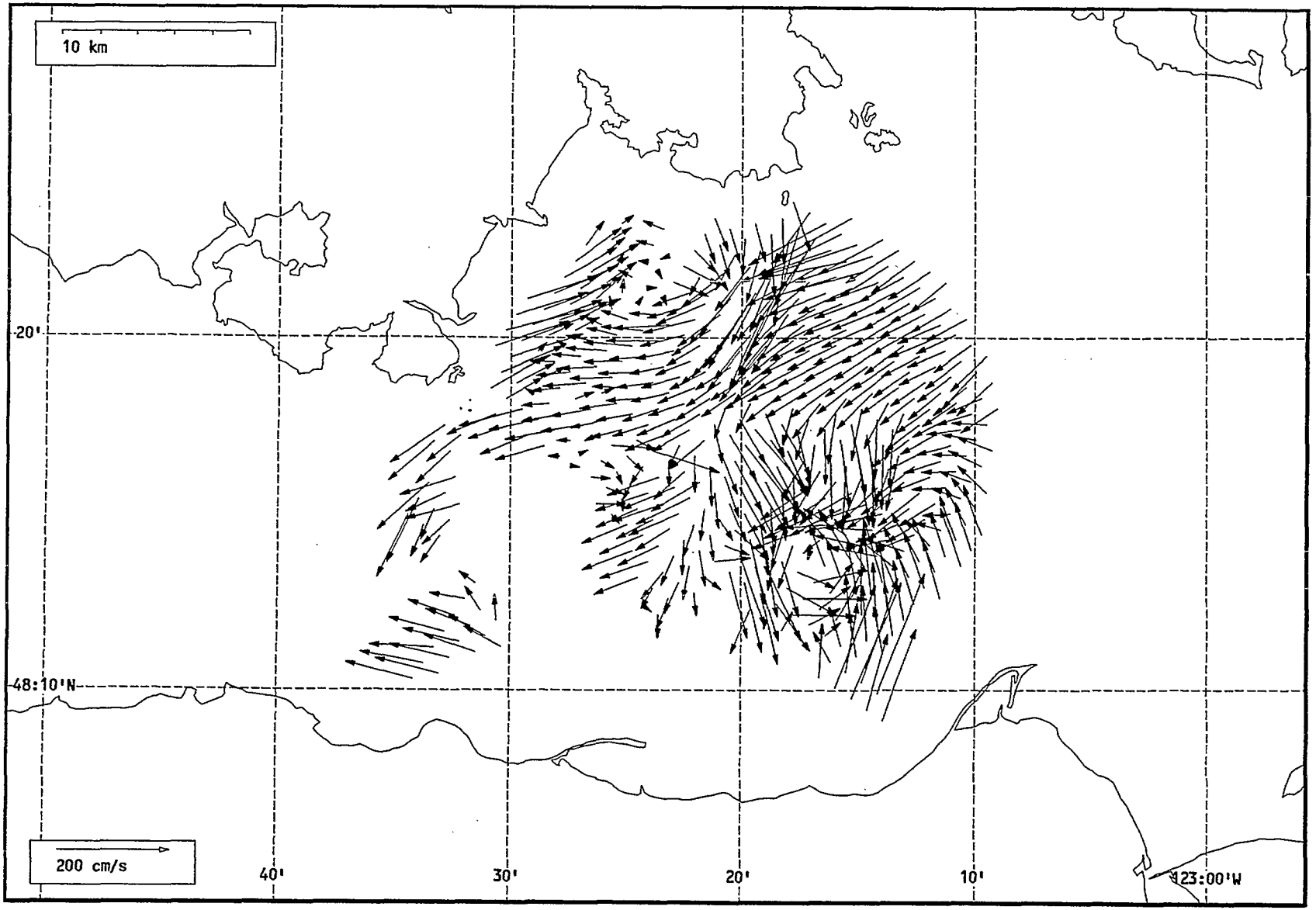

Total current vectors, Juan de Fuca Strait, 1992-07-22 10:00 Z.

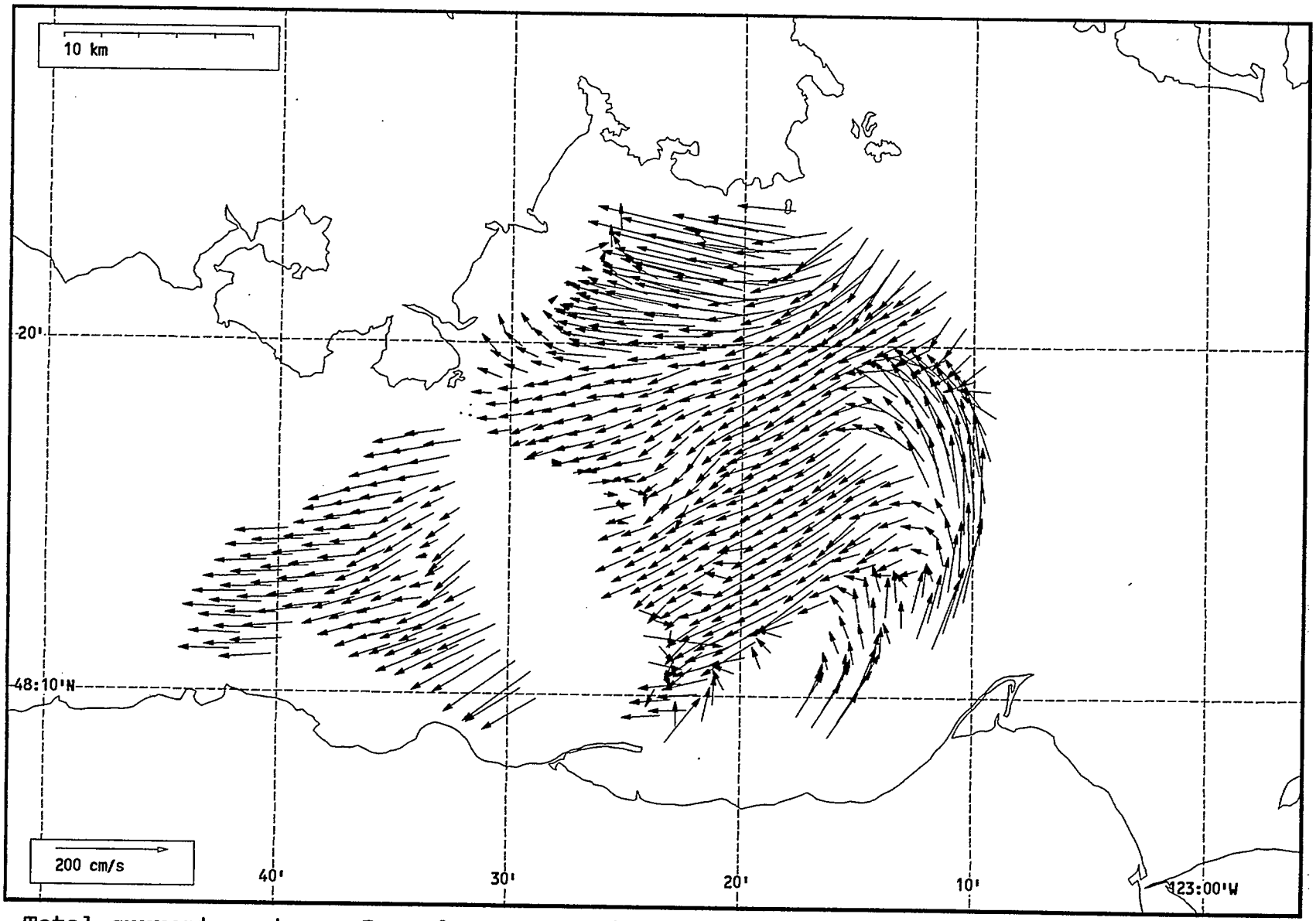

Total current vectors, Juan de Fuca Strait, 1992-07-22 11:00 Z.

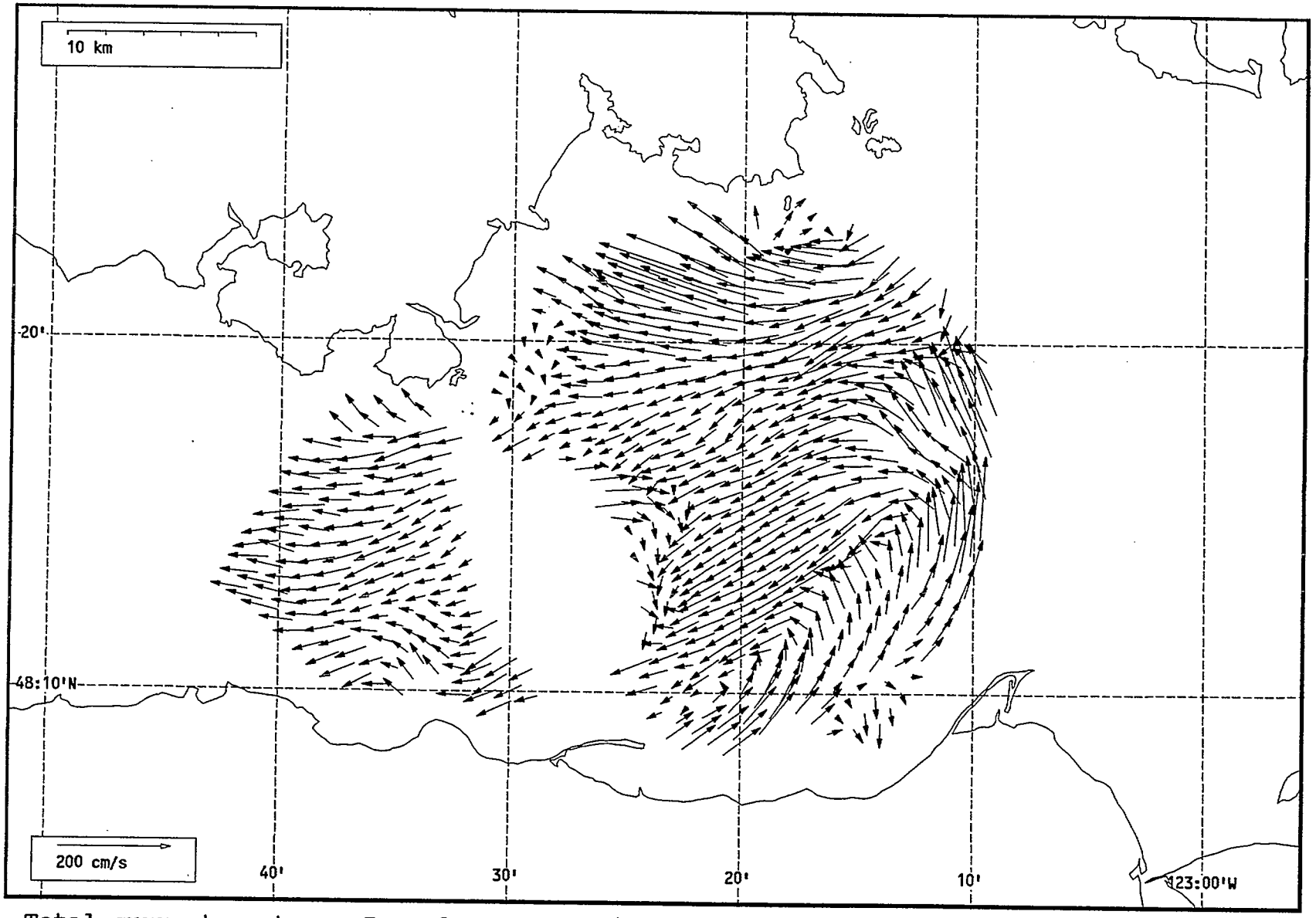

Total current vectors, Juan de Fuca Strait, 1992-07-22 12:00 Z.

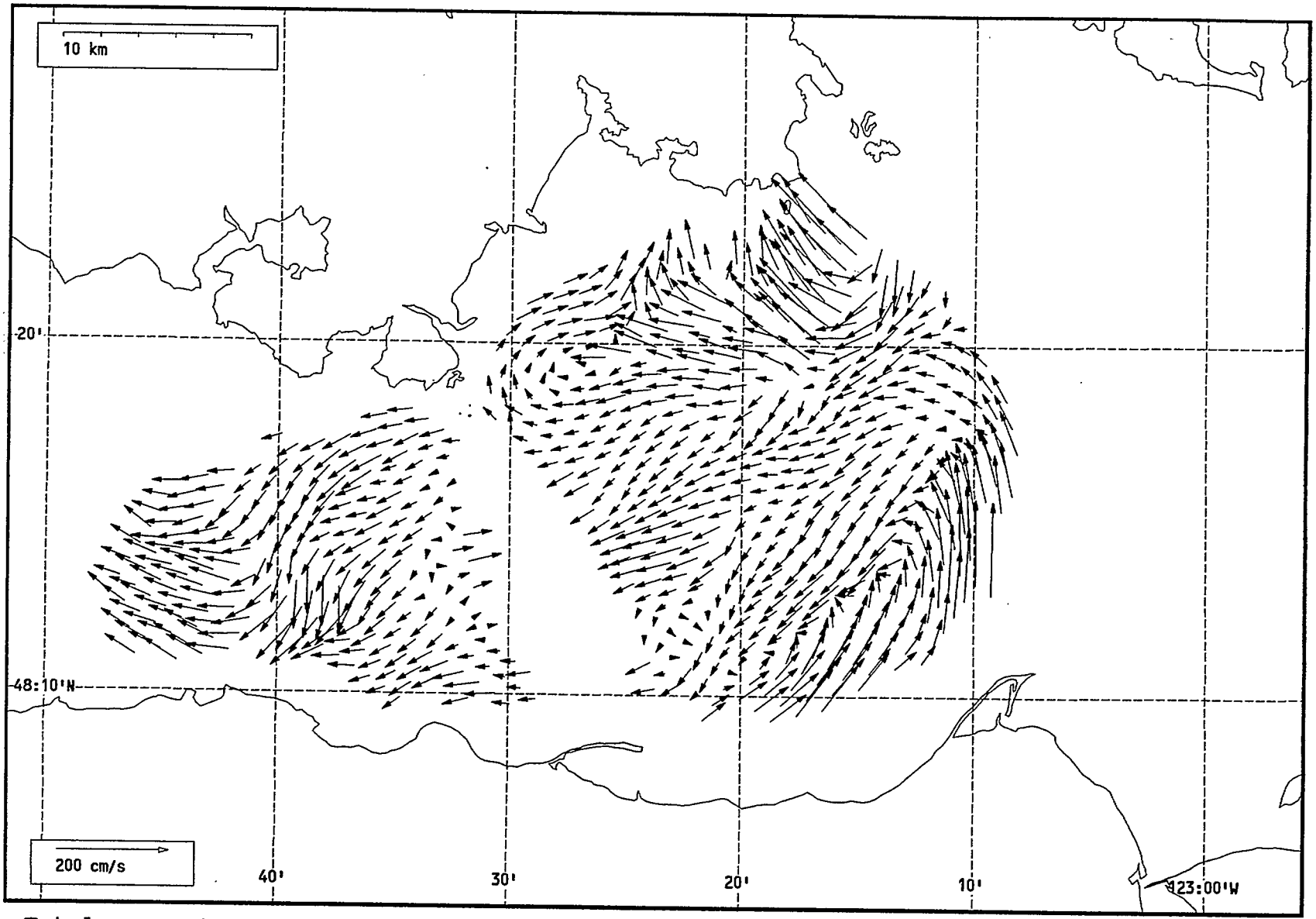

Total current vectors, Juan de Fuca Strait, 1992-07-22 13:00 Z.

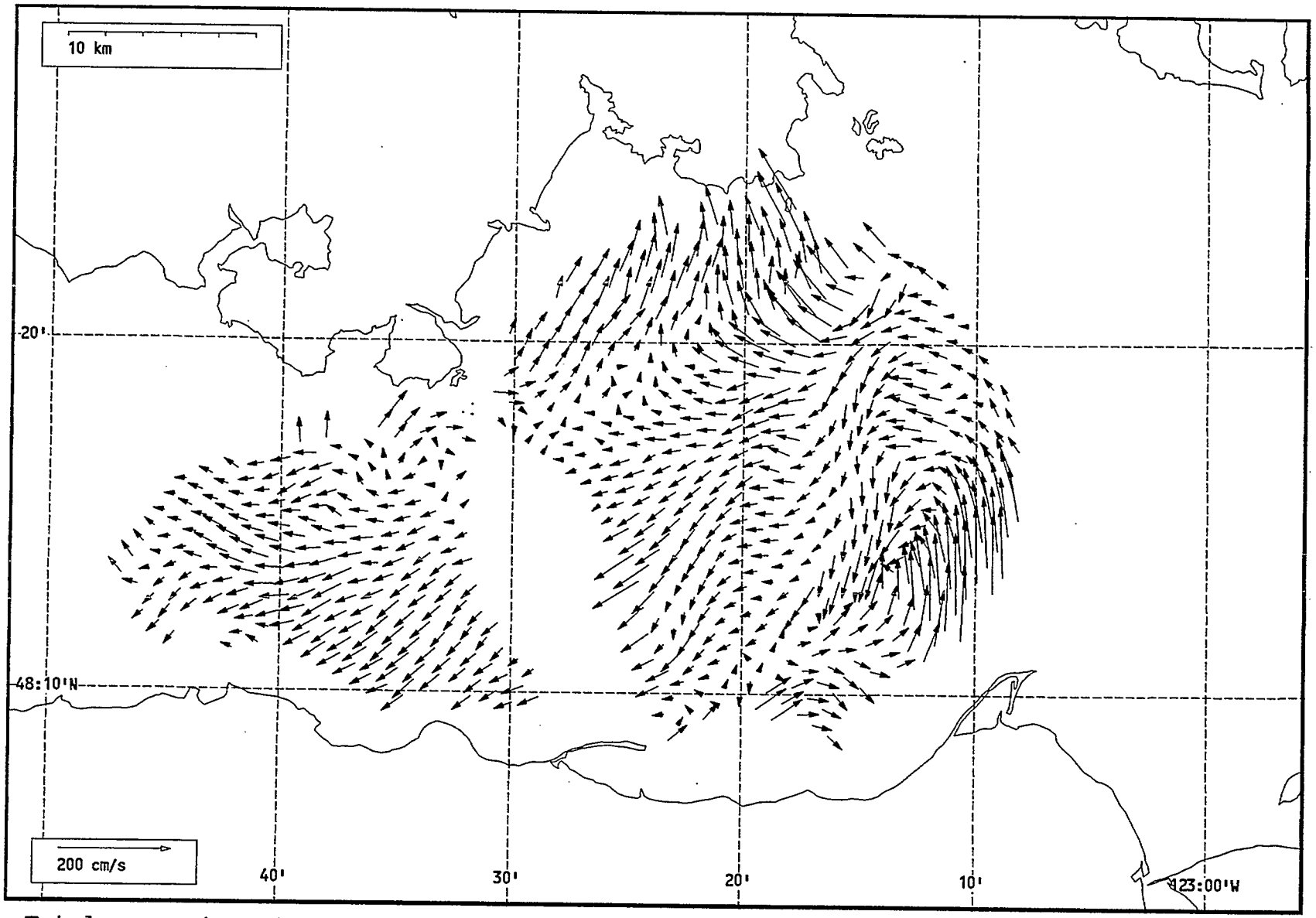

Total current vectors, Juan de Fuca Strait, 1992-07-22 14:00 Z.

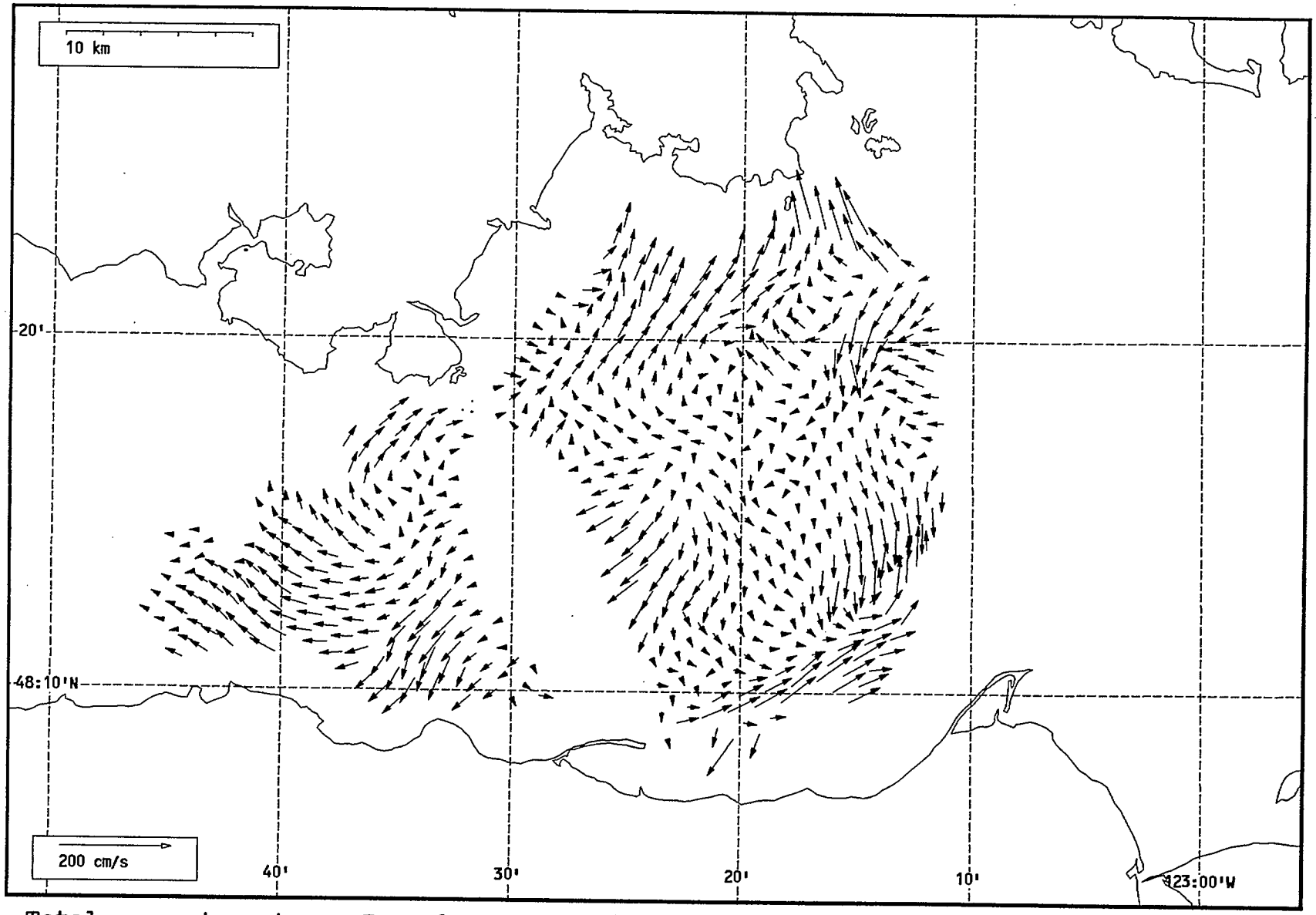

Total current vectors, Juan de Fuca Strait, 1992-07-22 15:00 Z.

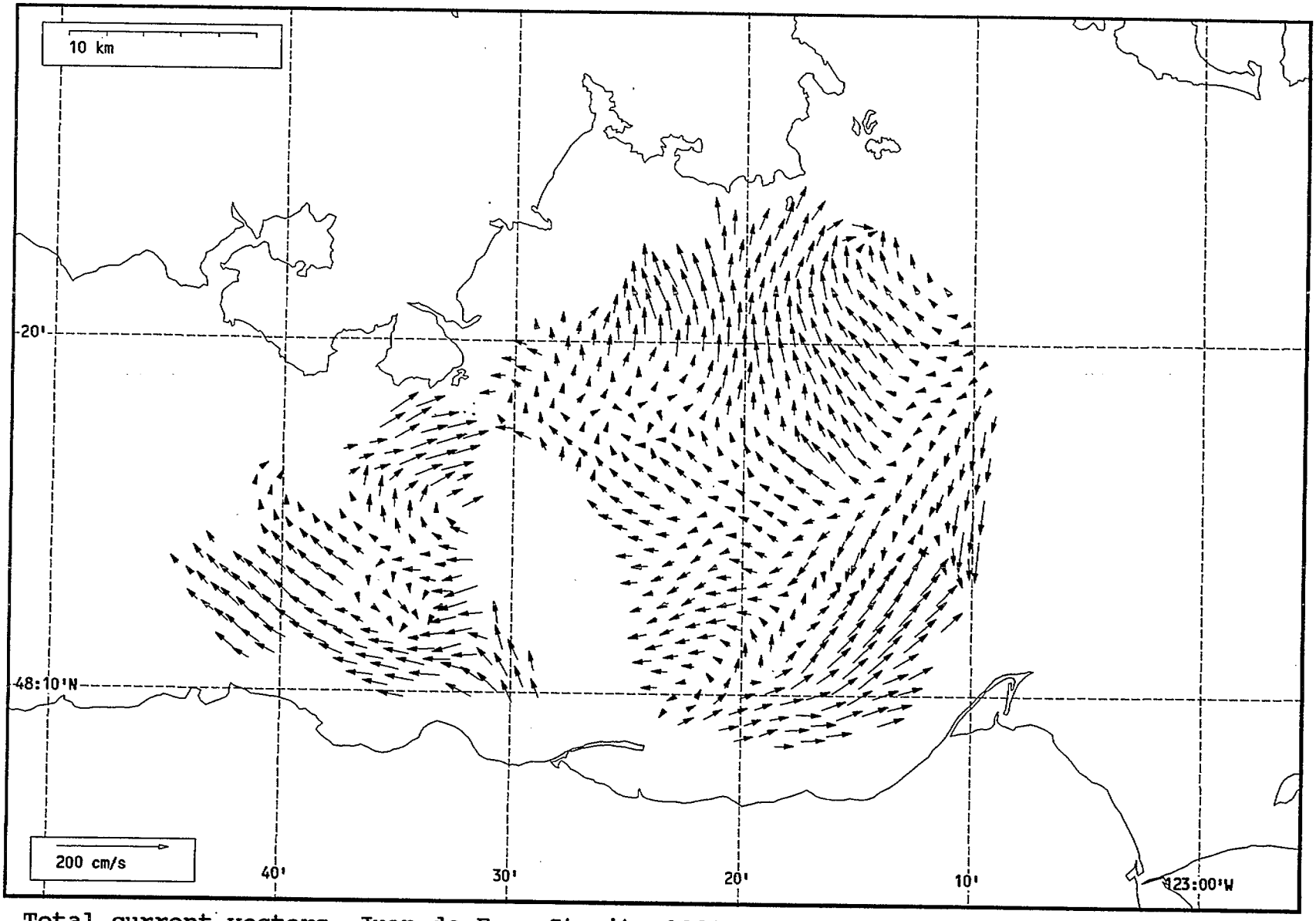

Total current vectors, Juan de Fuca Strait, 1992-07-22 17:00 Z.

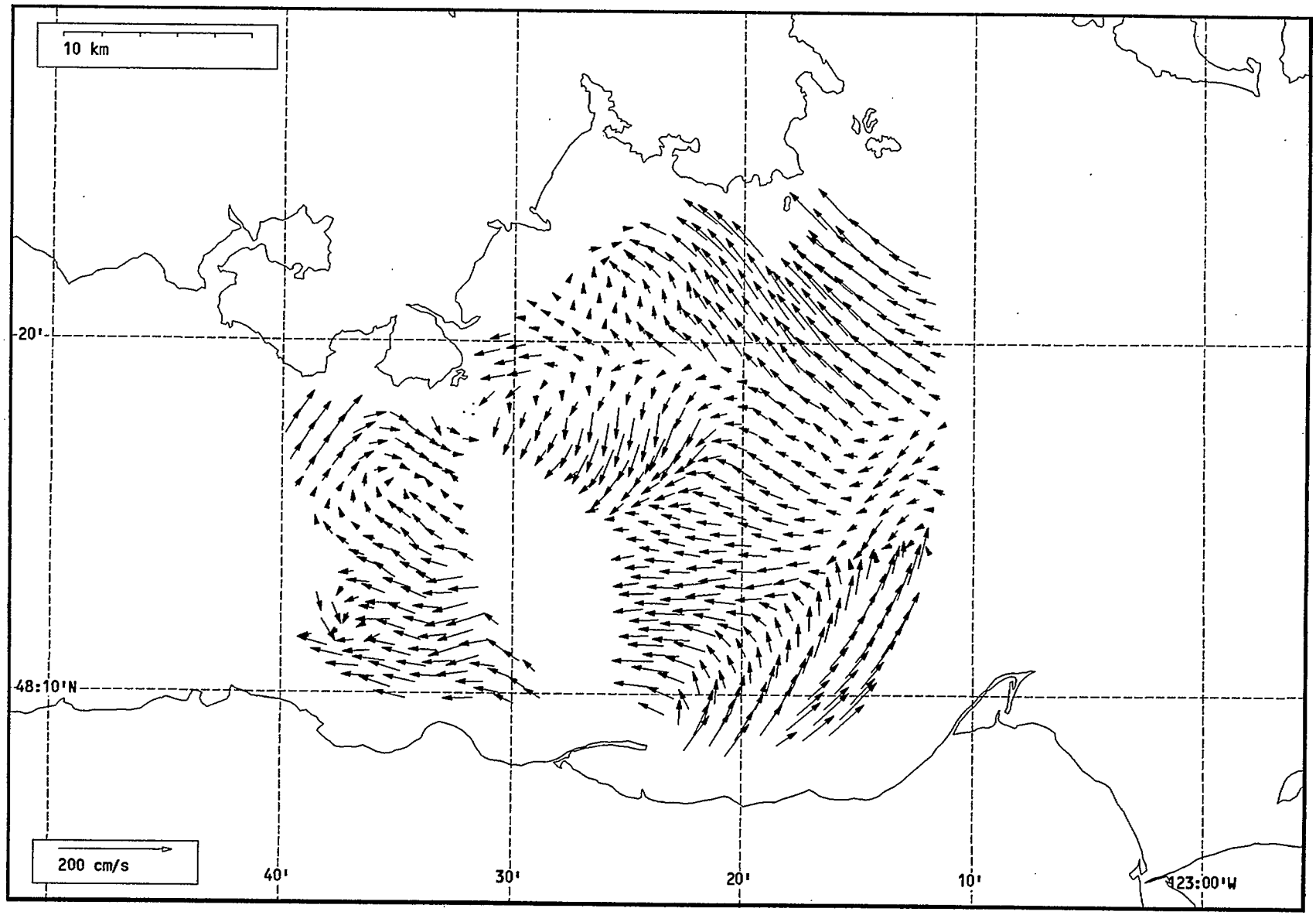

Total current vectors, Juan de Fuca Strait, 1992-07-22 18:00 Z.

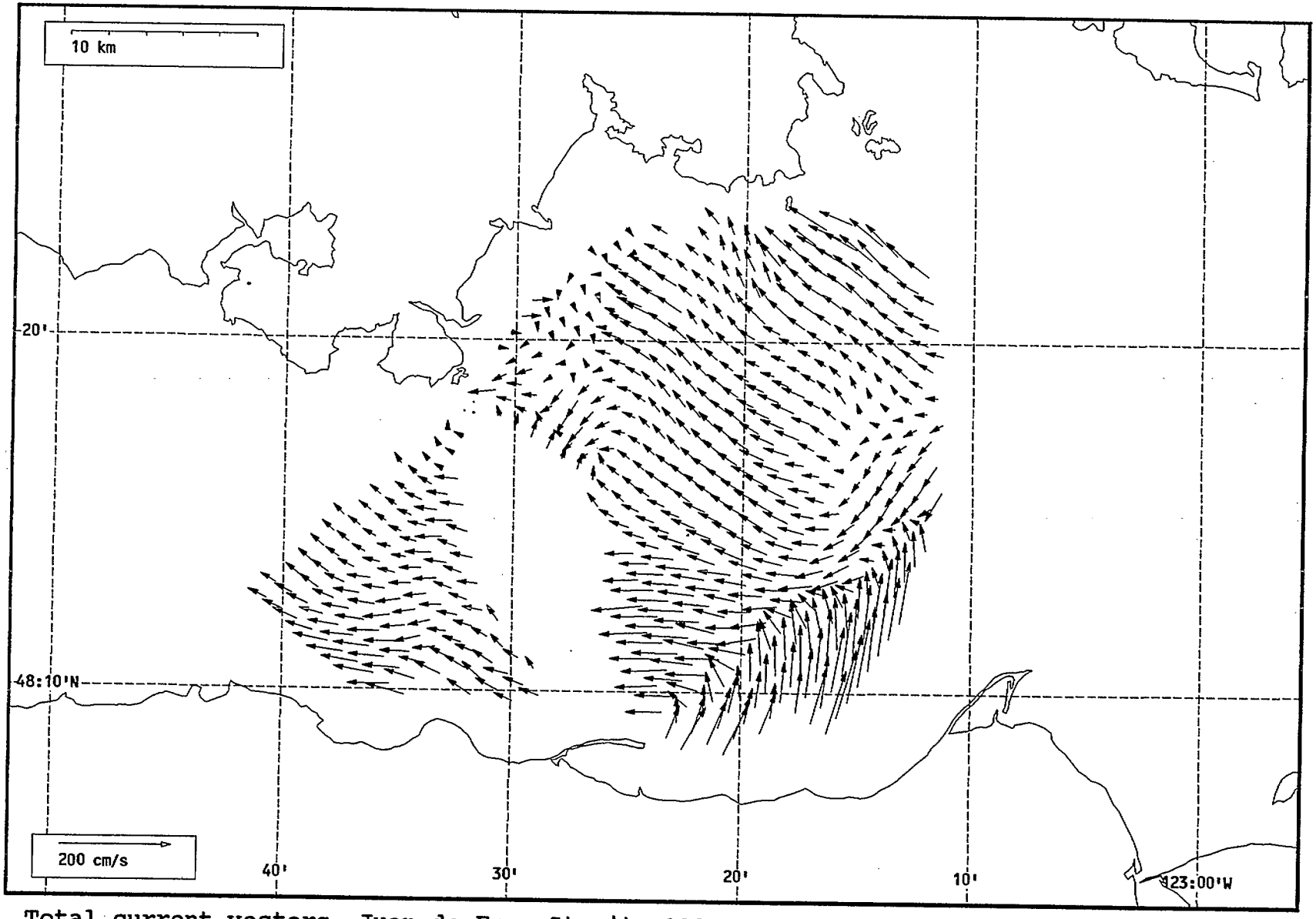

Total current vectors, Juan de Fuca Strait, 1992-07-22 19:00 Z.

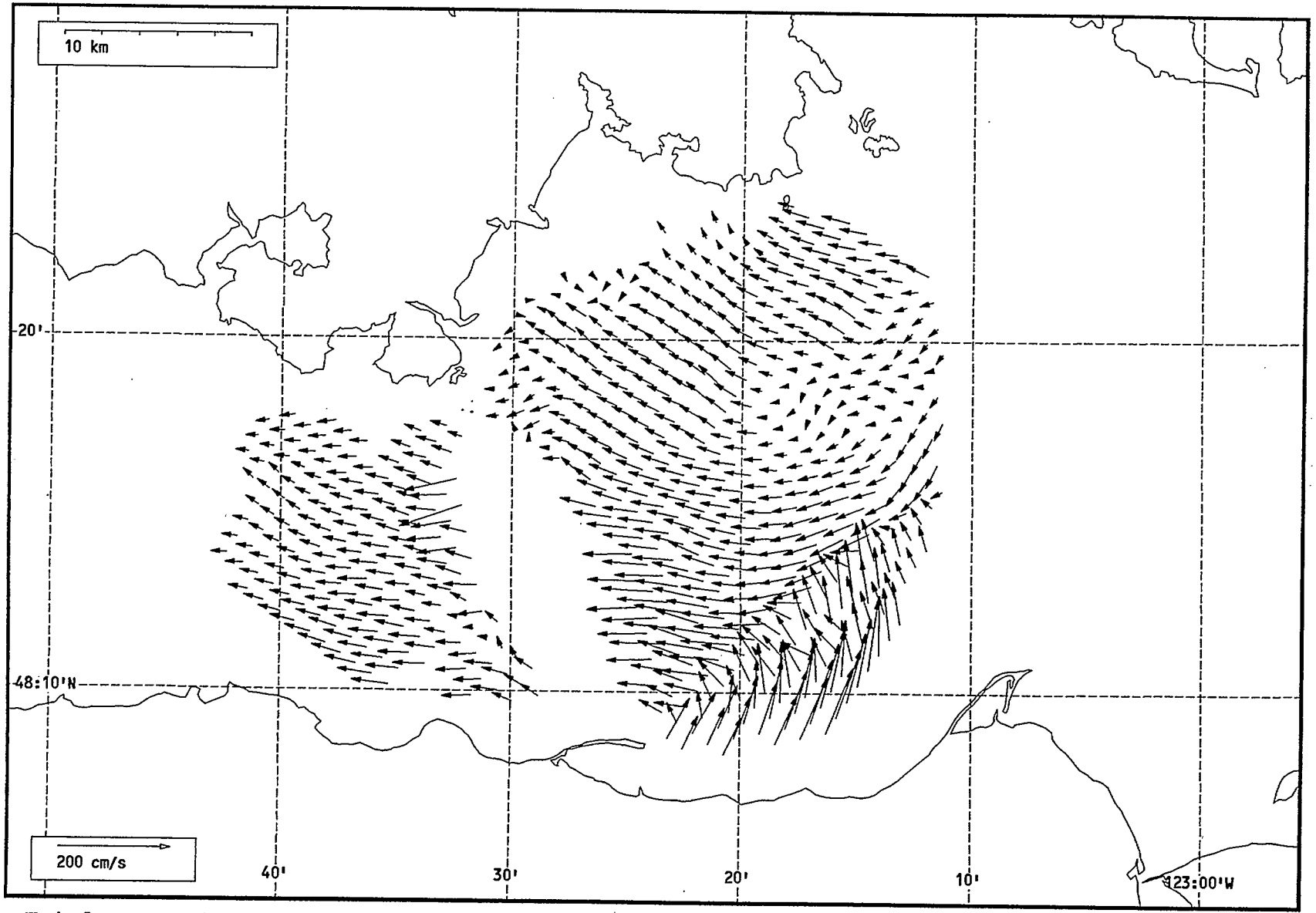

Total current vectors, Juan de Fuca Strait, 1992-07-22 20:00 Z.

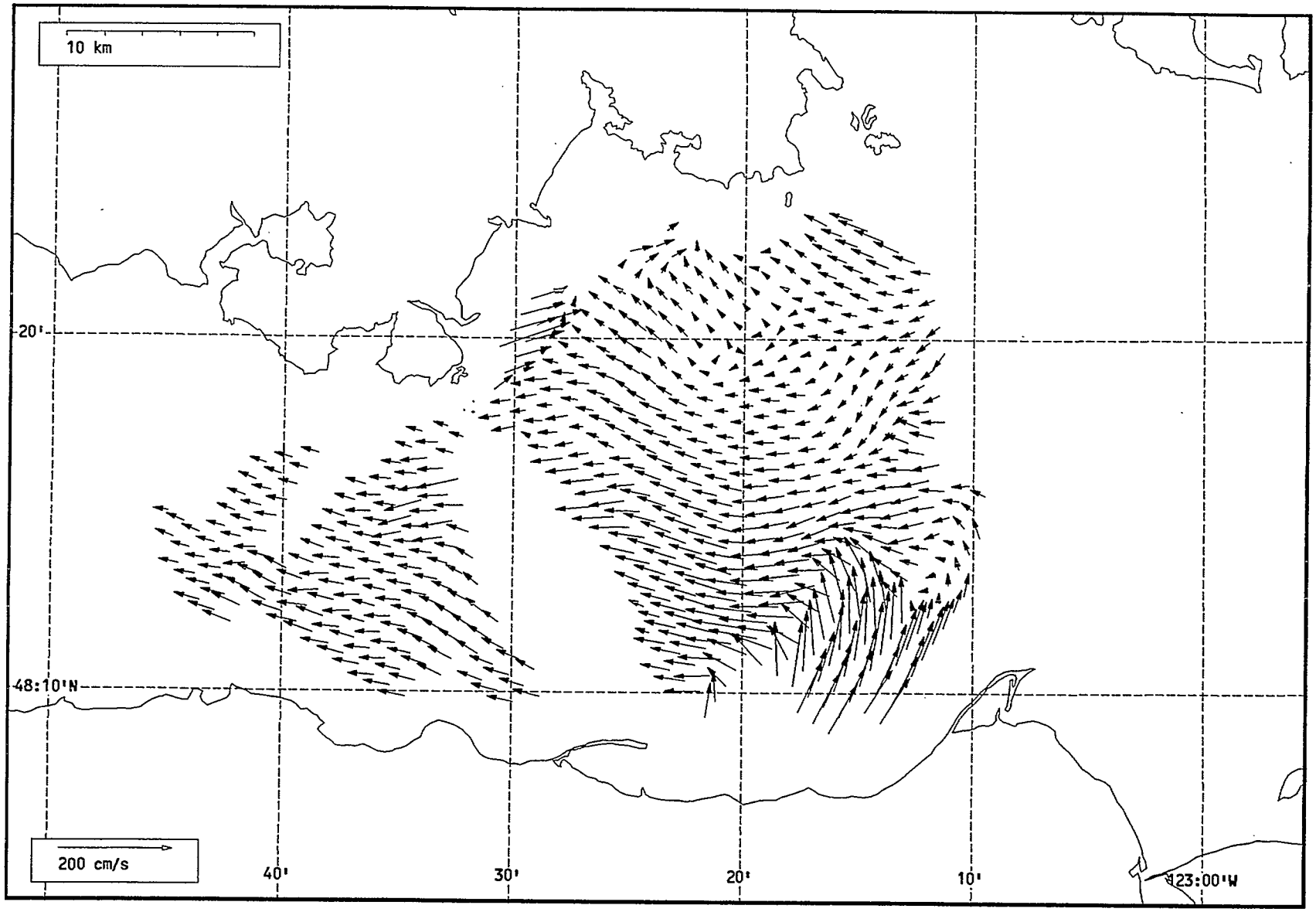

Total current vectors, Juan de Fuca Strait, 1992-07-22 21:00 Z.

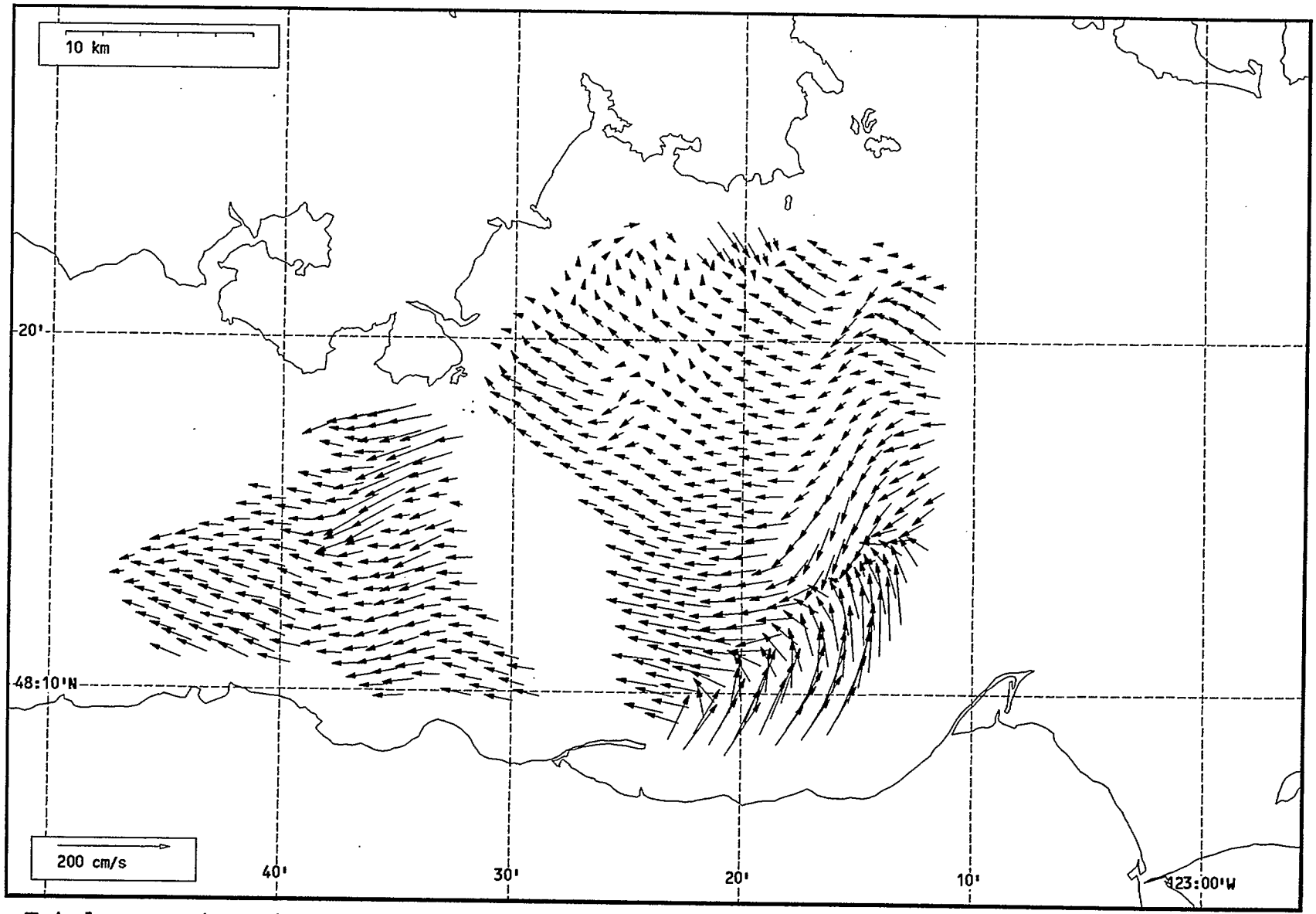

Total current vectors, Juan de Fuca Strait, 1992-07-22 22:00 Z.

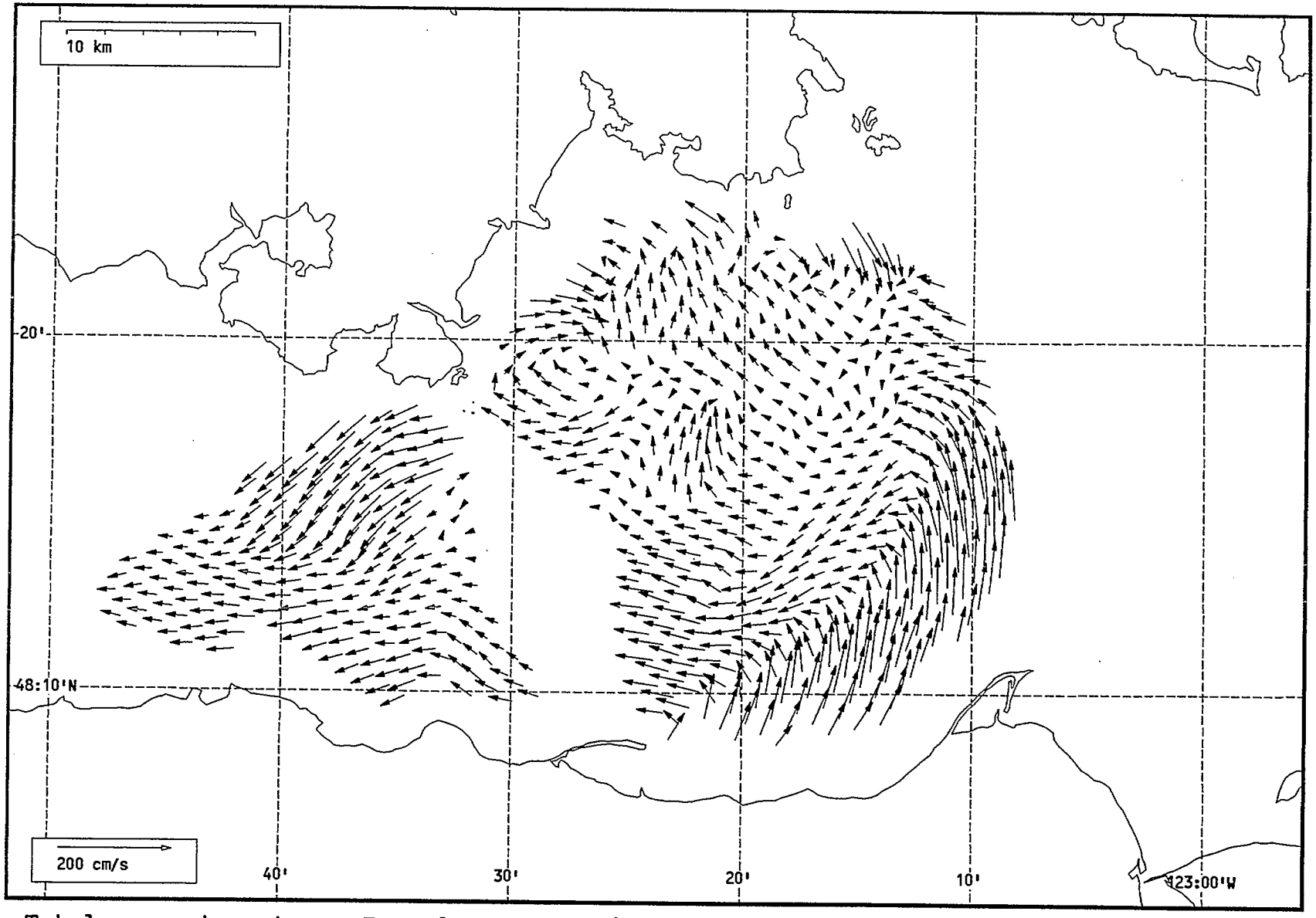

Total current vectors, Juan de Fuca Strait, 1992-07-22 23:00 Z.

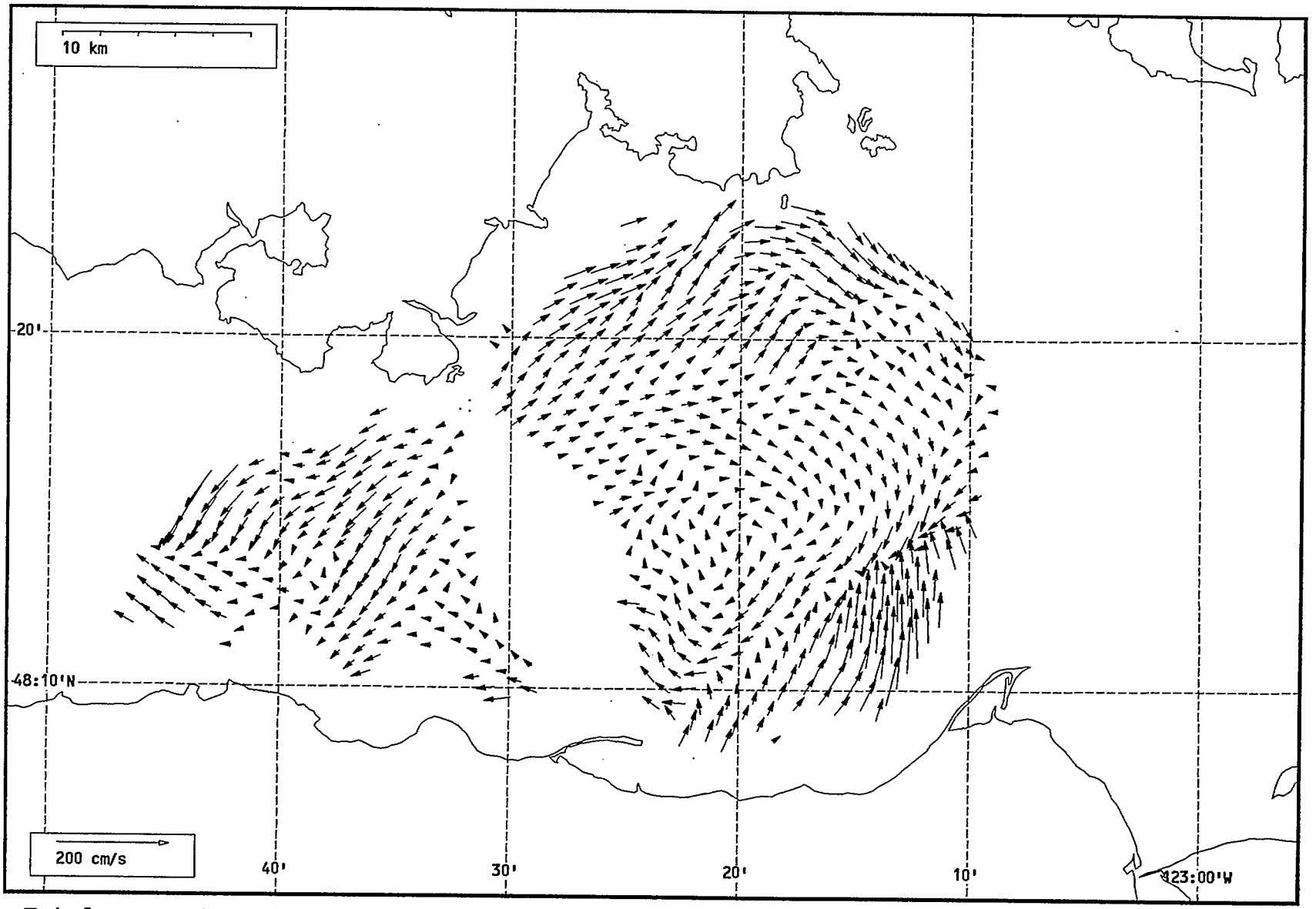

Total current vectors, Juan de Fuca Strait, 1992-07-23 00:00 Z.

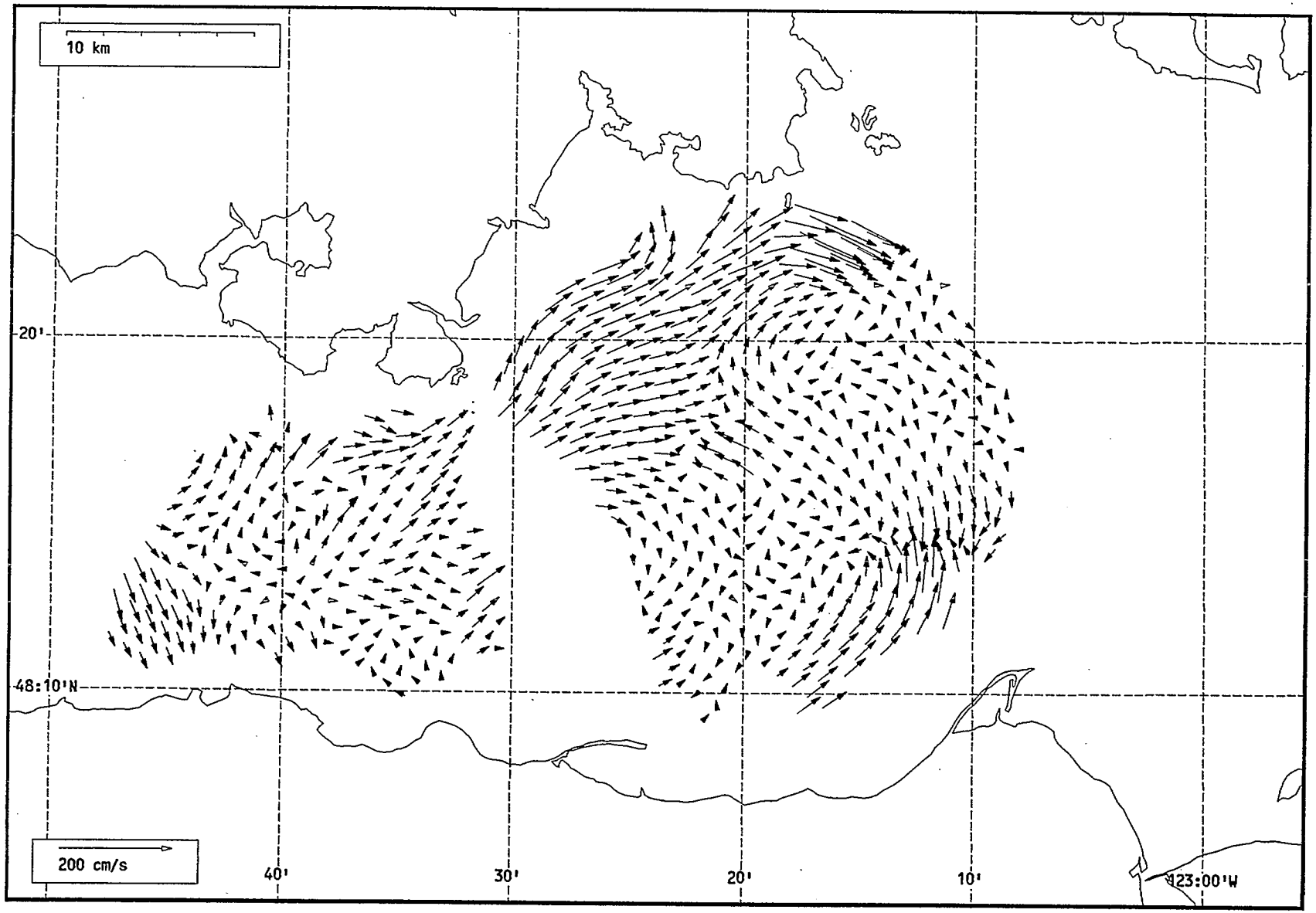

Total current vectors, Juan de Fuca Strait, 1992-07-23 01:00 Z.

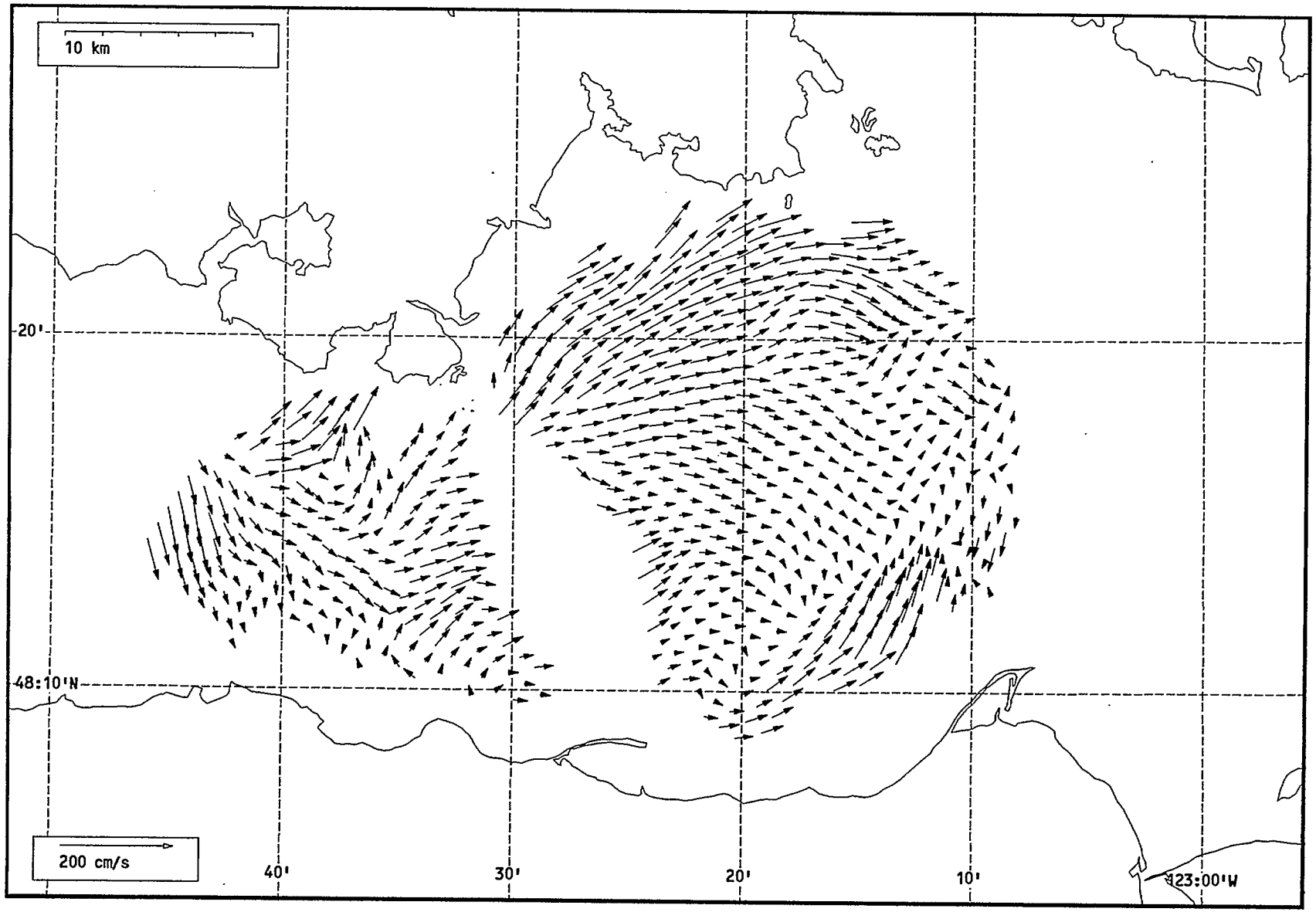

Total current vectors, Juan de Fuca Strait, 1992-07-23 02:00 Z..

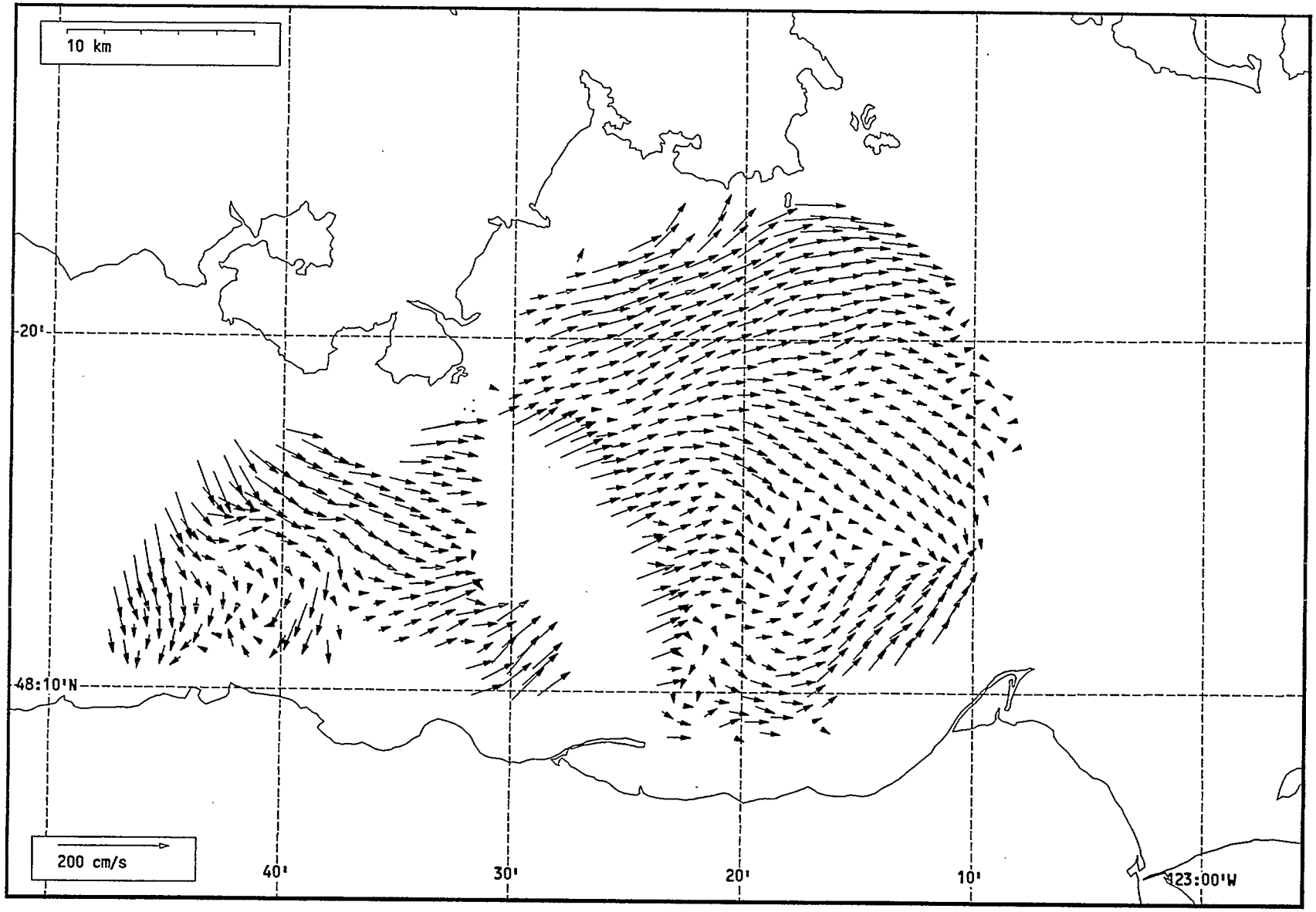

Total current vectors, Juan de Fuca Strait, 1992-07-23 03:00 Z.

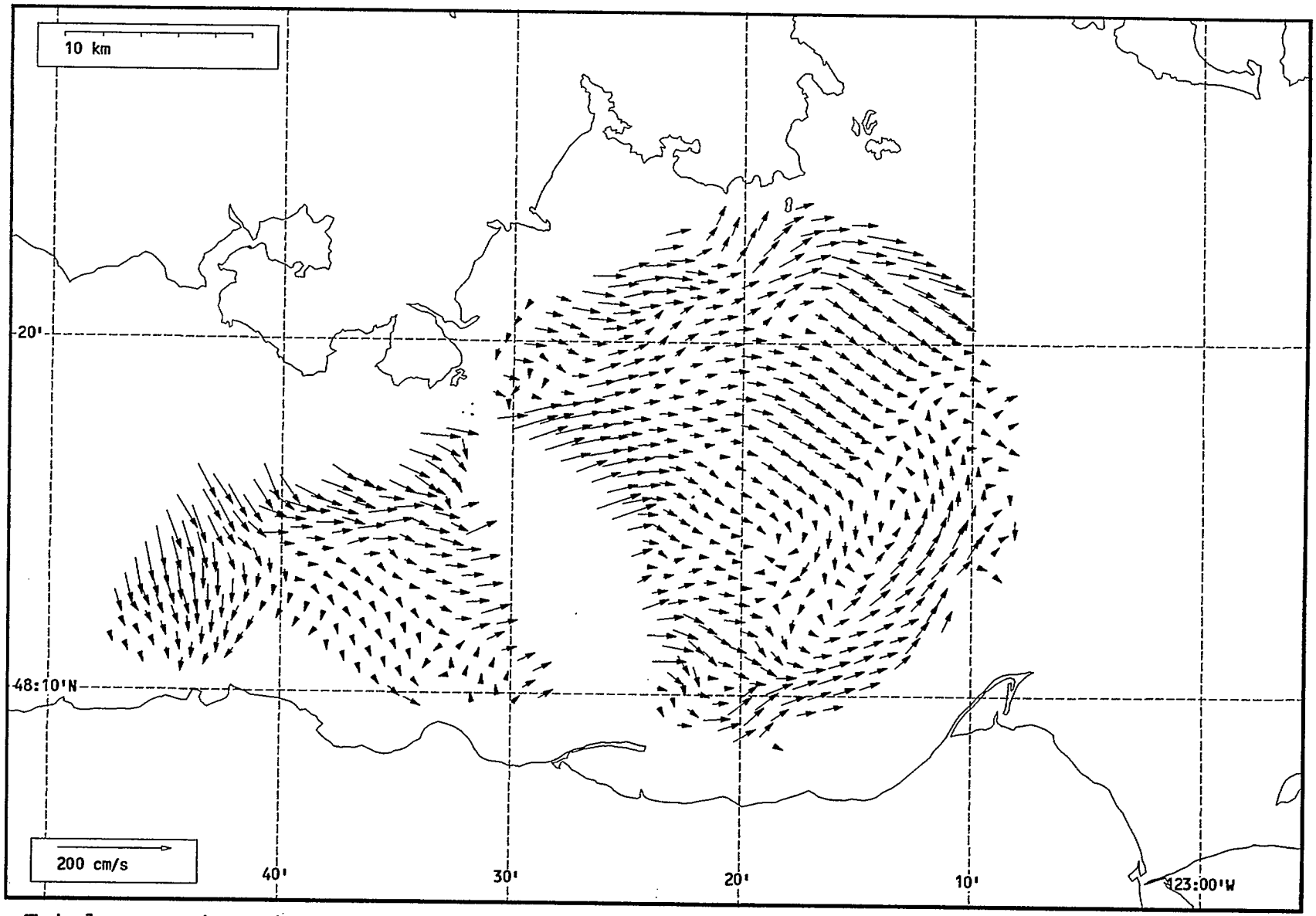

Total current vectors, Juan de Fuca Strait, 1992-07-23 04:00 Z.

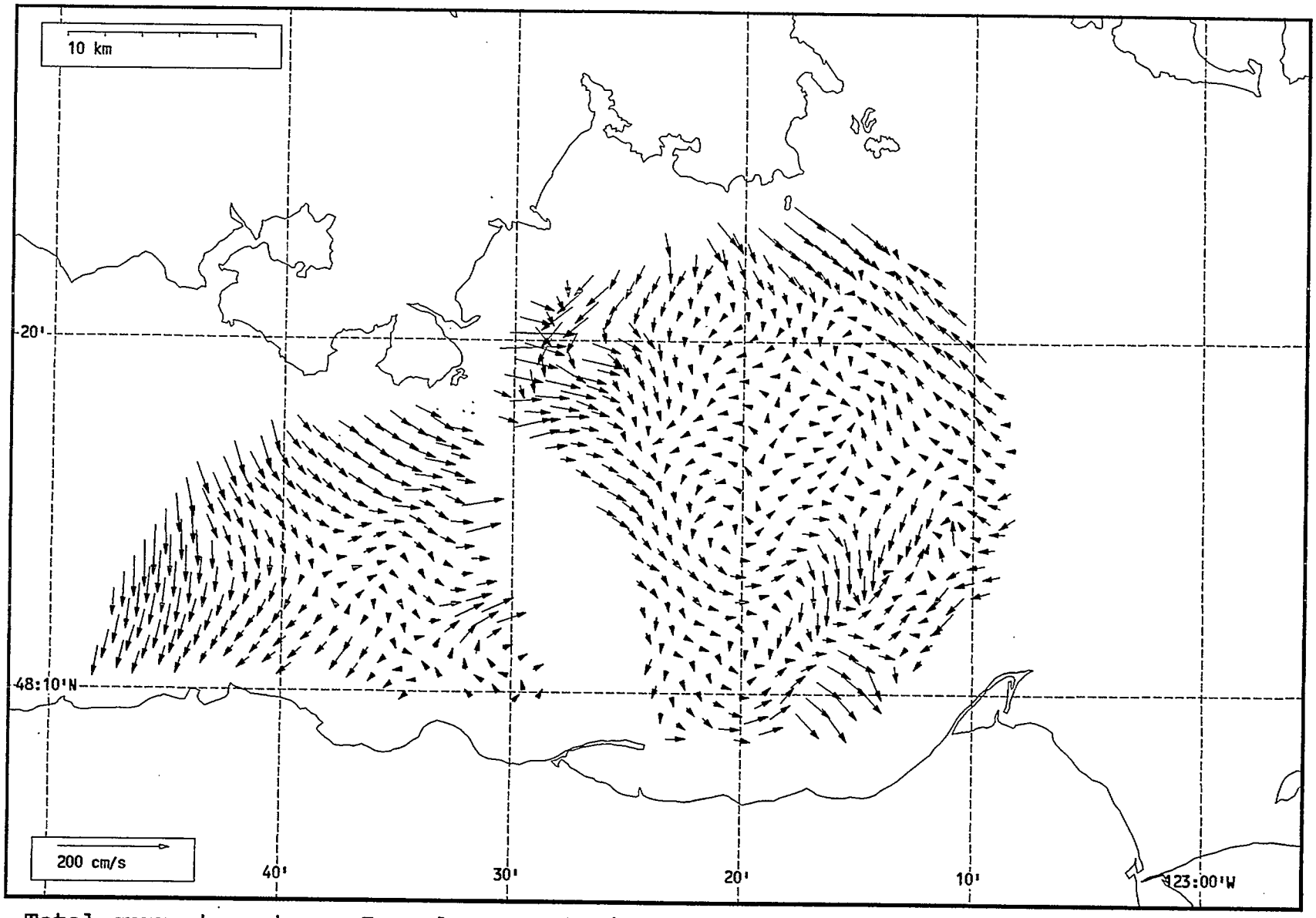

Total current vectors, Juan de Fuca Strait, 1992-07-23 05:00 Z.

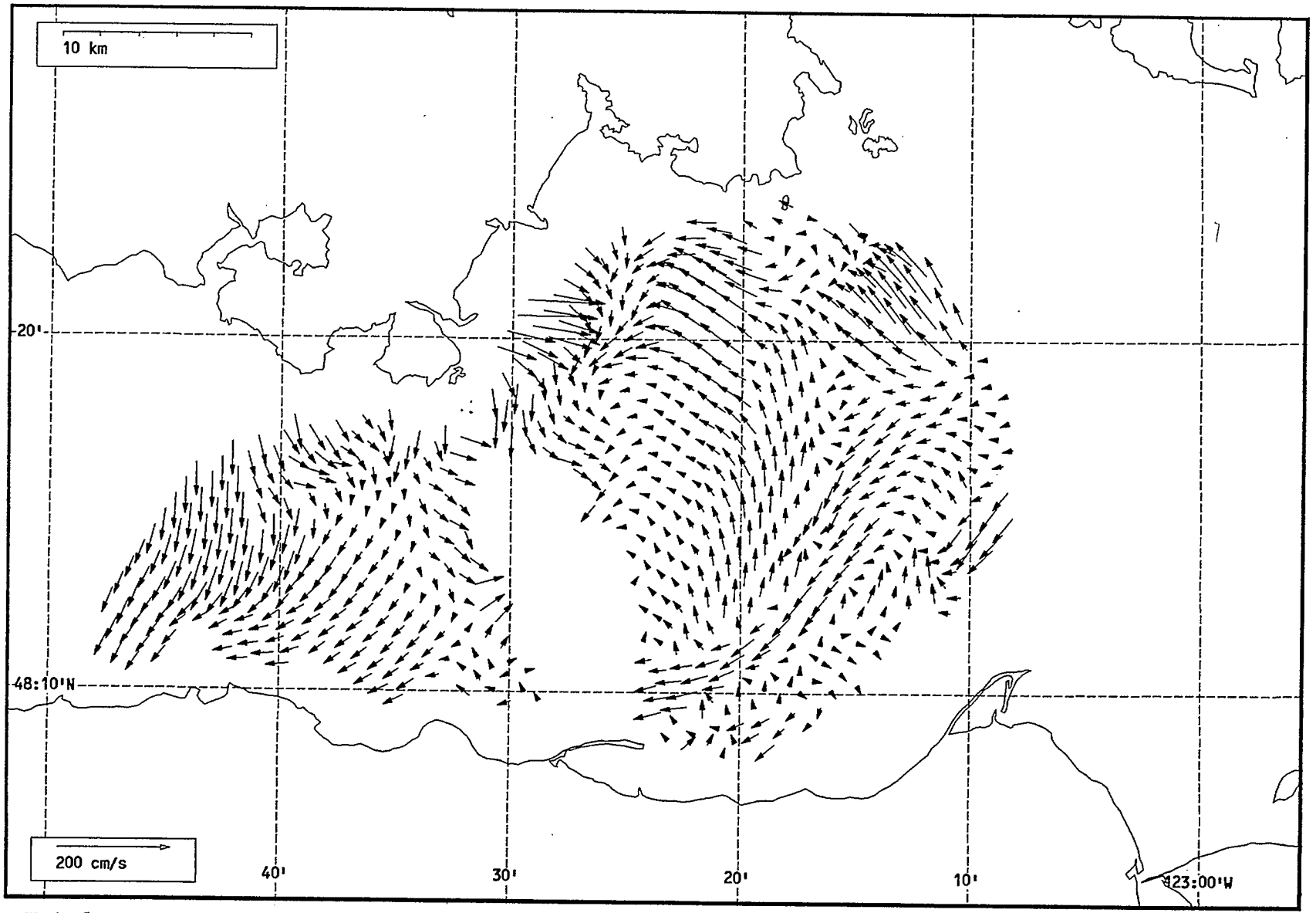

Total current vectors, Juan de Fuca Strait, 1992-07-23 06:00 Z.

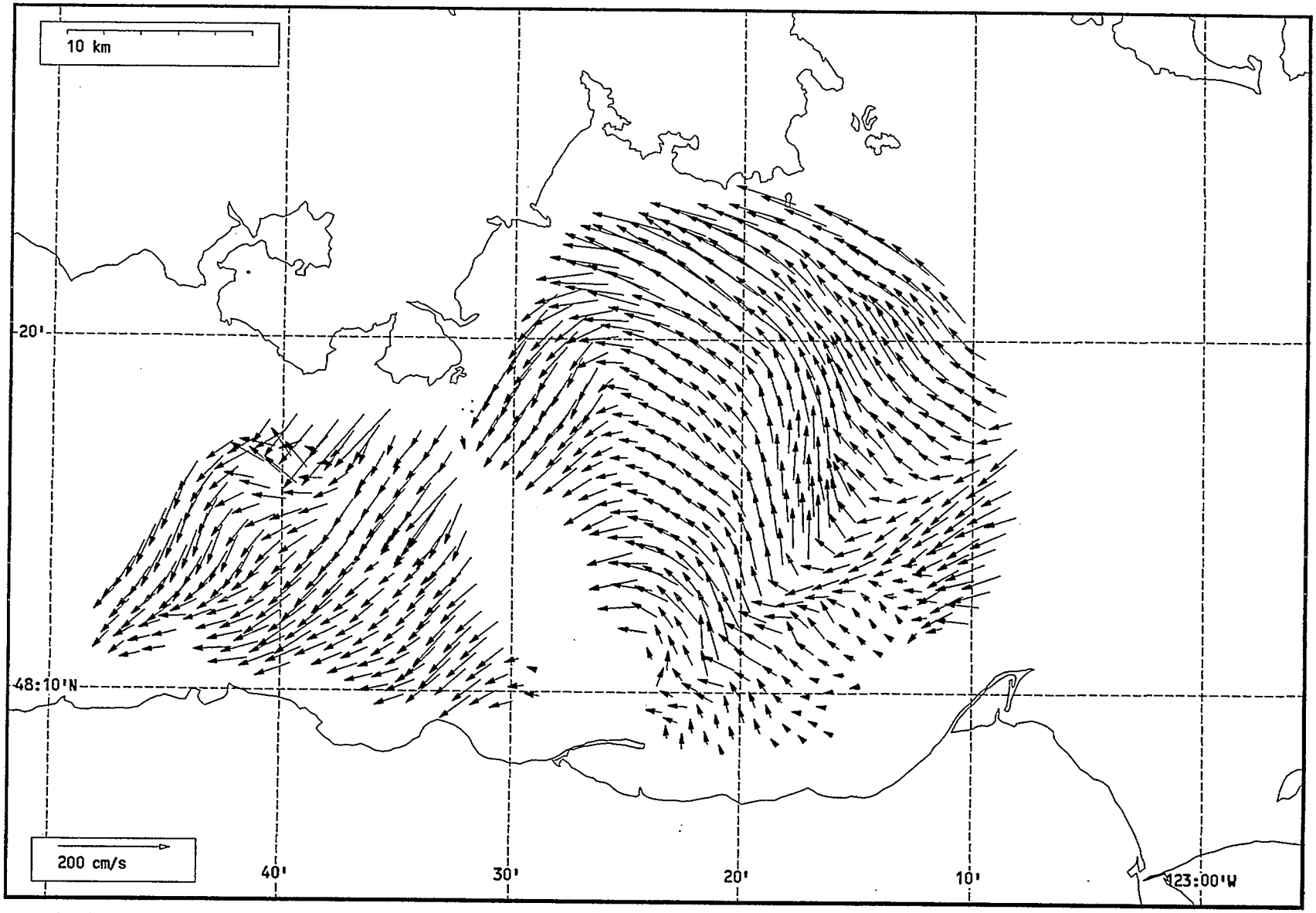

Total current vectors, Juan de Fuca Strait, 1992-07-23 07:00 Z.

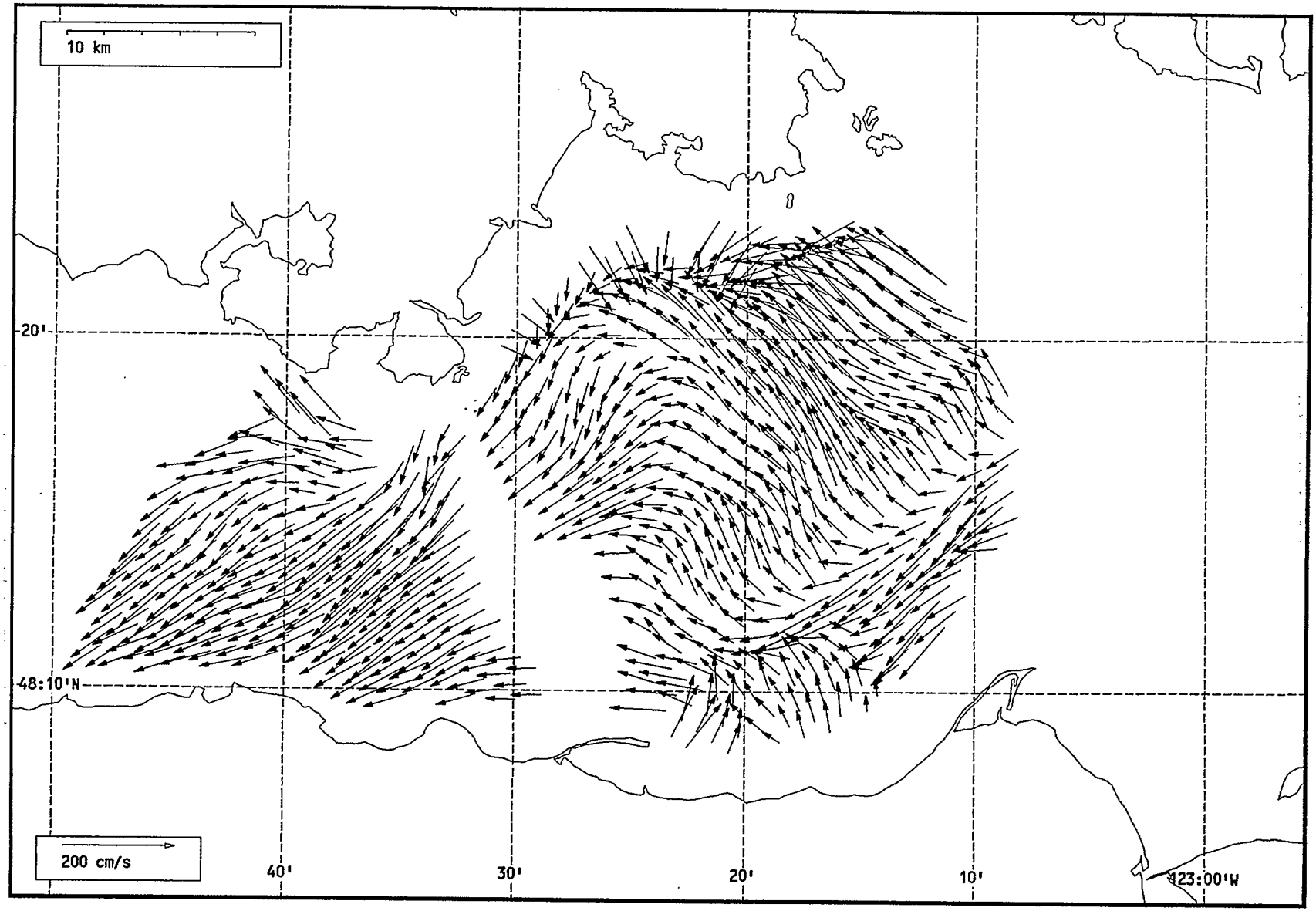

Total current vectors, Juan de Fuca Strait, 1992-07-23 08:00 Z.

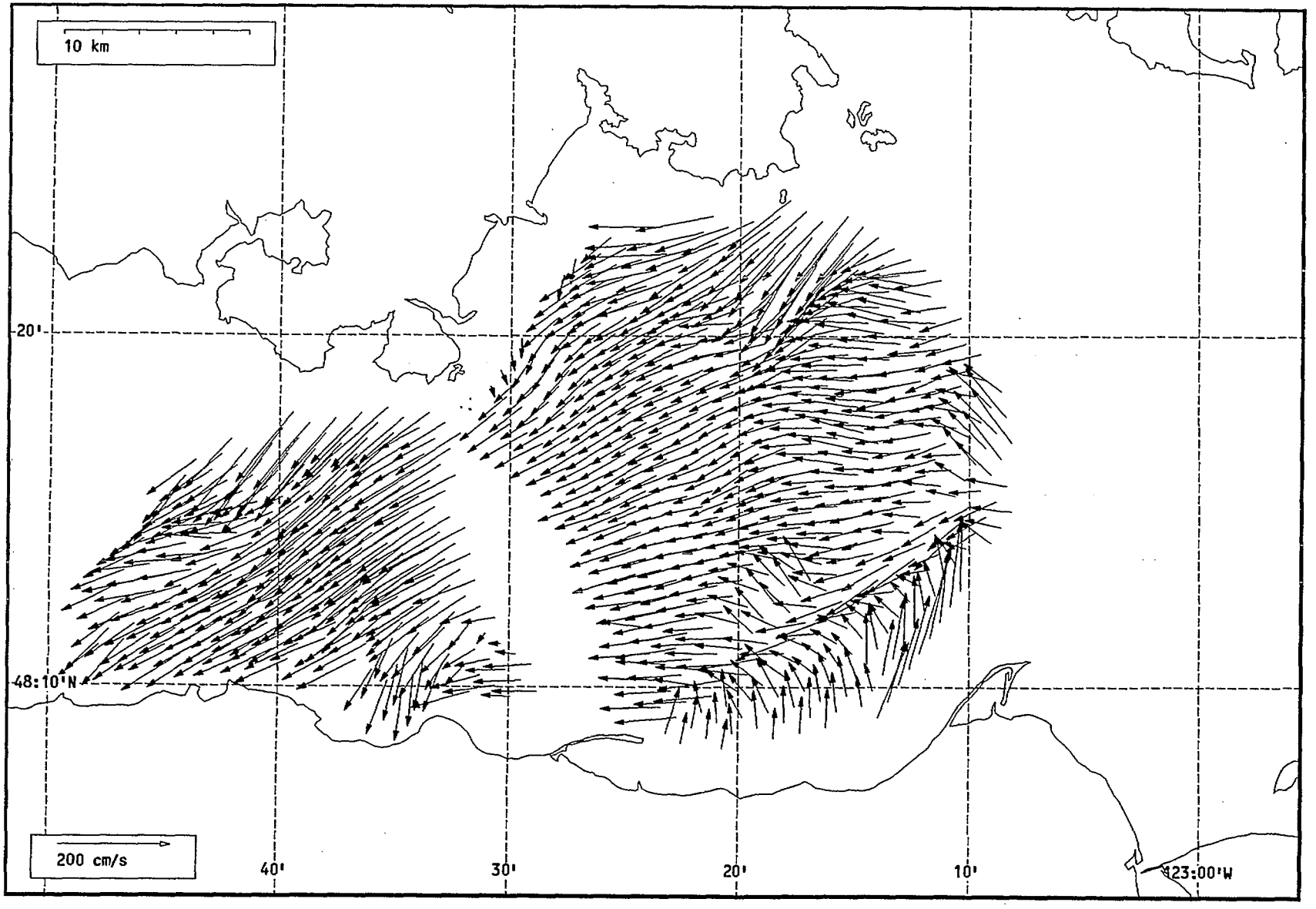

Total current vectors, Juan de Fuca Strait, 1992-07-23 09:00 Z.

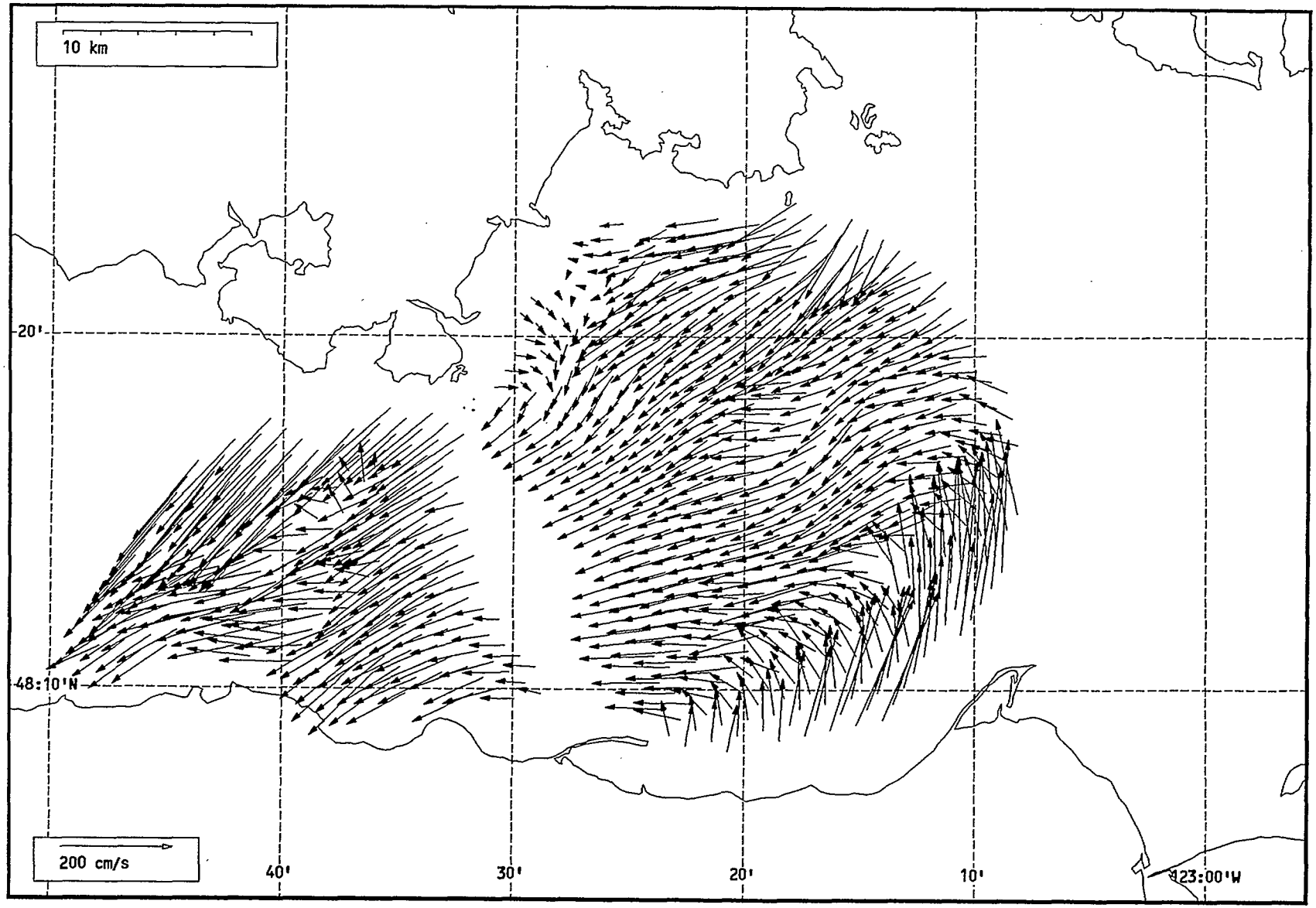

Total current vectors, Juan de Fuca Strait, 1992-07-23 10:00 Z.

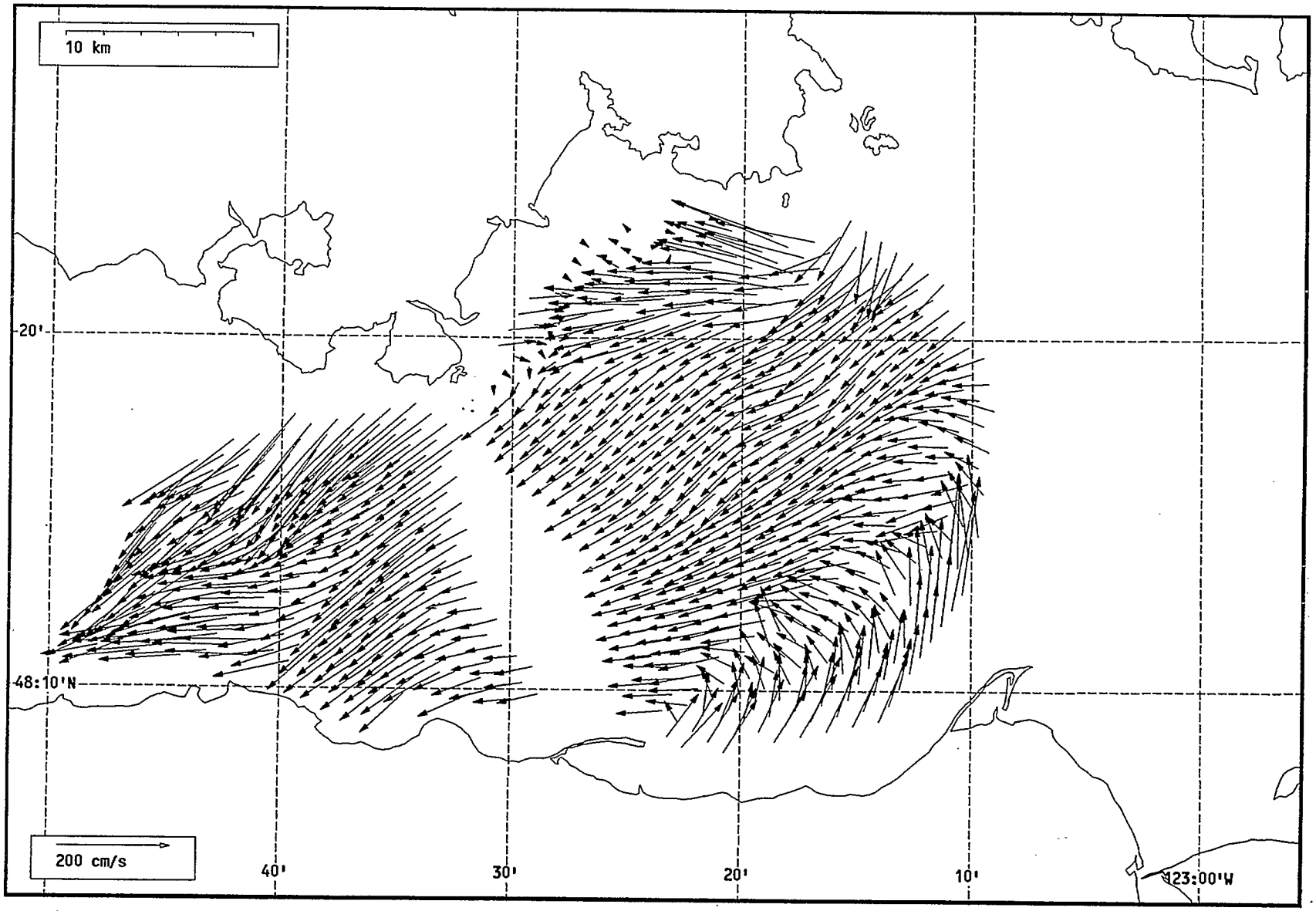

Total current vectors, Juan de Fuca Strait, 1992-07-23 11:00 Z.

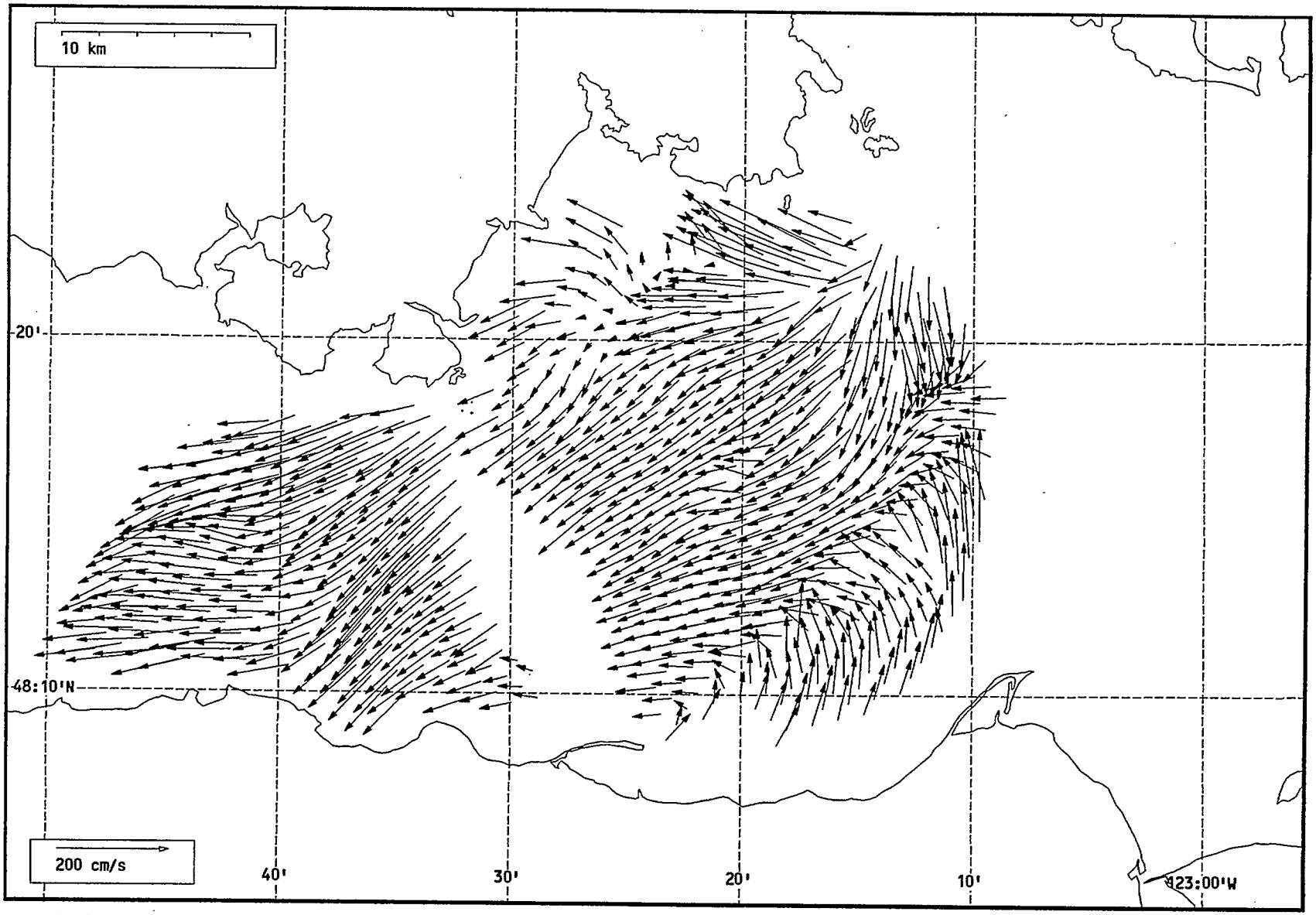

Total current vectors, Juan de Fuca Strait, 1992-07-23 12:00 Z.

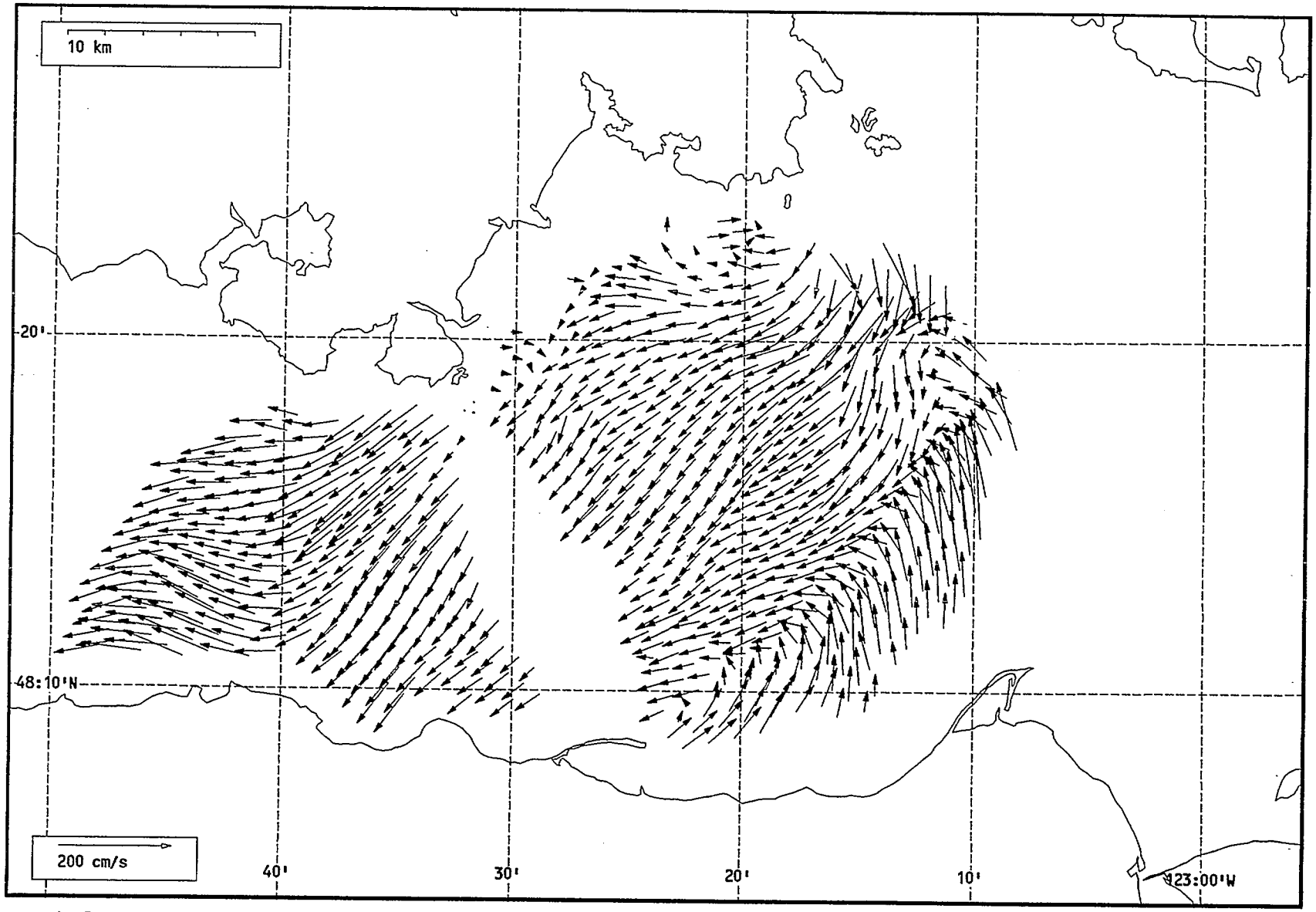

Total current vectors, Juan de Fuca Strait, 1992-07-23 13:00 Z.

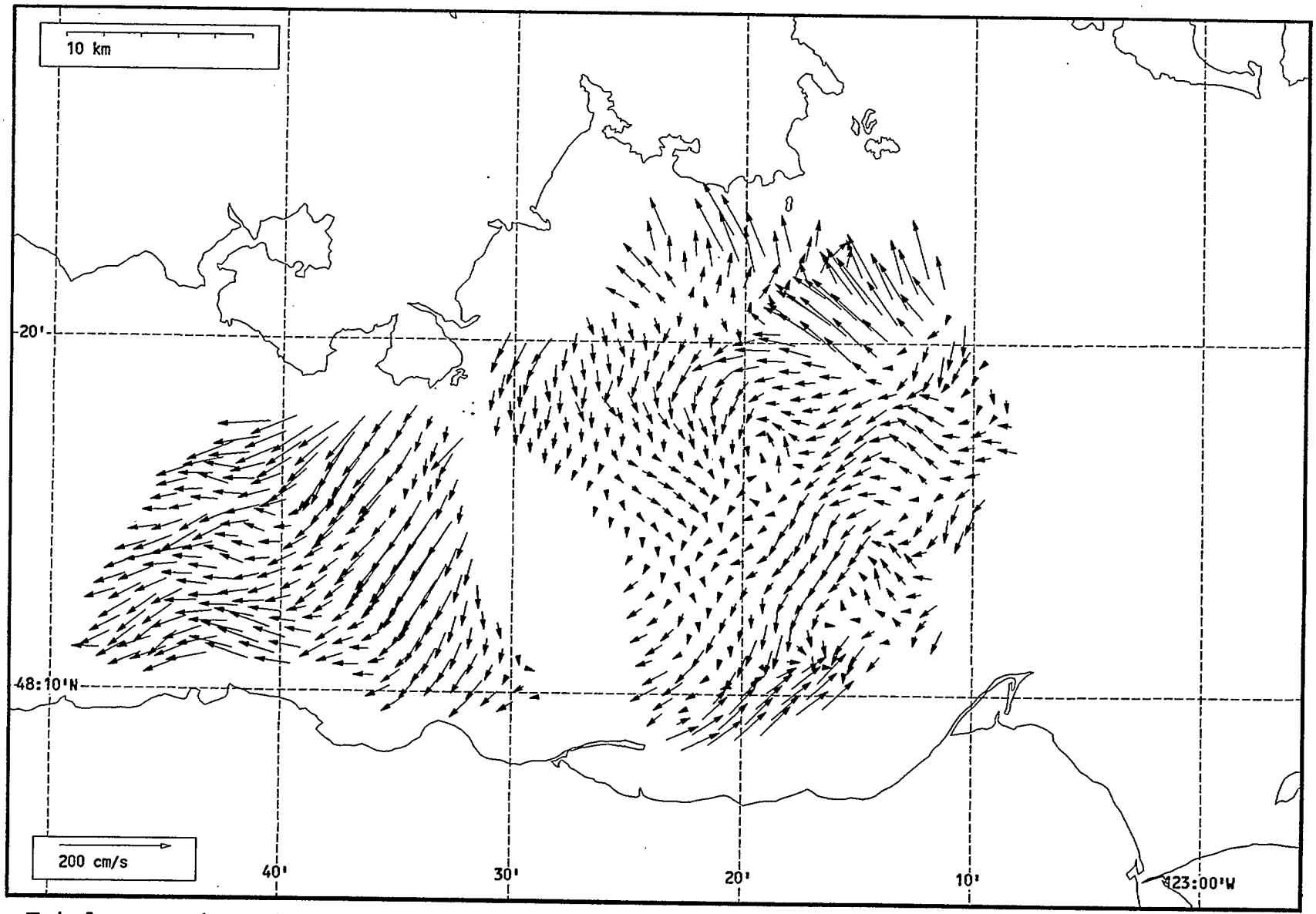

Total current vectors, Juan de Fuca Strait, 1992-07-23 14:00 Z..

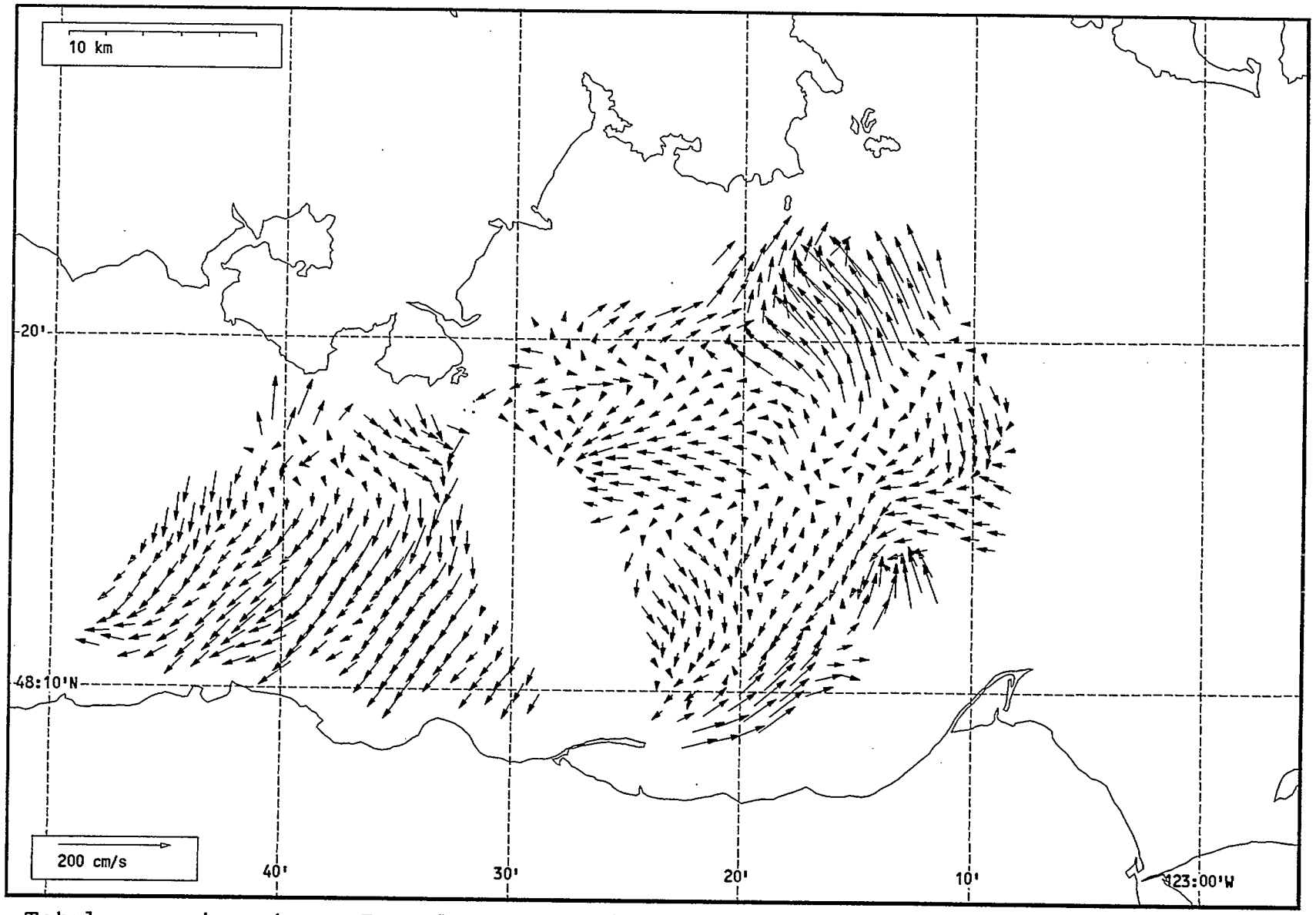

Total current vectors, Juan de Fuca Strait, 1992-07-23 15:00 Z.

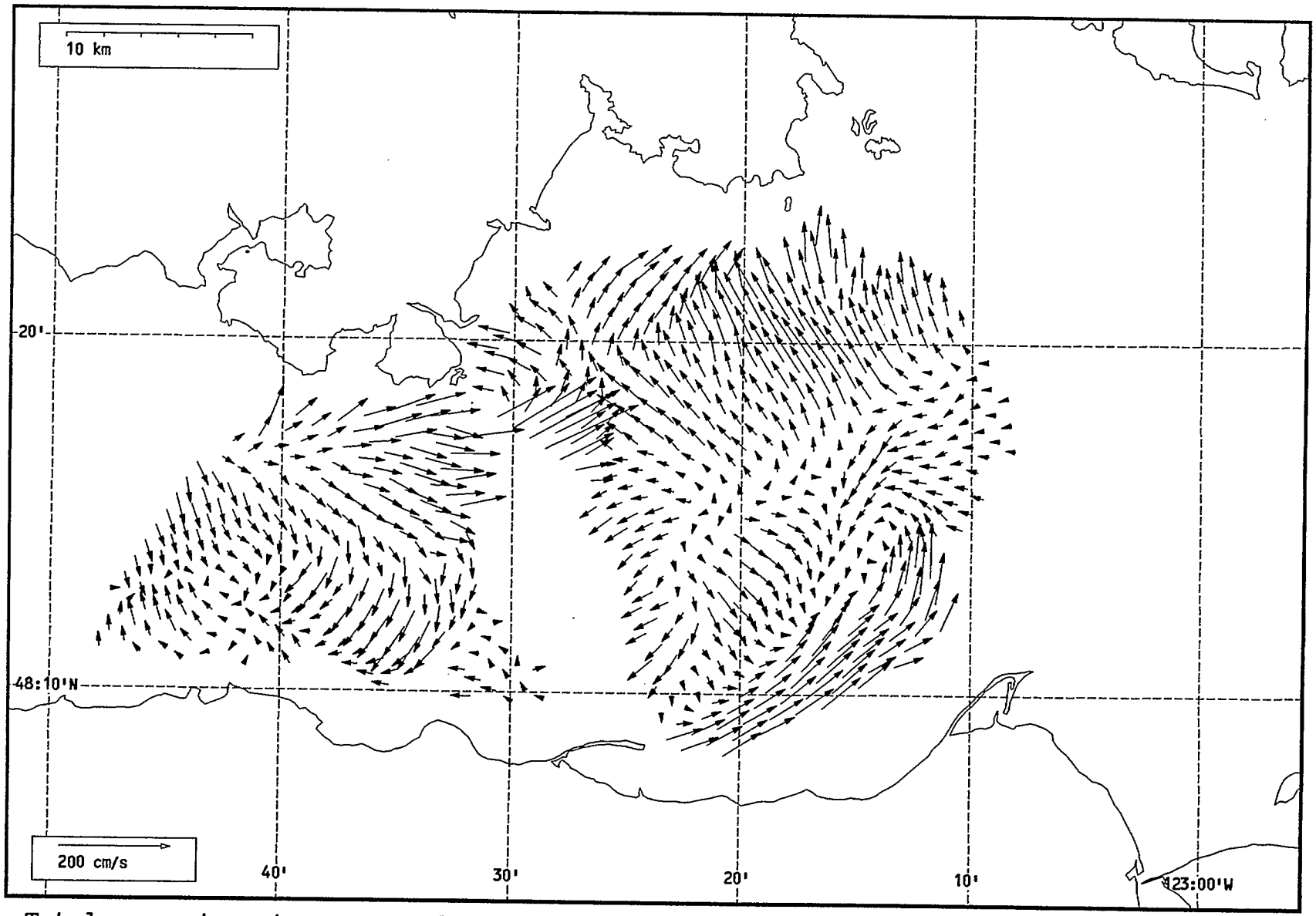

Total current vectors, Juan de Fuca Strait, 1992-07-23 16:00 Z.

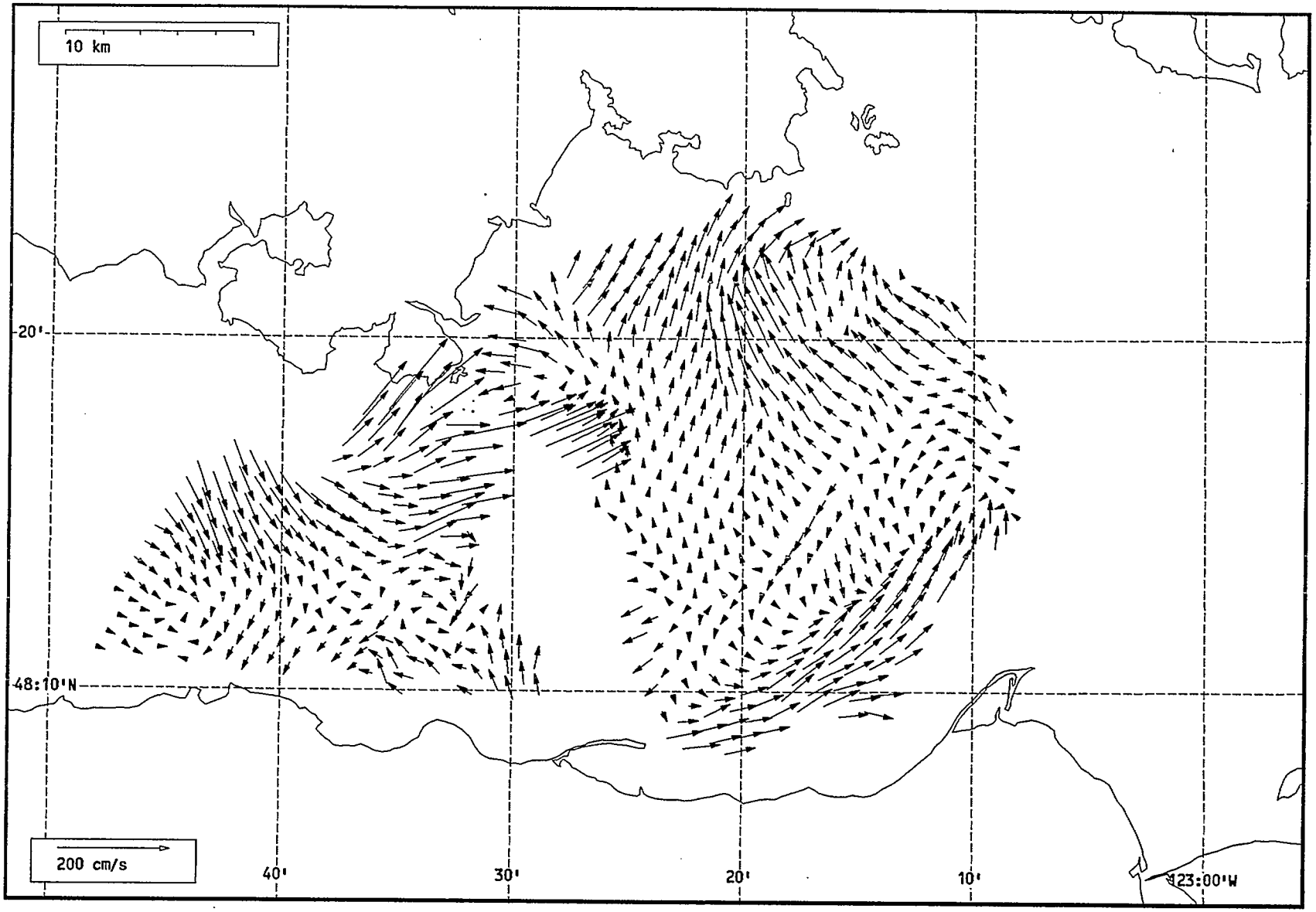

Total current vectors, Juan de Fuca Strait, 1992-07-23 17:00 Z.

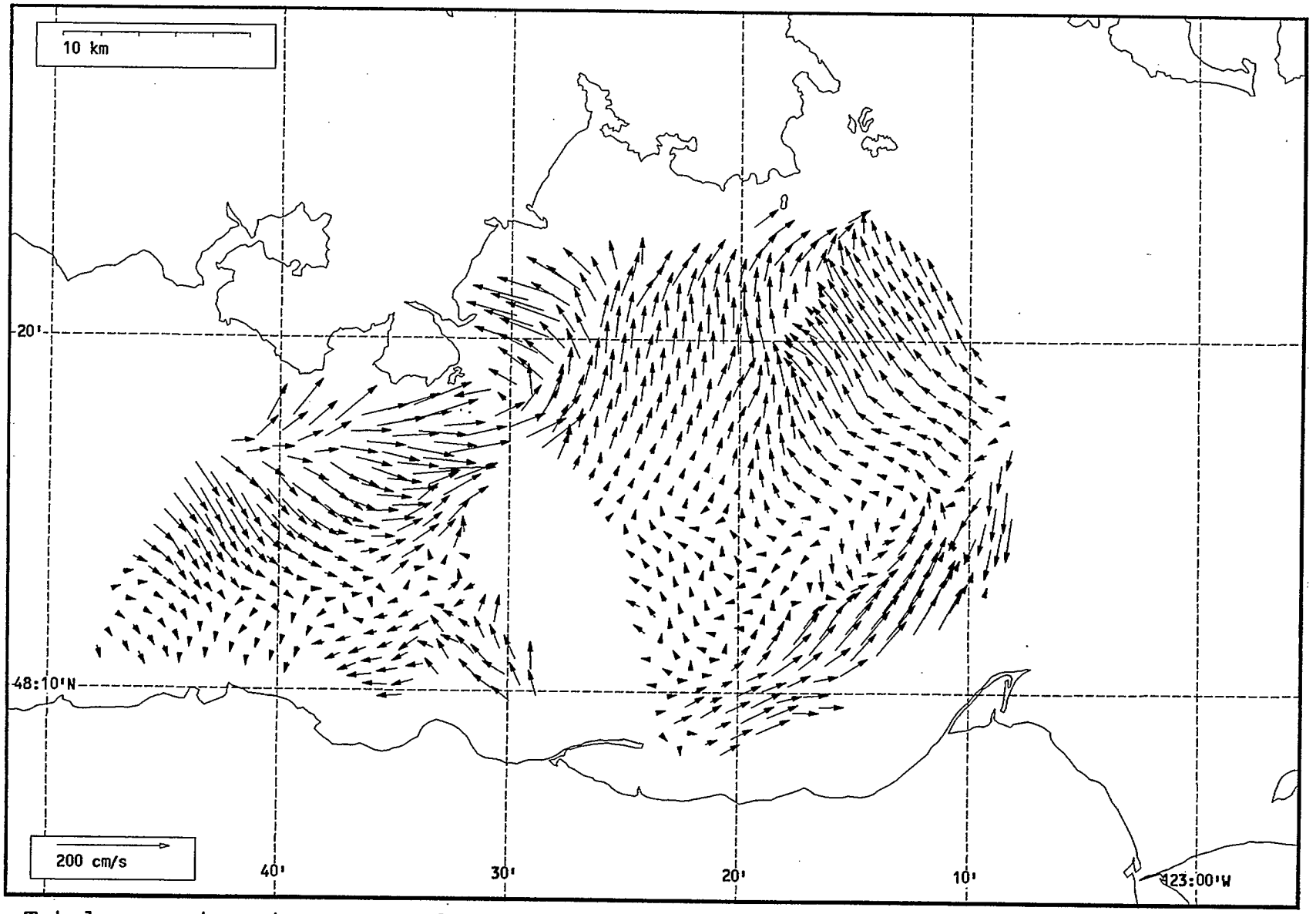

Total current vectors, Juan de Fuca Strait, 1992-07-23 18:00 Z.

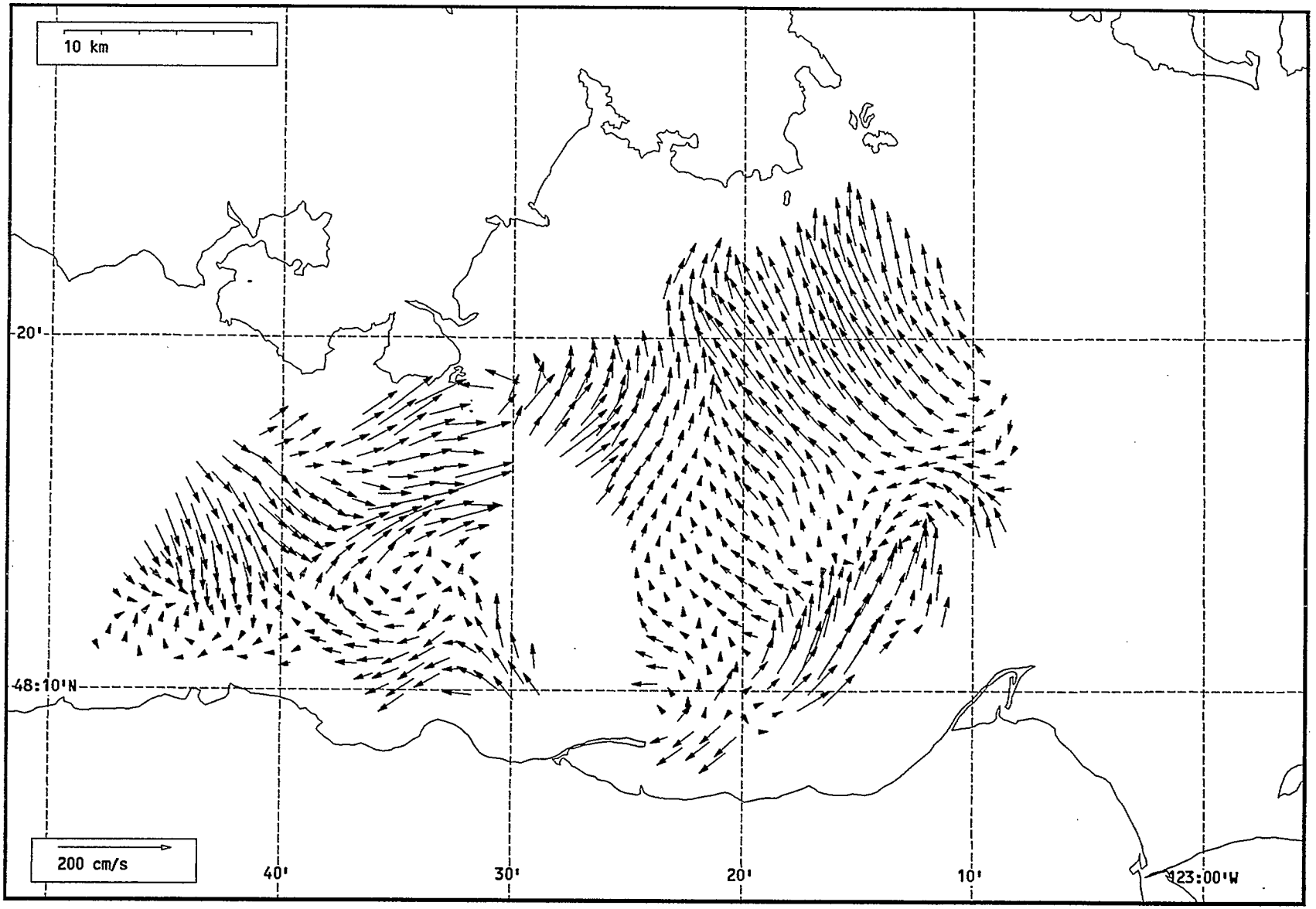

Total current vectors, Juan de Fuca Strait, 1992-07-23 19:00 Z.

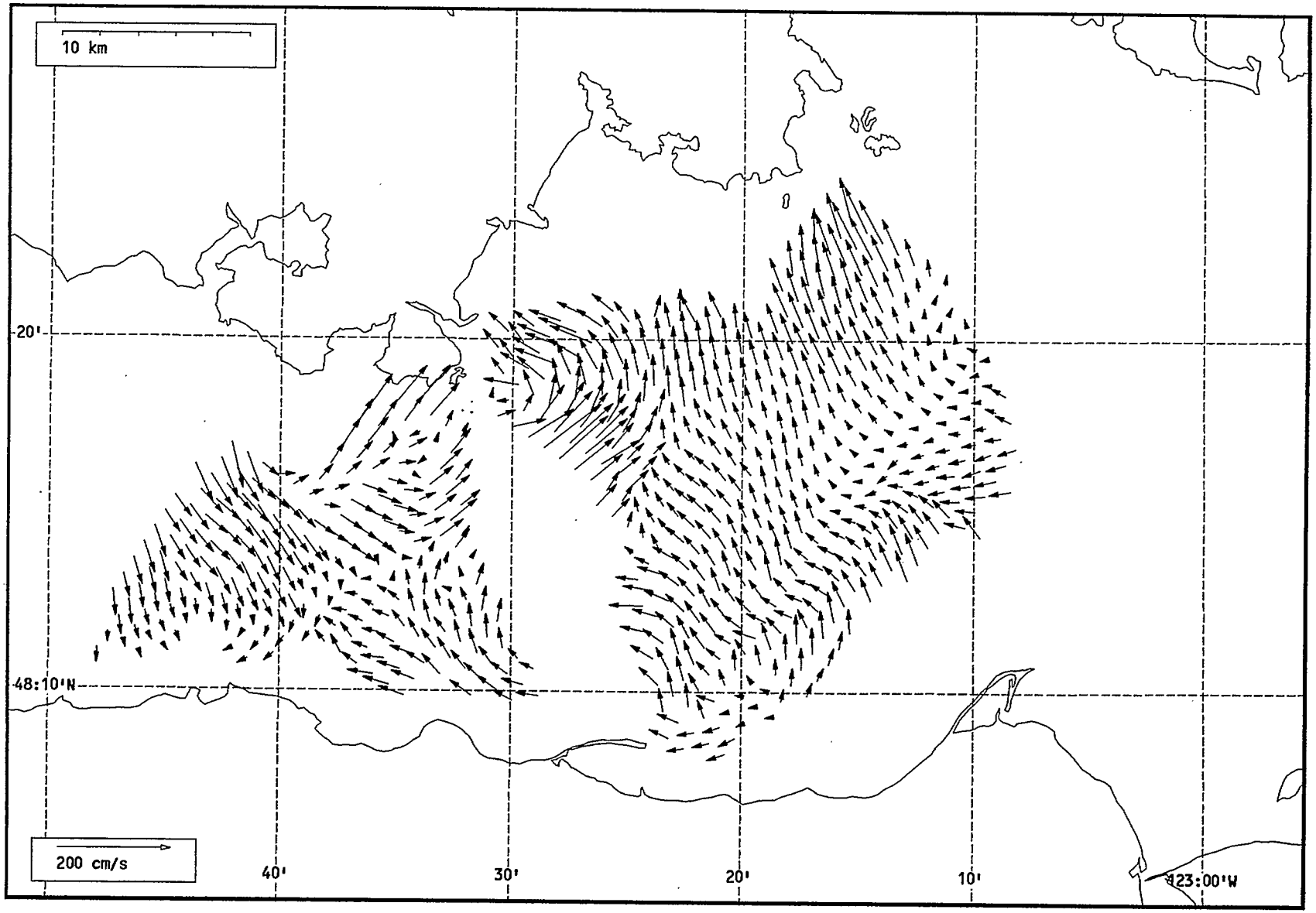

Total current vectors, Juan de Fuca Strait, 1992-07-23 20:00 Z.

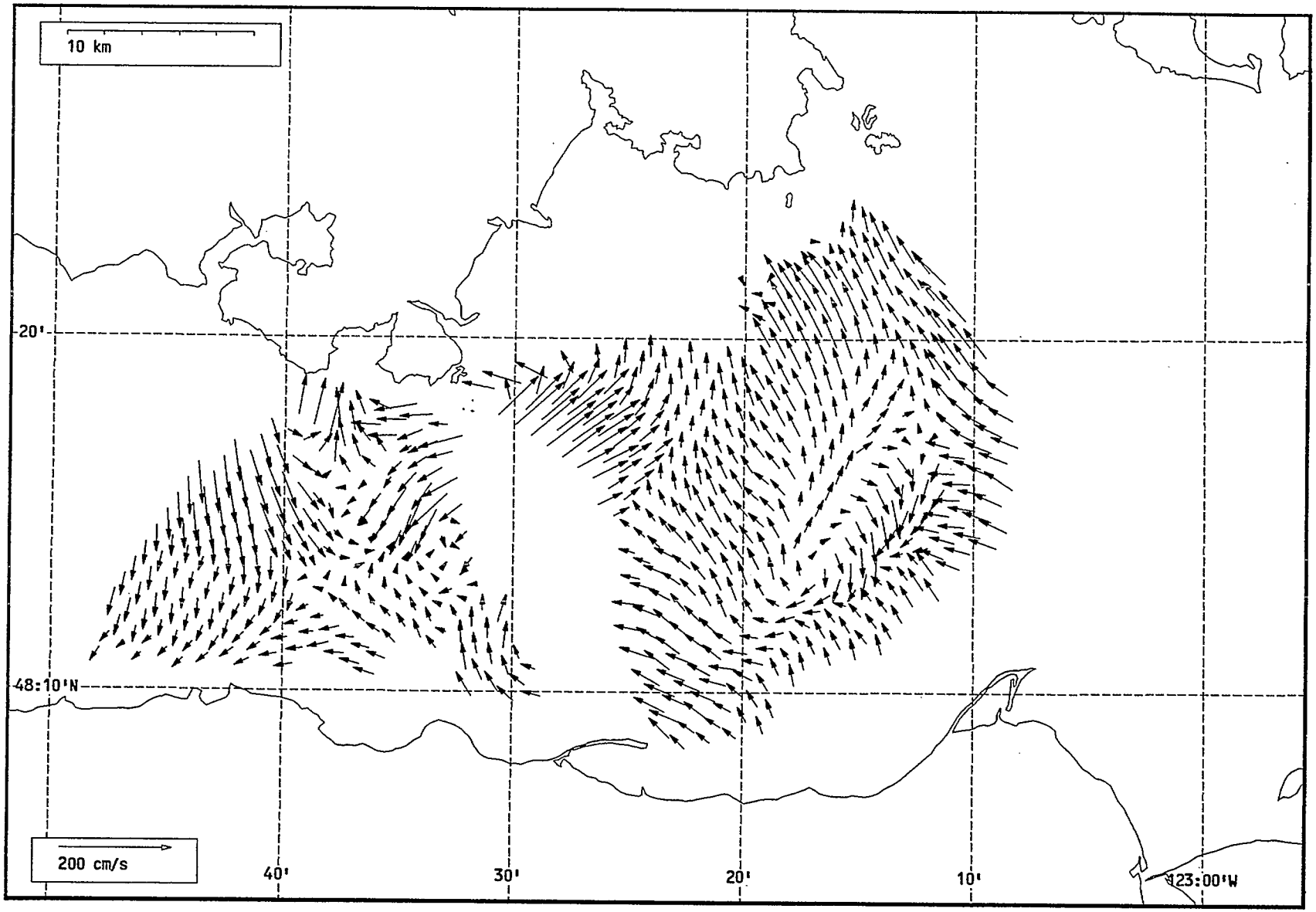

Total current vectors, Juan de Fuca Strait, 1992-07-23 21:00 Z.

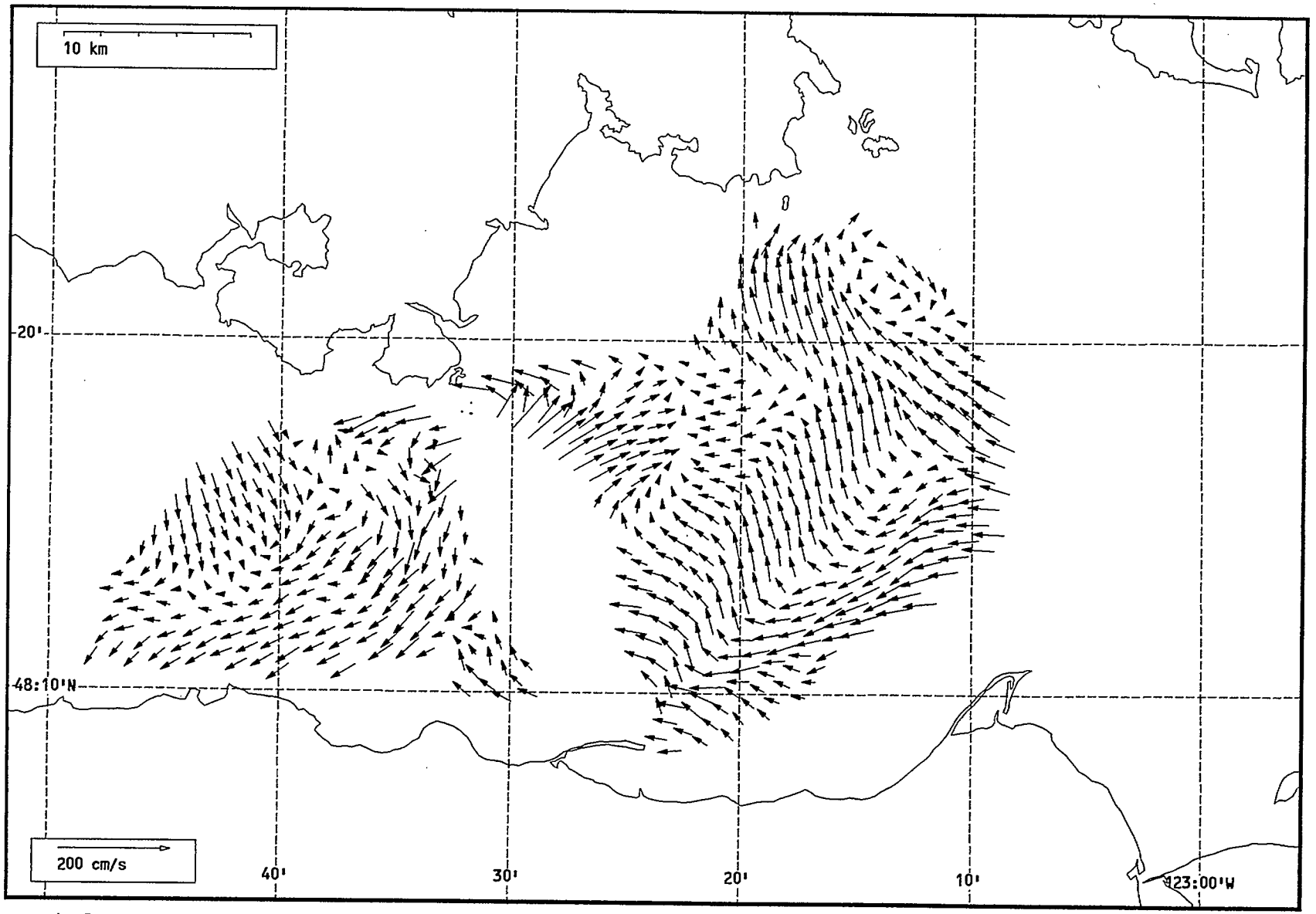

Total current vectors, Juan de Fuca Strait, 1992-07-23 22:00 Z.

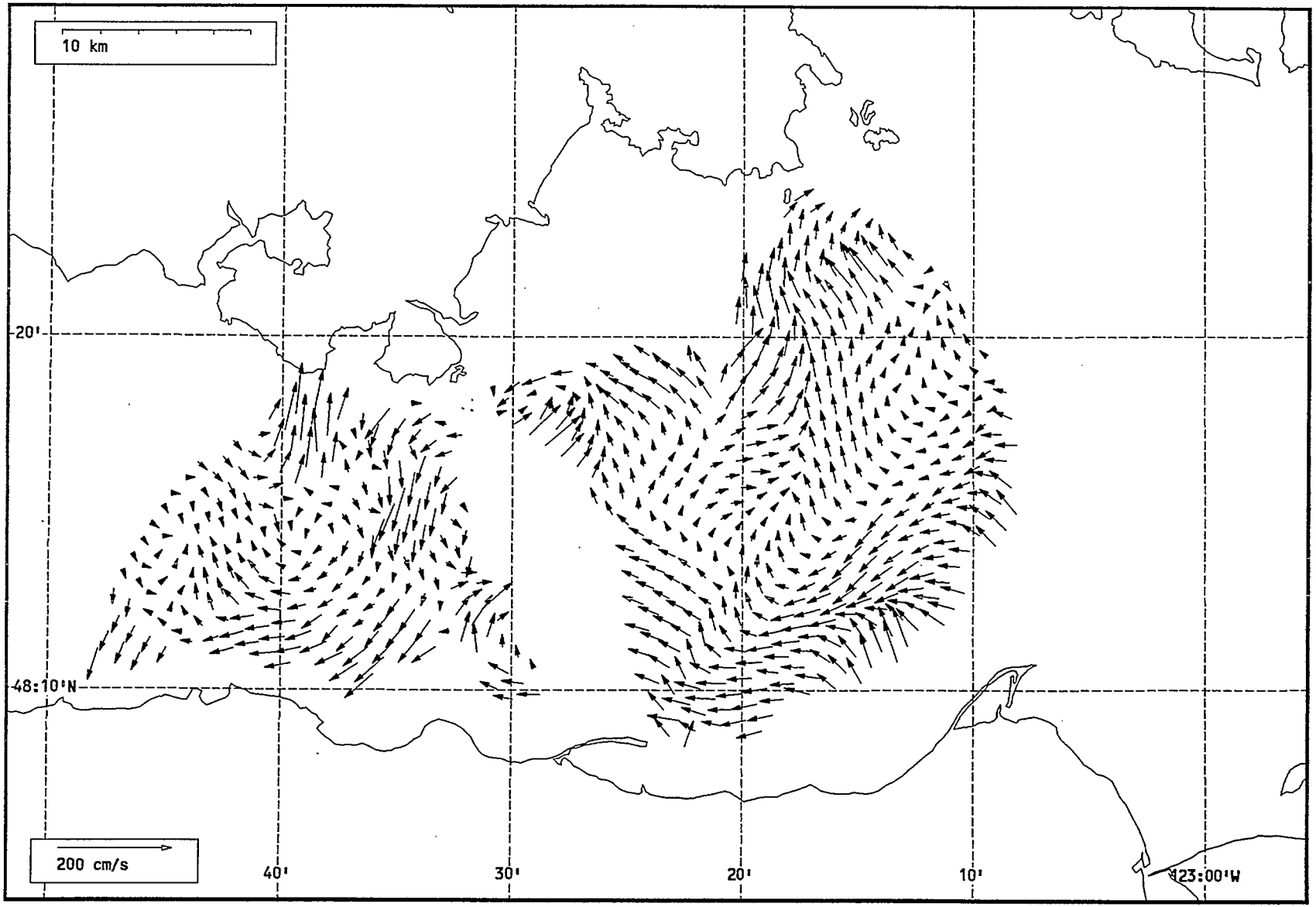

Total current vectors, Juan de Fuca Strait, 1992-07-23 23:00 Z.

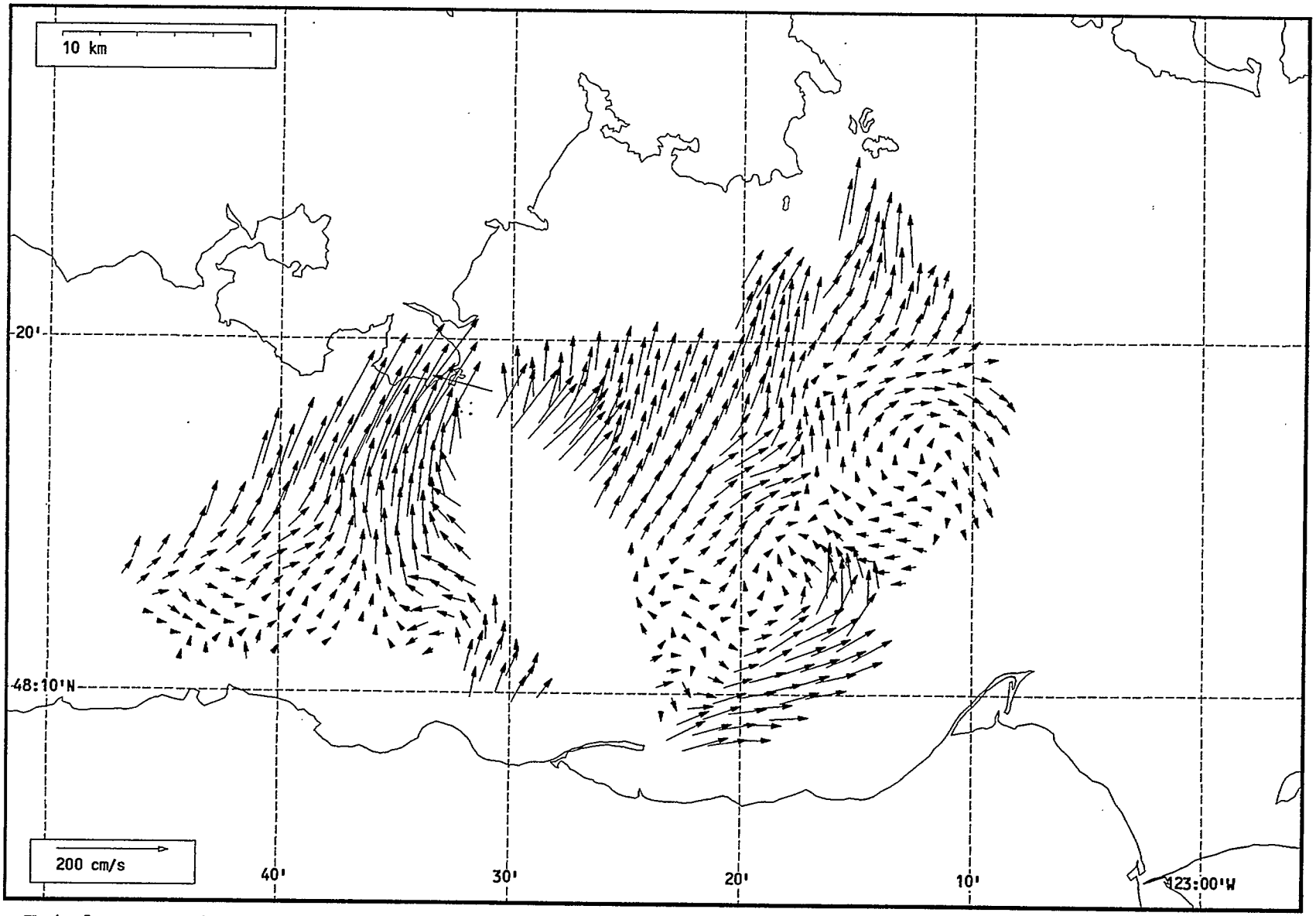

Total current vectors, Juan de Fuca Strait, 1992-07-24 18:00 Z.

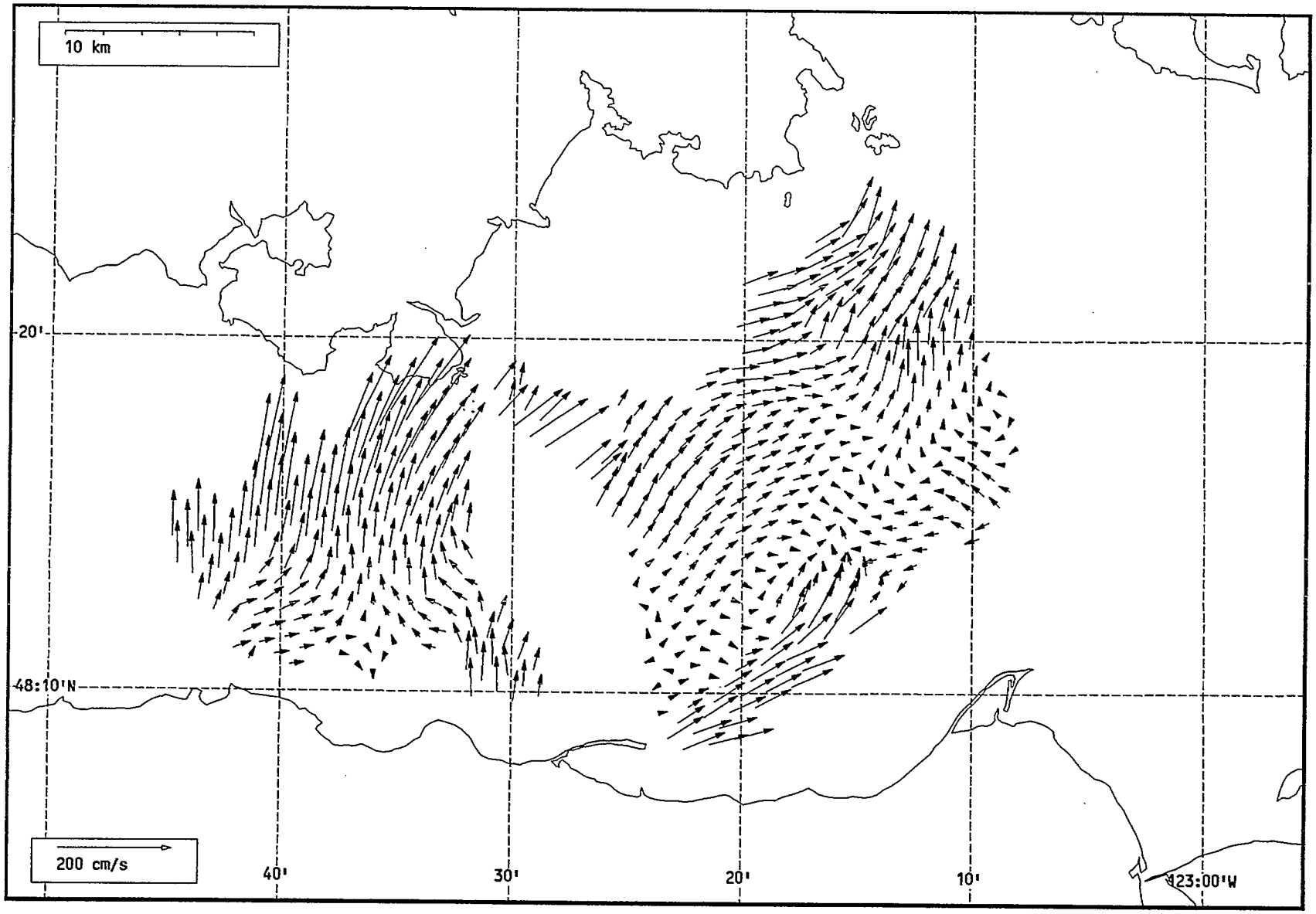

Total current vectors, Juan de Fuca Strait, 1992-07-24 19:00 Z.

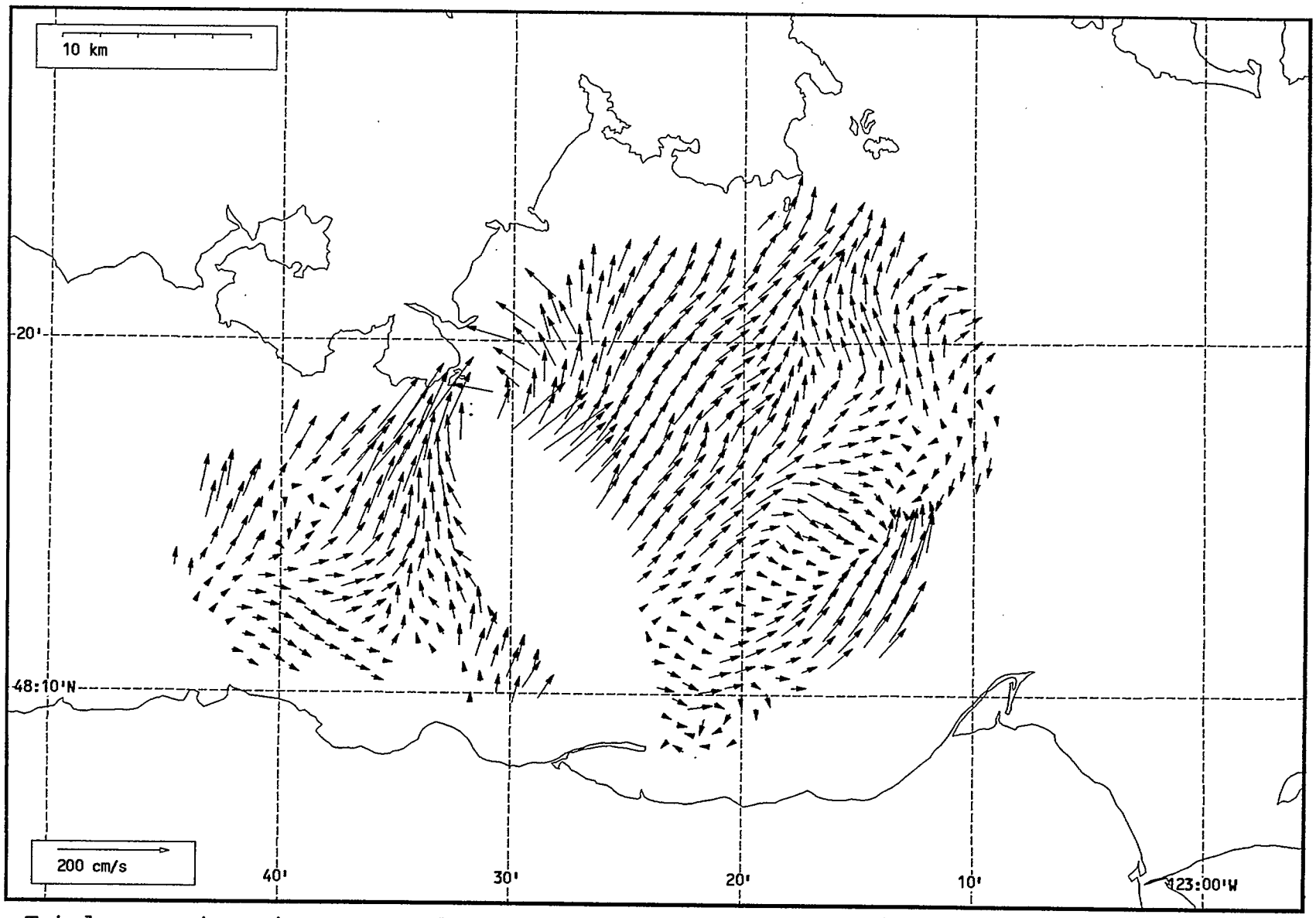

Total current vectors, Juan de Fuca Strait, 1992-07-24 20:00 Z.

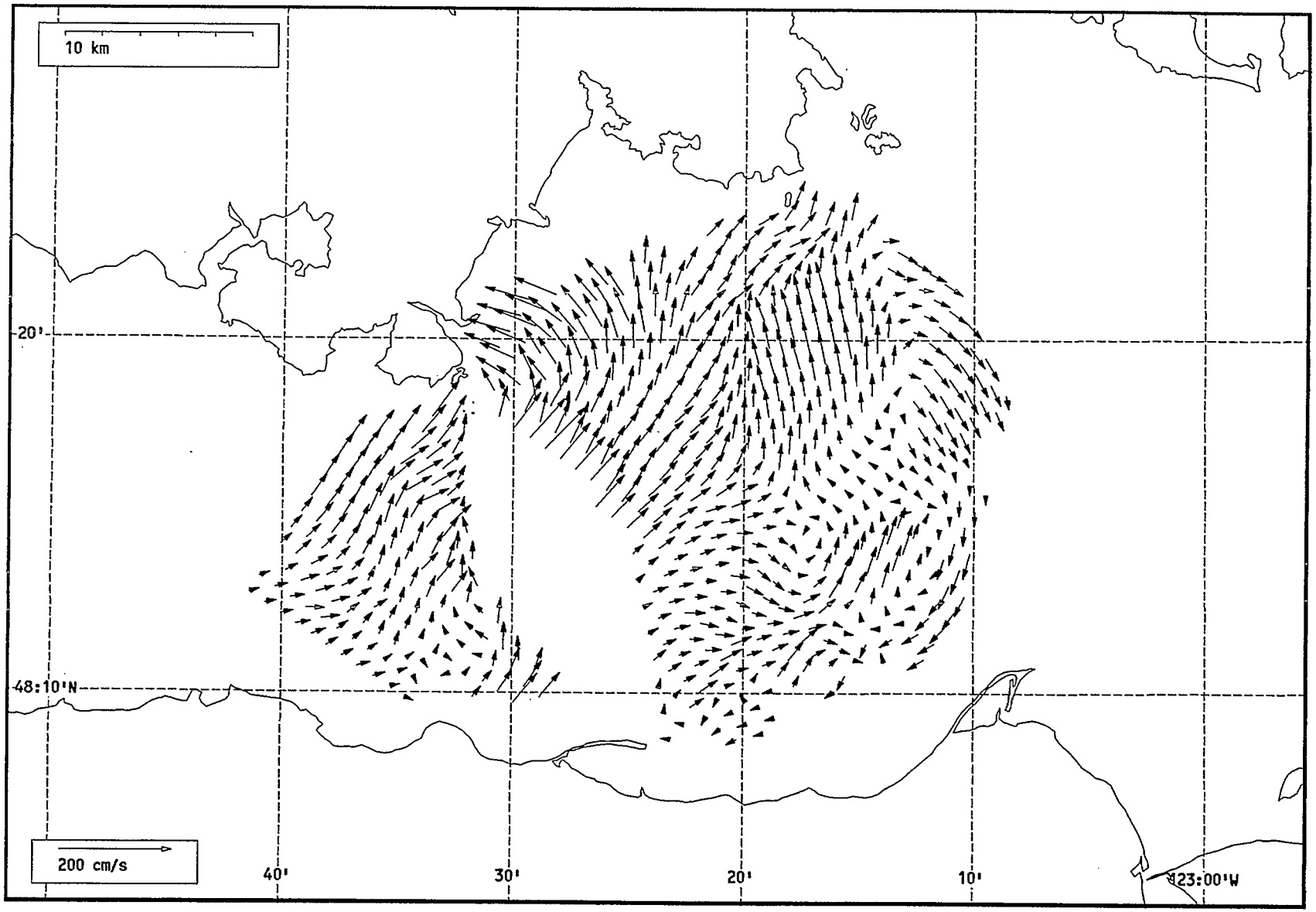

Total current vectors, Juan de Fuca Strait, 1992-07-24 21:00 Z.

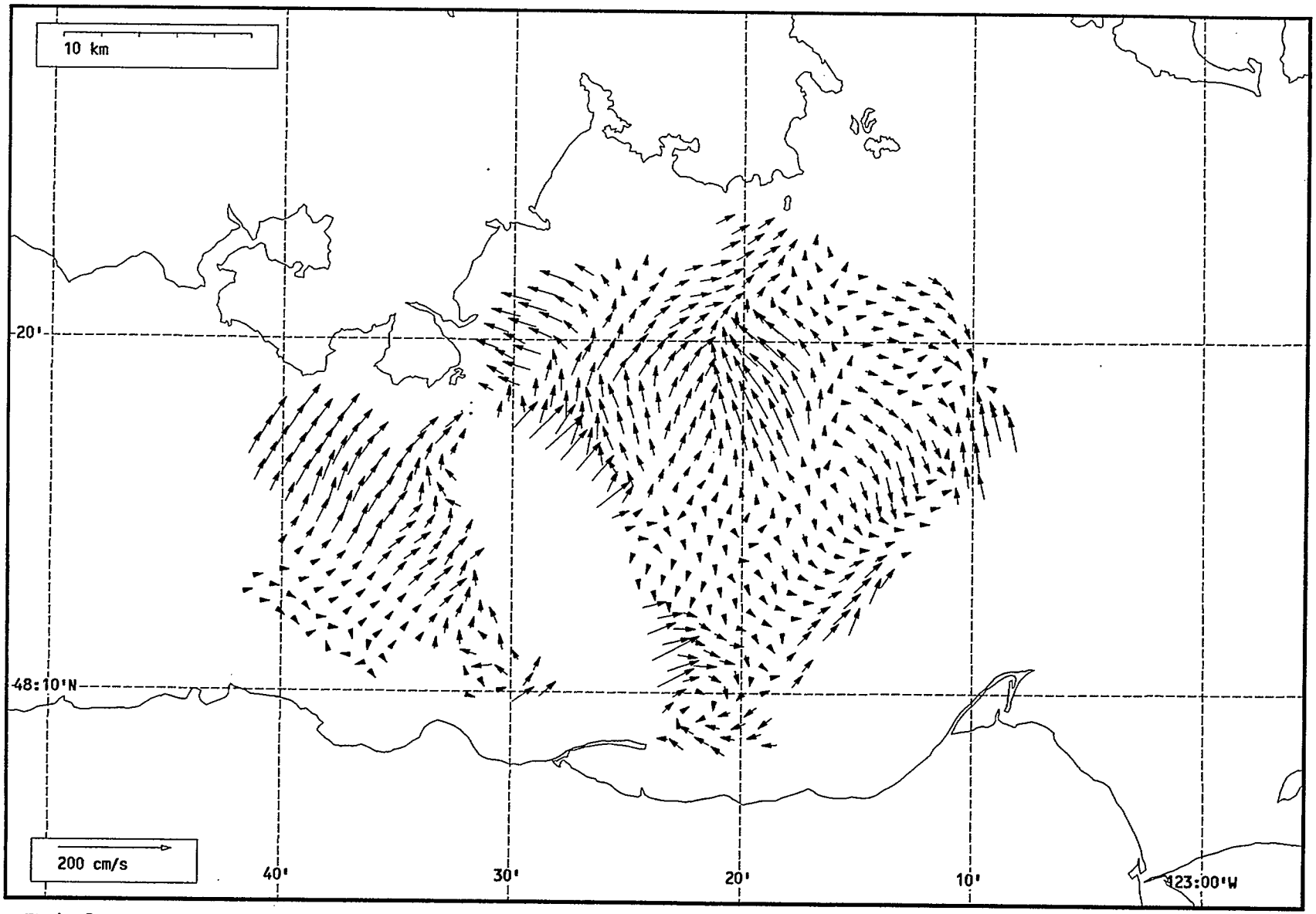

Total current vectors, Juan de Fuca Strait, 1992-07-24 22:00 Z.

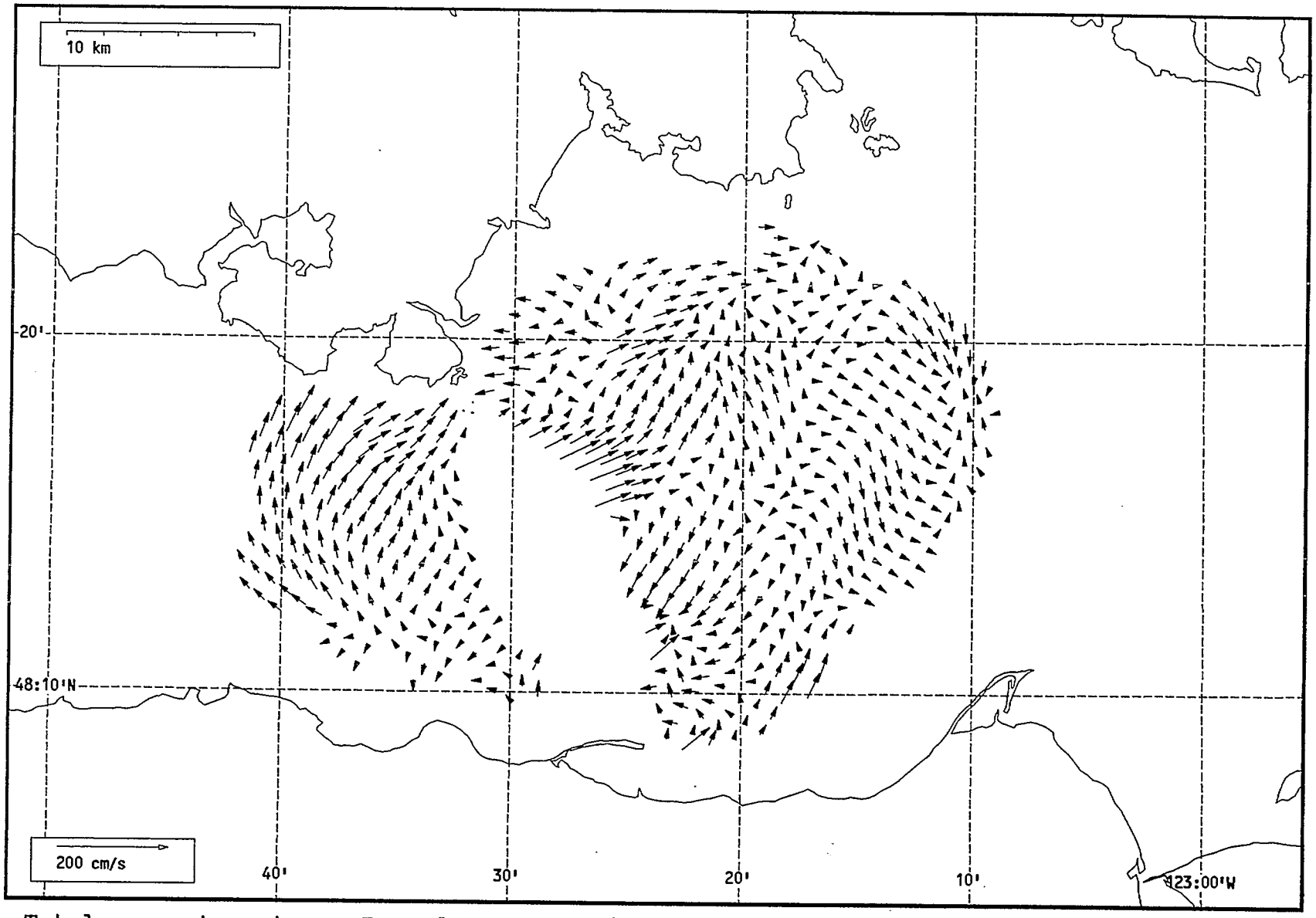

Total current vectors, Juan de Fuca Strait, 1992-07-24 23:00 Z.

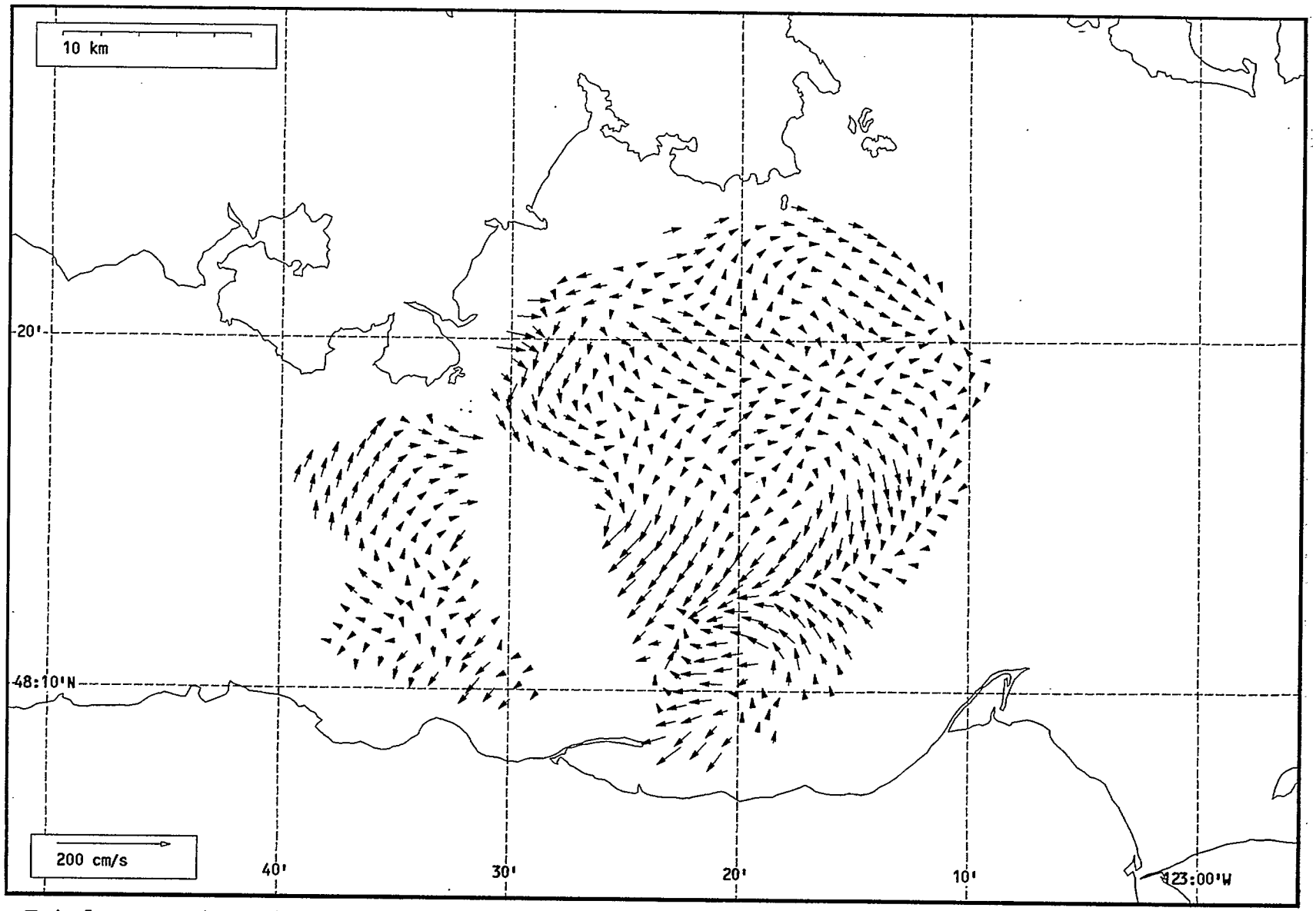

Total current vectors, Juan de Fuca Strait, 1992-07-25 00:00 Z.

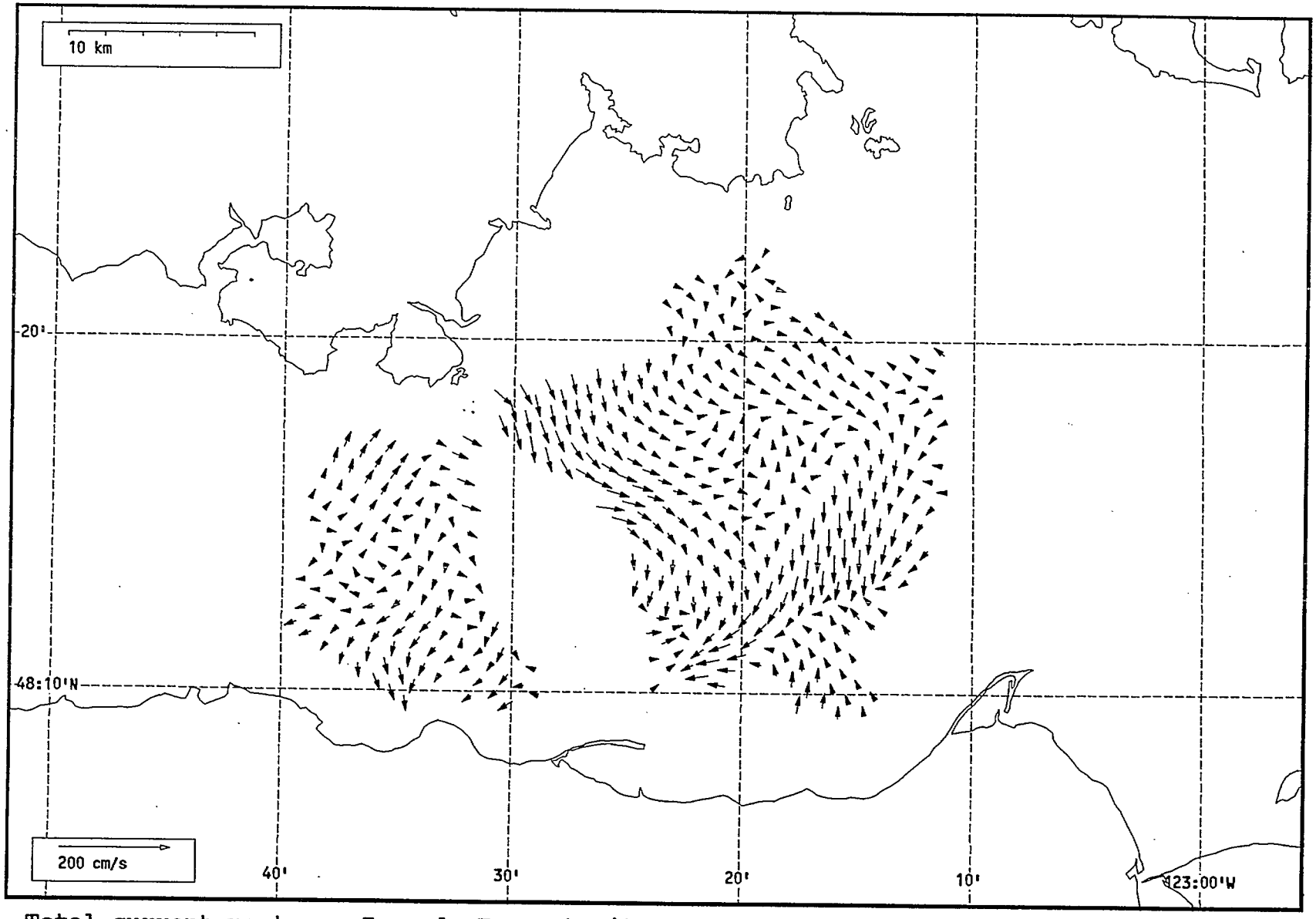

Total current vectors, Juan de Fuca Strait, 1992-07-25 01:00 Z.

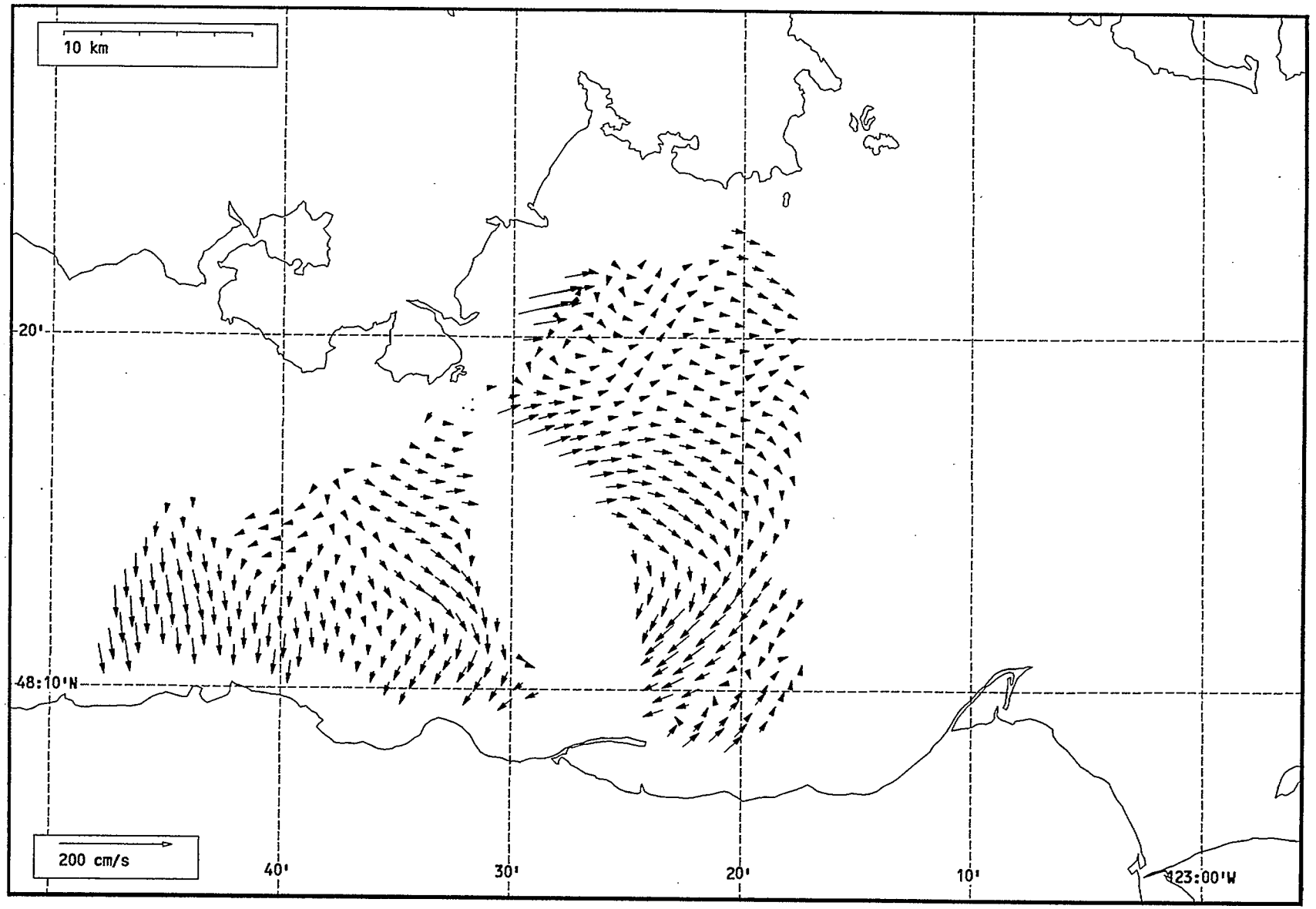

Total current vectors, Juan de Fuca Strait, 1992-07-25 02:00 Z.

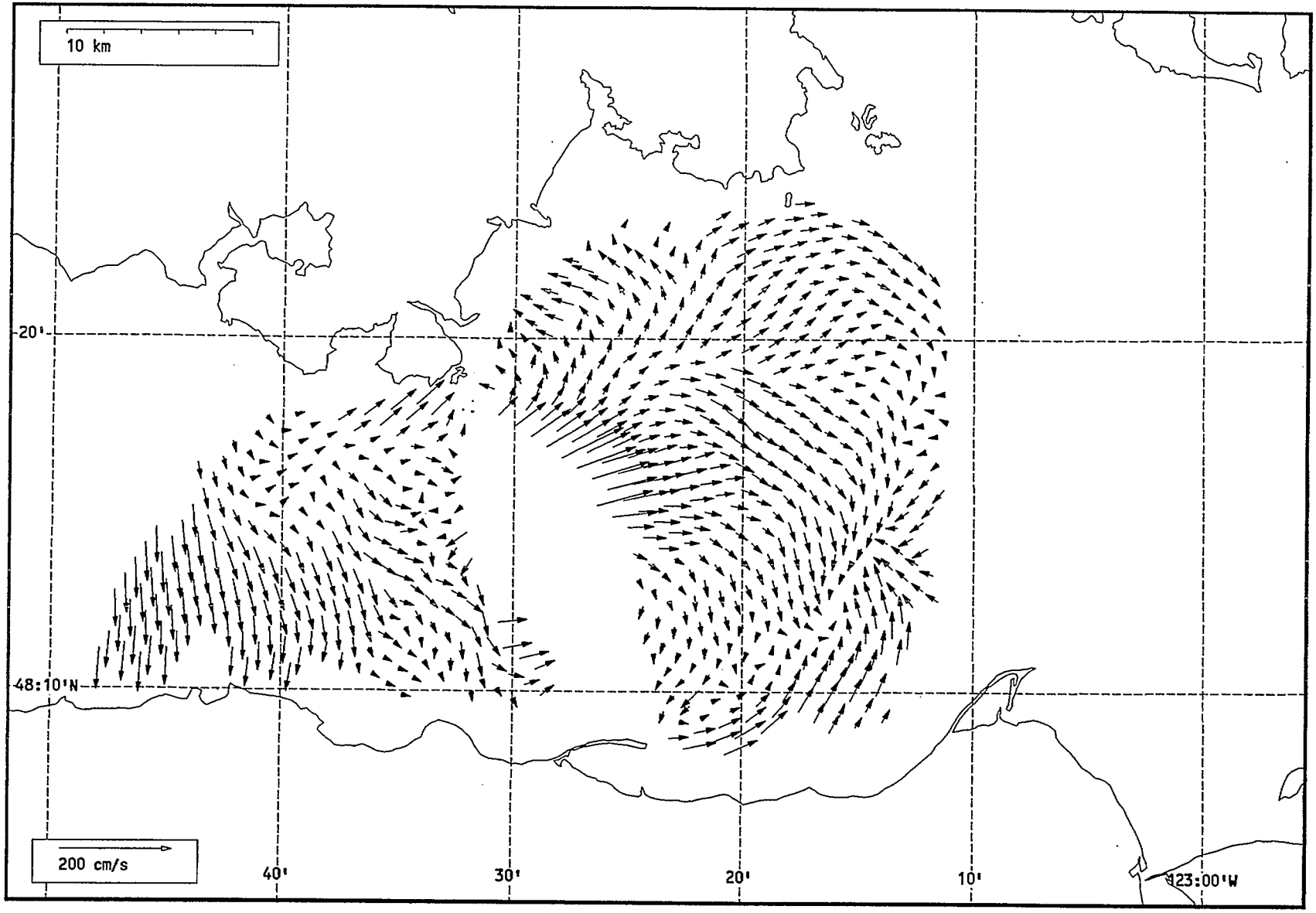

Total current vectors, Juan de Fuca Strait, 1992-07-25 03:00 Z.

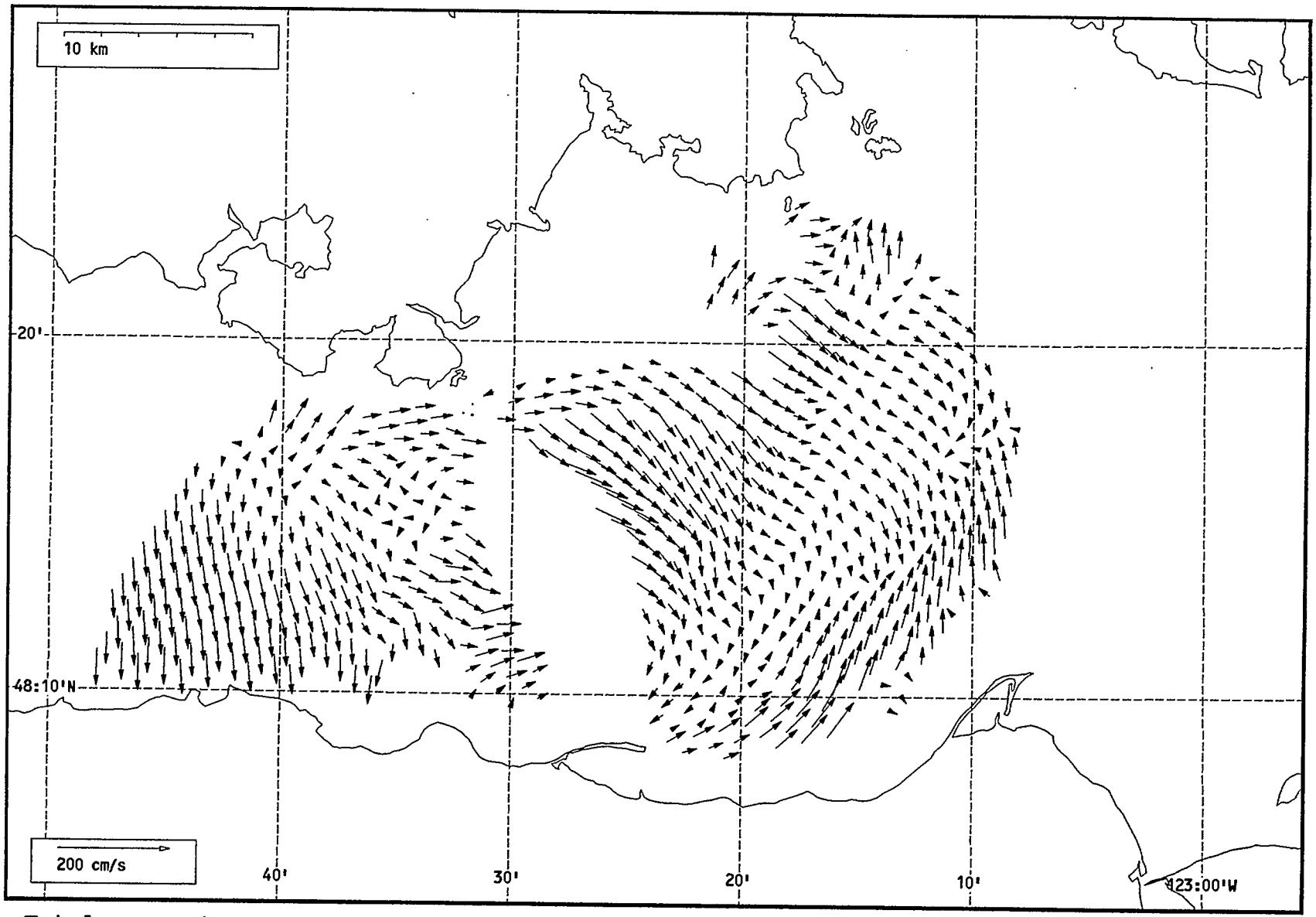

Total current vectors, Juan de Fuca Strait, 1992-07-25 04:00 Z.

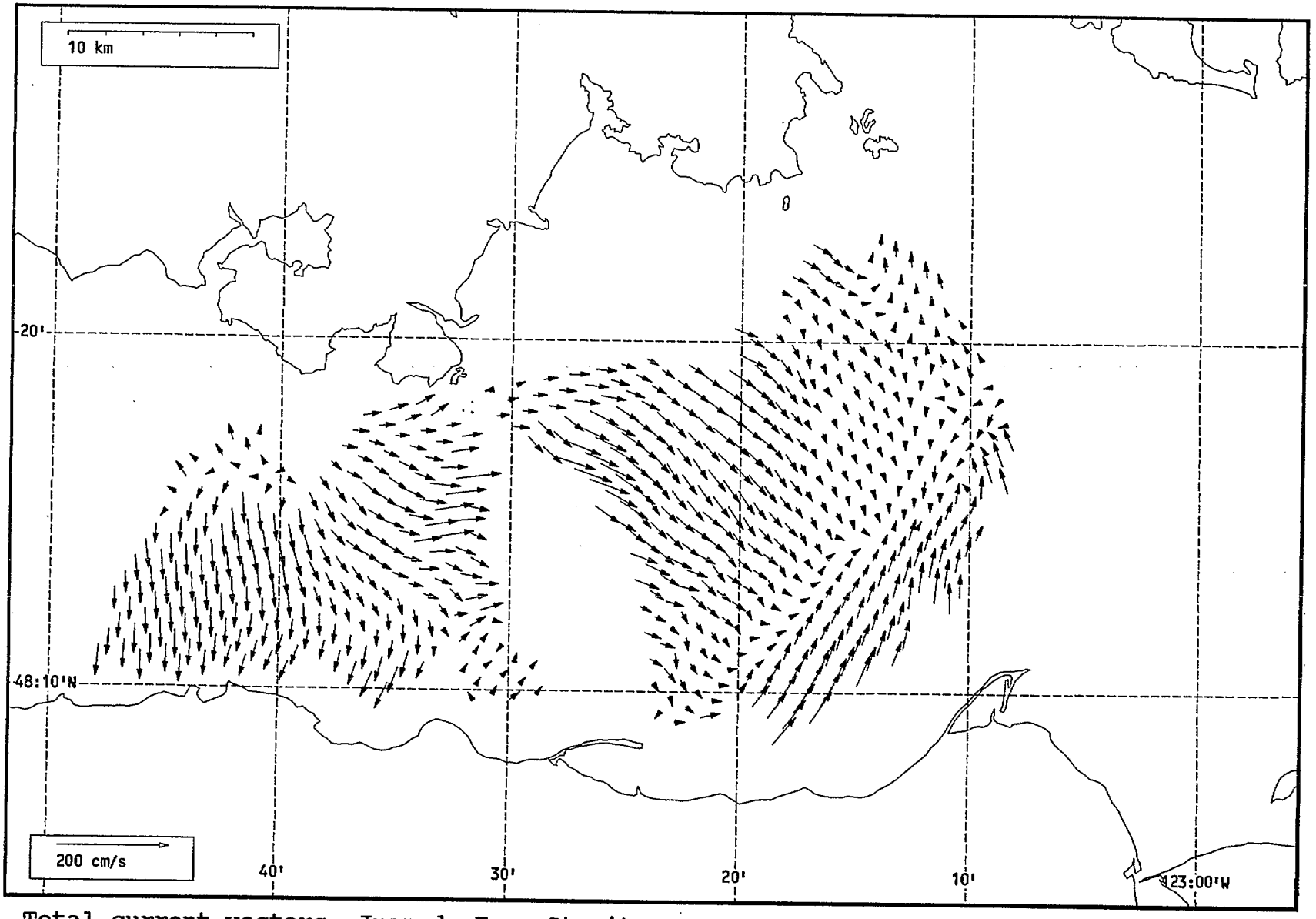

Total current vectors, Juan de Fuca Strait, 1992-07-25 05:00 Z.

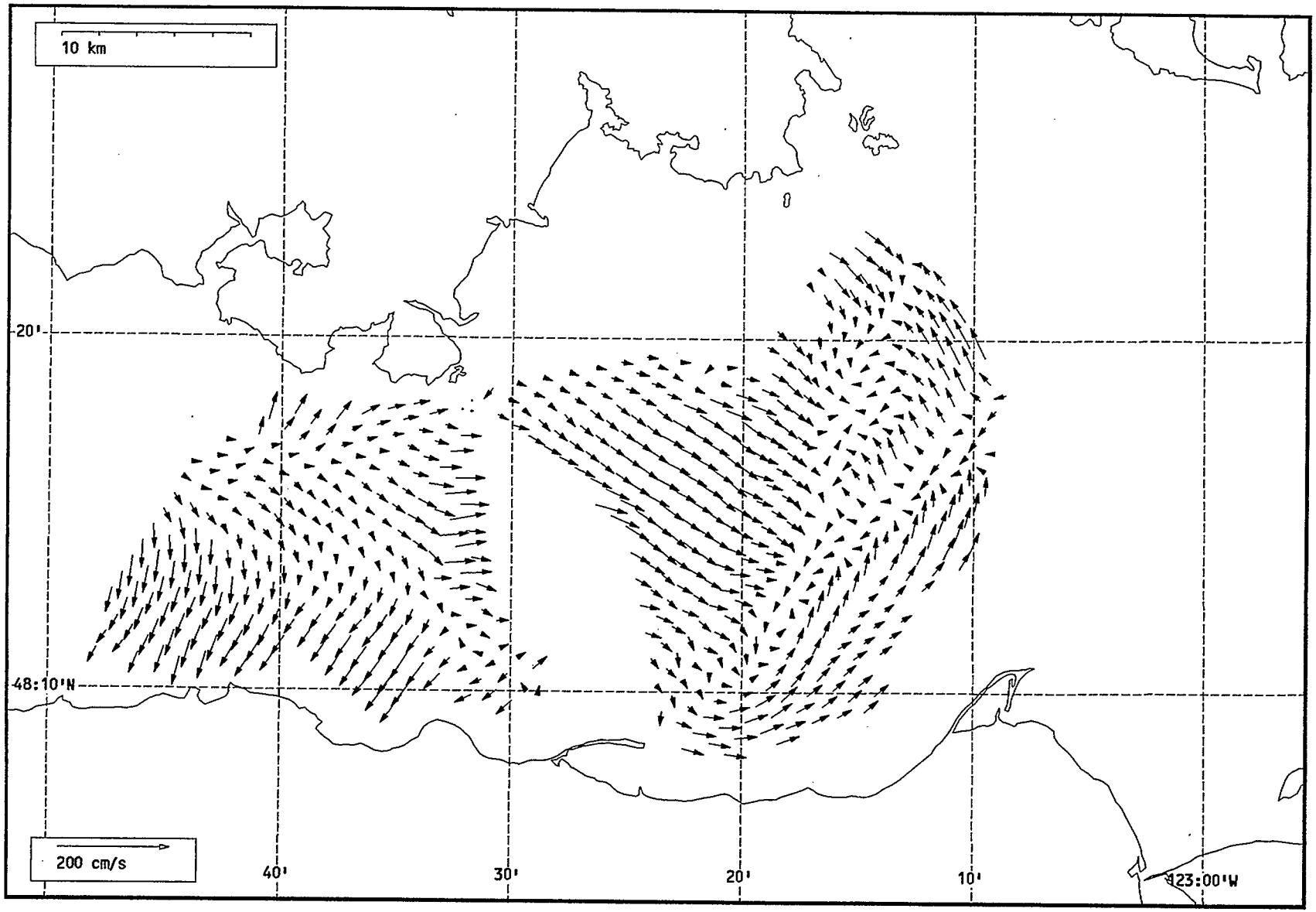

Total current vectors, Juan de Fuca Strait, 1992-07-25 06:00 Z.

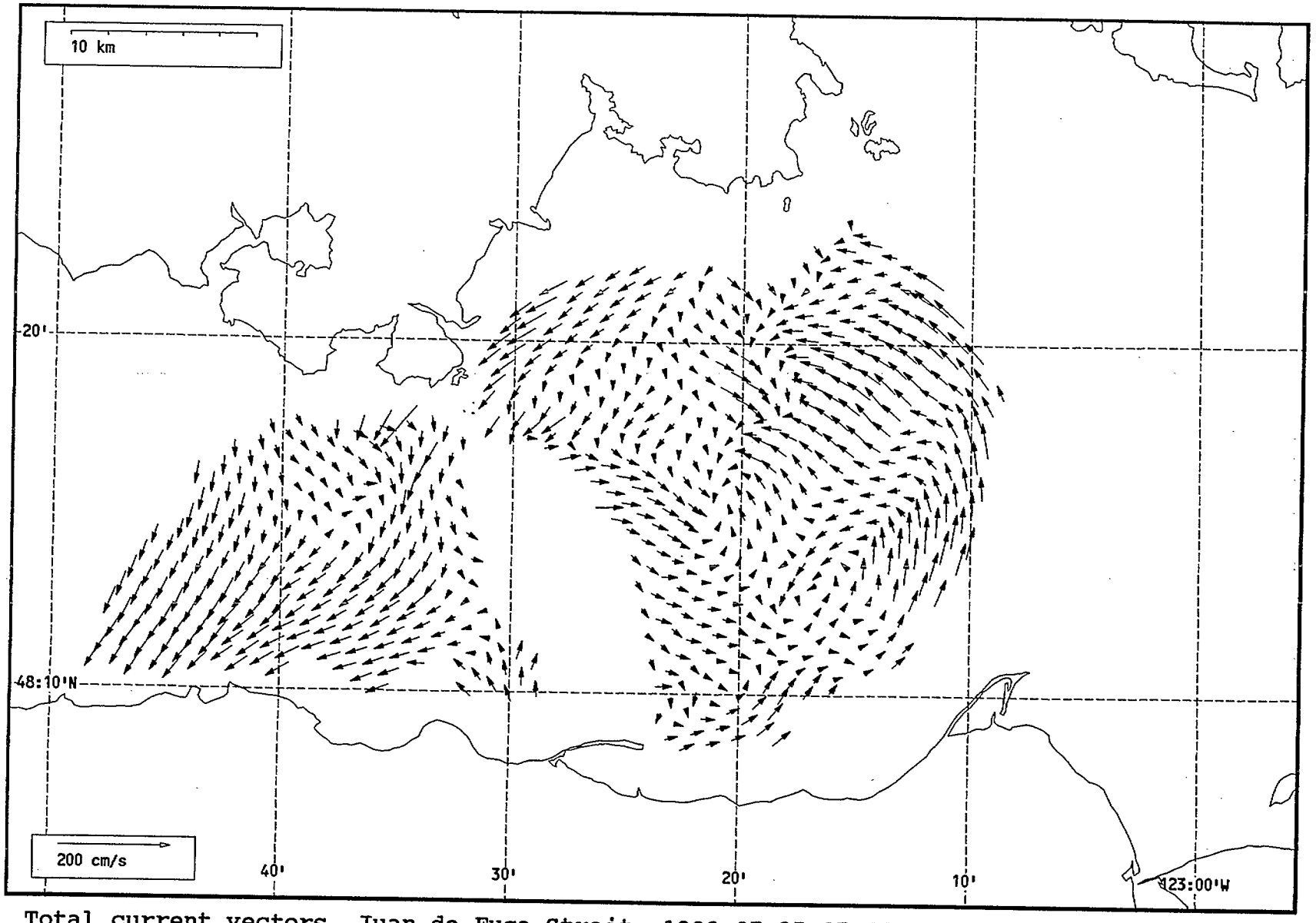

Total current vectors, Juan de Fuca Strait, 1992-07-25 07:00 Z.

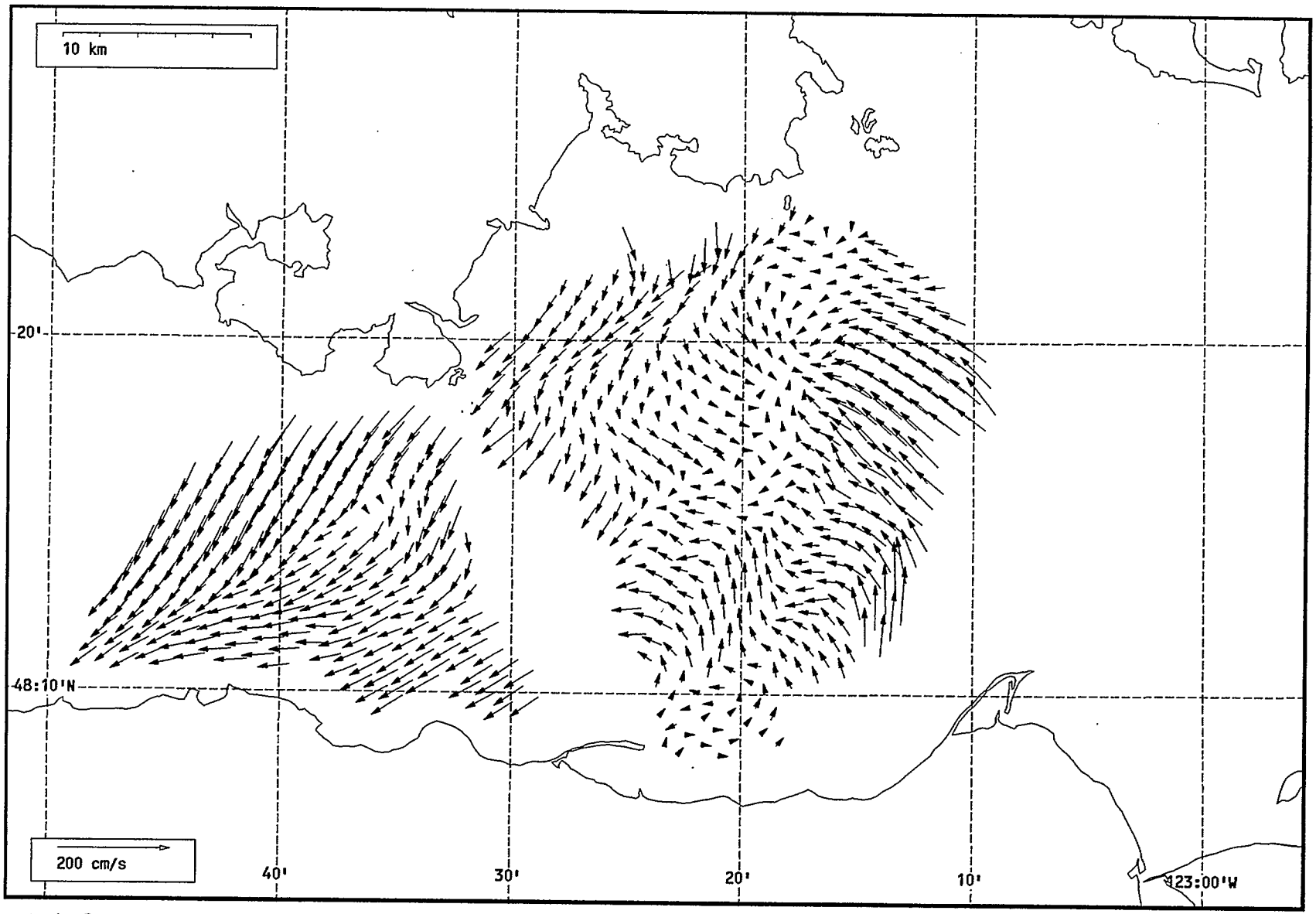

Total current vectors, Juan de Fuca Strait, 1992-07-25 08:00 Z.

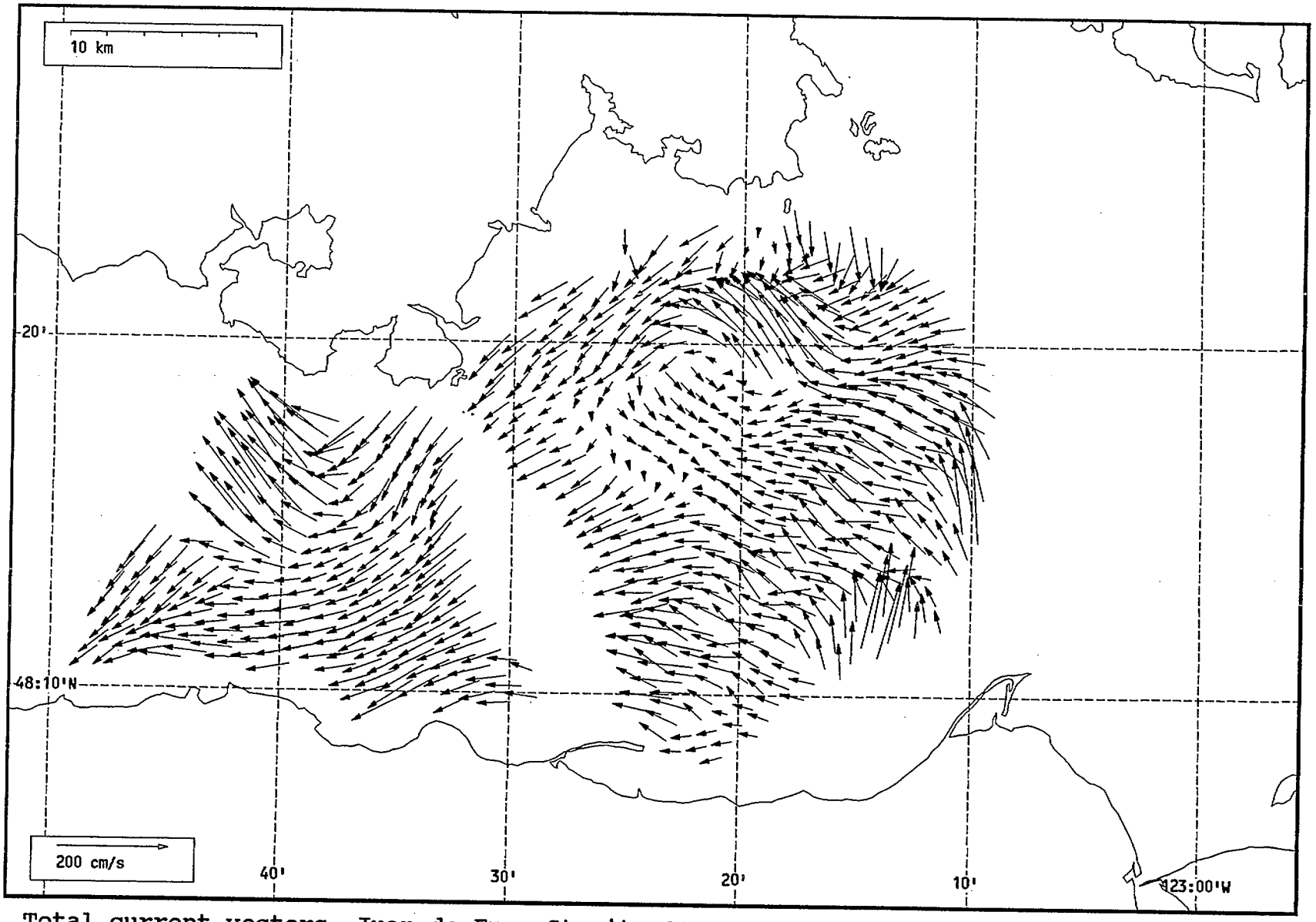

Total current vectors, Juan de Fuca Strait, 1992-07-25 09:00 Z.

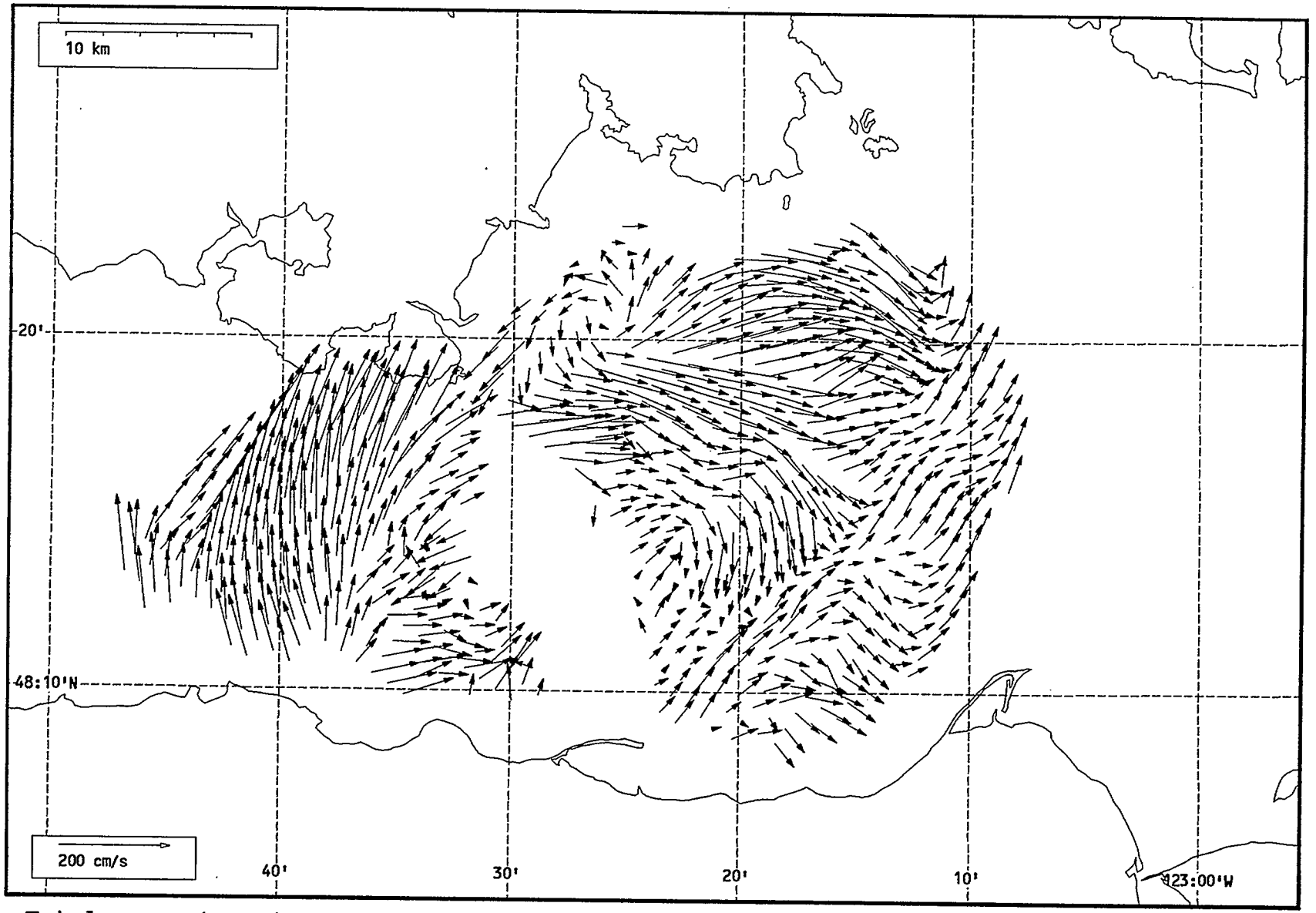

Total current vectors, Juan de Fuca Strait, 1992-07-26 21:00 Z.

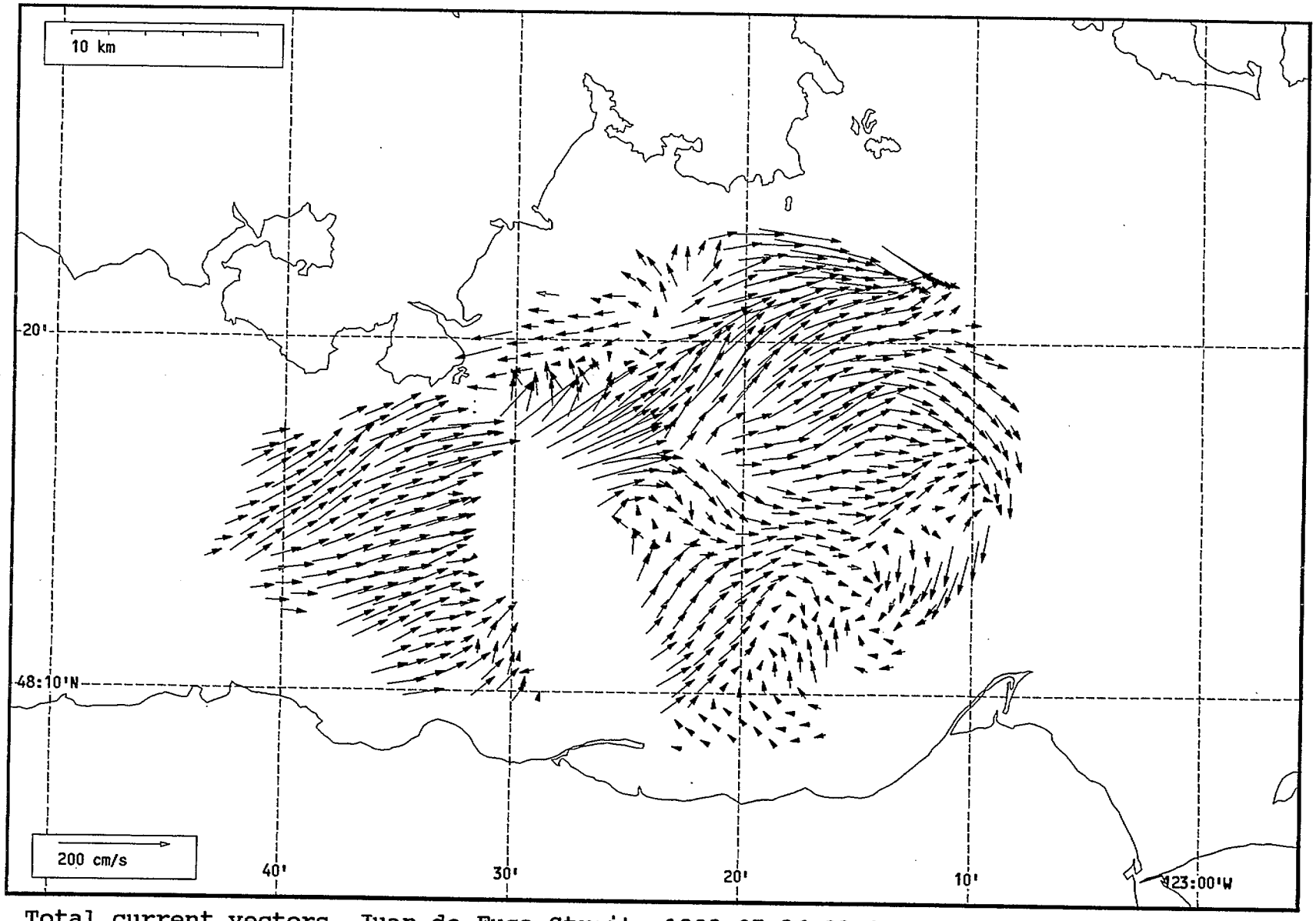

Total current vectors, Juan de Fuca Strait, 1992-07-26 22:00 Z.

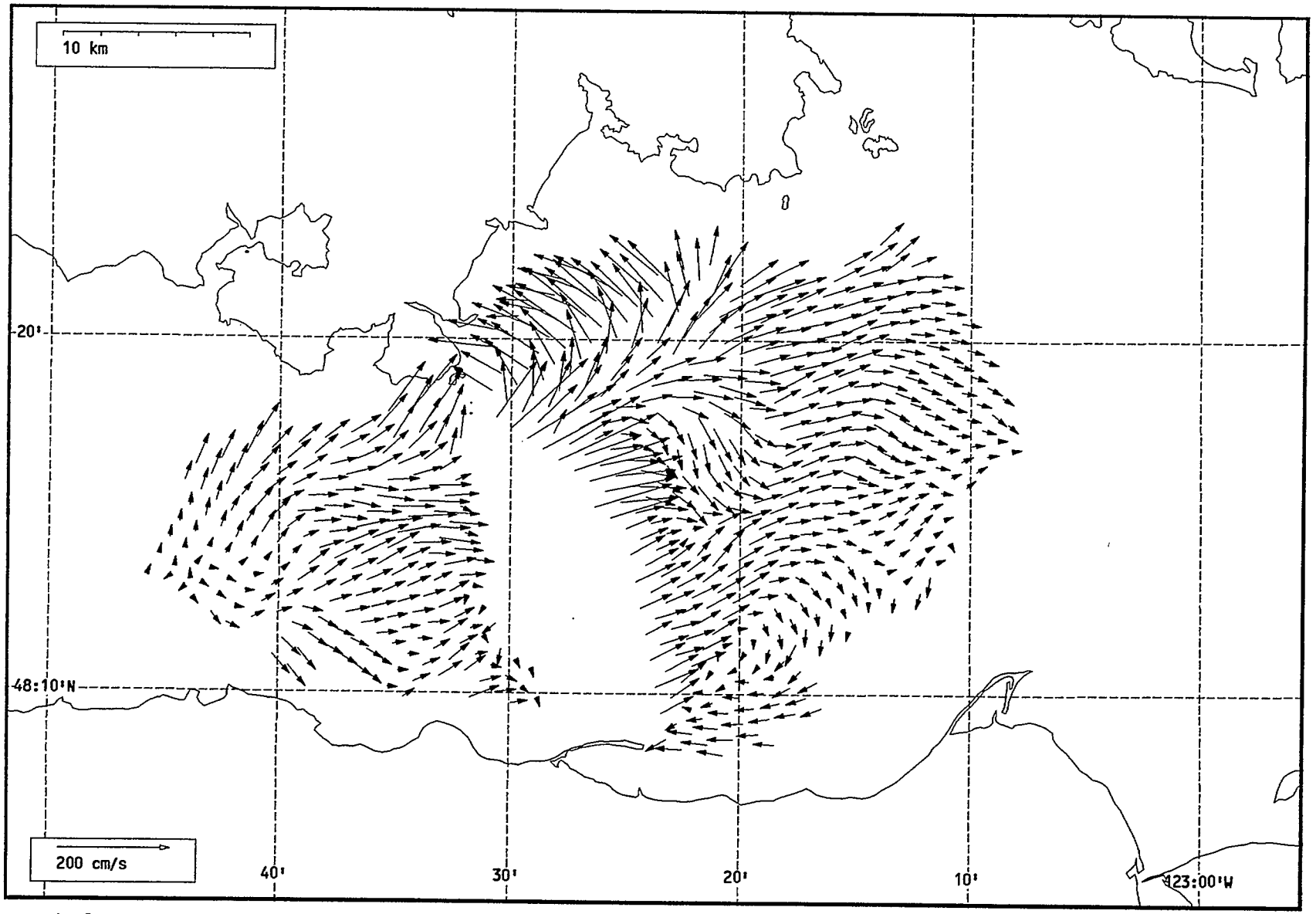

Total current vectors, Juan de Fuca Strait, 1992-07-26 23:00 Z.

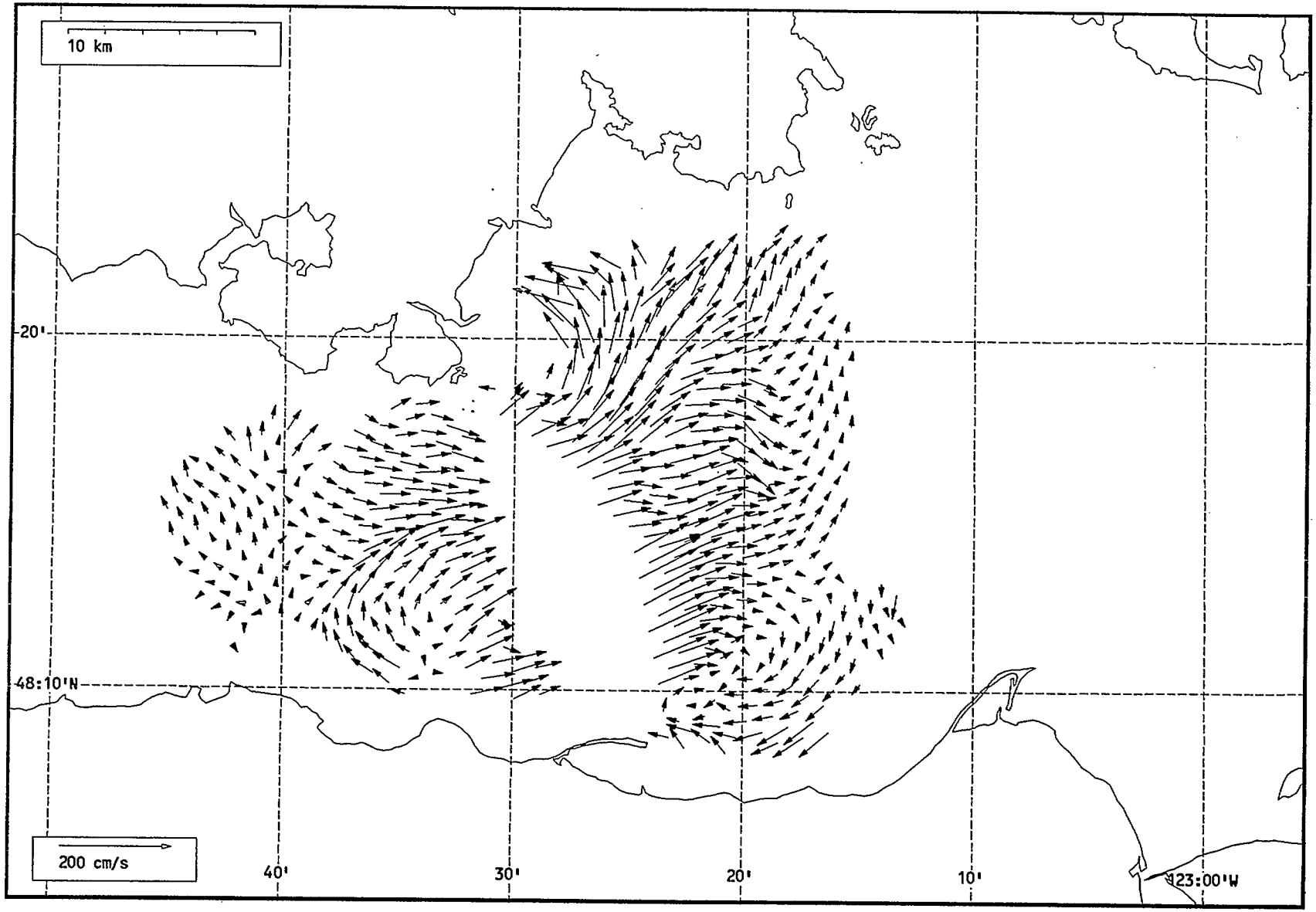

Total current vectors, Juan de Fuca Strait, 1992-07-27 00:00 Z.

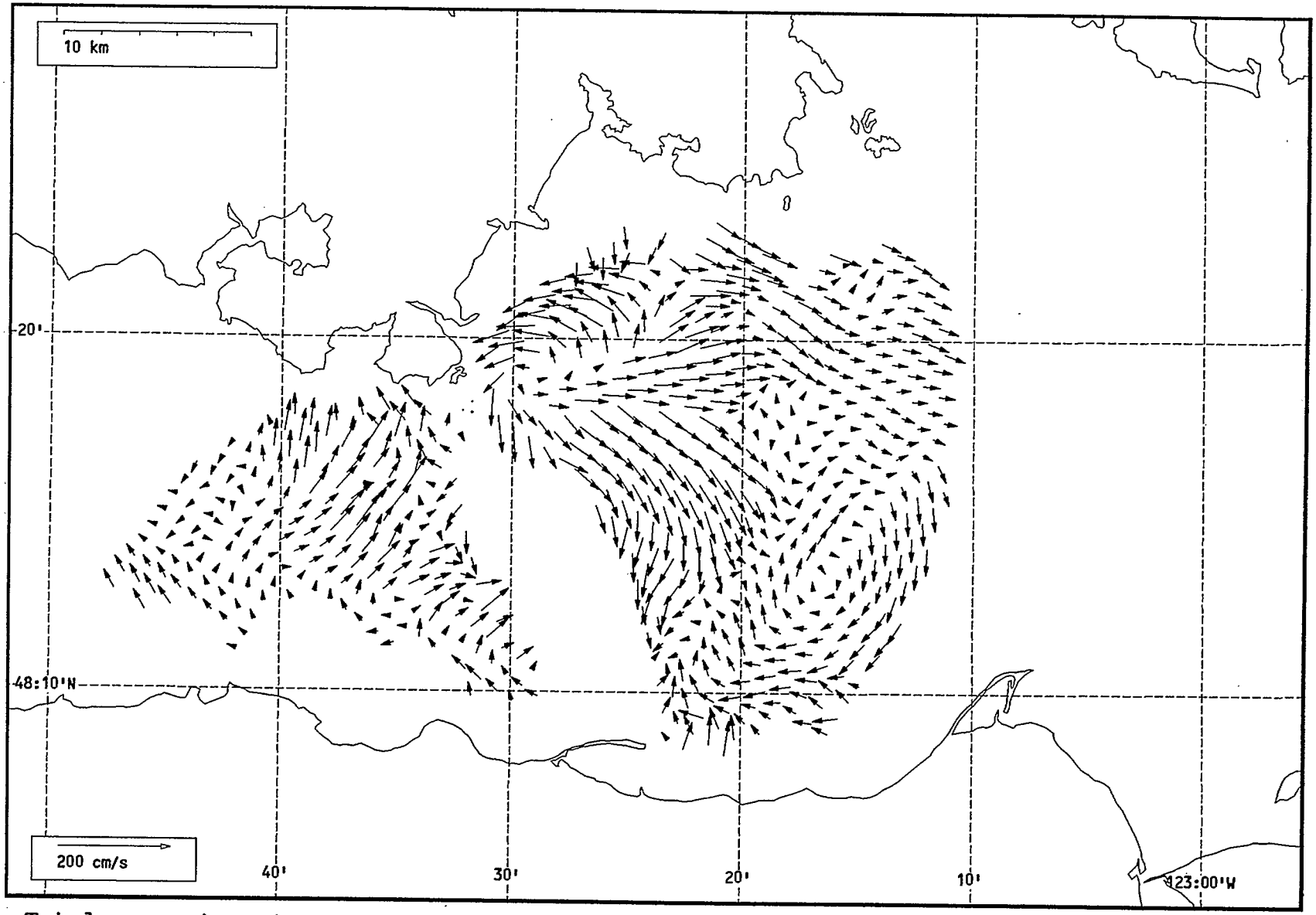

Total current vectors, Juan de Fuca Strait, 1992-07-27 01:00 Z.

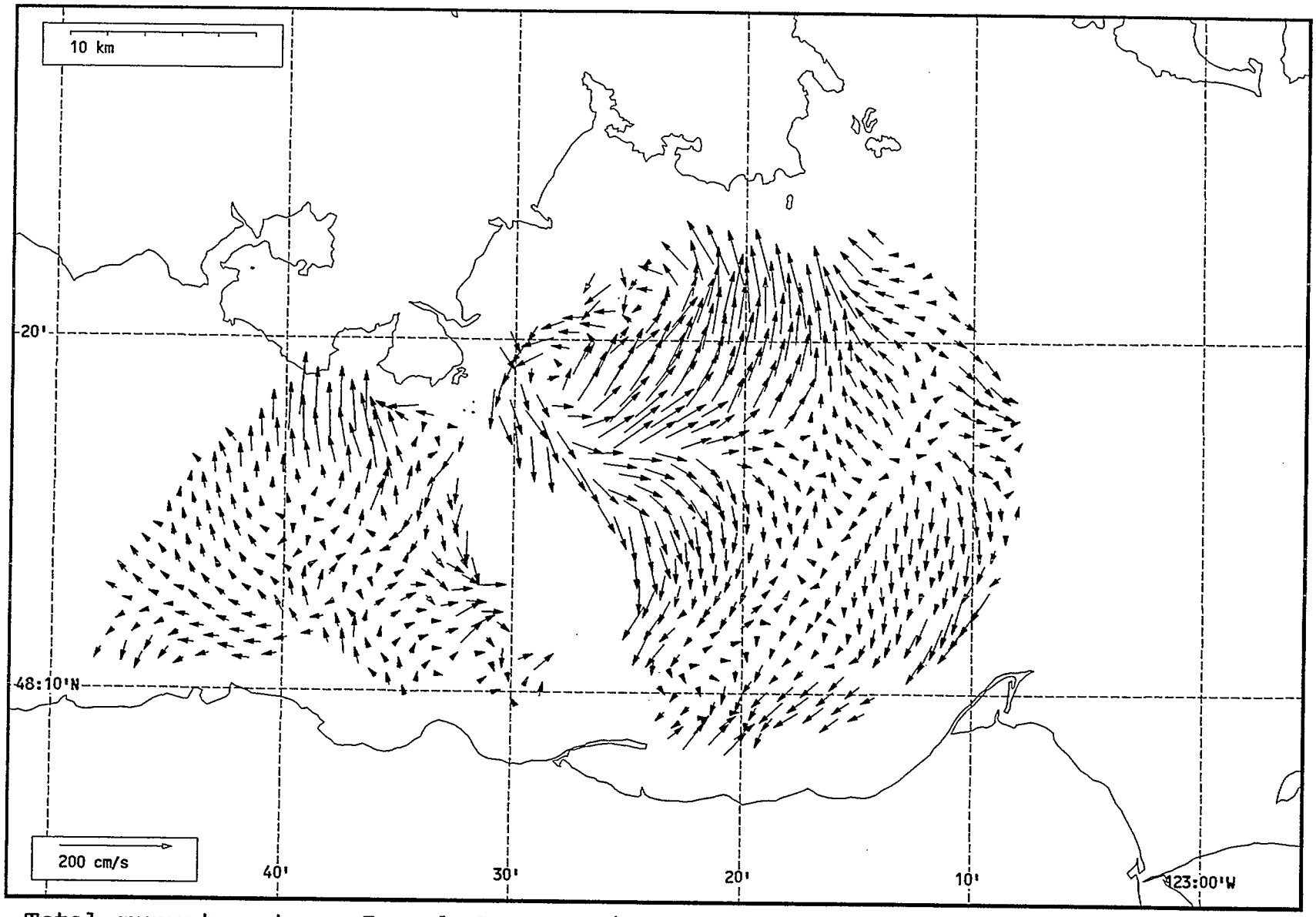

Total current vectors, Juan de Fuca Strait, 1992-07-27 02:00 Z.

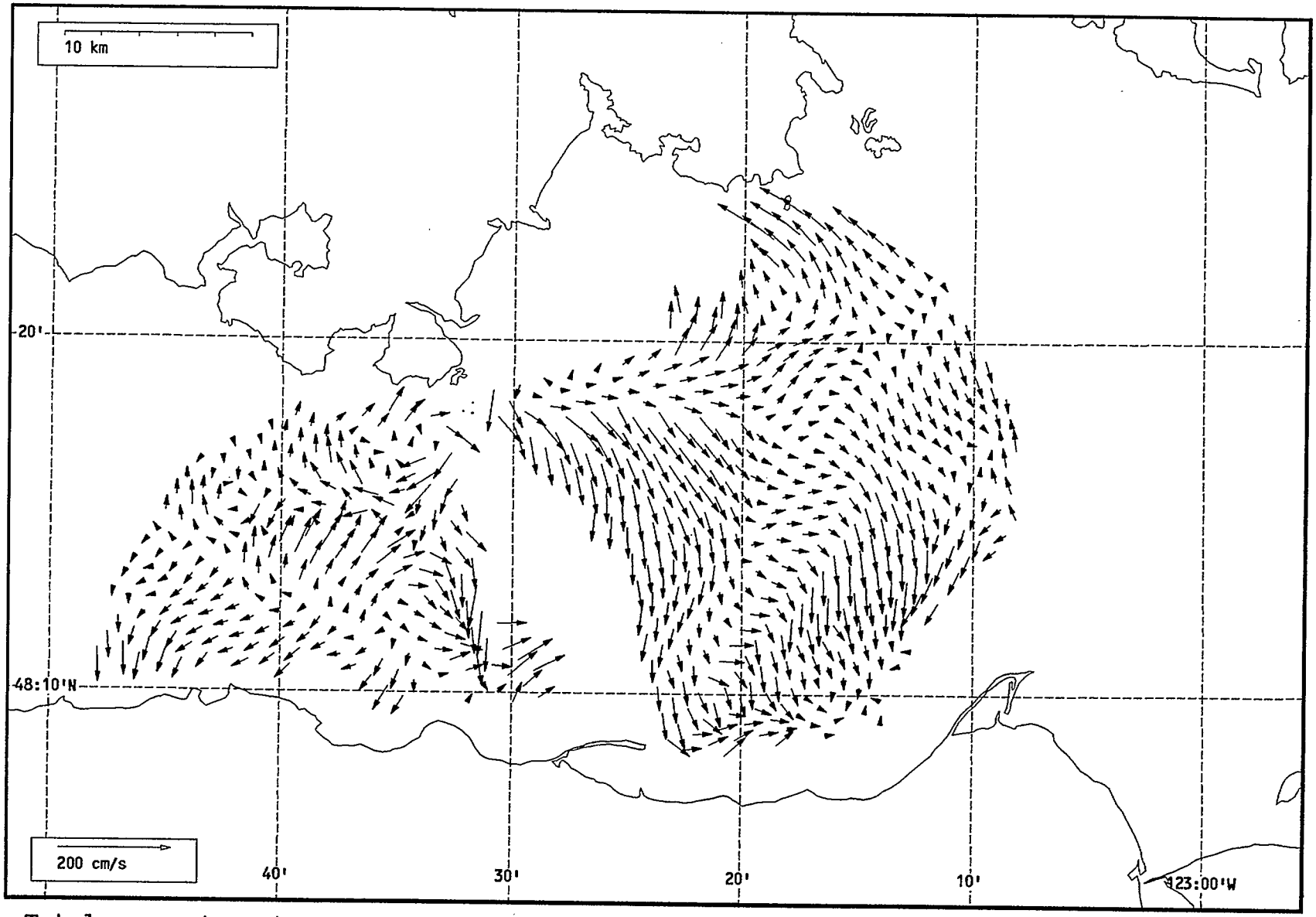

Total current vectors, Juan de Fuca Strait, 1992-07-27 03:00 Z.

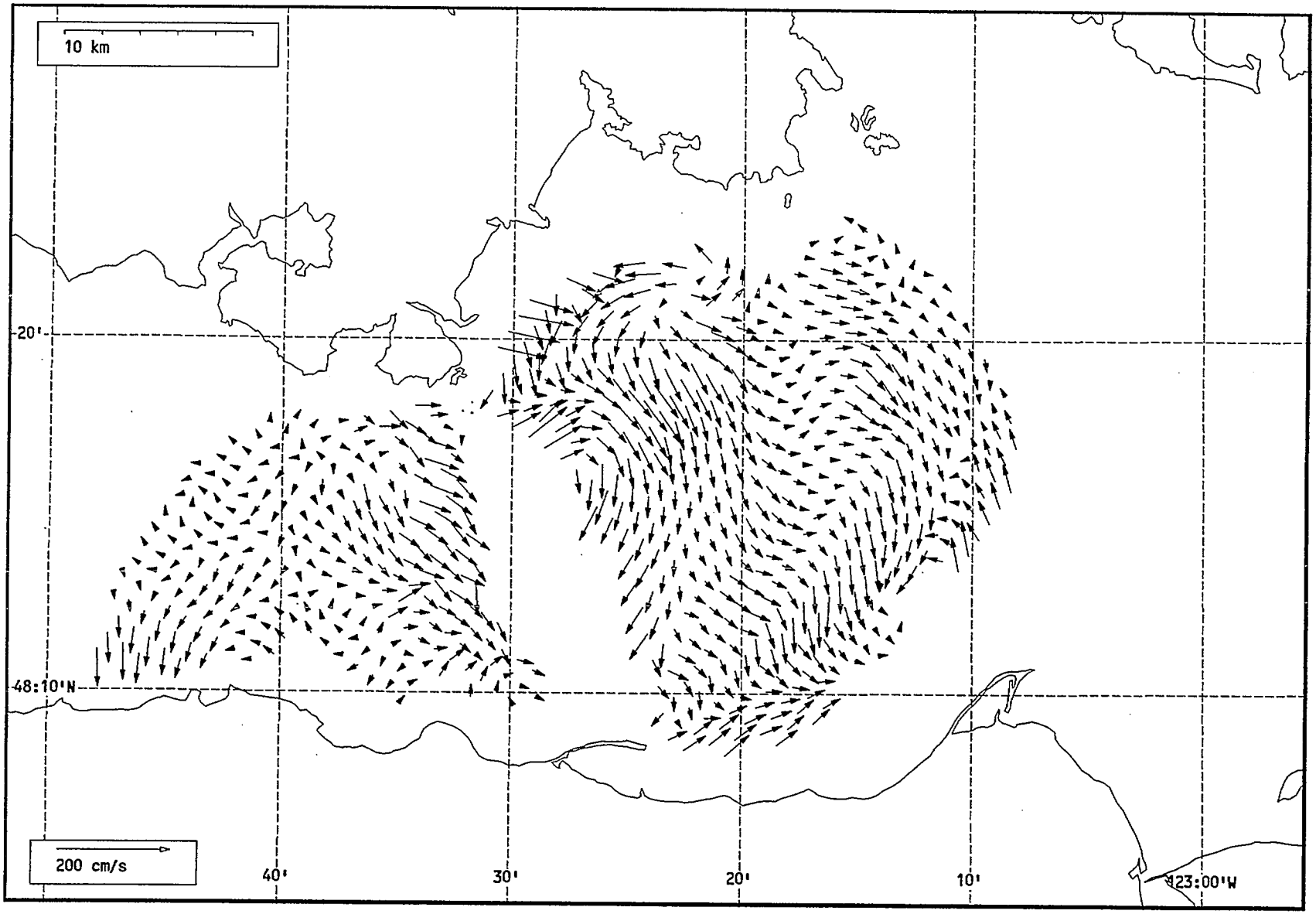

Total current vectors, Juan de Fuca Strait, 1992-07-27 04:00 Z.

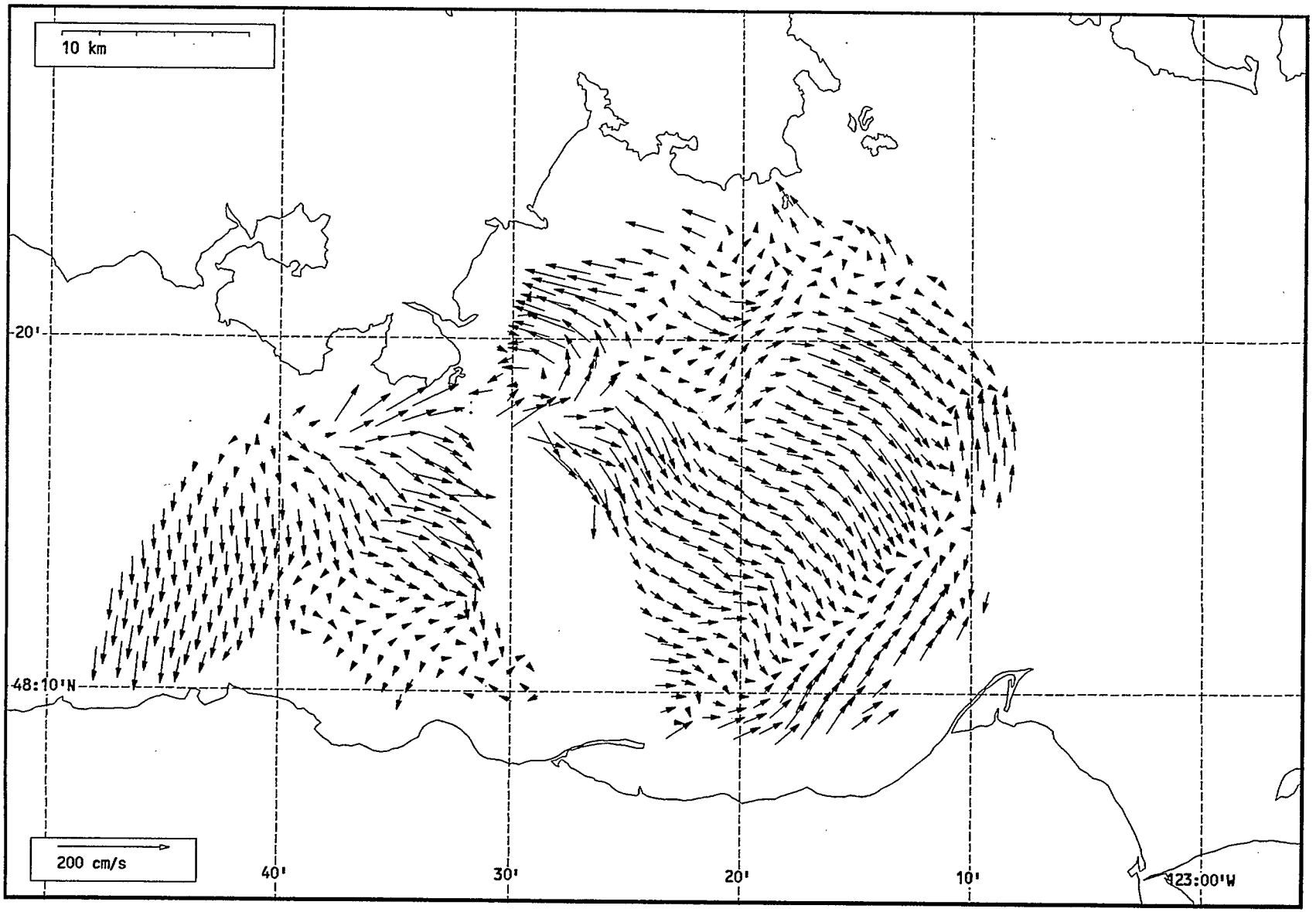

Total current vectors, Juan de Fuca Strait, 1992-07-27 05:00 Z.

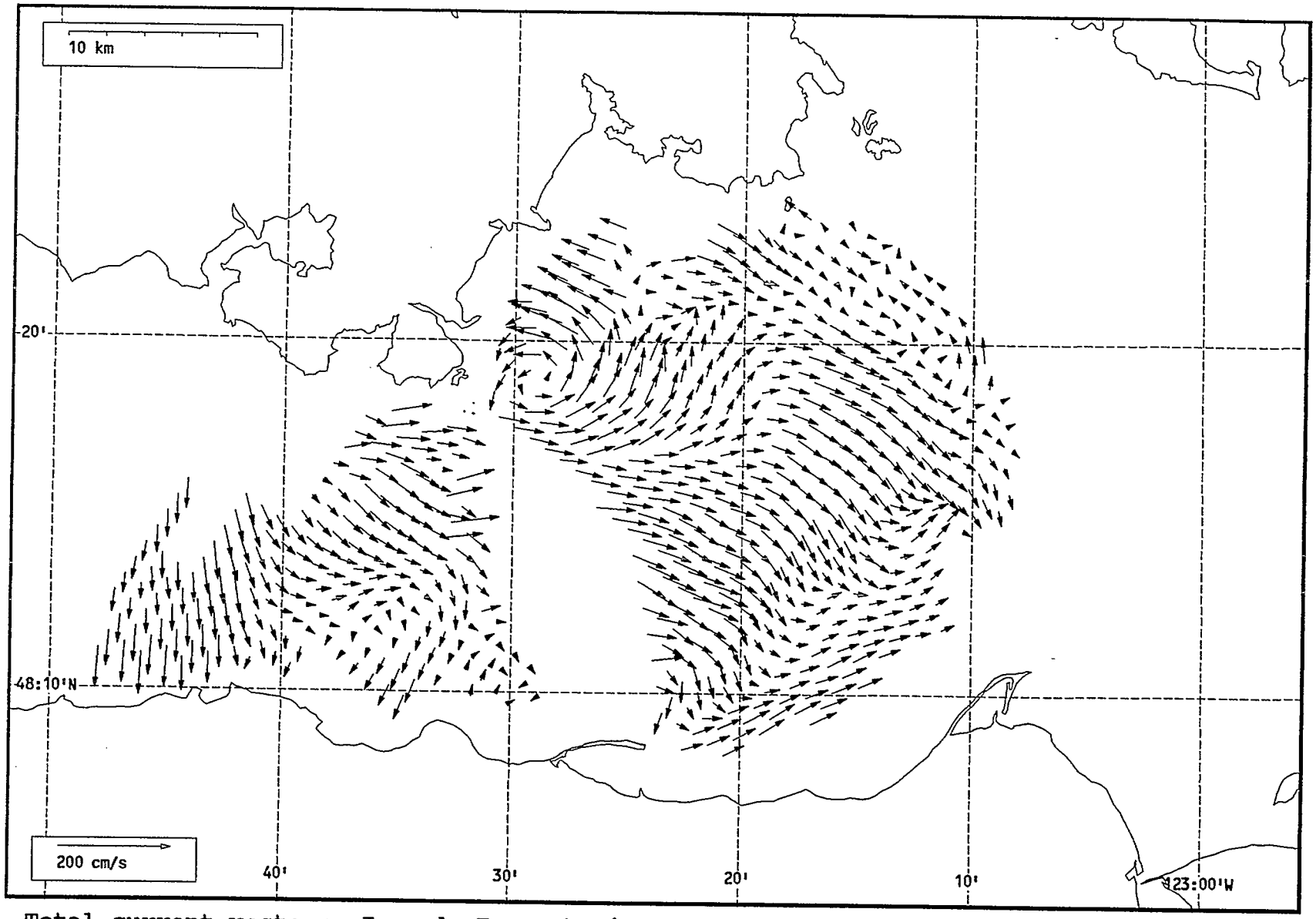

Total current vectors, Juan de Fuca Strait, 1992-07-27 06:00 Z.

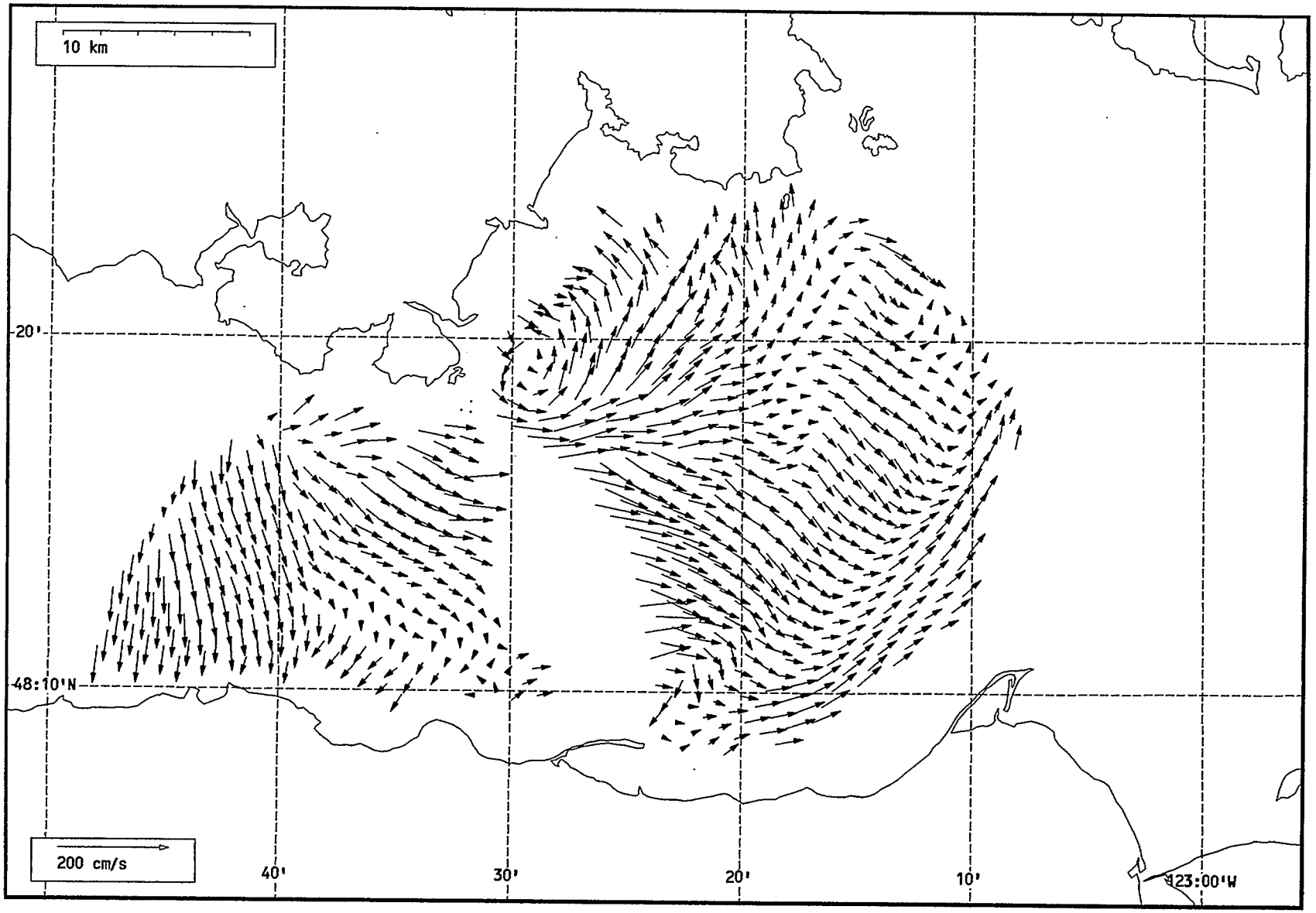

Total current vectors, Juan de Fuca Strait, 1992-07-27 07:00 Z.

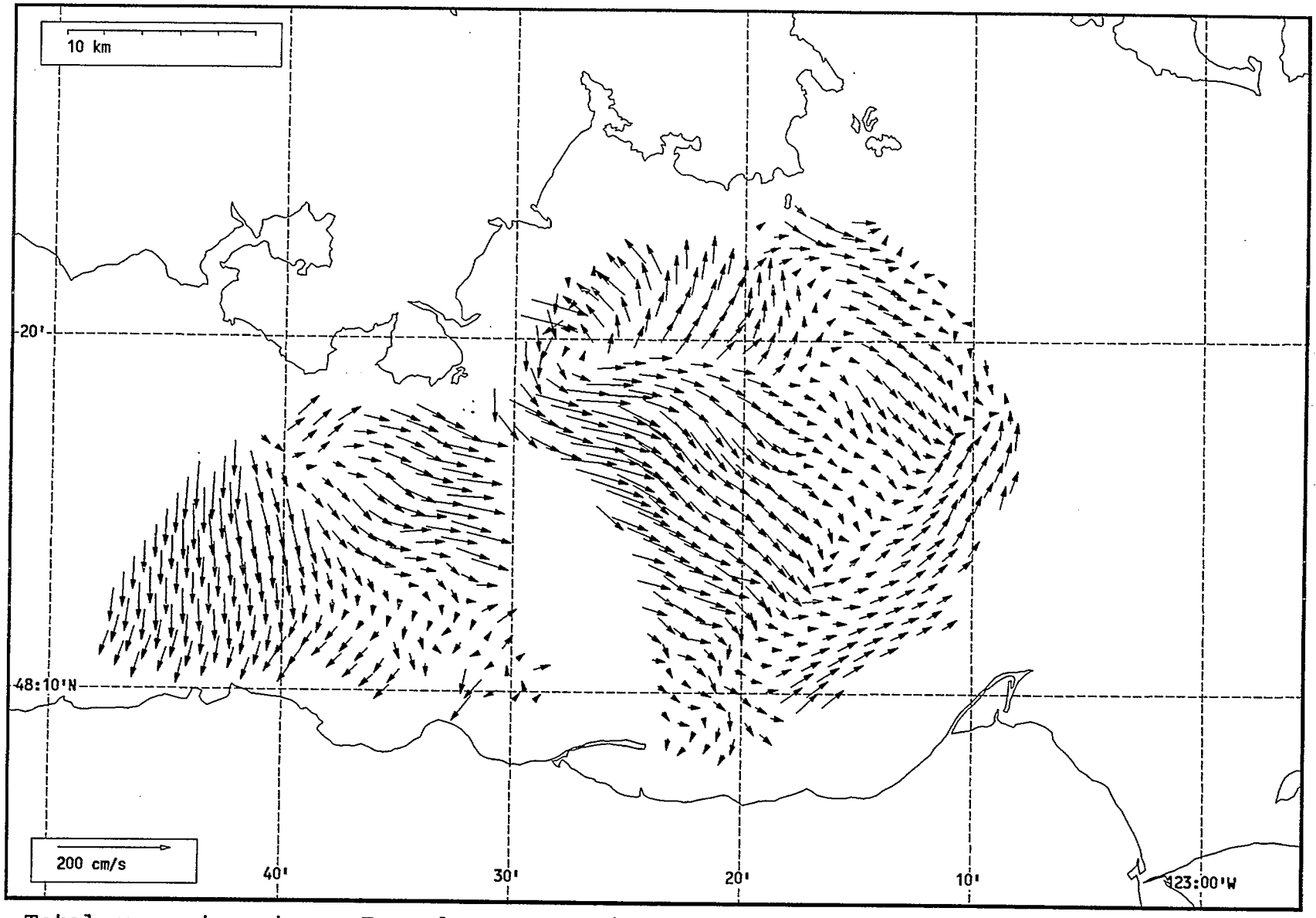

Total current vectors, Juan de Fuca Strait, 1992-07-27 08:00 Z.

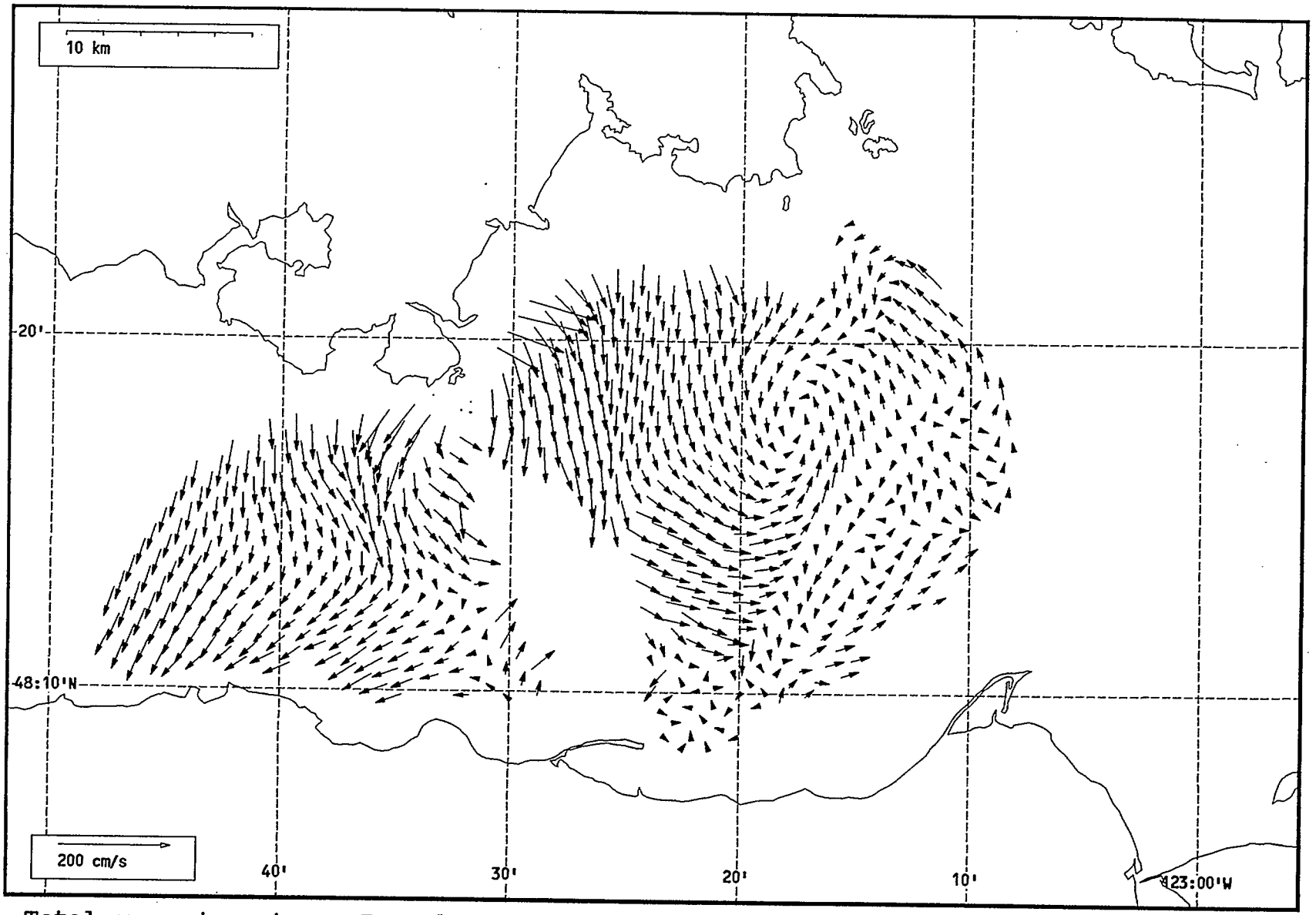

Total current vectors, Juan de Fuca Strait, 1992-07-27 09:00 Z.

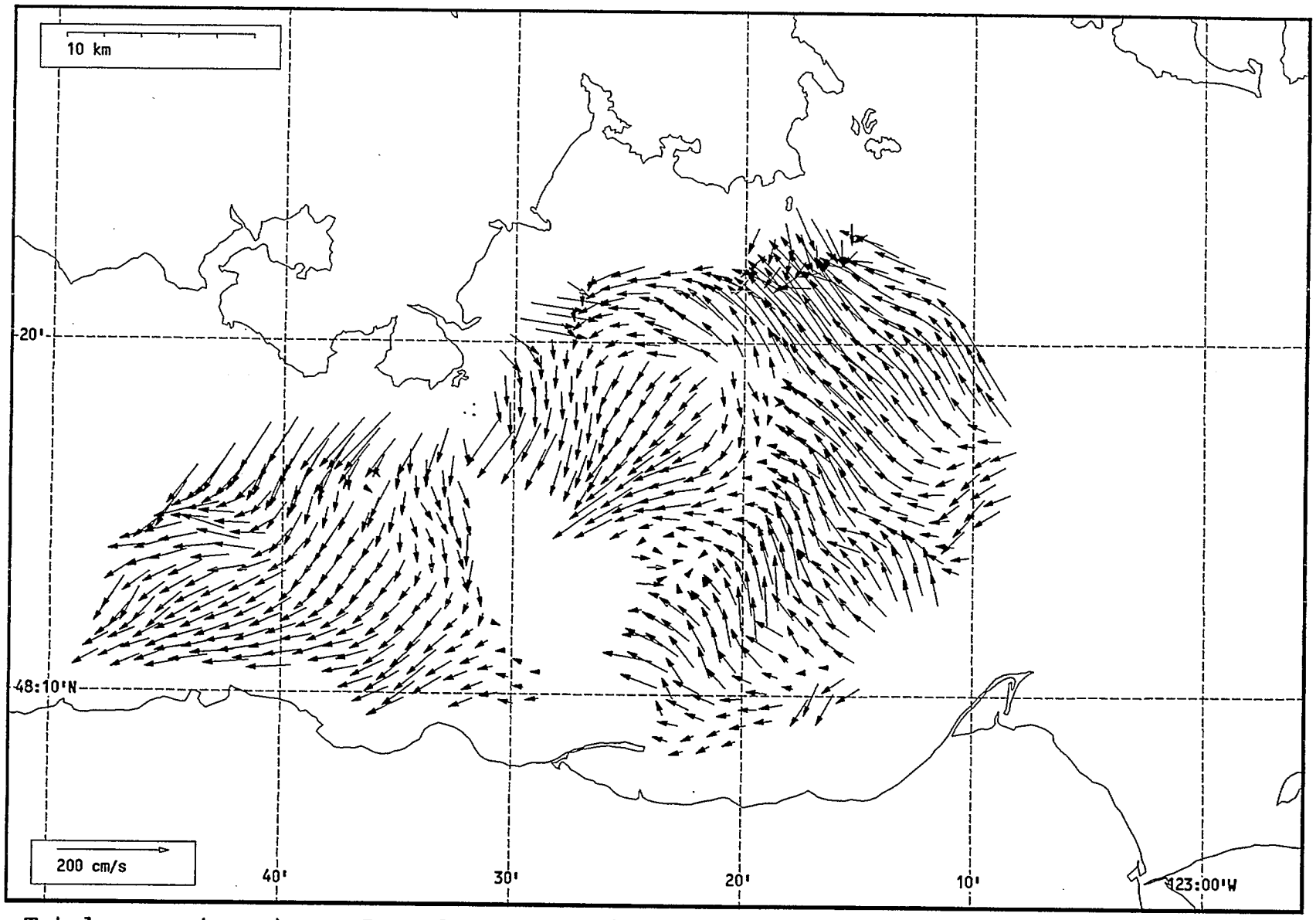

Total current vectors, Juan de Fuca Strait, 1992-07-27 10:00 Z.

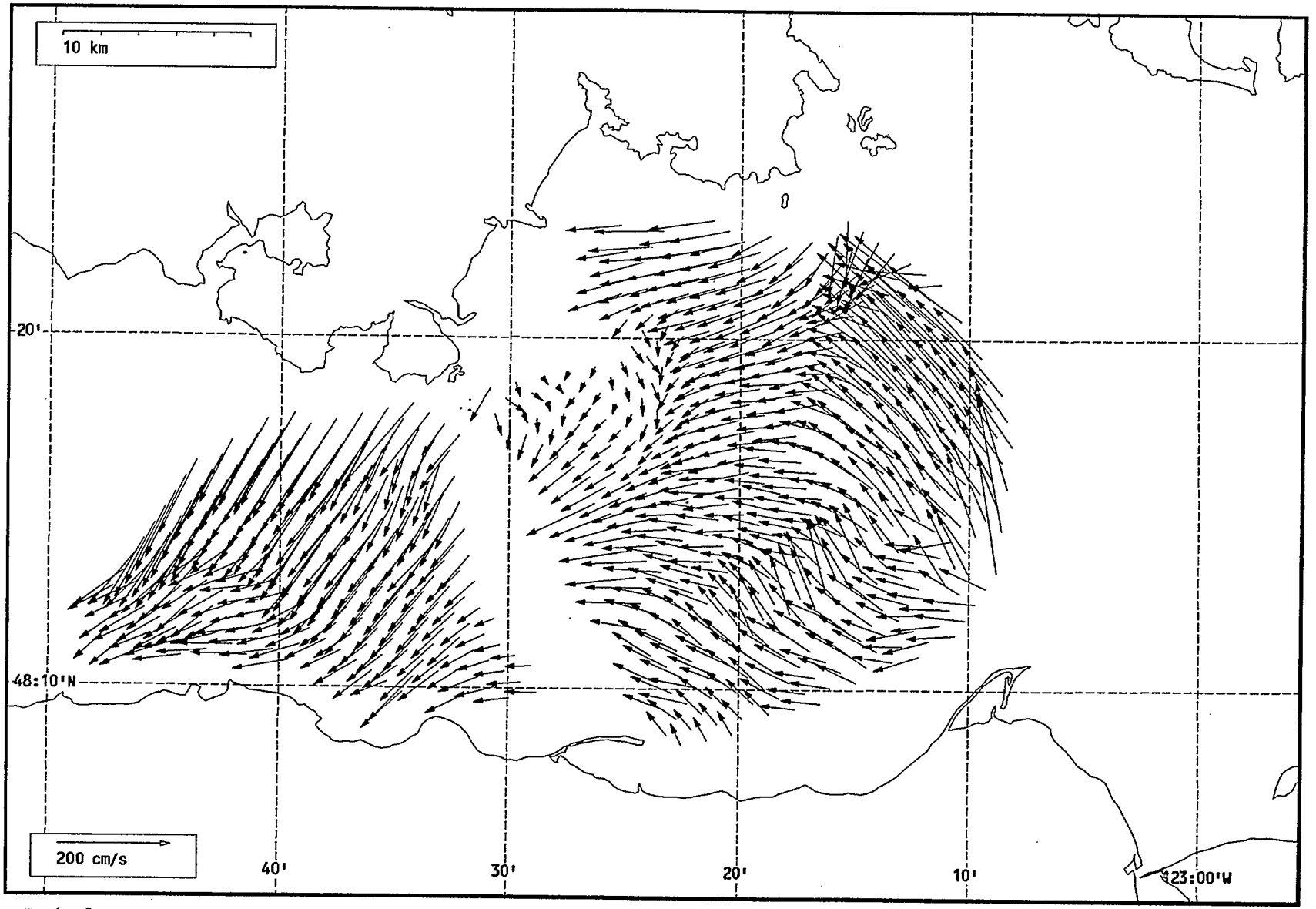

Total current vectors, Juan de Fuca Strait, 1992-07-27 11:00 Z.

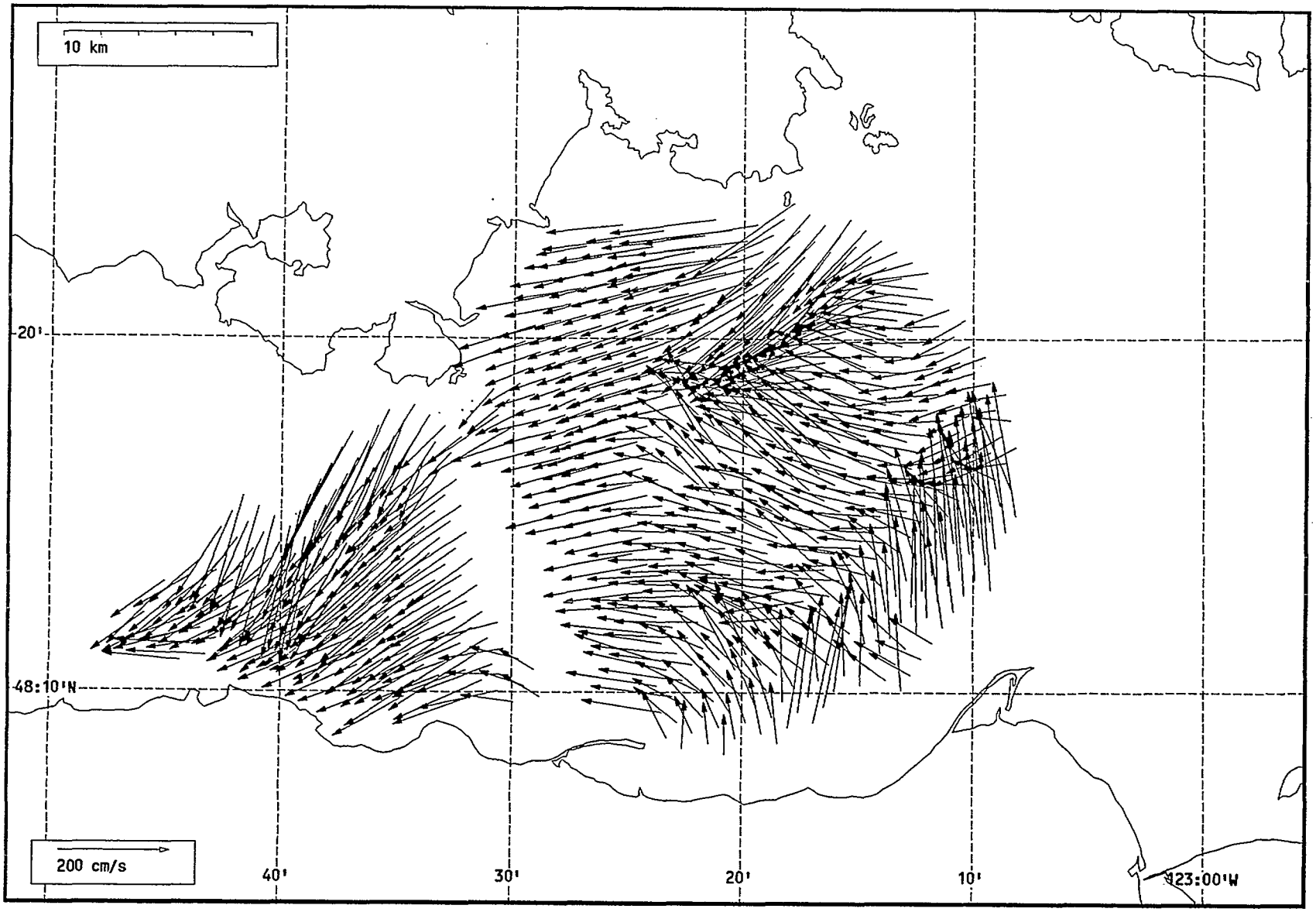

Total current vectors, Juan de Fuca Strait, 1992-07-27 12:00 Z.

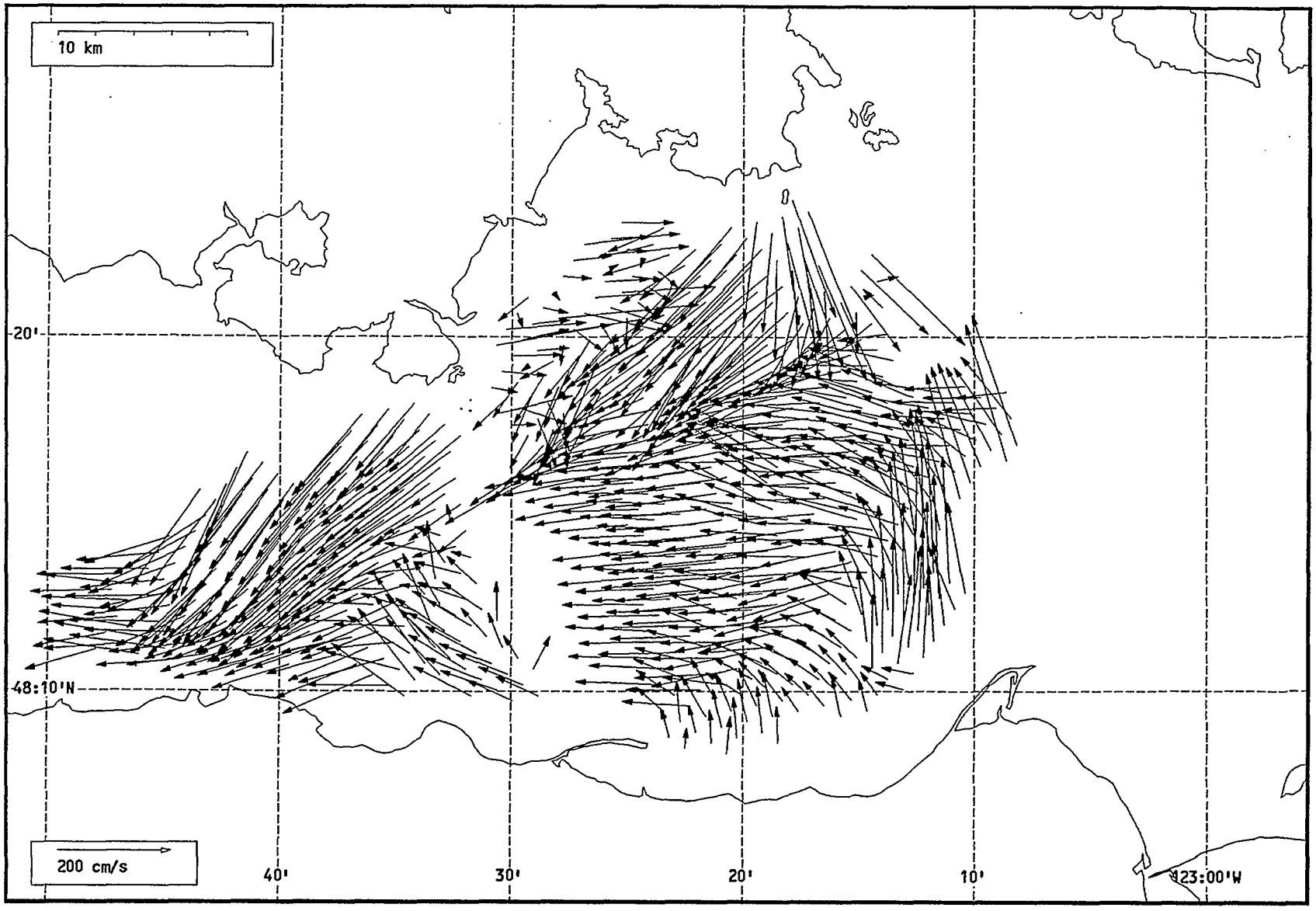

Total current vectors, Juan de Fuca Strait, 1992-07-27 13:00 Z.

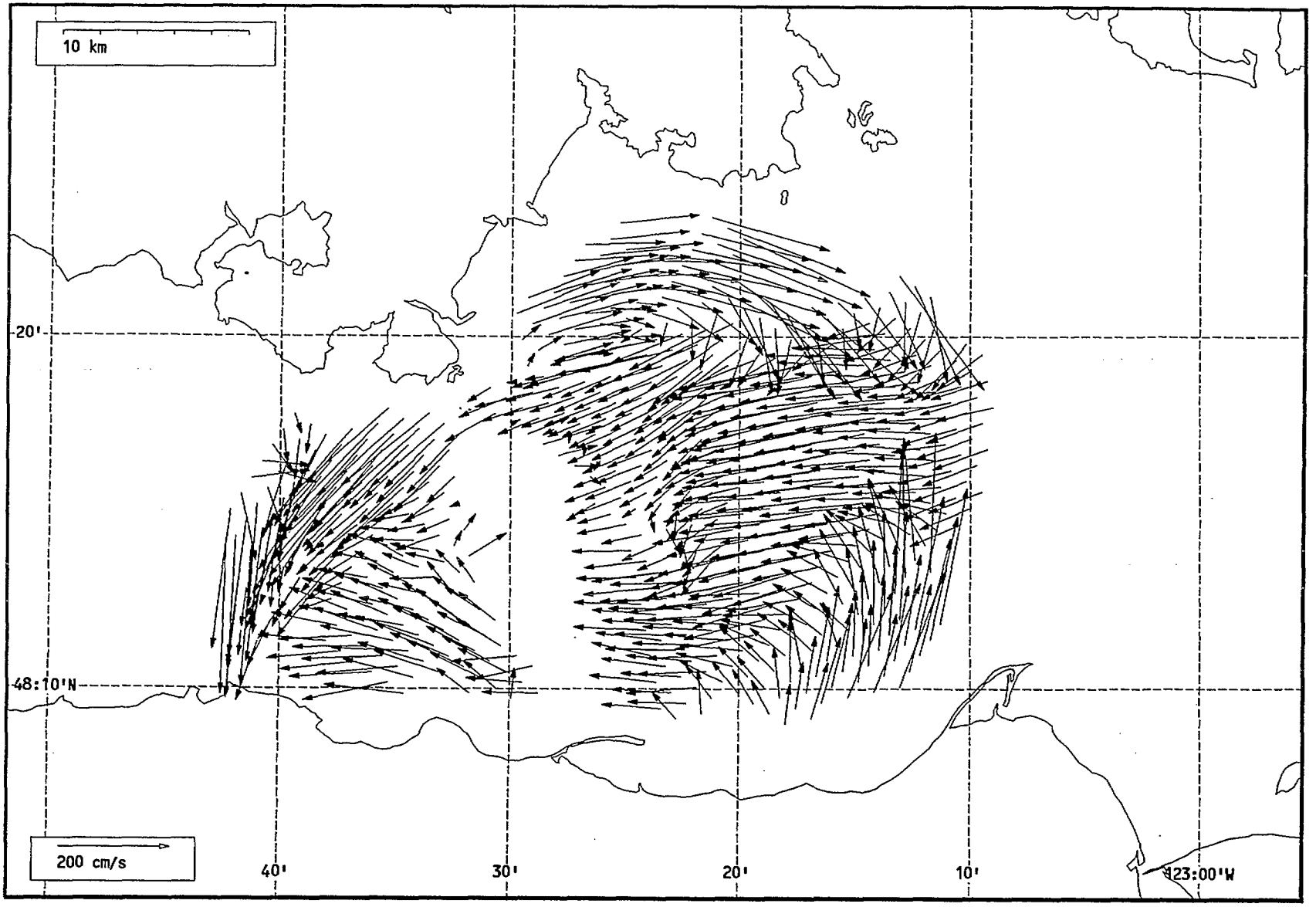

Total current vectors, Juan de Fuca Strait, 1992-07-27 14:00 Z.

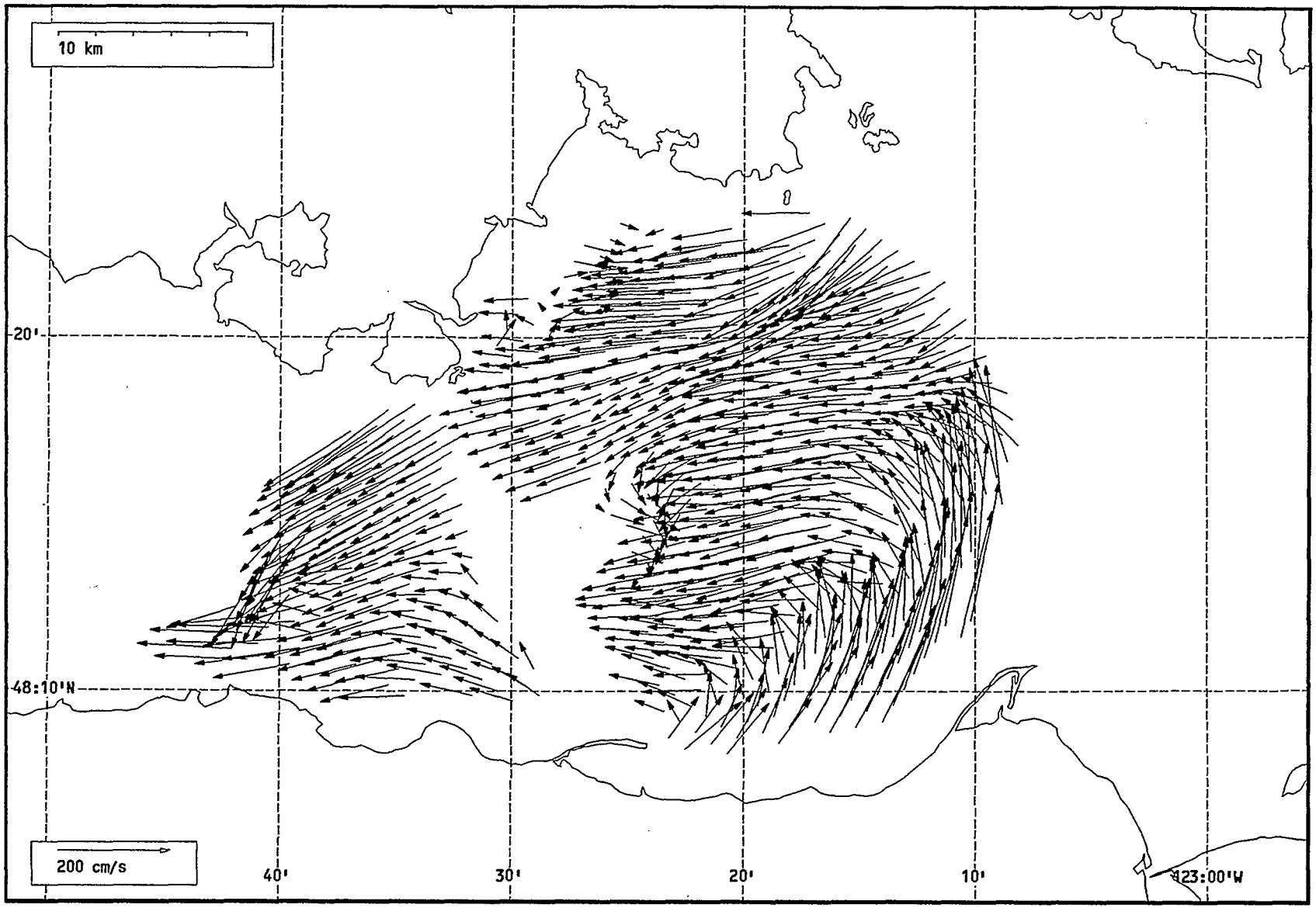

Total current vectors, Juan de Fuca Strait, 1992-07-27 15:00 Z.

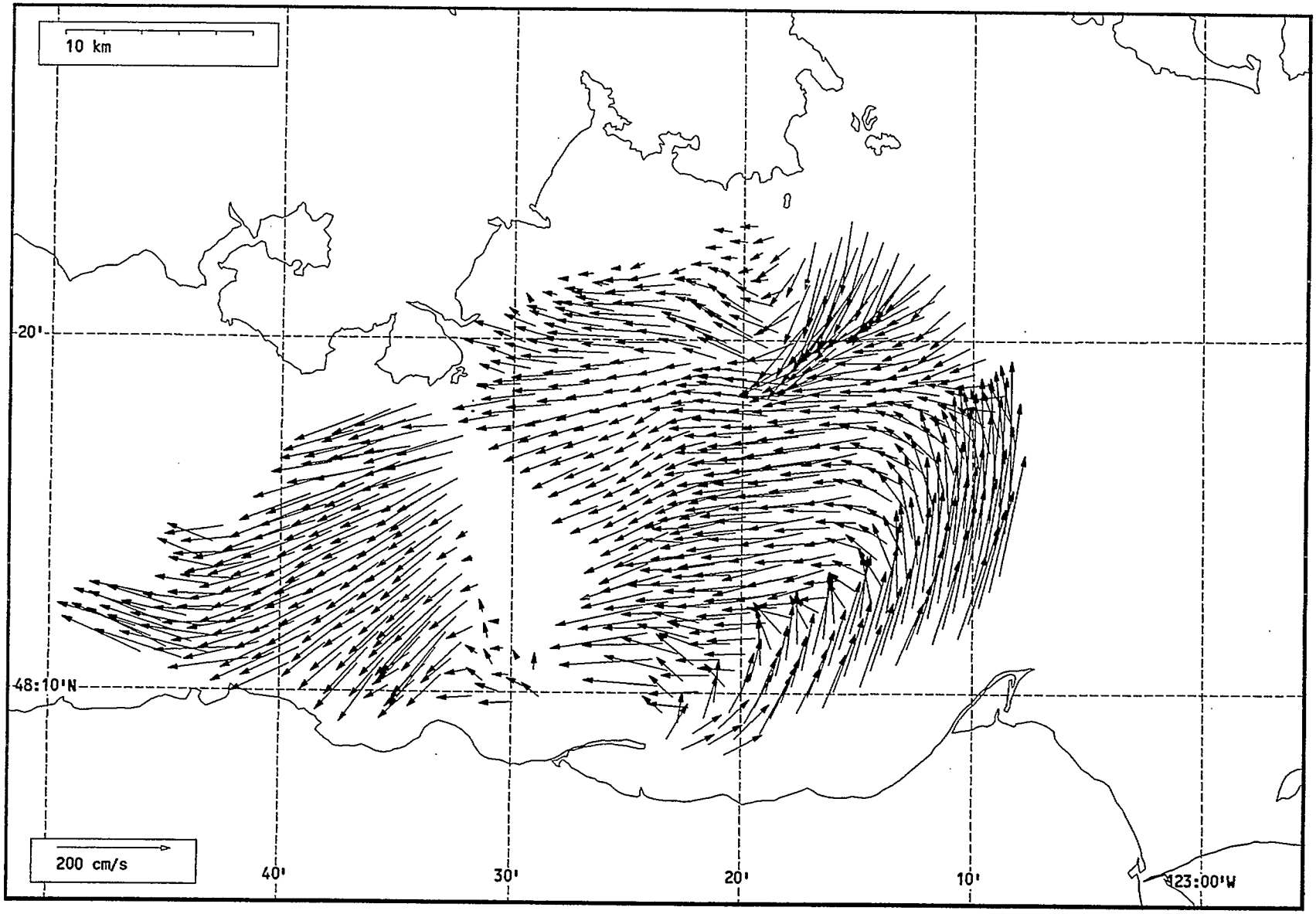

Total current vectors, Juan de Fuca Strait, 1992-07-27 16:00 Z.

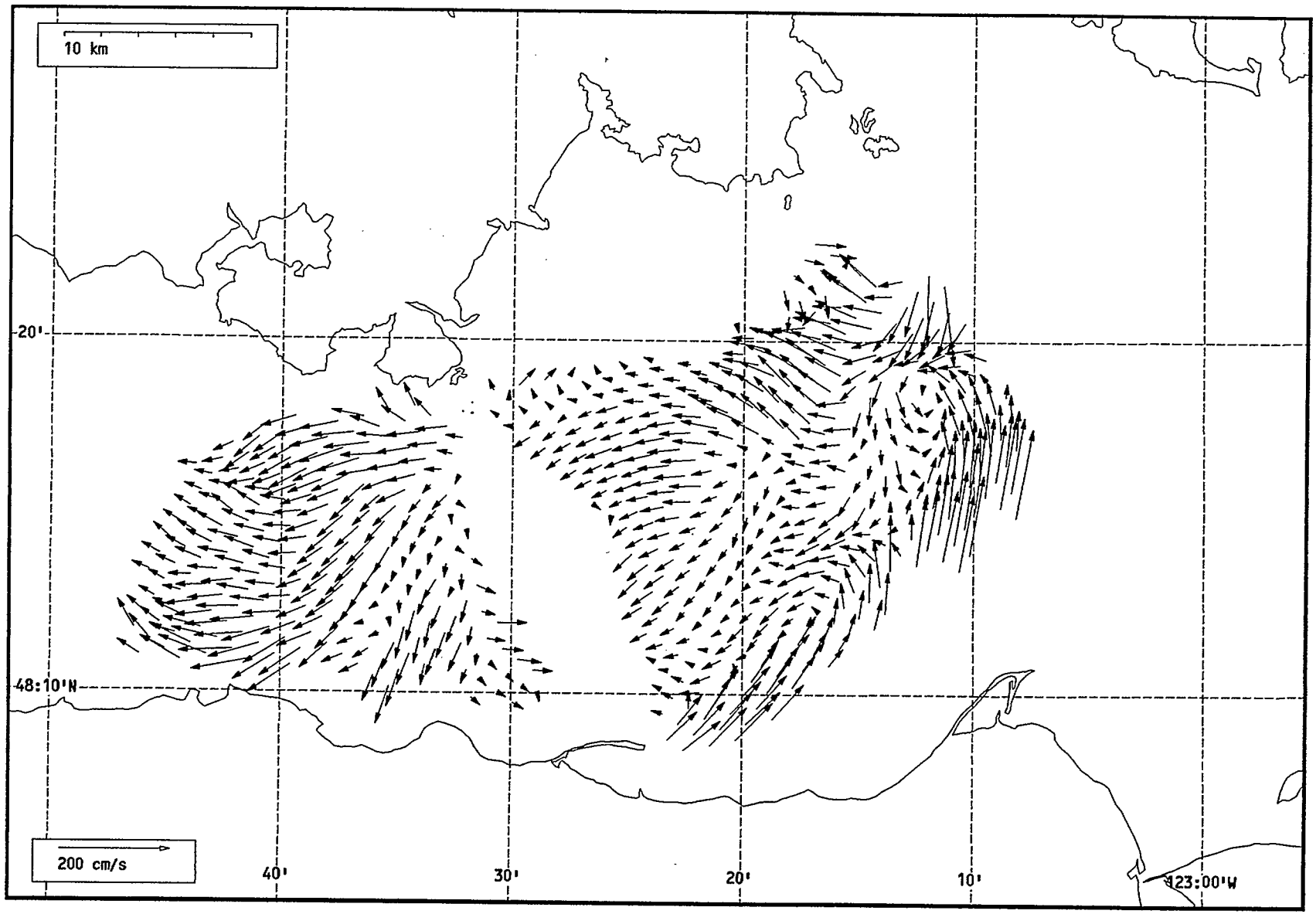

Total current vectors, Juan de Fuca Strait, 1992-07-27 17:00 Z.

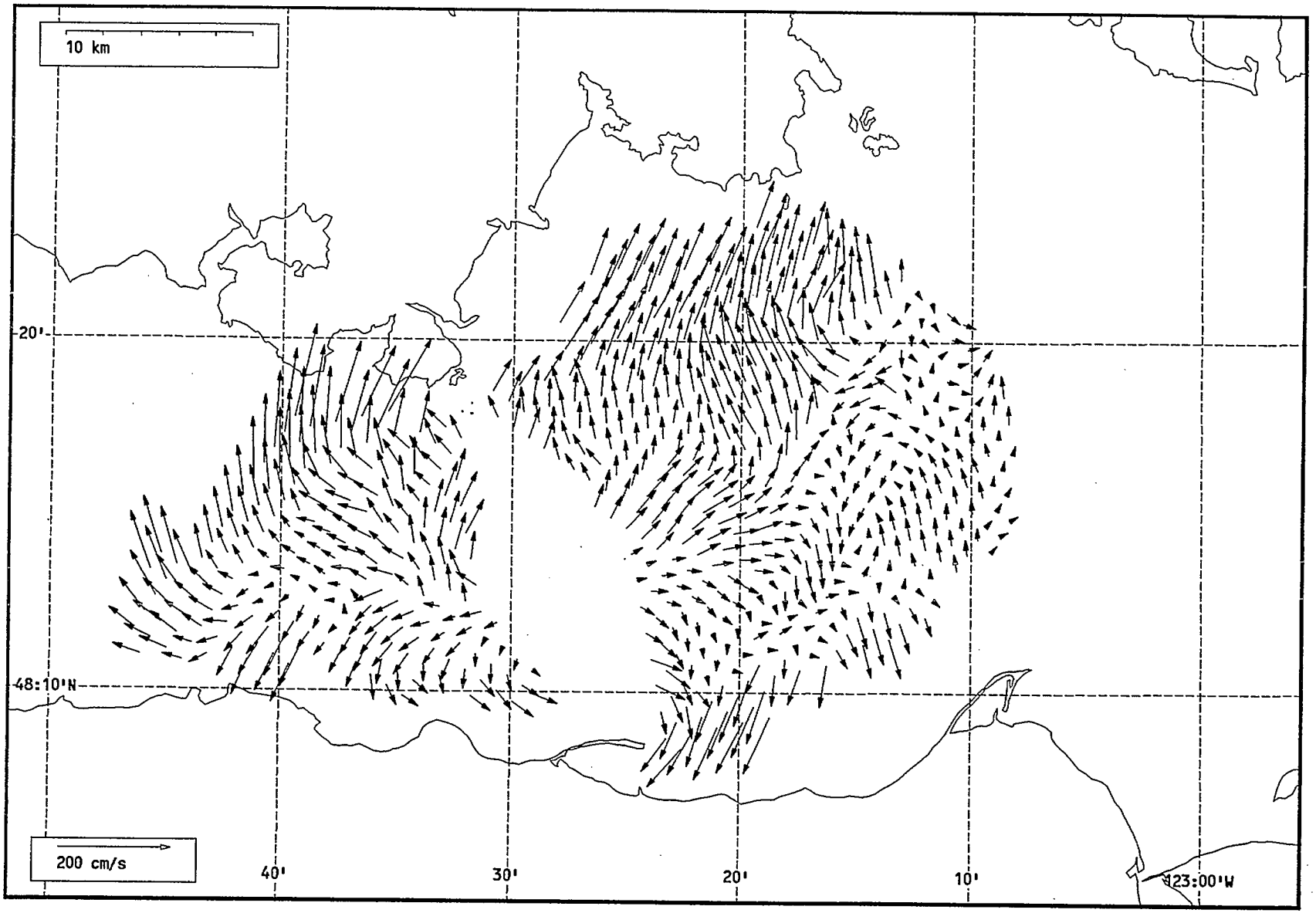

Total current vectors, Juan de Fuca Strait, 1992-07-27 18:00 Z.

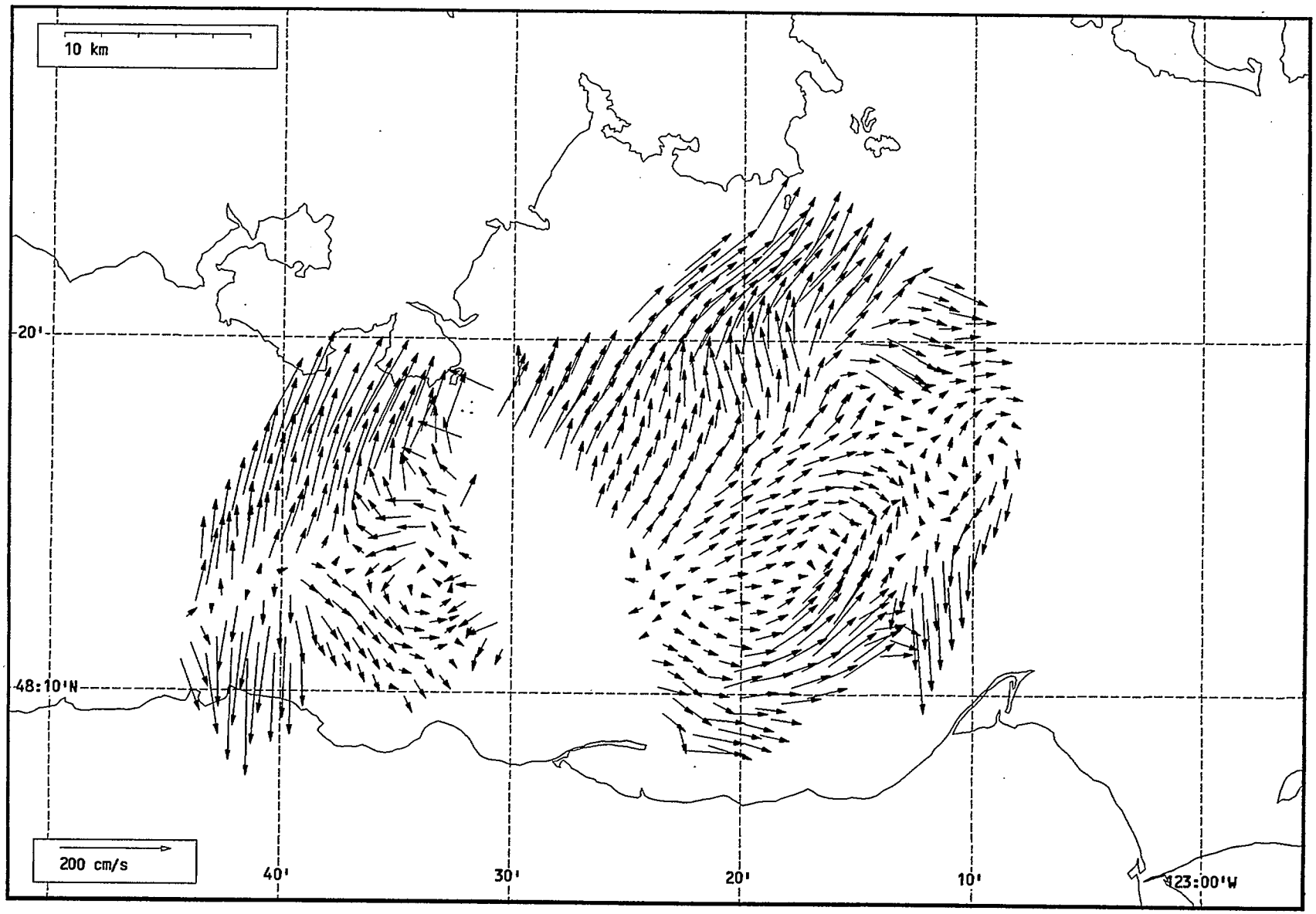

Total current vectors, Juan de Fuca Strait, 1992-07-27 19:00 Z.

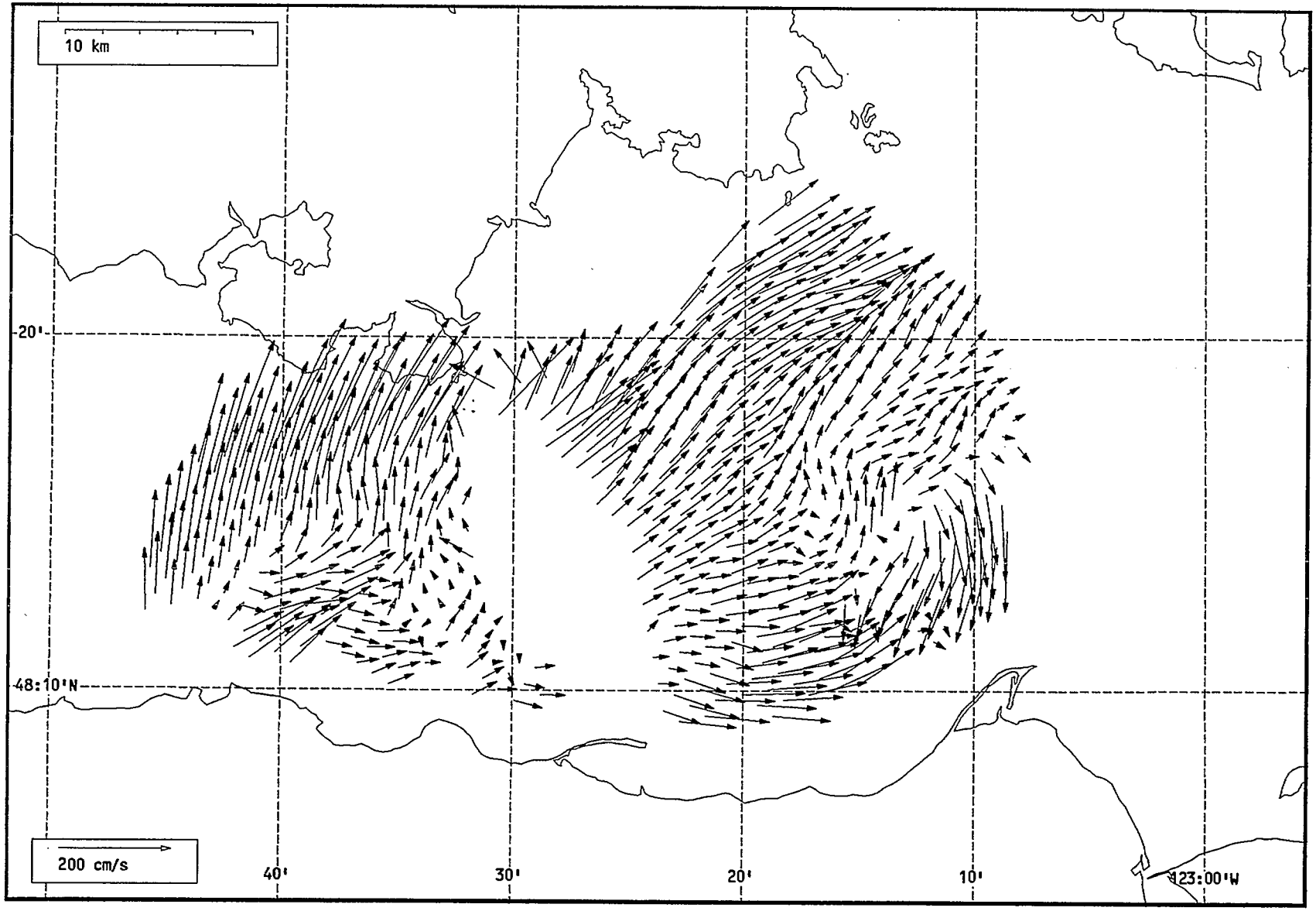

Total current vectors, Juan de Fuca Strait, 1992-07-27 20:00 Z.

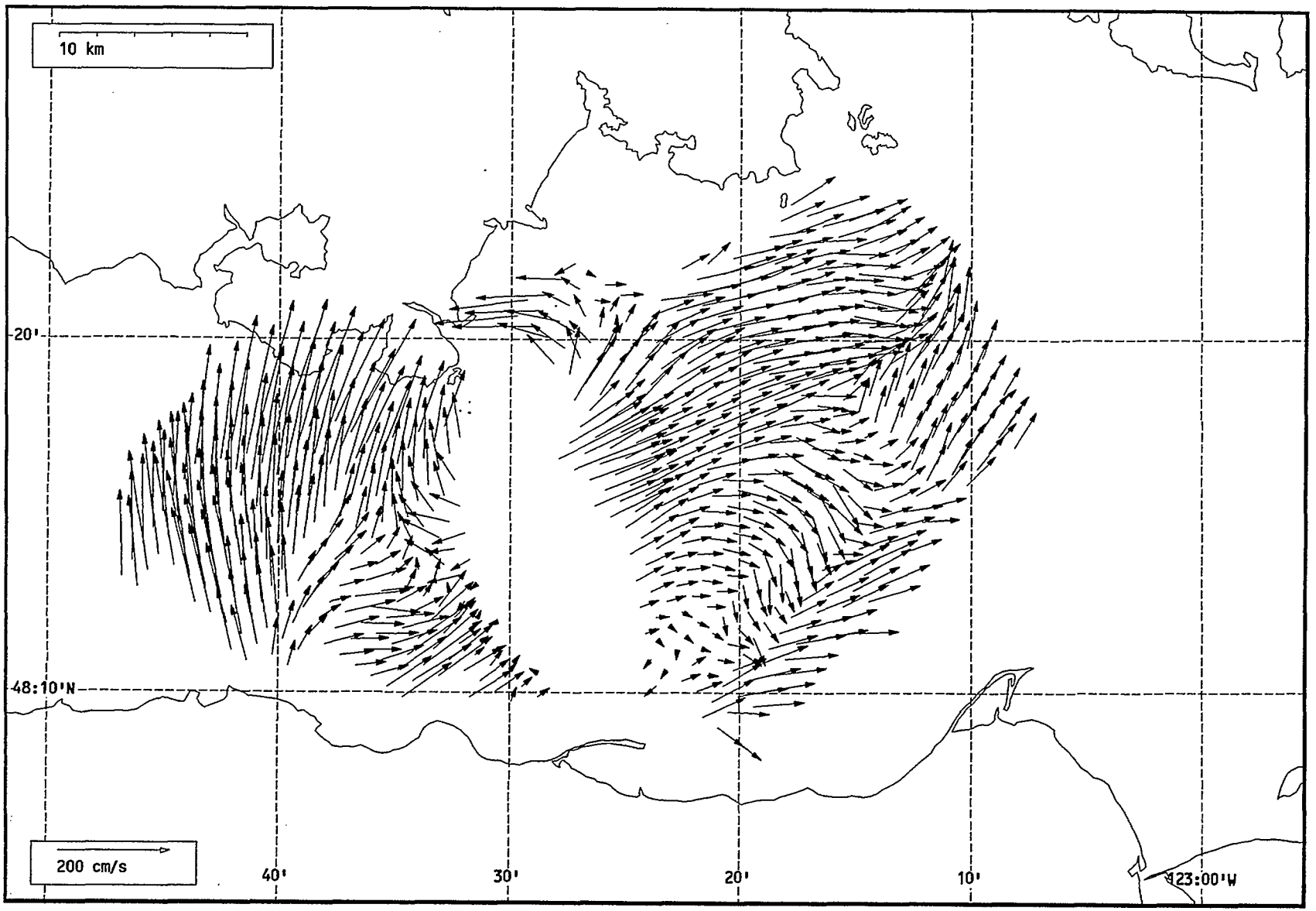

Total current vectors, Juan de Fuca Strait, 1992-07-27 21:00 Z.

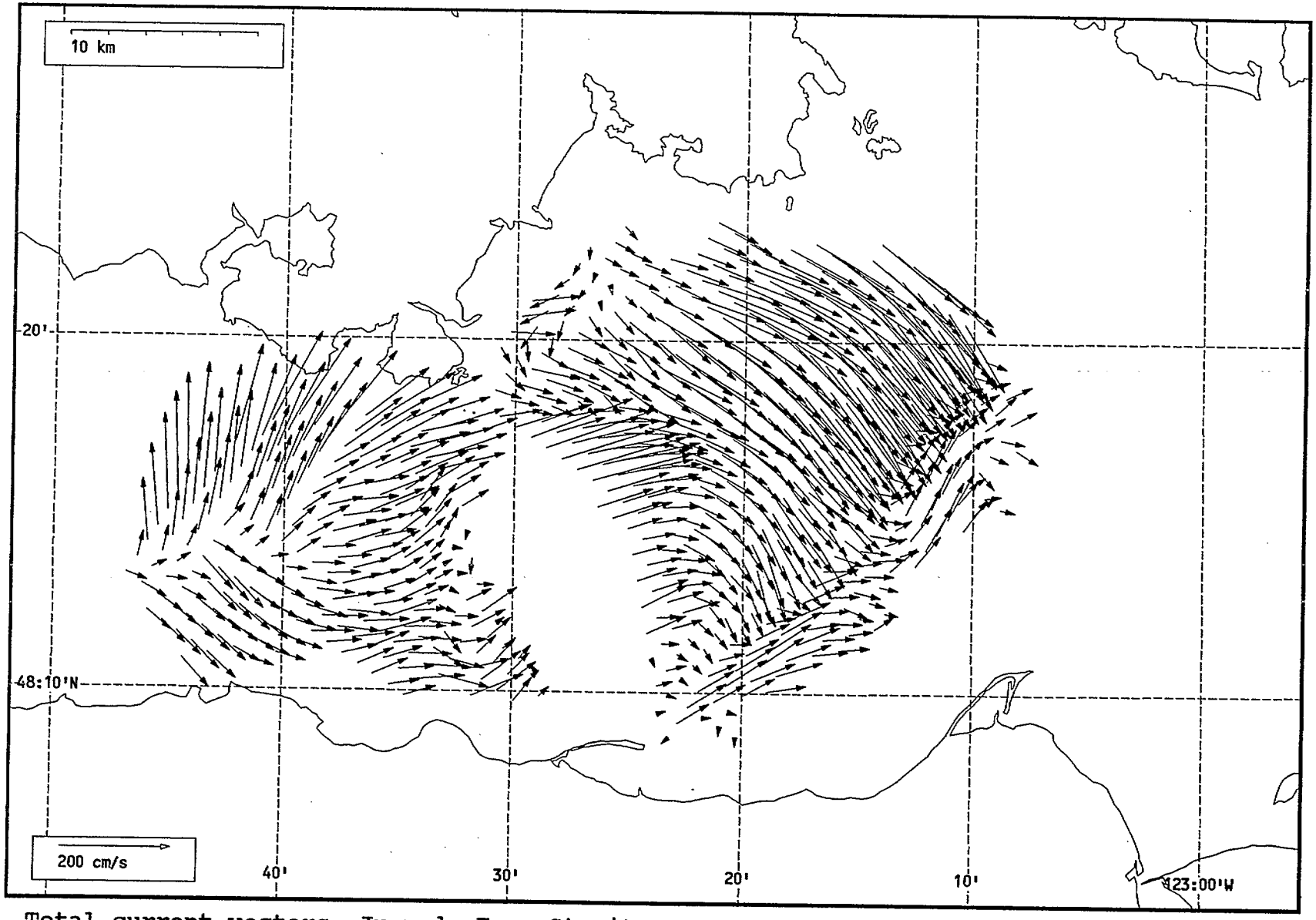

Total current vectors, Juan de Fuca Strait, 1992-07-27 22:00 Z.

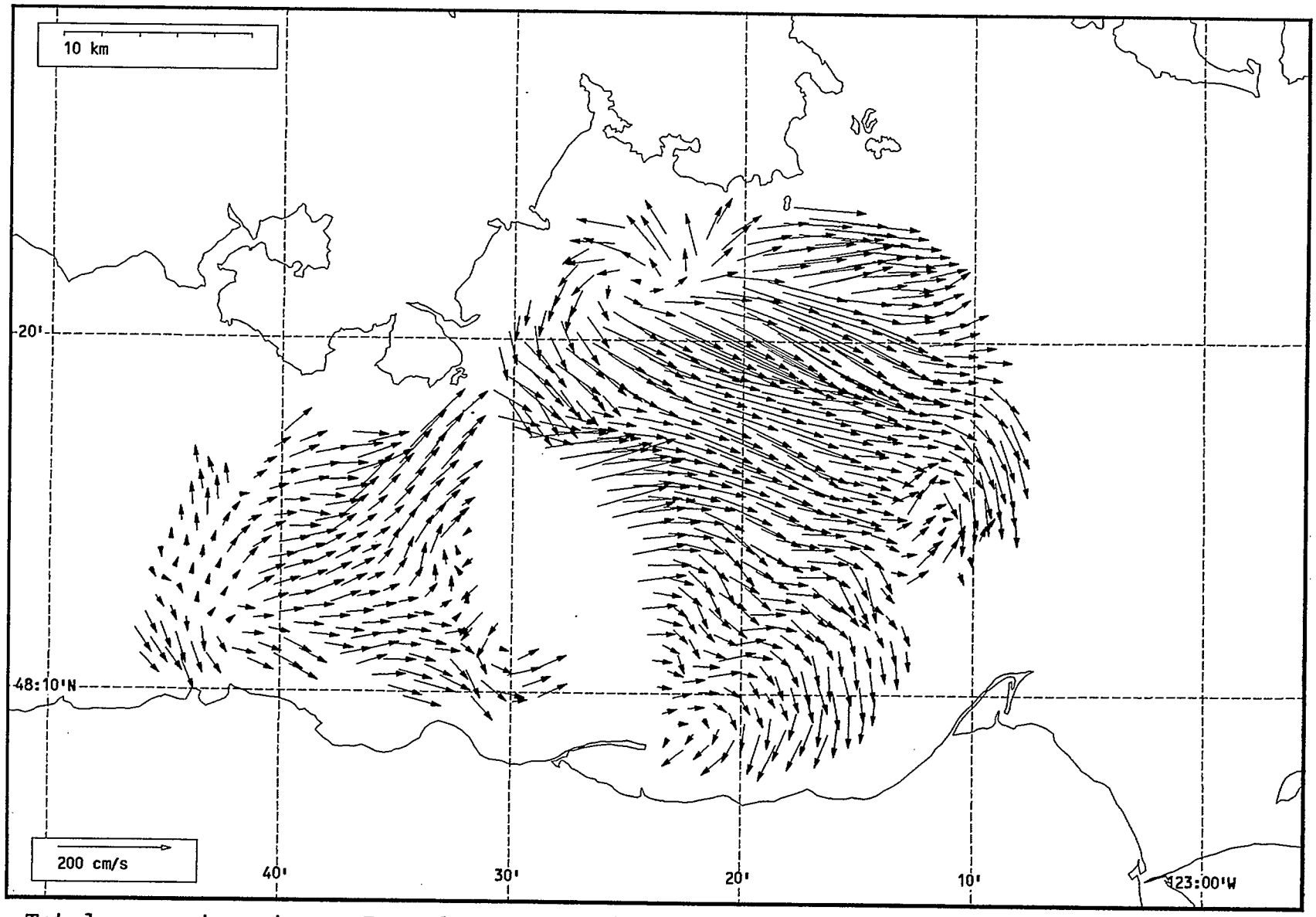

Total current vectors, Juan de Fuca Strait, 1992-07-27 23:00 Z.

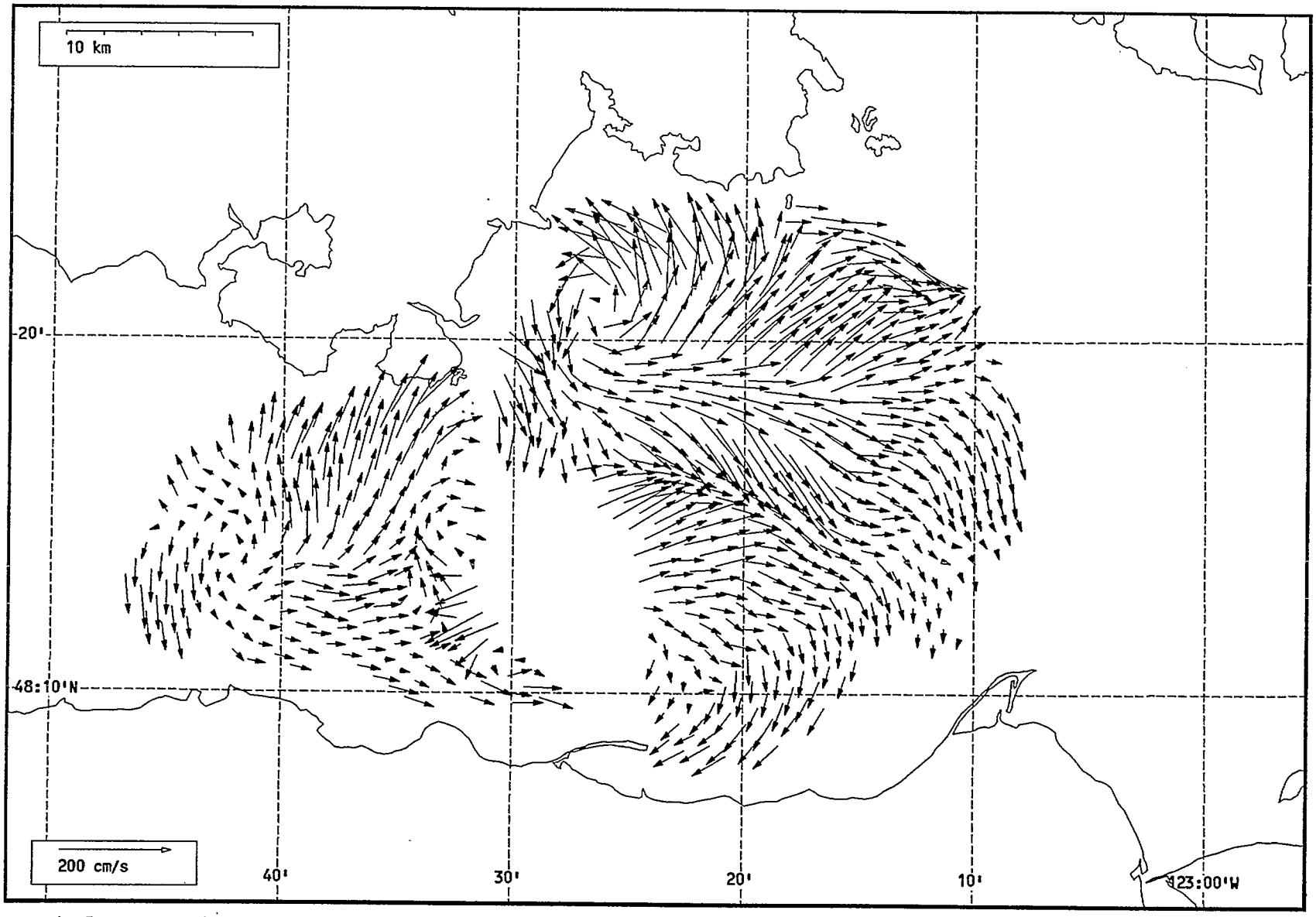

Total current vectors, Juan de Fuca Strait, 1992-07-28 00:00 Z.

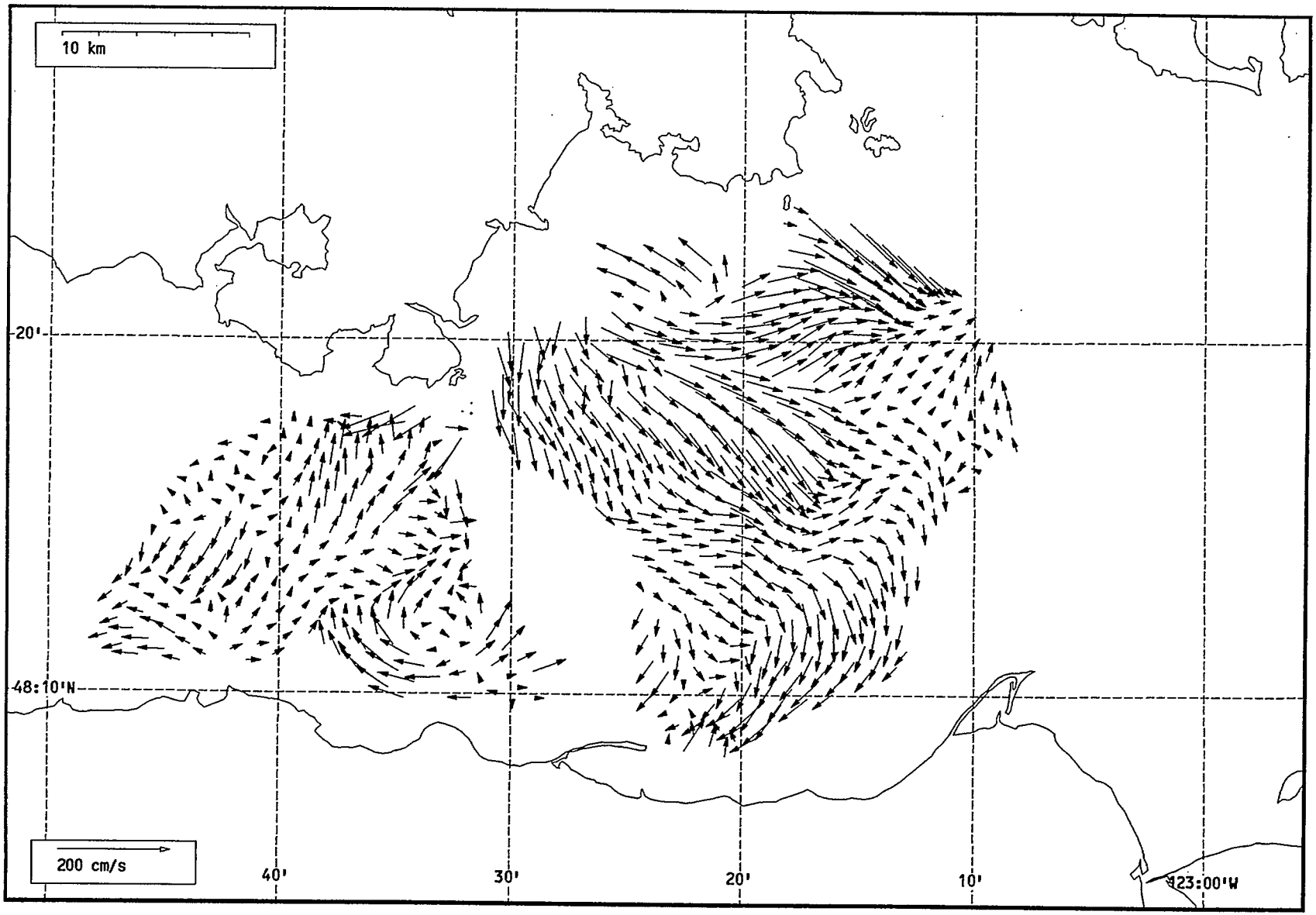

Total current vectors, Juan de Fuca Strait, 1992-07-28 01:00 Z.

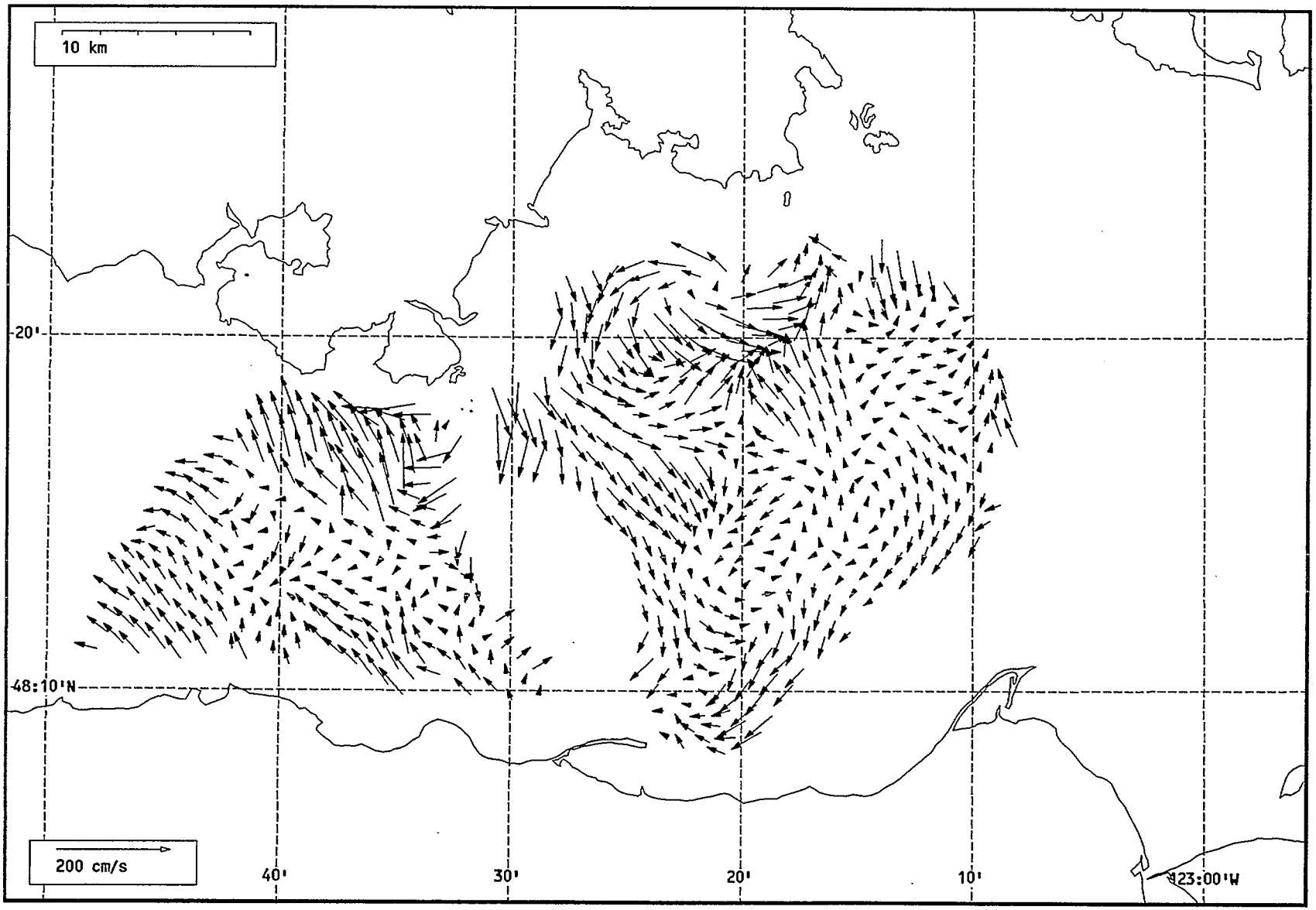

Total current vectors, Juan de Fuca Strait, 1992-07-28 02:00 Z.

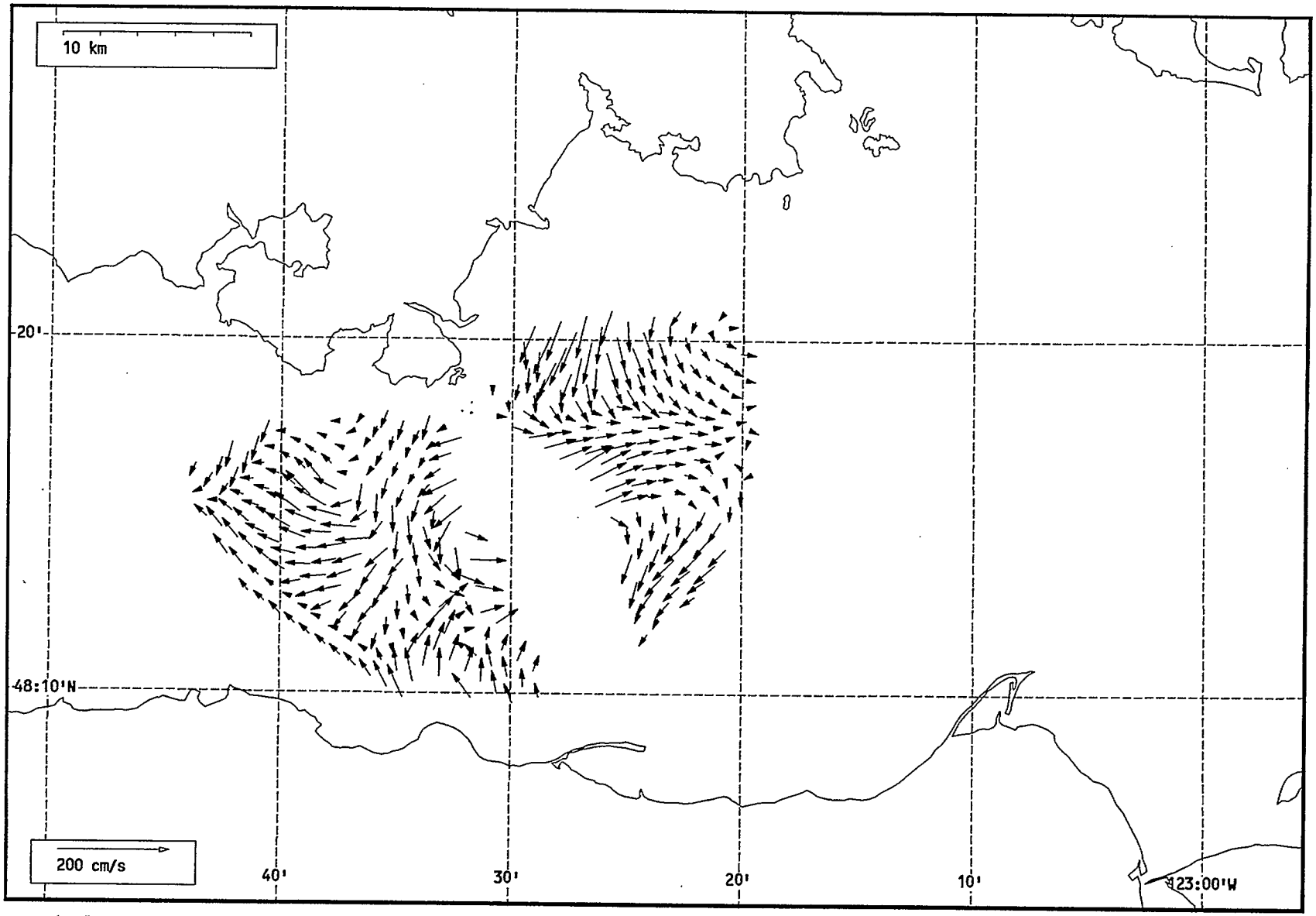

Total current vectors, Juan de Fuca Strait, 1992-07-28 03:00 Z.

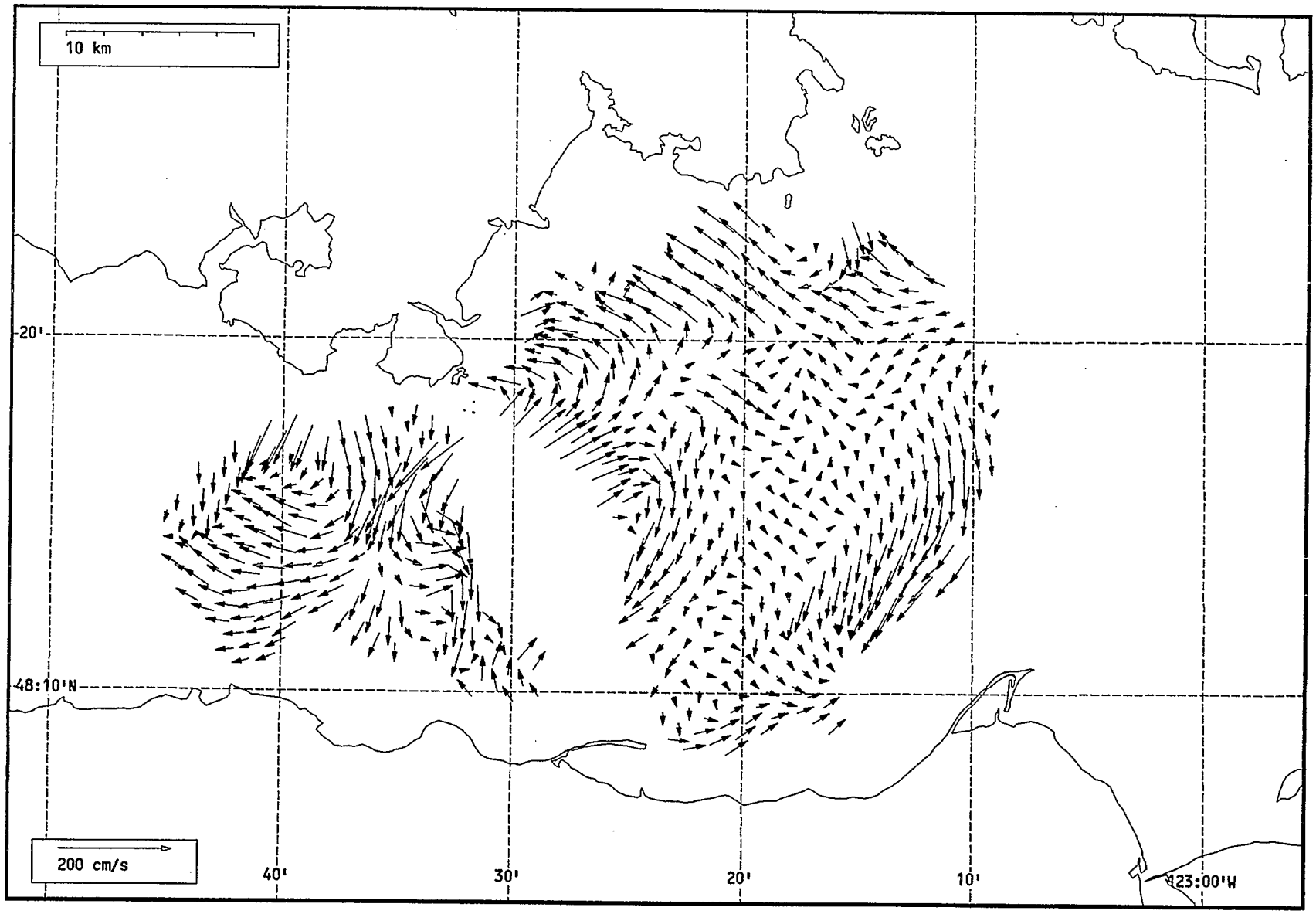

Total current vectors, Juan de Fuca Strait, 1992-07-28 04:00 Z.

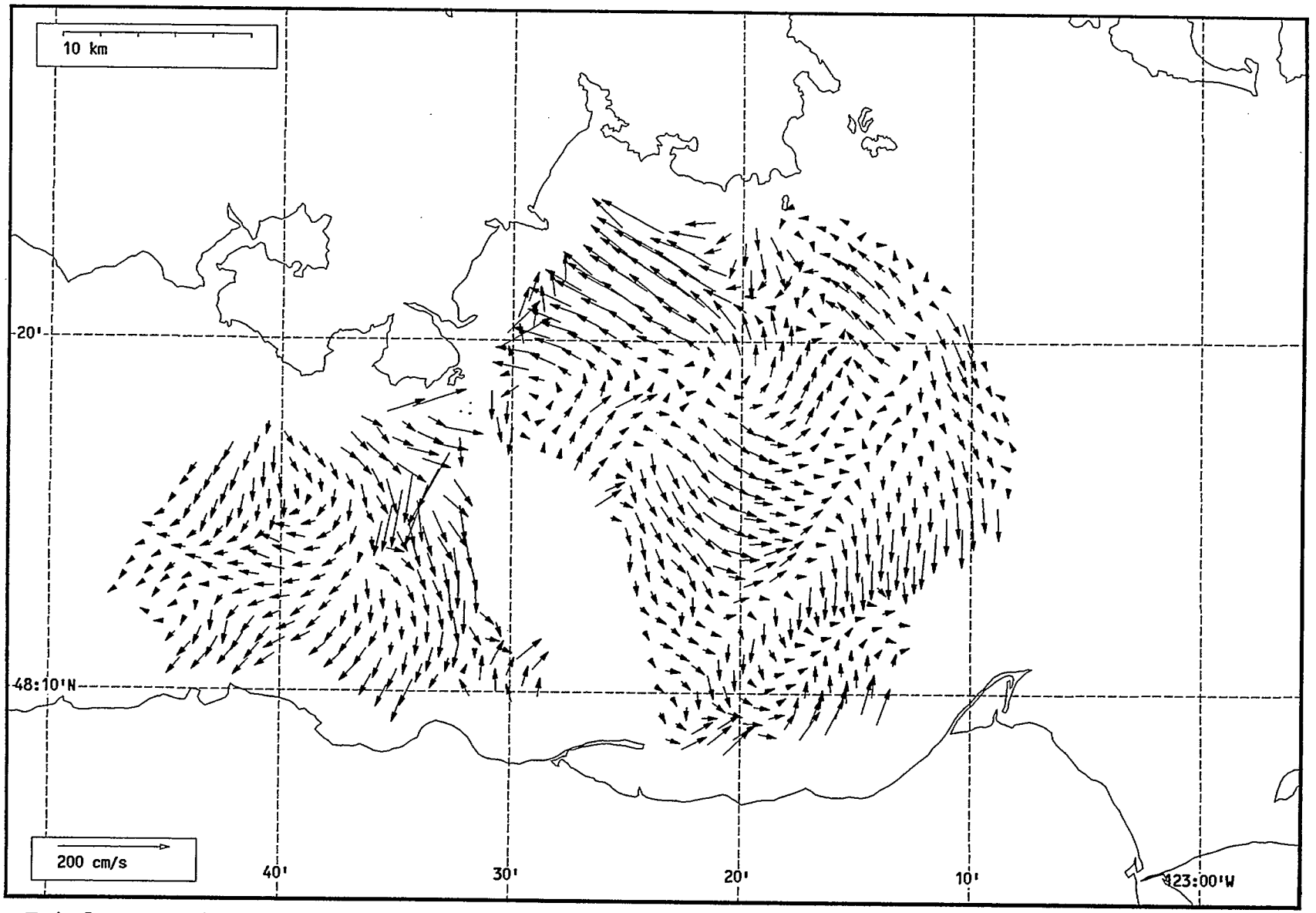

Total current vectors, Juan de Fuca Strait, 1992-07-28 05:00 Z.

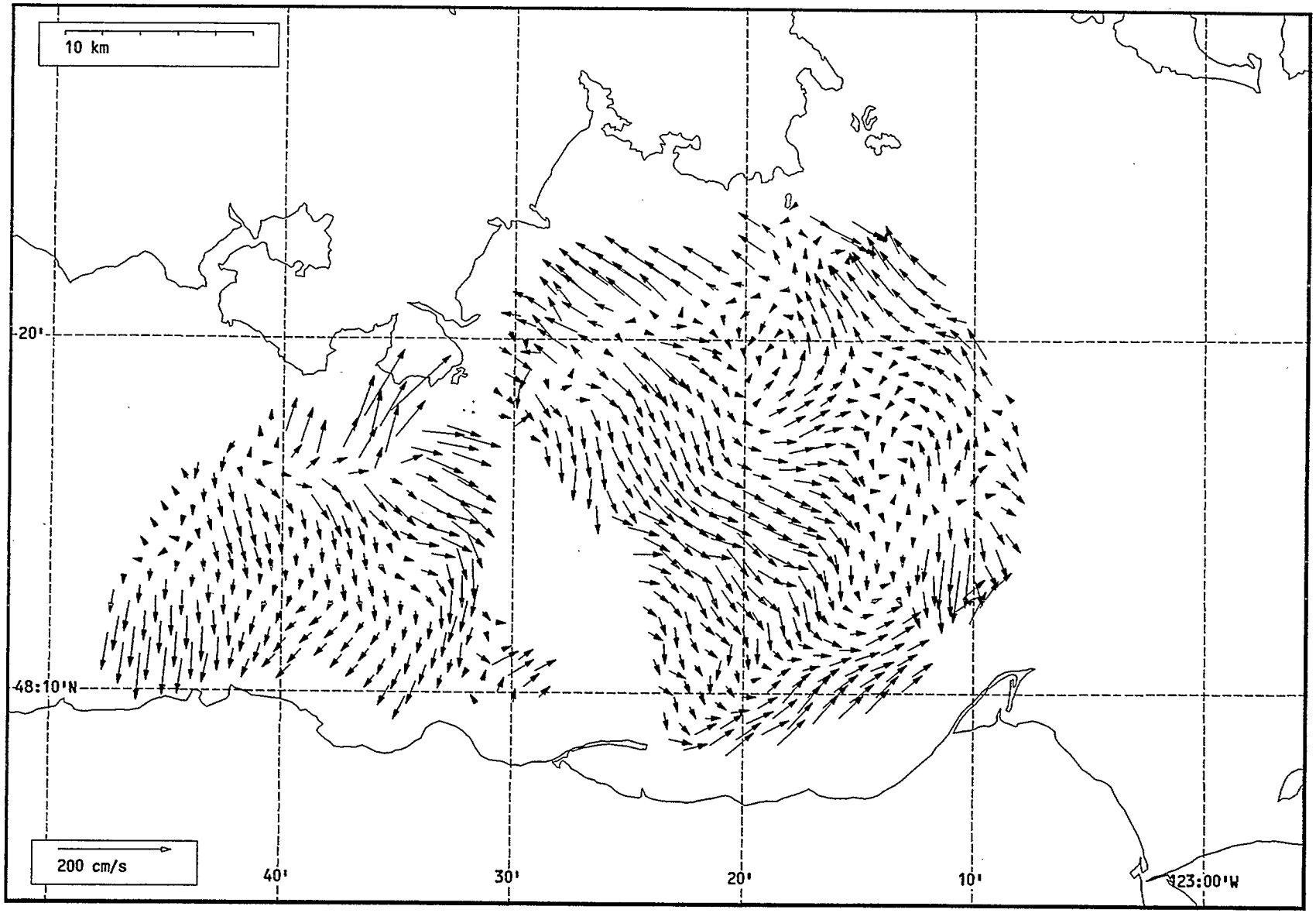

Total current vectors, Juan de Fuca Strait, 1992-07-28 06:00 Z.

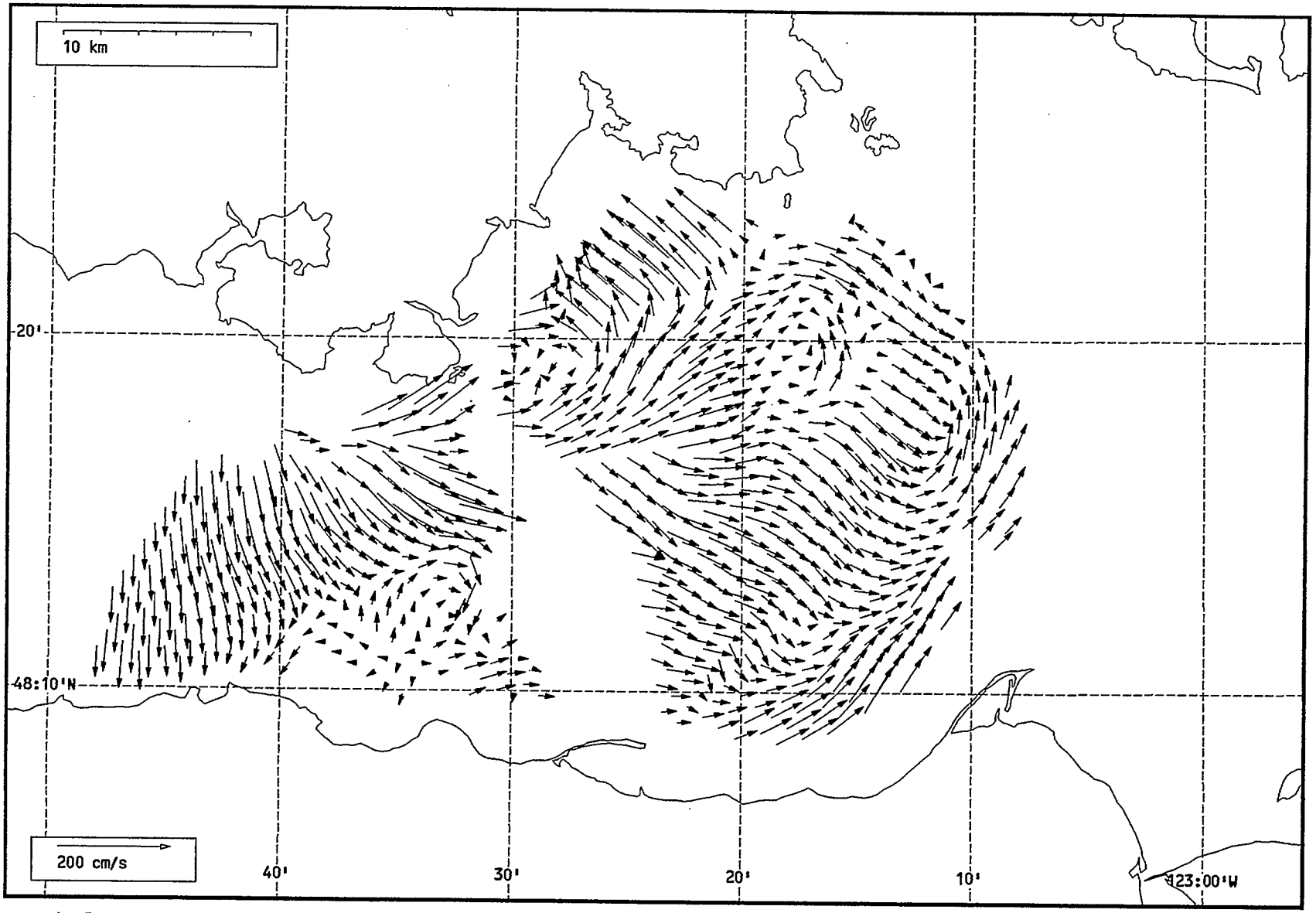

Total current vectors, Juan de Fuca Strait, 1992-07-28 07:00 Z.

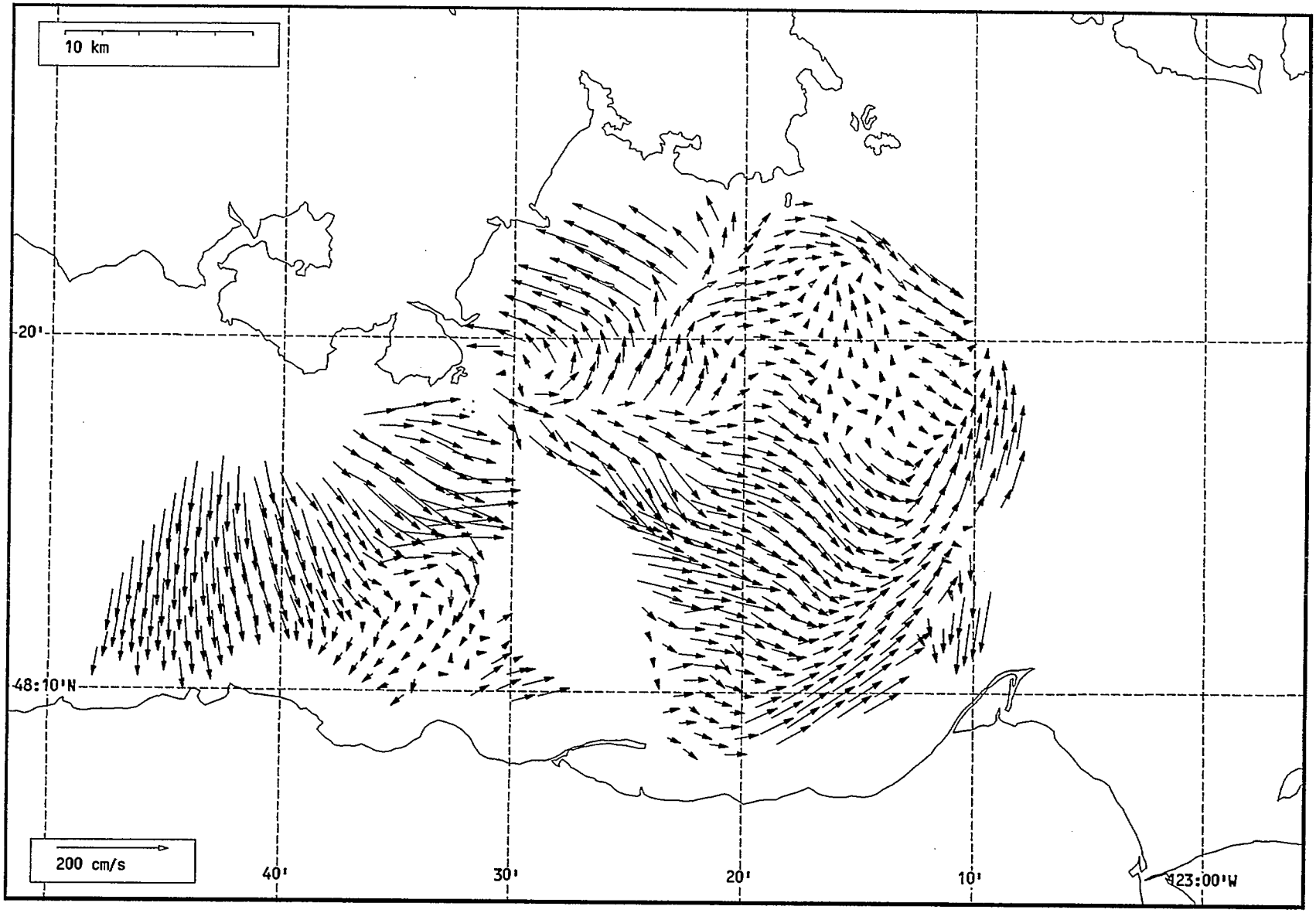

Total current vectors, Juan de Fuca Strait, 1992-07-28 08:00 Z.

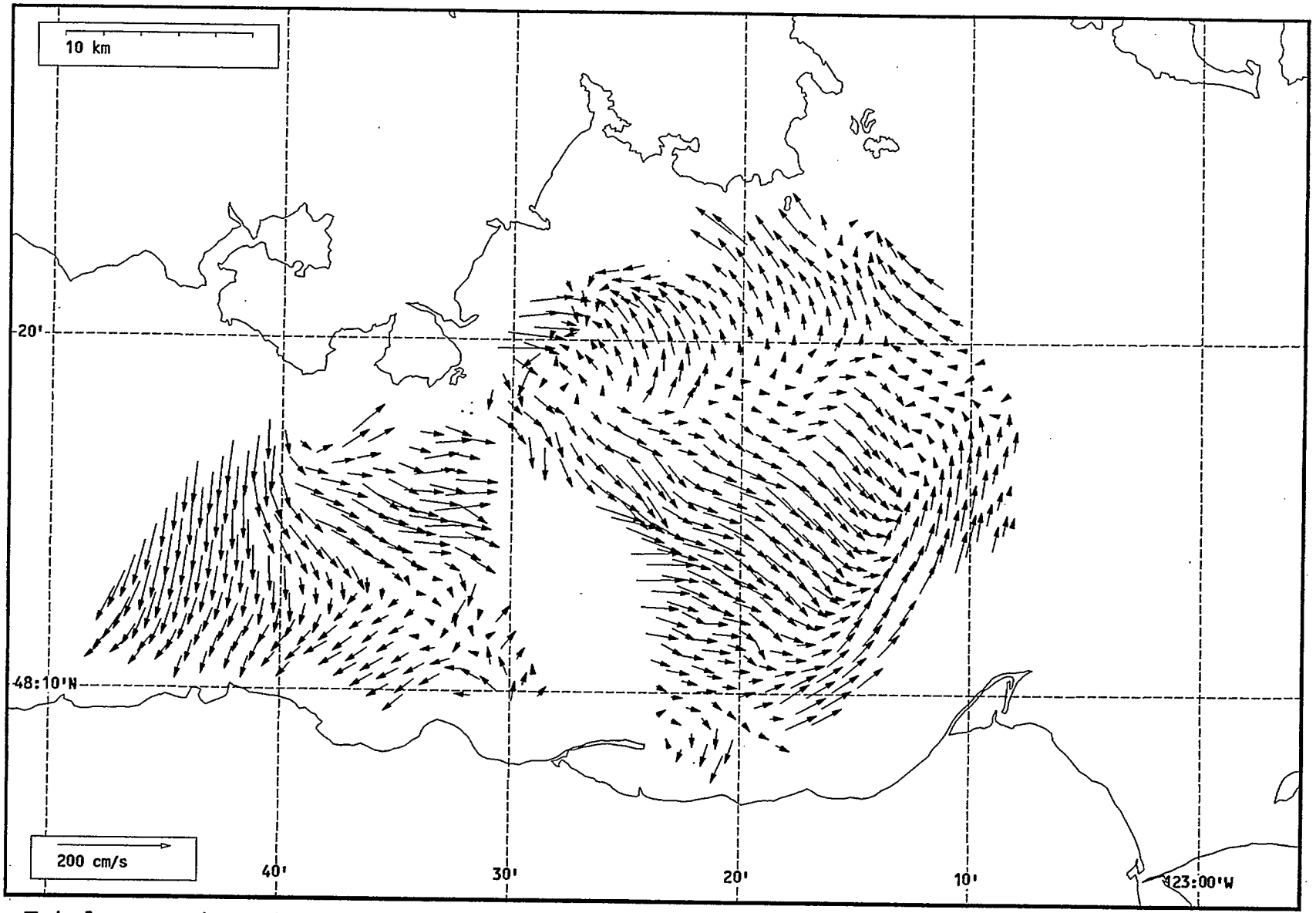

Total current vectors, Juan de Fuca Strait, 1992-07-28 09:00 Z.

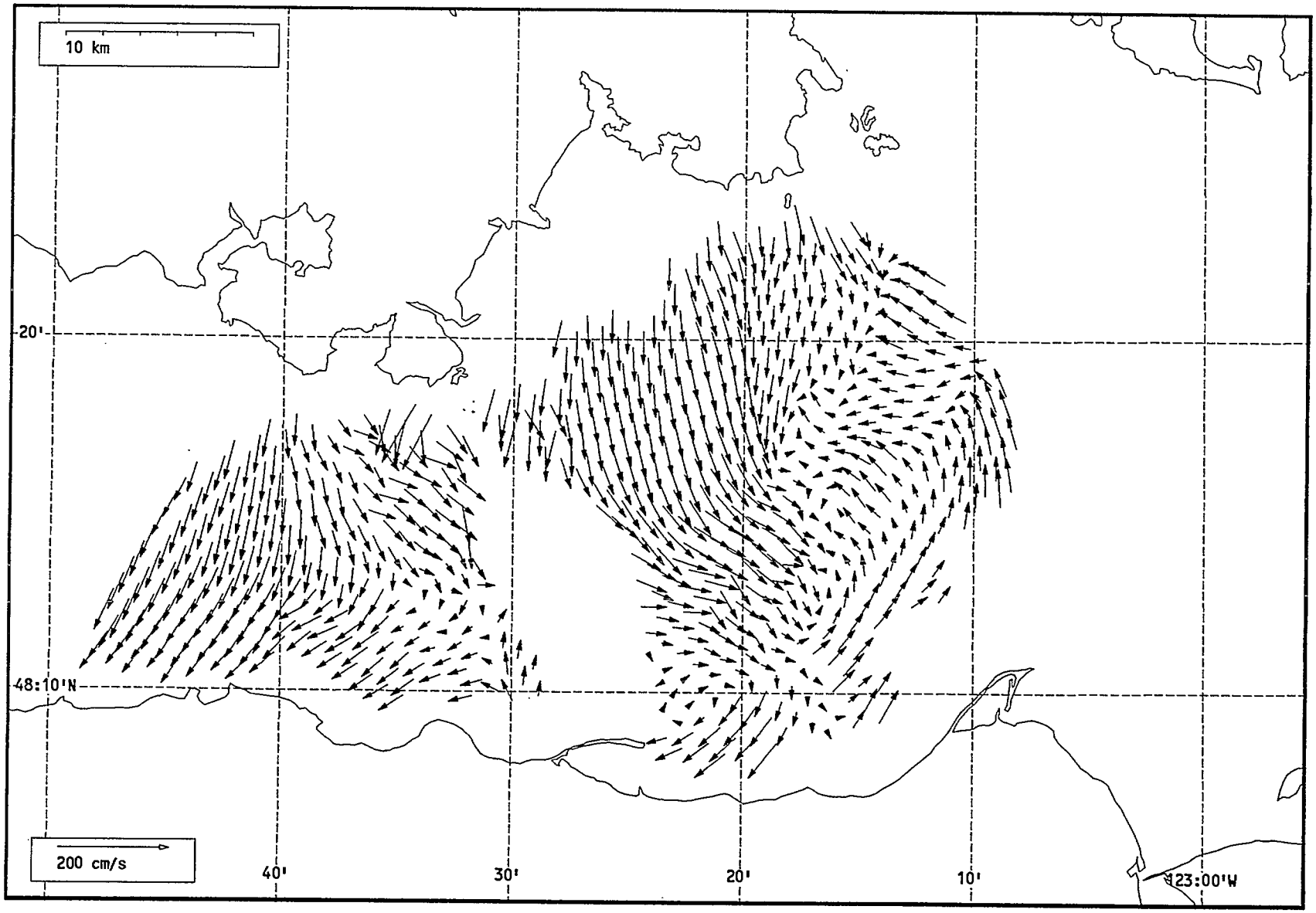

Total current vectors, Juan de Fuca Strait, 1992-07-28 10:00 Z.

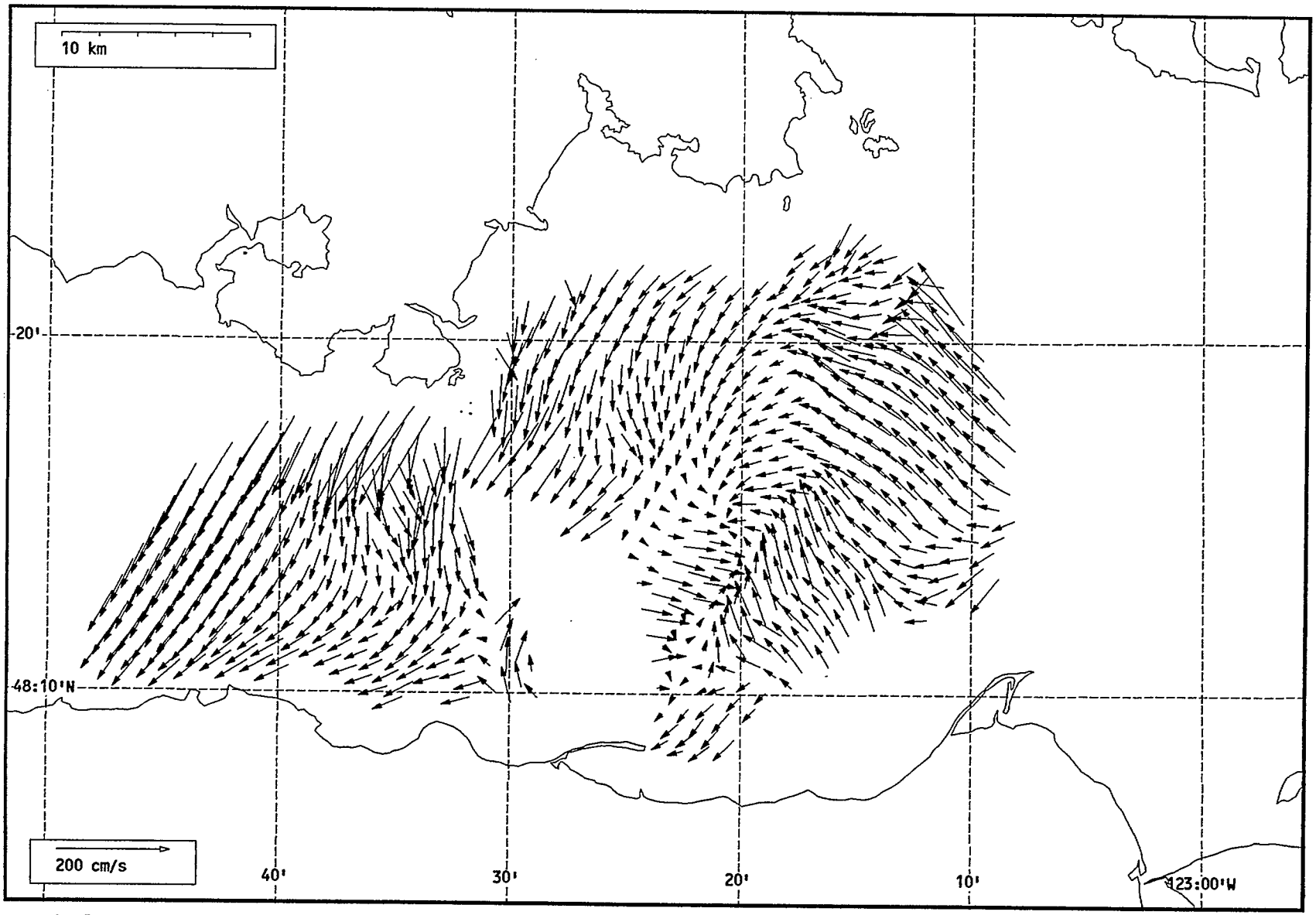

Total current vectors, Juan de Fuca Strait, 1992-07-28 11:00 Z.

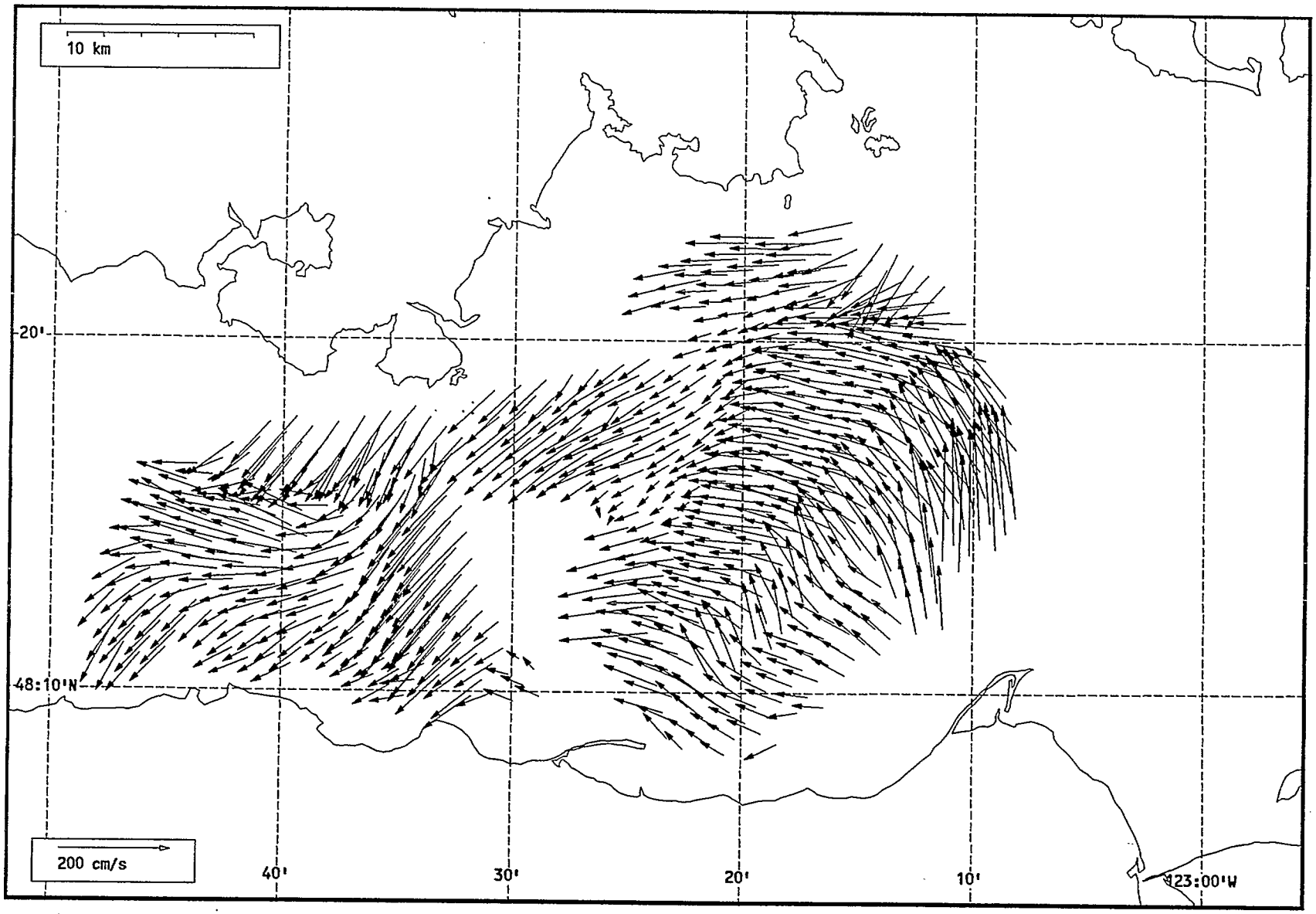

Total current vectors, Juan de Fuca Strait, 1992-07-28 12:00 Z.

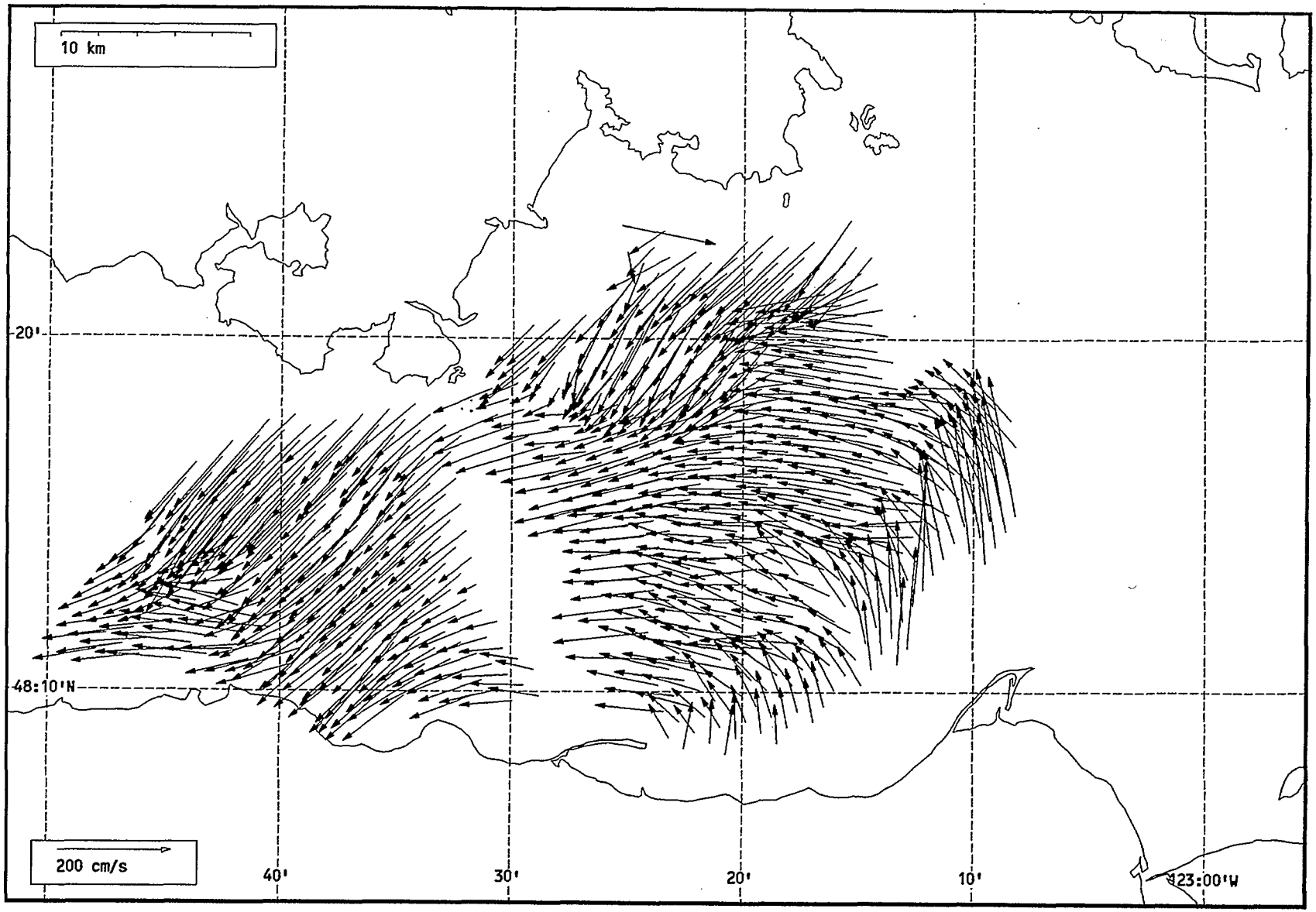

Total current vectors, Juan de Fuca Strait, 1992-07-28 13:00 Z.

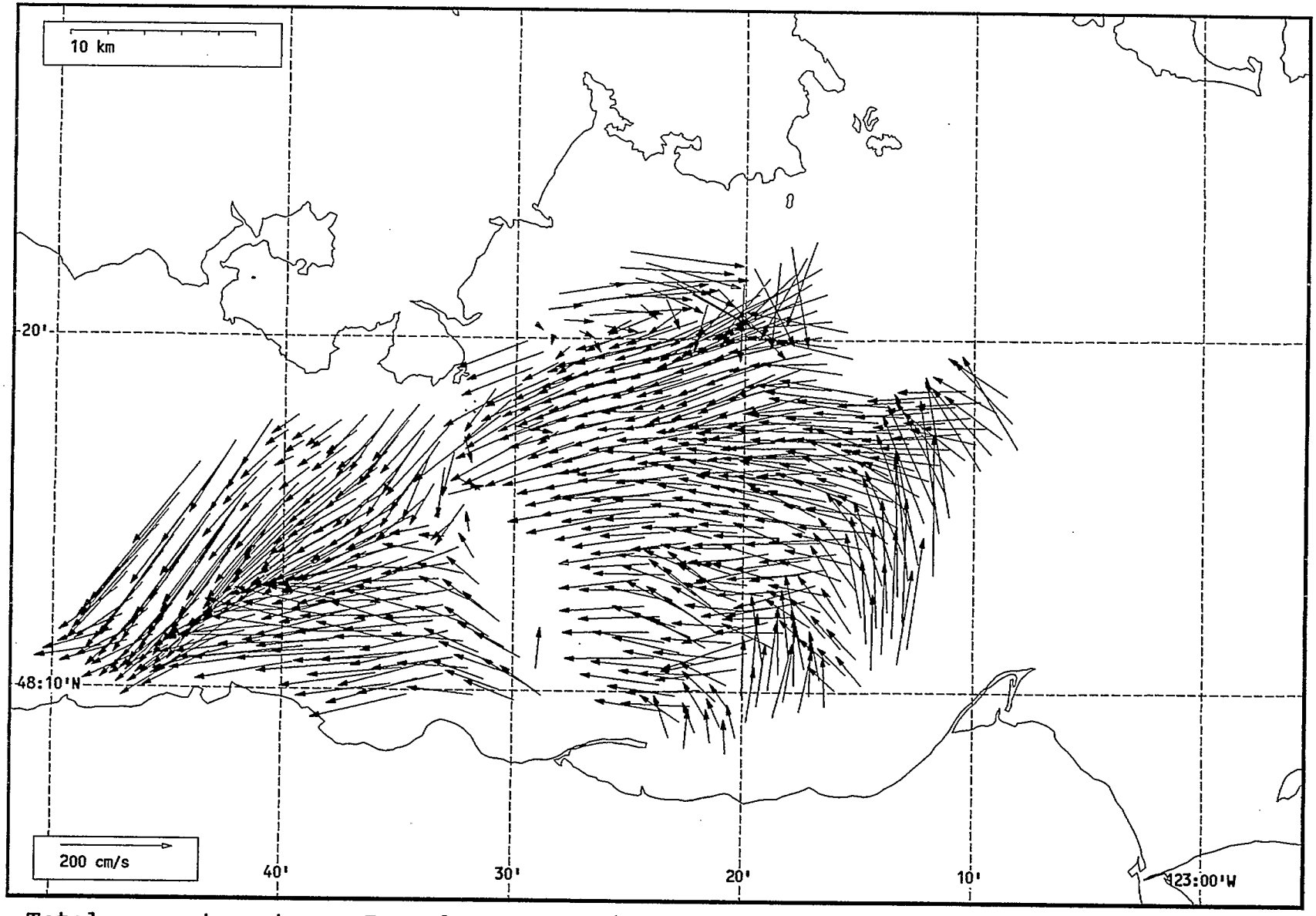

Total current vectors, Juan de Fuca Strait, 1992-07-28 14:00 Z.

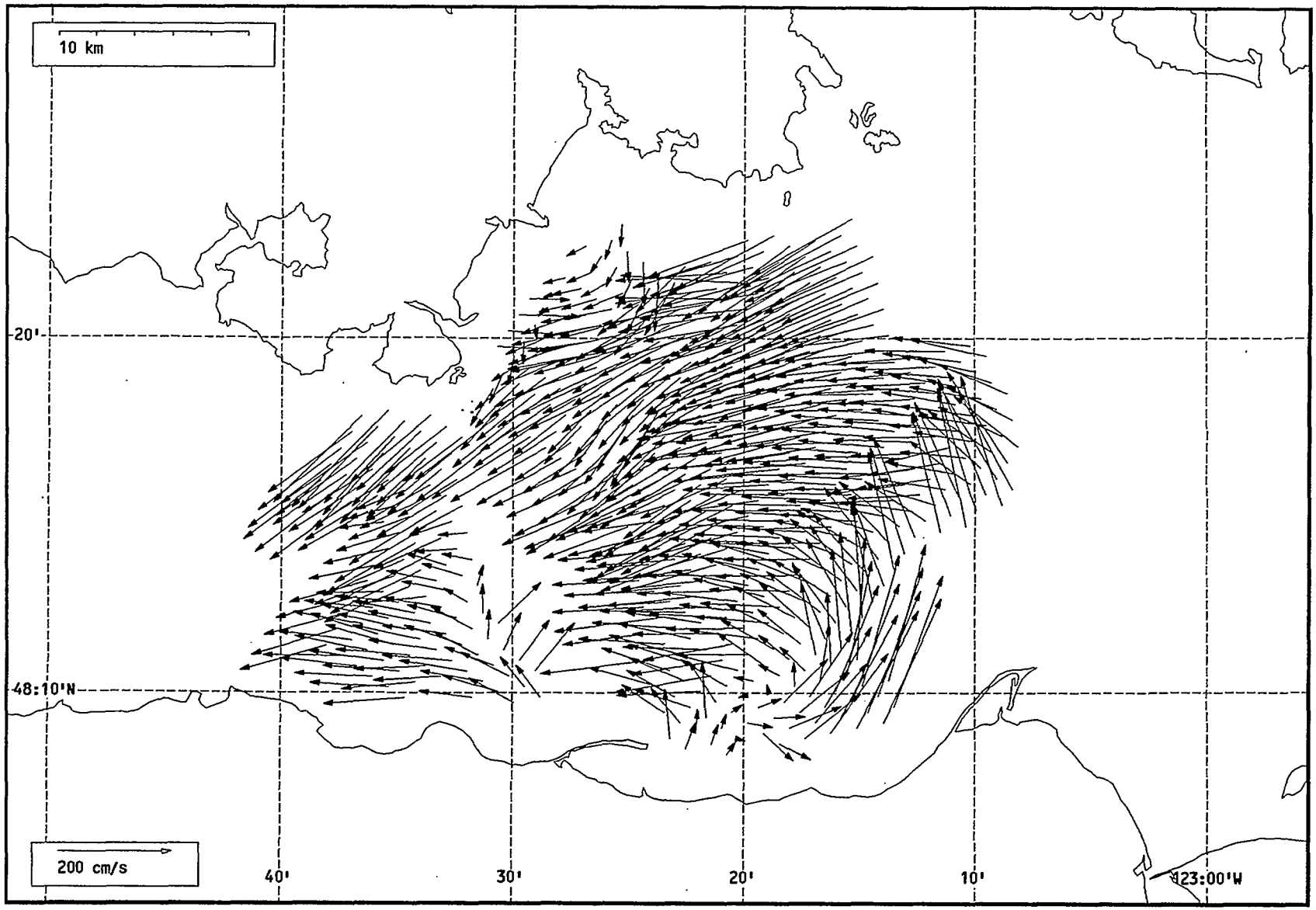

Total current vectors, Juan de Fuca Strait, 1992-07-28 15:00 Z.

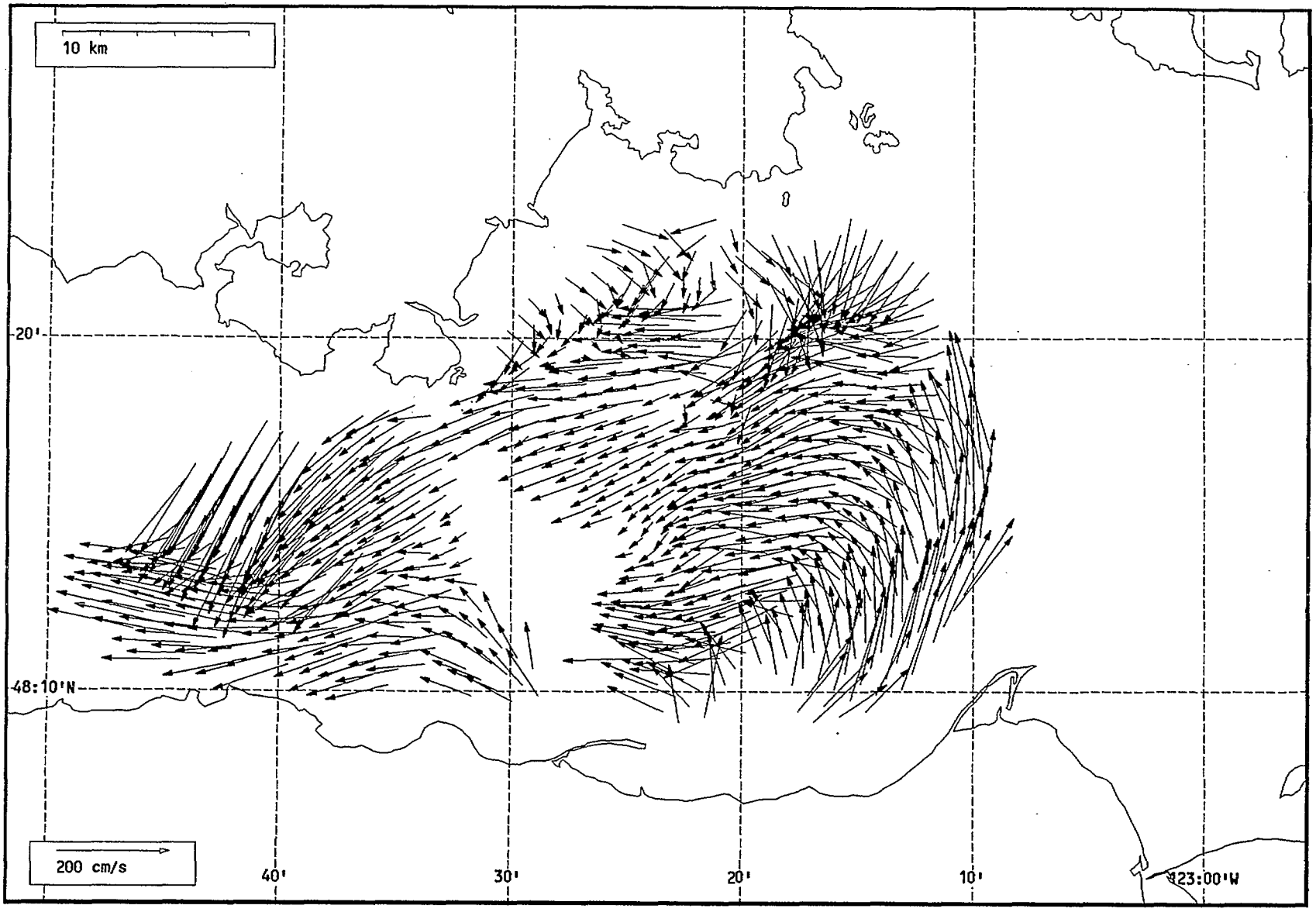

Total current vectors, Juan de Fuca Strait, 1992-07-28 16:00 Z.

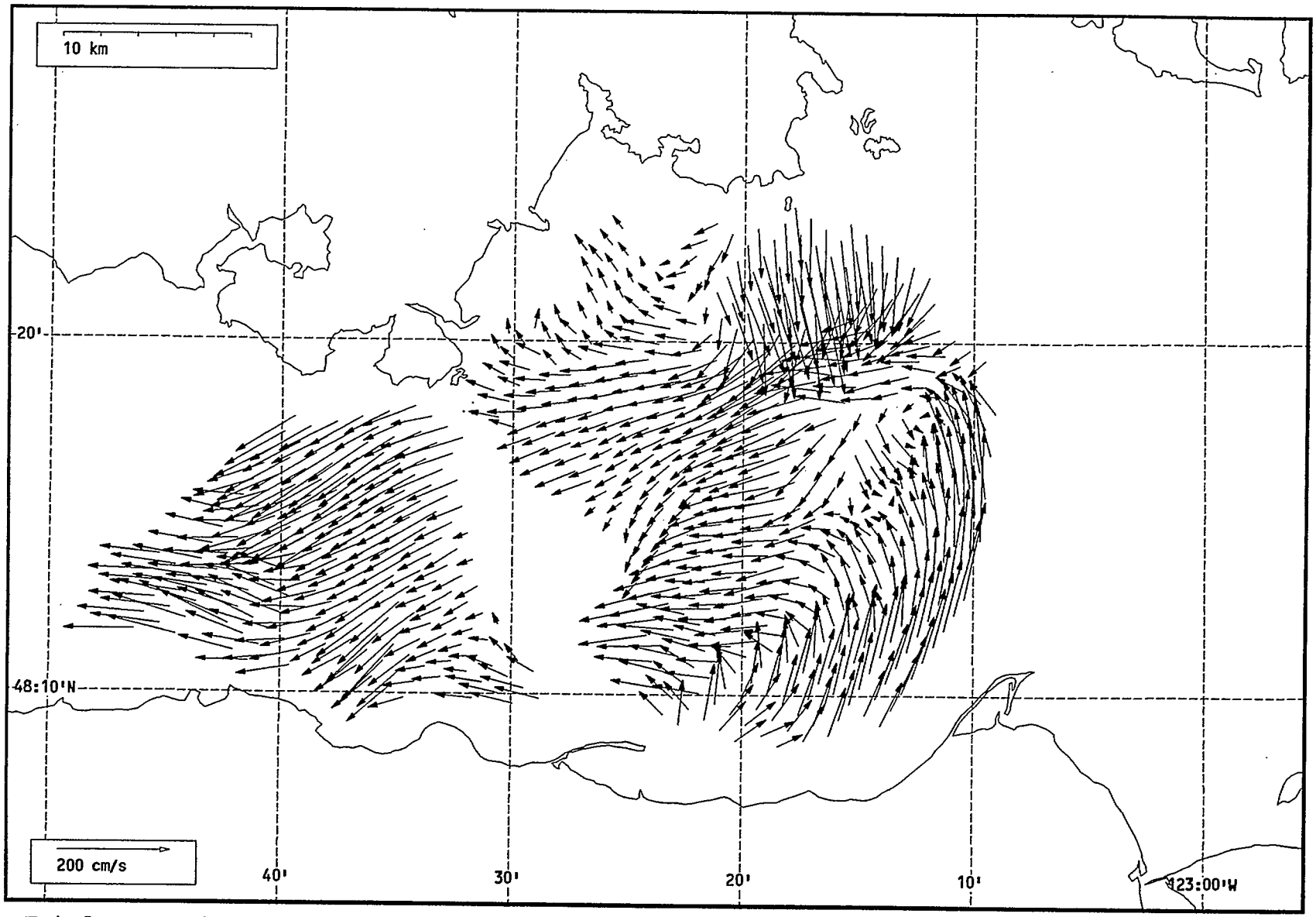

Total current vectors, Juan de Fuca Strait, 1992-07-28 17:00 Z.

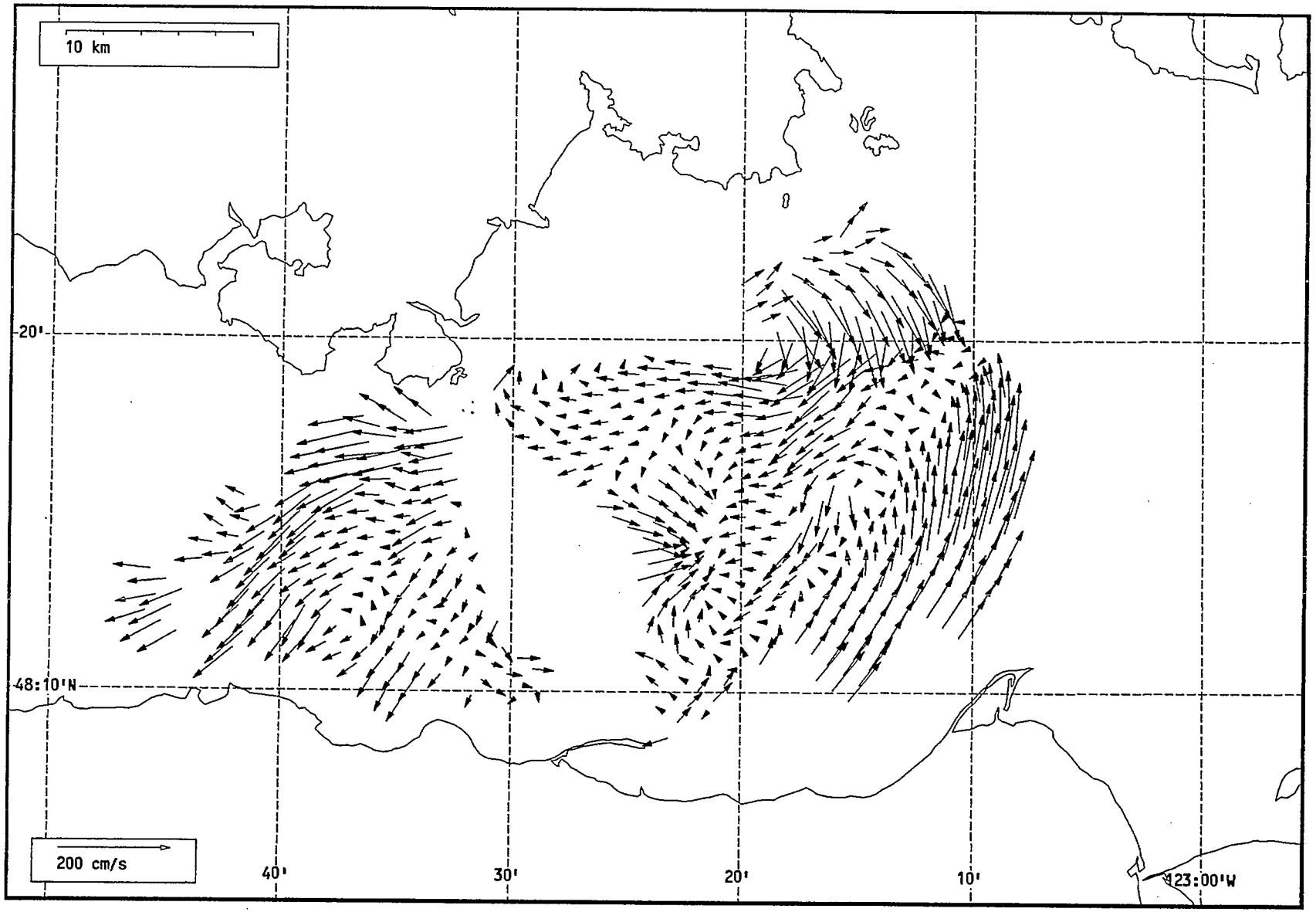

Total current vectors, Juan de Fuca Strait, 1992-07-28 18:00 Z.

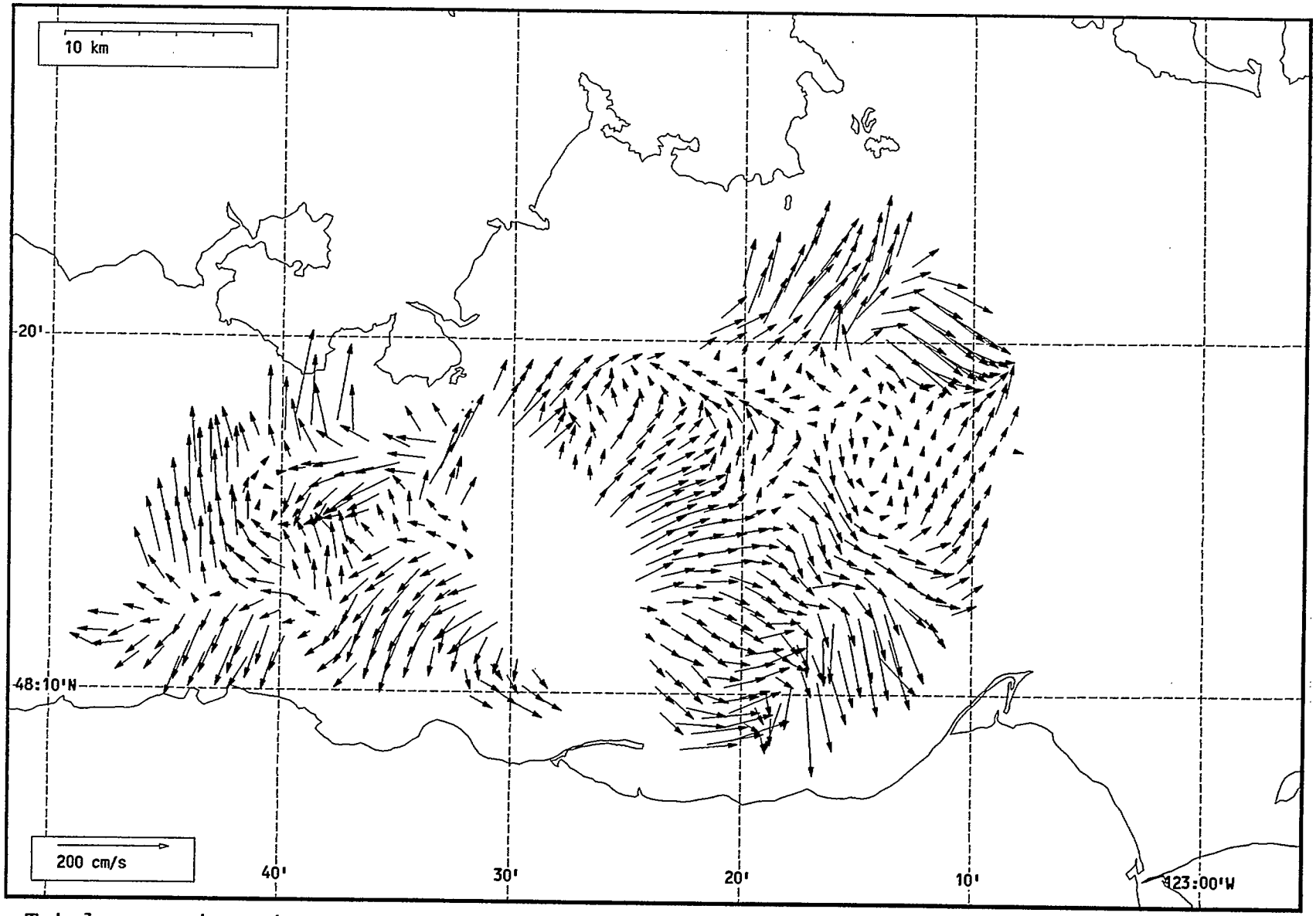

Total current vectors, Juan de Fuca Strait, 1992-07-28 19:00 Z.

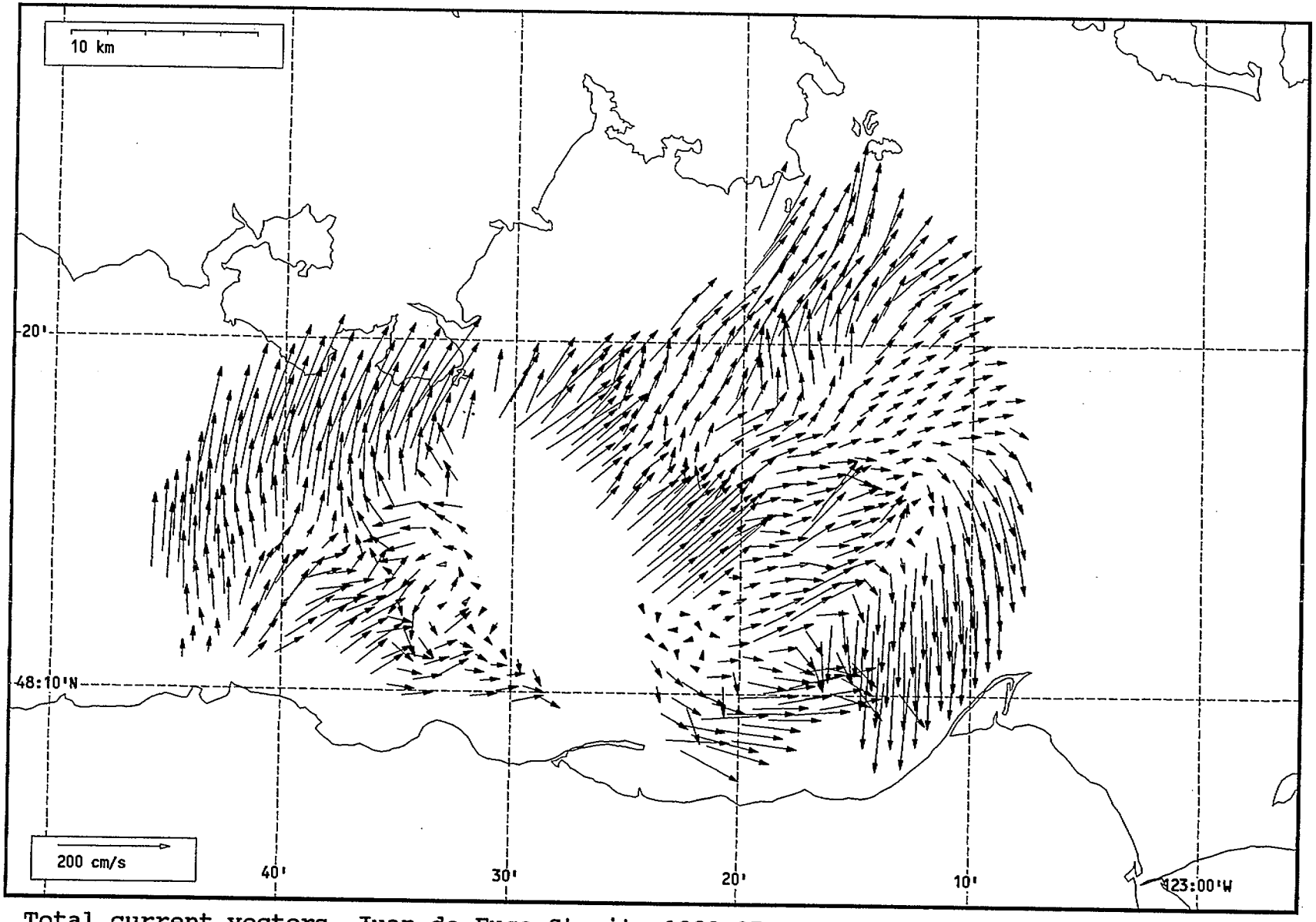

Total current vectors, Juan de Fuca Strait, 1992-07-28 20:00 Z.

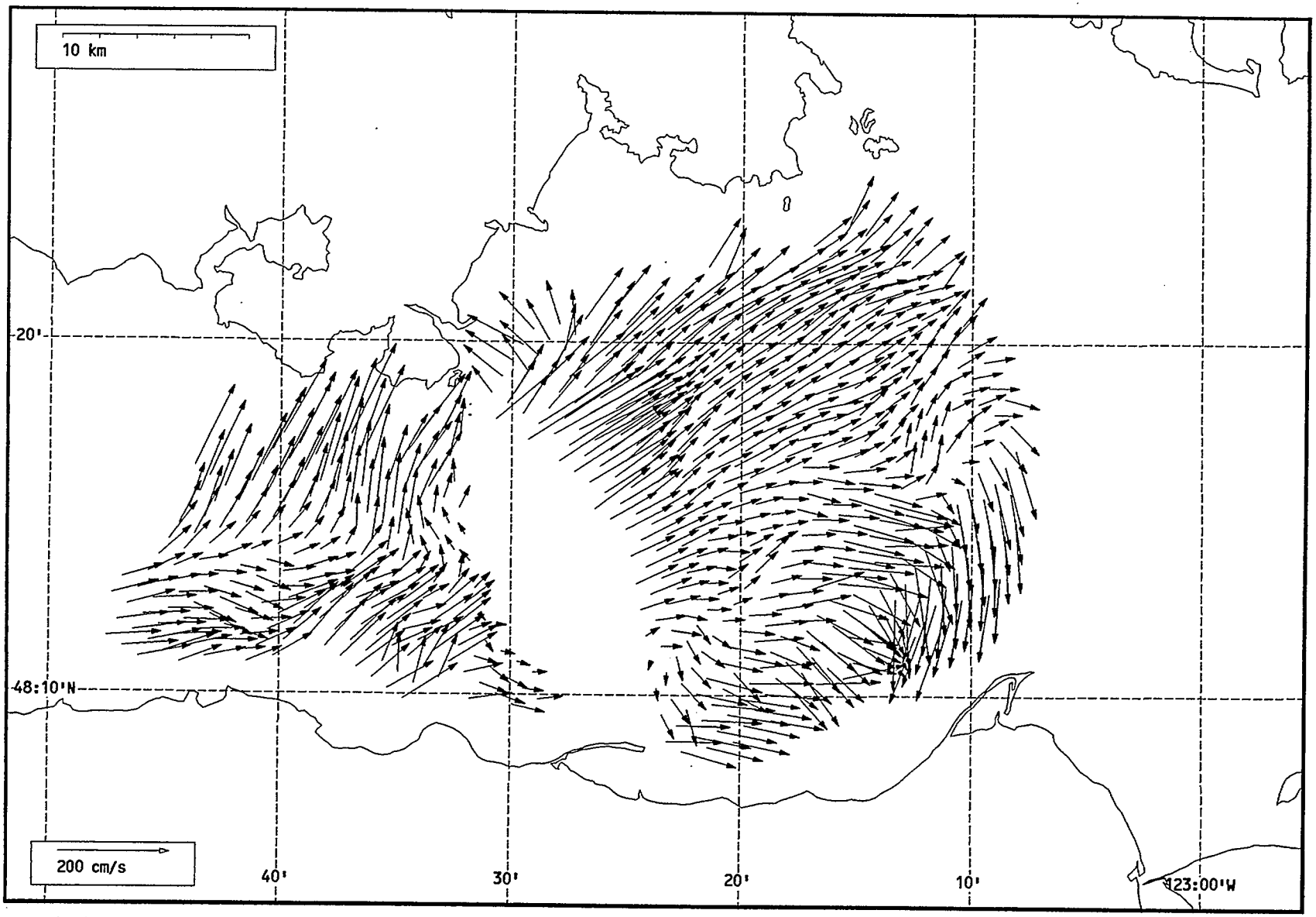

Total current vectors, Juan de Fuca Strait, 1992-07-28 21:00 Z.

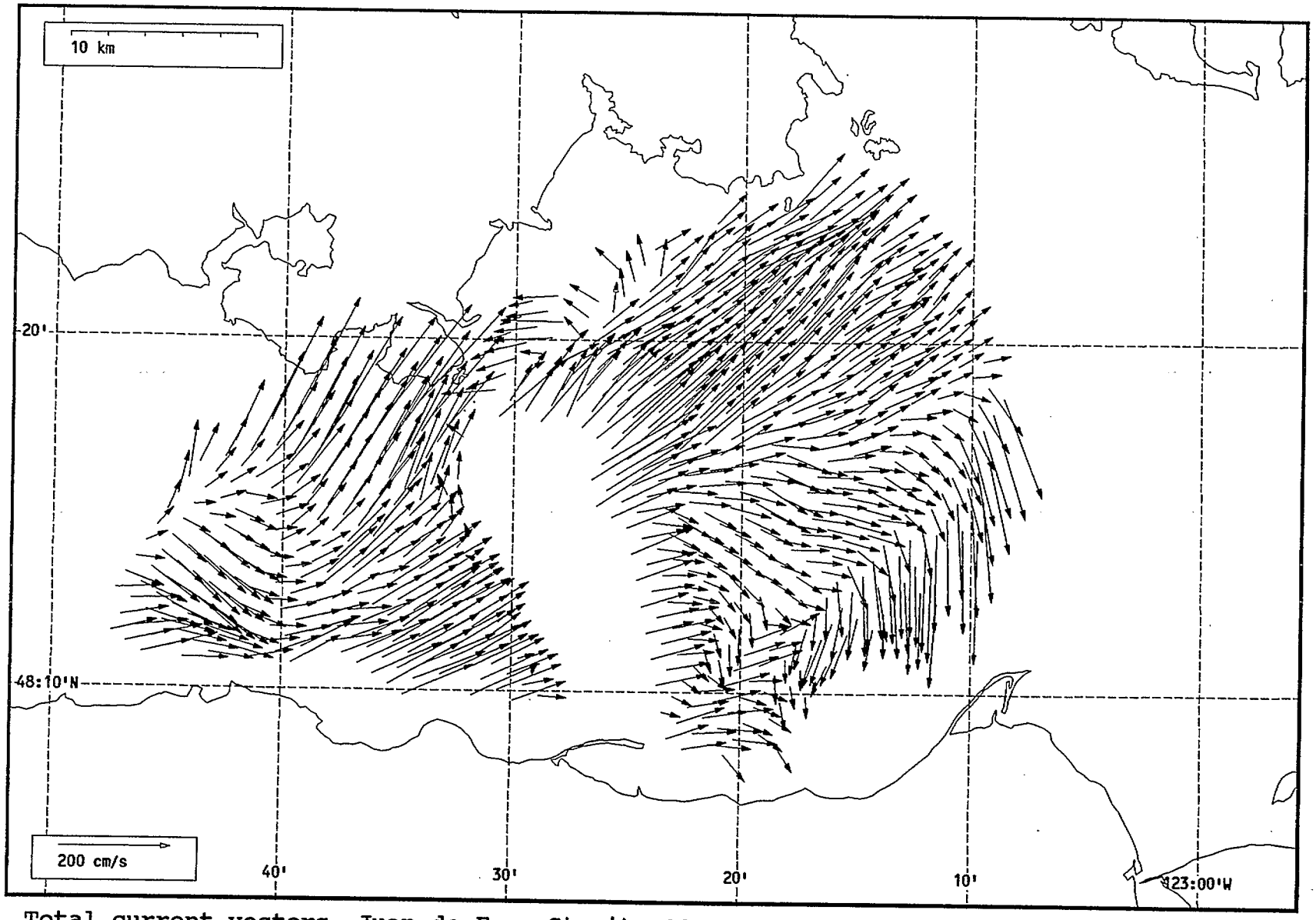

Total current vectors, Juan de Fuca Strait, 1992-07-28 22:00 Z.

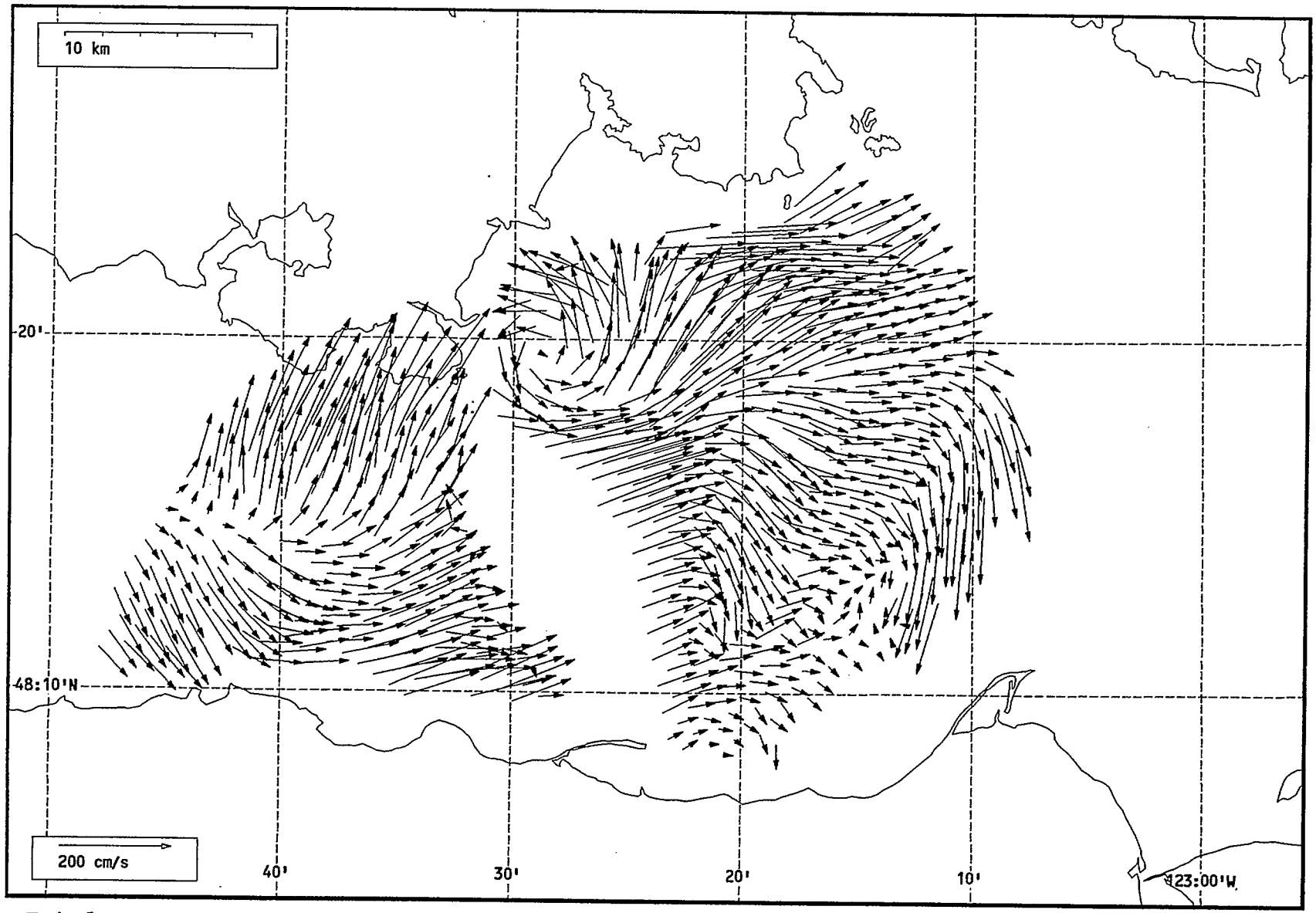

Total current vectors, Juan de Fuca Strait, 1992-07-28 23:00 Z..

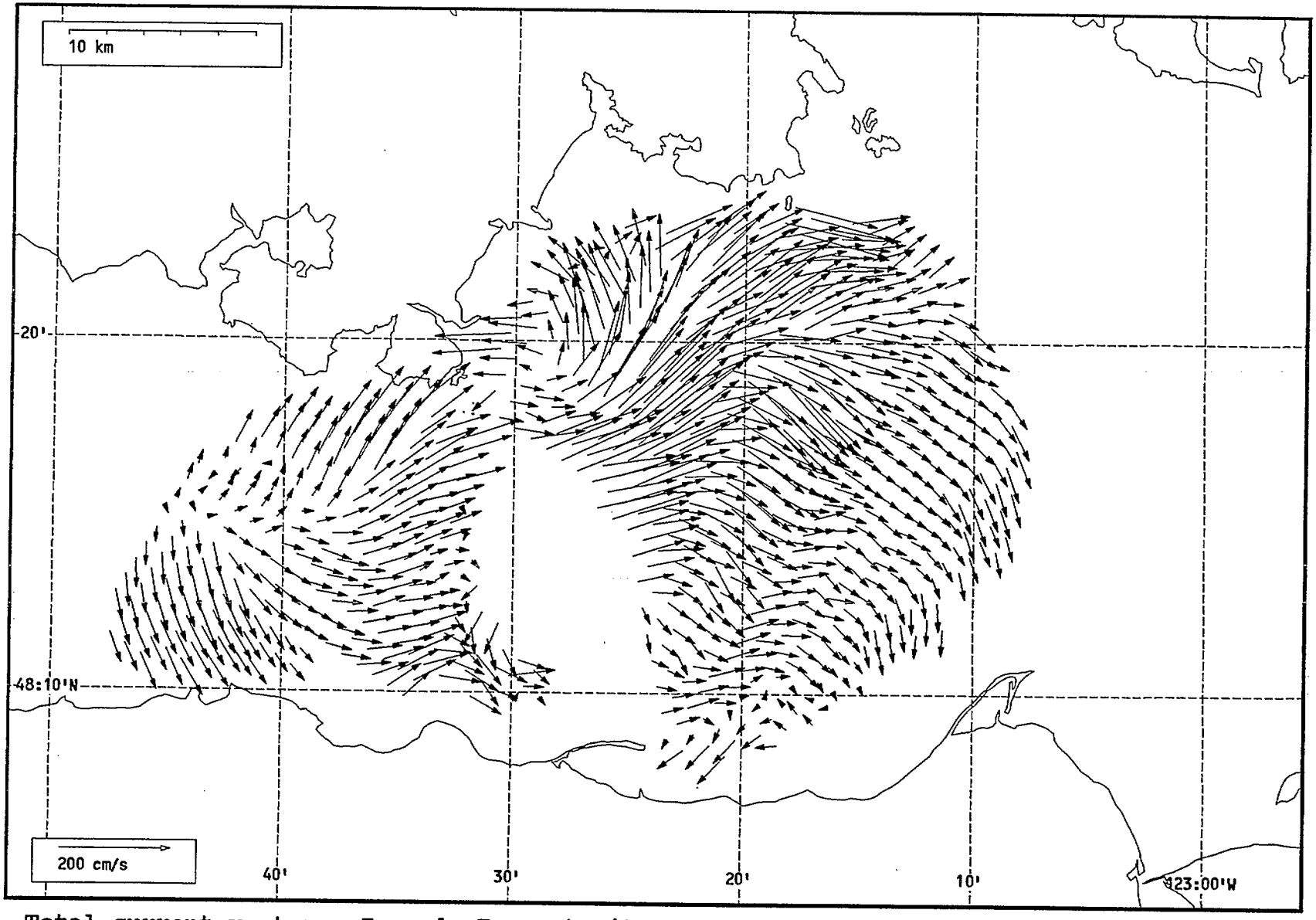

Total current vectors, Juan de Fuca Strait, 1992-07-29 00:00 Z.

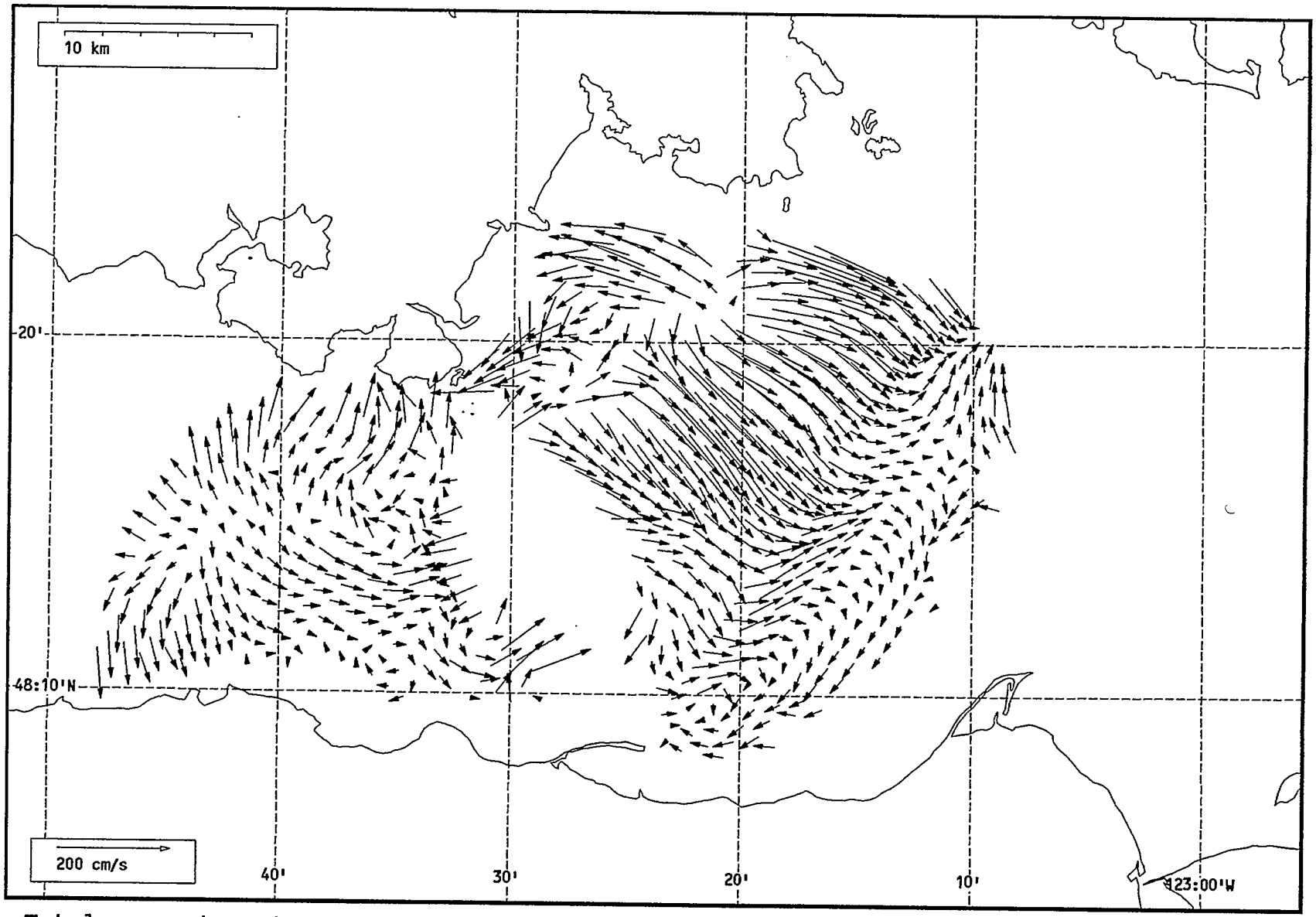

Total current vectors, Juan de Fuca Strait, 1992-07-29 01:00 Z.

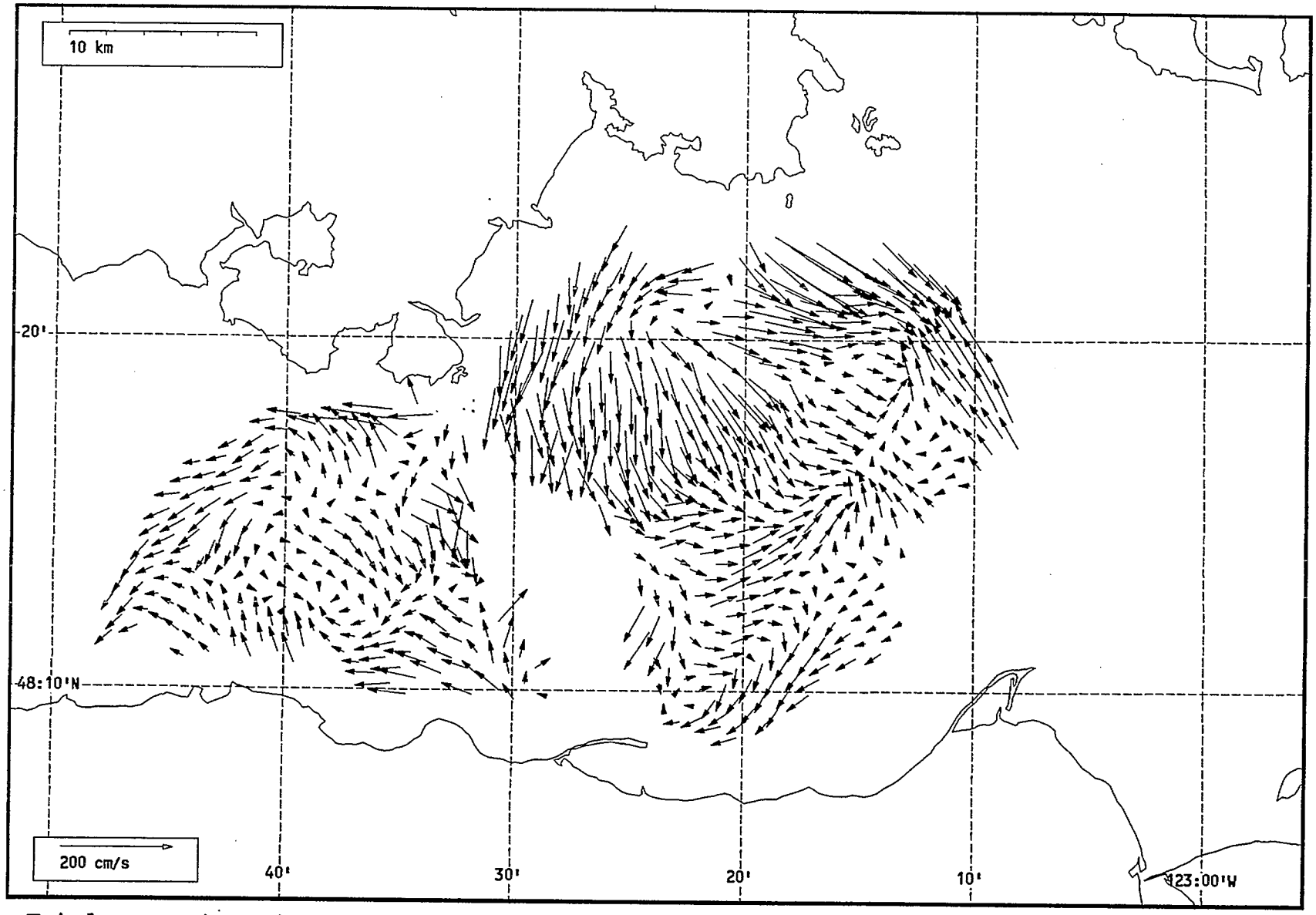

Total current vectors, Juan de Fuca Strait, 1992-07-29 02:00 Z.

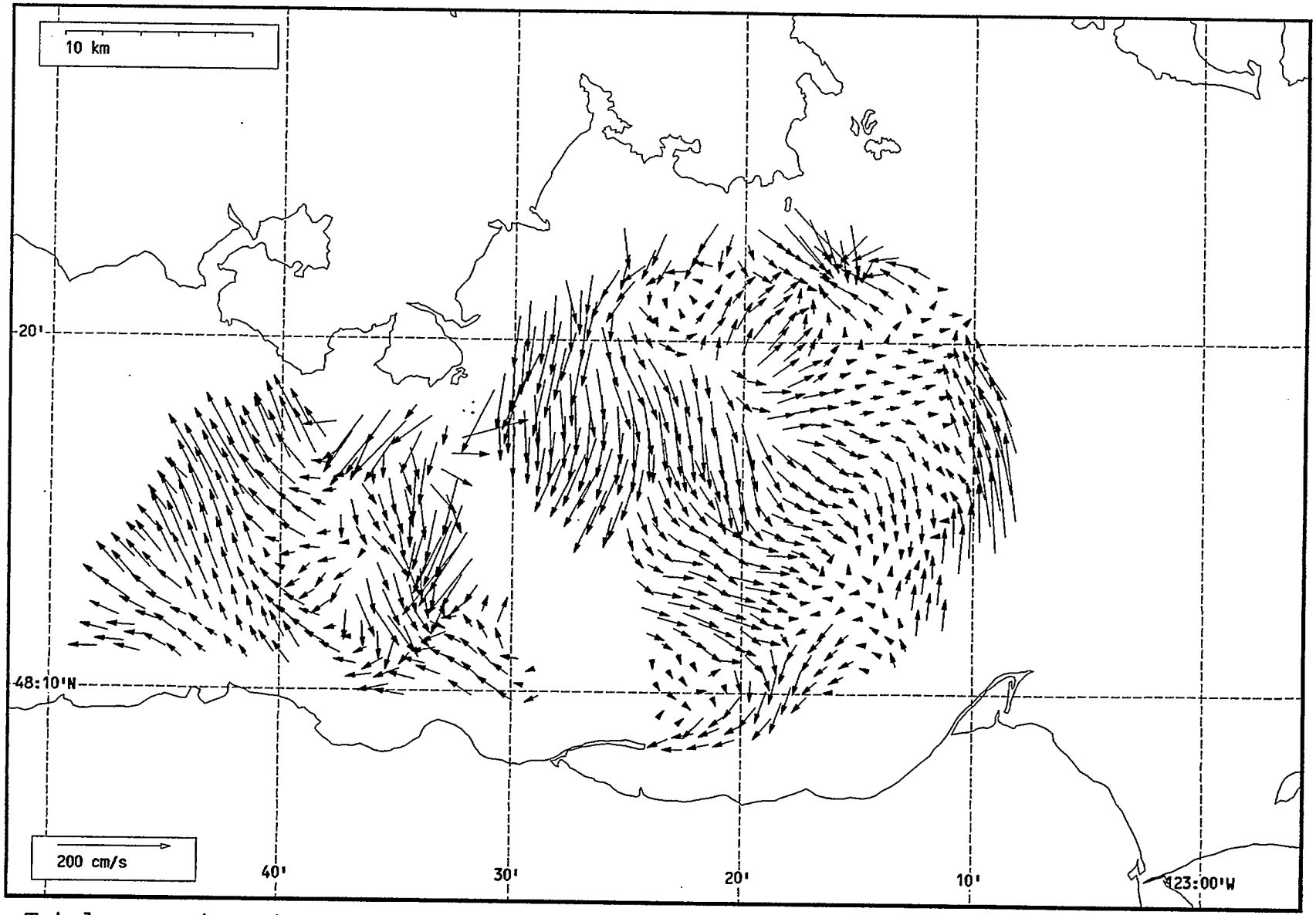

Total current vectors, Juan de Fuca Strait, 1992-07-29 03:00 Z.

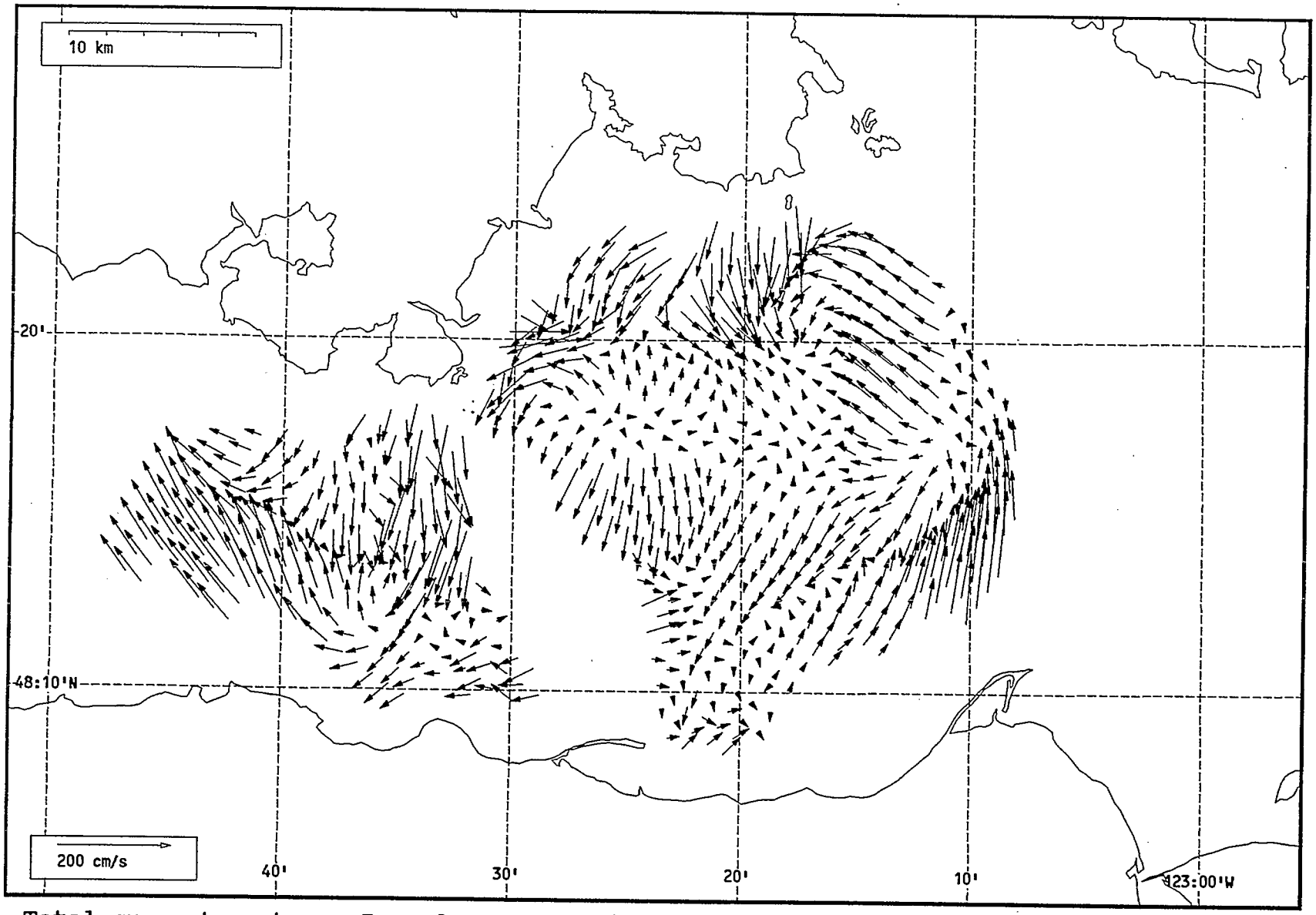

Total current vectors, Juan de Fuca Strait, 1992-07-29 04:00 Z.

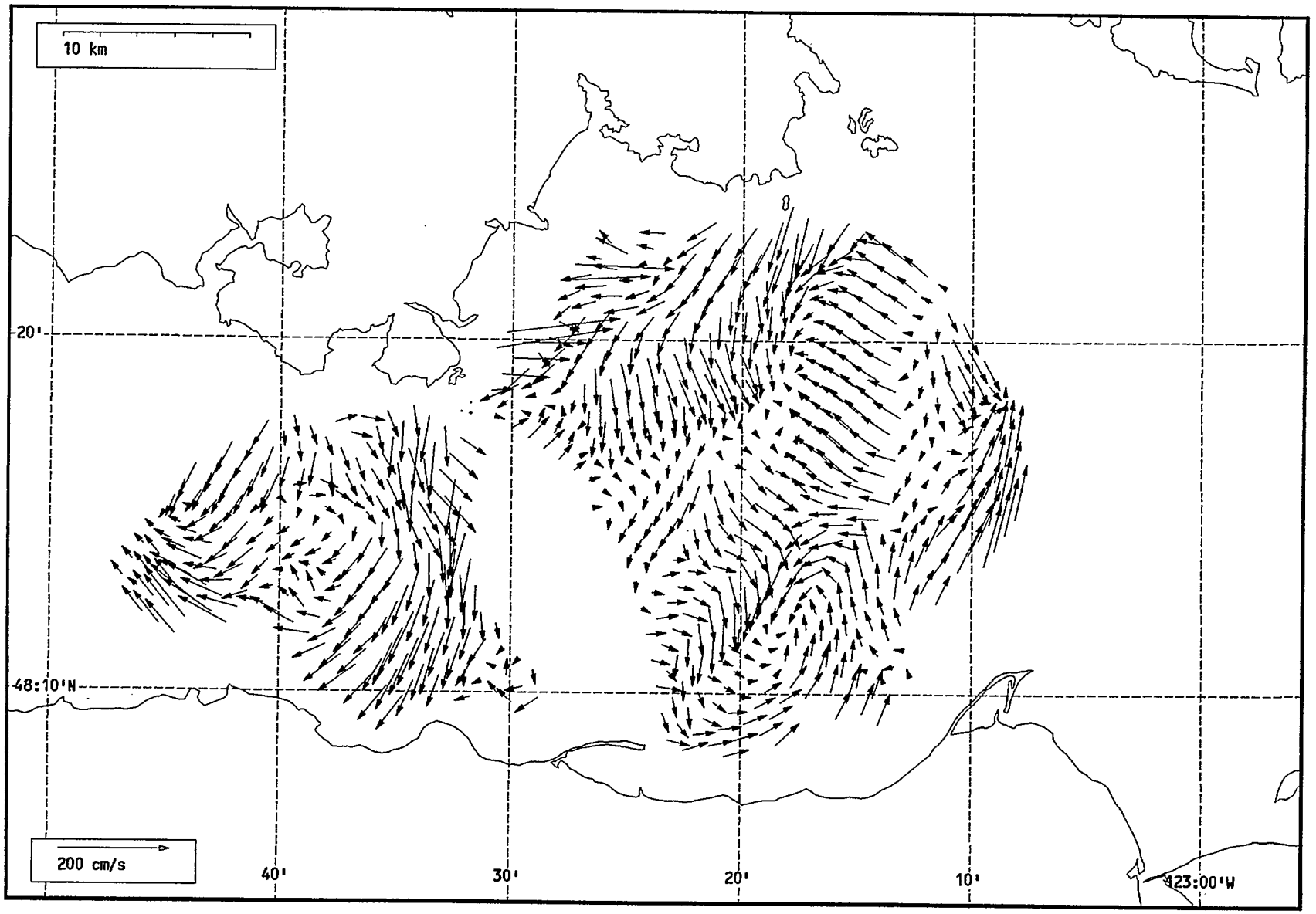

Total current vectors, Juan de Fuca Strait, 1992-07-29 05:00 Z.

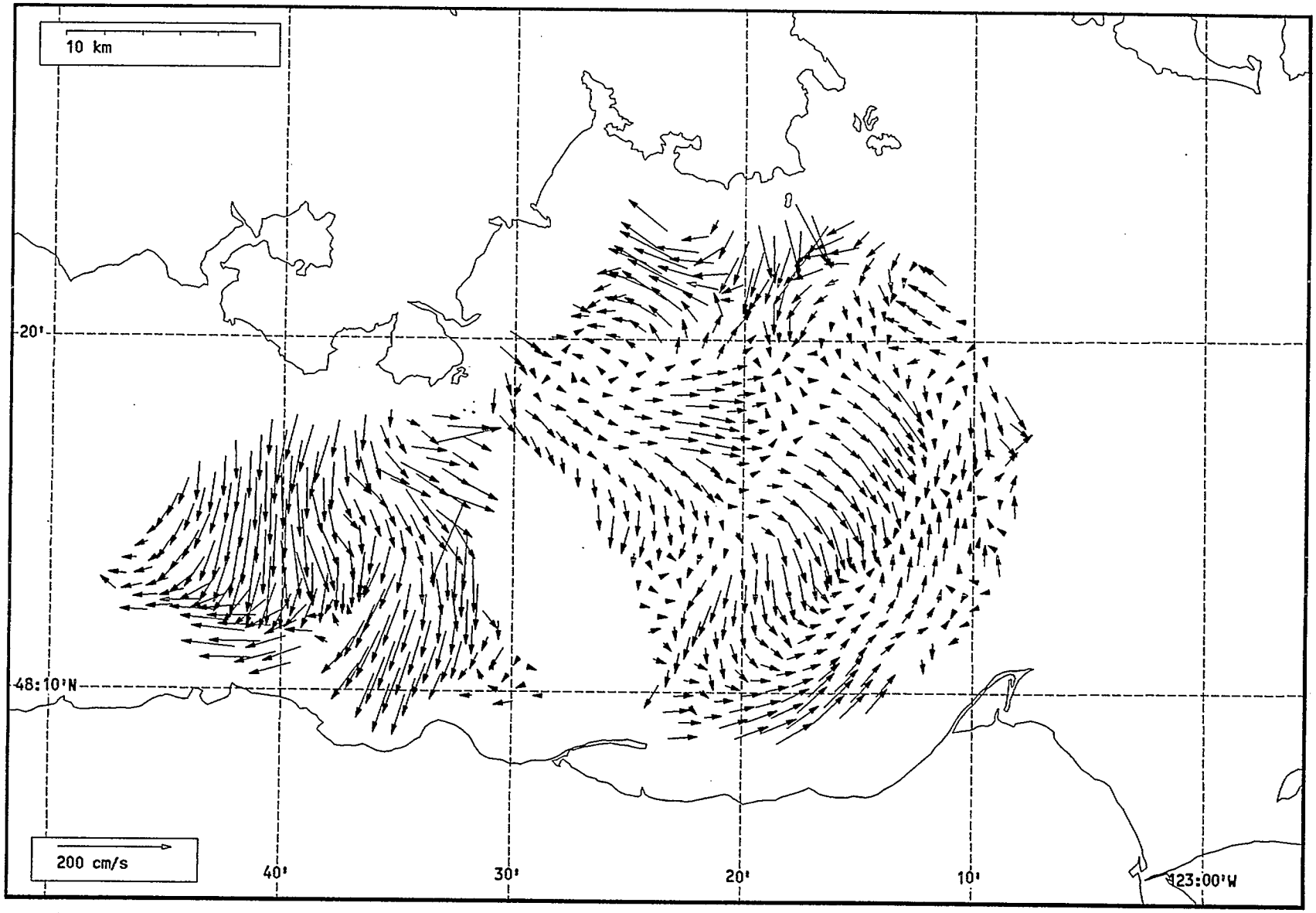

Total current vectors, Juan de Fuca Strait, 1992-07-29 06:00 Z.

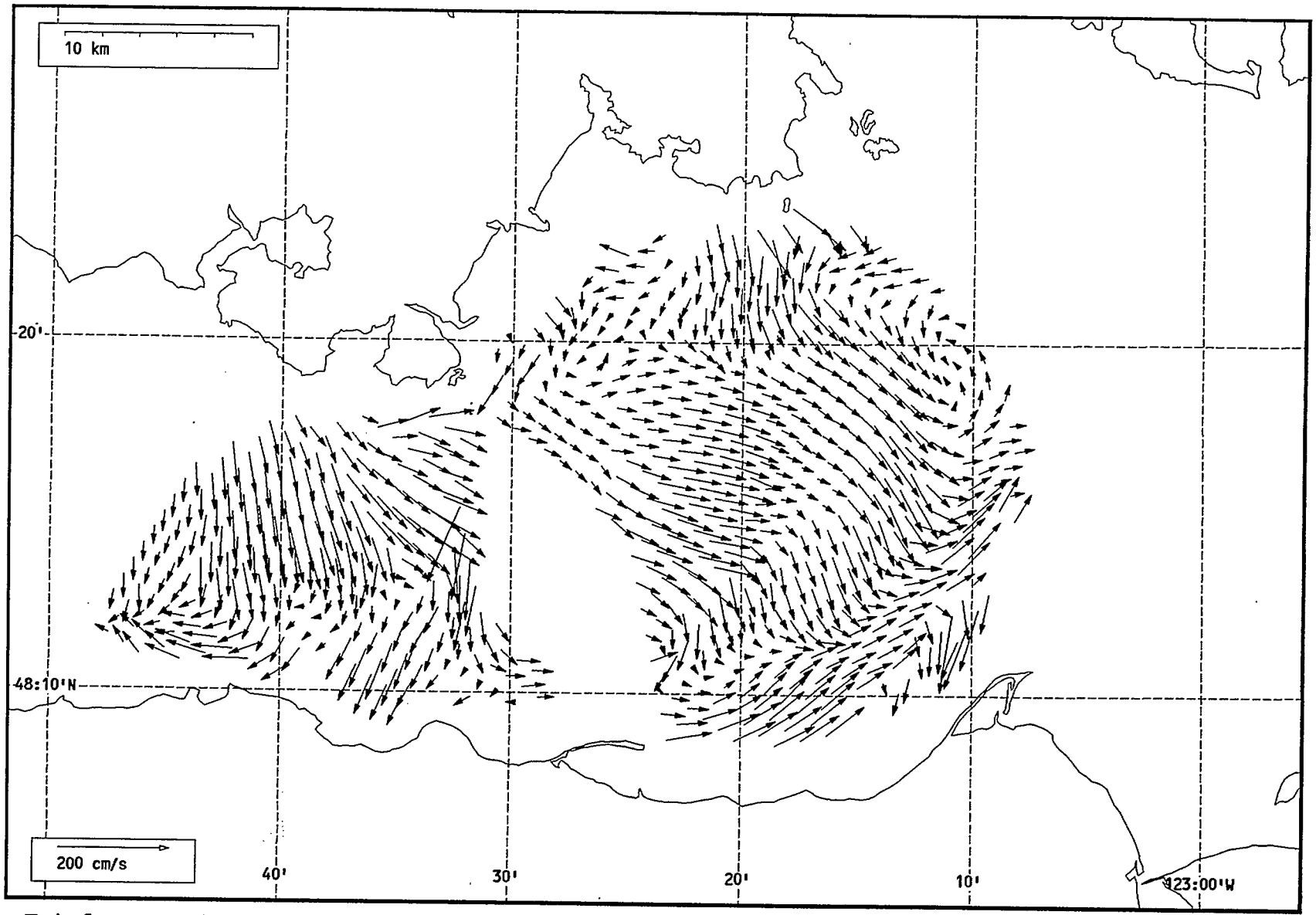

Total current vectors, Juan de Fuca Strait, 1992-07-29 07:00 Z.

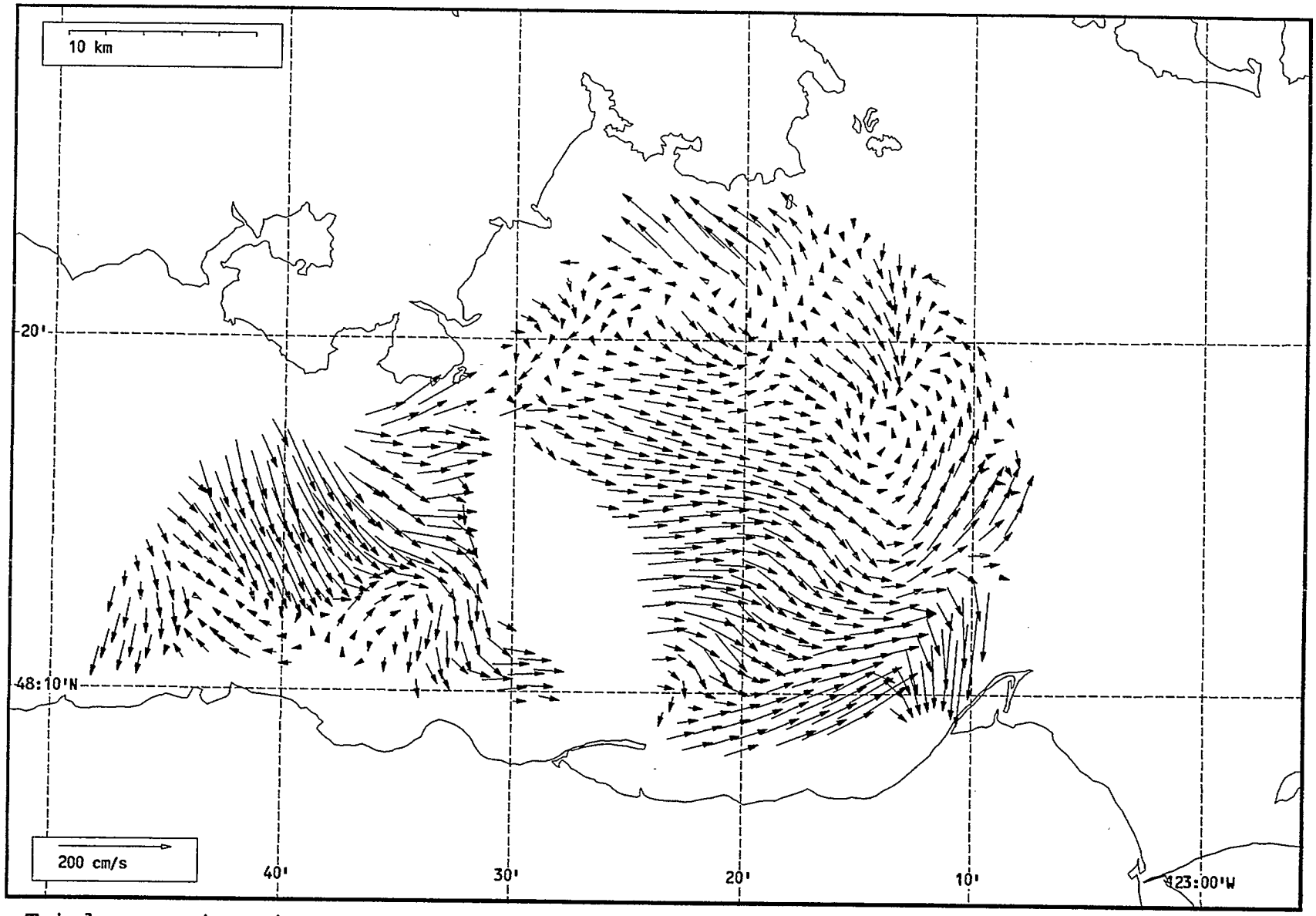

Total current vectors, Juan de Fuca Strait, 1992-07-29 08:00 Z.

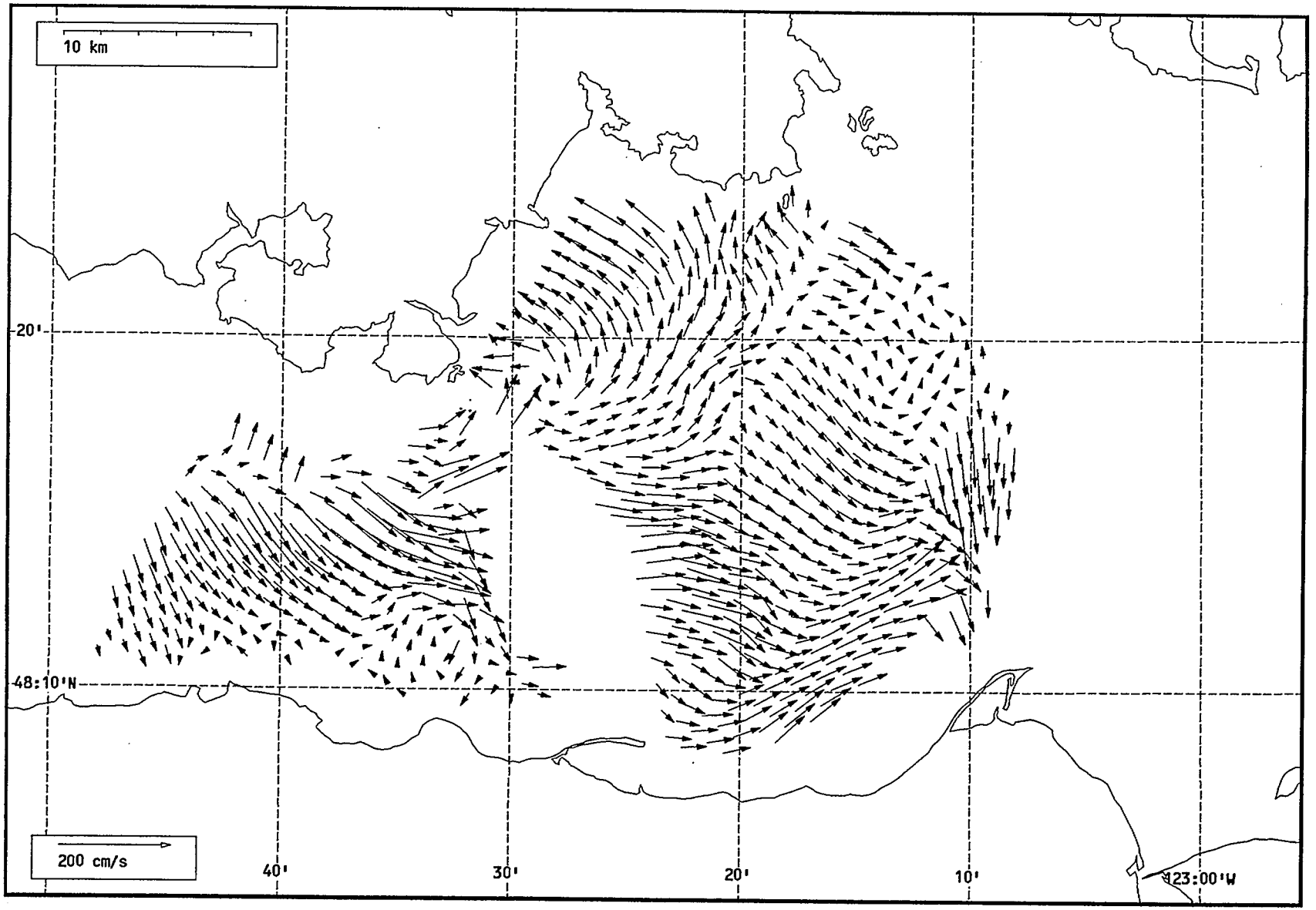

Total current vectors, Juan de Fuca Strait, 1992-07-29 09:00 Z.

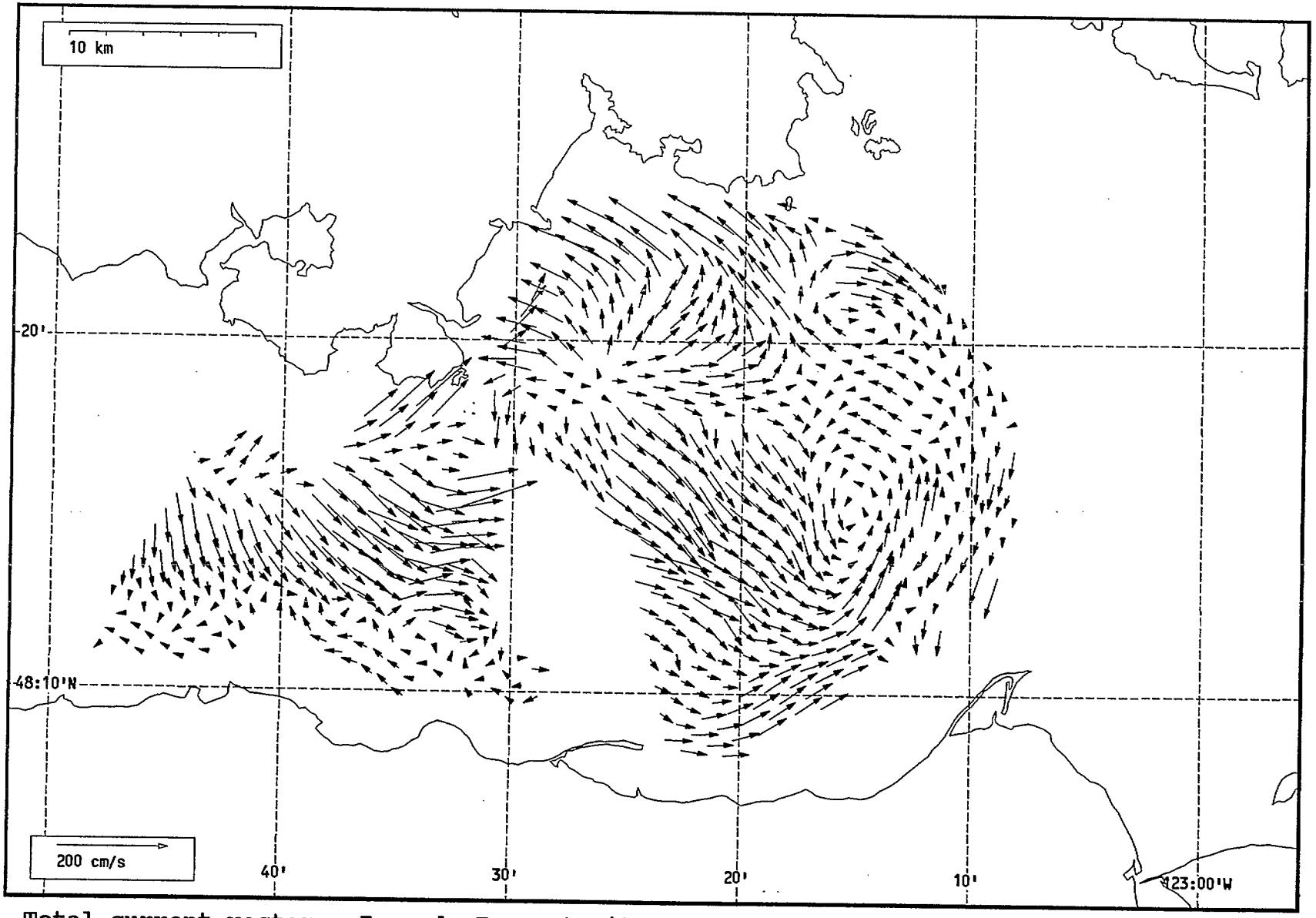

Total current vectors, Juan de Fuca Strait, 1992-07-29 10:00 Z.

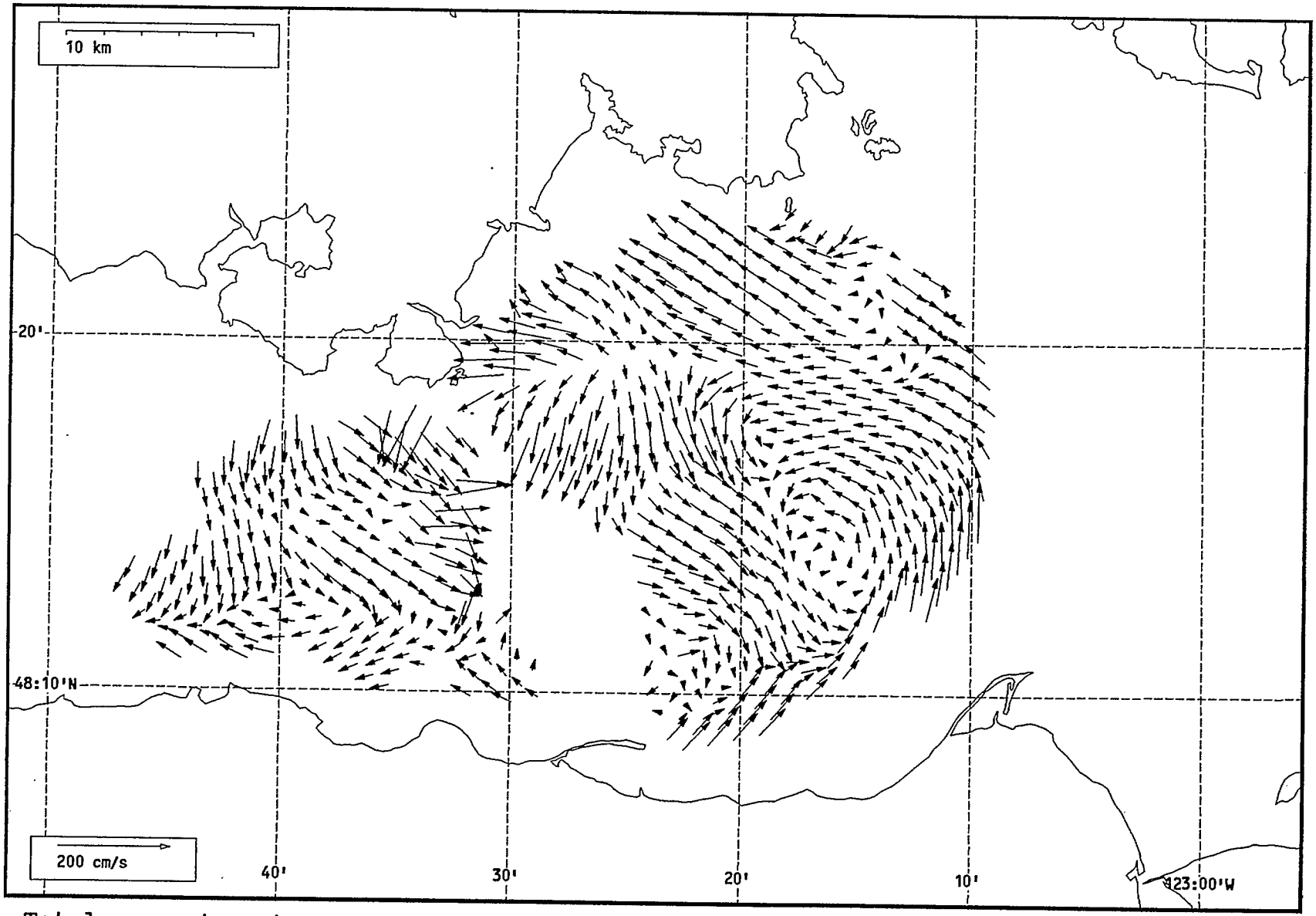

Total current vectors, Juan de Fuca Strait, 1992-07-29 11:00 Z.

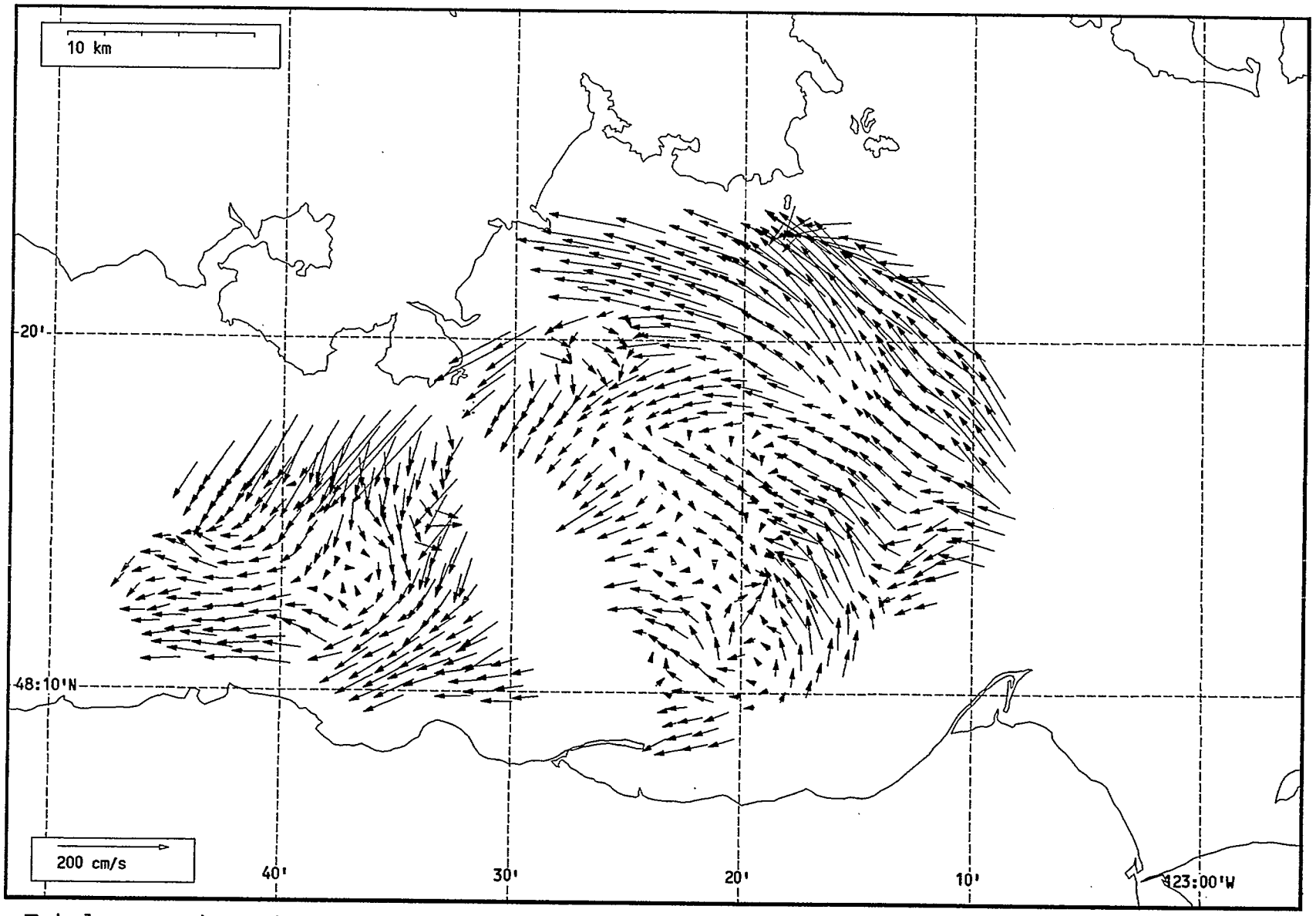

Total current vectors, Juan de Fuca Strait, 1992-07-29 12:00 Z.

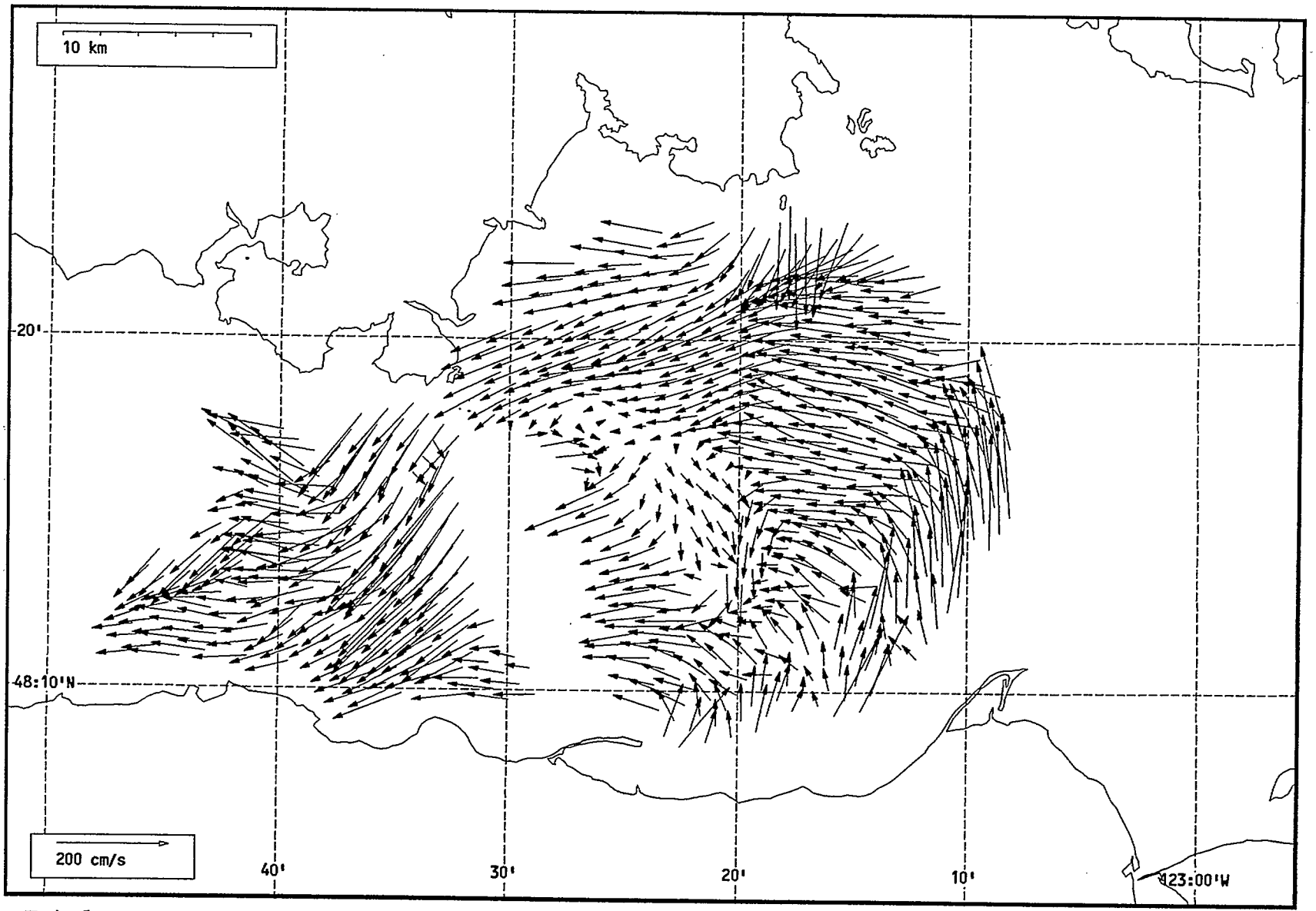

Total current vectors, Juan de Fuca Strait, 1992-07-29 13:00 Z.

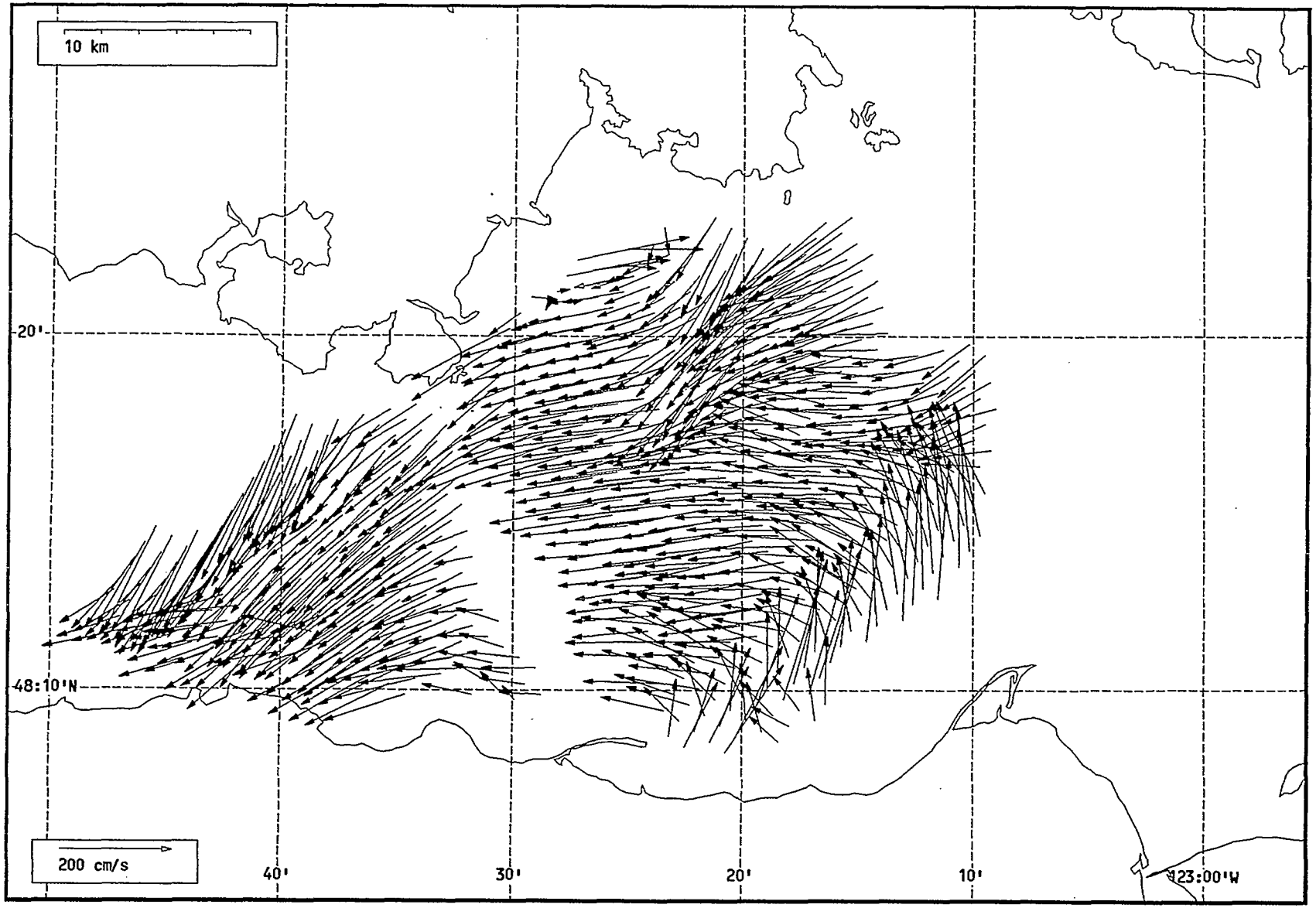

Total current vectors, Juan de Fuca Strait, 1992-07-29 14:00 Z.

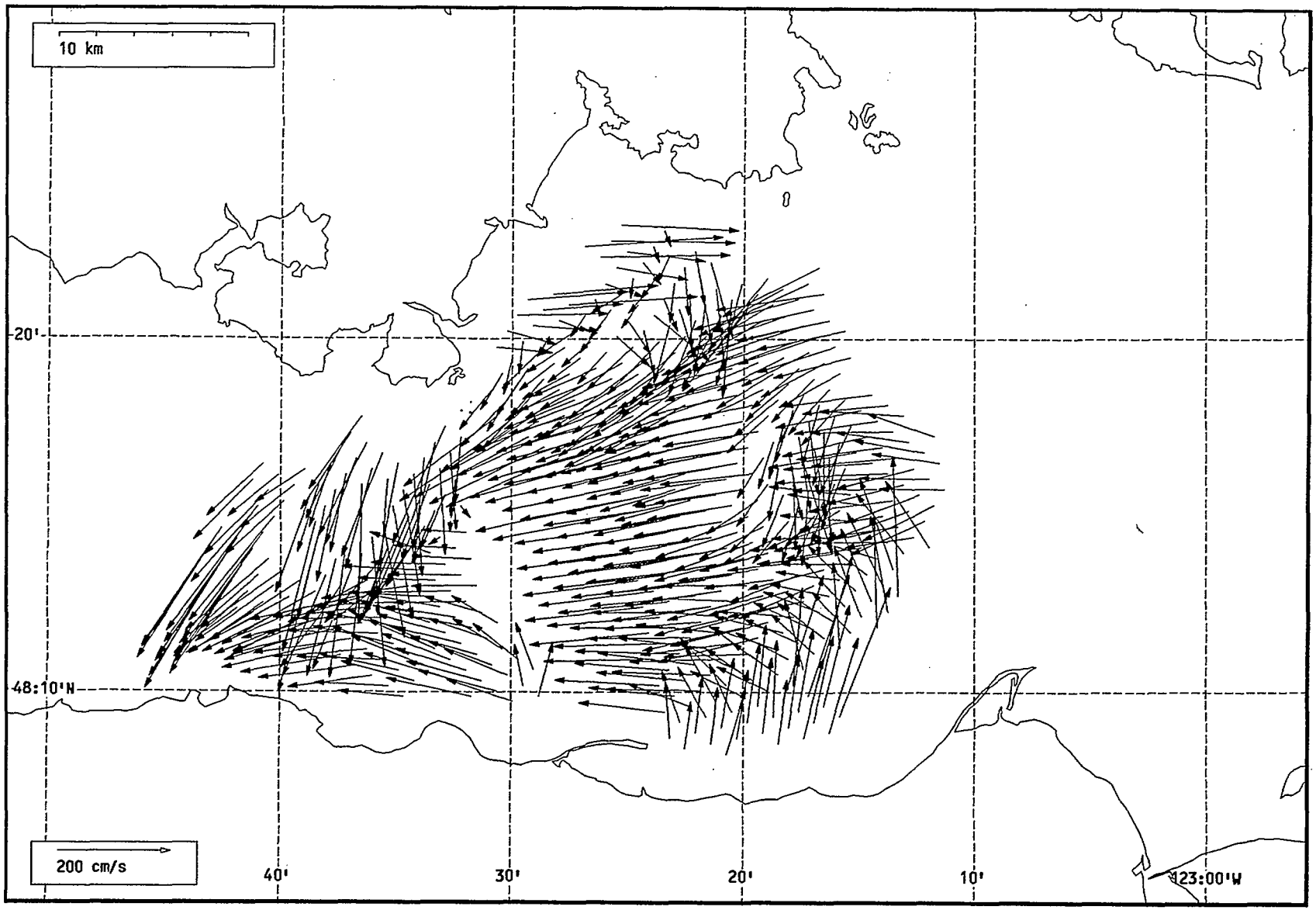

Total current vectors, Juan de Fuca Strait, 1992-07-29 15:00 Z.

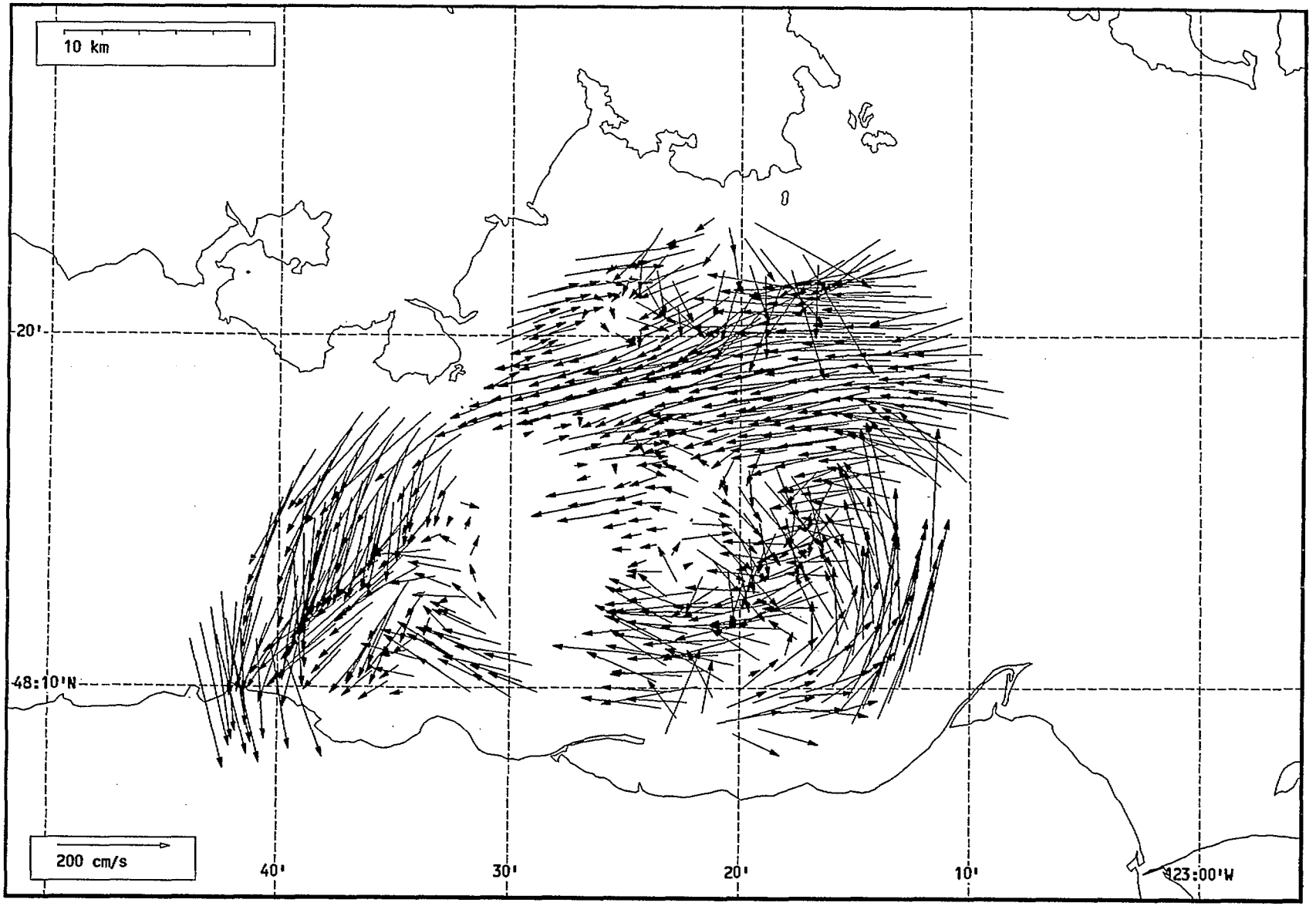

Total current vectors, Juan de Fuca Strait, 1992-07-29 16:00 Z.

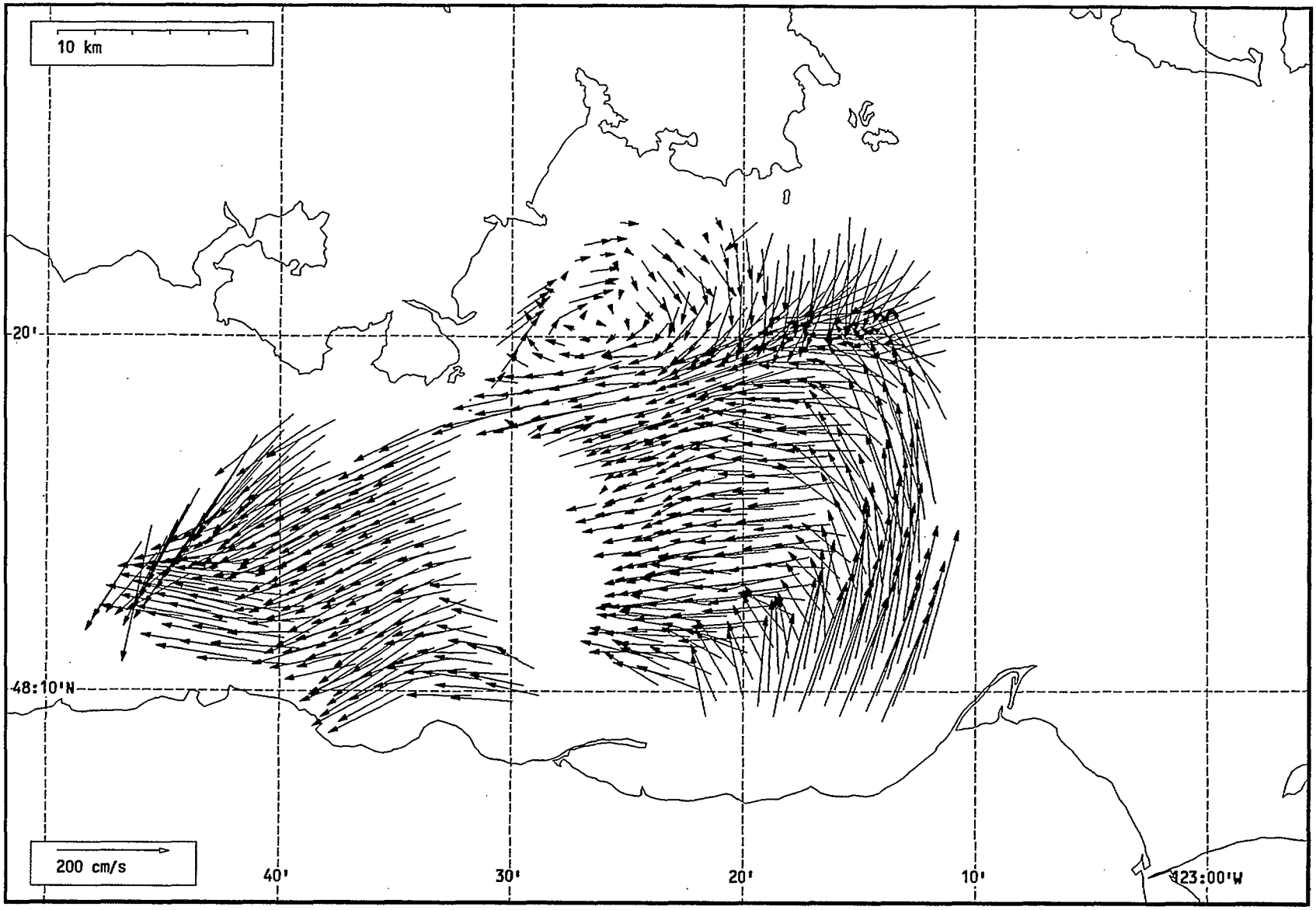

Total current vectors, Juan de Fuca Strait, 1992-07-29 17:00 Z.

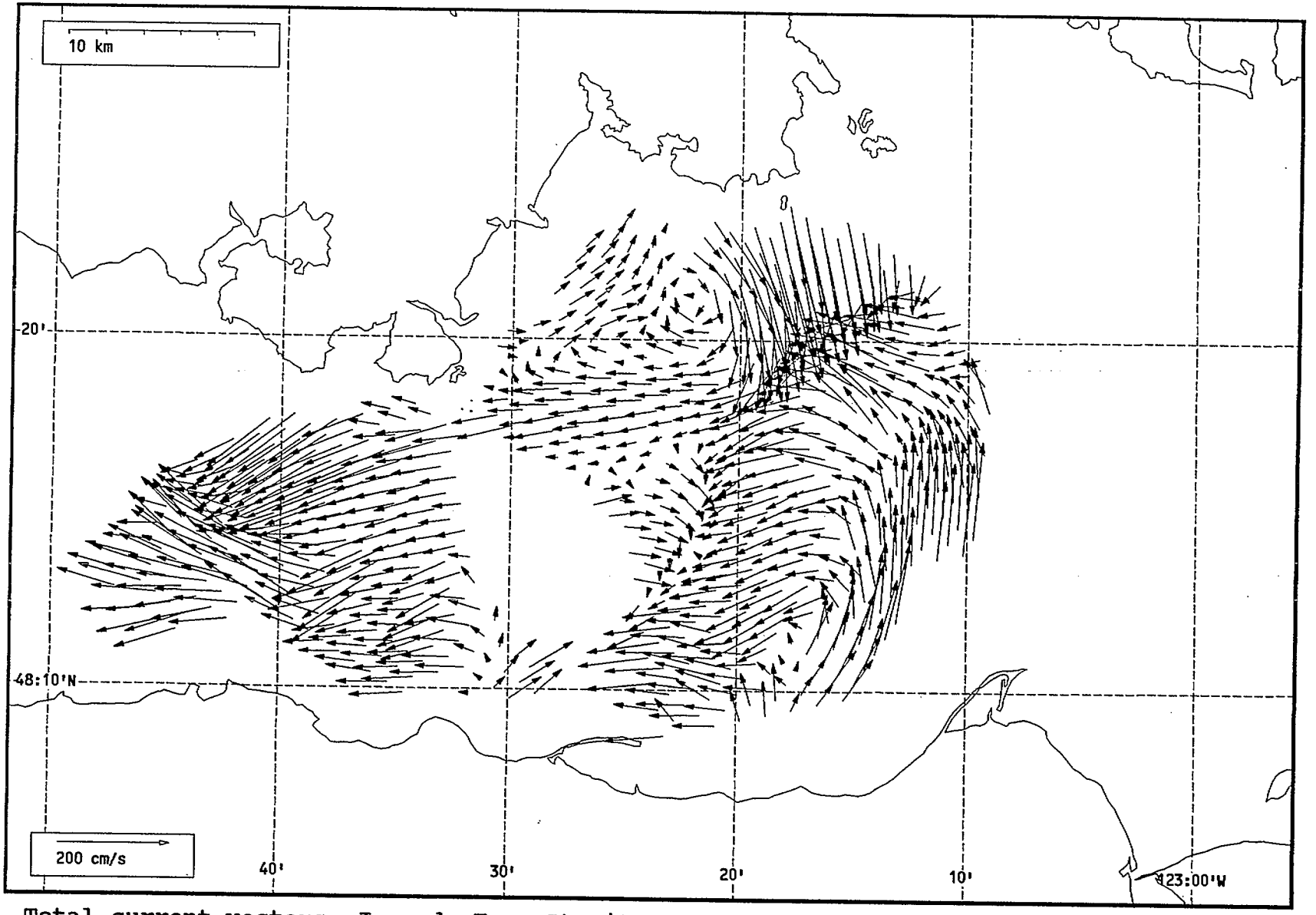

Total current vectors, Juan de Fuca Strait, 1992-07-29 18:00 Z.

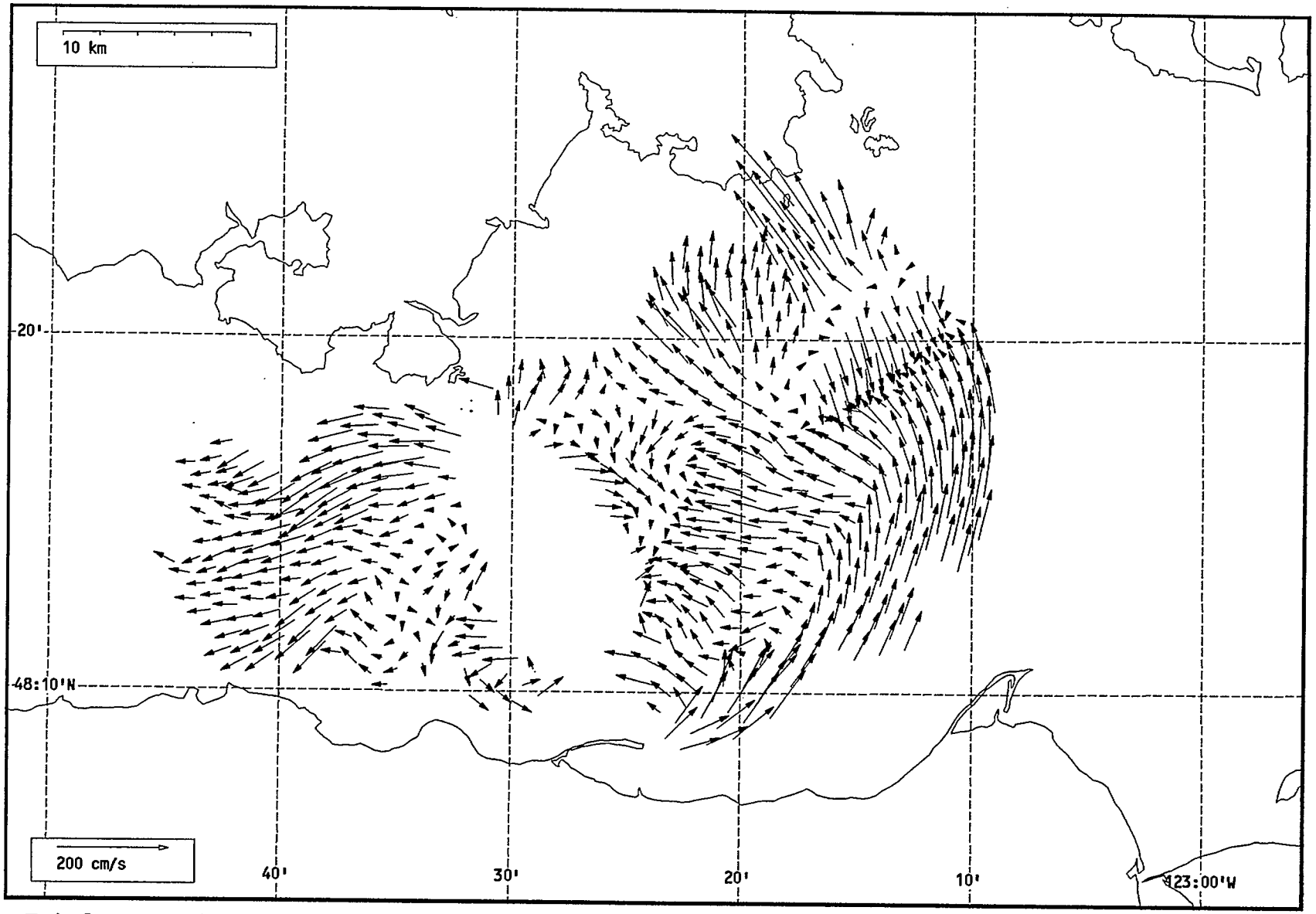

Total current vectors, Juan de Fuca Strait, 1992-07-29 19:00 Z.

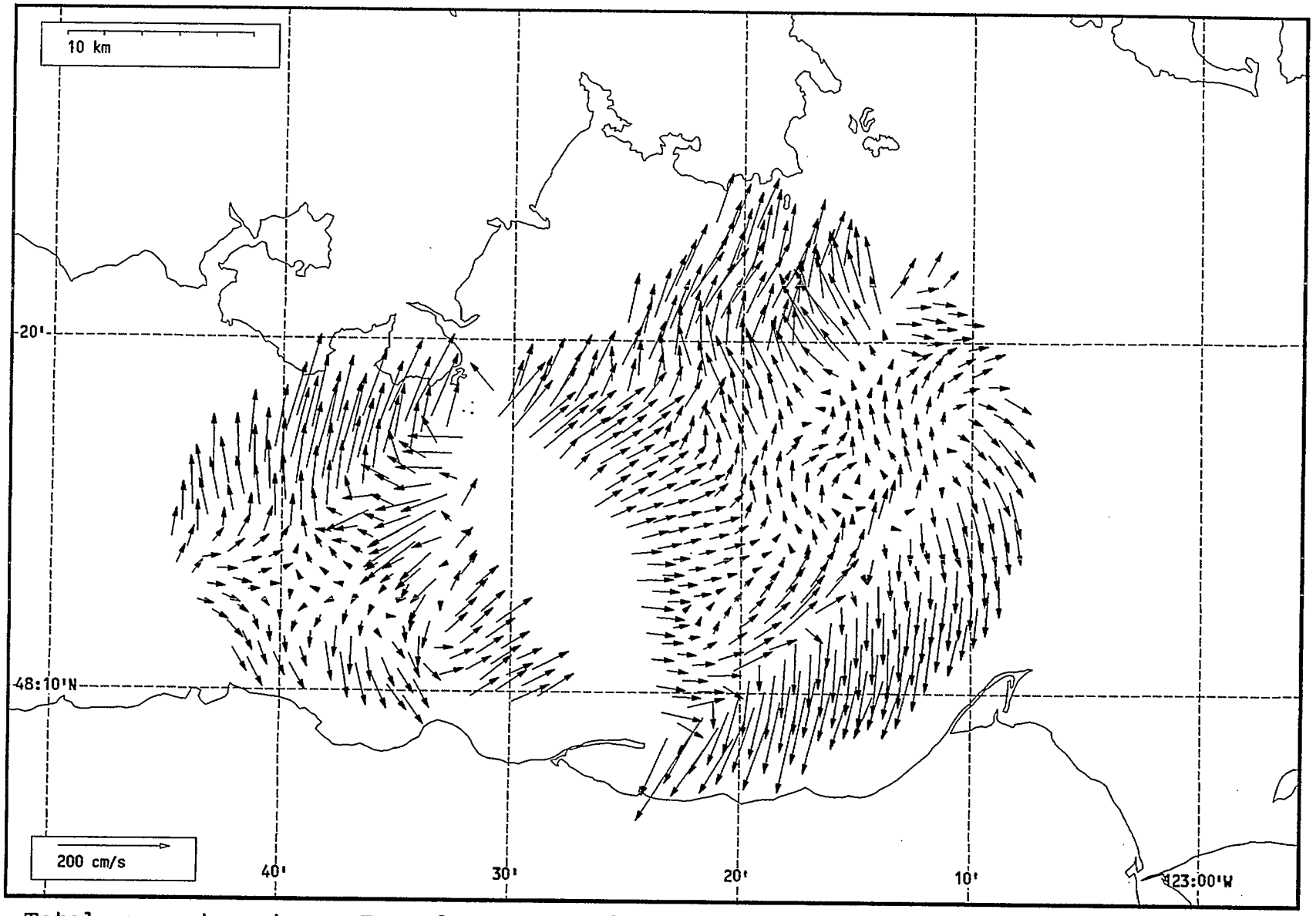

Total current vectors, Juan de Fuca Strait, 1992-07-29 20:00 Z.

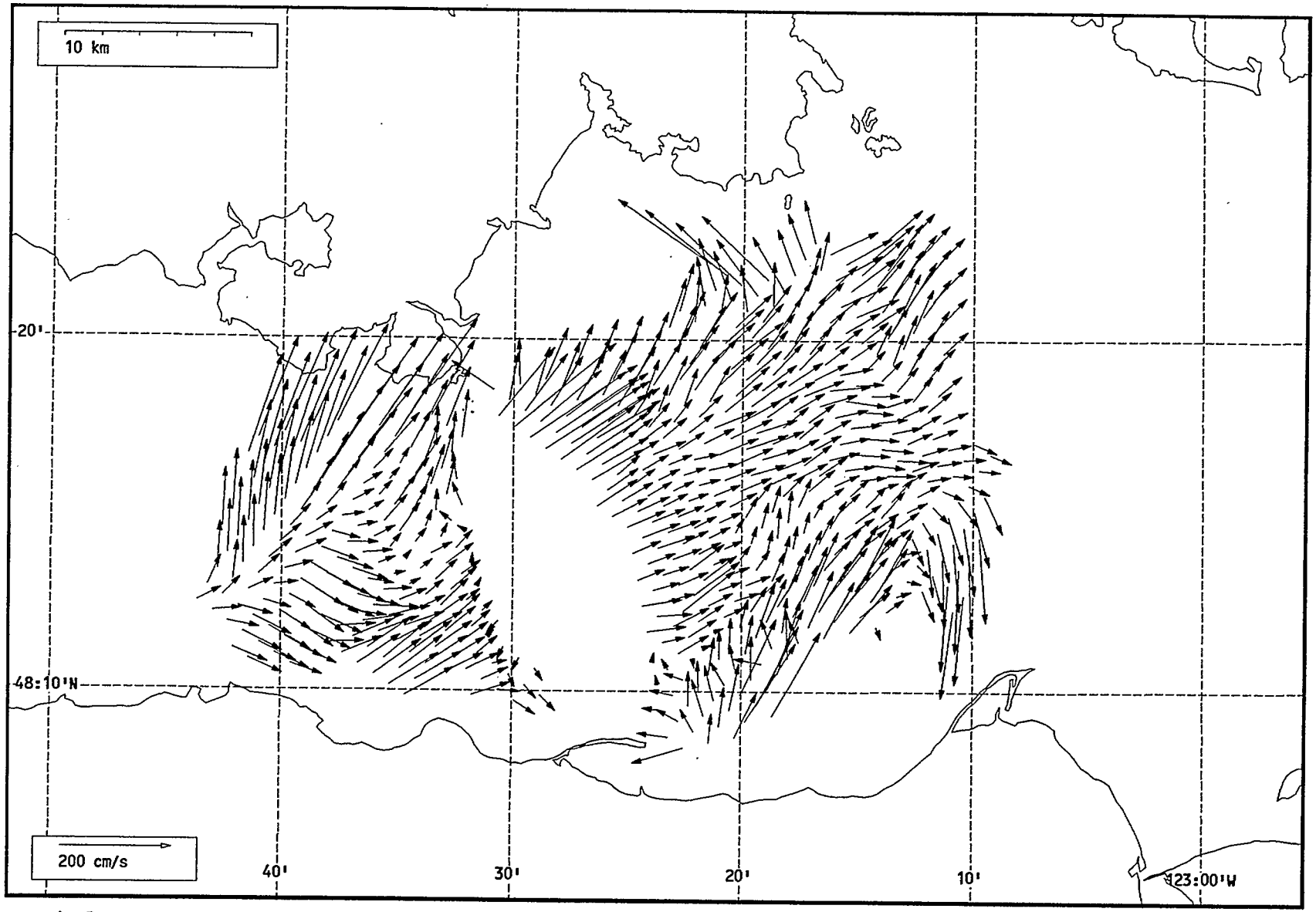

Total current vectors, Juan de Fuca Strait, 1992-07-29 21:00 Z.

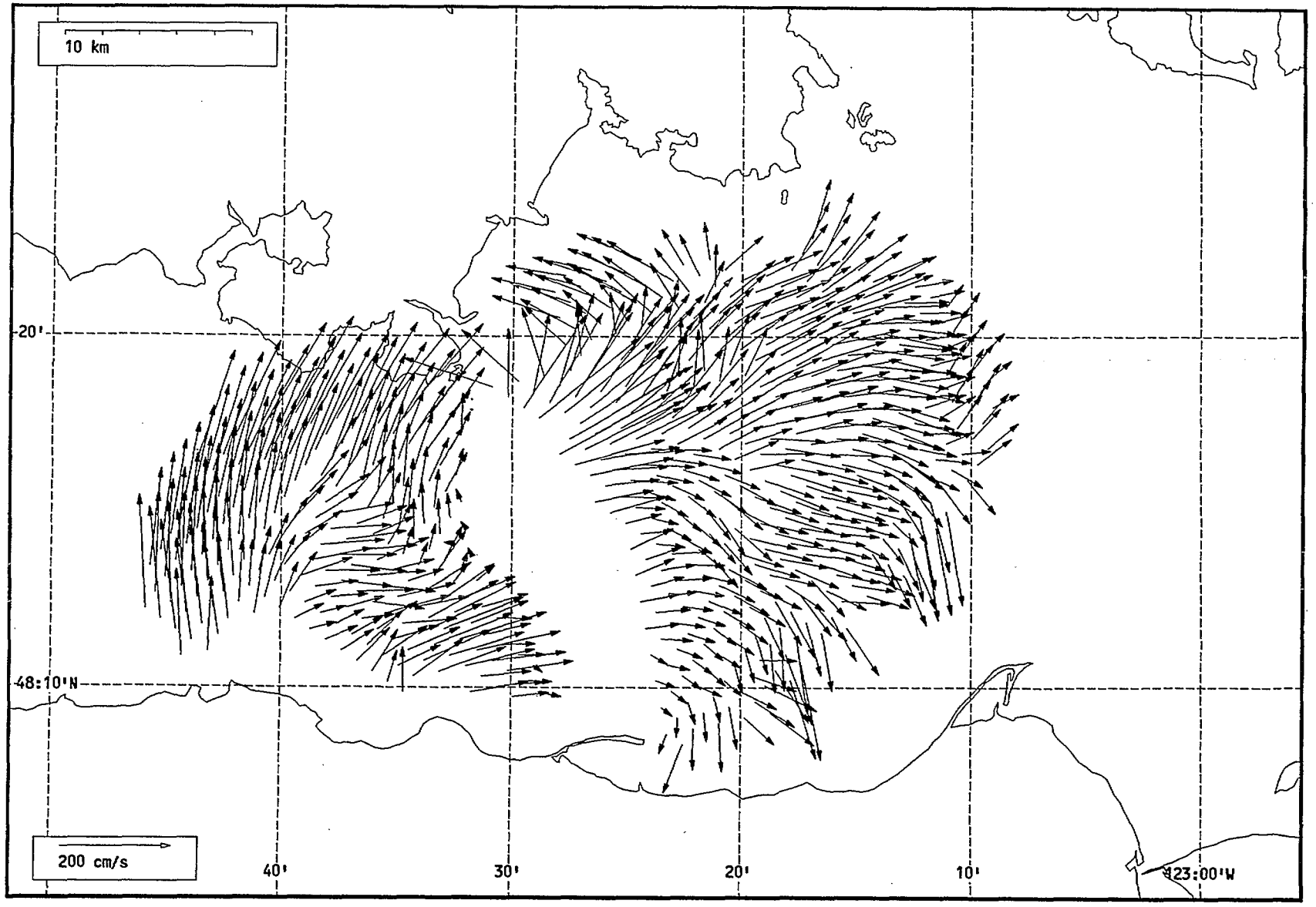

Total current vectors, Juan de Fuca Strait, 1992-07-29 22:00 Z.

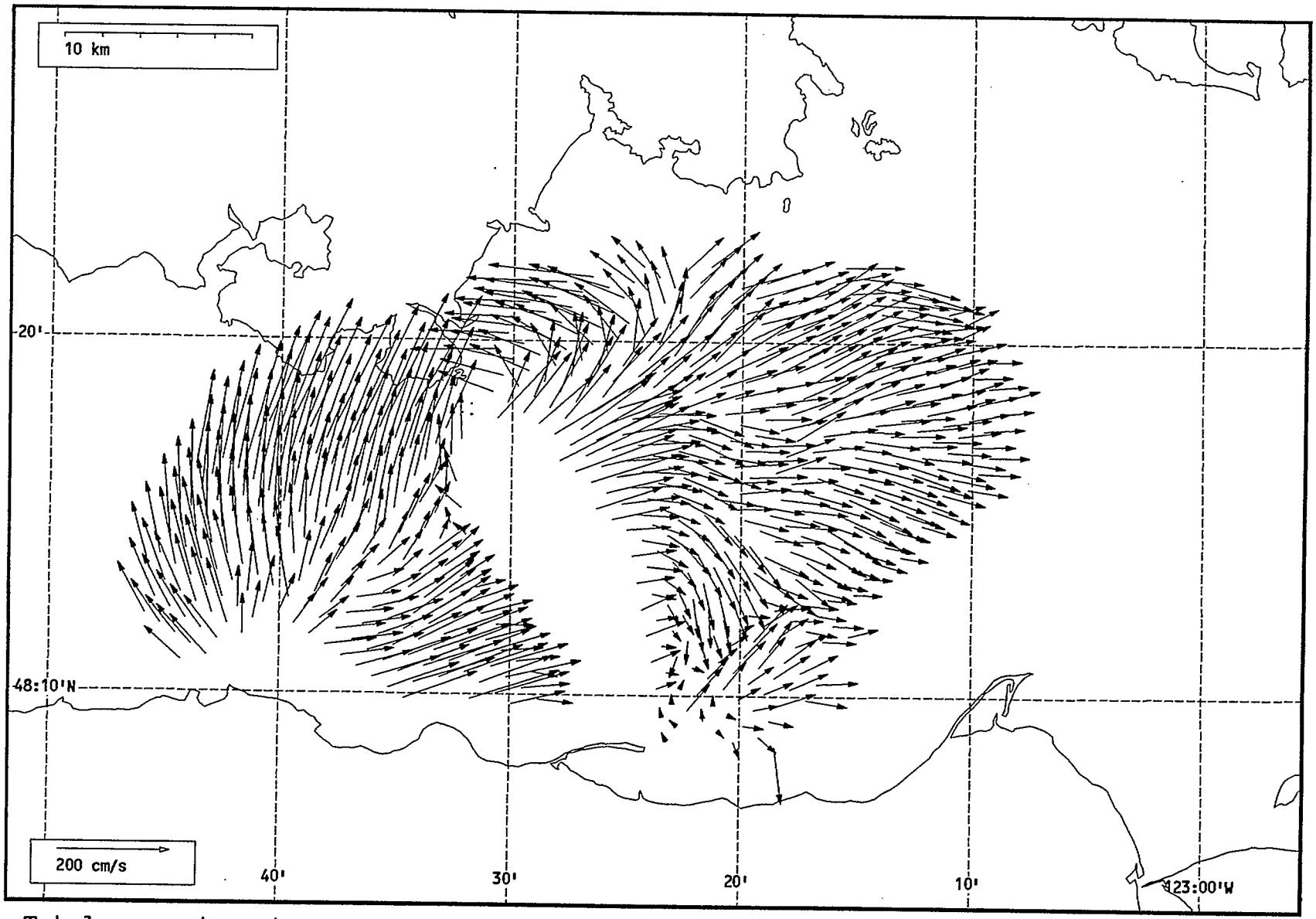

Total current vectors, Juan de Fuca Strait, 1992-07-29 23:00 Z.

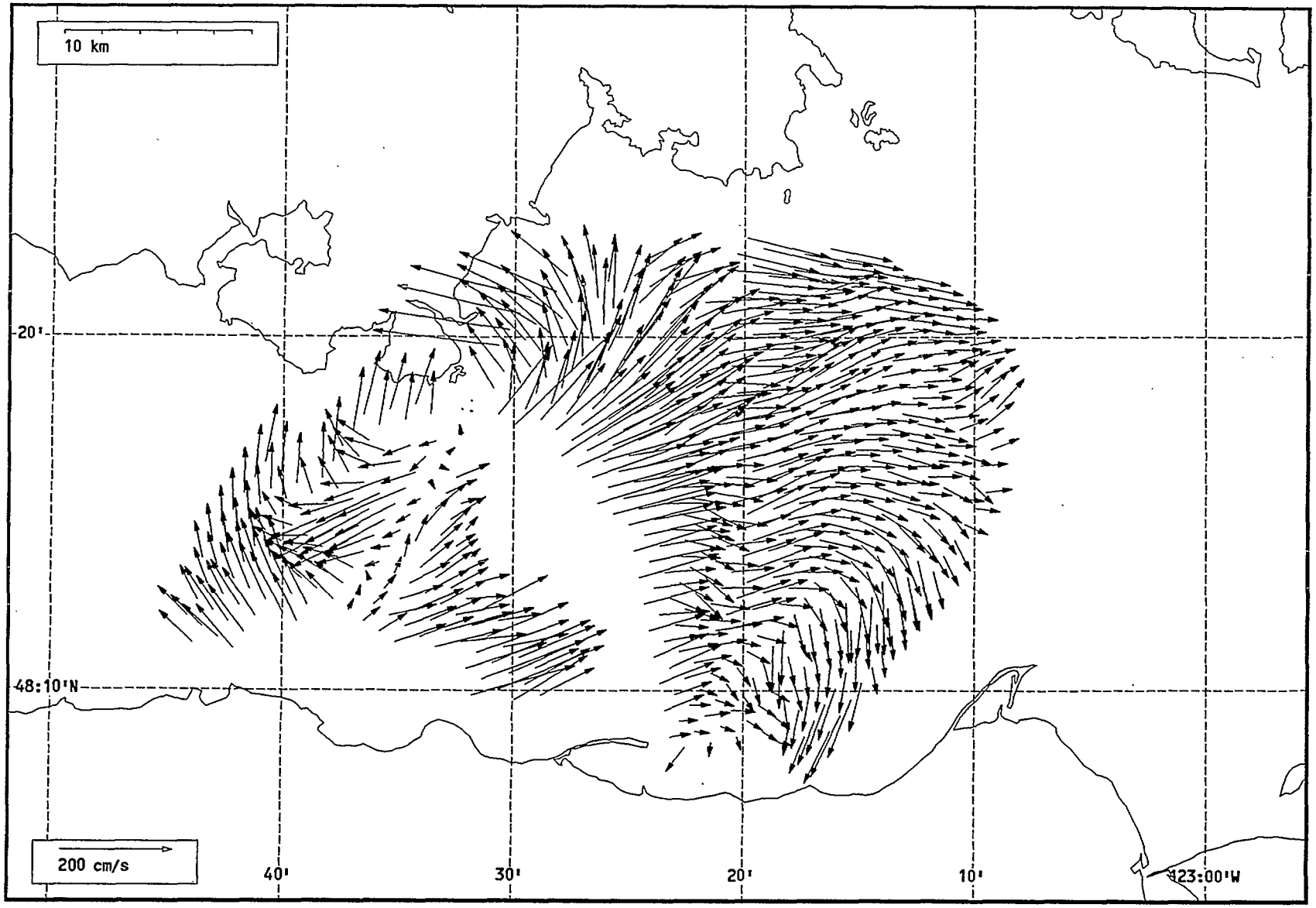

Total current vectors, Juan de Fuca Strait, 1992-07-30 00:00 Z.

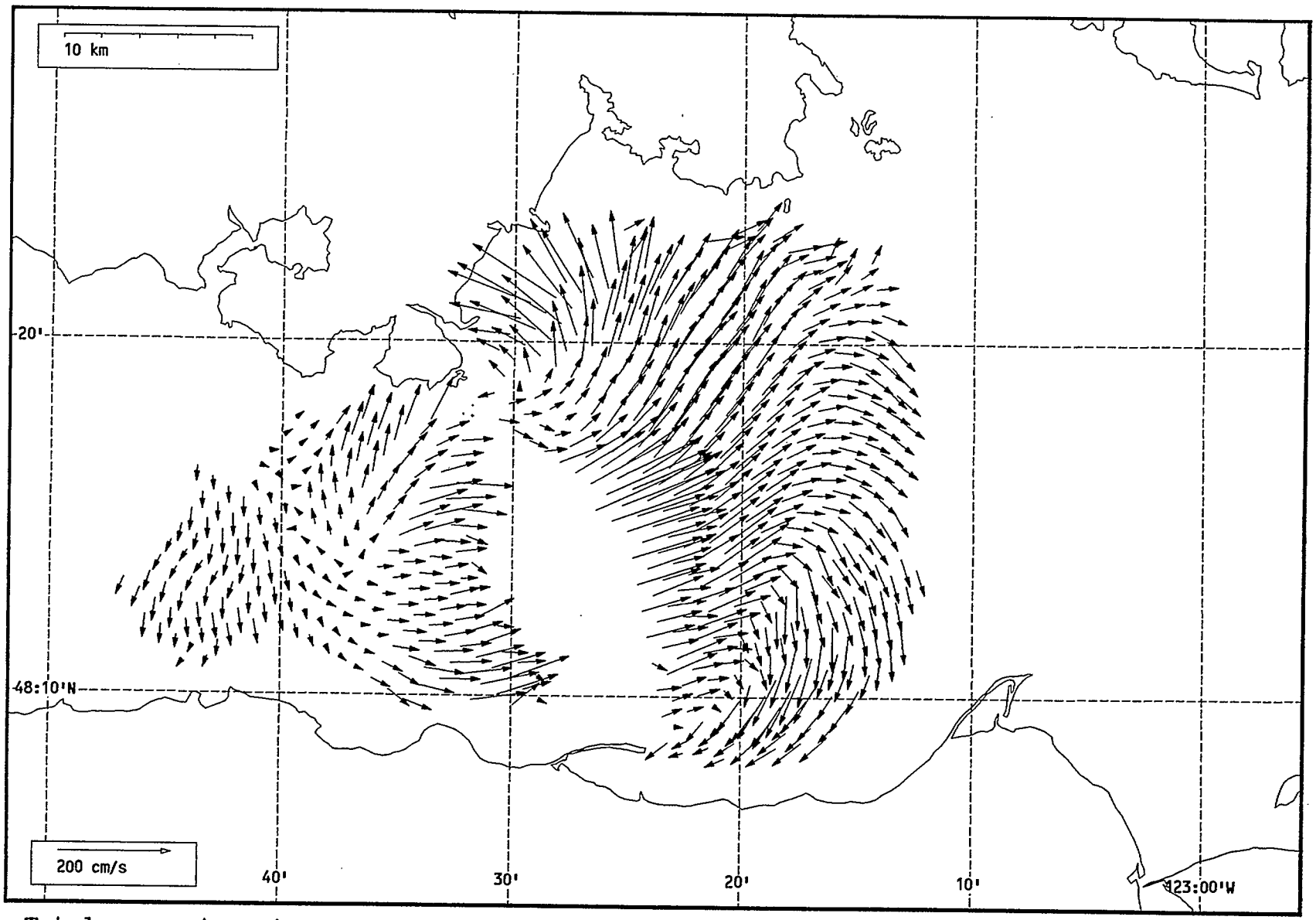

Total current vectors, Juan de Fuca Strait, 1992-07-30 01:00 Z.

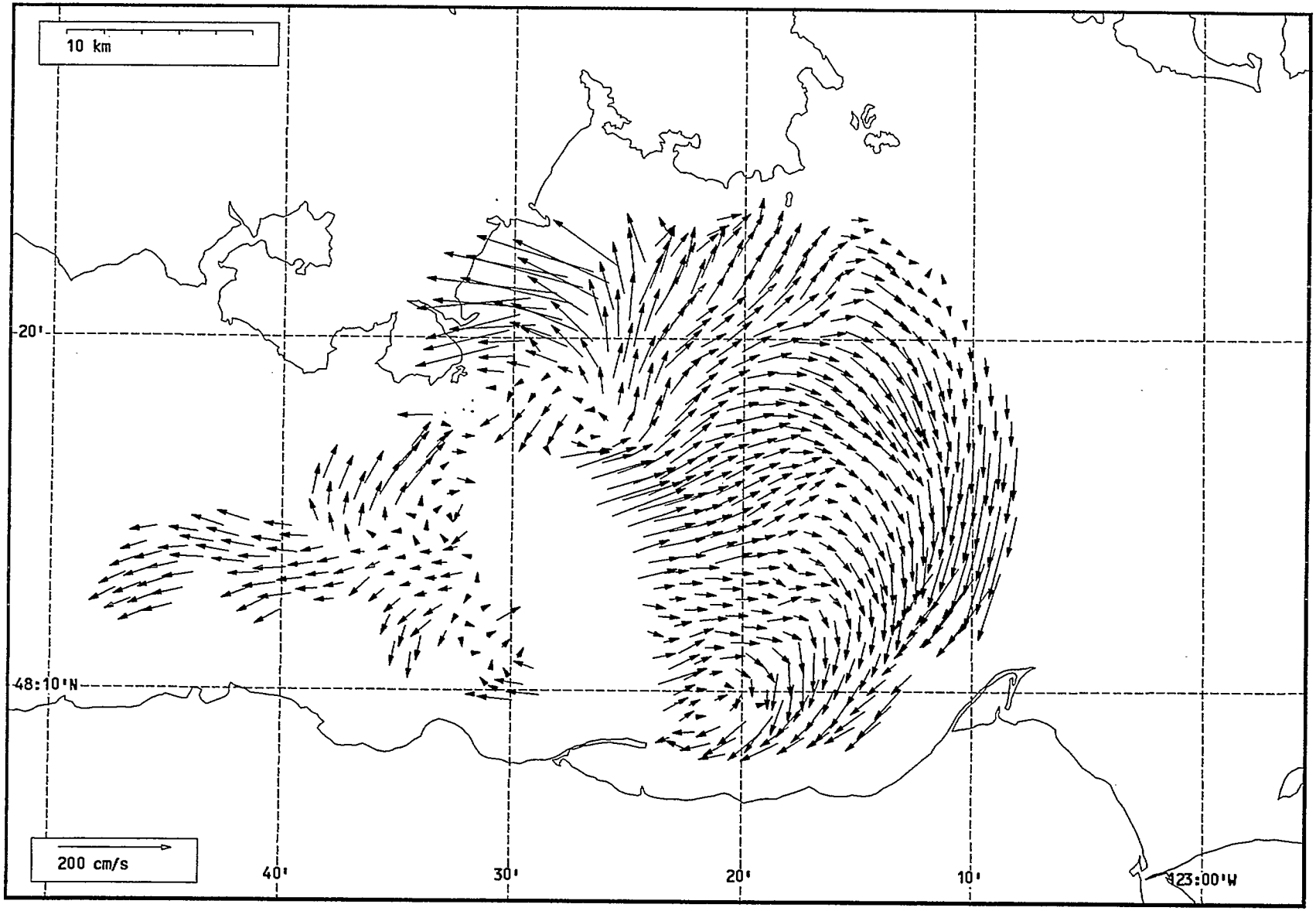

Total current vectors, Juan de Fuca Strait, 1992-07-30 02:00 Z.

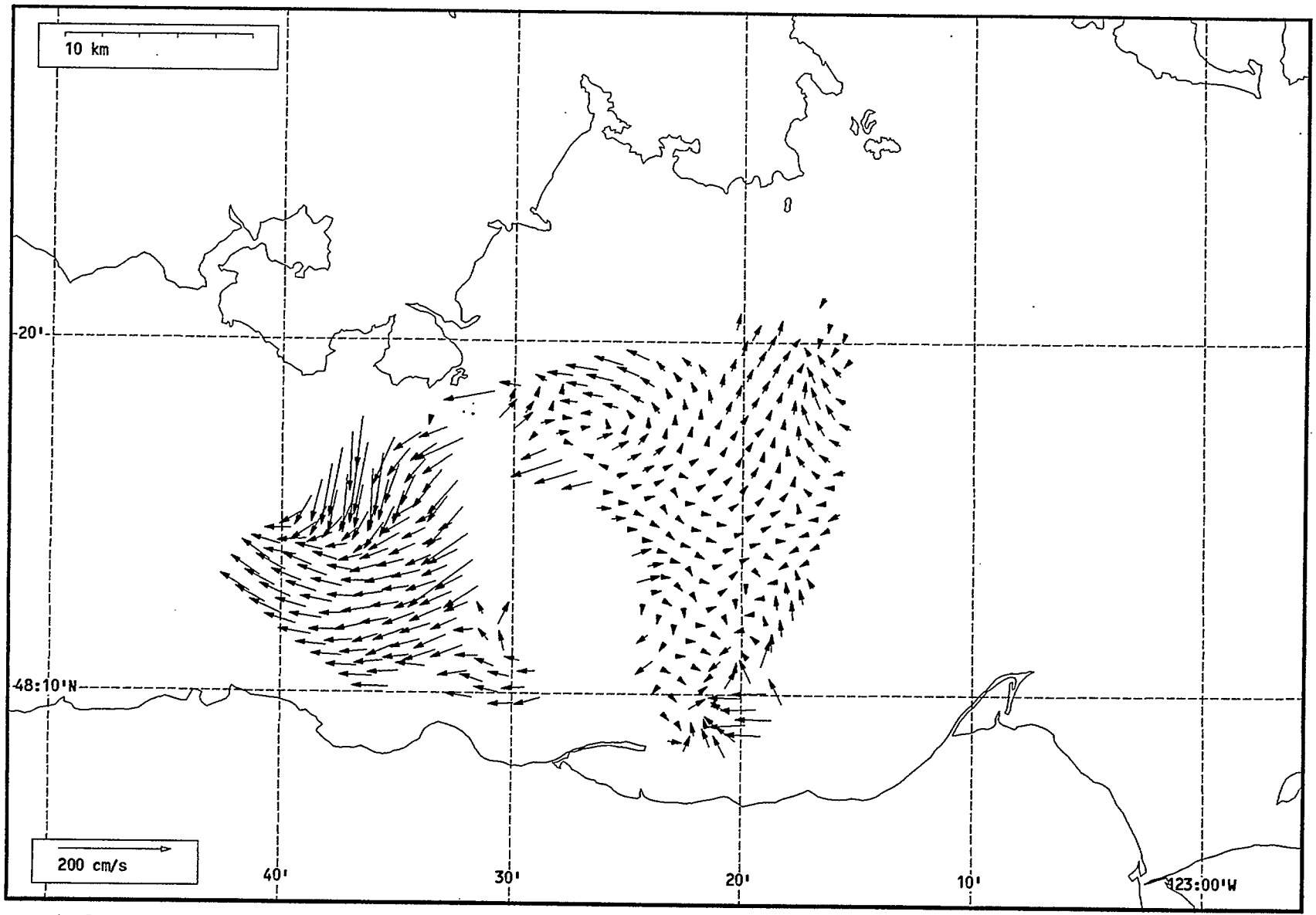

Total current vectors, Juan de Fuca Strait, 1992-07-30 03:00 Z.

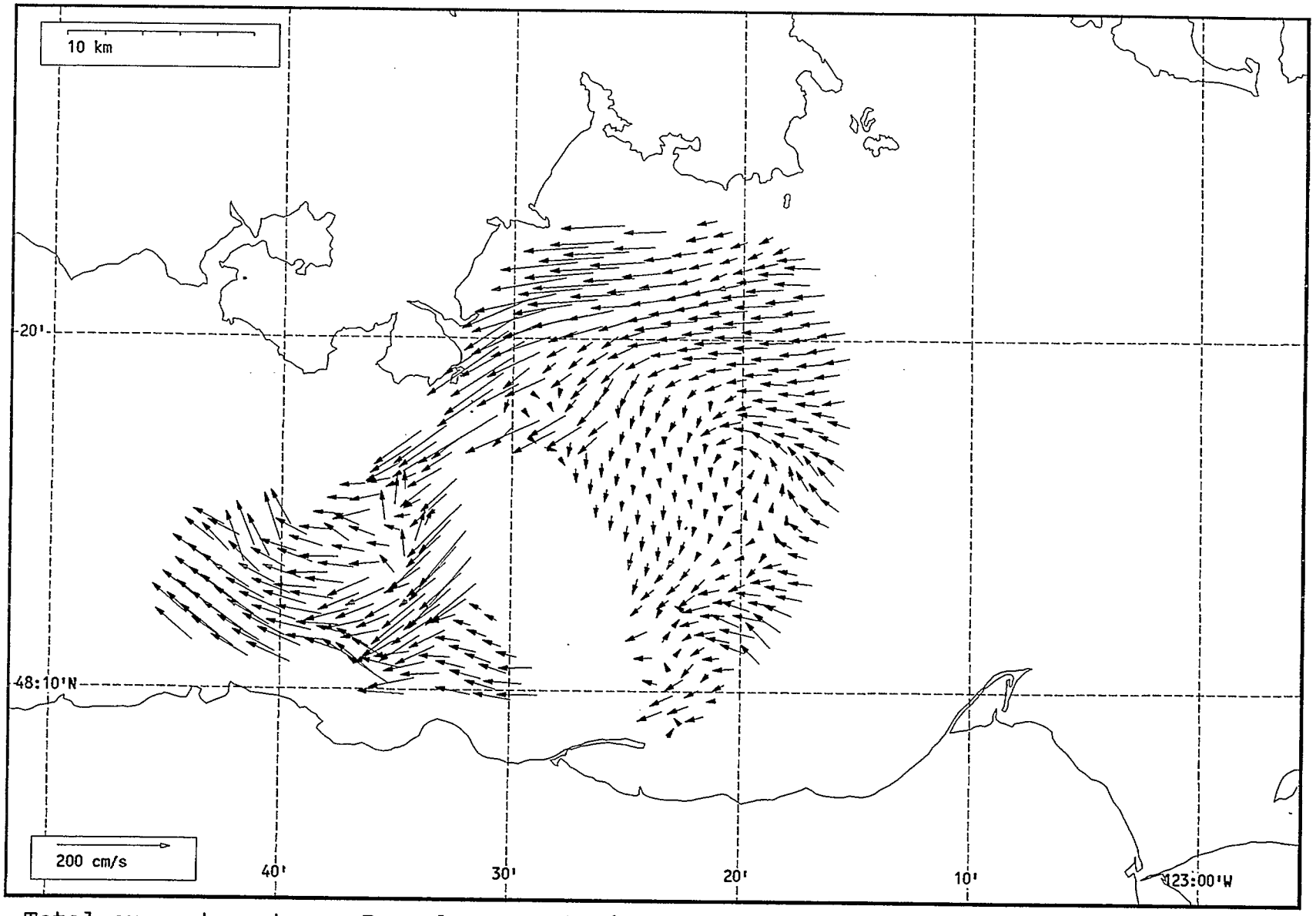

Total current vectors, Juan de Fuca Strait, 1992-07-30 04:00 Z.

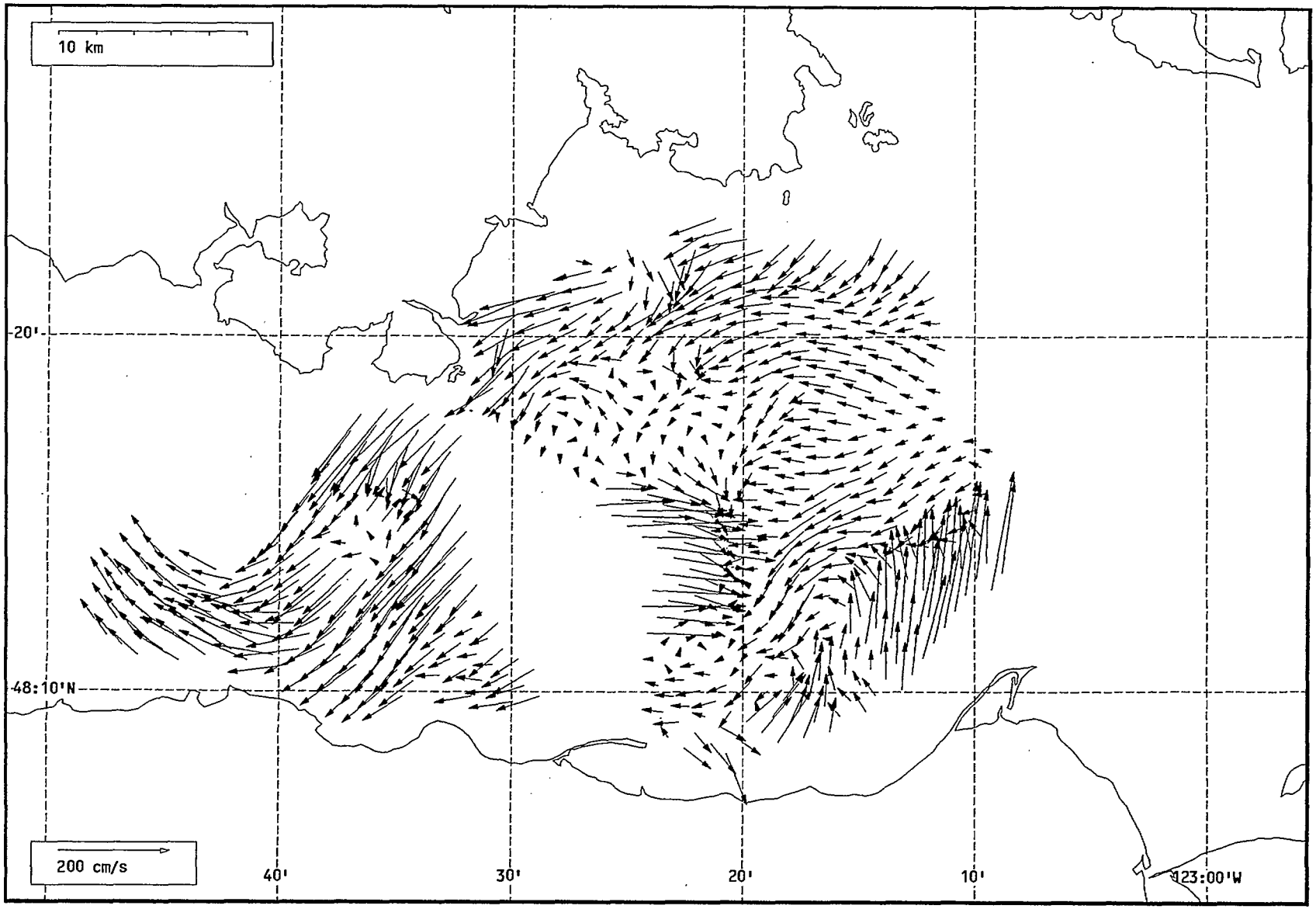

Total current vectors, Juan de Fuca Strait, 1992-07-30 05:00 Z.

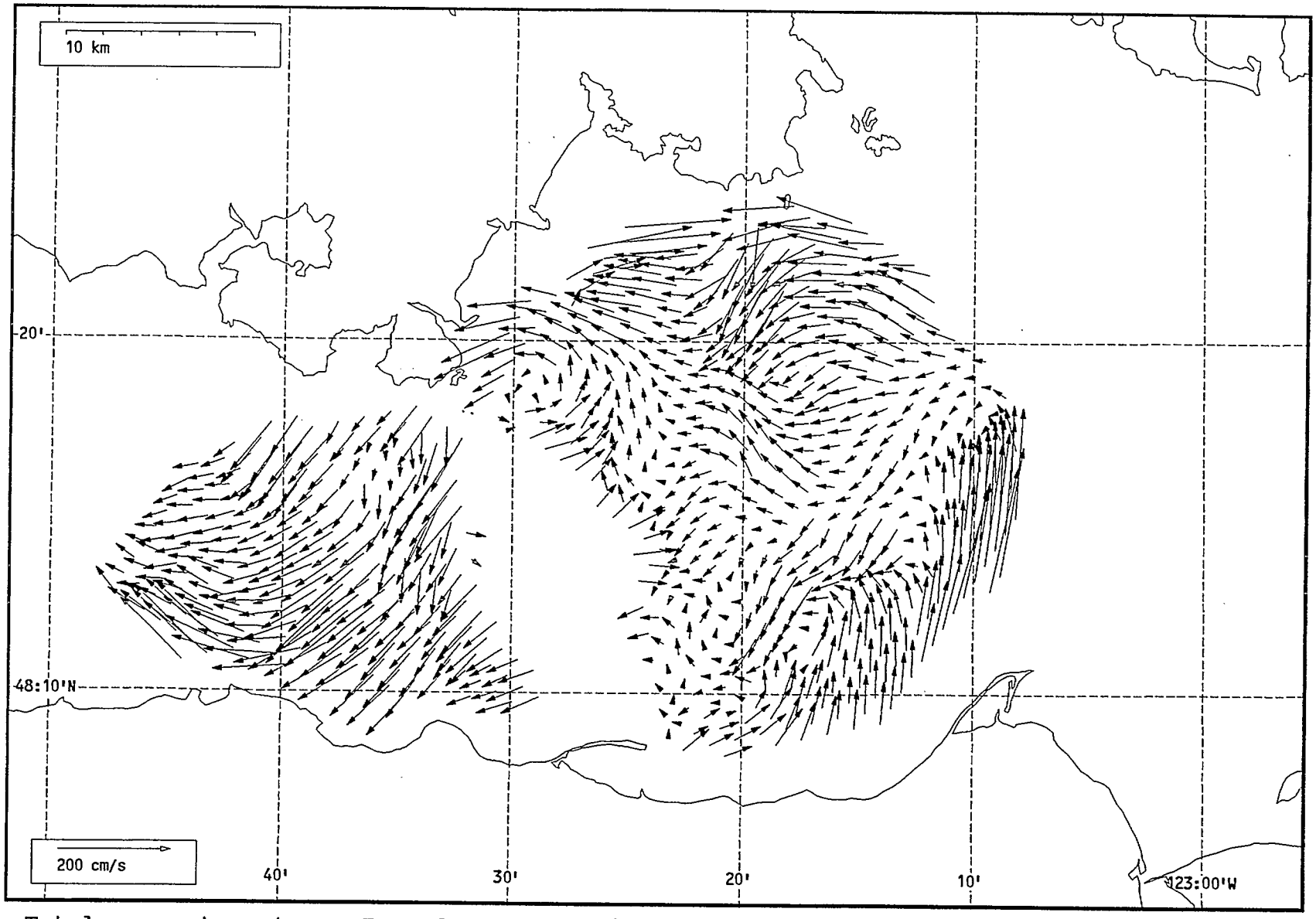

Total current vectors, Juan de Fuca Strait, 1992-07-30 06:00 Z.

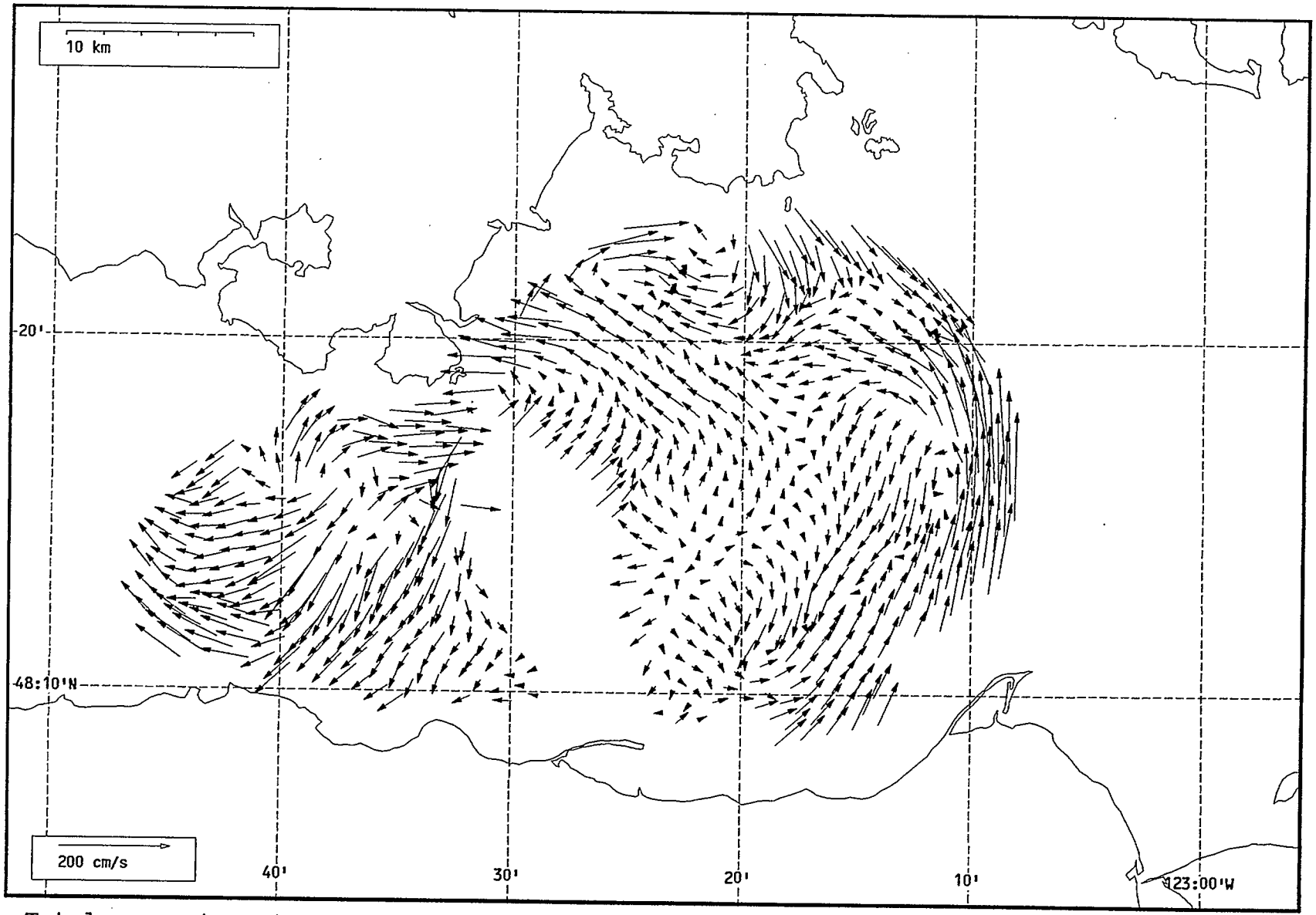

Total current vectors, Juan de Fuca Strait, 1992-07-30 07:00 Z.

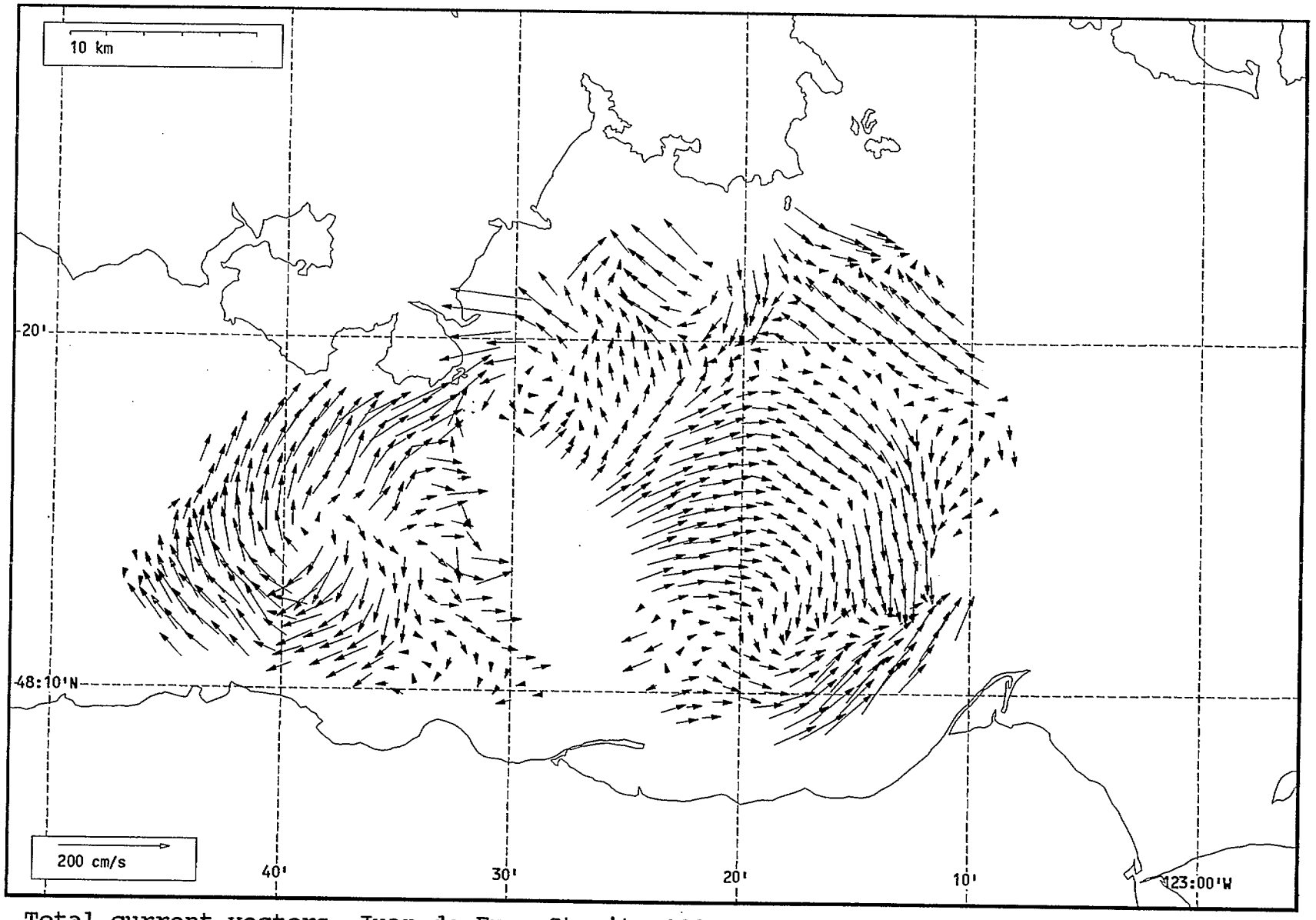

Total current vectors, Juan de Fuca Strait, 1992-07-30 08:00 Z.

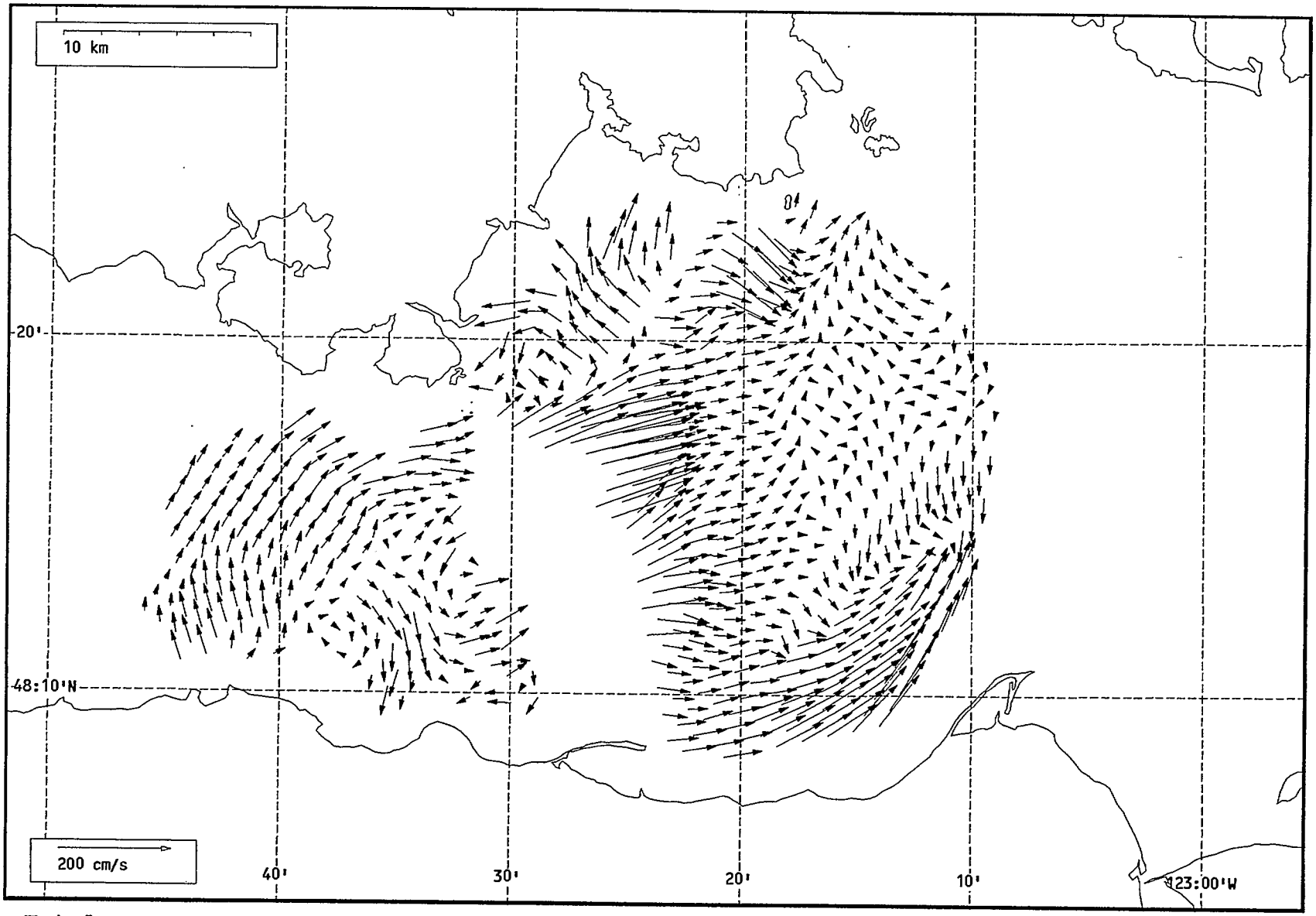

Total current vectors, Juan de Fuca Strait, 1992-07-30 09:00 Z.

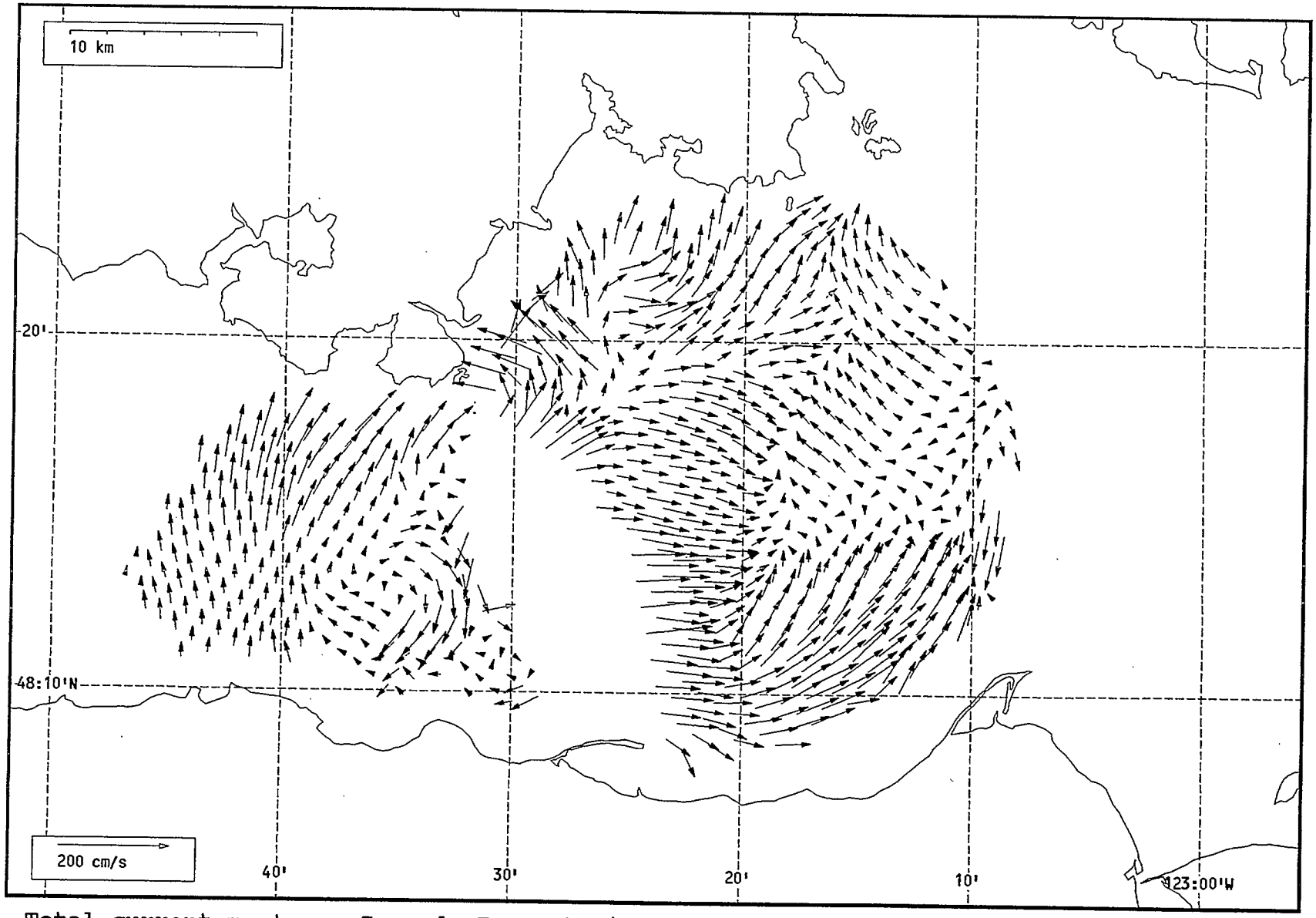

Total current vectors, Juan de Fuca Strait, 1992-07-30 10:00 Z.

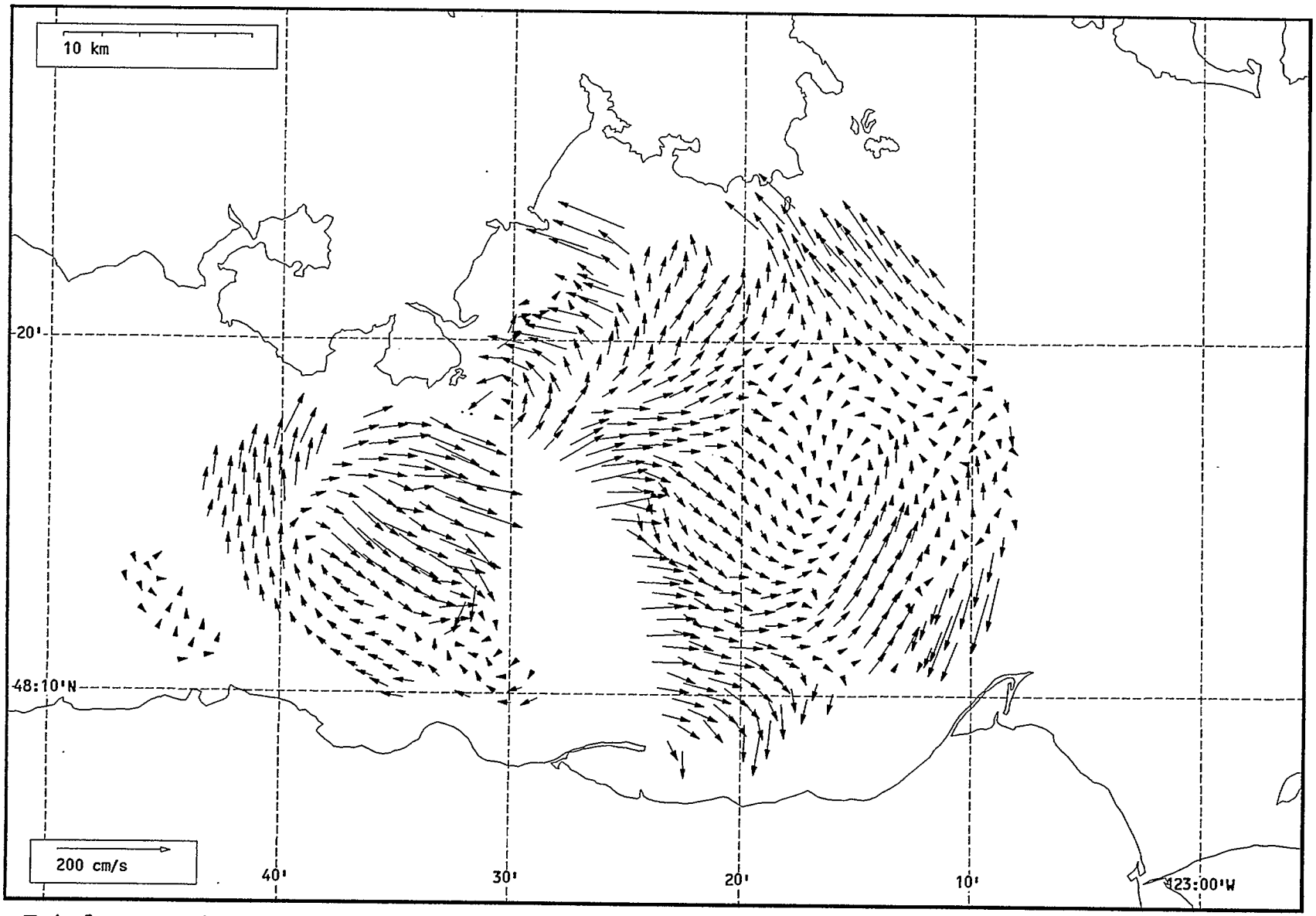

Total current vectors, Juan de Fuca Strait, 1992-07-30 11:00 Z..

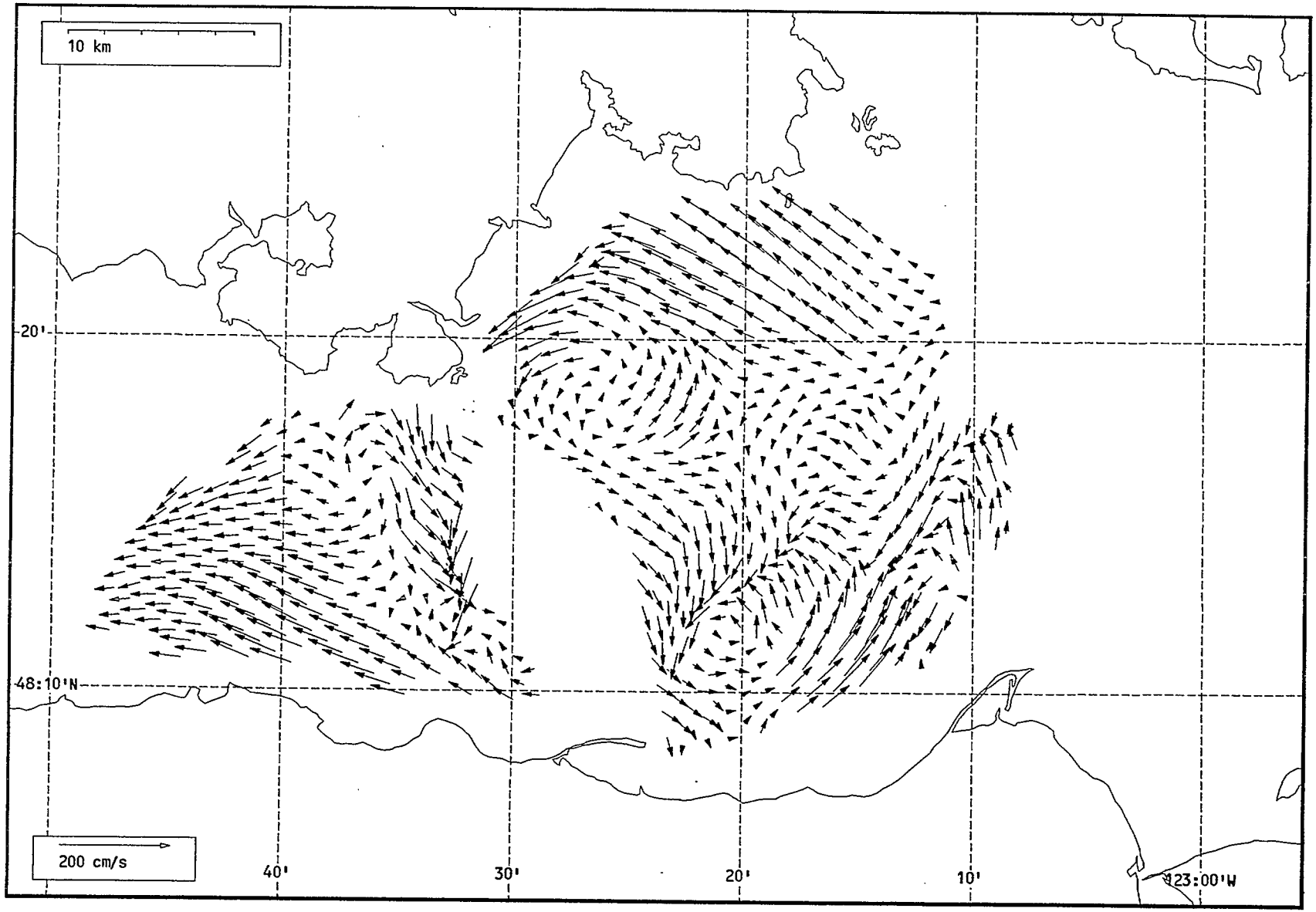

Total current vectors, Juan de Fuca Strait, 1992-07-30 12:00 Z.

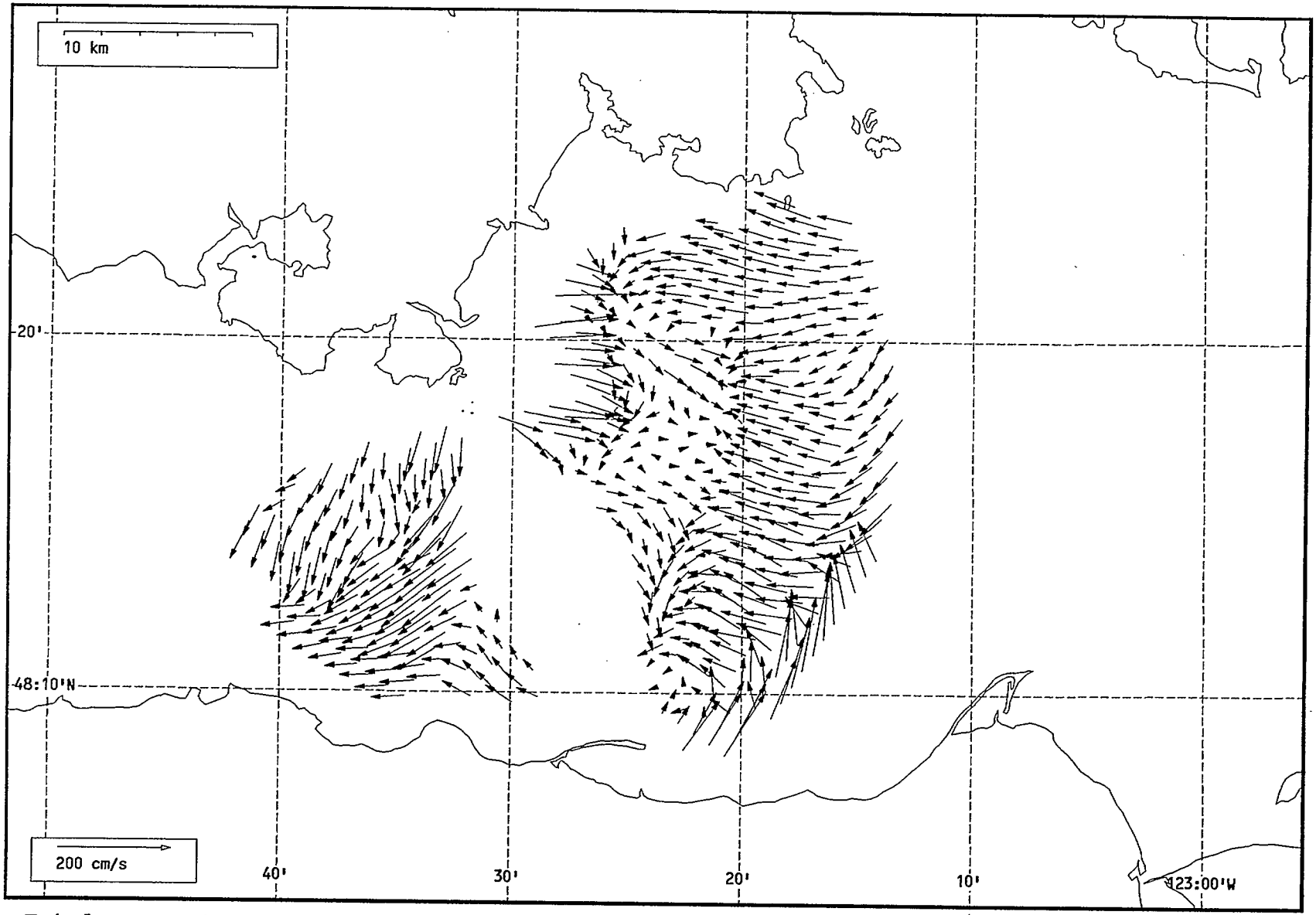

Total current vectors, Juan de Fuca Strait, 1992-07-30 13:00 Z.

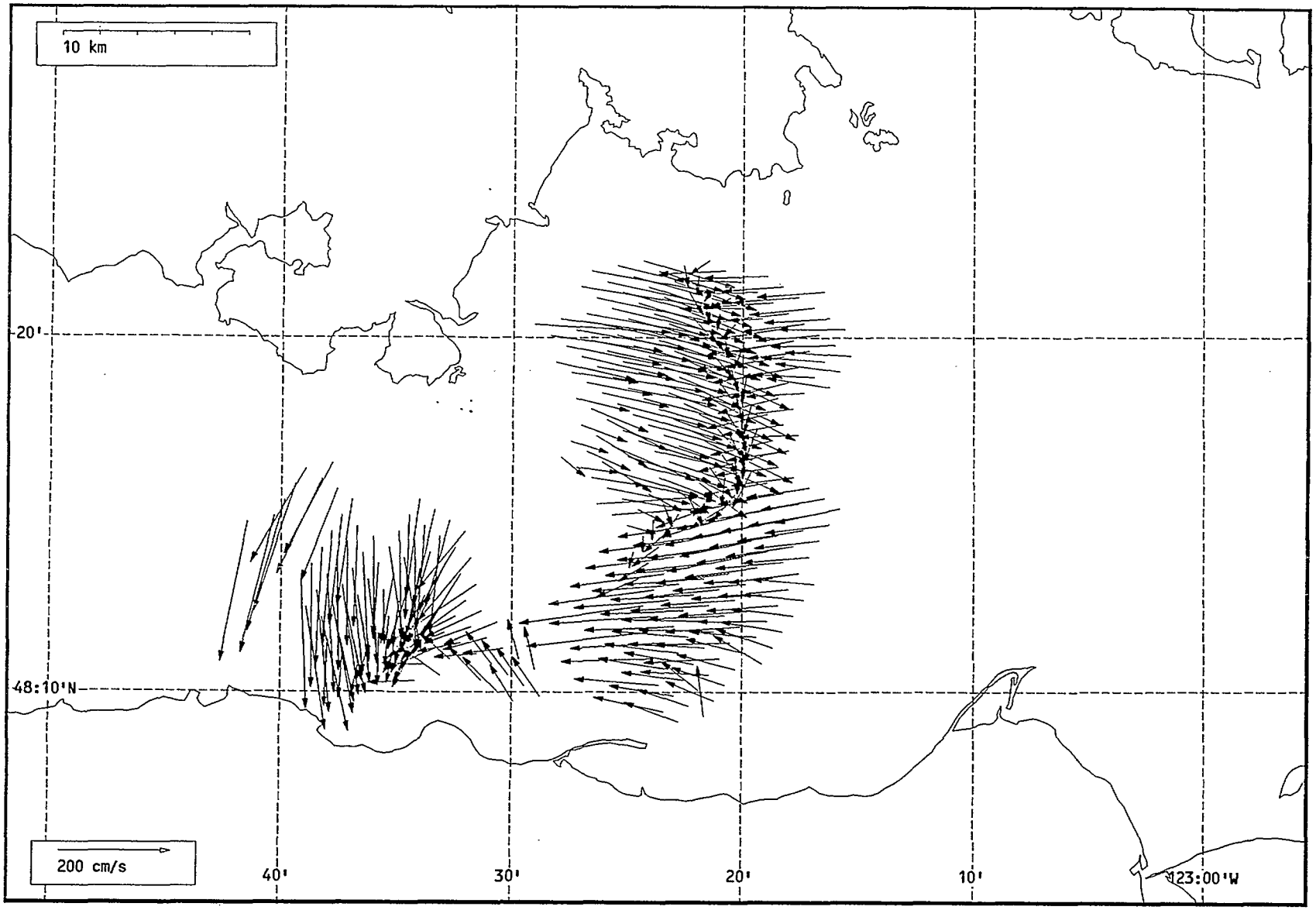

Total current vectors, Juan de Fuca Strait, 1992-07-30 14:00 Z.

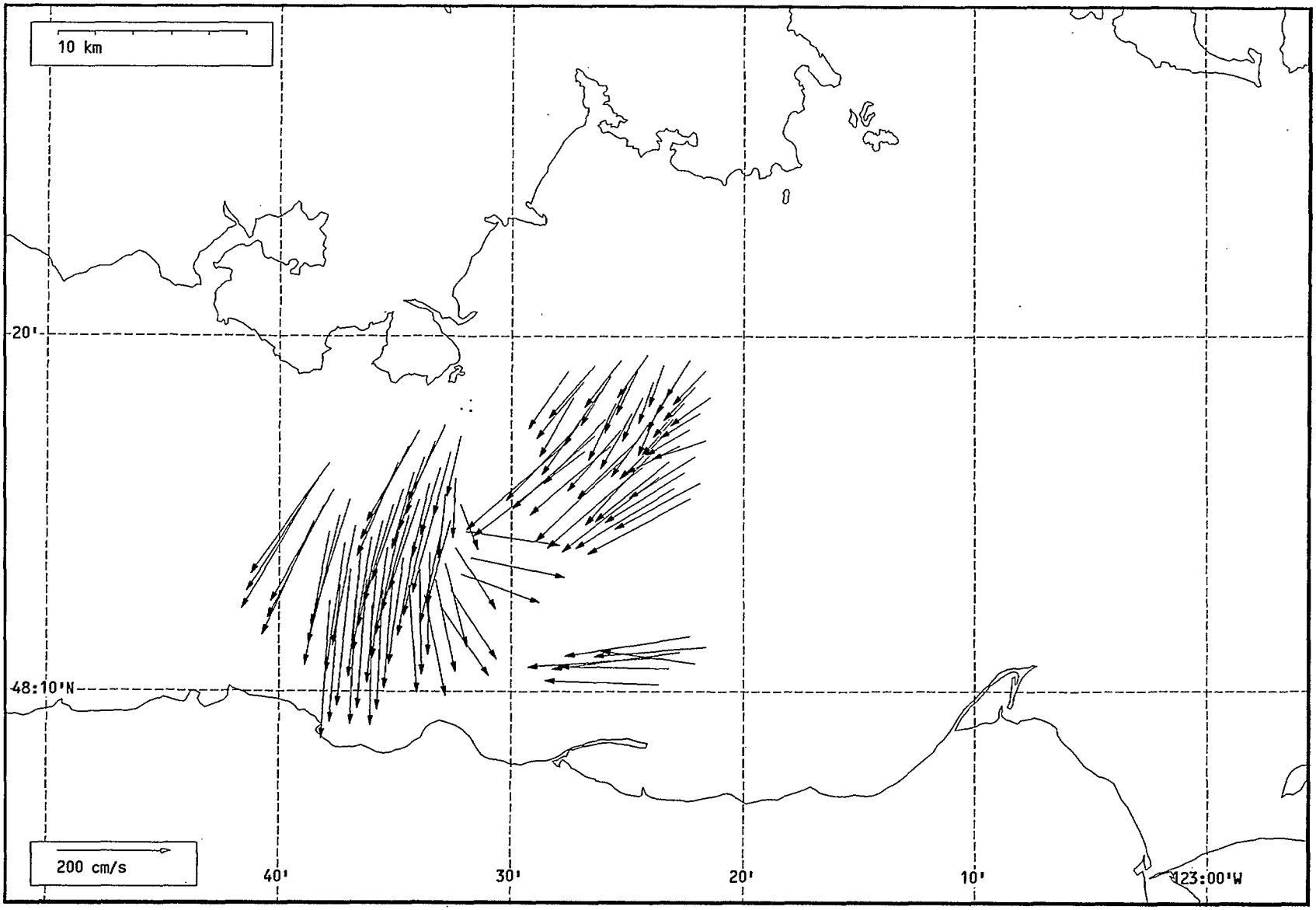

Total current vectors, Juan de Fuca Strait, 1992-07-30 15:00 Z.

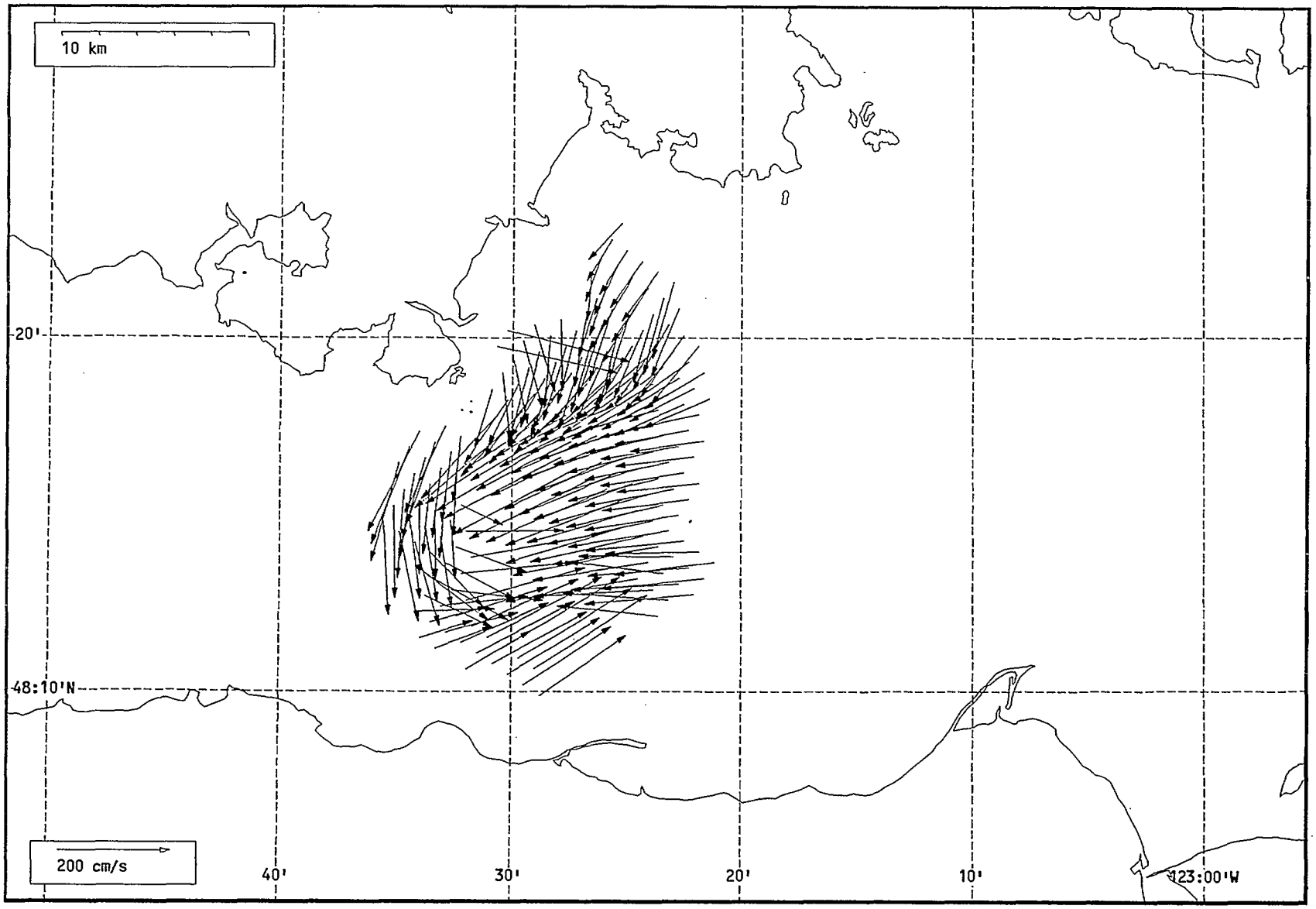

Total current vectors, Juan de Fuca Strait, 1992-07-30 16:00 Z.

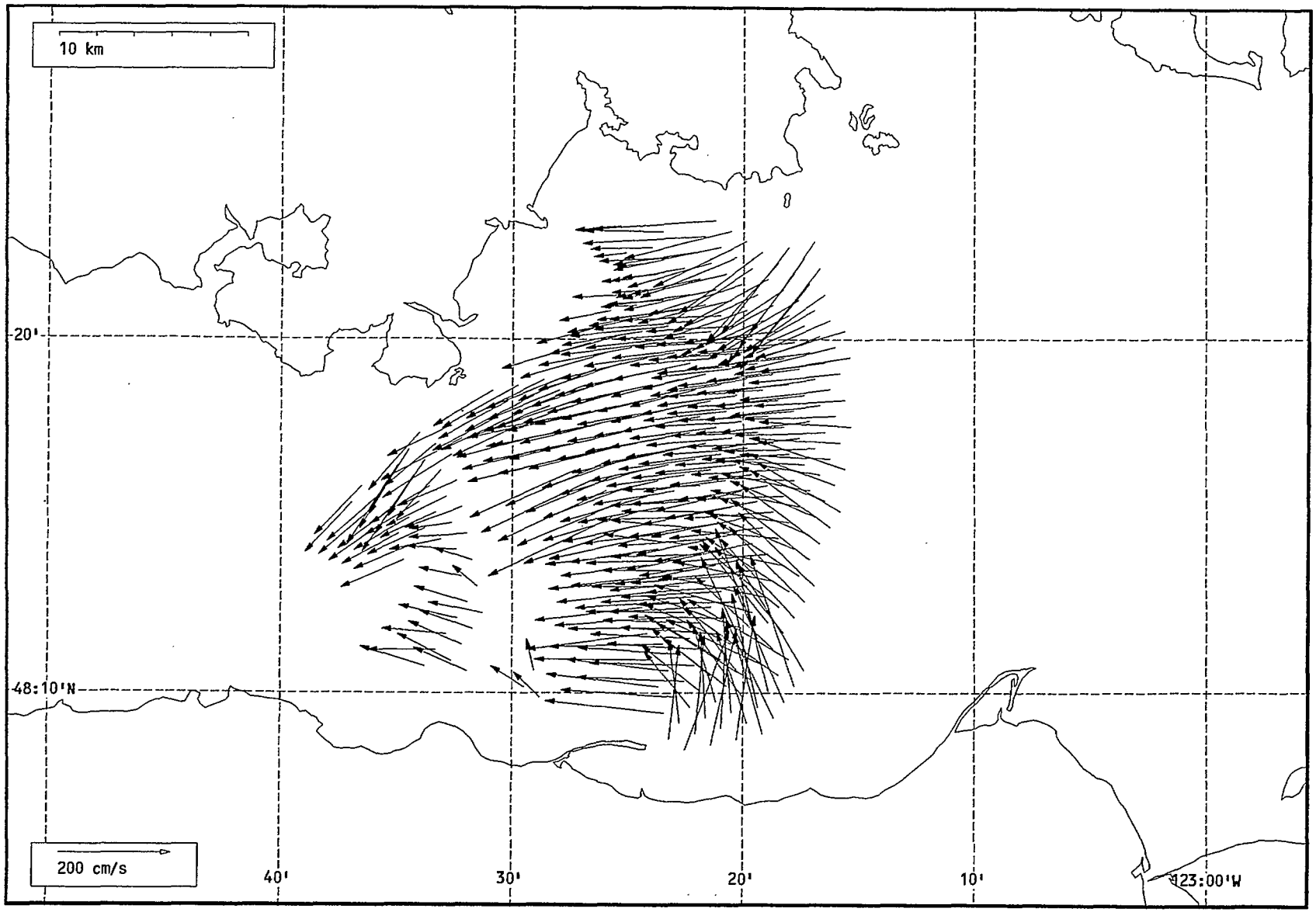

Total current vectors, Juan de Fuca Strait, 1992-07-30 17:00 Z.

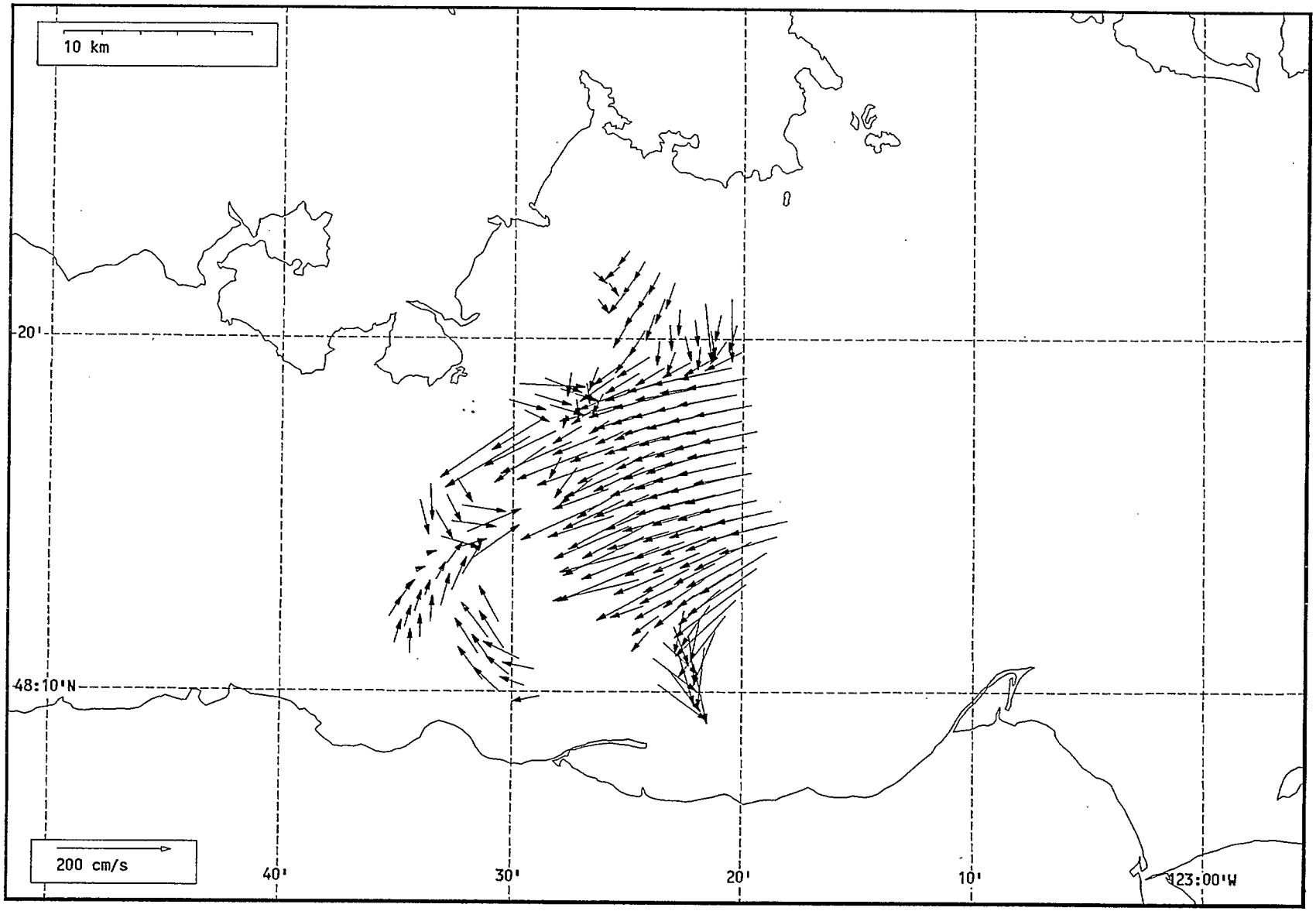

Total current vectors, Juan de Fuca Strait, 1992-07-30 18:00 Z.

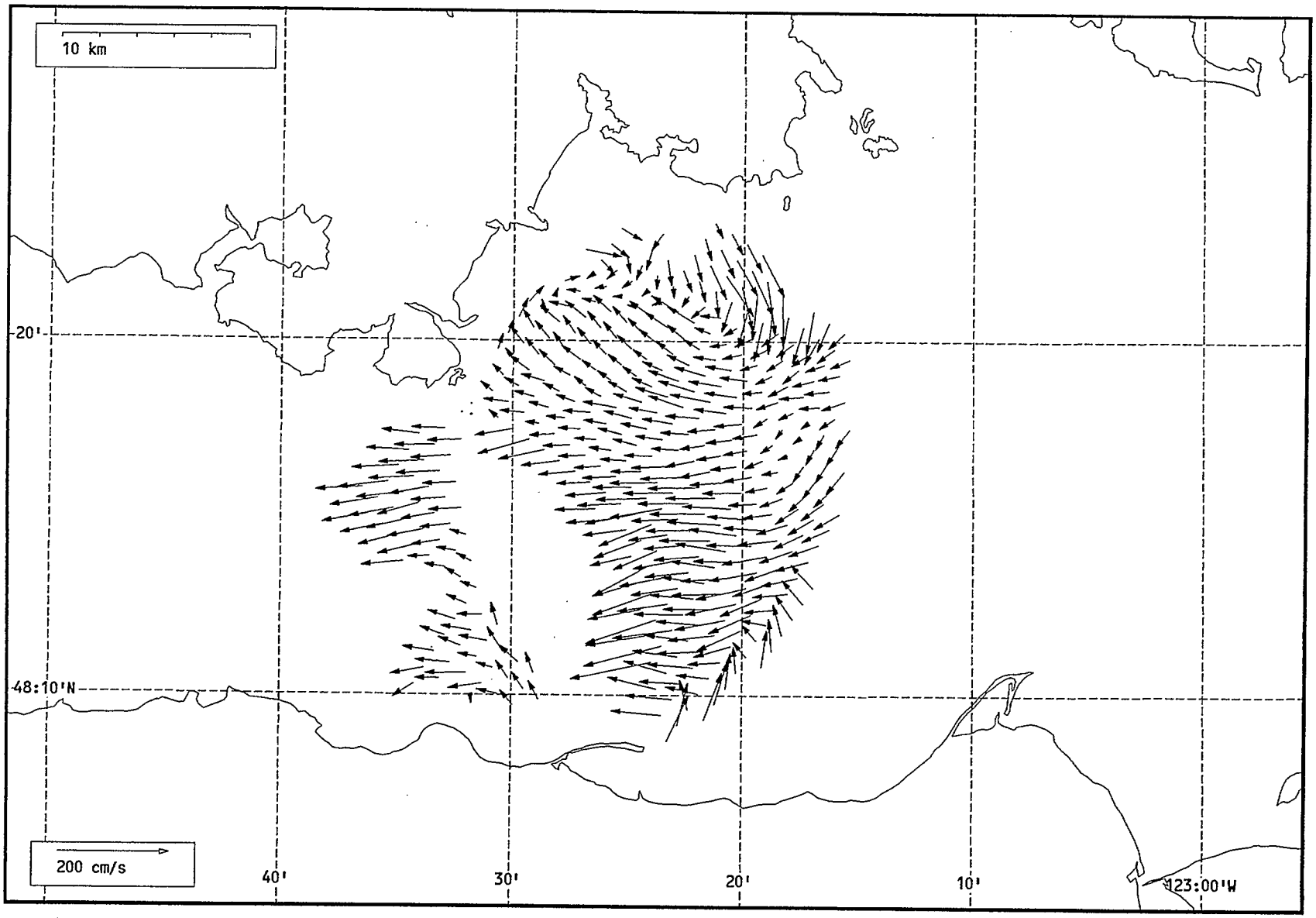

Total current vectors, Juan de Fuca Strait, 1992-07-30 19:00 Z.

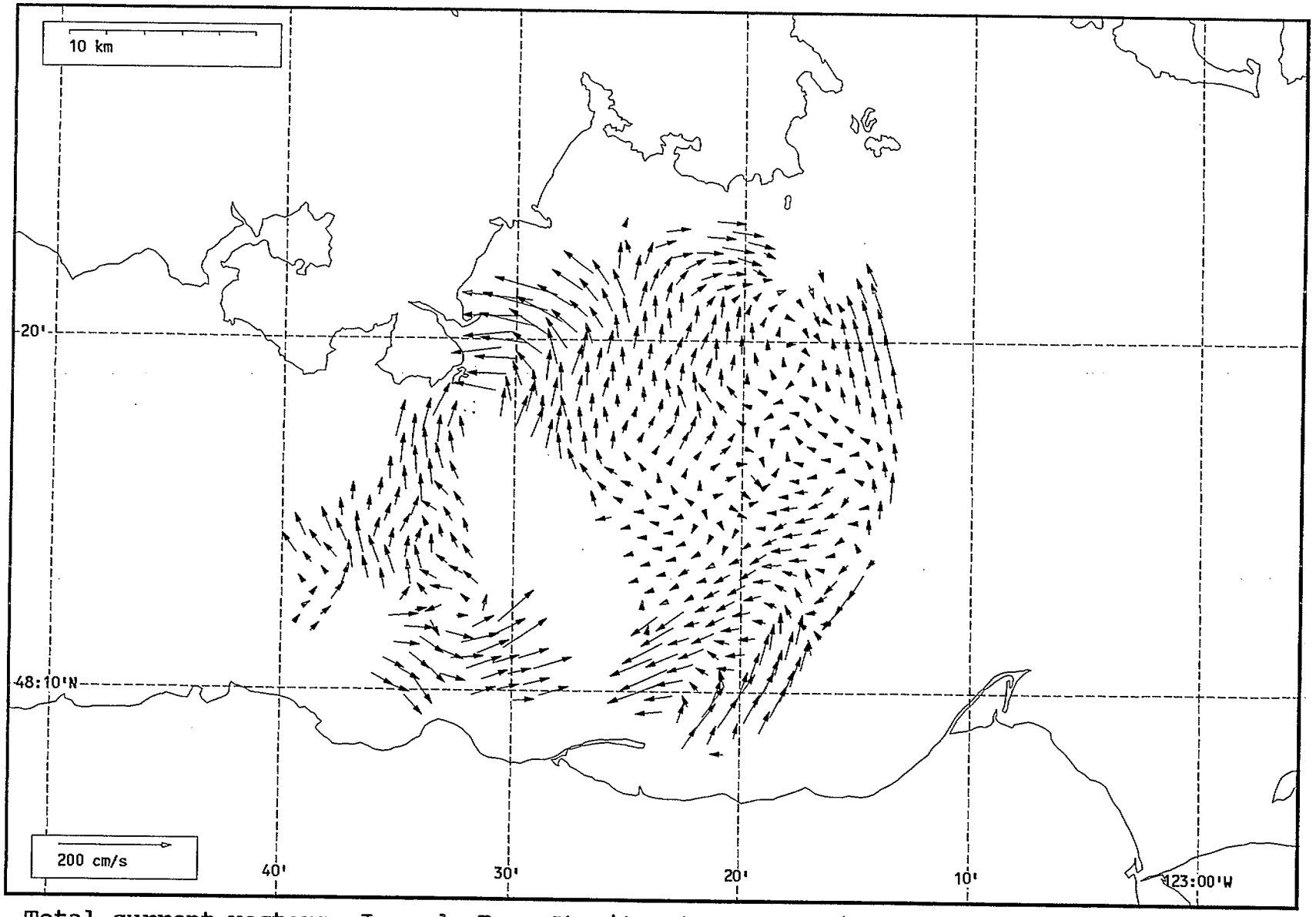

Total current vectors, Juan de Fuca Strait, 1992-07-30 20:00 Z.

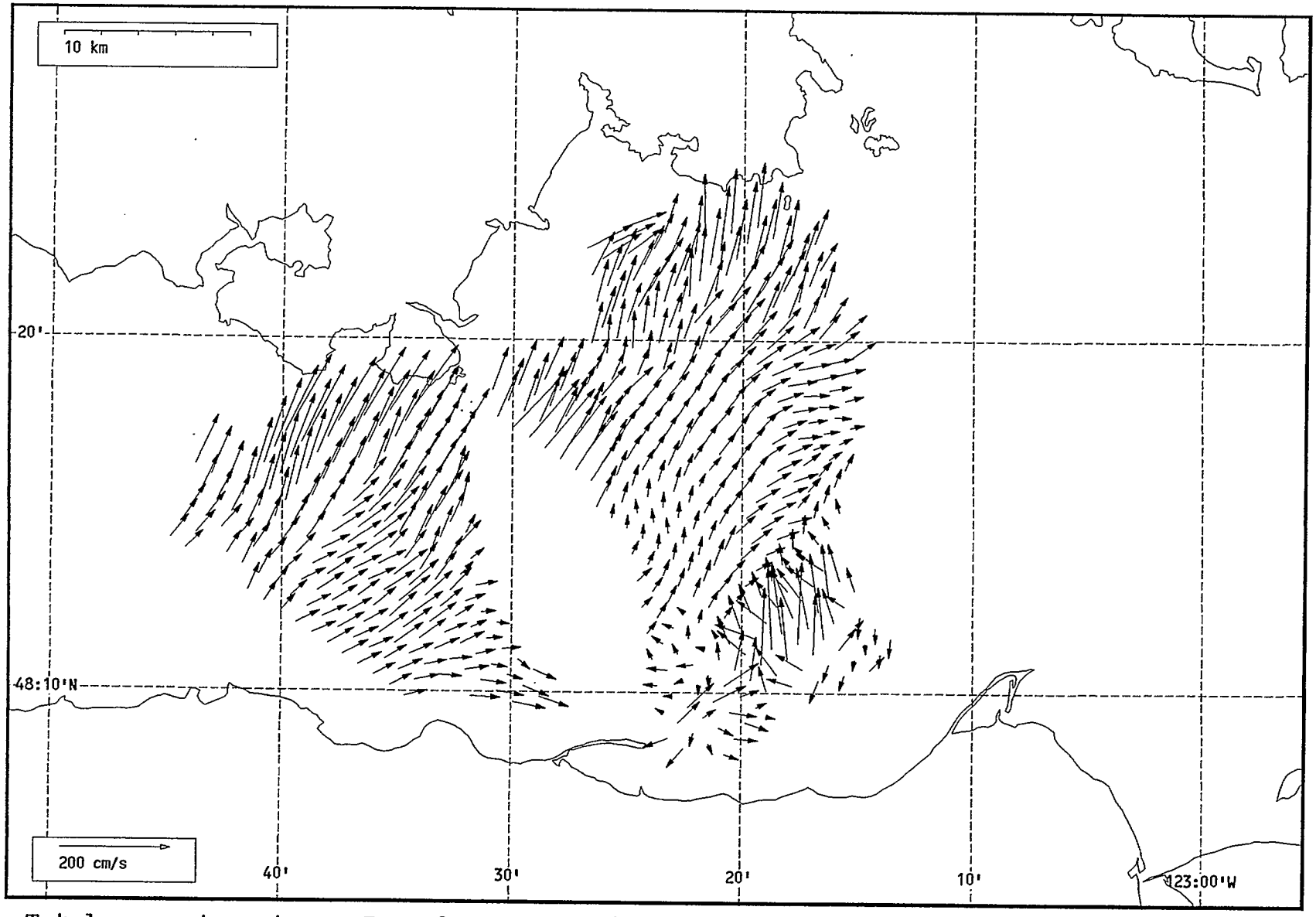

Total current vectors, Juan de Fuca Strait, 1992-07-30 21:00 Z.

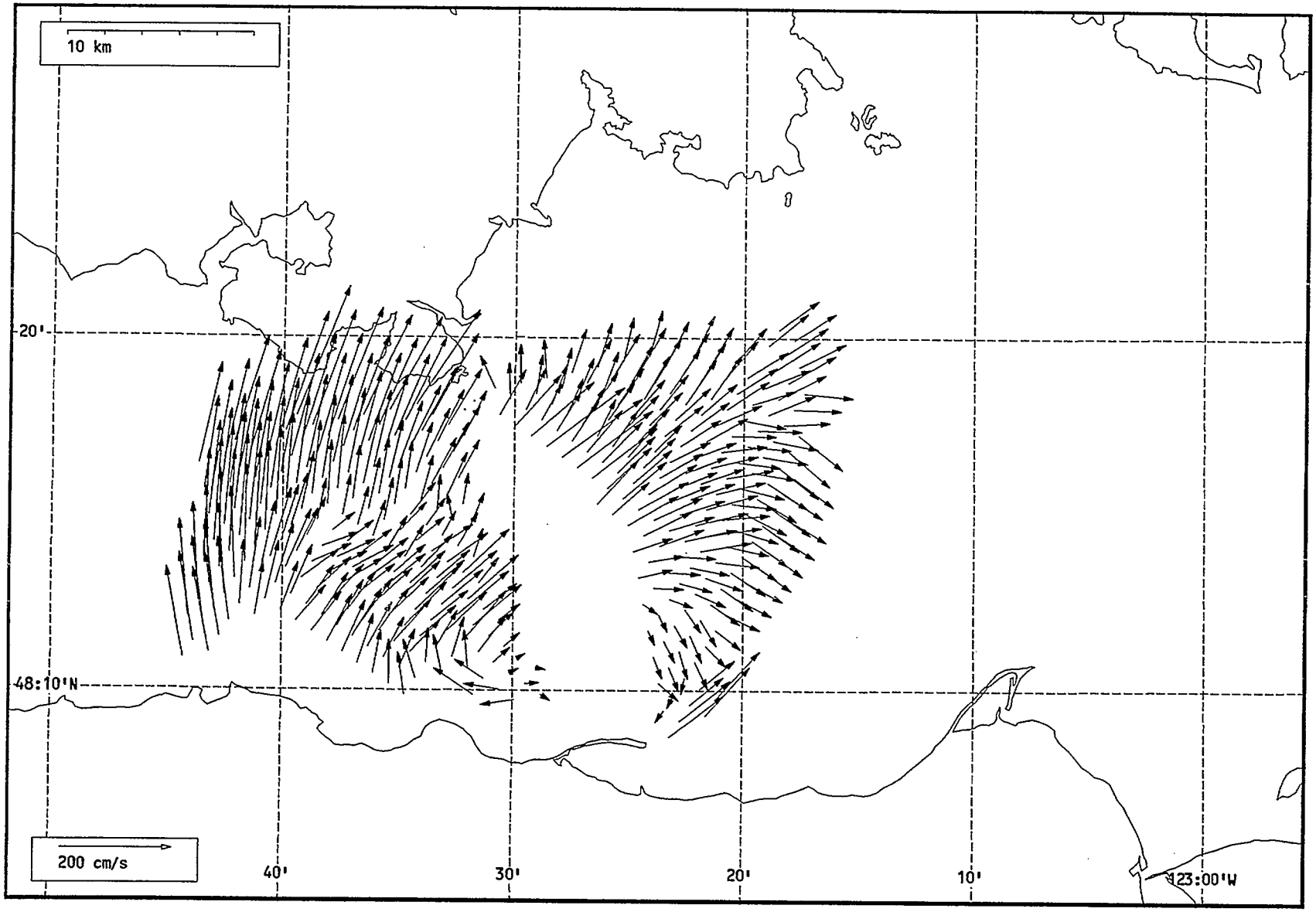

Total current vectors, Juan de Fuca Strait, 1992-07-30 22:00 Z.

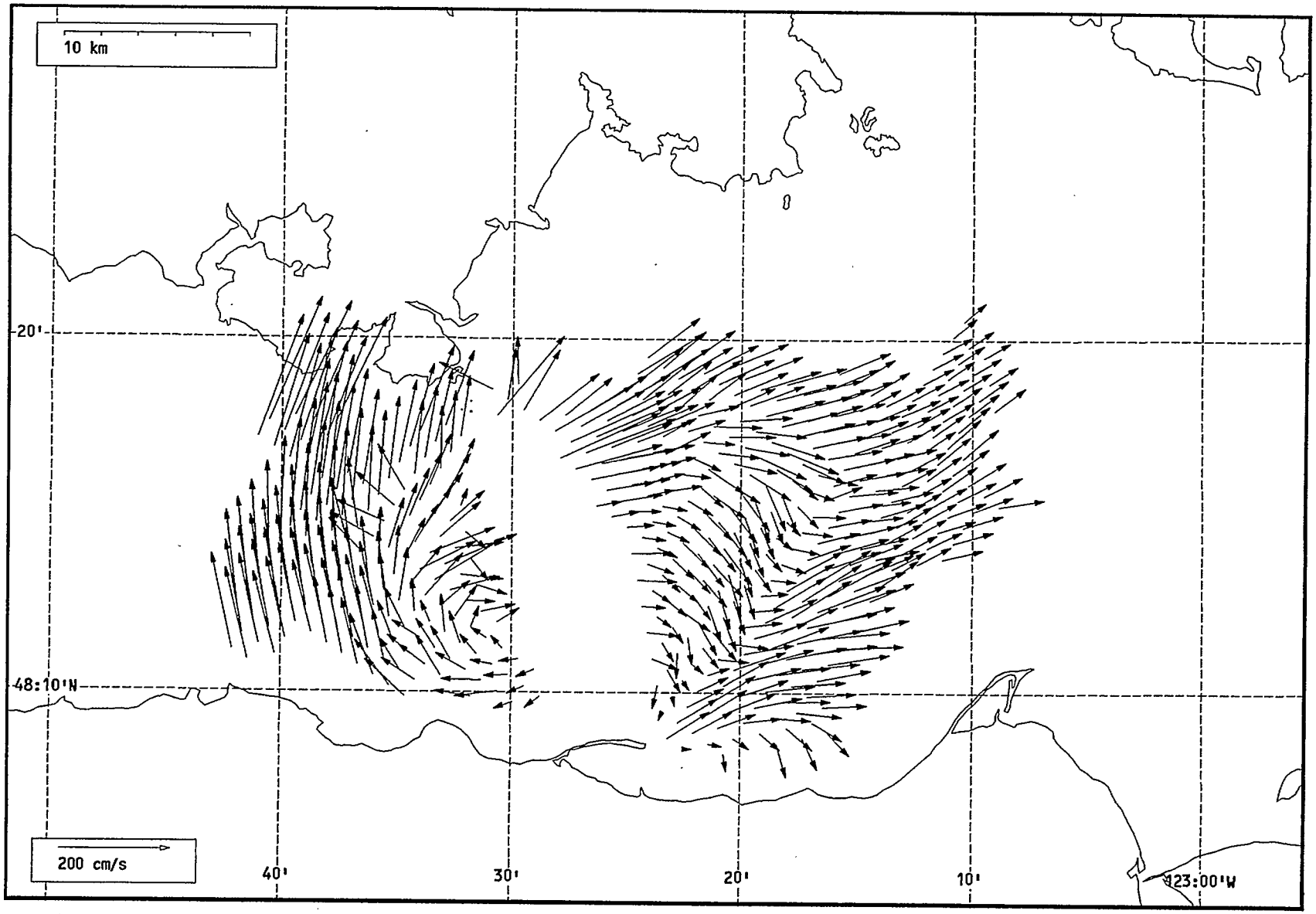

Total current vectors, Juan de Fuca Strait, 1992-07-30 23:00 Z.

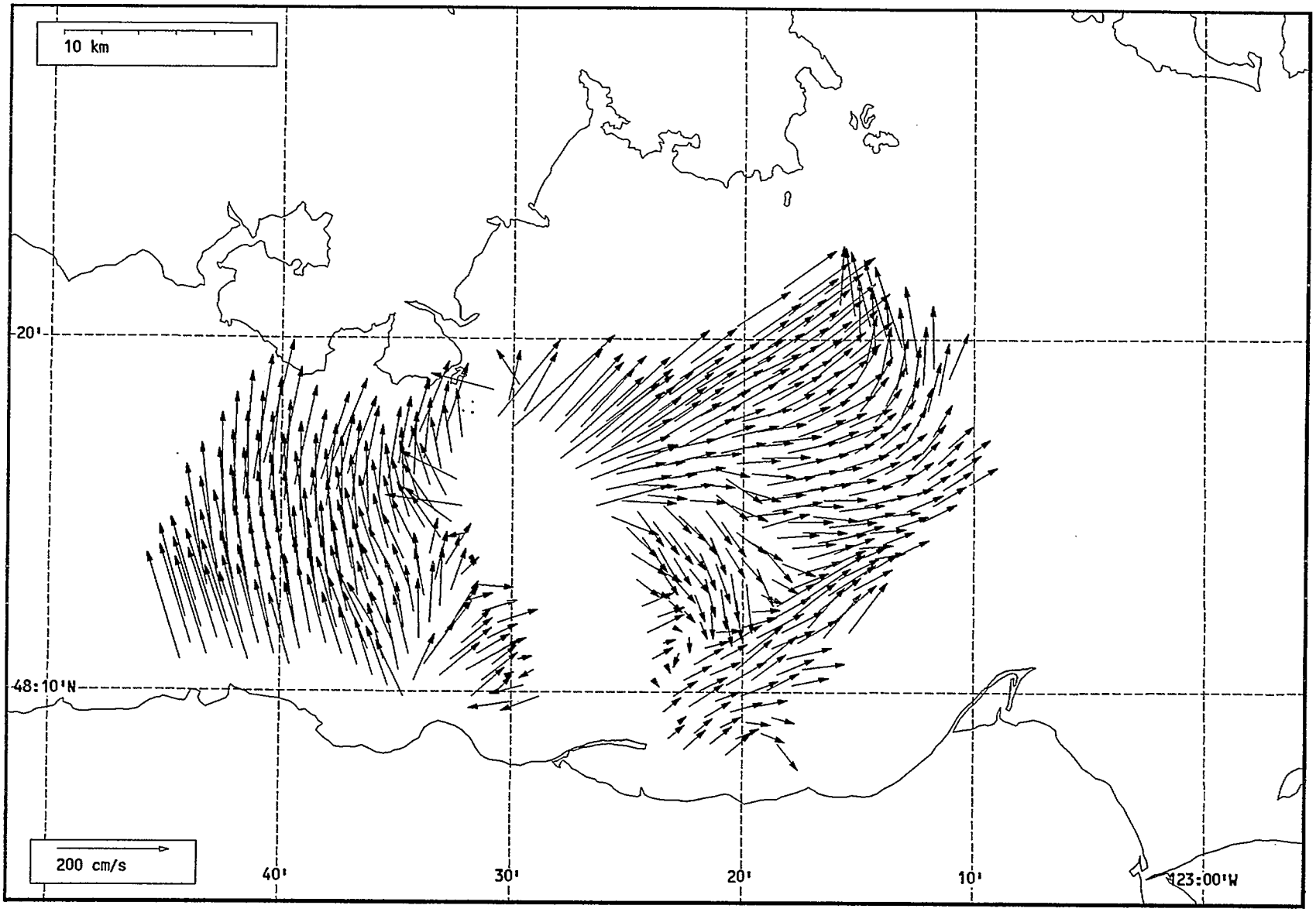

Total current vectors, Juan de Fuca Strait, 1992-07-31 00:00 Z.

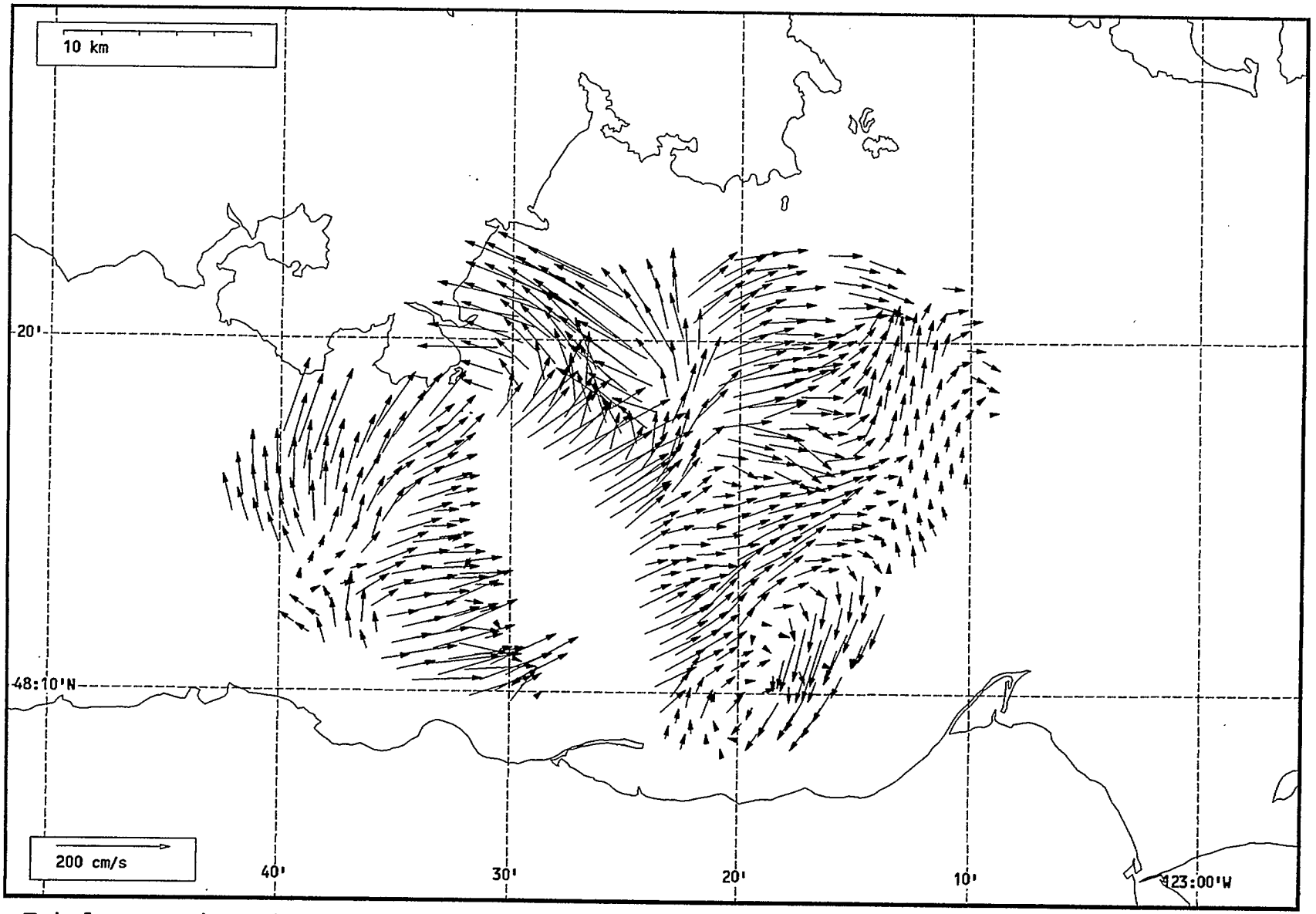

Total current vectors, Juan de Fuca Strait, 1992-07-31 01:00 Z.

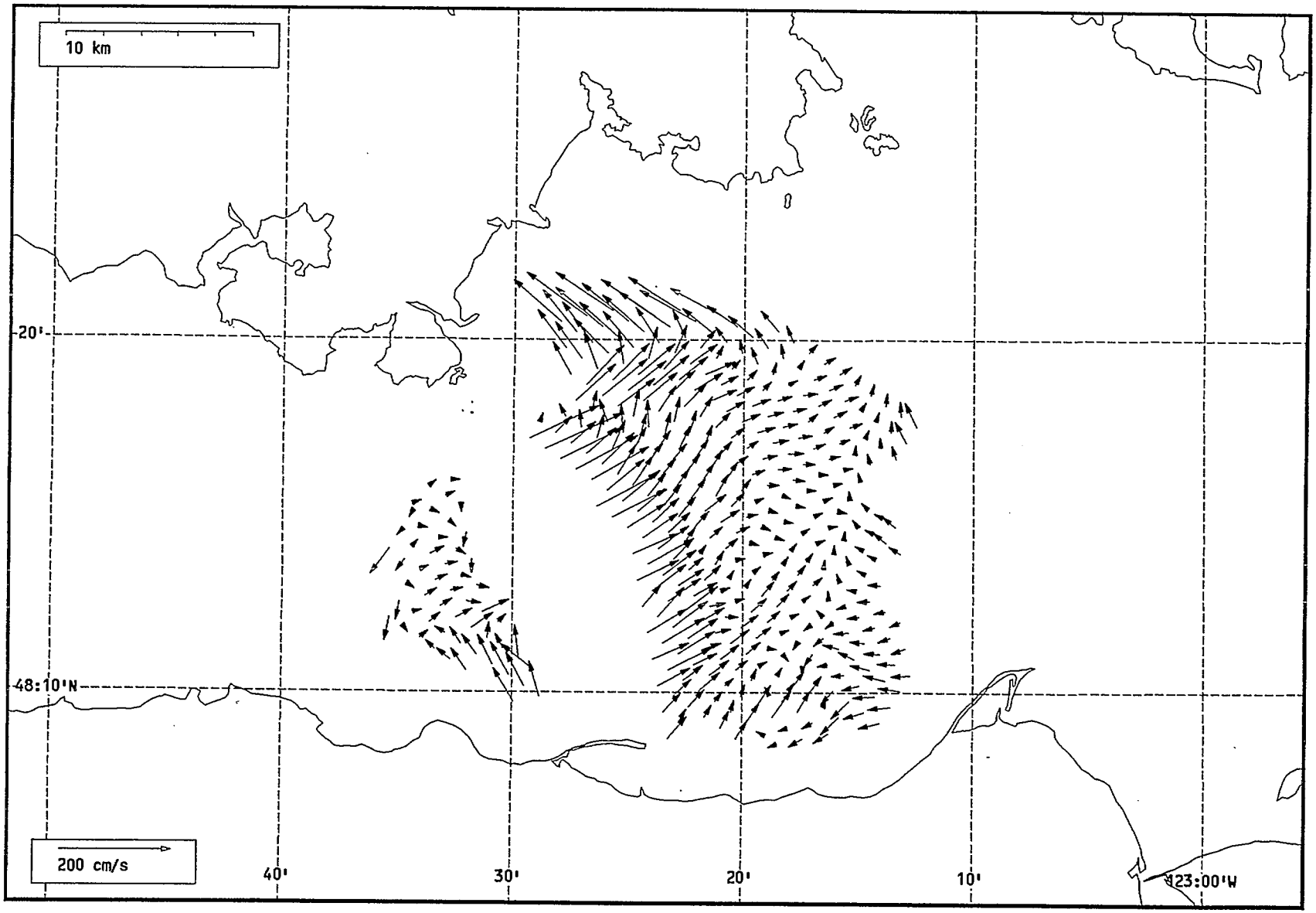

Total current vectors, Juan de Fuca Strait, 1992-07-31 02:00 Z.

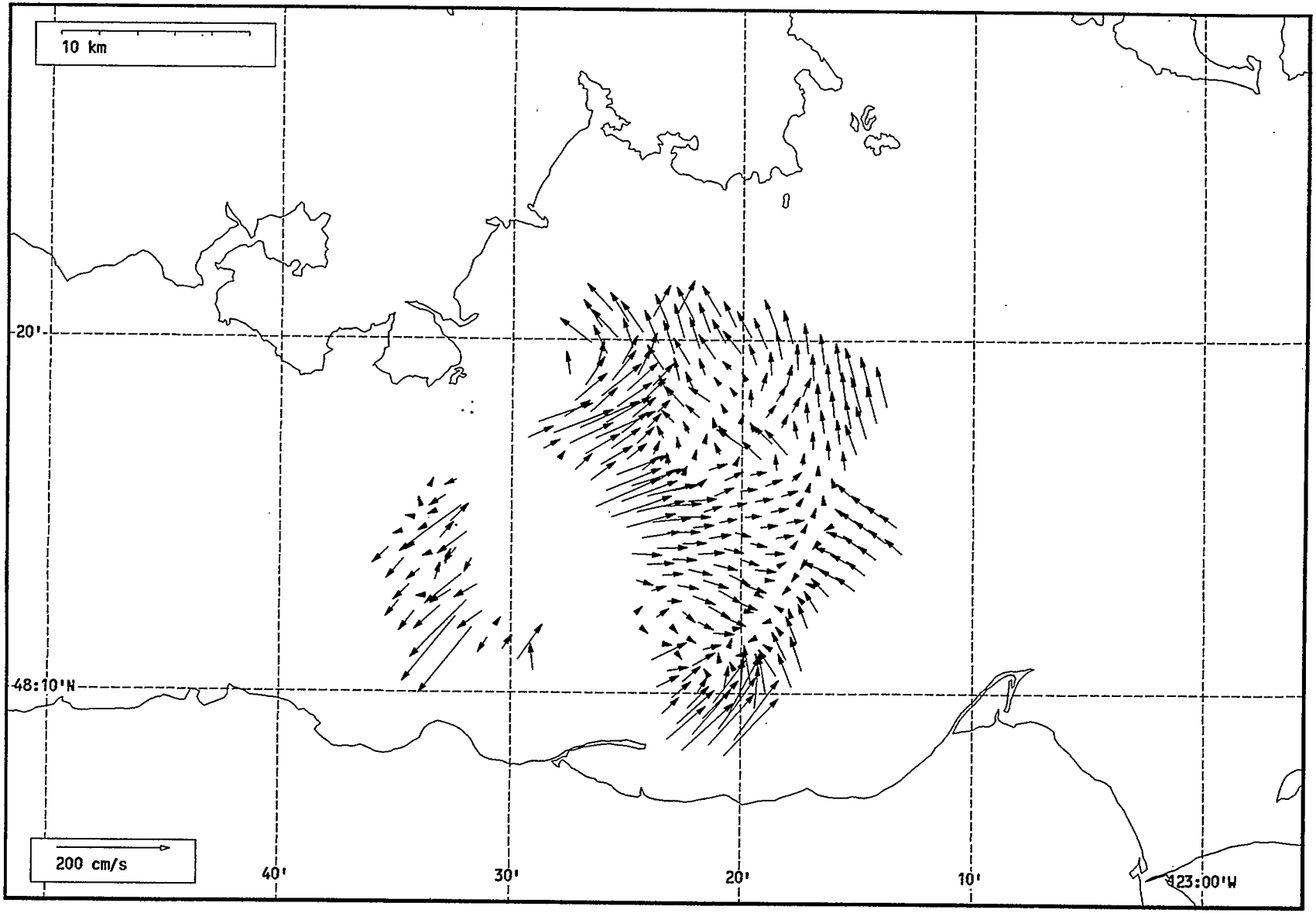

Total current vectors, Juan de Fuca Strait, 1992-07-31 03:00 Z.

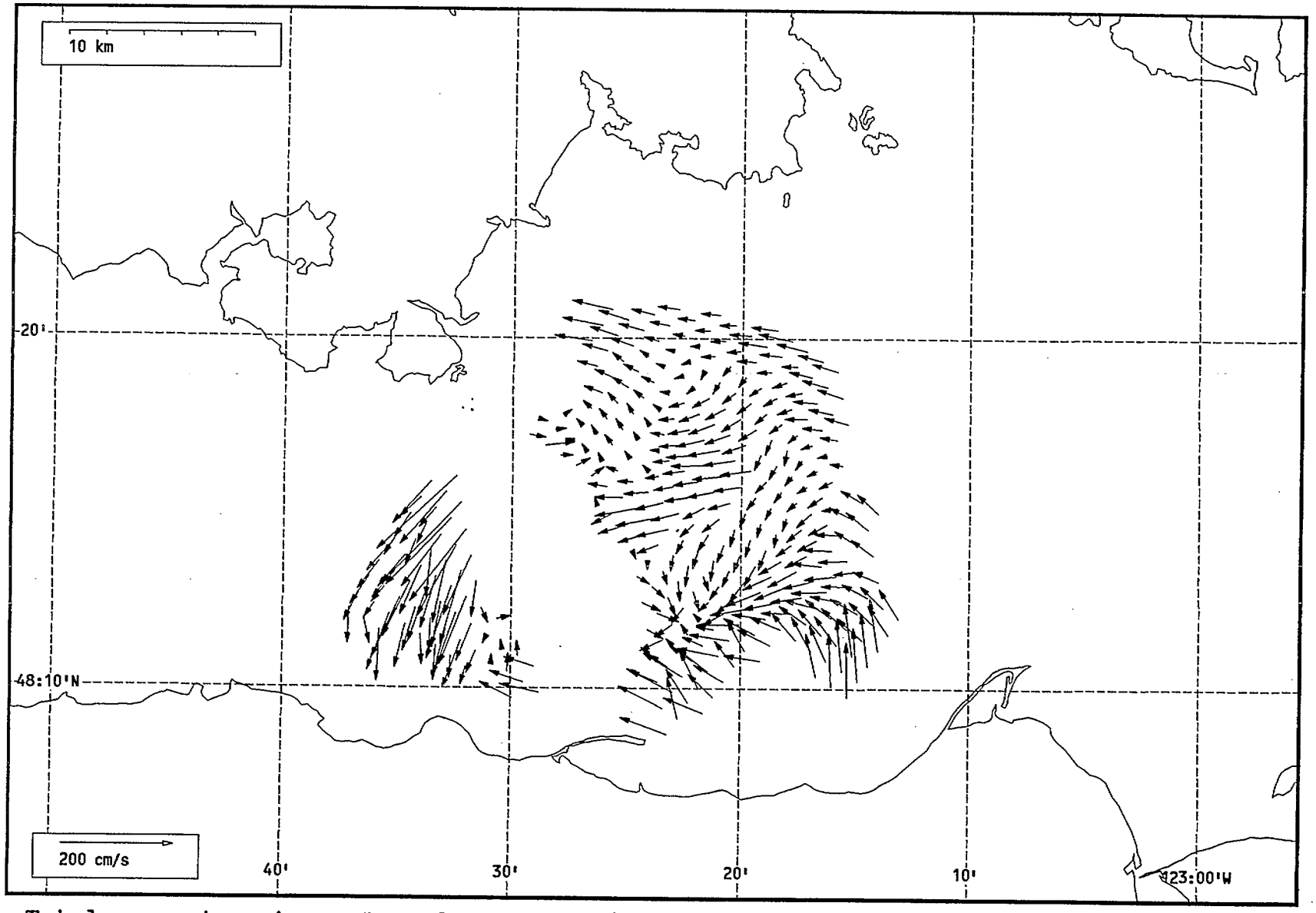

Total current vectors, Juan de Fuca Strait, 1992-07-31 04:00 Z.

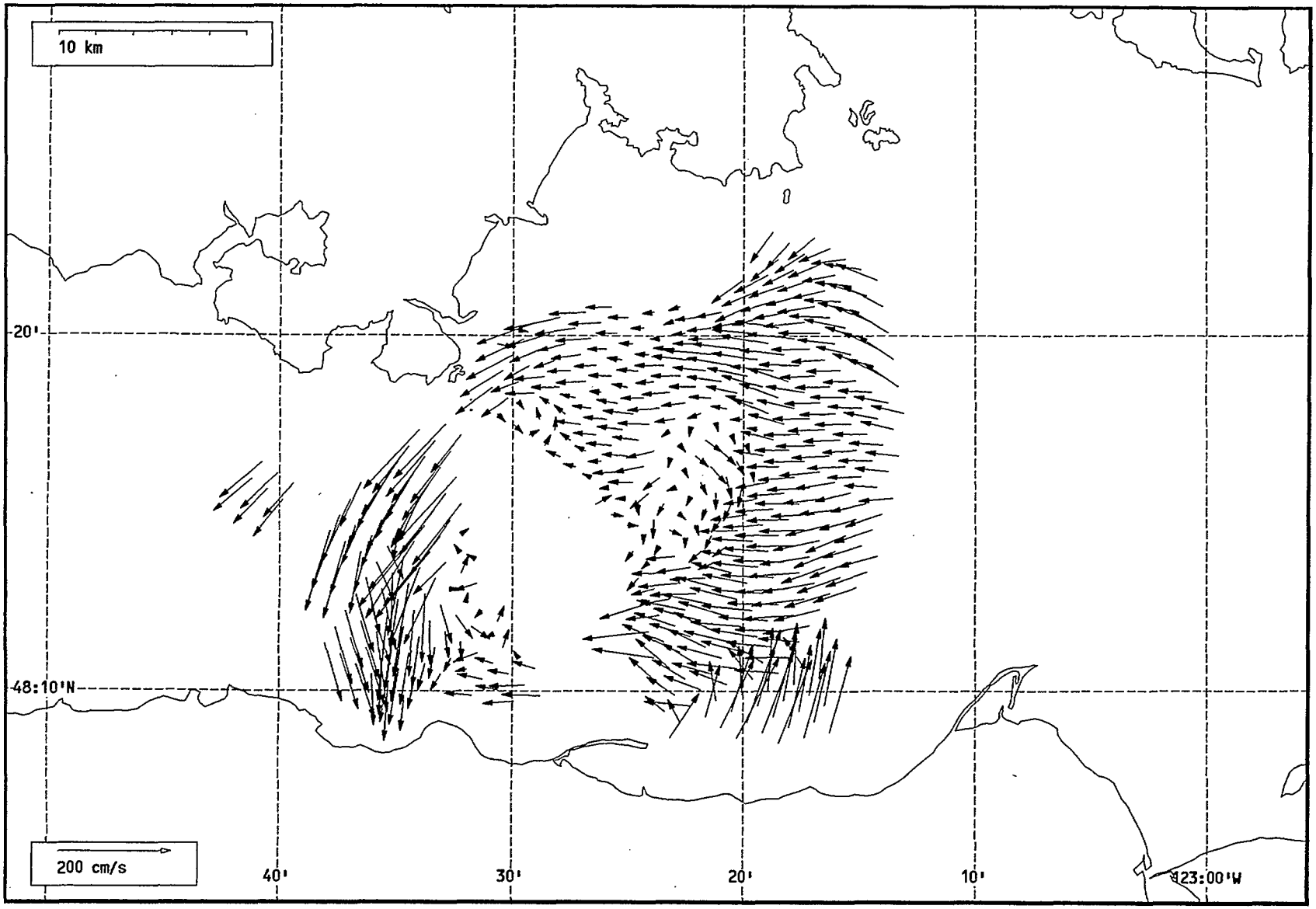

Total current vectors, Juan de Fuca Strait, 1992-07-31 05:00 Z.

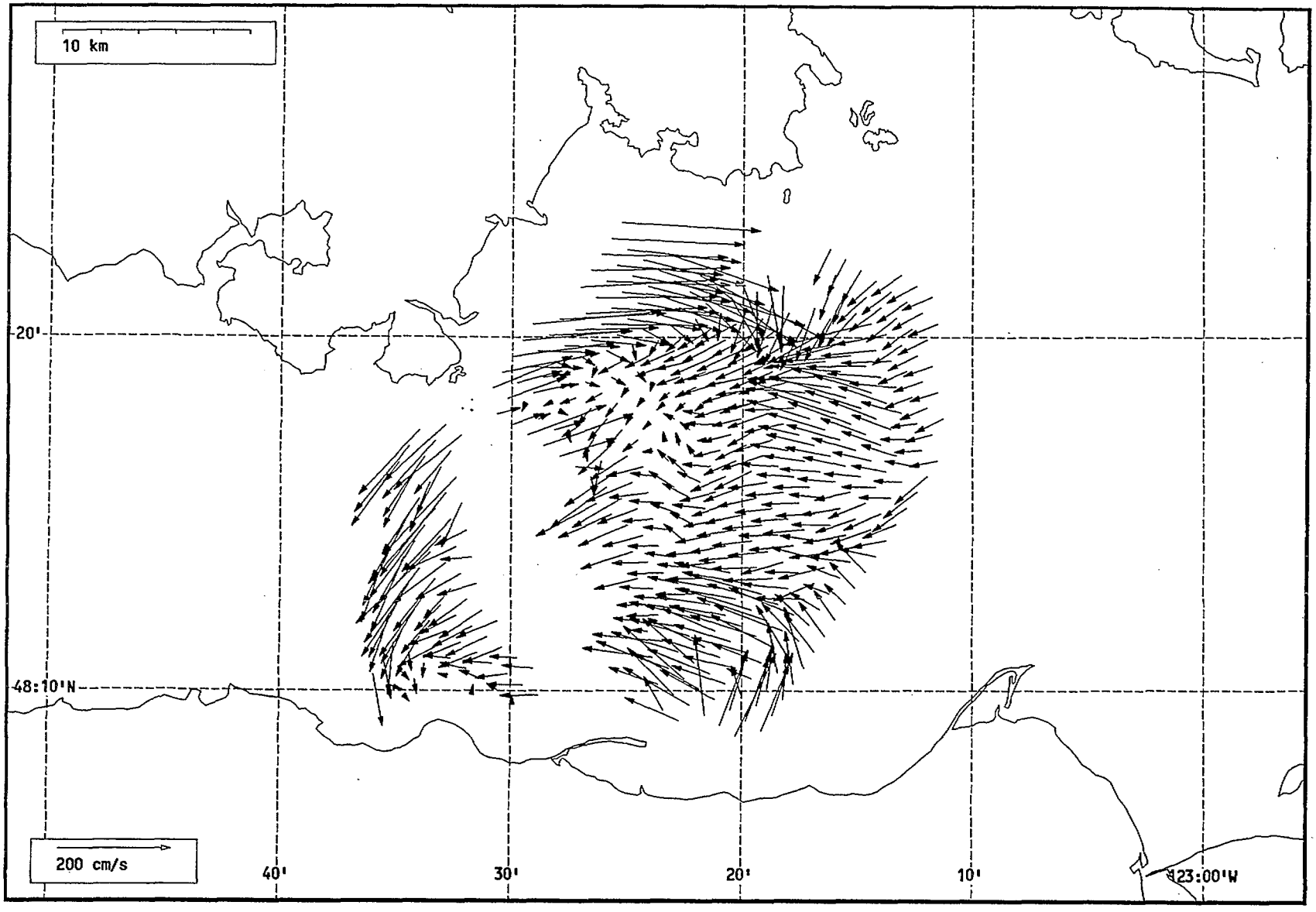

Total current vectors, Juan de Fuca Strait, 1992-07-31 06:00 Z.

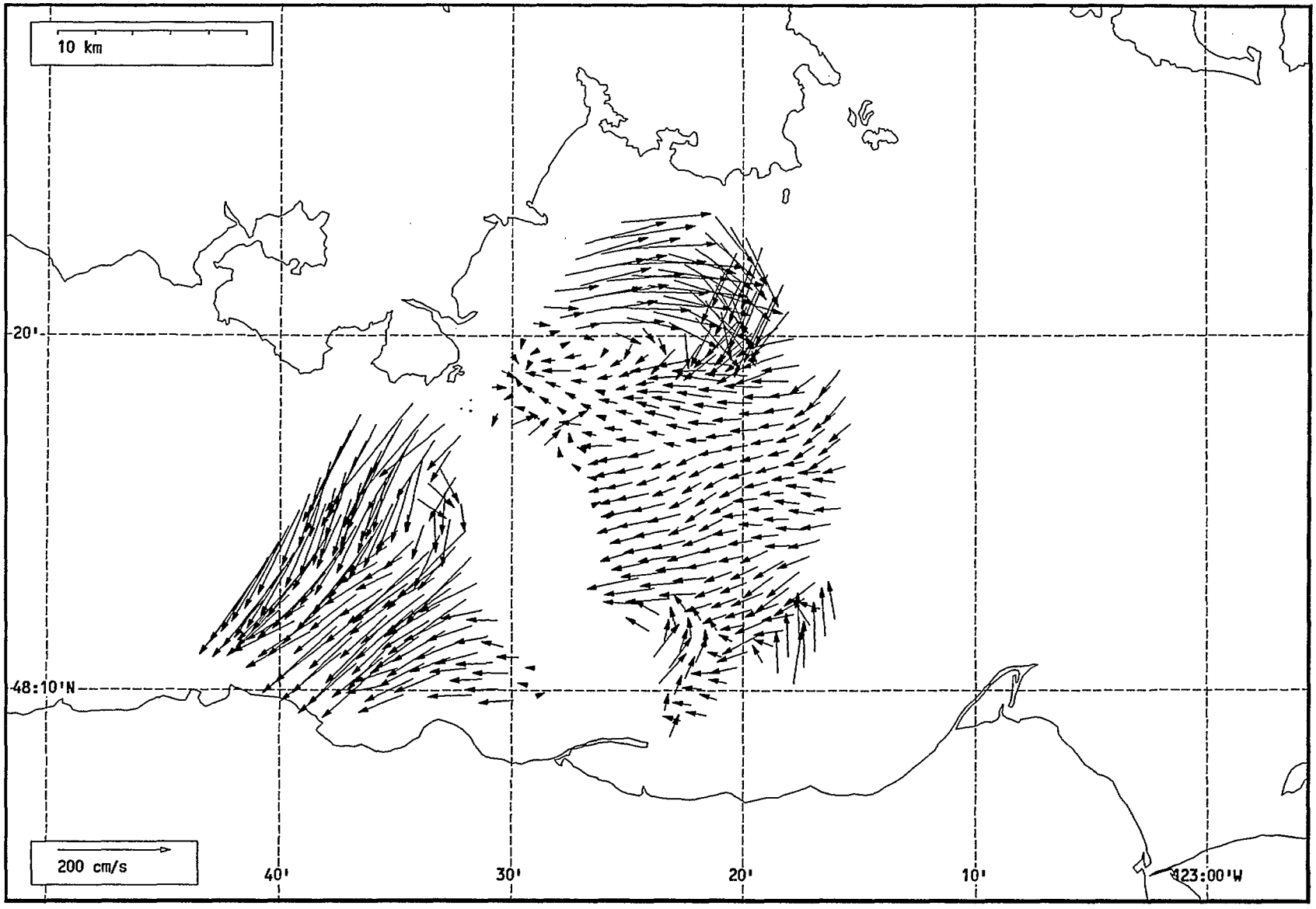

Total current vectors, Juan de Fuca Strait, 1992-07-31 07:00 Z.

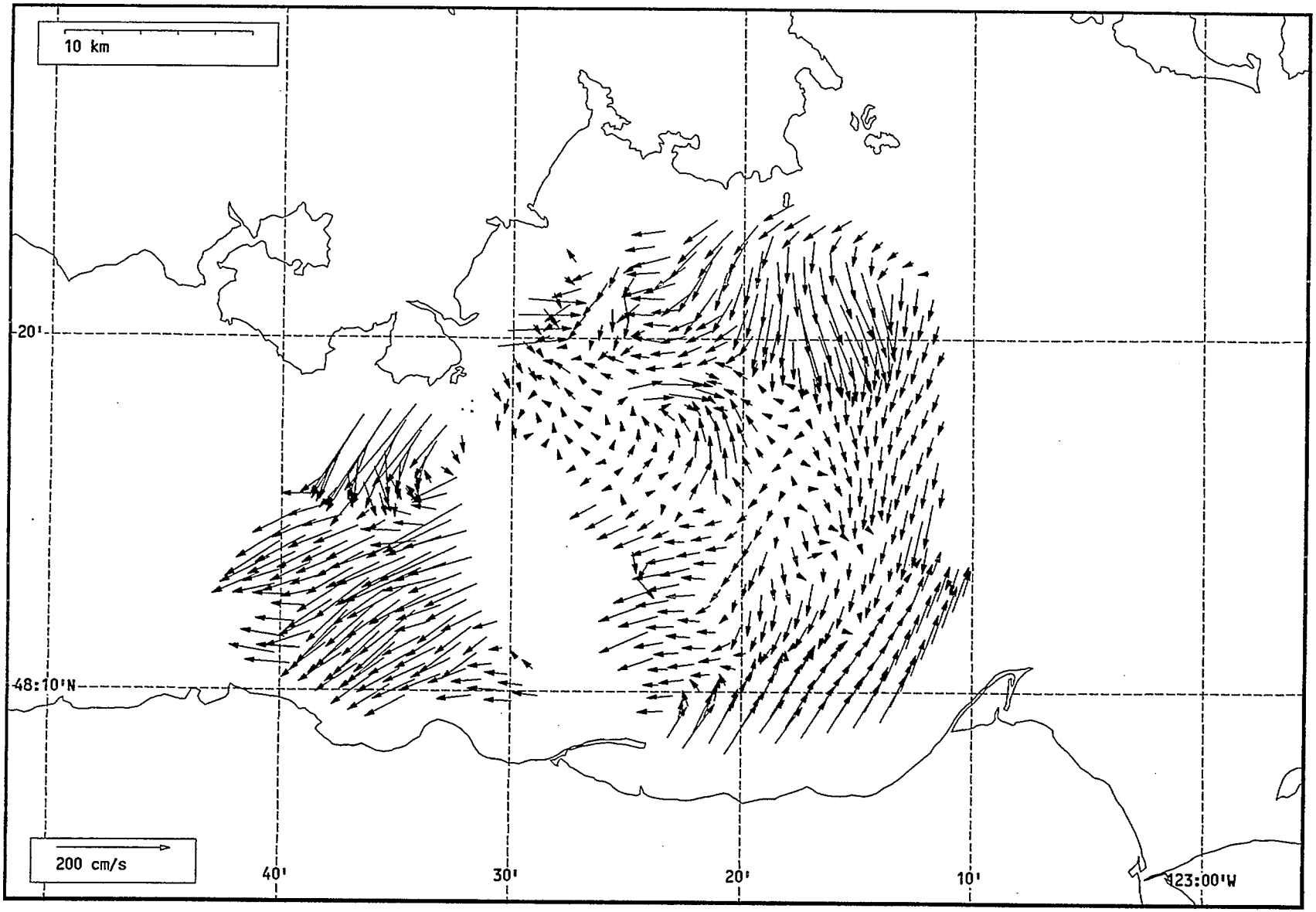

Total current vectors, Juan de Fuca Strait, 1992-07-31 08:00 Z.

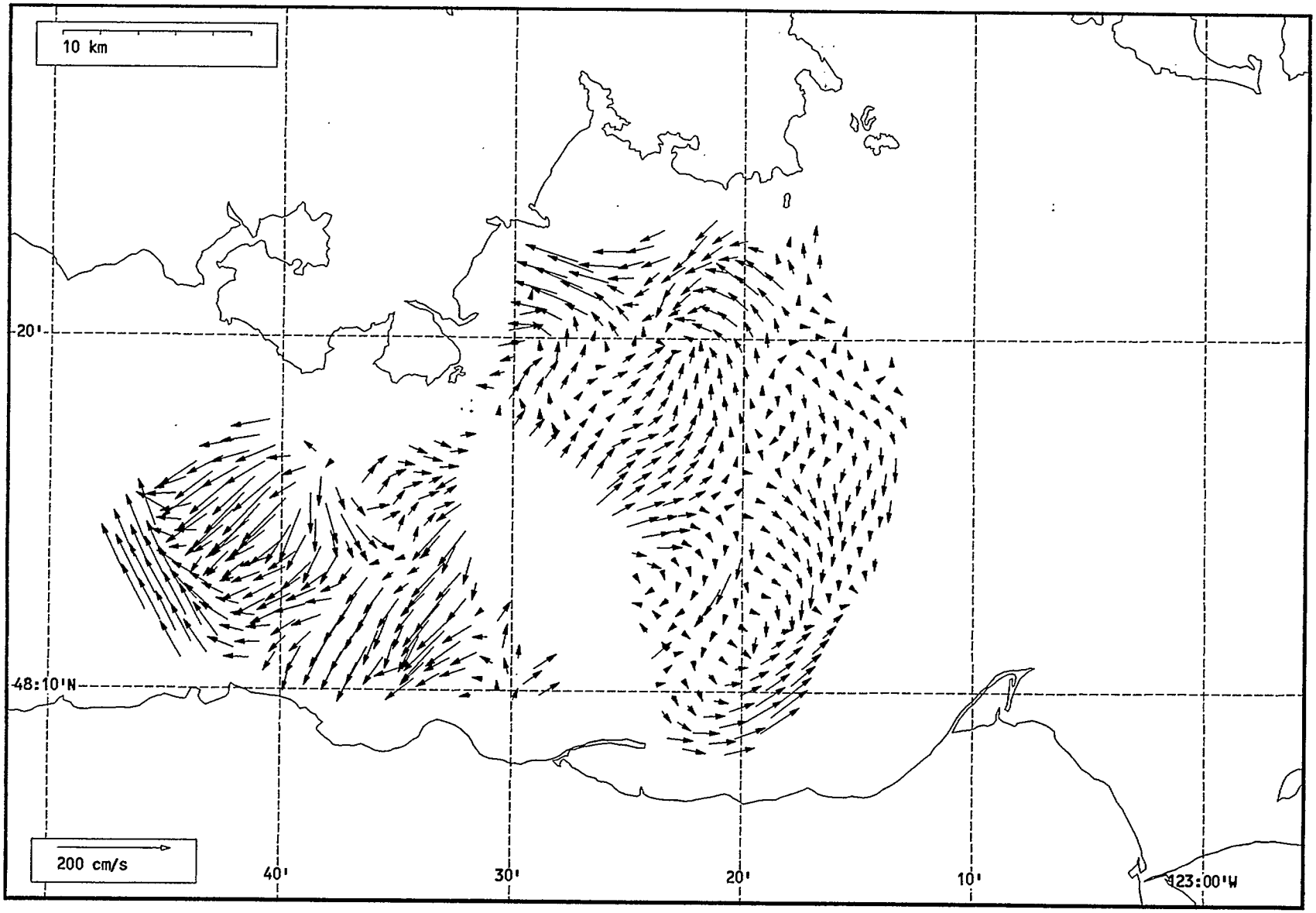

Total current vectors, Juan de Fuca Strait, 1992-07-31 09:00 Z.

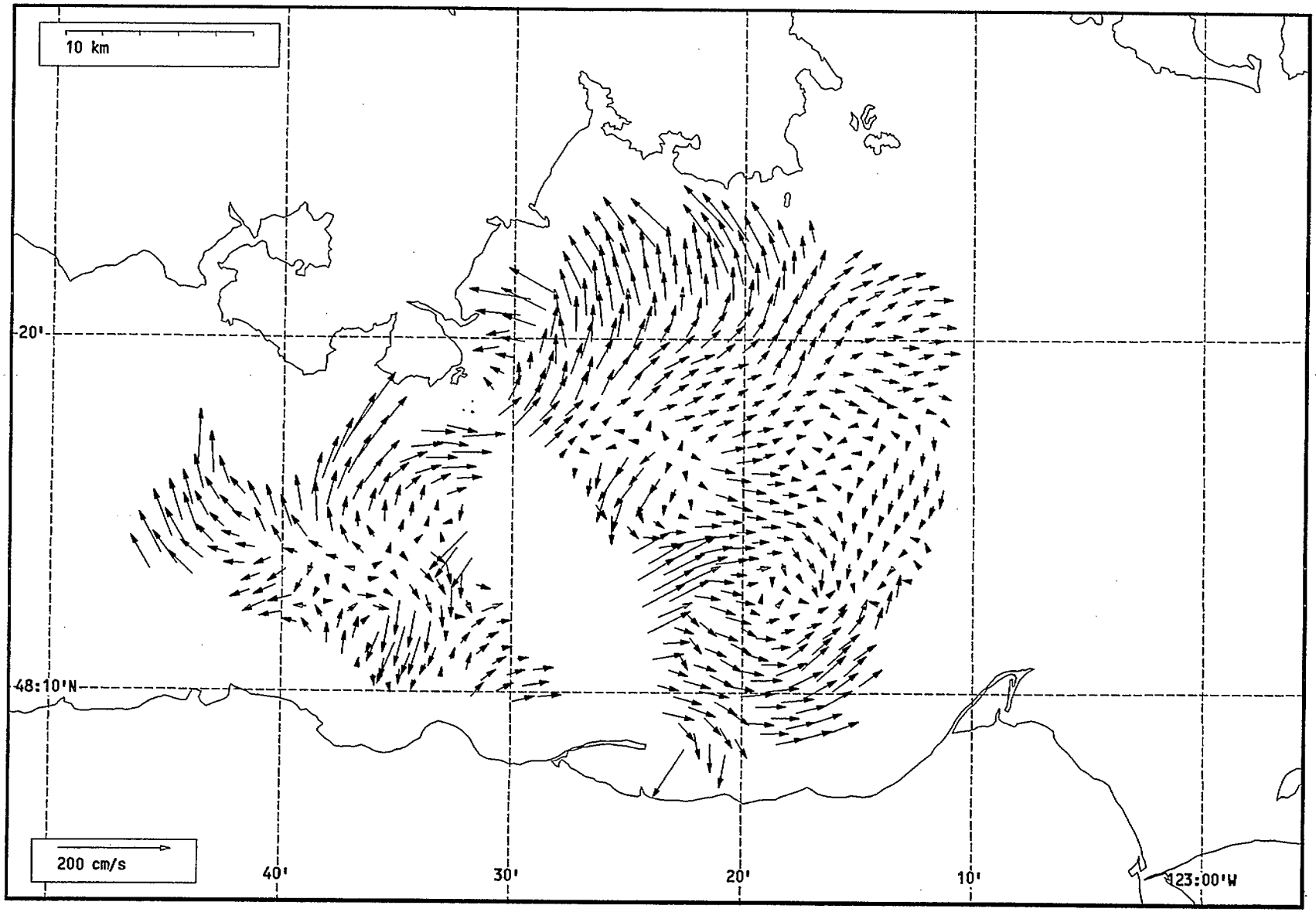

Total current vectors, Juan de Fuca Strait, 1992-07-31 10:00 Z.

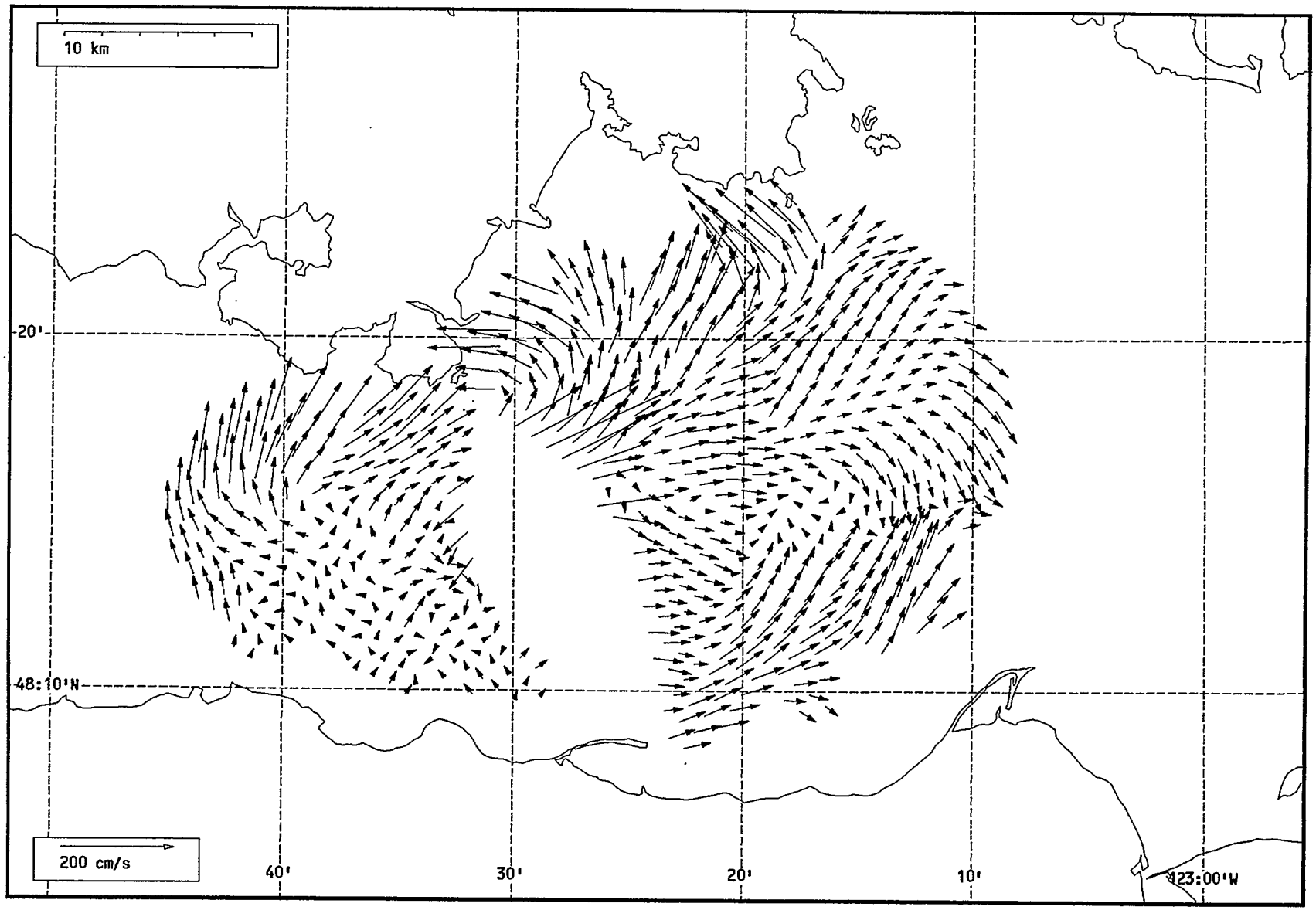

Total current vectors, Juan de Fuca Strait, 1992-07-31 11:00 Z.

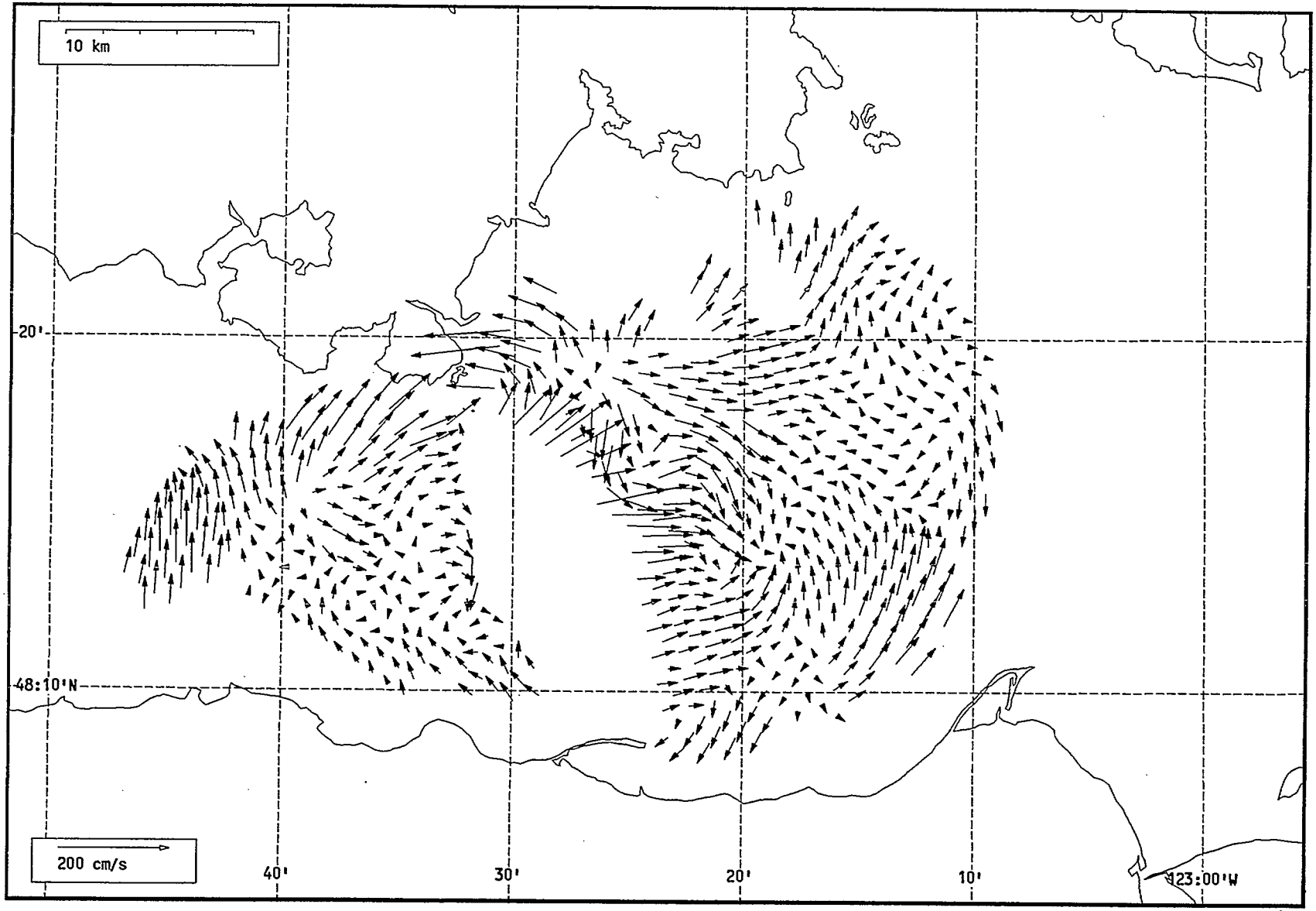

Total current vectors, Juan de Fuca Strait, 1992-07-31 12:00 Z.

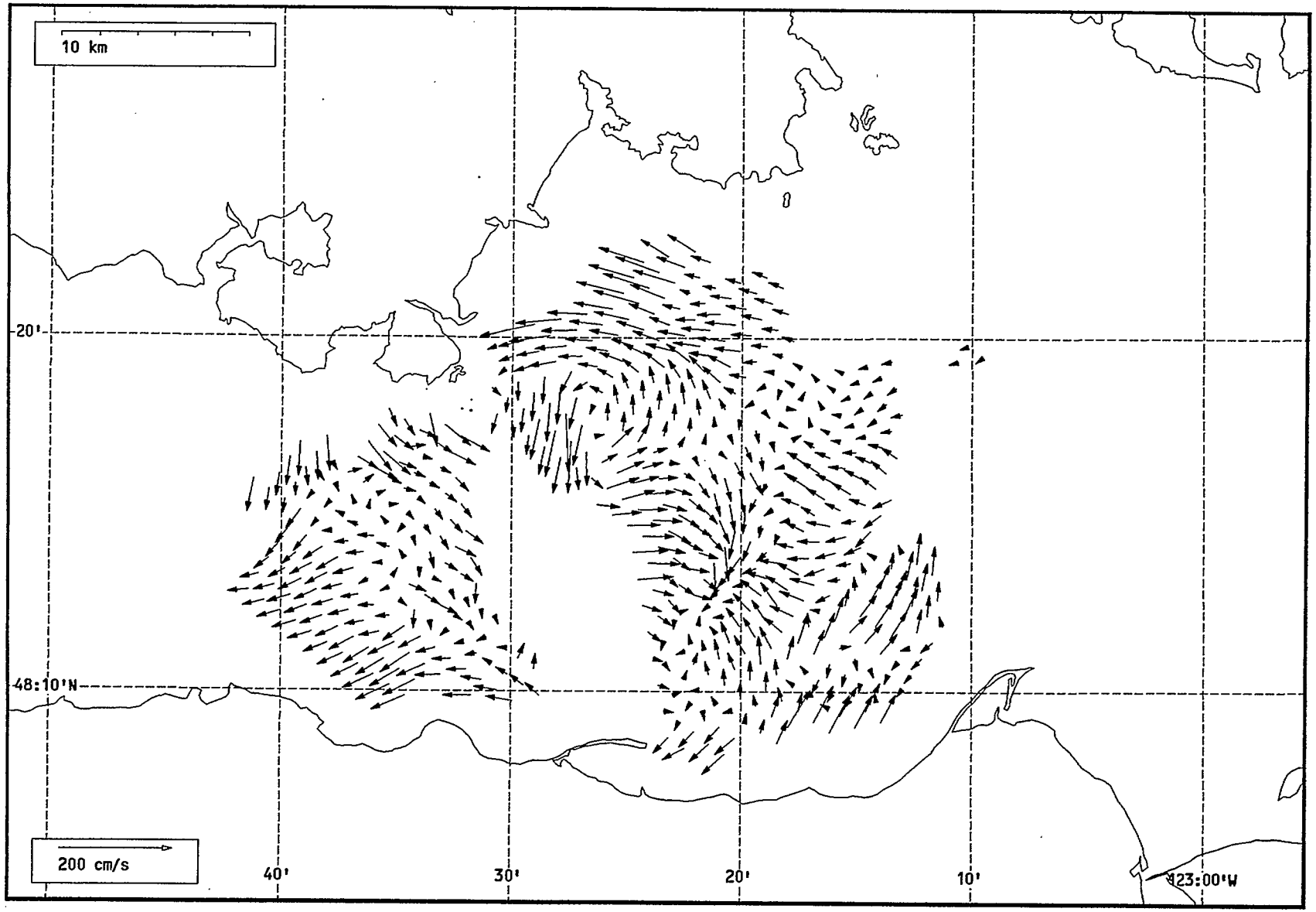

Total current vectors, Juan de Fuca Strait, 1992-07-31 13:00 Z.

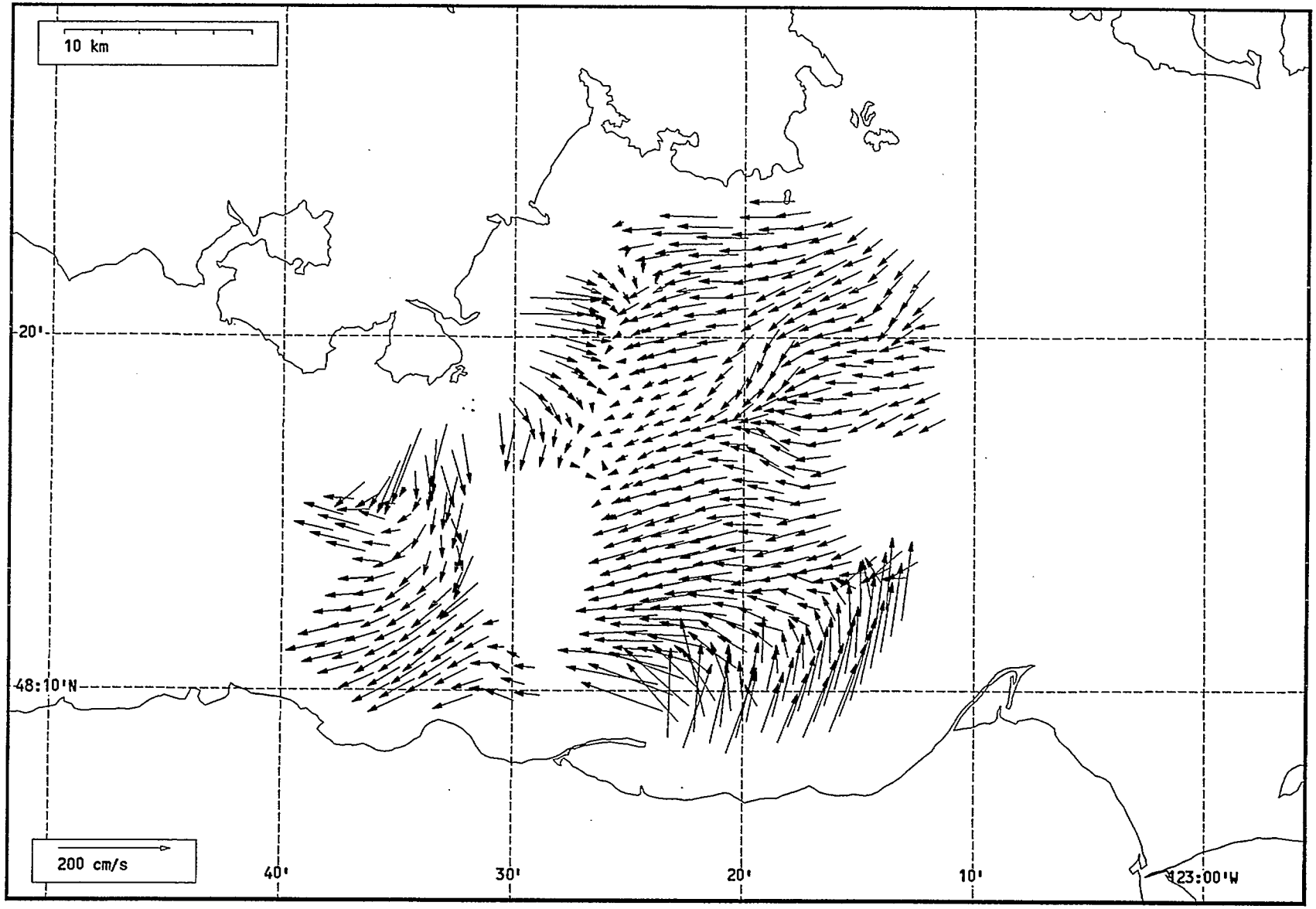

Total current vectors, Juan de Fuca Strait, 1992-07-31 14:00 Z.

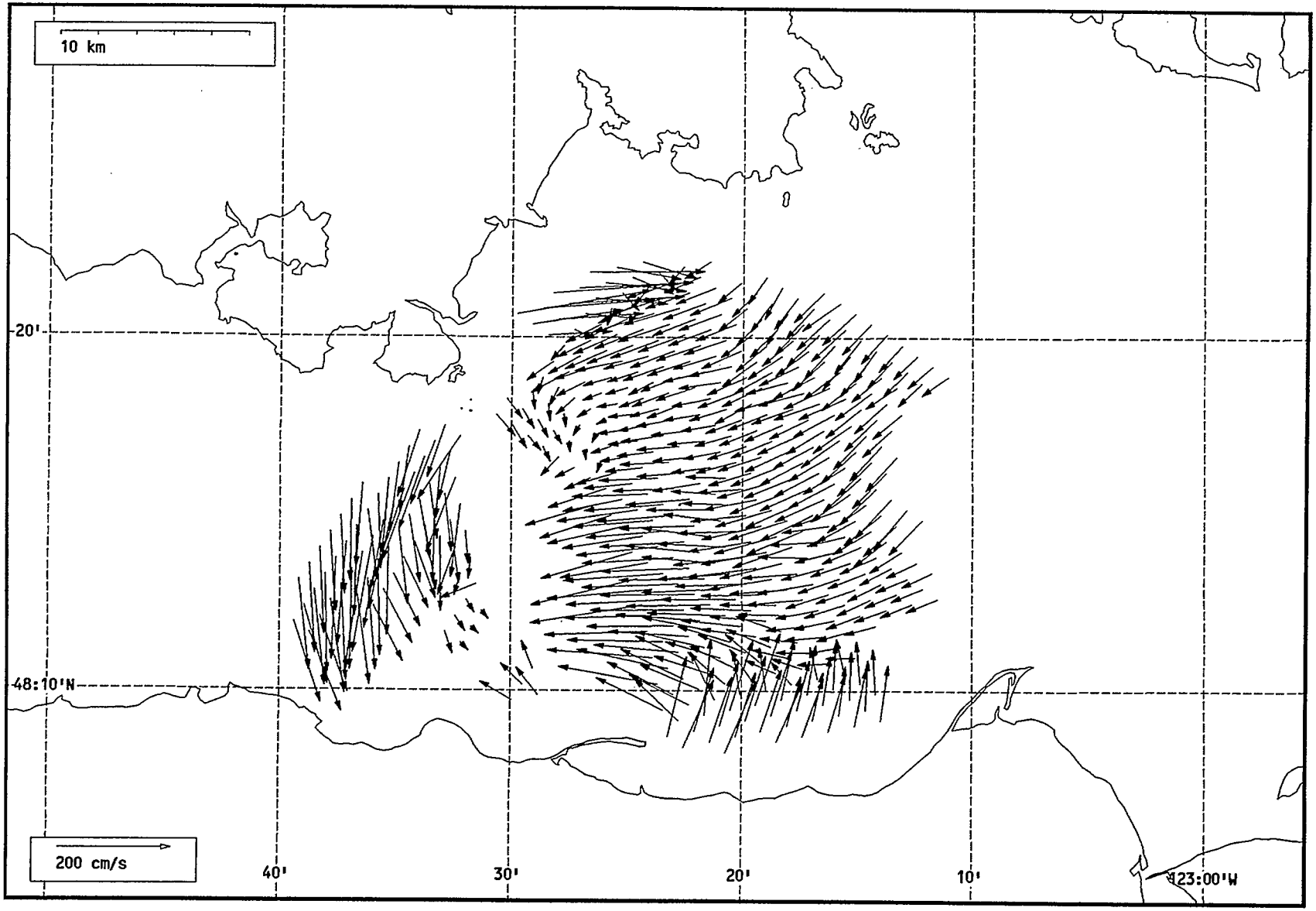

Total current vectors, Juan de Fuca Strait, 1992-07-31 15:00 Z.

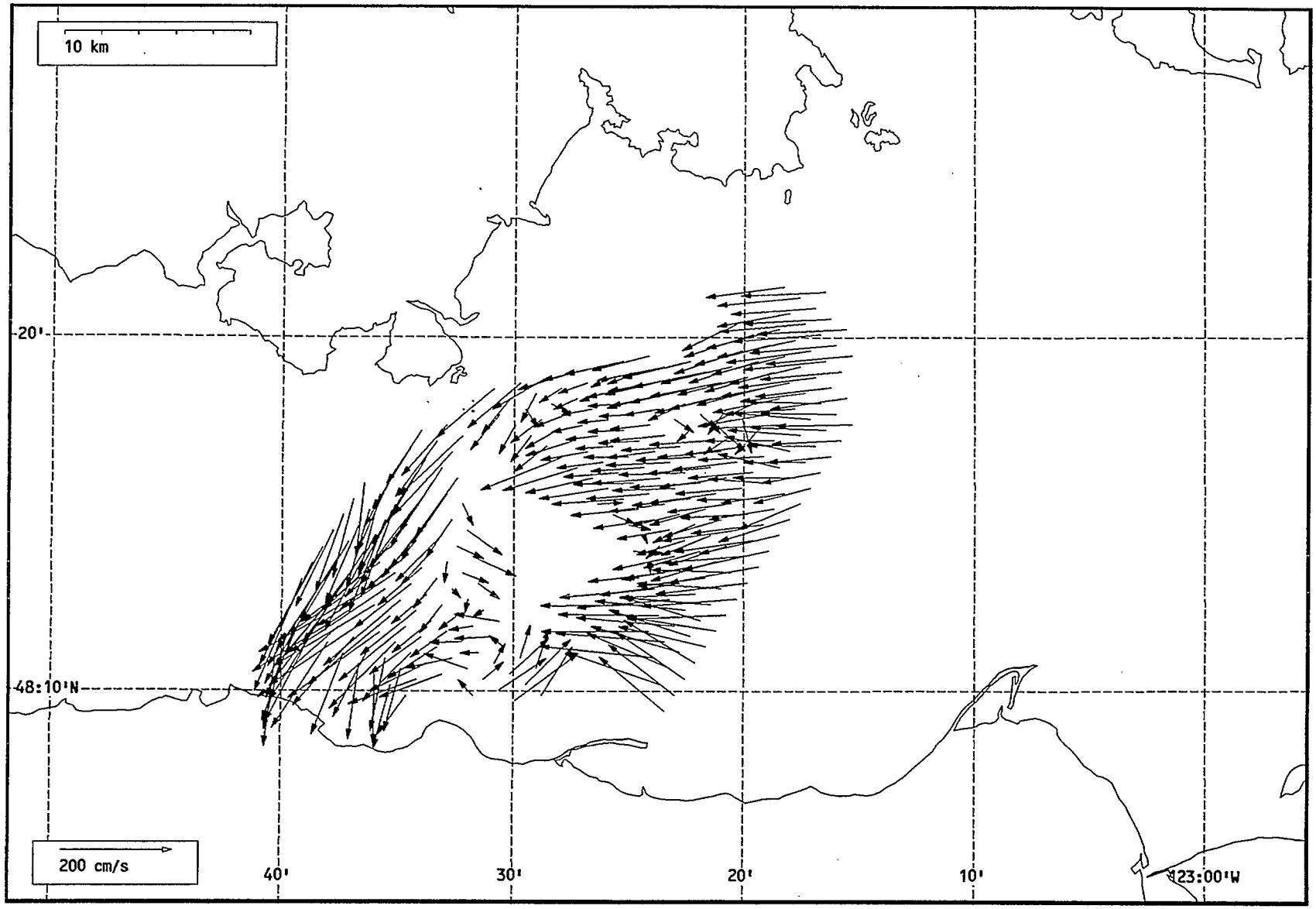

Total current vectors, Juan de Fuca Strait, 1992-07-31 16:00 Z.

APPENDIX 2: DATA FILE DOCUMENTATION

A total of 437 surface current data files are supplied in compressed form on the 3.5" floppy disks named RACEROCK1, RACEROCK2, RACEROCK3 and RACEROCK4. 'RACEROCK' is used to refer to the entire Juan de Fuca study area, not just the radar site situated at Race Rocks. The files are named according to the applicable date and time (the center of the hourly interval):

yymddhmm.zip

where yy is the year (last two digits), m is a one-digit month code (hexadecimal 1-9, A, B), dd is the two-digit day, h is a one-digit hour code (extended hexadecimal 0-9, A-N), and mm is the two-digit minute. For example, the first current file is named 92706H00.ZIP.

The file extension ZIP refers to files that have been compressed using the PKZIP file compression utility, which reduces the space required for storage by about 63%. Regular current files have the extension VEC. To decompress the file, use the PKUNZIP utility program. For example, to extract the current file 92706HOO.VEC from the archive file 92706HOO.ZIP, enter

PKUNZIP 92706HOO.ZIP

This procedure does not destroy the compressed file. However, if for some reason the compressed file has been lost, the current file can be recompressed by entering

PKZIP 92706HOO.ZIP 92706HOO.VEC

Both of these shareware PC utility programs have been provided with the data set, on disk RACEROCK4. Help is available for both programs by typing the name of the program on the command line.

Surface Current File Header

Sample:

17:00:00 07-06-92 Z
Longitude Latitude Speed [cm/s] Dir [radians ccw from East]

Meaning of each line:

1st line: the date and time (in GMT) of the current data. The sample date and time is July 6, 1992, at 17:00 GMT.

2nd line: an informative header for the body of the data file.

Surface Current File Body

Sample:

123.1546 W 48.2149 N 34.422 29.245 2.081 32.640

Meaning of each parameter:

1st parameter:	longitude of the current datum in the grid
2nd parameter:	latitude of the current datum in the grid
3rd parameter:	current speed (cm/s)
4th parameter:	confidence level in the speed (cm/s)
5th parameter:	current direction (radians ccw from East)
6th parameter:	confidence level in the direction (radians)

DATE DUE

MAY MAI -2 1997			
			Printed in USA